Des étoiles céphéides aux mers d'hydrocarbures de Titan

Daniel Cordier

▶ **To cite this version:**

Daniel Cordier. Des étoiles céphéides aux mers d'hydrocarbures de Titan. Physique [physics]. URCA, 2018. tel-02268570

HAL Id: tel-02268570
https://hal.science/tel-02268570

Submitted on 23 Aug 2019

HAL is a multi-disciplinary open access archive for the deposit and dissemination of scientific research documents, whether they are published or not. The documents may come from teaching and research institutions in France or abroad, or from public or private research centers.

L'archive ouverte pluridisciplinaire **HAL**, est destinée au dépôt et à la diffusion de documents scientifiques de niveau recherche, publiés ou non, émanant des établissements d'enseignement et de recherche français ou étrangers, des laboratoires publics ou privés.

UNIVERSITÉ DE REIMS CHAMPAGNE-ARDENNE

Université de Reims-Champagne-Ardenne

École Doctorale Sciences Technologie Santé

Habilitation à Diriger des Recherches

présentée et soutenue publiquement par

Daniel CORDIER

Chargé de Recherche au CNRS — Section 17

Groupe de Spectrométrie Moléculaire et Atmosphérique (UMR 7331)

le 10 octobre 2018

Des étoiles céphéides aux mers d'hydrocarbures de Titan

Jury

M. Robert Georges,	Professeur	Examinateur
M. Sébastien Lebonnois,	Directeur de Recherche au CNRS	Rapporteur
Mme Nathalie Carrasco,	Professeur	Rapportrice
M. Gérard Liger-Belair,	Professeur	Examinateur
M. Olivier Bourgeois,	Professeur	Rapporteur
M. Sébastien Rodriguez,	Maître de Conférence	Examinateur

Table des matières

Table des matières iii

Dédicace 1

Remerciements 3

Introduction 5

I Quelques propriétés de la surface de Titan 7

1 Titan : une introduction historique 9
1.1 La découverte de Titan et de son atmosphère . . . 9
1.2 Titan à l'ère de l'exploration spatiale . . . 11
1.3 Références . . . 17

2 Titan : surface et modèles numériques 19
2.1 Introduction . . . 19
2.2 Les modèles d'équilibre liquide-gaz basés sur la RST . . . 20
2.3 Autres applications du modèle basé sur la RST . . . 25
2.4 Discussion sur la RST . . . 28
2.5 Modèles thermodynamiques basés sur PC-SAFT . . . 30
2.6 Références . . . 36

3 Surfaces planétaires : projet scientifique 41
3.1 Les gradients verticaux de composition chimique . . . 41
3.2 Modélisation des écoulements et/ou du cryovolcanisme . . . 46
3.3 Caractérisation de la surface de Titan . . . 47
3.4 Références . . . 50

4 Articles : surface de Titan 57
4.1 Article sur la composition des lacs/mers de Titan . . . 58
4.2 Article sur la dissolution des gaz rares dans les lacs de Titan . . . 62
4.3 Article sur la séquestration des gaz rares dans des clathrates de la surface de Titan . . . 66
4.4 Article sur les incertitudes des modèles basés sur la RST . . . 70
4.5 Article sur la composition de surface des évaporites . . . 79
4.6 Article sur la structure des évaporites . . . 86
4.7 Article sur un concept de mission vers Titan et Encelade . . . 102
4.8 Article sur l'évaporation des lacs . . . 121
4.9 Article sur la formation des dépressions lacustres . . . 130
4.10 Article sur la vitesse du son comme contrainte sur la composition chimique . . . 161
4.11 Article sur l'apparition de bulles de N_2 dans au fond des lacs . . . 167
4.12 Article sur la solubilité de l'acétylène et l'éthylène dans le méthane et l'éthane liquide 171

4.13 Article sur la solubilité de l'éthylène et d'autres molécules dans l'argon liquide . . . 187
4.14 Article sur la nucléation, la croissance et la signature RADAR des bulles 195

5 Articles : atmosphère de Titan **205**
5.1 Article sur le D/H dans l'atmosphère de Titan 206
5.2 Article sur l'évolution des isotopes dans l'atmosphère de Titan 210
5.3 Article sur la croissance des anions dans l'atmosphère de Titan 224

II Origine du système solaire **233**

6 Modélisation des disques proto-planétaires : généralités **235**
6.1 Préambule 236
6.2 Introduction 238
6.3 Une modélisation de l'évolution temporelle d'un disque protoplanétaire 240
6.4 Structure verticale d'un disque d'accrétion 242
6.5 Evolution temporelle d'un disque protoplanétaire 246
6.6 Références 247

7 Equation d'évolution d'un disque α et méthode numérique de résolution **249**
7.1 Une très brève introduction 249
7.2 L'équation d'évolution et les conditions aux limites 249
7.3 Discrétisation de l'équation d'évolution 253
7.4 Références 257

8 Intégration verticale **259**
8.1 Le système d'équations et son intégration 259
8.2 Interpolation des valeurs de $< \nu >$ 261
8.3 Validation du programme 262
8.4 Résultats 263
8.5 Références 268

9 Origine du système solaire : projet scientifique **269**
9.1 Références 270

10 Articles : origine du système solaire **273**
10.1 Article sur le transport par photophorèse au voisinage d'une T Tauri 274
10.2 Article sur le transport par photophorèse 288
10.3 Article sur l'origine du méthane de Titan 299
10.4 Article sur l'origine du méthane d'Encelade 302
10.5 Article sur la clathration dans la nébuleuse primordiale et l'origine de l'atmosphère de Titan 306
10.6 Article sur la clathration des volatiles dans la nébuleuse primordiale 313

III Le champagne **331**

11 La physico-chimie du champagne : approche transdisciplinaire **333**
11.1 Bleu et blanc au-dessus d'une bouteille 333
11.2 Projet scientifique pétillant 336
11.3 Références 341

12 Articles : le champagne **343**
12.1 Article la lueur bleue lors du débouchage 344

IV Physique stellaire **357**

13 La physique stellaire **359**
13.1 Références 360

14 Articles : physique stellaire **361**
14.1 Article sur la variation de l'overshooting en fonction de la métallicité 362
14.2 Article sur les céphéides du SMC 374
14.3 Article sur la branche des géantes et BaSTI 385
14.4 Article sur BaSTI comme part du Virtual Observatory italien 397
14.5 Article sur Omega Centauri 409

Conclusion **421**

A Curriculum vitæ **I**

B Production bibliographique complète **III**
B.1 Travaux Publiés III
B.2 Actes de colloques VIII

C Articles divers **XIII**
C.1 Article sur HD 189733b XIV
C.2 Article sur la séquestration des gaz rares dans la cryosphère de Mars XXI
C.3 Article sur la détermination du rapport $^{14}N/^{15}N$ dans les comètes XXIX
C.4 Article sur le concept de mission EChO XXXIV

Dédicace

à Marianne, Sibylle, Léopold et Hippolyte ;
à mon épouse Gaëlle

Remerciements

Je remercie chaleureusement les membres de mon Jury, en particulier les rapporteurs, qui m'ont fait le plaisir et l'honneur de ce plonger dans ce manuscrit.

Depuis 1995, j'utilise de nombreux logiciels libres : l'OS `Linux`, dans sa variante Debian, les compilateurs ou interpréteurs `gfortran`, `PERL` ou `Python`, les logiciels de traitement de texte LaTeX et `LibreOffice`, les outils graphiques `Gimp`, `XFig` et `Inkscape` ; j'adresse donc d'amicals remerciements à tous ceux qui ont contribué, d'une manière ou d'une autre, au développement de cette informatique libre qui m'a permis de réaliser tout mon travail scientifique.

Enfin, je salue la grande aide bibliographique que m'a apporté Alexandra Elbakyan.

Introduction

« *Le monde moderne est un monde de jouets.* »

Bernard Maris,
Houellebecq économiste, p. 74,
Editions Flammarion, 2014.

De façon assez curieuse, mes études portant sur les propriétés de surface de Titan conjuguent de lointains développements des travaux séminaux de Christiaan Huygens, Johannes Van der Waals et Gerard Kuiper, trois hommes de sciences hollandais. Au premier on doit la découverte du plus imposant satellite de Saturne ; le second nous a légué une équation d'état qui a ouvert la voie à de fructueuses recherches. Certaines ont abouti aux équations d'états sophistiquées utilisées aujourd'hui, notamment dans les modèles «titaniens» de liquides cryogéniques. Gerard Kuiper a, pour sa part, montré l'existence d'une atmosphère sur Titan. Sans cette dernière, le plus imposant satellite de Saturne n'aurait pas toutes les caractéristiques extraordinaires qu'on lui connaît maintenant.

Il est assez remarquable que ces trois hommes aient eu des champs d'activité assez différents. Huygens, tout en étant astronome, était également opticien et mécanicien, on lui est redevable, dans ce dernier domaine, d'importantes améliorations des horloges. Van der Waals a consacré ses investigations aux propriétés de la matière, renforçant la théorie moléculaire par l'introduction des idées d'interaction intermoléculaire et de volume fini des molécules. Kuiper, un des pères de la planétologie moderne, fut un astronome spectroscopiste, auteur de nombreuses découvertes, allant de celle de petits satellites d'Uranus, à la présence de méthane dans l'atmosphère de Titan. Il est à noter que, malgré la dénomination usuelle, Kuiper n'est pas le découvreur de la ceinture de Kuiper. Il fut aussi le directeur de thèse de Carl Sagan, un autre grand nom attaché à Titan. Cette diversité peut être vue comme un signe de la richesse disciplinaire qui est attachée à la planétologie. Celle-ci représente aujourd'hui des pans entiers de l'astrophysique et de l'astrochimie. La pluridisciplinarité de la planétologie vient de la présence, dans les systèmes qu'elle étudie, des quatre états de la matière, et de conditions dans lesquelles une chimie peut parfois se développer. Cette matière, placée dans un contexte astronomique conduit à des objets aux propriétés originales, parfois totalement exotiques. Même si je suis venu à la planétologie un peu par hasard, c'est cette variété d'objets et de propriétés que je trouve très attrayante.

Dans mon travail, j'ai essayé de marier ces aspects transdisciplinaires de la physique-chimie, avec la simulation numérique. La modélisation obtenue, une fois validée, me procure un sentiment voisin de celui que j'éprouvais enfant, lorsque je découvrais un nouveau jouet. Je souhaite partager, même très partiellement, avec le lecteur, la lectrice, un peu de ces petites joies scienti-

fiques.

Ce manuscrit est divisée en quatre parties d'inégales importances : les propriétés des surfaces planétaires, l'origine du système solaire, le champagne et la physique stellaire. Les propriétés de surfaces sont essentiellement consacrées à Titan. Une description détaillée de mon modèle de disque protoplanétaire est proposée, j'ai en effet profité de cette HDR pour fournir ce type de description malheureusement absente de la littérature. La partie dédiée au champagne, concrétisation de mon encrage régional, fait le point sur le travail déjà effectué et sur les perspectives de développements. La dernière partie, ayant pour objet la physique stellaire représente un domaine dans lequel je ne suis plus actif, mais qui a été mon point de départ en recherche.

Dans la version numérique de ce document, des liens cliquables permettent une navigation facile entre la table des matières et les différentes sections. De même un renvoi aisée des chapitres en français, vers les articles correspondants, est actif.

Première partie

Quelques propriétés de la surface de Titan

Chapitre 1

Titan : une introduction historique

« *Les satellites de Saturne ont été jusqu'ici beaucoup moins étudiés. Le plus distant de la planète l'emporte beaucoup sur les autres par ses dimensions, qui probablement ne le cèdent guère à celles de Mars. Son orbite a aussi une inclinaison sensible sur le plan de l'anneau, avec lequel les orbites de tous les autres coïncident à très-peu près. Il est le seul dont on ait poussé la théorie au-delà de ce qu'il fallait pour assurer que la troisième loi de Képler subsiste dans le système des satellites de Saturne, aussi bien que dans celui des satellites de Jupiter et sous les mêmes restrictions. Ce satellite offre, comme ceux de Jupiter, des variations périodiques dans sa lumière, d'où l'on a conclu qu'il tourne sur son axe, dans le même temps qu'il se met à accomplir une révolution autour de Saturne.* »

— Sir John F.-W. Herschel, *Traité d'Astronomie*, p. 350,
traduit de l'anglais par Augustin Cournot,
Paris, Paulin, Libraire, Éditeur, 51, place de la bourse, 1834

Sommaire

1.1 La découverte de Titan et de son atmosphère 9
1.2 Titan à l'ère de l'exploration spatiale 11
1.3 Références 17

1.1 La découverte de Titan et de son atmosphère

Le 14 avril 1629, Christiaan Huygens naît à La Haye dans une famille hollandaise aussi aisée qu'influente [SAMUELI et BOUDENOT, 2017]. Il fait partie d'une fratrie de cinq enfants et, très jeune, fait preuve de grands talents aussi bien dans le domaine expérimental qu'en mathématique. Laissons un instant la parole à son père qui le surnommait son «petit Archimède», voici ce qu'il disait de son fils Christiaan :

> «*Dès 1643, il faisait preuve d'une aptitude exceptionnelle pour comprendre tout ce qui a trait à la mécanique ou à n'importe quel autre domaine des mathématiques. Il trouve toujours une solution lorsqu'il s'agit d'exécuter un modèle ou n'importe quel ouvrage manuel, il lui suffit, simplement d'avoir lu ou appris par d'autres, de quoi il a besoin pour le réaliser.* [...] *En 1644, il a commencé à étudier les mathématiques en faisant des progrès extraordinaires. Il ne se contentait pas de tout comprendre et de tout retenir, mais il inventait encore chaque jour toutes sortes de choses très ingénieuses. De plus, il apprenait la danse et l'équitation.*»

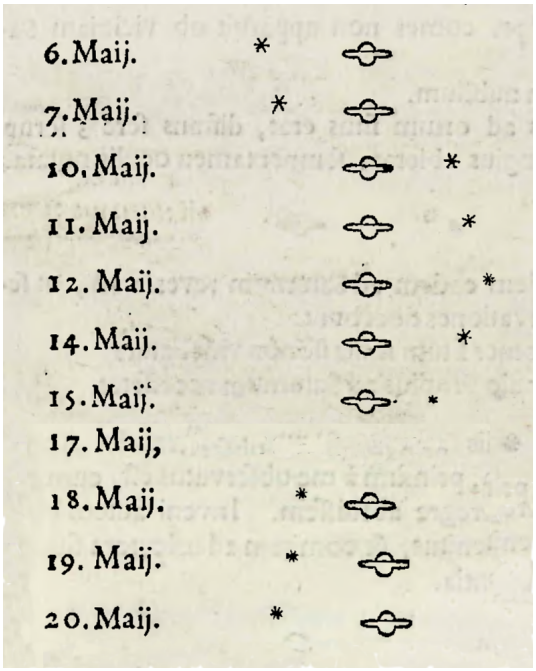

FIGURE 1.1 – Reproduction des dessins p.32 et 33 du *Systema Saturnium* de Huygens, dont une copie au format PDF est disponible sur Internet (https://www.wdl.org/en/item/4302/). On distingue clairement sur ces dessins le mouvement de Titan, avec une période de révolution d'environ 15 jours.

Même si l'amour paternel peut biaiser le jugement, cette citation donne un aperçu des capacité du jeune Christiaan Huygens. C'est donc à 16 ans qu'il rentre à l'Université de Leyde pour y étudier le droit et les mathématiques. Toujours précoce, il écrit un premier essai scientifique à 22 ans. En 1654, avec un de ses frères Constantijn, il décide de construire des lunettes en fabriquant eux-mêmes des lentilles. Le premier instrument opérationnel mesure 12 pieds de long, soit environ 3,5 mètres, et possède un grossissement de 50. Au début de 1655 il observe Saturne et découvre un satellite gravitant autour de la planète géante. Ce satellite est celui que nous appelons aujourd'hui Titan. En effet, jusqu'au milieu du 19e siècle, les satellites connues, alors peu nombreux, n'étaient désignés que par leur numéro. C'est John Herschel, le fils de William, qui proposera de nommer les satellites. Ceci explique l'absence de nom dans la citation du *Traité d'Astronomie*, publié en 1834 par John Herschel, insérée au début de ce chapitre.

Après un séjour à Paris, Huygens reprend les observations de Saturne début 1656 : «*Elle est entourée d'un anneau plat et mince qui nulle part ne la touche et fait un angle avec l'écliptique*», c'est donc avec ces mots qu'il décrit sa découverte de la nature annulaire de ce qu'on sait maintenant être les anneaux de Saturne. En 1659, Huygens publie son *Systema Saturnium*, livre d'astronomie observationnelle qui fait date, le précédent ouvrage d'égale importance étant *Siderius Nuncius* de Galilée, paru en 1610 (voir Fig. 1.1).

Outre en astronomie, Huygens apportera des contributions majeures en optique et en mécanique, avec pour cette dernière des innovations importantes en horlogerie. Il faudra plus de 250 ans pour que Titan revienne sur le devant de la scène. C'est en effet au tout début du 20^{e} siècle que l'astronome catalan Josep Comas i Solà annonça avoir observé un assombrissement centre-bord sur le disque de Titan [COMAS I SOLÀ, 1907, 1908]. Cette observation, apparemment non-confirmée dans les années qui suivirent, est à considérer cependant avec quelques réserves. Comme souligné par Ralph Lorenz [LORENZ, 1997], l'utilisation de la lunette de 38 cm de diamètre de l'observatoire de Fabra à Barcelone, implique, due à la seule diffraction, une limite de résolution de $\sim$ 1 microradian. Le disque de Titan, distant de 9 unité astronomique de la Terre, a une taille

d'à peine 4 microradians, soit environ 1 arcseconde. Du fait de la turbulence atmosphérique, une valeur typique de «seeing» est de l'ordre de 1 arcseconde, l'observation de Comas i Solà suppose donc de très bonnes conditions d'observation, caractérisées par une atmosphère terrestre particulièrement calme. Toutefois, bien que très difficile, cette observation n'a pas dû être impossible.

Une vingtaine d'années après l'annonce de Josep Comas i Solà, ce sont des arguments théoriques qui sont avancés. Dans un livre consacré à la théorie cinétique des gaz [JEANS, 1925], Sir James Hopwood Jeans, astronome, physicien et mathématicien anglais, montre que Titan peut potentiellement retenir une atmosphère dense, ceci sur une échelle de temps équivalent à l'âge du système solaire. Il précise cependant que les molécules, composant cette possible atmosphère, doivent être plus massives que l'hydrogène ou l'hélium. Cela laissait la possibilité d'une atmosphère d'argon, de néon, de diazote ou de méthane ; ou toute combinaison de ces espèces [LORENZ et MITTON, 2008].

Durant l'hiver 1943-1944, l'astronome américain, d'origine néerlandaise, Gerard Kuiper réalise des observations spectroscopiques, à l'observatoire McDonald au Texas. A l'aide d'un spectroscope à prisme, monté sur une télescope de 2 mètres de diamètre, il étudie les 10 plus gros satellites du système solaire, et quelques planètes. C'est ainsi qu'il met en évidence les bandes d'absorption du méthane à 6190 et 7260 Å sur le disque de Titan [KUIPER, 1944]. La preuve de l'existence d'une atmosphère sur Titan est faite. De façon amusante, à la fin de son article, Kuiper cite deux passages du livre de Jeans : «An atmosphere has been observed on Titan» et encore «the suspected atmosphere on two of Jupiter's satellites». Jeans ne citant pas ses sources, Kuiper souligne alors qu'il n'a pas trouvé de références rapportant de telles informations, et citent les ouvrages/articles (tous anglo-saxons !) qu'il a pu consulter, et où il n'y a aucune mention d'atmosphère autour de satellites. Pour finir, Kuiper souligne la difficulté, pour ne pas dire l'impossibilité, d'observer visuellement une atmosphère sur un objet de ~ 1 arcseconde de diamètre. Si l'existence de cette atmosphère titanienne est alors bien établie, de nombreuses questions se posent encore, et en premier lieu sa composition exacte. Les réponses seront apportées par l'exploration spatiale.

1.2 Titan à l'ère de l'exploration spatiale

La première sonde spatiale à s'approcher du système de Saturne a été *Pioneer 11*. Durant l'été 1979, elle «survolera» Titan, en restant toutefois à la distance respectable de 360 000 km. *Pioneer 11* réalise le premier cliché spatial de Titan [SEIGNOVERT, 2017], et ses mesures permettent de mieux contraindre le rayon de Titan [SMITH, 1980] ainsi que les propriétés des aérosols de son atmosphère [TOMASKO, 1980; TOMASKO et SMITH, 1982]. Les premières avancées majeures viendront avec la sonde *Voyager 1*.

Le 11 novembre 1980, entre 11h12 et 11h24, heure de la côte ouest des USA, des signaux radio en provenance de la sonde *Voyager 1* sont reçus par les antennes du NASA Deep Space Network. Ces signaux ont été émis lors du passage de *Voyager 1* dans le système de Saturne. La trajectoire de cette rencontre est disponible dans le *Voyager Bulletin* n° 57, elle est reproduite sur la Fig. 1.2. Cet événement avait été spécialement planifié pour que Titan, dont l'intérêt scientifique était considéré comme de toute première importance, soit survolé au plus près, la distance minimale entre la sonde et le plus gros satellite de Saturne sera alors d'environ 4000 km, comptés à partir de la surface. La trajectoire avait été préparée afin que Titan se trouve, pendant une dizaine de minutes, entre *Voyager* et la Terre, réalisant ainsi une occultation du faisceau radio. Les techniques d'occultation, presque aussi anciennes que l'astronomie elle-même, sont des moyens d'investigations extrêmement puissants, dont on tire beaucoup d'informations. Dans notre cas, l'occultation de *Voyageur* par Titan a permis d'en savoir beaucoup plus, entre autres choses, sur les propriétés de son atmosphère. Les données obtenues ont ainsi permis de montrer que le diazote est le principal constituant de l'atmosphère, ne laissant au méthane que quelques pourcents. Dans leur analyse

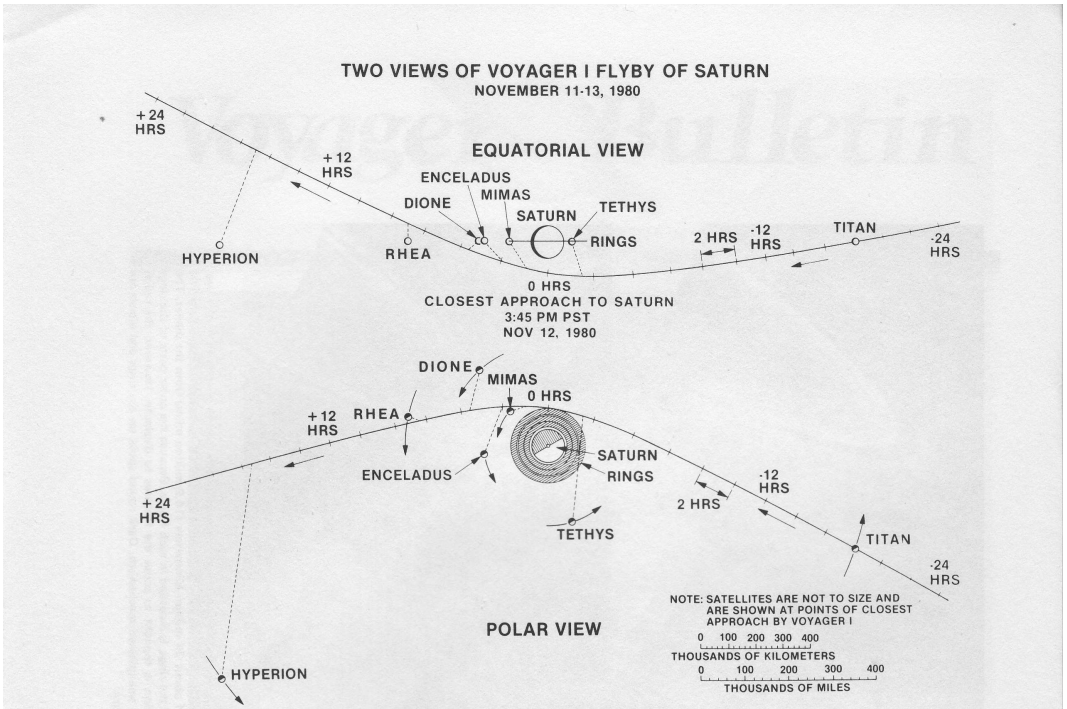

Encounter Highlights

All times are Pacific Standard Earth-received time of event. All distances are from surfaces of satellites except where noted.

November 11

9:52 – 10:36 a.m.	Spacecraft maneuver to sample fields and particles near Saturn; reference star is Miaplacidus
11:05 p.m.	Titan closest approach (4000 kilometers)
11:11 – 11:22 p.m.	Titan/Sun occultation
11:12 – 11:24 p.m.	Titan/Earth occultation
11:22 p.m.	Inbound ring plane crossing

November 12

3:41 p.m.	Tethys closest approach (415,320 kilometers)
5:10 p.m.	Saturn closest approach (124,200 kilometers above clouds)
7:07 p.m.	Mimas closest approach (88,820 kilometers)
7:15 p.m.	Enceladus closest approach (202,251 kilometers)
6:09 – 6:33 p.m.	Spacecraft maneuver to sample fields and particles
7:08 – 8:35 p.m.	Saturn/Earth occultation
7:22 – 8:02 p.m.	Saturn/Sun occultation
9:03 p.m.	Dione closest approach (161,131 kilometers)
8:44 – 9:00 p.m.	Ring/Earth occultation
9:45 p.m.	Outbound ring plane crossing
11:46 p.m.	Rhea closest approach (72,000 kilometers)
11:09 – 11:26 p.m.	Spacecraft maneuver to sample fields and particles; reference star is Alhena
11:38 p.m. – 12:41 a.m.	Rhea image motion compensation maneuver; reference star is Vega

November 13

10:09 a.m.	Hyperion closest approach (879,127 kilometers)
2:42 – 4:43 p.m.	Spacecraft maneuver; return to Vega

November 14

12:50 a.m.	Iapetus closest approach (2,474,000 kilometers)

3

FIGURE 1.2 – La trajectoire de la sonde *Voyager 1* lors de sa visite du système de Saturne les 11-13 novembre 1980.

préliminaires de ces données d'occultation, TYLER et collab. [1981] obtiennent une pression au sol de 1.6 bar, et une température de 93 K, valeurs très proches de résultats définitifs publiés par LINDAL et collab. [1983]. Dans leur article, TYLER et collab. [1981] remarquent qu'avec de pareilles valeurs, le méthane se trouve, à la surface du satellite, proche de son point triple, lieu du diagramme de phase où les trois phases peuvent coexister. Pour mémoire la température du point triple est 90.7 K et sa pression vaut 117 mbars (source : NIST [1]). C'est donc tout naturellement que TYLER et collab. [1981] émettent l'hypothèse de possibles océans de méthane liquide à la surface de Titan. Ces auteurs notèrent que, si le carbone (*i.e.* le carbone atomique) et l'azote (*i.e.* l'azote

1. https://webbook.nist.gov/chemistry/

atomique) avaient été sur Titan dans des proportions solaires, alors il aurait dû y avoir environ 100 fois plus de méthane à la surface que contenu dans l'atmosphère. Ils évaluèrent l'épaisseur de l'océan global de méthane (éventuellement gelé) à 1 km. Ce travail, qui est une présentation générale de résultats obtenus grâce à l'occultation, n'est pas allé plus loin au sujet du possible océan, mais il a suscité de nombreuses études et idées nouvelles.

Environ un an après l'article de TYLER et collab. [1981], Tobias Owen publie un article de vulgarisation dans *Scientific American* [OWEN, 1982] dans lequel il passe en revue les apports de *Voyager*. Owen reprend à son compte la possibilité d'avoir un cycle hydrologique du méthane, avec comme corollaire la présence de mers de méthane. La même année, mais en novembre, SAGAN et DERMOTT [1982] publient un article dans lequel ils discutent la possibilité d'un océan de méthane liquide. Leurs arguments portent essentiellement sur des considérations orbitales et sur les effets de marée qui leurs sont associés. Dans leur conclusion, ces auteurs proposent deux possibilités : (1) un océan existe et il recouvre la quasi-totalité de la surface, avec une profondeur supérieure à 400 m, (2) il n'y a pratiquement pas de méthane liquide à la surface de Titan. De façon très intéressante, ils proposent un moyen de trancher entre ces deux alternatives. Leur méthode repose sur l'utilisation d'un radiotélescope en mode RADAR. Sagan et Dermott rapportent, suite à leurs échanges avec Campbell et Ostro, qu'une tentative d'utilisation du radiotélescope d'Arecibo, au cours de l'opposition de 1979, n'a conduit qu'à l'obtention d'une limite supérieure à la réflectivité moyenne de la surface de Titan. Ils indiquent finalement qu'une nouvelle tentative pourra être faite mi-1990, époque à laquelle Titan s'est trouvé à nouveau dans le champ du radiotélescope d'Arecibo.

En 1983, Michael Flasar propose un nouvelle interprétation des données de radio-occultations réalisées grâce à *Voyager 1* [FLASAR, 1983]. Il montre que, pour les deux régions sondées par les radio-occultations, à savoir 6.2°N et 8.5°S, donc espacées d'environ 180°, l'humidité relative en méthane doit être de l'ordre de 70%. Dans le même temps, M. Flasar établit qu'au-dessus d'un océan de méthane liquide, l'humidité doit être au minimum de 98%. Cet auteur en conclut que les régions sondées doivent être sèches. Il ajoute que l'absence de topographie importante doit probablement impliquer l'absence totale de mers/océans de méthane sur Titan. Toutefois, il ajoute à la fin de son article, dans une petite section *Note added in proof*, qu'une autre possibilité d'océan est offerte par la production, par la photochimie atmosphérique, d'hydrocarbures plus lourds, donc moins volatiles que le méthane. Un article, très proche par sa méthode et sa conclusion, est publié également la même année par ESHLEMAN et collab. [1983]. Ces auteurs concluent également à une faible probabilité de trouver du méthane liquide, au sol, et même dans l'atmosphère, au niveau des régions équatoriales de Titan.

L'impossibilité d'avoir un réservoir de méthane liquide, à la surface de Titan, se dessine alors. A la même période, les premiers modèles de photochimie atmosphérique indiquent un temps de vie du méthane dans l'atmosphère de l'ordre de quelques millions d'années [YUNG et collab., 1984], ce qui pose la question de l'existence d'une source de CH_4, alimentant l'atmosphère. De façon concomitante à la destruction de CH_4, les modèles de photochimie montrent que C_2H_6 semble produit en masse. L'éthane étant liquide dans les conditions thermodynamiques de la surface, LUNINE et collab. [1983] proposent l'existence d'un océan d'éthane liquide, dans lequel serait dissout environ 25% de méthane. Ce scénario étant compatible avec les contraintes liées aux observations de *Voyager*, il restait à obtenir de nouvelles mesures pour confirmer, ou infirmer, l'existence d'un tel océan.

Durant les nuits du 3 au 6 juin 1989, Duane Muhleman et ses collègues menèrent des expériences radar vers Titan, dans le but d'identifier, ou non, la présence d'un océan global d'éthane. Des faisceaux de 360 kW furent émis depuis un radiotélescope de 70 m en Californie, l'énergie réfléchie par Titan étant collectée par le *Very Large Array* au Nouveau Mexique [MUHLEMAN et col-

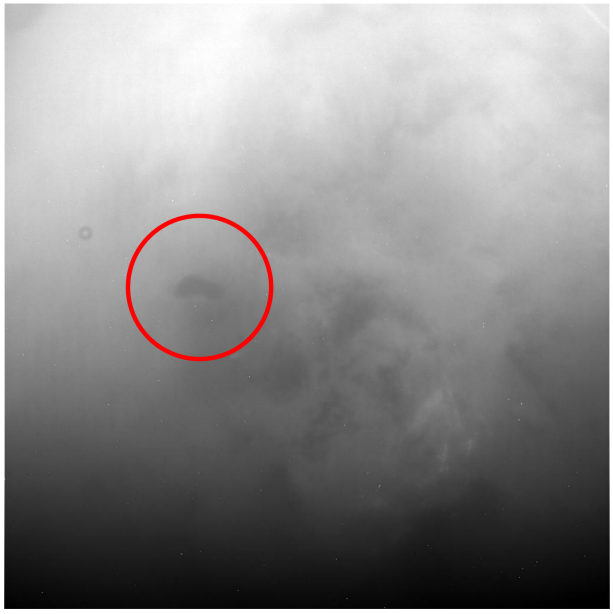

FIGURE 1.3 – Image ISS (N1496753247_1) du pôle sud de Titan, prise en juin 2005, où on distingue Ontario Lacus (dans le cercle rouge).

lab., 1990]. Le but était de mesurer la réflectivité radar de la surface de Titan, l'éthane liquide ayant une permittivité diélectrique beaucoup plus faible que celle de la glace d'eau ou de le régolithe dont est faite la surface d'autres satellites, la distinction devait être aisée. Les déterminations de MUHLEMAN et collab. [1990] exclurent la présence d'un océan global d'éthane.
Quelques années plus tard, une autre équipe [CAMPBELL et collab., 2003] utilise le radiotélescope d'Arecibo avec une technique différente de celle employée par D. Muhleman et ses collègues. Cette fois un faisceau polarisé circulairement est utilisé, et sa réponse spectrale est analysée. Les investigations de CAMPBELL et collab. [2003] montrent alors que le faisceau réfléchi contient jusqu'à 25% en puissance de photons radio ayant subi une réflexion spéculaire, à la longueur d'onde près, *i.e.* 13 cm. Une étendue liquide est l'explication naturelle à ce genre de réflexion. Bien sûr, d'autres situations peuvent également rendre compte de ce résultat, par exemple des lits de lacs asséchés, similaires aux playas terrestres. Il reste donc à se rendre sur place, par robot interposé [2].

Un fois le passage de *Voyager 1* accompli, des idées d'une mission, entièrement dédiée au système de Saturne, germe dans les esprits. En 1982, l'Agence Spatiale Européenne lance un appel à projet, auquel répondent un consortium international dont les leaders sont Wing Ip pour l'Allemagne, Daniel Gautier pour la France et Tobias Owen pour les USA. La mission s'appellera *Cassini* et sera composée d'un orbiteur et d'un atterrisseur devant se poser sur Titan.
Le lancement a lieu le 15 octobre 1997 et l'insertion en orbite autour de Saturne le 1er juillet 2004. La recherche du cycle hydrologique de Titan allait pouvoir se poursuivre, cette fois *in situ*. L'atterrisseur *Huygens* plonge dans l'atmosphère de Titan le 14 janvier 2005 pour atteindre le sol sur un site localisé dans les régions équatoriales. Même si la fameuse, et seule, image prise par *Huygens* depuis la surface, montre des galets suggérant des écoulements liquides par le passé, on est loin de devoir profiter des capacités de flottaison qui avaient été prévues pour *Huygens*. Néanmoins des mesures effectuées lors de l'impact ont laissé deviner un sol relativement meuble, dont les propriétés mécaniques pouvaient être compatibles avec du sable humide. La recherche de liquides va donc se poursuivre avec l'ensemble des instruments de l'orbiteur *Cassini*. La première approche de Titan par *Cassini* a lieu au moment de l'insertion, cette approche, en date du 2 juillet

2. Le paradoxe entre les observations de CAMPBELL et collab. [2003] et celles de *Cassini*, qui n'a pas détecté de vastes étendues liquides à l'équateur, devrait être levé. En effet, suivant un échange d'e-mails avec Jason Hofgartner (mai 2018) un article sur le sujet devrait être publié bientôt.

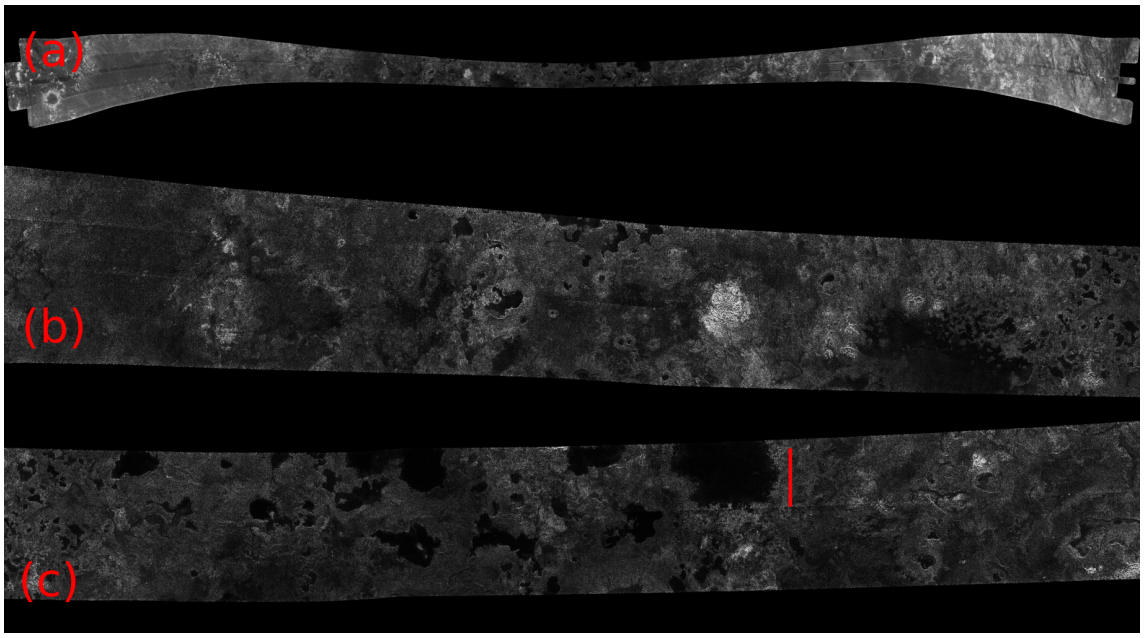

FIGURE 1.4 – Le «swath» radar obtenu lors du flyby T16 de *Cassini* sur Titan. (a) Le «swath» entier, dont la taille correspond à une longueur de 6 700 km, pour une largeur minimale de l'ordre de 140 km. (b) est un zoom sur environ la moitié de la région polaire nord des lacs, (c) est la même chose sur l'autre moitié. Le trait rouge donne l'échelle, il correspond à environ 60 km. Des «swath» radar peuvent être trouvé sur : http://pirlwww.lpl.arizona.edu/~perry/RADAR/.

2004, est nommée «T0» («T» pour «Titan»). Bien que la distance soit restée très respectable, avec un minimum de 339 000 km, les clichés du spectro-imageurs VIMS [3] [voir LORENZ et MITTON, 2008, Fig. 4.01 p. 102] et ISS [4] [voir LORENZ et MITTON, 2008, Fig. 4.04 p. 105] laissent voir des motifs très réfléchissants qui seront interprétés comme des nuages un peu plus tard. Cela sera, en effet, lors du flyby TB (13 décembre 2004) que Caitlin Griffith et ses collègues identifient clairement une activité nuageuse à des latitudes moyennes de Titan [GRIFFITH et collab., 2005]. La présence de gouttelettes de méthane liquide, dans l'atmosphère, ne fait plus guère de doute. Cependant, ce qui nous intéresse le plus ici : la détection d'une quantité massive de liquide en surface, n'est pas réalisée. Le radar de *Cassini*, spécialement embarqué sur la sonde pour travailler au travers de l'atmosphère, produit sa première image lors du premier véritable survol de Titan : le flyby TA, effectué à une altitude minimum de 1200 km le 27 octobre 2004. Lors de cette opération, le vaisseau dut tourner plusieurs fois sur lui-même afin de pointer successivement ses instruments vers Titan. Ce premier «swath» [5] radar révèle de nombreuses structures géologiques, notamment des chenaux d'écoulement, mais rien pouvant s'apparenter à un lac ou une mer d'hydrocarbures.

Les lacs vont d'abord être observés sans qu'on sache de quoi il s'agissait. Cela a été le cas dès juin 2005, avec une série d'images d'ISS du pôle sud, prise à une distance de 450 000 km, où une zone sombre en forme de haricot [voir LORENZ et MITTON, 2008, Fig. 6.08 p. 186, et aussi Fig. 1.3 page 14 de ce chapitre] est remarquée sans qu'on puisse en faire une interprétation univoque.

Les chercheurs commençaient à admettre l'idée d'un satellite très sec. La dernière zone à explorer, via les ondes électromagnétiques, était le pôle nord. Ce dernier devait être l'endroit le plus propice à l'existence d'étendues liquides en surface : c'était, au début de la mission *Cassini*, la région la plus froide de Titan car plongée dans l'hiver polaire.

Le survol T16 du 22 juillet 2006, fut une «mission de dernière chance», couronnée de succès.

3. Visual and Infrared Mapping Spectrometer
4. Imaging Science Subsystem
5. «Image-bande» correspondant à la projection de la trajectoire de *Cassini* sur le sol de Titan

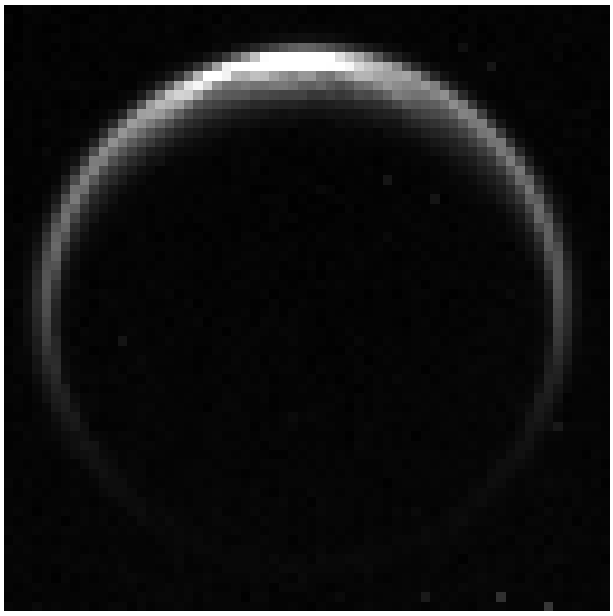

FIGURE 1.5 – Un des cubes VIMS (V1625730355_1), issus du flyby T58, utilisés par STEPHAN et collab. [2010] dans leur identification d'un reflet spéculaire sur Jingpo Lacus [SODERBLOM et collab., 2012].

Des dizaines de motifs, très sombres au radar, peuplaient les latitudes au-delà de 80° nord. Leurs contours rappelaient ceux des lacs terrestres et certains possédaient des chenaux de drainage et d'autres des «bathtube rings». Leur localisation étaient en accord avec les modèles climatiques qui prédisaient des précipitations d'éthane à ces latitudes [RANNOU et collab., 2006].

Plusieurs hypothèses pouvaient expliquer les observations : (1) un dépôt très lisse de boue, de glace ou de métal, (2) des lits de lacs asséchés recouverts d'une couche (de nature inconnues) très absorbante au radar, (3) des lacs/mers d'hydrocarbures liquides [LORENZ et MITTON, 2008]. Le scénario le plus probable est le dernier de la liste, c'est donc celui qui a été retenu par les auteurs de la publication STOFAN et collab. [2007]. Ce qui avait été imaginé 26 ans plus tôt était enfin identifié.

Depuis la découverte de STOFAN et collab. [2007], les flybys de *Cassini* au-dessus des pôles de Titan se sont enchaînés, améliorant à chaque fois la couverture géographique de ces régions. Il restait à avoir d'autres arguments en faveur de l'existence de ces lacs, c'est ce qu'ont apporté STEPHAN et collab. [2010]. Cette équipe a observé le pôle nord de Titan avec le spectro-imageur VIMS, ce dernier permettant de faire, notamment, des enregistrements dans l'infrarouge autour de 5 µm, il y avait là une possibilité d'apercevoir la surface, car à ~ 5 µm se trouve une des «fenêtres spectrales», aux longueurs d'onde desquelles l'atmosphère de Titan est transparente. En mettant la sonde dans une configuration compatible avec une réflexion spéculaire dans la région du pôle nord, STEPHAN et collab. [2010] ont pu détecter une telle réflexion, confirmant de façon très convaincante l'existence de surfaces très lisses, sur des objets à la morphologie lacustre. Le travail de STEPHAN et collab. [2010] a été ensuite affiné par SODERBLOM et collab. [2012] qui ont construit une modèle sophistiqué de la réflexion spéculaire en tenant compte de la sphéricité de la surface réfléchissante. Ils ont de plus mieux identifié la localisation géographique de ce «glint», selon ces auteurs il s'est produit non pas sur Kraken Mare mais sur Jingpo Lacus. Ces cubes VIMS ont été aussi, par la suite, exploités par BARNES et collab. [2011] afin de contraindre la taille des vagues à la surface du lac en question.

Pour les lacs et les mers de Titan, une classification a été établie : on distingue ainsi les *lacus* et les *mare*, ils forment le premier exemple d'étendues liquides extraterrestres. L'intérêt de leur étude

scientifique est grand, car elle offre les prémices de ce que pourrait être une exo-océanographie. Les questions scientifiques qu'ils soulèvent sont nombreuses, on peut s'interroger par exemple sur leur mode de formation, sur leur état réellement liquide ou non, sur leur composition chimique, sur leur participation aux cycles du méthane, et sur leur étonnante absence de vagues ou encore les manifestations des fameuses «*Magic Island*». Ceci sans évoquer une possible chimie prébiotique prenant naissance dans un solvant cryogénique. Le chapitre suivant propose une présentation générale des travaux de modélisation numérique que j'ai publié depuis 2009, et qui ont pour principal objet les lacs de Titan.

1.3 Références

BARNES, J. W., J. M. SODERBLOM, R. H. BROWN, L. A. SODERBLOM, K. STEPHAN, R. JAUMANN, S. L. MOUÉLIC, S. RODRIGUEZ, C. SOTIN, B. J. BURATTI, K. H. BAINES, R. N. CLARK et P. D. NICHOLSON. 2011, «Wave constraints for Titan's Jingpo Lacus and Kraken Mare from VIMS specular reflection lightcurves», *Icarus*, vol. 211, doi: 10.1016/j.icarus.2010.09.022, p. 722–731. 16

CAMPBELL, D. B., G. J. BLACK, L. M. CARTER et S. J. OSTRO. 2003, «Radar Evidence for Liquid Surfaces on Titan», *Science*, vol. 302, doi: 10.1126/science.1088969, p. 431–434. 14

COMAS I SOLÀ, J. 1907, *Comptes Rendus de l'Academie des Sciences de Paris*, p. 1255–1256. 10

COMAS I SOLÀ, J. 1908, *Astronomische Nachrichten*, vol. 4290, p. 289–290. 10

ESHLEMAN, V. R., G. F. LINDAL et G. L. TYLER. 1983, «Is Titan wet or dry ?», *Science*, vol. 221, doi: 10.1126/science.221.4605.53, p. 53–55. 13

FLASAR, F. M. 1983, «Oceans on Titan ?», *Science*, vol. 221, doi: 10.1126/science.221.4605.55, p. 55–57. 13

GRIFFITH, C. A., P. PENTEADO, K. BAINES, P. DROSSART, J. BARNES, G. BELLUCCI, J. BIBRING, R. BROWN, B. BURATTI, F. CAPACCIONI, P. CERRONI, R. CLARK, M. COMBES, A. CORADINI, D. CRUIKSHANK, V. FORMISANO, R. JAUMANN, Y. LANGEVIN, D. MATSON, T. MCCORD, V. MENNELLA, R. NELSON, P. NICHOLSON, B. SICARDY, C. SOTIN, L. A. SODERBLOM et R. KURSINSKI. 2005, «The Evolution of Titan's Mid-Latitude Clouds», *Science*, vol. 310, doi: 10.1126/science.1117702, p. 474–477. 15

JEANS, J. H. 1925, *Dynamical Theory of Gases*, Cambridge University Press, Cambridge, UK. 11

KUIPER, G. P. 1944, «Titan : a Satellite with an Atmosphere.», *ApJ*, vol. 100, doi: 10.1086/144679, p. 378. 11

LINDAL, G. F., G. E. WOOD, H. B. HOTZ, D. N. SWEETNAM, V. R. ESHLEMAN et G. L. TYLER. 1983, «The atmosphere of Titan - an analysis of the Voyager 1 radio occultation measurements», *Icarus*, vol. 53, doi: 10.1016/0019-1035(83)90155-0, p. 348–363. 12

LORENZ, R. 1997, «Did Comas Solà discover Titan's atmosphere ?», *Astronomy & Geophysics*, vol. 38, doi: https://doi.org/10.1093/astrogeo/38.3.16, p. 16–18. 10

LORENZ, R. et J. MITTON, éd.. 2008, *Titan unveiled*, Princeton University Press, 41, William Street, Princeton, New Jersey, USA. 11, 15, 16

LUNINE, J. I., D. J. STEVENSON et Y. L. YUNG. 1983, «Ethane ocean on Titan», *Science*, vol. 222, doi: 10.1126/science.222.4629.1229, p. 1229–1230. 13

MUHLEMAN, D. O., A. W. GROSSMAN, B. J. BUTLER et M. A. SLADE. 1990, «Radar reflectivity of Titan», *Science*, vol. 248, doi: 10.1126/science.248.4958.975, p. 975–980. 13, 14

OWEN, T. 1982, «Titan», *Sci. Am.*, vol. 246,
doi: 10.1038/scientificamerican0282-98, p. 98–101. 13

RANNOU, P., F. MONTMESSIN, F. HOURDIN et S. LEBONNOIS. 2006, «The Latitudinal Distribution of Clouds on Titan», *Science*, vol. 311,
doi: 10.1126/science.1118424, p. 201–205. 16

SAGAN, C. et S. F. DERMOTT. 1982, «The tide in the seas of Titan», *Nature*, vol. 300,
doi: 10.1038/300731a0, p. 731–733. 13

SAMUELI, J.-J. et J.-C. BOUDENOT. 2017, *Trente livres de physique qui ont changé le monde*, 2e éd., Edition Ellipse, Paris. 9

SEIGNOVERT, B. 2017, *Analyse de la couche détachée de Titan à l'aide de l'instrument Cassini/ISS*, thèse de doctorat. 11

SMITH, P. H. 1980, «The radius of Titan from Pioneer Saturn data», *J. Geophys. Res.*, vol. 85,
doi: 10.1029/JA085iA11p05943, p. 5943–5947. 11

SODERBLOM, J. M., J. W. BARNES, L. A. SODERBLOM, R. H. BROWN, C. A. GRIFFITH, P. D. NICHOLSON, K. STEPHAN, R. JAUMANN, C. SOTIN, K. H. BAINES, B. J. BURATTI et R. N. CLARK. 2012, «Modeling specular reflections from hydrocarbon lakes on Titan», *Icarus*, vol. 220,
doi: 10.1016/j.icarus.2012.05.030, p. 744–751. 16

STEPHAN, K., R. JAUMANN, R. H. BROWN, J. M. SODERBLOM, L. A. SODERBLOM, J. W. BARNES, C. SOTIN, C. A. GRIFFITH, R. L. KIRK, K. H. BAINES, B. J. BURATTI, R. N. CLARK, D. M. LYTLE, R. M. NELSON et P. D. NICHOLSON. 2010, «Specular reflection on Titan : Liquids in Kraken Mare», *Geophys. Res. Lett.*. 16

STOFAN, E. R., C. ELACHI, J. I. LUNINE, R. D. LORENZ, B. STILES, K. L. MITCHELL, S. OSTRO, L. SODERBLOM, C. WOOD, H. ZEBKER, S. WALL, M. JANSSEN, R. KIRK, R. LOPES, F. PAGANELLI, J. RADEBAUGH, L. WYE, Y. ANDERSON, M. ALLISON, R. BOEHMER, P. CALLAHAN, P. ENCRENAZ, E. FLAMINI, G. FRANCESCETTI, Y. GIM, G. HAMILTON, S. HENSLEY, W. T. K. JOHNSON, K. KELLEHER, D. MUHLEMAN, P. PAILLOU, G. PICARDI, F. POSA, L. ROTH, R. SEU, S. SHAFFER, S. VETRELLA et R. WEST. 2007, «The lakes of Titan», *Nature*, vol. 445,
doi: 10.1038/nature05438, p. 61–64. 16

TOMASKO, M. G. 1980, «Preliminary results of polarimetry and photometry of Titan at large phase angles from Pioneer 11», *J. Geophys. Res.*, vol. 85,
doi: 10.1029/JA085iA11p05937, p. 5937–5942. 11

TOMASKO, M. G. et P. H. SMITH. 1982, «Photometry and polarimetry of Titan - Pioneer 11 observations and their implications for aerosol properties», *Icarus*, vol. 51,
doi: 10.1016/0019-1035(82)90030-6, p. 65–95. 11

TYLER, G. L., V. R. ESHLEMAN, J. D. ANDERSON, G. S. LEVY, G. F. LINDAL, G. E. WOOD et T. A. CROFT. 1981, «Radio science investigations of the Saturn system with Voyager 1 - Preliminary results», *Science*, vol. 212,
doi: 10.1126/science.212.4491.201, p. 201–206. 12, 13

YUNG, Y. L., M. ALLEN et J. P. PINTO. 1984, «Photochemistry of the atmosphere of Titan - Comparison between model and observations», *ApJS*, vol. 55,
doi: 10.1086/190963, p. 465–506. 13

Chapitre 2

Titan : surface et modèles numériques

« C'est à la chaleur que doivent être attribués les grands mouvements qui frappent nos regards sur la terre ; c'est à elle que sont dues les agitation de l'atmosphère, l'ascension des nuages, la chute des pluies et des autres météores, les courants d'eau qui sillonnent la surface du globe et dont l'homme est parvenu à employer pour son usage une faible partie ; enfin les tremblements de terre, les éruptions volcaniques reconnaissent aussi pour cause la chaleur. »

— Sadi Carnot, *Réflexions sur la puissance motrice du feu et sur les machines propres à développer cette puissance,*
Annales scientifiques de l'É.N.S. 2e série, tome 1, 1872, p. 393-457.
1834

Sommaire

2.1 Introduction . . . 19
2.2 Les modèles d'équilibre liquide-gaz basés sur la RST . . . 20
2.2.1 Introduction : le problème de l'écart à l'idéalité . . . 20
2.2.2 Quelques rappels de thermodynamique . . . 21
2.2.3 Le modèle basé sur la RST . . . 22
2.2.4 Résultats . . . 24
2.3 Autres applications du modèle basé sur la RST . . . 25
2.3.1 Séquestration des gaz rares . . . 25
2.3.2 La composition de surface des évaporites . . . 26
2.4 Discussion sur la RST . . . 28
2.5 Modèles thermodynamiques basés sur PC-SAFT . . . 30
2.5.1 Introduction – Implémentation de PC-SAFT . . . 30
2.5.2 Quelques applications de PC-SAFT . . . 32
2.6 Références . . . 36

2.1 Introduction

Comme indiqué dans le chapitre introductif, un des problèmes importants concernant les lacs et mers de Titan est celui de leur composition chimique. On a pu voir qu'au cours des années 80 la discussion portait plutôt sur la prédominance du méthane ou de l'éthane comme constituant majeur ; la détection du diazote comme constituant principal de l'atmosphère a ajouté la question de sa dissolution dans un mélange liquide de CH_4–C_2H_6.

D'un point de vue observationnel, la détermination spectroscopique de la composition chimique des lacs et mers de Titan est très difficile, si cela n'est pas impossible. Le problème est causé

par la présence importante de diazote et de méthane dans l'atmosphère. Une tentative a été réalisée par BROWN et collab. [2008], ces auteurs apportant des arguments en faveur de présence d'éthane liquide dans Ontario Lacus, le plus grand lac de la région polaire sud. Cette étude, bien qu'intéressante, demande cependant à être confirmée. En effet, BROWN et collab. [2008] utilisent des rapports de spectres, en particulier entre des spectres de pixels VIMS situés à la surface du lac, et d'autres correspondant à une localisation sur les terrains environnants. Une étude plus approfondies, basée sur l'utilisation d'un modèle de transfert radiatif, est intéressante à mener, cela fait d'ailleurs partie du travail de Maélie Coutelier, doctorante que je co-encadre.

Parallèlement aux observations, d'autres approches sont possibles : les expériences en laboratoire et les simulations numériques, chacune avec ses avantages et inconvénients. Dans mon travail j'ai construit des modèles numériques, avec dans certains cas des applications aux expériences. Dans la suite, je décris mes modèles, je rappelle leurs résultats et en discute leurs limites.

2.2 Les modèles d'équilibre liquide-gaz basés sur la RST

2.2.1 Introduction : le problème de l'écart à l'idéalité

L'idée la plus immédiate concernant un modèle, destiné à estimer la composition des lacs de Titan, est celle d'un équilibre thermodynamique entre le liquide du lac et le gaz de l'atmosphère. C'est une hypothèse assez forte, et simplificatrice, car un système mer-atmosphère est constamment en situation de hors-équilibre : le Soleil fournit en continue un flux d'énergie, et le cycle hydrologique qui est déclenché relève du hors équilibre. Cet état se manifeste par l'évaporation et les épisodes de précipitation. Au niveau moléculaires, l'équilibre thermodynamique correspond à des flux de particules dans le sens liquide vers gaz, égaux à ceux dans le sens contraire. On voit bien qu'on n'est pas dans cette situation lors, par exemple, d'une évaporation.
Néanmoins, l'hypothèse de l'équilibre permet une première approche, apportant des informations sur une sorte de comportement moyen d'un système liquide-vapeur. C'est l'hypothèse retenue dans un des premiers travaux du genre sur la composition chimique des mers de Titan, à savoir : DUBOULOZ et collab. [1989]. Pour ce type de modélisation, un aspect très important est la prise en compte de la non-idéalité du liquide. En effet, traiter un liquide comme un gaz parfait, revient à négliger les interactions inter-moléculaires alors qu'elles y jouent un rôle important, voire largement prépondérant. Un exemple frappant est celui de l'eau, qui est liquide à ~ 300 K, et en équilibre avec sa vapeur, ceci à une pression de l'ordre de ~ 1 bar. Si, dans ces conditions, on applique l'équation d'état des gaz parfaits à 1 litre d'eau liquide on a :

$$\mathrm{P} = \frac{m\,\mathrm{RT}}{\mathrm{M_{H_2O}V}} = \frac{1 \times 8{,}31 \times 300}{18 \times 10^{-3} \times 10^{-3}} \simeq 1{,}4 \times 10^{8}\ \mathrm{Pa} \tag{2.1}$$

Ce calcul montre que le système devrait avoir besoin d'une pression de ~ 1400 bars pour être à l'équilibre alors qu'en réalité, les liaisons hydrogènes entre molécules d'eau, abaissent cette valeur à 1 bar. La prise en compte des effets non-idéaux est donc une nécessité, même si en l'absence de liaisons hydrogène, ou encore dipôle-dipôle, ces effets devraient être moins marqués pour un système N_2–CH_4–C_2H_6.

La première manière de tenir compte des effets non-idéaux est l'utilisation de l'équation d'état développée au 19e siècle par Johannes Diderik Van der Waals [1]. Cette équation, dont on rappelle l'expression :

$$(\mathrm{P} + \frac{a}{\mathrm{V}^2})\,(\mathrm{V} - b) = \mathrm{RT} \tag{2.2}$$

1. Après avoir fait une première carrière d'instituteur, c'est à l'âge de trente ans passé que J. D. Van der Waals est rentré à l'Université de Leyde [ROUSSET et SIX, 2000] ; cet aspect biographique le rend sympathique aux yeux de l'auteur de ce manuscrit.

où a et b sont deux paramètres dépendant de l'espèce étudiée. Le paramètre a rend compte des forces d'attraction intermoléculaires, le second paramètres, b, représente le volume minimum occupé par le fluide à très haute pression. Cette équation a permis notamment de mieux représenter les mesures de compressibilités réalisées par V. Regnault [*e.g.* REGNAULT, *1842]* au cours du 19e siècle [pour plus d'information sur l'œuvre de V. Regnault, voir PONCET et DAHLBERG, 2011] ; de plus c'est grâce à elle qu'on a pu rendre compte de l'existence d'un point critique découvert par Thomas Andrews [ANREWS, 1869]. Pour l'ensemble de ces travaux, Van der Waals recevra le Prix Nobel de Physique en 1910.

Depuis ces travaux précurseurs, de nombreuses équations d'état ont été développées, chacune ayant un domaine de validité particulier, ou des performances plus ou moins bonnes. Les espèces qui nous intéressent, à savoir principalement le diazote, le méthane et l'éthane, sont les constituants majeurs du gaz naturel terrestre. Cela explique, vu l'intérêt industriel, que de très nombreux travaux [voir POLING et collab., 2007] aient été réalisés sur le sujet de la modélisation des mélanges d'hydrocarbures liquides, état qui facilite leur transport.
Ainsi, afin de tenir compte des effets non-idéaux, DUBOULOZ et collab. [1989] ont utilisé la *Regular Solution Theory* (*RST*, «théorie des solutions régulières» en français). Avant d'aller plus loin, il est nécessaire de rappeler quelques éléments de thermodynamiques.

2.2.2 Quelques rappels de thermodynamique

L'enthalpie peut être interprétée comme l'énergie nécessaire à la création du système qu'on étudie, *i.e.* l'énergie interne U, à laquelle on ajoute le travail nécessaire PV pour mettre en place les particules, *i.e.* créer un certain espace entre elles. Mathématiquement on a donc :

$$H = U + PV \tag{2.3}$$

Ainsi définie, l'enthalpie peut être vue comme l'énergie totale contenue dans le système.
On raisonne couramment à partir de l'enthalpie libre, notée G et appelée en anglais «Gibbs free energy», qui est l'enthalpie facilement disponible pour créer du travail, *i.e.* une forme d'énergie utilisable pour des applications pratiques. On écrit par définition :

$$G = H - TS \tag{2.4}$$

où le terme «TS» correspond à l'énergie associée au désordre lié à l'agitation thermique.

Pour un système composé de N_φ phases et de N_c espèces chimiques, la variation élémentaire dG d'enthalpie libre associée à une petite transformation du système s'écrit :

$$dG = V\,dP - S\,dT + \sum_{\alpha=1}^{N_\varphi} \sum_{i=1}^{N_c} \mu_i^{(\alpha)} dN_i^{(\alpha)} \tag{2.5}$$

A l'équilibre thermodynamique, l'enthalpie libre est minimale, et $dG = 0$. Pour un système à pression et température uniforme, on a alors :

$$\sum_{\alpha=1}^{N_\varphi} \sum_{i=1}^{N_c} \mu_i^{(\alpha)} dN_i^{(\alpha)} = 0 \tag{2.6}$$

on voit que s'il y a des mélanges de matières, entre phases, à l'intérieur du système, *i.e.* si on a des termes $dN_i^{(\alpha)} \neq 0$; l'état d'équilibre n'est préservé que si, pour toute espèce i, et pour –par exemple– deux phases α et β :

$$\mu_i^{(\alpha)} = \mu_i^{(\beta)} \tag{2.7}$$

Cette quantité μ_i, appelée «potentiel chimique» de l'espèce i, n'est autre que l'enthalpie libre partielle molaire.

Si on prend le cas particulier d'un gaz, on écrit, pour un gaz réel :

$$\mu_i = \mu_i^0(g) + \mathrm{RT}\ln\frac{f_i}{\mathrm{P}_0} \tag{2.8}$$

où P_0 est une pression de référence choisie arbitrairement (généralement 1 bar) et f_i la fugacité du gaz. Le potentiel $\mu_i^0(g)$ est le potentiel standard, *i.e.* le potentiel chimique du gaz i, dans l'état standard (*i.e.* gaz parfait) à la pression P_0.

On introduit parfois également le cœfficient de fugacité Φ_i défini par :

$$f_i = \Phi_i\, x_i\, \mathrm{P} \tag{2.9}$$

avec P la pression de travail et x_i la fraction molaire de l'espèce i.

On notera bien que lorsque $x_i \to 1$ (on a alors qu'une seule espèce) $f_i \to \Phi_i \mathrm{P}$. Si de plus $\mathrm{P} = \mathrm{P}_0$; alors :

$$\mu_i = \mu_i^0(gp) + \ln\Phi_i \tag{2.10}$$

avec «$\mu_i^0(gp)$» le potentiel standard du gaz parfait correspondant. Ceci montre que Φ_i mesure l'écart à l'idéalité, en d'autres termes c'est une mesure de l'énergie d'interaction entre les molécules en présence. Pour un gaz parfait $\Phi_i = 1$. Aussi bien f_i que Φ_i mesure la non-idéalité. Suivant les habitudes, et les domaines (chimie des gaz, des solutions, ...) on peut de façon équivalente travailler avec l'activité a_i définie par :

$$\mu_i = \mu_i^0(gp) + \ln a_i \tag{2.11}$$

on a alors $a_i = f_i/\mathrm{P}_0$; et on introduit aussi le cœfficient d'activité γ_i tel que :

$$a_i = \gamma_i\, x_i \tag{2.12}$$

dans le cas de l'idéalité $\gamma_i \to 1$. Dans tous les cas, f_i ou a_i (ou de façon associée Φ_i ou γ_i) mesure la distance à l'idéalité, *i.e.* ces quantités rendent compte des interactions intermoléculaires.

Ce qu'on vient de montrer au sujet des gaz ce généralise aux liquides. Une autre terminologie peut être également rencontrée : l'*excess Gibbs energy* $\mathrm{G_E}$:

$$\mathrm{G_E} = \mathrm{RT}\sum_i n_i \ln\gamma_i \tag{2.13}$$

comme on le voit, là encore, il s'agit d'écrire la contribution à l'énergie du système des forces d'interaction.

Le lecteur intéressé pourra se rendre sur http://chem.libretexts.org/Textbook_Maps, où une très bonne, et très complète, introduction à la thermodynamique est disponible.

2.2.3 Le modèle basé sur la RST

Le choix fait par DUBOULOZ et collab. [1989] est d'utiliser, parmi un grand nombre de possibilité plus ou moins équivalentes [POLING et collab., 2007], la RST qui donne les cœfficients d'activité γ_k par :

$$\mathrm{RT}\ln\gamma_k = v_k \sum_i \sum_j (\mathrm{A}_{ik} - \mathrm{A}_{ij}/2)\,\Phi_i\Phi_j \tag{2.14}$$

avec :

$$\mathrm{A}_{ij} = (\delta_i - \delta_j)^2 + 2l_{ij}\,\delta_i\delta_j \tag{2.15}$$

et

$$\Phi_i = \frac{x v_i}{\sum_j x_i x_j} \tag{2.16}$$

TABLEAU 2.1 – Composition des phases liquides calculée aux pôles de Titan, et également à la température relevée à l'équateur. Ces résultats sont issus de CORDIER et collab. [2009] (voir page 58).

	Equator (93.65 K)	Poles (90 K)
Main composition (lake mole fraction)		
N_2	3.67×10^{-3}	5.91×10^{-3}
CH_4	6.34×10^{-2}	1.09×10^{-1}
Ar	3.52×10^{-6}	5.52×10^{-6}
CO	2.57×10^{-7}	5.10×10^{-7}
C_2H_6	8.14×10^{-1}	7.72×10^{-1}
C_3H_8	7.90×10^{-2}	7.49×10^{-2}
C_4H_8	1.48×10^{-2}	1.41×10^{-2}
H_2	4.41×10^{-6}	3.92×10^{-6}
Solutes (lake mole fraction)		
HCN	2.42×10^{-5} (s)	1.17×10^{-5} (s)
C_4H_{10}	1.29×10^{-2} (ns)	1.23×10^{-2} (ns)
C_2H_2	1.22×10^{-2} (ns)	1.16×10^{-2} (ns)
C_6H_6	1.10×10^{-4} (s)	5.97×10^{-5} (s)
CH_3CN	9.90×10^{-5} (s)	5.12×10^{-5} (s)
CO_2	3.11×10^{-4} (ns)	2.95×10^{-4} (ns)

(s) : saturated ; (ns) non saturated.

Afin d'avoir des résultats qui puissent être comparés à ceux de DUBOULOZ et collab. [1989], j'ai donc utilisé la même approche dans CORDIER et collab. [2009] (voir page 58) avec des mises à jour substantielles apportées par les mesures *in situ* de la composition atmosphérique par *Huygens* [NIEMANN et collab., 2005].
Dans les équations (2.15) et (2.16), il est bon de s'arrêter sur deux types de termes : les δ_i et les l_{ij}.

Les δ_i sont appelés paramètres de solubilité d'Hildebrand, et sont donnés par :

$$\delta_i = \sqrt{\frac{\Delta H_{vap,i} - RT}{V_i}} \tag{2.17}$$

avec T la température, R la constante des gaz parfaits, $\Delta H_{vap,i}$ l'enthalpie de vaporisation et V_i le volume molaire. Comme on le voit δ_i est une manière de mesurer l'énergie de cohésion de l'espèce i à l'état liquide. Dans l'approche d'Hildebrand [HIDEBRAND, 1936] deux espèces avec des δ_i voisins sont très solubles, alors que celles avec des δ_i différents le sont peu.

Si on regarde le cas limite où $\delta_i = \delta_j$, en laissant pour le moment de côté le terme avec l_{ij} dans (2.15) on voit que cela conduit à $\gamma_k = 1$, cas idéal où les solubilités sont sans limitation.

Le terme en «$2 l_{ij} \delta_i \delta_j$» rend compte des interactions interspécifiques, avec les l_{ij} qui sont des paramètres libres du système, et dont on ne connaît souvent pas les valeurs. Cette dernière remarque vaut également pour les enthalpies de vaporisation $\Delta H_{vap,i}$. Dans le modèle de CORDIER et collab. [2009] (voir page 58), pour les espèces présentes à la fois dans l'atmosphère et la phase liquide, on écrit :

$$y_i P = \gamma_i x_i P_{vap,i} \tag{2.18}$$

où le membre de gauche représente le gaz et celui de droite le liquide. À ces égalités on ajoute une relation rendant compte de l'équilibre solide-liquide pour les espèces initialement solides

tombant vers la surface (comme HCN) et ensuite dissoutes dans le liquide :

$$\ln(\gamma_i\, x_{i,\mathrm{sat}}) = \frac{\Delta \mathrm{H}_m}{\mathrm{R}\mathrm{T}_m}\left(1 - \frac{\mathrm{T}_m}{\mathrm{T}}\right) \tag{2.19}$$

lorsque x_i atteint la valeur $x_{i,\mathrm{sat}}$, fraction molaire à saturation, on fixe $x_i = x_{i,\mathrm{sat}}$.

Concernant les produits de la photochimie atmosphérique, dont la pression de vapeur est trop faible pour être mesurée, on calcule leur fraction molaire dans le liquide ajustée proportionnellement à l'abondance de celle de l'éthane dans les précipitations, ce qui s'écrit :

$$x_i = \frac{\tau_i}{\tau_{\mathrm{C_2H_6}}}\, x_{\mathrm{C_2H_6}} \tag{2.20}$$

avec les τ_i les taux de précipitation de l'espèce i. Ces τ_i sont donnés par les modèles de photochimie, comme ceux de LAVVAS et collab. [2008a,b].

En définitive, c'est un système non-linéaire à N équations, et N inconnues, qui est à résoudre. Pour cela on emploie une méthode de Newton-Raphson [PRESS et collab., 1992].

2.2.4 Résultats

Les résultats de ce premier modèle, basé sur la RST, sont présentés dans la table 2.1, ceci pour deux températures différentes : 93.65 K qui est celle mesurée par *Huygens* sur son site d'atterrissage [NIEMANN et collab., 2005], et 90 K qui est certainement celle dans les régions polaires [JENNINGS et collab., 2016, 2009]. Ce qui frappe dans ces résultats c'est le faible taux de N_2, dissout dans le liquide, j'en reparlerai plus tard. Le cas est important, car il conditionne le fait que le liquide puisse geler ou non. A ce propos, ce modèle n'indique rien, car la question de l'équilibre «solution liquide–solution solide de CH_4» n'est pas incluse.

Un autre point saillant est l'abondance relativement élevée [comparée à celle publiée par DUBOULOZ et collab., 1989] de l'acétylène C_2H_2. Ce dernier pourrait être, à la base d'un métabolisme de micro-organismes «titaniens» mangeant du C_2H_2 solide en respirant H_2 faiblement présent dans l'atmosphère [LUNINE, 2010; SCHULZE-MAKUCH et GRINSPOON, 2005]. Cette hypothèse, intellectuellement excitante, reste pour le moment extrêmement spéculative. Finalement le comportement vis-à-vis de la température (voir figure 2.1) montre généralement un abaissement de la concentration des espèces les plus volatiles, alors que les solides se dissolvent de plus en plus facilement. Le rupture de pente dans la solubilité de HCN est causée par la saturation de cette espèce.

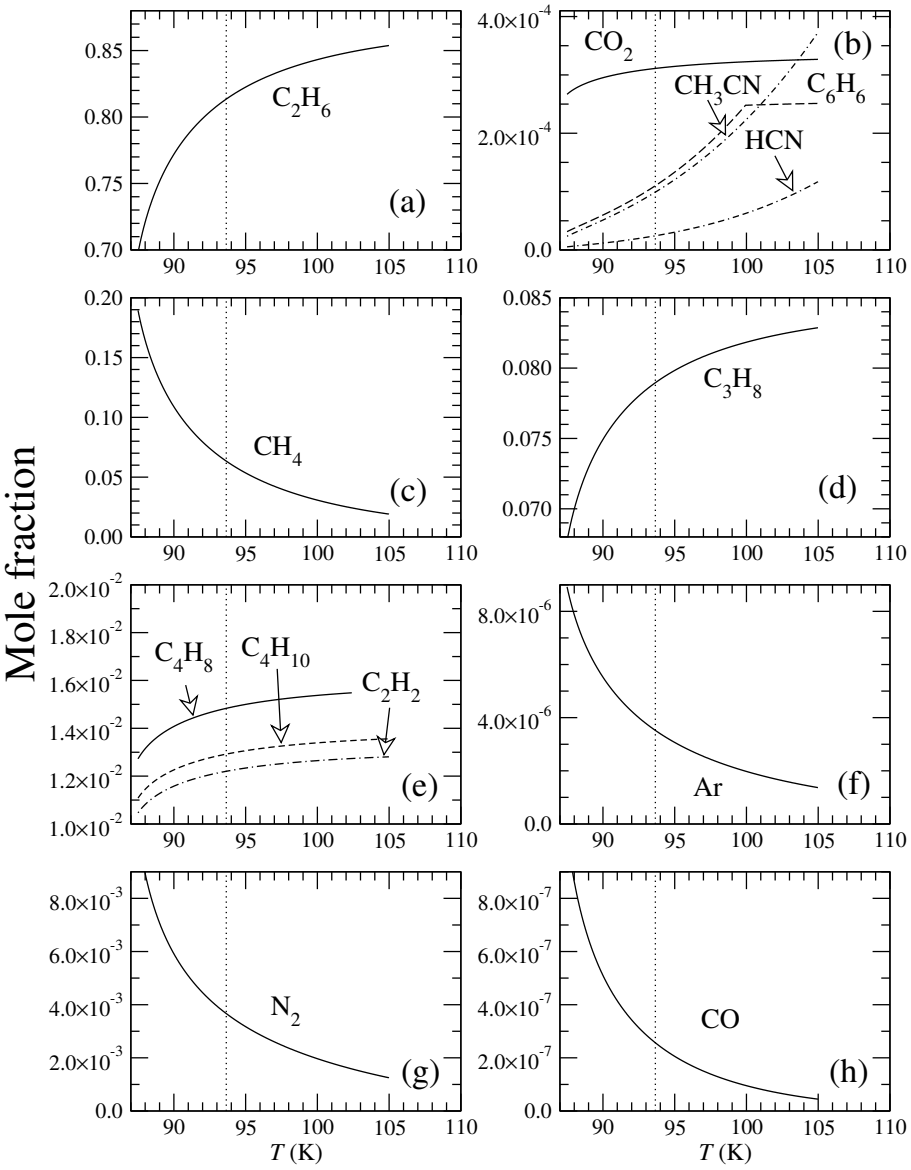

FIGURE 2.1 – (a)–(h) : Composition des lacs de Titan en fonction de la température. La droite verticale en pointillés représente la température 93.65 K relevée par *Huygens* sur son site d'atterrissage. Ces résultats sont issus de CORDIER et collab. [2009] (voir page 58).

2.3 Autres applications du modèle basé sur la RST

2.3.1 Séquestration des gaz rares

L'argon possède, entre autres, deux isotopes d'intérêt titanien : ^{36}Ar et ^{40}Ar. Le premier est considéré comme primordial, *i.e.* il provient des tout premiers temps du système solaire ; alors que le deuxième, ^{40}Ar, est un produit de désintégration de ^{40}K, d'origine géologique.
Lors de sa descente dans l'atmosphère de Titan, la sonde *Huygens* a procédé à des mesures d'abondances avec l'instrument GCMS. Concernant les gaz rares, aussi bien le krypton que le xénon sont restés en dessous du seuil de détection ; *i.e.* eu dessous de 10^{-8} en fraction molaire. L'argon a été détecté, surtout sous la forme ^{40}Ar (4.32×10^{-5}), l'argon 36 (2.80×10^{-7}) ayant une abondance relative à l'azote 14 (*i.e.* ^{36}Ar/^{14}N) pratiquement 6 ordres de grandeur inférieure à celle généralement acceptée pour la nébuleuse proto-solaire [LODDERS, 2003]. Lors de la formation, ou au cours de l'évolution de Titan, il y a eu un processus physico-chimique qui a conduit à la séquestration de ^{36}Ar.

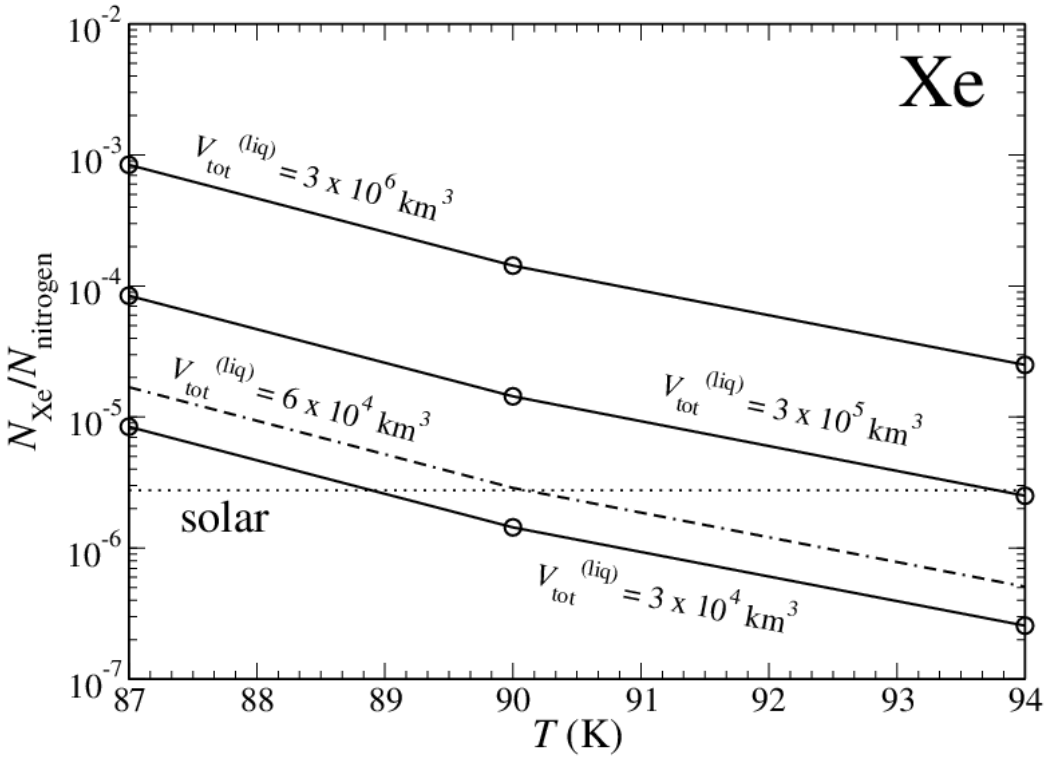

FIGURE 2.2 – Le rapport $N_{Xe}/N_{nitrogen}$ global pour Titan en fonction de la température au sol. La ligne horizontale représente la valeur solaire. Les autres lignes, de haut en bas, correspondent à différentes valeurs du volume totale de liquide. La valeur de la fraction molaire atmosphérique correspond au seuil de détection du GCMS de *Huygens* ($y_{Xe} = 10^{-8}$). Cette figure est issue de CORDIER et collab. [2010] (voir page 62).

Plusieurs idées ont été proposées : le stockage dans les clathrates [OSEGOVIC et MAX, 2005] ; ou la capture par les aérosols de l'atmosphère [JACOVI et BAR-NUN, 2008]. J'ai envisagé une autre alternative : la dissolution des ces gaz rares dans les phases liquides présentes sur Titan.

En utilisant le modèle de dissolution décrit en section 2.2.3, et en prenant compte des quantités présentes dans l'atmosphère et les phases liquides, on a pu calculer [CORDIER et collab., 2010] (voir page 62) les ratios N_{gr}/N_{N_2} (N_{gr} : nombre de particules d'un gaz rare donné, par unité de volume), en faisant une hypothèse raisonnables sur le volume total d'hydrocarbures liquides disponibles.

Le résultat pour Ar est sans appel : le rapport N_{Ar}/N_{N_2} reste trois ordres de grandeurs trop élevé. Cette situation se répète pour le krypton où, là non plus la déplétion observée ne peut pas s'expliquer par une dissolution dans les phases liquides actuelles. Le cas du xénon est moins tranché. En effet (voir figure 2.2), à la température des pôles, *i.e.* ~ 90 K, une valeur raisonnable de liquide (*i.e.* 6×10^4 km^3) peut être trouvée pour séquestrer suffisamment de Xe pour expliquer les mesures de *Huygens*. Le problème reste largement ouvert.

2.3.2 La composition de surface des évaporites

Lors de la découverte de l'existence des lacs et mers dans la région arctique de Titan [STOFAN et collab., 2007] ; de nombreuses structures paraissaient, d'un point de vue morphologique, être des lits de lacs asséchés. Des indices d'une activité du cycle du méthane ont été clairement mis en évidence [*e.g.* TURTLE et collab., 2011a], ainsi qu'une suspicion d'activité sur les rives d'Ontario Lacus [CORNET et collab., 2012; TURTLE et collab., 2011b]. C'est BARNES et collab. [2011] qui mettent

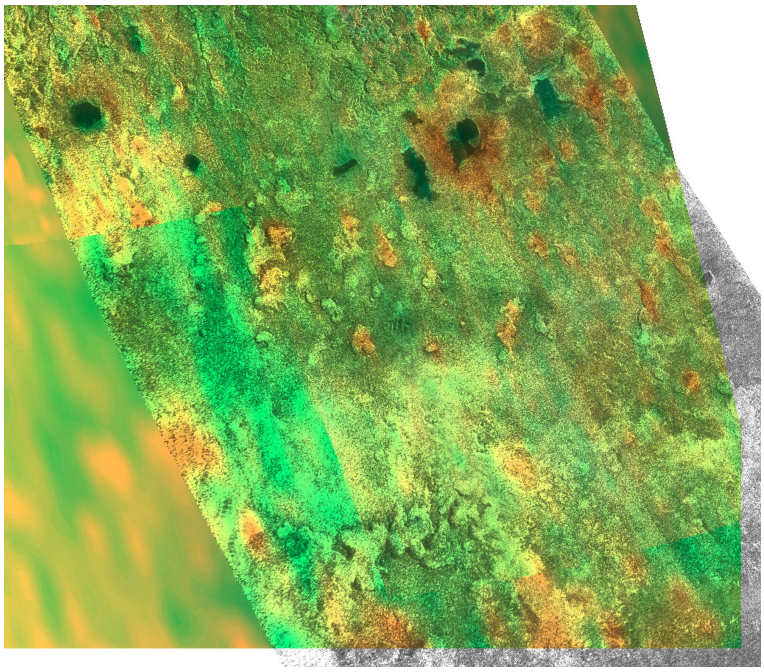

FIGURE 2.3 – Image composite : les données RADAR sont représentées par une échelle de gris, à ceci il a été superposé un cliché issu de l'instrument VIMS, dans ce cas les zones riches en glace d'eau sont en vert, alors que celles qui semblent pauvres sont codées en orange. Cette figure m'a été aimablement communiquée par Jason Barnes [BARNES et collab., 2011].

en évidence une corrélation entre d'une part les lits de lacs asséchés vus au radar, et, d'autre part une indication, dans l'infrarouge, d'une pauvreté du sol en glace. Les résultats de [BARNES et collab., 2011] suggèrent donc la formation de dépôts organiques au niveau des lits asséchés. Ces dépôts, nommés «évaporites» seraient l'analogue des dépôts de sel des marais salants terrestres.

La question a été de discuter la composition possible de la surface de ces évaporites [CORDIER et collab., 2013] (voir page 79). Aucun modèle n'étant disponible pour ce type de système, il a fallu réfléchir à la manière d'aborder le problème. Les modèles thermodynamiques précédents faisaient l'hypothèse d'un équilibre entre le liquide et l'atmosphère. Dans le cas des évaporites ce n'est clairement pas applicable car, lors de leur formation, il y a évaporation du solvant.
L'aspect «équilibre avec l'atmosphère» a donc été enlevé, pour laisser la place à une perte de matière en solvant. Cette perte de matière a été associée à un taux d'évaporation arbitraire, en d'autres termes le modèle ne pourrait pas fournir le temps de formation des évaporites, mais seulement le résultat final. Le modèle est donc construit sur un équilibre (espèce en solution)–(espèce solide), cet équilibre étant atteint lorsque l'espèce i a sa fraction molaire à sa valeur à saturation $x_{i,\mathrm{sat}}$ donnée par :

$$\ln \gamma_i \, x_{i,\mathrm{sat}} = -\frac{\Delta \mathrm{H}_{i,\mathrm{m}}}{\mathrm{R}\,\mathrm{T}_{i,\mathrm{m}}} \left(\frac{\mathrm{T}_{i,\mathrm{m}}}{\mathrm{T}} - 1 \right) \tag{2.21}$$

le cœfficient d'activité γ_i étant estimé dans le cadre de la RST. Lorsqu'à un «pas de temps» donné une espèce a sa fraction molaire x_i dépassant $x_{i,\mathrm{sat}}$; on fixe $x_i = x_{i,\mathrm{sat}}$; la matière excédentaire étant déposée sur le fond du lac. Ainsi, avec une gestion de la conservation de la matière, on peut suivre la construction d'un dépôt dans le lit lacustre. Lorsqu'il ne reste plus de solvant, on obtient alors la composition à la surface des évaporites [CORDIER et collab., 2013] (voir page 79).
Le premier présupposé à fixer, avant de calculer la formation d'un dépôt évaporitique, est de déterminer la composition initiale. Dans CORDIER et collab. [2013] (voir page 79) nous avons considéré que le solvant était formé par un mélange N_2–CH_4–C_2H_6, riche ou pauvre en méthane. Pour les solutés, le jeu d'espèces considérées vient des modèles de photochimie [LAVVAS et collab., 2008a,b; VUITTON et collab., 2008] et nous avons suivi deux scénarios :

- **Type 1 :** les solides dissous ont leurs abondances initiales prises proportionnelles aux taux de précipitations atmosphériques, l'espèce la plus abondante (*i.e.* HCN) ayant une fraction molaire initiale à sa valeur à saturation. Ainsi, dans ce scénario, HCN commence à sédimenter dès le début de l'évaporation.

- **Type 2 :** tous les solides ont la même concentration initiale, ajustée à la plus petite des fractions molaires à saturation. Ce scénario permet de mieux appréhender l'effet du seul processus d'évaporation/sédimentation.

Nous avons étudié l'influence de différentes paramètres : richesse en méthane ou idéalité de la solution. Dans tous les cas, ce sont les espèces identifiées comme les plus solubles, à savoir l'acétylène C_2H_2 et le butane C_4H_{10}, qui, étant restées en solution le plus longtemps se retrouvent à la surface des évaporites.

Par exemple, pour un mélange non-idéal, de type 2, riche en méthane, la surface finale est composée de 67% de C_4H_{10} et 32% de C_2H_2. Bien sûr, de nombreuses réserves sont à émettre au sujet de ces résultats. A commencer par la fiabilité des prédictions des modèles de chimie atmosphérique, par exemple le butane (C_4H_{10}) n'a toujours pas été détecté. Du côté de la modélisation thermodynamique, l'équation (2.21) est approchée et tous les effets de nucléation ont été ignorés. Néanmoins, CORDIER et collab. [2013] a fait l'objet d'un *Research Highlight* dans la revue *Nature Geoscience*. Le problème des évaporites sera repris dans la section 2.5.2, avec un modèle basé sur PC-SAFT, au lieu de la RST, et donnant non seulement la composition de la surface, mais aussi la structure verticale.

2.4 Discussion sur la RST

L'approche thermodynamique décrite ci-avant est est naturellement discutable. En premier lieu l'hypothèse d'équilibre océan-atmosphère n'est sans doute pas systématiquement vérifiée ; des épisodes d'évaporation ont certainement lieu, tout comme des périodes où des précipitations se produisent. D'autre part, concernant les modèles de formation d'évaporites, les résultats dépendent des espèces considérées, celles-ci venant des modèles de photochimie atmosphérique, qui ont eux mêmes des résultats qui ne sont pas tous en accord [KRASNOPOLSKY, 2009, 2010, 2014; LAVVAS et collab., 2008a,b].
Dans le cas particulier de la RST, approche qui a été mise au point pour des applications en génie chimique (*i.e.* pour l'industrie pétrochimique) la justification de la théorie est plus de l'ordre de la «recette» que de quelque chose qui repose sur des fondements physiques solides. De plus les modèles basés sur la RST dépendent de nombreuses données thermodynamiques : pressions de vapeur, enthalpie de vaporisation et de fusion, volumes molaires ; qui ne sont pas toujours bien connus, en particulier dans le domaine de température pertinent pour la surface de Titan. Par exemple les enthalpies de vaporisation de C_2H_6, C_3H_8 et C_4H_8 doivent être extrapolées sur plus de 100 K. C'est pourquoi dans CORDIER et collab. [2012] (voir page 70) une étude extensive, basée sur un algorithme de Monte-Carlo, a été entreprise, avec pour but d'évaluer l'influence des incertitudes sur les paramètres d'entrée. Etaient inclus les paramètres d'interaction inter-espèces, les l_{ij}, en général très mal connus, ont été également inclus dans cette étude.
Afin d'utiliser Monte-Carlo, nous avons dû toutefois toutefois fixer une «plage raisonnable» d'erreur sur les quantités thermodynamiques testées : par exemple un maximum de 10% d'erreur sur les pressions de vapeur. Pour une simulation donnée, la valeur d'une pression de vapeur étant tirée au sort sur un intervalle allant de la valeur «nominale» −10%, à la valeur nominale +10%, ceci avec une distribution uniforme. La même démarche étant généralisée aux autres grandeurs. L'influence sur les concentrations obtenues pour le liquide est finalement mesurée grâce à un écart-type relatif σ^* des valeurs obtenues pour 10000 simulations. En prenant en compte toutes les grandeurs

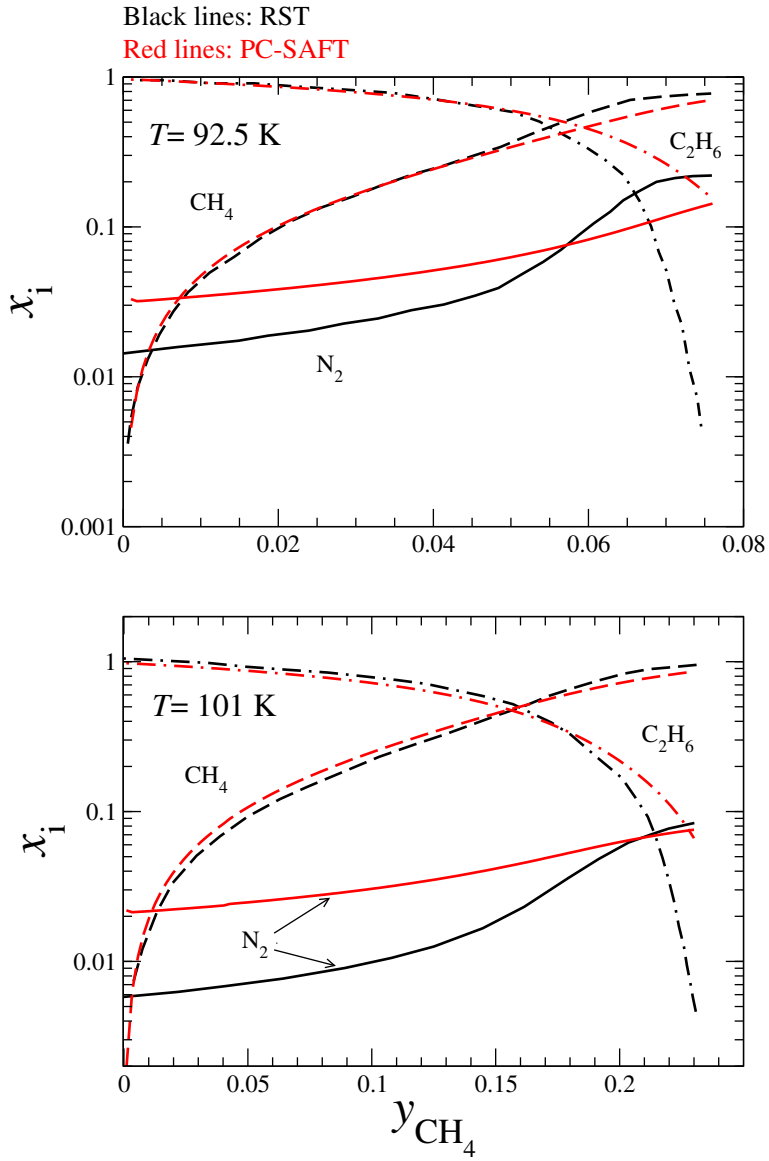

FIGURE 2.4 – Comparaison entre les résultats de la RST (en noir) et de PC-SAFT (en rouge). Cette figure reprend le principe de la figure 1 de DUBOULOZ et collab. [1989].

thermodynamiques on a obtenu des σ^* entre 100 et 300%, pour les espèces présentes dans l'atmosphère, donc sujettes à l'équilibre liquide-vapeur. Les σ^* restant plus petits, avec des valeurs de l'ordre de 10% pour les solides dissous. Ces expériences numériques mesurent naturellement l'incertitude internes à la RST, mais pas celles dues au choix de la RST, parmi les modèles de cœfficients d'activité disponibles.

Dans CORDIER et collab. [2012] (voir page 70) ont été également testés les possibles influences du climat de Titan. Les calculs de circulation globale (GCM) par CRESPIN et collab. [2008], montrent une forte variabilité en latitude des rapports de l'espèce X/C_2H_6. Si pour les pôles on a sensiblement la même chose, ce n'est pas le cas entre les pôles et les régions équatoriales [*cf.* Fig. 4 de CORDIER et collab., 2012]. Là encore des incertitudes existent, car dans ces modèles d'atmosphère, la microphysique, *i.e.* principalement la nucléation et la croissance des gouttelettes et des cristaux, n'est pas encore prise en compte.

Comparé à d'autres modèles [par exemple TAN et collab., 2013], mon modèle de composition des lacs de Titan, et en particulier l'aspect «équilibre liquide-valeur» semble minimiser la concen-

tration de diazote dissout avec une fraction molaire inférieure à ~ 1% pour CORDIER et collab. [2009] (voir page 58) et de l'ordre de 10–20% pour TAN et collab. [2013].

Je me suis penché sur ce problème grâce, en particulier, à des données de laboratoire et en mettant au point une implémentation de l'équation d'état dite PC-SAFT [GROSS et SADOWSKI, 2001] dont je reparlerai plus loin. PC-SAFT a un fondement physique plus solide que la RST qui est seulement semi-empirique. PC-SAFT permet de très bons accord avec les données expérimentales disponibles.

Sur la figure 2.4 (non publiée), j'ai réalisé une comparaison RST/PC-SAFT à partir des résultats de DUBOULOZ et collab. [1989], auteurs dont j'ai suivi l'approche basée sur la RST. Comme on peut le constater, par rapport à PC-SAFT, la RST a tendance à sous-estimer le contenu en N_2. Je ne suis pas allé plus loin dans les investigations, mais je soupçonne fort les paramètres d'entrée de la RST de ne pas être ceux valides pour les équilibres liquide-vapeur dans le contexte titanien.

2.5 Modèles thermodynamiques basés sur PC-SAFT

2.5.1 Introduction – Implémentation de PC-SAFT

Rendre compte de l'histoire des équations d'état seraient très long et dépasserait largement le cadre de ce manuscrit, je vais cependant rappeler quelques points importants. Le lecteur intéressé par le sujet pourra cependant lire le chapitre II de BELKADI [2008].

Fondamentalement une équation d'état est une expression mathématique liant plusieurs fonctions d'état liées à la matière, comme par exemple la pression P ou le volume molaire V ; mais cela peut être aussi l'aimantation, le champ électrique appliqué, etc. Toutes les équations d'état ont un domaine d'application spécifique, il en existe de ce fait un très grand nombre. La première, et sans doute la plus connue, des équations d'état est celle des gaz parfaits :

$$\mathrm{P}\,v = \mathrm{R}\,\mathrm{T} \tag{2.22}$$

avec v le volume molaire et T la température absolue. Elle date du 17$^{\mathrm{e}}$ siècle et on la doit à Robert Boyle et Edme Mariotte. Cette équation fait l'hypothèse d'une énergie d'interaction nulle entre les molécules, elle n'est donc pas applicable aux états de la matière dense comme les liquides.

Les gaz, dit «réels» par opposition aux gaz parfaits (ou «idéaux» en anglais) prennent en compte l'interaction entre molécules. Un liquide peut être représenté par une équation valable pour un «gaz réel». Au milieu du 19$^{\mathrm{e}}$ siècle, Hirn et Van der Waals proposent un aménagement de l'équation d'état des gaz parfaits prenant en compte une forme d'interaction ainsi que le volume occupé par les molécules.

En 1873, Johannes Van der Waals montre que la «pression interne» d'un gaz est proportionnelle à $1/v^2$ (avec v le volume molaire), on a alors sa fameuse équation :

$$\left(\mathrm{P} + \frac{a}{v^2}\right)(v - b) = \mathrm{R}\,\mathrm{T} \tag{2.23}$$

qui en plus de mieux décrire les gaz, décrit aussi les liquides (au moins certains) et permet de prédire l'existence du point critique. C'est aussi, et c'est sans doute aussi important, un des éléments qui consolidera la théorie moléculaire de la matière. Au 19$^{\mathrm{e}}$ siècle, l'existence des molécules n'était pas admise par tous les scientifiques.
L'approche de Van der Waals a inspiré de nombreux travaux, donnant naissance à une famille d'équations d'état : les équations dites «cubiques». Parmi les plus célèbres de ces équations on citera : celle de Redlich et Kwong [REDLICH et KWONG, 1949], WILSON [1964], et PENG et ROBINSON

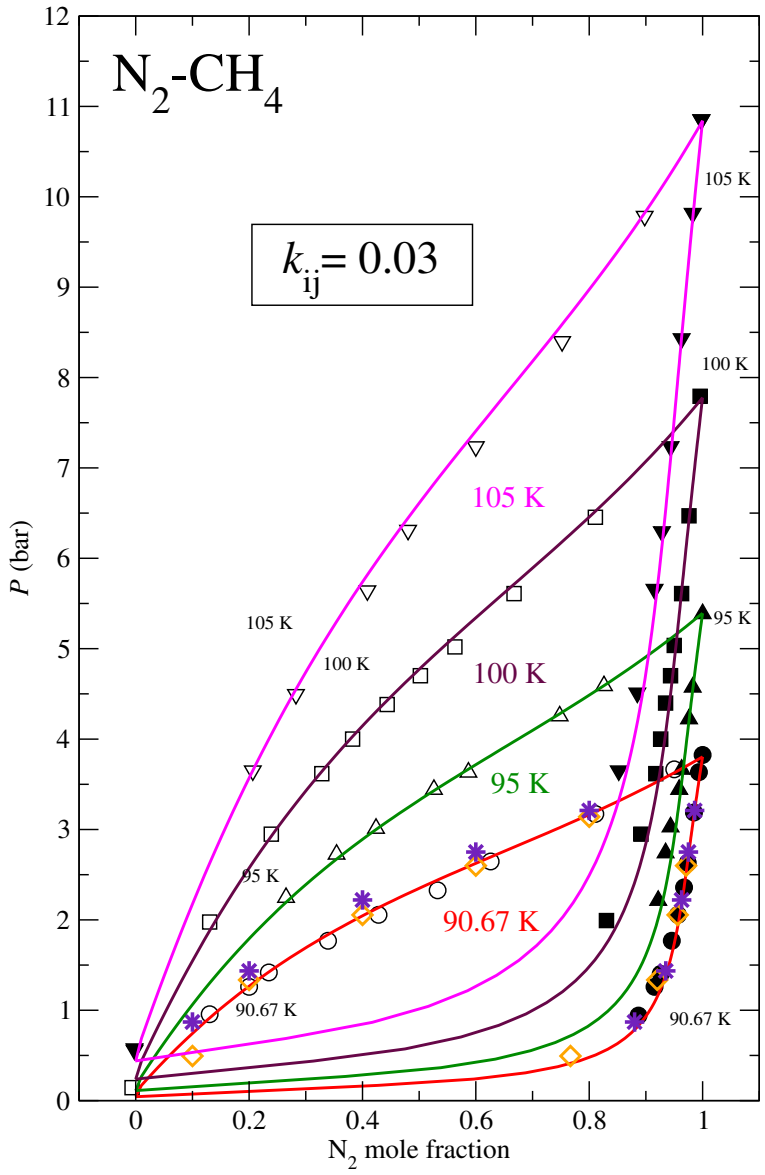

FIGURE 2.5 – Un exemple de comparaison entre les résultats de PC-SAFT (les différentes lignes) et des mesures de laboratoire. Le système est le binaire N_2–CH_4, les températures s'étalent de 90.67 K à 105 K. Pour ces équilibres liquide-valeur, le paramètre d'interaction pour le couple N_2–CH_4 est $k_{N_2-CH_4} = 0.03$.

[1976]. Toutes ces équations ont été largement utilisées dans l'industrie pétrochimique et au-delà de ce domaine.

Toutes ces équations donnent de bons résultats pour des molécules dont la forme n'est pas trop éloignée de la sphère. Pour certaines espèces, comme les polymères, on s'écarte largement de cette condition. La physique statistique a été le cadre de développements de nombreuses équations d'état, où le point de départ est le potentiel d'interaction intermoléculaire. Un des potentiels les plus utilisés étant le potentiel de Lennard-Jones.

L'équation SAFT (Statistical Association Fluid Theory) CHAPMAN et collab. [1990], puis PC-SAFT (Perturbed Chain-SAFT) par GROSS et SADOWSKI [2001] repose sur un traitement de physique statistique des molécules décrites comme des associations («chains») de sphères, un type de molécule est caractérisé par la donnée de trois paramètres : le nombre de segments m, les paramètres de Lennard-Jones σ (taille en Å d'un segment) et ϵ la profondeur du puits de potentiel d'un

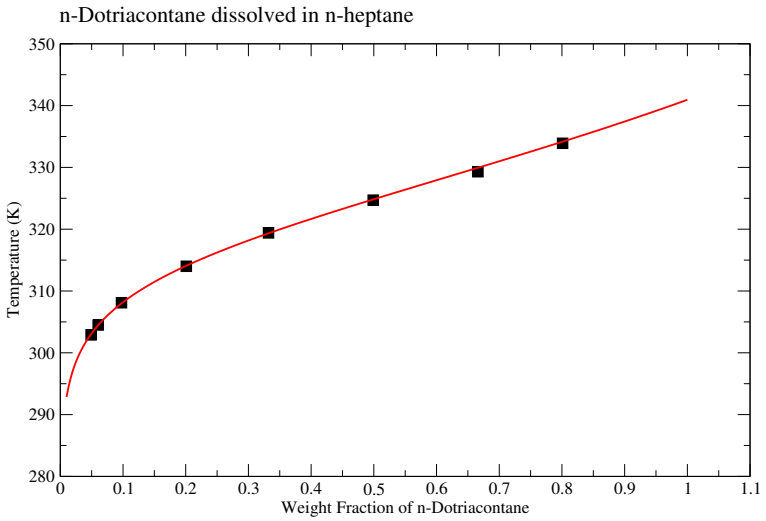

FIGURE 2.6 – Un exemple de résultat de dissolution d'un solide, ici la n-dotriacontane dans de l'heptane. La ligne rouge représente le calcul mené avec PC-SAFT, les carrés sont les données expérimentales. Pour chaque valeur de fraction massique de n-dotriacontane, la température à laquelle on a saturation de la solution est calculée grâce à PC-SAFT.

segment. De plus, pour les mélanges on doit faire intervenir un paramètre d'interaction k_{ij}. Tous les paramètres ont leurs valeurs déterminées par des ajustements sur des mesures de laboratoires, comme celles issues des diagrammes de phase. PC-SAFT étant une équation d'état, à P et T fixées on peut obtenir la masse volumique, l'activité d'une espèce dans le mélange, etc. PC-SAFT est très utilisée pour les applications industrielles du fait de ses très bonnes performances, quand les paramètres sont connus. Mon implémentation de PC-SAFT, à partir de l'article de GROSS et SADOWSKI [2001] représente environ 12 000 lignes de FORTRAN 2008, avec une écriture orientée objet, ce qui facilite son utilisation dans le cas d'une application à la chimie. Pour un équilibre liquide-vapeur, on écrira :

$$\Phi_i^{\mathrm{V}}(y_1,\ldots,y_{\mathrm{N}},\mathrm{P},\mathrm{T})\,y_i\,\mathrm{P} = \Phi_i^{\mathrm{L}}(x_1,\ldots,x_{\mathrm{N}},\mathrm{P},\mathrm{T})\,x_i\,\mathrm{P} \tag{2.24}$$

pour chaque espèce i. Les fractions molaires dans la phase vapeur sont les y_i, alors que dans le liquide elles sont notées x_i. Les cœfficients d'activité, donnés par PC-SAFT, sont respectivement Φ_i^{V} et Φ_i^{L} pour la phase vapeur et la phase liquide. Pour N espèces en présence, on a N équations de type (2.24) ; les inconnues variant suivant le type de problème traité. En général, les solutions sont cherchées avec un algorithme de Newton-Raphson. Un exemple de performance de PC-SAFT est fourni pour le système binaire N_2–CH_4, par la figure 2.5, on peut constater le bon accord entre modèle et les mesures de laboratoire. En résolvant une équation du type :

$$\ln\left(\frac{\Phi_2^{\mathrm{L}} x_2}{\Phi_2^0}\right) = -\frac{\Delta \mathrm{H}_{2,\mathrm{m}}}{\mathrm{R}\,\mathrm{T}_{2,\mathrm{m}}}\left(\frac{\mathrm{T}_{2,\mathrm{m}}}{\mathrm{T}} - 1\right) \tag{2.25}$$

d'un composé (2) dissout dans un solvant (1), on peut en déduire la solubilité x_2^{L} de l'espèce (2) dans le liquide en question. Les cœfficients d'activité sont Φ_2^{L} et Φ_2^0, ce dernier calculé pour l'espèce 2 seule. Un exemple de résultat, pour un équilibre solide-liquide, est donné pour la figure 2.6, où la température de dissolution du n-dotriacontane dans de l'heptane est reportée. Là encore un bon accord expérience-modèle peut être trouvé.

2.5.2 Quelques applications de PC-SAFT

Estimation de la composition d'Ontario Lacus à partir des taux d'évaporation

A l'Université d'Arkansas, une chambre d'expérimentation, dans laquelle l'évaporation de mélange N_2–CH_4–C_2H_6 peut être étudiée, a été développé. Ce projet a été mené par Vincent Chevrier,

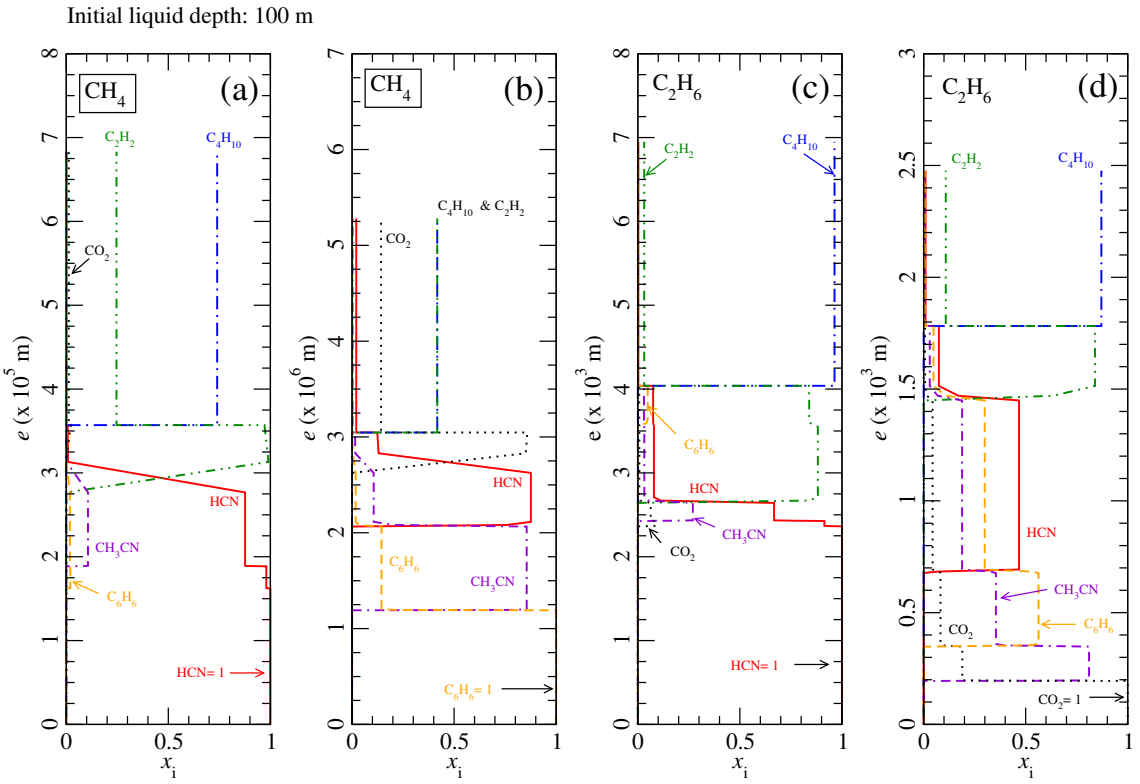

FIGURE 2.7 – Structure 1D des couches d'évaporites, calculée pour une profondeur initiale de liquide de 100 m. L'axe des ordonnées représente le hauteur e de dépôt au-dessus du substrat géologique, supposé insoluble. L'axe des abscisses montre la fraction molaire x_i des différentes espèces à une hauteur donnée. Deux types de solvants sont considérés : le méthane (panels (a) et (b)), et l'éthane (panels (c) et (d)). Pour les simulations reportées dans les panels (a) et (c), le mélange initial de solutés est construit proportionnellement à l'abondance de HCN, l'espèce la plus abondante dans les précipitations solides. La concentration initiale de HCN est fixée à sa valeur à saturation dans le solvant considéré. Les résultats correspondant aux simulations faisant l'hypothèse de concentrations initiales uniformes ont été utilisés dans les panels (b) et (d). La valeur de la concentration initiale a été fixée, dans ce cas, à celle de l'espèce la moins soluble.

et son étudiante d'alors Adrienn Luspay-Kuti, à l'encadrement de laquelle j'ai participé [LUSPAY-KUTI et collab., 2015] (voir page 121). Des taux d'évaporation E (kg m^{-2} s^{-1}) pouvait être mesuré en fonction de la composition du liquide. Sur le plan numérique, un taux d'évaporation théorique J pouvait être calculé grâce à [adapté de INGERSOLL, 1970] :

$$J = 0.17 D_{CH_4/N_2} \Delta\eta \left(\frac{\frac{\Delta\rho}{\rho_{surf}} g}{\nu^2} \right)^{1/3} \tag{2.26}$$

avec D_{CH_4/N_2} le cœfficient de diffusion de CH_4 (gaz) dans N_2 (gaz), $\Delta\eta = \rho_{CH_4,surf} - \rho_{CH_4,atm}$ le gradient de composition entre la surface du liquide et l'atmosphère ambiante, $\Delta\rho = \rho_{atm} - \rho_{surf}$ la différence de masse volumique entre le gaz ambiant et le liquide de la couche de contact. La gravité est notée g, alors que ν est la viscosité du méthane. Toutes les masses volumiques ρ_i sont ici calculées avec PC-SAFT.

Le calcul de J permet de faire le lien entre les taux d'évaporation expérimentaux E et la composition du liquide, car la quantité exacte de N_2 dissout n'était pas mesurée.

Une comparaison entre taux d'évaporation d'Ontario Lacus, estimé à 1 m y^{-1} par [HAYES et collab., 2011], a permis d'estimer une composition de celui-ci : entre 5 et 10% de CH_4, 50 à 80% de C_2H_6, et 5 à 10 de N_2 ; montrant ainsi un Ontario Lacus riche en éthane, comme suspecté par BROWN et collab. [2008].

La structure des dépôts évaporitiques

Par rapport au premier article sur les évaporites [CORDIER et collab., 2013] (voir page 79), PC-SAFT est utilisée dans CORDIER et collab. [2016] (voir page 86) en lieu et place de la RST. De plus, des calculs de chimie quantique (réalisés par Tangui Le Bahers, que j'ai eu, dans une autre vie, comme étudiant au CPI[2], à l'Ecole de Chimie de Rennes) ont confirmé les masses volumiques des différents solides organiques pris en compte, à savoir : HCN, C_4H_{10}, C_2H_2, CH_3CN, CO_2 et C_6H_6. Construit à partir de CORDIER et collab. [2013], le modèle permet alors d'obtenir la structure verticale des évaporites, ceci dans le cadre de différents scénarios. Cette structure permet également de prédire la composition des «bathtub rings» observés autours de certains lacs.

Les résultats de la structure ont été reporté sur la figure 2.7 [figure 5 de CORDIER et collab., 2016]. Comme on peut le constater, encore une fois C_2H_2 et C_4H_{10} dominent la composition de la surface, car ils sont les espèces les plus solubles. Les espèces les moins solubles, en particulier HCN sont enfouies. Concernant les «bathtub rings», suivant le scénario adopté, HCN (ou alternativement CO_2 ou C_6H_6) sont retrouvés sur les zones les plus périphériques des lits asséchés.
On a également montré que l'éthane, bien meilleur solvant que le méthane, permettait potentiellement d'atteindre des épaisseurs d'évaporites de plusieurs mètres à partir d'une colonne initiale de liquide de 100 m.

Un instrument pour un sous-marin

Dans CORDIER [2016] (voir page 161) je décris un concept d'instrument, principalement basé sur un tube de Kundt [KUNDT, 1866]. Ce tube autorise des mesures précises de la vitesse du son dans le fluide dont il est rempli. On peut imaginer un sous-marin explorant les profondeurs d'une mer de Titan, c'est ce qui a d'ailleurs été proposé par LORENZ et collab. [2015] et HARTWIG et collab. [2016]. On notera que *Huygens* était aussi équipé d'un système acoustique (API : Acoustic Properties Investigation).

PC-SAFT m'a permis de simuler le comportement d'un tel dispositif dans une mer de Titan. Je montre que la composition en N_2:CH_4:C_2H_6 pourrait être contrainte à une précision de l'ordre de 10% si 50 mesures de vitesse du son sont réalisées en faisant varier la température de 90 K à 100 K dans la cellule.

Des bulles dans les profondeurs de Ligeia Mare

Alors que les grandes mers de la région arctique de Titan semblent, aux RADAR, extrêmement lisses [GRIMA et collab., 2017; WYE et collab., 2009; ZEBKER et collab., 2014] ; des épisodes de surbrillance locale ont été plusieurs fois détectés par le RADAR [HOFGARTNER et collab., 2016, 2014]. Plusieurs idées peuvent être avancées pour expliquer ce genre de phénomène : vagues, sédiments en suspension ou des bulles. C'est cette dernière possibilité qu'on a exploré dans CORDIER et collab. [2017] (voir page 167).

Pour les mélanges ternaires N_2:CH_4:C_2H_6, il est connu depuis longtemps que, dans certaines conditions de température, de pression et de composition, le mélange peut démixer et se retrouver sous la forme de trois phases : deux liquides (de compositions différentes) et une vapeur [LU et collab., 1970]. Malheureusement les données de laboratoire disponibles correspondaient à des pressions supérieures à 4 bars, alors que les pressions attendues pour les profondeurs (100 à 200 m) de Ligeia Mare étaient au maximum de 3.3 bars.

A l'Institut Mexicain du Pétrole, Fernando García-Sánchez et Daimler Justo-García ont, à partir de PC-SAFT, réalisé une analyse en stabilité. Cette analyse permettait de déterminer les domaines de composition, pour P et T fixées, qui menaient à une séparation de phase. Les résultats sont

2. Cycle Préparatoire Intégré

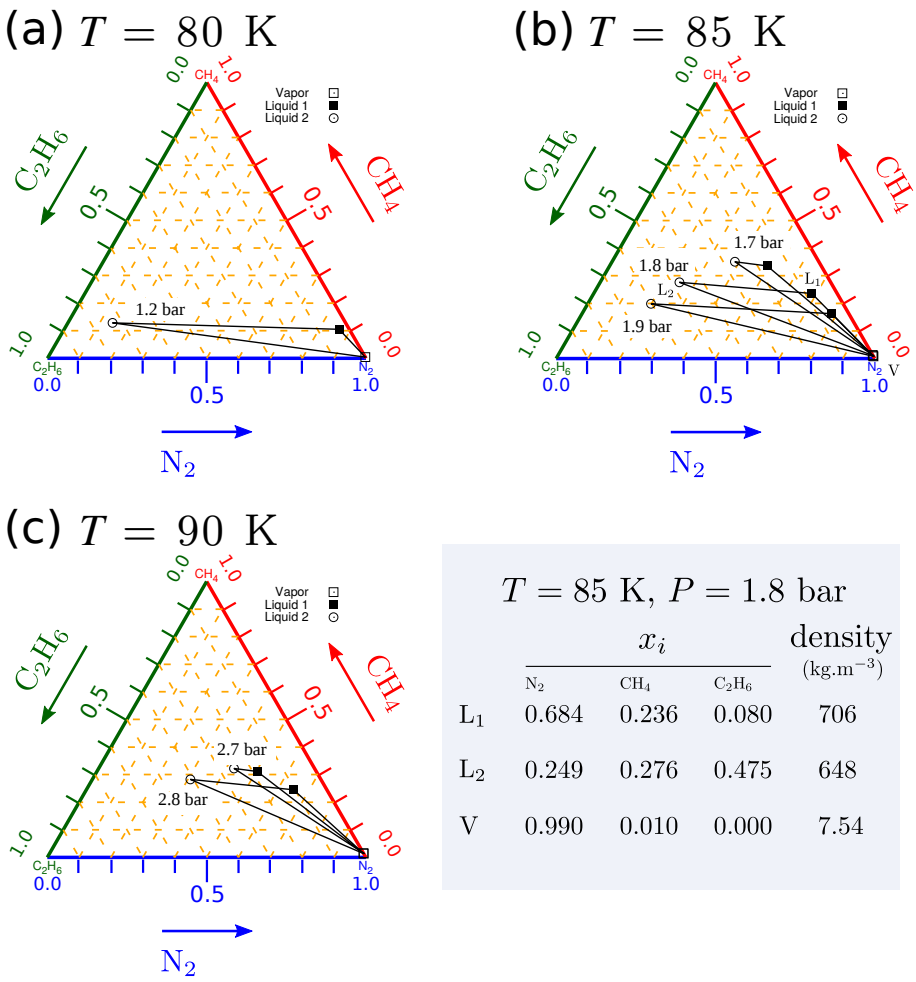

$T = 85$ K, $P = 1.8$ bar

	x_i			density ($kg.m^{-3}$)
	N_2	CH_4	C_2H_6	
L_1	0.684	0.236	0.080	706
L_2	0.249	0.276	0.475	648
V	0.990	0.010	0.000	7.54

FIGURE 2.8 – Les équilibres ternaires pour le système N_2:CH_4:C_2H_6, pour trois valeurs de pression : 80 K, 85 K et 90 K.

résumés sur la figure 2.8. Comme on peut le constater sur cette figure, pour des températures pertinentes (au fond de Ligeia Mare il peut faire plus froid qu'en surface) ; des équilibres liquide-liquide-vapeur peuvent apparaître à des pressions entre 2 et 3 bars, qu'on trouve dans les profondeurs de Ligeia Mare. Les événements TFL 1 et TFL 2 (comme on peut le voir sur la figure 2.9) correspondent à des endroits où Ligeia Mare est suffisamment profonde pour que des pressions de 2-3 bars puissent être atteintes. On peut donc imaginer des masses de fluide riches en CH_4 et N_2, initialement proches de la surface, rencontrer un liquide riche en C_2H_6 stagnant au fond. Ceci en lien avec les mouvements de circulation dans la mer. La condition d'avoir une composition, une pression et une température bien précise, correspond à un équilibre liquide–liquide–vapeur particulier, expliquerait l'aspect occasionnel du phénomène observé.

D'autres auteurs proposent un dégazage du N_2 par simple chauffage du liquide, la source du réchauffement restant inexpliquée [MALASKA et collab., 2017]. Dans CORDIER et LIGER-BELAIR [2018] (voir page 195) nous avons donc entrepris une discussion sur la nucléation et le croissance de bulles de N_2 dans Ligeia Mare. Il en ressort que la nucléation homogène est impossible, seule la nucléation hétérogène sur le lit de la mer offre une possibilité d'apparition de bulles de gaz.

De plus, dans ce même travail, nous avons montré que la rétro-diffusion d'une onde RADAR, par diffusion de Mie, sur une colonne de liquide remplie de bulles, nécessite une hauteur équivalente à la profondeur de Ligeia Mare pour reproduire les signaux observés. L'étude de CORDIER et LIGER-BELAIR [2018] favorise nettement les scénarios avec apparition de bulles en profondeur,

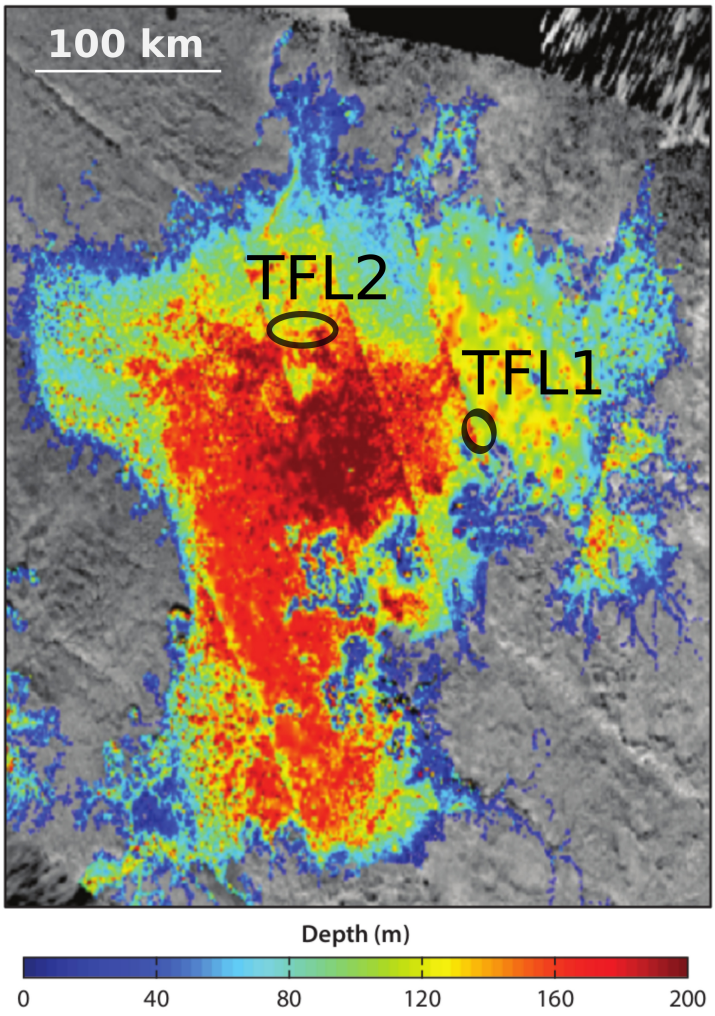

FIGURE 2.9 – Positions des deux événements de «transient feature» (TFL 1 et TFL 2) sur ligeia Mare, et comparaison avec la carte des profondeurs obtenues par HAYES [2016].

ceci grâce au mécanisme proposé par CORDIER et collab. [2017] ou simplement par échappement de gaz depuis les couches géologiques sous-jacents.

2.6 Références

ANREWS, T. 1869, «The Bakerian lecture : On the continuity of the gaseous and liquid states of matter», *Philos. Trans. Royal Soc.*, vol. 159, p. 575–590. 21

BARNES, J. W., J. BOW, J. SCHWARTZ, R. H. BROWN, J. M. SODERBLOM, A. G. HAYES, G. VIXIE, S. LE MOUÉLIC, S. RODRIGUEZ, C. SOTIN, R. JAUMANN, K. STEPHAN, L. A. SODERBLOM, R. N. CLARK, B. J. BURATTI, K. H. BAINES et P. D. NICHOLSON. 2011, «Organic sedimentary deposits in Titan's dry lakebeds : Probable evaporite», *Icarus*, vol. 216, doi: 10.1016/j.icarus.2011.08.022, p. 136–140. 26, 27

BELKADI, A. 2008, *Modélisation de la matière avec l'équation SAFT pour la prédiction des propriétés thermodynamiques des fluides complexes à travers SIMULIS THERMODYNAMICS*, thèse de doctorat, Université de Toulouse (France). 30

BROWN, R. H., L. A. SODERBLOM, J. M. SODERBLOM, R. N. CLARK, R. JAUMANN, J. W. BARNES, C. SOTIN, B. BURATTI, K. H. BAINES et P. D. NICHOLSON. 2008, «The identification of liquid

ethane in Titan's Ontario Lacus», *Nature*, vol. 454,
doi: 10.1038/nature07100, p. 607–610. 20, 33

CHAPMAN, W. G., K. E. GUBBINS, G. JACKSON et M. RADOSD. 1990, «New Reference Equation of State for Associating Liquids», *Ind. Eng. Chem. Res.*, vol. 29, p. 1709–1721. 31

CORDIER, D. 2016, «How speed-of-sound measurements could bring constraints on the composition of Titan's seas», *MNRAS*, vol. 459,
doi: 10.1093/mnras/stw732, p. 2008–2013. 34

CORDIER, D., J. W. BARNES et A. G. FERREIRA. 2013, «On the chemical composition of titan's dry lakebed evaporites», *Icarus*, vol. 226, nº 2,
doi: http://dx.doi.org/10.1016/j.icarus.2013.07.026, p. 1431 – 1437, ISSN 0019-1035. URL http://www.sciencedirect.com/science/article/pii/S0019103513003278. 27, 28, 34

CORDIER, D., T. CORNET, J. W. BARNES, S. M. MACKENZIE, T. LE BAHERS, D. NNA MVONDO et A. G. FERREIRA. 2016, «Structure of titan's evaporites», *Icarus*, vol. 270,
doi: 10.1016/j.icarus.2015.12.034, p. 41–56. 34

CORDIER, D., F. GARCÍA-SÁNCHEZ, D. N. JUSTO-GARCÍA et G. LIGER-BELAIR. 2017, «Bubble streams in Titan's seas as a product of liquid N_2 + CH_4 + C_2H_6 cryogenic mixture», *Nat. Astron.*, vol. 1,
doi: 10.1038/s41550-017-0102, 0102. 34, 36

CORDIER, D. et G. LIGER-BELAIR. 2018, «Bubbles in Titan's Seas : Nucleation, Growth, and RADAR Signature», *ApJ*, vol. 859, nº 1,
doi: 10.3847/1538-4357/aabc10, p. 26. URL http://stacks.iop.org/0004-637X/859/i=1/a=26. 35

CORDIER, D., O. MOUSIS, J. I. LUNINE, P. LAVVAS et V. VUITTON. 2009, «An Estimate of the Chemical Composition of Titan's Lakes», *ApJL*, vol. 707,
doi: 10.1088/0004-637X/707/2/L128, p. L128–L131. 23, 25, 30

CORDIER, D., O. MOUSIS, J. I. LUNINE, S. LEBONNOIS, P. LAVVAS, L. Q. LOBO et A. G. M. FERREIRA. 2010, «About the Possible Role of Hydrocarbon Lakes in the Origin of Titan's Noble Gas Atmospheric Depletion», *ApJL*, vol. 721,
doi: 10.1088/2041-8205/721/2/L117, p. L117–L120. 26

CORDIER, D., O. MOUSIS, J. I. LUNINE, S. LEBONNOIS, P. RANNOU, P. LAVVAS, L. Q. LOBO et A. G. M. FERREIRA. 2012, «Titan's lakes chemical composition : Sources of uncertainties and variability», *Planet. Space Sci.*, vol. 61,
doi: 10.1016/j.pss.2011.05.009, p. 99–107. 28, 29

CORNET, T., O. BOURGEOIS, S. LE MOUÉLIC, S. RODRIGUEZ, C. SOTIN, J. W. BARNES, R. H. BROWN, K. H. BAINES, B. J. BURATTI, R. N. CLARK et P. D. NICHOLSON. 2012, «Edge detection applied to Cassini images reveals no measurable displacement of Ontario Lacus' margin between 2005 and 2010», *J. Geophys. Res.*, vol. 117,
doi: 10.1029/2012JE004073, E07005. 26

CRESPIN, A., S. LEBONNOIS, S. VINATIER, B. BÉZARD, A. COUSTENIS, N. A. TEANBY, R. K. ACHTERBERG, P. RANNOU et F. HOURDIN. 2008, «Diagnostics of Titan's stratospheric dynamics using Cassini/CIRS data and the 2-dimensional IPSL circulation model», *Icarus*, vol. 197,
doi: 10.1016/j.icarus.2008.05.010, p. 556–571. 29

DUBOULOZ, N., F. RAULIN, E. LELLOUCH et D. GAUTIER. 1989, «Titan's hypothesized ocean properties - The influence of surface temperature and atmospheric composition uncertainties», *Icarus*, vol. 82,
doi: 10.1016/0019-1035(89)90025-0, p. 81–96. 20, 21, 22, 23, 24, 29, 30

GRIMA, C., M. MASTROGIUSEPPE, A. G. HAYES, S. D. WALL, R. D. LORENZ, J. D. HOFGARTNER, B. STILES, C. ELACHI et CASSINI RADAR TEAM. 2017, «Surface roughness of Titan's hydrocarbon seas», *Earth Planet. Sci. Lett.*, vol. 474,
doi: 10.1016/j.epsl.2017.06.007, p. 20–24. 34

GROSS, J. et G. SADOWSKI. 2001, «Perturbed-Chain SAFT : An Equation of State Based on a Perturbation Theory for Chain Molecules», *Ind. Eng. Chem. Res.*, vol. 40, doi: 10.1021/ie0003887, p. 1244–1260. 30, 31, 32

HARTWIG, J. W., A. COLOZZA, R. D. LORENZ, S. OLESON, G. LANDIS, P. SCHMITZ, M. PAUL et J. WALSH. 2016, «Exploring the depths of Kraken Mare - Power, thermal analysis, and ballast control for the Saturn Titan submarine», *Cryogenics*, vol. 74, doi: 10.1016/j.cryogenics.2015.09.009, p. 31–46. 34

HAYES, A. G. 2016, «The Lakes and Seas of Titan», *Annu. Rev. Earth Planet. Sci.*, vol. 44, doi: 10.1146/annurev-earth-060115-012247, p. 57–83. 36

HAYES, A. G., O. AHARONSON, J. I. LUNINE, R. L. KIRK, H. A. ZEBKER, L. C. WYE, R. D. LORENZ, E. P. TURTLE, P. PAILLOU, G. MITRI, S. D. WALL, E. R. STOFAN, K. L. MITCHELL et C. ELACHI. 2011, «Transient surface liquid in Titan's polar regions from Cassini», *Icarus*, vol. 211, doi: 10.1016/j.icarus.2010.08.017, p. 655–671. 33

HIDEBRAND, J. H. 1936, *The Solubility of Non-Electrolytes*, Reinhold, New York, USA. 23

HOFGARTNER, J. D., A. G. HAYES, J. I. LUNINE, H. ZEBKER, R. D. LORENZ, M. J. MALASKA, M. MASTROGIUSEPPE, C. NOTARNICOLA et J. M. SODERBLOM. 2016, «Titan's "Magic Islands" : Transient features in a hydrocarbon sea», *Icarus*, vol. 271, doi: 10.1016/j.icarus.2016.02.022, p. 338–349. 34

HOFGARTNER, J. D., A. G. HAYES, J. I. LUNINE, H. ZEBKER, B. W. STILES, C. SOTIN, J. W. BARNES, E. P. TURTLE, K. H. BAINES, R. H. BROWN, B. J. BURATTI, R. N. CLARCK, P. ENCRENAZ, R. D. KIRK, A. LE GALL, R. M. LOPES, R. D. LORENZ, M. J. MALASKA, K. L. MITCHELL, P. NICHOLSON, P. D. PAILLOU, J. RADEBAUGH, S. D. WALL et C. WOOD. 2014, «Transient features in a Titan sea», *Nat. Geosci.*, vol. 7, doi: 10.1038/NGEO2190, p. 493–496. 34

INGERSOLL, A. P. 1970, «Mars : Occurrence of Liquid Water», *Science*, vol. 168, doi: 10.1126/science.168.3934.972, p. 972–973. 33

JACOVI, R. et A. BAR-NUN. 2008, «Removal of Titan's noble gases by their trapping in its haze», *Icarus*, vol. 196, doi: 10.1016/j.icarus.2008.02.014, p. 302–304. 26

JENNINGS, D. E., V. COTTINI, C. A. NIXON, R. K. ACHTERBERG, F. M. FLASAR, V. G. KUNDE, P. N. ROMANI, R. E. SAMUELSON, A. MAMOUTKINE, N. J. P. GORIUS, A. COUSTENIS et T. TOKANO. 2016, «Surface Temperatures on Titan during Northern Winter and Spring», vol. 816, doi: 10.3847/2041-8205/816/1/L17, L17. 24

JENNINGS, D. E., F. M. FLASAR, V. G. KUNDE, R. E. SAMUELSON, J. C. PEARL, C. A. NIXON, R. C. CARLSON, A. A. MAMOUTKINE, J. C. BRASUNAS, E. GUANDIQUE, R. K. ACHTERBERG, G. L. BJORAKER, P. N. ROMANI, M. E. SEGURA, S. A. ALBRIGHT, M. H. ELLIOTT, J. S. TINGLEY, S. CALCUTT, A. COUSTENIS et R. COURTIN. 2009, «Titan's Surface Brightness Temperatures», *ApJL*, vol. 691, doi: 10.1088/0004-637X/691/2/L103, p. L103–L105. 24

KRASNOPOLSKY, V. A. 2009, «A photochemical model of Titan's atmosphere and ionosphere», *Icarus*, vol. 201, doi: 10.1016/j.icarus.2008.12.038, p. 226–256. 28

KRASNOPOLSKY, V. A. 2010, «The photochemical model of Titan's atmosphere and ionosphere : A version without hydrodynamic escape», *Planet. Space Sci.*, vol. 58, doi: 10.1016/j.pss.2010.07.010, p. 1507–1515. 28

KRASNOPOLSKY, V. A. 2014, «Chemical composition of Titan's atmosphere and ionosphere : Observations and the photochemical model», *Icarus*, vol. 236, doi: 10.1016/j.icarus.2014.03.041, p. 83–91. 28

KUNDT, A. 1866, «Ueber eine neue Art Akustischer Staubfiguren und über die Anwendung derselben zur Bestimmung der Shallgeschwindigkeit in festen Körpern und Gasen», *Annalen der Physik*, vol. 127, p. 497–523. 34

LAVVAS, P. P., A. COUSTENIS et I. M. VARDAVAS. 2008a, «Coupling photochemistry with haze formation in Titan's atmosphere, Part I : Model description», *Planet. Space Sci.*, vol. 56, doi: 10.1016/j.pss.2007.05.026, p. 27–66. 24, 27, 28

LAVVAS, P. P., A. COUSTENIS et I. M. VARDAVAS. 2008b, «Coupling photochemistry with haze formation in Titan's atmosphere, Part II : Results and validation with Cassini/Huygens data», *Planet. Space Sci.*, vol. 56, doi: 10.1016/j.pss.2007.05.027, p. 67–99. 24, 27, 28

LODDERS, K. 2003, «Solar System Abundances and Condensation Temperatures of the Elements», *ApJ*, vol. 591, doi: 10.1086/375492, p. 1220–1247. 25

LORENZ, R. D., S. OLESON, J. WOYTACH, R. JONES, A. COLOZZA, P. SCHMITZ, G. LANDIS, M. PAUL et J. WALSH. 2015, «Titan Submarine : Vehicle Design and Operations Concept for the Exploration of the Hydrocarbon Seas of Saturn's Giant Moon», dans *Lunar and Planetary Science Conference*, *Lunar and Planetary Inst. Technical Report*, vol. 46, p. 1259. 34

LU, B. C. Y., P. YU et D. P. L. POON. 1970, «Liquid phase inversion», *Nature*, vol. 225, p. 1128–1129. 34

LUNINE, J. I. 2010, «Titan and habitable planets around M-dwarfs», *Farad. Discuss.*, vol. 147, doi: 10.1039/c004788k, p. 405–418. 24

LUSPAY-KUTI, A., V. F. CHEVRIER, D. CORDIER, E. G. RIVERA-VALENTIN, S. SINGH, A. WAGNER et F. C. WASIAK. 2015, «Experimental Constraints on the Composition and Dynamics of Titan's Polar Lakes», *EPSL*, vol. 410C, p. 75–83. 33

MALASKA, M. J., R. HODYSS, J. I. LUNINE, A. G. HAYES, J. D. HOFGARTNER, G. HOLLYDAY et R. D. LORENZ. 2017, « Laboratory measurements of nitrogen dissolution in Titan lake fluids», *Icarus*, vol. 289, doi: 10.1016/j.icarus.2017.01.033, p. 94–105. 35

NIEMANN, H. B., S. K. ATREYA, S. J. BAUER, G. R. CARIGNAN, J. E. DEMICK, R. L. FROST, D. GAUTIER, J. A. HABERMAN, D. N. HARPOLD, D. M. HUNTEN, G. ISRAEL, J. I. LUNINE, W. T. KASPRZAK, T. C. OWEN, M. PAULKOVICH, F. RAULIN, E. RAAEN et S. H. WAY. 2005, «The abundances of constituents of Titan's atmosphere from the GCMS instrument on the Huygens probe», *Nature*, vol. 438, doi: 10.1038/nature04122, p. 779–784. 23, 24

OSEGOVIC, J. P. et M. D. MAX. 2005, «Compound clathrate hydrate on Titan's surface», *J. Geophys. Res.*, vol. 110, doi: 10.1029/2005JE002435, E08004. 26

PENG, D. Y. et D. B. ROBINSON. 1976, *Ind. Eng. Chem. Fundam.*, vol. 15, p. 59. 30

POLING, B. E., J. M. PRAUSNITZ et J. O'CONNELL. 2007, *The Properties of Gases and Liquids*, 5e éd., McGraw-Hill Professional, Englewood Cliffs. 21, 22

PONCET, S. et L. DAHLBERG. 2011, «The legacy of Henri Victor Regnault in the arts and sciences», *International Journal of Arts and Sciences*, vol. 4, no 13, p. 377–400. URL https://hal.archives-ouvertes.fr/hal-00678894. 21

PRESS, W., S. TEUKOLSKY, W. VETTERLING et B. FLANNERY. 1992, *Numerical Recipes in Fortran 77*, Cambridge University Press. 24

REDLICH, O. et J. N. S. KWONG. 1949, «On the Thermodynamics of Solutions. V. An Equation of State. Fugacities of Gaseous Solutions.», *Chem. Rev.*, vol. 44, no 1, doi: 10.1021/cr60137a013, p. 233–244. 30

REGNAULT, H. V. 1842, «Recherches sur la dilatation des gaz», *Ann. chem. phys*, vol. 4, p. 4–67. 21

ROUSSET, A. et J. SIX, éd.. 2000, *Des physiciens de A à Z*, Ellipses, Paris, France. 20

SCHULZE-MAKUCH, D. et D. H. GRINSPOON. 2005, «Biologically Enhanced Energy and Carbon Cylcing on Titan ?», *Astrobiology*, vol. 5, p. 560–567. 24

STOFAN, E. R., C. ELACHI, J. I. LUNINE, R. D. LORENZ, B. STILES, K. L. MITCHELL, S. OSTRO, L. SODERBLOM, C. WOOD, H. ZEBKER, S. WALL, M. JANSSEN, R. KIRK, R. LOPES, F. PAGANELLI, J. RADEBAUGH, L. WYE, Y. ANDERSON, M. ALLISON, R. BOEHMER, P. CALLAHAN, P. ENCRENAZ, E. FLAMINI, G. FRANCESCETTI, Y. GIM, G. HAMILTON, S. HENSLEY, W. T. K. JOHNSON, K. KELLEHER, D. MUHLEMAN, P. PAILLOU, G. PICARDI, F. POSA, L. ROTH, R. SEU, S. SHAFFER, S. VETRELLA et R. WEST. 2007, «The lakes of Titan», *Nature*, vol. 445, doi: 10.1038/nature05438, p. 61–64. 26

TAN, S. P., J. S. KARGEL et G. M. MARION. 2013, «Titan's atmosphere and surface liquid : New calculation using Statistical Associating Fluid Theory», *Icarus*, vol. 222, doi: 10.1016/j.icarus.2012.10.032, p. 53–72. 29, 30

TURTLE, E. P., J. E. PERRY, A. G. HAYES, R. D. LORENZ, J. W. BARNES, A. S. MCEWEN, R. A. WEST, A. D. DEL GENIO, J. M. BARBARA, J. I. LUNINE, E. L. SCHALLER, T. L. RAY, R. M. C. LOPES et E. R. STOFAN. 2011a, «Rapid and Extensive Surface Changes Near Titan's Equator : Evidence of April Showers», *Science*, vol. 331, doi: 10.1126/science.1201063, p. 1414–1417. 26

TURTLE, E. P., J. E. PERRY, A. G. HAYES et A. S. MCEWEN. 2011b, «Shoreline retreat at Titan's Ontario Lacus and Arrakis Planitia from Cassini Imaging Science Subsystem observations», *Icarus*, vol. 212, doi: 10.1016/j.icarus.2011.02.005, p. 957–959. 26

VUITTON, V., R. V. YELLE et J. CUI. 2008, «Formation and distribution of benzene on Titan», *Journal of Geophysical Research (Planets)*, vol. 113, doi: 10.1029/2007JE002997, p. 5007–+. 27

WILSON, G. M. 1964, «Vapor–Liquid Equilibrium. XI. A New Expression for the Excess Free Energy of Mixing», *J. Am. Chem. Soc.*, vol. 86, p. 127–130. 30

WYE, L. C., H. A. ZEBKER et R. D. LORENZ. 2009, «Smoothness of Titan's Ontario Lacus : Constraints from Cassini RADAR specular reflection data», *Geophys. Res. Lett.*, vol. 36, doi: 10.1029/2009GL039588, L16201. 34

ZEBKER, H., A. HAYES, M. JANSSEN, A. LE GALL, R. LORENZ et L. WYE. 2014, «Surface of Ligeia Mare, Titan, from Cassini altimeter and radiometer analysis», *Geophys. Res. Lett.*, vol. 41, doi: 10.1002/2013GL058877, p. 308–313. 34

Chapitre 3

Surfaces planétaires : projet scientifique

Sommaire

3.1 Les gradients verticaux de composition chimique 41
3.1.1 L'alcanofère de Titan 41
3.1.2 L'atmosphère profonde de Vénus 44
3.2 Modélisation des écoulements et/ou du cryovolcanisme 46
3.3 Caractérisation de la surface de Titan 47
3.3.1 Exploitation des données VIMS 47
3.3.2 Exploitation des données ISS 48
3.4 Références 50

Très concentré sur la surface de Titan, je souhaiterais, dans les années à venir, diversifier mon champ d'action. Dans ce chapitre, je propose quelques pistes que je pourrais suivre pour développer mon activité dans ce domaine. Certaines sont déjà en cours d'exploration, quand d'autres demandent un travail sur un moyen ou long terme.

3.1 Les gradients verticaux de composition chimique

3.1.1 L'alcanofère de Titan

Deux articles récents [Corlies et collab., 2017; Hayes et collab., 2017] suggèrent, à partir des dernières observations RADAR de Cassini, qu'il pourrait exister un «alcanofère» reliant souterrainement certaines mers, ou lacs, du pôle nord de Titan. Des études antérieures [Mousis et collab., 2014] au sujet de ce possible «alcanofère» ont été menées, en lien avec l'éventuelle clathration de l'éthane. Cette espèce pose d'ailleurs problème, car sa production par la photochimie, depuis la formation de Titan, représente une quantité totale de matière correspondant à un océan global d'une profondeur de l'ordre de ~ 160 m [Atreya et collab., 2006; Mousis et Schmitt, 2008]. La question du devenir de cette quantité d'éthane est donc intéressante, comme manifestement l'océan global n'existe pas, ou plus.

Sur Terre, les gisements d'hydrocarbures, piégés dans des milieux poreux que sont les roches mères, présentent d'importants gradients verticaux de composition [voir par exemple Obidi, 2014]. Ces gradients se mettent en place au cours des temps géologiques grâce à la diffusion moléculaire. De nombreux modèles numériques existent, je travaille actuellement à la mise au point d'un tel modèle pour l'alcanofère de Titan. Ceci pour savoir comment l'éthane se comporte dans un alcanofère formé d'un mélange N_2:CH_4:C_2H_6 sous la gravité titanienne.

De façon général, une espèce (1) peut être transportée par diffusion, dans un milieu contenant l'espèce (2), avec un flux de matière $\overrightarrow{J_1}$ donné par [Bird et collab., 1960; Ghorayeb et Firooza-

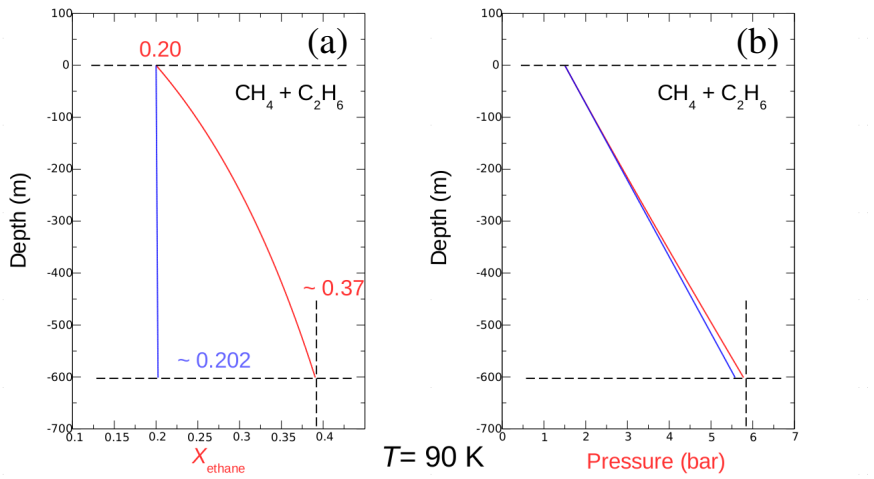

FIGURE 3.1 – (a) La fraction molaire d'éthane en fonction de la profondeur dans un alcanofère. En rouge : le modèle semi-idéal, en bleu : le modèle non-idéal basé sur PC-SAFT. (b) Les variation de pression correspondantes. Pour tous ces modèles la température est uniforme et vaut 90 K.

BADI, 2000] :

$$\vec{J_1} = -\rho D_{12} \frac{M_1 M_2}{\bar{M}^2} \left\{ \left.\frac{\partial \ln f_1}{\partial \ln x_1}\right|_{P,T} \vec{\nabla} x_1 + \frac{x_1}{RT}\left(\bar{V}_1 - \frac{M_1}{\rho}\right)\vec{\nabla} P + \frac{k_{T\,1,2}}{T}\vec{\nabla} T \right\} \tag{3.1}$$

avec M_1, M_2 et $\bar{M}$ respectivement la masse molaire (kg mol^{-1}) de (1), de (2) et la masse molaire moyenne. La masse volumique est notée ρ (kg m^{-3}), D_{12} est le cœfficient de diffusion de (1) dans (2) (m^2 s^{-1}), f_1 est la fugacité de (1), x_1 sa fraction molaire, R est la constante des gaz parfaits et T la température absolue, $\bar{V}_1$ représente le volume molaire partiel de (1) :

$$\bar{V}_1 = \frac{RT}{P}\left\{1 + P \left.\frac{\partial \ln \Phi_1}{\partial P}\right|_{T,\{x_{i\neq 1}\}}\right\} \tag{3.2}$$

avec Φ_1 le cœfficient de fugacité de (1). La dérivée de la fugacité est, elle, donnée par :

$$\left.\frac{\partial \ln f_1}{\partial \ln x_1}\right|_{P,T} = 1 + \left.\frac{\partial \ln \Phi_1}{\partial \ln x_1}\right|_{P,T} \tag{3.3}$$

Φ_1 étant obtenu grâce à une équation d'état appropriée, PC-SAFT dans le cas des hydrocarbures liquides de Titan. Le cœfficient $k_{T,12}$ est le *thermal diffusion ratio*, il s'exprime généralement en fonction de $\alpha_{T,12}$ le *thermal diffusion coefficient* :

$$k_{T,12} = \alpha_{T,12}\, x_1\, (1 - x_1) \tag{3.4}$$

où $\alpha_{T,12}$ dépend de la masse et de la taille des molécules, de la température, de la composition du mélange et des interactions intermoléculaires. Ce cœfficient peut être positif ou négatif, en général il n'est pas très bien connu.
De manière assez lisible, le membre de droite de l'équation (3.1) contient trois termes correspondant respectivement à trois phénomènes physiques différents, de gauche à droite on a : la diffusion moléculaire fickéenne, la barodiffusion causée par un gradient de pression, et finalement la thermodiffusion présente lorsque le système est le siège d'un gradient de température. Dans le cas général, ces trois effets se combinent.

Dans le cas de l'équilibre, pour un système idéal (la dérivée de la fugacité vaut alors 1) l'équation (3.1) devient :

$$\frac{\partial x_1}{\partial z} = -\frac{x_1}{P}\left(1 - \frac{M_1}{\bar{M}}\right)\frac{\partial P}{\partial z} - \frac{\alpha_{T\,1,2}}{T}\, x_1 (1 - x_1)\frac{\partial T}{\partial z} \tag{3.5}$$

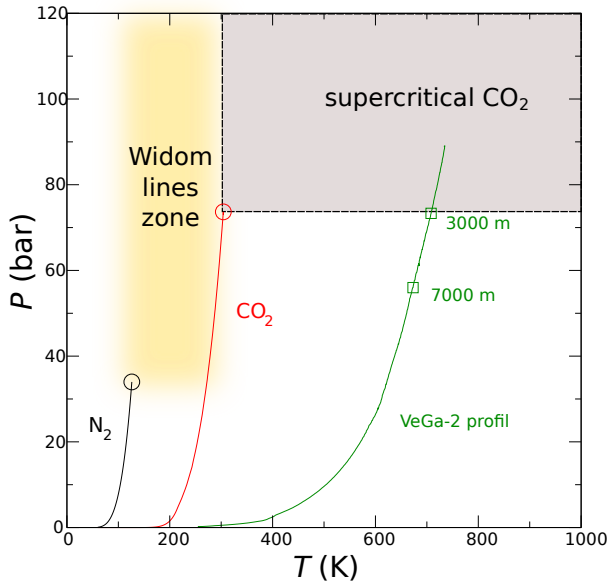

FIGURE 3.2 – Diagramme de phase simplifié du CO_2. La position du point critique est indiquée par un cercle rouge, ainsi que celle du point correspondant pour N_2. L'introduction d'un peu de N_2 dans CO_2 décale légèrement le point critique du mélange de quelques bar et quelques kelvins [GOOS et collab., 2011]. Le lignes verte et bleue se réfèrent respectivement aux profils P – T de l'atmosphère de Vénus obtenus grâce à des simulations de GCM[a] [LEBONNOIS et SCHUBERT, 2017] ou aux mesures *in situ* effectuées par la sonde VeGa-1 [LORENZ et collab., 2018].

[a] Global Circulation Model.

Si dans une première approche on considère un système à la température uniforme, on a alors à intégrer le système :

$$\frac{\partial x_1}{\partial z} = -\frac{x_1}{\mathrm{P}}\left(1-\frac{\mathrm{M}_1}{\bar{\mathrm{M}}}\right)\rho g_{\mathrm{Tit}} \tag{3.6}$$

$$\frac{\partial \mathrm{P}}{\partial z} = -\rho g_{\mathrm{Tit}} \tag{3.7}$$

si cependant on évalue ρ avec PC-SAFT on a un modèle «semi-idéal», dont les résultats, après intégration, sont présentés par les courbes rouges de la Fig. 3.1. Comme on le voit, dans le cadre de ce premier modèle, on obtient sur une hauteur totale de 600 m, un gradient d'abondance en éthane non-négligeable. La fraction molaire de C_2H_6 passant de 0.20 (valeur arbitraire mais plausible) à la surface, à presque le double en profondeur avec 0.37. Examinons maintenant un cas non-idéal où la dérivée de la fugacité est prise en compte :

$$\left.\frac{\partial \ln f_1}{\partial \ln x_1}\right|_{\mathrm{P,T}} \frac{\partial x_1}{\partial z} = -\frac{x_1}{\mathrm{P}}\left(1-\frac{\mathrm{M}_1}{\bar{\mathrm{M}}}\right)\rho g_{\mathrm{Tit}} \tag{3.8}$$

Les résultats sont représentés sur la Fig. 3.1 par les lignes bleues. Cette fois-ci, le gradient de composition chimique disparaît presque complètement. Ces simulations, encore très préliminaires et qui demandent donc à être confirmées, tendent à montrer que l'éthane ne peut pas être séquestré dans les parties basses de l'alcanofère titanien. Il reste bien sûr à évaluer l'effet d'un éventuel gradient géophysique de température.

Dans le même travail, je pourrai répondre à la question : en combien de temps une couche de méthane liquide, posée sur une autre, composée uniquement d'éthane, met pour atteindre un mélange complet. Cette question, que m'a posée par Michael Malaska à la suite de ma présentation au Workshop Titan's surface en mai 2018 à l'Université de Cornell, correspond à un dépôt de méthane consécutif à une averse. Sur le plan de la physique, pour traiter cette question, il suffit de

combiner l'équation de continuité à l'équation (3.1) donnant le flux $\overrightarrow{J_1}$. L'algorithme numérique, nécessaire à l'intégration de l'équation, est très similaire à celui, basé sur des différences finies, et développé pour le modèle de disque protoplanétaire décrit au chapitre 7.

3.1.2 L'atmosphère profonde de Vénus

Une problématique voisine, de celle décrite dans la section précédente, concerne les couches profondes de l'atmosphère de Vénus. En effet, LEBONNOIS et SCHUBERT [2017] ont montré qu'il existait probablement un gradient de N_2 dans les toutes premières couches de cette atmosphère composée essentiellement de CO_2. Ce dernier, dans le domaine supercritique aux altitudes considérées (voir Fig. 3.2), pourrait présenter des propriétés extraordinaires comme l'ont suggéré les expériences de HENDRY et collab. [2013] et ESPANANI et collab. [2016]. Ces résultats, aujourd'hui remis en cause (F. García-Sánchez et S. Lebonnois, communications privées), semblaient montrer une séparation de N_2 et CO_2 lorsque le mélange était porté en conditions supercritiques. On pouvait donc se poser légitimement la question d'un effet, amplifié par la supercriticité, d'une stratification engendrée par la diffusion moléculaire, ceci pendant une période où la convection est absente.
J'ai donc repris l'approche utilisée pour les gisements d'hydrocarbures terrestres et déjà appliquée dans le paragraphe 3.1.1 au sujet de l'alcanofère de Titan. Dans un premier temps un calcul basé sur l'équation d'état des gaz parfaits a permis de trouver un gradient d'abondance en CO_2 de l'ordre de 0.6 ppm, au lieu des ~ 5 ppm avancés par LEBONNOIS et SCHUBERT [2017]. Le cas non-idéal a été traité en utilisant l'équation d'état de [DUAN et collab., 1996], développée spécifiquement pour les mélanges en conditions supercritiques. Sachant que la dérivée $\partial \ln f_1 / \partial \ln x_1$ tend vers 0 lorsqu'on s'approche du point critique, un espoir était permis d'avoir le gradient en CO_2, *i.e.* $\partial x_1 / \partial z$ (voir Eq. 3.8) prendre une valeur très grande. Malheureusement, les calculs montrent que, le long du profil en pression et température de Vénus (voir Fig. 3.2), le terme en dérivée de la fugacité reste proche de l'unité, laissant le gradient de composition chimique très proche de celui déduit dans le cas d'un gaz parfait.

Alors que ces calculs de gradient ont été menés dans le cadre de l'équilibre thermodynamique, on doit se poser la question de la cinétique du processus, *i.e.* la question de l'échelle de temps requise pour atteindre l'équilibre. Dans leur article, LEBONNOIS et SCHUBERT [2017] indiquent que le temps de mélange dynamique τ_{dyn} des couches profondes est de l'ordre de 20 jours [1] de Vénus, soit $\tau_{dyn} \sim 4.2 \times 10^8$ s. Le temps de séparation de CO_2 et N_2 doit donc être plus court que cette valeur de τ_{dyn}. L'échelle de temps liée aux phénomènes de diffusion τ_{diff} peut être évaluée avec une expression du type :

$$\tau_{diff} \sim \frac{H^2}{D} \tag{3.9}$$

avec H la distance sur laquelle la diffusion a lieu, et D le cœfficient de diffusion. Pour évaluer le cœfficient d'auto-diffusion du CO_2 supercritique on peut utiliser la formule de Wilke-Chang [WILKE et CHANG, 1955] :

$$D_{CO_2,sp} \simeq 7.4 \times 10^{-15} \frac{TM_s^{1/2}}{\eta_{CO_2,sp} V_{eb}^{0.6}} \tag{3.10}$$

on obtient alors $D_{CO_2,sp} \sim 10^{-7}$ m^2 s^{-1}. Ce qui, pour une atmosphère profonde d'une épaisseur de $H \sim 7000$ m [LEBONNOIS et SCHUBERT, 2017], correspond à une échelle de temps de diffusion de l'ordre de $\tau_{diff} \sim 10^{14}$ s, largement supérieure à τ_{dyn}. Il y a là un argument supplémentaire, clairement en défaveur d'une origine «diffusive» du possible gradient de composition de l'atmosphère vénusienne. Les expériences de laboratoires de HENDRY et collab. [2013] et ESPANANI et collab. [2016] semblaient montrer des temps de séparation très courts, *i.e.* de l'ordre de quelques dizaines de secondes. Ces durées suggéraient l'existence d'un phénomène hydrodynamique, donc macroscopique ; et non pas microscopique comme les phénomènes diffusifs discutés ci-avant. Cepen-

1. La période de rotation propre de Vénus vaut 243.0187 jours terrestres.

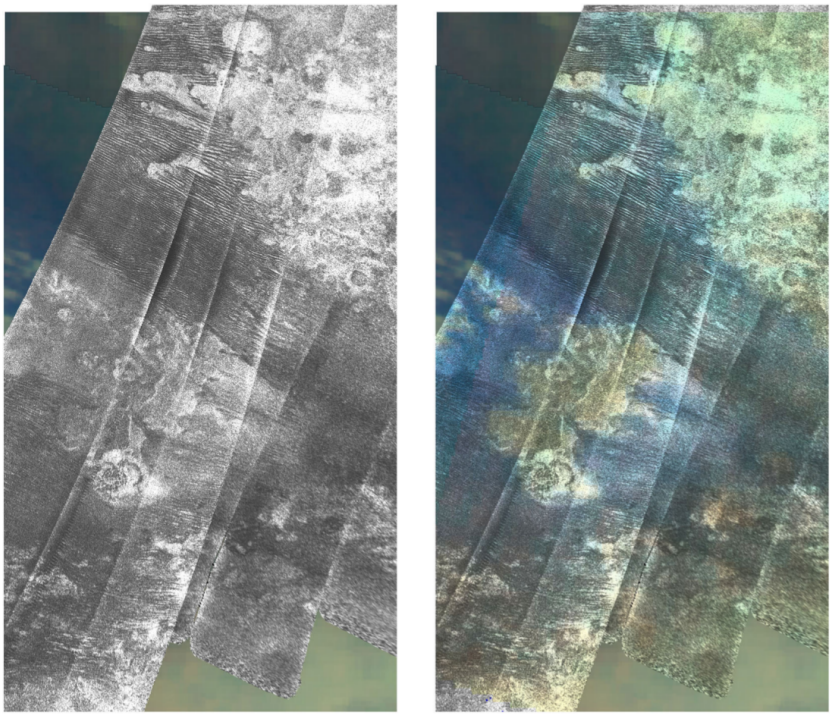

FIGURE 3.3 – Combinaison de données RADAR (SAR) et VIMS du candidat cryovolcan Sotra Patera, repris sur la Fig. 8 de LOPES et collab. [2013].

dant, comme déjà mentionné, ces résultats expérimentaux sont critiquables du fait du protocole mis en œuvre (F. García-Sánchez, communication privée), et de récentes expériences menées au *NASA Glenn Research Center* à Cleveland (USA) ont montré que les résultats de HENDRY et collab. [2013] ne sont reproductibles que si N_2 et CO_2 sont introduits séparément dans la chambre expérimentale. Lorsque que ces deux espèces sont au préalable bien mélangées, aucune séparation ne se produit sur le temps de l'expérience (S. Lebonnois, communication privée, août 2018). Cependant, et de façon très intéressante, lorsque N_2 et CO_2 sont introduits séparément, leur séparation reste stable, ce qui suggère leur difficulté à se mélanger.

Sur le plan théorique, des comportements exotiques du CO_2 supercritique ont été mis en évidence par les simulations de dynamique moléculaire de BOLMATOV et collab. [2013], BRAZHKIN et collab. [2013] et BOLMATOV et collab. [2014]. Dans un état supercritique, le CO_2, seul, semble former, au niveau moléculaire, des agrégats. Une transposition aux mélanges binaires CO_2:N_2 pourrait laisser penser qu'il serait possible d'avoir un phénomène analogue, mais cette fois avec formation de deux types d'agrégats : l'un riche en azote, l'autre pauvre. Les expériences faites au *NASA Glenn Research Center* semblent aller à l'encontre de ce type de processus. Cependant, afin d'éclaircir les choses sur cet aspect, ainsi que sur celui de la pauvre miscibilité apparente de CO_2 et N_2 dans le domaine supercritique, j'ai entrepris une collaboration avec David Bonhommeau, spécialiste de dynamique moléculaire au GSMA.

Au moment où j'écris ces lignes (22 août 2018), le scénario que je souhaite tester est celui d'un dégazage du sous-sol vénusien, produisant un enrichissement en CO_2 de la basse atmosphère, à la faveur de la faible miscibilité indiquée par les plus récentes expériences de laboratoire.

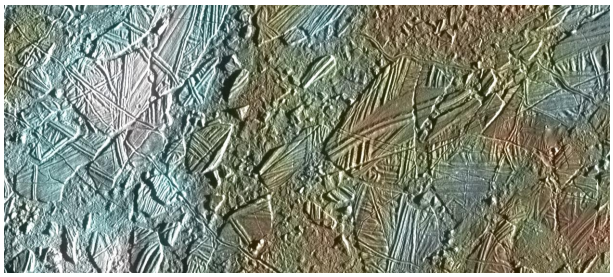

FIGURE 3.4 – Cliché du terrain chaotique de la région de Conamara à la surface d'Europe (Image : NASA/JPL/University of Arizona, https://www.jpl.nasa.gov/spaceimages/details.php?id=PIA01127).

3.2 Modélisation des écoulements et/ou du cryovolcanisme

Les traces d'écoulements, détectées à la surface de Titan, sont très nombreuses. Elles semblent avoir deux origines bien distinctes : d'une part l'érosion liée au probable ruissellement de méthane liquide, on pourra se reporter par exemple aux références citées dans BURR et collab. [2013] ; d'autre part les possibles flots de «cryolave» [voir Fig. 3.3 et LOPES et collab., 2013]. Même si les plus importants lacs de Titan (Kraken Mare, Ligeia Mare, Punga Mare) présentent des empreintes fluviales à la périphérie de leurs rives ; nombreux sont ceux qui ont une morphologie qui suggèrent fortement la dissolution d'un substrat géologique, suivant en cela un mode de formation de type karstique [CORNET et collab., 2012a,b, 2015]. Celui-ci suppose également un déplacement de fluides lors d'interactions entre la surface et un possible «alcanofère» souterrain. Dans tous les cas, une modélisation de ces écoulements, prenant en compte les effets concomitants, est très intéressante. Ceci pouvant mener à un modèle de «landforming» directement comparable aux observations RADAR et infrarouges réalisées à partir de Cassini. Pour ce faire, plusieurs techniques sont disponibles : la technique de Smoothed Particle Hydrodynamics (SPH) déjà introduite en astrophysique [MONAGHAN, 1992], celle des automates cellulaires [SCHIFF, 2008] ainsi que la Lattice Boltzmann Method (LBM) développée par Sauro Succi [SUCCI, 2001]. Dans le prolongement des études sur la thermochimie des formations lacustres de Titan, on pourra étudier en détail leur mode de formation en mariant dissolution, érosion mécanique, interaction avec un «alcanofère» et écoulement ; ceci grâce à la mise en œuvre d'une technique d'automates cellulaires ou basée sur la LBM, techniques qui semblent les plus abordables et les moins coûteuses en ressources informatiques. La question du cryovolcanisme sur Titan reste largement débattue ; alors que son existence apporterait une explication à la persistance du méthane atmosphérique. Le cryovolcanisme aurait également pu avoir une implication dans la production de molécules complexes dans l'atmosphère [BRASSÉ et collab., 2017; POCH et collab., 2012]. Peu d'indice morphologique, de ce volcanisme, ont été observés, seuls restent quelques candidats [LOPES et collab., 2013; SOLOMONIDOU et collab., 2014]. Grâce aux automates cellulaires, et en reprenant la démarche suivie par [MIYAMOTO et SASAKI, 1997] pour des coulées de lave terrestres, on pourra étudier la compatibilité des propriétés physiques (composition, conduction thermique, viscosité, ...) attendues pour la «cryolave» avec la morphologie observée. Ceci pourrait de conforter éventuellement le statut des candidats «cryovolcans», ou au contraire de l'affaiblir. Dans un deuxième temps, l'application des automates cellulaires pourrait être faite à la formation des lacs et éventuellement à celle des lits fluviaux (comme cela a été fait dans le contexte terrestre au bassin de l'Armaconi en Calabre (Italie) par D'AMBROSIO et collab. [2001].

La SPH est une technique également applicable à la modélisation des geysers d'Encelade, ou même, de façon sans doute plus exotique à la formation de surface solide à la géométrie bien particulière comme celle de la région de Conamara [SCHMIDT et collab., 2011] à la surface d'Europe (voir Fig. 3.4), la lune de Jupiter. En effet, la démarche de la SPH peut être adapté au cas des solides [voir le chapitre 8 «SPH for Hydrodynamics with Material Strengh» de LIU et LIU, 2003].

Les aspects de transitions de phases solide-liquide, ainsi que la conduction thermique peuvent être inclus [CLEARY et MONAGHAN, 1999; FARROKHPANAH et collab., 2017]. A l'instant où je rédige, je ne sais pas encore si le cas des solides peut être traité avec la LBM.

3.3 Caractérisation de la surface de Titan

3.3.1 Exploitation des données VIMS

Alors que la composition de l'atmosphère de Titan est assez bien connue [voir par exemple COUSTENIS et collab., 2007; FLASAR et collab., 2005; LELLOUCH et collab., 2014; VINATIER et collab., 2010] ; il n'en n'est pas de même pour le sol. En effet, entre autres choses, la présence d'une brume permanente dans la haute atmosphère, rend difficile les observations spectroscopiques de la surface. Sur cette dernière, les composés susceptibles d'être détectés sont d'abord la glace d'eau Ih, dont la possible existence est suggérée par la densité moyenne de Titan et les modèles de structure interne [TOBIE et collab., 2010] ; ensuite de nombreuses espèces organiques, plus ou moins complexes, mais toutes issues de la photochimie atmosphérique [LAVVAS et collab., 2008a,b; VUITTON et collab., 2008; YUNG et DEMORE, 1999] sont attendues, y compris des «tholins» dont le concept a été introduit par SAGAN et collab. [1992], mais dont la structure reste encore très mal connue [NNA-MVONDO et collab., 2013].

La composition de la surface de Titan, dans la région de l'atterrissage de Huygens, a fait l'objet d'une première étude détaillée par TOMASKO et collab. [2005]. Ce travail a été ensuite repris et amélioré par SCHRÖDER et KELLER [2008] et KELLER et collab. [2008] ; mais malgré ce qui pourrait être interprété comme une signature de la glace d'eau vers 1500 nm ; les résultats restent ambigus car à ces longueurs d'onde il existe une bande d'absorption de la glace d'eau CLARK [1981] et les tholins synthétisés en laboratoire [BERNARD et collab., 2006; CRUIKSHANK et collab., 1991] semblent également avoir le même genre de propriétés spectrales dans ce domaine. Concernant VIMS, la possible présence d'éthane liquide a pu être mis en évidence dans le lac Ontario [BROWN et collab., 2008]. Dans le même temps, grâce à des mesures photométriques de laboratoire, CLARK et collab. [2010] avancent des arguments en faveur de dépôts de benzène à la surface de Titan. Cependant, l'utilisation d'un modèle de transfert radiatif en géométrie plan-parallèle, appellent quelques réserves quant à la robustesse de leurs résultats. En effet, de nombreuses données VIMS ont été acquises avec des angles de phases qui rendent ce type de géométrie inadéquate.

Certains auteurs tentent de contourner les difficultés liées à la modélisation du transfert radiatif dans l'atmosphère de Titan. Par exemple, toutes les identifications de candidats évaporites effectuées par BARNES et collab. [2011a] et MACKENZIE et collab. [2014] ont été menées sur la base de détermination de la «pente» spectrale entre les fenêtres à 2.7 microns et 2.8 microns. En effet, BARNES et collab. [2009] indiquent qu'une pente positive, bien qu'interprétée comme caractéristique du dioxyde de carbone solide par MCCORD et collab. [2008], peut surtout être considérée comme un indice fort de pauvreté en glace d'eau, ceci du fait de la forte décroissance de la réflectivité de la glace d'eau entre 2.7 et 2.8 microns [voir par exemple le spectre bleu sur le Fig. 8 de CLARK et collab., 2010]. Cette conclusion repose cependant sur l'hypothèse d'une absorption atmosphérique uniforme entre 2.7 et 2.8 microns, celle-ci vient d'être remise en cause par HAYNE et collab. [2014]. En utilisant une technique d'occultation, ces derniers ont en effet mesuré une plus forte absorption atmosphérique (au-dessus de 40 km d'altitude) à 2.7 et qu'à 2.8 microns. Bien sûr, rien n'interdit un comportement inverse dans la troposphère, ce qui viendrait rétablir la pertinence du critère employé par BARNES et collab. [2011a] et MACKENZIE et collab. [2014]. Tous ces éléments font qu'une étude précise des fenêtres à 1.6 microns (qui est une des fenêtres dont les propriétés sont les mieux connues) et 2.7 – 2.8 microns est aussi nécessaire qu'intéressante.

Ce travail de caractérisation de la surface, à l'aide des images VIMS fait l'objet du sujet de thèse de Maélie Coutelier, étudiante que je co-encadre avec Pascal Rannou.

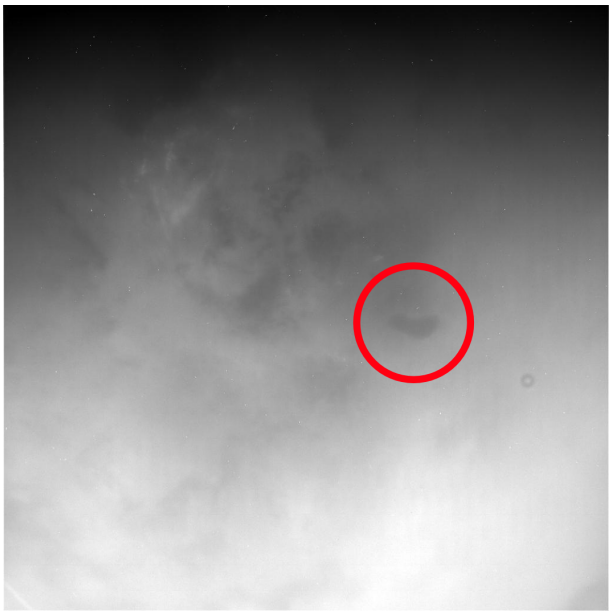

FIGURE 3.5 – Un exemple d'image ISS, acquise avec la NAC, sur laquelle on peut distinguer Ontario Lacus (signalé par le cercle rouge) grâce à la combinaison des filtres CB3 et IRP0.

3.3.2 Exploitation des données ISS

La surface des lacs et mers de Titan ont montré d'étonnantes propriétés, en particulier leur surprenant aspect lisse, avec des «aspérités» qui devraient avoir une taille inférieure au millimètre. Ceci a été montré avec les observations RADAR lors de survols d'Ontario Lacus [flyby T49 WYE et collab., 2009], et de Ligeia Mare [flyby T91 ZEBKER et collab., 2014], les résultats ayant été confirmés par de nouvelles analyses des signaux RADAR par GRIMA et collab. [2017]. De façon complémentaire, des observations à 5 µm, longueur d'onde à laquelle l'atmosphère est transparente, de Jingpo Lacus et Punga Mare, on également révélé une surface extrêmement lisse [BARNES et collab., 2011b; STEPHAN et collab., 2010]. Seule un zone légèrement «rugueuse» a été mise en évidence sur Punga Mare [BARNES et collab., 2014], mais ce dernier résultat est sujet à caution car les I/F produits par le modèle de surface des auteurs est en contradiction avec ce que cette même équipe obtient de façon observationnelle.

L'observation d'une surface en lumière polarisée apporte des informations intéressantes. En effet, ce genre de réflexion modifie l'état de polarisation de l'onde, ce dont on peut éventuellement déduire des contraintes sur la nature et l'état de surface du système observé. On peut donc envisager d'utiliser des observations, avec polarisation, pour tenter d'en apprendre plus sur l'état de la surface des mers de Titan. A bord de Cassini, les caméras de l'instrument ISS [2] disposaient de trois filtres polarisés dans le domaine visible : P0, P60 et P120, cependant ces derniers ne permettaient d'observer que l'atmosphère. Dans l'infrarouge, deux filtres étaient disponibles : IRP0 (axe passant parallèle à l'axe vertical de l'image) et IRP90 (axe horizontal) [voir Table VIII p. 446 de PORCO et collab., 2004]. Seul IRP0 est présent sur la NAC [3], IRP0 et IRP90 sont tout deux disponibles sur la WAC [4]. C'est filtres polarisants se combinent avec d'autres, sélectionnant un intervalle de longueur d'onde. Pour ISS, c'est avec les filtres CB2 et CB3 qu'on peut apercevoir la surface. Une première recherche dans les bases de données révèle quelques clichés où les lacs sont dans le champ. La Fig. 3.5 donne un exemple d'image utilisant la polarisation et sur laquelle on a un des lacs de Titan. Malheureusement, on a seulement que l'orientation IRP0 car IRP90 n'est pas

2. Imaging Science Subsystem
3. Narrow Angle Camera
4. Wide Angle Camera

disponible sur la NAC. Des images WAC, avec les deux orientations, sont également disponibles, la Fig. 3.6 montre un couple d'images du pôle nord où on distingue les «Maria», cette fois-ci les

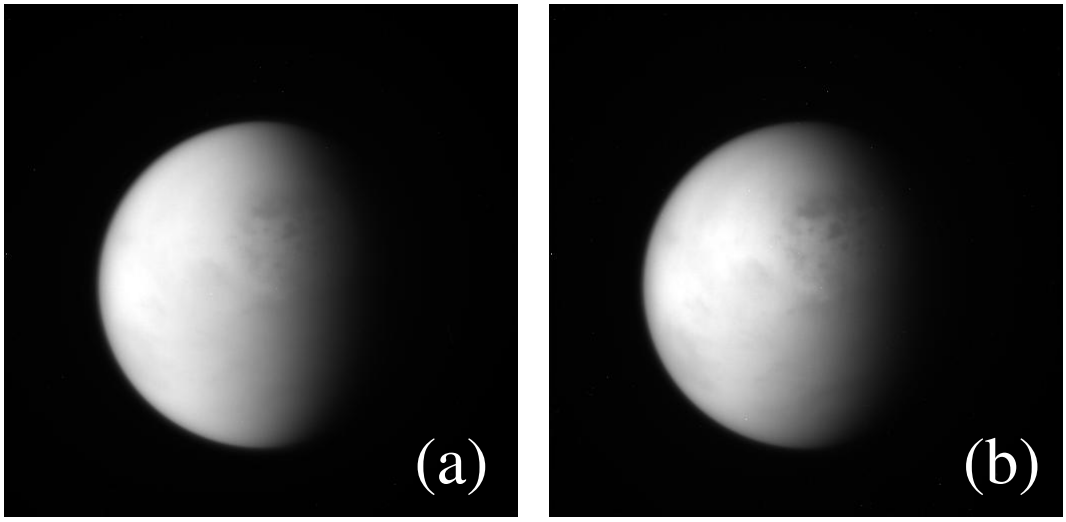

FIGURE 3.6 – Vues du pôle nord, avec une sélection du couple CB3+IRPOL (images WAC). (a) filtre IRP90. (b) filtre IRP0. La différence de polarisation entre les deux images est clairement visible, il reste cependant à faire la distinction entre la contribution de la surface et celle de l'atmosphère.

deux directions de polarisation ont été acquises. Un aspect important, dans l'interprétation de ce genre d'image, est la possibilité de les corriger des effets apportés par l'atmosphère. Une façon de faire est de construire un modèle de transfert radiatif de l'atmosphère, une autre consiste à appliquer une correction empirique déterminée à partir d'un cliché réalisé à une longueur d'onde pour laquelle on ne voit que l'atmosphère. En explorant la base de données de Cassini, j'ai pu trouver quelques cas où on a à la fois une vue des lacs grâce au filtre CB2, ceci pour les deux directions de polarisation, et une image de l'atmosphère seule, cette fois-ci grâce au filtre MT2. Cette situation ouvre la voie à un traitement d'image, similaire à celui proposé par exemple par PERRY et collab. [2005], et qui, dans un premier temps, dispense de développer un modèle de transfert radiatif valable dans le cas d'ondes polarisées.

De façon générale, un code de transfert radiatif, incluant la polarisation, devrait être nécessaire pour une interprétation fine des images ISS. J'ai déjà réfléchi à un algorithme, en particulier pour ce qui est de la recherche du trajet des paquets de photons, dans une approche de type Monte-Carlo [CHANDRASEKHAR, 1950], avec mise en œuvre des algorithmes d'optimisation [mis au point dans le contexte de l'étude des galaxies BAES et collab., 2016] afin d'améliorer l'efficacité du calcul, par essence assez mauvaise avec une approche de type Metropolis [5].

Ce type de modèle, utile dans le cadre de recherches concernant Titan, serait également utile dans le contexte d'un disque protoplanétaire, ou même dans celui d'une étude d'un panache au-dessus d'une bouteille de champagne débouchée. En effet, les calculs de transfert radiatif par méthode de Monte-Carlo ont l'avantage de pouvoir, au moins en principe, s'adapter à une géométrie quelconque.

5. Synonyme de Monte-Carlo.

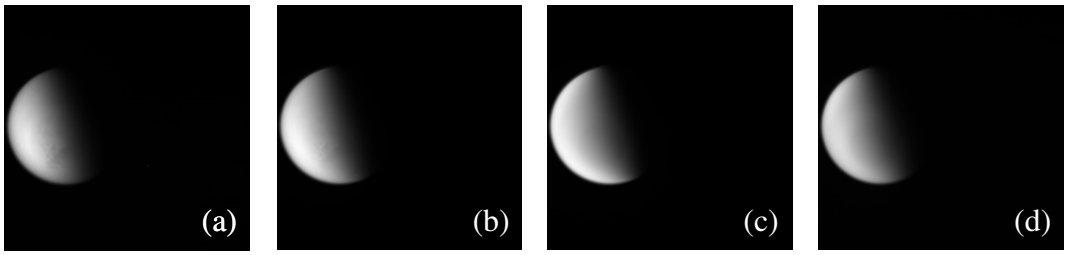

FIGURE 3.7 – Un exemple du pôle nord, avec sélection `CB2 + IRPOL` et `MT2 + IRPOL`. (a) filtres `CB2 + IRP90`. (b) filtres `CB2 + IRP0`. (c) filtres `MT2 + IRP0`. (d) filtres `MT2 + IRP90`.

3.4 Références

ATREYA, S. K., E. Y. ADAMS, H. B. NIEMANN, J. E. DEMICK-MONTELARA, T. C. OWEN, M. FULCHIGNONI, F. FERRI et E. H. WILSON. 2006, «Titan's methane cycle», *Planet. Space Sci.*, vol. 54, doi: 10.1016/j.pss.2006.05.028, p. 1177–1187. 41

BAES, M., K. D. GORDON, T. LUNTTILA, S. BIANCHI, P. CAMPS, M. JUVELA et R. KUIPER. 2016, «Composite biasing in Monte Carlo radiative transfer», *A&A*, vol. 590, doi: 10.1051/0004-6361/201528063, A55. 49

BARNES, J. W., J. BOW, J. SCHWARTZ, R. H. BROWN, J. M. SODERBLOM, A. G. HAYES, G. VIXIE, S. LE MOUÉLIC, S. RODRIGUEZ, C. SOTIN, R. JAUMANN, K. STEPHAN, L. A. SODERBLOM, R. N. CLARK, B. J. BURATTI, K. H. BAINES et P. D. NICHOLSON. 2011a, «Organic sedimentary deposits in Titan's dry lakebeds : Probable evaporite», *Icarus*, vol. 216, doi: 10.1016/j.icarus.2011.08.022, p. 136–140. 47

BARNES, J. W., R. H. BROWN, J. M. SODERBLOM, L. A. SODERBLOM, R. JAUMANN, B. JACKSON, S. LE MOUÉLIC, C. SOTIN, B. J. BURATTI, K. M. PITMAN, K. H. BAINES, R. N. CLARK, P. D. NICHOLSON, E. P. TURTLE et J. PERRY. 2009, «Shoreline features of Titan's Ontario Lacus from Cassini/VIMS observations», *Icarus*, vol. 201, doi: 10.1016/j.icarus.2008.12.028, p. 217–225. 47

BARNES, J. W., J. M. SODERBLOM, R. H. BROWN, L. A. SODERBLOM, K. STEPHAN, R. JAUMANN, S. L. MOUÉLIC, S. RODRIGUEZ, C. SOTIN, B. J. BURATTI, K. H. BAINES, R. N. CLARK et P. D. NICHOLSON. 2011b, «Wave constraints for Titan's Jingpo Lacus and Kraken Mare from VIMS specular reflection lightcurves», *Icarus*, vol. 211, doi: 10.1016/j.icarus.2010.09.022, p. 722–731. 48

BARNES, J. W., C. SOTIN, J. M. SODERBLOM, R. H. BROWN, A. G. HAYES, M. DONELAN, S. RODRIGUEZ, S. LE MOUELIC, K. H. BAINES et T. B. MCCORD. 2014, «Cassini/VIMS Observes Rough Surfaces on Titan's Punga Mare in Specular Reflection», *Planet. Sci.*, vol. 3, doi: 10.1186/s13535-014-0003-4, 3. 48

BERNARD, J.-M., E. QUIRICO, O. BRISSAUD, G. MONTAGNAC, B. REYNARD, P. MCMILLAN, P. COLL, M.-J. NGUYEN, F. RAULIN et B. SCHMITT. 2006, «Reflectance spectra and chemical structure of Titan's tholins : Application to the analysis of Cassini Huygens observations», *icarus*, vol. 185, doi: 10.1016/j.icarus.2006.06.004, p. 301–307. 47

BIRD, R. B., W. E. STEWART et E. N. LIGHTFOOT, éd.. 1960, *Transport Phenomena*, John Wiley and Sons, New York, ISBN 978-0470115398. 41

BOLMATOV, D., V. V. BRAZHKIN et K. TRACHENKO. 2013, «Thermodynamic behavior of supercritical matter», *Nat. Commun.*, vol. 4, nº 2331, doi: 10.1038/ncomms3331. 45

BOLMATOV, D., D. ZAV'YALOV et M. ZHERNENKOV. 2014, «Structural Evolution of Supercritical CO_2 across the Frenkel Line», *J. Phys. Chem. Lett.*, vol. 5, doi: 10.1021/jz5012127, p. 2785–2790. 45

BRASSÉ, C., A. BUCH, P. COLL et F. RAULIN. 2017, «Low-Temperature Alkaline pH Hydrolysis of Oxygen-Free Titan Tholins : Carbonates' Impact», *Astrobiology*, vol. 17, doi: 10.1089/ast.2016.1524, p. 8–26. 46

BRAZHKIN, V. V., A. G. FOMIN, Y. D. LYAPIN, V. N. RYZHOV, E. N. TSIOK et K. TRACHENKO. 2013, «"Liquid-Gas" Transition in the Supercritical Region : Fundamental Changes in the Particle Dynamics», *Phys. Rev. Lett.*, vol. 111, nº 145901, doi: 10.1103/PhysRevLett.111.145901. 45

BROWN, R. H., L. A. SODERBLOM, J. M. SODERBLOM, R. N. CLARK, R. JAUMANN, J. W. BARNES, C. SOTIN, B. BURATTI, K. H. BAINES et P. D. NICHOLSON. 2008, «The identification of liquid ethane in Titan's Ontario Lacus», *Nature*, vol. 454, doi: 10.1038/nature07100, p. 607–610. 47

BURR, D. M., S. A. DRUMMOND, R. CARTWRIGHT, B. A. BLACK et J. T. PERRON. 2013, «Morphology of fluvial networks on Titan : Evidence for structural control», *Icarus*, vol. 226, doi: 10.1016/j.icarus.2013.06.016, p. 742–759. 46

CHANDRASEKHAR, S. 1950, *Radiative Transfer*, Oxford Clarendon Press, Oxford. 49

CLARK, R. N. 1981, «Water frost and ice - The near-infrared spectral reflectance 0.65-2.5 microns», *J. Geophys. Res.*, vol. 86, doi: 10.1029/JB086iB04p03087, p. 3087–3096. 47

CLARK, R. N., J. M. CURCHIN, J. W. BARNES, R. JAUMANN, L. SODERBLOM, D. P. CRUIKSHANK, R. H. BROWN, S. RODRIGUEZ, J. LUNINE, K. STEPHAN, T. M. HOEFEN, S. LE MOUÉLIC, C. SOTIN, K. H. BAINES, B. J. BURATTI et P. D. NICHOLSON. 2010, «Detection and mapping of hydrocarbon deposits on Titan», *J. Geophys. Res.*, vol. 115, doi: 10.1029/2009JE003369, E10005. 47

CLEARY, P. W. et J. J. MONAGHAN. 1999, «Conduction Modelling Using Smoothed», *J. Comput. Phys.*, vol. 148, doi: 10.1002/fld.2481, p. 227–264. 47

CORLIES, P., A. G. HAYES, S. P. D. BIRCH, R. LORENZ, B. W. STILES, R. KIRK, V. POGGIALI, H. ZEBKER et L. IESS. 2017, «Titan's Topography and Shape at the End of the Cassini Mission», *Geophys. Res. Lett.*, vol. 44, doi: 10.1002/2017GL075518, p. 11. 41

CORNET, T., O. BOURGEOIS, S. LE MOUÉLIC, S. RODRIGUEZ, T. LOPEZ GONZALEZ, C. SOTIN, G. TOBIE, C. FLEURANT, J. W. BARNES, R. H. BROWN, K. H. BAINES, B. J. BURATTI, R. N. CLARK et P. D. NICHOLSON. 2012a, «Geomorphological significance of Ontario Lacus on Titan : Integrated interpretation of Cassini VIMS, ISS and RADAR data and comparison with the Etosha Pan (Namibia)», *Icarus*, vol. 218, doi: 10.1016/j.icarus.2012.01.013, p. 788–806. 46

CORNET, T., O. BOURGEOIS, S. LE MOUÉLIC, S. RODRIGUEZ, C. SOTIN, J. W. BARNES, R. H. BROWN, K. H. BAINES, B. J. BURATTI, R. N. CLARK et P. D. NICHOLSON. 2012b, «Edge detection applied to Cassini images reveals no measurable displacement of Ontario Lacus' margin between 2005 and 2010», *J. Geophys. Res.*, vol. 117, doi: 10.1029/2012JE004073, E07005. 46

CORNET, T., D. CORDIER, T. L. BAHERS, O. BOURGEOIS, C. FLEURANT, S. L. MOUÉLIC et N. ALTOBELLI. 2015, «Dissolution on Titan and on Earth : Toward the age of Titan's karstic landscapes», *J. Geophys. Res.*, vol. 120, doi: 10.1002/2014JE004738, p. 1044–1074. 46

COUSTENIS, A., R. K. ACHTERBERG, B. J. CONRATH, D. E. JENNINGS, A. MARTEN, D. GAUTIER, C. A. NIXON, F. M. FLASAR, N. A. TEANBY, B. BÉZARD, R. E. SAMUELSON, R. C. CARLSON, E. LELLOUCH, G. L. BJORAKER, P. N. ROMANI, F. W. TAYLOR, P. G. J. IRWIN, T. FOUCHET, A. HUBERT, G. S. ORTON, V. G. KUNDE, S. VINATIER, J. MONDELLINI, M. M. ABBAS et R. COURTIN. 2007,

«The composition of Titan's stratosphere from Cassini/CIRS mid-infrared spectra», *Icarus*, vol. 189,
doi: 10.1016/j.icarus.2006.12.022, p. 35–62. 47

CRUIKSHANK, D. P., L. J. ALLAMANDOLA, W. K. HARTMANN, D. J. THOLEN, R. H. BROWN, C. N. MATTHEWS et J. F. BELL. 1991, «Solid C triple bond N bearing material on outer solar system bodies», *Icarus*, vol. 94,
doi: 10.1016/0019-1035(91)90233-J, p. 345–353. 47

D'AMBROSIO, D., S. DI GREGORIO, S. GABRIELE et R. GAUDIO. 2001, «A Cellular Automata model for soil erosion by water», *Physics and Chemistry of the Earth, Part B : Hydrology, Oceans and Atmosphere*, vol. 26, nº 1,
doi: https://doi.org/10.1016/S1464-1909(01)85011-5, p. 33–39, ISSN 1464-1909. 46

DUAN, Z., N. MØLLER et J. H. WEARE. 1996, «A general equation of state for supercritical fluid mixtures and molecular dynamics simulation of mixture *PVTX* properties», *Geochim. Cosmochim. Ac.*, vol. 60, nº 7,
doi: 10.1016/0016-7037(96)00004-X, p. 1209–1216. 44

ESPANANI, R., A. MILLER, A. BUSICK, D. HENDRY et W. JACOBY. 2016, «Separation of N_2/CO_2 mixture using a continuous high-pressure density-driven separator», *J. CO_2 Util.*, vol. 14,
doi: 10.1016/j.jcou.2016.02.012, p. 67–75. 44

FARROKHPANAH, A., M. BUSSMANN et J. MOSTAGHIMI. 2017, «New smoothed particle hydrodynamics (SPH) formulation for modeling heat conduction with solidification and melting», *Numerical Heat Transfer, Part B : Fundamentals*, vol. 71,
doi: 10.1080/10407790.2017.1293972, p. 299–312. 47

FLASAR, F. M., R. K. ACHTERBERG, B. J. CONRATH, P. J. GIERASCH, V. G. KUNDE, C. A. NIXON, G. L. BJORAKER, D. E. JENNINGS, P. N. ROMANI, A. A. SIMON-MILLER, B. BÉZARD, A. COUSTENIS, P. G. J. IRWIN, N. A. TEANBY, J. BRASUNAS, J. C. PEARL, M. E. SEGURA, R. C. CARLSON, A. MAMOUTKINE, P. J. SCHINDER, A. BARUCCI, R. COURTIN, T. FOUCHET, D. GAUTIER, E. LELLOUCH, A. MARTEN, R. PRANGÉ, S. VINATIER, D. F. STROBEL, S. B. CALCUTT, P. L. READ, F. W. TAYLOR, N. BOWLES, R. E. SAMUELSON, G. S. ORTON, L. J. SPILKER, T. C. OWEN, J. R. SPENCER, M. R. SHOWALTER, C. FERRARI, M. M. ABBAS, F. RAULIN, S. EDGINGTON, P. ADE et E. H. WISHNOW. 2005, «Titan's Atmospheric Temperatures, Winds, and Composition», *Science*, vol. 308,
doi: 10.1126/science.1111150, p. 975–978. 47

GHORAYEB, K. et A. FIROOZABADI. 2000, «Molecular, Pressure, and Thermal Diffusion in Nonideal Multicomponent Mixtures», *AlChE J.*, vol. 46,
doi: 10.1002/aic.690460503, p. 883–891. 41

GOOS, E., U. RIEDEL, L. ZHAO et L. BLUM. 2011, «Phase diagrams of CO_2 and CO_2-N_2 gas mixtures and their», *Energy Procedia*, vol. 4,
doi: 10.1016/j.egypro.2011.02.312, p. 3778–3785. 43

GRIMA, C., M. MASTROGIUSEPPE, A. G. HAYES, S. D. WALL, R. D. LORENZ, J. D. HOFGARTNER, B. STILES, C. ELACHI et CASSINI RADAR TEAM. 2017, «Surface roughness of Titan's hydrocarbon seas», *Earth Planet. Sci. Lett.*, vol. 474,
doi: 10.1016/j.epsl.2017.06.007, p. 20–24. 48

HAYES, A. G., S. P. D. BIRCH, W. E. DIETRICH, A. D. HOWARD, R. L. KIRK, V. POGGIALI, M. MASTROGIUSEPPE, R. J. MICHAELIDES, P. M. CORLIES, J. M. MOORE, M. J. MALASKA, K. L. MITCHELL, R. D. LORENZ et C. A. WOOD. 2017, «Topographic Constraints on the Evolution and Connectivity of Titan's Lacustrine Basins», *Geophys. Res. Lett.*, vol. 44,
doi: 10.1002/2017GL075468, p. 11. 41

HAYNE, P. O., T. B. MCCORD et C. SOTIN. 2014, «Titan's surface composition and atmospheric transmission with solar occultation measurements by Cassini VIMS», *Icarus*, vol. 243,
doi: 10.1016/j.icarus.2014.08.045, p. 158–172. 47

HENDRY, D., W. N. MILLER, A, M. , WICKRAMATHILAKA, R. ESPANANI et W. JACOBY. 2013, «Exploration of high pressure equilibrium separations of nitrogen and carbon dioxide», *J. CO_2 Util.*, vol. 3-4,
doi: 10.1016/j.jcou.2013.09.002, p. 37–43. 44, 45

KELLER, H. U., B. GRIEGER, M. KÜPPERS, S. E. SCHRÖDER, Y. V. SKOROV et M. G. TOMASKO. 2008, «The properties of Titan's surface at the Huygens landing site from DISR observations», *planss*, vol. 56,
doi: 10.1016/j.pss.2007.11.020, p. 728–752. 47

LAVVAS, P. P., A. COUSTENIS et I. M. VARDAVAS. 2008a, «Coupling photochemistry with haze formation in Titan's atmosphere, Part I : Model description», *Planet. Space Sci.*, vol. 56,
doi: 10.1016/j.pss.2007.05.026, p. 27–66. 47

LAVVAS, P. P., A. COUSTENIS et I. M. VARDAVAS. 2008b, «Coupling photochemistry with haze formation in Titan's atmosphere, Part II : Results and validation with Cassini/Huygens data», *Planet. Space Sci.*, vol. 56,
doi: 10.1016/j.pss.2007.05.027, p. 67–99. 47

LEBONNOIS, S. et G. SCHUBERT. 2017, «The deep atmosphere of Venus and the possible role of density-driven separation of CO_2 and N_2», *Nat. Geosci.*, vol. 10,
doi: 10.1038/NGEO2971, p. 473–477. 43, 44

LELLOUCH, E., B. BÉZARD, F. M. FLASAR, S. VINATIER, R. ACHTERBERG, C. A. NIXON, G. L. BJORAKER et N. GORIUS. 2014, «The distribution of methane in Titan's stratosphere from Cassini/CIRS observations», *icarus*, vol. 231,
doi: 10.1016/j.icarus.2013.12.016, p. 323–337. 47

LIU, G. R. et M. B. LIU. 2003, *Smoothed Particle Hydrodynamics – A Meshfree Particle Method*, 1re éd., World Scientific Publishing, 5 Toh Tuck Link, Singapore 596224, ISBN 981-238-456-1. 46

LOPES, R. M. C., R. L. KIRK, K. L. MITCHELL, A. LEGALL, J. W. BARNES, A. HAYES, J. KARGEL, L. WYE, J. RADEBAUGH, E. R. STOFAN, M. A. JANSSEN, C. D. NEISH, S. D. WALL, C. A. WOOD, J. I. LUNINE et M. J. MALASKA. 2013, «Cryovolcanism on Titan : New results from Cassini RADAR and VIMS», *JGR*, vol. 118,
doi: 10.1002/jgre.20062, p. 416–435. 45, 46

LORENZ, R. D., D. CRISP et L. HUBER. 2018, «Venus atmospheric structure and dynamics from the VEGA lander and balloons : New results and PDS archive», *Icarus*, vol. 305,
doi: 10.1016/j.icarus.2017.12.044, p. 277–283. 43

MACKENZIE, S. M., J. W. BARNES, C. SOTIN, J. M. SODERBLOM, S. LE MOUÉLIC, S. RODRIGUEZ, K. H. BAINES, B. J. BURATTI, R. N. CLARK, P. D. NICHOLSON et T. B. MCCORD. 2014, «Evidence of Titan's climate history from evaporite distribution», *Icarus*, vol. 243,
doi: 10.1016/j.icarus.2014.08.022, p. 191–207. 47

MCCORD, T. B., P. HAYNE, J.-P. COMBE, G. B. HANSEN, J. W. BARNES, S. RODRIGUEZ, S. LE MOUÉLIC, E. K. H. BAINES, B. J. BURATTI, C. SOTIN, P. NICHOLSON, R. JAUMANN, R. NELSON et THE CASSINI VIMS TEAM. 2008, «Titan's surface : Search for spectral diversity and composition using the Cassini VIMS investigation», *icarus*, vol. 194,
doi: 10.1016/j.icarus.2007.08.039, p. 212–242. 47

MIYAMOTO, H. et S. SASAKI. 1997, «Simulating Lava Flows by an Improved Cellular Automata Method», *Computers & Geosciences*, vol. 23, p. 283–292. 46

MONAGHAN, J. J. 1992, «Smoothed particle hydrodynamics», *Annu. Rev. Astron. Astrophys.*, vol. 30,
doi: 10.1146/annurev.aa.30.090192.002551, p. 543–574. 46

MOUSIS, O., M. CHOUKROUN, J. I. LUNINE et C. SOTIN. 2014, «Equilibrium composition between liquid and clathrate reservoirs on Titan», *Icarus*, vol. 239,
doi: 10.1016/j.icarus.2014.05.032, p. 39–45. 41

MOUSIS, O. et B. SCHMITT. 2008, «Sequestration of Ethane in the Cryovolcanic Subsurface of Titan», *ApJL*, vol. 677, doi: 10.1086/587141, p. L67–L70. 41

NNA-MVONDO, D., J. L. DE LA FUENTE, M. RUIZ-BERMEJO, B. KHARE et C. P. MCKAY. 2013, «Thermal characterization of Titan's tholins by simultaneous TG-MS, DTA, DSC analysis», *Planet. Space Sci.*, vol. 85, doi: 10.1016/j.pss.2013.06.025, p. 279–288. 47

OBIDI, O. C. 2014, *Timescales for the Development of Thermodynamic Equilibrium in Hydrocarbon Reservoirs*, thèse de doctorat, Imperial College London. 41

PERRY, J. E., A. S. MCEWEN, S. FUSSNER, E. P. TURTLE, R. A. WEST, C. C. PORCO, B. KNOWLES, D. D. DAWSON et CASSINI ISS TEAM. 2005, «Processing ISS Images of Titan's Surface», dans *36th Annual Lunar and Planetary Science Conference, Lunar and Planetary Science Conference*, vol. 36, édité par S. Mackwell et E. Stansbery. 49

POCH, O., P. COLL, A. BUCH, S. I. RAMÍREZ et F. RAULIN. 2012, «Production yields of organics of astrobiological interest from H_2O-NH_3 hydrolysis of Titan's tholins», *Planet. Space Sci.*, vol. 61, doi: 10.1016/j.pss.2011.04.009, p. 114–123. 46

PORCO, C. C., R. A. WEST, S. SQUYRES, A. MCEWEN, P. THOMAS, C. D. MURRAY, A. DEL GENIO, A. P. INGERSOLL, T. V. JOHNSON, G. NEUKUM, J. VEVERKA, L. DONES, A. BRAHIC, J. A. BURNS, V. HAEMMERLE, B. KNOWLES, D. DAWSON, T. ROATSCH, K. BEURLE et W. OWEN. 2004, «Cassini Imaging Science : Instrument Characteristics And Anticipated Scientific Investigations At Saturn», *Space Sci. Rev.*, vol. 115, doi: 10.1007/s11214-004-1456-7, p. 363–497. 48

SAGAN, C., W. R. THOMSON et B. KHARE. 1992, «Titan : A laboratory for pre-biological organic chemistry», *Acc. Chem. Res.*, vol. 25, doi: 10.1021/ar00019a003, p. 286–292. 47

SCHIFF, J. L. 2008, *Cellular Automata – A Discrete View of the World*, 1re éd., Wiley-Interscience, Hoboken, New Jersey, USA, ISBN 978-0470168790. 46

SCHMIDT, B. E., D. D. BLANKENSHIP, G. W. PATTERSON et P. M. SCHENK. 2011, «Active formation of 'chaos terrain' over shallow subsurface water on Europa», *Nature*, vol. 479, doi: 10.1038/nature10608, p. 502–505. 46

SCHRÖDER, S. E. et H. U. KELLER. 2008, «The reflectance spectrum of Titan's surface at the Huygens landing site determined by the descent imager/spectral radiometer», *Planet. Space Sci.*, vol. 56, doi: 10.1016/j.pss.2007.10.011, p. 753–769. 47

SOLOMONIDOU, A., M. HIRTZIG, A. COUSTENIS, E. BRATSOLIS, S. LE MOUÉLIC, S. RODRIGUEZ, K. STEPHAN, P. DROSSART, C. SOTIN, R. JAUMANN, R. H. BROWN, K. KYRIAKOPOULOS, R. M. C. LOPES, G. BAMPASIDIS, K. STAMATELOPOULOU-SEYMOUR et X. MOUSSAS. 2014, «Surface albedo spectral properties of geologically interesting areas on Titan», *JGR*, vol. 119, doi: 10.1002/2014JE004634, p. 1729–1747. 46

STEPHAN, K., R. JAUMANN, R. H. BROWN, J. M. SODERBLOM, L. A. SODERBLOM, J. W. BARNES, C. SOTIN, C. A. GRIFFITH, R. L. KIRK, K. H. BAINES, B. J. BURATTI, R. N. CLARK, D. M. LYTLE, R. M. NELSON et P. D. NICHOLSON. 2010, «Specular reflection on Titan : Liquids in Kraken Mare», *Geophys. Res. Lett.*. 48

SUCCI, S. 2001, *The Lattice Boltzmann Equation – For Fluid Dynamics and Beyond*, 1re éd., Oxford University Press, USA, New-York, USA, ISBN 9780198503989. 46

TOBIE, G., B. GIESE, T. A. HURFORD, R. M. LOPES, F. NIMMO, F. POSTBERG, K. D. RETHERFORD, J. SCHMIDT, J. R. SPENCER, T. TOKANO et E. P. TURTLE. 2010, «Surface, Subsurface and Atmosphere Exchanges on the Satellites of the Outer Solar System», *SSRv*, vol. 153, doi: 10.1007/s11214-010-9641-3, p. 375–410. 47

TOMASKO, M. G., B. ARCHINAL, T. BECKER, B. BÉZARD, M. BUSHROE, M. COMBES, D. COOK, A. COUSTENIS, C. DE BERGH, L. E. DAFOE, L. DOOSE, S. DOUTÉ, A. EIBL, S. ENGEL, F. GLIEM, B. GRIEGER, K. HOLSO, E. HOWINGTON-KRAUS, E. KARKOSCHKA, H. U. KELLER, R. KIRK, R. KRAMM, M. KÜPPERS, P. LANAGAN, E. LELLOUCH, M. LEMMON, J. LUNINE, E. MCFARLANE, J. MOORES, G. M. PROUT, B. RIZK, M. ROSIEK, P. RUEFFER, S. E. SCHRÖDER, B. SCHMITT, C. SEE, P. SMITH, L. SODERBLOM, N. THOMAS et R. WEST. 2005, «Rain, winds and haze during the Huygens probe's descent to Titan's surface», *nat*, vol. 438,
doi: 10.1038/nature04126, p. 765–778. 47

VINATIER, S., B. BÉZARD, C. A. NIXON, A. MAMOUTKINE, R. C. CARLSON, D. E. JENNINGS, E. A. GUANDIQUE, N. A. TEANBY, G. L. BJORAKER, F. MICHAEL FLASAR et V. G. KUNDE. 2010, «Analysis of Cassini/CIRS limb spectra of Titan acquired during the nominal mission. I. Hydrocarbons, nitriles and CO_2 vertical mixing ratio profiles», *Icarus*, vol. 205,
doi: 10.1016/j.icarus.2009.08.013, p. 559–570. 47

VUITTON, V., R. V. YELLE et J. CUI. 2008, «Formation and distribution of benzene on Titan», *Journal of Geophysical Research (Planets)*, vol. 113,
doi: 10.1029/2007JE002997, p. 5007–+. 47

WILKE, C. R. et P. CHANG. 1955, «Correlation of diffusion coefficients in dilute solutions», *AlChE J.*, vol. 1,
doi: 10.1002/aic.690010222, p. 264–270. 44

WYE, L. C., H. A. ZEBKER et R. D. LORENZ. 2009, «Smoothness of Titan's Ontario Lacus : Constraints from Cassini RADAR specular reflection data», *Geophys. Res. Lett.*, vol. 36,
doi: 10.1029/2009GL039588, L16201. 48

YUNG, Y. L. et DEMORE. 1999, *Photochemistry of Planetary Atmospheres*, Oxford Univ. Press, New York. 47

ZEBKER, H., A. HAYES, M. JANSSEN, A. LE GALL, R. LORENZ et L. WYE. 2014, «Surface of Ligeia Mare, Titan, from Cassini altimeter and radiometer analysis», *Geophys. Res. Lett.*, vol. 41,
doi: 10.1002/2013GL058877, p. 308–313. 48

Chapitre 4

Articles : surface de Titan

FIGURE 4.1 – Dessin réalisé par Catherine Créhange lors de la journée des 40 ans de la DR06 au GSMA, le 18 mai 2017.

4.1 Article sur la composition des lacs/mers de Titan

The Astrophysical Journal, 707:L128–L131, 2009 December 20 doi:10.1088/0004-637X/707/2/L128
© 2009. The American Astronomical Society. All rights reserved. Printed in the U.S.A.

AN ESTIMATE OF THE CHEMICAL COMPOSITION OF TITAN's LAKES

Daniel Cordier[1,2,3], Olivier Mousis[4,5], Jonathan I. Lunine[4], Panayotis Lavvas[4], and Véronique Vuitton[6]
[1] Ecole Nationale Supérieure de Chimie de Rennes, CNRS, UMR 6226, Avenue du Général Leclerc, CS 50837, 35708 Rennes Cedex 7, France; daniel.cordier@ensc-rennes.fr
[2] Université européenne de Bretagne, Rennes, France
[3] Institut de Physique de Rennes, CNRS, UMR 6251, Université de Rennes 1, Campus de Beaulieu, 35042 Rennes, France
[4] Lunar and Planetary Laboratory, University of Arizona, Tucson, AZ, USA
[5] Université de Franche-Comté, Institut UTINAM, CNRS/INSU, UMR 6213, 25030 Besançon Cedex, France
[6] Université Joseph Fourier, Laboratoire de Planétologie de Grenoble, CNRS/INSU, France
Received 2009 July 24; accepted 2009 November 9; published 2009 December 4

ABSTRACT

Hundreds of radar-dark patches interpreted as lakes have been discovered in the north and south polar regions of Titan. We have estimated the composition of these lakes by using the direct abundance measurements from the Gas Chromatograph Mass Spectrometer aboard the Huygens probe and recent photochemical models based on the vertical temperature profile derived by the Huygens Atmospheric Structure Instrument. Thermodynamic equilibrium is assumed between the atmosphere and the lakes, which are also considered nonideal solutions. We find that the main constituents of the lakes are ethane (C_2H_6) (∼76%–79%), propane (C_3H_8) (∼7%–8%), methane (CH_4) (∼5%–10%), hydrogen cyanide (HCN) (∼2%–3%), butene (C_4H_8) (∼1%), butane (C_4H_{10}) (∼1%), and acetylene (C_2H_2) (∼1%). The calculated composition of lakes is then substantially different from what has been expected from models elaborated prior to the exploration of Titan by the Cassini–Huygens spacecraft.

Key words: planets and satellites: general – planets and satellites: individual (Titan) – solar system: general

1. INTRODUCTION

The surface of Saturn's haze-shrouded moon Titan had long been proposed to have oceans or seas, on the basis of the stability of liquid methane and ethane at the ground level (Flasar 1983; Lunine et al. 1983; Lorenz et al. 2003). Ground-based radar observations ruled out the presence of a global ocean in the 1990s (Muhleman et al. 1995), but the presence of isolated lakes was not precluded (Campbell et al. 2003). A large, dark, lake-like feature subsequently named Ontario Lacus was detected at Titan's south polar region by the Cassini ISS system in 2005 (Mc Ewen et al. 2005) and hundreds of radar dark features with a variety of properties consistent with liquid-filled lakes were found in the northern hemisphere by the Cassini RADAR system (Stofan et al. 2007).

The chemical composition of the lakes of Titan is still not well determined. Good quality spectral data of the Ontario Lacus have been obtained by the Visual and Infrared Mapping Spectrometer (VIMS) aboard Cassini but the only species that seems firmly identified is C_2H_6 (Brown et al. 2008); the atmosphere contains so much CH_4 that it is very difficult to detect the surface liquid phase of this molecule even if it is dominant in the lakes. Because the detection of other compounds in the lakes of Titan remains challenging in the absence of in situ measurements, the only way to get a good estimate of the chemical composition of these lakes is to elaborate a thermodynamic model based on theoretical calculations and laboratory data. Several models that investigate the influence of photochemistry and the atmospheric composition on the chemical composition of liquids formed on the surface of Titan have been elaborated in the pre-Cassini years (Lunine et al. 1983; Dubouloz et al. 1989; Mc Kay et al. 1993; Tokano 2005). Based on atmospheric observations these models assumed surface bodies of liquid on Titan to contain a mixture of C_2H_6, CH_4, and N_2 and a large number of dissolved minor species.

However, Cassini–Huygens measurements have improved our knowledge of the structure and composition of Titan's atmosphere, requiring the solubilities to be recomputed under actual Titan conditions. In particular, the Gas Chromatograph Mass Spectrometer (GCMS) aboard Huygens and the Cassini Composite Infrared Spectrometer (CIRS) provided new atmospheric mole fraction data (see Table 1 and Niemann et al. 2005). Moreover, near-surface brightness temperatures at the high latitudes where the lakes exist have now been determined (Jennings et al. 2009).

Here, we propose a model that takes into account these recent advances and thus provides the most up-to-date chemical composition of Titan's lakes as a function of their location on the satellite's surface. Our model considers the same assumptions as those made by Dubouloz et al. (1989; hereafter D89) when they calculated the composition of the hypothetical ocean proposed to exist on Titan in the years prior to the Cassini–Huygens exploration. The lakes are then considered nonideal solutions in thermodynamic equilibrium with the atmosphere. This assumption is supported by recent calculations that showed that raindrops could reach the ground in compositional equilibrium with the atmosphere (Graves et al. 2008).

2. THE MODEL OF LAKE–ATMOSPHERE EQUILIBRIUM

The general phenomenological picture of our model is the following: high altitude photochemistry produces gases and aerosols in Titan's atmosphere, which are transported to lower altitude via atmospheric mixing, molecular diffusion, and sedimentation. At low temperature conditions found in the lower stratophere and troposphere, the formed gases can condense on the aerosols and their precipitation rates (see Table 2) are given by photochemical models (Lavvas et al. 2008a, 2008b; Vuitton et al. 2008). From the different vapor pressures of the molecules that condense in Titan's atmosphere, these models define the altitude (i.e., temperature) at which the condensation of each gas will start. Although the condensed phase can start as a liquid, the temperature of the surface is smaller than the temperature at the altitude where condensation begins for some

Table 1
Assumed Composition of Titan's Atmosphere at the Ground Level

Atmosphere	Mole Fraction	Determination
H_2	9.8×10^{-4}	Huygens GCMS[a]
N_2	0.95	This work
CH_4	0.0492	Huygens GCMS[b]
CO	4.70×10^{-5}	Cassini CIRS[c]
^{40}Ar	4.32×10^{-5}	Huygens GCMS[b]
C_2H_6	1.49×10^{-5}	This work

Notes. [a] Owen & Niemann 2009;
[b] Niemann et al. 2005;
[c] De Kok et al. 2007. N_2 and C_2H_6 abundances are determined from our model (see the text).

of the molecules. This allows some of the condensables to reach the surface in the solid phase. The physical state of these precipitates as they enter the seas at Titan's surface level does not matter as they are assumed to dissolve in thermodynamic equilibrium. The considered gas phase is representative of Titan's atmosphere (see Table 1) and the ethane mole fractions in liquid and gas are considered as unknowns of the problem. Mole fractions of other species present in precipitation are supposed to have negligible gas phase abundances. We place our model in the framework of the regular solution theory. Thus, because the thermodynamic equilibrium is assumed between lakes and atmosphere, the equality of chemical potentials for each species listed in Table 1 can be written as (Equation (1) of D89):

$$Y_i P = \Gamma_i X_i P_{\mathrm{vp},i}, \quad (1)$$

where P is the total pressure at Titan's surface, Y_i and X_i are respectively the mole fractions of the i compound in the atmosphere and the liquid, $P_{\mathrm{vp},i}$ is its vapor pressure, and Γ_i is its activity coefficient in the liquid given by Equation (2) of D89. Abundances of compounds below C_2H_6 in Table 2 are expressed proportionally to that of C_2H_6 both in the precipitation and in the lakes. Because the system of involved equations is nonlinear, it is solved with the use of Newton–Raphson's method.

Our model also allows us to estimate the fractions of solid precipitates that can be dissolved in the lakes of Titan. To this end, we calculate the *saturation* mole fraction[7] $X_{i,\mathrm{sat}}$ of the i compound, which is given by (Equation (7) of D89):

$$\ln(\Gamma_i X_{i,\mathrm{sat}}) = (\Delta H_m / R T_m)(1 - T_m / T), \quad (2)$$

where T_m is the component's melting temperature and ΔH_m is its enthalpy of fusion. Our calculation procedure is then conducted as follows:

1. The unknown X_is and Y_is are computed via the Newton–Raphson method.
2. Once the X_is have been determined, the $X_{i,\mathrm{sat}}$s are in turn calculated and compared to the X_is for each species. If for compound i we get $X_{i,\mathrm{sat}} < X_i$, then we fix $X_i = X_{i,\mathrm{sat}}$.
3. We get new values of X_is and $X_{i,\mathrm{sat}}$s via the resolution of the nonlinear system.
4. The iterations are continued until we get a difference between $X_{i,\mathrm{sat}}$ and X_i lower than 10^{-6}, value for which the numerical inaccuracy is clearly negligible compared to other sources of uncertainties.

[7] The saturation mole fraction of the i compound corresponds to the maximum mole fraction of i in the liquid form. Above this value, the i material in excess remains in solid form.

Table 2
Precipitation Rates (τ) Assumed at the Ground Level

Form	Compound	Rate τ (cm^{-2} s^{-1})
Liquid	C_2H_6	3.4×10^{9}[a]
	C_3H_8	3.3×10^{8}[a]
	C_4H_8	6.2×10^{7}[a]
Solid	HCN	1.3×10^{8}[a]
	C_4H_{10}	5.4×10^{7}[a]
	C_2H_2	5.1×10^{7}[a]
	CH_3CN	4.4×10^{6}[a]
	CO_2	1.3×10^{6}[a]
	C_6H_6	1.0×10^{6}[b]

Notes.
[a] Lavvas et al. (2008a, 2008b);
[b] Vuitton et al. (2008).

The known Y_is are given in Table 1. The precipitation rates used here are given in Table 2 and derived from the photochemical models of Lavvas et al. (2008a, 2008b) and Vuitton et al. (2008). They correspond to the main products of CH_4 and N_2 photolysis. These rates allow us to express each i compound that precipitates in the form $X_i = \frac{\tau_i}{\tau_{C_2H_6}} \times X_{C_2H_6}$. We also ensure that $\sum_i X_i = 1$ and $\sum_i Y_i = 1$. The thermodynamic data used in our calculations are derived from the NIST database[8] when they are available and the remaining ones have been taken from D89. Note that H_2 is the only compound whose mole fraction in the liquid is not determined with the aforementioned procedure. Instead, we calculate the amount of dissolved H_2 in the liquid via Henry's law (D89).

3. RESULTS

Our calculations in the framework of thermodynamic equilibrium have been performed for two different regions of Titan's surface. The first zone corresponds to the vicinity of the landing site of the Huygens probe, where the surface temperature was measured to be 93.65 K (Niemann et al. 2005). The Huygens probe detected drainage-like features and a high surface relative humidity, so the presence of liquids cannot be excluded in this area (Tomasko et al. 2005; Niemann et al. 2005). The second zone corresponds to the north pole of Titan where the surface temperature is around ∼90 K based on near-surface brightness temperature measurements (Jennings et al. 2009). In both cases, the atmospheric pressure is assumed to be identical and corresponds to that (1.46 bar) measured by Huygens at the ground level (Niemann et al. 2005).

Figure 1 shows the variation of the composition of Titan's lakes as a function of the surface temperature. It appears that the mole fractions of CH_4, N_2, CO, and Ar decrease with the increase of temperature, while the mole fraction of C_2H_6 and of the precipitates increase. This is due to the vapor pressure of C_2H_6, whose temperature dependence is lower than those of CH_4, N_2, CO, and Ar. Figure 2 displays the variation of the composition of the lakes of Titan as a function of the atmospheric CH_4 mole fraction at the ground level, assuming a surface temperature of 93.65 K. It shows that an increase of the CH_4 atmospheric mixing ratio enhances its corresponding mole fraction in the liquid, as well as those of N_2, CO, and Ar. Interestingly enough, HCN is the only compound reaching saturation within the considered ranges of temperature and atmospheric methane mole fraction. Indeed, the HCN mole fraction represented as a function of

[8] http://webbook.nist.gov

Retour à la table des matières : p. v

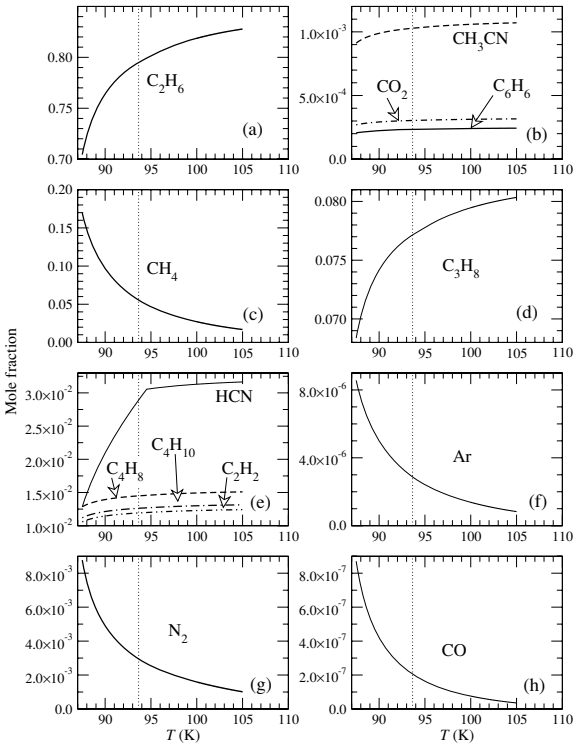

Figure 1. (a)–(h) Composition of lakes as a function of the surface temperature. The vertical dashed line corresponds to the surface temperature of 93.65 K measured by Huygens.

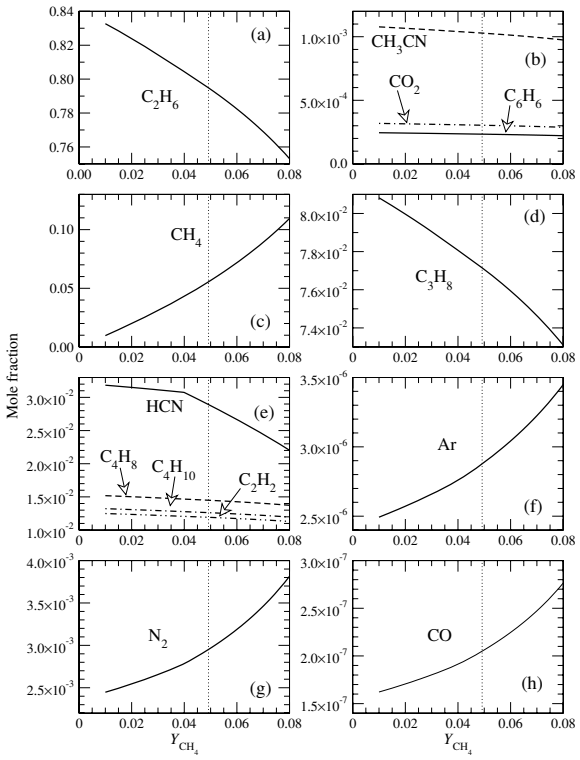

Figure 2. (a)–(h) Composition of lakes as a function of the methane atmospheric mole fraction, assuming a surface temperature of 93.65 K. The vertical dashed line corresponds to the methane atmospheric mole fraction measured by Huygens at the ground level.

the soil temperature in Figure 1(e) corresponds to the saturation limit for any temperature lower than 94.5 K (change of the curve's slope). This is due to the solubility of this compound diminishing with decreasing temperature. Moreover, Figure 2(c) shows that when Y_{CH_4} is larger than ~ 0.04, the lake is saturated in HCN. Because it is denser than the liquid,[9] the non-dissolved HCN should sink in the lakes of Titan.

Table 3 gives the mole fractions of the main compounds in lakes formed on the surface of Titan and shows that, whatever the considered site, their composition is dominated by C_2H_6, C_3H_8, CH_4, HCN, C_4H_8, C_4H_{10}, and C_2H_2. On the other hand, with mole fractions much lower than 1%, N_2, C_6H_6, CH_3CN, CO_2, Ar, CO, and H_2 are found to be minor compounds in the lakes.

4. DISCUSSION

The use of more up-to-date thermodynamic data and the recent Cassini–Huygens measurements, results in our calculated composition of the lakes differing from that of the hypothetical global ocean determined by D89. Indeed, considering the D89 case most closely corresponding to actual Titan conditions ($T = 92.5$ K, $Y_{Ar} = 0$, and $Y_{CH_4} = 0.0492$; see their Figure 1), they obtained mole fractions of C_2H_6, CH_4, and N_2 of ~0.35, 0.60, and 0.05, respectively. The most striking difference in the comparison is that the mole fraction of N_2 is more than 10 times lower in our results than in theirs, and some compounds considered as minor in the ocean of D89 are not negligible in the composition of our lakes. However, our model reproduces the results of D89 when we adopt precisely the same thermodynamic parameters. The fact that relatively small differences (order of a few percent) between our thermodynamic data extracted from the NIST database and those of D89 lead to significantly different results illustrates the nonlinearity of the system of equations determining the composition of the

Table 3
Chemical Composition of Lakes at the Poles and the Equator

	Equator (93.65 K)	Poles (90 K)
Main composition (lake mole fraction)		
N_2	2.95×10^{-3}	4.90×10^{-3}
CH_4	5.55×10^{-2}	9.69×10^{-2}
Ar	2.88×10^{-6}	5.01×10^{-6}
CO	2.05×10^{-7}	4.21×10^{-7}
C_2H_6	7.95×10^{-1}	7.64×10^{-1}
C_3H_8	7.71×10^{-2}	7.42×10^{-2}
C_4H_8	1.45×10^{-2}	1.39×10^{-2}
H_2	5.09×10^{-11}	3.99×10^{-11}
Solutes (lake mole fraction)		
HCN	2.89×10^{-2}(s)	2.09×10^{-2}(s)
C_4H_{10}	1.26×10^{-2} (ns)	1.21×10^{-2}(ns)
C_2H_2	1.19×10^{-2} (ns)	1.15×10^{-2}(ns)
C_6H_6	2.34×10^{-4} **(ns)**	2.25×10^{-4}**(ns)**
CH_3CN	1.03×10^{-3} (ns)	9.89×10^{-4}(ns)
CO_2	3.04×10^{-4} (ns)	2.92×10^{-4}(ns)

Notes. (s): saturated; (ns) non-saturated.

[9] The mean molar volume of the liquid HCN is 4.8×10^{-5} m^3 mol^{-1} while that of solid HCN is lower than 3.8×10^{-5} m^3 mol^{-1}.

Retour à la table des matières : p. v

liquid. It is difficult to quantify the errors on the predicted mole fractions of the different species because our model is based on thermodynamic data much of which is provided either without uncertainties or is derived from extrapolation of data to low temperature. However, numerical tests aiming to investigate the sensitivity of our model to the photochemical models we employ indicate that a $\pm$ 30% variation of the C_2H_6 precipitation rate induces similar variations for the C_3H_8 to C_6H_6 lake mole fractions but poorly alters the N_2 to C_2H_6 lake mole fractions given in Table 3. Moreover, as shown by Figure 2, a variation of the methane atmospheric abundance hardly affects the lake mole fractions of the precipitates. Pure numerical errors due to the algorithm have been estimated absolutely negligible.

We also outline that the assumption of thermodynamic equilibrium between the lakes and the atmosphere is a crude approximation since in fact the humidity and temperature of the atmosphere in contact with the lakes are determined by dynamic processes such as convection and wind advection (Mitri et al. 2007).

Our solubility calculations imply that a number of species produced by methane photolysis and energetic particle chemistry in Titan's upper atmosphere should be readily detectable with a mass spectrometer carried to the surface of a liquid-filled lake by a Huygens-like entry probe (Coustenis et al. 2009). The measured abundances of multiple minor constituents in the lake, coupled to measurements and models of stratospheric abundances and production rates, and direct temperature measurements of the lake surface, will constrain lake properties that are of interest in understanding the methane hydrologic cycle. For example, at the winter pole a seasonally deposited upper layer of liquid methane might exist on top of a longer-lived ethane–methane liquid reservoir by virtue of methane's lower density and limited vertical mixing in the cold lakes (Stevenson & Potter 1986). Such a transient layer would be bereft of minor components compared with our values thanks to the slow sedimentation rate of the high altitude aerosols compared to the seasonal (meteorological) methane deposition rate; our solubility values provide a means of calculating the extent to which the longer-lived liquid reservoir below has mixed into the methane meteorological layer. (The extreme cold of the tropopause of Titan prevents the hydrocarbon constituents other than methane and possibly ethane from passing directly to the lower atmosphere in the gas phase; thus the lakes must be seeded by stratospheric aerosol sedimentation.)

A longer-lived ethane–methane lake sampled at the summer pole might still have undergone pole-to-pole transport on timescales of tens of millenia thanks to the precession of perihelion of Saturn's orbit around the Sun (Aharonson et al. 2009). The abundances of minor constituents compared to our values which assume accumulation over geologic time, coupled with the aerosol sedimentation rate, could be used to "date" the liquid reservoir and hence test whether they have been cycled on the "Milankovitch" timescale. For species that are chemically inactive and occur as gas only in the atmosphere, such as the noble gases, the lakes provide a second reservoir other than the atmosphere to measure abundances. Variations from the atmospheric value of, for example, $^{40}Ar/^{36}Ar$, might hint at contact between the lakes and a much deeper crustal reservoir of liquid methane and ethane not in contact with the atmosphere (Hayes et al. 2008). Finally, our results provide the chemical data needed to compute the amount of deposition of various hydrocarbons and nitriles in fluvial valleys in the Titan's midlatitudes, as a function of the flow of methane runoff from convective storms, allowing potential tests of models of fluvial erosion (Perron et al. 2006).

This work was supported in part by the CNES. Support from the PID program "Origines des Planètes et de la Vie" of the CNRS, and the *Cassini* project, is also gratefully acknowledged. We acknowledge Bruno Bézard, Sébastien Lebonnois, and Pascal Rannou for helpful discussions about Titan's atmosphere. We thank John Prausnitz for providing us with some unpublished thermodynamic data. We thank an anonymous reviewer for his constructive comments which helped us improve our manuscript.

REFERENCES

Aharonson, O., Hayes, A. G., Lunine, J. I., Lorenz, R. D., Allison, M. D., & Elachi, C. 2009, Nat. Geosci., submitted
Brown, R. H., et al. 2008, Nature, 454, 607
Campbell, D. B., Black, G. J., Carter, L. M., & Ostro, S. J. 2003, Science, 302, 431
Coustenis, A., Lunine, J., Matson, D. L., Hansen, C., Reh, K., Beauchamp, P., Lebreton, J.-P., & Erd, C. 2009, Lunar and Planetary Institute Science Conf. Abstracts, 40, 1060
de Kok, R., et al. 2007, Icarus, 186, 354
Dubouloz, N., Raulin, F., Lellouch, E., & Gautier, D. 1989, Icarus, 82, 81
Flasar, F. M. 1983, Science, 221, 55
Graves, S. D. B., Mc Kay, C. P., Griffith, C. A., Ferri, F., & Fulchignoni, M. 2008, Planet. Space Sci., 56, 346
Hayes, A., et al. 2008, Geophys. Res. Lett., 35, 9204
Jennings, D. E., et al. 2009, ApJ, 691, L103
Lavvas, P. P., Coustenis, A., & Vardavas, I. M. 2008a, Planet. Space Sci., 56, 27
Lavvas, P. P., Coustenis, A., & Vardavas, I. M. 2008b, Planet. Space Sci., 56, 67
Lorenz, R. D., Biolluz, G., Encrenaz, P., Janssen, M. A., West, R. D., & Muhleman, D. O. 2003, Planet. Space Sci., 51, 353
Lunine, J. I., Stevenson, D. J., & Yung, Y. L. 1983, Science, 222, 1229
Mc Ewen, A., et al. 2005, BAAS, 37, 739
Mc Kay, C. P., Pollack, J. B., Lunine, J. I., & Courtin, R. 1993, Icarus, 102, 88
Mitri, G., Showman, A. P., Lunine, J. I., & Lorenz, R. D. 2007, Icarus, 186, 385
Muhleman, D. O., Grossman, A. W., & Butler, B. J. 1995, Annu. Rev. Earth Planet. Sci., 23, 337
Niemann, H. B., et al. 2005, Nature, 438, 779
Owen, T., & Niemann, H. B. 2009, R. Soc. Lond. Philos. Trans. Ser. A, 367, 607
Perron, J. T., Lamb, M. P., Koven, C. D., Fung, I. Y., Yager, R., & Adamkovics, M. 2006, J. Geophys. Res., 111, E11001
Stevenson, D. J., & Potter, B. E. 1986, Geophys. Res. Lett., 13, 93
Stofan, E. R., et al. 2007, Nature, 445, 61
Tokano, T. 2005, Adv. Space Res., 36, 286
Tomasko, M. G., et al. 2005, Nature, 438, 765
Vuitton, V., Yelle, R. V., & Cui, J. 2008, J. Geophys. Res. (Planets), 113, 5007

Retour à la table des matières : p. v

4.2 Article sur la dissolution des gaz rares dans les lacs de Titan

The Astrophysical Journal Letters, 721:L117–L120, 2010 October 1 doi:10.1088/2041-8205/721/2/L117
© 2010. The American Astronomical Society. All rights reserved. Printed in the U.S.A.

ABOUT THE POSSIBLE ROLE OF HYDROCARBON LAKES IN THE ORIGIN OF TITAN'S NOBLE GAS ATMOSPHERIC DEPLETION

D. Cordier[1,2,3], O. Mousis[4], J. I. Lunine[5], S. Lebonnois[6], P. Lavvas[7], L. Q. Lobo[8], and A. G. M. Ferreira[8]
[1] Ecole Nationale Supérieure de Chimie de Rennes, CNRS, UMR 6226, Avenue du Général Leclerc, CS 50837, 35708 Rennes Cedex 7, France; daniel.cordier@ensc-rennes.fr
[2] Université européenne de Bretagne, Rennes, France
[3] Institut de Physique de Rennes, CNRS, UMR 6251, Université de Rennes 1, Campus de Beaulieu, 35042 Rennes, France
[4] Université de Franche-Comté, Institut UTINAM, CNRS/INSU, UMR 6213, 25030 Besançon Cedex, France
[5] Dipartimento di Fisica, Università degli Studi di Roma "Tor Vergata," Rome, Italy
[6] Laboratoire de Météorologie Dynamique, Jussieu, P.O. Box 99, 75252 PARIS cedex 05, France
[7] Lunar and Planetary Laboratory, University of Arizona, Tucson, AZ, USA
[8] Departamento de Engenharia Quimica, Universidade de Coimbra, Coimbra 3030-290, Portugal
Received 2010 May 10; accepted 2010 August 11; published 2010 September 9

ABSTRACT

An unexpected feature of Titan's atmosphere is the strong depletion in primordial noble gases revealed by the Gas Chromatograph Mass Spectrometer aboard the *Huygens* probe during its descent on 2005 January 14. Although several plausible explanations have already been formulated, no definitive response to this issue has yet been found. Here, we investigate the possible sequestration of these noble gases in the liquid contained in lakes and wet terrains on Titan and the consequences for their atmospheric abundances. Considering the atmosphere and the liquid existing on the soil as a whole system, we compute the abundance of each noble gas relative to nitrogen. To do so, we make the assumption of thermodynamic equilibrium between the liquid and the atmosphere, the abundances of the different constituents being determined via regular solution theory. We find that xenon's atmospheric depletion can be explained by its dissolution at ambient temperature in the liquid presumably present on Titan's soil. In the cases of argon and krypton, we find that the fractions incorporated in the liquid are negligible, implying that an alternative mechanism must be invoked to explain their atmospheric depletion.

Key words: planets and satellites: atmospheres – planets and satellites: individual (Titan) – planets and satellites: general

1. INTRODUCTION

A striking feature of the atmosphere of Titan is that no primordial noble gases other than argon were detected by the Gas Chromatograph Mass Spectrometer (GCMS) on board the *Huygens* probe during its descent to Titan's surface in 2005 January. The detected argon includes primordial ^{36}Ar present in subsolar abundance in Titan's atmosphere (^{36}Ar/^{14}N is found to be about six orders of magnitude lower than the solar value) and the radiogenic isotope ^{40}Ar, which is a decay product of ^{40}K (Niemann et al. 2005). The other primordial noble gases ^{38}Ar, Kr, and Xe were not detected by the GCMS instrument, yielding upper limits of 10^{-8} for their atmospheric mole fractions.

The interpretation of the noble gas deficiency measured in Titan's atmosphere has been the subject of several studies in the recent literature. Thus, Osegovic & Max (2005) proposed that these species could be preferentially stored in clathrates present on the satellite's surface. They calculated the composition of clathrates on the surface of Titan using the program CSMHYD developed by Sloan (1998) and showed that such crystalline ice structures may act as a sink for Xe. However, the CSMHYD code used by Osegovic & Max (2005) is not suitable below 140 K for the gas mixtures of interest, whereas the mean surface temperature of Titan is below 95 K (Cordier et al. 2009), and the authors did not explicitly calculate the trapping efficiencies of Ar and Kr in clathrates on the surface of the satellite. These considerations led Thomas et al. (2007, 2008) to rethink their results. In both studies, the authors found that the trapping efficiency of clathrates is high enough to significantly decrease the atmospheric concentrations of Xe and Kr irrespective of the initial gas phase composition, provided that these clathrates are abundant enough on the surface of Titan. In contrast, they found that Ar is poorly trapped in clathrates and that this mechanism alone could not explain the argon impoverishment measured in Titan's atmosphere. Another interpretation of the Ar, Kr, and Xe deficiencies is that the haze present in Titan's atmosphere could simultaneously trap these three noble gases in a way consistent with the observed atmospheric abundances (Jacovi & Bar-Nun 2008). In this mechanism, the open structure of the small aerosol particles would allow the noble gas atoms to fill their pores. All these hypotheses are based on different assumptions (requirement of large amounts of clathrates on the satellite's surface or formation of Titan's aerosols in exactly the same conditions as those used during laboratory experiments) that will need to be investigated by in situ measurements or observations performed by future spacecraft missions.

In this Letter, we offer another hypothesis that Titan's hydrocarbon lakes play a key role in the impoverishment of its atmospheric noble gases. Indeed, hundreds of radar dark features interpreted as hydrocarbon lakes have been detected in the polar regions (Stofan et al. 2007). Recently, Cordier et al. (2009) have published a study of the chemical composition of Titan's lakes, which is based on the direct abundance measurements from the GCMS on board the *Huygens* probe and recent photochemical models based on the vertical temperature profile derived by the *Huygens* Atmospheric Structure Instrument. Here, we extend the model of Cordier et al. (2009) by including simultaneously Ar, Kr, and Xe in the composition of the liquid phase. We then explore the amount of liquid that is needed on the surface of Titan to account for the measured noble gas atmospheric abundances assuming solar abundances in the bulk system.

2. NOBLE GASES SEQUESTRATION IN TITAN'S SURFACE LIQUID PHASE

Here, we consider the atmosphere and the liquid existing on the surface of Titan as a single, fully coupled system. Our approach consists in 1) computing the ratio $N_{\rm NG}/N_{\rm nitrogen}$, where $N_{\rm NG}$ and $N_{\rm nitrogen}$ are the total numbers of atoms of a given noble gas NG and of nitrogen, respectively, and 2) comparing this result to the ratio $(N_{\rm NG}/N_{\rm nitrogen})_{\odot}$ derived from protosolar abundances (Lodders 2003). Our calculations always refer to nitrogen because it is the most abundant compound detected in Titan's atmosphere and because thermodynamic equilibrium models predict that it is also present in the lakes (see Cordier et al. 2009). Under these conditions, for a noble gas (NG), we can write

$$\frac{N_{\rm NG}}{N_{\rm nitrogen}} = \frac{N^{\rm (liq)}_{\rm tot,NG} + N^{\rm (atm)}_{\rm tot,NG}}{N^{\rm (liq)}_{\rm tot,nitrogen} + N^{\rm (atm)}_{\rm tot,nitrogen}}, \quad (1)$$

where $N^{\rm (liq)}_{\rm tot}$ and $N^{\rm (atm)}_{\rm tot}$ are the total number of atoms of the NG element or nitrogen in the liquid and in the atmosphere of Titan, respectively.

The total mole number of element NG in Titan's liquid is given by

$$N^{\rm (liq)}_{\rm tot,NG} = \frac{x^{\rm (liq)}_{\rm NG} \times V^{\rm (liq)}_{\rm tot} \times \rho^{\rm (liq)}}{\bar{M}}, \quad (2)$$

where $x^{\rm (liq)}_{\rm NG}$ is the mole fraction of atoms of NG in lakes computed following the method described in Cordier et al. (2009), $V^{\rm (liq)}_{\rm tot}$ is the total volume of Titan's liquid in contact with the atmosphere, $\rho^{\rm (liq)}$ is their mean density (in kg.m^{-3}), and $\bar{M}$ is the mean molecular weight of the liquid. $\bar{M}$ is given by

$$\bar{M} = \sum_j x_j \times M_j, \quad (3)$$

where the sum $\sum_j$ runs over all species present in the liquid phase. The composition of the liquid is calculated via the thermodynamic equilibrium model of Titan's lakes described by Cordier et al. (2009). In this approach, thermodynamic equilibrium, which translates into the equality of chemical potentials for each species listed in Table 1 from N_2 to C_2H_6 (except for H_2), can be expressed as

$$y_i\ P = \Gamma_i\ x_i\ P_{vp,i}, \quad (4)$$

where P is the total pressure at Titan's surface, y_i and x_i are, respectively, the mole fractions of the i compound in the atmosphere and in the liquid, $P_{vp,i}$ is its vapor pressure, and Γ_i is its activity coefficient in the liquid determined with Equation (2) of Dubouloz et al. (1989). Abundances of compounds below C_2H_6 in Table 1 are expressed proportionally to that of C_2H_6 both in the precipitation and in the liquid existing in the lakes or in the putative porous network.

In order to compute $N^{\rm (liq)}_{\rm tot,NG}$ for all noble gases, we have extended the thermodynamic equilibrium model by adding Kr and Xe to the list of species already taken into account by Cordier et al. (2009). The thermodynamic data essentially derive from the NIST database[9] in which the vapor pressures are expressed in the forms of Antoine's equations. On the other hand, the enthalpies of vaporization and molar volume of Ar, which are needed in the computation of its activity coefficient via the determination of its solubility parameter (see Prausnitz et al. 1986), have been updated relative to the value adopted by Cordier et al. (2009) and now are derived from the laboratory measurements published by Ferreira & Lobo (2008) and Tegeler et al. (1999), respectively. On the other hand, the enthalpies of vaporization and molar volumes of Kr and Xe all derive from the experimental data published by Ferreira & Lobo (2009).

[9] http://webbook.nist.gov/chemistry

Table 1
Composition of Liquid (Mole Fraction at Given Temperature)

Species	87 K	90 K	93.65 K	
N_2	1.22×10^{-2}	4.94×10^{-3}	2.96×10^{-3}	
CH_4	2.18×10^{-1}	9.74×10^{-2}	5.56×10^{-2}	
Ar	1.01×10^{-5}	4.95×10^{-6}	3.09×10^{-6}	
Xe	8.55×10^{-3}	1.52×10^{-3}	3.09×10^{-4}	
Kr	7.72×10^{-9}	3.13×10^{-9}	1.92×10^{-9}	
CO	1.24×10^{-6}	4.25×10^{-7}	2.05×10^{-7}	
H_2	2.94×10^{-11}	4.08×10^{-11}	5.12×10^{-11}	
C_2H_6	6.55×10^{-1}	7.62×10^{-1}	7.95×10^{-1}	
C_3H_8	6.36×10^{-2}	7.40×10^{-2}	7.71×10^{-2}	
C_4H_8	1.19×10^{-2}	1.39×10^{-2}	1.45×10^{-2}	
HCN	9.06×10^{-3}	2.08×10^{-2}	2.89×10^{-2}	(s)
C_4H_{10}	1.04×10^{-2}	1.21×10^{-2}	1.26×10^{-2}	(ns)
C_2H_2	9.83×10^{-3}	1.14×10^{-2}	1.19×10^{-2}	(ns)
CH_3CN	8.48×10^{-4}	9.87×10^{-4}	1.03×10^{-3}	(ns)
CO_2	2.50×10^{-4}	2.92×10^{-4}	3.04×10^{-4}	(ns)
C_6H_6	1.93×10^{-4}	2.24×10^{-4}	2.34×10^{-4}	(ns)

Notes. From HCN to C_6H_6, compounds are in the solid state in precipitates and are assumed to dissolve when they reach the liquid phase. (s): saturated; (ns): non saturated. Ar is the total argon contained in all isotopes.

The total mole number of element NG in Titan's atmosphere is determined via the following vertical integration:

$$N^{\rm (atm)}_{\rm tot,NG} = \int_{z=0}^{z=H} \frac{y^{\rm (atm)}_{\rm NG} \times \rho^{\rm (atm)}(z)}{\bar{M}^{\rm (atm)}(z)}\, 4\pi\, (R_{\rm Titan} + z)^2 dz, \quad (5)$$

where $R_{\rm Titan}$ is the radius of Titan, z the altitude and H the maximum elevation at which the *Huygens* GCMS started to collect data, $\rho^{\rm (atm)}(z)$ is the atmospheric density at the elevation z whose determination derives from the *Huygens* HASI data (Fulchignoni et al. 2005), and $x^{\rm (atm)}_{\rm NG}$ is the mole fraction of element NG derived from the GCMS data at the ground level (Niemann et al. 2005) and is assumed to be constant whatever the altitude. The mean molecular weight $\bar{M}^{\rm (atm)}(z)$ of the atmosphere is also derived from the *Huygens* GCMS data using an approach similar to the one used to calculate the mean molecular weight of the liquid (see Equation (3)).

3. ASSUMPTIONS ABOUT THE TITAN ENVIRONMENT

Atmospheric mole fraction data used as inputs in our model are gathered in Table 2. The atmospheric abundances of species which are not included in this table are assumed negligible. We have set the atmospheric mole fractions of Kr and Xe to 10^{-8} because they correspond to the detection limit of the *Huygens* GCMS instrument. Following the approach of Cordier et al. (2009), atmospheric mole fractions of N_2 and C_2H_6 are treated as unknowns of our problem and atmospheric abundances of compounds below the one of C_2H_6 are neglected. In order to investigate the temperature dependence of the mole fractions of noble gases trapped in Titan's surface liquid, we have allowed

Retour à la table des matières : p. v

Table 2
Assumed Composition of Titan's Atmosphere at the Ground Level.

Atmosphere	Mole Fraction	Determination
H_2	9.8×10^{-4}	*Huygens* GCMS[a]
N_2	0.95	This work
CH_4	0.0492	*Huygens* GCMS[b]
CO	4.70×10^{-5}	*Cassini* CIRS[c]
^{40}Ar	4.32×10^{-5}	*Huygens* GCMS[b]
^{36}Ar	2.80×10^{-7}	*Huygens* GCMS[b]
Kr	10^{-8}	*Huygens* GCMS[b]
Xe	10^{-8}	*Huygens* GCMS[b]
C_2H_6	1.49×10^{-5}	This work

Notes. N_2 and C_2H_6 abundances are determined from our model (see the text).
[a] Owen & Niemann (2009).
[b] Niemann et al. (2005).
[c] de Kok et al. (2007).

the ground temperature to range between 87 and 94 K. These extreme values bracket the mean ground temperature estimated to be ~90–91 K in northern polar regions where lake candidates are located (Janssen et al. 2009) and the temperature of 93.65 K measured by the *Huygens* probe at its landing site (Niemann et al. 2005).

Current inventories of Titan's lakes are estimated to range between 3×10^4 and 3×10^5 km^3 (Lorenz et al. 2008). In the present study, we consider a more generous range for the total volume of liquid existing at the surface of Titan, including a fraction that might reside in wet terrains. A substantial fraction of liquid incorporated in Titan's soil, even at the equator, is plausible because the *Huygens* probe firmly identified ethane in the mass spectra taken from the surface (Niemann et al. 2005). Moreover, it has been proposed that the subsurface of Titan is porous, implying that large amounts of liquid hydrocarbons could remain in contact with the atmosphere via open pores in the soil (Mousis & Schmitt 2008). Hence, assuming that the total volume of liquid existing on Titan's surface could be up to 10 times the total volume estimated for the lakes, we consider here three different liquid volume values: 3×10^4, 3×10^5, and 3×10^6 km^3. Note that the larger volume of liquid considered here remains ~10 times lower than the total amount of ethane that could have precipitated on Titan's surface if one assumes a precipitation rate of 3.4×10^9 molecules cm^{-2} s^{-1} (Lavvas et al. 2008a, 2008b) over 4.5 Gyr.

4. RESULTS

Our calculations, including both ^{36}Ar and ^{40}Ar isotopes, produce an $N_{Ar}/N_{nitrogen}$ ratio (~2.24×10^{-5}) that remains more than three orders of magnitude lower than the value inferred from solar abundances ($(N_{Ar}/N_{nitrogen})_\odot = 5.26 \times 10^{-2}$), irrespective of the adopted values for the temperature and total volume of lakes. Because ^{36}Ar is the main primordial argon isotope (Lodders 2003), we note that even if all the argon dissolved in the liquid was in the form of this isotope, this could not explain its apparent depletion in Titan's atmosphere. This behavior is explained by the very low solubility of argon in the C_2H_6-dominated liquid in the considered temperature range. Even if the liquid volume is of the order of 3×10^6 km^3, almost all argon remains in the atmosphere, the fraction incorporated in liquid playing only a negligible role. Hence, whatever the source of argon, i.e., primordial or radiogenic, we conclude that the argon depletion observed in Titan's atmosphere cannot be explained by its sequestration in the liquid in contact with Titan's atmosphere.

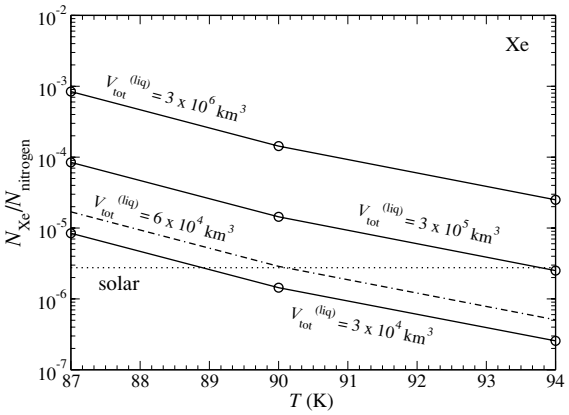

Figure 1. Global $N_{Xe}/N_{nitrogen}$ ratio in Titan versus ground temperature for different volumes of lakes. The horizontal line represents the solar value. Other lines, from top to bottom, derive from our calculations for the considered volumes of liquid available at ground level. The assumed atmospheric mole fraction corresponds to the GCMS detection threshold ($y_{Xe} = 10^{-8}$).

In the case of krypton, the computed $N_{Kr}/N_{nitrogen}$ ratio (~5×10^{-9}) is about three to four orders of magnitude lower than the solar value ($(N_{Kr}/N_{nitrogen})_\odot = 2.83 \times 10^{-5}$), irrespective of the adopted values for the temperature and total volume of lakes. Similarly to the case of argon, the dissolution of krypton in liquid hydrocarbon on the surface of Titan cannot explain the observed depletion.

Figure 1 summarizes the behavior of the global ratio $N_{Xe}/N_{nitrogen}$ as a function of the temperature of Titan's surface and of the available volume of liquid. Because the thermodynamic equilibrium between the liquid phase and the atmosphere requires a larger mole fraction of xenon in the liquid, the resulting $N_{Xe}/N_{nitrogen}$ ratio is larger than the one calculated from the detection limit of the GCMS instrument. Moreover, since the atmospheric mole fraction of xenon remains fixed in our system, its solubility diminishes in the liquid with an increase of temperature.

Figure 1 shows that only the $N_{Xe}/N_{nitrogen}$ ratio reaches or exceeds the value determined from solar abundances in a temperature range consistent with the temperature inferred in polar regions and for a plausible amount of liquid on Titan's surface. Thus, a volume of liquid of about ~6×10^4 km^3 is required at 90 K to trap enough xenon to explain its apparent atmospheric depletion. The fact that xenon is much more soluble in liquid hydrocarbon than the other noble gases is consistent with their molar masses, i.e., ~39.95 g mol^{-1}, 83.80 g mol^{-1}, and 131.30 g mol^{-1} for Ar, Kr, and Xe, respectively. The most massive element remains the easiest to condense.

5. DISCUSSION

If one considers an atmospheric mole fraction of krypton lower than the detection limit ($y_{Kr} = 10^{-8}$) of the GCMS instrument, the global ratio $N_{Kr}/N_{nitrogen}$ should decrease linearly because $N_{Kr}/N_{nitrogen} \simeq N_{tot,Kr}^{(atm)}/N_{nitrogen}$ (the solubility of krypton appears to be very low: $N_{tot,Kr}^{(liq)} \ll N_{tot,Kr}^{(atm)}$) and $N_{tot,Kr}^{(atm)} \propto y_{Kr}$ (see Equation (5)). In contrast, because xenon is much more soluble than the other noble gases in the liquid hydrocarbon, we have $N_{tot,Xe}^{(liq)} \gg N_{tot,Xe}^{(atm)}$. Assuming an atmospheric abundance of

Retour à la table des matières : p. v

xenon lower than the GCMS detection threshold would also lead to a linear decrease of $N_{Xe}/N_{nitrogen}$ because $N^{(liq)}_{tot,Xe} \gg N^{(atm)}_{tot,Xe}$ and $x_{Xe} \propto y_{Xe}$, implying that $N^{(liq)}_{tot,Xe} \propto x_{Xe}$ (see Equation (2)). We find here a behavior close to Henry's law.

The variation of pressure at ground level could also play a role in the dissolution of atmospheric compounds. However, Global Circulation Models (GCMs) show that surface pressure fluctuations due to weather conditions or Saturn's tidal effects should not exceed 0.1% (Tokano & Neubauer 2002). On the other hand, using the *Cassini* Synthetic Aperture Radar (SAR), Stiles et al. (2009) have recorded surface height (referenced to the nominal 2575 km radius) in the range −1500 m to +1000 m, yielding a maximum altitude difference of ∼2500 m. We made a test at $T = 90$ K with a pressure 10% higher than the one measured by *Huygens*, i.e., a value corresponding to the unrealistic case where all the lakes and wet terrains are located at an altitude ∼1500 m below the *Huygens* landing site. Even with this pressure variation, our calculations show that the fraction of dissolved noble gases is almost unchanged and that the aforementioned results remain unaltered.

We conclude that noble gas trapping in Titan's hydrocarbon lakes and liquid contained in wet surfaces cannot be the unique answer to the problem of their apparent atmospheric depletion. The physical reality is probably a composite and several combined effects might play a role with different efficiencies. For example, in order to explain the Ar deficiency, it has been proposed that Titan's building blocks were formed in a relatively warm nebular environment which excluded both argon and molecular nitrogen (Owen 1982) or partly devolatilized during their migration within Saturn's subnebula (Alibert & Mousis 2007; Mousis et al. 2009). If the lakes of Titan are the main sink of atmospheric xenon, then krypton must have remained sequestrated in the interior of Titan because none of the alternative trapping scenarios cited in the introduction predict a krypton impoverishment relative to xenon. This study encourages direct measurements by future probes of the noble gas abundances in Saturn's atmosphere and/or in Titan's hydrocarbon lakes.

We thank an anonymous reviewer for his constructive comments which helped us improve our manuscript. We also thank Bruno Bézard and Pascal Rannou for enlightening comments.

REFERENCES

Alibert, Y., & Mousis, O. 2007, A&A, 465, 1051
Cordier, D., Mousis, O., Lunine, J. I., Lavvas, P., & Vuitton, V. 2009, ApJ, 707, L128
de Kok, R., et al. 2007, Icarus, 186, 354
Dubouloz, N., Raulin, F., Lellouch, E., & Gautier, D. 1989, Icarus, 82, 81
Ferreira, A., & Lobo, L. 2008, J. Chem. Thermodyn., 40, 1621
Ferreira, A., & Lobo, L. 2009, J. Chem. Thermodyn., 41, 809
Fulchignoni, M., et al. 2005, Nature, 438, 785
Jacovi, R., & Bar-Nun, A. 2008, Icarus, 196, 302
Janssen, M., et al. 2009, Icarus, 200, 222
Lavvas, P. P., Coustenis, A., & Vardavas, I. M. 2008a, Planet. Space Sci., 56, 27
Lavvas, P. P., Coustenis, A., & Vardavas, I. M. 2008b, Planet. Space Sci., 56, 67
Lodders, K. 2003, ApJ, 591, 1220
Lorenz, R. D., et al. 2008, Geophys. Res. Lett., 35, L02406
Mousis, O., & Schmitt, B. 2008, ApJ, 677, L67
Mousis, O., et al. 2009, ApJ, 691, 1780
Niemann, H. B., et al. 2005, Nature, 438, 779
Osegovic, J. P., & Max, M. D. 2005, J. Geophys. Res. (Planet), 110, 8004
Owen, T. 1982, Planet. Space Sci., 30, 833
Owen, T., & Niemann, H. B. 2009, Phil. Trans. R. Soc. A, 367, 607
Prausnitz, J. M., Lichtenthaler, R. N., & Azevedo, E. G. 1986, Molecular Thermodynamics of Fluid-Phase Equilibria (2nd ed.; Englewood Cliffs, NJ: Prentice-Hall)
Sloan, E. D. 1998, Clathrates Hydrates of Natural Gases (New York: Marcel Decker)
Stiles, B. W., et al. 2009, Icarus, 202, 584
Stofan, E. R., et al. 2007, Nature, 445, 61
Tegeler, C., Span, S., & Wagner, W. 1999, J. Phys. Chem. Ref. Data., 779, 829
Thomas, C., Mousis, O., Ballenegger, V., & Picaud, S. 2007, A&A, 474, L17
Thomas, C., Picaud, S., Mousis, O., & Ballenegger, V. 2008, Planet. Space Sci., 56, 1607
Tokano, T., & Neubauer, F. M. 2002, Icarus, 158, 499

Retour à la table des matières : p. v

4.3 Article sur la séquestration des gaz rares dans des clathrates de la surface de Titan

The Astrophysical Journal Letters, 740:L9 (4pp), 2011 October 10 doi:10.1088/2041-8205/740/1/L9
© 2011. The American Astronomical Society. All rights reserved. Printed in the U.S.A.

REMOVAL OF TITAN'S ATMOSPHERIC NOBLE GASES BY THEIR SEQUESTRATION IN SURFACE CLATHRATES

Olivier Mousis[1], Jonathan I. Lunine[2], Sylvain Picaud[1], Daniel Cordier[3,4], J. Hunter Waite, Jr.[5], and Kathleen E. Mandt[5]
[1] Université de Franche-Comté, Institut UTINAM, CNRS/INSU, UMR 6213, Observatoire des Sciences de l'Univers de Besancon, France; olivier.mousis@obs-besancon.fr
[2] CRSR, Cornell University, Ithaca, NY 14853, USA
[3] Université de Rennes 1, Institut de Physique de Rennes, CNRS, UMR 6251, France
[4] Ecole Nationale Supérieure de Chimie de Rennes, CNRS, UMR 6226, France
[5] Space Science and Engineering Division, Southwest Research Institute, San Antonio, TX 78228, USA
Received 2011 May 2; accepted 2011 August 23; published 2011 September 19

ABSTRACT

A striking feature of the atmosphere of Titan is that no heavy noble gases other than argon were detected by the Gas Chromatograph Mass Spectrometer aboard the *Huygens* probe during its descent to Titan's surface in 2005 January. Here we provide an explanation of the mysterious absence or rarity of these noble gases in Titan's atmosphere: the thermodynamic conditions prevailing at the surface–atmosphere interface of the satellite allow the formation of multiple guest clathrates that preferentially store some species, including all heavy noble gases, over others. The clean water ice needed for the formation of these clathrates could be delivered by successive episodes of cryovolcanic lavas that have been hypothesized to regularly cover the surface of Titan. The formation of clathrates in the porous lavas and their propensity for trapping Ar, Kr, and Xe would progressively remove these species from the atmosphere of Titan over the course of its history. In some circumstances, a global clathrate crust with an average thickness not exceeding a few meters could be sufficient on Titan for a complete removal of the heavy noble gases from the atmosphere.

Key words: planets and satellites: atmospheres – planets and satellites: composition – planets and satellites: individual (Titan) – planets and satellites: surfaces

1. INTRODUCTION

A striking feature of the atmosphere of Titan is that no heavy noble gases other than argon were detected by the Gas Chromatograph Mass Spectrometer (GCMS) aboard the *Huygens* probe during its descent to Titan's surface in 2005 January (Niemann et al. 2005, 2010). The detected argon includes primordial ^{36}Ar, present in subsolar abundance in Titan's atmosphere (^{36}Ar/^{14}N is found to be about six orders of magnitude lower than the solar value), and the radiogenic isotope ^{40}Ar, which is a decay product of ^{40}K (Niemann et al. 2005). The other primordial noble gases ^{38}Ar, Kr, and Xe were not detected by the GCMS instrument, yielding upper limits of 10^{-8} for their atmospheric mole fractions (Niemann et al. 2005, 2010).

In order to interpret this deficiency, it has been proposed that the atmospheric depletion of these species could be explained by their dissolution at ambient temperature in the hydrocarbon lakes and seas present on Titan's surface (Cordier et al. 2010). However, the fractions of argon and krypton that would dissolve in these liquids were found to be negligible (Cordier et al. 2010). Another interpretation of the lack of heavy noble gas abundances above 10 ppb in Titan's atmosphere is based on laboratory results suggesting that the haze present in Titan's atmosphere could efficiently trap argon, krypton, and xenon during its formation (Jacovi & Bar-Nun 2008). In this mechanism, the open structure of the small aerosol particles would allow the noble gas atoms to fill their pores. However, even if this trapping mechanism is effective, the erosion of sedimented aerosols might induce the progressive release of the trapped noble gases in Titan's atmosphere.

The presence of clathrate hydrates on Titan's surface has also been proposed to be the origin of the heavy noble gas deficiency measured in its atmosphere (Osegovic & Max 2005). A series of theoretical investigations showed that the trapping efficiency of these ice structures is high enough to significantly decrease the atmospheric concentrations of xenon and krypton, but failed to explain the observed argon atmospheric deficiency (Thomas et al. 2007, 2008). It was then argued that Titan's building blocks were partly devolatilized within a subnebula around the forming Saturn, implying the loss of argon initially incorporated as pure condensate prior to satellite formation (Mousis et al. 2009). However, more recent work showed that argon could have been retrapped in primordial clathrates so as to remain abundant in the planetesimals incorporated in Titan (Mousis et al. 2010). Given the evidence from ^{40}Ar that Titan is extensively outgassed (Niemann et al. 2010), it is difficult to explain the observed ^{36}Ar rarity in the atmosphere in the absence of a sink over geologic time.

Here we show that trapping over time of atmospheric argon in clathrates could indeed provide such a sink. This conclusion is based on the use of recent intermolecular potential parameters in a statistical thermodynamic model describing clathrate composition. The fresh water ice needed for the formation of these clathrates could be delivered by successive episodes of cryovolcanic lavas hypothesized to periodically cover the surface of Titan. The formation of clathrates in the porous cryolavas and their propensity for trapping Ar, Kr, and Xe would progressively remove these species from the atmosphere of Titan over the course of its history. A global clathrate crust with an average thickness not exceeding a few meters could be sufficient on Titan for a complete removal of the heavy noble gases from the atmosphere.

2. THE STATISTICAL THERMODYNAMIC MODEL

To calculate the relative abundances of guest species incorporated in a clathrate from a coexisting gas of specified

Table 1
Parameters for the Kihara Potential

Molecule	σ (Å)	ϵ/k_B (K)	a (Å)	Reference
N_2	3.13512	127.426	0.3526	SK08
CH_4	3.14393	155.593	0.3834	SK08
C_2H_6	3.24693	188.181	0.5651	SK08
Ar	2.9434	170.50	0.184	PP72
Kr	2.9739	198.34	0.230	PP72
Xe	3.32968	193.708	0.2357	SK08

Note. σ is the Lennard-Jones diameter, ϵ is the depth of the potential well, and a is the radius of the impenetrable core.

composition at given temperature and pressure, we use a model applying classical statistical mechanics that relates the macroscopic thermodynamic properties of clathrates to the molecular structure and interaction energies (van der Waals & Platteeuw 1959; Lunine & Stevenson 1985). It is based on the original ideas of van der Waals and Platteeuw for clathrate formation, which assume that trapping of guest molecules into cages corresponds to the three-dimensional generalization of ideal localized adsorption. In this work, the availability of recent intermolecular potential parameters retrieved from experiments (Sloan & Koh 2008, hereafter SK08) allows us to revise the relative abundances of guest species incorporated in a clathrate from a coexisting gas of specified composition at a temperature and pressure relevant to Titan's surface conditions.

In this formalism, the fractional occupancy of a guest molecule K for a given type t (t = small or large) of the cage can be written as

$$y_{K,t} = \frac{C_{K,t} P_K}{1 + \sum_J C_{J,t} P_J}, \quad (1)$$

where the sum in the denominator includes all the species which are present in the initial gas phase. $C_{K,t}$ is the Langmuir constant of species K in the cage of type t and P_K is the partial pressure of species K. This partial pressure is given by $P_K = x_K \times P$ (we assume that the sample behaves as an ideal gas), with x_K the mole fraction of species K in the initial gas, and P the total atmospheric gas pressure, which is dominated by N_2. The Langmuir constant depends on the strength of the interaction between each guest species and each type of cage, and can be determined by integrating the molecular potential within the cavity as

$$C_{K,t} = \frac{4\pi}{k_B T} \int_0^{R_c} \exp\left(-\frac{w_{K,t}(r)}{k_B T}\right) r^2 dr, \quad (2)$$

where R_c represents the radius of the cavity assumed to be spherical, k_B is the Boltzmann constant, and $w_{K,t}(r)$ is the spherically averaged Kihara potential representing the interactions between the guest molecules K and the H_2O molecules forming the surrounding cage t. This potential $w(r)$ can be written for a spherical guest molecule as (McKoy & Sinanoğlu 1963)

$$w(r) = 2z\epsilon\left[\frac{\sigma^{12}}{R_c^{11} r}\left(\delta^{10}(r) + \frac{a}{R_c}\delta^{11}(r)\right) - \frac{\sigma^6}{R_c^5 r}\left(\delta^4(r) + \frac{a}{R_c}\delta^5(r)\right)\right], \quad (3)$$

Table 2
Assumed Composition of Titan's Atmosphere at the Ground Level

Species K	Mole Fraction f_K	Reference
N_2	8.80×10^{-1}	This work
CH_4	4.92×10^{-2}	Niemann et al. (2005)
C_2H_6	1.49×10^{-5}	Cordier et al. (2009)
Ar	7.07×10^{-2}	This work
Kr	5.01×10^{-5}	This work
Xe	4.89×10^{-6}	This work

with

$$\delta^N(r) = \frac{1}{N}\left[\left(1 - \frac{r}{R_c} - \frac{a}{R_c}\right)^{-N} - \left(1 + \frac{r}{R_c} - \frac{a}{R_c}\right)^{-N}\right]. \quad (4)$$

In Equation (3), z is the coordination number of the cell. This parameter depends on the structure of the clathrate (I or II) and on the type of the cage (small or large). The Kihara parameters a, σ, and ϵ for the molecule–water interactions, given in Table 1, have been taken from the recent work of SK08 when available and from Parrish & Prausnitz (1972, hereafter PP72) for the remaining species.

Finally, the mole fraction f_K of a guest molecule K in a clathrate can be calculated with respect to the whole set of species considered in the system as

$$f_K = \frac{b_s y_{K,s} + b_\ell y_{K,\ell}}{b_s \sum_J y_{J,s} + b_\ell \sum_J y_{J,\ell}}, \quad (5)$$

where b_s and b_l are the number of small and large cages per unit cell, respectively, for the clathrate structure under consideration, and with $\sum_K f_K = 1$. Values of R_c, z, b_s, and b_l are taken from PP72.

3. RESULTS

Table 2 gives the composition of Titan's atmosphere used in our calculations. We made the conservative assumption that all noble gases were initially present in the atmosphere of Titan, with Ar/N, Kr/N, and Xe/N ratios assigned to be solar (Asplund et al. 2009). Because our composition calculations are only valid along the equilibrium curve of the clathrate of interest, they were performed at 165.8 K, i.e., the equilibrium temperature of a multiple guest clathrate formed from the atmosphere of Titan possessing a pressure of 1.46 bar at the surface (see the Appendix). Composition calculations have been performed in the cases of structure I and II clathrates. We have also taken into account the influence of variation of the cage sizes on the mole fractions of guests encaged in clathrates by modifying the values of their initial radius by up to 3%. Indeed, thermal expansion or contraction measured in the temperature range of 90–270 K has been found to significantly affect the composition of clathrates as well as their dissociation pressures that define the (P,T) loci of stability (Mousis et al. 2010; Belosludov et al. 2002).

Figure 1 gives the composition of structure I and II clathrates expected to form on the surface of Titan from the nitrogen-dominated atmosphere in the cases of our nominal model (no cage variation) and a 2% contraction of the cages (Belosludov et al. 2002). Assuming that noble gases are in solar abundances relative to elemental nitrogen (Asplund et al. 2009), the total number of Ar, Kr, and Xe atoms that would exist in the atmosphere of Titan is of the order of 1.06×10^{43}, 3.23×10^{39}, and 2.02×10^{38}, respectively. The equivalent volume of

Retour à la table des matières : p. v

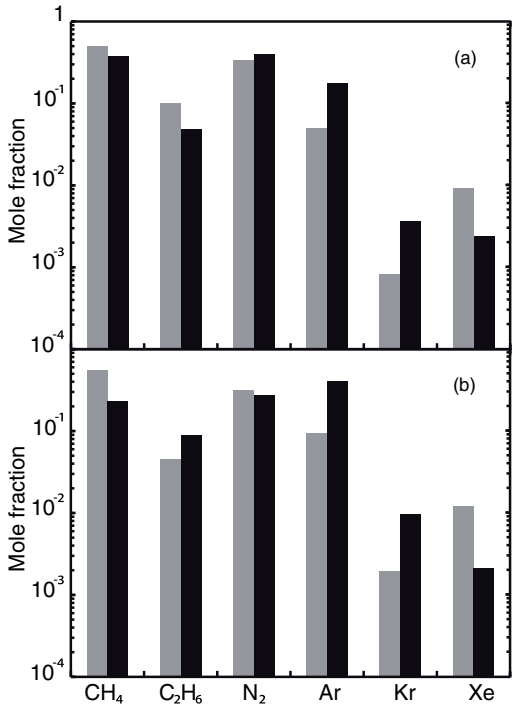

Figure 1. Mole fraction F_K of volatile K encaged in multiple guest clathrate formed on Titan's surface at $T = 165.8$ K and $P = 1.46$ bar. Calculations are performed in the cases of (a) our nominal model (no cage variation) and (b) a 2% contraction of the cages. Gray and dark bars correspond to structure I and structure II clathrates, respectively.

clathrate needed to fully trap argon, the most abundant noble gas, would then be about 2.29×10^{15} m^3 in clathrates, irrespective of the considered structure.[6] On the other hand, since the mole fraction of Ar has been found to be about 5.01×10^{-2} and 1.78×10^{-1} in structure I and II clathrates of our nominal model, we then obtain a total clathrate volume of 4.55×10^{16} and 1.28×10^{16} m^3 needed to trap simultaneously the three noble gases in these two structures, respectively. In the case of a 2% contraction of the cages, the mole fraction of Ar becomes 9.24×10^{-2} and 4.02×10^{-1} in structure I and II clathrates, corresponding to a total clathrate volume of 2.47×10^{16} and 5.67×10^{15} m^3 in these two structures, respectively. Interestingly, irrespective of the considered case, Ar remains the less efficiently trapped of the three considered noble gases (respectively, to their initial atmospheric abundances) so its complete enclathration also implies the full trapping of krypton and xenon.

Figure 2 represents the thickness of the clathrate layer needed to trap the three noble gases as a function of the variation of the cage sizes in the cases of structure I and II clathrates. In the case of the nominal model, the total clathrate volume translates into a multiple guest clathrate layer with an equivalent thickness of about 549.6 and 154.7 m globally averaged in structures I and II, respectively. If one considers the case corresponding to a 2% contraction of the clathrate cages, then the equivalent thickness of the clathrate layer would be reduced to about 298.0 and 68.6 m over the surface of Titan in structures I and II, respectively.

[6] The unit cell of structure I consists of 8 cages for a unit volume of 1.73×10^{-27} m^3 while the unit cell of structure II consists of 24 cages for a unit volume of 5.18×10^{-27} m^3.

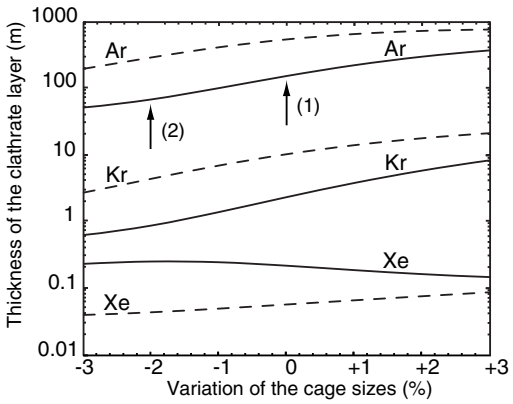

Figure 2. Thickness of structure I (dashed lines) and structure II (solid lines) clathrate layers needed to trap Ar, Kr, or Xe as a function of the cage sizes. Vertical arrows give the value of the thickness of the structure II clathrate layer needed to simultaneously trap all noble gases in the cases of (1) our nominal model (no cage variation) and (2) a 2% contraction of the cages. Calculations have been made at $T = 165.8$ K and $P = 1.46$ bar.

4. DISCUSSION

Formation scenarios predict that Titan only accreted elemental nitrogen in the form of ammonia during its formation (Mousis et al. 2002, 2009), the latter being converted into molecular nitrogen via photolysis (Atreya et al. 1978) or shock chemistry (McKay et al. 1988) in the atmosphere. If 5% of solar elemental nitrogen was accreted by Titan in the form of ammonia (Mousis et al. 2002), then the equivalent thickness of the clathrate layer would reduce to about 27.4 and 7.7 m in the nominal model and 14.8 and 3.4 m in the case of a 2% contraction of the cages in structures I and II, respectively. Our model then suggests that formation scenarios favoring the accretion of Titan from NH_3-rich and N_2-poor planetesimals are preferable because the amount of clathrates needed to explain the noble gas atmospheric deficiency is much less important than in the case of satellite accretion from N_2-rich planetesimals. It should be noted that, because (1) the atmosphere of Titan is by far dominated by N_2 and (2) N_2 clathrate is of structure II (Lunine & Stevenson 1985; SK08), we should expect the presence of structure II clathrates on the satellite's surface. In any case, future laboratory experiments aiming at investigating the formation of clathrates formed from a mixture analogous to that of Titan's atmosphere could help to disentangle between the two possible structures.

Our calculations imply that noble gas-rich clathrates either formed (1) when the surface of the satellite of Saturn was warmer than today (Thomas et al. 2007) and/or (2) during more recent release events of hot and porous cryolava possibly associated with methane delivery toward the surface (Mousis & Schmitt 2008; Tobie et al. 2006). In the first case, Titan's accretional heating would have resulted in an initially warm surface (∼300–500 K), implying the melting of the ice (Kuramoto & Matsui 1994; Lunine et al. 2010). With time, crustal freezing would have allowed formation of multiple guest clathrates at the surface/atmosphere interface (Tobie et al. 2006; Lunine et al. 2010). In the second case, a highly porous icy material should be generated from the decomposition of methane clathrates (Mousis & Schmitt 2008) and the formation of multiple guest clathrates at the surface–atmosphere interface would take place during the cooling of the cryolava, which needs about

Retour à la table des matières : p. v

1 Earth year to decrease to Titan's surface temperature (Lorenz 1996). In both cases, the clathrates' composition is assumed to remain fixed during the cooling of Titan's surface.

Because the volume expansion induced by clathrate formation (∼20% compared to that of water ice; Mousis & Schmitt 2008) may well cause its self-isolation by closing the pores of the ice that is not in direct contact with the atmosphere, the thickness of the clathrate layer formed during the satellite cooling should be very limited, unless events such as impacts (Sekine et al. 2011) expose clean ice. Cryovolcanic activity, whose features are visible in some regions of Titan (Wall et al. 2009), is probably required to create substantial amounts of porous water ice spread across the surface, in a way similar to basaltic lava flows on Earth. Long periods of active cryovolcanism on Titan (Tobie et al. 2006) should lead to the continuous buildup of consecutive layers of cryolava (Mousis & Schmitt 2008) and thus favor the formation of noble gas-rich clathrate layers. The GCMS detection of ^{40}Ar remains consistent with our model and implies that it is the most abundant argon isotope trapped in the clathrate layers. Its release into the atmosphere would then result from outgassing events (Waite et al. 2005) that occurred later than the removal of all the atmospheric noble gases.

However, the formation of noble gas-rich clathrate layers from water ice delivered via cryovolcanism might meet two limitations. First, once in contact with the atmosphere, the cryolava flows might be too hot to directly form noble gas-rich clathrate layers. Second, cryolava flows could act as sources of noble gases by liberating them from underlying clathrates through melting. The volume (temporarily) melted by the flow may well exceed the volume of the flow itself that is available for sequestering, resulting in a net release of noble gas, instead of net sequestration. On the other hand, clathrate formation should remain possible during the rapid cooling of the cryolava. Indeed, the equilibrium pressure of an N_2-dominated clathrate (similar to our structure II nominal model) is about 10^{-3} bar for a surface temperature of 94 K. With a value of ∼1.3 bar, the partial pressure of N_2 in the atmosphere greatly exceeds the equilibrium pressure of N_2-dominated clathrate and then favors the formation of this structure at the current surface temperature. As such, the newly formed clathrate layers could at least partially absorb the noble gases recently released into the atmosphere by hot cryolava flows.

We thank an anonymous referee whose comments have helped us improve our manuscript.

APPENDIX

In the present study, the temperature dependence of the dissociation pressure of the multiple guest clathrate is determined from available experimental data and from a combination rule due to Lipenkov & Istomin (2001). Thus, the dissociation pressure $P_{\rm mix}^{\rm diss}$ of a multiple guest clathrate is calculated from the dissociation pressure $P_K^{\rm diss}$ of a pure clathrate of guest species K as

$$P_{\rm mix}^{\rm diss} = \left[\sum_K \frac{x_K}{P_K^{\rm diss}} \right]^{-1}, \quad \text{(A1)}$$

where x_K is the molar fraction of species K in the gas phase. The dissociation pressure $P_K^{\rm diss}$ is derived from laboratory measurements and follows an Arrhenius law (Miller 1961):

$$\log\left(P_K^{\rm diss}\right) = A + \frac{B}{T}, \quad \text{(A2)}$$

where $P_K^{\rm diss}$ and T are expressed in Pa and K, respectively. The constants A and B used in the present study have been fitted to the experimental data used by Thomas et al. (2007) and derived from Lunine & Stevenson (1985) and SK08.

REFERENCES

Asplund, M., Grevesse, N., Sauval, A. J., & Scott, P. 2009, ARA&A, 47, 481
Atreya, S. K., Donahue, T. M., & Kuhn, W. R. 1978, Science, 201, 611
Belosludov, V. R., Inerbaev, T. M., Subbotin, O. S., et al. 2002, J. Supramol. Chem., 2, 453
Cordier, D., Mousis, O., Lunine, J. I., Lavvas, P., & Vuitton, V. 2009, ApJ, 707, L128
Cordier, D., Mousis, O., Lunine, J. I., et al. 2010, ApJ, 721, L117
Jacovi, R., & Bar-Nun, A. 2008, Icarus, 196, 302
Kuramoto, K., & Matsui, T. 1994, J. Geophys. Res., 99, 21183
Lipenkov, V. Ya., & Istomin, V. A. 2001, Mater. Glyatsiol. Issled., 91, 129
Lorenz, R. D. 1996, Planet. Space Sci., 44, 1021
Lunine, J., Choukroun, M., Stevenson, D., & Tobie, G. 2010, in Titan from Cassini-Huygens, ed. R. H. Brown, J.-P. Lebreton, & J. H. Waite (Dordrecht: Springer), 35
Lunine, J. I., & Stevenson, D. J. 1985, ApJS, 58, 493
McKay, C. P., Scattergood, T. W., Pollack, J. B., Borucki, W. J., & van Ghyseghem, H. T. 1988, Nature, 332, 520
McKoy, V., & Sinanoğlu, O. 1963, J. Chem. Phys., 38, 2946
Miller, S. L. 1961, Proc. Natl Acad. Sci., 47, 1798
Mousis, O., Gautier, D., & Bockelée-Morvan, D. 2002, Icarus, 156, 162
Mousis, O., Lunine, J. I., Picaud, S., & Cordier, D. 2010, Faraday Discuss., 147, 509
Mousis, O., Lunine, J. I., Thomas, C., et al. 2009, ApJ, 691, 1780
Mousis, O., & Schmitt, B. 2008, ApJ, 677, L67
Niemann, H. B., Atreya, S. K., Bauer, S. J., et al. 2005, Nature, 438, 779
Niemann, H. B., Atreya, S. K., Demick, J. E., et al. 2010, J. Geophys. Res. (Planets), 115, 12006
Osegovic, J. P., & Max, M. D. 2005, J. Geophys. Res. (Planets), 110, 8004
Parrish, W. R., & Prausnitz, J. M. 1972, Ind. Eng. Chem. Process Des. Dev., 11, 26 (erratum: 11, 462) (PP72)
Sekine, Y., Genda, H., Sugita, S., Kadono, T., & Matsui, T. 2011, Nature Geosci., 4, 359
Sloan, E. D., & Koh, C. A. 2008, Clathrate Hydrates of Natural Gases (3rd ed.; Boca Raton: CRC Press) (SK08)
Thomas, C., Mousis, O., Ballenegger, V., & Picaud, S. 2007, A&A, 474, L17
Thomas, C., Picaud, S., Mousis, O., & Ballenegger, V. 2008, Planet. Space Sci., 56, 1607
Tobie, G., Lunine, J. I., & Sotin, C. 2006, Nature, 440, 61
van der Waals, J. H., & Platteeuw, J. C. 1959, Adv. Chem. Phys., Clathrate Solutions, Vol. 2 (New York: Interscience), 1
Waite, J. H., Niemann, H., Yelle, R. V., et al. 2005, Science, 308, 982
Wall, S. D., Lopes, R. M., Stofan, E. R., et al. 2009, Geophys. Res. Lett., 36, 4203

Retour à la table des matières : p. v

4.4 Article sur les incertitudes des modèles basés sur la RST

Planetary and Space Science 61 (2012) 99–107

Contents lists available at ScienceDirect

Planetary and Space Science

journal homepage: www.elsevier.com/locate/pss

Titan's lakes chemical composition: Sources of uncertainties and variability

D. Cordier [a,b,c,*], O. Mousis [d], J.I. Lunine [e,f], S. Lebonnois [g], P. Rannou [h], P. Lavvas [f], L.Q. Lobo [i], A.G.M. Ferreira [i]

[a] Institut de Physique de Rennes, CNRS, UMR 6251, Université de Rennes 1, Campus de Beaulieu, 35042 Rennes, France
[b] Ecole Nationale Supérieure de Chimie de Rennes, CNRS, UMR 6226, Avenue du Général Leclerc, CS 50837, 35708 Rennes Cedex 7, France
[c] Université européenne de Bretagne, Rennes, France
[d] Université de Franche-Comté, Institut UTINAM, CNRS/INSU, UMR 6213, 25030 Besançon Cedex, France
[e] Dipartimento di Fisica, Università degli Studi di Roma "Tor Vergata", Rome, Italy
[f] Lunar and Planetary Laboratory, University of Arizona, Tucson, AZ, USA
[g] Laboratoire de Météorologie Dynamique, Jussieu, Box 99, 75252 Paris Cedex 05, France
[h] Groupe de Spectrométrie Moléculaire et Atmosphérique, UMR 6089 Campus Moulin de la Housse, BP 1039, Université de Reims Champagne-Ardenne, 51687 REIMS, France
[i] Departamento de Engenharia Quimica, Universidade de Coimbra, Coimbra 3030-290, Portugal

ARTICLE INFO

Article history:
Received 14 December 2010
Received in revised form
6 April 2011
Accepted 24 May 2011
Available online 1 June 2011

Keywords:
Planets and satellites
Individual
Titan—planets and satellites
General—solar system
General

ABSTRACT

Between 2004 and 2007 the instruments of the Cassini spacecraft, orbiting within the Saturn system, discovered dark patches in the polar regions of Titan. These features are interpreted as hydrocarbon lakes and seas with ethane and methane identified as the main compounds. In this context, we have developed a lake–atmosphere equilibrium model allowing the determination of the chemical composition of these liquid areas present on Titan. The model is based on uncertain thermodynamic data and precipitation rates of organic species predicted to be present in the lakes and seas that are subject to spatial and temporal variations. Here we explore and discuss the influence of these uncertainties and variations. The errors and uncertainties relevant to thermodynamic data are simulated via Monte Carlo simulations. Global circulation models (GCM) are also employed in order to investigate the possibility of chemical asymmetry between the south and the north poles, due to differences in precipitation rates. We find that mole fractions of compounds in the liquid phase have a high sensitivity to thermodynamic data used as inputs, in particular molar volumes and enthalpies of vaporization. When we combine all considered uncertainties, the ranges of obtained mole fractions are rather large (up to $\sim$8500%) but the distributions of values are narrow. The relative standard deviations remain between 10% and $\sim$300% depending on the compound considered. Compared to other sources of uncertainties and variability, deviation caused by surface pressure variations are clearly negligible, remaining of the order of a few percent up to $\sim$20%. Moreover, no significant difference is found between the composition of lakes located in north and south poles. Because the theory of regular solutions employed here is sensitive to thermodynamic data and is not suitable for polar molecules such as HCN and CH_3CN, our work strongly underlines the need for experimental simulations and the improvement of Titan's atmospheric models.

© 2011 Elsevier Ltd. All rights reserved.

1. Introduction

The surface of Saturn's haze-shrouded moon Titan had long been proposed to be at least partly hidden by oceans or seas, on the basis of the stability of liquid methane and ethane at the surface (Flasar, 1983; Lunine et al., 1983; Lorenz et al., 2003). The presence of a global ocean on Titan was excluded from ground-based radar observations in the mid 1990s (Muhleman et al., 1995). In mid 2006, dark, lake-like features of a range of sizes were detected at Titan's north polar region by the Cassini RADAR (Stofan et al., 2007). The chemical composition of these lakes remains, however, poorly determined. Spectra of the southern hemisphere lake Ontario Lacus have been obtained by the visual and infrared mapping spectrometer (VIMS) aboard Cassini but the only species that has been firmly identified is C_2H_6 (Brown et al., 2008). The difficulty in determining the composition of the lakes is essentially due to the presence of a large atmospheric fraction of CH_4 that impedes this molecule's identification in the liquid phase present on the surface, irrespective of the value of its mole fraction. However, methane is indirectly inferred in Ontario Lacus by the secular decline of the lake extent over the Titan summer

* Corresponding author at: Institut de Physique de Rennes, CNRS, UMR 6251, Université de Rennes 1, Campus de Beaulieu, 35042 Rennes, France.
E-mail address: daniel.cordier@obs-besancon.fr (D. Cordier).

0032-0633/$ - see front matter © 2011 Elsevier Ltd. All rights reserved.
doi:10.1016/j.pss.2011.05.009

Retour à la table des matières : p. v

(Hayes et al., 2010) and the observation of troposphere clouds, which must be methane, coincident with surface darkening over the southern pole during the summer (Turtle et al., 2007). Because the detection of other compounds in the lakes of Titan remains challenging in the absence of in situ measurements, the only way to get a good estimate of their chemical composition is to develop and utilize a thermodynamic model based on theoretical calculations and laboratory data. Several models investigating the influence of photochemistry and the atmospheric composition on the chemical composition of putative hydrocarbon oceans or seas formed on the surface of Titan have been elaborated in the pre-Cassini years (Lunine et al., 1983; Dubouloz et al., 1989; McKay et al., 1993; Tokano, 2005). These models suggested that the liquid phase existing on Titan contains a mixture made from C_2H_6, CH_4 and N_2, and a large number of dissolved minor species.

On the other hand, the Cassini–Huygens measurements have improved our knowledge of the structure and composition of Titan's atmosphere. In particular, the gas chromatograph mass spectrometer (GCMS) aboard Huygens and the Cassini composite infrared spectrometer (CIRS) provided new atmospheric mole fraction data (see Niemann et al., 2005, and Table 1). Moreover, near-surface brightness temperatures and corresponding estimates for physical temperatures in the high latitudes at which numerous lakes are found have now been determined (Jennings et al., 2009). These atmospheric and surface conditions have been recently used to recompute the solubilities of the different compounds in the hydrocarbon lakes (Cordier et al., 2009, hereafter C09). The same model has also been employed to explore the possibility of noble gas trapping in the lakes of Titan in order to provide an attempt of explanation of their atmospheric depletion (Cordier et al., 2010).

The assumptions considered by C09 are similar to those made by Dubouloz et al. (1989) (hereafter DUB89): in both cases, lakes are considered as nonideal solutions in thermodynamic equilibrium with the atmosphere. However, neither DUB89 nor C09 have taken into consideration the influence of uncertainties on the data used as inputs in their models. Indeed, some thermodynamic data are measured at much higher temperature and extrapolated down to temperatures relevant to Titan's conditions. Precipitation rates are also supposed to vary with respect to latitude, longitude and time. In this work, we investigate the influence of thermodynamic uncertainties, and in a lesser extent, the geographic influence of the variation of precipitations on the lakes composition. In the latter case, we restrict our study to a supposed north/south poles asymmetry in chemical composition.

In Section 2 we detail our lake–atmosphere equilibrium model. Section 3 is dedicated to the study of the influence of uncertainties on thermodynamic data (vapor pressures, molar volumes, enthalpies of vaporization and parameters of interaction) on the resulting lakes composition. In Section 4, simulations are conducted with the use of precipitation rates derived from a version of the IPSL[1] two-dimensional climate model of Titan's atmosphere (Crespin et al., 2008) and allow comparison between chemical composition of south pole and north pole lakes. Section 5 is devoted to discussion and conclusions.

Table 1
Assumed composition of Titan's atmosphere at the ground level.

Atmosphere	Mole fraction	Determination
H_2	9.8×10^{-4}	Huygens GCMS[a]
CH_4	0.0492	Huygens GCMS[b]
CO	4.70×10^{-5}	Cassini CIRS[c]
^{40}Ar	4.32×10^{-5}	Huygens GCMS[b]
N_2	0.95	C09[d]
C_2H_6	1.49×10^{-5}	C09[d]

[a] Owen and Niemann (2009).
[b] Niemann et al. (2005).
[c] De Kok et al. (2007).
[d] N_2 and C_2H_6 abundances have been calculated by C09 and correspond to a ground temperature of 93.65 K. In Monte Carlo simulations presented here, the mole fractions of N_2 and C_2H_6 are varying (see text).

2. Description of the lake–atmosphere equilibrium model

Our model is based on regular solution theory and thermodynamic equilibrium is assumed between the liquid and the atmosphere. This equilibrium, which is expressed by the equality of chemical potentials, can be written as follows (Eq. (1) of DUB89):

$$Y_k P = \Gamma_k X_k P_{vp,k}, \tag{1}$$

where P is the total pressure at Titan's surface, Y_k and X_k respectively the mole fractions of the k compound in the atmosphere and in the liquid, and $P_{vp,k}$ its vapor pressure. The activity coefficient Γ_k (dimensionless) of the k compound is given by (frame of the regular solution theory—see Poling et al., 2007)

$$RT\ln\Gamma_k = V_{m,k}\sum_i\sum_j (A_{ik}-A_{ij})\Phi_i\Phi_j, \tag{2}$$

where

$$A_{ij} = (\delta_i-\delta_j)^2 + 2l_{ij}\delta_i\delta_j \tag{3}$$

and

$$\Phi_i = X_i V_{m,i} \Big/ \sum_j X_j V_{m,j}. \tag{4}$$

δ_i ($(J\,m^{-3})^{1/2}$) is the Hildebrand's solubility parameter of the ith compound. The value of this parameter is given by

$$\delta_i = \sqrt{\frac{\Delta H_{v,i}-RT}{V_{m,i}}}, \tag{5}$$

where $\Delta H_{v,i}$ ($J\,mol^{-1}$) is the enthalpy of vaporization and $V_{m,i}$ ($m^3\,mol^{-1}$) the molar volume. A δ_i represents a measure of the molecular cohesion energy of the pure component i. It depends on the nature and the *strength* of intermolecular forces (hydrogen bond, etc.) between molecules of the same species. In general, two components i and j with δ_i and δ_j presenting close values, have a high solubility. Beside this, the l_{ij}'s parameters represent the effects of interactions between molecules of different species. These l_{ij}'s are empirically determined and are generally poorly known. The situation $\forall i,j$: $\delta_i=\delta_j$ and $l_{ij}=0$ corresponds to all activity coefficient equal to one, in other words this is an ideal solution in which all intermolecular forces are negligible.

Our model also allows us to estimate the mole fraction of each solid precipitate that is dissolved in the lakes of Titan. To this end, we calculate the *saturation* mole fraction[2] $X_{i,sat}$ of the compound i, which is given by (Eq. (7) of DUB89)

$$\ln(\Gamma_i X_{i,sat}) = (\Delta H_m/RT_m)(1-T_m/T), \tag{6}$$

where T_m is the component's melting temperature and ΔH_m its enthalpy of fusion. Our calculation procedure is then as follows:

1. The unknown X_i's and Y_i's are computed via the Newton–Raphson method.

[1] Institut Pierre-Simon Laplace.
[2] The saturation mole fraction of the compound i corresponds to the maximum mole fraction of i in the liquid form. Above this value, the i material in excess remains in solid form.

Retour à la table des matières : p. v

2. Once the X_i's have been determined, the $X_{i,sat}$'s are in turn calculated and compared to the X_i's for each species. If for i compound we get $X_{i,sat} < X_i$, then we fix $X_i = X_{i,sat}$.
3. We get new values of X_i's and $X_{i,sat}$'s via the resolution of the nonlinear system.
4. The iterations are continued until we get a difference between $X_{i,sat}$ and X_i lower than 10^{-6}, value for which the numerical inaccuracy is clearly negligible, are compared to other sources of uncertainties.

The known Y_i's are given in Table 1. The precipitation rates τ_i's represent the number of molecules of a given species, reaching the surface of Titan by unit of time and by unit of surface (molecules $m^{-2}\,s^{-1}$). The τ_i's used in C09 were derived from the photochemical models of Lavvas et al. (2008a,b) and Vuitton et al. (2008), and correspond to the main products of CH_4 and N_2 photolysis. These rates allow us to express each i compound that falls from the atmosphere in the form

$$X_i = \frac{\tau_i}{\tau_{C_2H_6}} \times X_{C_2H_6}. \quad (7)$$

We also ensure that $\sum_i X_i = 1$ and $\sum_i Y_i = 1$. In this way, we get 15 unknowns and 15 equations, allowing the system to be solved. The thermodynamic data used in our calculations derive mainly from the NIST database.[3] As discussed in the following section, these data are often not well known and the large uncertainties associated to their determination may induce strong variations of the lakes chemical composition.

3. Uncertainties due to thermodynamic data

In the calculations of C09, the thermodynamic data (vapor pressures, molar volumes, enthalpies of vaporization and l_{ij}'s) have been set to their nominal values in the lake–atmosphere equilibrium model. However, each of these nominal values is accompanied by a given "deviation" or "error" and the consideration of the full range of possibilities for these thermodynamic data may strongly alter the lakes composition compared to the one calculated by C09. In order to investigate up to which point the composition of these lakes may depart from the one of C09, we use here a Monte Carlo numerical method (see for instance Metropolis and Ulam, 1949), allowing us to perform error simulations for vapor pressures, molar volumes, enthalpies of vaporization and parameters of interaction l_{ij}'s. A first set of computations consists in calculating the composition of lakes from numbers randomly chosen within the range of possible values attributed to a set of thermodynamic data. For each mole fraction X_i, the minimum $X_{i,min}$, the maximum $X_{i,max}$ and the average value $\overline{X}_i$ are recorded. The procedure is repeated 10,000 times for each set of thermodynamic data. The choice of the total number of Monte Carlo iterations is a compromise that has been fixed to get a statistically significant population while maintaining reasonable computation time. Simulations with 5000 and 20,000 iterations do not give significantly different results. Additionally we perform a simulation addressing the case where all sets of thermodynamic data are simultaneously considered with synthetic errors. This procedure is also repeated 10,000 times.

Note that the enthalpies of melting ΔH_m are not considered in our investigation because (i) they seem to be reasonably well known compared to other thermodynamic quantities and (ii) they only play a role in case of saturation, e.g. here with HCN. For this compound the measurement, provided by the NIST database, comes from Giauque and Ruehrwein (1939) with an accuracy of about 10^{-4}. Such a level of uncertainty is clearly negligible compared to other sources, allowing us to keep these thermodynamic quantities out of our study.

3.1. Influence of vapor pressure uncertainties

Vapor pressures of species, for which Eq. (1) is written, are taken from the NIST database in the form of an Antoine's law in the cases of N_2, CH_4, Ar and C_2H_6 or from a vapor pressure law given by Lide (1974) in the case of CO.[4] In general the domains of validity of Antoine's laws used in this work include the range of temperatures relevant for Titan's lakes (i.e. 90 ± 3 K). For instance, in the cases of CH_4 and C_2H_6, the lower boundaries are 90.99 and 91.33 K respectively, implying moderate extrapolations for temperatures slightly below ~ 90 K.

On the other hand, evaluating the accuracy of Antoine's equations brought by the NIST database is not straightforward. To do so, we have first considered the case of N_2 for which NIST maintainers derived an Antoine's equation from Edejer and Thodos (1967). These authors published a Frost–Kalkwarf equation based on 180 experimental vapor pressure measurements derived from 13 references. The equation obtained by Edejer and Thodos (1967) reproduces the experimental measurements with a deviation ranging between 0.13% and 2.04%. Comparing the vapor pressure computed with the NIST Antoine's equation with the one given by Edejer and Thodos (1967), we found differences reaching $\sim 10\%$ for the lowest temperatures (i.e. around 67 K) and $\sim 1\%$ for temperatures close to 90 K. Following a similar approach, we compared pressure computed with the NIST Antoine's equation and original data from Carruth and Kobayashi (1973). We also made a comparison between our own fit and pressure data given by Lide (1974) for carbon monoxide. For the relevant temperature domain, the deviation for C_2H_6 remains between 0.1% and 1%, while the vapor pressure of CO reaches a difference of about 9%. Consequently we have fixed the maximum errors on vapor pressures, for all relevant species (i.e. N_2, CH_4, Ar, CO and C_2H_6) to $\pm 10\%$ relative to previously used values (see C09). This range should bracket all the vapor pressures expected for each compound. This approach allows us to explore a wide range of possibilities, including combinations which do not correspond to physical reality. In this sense, results corresponding to extreme deviations should be regarded as unlikely cases.

Table 2 gathers our results which are quantified by $\Delta_{P_{vap}} = (X_{max} - X_{min})/\overline{X}$ and the relative standard deviation σ^* (both expressed in percentage). $\Delta_{P_{vap}}$ measures the total spread (over 10,000 computations of chemical compositions) of mole fraction values for a given species, including the results of the most unlikely combinations of synthetic errors. The relative standard deviation $\sigma^*(i) = \sqrt{\overline{X_i^2} - \overline{X_i}^2}/\overline{X}_i$ (the upper bar denotes the average value over 10,000 computations) shows how much variation or "dispersion" there is from the "average" X_i. Table 2 shows that $\sigma^*(i)$'s differ strongly from $\Delta_{P_{vap}}$'s. This feature corresponds to the signature of extremely narrow distributions of values around the average ones and can be explained by the non-linearity of the equations of our model. Indeed, synthetic errors are chosen with **a** uniform distribution but the resulting distribution of mole fractions is heterogeneous. The shapes of X_i's distributions are shown in Section 3.5 in which errors for all thermodynamic inputs are taken into consideration.

Errors on vapor pressure mainly affect mole fractions of species for which Eq. (1) is written. This behavior is not surprising as Eq. (1) contains explicitly the vapor pressure. The entire set of equations being coupled, even a variation of one vapor pressure

[3] http://webbook.nist.gov

[4] CO data are unavailable in the NIST.

Retour à la table des matières : p. v

Table 2
Results of Monte Carlo simulations showing the space of possible values for thermodynamic inputs explored randomly within a $\pm 10\%$ range centered on the nominal values used by C09. X_{min}, $\overline{X}$ and X_{max} are recorded for each species and results are presented in the form of Δ's and relative standard deviations σ^* (see text). X_{min}, $\overline{X}$ and X_{max} are shown only in the cases where the space of vapor pressures is explored. $\Delta_{P_{vap}}$ ($\sigma^*_{P_{vap}}$) refers to Monte Carlo simulations for which only vapor pressures are affected by synthetic errors. $\Delta_{V_m}(\sigma^*_{V_m})$, $\Delta_{\Delta H_{vap}}(\sigma^*_{\Delta H_{vap}})$, and $\Delta_{l_{ij}}(\sigma^*_{l_{ij}})$ refer to molar volumes, enthalpies of vaporization and interaction parameters l_{ij}, respectively. $\Delta_{All}(\sigma^*_{All})$ are resulting uncertainties when all thermodynamic quantities are considered with errors.

	X_{min} (P_{vap})	$\overline{X}$ (P_{vap})	X_{max} (P_{vap})	$\Delta_{P_{vap}}$ (%)	$\sigma^*_{P_{vap}}$ (%)	Δ_{V_m} (%)	$\sigma^*_{V_m}$ (%)	$\Delta_{\Delta H_{vap}}$ (%)	$\sigma^*_{\Delta H_{vap}}$ (%)	$\Delta_{l_{ij}}$ (%)	$\sigma^*_{l_{ij}}$ (%)	Δ_{All} (%)	σ^*_{All} (%)
N_2	4.1×10^{-3}	4.9×10^{-3}	5.9×10^{-3}	37	8	792	94	2310	105	445	65	8540	282
CH_4	8.3×10^{-2}	9.7×10^{-2}	1.1×10^{-1}	32	9	346	61	570	63	379	84	1370	157
Ar	4.3×10^{-6}	4.9×10^{-6}	5.8×10^{-6}	31	7	333	53	557	56	288	54	1270	104
CO	3.5×10^{-7}	4.2×10^{-7}	5.1×10^{-7}	37	8	734	88	244	102	386	59	5840	223
C_2H_6	7.5×10^{-1}	7.6×10^{-1}	7.7×10^{-1}	3	1	50	8	96	9	17	4	108	10
C_3H_8	7.3×10^{-2}	7.4×10^{-2}	7.5×10^{-2}	3	1	50	8	96	9	17	4	108	10
C_4H_8	1.4×10^{-2}	1.4×10^{-2}	1.4×10^{-2}	3	1	50	8	96	9	17	4	108	10
HCN	2.0×10^{-2}	2.2×10^{-2}	2.3×10^{-2}	16	4	156	50	167	56	52	13	150	52
C_4H_{10}	1.2×10^{-2}	1.2×10^{-2}	1.2×10^{-2}	3	1	50	8	96	9	17	4	108	10
C_2H_2	1.1×10^{-2}	1.1×10^{-2}	1.2×10^{-2}	3	1	50	8	96	9	17	4	108	10
CH_3CN	9.7×10^{-4}	9.9×10^{-4}	1.0×10^{-3}	3	1	52	8	112	11	17	4	109	14
CO_2	2.9×10^{-4}	2.9×10^{-4}	3.0×10^{-4}	3	1	50	8	96	9	17	4	108	10
C_6H_6	2.2×10^{-4}	2.3×10^{-4}	2.3×10^{-4}	3	1	50	8	96	9	17	4	108	10

affects the mole fractions of all the other species determined with our model. Note that the case of ethane is particular because its atmospheric mole fraction $Y_{C_2H_6}$ is an unknown of our mathematical problem, while atmospheric abundances of N_2, CH_4, Ar and CO are fixed by the observations. Compared to other compounds belonging to precipitated species HCN shows a relatively high $\Delta_{P_{vap}}$ (σ^*). In this case, this is also due to the use of an equation (Eq. (6)) where vapor pressures play a role via Γ_i. Average values $\overline{X}_i$ differ slightly from previous results (C09).

3.2. Influence of molar volume uncertainties

Molar volumes have been estimated via Rackett's method (see Poling et al., 2007). Tables 4–11 and pages 4.36–4.37 of Poling et al. (2007) present comparisons between measured molar volumes and estimated ones for some organic compounds at the boiling temperature. These comparisons show that maximum deviations typically reach the levels of a few percent. We then adopted a maximum "error" of $\pm 10\%$ for Monte Carlo simulations only applied to molar volumes. These simulations allow a sensitivity comparison with those performed for vapor pressure. Resulting Δ_{V_m} and $\sigma^*_{V_m}$ are displayed in Table 2.

Similar to simulations related to vapor pressure, large differences between Δ_{V_m} and $\sigma^*_{V_m}$ indicate a very narrow spread of mole fractions in lakes. As would be expected, species for which thermodynamic equations (1) are explicitly used show the highest deviations. As also shown by Table 2, a general trend is that mole fractions appear to be much more sensitive to molar volume than to vapor pressures.

3.3. Influence of enthalpies of vaporization uncertainties

The NIST and the literature provide numerous interpolation formulae for enthalpies of vaporization. Getting reliable estimates of their actual accuracy is not easy because the domains of validity of these formulae do not often include the ground temperature of Titan. For instance for C_2H_6, C_3H_8 and C_4H_8 extrapolations over about 100 K are required. However we have performed error estimates only for methane, ethane and argon. In the cases of methane and ethane, we compared the enthalpies of vaporization given by the NIST database (originally published by Majer and Svoboda, 1985) to those computed with the equations provided by Somayajulu (1988). For methane, in the temperature range of interest for the surface on Titan, we obtained differences lower than 1%. In the case of ethane, these differences are much more important and lie between 26% and 30%. Considering the work of Tegeler et al. (1999), we estimate an internal uncertainty of about 1% for the enthalpy of vaporization of argon. Again, in order to be consistent with others Monte Carlo simulations, we fixed the maximum "error" on the enthalpy of vaporization of each species to $\pm 10\%$, a value which is well within the range of uncertainties found from comparisons. The results are displayed in Table 2 and show that the induced uncertainties on mole fractions are similar or higher than those obtained for the molar volumes.

3.4. Influence of l_{ij} uncertainties

The interaction parameters l_{ij}'s represent the interaction between molecules of different species and are essentially determined empirically. These parameters are fixed to zero in the case of interactions between the same molecules ($\forall i\ l_{ii}=0$). In principle these l_{ij} depend on temperature, however for typical nonpolar mixtures over a modest range of temperature, that dependence is usually small (see Poling et al., 2007). As stated by DUB89, they are unknown in many situations. In this work, as 13 species are taken into account in the liquid phase, we need to know 156 parameters ($13\times13-13=156$; the 13 l_{ii} being set to zero) and testing the possible influence of each of them in our system does not really make sense. Given the fact that the values of l_{ij} range between ~ 0.02 (DUB89) and 0.09 (Poling et al., 2007), we have performed Monte Carlo simulations with these parameters set randomly between 0 and 0.10 (except $l_{ii}=0$). The sensitivity of mole fractions to l_{ij}'s is presented in Table 2 and appears lower than in the cases of molar volume and enthalpy of vaporization.

3.5. Combination of all thermodynamic uncertainties

Here we have combined all sources of uncertainties (i.e. errors on P_{vap}, V_m, ΔH_{vap} and l_{ij}) and the results are represented by Δ_{All} and σ^*_{All} in Table 2. The combination of uncertainties on thermodynamic data can induce mole fraction fluctuations up to a factor of ~ 100 for Δ_{All} and slightly lower than ~ 4 if we consider the relative standard deviation σ^*_{All}. The distribution of mole fractions X_i is represented in the form of histograms in Figs. 1 and 2.

For each species, the range $X_{i,min}-X_{i,max}$ has been divided into 100 intervals. For the k-th interval, the number N_k of mole fractions owning a given value has been normalized via $N^*_k=N_k/N_{peak}$, where N_{peak} corresponds to the largest N_k. We stress that N_{peak} has a specific value for each compound.

Retour à la table des matières : p. v

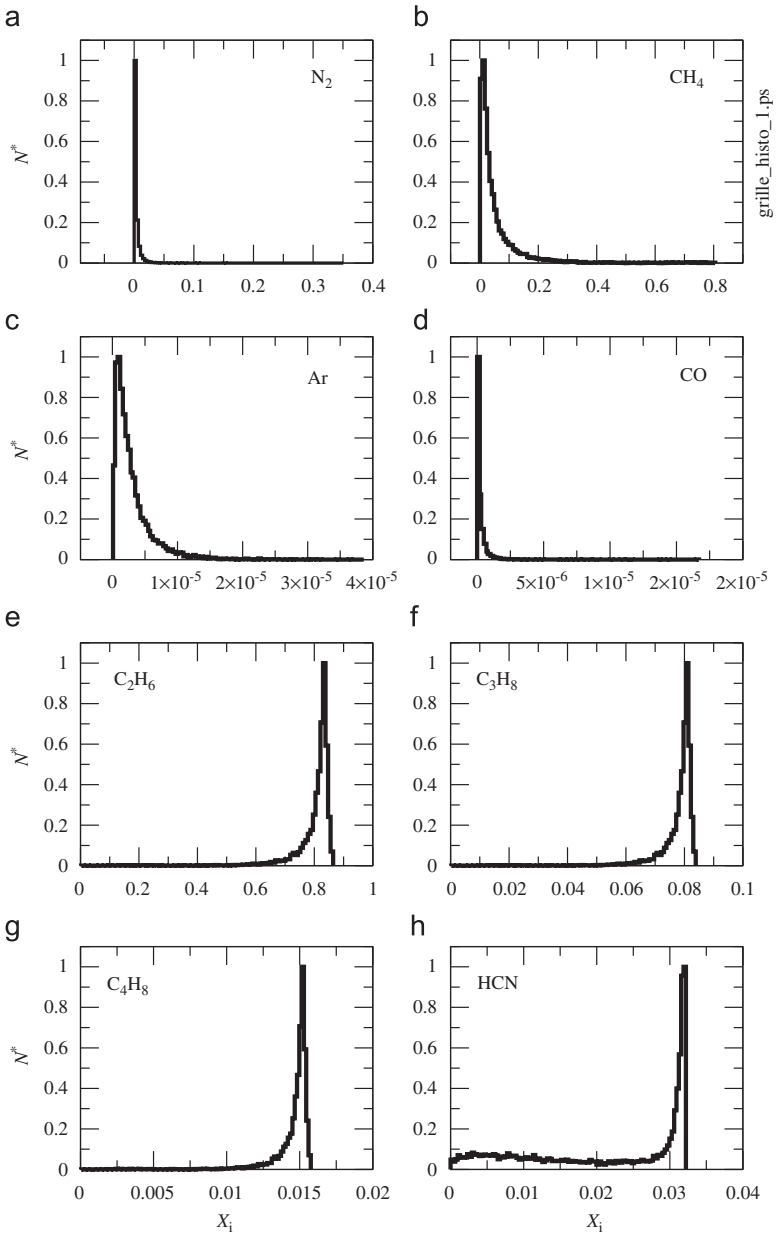

Fig. 1. (a–h) Histogram of mole fractions of Titan's hydrocarbon lakes. N^* is the normalized number of mole fractions owning the value X_i computed within a given range of uncertainties for compound i (indicated in the top left of each panel). The 10,000 computations of chemical compositions have been performed at $T=90$ K, assuming a maximum error of $\pm 10\%$ for all P_{vap}, V_m, ΔH_m, and assuming a 0–0.1 range of values for the l_{ij}'s.

Distributions are very narrow and clearly asymmetric. The smallest abundances are limited by $X=0$. HCN is a particular case for which the highest abundances are limited by the saturation. Curiously, the HCN distribution presents a "residual tail" located at lake mole fractions between 0 and ~ 0.032.

If we consider case 1 of DUB89 (i.e. $T=92.5$ K, $Y_{Ar}=0$ and $Y_{CH_4}=0.0155$), our results bracket the abundances found by these authors. For instance we find $7.7\times10^{-6}\leq X_{N_2}\leq 0.039$ while DUB89 got $X_{N_2}=0.018$. The case of methane is similar since we find $1.8\times10^{-4}\leq X_{CH_4}\leq 0.083$ whereas DUB89 inferred $X_{CH_4}=7.3\%$. This illustrates the fact that differences between C09 and DUB89 are consistent with uncertainties caused by poorly known thermodynamic data.

One could argue that the choice of a maximum deviation of $\pm 10\%$ is arbitrary, even if that level of uncertainty has been discussed in previous subsections. Fig. 3 shows the sensitivity of σ^* to the adopted maximum error for N_2, CH_4, Ar and CO. As expected, the standard deviation increases with the value of the maximum error but this behavior appears to be nonlinear. During a Monte Carlo simulation, some combinations of errors yield to a non-convergence of the model, these occurrences corresponding more likely to unphysical situations and/or to an initial input (in practice the nominal solution for $T=90$ K published in C09) in the Newton–Raphson algorithm which is too far from the solution of the system of the equations. In addition, a maximum error of $\pm 10\%$ in the thermodynamic data is probably an

Retour à la table des matières : p. v

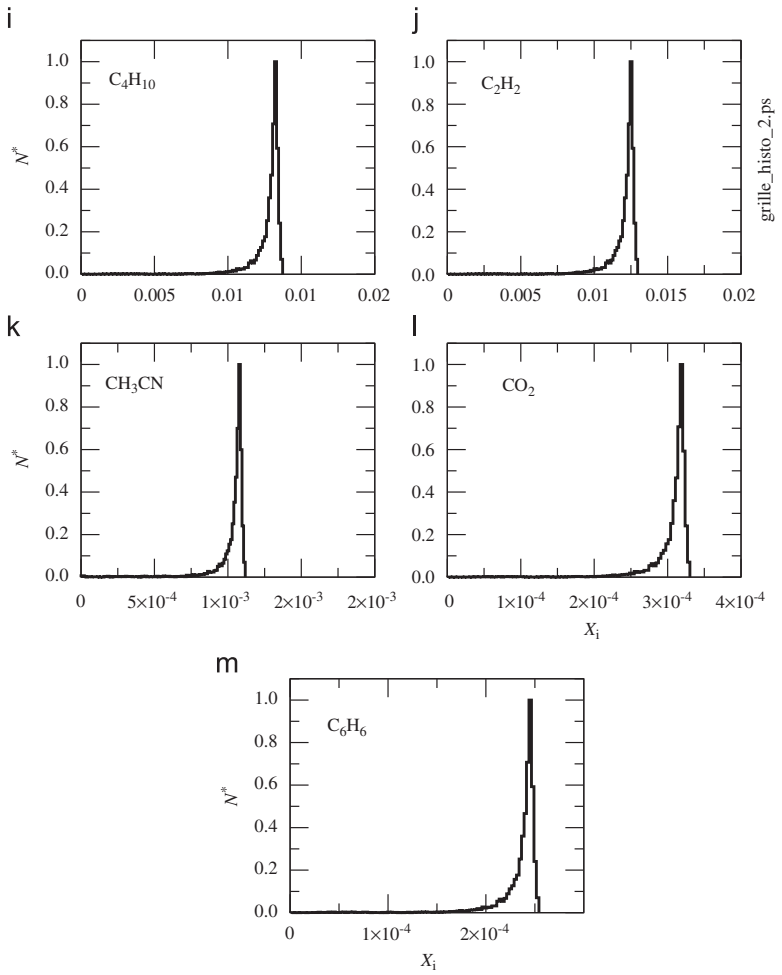

Fig. 2. Same as in Fig. 1.

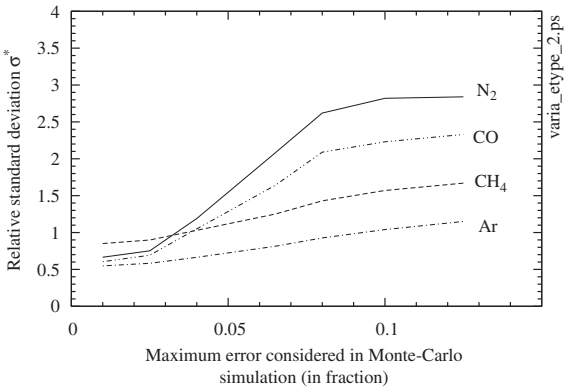

Fig. 3. Relative standard deviation σ_i^* corresponding to the mole fractions of N_2, CH_4, Ar and CO. σ_i^* are plotted as functions of the maximum errors obtained for $P_{vap,i}$, $V_{m,i}$, $\delta H_{vap,i}$ in Monte Carlo simulations. l_{ij}'s have been set to 0.1 in all these computations.

overestimated value even if we do not really know how these data depart from the "real" ones. However, we consider that the most important point here was to address the sensitivity of the model to the different sources of uncertainties.

4. Influence of geographic variations of precipitation

On Earth, precipitation is almost entirely water, with the rate dependent on location and time. In the case of Titan, the situation is more complex because the slow sedimentation of stratospheric aerosols to the surface is key to filling the lakes with the dominant photochemical byproducts of methane as well as less abundant species.

Moreover, the sedimentation rates are also a function of location and time. In this section we restrict our study to the geographic dependence of lakes composition and more precisely to a possible south/north asymmetry as the distribution of lakes seems to be itself asymmetric (see Aharonson et al., 2009).

As mentioned in Section 2, the calculations are based on precipitation rates derived from a slightly improved version of Lavvas et al. (2008a,b) (hereafter LAV08) models that included the atmospheric profile of Titan's atmosphere measured with the Huygens atmosphere structure instrument (Fulchignoni et al., 2005) and some updated reaction rates. In the following we refer to this set of precipitation rates as LAV09. These models are clearly inadequate for a geographical study, this is why we used a 2D models originally developed by Lebonnois et al. (2001). These authors used an analytic description of the meridional circulation of Titan's atmosphere to take advection into account in a

Retour à la table des matières : p. v

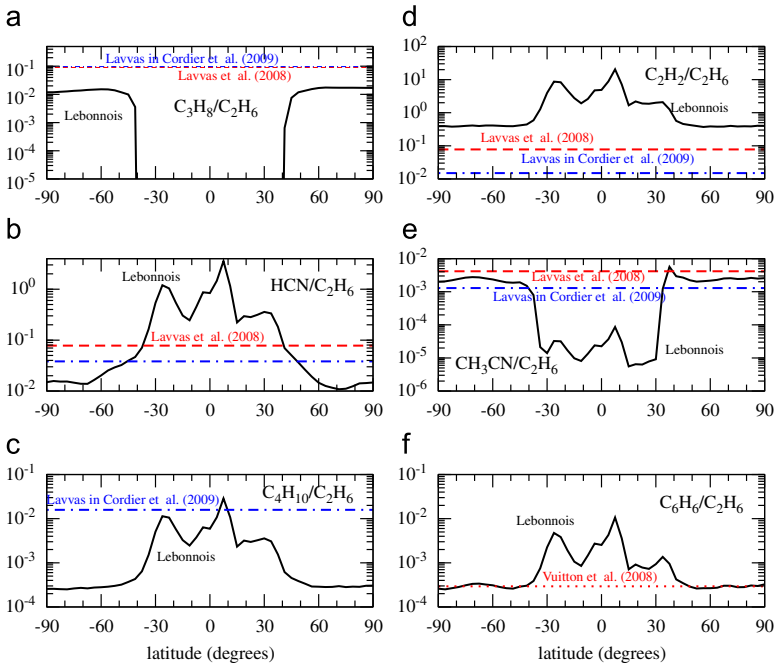

Fig. 4. (a–f) Solid lines: time averaged ratios $\tau_i/\tau_{C_2H_6}$ from LEB08 models represented as a function of Titan's latitude. Dashed lines: the same ratios computed with the LAV09 model and taken from Vuitton et al. (2008) in the case of C_6H_6.

two-dimensional photochemical model. This coupling between dynamics and photochemistry was subsequently improved by the implementation of the same photochemical model in the IPSL two-dimensional climate model (Crespin et al., 2008, hereafter LEB08).

Precipitates are included in our thermochemical model via the relation $X_i = (\tau_i/\tau_{C_2H_6}) \times X_{C_2H_6}$. At the first sight, one could believe that multiplying a given τ_i by an arbitrary factor α_i yields a multiplication by α_i of the resulting mole fraction X_i. This is not the case because the mole fraction of ethane $X_{C_2H_6}$ depends on all the other mole fractions. Indeed Eq. (1) depends on Eq. (4), and both equations are solved simultaneously. Hence, the influence of precipitation rates τ_i on mole fractions can only be estimated with a complete calculation. As these rates play a role in our set of equations via the ratios $\tau_i/\tau_{C_2H_6}$, we then consider these ratios instead of absolute τ_i values. For species available in LEB08's models, we computed the time averaged ratios $\tau_i/\tau_{C_2H_6}$, results are displayed in Fig. 4, ratios deduced from LAV08 and LAV09 have been displayed for comparison.

While we have noticed in LEB08 data absolute precipitation rates have huge latitudinal variations, the ratios $\tau_i/\tau_{C_2H_6}$ do not exhibit such steep dependence in regions located poleward of latitudes around $\pm 60^\circ$. In equatorial regions, the precipitation rates computed by LEB08 can be very small, implying that the ratio $\tau_i/\tau_{C_2H_6}$ probably has no great physical meaning in these regions. Fortunately, as hydrocarbon lakes have presumably been detected in polar regions, this observational evidence allows us to identify the questionable values.

With LEB08 polar ratios $\tau_i/\tau_{C_2H_6}$ we compute two sets of mole fractions: one for the south pole, another for the north pole. In both cases, the temperature and the pressure have been respectively fixed to 90 K and 1.467 bar. We did not find any significant differences between the composition of south and north lakes (i.e. differences of the order of 1%) excepted for C_3H_8 ($\sim 30\%$), C_4H_{10}, CH_3CN and C_6H_6 (both around $\sim 20\%$). The north mole fractions being systematically larger than those computed for the south pole, this behavior corresponds to LEB08 large ratios at north pole (see Fig. 4). These results have to be considered carefully because even up-to-data 2D Titan's atmosphere models have to be improved. For instance, LEB08 precipitation rates are in fact condensation rates. In this approach, when a given species is in an atmospheric layer where the local temperature corresponds to the saturation temperature of this species, then all the molecules in this layer are supposed to precipitate on Titan's surface. In this picture, the microphysics of clouds is not taken into account. Models including this microphysics for a lot of species have to be developed.

5. Discussion and conclusion

Beside vapor pressures, molar volumes and other parameters already studied in previous sections, total pressure P and temperature T at ground level could have also an influence on lakes composition.

The influence of temperature has been already discussed in C09. The variations of ground pressure, as P appears in Eq. (1), could change the thermodynamic equilibrium. Using the Cassini synthetic aperture radar (SAR) Stiles et al. (2009) have developed models of the topography of limited portions of the surface, finding surface heights typically in the range -1500 to $+1000$ m, yielding a maximum altitude difference of about 2500 m. More recently, radar altimetry analyzed by Wall et al. (2010) across Ontario Lacus and its surroundings shows a maximum amplitude of the altimetry echo center of mass of about ~ 500 m. This local determination is compatible with Stiles et al. (2009) work. HASI data (Fulchignoni et al., 2005) contain pressure records, measured on January 14th, 2005 during the Huygens probe descent. Between the Huygens landing site and an altitude of 2500 m, the pressure ranges between 1467 and 1296 hPa, i.e. a relative variation of 10%. By means of their 3D general circulation model, Tokano and Neubauer (2002) have investigated the

Retour à la table des matières : p. v

Table 3
Mole fractions of lakes species sensitivity to ground total pressure.

Compound	Molar fraction in liquid at $P_{Huy} = 1467$ hPa	Molar fraction in liquid at $P = P_{Huy} \times 0.9$		Molar fraction in liquid at $P = P_{Huy} \times 1.1$	
N_2	4.90×10^{-3}	4.07×10^{-3}	−17%	5.92×10^{-3}	+21%
CH_4	9.69×10^{-2}	8.26×10^{-2}	−15%	1.13×10^{-1}	+17%
Ar	5.01×10^{-6}	4.29×10^{-6}	−14%	5.83×10^{-6}	+16%
CO	4.21×10^{-7}	3.49×10^{-7}	−17%	5.09×10^{-7}	+21%
C_2H_6	7.64×10^{-1}	7.76×10^{-1}	+1.6%	7.50×10^{-1}	−1.8%
C_3H_8	7.42×10^{-2}	7.53×10^{-2}	+1.5%	7.28×10^{-2}	−1.9%
C_4H_8	1.39×10^{-2}	1.41×10^{-2}	+1.4%	1.37×10^{-2}	−1.4%
HCN	2.09×10^{-2} (s)	2.27×10^{-2} (s)	+8.6%	1.91×10^{-2} (s)	−8.6%
C_4H_{10}	1.21×10^{-2} (ns)	1.23×10^{-2} (ns)	+1.7%	1.19×10^{-2} (ns)	−1.7%
C_2H_2	1.15×10^{-2} (ns)	1.16×10^{-2} (ns)	+0.9%	1.13×10^{-2} (ns)	−1.7%
CH_3CN	9.89×10^{-4} (ns)	1.00×10^{-3} (ns)	+1.1%	9.71×10^{-4} (ns)	−1.8%
CO_2	2.92×10^{-4} (ns)	2.97×10^{-4} (ns)	+1.7%	2.87×10^{-4} (ns)	−1.7%
C_6H_6	2.25×10^{-4} (ns)	2.28×10^{-4} (ns)	+1.3%	2.21×10^{-4} (ns)	−1.8%

influence of Saturn's gravitational tide on the atmosphere of Titan. They found that induced surface pressure variations remains lower than 1.5 hPa, i.e. 0.1%, which is negligible in our context. Table 3 summarizes our results when we change the pressure value by $\pm 10\%$ from the *Huygens* Huygens-derived values P_{Huy}.

It is a valid question as to whether thermodynamic equilibrium is a reasonable assumption or not. For that purpose one can calculate the thermal relaxation time of a lake with a depth of H given by

$$\tau \sim H^2/\chi \tag{8}$$

(see the classical textbook Landau and Lifshitz, 1987), with χ the thermal diffusivity which is given by $\chi = \kappa/\rho C_P$ where κ (W m^{-1} K^{-1}) is the thermal conductivity, ρ (kg m^{-3}) the density and C_P (J kg^{-1} K^{-1}) the mass, specific heat capacity at constant pressure. We estimated κ thanks to the Enskog's theory (see Dymond, 1985), we found $\kappa \sim 0.59$ W m^{-1} K^{-1} for pure liquid ethane at $T = 90$ K. This value is of the same order of magnitude as that found by Lorenz et al. (2010) (see their Table 1), who got $\kappa \sim 0.25$ W m^{-1} K^{-1}. Finally we obtained $\tau \sim 2$ Titan's days for $H = 1$ m. As it can be seen in Tokano (2005) Titan's surface temperature variations in the polar regions are of the order of 1–2 K over a Titan's year (about 673 Titan's days[5]), that means that – at least the first meter of the lakes – have enough time to be in thermal equilibrium with the atmosphere. Following the models of Tokano (2005), during spring and summer the lakes are thermally stratified (which may imply a stratified chemical composition), but by the autumnal equinox convection renders the upper layer of the lakes isothermal.

In our work we use the semi-empirical regular solution theory already employed in previous works (Dubouloz et al., 1989; Cordier et al., 2009, 2010) but this also has its limits of validity. Particularly, it has been introduced for binary mixtures of non-polar molecules (Hildebrand and Scott, 1962) and generalized to multicomponent mixtures (see Poling et al., 2007, Chapter 8). Even though this generalization appears to be reasonable it has never been properly validated in a context relevant for Titan's hydrocarbon lakes. Moreover, the interaction parameters (the l_{ij}'s) are not well known in the case of nonpolar molecules and are probably an inadequate formalism when polar components are in the solution. We recall that the mixture considered in this work includes two polar molecules: HCN (with a dipole moment of 2.98 D, which could be compared to the water dipole moment of 1.85 D) and acetonitrile CH_3CN (with a dipole moment of 3.84 D).

[5] One Titan's day corresponds approximately to 16 terrestrial days.

Our work stresses the great impact on predicted composition of uncertainties in the thermodynamic inputs. In the framework of our model, this influence appears to be more important than abundance differences between north and south pole lakes, assuming a maximum "error" level of $\pm 10\%$ considered in our Monte Carlo simulations. Our computations show also that the influence of pressure variations is purely negligible.

It is important to note that, in this work, we did not consider the temporal variation of lakes chemical composition. Indeed, many phenomena could contribute to these variations, among which seasonal variations for short timescales and the Milankovitch cycle for longer timescales (see Aharonson et al., 2009). We stress that all these phenomena involve processes of evaporation/condensation of various species (in particular CH_4), which clearly represent non-equilibrium situations. A more realistic model will have to take into account energy and mass fluxes between lakes and the atmosphere (see Tokano, 2005) and incorporate a chemical model similar to the one used in the present work. Future works will have to integrate these two aspects of modeling to provide a more accurate description of lakes evolution.

We also underline the need for more realistic photochemistry models as already stated by Hébrard et al. (2007) among others. If we concentrate on the properties of the liquid of the lakes themselves, two kinds of approaches can be considered to make progress beyond what has been done here: (1) the development of more accurate thermodynamic data (measured in dedicated experiments and/or determined by *ab initio* computations); (2) Titan's lakes *in vitro* simulations, in which one explicitly attempts to simulate Titan's lakes through a liquid hydrocarbon mixture in contact with an atmosphere in a laboratory chamber. The second approach is surely more relevant because a model is not required to apply pure thermodynamic data, but the first approach may be more practical in the absence of a major experimental effort tied to proposed future missions to Titan like *Titan Saturn System Mission* (TSSM, see Matson et al., 2009) or *Titan Mare Explorer* (TiME, see Stofan et al., 2010), this latter being dedicated to lakes study and analysis.

References

Aharonson, O., Hayes, A.G., Lunine, J.I., Lorenz, R.D., Allison, M.D., Elachi, C., 2009. An asymmetric distribution of lakes on Titan as a possible consequence of orbital forcing. Nat. Geosci. 2 (December), 851–854.

Brown, R.H., Soderblom, L.A., Soderblom, J.M., Clark, R.N., Jaumann, R., Barnes, J.W., Sotin, C., Buratti, B., Baines, K.H., Nicholson, P.D., 2008. The identification of liquid ethane in Titan's Ontario Lacus. Nature 454 (July), 607–610.

Carruth, G.F., Kobayashi, R., 1973. Vapor pressure of normal paraffins ethane through n-decane from their triple points to about 10 Mm Hg. J. Chem. Eng. Data 18, 115–126.

Retour à la table des matières : p. v

Cordier, D., Mousis, O., Lunine, J.I., Lavvas, P., Vuitton, V., 2009. An estimate of the chemical composition of Titan's lakes. Astrophys. J. Lett. 707 (December), L128–L131.
Cordier, D., Mousis, O., Lunine, J.I., Lebonnois, S., Lavvas, P., Lobo, L.Q., Ferreira, A.G.M., 2010. About the possible role of hydrocarbon lakes in the origin of Titan's noble gas atmospheric depletion. ArXiv e-prints (August).
Crespin, A., Lebonnois, S., Vinatier, S., Bézard, B., Coustenis, A., Teanby, N.A., Achterberg, R.K., Rannou, P., Hourdin, F., 2008. Diagnostics of Titan's stratospheric dynamics using Cassini/CIRS data and the 2-dimensional IPSL circulation model. Icarus 197 (October), 556–571.
Dubouloz, N., Raulin, F., Lellouch, E., Gautier, D., 1989. Titan's hypothesized ocean properties—the influence of surface temperature and atmospheric composition uncertainties. Icarus 82 (November), 81–96.
Dymond, J.H., 1985. Hard-sphere theories of transport properties. Chem. Soc. Rev. 14, 317–356.
Edejer, M.R., Thodos, G., 1967. J. Chem. Eng. Data 12, 206–209.
Flasar, F.M., 1983. Oceans on Titan? Science 221 (July), 55–57.
Fulchignoni, M., Ferri, F., Angrilli, F., Ball, A.J., Bar-Nun, A., Barucci, M.A., Bettanini, C., Bianchini, G., Borucki, W., Colombatti, G., Coradini, M., Coustenis, A., Debei, S., Falkner, P., Fanti, G., Flamini, E., Gaborit, V., Grard, R., Hamelin, M., Harri, A.M., Hathi, B., Jernej, I., Leese, M.R., Lehto, A., Lion Stoppato, P.F., López-Moreno, J.J., Mäkinen, T., McDonnell, J.A.M., McKay, C.P., Molina-Cuberos, G., Neubauer, F.M., Pirronello, V., Rodrigo, R., Saggin, B., Schwingenschuh, K., Seiff, A., Simões, F., Svedhem, H., Tokano, T., Towner, M.C., Trautner, R., Withers, P., Zarnecki, J.C., 2005. In situ measurements of the physical characteristics of Titan's environment. Nature 438 (Dec), 785–791.
Giauque, W.F., Ruehrwein, R.A., 1939. The entropy of hydrogen cyanide. Heat capacity, heat of vaporization and vapor pressure. Hydrogen bond polymerization of the gas in chains of indefinite length. J. Am. Chem. Soc. 61, 2626.
Hayes, A.G., Wolf, A.S., Aharonson, O., Zebker, H., Lorenz, R., Kirk, R.L., Paillou, P., Lunine, J., Wye, L., Callahan, P., Wall, S., Elachi, C., 2008. Bathymetry and absorptivity of Titan's Ontario Lacus. J. Geophys. Res. 115, E09009. doi:10.1029/2009JE003557.
Hébrard, E., Dobrijevic, M., Bénilan, Y., Raulin, F., 2007. Photochemical kinetics uncertainties in modeling Titan's atmosphere: first consequences. Planet. Space Sci. 55 (July), 1470–1489.
Hildebrand, J.H., Scott, R.L., 1962. Regular Solutions. Prentice-Hall, Englewood Cliffs, NJ.
Jennings, D.E., Flasar, F.M., Kunde, V.G., Samuelson, R.E., Pearl, J.C., Nixon, C.A., Carlson, R.C., Mamoutkine, A.A., Brasunas, J.C., Guandique, E., Achterberg, R.K., Bjoraker, G.L., Romani, P.N., Segura, M.E., Albright, S.A., Elliott, M.H., Tingley, J.S., Calcutt, S., Coustenis, A., Courtin, R., 2009. Titan's surface brightness temperatures. Astrophys. J. Lett. 691 (February), L103–L105.
Landau, L.D., Lifshitz, E.M., 1987. Fluid Mechanics (Course of Theoretical Physics), second ed. Butterworth-Heinemann.
Lavvas, P.P., Coustenis, A., Vardavas, I.M., 2008a. Coupling photochemistry with haze formation in Titan's atmosphere, part I: model description. Planet. Space Sci. 56 (January), 27–66.
Lavvas, P.P., Coustenis, A., Vardavas, I.M., 2008b. Coupling photochemistry with haze formation in Titan's atmosphere, part II: results and validation with Cassini/Huygens data. Planet. Space Sci. 56 (January), 67–99.
Lebonnois, S., Toublanc, D., Hourdin, F., Rannou, P., 2001. Seasonal variations of Titan's atmospheric composition. Icarus 152 (August), 384–406.
Lide, D.P. (Ed.), 1974. CRC Handbook of Chemistry and Physics seventy fourth ed. CRC Press.
Lorenz, R.D., Biolluz, G., Encrenaz, P., Janssen, M.A., West, R.D., Muhleman, D.O., 2003. Cassini RADAR: prospects for Titan surface investigations using the microwave radiometer. Planet. Space Sci. 51 (April), 353–364.
Lorenz, R.D., Newman, C., Lunine, J.I., 2010. Threshold of wave generation on Titan's lakes and seas: effect of viscosity and implications for Cassini observations. Icarus 207 (June), 932–937.
Lunine, J.I., Stevenson, D.J., Yung, Y.L., 1967. Ethane ocean on Titan. Science 222, 1229–1230.
Majer, V., Svoboda, V., 1985. Enthalpies of Vaporization of Organic Compounds: A Critical Review and Data Compilation. Blackwell Scientific Publications, Oxford.
Matson, D., Coustenis, A., Lunine, J.I., Lebreton, J., Reh, K., Beauchamp, P., Erd, C., 2009. Spacecraft Exploration of Titan and Enceladus. AGU Fall Meeting Abstracts, D1474+ (December).
McKay, C.P., Pollack, J.B., Lunine, J.I., Courtin, R., 1993. Coupled atmosphere-ocean models of Titan's past. Icarus 102 (March), 88–98.
Metropolis, N., Ulam, S., 1949. J. Am. Statist. Assoc. 44, 335.
Muhleman, D.O., Grossman, A.W., Butler, B.J., 1995. Radar investigations of Mars, Mercury, and Titan. Ann. Rev. Earth Planet. Sci. 23, 337–374.
Niemann, H.B., Atreya, S.K., Bauer, S.J., Carignan, G.R., Demick, J.E., Frost, R.L., Gautier, D., Haberman, J.A., Harpold, D.N., Hunten, D.M., Israel, G., Lunine, J.I., Kasprzak, W.T., Owen, T.C., Paulkovich, M., Raulin, F., Raaen, E., Way, S.H., 2005. The abundances of constituents of Titan's atmosphere from the GCMS instrument on the Huygens probe. Nature 438 (December), 779–784.
Poling, B.E., Prausnitz, J.M., O'Connell, J., 2007. The Properties of Gases and Liquids, fifth ed. McGraw-Hill Professional, Englewood Cliffs.
Somayajulu, G.R., 1988. Int. J. Thermophys. 9, 567.
Stiles, B.W., Hensley, S., Gim, Y., Bates, D.M., Kirk, R.L., Hayes, A., Radebaugh, J., Lorenz, R.D., Mitchell, K.L., Callahan, P.S., Zebker, H., Johnson, W.T.K., Wall, S.D., Lunine, J.I., Wood, C.A., Janssen, M., Pelletier, F., West, R.D., Veeramacheneni, C., 2009. Cassini RADAR Team, 2009. Determining Titan surface topography from Cassini SAR data. Icarus 202 (August), 584–598.
Stofan, E.R., Elachi, C., Lunine, J.I., Lorenz, R.D., Stiles, B., Mitchell, K.L., Ostro, S., Soderblom, L., Wood, C., Zebker, H., Wall, S., Janssen, M., Kirk, R., Lopes, R., Paganelli, F., Radebaugh, J., Wye, L., Anderson, Y., Allison, M., Boehmer, R., Callahan, P., Encrenaz, P., Flamini, E., Francescetti, G., Gim, Y., Hamilton, G., Hensley, S., Johnson, W.T.K., Kelleher, K., Muhleman, D., Paillou, P., Picardi, G., Posa, F., Roth, L., Seu, R., Shaffer, S., Vetrella, S., West, R., 2007. The lakes of Titan. Nature 445 (January), 61–64.
Stofan, E.R., Lunine, J., Lorenz, R., 2010. The lakes and seas of Titan: outstanding questions and future exploration. In: Cottini, V., Nixon, C., Lorenz, R. (Ed.), Through Time; A Workshop On Titan's Past, Present and Future. p. 48 (April).
Tegeler, C., Span, S., Wagner, W., 1999. A new equation of state for argon covering the fluid region for temperatures from the melting line to 700 K at pressures up to 1000 MPa. J. Phys. Chem. Ref. Data 779, 829.
Tokano, T., 2005. Thermal structure of putative hydrocarbon lakes on Titan. Adv. Space Res. 36, 286–294.
Tokano, T., Neubauer, F.M., 2002. Tidal winds on Titan caused by Saturn. Icarus 158 (August), 499–515.
Turtle, E.P., Perry, J.E., McEwen, A.S., West, R.A., Dawson, D.D., Porco, C.C., Fussner, S., 2007. Cassini imaging science subsystem observations of Titan's high-latitude lakes. LPI Contrib. 1357 (August), 142–143.
Vuitton, V., Yelle, R.V., Cui, J., 2008. Formation and distribution of benzene on Titan. J. Geophys. Res. 113, E05007. doi:10.1029/2007JE002997.
Wall, S., Hayes, A., Bristow, C., Lorenz, R., Stofan, E., Lunine, J., Le Gall, A., Janssen, M., Lopes, R., Wye, L., Soderblom, L., Paillou, P., Aharonson, O., Zebker, H., Farr, T., Mitri, R., Kirk, R., Mitchell, K., Notarnicola, C., Casarano, D., Ventura, B., 2010. Active shoreline of Ontario Lacus Titan: a morphological study of the lake and its surroundings. Geophys. Res. Lett. 37, L05202.

Retour à la table des matières : p. v

4.5 Article sur la composition de surface des évaporites

Icarus 226 (2013) 1431–1437

Contents lists available at ScienceDirect

Icarus

journal homepage: www.elsevier.com/locate/icarus

On the chemical composition of Titan's dry lakebed evaporites

D. Cordier [a,*], J.W. Barnes [b], A.G. Ferreira [c]

[a] Université de Franche-Comté, Institut UTINAM, CNRS/INSU, UMR 6213, 25030 Besançon Cedex, France
[b] Department of Physics, University of Idaho, Engineering-Physics Building, Moscow, ID 83844, USA
[c] Departamento de Engenharia Quimica, Universidade de Coimbra, Coimbra 3030-290, Portugal

ARTICLE INFO

Article history:
Received 10 March 2013
Revised 15 July 2013
Accepted 22 July 2013
Available online 2 August 2013

Keyword:
Satellites, surfaces
Saturn, satellites
Titan
Titan, hydrology
Titan, surface
Prebiotic environments

ABSTRACT

Titan, the main satellite of Saturn, has an active cycle of methane in its troposphere. Among other evidence for a mechanism of evaporation at work on the ground, dry lakebeds have been discovered. Recent *Cassini* infrared observations of these empty lakes have revealed a surface composition poor in water ice compared to that of the surrounding terrains—suggesting the existence of organic evaporites deposits. The chemical composition of these possible evaporites is unknown. In this paper, we study evaporite composition using a model that treats both organic solids dissolution and solvent evaporation. Our results suggest the possibility of large abundances of butane and acetylene in the lake evaporites. However, due to uncertainties of the employed theory, these determinations have to be confirmed by laboratory experiments.

© 2013 Elsevier Inc. All rights reserved.

1. Introduction

For a long time the existence of liquid hydrocarbons at the surface of Titan has been suspected (Sagan and Dermott, 1982; Lunine et al., 1983; Lunine, 1993a,b). The dark features observed by Stofan et al. (2007) in the north polar region were the first confirmed lakes or seas of hydrocarbons. Subsequently, other evidence for the RADAR-dark areas' lacustrine nature was found in the RADAR and IR ranges, to the extent that the existence of lakes/seas is now rather well established. In fact, the number of detected manifestations (e.g. Turtle et al., 2011a,b) of an active tropospheric methane hydrologic cycle is increasing. The lakes are expected to take part in this cycle, providing methane and/or ethane to the atmosphere through evaporation processes.

In past years, the signature of lake evaporation has been actively researched. Already, Stofan et al. (2007) noticed features showing margins similar to those of established lakes but having a RADAR surface backscatter similar to the surrounding terrain, suggesting the occurrence of an evaporation process in the recent past. Barnes et al. (2009) performed a detailed study of shoreline features of Ontario Lacus, the largest southern latitude lake. These authors interpreted the 5-μm bright annulus around Ontario Lacus as a dry, low-water ice content zone, possibly corresponding to a deposit of fine-grained organic condensates. These patterns, created by the shoreline recession, could have been caused by an evaporation episode. In their study of the same system, Wall et al. (2010) reported evidences for active shoreline processes. Although evidence for short-term changes in the extent of Ontario Lacus has been put forward (Turtle et al., 2011b), a subsequent reanalysis came to the conclusion that there is no indication of lake extent changes in the *Cassini* dataset (Cornet et al., 2012). Hayes et al. (2011) noticed that some observed dry lakebeds in Titan's arctic appear to be brighter than their exteriors in both nadir and off-nadir observations, which suggests compositional differences. However Hayes et al. (2011) were not able to exclude the possibility of an infiltration of liquids into a subsurface hydrologic system. Barnes et al. (2011a) used a sample of several lakes and lakebeds located in a region south of the Ligeia Mare. They obtained a strong correlation between RADAR-empty lakes and 5-μm-bright unit interpreted as low-water ice content areas.

As mentioned by Barnes et al. (2011a) these observed dry lake floors cannot be made only of sediments, indeed a pure sedimentary origin of these deposits would produce lakebed showing a 5-μm-brightness similar to that of their surrounding zones. One possible explanation proposed by Barnes et al. (2011a) consists of evaporation of the solvent (here a mixture of methane and ethane) yielding to the saturation of the dissolved solutes. The top layer of the resulting evaporites is being observed now in dry lakebeds if this idea is correct. This paper is devoted to an exploration of the evaporite scenario on the theoretical side. We have developed a model allowing for the computation of the chemical composition of such evaporites.

This paper is organized as follows. In Section 2, we outline our model for calculating chemical composition of putative evaporite deposits in dry lakebeds. Section 3 is devoted to evaporite

* Corresponding author.
E-mail address: daniel.cordier@obs-besancon.fr (D. Cordier).

0019-1035/$ - see front matter © 2013 Elsevier Inc. All rights reserved.
http://dx.doi.org/10.1016/j.icarus.2013.07.026

Table 1
Solids assumed to be dissolved in the lake and some of their properties. The Hildebrand's solubity parameter δ has to be compared to the value for methane and ethane at the same temperature (i.e. 90 K), which are respectively 1.52×10^4 (J m^{-3})$^{1/2}$ and 2.19×10^4 (J m^{-3})$^{1/2}$. For comparison purposes, for H_2O $\delta \sim 5 \times 10^4$ (J m^{-3})$^{1/2}$.

Species	Precipitation rate molecules (m^{-2} s^{-1})	δ 10^4 (J m^{-3})$^{1/2}$	Melting temperature (K)	Enthalpy of melting (kJ mol^{-1})
HCN	1.3×10^8[a]	2.99	260.0	8.406
C_4H_{10}	5.4×10^7[a]	1.91	136.0	4.661
C_2H_2	5.1×10^7[a]	2.28	192.4	4.105
CH_3CN	4.4×10^6[a]	*2.92*	229.3	6.887
CO_2	1.3×10^6[a]	*1.98*	216.6	9.020
C_6H_6	1.0×10^6[b]	2.48	279.1	9.300

[a] Lavvas et al. (2008a,b).
[b] Vuitton et al. (2008).

composition computations, and we discuss our results and conclude in Section 4.

2. Model description

We consider a portion of a Titan lake of uniform depth h that has a free surface of area S in contact with the atmosphere. For the sake of simplicity, methane, ethane and nitrogen are considered to be the only volatile compounds; they form a ternary mixture which will be our solvent. The presence of H_2, Ar and CO is neglected as they have low abundances in the atmosphere and as a consequence in the solution; C_3H_8 and C_4H_8 are also not taken into account because C_2H_6 seems to be much more abundant and their behaviors should not be very different than that of ethane. In addition to the solvent chemistry itself, we considered species in the solid state under Titan's surface thermodynamic conditions that may dissolve in the solvent. In the following, for short, we will simply call these compounds "dissolved solids" or "solutes": they include all the species, except those belonging to the solvent (i.e., methane, ethane and nitrogen). These supposed dissolved species are ultimately the products of the complex photochemistry taking place in the upper Titan atmosphere. In this work, we used the same list of solid compounds as in previous papers (Cordier et al., 2009, 2010, 2012 hereafter respectively C09, C10 and C12. Note that Cordier et al. (2013) is an erratum of Cordier et al. (2009).) These species appear to be among the main products found by photochemical 1D-models of Lavvas et al. (2008a,b) and Vuitton et al. (2008); the list is displayed in Table 1. This list differs from the list of species detected by CIRS[1] (*i.e.*, CH_4, C_2H_2, C_2H_4, C_2H_6, C_3H_8, CH_3C_2H, C_4H_2, C_6H_6, HCN, HC_3N, C_2N_2, CO, CO_2 and H_2O, see Vinatier et al., 2010) as CIRS observations relate to Titan's stratosphere and do not imply that these species reach the thermodynamic conditions of their precipitation to the ground. In addition, some species (for instance C_4H_3, C_4H_4, C_4H_5; see Table 5 of Lavvas et al., 2008a) are included in models while they are not yet observed by Cassini instruments. Thanks to their melting temperatures ranging between 136.0 K (C_4H_{10}) and 279.1 K (C_6H_6), all these molecules are in solid state under the Titan's surface conditions ($T \sim 90$ K in the region of lakes; Jennings et al., 2009). Although it has still to be confirmed by laboratory experiments, the materials listed in Table 1 are theoretically predicted to be soluble in a mixture of methane and ethane. Indeed, the Hildebrand's solubility parameters δ's for these solids (see Poling et al., 2007; Ahuja, 2009) are close to the ethane value (see Table 1). We implement a numerical calculation for the dynamic composition evolution of liquid mixtures using discrete timesteps. At each time t, the saturation mole fraction $X_{i,\mathrm{sat}}$ of each dissolved solid species i is computed via

$$\ln \Gamma_i X_{i,\mathrm{sat}} = -\frac{\Delta H_{i,\mathrm{m}}}{RT_{i,\mathrm{m}}}\left(\frac{T_{i,\mathrm{m}}}{T} - 1\right) \quad (1)$$

This relation can be found, for instance, in Section 8s–16 of the textbook by Poling et al. (2007) (hereafter POL07). The physical significance of Eq. (1) is the existence of a thermodynamic equilibrium between the considered precipitated solid i and the liquid solution. The enthalpy of melting is denoted $\Delta H_{i,\mathrm{m}}$, whereas T and $T_{i,\mathrm{m}}$ are respectively the current temperature of the lake and the melting temperature of molecule i; R is the constant of ideal gases and Γ_i is the activity coefficient. Although Eq. (1) has previously been used in several published works (Dubouloz et al., 1989, hereafter D89, and also C09, C10 and C12), we recall that it is approximate and its validity will be discussed in Section 4.

As the thermodynamic computations in the frame of the regular solution theory are uncertain (see C12) due to the lack of knowledge of thermodynamic data, we have distinguished two cases: the approximation of the ideal solution for which all the Γ_i's are equal to unity, and the non-ideal regular solution. In the case of an ideal solution, the molecules of the same species and those of different species interact with same intensity. For a non-ideal solution model, the Γ_i's are computed in the frame of regular solution theory (see D89, C09, POL07) in which the intermolecular interactions of involved species are such that the resulting entropy of mixing is equal to that of an ideal solution with the same composition: zero excess entropy, with the volume of mixing at zero. However in contrast with ideal solutions, regular solutions have mixing enthalpy with nonzero values. The regular-solution theory provides a good and useful semiquantitative representation of real behavior for solution containing nonpolar components as is the case of the mixtures under study in this work and the results based on this theory are in general considerably improved over those calculated by Raoult's law. In the context of the mixtures studied here it is expected that even though results may not possess extreme accuracy they are also hardly ever very bad, providing a valuable guide for future work. We emphasize that the Γ_i's are functions of X_i's, a fact which leads to numerical complications. The temperature T of the liquid remains unchanged during the whole evaporation process. Note, by the way, that for the temperatures relevant (see Table 1 for melting temperatures values) in our context, the right-hand side of Eq. (1) is negative, leading to mole fractions lower than the unity, at least in the case of an ideal solution.

The equilibrium solid-solution written as Eq. (1) must be complemented by the Principle of Matter Conservation. If we denote the total number of moles of all species at time t in the liquid by $N(t)$; at time $t + \mathrm{d}t$, one can write for a lake with surface area S

$$N(t+\mathrm{d}t) = N(t) - F_{\mathrm{CH_4}} \times S \times \mathrm{d}t - F_{\mathrm{C_2H_6}} \times S \times \mathrm{d}t - F_{\mathrm{N_2}} \times S \times \mathrm{d}t - \sum_{i,\mathrm{sat},t+\mathrm{d}t}\left(X_i(t)\,N(t) - X_{i,\mathrm{sat}}^{\mathrm{ideal}} N(t+\mathrm{d}t)\right) \quad (2)$$

where $F_{\mathrm{CH_4}}$, $F_{\mathrm{C_2H_6}}$ and $F_{\mathrm{N_2}}$ are the assumed respective evaporation rates (in mole m^{-2} s^{-1}) of CH_4, C_2H_6 and N_2. The terms containing the F_i's represent the evaporation while the sum, which refers to species reaching the saturation at $t + \mathrm{d}t$, corresponds to matter that precipitates and deposits on the lake floor.

The number of mole of species i available in the volume $S \times H$ of lake, at time t, is denoted by $n_i(t)$. Thus we arrive at the simple relation $n_i(t) = X_i N(t)$. Our algorithm consists of several steps. For the first one, we compute $N^{(0)}(t + \mathrm{d}t)$. This is an estimation of the total number of moles (in volume $S \times H$ of lake) remaining after the time step $\mathrm{d}t$ during which only evaporation of methane, ethane and nitrogen is taken into account:

$$N^{(0)}(t+\mathrm{d}t) = N(t) - (F_{\mathrm{CH_4}} + F_{\mathrm{C_2H_6}} + F_{\mathrm{N_2}}) \times S \times \mathrm{d}t. \quad (3)$$

[1] Composite Infrared Spectrometer, an instrument onboard the Cassini spacecraft.

Retour à la table des matières : p. v

From this, we can infer the corresponding mole fraction

$$X_i^{(0)} = \frac{n_i(t+\mathrm{d}t)}{N^{(0)}(t+\mathrm{d}t)} \tag{4}$$

with $n_i(t+\mathrm{d}t) = n_i(t)$ for all species except those belonging to the solvent. If, as a first attempt, we work in the frame of the ideal solution theory, then we have to compare the $X_i^{(0)}$'s to the mole fractions at saturation (for an ideal solution) $X_{i,\mathrm{sat}}^{\mathrm{ideal}}$. The molecules for which the criterion is fulfilled are presumed to precipitate. Their abundances are fixed to the saturation value

$$X_i(t+\mathrm{d}t) = X_{i,\mathrm{sat}}^{\mathrm{ideal}} \text{ (only species that saturate)}, \tag{5}$$

and the total number of moles at $t+\mathrm{d}t$ in the volume $S\times H$ is recomputed to be

$$N(t+\mathrm{d}t) = \frac{[1-\sum_{\mathrm{sat}} X_{i,\mathrm{sat}}]N(t) - (F_{\mathrm{CH_4}} + F_{\mathrm{C_2H_6}} + F_{\mathrm{N_2}}) \times S \times \mathrm{d}t}{1-\sum_{\mathrm{sat}} X_{i,\mathrm{sat}}^{\mathrm{ideal}}}. \tag{6}$$

Finally, the abundances at $t+\mathrm{d}t$ of species that do not saturate can be easily derived

$$X_i(t+\mathrm{d}t) = \frac{n_i(t)}{N(t+\mathrm{d}t)} \tag{7}$$

For a given species i that saturates, the rate of evaporite formation is then given by

$$F_i^{\mathrm{evap}}(t+\mathrm{d}t) = \frac{X_i(t)N(t) - X_{i,\mathrm{sat}}^{\mathrm{ideal}} N(t+\mathrm{d}t)}{S\times \mathrm{d}t}. \tag{8}$$

The chemical composition of the formed evaporite at time $t+\mathrm{d}t$ is given by

$$X_i^{\mathrm{evap}}(t+\mathrm{d}t) = \frac{F_i^{\mathrm{evap}}(t+\mathrm{d}t)}{\sum_{j,\mathrm{sat}} F_j^{\mathrm{evap}}(t+\mathrm{d}t)}. \tag{9}$$

When the solution is considered as a "real" solution, i.e. the activity coefficients are not taken to be equal to the unity and depend on the mole fractions, then

$$\Gamma_i(t+\mathrm{d}t) = \Gamma_i(X_1(t+\mathrm{d}t), X_2(t+\mathrm{d}t), \ldots). \tag{10}$$

The scheme allowing the computation of evaporite composition when the solution is non-ideal is rather similar to that of the case of an ideal solution. However, there are some differences: the total number of moles $N(t+\mathrm{d}t)$ can no longer be computed with Eq. (6). Instead, if N_{sat} is the number of species saturating at $t+\mathrm{d}t$, then we solve the system of $(N_{\mathrm{sat}}+1)$ equations composed of Eq. (2) and the N_{sat} equations similar to Eq. (1). The unknowns are $N(t+\mathrm{d}t)$ and the N_{sat} mole fractions at saturation $X_{k,\mathrm{sat}}^{\mathrm{non-ideal}}$. The resolution of that non-linear system is performed using a multi-dimensional Newton–Raphson's method (see Press et al., 1992).

Several authors (Mitri et al., 2007; Tokano, 2005, 2009) have studied the dynamics of Titan's lakes. They have used the bulk aerodynamical model, introduced for Earth's climate model by Fairall et al. (1996). In this model the evaporation rate is given by

$$E = \rho_{\mathrm{air}} K(q^* - q)u_r \tag{11}$$

where E is expressed in kg m^{-2} s^{-1}, ρ_{air} as the density of the air, K is a transport coefficient (a purely aerodynamic quantity), q^* and q are saturation specific humidity and specific humidity respectively, and u_r is the horizontal component of the averaged wind speed relative to the surface at a given height z_r. As we can see, the rate E depends on q and u_r, quantities that are supposed to undergo substantial variations during a Titan's year. Thus the rate E is expected to experience significant variations during Titan's seasonal cycle. To obviate this problem we have chosen to use two definitions of time and two time-scales, respectively corresponding to the evaporation of CH_4 and the evaporation of C_2H_6. Methane is known to be much more volatile than ethane. An order of magnitude of the ratio $\alpha_{\mathrm{evap}} = F_{\mathrm{C_2H_6}}/F_{\mathrm{CH_4}}$ can be evaluated thanks to the Hertz-Knudsen (see Ward and Fang, 1999, and references therein): one finds that $\alpha_{\mathrm{evap}} \sim 10^{-4}$ for a temperature $T \simeq 90$ K. In our model we fixed α_{evap} to this value. The evaporation rate of nitrogen is scaled to the C_2H_6 one, in order to insure a N_2 content in the liquid preventing it from freezing (see Mitri et al., 2007). Therefore, all the CH_4 content evaporates on a short time-scale $\tau_{\mathrm{CH_4}}$ during which the time $t_{\mathrm{CH_4}}$ is defined so that the evaporation rate $F_{\mathrm{CH_4}}$ is constant. We emphasize that this operation is equivalent to an implicit non-linear re-scaling of time. A similar definition is adopted for $t_{\mathrm{C_2H_6}}$, the "variable time" valid during ethane evaporation, as $F_{\mathrm{CH_4}} \gg F_{\mathrm{C_2H_6}}$, the quantity of ethane escaping the lake during methane evaporation, is negligible. This way, all the details of the possible events (*e.g.*, low or high humidity, strong winds) that could affect the evaporation rates can be ignored.

3. Evaporites upper layer composition calculation

First we build plausible chemical compositions relevant for a lake before its evaporation. Previous calculations made at thermodynamic equilibrium (D89, C09) correspond to an averaged composition in time and space. Atmospheric precipitation rates are likely to undergo substantial secular variations—this is supported by some *Cassini* observations (see for instance Turtle et al., 2011a). In addition, the flux of hydrocarbons falling from the atmosphere likely varies significantly from one location to another: in the equatorial regions the presence of the dune fields indicates an arid climate while lakes, evidences for a wet weather, are located in the polar regions. These tendencies are confirmed by Global Circulation Models (see for instance Fig. 4 of C12 based on Crespin et al., 2008). Thus we have considered methane-poor and -rich solvents, always containing a few percent of N_2. Concerning the solids possibly in solution, we used precipitation rates derived from 1D photochemical models by Lavvas et al. (2008a,b) and Vuitton et al. (2008)—the precipitation rates are recalled in Table 1. We stress that these rates have to be taken with caution because of the lack of micro-physics in the models. A compound that meets an altitude where the temperature equals its condensation temperature rains out. In addition, 3D physical processes (mainly transport) are ignored, although they can affect significantly the amounts of solid hydrocarbons reaching the surface at a given place at a particular time. Two possibilities have been studied.

- In Type 1 solids mixture, where the abundances of these solids have been scaled to atmospheric precipitation rates, the most abundant species (i.e., HCN) has its mole fraction set to its value at saturation (ideal solution case). This way, the precipitation (i.e., saturation) of solids in solution in the liquid begins at the initial time. An assumed initial value below the saturation one, only delaying the starting time of precipitation, keeps the final composition of the upper layer of evaporites unchanged.
- Type 2 solids mixture, in order to appreciate the effect of evaporation/solids evaporites deposition, we constructed also initial mixtures with uniform abundances, and starting values fixed to the smallest mole fraction at saturation (i.e. that relative to C_6H_6). At the evaporation initial time, one species begins to precipitate (i.e. C_6H_6); the others saturate latter.

In Table 2, results relevant for an ideal solution have been gathered. Two initial mixtures have been considered—both ethane rich (~89% of C_2H_6 when evaporation begins) with ~1% of nitrogen to ensure the liquid physical state. This abundance of N_2 is typical of what has been inferred by computations at equilibrium in previous works. While $X_{\mathrm{liq}}^{\mathrm{ini}}$ quantifies the initial chemical composition of

Retour à la table des matières : p. v

Table 2
Computed chemical composition $\left(X_{\text{evap}}^{\text{fin}}\right)$ of upper layer Titan's lakes drybeds evaporites, in the ideal solution hypothesis. Two types of dissolved solids composition have been considered (see text for explanation). $X_{i,\text{sat}}$ is the mole fraction at saturation, $X_{i,\text{liq}}$ represents the initial composition of the liquid and $X_{i,\text{sol}}$ represents the initial abundances of dissolved solids. The Δ's show enrichment/empoverishment of the resulting upper layer of the evaporite deposit. The assumed temperature is $T = 90$ K. The notation $x \cdot y(-n) = x \cdot y \times 10^{-n}$ has been used. One can notice that ideal solubility of CO_2 is comparable to the values reported by Preston and Prausnitz (1970) and Preston et al. (1971) for somewhat higher temperatures around 130–140 K.

Ideal solution					
Species	$X_{i,\text{sat}}$ (ideal)	$X_{\text{liq}}^{\text{ini}}$	$X_{\text{sol}}^{\text{ini}}$	$X_{\text{evap}}^{\text{fin}}$	Δ (%)
		Mixture type 1			
CH_4	–	10.018%	–	–	–
C_2H_6	–	88.804%	–	–	–
N_2	–	1.002%	–	–	–
HCN	6.46(−4)	6.46(−4)	3.65(−1)	3.82(−3)	−99
C_4H_{10}	1.22(−1)	5.93(−4)	3.35(−1)	6.48(−1)	+94
C_2H_2	5.40(−2)	3.62(−4)	2.05(−1)	3.20(−1)	+56
CH_3CN	3.73(−3)	5.42(−5)	3.06(−2)	2.21(−2)	−28
CO_2	8.72(−4)	3.43(−5)	1.94(−2)	5.16(−3)	−73
C_6H_6	2.20(−4)	8.06(−5)	4.55(−2)	1.31(−3)	−97
		Mixture type 2			
CH_4	–	10.013%	–	–	–
C_2H_6	–	88.853%	–	–	–
N_2	–	1.001%	–	–	–
HCN	6.46(−4)	2.20(−4)	1.67(−1)	6.86(−3)	−96
C_4H_{10}	1.22(−1)	2.20(−4)	1.67(−1)	4.71(−1)	+183
C_2H_2	5.40(−2)	2.20(−4)	1.67(−1)	4.71(−1)	+183
CH_3CN	3.73(−3)	2.20(−4)	1.67(−1)	3.96(−2)	−76
CO_2	8.72(−4)	2.20(−4)	1.67(−1)	9.26(−3)	−94
C_6H_6	2.20(−4)	2.20(−4)	1.67(−1)	2.34(−3)	−99

the solution, $X_{\text{sol}}^{\text{ini}}$ represents the abundances of solutes regarded as a single set: $\sum X_{\text{sol}}^{\text{ini}} = 1$. The $X_{\text{evap}}^{\text{fin}}$'s are the mole fractions of compounds finally deposited in the evaporites upper layer. The parameter of enrichment Δ measures the relative enrichment/empoverishment of a given species in the surface evaporites, as compared to the initial composition of solids in solution.

As can be noticed in Table 2, the only species undergoing an enrichment in the surface evaporites layer, compared to abundances initially taken into account for the dissolved solids, are butane (C_4H_{10}) and acetylene (C_2H_2). This behavior can be explained by their high solubilities (i.e. high $X_{i,\text{sat}}$'s). The higher $X_{i,\text{sat}}$ is, the greater the quantity of dissolved material is. Consequently the saturation occurs later during the evaporation process. If we compare $X_{\text{fin}}^{\text{evap}}$ obtained for type 1 and type 2 mixtures of solids, we see that evaporite composition (perhaps unsurprisingly) depends on the initial abundances of solutes. Our simulation clearly shows, within the framework of our current assumptions, that dissolution in methane/ethane solution, followed by evaporation of the solvent, yields surface evaporite compositions with high abundances of the most soluble species.

We stress that an identical value of the enrichment Δ is the consequence of a saturation of solutes that occurs at the very end of the evaporation. Of course, a solvent of a different composition (e.g., a methane rich one) leads strictly to the same result because here we are making the calculations by adopting the ideal solution hypothesis.

The results of non-ideal simulations for the regular solution Γ_i's have been gathered in Tables 3 and 4. Tables 3 and 4 are respectively devoted to dissolved solids mixture type 1 and type 2. For each of these types, cases of methane rich and poor solvent are considered. As can be noticed in Tables 3 and 4, the general trend remains the same: butane and acetylene, if present in the initial mixture, are the dominant species in the upper evaporite layer.

Table 3
Type 1 mixtures in the case of a non-ideal solution. A methane poor and a methane rich case are considered.

Non-ideal solution				
Species	$X_{\text{liq}}^{\text{ini}}$	$X_{\text{sol}}^{\text{ini}}$	$X_{\text{evap}}^{\text{fin}}$	Δ (%)
	Mixture type 1, methane poor			
CH_4	10.018%	–	–	–
C_2H_6	88.804%	–	–	–
N_2	1.002%	–	–	–
HCN	6.46(−4)	3.65(−1)	1.52(−4)	−100
C_4H_{10}	5.93(−4)	3.35(−1)	5.72(−1)	+71
C_2H_2	3.62(−4)	2.05(−1)	4.20(−1)	+105
CH_3CN	5.42(−5)	3.06(−2)	7.14(−4)	−98
CO_2	3.43(−5)	1.94(−2)	6.53(−3)	−66
C_6H_6	8.06(−5)	4.55(−2)	6.82(−4)	−99
	Mixture type 1, methane rich			
CH_4	90.160%	–	–	–
C_2H_6	8.662%	–	–	–
N_2	1.002%	–	–	–
HCN	6.46(−4)	3.65(−1)	6.92(−5)	−100
C_4H_{10}	5.93(−4)	3.35(−1)	6.69(−1)	+100
C_2H_2	3.62(−4)	2.05(−1)	3.24(−1)	+58
CH_3CN	5.42(−5)	3.06(−2)	2.94(−4)	−99
CO_2	3.43(−5)	1.94(−2)	6.03(−3)	−69
C_6H_6	8.06(−5)	4.55(−2)	3.65(−4)	−99

Table 4
Type 2 mixtures in the case of a non-ideal solution. A methane poor and a methane rich case are considered.

Non-ideal solution				
Species	$X_{\text{liq}}^{\text{ini}}$	$X_{\text{sol}}^{\text{ini}}$	$X_{\text{evap}}^{\text{fin}}$	Δ (%)
	Mixture type 2 methane poor			
CH_4	10.013%	–	–	–
C_2H_6	88.853%	–	–	–
N_2	1.001%	–	–	–
HCN	2.20(−4)	1.67(−1)	2.18(−4)	−100
C_4H_{10}	2.20(−4)	1.67(−1)	4.95(−1)	+197
C_2H_2	2.20(−4)	1.67(−1)	4.95(−1)	+197
CH_3CN	2.20(−4)	1.67(−1)	1.04(−3)	−99
CO_2	2.20(−4)	1.67(−1)	8.54(−3)	−95
C_6H_6	2.20(−4)	1.67(−1)	9.55(−4)	−99
	Mixture type 2 methane rich			
CH_4	90.119%	–	–	–
C_2H_6	8.747%	–	–	–
N_2	1.001%	–	–	–
HCN	2.20(−4)	1.67(−1)	6.97(−5)	−100
C_4H_{10}	2.20(−4)	1.67(−1)	6.68(−1)	+301
C_2H_2	2.20(−4)	1.67(−1)	3.25(−1)	+95
CH_3CN	2.20(−4)	1.67(−1)	2.97(−4)	−100
CO_2	2.20(−4)	1.67(−1)	6.03(−3)	−96
C_6H_6	2.20(−4)	1.67(−1)	3.67(−4)	−100

The difference between the results of methane rich and poor are explained by the non-ideality of the solution: in such a situation the molecules undergo interactions. In this way, solvents with different compositions are not equivalent.

The content of nitrogen is expected to vary slightly for different bodies of liquid. Hence we test for sensitivity of evaporite composition regarding the abundances of nitrogen in the solvent. Table 5 shows the enrichment parameter Δ for all solutes in three cases: $X_{N_2}^{\text{ini}} = 0.5\%$, 1% and 3%. All of these computations have been made for a methane rich solvent for a temperature of 90 K. Clearly, solvents with a high nitrogen abundance appear to favor C_4H_{10} as a main constituent of surface evaporites.

Retour à la table des matières : p. v

Table 5
Influence of the initial nitrogen abundance on final evaporite layer composition. T = 90 K, non-ideal. Methane rich solvent $\left(X^{ini}_{CH_4} \simeq 90\right)\%$

$X^{ini}_{N_2}$	0.5%	1%	3%
	Δ	Δ	Δ
HCN	−99.9	−100.0	−100.0
C_4H_{10}	+270.5	+300.9	+377.5
C_2H_2	+125.0	+95.1	+19.1
CH_3CN	−99.7	−99.8	−100.0
CO_2	−96.2	−96.4	−96.7
C_6H_6	−99.7	−99.8	−100.0

Table 6
Influence of the temperature on final evaporite layer composition. The initial nitrogen mole fraction is fixed to $X^{ini}_{N_2} = 1\%$, the solution is a non-ideal one, and type 1 for the initial dissolved solids mixture has been considered.

Species	T = 85 K		T = 90 K		T = 95 K	
	X^{fin}_{evap}	Δ	X^{fin}_{evap}	Δ	X^{fin}_{evap}	Δ
Methane poor solvent						
HCN	1.17(−4)	−100	1.52(−4)	−100	1.84(−4)	−100
C_4H_{10}	5.19(−1)	+54.9	5.72(−1)	+70.7	6.20(−1)	+85.0
C_2H_2	4.76(−1)	+132.4	4.20(−1)	+105.3	3.70(−1)	+80.8
CH_3CN	6.52(−4)	−97.9	7.14(−4)	−97.7	7.39 (−4)	−97.6
CO_2	4.59(−3)	−76.3	6.53(−3)	−66.3	8.77 (−3)	−54.7
C_6H_6	5.54(−4)	−98.8	6.82(−4)	−98.5	7.88(−4)	−98.3
Methane rich solvent						
HCN	5.18(−5)	−100	6.92(−5)	−100	8.76(−5)	−100
C_4H_{10}	6.31(−1)	+88.3	6.69(−1)	+99.8	7.01(−1)	+109.4
C_2H_2	3.65(−1)	+78.1	3.24(−1)	+58.4	2.90(−1)	+41.6
CH_3CN	2.62(−4)	−99.2	2.94(−4)	−99.0	3.17 (−4)	−99.0
CO_2	4.29(−3)	−77.9	6.03(−3)	−68.9	8.07 (−3)	−58.3
C_6H_6	2.96(−4)	−99.4	3.65(−4)	−99.2	4.28(−4)	−99.1

The temperature also influences the solubility of solids. For a range of temperatures (i.e., 85 K, 90 K, and 95 K), the computed final compositions have been reported in Table 6. High values of temperature favors high-butane evaporite content, while acetylene is disfavored at high temperature. However the major tendency, the prominence of butane and acetylene, is robust. Finally, we stress that during all our calculations, for each time, we have checked that the density of species precipitating remained lower than the liquid solution value. Then, according to the simulations performed in this work, the organic precipitated solids would never float at the surface of the Titan's lakes (at least not without unusual circumstances such as those suggested by Hofgartner and Lunine, 2013).

4. Discussion and conclusion

As it has been shown in the previous section, the composition obtained for the superficial layer of evaporite is the result of the influence of two main factors: (1) the initial composition of dissolved solids, and (2) the mole fraction at saturation values of the solids, provided by Eq. (1). For a given initial composition, species with the highest $X_{i,sat}$ (i.e., the lowest energy of cohesion) remain dissolved for a longer time in the solvent during the evaporation and finally become the major constituents of the last layer of deposits. The value of the melting temperature T_m and enthalpy of melting determine the concentration at saturation. We furthermore emphasize that, due to the special non-linear scale of time used in this work, the depth of different layers of evaporite cannot be computed. In a same way, the composition of possible evaporite annuli around a lake (see for instance Hayes et al., 2010) could not be estimated. For a given initial composition of solids in solution, we can only compute the composition of the external surface of the evaporite deposit.

The behavior of those solid species that are not taken into consideration in this work could be estimated if their enthalpy of melting were known. For instance, laboratory experiments suggest that HC_3N could be an evaporite candidate in lake drybeds (Clark et al., 2010). In their Appendix II, Sagan and Thompson (1984) published a list of species with their estimated or estimated enthalpies of melting. HC_3N belongs to this list, these authors have found $\Delta H_m(HC_3N) = 40$ cal g^{-1}, corresponding to 8.5 kJ mol^{-1}. This value is a factor of 2 larger than enthalpies of melting for C_4H_{10} and C_2H_2. Coupled to an estimation of the temperature of melting of this molecule ~235 K (~235 K, obtained using a "group contribution" method, see Poling et al., 2007), one can derive that $X^{ideal}_{sat,HC_3N} \simeq 10^{-3}$. Consequently, HC_3N should have a behavior reassembling that of CH_3CN. Thus, even if HC_3N has a precipitation rate larger than the acetylene rate, after a dissolution/evaporation process C_2H_2 should remain a dominant species in the final deposits layer.

Although the composition of tholins has not been directly measured, Quirico et al. (2008) identified in their experiments that molecules derived from hydrazine $R_1R_2N–NH_2$ as a possible constituent of Titan's atmosphere tholins. Taking the most simple molecules of that family: $CH_3CH_3N–NH_2$, one can estimate the value of the enthalpy ΔH_m thanks to a "group contribution" method (see Poling et al., 2007). We found $\Delta H_m \simeq 9.15$ kJ mol^{-1} and $T_m \simeq$ 228 K (for methylhydrazine Aston et al., 1951, found $\Delta H_m \sim 10.42$ kJ mol^{-1} and $T_m \simeq 220.8$ K), yielding X^{ideal}_{sat} ($CH_3CH_3N–NH_2$) $\simeq 6 \times 10^{-4}$—a value much smaller than the butane or acetylene ones.

However, hydrazine derivatives probably belong to tholins but are probably not representative of the whole. We recall that experiments and theoretical works made in the past have shown the poor solubility of tholins in non-polar solvents (McKay, 1996; Raulin, 1987). In a general manner, we can notice that ΔH_m increases when the number of -CH_3 get larger, suggesting that molecules with long carbon chains would be easily buried under layers rich in C_4H_{10} and C_2H_2.

The precipitation of solids previously dissolved in ternary solvent $CH_4–C_2H_6–N_2$ implies heterogeneous nucleation, which occurs much more often than homogeneous nucleation in the real world. Nucleation that forms at preferential sites such as phase boundaries or impurities like dust requires less energy than homogeneous nucleation (see for instance Vehkamäki, 2006). Depending on the initial turbidity of the lake, which might possibly caused by sediments produced during drainage and/or organic aggregates fallen from the atmosphere, the deposition of evaporites could begin either on the lake floor alone or simultaneously on this floor and on the particules contributing to the initial turbidity. Moreover, the formation of evaporite has to occur on a time-scale significantly shorter than that of evaporation, otherwise the concept used for our non-linear evaporation time-scale would no longer be relevant. In other words, solution cannot remain "supersaturated" for a long time.

If the formation of evaporite on the lake bed is the dominant effect, then a model based on solubility is fully valid. Otherwise, if the evaporites form preferentially on possible turbidity particulates, then the scenario of lake drybed deposition formation could be very different as it could involve transport processes like convection and sedimentation. Unfortunately, given that the turbidity of Titan's lakes is unknown, one can only guess that it should be very variable from one lake to another, being a function of the exact history of the lake (drainage, occurence of a recent methane rainfall, etc.). Insight into turbidity and its time-variability could be acquired by direct measurements from a floating capsule, as were proposed by the Titan Mare Explorer (TiME) (Lorenz et al., 2012).

Retour à la table des matières : p. v

Finally, the validity of the theory presented in this article has to be considered. As indicated in Section 2, the Eq. (1) is an approximation, and the rigourous formula is (see or instance Hojjati and Rohani, 2006)

$$\ln \Gamma_i X_{i,\mathrm{sat}} = -\frac{\Delta H_{i,\mathrm{m}}}{RT_{i,\mathrm{m}}}\left(\frac{T_{i,\mathrm{m}}}{T}-1\right) - \frac{1}{RT}\int_{T_m}^{T}\Delta c_p\,\mathrm{d}T + \frac{1}{R}\int_{T_m}^{T}\frac{\Delta c_p}{T}\,\mathrm{d}T \tag{12}$$

with

$$\Delta c_p = c_p\ (\text{subcooled liquid solute}) - c_p(\text{solid solute}) \tag{13}$$

(see p. 8.181 of POL07). Eq. (1) is a good approximation of Eq. (12) when the contributions of the second and the third terms of the right-hand side are negligible, as is often the case as emphasized in the literature (see Poling et al., 2007; Hojjati and Rohani, 2006). This assumption has been made in previous work (D89, C09, C10 and C12). Unfortunately, reliable estimations of Δc_p are not feasible with available data. The Dulong and Petit law is probably not adequate for c_p (solid solute) at such a low temperature (~90 K), in which case the use of more sophisticated formulation like Debye's model (Kittel et al., 2004) would be required. However a Debye formulation is not currently applicable due to the lack of data. Besides this, Rùzicka and Domalski's method for determining c_p (subcooled liquid solute) (see p. 6.19 of POL07) is not relevant as interpolation expressions have a domain of validity limited to temperatures ranging from the melting point to the boiling point. For our purposes, the relevant temperature is well below the typical boiling point temperatures of considered species (see Table 1).

However, even if the second and the third terms of the right-hand side of Eq. (12) have significant values compared to that of the first term, the process of solid dissolution and formation of an evaporite deposit is certainly not neutral concerning the chemical composition of the solids visible at the surface. If quantitative determinations could be changed by the contribution of those two additional terms compared to present results, then the scenario of dissolution of solids coming directly from the atmospheric precipitation or surrounding terrains (washing and deposition in lakebeds) after an evaporation episode would be robust. Such a scenario provides an explanation for the strong correlation of 5-μm brightness observations with morphologic dry beds RADAR detections. Several authors (McKay and Smith, 2005; Schulze-Makuch and Grinspoon, 2005; Lunine, 2010) have proposed the hypothesis of an exotic form of life based on a metabolism involving a chemical reaction between surface acetylene and atmospheric hydrogen. We underline that in such a context, our results have to be handled with extreme caution.

As previously suggested by C12 for the composition of lakes, more reliable predictions of Titan's lakes' drybeds could be made using in vitro simulations. But that would require a huge experimental effort that couples the evaporation of a ternary mixture and dissolution of solids hydrocarbons and nitriles in a cryogenic range of temperature. Already, Luspay-Kuti et al. (2012) have determined the evaporation rate of CH_4 and Malaska and Hodyss (2013) haved obtained promising preliminary results concerning the solubility of benzene.

In the recent past, an infrared VIMS observation (Stephan et al., 2010; Barnes et al., 2011b; Soderblom et al., 2012) has been explained by the occurrence of a probable specular reflection on a filled Titan's lake. A search for similar specular or near-specular reflections over dry beds could be of interest to constrain the nature of the evaporitic surface. A glint associated to an empty lake could be the signature of a smooth and thick evaporite layer, while no glint or a diffuse glint could help to constrain the evaporites' particle size distribution.

Acknowledgments

We acknowledge financial support from the Observatoire des Sciences de l'Univers THETA Franche-Comt-Bourgogne, France. We thank Sandrine Vinatier and Panayotis Lavvas for scientific discussion; and the anonymous Reviewers who improved the clarity of the paper with their remarks and comments. J.W.B. is funded by the NASA CDAPS Program Grant #NNX12AC28G.

References

Ahuja, P., 2009. Chemical Engineering Thermodynamics. Prentice-Hall of India, New Dehli.
Aston, J.G., Finke, H.L., Janz, G.J., Russell, K.E., 1951. The heat capacity, heats of fusion and vaporization, vapor pressures, entropy and thermodynamic functions of methylhydrazine. J. Am. Chem. Soc. 73, 1939–1943.
Barnes, J.W., Brown, R.H., Soderblom, J.M., Soderblom, L.A., Jaumann, R., Jackson, B., Le Mouélic, S., Sotin, C., Buratti, B.J., Pitman, K.M., Baines, K.H., Clark, R.N., Nicholson, P.D., Turtle, E.P., Perry, J., 2009. Shoreline features of Titan's Ontario Lacus from Cassini/VIMS observations. Icarus 201 (May), 217–225.
Barnes, J.W., Bow, J., Schwartz, J., Brown, R.H., Soderblom, J.M., Hayes, A.G., Vixie, G., Le Mouélic, S., Rodriguez, S., Sotin, C., Jaumann, R., Stephan, K., Soderblom, L.A., Clark, R.N., Buratti, B.J., Baines, K.H., Nicholson, P.D., 2011a. Organic sedimentary deposits in Titan's dry lakebeds: Probable evaporite. Icarus 216 (November), 136–140.
Barnes, J.W., Soderblom, J.M., Brown, R.H., Soderblom, L.A., Stephan, K., Jaumann, R., Mouélic, S.L., Rodriguez, S., Sotin, C., Buratti, B.J., Baines, K.H., Clark, R.N., Nicholson, P.D., 2011b. Wave constraints for Titan's Jingpo Lacus and Kraken Mare from VIMS specular reflection lightcurves. Icarus 211 (January), 722–731.
Clark, R.N., Curchin, J.M., Barnes, J.W., Jaumann, R., Soderblom, L., Cruikshank, D.P., Brown, R.H., Rodriguez, S., Lunine, J., Stephan, K., Hoefen, T.M., Le Mouélic, S., Sotin, C., Baines, K.H, Buratti, B.J., Nicholson, P.D., 2010. Detection and mapping of hydrocarbon deposits on Titan. J. Geophys. Res. (Planets) 115 (October), 10005. http://dx.doi.org/10.1029/2009JE003369.
Cordier, D., Mousis, O., Lunine, J.I., Lavvas, P., Vuitton, V., 2009. An estimate of the chemical composition of Titan's lakes. Astrophys. J. 707 (December), L128–L131.
Cordier, D. et al., 2010. About the possible role of hydrocarbon lakes in the origin of Titan's noble gas atmospheric depletion. Astrophys. J. 721 (October), L117–L120.
Cordier, D. et al., 2012. Titan's lakes chemical composition: Sources of uncertainties and variability. Planet. Space Sci. 61 (February), 99–107.
Cordier, D., Mousis, O., Lunine, J.I., Lavvas, P., Vuitton, V., 2013. Erratum: "An estimate of the chemical composition of Titan's lakes" (2009, ApJL, 707, L128). Astrophys. J. 768 (May), L23–L25.
Cornet, T. et al., 2012. Edge detection applied to Cassini images reveals no measurable displacement of Ontario Lacus' margin between 2005 and 2010. J. Geophys. Res. (Planets) 117 (July), 7005.
Crespin, A., Lebonnois, S., Vinatier, S., Bézard, B., Coustenis, A., Teanby, N.A., Achterberg, R.K., Rannou, P., Hourdin, F., 2008. Diagnostics of Titan's stratospheric dynamics using Cassini/CIRS data and the 2-dimensional IPSL circulation model. Icarus 197 (October), 556–571.
Dubouloz, N., Raulin, F., Lellouch, E., Gautier, D., 1989. Titan's hypothesized ocean properties – The influence of surface temperature and atmospheric composition uncertainties. Icarus 82 (November), 81–96.
Fairall, C.W., Bradley, E.F., Rogers, D.P., Edson, J.B., Young, G.S., 1996. Bulk parameterization of air–sea fluxes for tropical ocean-global atmosphere coupled-ocean atmosphere response experiment. J. Geophys. Res. 101 (C2), 3747–3764.
Hayes, A.G., Wolf, A.S., Aharonson, O., Zebker, H., Lorenz, R., Kirk, R.L., Paillou, P., Paillou, P., Lunine, J., Wye, L., Callahan, P., Wall, S., Elachi, C., 2010. Bathymetry and absorptivity of Titan's Ontario Lacus. J. Geophys. Res. (Planets) 115 (September), 9009. http://dx.doi.org/10.1029/2009JE003557.
Hayes, A.G., Aharonson, O., Lunine, J.I., Kirk, R.L., Zebker, H.A., Wye, L.C., Lorenz, R.D., Turtle, E.P., Paillou, P., Mitri, G., Wall, S.D., Stofan, E.R., Mitchell, K.L., Elachi, C., 2011. Transient surface liquid in Titan's polar regions from Cassini. Icarus 211 (January), 655–671.
Hofgartner, J.D., Lunine, J.I., 2013. Does ice float in Titan's lakes and seas? Icarus 223 (March), 628–631.
Hojjati, H., Rohani, S., 2006. Measurement and prediction of solubility of paracetamol in water – Isopropanol solution. Part 2. Prediction. Org. Process Res. Develop. 10, 1110–1118.
Jennings, D.E. et al., 2009. Titan's surface brightness temperatures. Astrophys. J. 691 (February), L103–L105.
Kittel, C., Zettl, A., McEuen, P., 2004. Introduction to Solid State Physics. John Wiley & Sons.
Lavvas, P.P., Coustenis, A., Vardavas, I.M., 2008a. Coupling photochemistry with haze formation in Titan's atmosphere. Part I: Model description. Planet. Space Sci. 56 (January), 27–66.
Lavvas, P.P., Coustenis, A., Vardavas, I.M., 2008b. Coupling photochemistry with haze formation in Titan's atmosphere. Part II: Results and validation with Cassini/Huygens data. Planet. Space Sci. 56 (January), 67–99.

Retour à la table des matières : p. v

Lorenz, R.D., Stofan, E., Lunine, J.I., Zarnecki, J.C., Harri, A.M., Karkoschka, E., Newman, C.E., Bierhaus, E.B., Clark, B.C., Yelland, M., Leese, M.R., Boldt, J., Darlington, E., Neish, C.D., Sotzen, K., Arvelo, J., Rasbach, C., Kretsch, W., Strohbehn, K., Grey, M., Mann, J., Zimmerman, H., Reed, C., 2012. MP3 – A meteorology and physical properties package for Titan air–sea studies. LPI Contrib. 1683 (October), 1072–1073.
Lunine, J.I., 1993a. Does Titan have an ocean? A review of current understanding of Titan's surface. Rev. Geophys. 31 (May), 133–149.
Lunine, J.I., 1993b. Erratum: "Does Titan have an ocean? A review of current understanding of Titan's surface" [Rev. Geophys. 31, 133–149 (1993)]. Rev. Geophys. 31, 355–356.
Lunine, J.I., 2010. Titan and habitable planets around M-dwarfs. Faraday Discuss. 147, 405–418.
Lunine, J.I., Stevenson, D.J., Yung, Y.L., 1983. Ethane ocean on Titan. Science 222 (December), 1229–1230.
Luspay-Kuti, A. et al., 2012. Experimental simulations of CH_4 evaporation on Titan. Geophys. Res. Lett. 39 (October), L23203.
Malaska, M., Hodyss, R., 2013. Laboratory investigation of benzene dissolving in a Titan Lake. LPI Contrib. 1719 (March), 2744–2745.
McKay, C.P., 1996. Elemental composition, solubility, and optical properties of Titan's organic haze. Planet. Space Sci. 44 (August), 741–747.
McKay, C.P., Smith, H.D., 2005. Possibilities for methanogenic life in liquid methane on the surface of Titan. Icarus 178 (November), 274–276.
Mitri, G., Showman, A.P., Lunine, J.I., Lorenz, R.D., 2007. Hydrocarbon lakes on Titan. Icarus 186 (February), 385–394.
Poling, B.E., Prausnitz, J.M., O'Connell, J., 2007. The Properties of Gases and Liquids, fifth ed. McGraw-Hill Professional, Englewood Cliffs.
Press, W., Teukolsky, S., Vetterling, W., Flannery, B., 1992. Numerical Recipes in Fortran 77. Cambridge University Press.
Preston, G.T., Prausnitz, J.M., 1970. Thermodynamics of solid solubility in cryogenic solvents. Ind. Eng. Chem. Process Des. Develop. 9, 264–271.
Preston, G.T., Funk, E.W., Prausnitz, J.M., 1971. Solubilities of hydrocarbons and carbon dioxide in liquid methane and in liquid argon. J. Phys. Chem. 75, 2345–2352.
Quirico, E., Montagnac, G., Lees, V., McMillan, P.F., Szopa, C., Cernogora, G., Rouzaud, J.-N., Simon, P., Bernard, J.-M., Coll, P., Fray, N., Minard, R.D., Raulin, F., Reynard, B., Schmitt, B., 2008. New experimental constraints on the composition and structure of Tholins. Icarus 198 (November), 218–231.
Raulin, F., 1987. Organic chemistry in the oceans of Titan. Adv. Space Res. 7, 71–81.
Sagan, C., Dermott, S.F., 1982. The tide in the seas of Titan. Natur 300 (December), 731–733.
Sagan, C., Thompson, W.R., 1984. Production and condensation of organic gases in the atmosphere of Titan. Icarus 59 (August), 133–161.
Schulze-Makuch, D., Grinspoon, D.H., 2005. Biologically enhanced energy and carbon cylcing on Titan? Astrobiology 5, 560–567.
Soderblom, J.M., Barnes, J.W., Soderblom, L.A., Brown, R.H., Griffith, C.A., Nicholson, P.D., Stephan, K., Jaumann, R., Sotin, C., Baines, K.H., Buratti, B.J., Clark, R.N., 2012. Modeling specular reflections from hydrocarbon lakes on Titan. Icarus 220 (August), 744–751.
Stephan, K., Jaumann, R., Brown, R.H., Soderblom, J.M., Soderblom, L.A., Barnes, J.W., Sotin, C., Griffith, C.A., Kirk, R.L., Baines, K.H., Buratti, B.J., Clark, R.N., Lytle, D.M., Nelson, R.M., Nicholson, P.D., 2010. Specular reflection on Titan: Liquids in Kraken Mare. Geophys. Res. Lett. 37 (April), 7104. http://dx.doi.org/10.1029/2009GL042312.
Stofan, E.R. et al., 2007. The lakes of Titan. Nature 445 (January), 61–64.
Tokano, T., 2005. Thermal structure of putative hydrocarbon lakes on Titan. Adv. Space Res. 36, 286–294.
Tokano, T., 2009. Limnological structure of Titan's hydrocarbon lakes and its astrobiological implication. Astrobiology 9 (March), 147–164.
Turtle, E.P., Perry, J.E., Hayes, A.G., Lorenz, R.D., Barnes, J.W., McEwen, A.S., West, R.A., Del Genio, A.D., Barbara, J.M., Lunine, J.I., Schaller, E.L., Ray, T.L., Lopes, R.M.C., Stofan, E.R., 2011a. Rapid and extensive surface changes near Titan's equator: Evidence of April showers. Science 331 (March), 1414–1417.
Turtle, E.P., Perry, J.E., Hayes, A.G., McEwen, A.S., 2011b. Shoreline retreat at Titan's Ontario Lacus and Arrakis Planitia from Cassini Imaging Science Subsystem observations. Icarus 212 (April), 957–959.
Vehkamäki, H., 2006. Classical Nucleation Theory in Multicomponent Systems. Springer, Berlin, Heidelberg.
Vinatier, S., Bézard, B., Nixon, C.A., Mamoutkine, A., Carlson, R.C., Jennings, D.E., Guandique, E.A., Teanby, N.A., Bjoraker, G.L., Michael Flasar, F., Kunde, V.G., 2010. Analysis of Cassini/CIRS limb spectra of Titan acquired during the nominal mission. I. Hydrocarbons, nitriles and CO_2 vertical mixing ratio profiles. Icarus 205 (February), 559–570.
Vuitton, V., Yelle, R.V., Cui, J., 2008. Formation and distribution of benzene on Titan. J. Geophys. Res. (Planets) 113 (May), E05007. http://dx.doi.org/10.1029/2007JE002997.
Wall, S. et al., 2010. Active shoreline of Ontario Lacus, Titan: A morphological study of the lake and its surroundings. Geophys. Res. Lett. 37, L05202.
Ward, C.A., Fang, G., 1999. Expression for predicting liquid evaporation flux: Statistical rate theory approach. Phys. Rev. E 59, 429–440.

Retour à la table des matières : p. v

4.6 Article sur la structure des évaporites

Icarus 270 (2016) 41–56

Contents lists available at ScienceDirect

Icarus

journal homepage: www.journals.elsevier.com/icarus

Structure of Titan's evaporites

D. Cordier [a,b,*], T. Cornet [c], J.W. Barnes [d], S.M. MacKenzie [d], T. Le Bahers [e], D. Nna-Mvondo [f], P. Rannou [a], A.G. Ferreira [g]

[a] Groupe de Spectrométrie Moléculaire et Atmosphérique, UMR 6089 Campus Moulin de la Housse, BP 1039, Université de Reims Champagne-Ardenne, 51687 Reims, France
[b] Université de Franche-Comté, Institut UTINAM, CNRS/INSU, UMR 6213, 25030 Besançon Cedex, France
[c] European Space Agency (ESA), European Space Astronomy Centre (ESAC), P.O. BOX 78, E-28691 Villanueva de la Cañada (Madrid), Spain
[d] Department of Physics, University of Idaho, Engineering-Physics Building, Moscow, ID 83844, USA
[e] Université de Lyon, Université Claude Bernard Lyon 1, ENS Lyon, Laboratoire de Chimie UMR5182, 46 allée d'Italie, 69007 Lyon Cedex 07, France
[f] Laboratoire de Planétologie et Géodynamique LPGNantes, UMR CNRS 6112, 2, rue de la Houssinière, BP 92208, 44322 Nantes Cedex 3, France
[g] Departamento de Engenharia Quimica, Universidade de Coimbra, Coimbra 3030-290, Portugal

ARTICLE INFO

Article history:
Received 31 March 2015
Revised 2 December 2015
Accepted 22 December 2015
Available online 31 December 2015

Keywords:
Satellites, surfaces
Saturn, satellites
Titan, surface

ABSTRACT

Numerous geological features that could be evaporitic in origin have been identified on the surface of Titan. Although they seem to be water–ice poor, their main properties – chemical composition, thickness, stratification – are essentially unknown. In this paper, which follows on a previous one focusing on the surface composition (Cordier, D., Barnes, J.W., Ferreira, A.G. [2013b]. Icarus 226(2),1431–1437), we provide some answers to these questions derived from a new model. This model, based on the up-to-date thermodynamic theory known as "PC-SAFT", has been validated with available laboratory measurements and specifically developed for our purpose. 1-D models confirm the possibility of an acetylene and/or butane enriched central layer of evaporitic deposit. The estimated thickness of this acetylene–butane layer could explain the strong RADAR brightness of the evaporites. The 2-D computations indicate an accumulation of poorly soluble species at the deposit's margin. Among these species, HCN or aerosols similar to tholins could play a dominant role. Our model predicts the existence of chemically trimodal "bathtub rings" which is consistent with what it is observed at the south polar lake Ontario Lacus. This work also provides plausible explanations to the lack of evaporites in the south polar region and to the high radar reflectivity of dry lakebeds.

© 2015 Elsevier Inc. All rights reserved.

1. Introduction

Among many other fascinating features, Titan, the largest satellite of Saturn, hosts lakes and seas (Stofan et al., 2007) likely filled by liquid hydrocarbons containing some amount of dissolved atmospheric nitrogen and various organic compounds (Dubouloz et al., 1989; Cordier et al., 2009, 2013a).

In Cordier et al. (2013b) (hereafter PAP1), the authors only derived a chemical composition for the external surface of Titan's putative evaporites. Butane and acetylene were found to be the most likely main components of these external layers, but this result has several restrictions, the most obvious being the lack of information concerning the spatial structure of the evaporitic deposits. Indeed, in PAP1, neither vertical stratification nor horizontal variations of composition were considered; consequently the model can be labeled "0-D". The 1-D or 2-D models of evaporitic deposition are of interest as the subsequent structure is potentially observable at the margins of these geological units. Moreover, a future lander could drill into these layers and perform detailed analysis or a Titan boat could directly measure dissolved solids with a mass spectrometer (Stofan et al., 2011).

In a laboratory study, Malaska et al. (2012) obtained interesting and illustrative result on the evaporitic crystallization process with exotic materials. After full evaporation of their working fluid (heptane at room temperature in replacement of methane and/or ethane in cryogenic conditions), a "playa" composed of the sequence of the four organic compounds initially dissolved in the

Abbreviations: PC-SAFT, Perturbed-Chain Statistical Associating Fluid Theory; VIMS, Visual and Infrared Mapping Spectrometer; RST, Regular Solution Theory; EoS, equation of state; VLE, vapor–liquid equilibrium; SLE, solid–liquid equilibrium; NIST, National Institute of Standards and Technology; DST, density functional theory; GCM, Global Circulation Model.

* Corresponding author at: Groupe de Spectrométrie Moléculaire et Atmosphérique, UMR 6089 Campus Moulin de la Housse, BP 1039, Université de Reims Champagne-Ardenne, 51687 Reims, France.
E-mail address: daniel.cordier@univ-reims.fr (D. Cordier).

http://dx.doi.org/10.1016/j.icarus.2015.12.034
0019-1035/© 2015 Elsevier Inc. All rights reserved.

Retour à la table des matières : p. v

liquid was left behind. It should be noticed that some species used as analogs in this experimental approach do not follow the expected behavior based on their respective solubilities. This could be explained by the specific conditions of the laboratory simulation. Already in both VIMS[1] and RADAR data, chemical composition gradients appear to surround lakebeds (Barnes et al., 2009, 2011). Barnes et al. (2009) observed several separate *annuli* following the contour of the partially evaporated lake Ontario Lacus at Titan's south pole. Moriconi et al. (2010) tentatively detected organics and nitriles in a ramp along the shore of the same lake, suggesting that sediments and evaporites could coexist around this object. A model of evaporite layer structure may also shed light on the possible cause of the relatively high RADAR reflectivity observed in dry lakebeds. Indeed, as noticed by Barnes et al. (2011), this high reflectivity remains unexplained and could be caused by volume scattering if the evaporite layer is at least several centimeter thick or contains subsurface horizons (see also Section 3.3).

As a first step in PAP1, the Regular Solution Theory (hereafter RST) was employed to mimic the non-ideal effect in cryogenic solutions. Unfortunately, this approach is clearly limited (Cordier et al., 2012). Thus, the model of dissolution has been substantially improved in this work by the use of the Perturbed-Chain Statistical Associating Fluid Theory (hereafter PC-SAFT) equation of state (Gross and Sadowski, 2001) which is widely employed in the chemical engineering community. The PC-SAFT has been successfully introduced to the study of Titan by Tan et al. (2013, 2015) and Luspay-Kuti et al. (2015). Another improvement on the RST approach from PAP1 is the derivation of molar volumes of the relevant molecular solids from the properties of their crystal structure. The influence of the pressure on these volumes is moreover studied using state of the art quantum chemical calculations. We emphasize that the Modified Van Laar (MLV) model developed by Glein and Shock (2013) belongs to the RST family and relies, as does our model, on parameters regressed on empirical data. For the only solid organic considered by Glein and Shock (2013), *i.e.* acetylene, we have used the same experimental measurements, namely those published by Neumann and Mann (1969).

Our paper is organized as follows. In Section 2, we describe our new PC-SAFT based model, and we give details concerning the properties of the different molecular solids involved. We also specify the atmospheric model taken into consideration. Section 3 is devoted to results obtained with our 1-D model: for a given initial state (*i.e.* depth of liquid, assumed composition of solutes and solvents) a possible vertical structure is proposed. The question of the maximum thickness of evaporite deposited is also addressed. Adopting a plausible topography, in Section 4 we compute what could be the species segregation across a lakebed shore. Finally, we discuss our results and conclude in Sections 5 and 6.

2. The model of solutes properties

Although other possible sources are available in the literature, we have chosen to keep the list of studied solutes from the work of Lavvas et al. (2008a,b). This has the advantage of facilitating the comparisons with previous work (PAP1) and limits the potential sources of uncertainties which are inevitably multiplied by introducing more species. However, in the last section of the paper we will discuss the occurrence and the possible role of the compounds not included in our "standard" mixture. Although theoretical models (Lavvas et al., 2008a,b) argue in favor of their presence, we are aware that acetylene has not yet been firmly detected at the surface (Clark et al., 2010; Moriconi et al., 2010) and that butane has not been observed in the atmosphere.

Beside the solvents, considered as a ternary mixture of N_2, CH_4 and C_2H_6, we therefore consider a set of six species, listed in Table 1, which are assumed to be deposited to the surface of Titan or extracted from the "soil" by cryogenic solvents (after being previously produced in the atmosphere). In photochemical models (Lavvas et al., 2008a,b), they reach their temperature of solidification; therefore it can be hypothesized that they form exotic organic snows. Once they fall to the surface of Titan, these six species (*i.e.* HCN, C_4H_{10}, C_2H_2, CH_3CN, CO_2, C_6H_6) either remain in the solid state due to local conditions or will be dissolved in cryogenic solvents. Species that have been detected by observations or produced in photochemical models but are never found at temperatures below their freezing point are not considered as potential lake solutes – this is the case for ethylene. The microphysics of the formation of organic snows is ignored, although it could be the subject of interesting research in the future.

In the next section, we describe the adopted solubility theory and the method employed to get reliable molar volumes for organic solids.

2.1. The model of solubility

Similar to what has been done in PAP1, our solubility estimations are made by solving the equation

$$\ln \Gamma_i X_{i,sat} = -\frac{\Delta H_{i,m}}{RT_{i,m}}\left(\frac{T_{i,m}}{T} - 1\right) \quad (1)$$

where $X_{i,sat}$ is the mole fraction of the compound i at saturation and Γ_i is the activity coefficient of the considered species. $T_{i,m}$ and $\Delta H_{i,m}$ are melting temperature and enthalpy of melting respectively. The temperature of the system is denoted T, and R is the gas constant. This relation can be found, for instance, in the textbook by Poling et al. (2007). The physical meaning of Eq. (1) is that a thermodynamic equilibrium between the considered precipitated solid i and the liquid solution – Eq. (1) is nothing more than an equality of chemical potential. We emphasize that $X_i < X_{i,sat}$ can easily occur for a stable state, while situations where $X_i > X_{i,sat}$ are metastable. Commonly, metastable states are not sustainable: any perturbation ignites crystallization and the corresponding mole fractions are adjusted such as $X_i = X_{i,sat}$. The overabundance of species i is deposited at the bottom of the system. In PAP1 and in Glein and Shock (2013), the limitation of the validity of Eq. (1) is mentioned, an in depth discussion of that aspect will be put forward in the appendix of this paper. Cordier et al. (2012) have shown the flaws of the RST, as have other authors (Glein and Shock, 2013). At its core, the RST is a generalization of a model established for binary mixtures. The main caveat concerning the RST probably lies in its weak physical foundation. In contrast, the equation of state (EoS) called PC-SAFT[2] Gross and Sadowski (2001), which belongs to the vast family of the SAFT EoS, is molecular based. Indeed, PC-SAFT is derived, contrary to the RST, from the statistical physics. Each type of molecule is represented by parameters related to its individual microscopic properties. In that sense, PC-SAFT can be considered more profound than theories belonging to the RST family. Furthermore, PC-SAFT has proved to be one of the most powerful types of EoS for the liquid and vapor states. This theory is the subject of numerous works in the field of thermophysics. Here, the activity coefficient Γ_i that appears in Eq. (1) will be computed with the help of PC-SAFT. For this application to solid–liquid equilibrium (SLE), the activity coefficient is written as the ratio $\Gamma_i = \Phi_i^L/\Phi_i^{L0}$, where Φ_i^L is the fugacity coefficient of the species i and Φ_i^{L0} is the fugacity coefficient of the pure subcooled liquid of the same compound. In the frame of PC-SAFT, molecules are considered as "chains" of segments where each molecule is

[1] Visual and Infrared Mapping Spectrometer.

[2] Perturbed-Chain Statistical Associating Fluid Theory.

Retour à la table des matières : p. v

Table 1
Solids assumed to be dissolved in the lake and some of their properties.

Species	Precipitation rate molecules ($cm^{-2}\ s^{-1}$)	Melting temperature (K)	Enthalpy melting ($kJ\ mol^{-1}$)
HCN	1.3×10^{8}[a]	260.0	8.406
C_4H_{10}	5.4×10^{7}[a]	136.0	4.661
C_2H_2	5.1×10^{7}[a]	192.4	4.105
CH_3CN	4.4×10^{6}[a]	229.3	6.887
CO_2	1.3×10^{6}[a]	216.6	9.020
C_6H_6	1.0×10^{6}[b]	279.1	9.300

[a] Lavvas et al. (2008a,b).
[b] Vuitton et al. (2008).

characterized by its pure-component parameters: the number of segments m, the segment diameter σ (Å) and the segment energy of interaction ϵ/k_B (K). The PC-SAFT is extended to mixtures using the Berthelot–Lorentz combining rule for the dispersive energy, resulting in a single binary parameter k_{ij}. The values of all these parameters are determined by comparison with experimental results. Our implementation of PC-SAFT consists of a set of FORTRAN 2008 object-oriented subroutines written from scratch. Our model has been validated in two ways. We compared its outputs with experimental unitary and binary mixtures data for vapor–liquid equilibrium (hereafter VLE), largely similar to those already used by Tan et al. (2013) with the exception of CH_4–C_2H_6 mixtures (see Luspay-Kuti et al., 2015). We also checked that SLE results were in good agreement with laboratory measurements (similar to the work of Maity (2003)). For instance we verified that we correctly reproduced the data of dissolution of dotriacontane in heptane at varying temperatures (see Fig. 1). Our pure-component parameters are mainly taken from Tan et al. (2013), who used their own optimized adjustments. The NIST database or other sources, like the PC-SAFT original paper by Gross and Sadowski (2001), complete the sample. Concerning CH_3CN, we used the parameters published by Spuhl et al. (2004) and decided to neglect the association terms in the Helmholtz energy since they only provide improvements of the order of a few percent (see for instance Table 7 of Spuhl et al., 2004). This correction remains small compared to the other uncertainties related to the present modeling approach (exact composition of the solvent, influence of the interaction parameter and validity[3] of Eq. (1)). Additionally, solubilities are very sensitive to the value of the interaction parameters k_{ij} which are not known for nitriles relevant to this study (Stevenson et al., 2015b). We did not find m, σ and ϵ/k_B for HCN in the literature. Thus, we determined our own values by fitting the VLE data published by Giauque and Ruehrwein (1939) (see their Table II). Our adjustment is compared to data from Giauque and Ruehrwein (1939) in Fig. 2. All the m, σ, and ϵ/k_B values used in this study are summarized in Table 2. PC-SAFT also needs interaction parameters k_{ij} to account for interspecies molecular interaction, which may not be included in the adopted expression of the Helmholtz energy. In general, these k_{ij} are derived from VLE experimental data and are related to binary mixtures. Table 3 summarizes the interaction parameters adopted here. It should be noted that C_2H_2, CO_2, and C_6H_6 parameters have been derived from laboratory measurements published by Neumann and Mann (1969), Cheung and Zander (1968) and Diez-y-Riega et al. (2014), respectively. The rather good agreement between our own model and experimental data is shown in Fig. 3. Concerning the dissolution of C_6H_6 in ethane, we recognize that the measured value by Malaska and Hodyss (2014) at 94 K disagrees somewhat with those determined by Diez-y-Riega et al. (2014) (see Fig. 3(c)) but we used the measurements derived from Diez-y-Riega et al. (2014) since they

[3] see Appendix A.

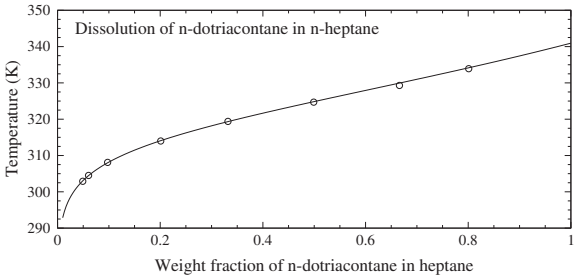

Fig. 1. Open circles: experimental solubility data for n-dotriacontane in n-heptane from Chang et al. (1983). Solid line: our model.

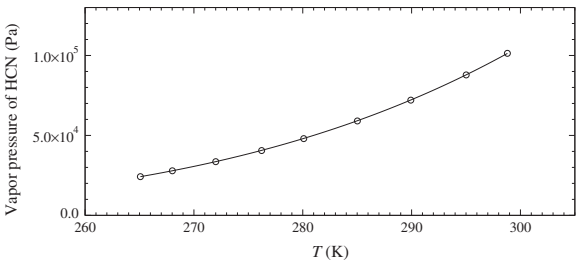

Fig. 2. Open circles: vapor pressure for a VLE of HCN, these experimental data are from Table II of Giauque and Ruehrwein (1939). Solid line: our best fit leading to the PC-SAFT parameters: $m = 2.434$, $\sigma = 3.2929$ Å and $\epsilon/k_B = 248.48$ K.

Table 2
The PC-SAFT pure-component parameters used in this study.

Name	m	σ (Å)	ϵ/k_B (K)	References
CH_4	1.000	3.7039	150.030	NIST, used by Tan et al. (2013)
N_2	1.2414	3.2992	89.2230	NIST, used by Tan et al. (2013)
C_2H_6	1.6114	3.5245	190.9926	NIST, used by Tan et al. (2013)
HCN	2.434	3.2929	248.48	This work
C_4H_{10}	2.6300	3.5100	190.900	Tamouza (2004)
C_2H_2	2.1569	2.9064	168.5506	Din (1962) used by Tan et al. (2013)
CH_3CN	2.2661	3.3587	313.04	Spuhl et al. (2004)
CO_2	2.0729	2.7852	169.210	Gross and Sadowski (2001)
C_6H_6	2.4653	3.6478	287.350	Gross and Sadowski (2001)

Table 3
The PC-SAFT binary interaction parameters k_{ij}. Only interactions between solute molecules and solvent ones have been taken into consideration in our model. By default, in the cases where dissolution data are not present in the literature, k_{ij} have been fixed to zero. For C_6H_6–C_2H_6, the best fit has been derived for a temperature dependent parameter. Solute-to-solute molecule interactions are ignored; this assumption can be considered a relatively safe assumption since solute abundances remains relatively low.

Name	CH_4	N_2	C_2H_6
CH_4	0	0.03 (1)	0.00 (1)
N_2		0	0.06 (2)
C_2H_6			0
HCN	0 (X)	0 (X)	0 (X)
C_4H_{10}	0.022 (4)	0 (X)	0 (X)
C_2H_2	0.115 (3)	0 (X)	0.105 (1)
CH_3CN	0 (X)	0 (X)	0 (X)
CO_2	0.085 (5)	0 (X)	0.13 (5)
C_6H_6	0.037 (4)	0 (X)	$-0.1388 + 15.070 \times 10^{-4} T$ (6)

(1) Tan et al. (2013); (2) this work, by fitting data from Gabis (1991) provided by Glein and Shock (2013); (3) this work, by fitting data from Neumann and Mann (1969) and Gross and Sadowski (2001); (5) this work, by fitting Cheung and Zander (1968) and previously used by Preston and Prausnitz (1970); (6) this work, by fitting data from Diez-y-Riega et al. (2014); (X) set to zero, as dissolution data were not found in the literature.

Retour à la table des matières : p. v

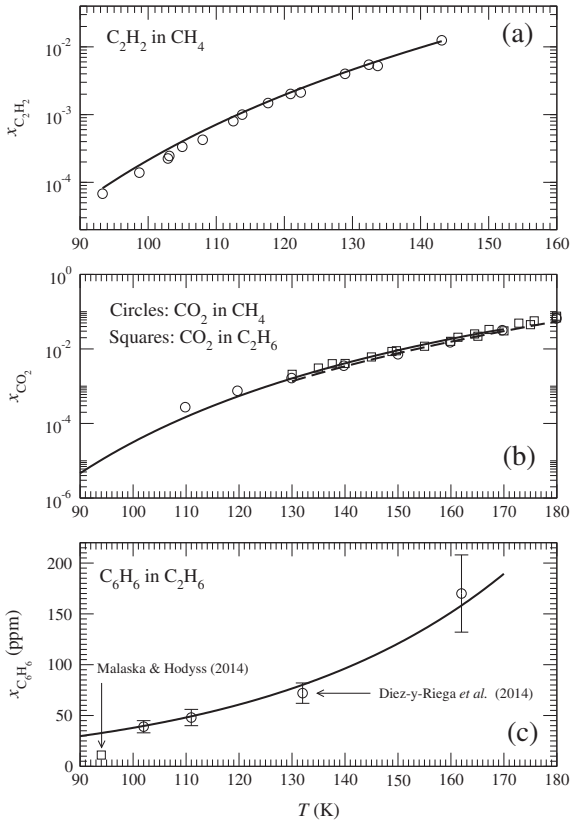

Fig. 3. Comparison between our solubility model and experimental data: the solubility of the considered species in a solvent (CH_4 or C_2H_6) is plotted as a function of temperature. (a) Mole fraction of dissolved acetylene in methane, the observed values have been taken in Neumann and Mann (1969) and the solid line represents our model. (b) The measured mole fraction of CO_2 dissolved in methane (circles) and in ethane (squares). (c) Dissolution of benzene (in ppm) in ethane, experimental data are from Diez-y-Riega et al. (2014) (circles) and Malaska and Hodyss (2014) (the square at 94 K).

were acquired over a temperature range and provide the necessary parameters for our PC-SAFT model. All unavailable interaction parameters have been set to zero.

2.2. The model for the evaporite layers thickness

The above-described model of liquid solutions provides only the number of moles of the various involved compounds that precipitate. Here we aim to estimate the thickness of the deposited layers; for this purpose, we thus need a model for the molar volumes of relevant species.

If during the time step Δt the precipitated quantities of organic matter are Δn_i (in mol), the resulting thickness Δe (in m) of the layer deposited over one square meter is given by $\Delta e = \sum_{i=1}^{N_{sat}} \Delta n_i \times V_{i,m}$. In this equation N_{sat} denotes the number of species that reach saturation during Δt, and $V_{i,m}$ represents the molar volume (in $m^3\ mol^{-1}$) of the solid i. It should be noted that inter-species possible interactions that could induce a deviation from the molar volume additivity and/or the problem of mechanical compaction are neglected. Hence, organic matter is assumed to form monocrystal structures, leaving no empty spaces in the evaporite layer as could be found in a porous medium. In that sense, the thicknesses calculated here are minimum values.

The molar volumes employed here are derived from the lattice parameters of the crystal cells of the organic compounds. For species where different crystal structures were experimentally observed, we chose the one stable at the temperature conditions found at the surface of Titan (*i.e.* 90–95 K). Table 4 brings together the crystal structures used in our model, which were measured at Earth ground atmospheric pressure. In the case where the volumes of the crystal cells were published for different temperatures, we verified that the influence of temperature variations on derived molar volumes is small enough to be ignored in our range of interest. The possible influence of pressure should be weak as the pressure at Titan's surface is ~1.5 bar; we evaluated its influence by means of a quantum chemical calculations along with the density functional theory (DFT). We found in general that the density of organic crystals decreases less than 1% over pressure ranges from 1 bar to 100 bar. C_2H_2, C_6H_6 and C_4H_{10} are exceptions for which the respective decreases were of −1.21%, −4.76% and −8.46%. We therefore conclude, as expected, that pressure variations are minor factors in the context of our work. The adopted molar volumes are listed in Table 5, slight differences between these molar volumes and those published in Cornet et al. (2015) are explained by a tentative correction to account for the temperature influence on the molar volumes in their paper (given at 91.5 K instead of 90 K). In addition, the difference in the mass density of CO_2 between the two studies is due to an error in the molar mass used for conversion to density (reported as $40\ g\ mol^{-1}$ instead of $44\ g\ mol^{-1}$).

3. Evaporite structure: a 1D model

3.1. Evaporite formation scenario

The formation of any evaporite layer requires a sequence of wet and dry periods. During the wet episode, methane and/or ethane rains dissolve the solid organics encountered along their runoff at the ground, and then finally they fill the lacustrine depressions. The subsequent dry period produces the evaporation of the solvents, and thus the formation of evaporites. The resulting vertical distribution of species depends on both the initial composition of the mixture and the individual concentrations at saturation. In this context, the precipitation of solid organics from the atmosphere in the form of exotic snows or hails has been supposed to have either taken place prior to the flowing episode or have happened at the same time as the runoff. However, any solid organic atmospheric precipitation that occurs during the evaporation process would complicate the global picture of the evaporitic layer formation as it would increase the abundances of certain dissolved species. The production of organics at the surface, or even in the satellite interior, cannot be excluded, although clear evidence for such processes are not available. These still speculative phenomena could provide an organic stratum prior to any rainfall.

The sequence of dry-wet periods can span over just a single year if driven by Titan's seasonal effect. Alternatively, the formation of observed putative evaporites observed by Barnes et al. (2011) and MacKenzie et al. (2014) could be the consequence of the climate change over much longer timescales. However, the map of evaporite distribution published by MacKenzie et al. (2014) (see their Fig. 2). is globally consistent with the latitudinal distribution of methane rains obtained by Rannou et al. (2006) (see our Fig. 4). The largest number of deposits is concentrated in polar regions where the highest cumulative rainfall is predicted to occur, whereas the 5-μm-bright material detected by MacKenzie et al. (2014) in the equatorial region (*i.e.* around $\lambda \sim -30°$) is consistent with the low, but non-zero, methane precipitation rates found by

Retour à la table des matières : p. v

Table 4
Cell parameters of the crystal of the different molecular solids, observed to be stable at the temperature range of Titan's surface, 90–95 K. The temperature listed in the fifth column is used to experimentally determine the cell parameters.

Name	a (Å)	b (Å)	c (Å)	β (°)	Ref
HCN	4.13	4.85	4.34	90	Dietrich et al. (1975) and Dulmage and Lipscomb (1951)
C_4H_{10}	4.1463	7.629	8.169	118.656	Refson and Pawley (1986)
C_2H_2	6.198	6.023	5.578	90	McMullan et al. (1992)
CH_3CN	6.05	5.24	7.79	90	Antson et al. (1987)
CO_2	5.624	5.624	5.624	90	Etters and Kuchta (1989) and Simon (1980)
C_6H_6	7.384	9.416	6.757	90	Craven et al. (1993)

Table 5
The densities and derived molar volumes of the crystal structures of the different molecular solids, observed stable in the temperature range 90–95 K.

Name	ρ_{solid} (g cm^{-3})	Molar mass (g mol^{-1})	$V_{i,m}$ (m^3 mol^{-1})
HCN	1.03	27.0253	2.624×10^{-5}
C_4H_{10}	0.851	58.1222	6.830×10^{-5}
C_2H_2	0.831	26.0373	3.133×10^{-5}
CH_3CN	1.10	41.0519	3.732×10^{-5}
CO_2	1.643	44.0095	2.679×10^{-5}
C_6H_6	1.104	78.1118	7.075×10^{-5}

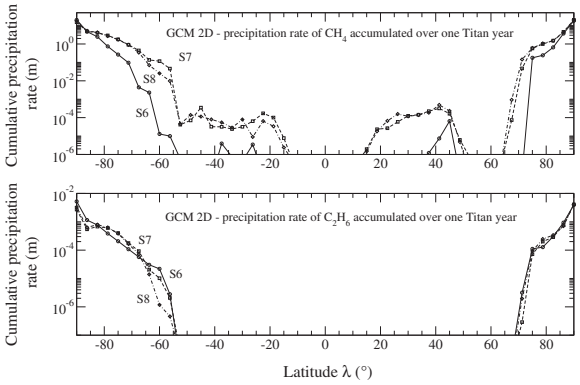

Fig. 4. (a) The cumulative precipitations (in meters) of methane as a function of Titan's latitude, computed by Rannou et al. (2006). (b) The same quantity for ethane. In both cases, labels S6, S7, and S8 correspond to various assumptions concerning the GCM 2D model inputs (*e.g.* thermal inertia and lake fraction at poles).

Rannou et al. (2006) and observational evidence Turtle et al. (2011) and Barnes et al. (2013).

Following Rannou et al.'s numerical simulations, the precipitation rate of CH_4 poleward from $\pm 80°$, ranges between 1 and 20 m per Titan year. In the case of ethane, this rate is much lower with values ranging from 3×10^{-4} to 5×10^{-3} m per Titan year. These numbers yield formation times for a column of liquid methane with a height of 100 m to be between 5 and 100 Titan years. Much longer periods of time are needed for ethane: the accumulation of a column of 100 m of ethane would take 20,000–300,000 Titan years.

However, these timescales of lake replenishment have to be considered as an upper limit because for one particular lake, as on Earth, the liquid catchment area (*i.e.* the drainage basin) is much more extended than the lakebed (*i.e.* the lacustrine depression) itself. For instance, an examination of Fig. 1 of Barnes et al. (2011) allows the reader to see that a collecting area with a surface ten (or even more) times that of the bed is quite common. The larger the surface of the drainage basin is, the shorter the lakebed replenishment time is. With a relatively large drainage basin, a replenishment timescale shorter than one Titan year is plausible.

In this work, we adopt a "standard" initial liquid depth of 100 m which is broadly consistent with the bathymetry of Ligeia Mare derived from altimetry measurements by Mastrogiuseppe et al. (2014). Besides, the computed evaporite layer structures could be easily rescaled to other initial liquid depths by applying a simple rule of proportionality. For example, a lake initially filled only with 10 m would correspond to a final layer tenfold thinner.

In the last decade, the application of GCMs has contributed much to our understanding of Titan's climate history and evolution. However, it is not straightforward, if even possible, to quantitatively compare all published GCM results because assumptions associated with each model differ significantly from one study to another. For instance, the microphysics required to approach realistic precipitation rates have been implemented in only two investigations (Tokano et al., 2001; Rannou et al., 2006); the radiative transfer could be based either on a two-stream model (e.g. GCM by Rannou et al., 2006; Tokano, 2009b) or on a gray atmosphere (e.g. GCM by Mitchell et al., 2011; Schneider et al., 2012); the dimensionality is either 2 or 3; and the methane reservoir could be considered finite or infinite. Most studies focus mainly on the predicted cloud activity, which presents the advantage of applicability to observational constraints. Unfortunately, the reported simulations cannot be taken at face value to derive cumulative methane/ethane precipitation rates. If we look at one of the most recent works, *i.e.* Schneider et al. (2012), and more specifically to their Fig. 1b in which the net evaporation rate $(E - P)$ has been plotted, a succession of wet and dry periods can be clearly seen at Titan's poles. Nevertheless, polar dry periods appear to undergo evaporation rates $(E - P) \sim 0$ mm day^{-1}, whereas slightly positive $(E - P)$'s seem to occur at latitudes around $\pm 30°$. At the first glance, this seems to be in contradiction with the evaporite distribution found by MacKenzie et al. (2014). However, Schneider et al. (2012) hypothesized a total methane content equivalent to 12 m of global liquid methane, and their results are averaged over 25 Titan years, which could erase the temporal fluctuations.

If we accept all the reservations mentioned above, and if we take cumulative methane precipitation rates computed by Rannou et al. (2006), then the existence (at least ephemerally) of local topological depressions filled by several tens of meters deep liquid methane looks plausible. Though the model is substantially different (microphysics is not included and the methane reservoir is finite), results from Schneider et al. (2012) lead to a similar conclusion. Mitri et al. (2007) have proposed estimations of hydrocarbon evaporation rates based on an equation originally published by Fairall et al. (1996). For instance, they found for a pure methane liquid layer an evaporation rate of $\sim 5 \times 10^3$ kg m^{-2} yr^{-1}; a value that yields to $\sim$10 terrestrial years for the complete evaporation of a column of 100 m of liquid methane. This estimation is clearly compatible with the duration of a Titan season (*i.e.* $\sim$7 Earth years) and allows the evaporation of a transient methane lake within that time period. The same authors obtained an evaporation rate of 1.5×10^3 kg m^{-2} yr^{-1} for a mixture of 35% of CH_4, 60% of ethane and 5% of nitrogen, an acceptable range. We note that Tokano (2009a) used the same prescription for his limnological study. Under slightly different conditions (no wind), Luspay-Kuti et al. (2012, 2015) obtained similar evaporation rates between $\sim 0.5 \times 10^{-4}$ and $\sim 2 \times 10^{-4}$ kg m^{-2} s^{-1} (equivalent to 1.58–6.31×10^3 kg m^{-2} yr^{-1}) in experimental simulations, depending on the actual content of ethane. In any case, the evaporation of several tens of meters deep hydrocarbon lake is likely possible within a few Titan months. Hence, the formation of at least a thin layer of evaporite is compatible with what we know about evaporation

Retour à la table des matières : p. v

Table 6
The solubility (in mole fraction) of considered solutes at $T = 90$ K and under 1.5 bar for an ideal solution and with our PC-SAFT based model. The solvent is only composed of either methane or ethane, e_{100} represents the final thickness of evaporites after the evaporation of an initial column of 100 m of liquid. These thicknesses were computed with PC-SAFT model solubilities. The notation $x \times 10^y = x(y)$ is used for conveniency.

Name	Ideal solution	PC-SAFT pure CH_4	PC-SAFT pure C_2H_6	e_{100} (m) pure CH_4	e_{100} (m) pure C_2H_6
HCN	6.46 (−4)	3.52 (−7)	4.64 (−5)	2.59 (−5)	2.65 (−3)
C_4H_{10}	1.26 (−1)	1.67 (−3)	9.14 (−2)	3.20 (−1)	13.6
C_2H_2	5.40 (−2)	4.84 (−5)	5.21 (−4)	4.26 (−3)	3.56 (−2)
CH_3CN	3.73 (−3)	4.27 (−8)	1.87 (−5)	4.47 (−6)	1.55 (−3)
CO_2	8.72 (−4)	2.45 (−6)	4.37 (−6)	1.84 (−4)	2.55 (−4)
C_6H_6	2.20 (−4)	7.20 (−9)	2.97 (−5)	1.43 (−6)	4.58 (−3)
Total thickness	(m)			0.324	13.65

rates, and it is plausible that the formation of the evaporites observed by Cassini have occured during the Titan's past. Some authors consider alternative mechanisms for the formation of features that are classified as "evaporites", which we discuss in more detail in Section 5.

Our model, based on PC-SAFT, has been mainly validated using data from solid organic dissolution where the solvent (methane or ethane) comprised the major components. However, our model has not been formally validated for very high concentration of solutes, *i.e.* for circumstances where the sum of their mole fractions is larger than ∼50%. We have then chosen to stop the evaporation algorithm when $\sum_{k(\text{solutes})} x_k > 0.5$. In practice, this criterion has been satisfied at the very end of the evaporation, *i.e.* when the ratio of the remaining volume and of the initial volume was approximately between 10^{-4} and 10^{-8}, depending on the particular composition adopted at the starting time. In fact, along the evaporation process the mole fraction of the solvent is nearly constant. Roughly, when a number of moles Δn are removed from the solvent by evaporation, a similar amount Δn of organics saturate and settled to the lakebed.

At the very end of the evaporation (*i.e.* during the last timestep), the remaining liquid is assumed to evaporate, and the total amount of still-dissolved compounds are deposited on the lakebed. In our model, when this evaporite final layer is composed of several species, they are assumed to be perfectly mixed.

3.2. The maximum thickness of evaporite: a first approach

Solution theory enables our model to estimate the allowed maximum thickness. For a given volume of liquid, the concentration at saturation of the considered compound gives the maximum quantity of matter that can be dissolved. Then, if we assume that all evaporite components are initially present in the solution at their saturation abundances, then the algorithm implemented in our model provides the thickness of the corresponding deposition. Table 6 shows the resulting depths, denoted e_{100}, corresponding to an initial height of solvent of 100 m. Unsurprisingly, ethane leads to greater final thicknesses because this molecule is a much better solvent than methane for the expected hydrocarbon solutes available to a Titan lake system. The resulting total thickness are respectively 0.324 and 13.65 m, for CH_4 and C_2H_6. The question remains, however, how easy it is to meet the conditions for the simultaneous saturations of all species. In other words, is the atmospheric photochemistry able to provide large enough quantities of organics to allow saturation in the lakes?

In Table 8, we estimated the dimensions of the catchment basins required to dissolve enough solid organics for the lake to reach saturation, for each investigated solute produced at the rates computed by Lavvas et al. (2008a,b) and accumulated during one Titan year. In this scenario, solid organics fall from the atmosphere (in the form of snows or hail) and would be washed into the lake with rainfall runoff flowing to the local topographic minimum, the lake. For idealized disk-shaped basins, we list the dimensions as a function of lake radius in Table 8 for either CH_4 or C_2H_6 playing the role of solvent. Different liquid depths H of the central are also considered. The lake itself is supposed to cover an area of 1 m^2. The computed radii correspond then to the catchment basin size required to get the saturation in a volume of $H \times 1$ (m^3) of liquid hydrocarbons.

HCN and C_4H_{10}, the solutes with respectively the smallest and largest mole fractions at saturation, need the smallest and the largest collecting area according to PC-SAFT calculation (see Table 6). More interestingly, these calculations indicate that butane is so soluble that reaching saturation requires an unreasonably large basin. In the most favorable case where methane is the solvent, for a diameter of ∼20 km (typical of some northern lakes (see Fig. 1 of Barnes et al., 2011)), and the initial depth fixed to 1 m, the drainage basin for butane must have a radius larger than the radius of Titan itself. In contrast, the saturation concentration of HCN is reached in a similar lake when this compound is drained over an area with a radius around 26 km while the assumed lake has a radius of 10 km.

Given the numbers reported in Table 8, we can safely conclude that all of the solutes considered in this study cannot be simultaneously at saturation in the initial state (*i.e.* before a significant evaporation episode) for a given lake. In addition, if the fraction of surface covered by evaporite in polar regions can be as high as ∼10% (see for instance Fig. 3 of MacKenzie et al., 2014), the average catchment area can only have a radius of 1.78 m for a central lake of 1 m^2 (a disk with a radius of 1.78 m has an area of ∼10 m^2). This value is lower than the majority of radii given in Table 8, indicating the improbability of lakes being saturated in their initial state. Thus we can firmly state that the thicknesses mentioned above, 0.324 and 13.65 m, are largely an overestimate if we impose a timescale of one Titan year. However, in Section 3.3, we will discuss a mechanism for repeated dissolution–evaporation–deposition that could overcome these limitations.

3.3. The possible 1D structure of evaporites

The structures of evaporitic deposit left at a lakebed after the entire evaporation of an assumed 100 m-high column of liquid have been computed. The results shown in Fig. 5 can be rescaled for any other initial liquid height. Two solvents have been employed: pure methane and pure ethane. In panel (a) of Fig. 5 the initial mixtures of dissolved organics are set by fixing the concentration of the most abundant species (*i.e.* HCN) to its value at saturation (*i.e.* 3.52×10^{-9}, see Table 6) while the abundances of other compounds are derived by scaling to the atmospheric production rates; the result is the "type A" mixture in Table 7. As a consequence, the initial total mole fraction of solutes reaches only

Retour à la table des matières : p. v

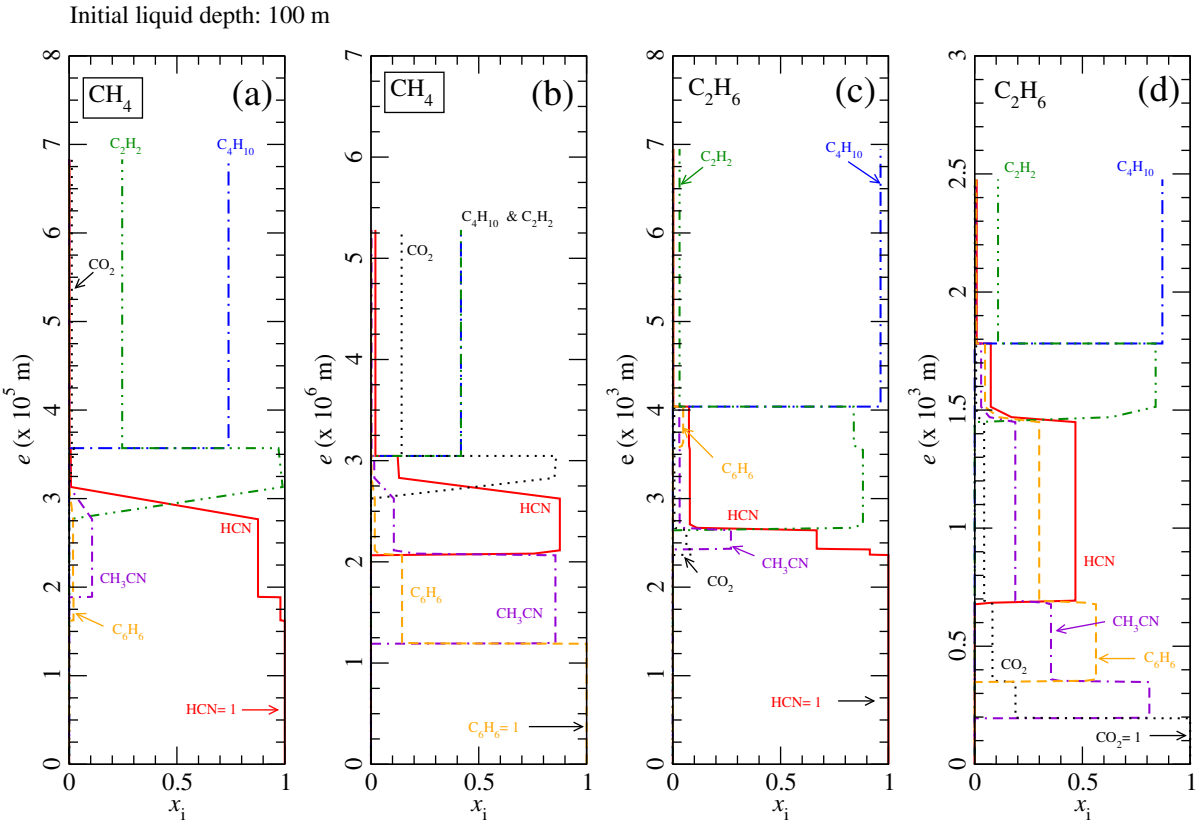

Fig. 5. 1D structure of evaporite layers, computed from an initial liquid depth of 100 m. The *y*-axis represents the height *e* of the resulting deposit over the non-soluble substrate. The *x*-axis shows the mole fractions x_i of the differing species at a given height. Two solvents are considered: methane (panels (a) and (b)), and ethane (panels (c) and (d)). In simulations reported in panels (a) and (c), the assumed initial mixture of solutes has a mole fraction of HCN (the most abundant species in atmospheric precipitation) set to its value at saturation in the considered solvent, and other concentration are derived by a scaling to atmospheric production rates. The results plotted in panels (b) and (d), have been obtained by adopting uniform solute concentrations, fixed to the lowest mole fraction at saturation.

Table 7
The initial mixtures of solutes taken into account. The entire set of compositions is divided into four types. Types A and B are used with a methane rich solvent whereas types C and D correspond to when ethane is the dominant solvent component. All abundances are expressed in mole fraction of the initial solution.

Species	Type A	Type B	Type C	Type D
HCN	3.519×10^{-7}	7.199×10^{-9}	4.635×10^{-5}	4.370×10^{-6}
C_4H_{10}	1.462×10^{-7}	7.199×10^{-9}	1.925×10^{-5}	4.370×10^{-6}
C_2H_2	1.381×10^{-7}	7.199×10^{-9}	1.818×10^{-5}	4.370×10^{-6}
CH_3CN	1.191×10^{-8}	7.199×10^{-9}	1.569×10^{-6}	4.370×10^{-6}
CO_2	3.519×10^{-9}	7.199×10^{-9}	4.635×10^{-7}	4.370×10^{-6}
C_6H_6	2.707×10^{-9}	7.199×10^{-9}	3.565×10^{-7}	4.370×10^{-6}

Table 8
Radius (in m) of possible idealized "catchment basins" of solid organics required to ensure the saturation of a given species in a column of solvent (CH_4 or C_2H_6) which height is *H*, and with a cross-section of 1 m^2 (corresponding to a disk with a radius of 0.56 m). All the computations were performed assuming an atmospheric precipitation timespan of one Titan year.

Name	CH_4 $H = 100$ m	CH_4 $H = 10$ m	CH_4 $H = 1$ m	C_2H_6 $H = 10$ m
HCN	15.18	4.799	1.518	48.41
C_4H_{10}	1621	512.5	162.06	3334
C_2H_2	284.2	89.88	28.42	259.0
CH_3CN	28.72	9.081	2.872	167.1
CO_2	400.2	126.5	40.02	148.7
C_6H_6	24.75	7.826	2.475	441.9

6.54×10^{-7}, a value that can be converted to a deposit thickness of a few tens of micrometers (6.83×10^{-5} m).

As already emphasized in PAP1, the most soluble species, *i.e.* C_4H_{10} and C_2H_2, remain dissolved until the very end of the evaporation process. Thus, these species dominate the final, top layer of the deposit. We noticed that the last droplet of solution to be evaporated contains the entire amount of dissolved C_4H_{10} and C_2H_2, around 50% of the volume of dissolved material. This is due to the small total amount of solute and the high solubilities of C_4H_{10} and C_2H_2 and explains the final vertical parts of the curves in the top of Fig. 5(a). Alternatively, the least soluble compounds (dominantly, for this mixture, HCN) are buried below the C_4H_{10}- and C_2H_2-enriched top layer.

The treatment of the "last droplet to be evaporated" is worth special attention. Indeed, our model has not been validated in situations where the solvent becomes a minor species of the "solution". Thus, we have simply adopted a principle of a well-mixed last layer, which is reflected in the top vertical parts of curves in Fig. 5(a) (and other panels). We therefore ignore possible segregation effects (presently unknown) that could occur during the late stages of evaporation. However, we are aware that different species can precipitate under different crystallographic phases leading

Retour à la table des matières : p. v

to an inhomogeneous mixture. This aspect will be the subject of a point of discussion further on in the paper.

Although the "type A" mixture is more realistic, we also use an uniform initial distribution of solutes ("type B" mixture displayed in Table 7). With this mixture, we eliminate the effect of the initial mixing ratios on the evaporite structure. HCN is no longer the solely dominant buried species; CH_3CN and C_6H_6 play a prominent role in this scenario. While butane and acetylene are still the major compounds of the external layer, carbon dioxide appears to reach abundances around 14%.

We also examine pure ethane as the solvent in the "type C" and "type D" mixtures of Table 7. Mixture "C" has an initial mixture corresponding to the most abundant species in precipitation (*i.e.* HCN) taken at its saturation. The initial solution for mixture "D" is similar to "type B" in that the uniform initial mole fractions are used: 4.37×10^{-6}, the lowest concentration at saturation of our set of solutes, *i.e.* that of CO_2. The results for these mixtures are displayed in Fig. 5(c) and (d), respectively, where the scale factor attached to the *y*-axis is 10^{-3}, meaning a depth of the order of a few millimeters. Solutions with methane (types "A" and "B") produce only micron-deep layers.

In the case where initial abundances are scaled to respective precipitation rates ("type C", Fig. 5(c)), the structure can be generally described as a layer of less solubles compounds (*i.e.* the nitriles CH_3CN and HCN) topped by a layer of butane. Comparison to Fig. 5 (a) shows unambiguously that the ethane-based mixture favors butane while the methane-based mixture favors acetylene in the surface layer. When uniform initial fractions are assumed (see mixture "type D" in Table 7), butane remains the most abundant species at the surface but leaves some space for C_2H_2. Not surprisingly, the interior structure is more complex with a non-negligible role of carbon dioxide and benzene.

If we focus on the external layer, these computations employing our new model based on PC-SAFT confirm the tendencies found in PAP1. However, we find here that the total thickness of the deposits is on the order of a few microns for a methane-rich solvent and a several millimeters for an ethane-rich solvent. In addition, when initial abundances of solutes are scaled to precipitation rates for either solvent, HCN seems to be the dominant buried species.

In order to assess the possible influence of dissolved N_2, we introduce an amount of nitrogen fixed at 10% of the current quantity of either CH_4 or C_2H_6. This mixing ratio seems realistic according to the current literature (Cordier et al., 2009, 2013a; Glein and Shock, 2013; Tan et al., 2013; Luspay-Kuti et al., 2015). Our results do not significantly differ with the inclusion of N_2 in the four mixture types. For instance, the resulting sequence of a 1D model of evaporites deposit structure remains essentially unchanged when the fraction of N_2 in the solvent (mainly composed by CH_4) is increased from 0.00 to 0.20. The most important change is a decrease of ~15% of the abundance of C_2H_2 in the top layer while an increase of the C_4H_{10} mole fraction of ~7% is found. This general low sensitivity to dissolved nitrogen abundances is not a surprise because the PC-SAFT interaction parameters k_{ij} between N_2 and the introduced solvent were set to zero due to the lack of relevant data. We emphasize, nevertheless, that except in the case of very strong interaction between these species, the role of N_2 should be of small importance, due to its relatively small abundance in the solutions.

Up to this point, all the simulated deposits were implicitly formed over an insoluble substrate. This approach is particularly relevant if this substrate is made of water ice and/or long chain hydrocarbons. Nevertheless, one can well imagine lakebeds successively flooding and drying year after year. If the atmospheric products are still the same in nature and quantities from one year to the next, we can expect an accumulation of evaporite at the bottom of these lakebeds. Additionally, liquid flowing into the system can re-dissolve, at least partially, the strata formed in previous cycles. We represent the end-member scenario where liquid runoff does not dissolve previously-formed evaporite layers in panels (a), (b) and (c) in Fig. 6, which could happen if the liquid runoff is too fast over the deposits. However, for liquid entering the system that is in contact with the deposits long enough to dissolve the evaporite (experiments by Malaska and Hodyss, 2014, give credence to this assumption), panels (d), (e) and (f) depict the evolution of evaporite layers. Around ~50% of the top layer formed during the previous year is brought into solution. As shown above, the most soluble species build the external layer of evaporite (deposited during some previous epochs). They are then the first "re-dissolved" material such that the current liquid solution becomes more enriched in the most soluble compounds. This leads to a secondary surface layer over-enriched in butane and/or acetylene (see panel (e) in Fig. 6). This process can be repeated from year to year, yielding to a very thick layer of the most soluble species (Fig. 6(f)), though the process might be limited by the saturation points of the solutes and the quantity of solvent running off.

Alternatively, if a much larger quantity of material is dissolved, for instance if all the deposited organics during the past year are redissolved, then, the new layers deposited in the next evaporation event are much thicker. In all cases, the dissolution of the previously formed layer increases the thickness of the external layers. This effect, however, is limited by the concentration at saturation and the average annual precipitation of liquid methane/ethane.

Regardless of the initial composition scenario, the surface layer of evaporite could be composed by a mixture of butane and acetylene. In addition, this top layer appears to be relatively thick compared to the depth of the whole deposit. With multi-annual repetition of the dissolution–evaporation process, the top butane–acetylene rich layer tends to grow in thickness. In Fig. 5, the uniform mole fractions of C_2H_2 and C_4H_{10} are only relevant on average. Indeed, it is extremely likely that these two species precipitate separately, each one in its own crystallographic phase. An homogeneous phase of C_2H_2–C_4H_{10} would imply the existence of something resembling an acetylene–butane "co-crystal" yet unknown but similar to what has been observed by Vu et al. (2014) for ethane and benzene. In addition, even if this kind of system exists, a perfectly homogeneous layer would require relative abundances of C_2H_2 and C_4H_{10} in agreement with the allowed stoichiometry of the "co-crystal". Thus, if butane and acetylene are present, the existence of a biphasic system seems more likely, and the structure of the top layer of evaporite could be similar to that depicted in Fig. 7, although the scales of heterogeneities are unknown.

The pebbles observed at *Huygens* landing site were probably formed by mechanical erosion and required relatively powerful liquid currents to flow in Titan's rivers (Tomasko et al., 2005). In contrast, evaporation in small lakes and ponds is a more gentle process but would also leave some irregularities like pebbles, evaporitic polygonal crusts, macroscopic crystals, that could produce high radar brightness as it has been also speculated in the case of channels observed by the Cassini RADAR (Le Gall et al., 2010). Indeed, on Earth, Devil's Golf Course (Death Valley, California) or Lucero Lake (White Sands National Monument, New Mexico) offer examples of evaporitic formations that show a several tenths of centimeters in size rugosity. Although these structures were largely due to erosion, there is no reason to ensure that this situation does not occur on Titan. Hence, the RADAR brightness of evaporites (see Barnes et al., 2011, Section 3) could be explained by processes occurring during either the lacustrine basin formation or the formation of evaporite deposits.

Unfortunately, we did not find frequency-dependent permittivity for solid butane and acetylene in the literature. However, since

Retour à la table des matières : p. v

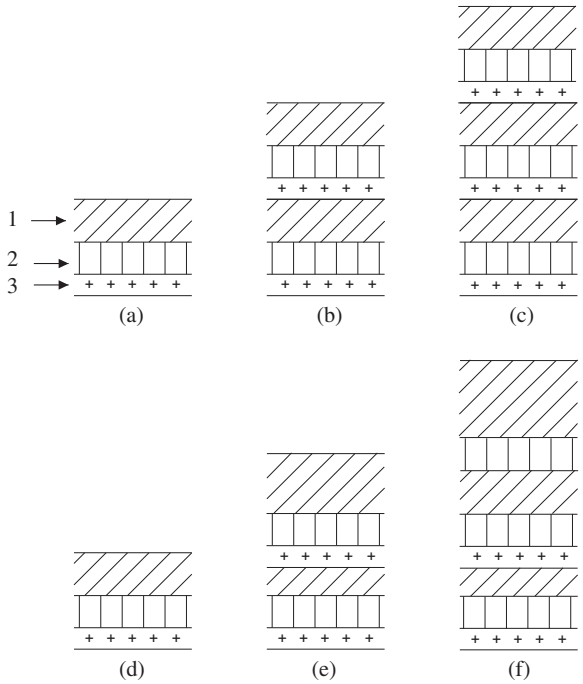

Fig. 6. Sketches of two scenarios of evaporites formation: three species (labeled 1, 2 and 3) are assumed for the sake of clarity. Both rows illustrate the evolution of a lakebed's evaporite layers over a period of three drying and evaporating cycles. The series (a), (b), and (c) corresponds to the accumulation of layers without any dissolution of the substrates deposited during the past years. At the bottom, the series (d), (e) and (f) presents schematically the evolution of evaporite layers if redissolution of previously laid-down layers is allowed to occur (in this example, between (e) and (f) only the two previous external layers were redissolved).

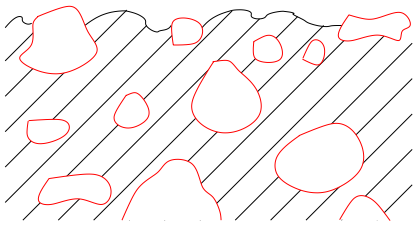

Fig. 7. Scheme of the plausible top layer structure of Titan's evaporite. The hatched area corresponds to a matrix made of the most abundant compound (forming a first macroscopic crystallographic phase), blank zones are composed by the less abundant, this corresponds to a second macroscopic phase. These heterogeneities have an effect on RADAR backscatter only if their scale is at least comparable to RADAR wavelength.

C_2H_2 and C_4H_{10} are both non-polar molecules, their polarizability provides the main contribution to the permittivity of their solid forms. We obtained the static permittivity $\epsilon_{r,0}$ at 195 K for both species ($\epsilon_{r,0}(C_4H_{10}) = 1.942$ and $\epsilon_{r,0}(C_2H_2) = 2.4841$) from *Handbook* (Lide, 1974). The difference in these values suggests substantially different permittivities in the microwave domain of the Cassini RADAR. We have shown that the thickness of evaporite can be as large as several tens of centimeters or even several meters, much larger than the wavelength of the Cassini RADAR (*i.e.* 2.18 cm) and therefore potentially affecting the RADAR signal. The observed RADAR brightness can be also caused by a layering but probably more likely by heterogeneities as depicted in Fig. 7.

In summary, the RADAR brightness at the evaporite (Barnes et al., 2011), if not produced by centimeter-sized surface roughness, could be also caused by heterogeneities within the top layer produced by the existence of at least two crystallographic phases. The subsurface horizons generated by stratification of evaporite (see Fig. 5) could also contribute to the effect, but the formation of plane interfaces between layers could be more difficult.

4. Evaporite deposits structure: a 2D model

Barnes et al. (2009, 2011) and MacKenzie et al. (2014) observed evaporite deposits along the periphery of lakebeds. The signal at 5 μm shows a gradient that could be explained by changes in chemical composition and/or thickness of the deposited organic material. On Earth, the combination of drought and increased water demand has produced significant drops in water levels of the well-known reservoirs Lake Mead and lake Powell. Consequently, "bathtub rings" have appeared along the shores of these lakes. These structures, mainly made of calcium carbonate, are observable in pictures taken from space (see for instance Barnes et al., 2009, Fig. 7). Similarly-formed "bathtub rings" around lakes on Titan are probably more complex due to the variety and different properties of the organic compounds involved. Consequently, these particular formations could be unique through the Solar System. Thus, a better understanding of evaporite formation is desirable.

For the sake of simplicity, we have adopted axisymmetric topography, as sketched out in Fig. 8. The bottom of the lakebed is represented by a disk-shaped flat terrain of radius R_1. This zone is surrounded by sloping ground that extends between the radii R_1 and $R_2 > R_1$. The value R_2 corresponds to the area covered by a volume with initial liquid depth H_0. Mastrogiuseppe et al. (2014) have performed bathymetric measurements along a RADAR track acquired during a nadir-looking altimetry flyby above Ligeia Mare. This sea is much larger than the class of lakes we are interested in. We note, however, that the shallow slope of the seabed revealed by the global bathymetric profile (see Fig. 4 of Mastrogiuseppe et al., 2014) generally agrees with the slope scheme we adopt here. Moreover, our results do not depend on the precise slope but rather on the exact shape of the shore terrain. In our baseline scenario, continuous evaporation removes liquid from the system while solid compounds are deposited in the bed. Parts of the lakebed deposits that are no longer immersed maintain their structure and composition until the end of the process. It is implicitly assumed that the kinetics of both precipitation and sedimentation are much faster than the kinetics of evaporation. Parts of the lakebed that are still submerged get covered by a growing layer of solid organics that stratifies gradually.

The properties and global characteristics of liquids mixing in Titan's lakes remain relatively unknown. Different physical processes can contribute to this mixing: vertical convection (Tokano, 2009a), tidal effects or global circulation (Tokano et al., 2014). In our approach, we chose to ignore the possible details of this mixing and instead consider two extreme cases: (1) only an efficient vertical mixing occurs and (2) a combined horizontal–vertical mixing scheme that ensures chemical homogeneity of the entire lake (see Fig. 8).

In case (1), the whole quantity of dissolved solutes contained in the initial column of liquid above a given point of the lake is precipitated on the bed following the behavior reported in our 1D model study (see Section 3). In such a case, the resulting composition of the evaporite deposition will show an uniform surface composition: only the depth will vary from one point to another. Locally the thickness of evaporite layers scales to the initial height of the local liquid column. No bathtub ring structures are expected

Retour à la table des matières : p. v

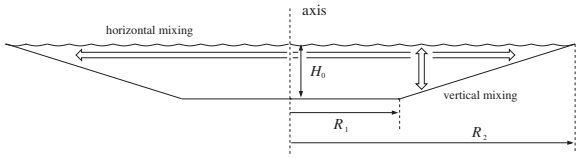

Fig. 8. Schematic cross-section of our idealized lakebed. We denote H_0 the initial liquid depth, R_1 and R_2 are defined in the text.

in case (1). Thus, observations of a Titan lakebed lacking evaporite rings could be understood as the mark of a weakly efficient horizontal mixing in the lake and/or evidence for an unsaturated solution.

In case (2), the time-dependent compositions and thickness of the deposits are easily computed by fixing the sizes of the lake to typical values, *i.e.* $R_1 = 15$ km, $R_2 = 30$ km (see for instance Fig. 1 panel C of Barnes et al., 2011) and an initial depth of $H_0 = 600$ m. This implies a shore slope of $\sim 2.3°$, similar to those reported in Table 9. The computation algorithm is divided in two main steps. First, for the corresponding total volume $V_{tot} = \pi H_0(R_1^2 + R_2^2 + R_1R_2)/3$, our thermodynamic model is employed to estimate the quantities of precipitated matter during each time step. The resulting outputs are then applied to the chosen particular geometry such that at each timestep, the total amount of over-saturated species is uniformly distributed over the immersed part of the bed. These operations are repeated until the solvent is exhausted.

The results are summarized in Fig. 9. The mixture types used for the 1D model are also used here. The solvents are pure methane (Fig. 9 panels (a) and (b)) and pure ethane (Fig. 9 panels (c) and (d)). For each solvent, two initial solutes compositions are considered: either the abundances are scaled to atmospheric precipitation rates (Fig. 9 panels (a) and (c)), or the initial mole fractions are all fixed to the smallest saturation value (Fig. 9 panels (b) and (d)). Unsurprisingly, the surface of the central part of the evaporite deposits, *i.e.* that which covers the flat bottom of the basin, has a composition dominated by butane and acetylene. This behavior is explained, as in the 1D results, by the large solubilities of these two species, which are thus able to remain dissolved until the very late stages of the liquid evaporation. During this last episode, the liquid stagnates above the bed bottom and the species, that are still dissolved, finally precipitate out. Clearly, this composition is consistent with the abundances of the top layers exhibited by the 1D model (see Fig. 5), although a slight difference is evident in the ethane solvent (Fig. 5(c)) where an almost pure butane region is surrounded by an acetylene rich crown.

The most external parts of the lacustrine basin are covered by a surface made of solid HCN when the solutes initial abundances are scaled to the atmospheric precipitation composition (see Fig. 9 panels (a) and (c)). In this scenario, the most plausible for an average lake, hydrogen cyanide is the most abundant dissolved compound though it is very poorly soluble. When the initial composition of solutes is uniform (Fig. 9 panels (b) and (d)), an external ring is made of either benzene (when CH_4 is the solvent, Fig. 9(b)) or carbon dioxide (when C_2H_6 is the solvent, Fig. 9(d)). These results indicate that the occurrence of an external HCN-rich ring would likely be caused by large initial content of the solution rather than a pure solubility effect. We emphasize that although HCN is clearly detected in the atmosphere (see for instance Vinatier et al., 2010; de Kok et al., 2014), its solubility in cryogenic solvents remains not well known, and values provided in this work are less reliable than those concerning other species, especially when the model outputs are compared to experimental works (see Section 2.1). Laboratory experiments are needed in order to determine the interaction parameters k_{ij}s related to HCN.

Table 9
Lake shore slopes derived from data published by Hayes et al. (2008) (Fig. 3, panel c). In this paper, the positions of the lakes are indicated by their respective abscissa along the RADAR track, *i.e.* "shore 1" is the one first crossed by the track. The central part of the "lake 1" bed has not been taken into consideration because of the lack of data. "Lake 1" and "lake 2" correspond respectively to features around ∼140 and ∼320 km along RADAR track in Fig. 3 of Hayes et al. (2008).

Object	Shore 1 Slope (in degrees)	Central region of the bed (in degrees)	Shore 2 Slope (in degrees)
Lake 1	1.812	–	1.773
Lake 2	4.445	0.420	3.180

Finally, between the outer portion (*i.e.* $r \gtrsim 22$ km) and the central area (*i.e.* $r \lesssim 15$ km) there lies a transitional zone that exhibits a chemically complex surface. Whatever the initial assumed composition, the resulting surface composition of evaporites appears to be "trimodal": a C_4H_{10}–C_2H_2 central region is bordered by a chemically complex narrow ring which is itself surrounded by an extended region where HCN is the dominant species (if the adopted atmospheric precipitations are representative of the actual weather conditions in Titan's troposphere). These conditions could either bring solutes to the lake directly from atmospheric fallout or wash the surrounding terrains and dissolve pre-existent solids that could cover these areas.

We underline that this chemically "trimodal" surface composition does not depend on the actual slope of the lacustrine basin shore. Indeed, a shore with a more gentle slope will be covered by thinner depositions, but will show more extended "bathtub rings", the aspect ratio being preserved. Narrower rings will be caused by steeper shores, again maintaining the aspect ratio. In terms of deposit thickness, low slopes correspond to shallow evaporite layers, whereas steep shores will exhibit thick strata.

The spectroscopic observation of all species involved in this study, is beyond the capabilities of an instrument like VIMS. However, the predicted "trimodal" surface composition of evaporite layers could be tentatively detected by VIMS if the spatial resolution is high enough (for instance $\lesssim 5$ km/pixel). The data spanning Ontario Lacus' evaporite-covered shorelines, analyzed by Barnes et al. (2009), have a high spatial resolution, as good as 330 m/pixel. These coastal features seem to be "bimodal" with two distinct zones (see Barnes et al., 2009, Fig. 4). After excluding several hypotheses (freezing, continental shelf, etc.), Barnes et al. (2009) proposed that the inner ring could be an intertidal zone showing exposed lake-bottom sediments. The external ring appears to have a low water–ice content, leading Barnes et al. (2009) to propose that it consists of fine-grained condensate, resulting of the evaporation of the liquid. These observations are consistent with our "trimodal" evaporation deposition. Indeed, in the case of Ontario Lacus, the liquid could still contain a large amount of solutes since it seems to be rich in ethane (Brown et al., 2008; Luspay-Kuti et al., 2015), a much more efficient solvent than methane. In our simulations, the central part of the deposit (see Fig. 9) is built up during the last stages of the evaporation, when butane and/or acetylene crystallize. Hence, the distinct two zones observed by Barnes et al. (2009) could correspond to two chemically different evaporite deposits: "unit 3" (the most external in Barnes et al. denomination) is perhaps composed of HCN while "unit 2" could be a "chemically complex" deposit. This interpretation is not mutually exclusive with that of an intertidal zone.

Also using VIMS data, Moriconi et al. (2010) have tentatively detected organic species within the rings observed around Ontario Lacus. They used the Spectral Angle Mapper technique to compare pixel spectra to the reference spectra of compounds of interest (C_2H_6, CH_4, C_4H_{10}, HCN, C_3H_8, C_2H_2 and C_6H_6). However, the definitive identification of surface compounds on Titan remains a matter of debate given the few opportunities left to see the surface with a

Retour à la table des matières : p. v

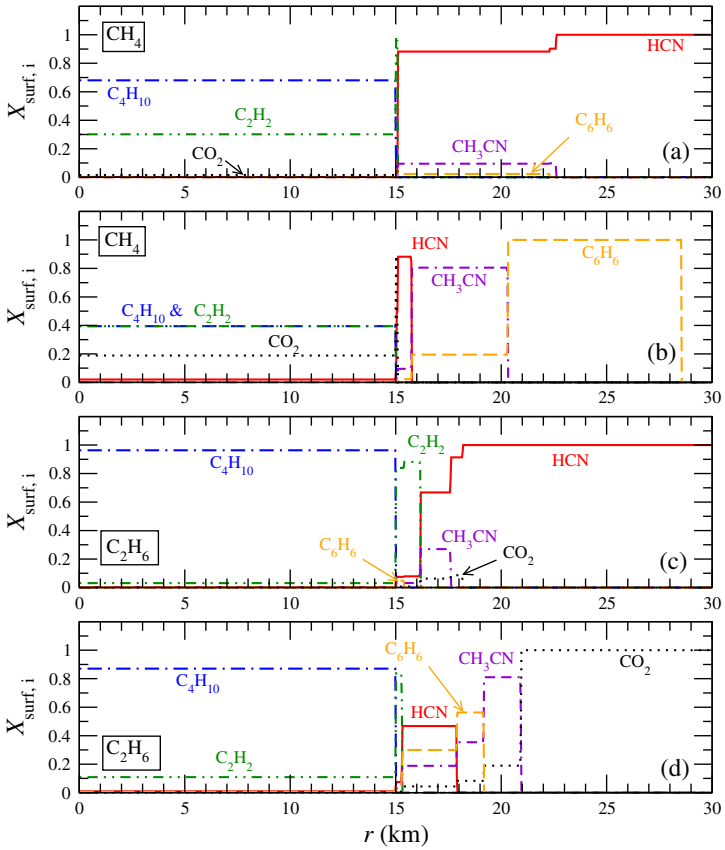

Fig. 9. Surface composition (in mole fraction) of a model lakebed with topography depicted in Fig. 8. The initial mixtures are those adopted for simulations reported in Fig. 5, *i.e.* in panels (a) and (b) the solvent is pure CH_4 while in panels (c) and (d) it is ethane. Two solute compositions are considered: the initial abundances are scaled to atmospheric precipitation rates (with HCN initially at saturation), corresponding to panels (a) and (c), and uniform abundances, as in panels (b) and (d). In order to be consistent with Fig. 5, species are represented by the same line style. The radius r represents the distance to the axis of the modeled lake basin.

reduced atmospheric contribution and an increased Signal-to-Noise Ratio with VIMS.

Nonetheless, the infrared data analyzed by Moriconi et al. (2010) appear to be compatible with the presence of C_4H_{10}, C_2H_2 and HCN within the area called "the ridge" by the authors (equivalent to unit 3 of the study of Barnes et al., 2009). The possible detection of species in liquid state under Titan's ground conditions, *i.e.* C_2H_6, CH_4 and C_3H_8, can be explained by either sediments still soaked in the corresponding liquid or an altimetric profile not as simple as that depicted in Fig. 8. Indeed, citing Lorenz et al. (2009); Moriconi et al. (2010) noted that the "ridge" could have a non-uniform elevation (see also Fig. 6 in Cornet et al., 2012). A lake shore altimetric profile with a changing slope could lead to a solid crystallization sequence within sporadic pools that could exist in the zone.

Globally, the findings of Moriconi et al. (2010) are in agreements with our predictions where C_4H_{10}, C_2H_2 and HCN appears to be the most abundant species at evaporites surface. Fig. 9 shows that C_6H_6 has a very discrete presence in scenarios where the initial compositions are scaled to atmospheric abundances (panels (a) and (c) in Fig. 9). Therefore, the non-detection of benzene can be interpreted as evidence that the composition of the atmospheric precipitation is similar to that computed by Lavvas et al. (2008a,b), as proposed in the interpretation of Moriconi et al. (2010). However, in their surface mapping of a 5.05-μm spectral feature on Titan's surface, Clark et al. (2010) shown that benzene could be present in a circular geological pattern (see Fig. 17.B of their study), which they interpreted as a dry lakebed. Unfortunately, this feature has not been imaged by the RADAR in order to confirm its exact geological nature, and mainly whether it pertains to the class of possible lakebeds or not.

Our model also predicts evaporite layer thickness. In Fig. 10, we have plotted the total thickness of the evaporite deposition in the scenario where solute abundances are scaled to production rate of solids (see Fig. 9) and using an ethane solvent. The central plateau is explained by the final deposition of C_4H_{10}, in agreement with the results of our 1D models (Fig. 5(c)). The change in slope observed between $r = 15$ km and 16 km is a consequence of the sudden saturation of acetylene (see Fig. 9(c)).

Fig. 10 is typical of the thickness distribution of evaporite deposits after one sequence of dissolution–evaporation. In Titan weather conditions, successive evaporation and flooding episodes can occur and thus drive thicker deposits via redissolution/precipitation mechanisms similar to those already discussed in Section 3.2.

5. Discussion

Throughout this article we have assumed that the main process that removes a solvent is evaporation. Several authors have discussed the possibility of fluids percolation within some porous

Retour à la table des matières : p. v

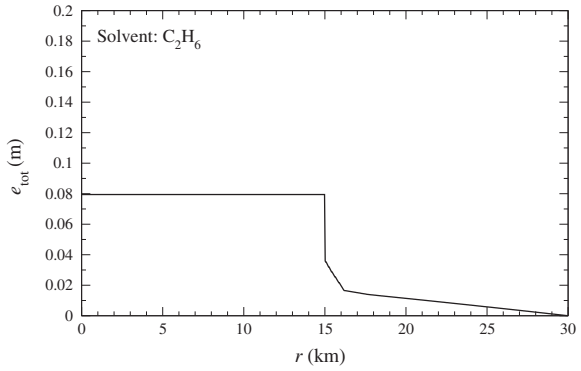

Fig. 10. The total thickness e_{tot} (in meter) of the resulting evaporite layer that appears after evaporation of the solvent. The adopted lakebed topography is described in Fig. 8, r (km) represents the typical radius of a lake initially containing solutes with abundances scaled to atmospheric precipitation rates (this model corresponds to what it is depicted by Fig. 9(c)).

regolith or terrain (Hayes et al., 2008; Choukroun and Sotin, 2012; MacKenzie et al., 2014). This process could be efficient only in the case where solid particles would not fill the regolith pores. A situation where the compounds belonging to the solvent could percolate, leaving behind initially dissolved species, seems particularly unrealistic since the pores would have very specific (and still unknown) properties; in addition, deposited layers at the lake bed would have to remain permeable to solutes, irrespective of its thickness. Nevertheless, we could wonder whether even in case of liquid percolation, the formation of evaporitic deposition could take place. Hence, if the bulk of the liquid, initially lying in a lacustrine depression, flows into a porous geologic formation instead of evaporate; at the end it will still remain a thin layer of liquid. The depth of this former layer depends on the wetting properties of the system solid substrate–liquid, namely the surface tensions liquid–vapor and liquid–solid (Butt et al., 2003), which are essentially unknown, although they do exist. A crude estimation of the possibly resulting depth of the coat of evaporite can be made. For that purpose, we assume a wetting film of a thickness around 1 mm. Table 6 provides the thickness equivalent to an initial depth of 100 m of saturated liquid. From these numbers, one can easily derive the possible thickness of the evaporite layer left after the evaporation of a final wetting film. One finds a thickness around a few microns, mainly due to butane. Thus, even if the geological substrate is porous, the formation of a fine evaporite layer remains possible.

All of our solubilities have been computed assuming a solvent that contains three major species: CH_4, C_2H_6 and N_2. This was clearly a reasonable assumption; however, it does not account for the potential role of a less abundant player like propane. Although photochemical models predict a relative precipitation rate of C_3H_8 one order of magnitude smaller than that of ethane (Lavvas et al., 2008b), propane could play a role in regions where it would be overabundant compared to its global average concentration. Brown et al. (2008), in their analysis of the 5-μm window, were not able to exclude the existence for a small amount of propane, butane and high-order alkanes in Ontario Lacus. Thus, we have calculated the mole fraction at saturation of considered solutes in pure C_3H_8. Unfortunately, among the PC-SAFT interaction parameters k_{ij} relevant for propane, the only one available is that of the couple (C_3H_8,C_2H_2) (taken from Tan et al., 2013), for others we used 0.0 (like in most cases involving C_2H_6 as a solvent). In general, for a solute X, adopting $k_{ij} = 0.0$ for both (C_2H_6, X) and (C_3H_8, X), we got a maximum solubility in propane roughly a factor of 2 higher than in ethane. This tendency is also found in the case of C_2H_2 where k_{ij} is known. The only noticeable exception is for CO_2; for this compound we use the $k_{ij} \neq 0.0$ determined for (C_2H_6, CO_2) (see Section 2), but we have not been able to draw any satisfactory conclusions. In short, the possible presence of some amount of propane could somewhat enhance the solubility of solid organics without changing essentially the formation scheme of evaporites.

It is difficult to compare our solubility estimations with previous works since the theoretical background (equilibrium with the atmosphere or not, the use of RST or PC-SAFT, etc.), the thermodynamical conditions (pressure and temperature) and the exact composition of the solvent and the solutes taken into account vary from one publication to another. For instance Dubouloz et al. (1989) and Cordier et al. (2013a) consider simultaneous equilibria of the liquid with solid organics, and the vapor phase of the atmosphere. Raulin (1987) consider a temperature of 94 K while we take 90 K, which is probably more realistic. In addition Raulin (1987) used a version of Eq. (1) that is slightly differ from our version, but the term introduced in their equation is questionable (see our discussion in Appendix A). A summary of solubilities found in previous works can be found in Cornet et al. (2015) (see their Table B.5). Making a detailed list of the explicit differences in the theoretical assumptions of each published model would not reveal any physical insight great enough to justify such an undertaking. However, one can notice that they have a significant dependence on free parameters in common. The values of these parameters are directly determined by adjustment on experimental data, as these are the best numbers currently available. There is never, however, a guarantee of their validity in the context of Titan. Sometimes the values are crudely estimated, like the δ_{ij} in the case of the RST, or a default value is adopted as is the case in Stevenson et al. (2015b) and in this work for nitrogen compounds (the k_{ij}'s are taken equal to zero for the nitrogen species). In this work, we made a substantial effort to get an agreement with available experimental data by adjusting free parameters. This could explain the differences between some previous works (Raulin, 1987; Dubouloz et al., 1989; Cordier et al., 2013a) and our results for C_2H_2, CO_2, and C_6H_6. We determined that a disagreement of the order of about a factor of ten remains acceptable. Recently Stevenson et al. (2015b) concentrated their experimental efforts on nitrogen compounds. As a general trend, they found HCN and CH_3CN less soluble than what we found. Nonetheless, the solubility of CH_3CN in pure methane at 94 K (see their Table 4) is close to our determination: both are around 10^{-8}. Other models provide higher values, *e.g.* COSMO-RS estimates around 10^{-7}. In the case of HCN, the output of the Stevenson et al.'s COSMO-RS model is not too far from our value with solubilities of the order of 10^{-7}–10^{-8}. The implementation of PC-SAFT by Stevenson et al. (2015b) yields values significantly smaller, with solubilities in the range of 10^{-11}–10^{-12}. We recall that this could be explained by parameters that are dissimilar between the two models: m, σ and ϵ were directly determined with laboratory data in our work (see our Fig. 2) while Stevenson et al. (2015b) used other sources. More importantly, together with Stevenson et al. (2015b), we did not find data which allow the determination of the k_{ij}'s for HCN and CH_3CN. As emphasized by Stevenson et al. (2015b) (see their Tables 11 and 12) results depend drastically on k_{ij}'s; this problem could only be solved by future theoretical chemistry simulations or experimental measurements. Finally, the "global picture" of the evaporite structure does not seem to depend on the chosen model: very soluble species (like C_2H_2 and C_4H_{10}, which are among the most soluble with an RST or PC-SAFT approach) should be predominant at the surface of the central region of the deposit, whereas less solubles like HCN (all models seem to indicate that nitrogen bearing molecules are

Retour à la table des matières : p. v

poorly soluble) should lay along the former shoreline. For instance, estimates of HCN solubility much smaller than ours must reenforce the tendency we found.

"Tholins", generated in laboratory experiments, have long been proposed as Titan's aerosol analogs (Khare et al., 1984; Sagan et al., 1992). Numerous experimental works show that they are complex combinations of C–N–H molecules, with a molecular weight ranging between ∼100 to ∼800 daltons (Imanaka et al., 2004; McDonald et al., 1994; Sarker et al., 2003; Nna-Mvondo et al., 2013). In addition, they have been found to be very poorly soluble in nonpolar solvents (McKay, 1996; Coll et al., 2001). Tholins are macromolecules much larger than those considered in this study. In the frame of the PC-SAFT theory, the segment number m increases with the molecular size, whereas the hard-core segment diameter σ and the segment–segment interaction energy parameter ϵ/k_B remain approximately constant. This behavior can be easily understood: m represents the number of "hard spheres" that are assumed to compose the molecule in question. One can check this tendency in Table 6 of Tihic et al. (2008), where the ratio m/MW (MW stands for the molecular weight) stays around ∼0.02 for a collection of polymers. At the same time, σ and ϵ/k_B keep values around ∼4 Å and ∼250 K respectively.

For a sensitivity analysis, we tried increasing progressively the segment number of butane, from its standard value 2.63 to 7 ($m = 8$ has lead to a non-convergence of PC-SAFT, due to an unphysical situation), leaving σ and ϵ/k_B unchanged. The solubility of butane has been computed in ethane at 90 K, under 1.5 bar. We found that the concentration of butane would fall from 9.14×10^{-2} (in mole fraction) to 1.04×10^{-3} (in our hypothetical $m = 7$ case). In other words the solubility is very sensitive to the value of m and decreases by several order of magnitude when m is increased by only a few units. More sophisticated numerical experiments (*e.g.* in which m is estimated using a group-contribution approach for a complex macromolecule, see Tihic et al., 2008) yield a similar conclusion.

As already emphasized in PAP1, the enthalpy of melting that appears in Eq. (1) has a strong influence of the resulting solubility. This enthalpy can be estimated using a group-contribution method (see for instance Joback, 1984); the relevant equation proposed in Appendix C of Poling et al. (2007) has the following form

$$\Delta H_m = -0.88 + \sum_k N_k(hmk) \times 0.004184 \qquad (2)$$

where N_k is the number of groups (–CH_3, –OH, ...) of type k, and the hmk's represent the corresponding contributions to the enthalpy; they are provided by dedicated tables. For the majority of these groups — first of all CH_3, CH_2 and CH — the hmk's are positive. Thus the general tendency is an increase of ΔH_m with the size of molecules leading to lower solubility. In PAP1, the authors discussed the case of the most simple molecule of the hydrazine family; (identified by Quirico et al., 2008, to be one of the possible components of tholins) CH_3CH_3N–CH_2; and also cyanoacetylene HC_3N. Unfortunately, for both molecules, we were not be able to find in the literature values of even estimations for their PC-SAFT parameters. Then, we cannot, for this moment, improve the solubility estimations computed in PAP1 for this particular species.

However, Titan's atmospheric aerosols that fall on its surface (Barth and Toon, 2006; Larson et al., 2014) –and that could be similar to tholins– have probably a very low solubility. Therefore, a layer of these aerosols may compose the lakebed, and most likely below the layers of butane and acetylene and those of HCN and CH_3CN. The "tholins" might be buried at the bottom of the evaporitic deposition or compose the external part of the bathtub.

Present knowledge of the Titan's surface chemical composition suffers from a lack of data. Brown et al. (2008) published clues in favor of the presence of the ethane in Ontario Lacus. In their work, Clark et al. (2010) identified benzene but they could not disentangle spectral signature of HC_3N and CO_2 while C_2H_2 has not been detected and CH_3CN could explain some spectral features. Beyond this, we have to keep in mind that *in situ* exploration could bring some surprises: for instance, in their experimental work, Vu et al. (2014) and Cable et al. (2014) have explored the formation of benzene–ethane co-crystals. Moreover, even if the low temperature of the surface disfavors the kinetics of chemical reactions, cosmics-ray particles could penetrate down to the surface (Sagan and Thompson, 1984; Zhou et al., 2010) and their energy deposition (see Molina-Cuberos et al., 1999) could speed-up some simple organics processes that could lead to the emergence of unexpected species over geological timescales. In short, molecules taken into account in this work as evaporites are supported by photochemical models, but we cannot exclude that future investigations or possible *in situ* exploration will reveal chemical surprises.

As emphasized in PAP1, possible turbidity is a major issue in our context. The presence of impurities may play a role in the nucleation of precipitating organics providing favorable nucleation sites, and they may also contribute to the deposits left on the ground after evaporation of the liquid. The authors of PAP1 have recalled that the laws of thermodynamics favor the heterogeneous nucleation since the cost in energy is lower in the case of a heterogeneous process compared to a homogeneous one, but Malaska and Hodyss (2013) observed, in their experiments, volume precipitation of benzene (M. Malaska, private communication) suggesting homogeneous precipitation. This unexpected phenomenon could be explained either by the presence of impurities in the liquid or by a very smooth internal surface of the experimental cell. Among our few observational constraints, Brown et al. (2008), using observation through the 5-µm window, have noticed that Ontario Lacus appears to be filled with a liquid free of particles larger than a few micrometers. In addition, in their study of Ligeia Mare Mastrogiuseppe et al. (2014) have also pointed out that the low attenuation of the RADAR signal is compatible with a ternary mixture of nitrogen, methane and ethane, excluding, after discussion, the possibility of significant turbidity caused by suspended scatterers. Despite this, the question of turbidity remains an open issue that could be answered by future space missions.

In their study of the geographical distribution of evaporite candidates, MacKenzie et al. (2014) noticed a clear lack of 5-µm-bright material in the south pole district. This observation cannot be explained by water snow falling from the atmosphere since Titan's atmosphere is particularly poor in water (Coustenis et al., 1998; de Kok et al., 2007; Moreno et al., 2012; Cottini et al., 2012). Therefore, MacKenzie et al. (2014) have proposed three possible explanations to this observation: (1) the evaporites layers could have been buried; being covered by a cap of aerosols, (2) the liquid could have percolated to a subsurface reservoir through a porous regolith, or (3) that there just haven't ever been deep, long-lived liquids at the south pole. However, the explanation offered by aerosols settling appears much more unlikely than percolation, since that implies a probable disappearance of difference between south zones which seems to be water–ice rich, and those consistent with water–ice in VIMS data.

Two alternative origins of this lack of southward evaporites can be proposed. First, if organic solutes are mainly produced in the atmosphere, one can imagine the existence of a low production rate above the south polar regions, phenomenon caused by the photochemistry itself and/or by properties of the atmospheric circulation that could disfavor the south pole. This hypothesis is supported by the asymmetrical distribution of lakes, which could be explained by the insolation asymmetry caused by Saturn's system orbital properties (Aharonson et al., 2009; Lora and Mitchell, 2015). Second, due to the high concentrations at saturation of potential

Retour à la table des matières : p. v

solutes into ethane (see Table 6), this solvent, by running off over the surface, could dissolve and trap almost the entire amount of solid organics that have been fallen from the atmosphere over the south polar region. The fact that Ontario Lacus is recognized to be enriched in ethane (Brown et al., 2008; Luspay-Kuti et al., 2015) strengthens this interpretation. Moreover, the RADAR very low loss tangent observed in Ligeia Mare by Mastrogiuseppe et al. (2014), contrasts with the much stronger absorption estimated at Ontario Lacus (Hayes et al., 2010); this fact could be interpreted as the consequence of the solvation of more absorbing compounds like long chain hydrocarbons, aromatics and nitriles (Mastrogiuseppe et al., 2014). Order of magnitude evaluations can be also invoked. For that purpose, we employed the least-square fit, established by Lorenz et al. (2008), that provides the average depth of the Earth's 20 largest lakes, as a function of their size (*i.e.* the square root of their surface area). Applied to Ontario Lacus, this law suggests an average depth of ∼200 m, for an adopted surface area of 15,600 km^2; finally leading to an approximate total volume of $\sim 4 \times 10^{12}$ m^3. If we assume a content made of pure ethane, this volume corresponds to $\sim 10^{17}$ mol, mole fractions at saturation gathered in Table 6 allow estimations of maximum quantities of solutes that can be contained in Ontario. On another side, we have estimated the total quantities of organic solids settled to the regions further south than Ontario Lacus, which represent a total area of about 2×10^{12} m^2; this, during a period equal to a Titan's year. To do so, we simply have multiplied the rates coming from Lavvas et al. (2008b), by both the considered area and the chosen period of time. The results show that the maximum dissolved quantities, allowed by our model, exceed by a factor of $\sim 10^3$–10^4 the amounts of potential solutes that are assumed to fall from the atmosphere according to photochemistry models. Thanks to Cassini RADAR data, Ventura et al. (2012) derived a more realistic average depth for Ontario Lacus, around ten times lower than our crude estimation. Obviously, even a much shallower lake does not alter our conclusion. Therefore, our scenario, postulating that the south polar regions are currently dominated by liquid ethane that could host the major part of soluble species, appears plausible.

6. Conclusion

We have developed a new model of dissolution based on the up-to-date theory called PC-SAFT. This model takes into account recent laboratory measurements. As a by-product, we have determined the PC-SAFT parameters for HCN. The absence of available interaction parameters k_{ij} for some species, among them HCN, encourages further experimental work on the solubility determinations in cryogenic solvents.

With our model, we have also computed the possible vertical structure of evaporite deposits. These 1-D simulations confirm the result already published in PAP1: butane and acetylene are good candidates for species that could compose the surface of evaporite. In addition, we found that a couple of compounds could form a thick external layer; and due to the combination of the existence of two crystallographic phases and of the rather thick layer, this external C_4H_{10}–C_2H_2 enriched layer could explain the RADAR brightness of evaporites, if the scale of the produced heterogeneities is similar or larger than the RADAR wavelength. We have also shown that the seasonal cycle may offer a mechanism which leads to a growth of evaporite thickness only limited by atmospheric production of organics. Thanks to our solubility calculation, we also suggest that ethane-enriched south pole lake Ontario Lacus could have trapped a large quantity of solutes, and this would explain – at least partially – the lack of evaporite in the south polar regions.

Under realistic conditions, with our 2-D model we confirm the possibility of the formation of "bathtub rings", showing a complex chemical composition. However our model suggests the possible existence of "trimodal bathtub ring compositions when the entire evaporation is completed. Our predictions are in agreement with past observations of Ontario Lacus by Barnes et al. (2009) and Moriconi et al. (2010) and suggest the need of a future Titan's space mission involving a lander, partly focused on the exploration of the lakes shores, where the chemical diversity is clearly high (Stevenson et al., 2015a).

Acknowledgments

We thank Giuseppe Mitri for scientific discussion. TC is funded by the ESA Research Fellowship in Space Science Programme. The authors acknowledge financial support from the ESAC Faculty (ESAC-358 proposal). Finally, we thank the anonymous Reviewers who improved the clarity of the paper with their remarks and comments.

Appendix A. The validity of the equation of liquid–solid equilibrium

The solubility calculations, presented throughout this paper, rely in Eq. (1), which is – as already mentioned in PAP1 – an approximation. The rigorous expression is given by (see for instance, annex of Maity, 2003)

$$\ln(\Gamma_i X_i^{\text{sat}}) = \underbrace{-\frac{\Delta H_{i,m}}{RT_{i,m}}\left(\frac{T_{i,m}}{T}-1\right)}_{(1)} \underbrace{-\frac{1}{RT}\int_P^{P_i^{\text{sat}}}\left(V_{i,m}^S - V_{i,m}^L\right)\mathrm{d}P}_{(2)} \underbrace{-\frac{1}{RT}\int_T^{T_{i,m}}\left(C_{p,i}^S - C_{p,i}^L\right)\mathrm{d}T}_{(3)} \underbrace{+\frac{1}{T}\int_T^{T_{i,m}}\left(C_{p,i}^S - C_{p,i}^L\right)\frac{\mathrm{d}T}{T}}_{(4)} \quad (A.1)$$

and one can legitimately wonder if terms (2), (3) and (4) have a global contribution negligible compared to term (1) or not. It is very striking to note that experimental data can be nicely reproduced even without these terms (see Figs. 1 and 3). It is probably safe then to assume that either terms 2, 3, and 4 have a tiny contribution or that their role is included in the effect of the interaction parameters k_{ij}. Nonetheless, we have tentatively tried to estimate the values of terms (2)–(4). We found in the literature laboratory measurements for the specific heats $C_{p,i}^S$ of some involved solids: C_4H_{10}, C_6H_6, CH_3-CN and HCN (respectively in Aston and Messerly, 1940; Oliver et al., 1948; Putnam et al., 1965; Giauque and Ruehrwein, 1939); and the specific heats $C_{p,i}^L$ of the subcooled liquids can – at least in principle – be evaluated by the use of PC-SAFT. This equation of state only provides their quantities if the Helmholtz energy (or equivalently the specific heat $C_{p,i}^{id}$ of the corresponding ideal gas) is known. Hence, we have estimated these $C_{p,i}^{id}$ using the group-contribution method developed by Joback (1984) and Joback and Reid (1987) and summarized by Poling et al. (2007). In order to test the validity of this approach, we compared the speed of sound

$$c_{\text{sound}} = \sqrt{\frac{C_p}{C_v}\frac{1}{k_T\rho}} \quad (A.2)$$

obtained by this method with experimental results for some cryogenic liquids. The agreement was not good enough to allow a firm validation of the method. The current development status of our model does not then permit reliable estimation for terms (3) and (4).

Retour à la table des matières : p. v

On one hand, measured molar volumes $V^S_{i,m}$ of solids are available (see Table 5); on the other hand the molar volume $V^L_{i,m}$ of subcooled liquids can be computed by PC-SAFT because it is not required to know the Helmholtz energy of the corresponding ideal gas. The vapor pressures P^{sat} are clearly negligible compared to the ambient pressure of ~1.5 bar, in addition solids and liquids have in general a very low compressibility, that way term (2) in Eq. (A.1) is not significantly different from $\sim|V^S_{i,m} - V^L_{i,m}| \times P/RT$. Then, for the solid species involved in this work, the term (1) ranges between ~1 and ~10, while $|V^S_{i,m} - V^L_{i,m}| \times P/RT$ has values of the order of $\sim 10^{-4}$–10^{-3}. We conclude that term (2) is negligible, whereas the precise role of the terms (3) and (4) remains questionable, even if the k_{ij}'s could partly mimic their effect.

References

Aharonson, O. et al., 2009. An asymmetric distribution of lakes on Titan as a possible consequence of orbital forcing. Nat. Geosci. 2, 851–854. http://dx.doi.org/10.1038/ngeo698.

Antson, O., Tilli, K., Andersen, N., 1987. Neutron powder diffraction study of deuterated β-acetonitrile. Acta Crystallogr., 296–301

Aston, J., Messerly, G.H., 1940. The heat capacity and entropy, heats of fusion and vaporization and the vapor pressure of n-butane. J. Am. Chem. Soc. 62, 1917–1923.

Barnes, J.W. et al., 2009. Shoreline features of Titan's Ontario Lacus from Cassini/VIMS observations. Icarus 201, 217–225. http://dx.doi.org/10.1016/j.icarus.2008.12.028.

Barnes, J.W. et al., 2011. Organic sedimentary deposits in Titan's dry lakebeds: Probable evaporite. Icarus 216, 136–140. http://dx.doi.org/10.1016/j.icarus.2011.08.022.

Barnes, J.W. et al., 2013. Precipitation-induced surface brightenings seen on Titan by Cassini VIMS and ISS. Planet. Sci. 2, 1–22.

Barth, E.L., Toon, O.B., 2006. Methane, ethane, and mixed clouds in Titan's atmosphere: Properties derived from microphysical modeling. Icarus 182, 230–250. http://dx.doi.org/10.1016/j.icarus.2005.12.017.

Brown, R.H. et al., 2008. The identification of liquid ethane in Titan's Ontario Lacus. Nature 454, 607–610. http://dx.doi.org/10.1038/nature07100.

Butt, H.J., Graf, K., Kappl, M., 2003. Physics and Chemistry of Interfaces. Wiley-VCH Verlag, Weinheim.

Cable, M.L. et al., 2014. Experimental determination of the kinetics of formation of the benzene–ethane co-crystal and implications for Titan. Geophys. Res. Lett. 41, 5396–5401. http://dx.doi.org/10.1002/2014GL060531.

Chang, S., Maurey, J.R., Pummer, W.J., 1983. J. Chem. Eng. Data 28, 187–189.

Cheung, H., Zander, E.H., 1968. Chem. Eng. Progr.; Symp. Ser. No 88 64, 34.

Choukroun, M., Sotin, C., 2012. Is Titan's shape caused by its meteorology and carbon cycle? Geophys. Res. Lett. 39, L04201. http://dx.doi.org/10.1029/2011GL050747.

Clark, R.N. et al., 2010. Detection and mapping of hydrocarbon deposits on Titan. J. Geophys. Res. (Planets) 115, E10005. http://dx.doi.org/10.1029/2009JE003369.

Coll, P. et al., 2001. Chemical and optical behaviour of tholins, laboratory analogues of Titan aerosols. Adv. Space Res. 27, 289–297. http://dx.doi.org/10.1016/S0273-1177(01)00060-6.

Cordier, D. et al., 2009. An estimate of the chemical composition of Titan's lakes. Astrophys. J. Lett. 707, L128–L131. http://dx.doi.org/10.1088/0004-637X/707/2/L128. Available from: <0911.1860>.

Cordier, D. et al., 2012. Titan's lakes chemical composition: Sources of uncertainties and variability. Planet. Space Sci. 61, 99–107. http://dx.doi.org/10.1016/j.pss.2011.05.009. Available from: <1104.2131>.

Cordier, D. et al., 2013a. Erratum: "An estimate of the chemical composition of Titan's lakes". Astrophys. J. Lett. 768, L23. http://dx.doi.org/10.1088/2041-8205/768/1/L23.

Cordier, D., Barnes, J.W., Ferreira, A.G., 2013b. On the chemical composition of Titan's dry lakebed evaporites. Icarus 226 (2), 1431–1437. http://dx.doi.org/10.1016/j.icarus.2013.07.026.

Cornet, T. et al., 2012. Geomorphological significance of Ontario Lacus on Titan: Integrated interpretation of Cassini VIMS, ISS and RADAR data and comparison with the Etosha Pan (Namibia). Icarus 218, 788–806. http://dx.doi.org/10.1016/j.icarus.2012.01.013.

Cornet, T. et al., 2015. Dissolution on Titan and on Earth: Toward the age of Titan's karstic landscapes. J. Geophys. Res. (Planets) 120, 1044–1074. http://dx.doi.org/10.1002/2014JE004738. Available from: <1505.08109>.

Cottini, V. et al., 2012. Water vapor in Titan's stratosphere from Cassini CIRS far-infrared spectra. Icarus 220, 855–862. http://dx.doi.org/10.1016/j.icarus.2012.06.014.

Coustenis, A. et al., 1998. Evidence for water vapor in Titan's atmosphere from ISO/SWS data. Astron. Astrophys. 336, L85–L89.

Craven, C. et al., 1993. The structure and dynamics of solid benzene. I. A neutron powder diffraction study of deuterated benzene from 4 K to the melting point. J. Chem. Phys. 98, 8236–8243.

de Kok, R. et al., 2007. Oxygen compounds in Titan's stratosphere as observed by Cassini CIRS. Icarus 186, 354–363. http://dx.doi.org/10.1016/j.icarus.2006.09.016.

de Kok, R.J. et al., 2014. HCN ice in Titan's high-altitude southern polar cloud. Nature 514, 65–67. http://dx.doi.org/10.1038/nature13789. Available from: <1410.5563>.

Dietrich, O., Mackenzie, G., Pawley, G., 1975. The structural phase transition in solid DCN. J. Phys. C: Solid State Phys. 8, L98–L102.

Diez-y-Riega, H. et al., 2014. Unsaturated hydrocarbons in the lakes of Titan: Benzene solubility in liquid ethane and methane at cryogenic temperatures. Planet Space Sci. 99, 28–35. http://dx.doi.org/10.1016/j.pss.2014.05.003.

Din, F., 1962. Thermodynamic Functions of Gases, vol. 2. Butterworth Inc., Washington.

Dubouloz, N. et al., 1989. Titan's hypothesized ocean properties – The influence of surface temperature and atmospheric composition uncertainties. Icarus 82, 81–96. http://dx.doi.org/10.1016/0019-1035(89)90025-0.

Dulmage, W., Lipscomb, W., 1951. The crystal structures of hydrogen cyanide, HCN. Acta Crystallogr. 4, 330–334.

Etters, R., Kuchta, B., 1989. Static and dynamic properties of solid CO_2 at various temperatures and pressures. J. Chem. Phys. 90, 4537–4541.

Fairall, C.W. et al., 1996. Bulk parameterization of air-sea fluxes for tropical ocean-global atmosphere coupled-ocean atmosphere response experiment. J. Geophys. Res. 101 (C2), 3747–3764.

Gabis, D.H., 1991. Liquid–Vapor Equilibrium at 90–160 K for Systems Containing Nitrogen, Methane, and Ethane. Ph.D. Thesis, Cornell Univ.

Giauque, W.F., Ruehrwein, R.A., 1939. The entropy of hydrogen cyanide. Heat capacity, heat of vaporization and vapor pressure. Hydrogen bond polymerization of the gas in chains of indefinite length. J. Am. Chem. Soc. 61, 2626–2633.

Glein, C.R., Shock, E.L., 2013. A geochemical model of non-ideal solutions in the methane–ethane–propane–nitrogen–acetylene system on Titan. Geochim. Cosmochim. Acta 115, 217–240. http://dx.doi.org/10.1016/j.gca.2013.03.030.

Gross, J., Sadowski, G., 2001. Perturbed-chain SAFT: An equation of state based on a perturbation theory for chain molecules. Ind. Eng. Chem. Res. 40, 1244–1260. http://dx.doi.org/10.1021/ie0003887.

Hayes, A. et al., 2008. Hydrocarbon lakes on Titan: Distribution and interaction with a porous regolith. Geophys. Res. Lett. 35, L09204. http://dx.doi.org/10.1029/2008GL033409.

Hayes, A.G. et al., 2010. Bathymetry and absorptivity of Titan's Ontario Lacus. J. Geophys. Res. (Planets) 115, 9009. http://dx.doi.org/10.1029/2009JE003557.

Imanaka, H. et al., 2004. Laboratory experiments of Titan tholin formed in cold plasma at various pressures: Implications for nitrogen-containing polycyclic aromatic compounds in Titan haze. Icarus 168, 344–366. http://dx.doi.org/10.1016/j.icarus.2003.12.014.

Joback, K.G., 1984. Unified Approach to Physical Property Estimation Using Multivariate Statistical Techniques. Ph.D. Thesis, Massachusetts Institute of Technology.

Joback, K.G., Reid, R.C., 1987. Chemical potential – A quantity in search of recognition. Chem. Eng. Commun. 57, 233–243.

Khare, B.N. et al., 1984. The organic aerosols of Titan. Adv. Space Res. 4, 59–68. http://dx.doi.org/10.1016/0273-1177(84)90545-3.

Larson, E.J.L., Toon, O.B., Friedson, A.J., 2014. Simulating Titan's aerosols in a three dimensional general circulation model. Icarus 243, 400–419. http://dx.doi.org/10.1016/j.icarus.2014.09.003.

Lavvas, P.P., Coustenis, A., Vardavas, I.M., 2008a. Coupling photochemistry with haze formation in Titan's atmosphere, Part I: Model description. Planet Space Sci. 56, 27–66. http://dx.doi.org/10.1016/j.pss.2007.05.026.

Lavvas, P.P., Coustenis, A., Vardavas, I.M., 2008b. Coupling photochemistry with haze formation in Titan's atmosphere, Part II: Results and validation with Cassini/Huygens data. Planet Space Sci. 56, 67–99. http://dx.doi.org/10.1016/j.pss.2007.05.027.

Le Gall, A. et al., 2010. Radar-bright channels on Titan. Icarus 207, 948–958. http://dx.doi.org/10.1016/j.icarus.2009.12.027.

Lide, D.P. (Ed.), 1974. CRC Handbook of Chemistry and Physics, 74th ed. CRC Press.

Lora, J.M., Mitchell, J.L., 2015. Titan's asymmetric lake distribution mediated by methane transport due to atmospheric eddies. Geophys. Res. Lett. 42, 6213–6220. http://dx.doi.org/10.1002/2015GL064912.

Lorenz, R.D. et al., 2008. Titan's inventory of organic surface materials. Geophys. Res. Lett. 35, L02406. http://dx.doi.org/10.1029/2007GL032118.

Lorenz, R.D. et al., 2009. Ontario Lacus: Brilliant observations of a Titan lake by the Cassini Cassini RADAR altimeter. In: Lunar and Planetary Science Conference, vol. 40, p. 1990.

Luspay-Kuti, A. et al., 2012. Experimental simulations of CH_4 evaporation on Titan. Geophys. Res. Lett. 39, 5, L23203.

Luspay-Kuti, A. et al., 2015. Experimental constraints on the composition and dynamics of Titan's polar lakes. Earth Planet. Sci. Lett. 410C, 75–83.

MacKenzie, S.M. et al., 2014. Evidence of Titan's climate history from evaporite distribution. Icarus 243, 191–207. http://dx.doi.org/10.1016/j.icarus.2014.08.022. Available from: <1408.2899>.

Maity, S.K., 2003. Modeling and Simulation of Solid–liquid Equilibrium by Perturbed-Chain Statistical Associating Fluid Theory. Master's Thesis, Indian Institute of Technology; Kharagpur, India.

Malaska, M. et al., 2012. Titan in a fume hood: Room-temperature simulation of a Titan evaporite playa using a multi-component mixture of organic compounds. In: Lunar and Planetary Science Conference. Lunar and Planetary Inst. Technical Report, vol. 43, p. 2139.

Retour à la table des matières : p. v

Malaska, M., Hodyss, R., 2013. Laboratory investigation of benzene dissolving in a Titan lake. LPI Contrib. 1719, 2744–2745.
Malaska, M.J., Hodyss, R., 2014. Dissolution of benzene, naphthalene, and biphenyl in a simulated Titan lake. Icarus 242, 74–81. http://dx.doi.org/10.1016/j.icarus.2014.07.022.
Mastrogiuseppe, M. et al., 2014. The bathymetry of a Titan sea. Geophys. Res. Lett. 41, 1432–1437. http://dx.doi.org/10.1002/2013GL058618.
McDonald, G.D. et al., 1994. Chemical investigation of Titan and Triton tholins. Icarus 108, 137–145. http://dx.doi.org/10.1006/icar.1994.1046.
McKay, C.P., 1996. Elemental composition, solubility, and optical properties of Titan's organic haze. Planet. Space Sci. 44, 741–747. http://dx.doi.org/10.1016/0032-0633(96)00009-8.
McMullan, R., Kvick, A., Popelier, P., 1992. Structures of cubic and orthorhombic phases of acetylene by single-crystal neutron diffraction. Acta Crystallogr. Sect. B Struct. Sci. 48, 726–731.
Mitchell, J.L. et al., 2011. Locally enhanced precipitation organized by planetary-scale waves on Titan. Nat. Geosci. 4, 589–592. http://dx.doi.org/10.1038/ngeo1219.
Mitri, G. et al., 2007. Hydrocarbon lakes on Titan. Icarus 186, 385–394. http://dx.doi.org/10.1016/j.icarus.2006.09.004.
Molina-Cuberos, G.J. et al., 1999. Ionization by cosmic rays of the atmosphere of Titan. Planet. Space Sci. 47, 1347–1354. http://dx.doi.org/10.1016/S0032-0633(99)00056-2.
Moreno, R. et al., 2012. The abundance, vertical distribution and origin of H_2O in Titan's atmosphere: Herschel observations and photochemical modelling. Icarus 221, 753–767. http://dx.doi.org/10.1016/j.icarus.2012.09.006.
Moriconi, M.L. et al., 2010. Characterization of Titan's Ontario Lacus region from Cassini/VIMS observations. Icarus 210, 823–831. http://dx.doi.org/10.1016/j.icarus.2010.07.023.
Neumann, A., Mann, R., 1969. Die Loslichkeit von festem Acetylen in flussigen Methan/Athylen-Mischungen. Chem. Ing. Tech. 41, 708–711.
Nna-Mvondo, D. et al., 2013. Thermal characterization of Titan's tholins by simultaneous TG-MS, DTA, DSC analysis. Planet. Space Sci. 85, 279–288. http://dx.doi.org/10.1016/j.pss.2013.06.025.
Oliver, G.D., Eaton, M., Huffman, H.M., 1948. The heat capacity, heat of fusion and entropy of benzene. J. Am. Chem. Soc. 70, 1502–1505.
Poling, B.E., Prausnitz, J.M., O'Connell, J., 2007. The Properties of Gases and Liquids, fifth ed. McGraw-Hill Professional, Englewood Cliffs.
Preston, G.T., Prausnitz, J.M., 1970. Thermodynamics of solid solubility in cryogenic solvents. Ind. Eng. Chem. Process Des. Develop 9, 264–271.
Putnam, W.E., McEachern, D.M., Kilpatrick, J.E., 1965. Entropy and related thermodynamic properties of acetonitrile. J. Chem. Phys. 42, 749–755.
Quirico, E. et al., 2008. New experimental constraints on the composition and structure of tholins. Icarus 198, 218–231. http://dx.doi.org/10.1016/j.icarus.2008.07.012.
Rannou, P. et al., 2006. The latitudinal distribution of clouds on Titan. Science 311, 201–205. http://dx.doi.org/10.1126/science.1118424.
Raulin, F., 1987. Organic chemistry in the oceans of Titan. Adv. Space Res. 7, 71–81. http://dx.doi.org/10.1016/0273-1177(87)90358-9.
Refson, K., Pawley, G., 1986. The structure and orientational disorder in solid n-butane by neutron powder diffraction. Acta Crystallogr., 402–410
Sagan, C., Thompson, W.R., 1984. Production and condensation of organic gases in the atmosphere of Titan. Icarus 59, 133–161. http://dx.doi.org/10.1016/0019-1035(84)90018-6.
Sagan, C., Thompson, W.R., Khare, B., 1992. Titan: A laboratory for prebiological organic chemistry. Acc. Chem. Res. 25, 286–292. http://dx.doi.org/10.1021/ar00019a003.
Sarker, N. et al., 2003. Titan aerosol analogues: Analysis of the nonvolatile tholins. Astrobiology 3, 719–726. http://dx.doi.org/10.1089/153110703322736042.
Schneider, T. et al., 2012. Polar methane accumulation and rainstorms on Titan from simulations of the methane cycle. Nature 481, 58–61. http://dx.doi.org/10.1038/nature10666.
Simon, A.P.K., 1980. Single-crystal refinement of the structure of carbon dioxide. Acta Crystallogr., 2750–2751
Spuhl, O. et al., 2004. Ind. Eng. Chem. Res. 43, 4457–4464.
Stevenson, J., Lunine, J., Clancy, P., 2015a. Membrane alternatives in worlds without oxygen: Creation of an azotosome. Sci. Adv. 1, e1400067. http://dx.doi.org/10.1126/sciadv.1400067.
Stevenson, J.M. et al., 2015b. Solvation of nitrogen compounds in Titan's seas, precipitates, and atmosphere. Icarus 256, 1–12. http://dx.doi.org/10.1016/j.icarus.2015.04.019.
Stofan, E.R. et al., 2007. The lakes of Titan. Nature 445, 61–64. http://dx.doi.org/10.1038/nature05438.
Stofan, E.R. et al., 2011. The Titan Mare Explorer Mission (TiME): A discovery mission to a Titan sea. In: EPSC-DPS Joint Meeting 2011, p. 909.
Tamouza, S.M., 2004. Utilisation prédictive de l'équation d'état SAFT. Ph.D. Thesis, Université de Paris XIII, France.
Tan, S.P. et al., 2015. Titans liquids: Exotic behavior and its implications on global fluid circulation. Icarus 250 (0), 64–75. http://dx.doi.org/10.1016/j.icarus.2014.11.029.
Tan, S.P., Kargel, J.S., Marion, G.M., 2013. Titan's atmosphere and surface liquid: New calculation using Statistical Associating Fluid Theory. Icarus 222, 53–72. http://dx.doi.org/10.1016/j.icarus.2012.10.032.
Tihic, A. et al., 2008. A predictive group-contribution simplified PC-SAFT equation of state: Application to polymer systems. Ind. Eng. Chem. Res. 47, 5092–5101.
Tokano, T. et al., 2001. Three-dimensional modeling of the tropospheric methane cycle on Titan. Icarus 153, 130–147. http://dx.doi.org/10.1006/icar.2001.6659.
Tokano, T., 2009a. Limnological structure of Titan's hydrocarbon lakes and its astrobiological implication. Astrobiology 9, 147–164. http://dx.doi.org/10.1089/ast.2007.0220.
Tokano, T., 2009b. Impact of seas/lakes on polar meteorology of Titan: Simulation by a coupled GCM-Sea model. Icarus 204, 619–636. http://dx.doi.org/10.1016/j.icarus.2009.07.032.
Tokano, T., Lorenz, R.D., Van Hoolst, T., 2014. Numerical simulation of tides and oceanic angular momentum of Titan's hydrocarbon seas. Icarus 242, 188–201. http://dx.doi.org/10.1016/j.icarus.2014.08.021.
Tomasko, M.G. et al., 2005. Rain, winds and haze during the Huygens probe's descent to Titan's surface. Nature 438, 765–778. http://dx.doi.org/10.1038/nature04126.
Turtle, E.P. et al., 2011. Rapid and extensive surface changes near Titan's equator: Evidence of april showers. Science 331, 1414–1417. http://dx.doi.org/10.1126/science.1201063.
Vinatier, S. et al., 2010. Analysis of Cassini/CIRS limb spectra of Titan acquired during the nominal mission. I. Hydrocarbons, nitriles and CO_2 vertical mixing ratio profiles. Icarus 205, 559–570. http://dx.doi.org/10.1016/j.icarus.2009.08.013.
Ventura, B. et al., 2012. Electromagnetic models and inversion techniques for Titan's Ontario Lacus depth estimation from Cassini RADAR data. Icarus 221, 960–969. http://dx.doi.org/10.1016/j.icarus.2012.09.011.
Vu, T.H. et al., 2014. Formation of a new benzene–ethane co-crystalline structure under cryogenic conditions. J. Phys. Chem. A 118, 4087–4094.
Vuitton, V., Yelle, R.V., Cui, J., 2008. Formation and distribution of benzene on Titan. J. Geophys. Res. (Planets) 113, 5007. http://dx.doi.org/10.1029/2007JE002997.
Zhou, L. et al., 2010. Cosmic-ray-mediated formation of benzene on the surface of Saturn's Moon Titan. Astrophys. J. 718, 1243–1251. http://dx.doi.org/10.1088/0004-637X/718/2/1243.

Retour à la table des matières : p. v

4.7 Article sur un concept de mission vers Titan et Encelade

Planetary and Space Science 104 (2014) 59–77

Contents lists available at ScienceDirect

Planetary and Space Science

journal homepage: www.elsevier.com/locate/pss

Science goals and mission concept for the future exploration of Titan and Enceladus

G. Tobie [a,*], N.A. Teanby [b], A. Coustenis [c], R. Jaumann [d], F. Raulin [e], J. Schmidt [f], N. Carrasco [g], A.J. Coates [h], D. Cordier [i], R. De Kok [j], W.D. Geppert [k], J.-P. Lebreton [l], A. Lefevre [a], T.A. Livengood [m], K.E. Mandt [n], G. Mitri [a], F. Nimmo [o], C.A. Nixon [m], L. Norman [p], R.T. Pappalardo [q], F. Postberg [r], S. Rodriguez [s], D. Schulze-Makuch [t], J.M. Soderblom [u], A. Solomonidou [c,v], K. Stephan [d], E.R. Stofan [m], E.P. Turtle [w], R.J. Wagner [d], R.A. West [q], J.H. Westlake [w]

[a] Laboratoire de Planétologie et Géodynamique de Nantes, University of Nantes, CNRS, UMR-6112, 44322 Nantes cedex, France
[b] School of Earth Sciences, University of Bristol, Wills Memorial Building, Queen's Road, Bristol BS8 1RJ, UK
[c] LESIA-Observatoire de Paris, CNRS, Université Paris 6, Université Paris-Diderot, 5 place Jules Janssen, 92195 Meudon, France
[d] DLR, Institute of Planetary Research, Berlin, Germany
[e] Univ Paris Est Creteil, CNRS, UMR 7583, Lab Interuniv Syst Atmospher, IPSL, F-94010 Creteil, France
[f] Univ Potsdam, D-14469 Potsdam, Germany
[g] Univ Paris 06, Univ Versailles St Quentin, CNRS, LATMOS, F-78280 Guyancourt, France
[h] Univ Coll London, Mullard Space Sci Lab, Dorking RH5 6NT, Surrey, England
[i] Univ Franche Comte, Inst UTINAM, CNRS INSU, UMR 6213, Observ Sci Univers THETA, F-25030 Besancon, France
[j] SRON Netherlands Institute for Space Research, Sorbonnelaan 2, 3584 CA Utrecht, Netherlands
[k] Stockholm Univ, Dept Phys, SE-10691 Stockholm, Sweden
[l] European Space Agcy, Estec, NL-2200 AG Noordwijk, Netherlands
[m] NASA Goddard Space Flight Center, Greenbelt, MD, USA
[n] SW Res Inst, Space & Sci Engn Div, San Antonio, TX 78238, USA
[o] Univ Calif Santa Cruz, Dept Earth & Planetary Sci, Santa Cruz, CA 95064 USA
[p] UCL, Dept Space & Climate Phys, Inst Origins, London WC1E 6BT, England
[q] Jet Propulsion Laboratory, California Institute of Technology, Pasadena, CA, 91109 USA
[r] Heidelberg Univ, Inst Earth Sci, D-69120 Heidelberg, Germany
[s] Univ Paris 07, Lab AIM, CNRS, CEA, Ctr Orne Merisiers, F-91191 Gif Sur Yvette, France
[t] Washington State Univ, Pullman, WA 99163, USA
[u] Dept. Earth, Atmospheric and Planetary Sciences, MIT, Cambridge, MA 02139, USA
[v] Univ Athens, Dept Geol & Geoenvironm, Athens 15784, Greece
[w] Johns Hopkins Univ, Appl Phys Lab, Dept Space, Laurel, MD 20723, USA

ARTICLE INFO

Article history:
Received 31 December 2013
Received in revised form
23 September 2014
Accepted 6 October 2014
Available online 28 October 2014

Keywords:
Titan
Enceladus
Atmosphere
Surface
Ocean
Interior
Missions

ABSTRACT

Saturn's moons, Titan and Enceladus, are two of the Solar System's most enigmatic bodies and are prime targets for future space exploration. Titan provides an analogue for many processes relevant to the Earth, more generally to outer Solar System bodies, and a growing host of newly discovered icy exoplanets. Processes represented include atmospheric dynamics, complex organic chemistry, meteorological cycles (with methane as a working fluid), astrobiology, surface liquids and lakes, geology, fluvial and aeolian erosion, and interactions with an external plasma environment. In addition, exploring Enceladus over multiple targeted flybys will give us a unique opportunity to further study the most active icy moon in our Solar System as revealed by Cassini and to analyse in situ its active plume with highly capable instrumentation addressing its complex chemistry and dynamics. Enceladus' plume likely represents the most accessible samples from an extra-terrestrial liquid water environment in the Solar system, which has far reaching implications for many areas of planetary and biological science. Titan with its massive atmosphere and Enceladus with its active plume are prime planetary objects in the Outer Solar System to perform in situ investigations. In the present paper, we describe the science goals and key measurements to be performed by a future exploration mission involving a Saturn–Titan orbiter and a

* Corresponding author.
E-mail addresses: gabriel.tobie@univ-nantes.fr (G. Tobie), n.teanby@bristol.ac.uk (N.A. Teanby).

http://dx.doi.org/10.1016/j.pss.2014.10.002
0032-0633/© 2014 Elsevier Ltd. All rights reserved.

Titan balloon, which was proposed to ESA in response to the call for definition of the science themes of the next Large-class mission in 2013. The mission scenario is built around three complementary science goals: (A) Titan as an Earth-like system; (B) Enceladus as an active cryovolcanic moon; and (C) Chemistry of Titan and Enceladus – clues for the origin of life. The proposed measurements would provide a step change in our understanding of planetary processes and evolution, with many orders of magnitude improvement in temporal, spatial, and chemical resolution over that which is possible with Cassini–Huygens. This mission concept builds upon the successes of Cassini–Huygens and takes advantage of previous mission heritage in both remote sensing and in situ measurement technologies.

© 2014 Elsevier Ltd. All rights reserved.

1. Introduction

The Cassini–Huygens mission, which has been in orbit around Saturn since July 2004 and released the Huygens probe that landed on Titan's surface on January 14, 2005, has revealed Titan and Enceladus to be enigmatic objects – introducing extraordinary challenges for geologists, astrobiologists, organic chemists, and planetologists. Titan, Saturn's largest satellite, is unique in the Solar System with its extensive atmosphere made mostly of N_2, with a column density 10 times that of Earth's atmosphere. The presence of a few per cent methane provides the basis for rich organic chemistry, leading to production of complex CHON compounds from the upper atmosphere down to the surface (e.g. Israël et al., 2005; Waite et al., 2007; Bézard et al., 2014). Methane is close to its triple point on Titan, which gives rise to a methanological cycle analogous to the terrestrial hydrological cycle, characterized by cloud activity, precipitation, river networks and lakes (e.g. Tomasko et al., 2005; Stofan et al., 2007; Rodriguez et al., 2009). Exploring Titan in greater detail than ever possible with Cassini–Huygens offers the possibility to study physical processes analogous to those shaping the Earth's landscape, where methane takes on water's role, and to analyse complex chemical processes that may have prebiotic implications (e.g. Raulin et al., 2012).

The discovery of jets of water vapor and ice grains emanating from Enceladus' south pole in 2005 is one of the major highlights of the Cassini–Huygens mission (e.g. Dougherty et al., 2006; Porco et al., 2006; Spahn et al., 2006; Waite et al., 2006; Spencer et al., 2009). Despite its small size (10 times smaller than Titan), Enceladus is the most active moon of the Saturnian system. Although geyser-like plumes have been reported on Triton (Soderblom et al., 1990) and more recently transient water vapor activity around Europa (Roth et al., 2014), Enceladus is the only one proven to have current endogenic activity. The jets, which form a huge plume of vapor and ice grains above Enceladus' south pole, are associated with abnormally elevated heat flow along tectonic ridges, called 'Tiger stripes'. Sampling of the plume by Cassini's instruments revealed the presence of water vapor, organics and salt-rich ice grains (Hansen et al., 2008; Waite et al., 2009; Postberg et al., 2009, 2011), suggesting that the jet sources are connected to subsurface salt-water reservoirs (e.g. Postberg et al., 2011). The surprising activity of Enceladus provides a unique opportunity to analyse materials coming from its water-rich interior, potentially containing compounds of prebiotic interest, and to study today aqueous processes that may have been important on many other icy worlds in the past.

The objectives of the present paper is to present the science goals and mission concept that were defined in response to the ESA call for the definition of the science theme of the next L-class (L2/L3) missions of the Cosmic Vision programme and to discuss the possible next step in the exploration of these two moons. Here we focus on science goals that could be achieved from the combination of a Saturn–Titan orbiter and a Titan balloon. The science goals and key measurements that may be achieved from the combination of a Titan orbiter and a lake probe are described in a companion paper (Mitri et al., 2014). The mission scenario described here is built around three major science goals, which were identified as the highest priority for such a mission:

- *Goal* A: Understand how Titan functions as a world, in the same way that one would ask this question about Venus, Mars, and the Earth.
- *Goal* B: Characterize the present-day activity of Enceladus, to understand what processes power it and how it affects the Saturnian environment.
- *Goal* C: Determine the degree of chemical complexity on the two moons, to analyse complex chemical processes that may haveprebiotic implications.

These goals are explained in detail in Sections 2–4. In Section 5, we briefly discuss a possible mission concept and key measurements, and consider the technological issues involved in return to the Saturn system. Section 6 provides a brief conclusion and some perspectives for the preparation of future exploration mission projects.

2. Science goal a: Titan as an earth-like system

Titan is a complex world more like the Earth than any other: it is the only place besides Earth known to have a dense, predominantly nitrogen, atmosphere; it has an active climate and meteorological cycle where the working fluid – methane – behaves under Titan's conditions the way that water does on Earth; and its geology – from lakes and seas to broad river valleys and mountains – while carved in ice is, in its vast range of processes, again most like Earth. Beneath this panoply of terrestrial processes an ice crust floats atop what appears to be a liquid water ocean. Science Goal A seeks to understand how Titan functions as a world, in the same way that one would ask this question about Venus, Mars, and the Earth. How are the distinctions between Titan and other worlds in the Solar System understandable in the context of the complex interplay between geology, hydrology, meteorology, and aeronomy? Is Titan an analogue for some aspect of the Earth's history, past or future? Why is Titan endowed with an atmosphere when, for example, Jupiter's moon Ganymede, virtually identical in size and mass, is not? Although the Cassini–Huygens mission provided major advances for understanding the atmospheric and geological processes at work on Titan, many questions remain unanswered – addressing these questions require future missions designed to explore these worlds.

2.1. Titan's atmosphere

2.1.1. Meteorology and methane cycle

Titan is the only body in the Solar System besides Earth with an active "hydrologic" cycle, featuring methane rather than water as the condensable fluid in clouds, rain, and surface reservoirs (lakes). Titan has an obliquity of 26.7° (similar to Earth) giving pronounced seasonal change during its 29.5-year orbit around the Sun. Cassini

Retour à la table des matières : p. v

imaging shows that Titan's tropospheric clouds range from mid-latitude streaks, equatorial bands and patches, and summer polar convective outbursts, to a long-lived high-altitude winter polar cap (Rodriguez et al., 2009, 2011; Le Mouélic et al., 2012, Fig. 1). Polar cloud activity appears to disappear as equinox approaches (Fig. 1). Occasional equinoctial tropical methane monsoons have been speculated and recent observations of an equatorial arrow-shaped cloud (Turtle et al., 2011, Fig. 1) suggest an inter-tropical convergence zone following solar insolation maximum (Mitchell et al., 2011). Such storms and subsequent rainfall could explain the formation of equatorial fluvial surface erosion and intricate valley networks like those seen around the Huygens probe landing site (Tomasko et al., 2005, Fig. 2c).

Despite these major advances, Cassini's observations are limited by incomplete time coverage, due to the Saturn-centric orbit, which leads to a sporadic time series dependent on widely spaced Titan flybys/encounters. This makes it difficult to accurately assess global trends and seasonality in Titan's rapidly changing methane cycle. Continuous measurement of cloud distribution, characteristics, and evolution is now essential to constrain energy budgets, surface methane sources, and tropospheric circulation. It is unclear how often it rains on Titan, which determines erosion rates and how fluids are transferred around the globe. Investigating Titan's active meteorology will reveal the controlling factors that link surface and atmospheric interactions.

2.1.2. *Global dynamics, circulation, and seasonal change*

Titan provides a giant natural laboratory for testing Earth-based climate and general circulation models under different physical conditions. Much of Titan's general circulation, however, remains to be constrained – particularly above 500 km, below 100 km, within polar vortices, and in equatorial regions (Flasar et al., 2009). Measurements of circulation in these regions are important for constraining how strongly tropospheric and stratospheric circulation are coupled, whether the tropopause wind minimum and near-surface flow reversal observed by Huygens (Bird et al., 2005) are global features, and how thermal energy is redistributed in the upper atmosphere. A Titan orbiter would provide continuous coverage for remote sensing instruments and a regular series of radio occultations that would provide major advances. By comparing such measurements with legacy data from Voyager and Cassini, long-term climate trends could also be investigated.

Studying the seasonal variation of circulation patterns has been limited by the coverage available from each flyby, which is non-uniform and globally incomplete, but significant progress has been made. In addition to winds derived by Huygens probe radio tracking (Bird et al., 2005), there have also been cloud-tracking attempts, but these have been severely limited by Cassini's short flyby durations. Indirect measurements of the middle-atmospheric zonal winds have been derived from temperature fields via the thermal wind equation and vertical winds have been probed using chemical tracers and adiabatic heating (Teanby et al., 2008, 2009b, 2010b, 2012; Coustenis et al., 2010). Maps of atmospheric temperature and composition also show that Titan's atmospheric rotation axis is different from that of a solid body (Achterberg et al., 2008; Roman et al., 2009; Teanby et al., 2010a). The cause of this is currently unclear, but could be linked to thermal tides. Gravity waves appear to be an important and controlling feature of Titan's atmosphere and a major contributor to the super-rotation, but have only been directly profiled at a single point and a single season by the Huygens probe, so at present are very poorly constrained. Titan's detached haze varies in altitude from about 300 km to 500 km and is apparently synchronized to seasonal cycles (West et al., 2011) and reveals a strong coupling with the atmosphere dynamics (Cours et al., 2011). The nature of this coupling is still under debate, but the haze is clearly an important tracer of atmospheric dynamics in Titan's upper stratosphere. The vertical distribution of haze in the troposphere is also unknown and could provide nuclei for condensation. Further progress in all dynamical aspects of Titan's atmosphere now requires high temporal resolution monitoring from an orbiter.

2.1.3. *Temperature structure*

Titan's temperature structure and its evolution over seasonal timescales are essential for understanding climatic evolution, global circulation, photochemistry, and condensation processes. The chemical composition of Titan's atmosphere is similar to Earth's nitrogen-dominated atmosphere and both planets feature a distinct stratosphere. Titan's atmosphere is unique within the Solar System because it is so cold and extends to such high altitude, with evidence that upper atmospheric temperature is influenced by both magnetospheric plasma (external influence) (Westlake et al., 2011) and atmospheric waves (internal) (Hinson and Tyler, 1983), causing it to change rapidly (Snowden et al., 2013; Snowden and Yelle, 2014). Yet the existence of Titan's atmosphere appears relatively stable. Atmospheric escape (Yelle et al., 2008; Strobel, 2009) or irreversible photochemical conversion (Yung et al., 1984) are processes that could eliminate Titan's current atmosphere, although many aspects of these processes remain controversial (Bell et al., 2014). In any case, Titan's atmosphere is either begin replenished by processes not yet fully understood or

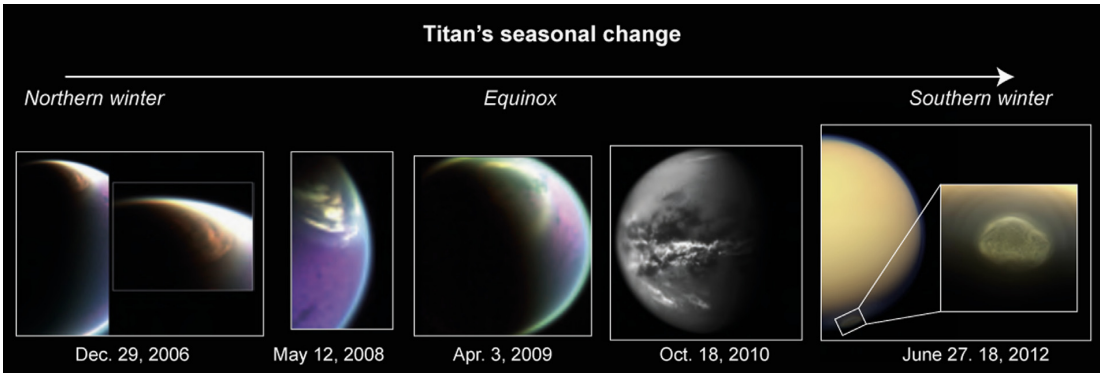

Fig. 1. Seasonal change witnessed from cloud activity, as observed by Cassini: (from left to right) first observation of the North Polar cloud system by VIMS at the end of 2006 and progressive disappearance at the equinox (Le Mouélic et al., 2012); Observation of a giant cloud system in the equatorial region by ISS after the equinox (October 18, 2010; Turtle et al., 2011); ISS observation of a polar vortex above the south pole while the pole is entering in the southern winter (credits: NASA/JPL-Caltech/Space Science Institute).

Retour à la table des matières : p. v

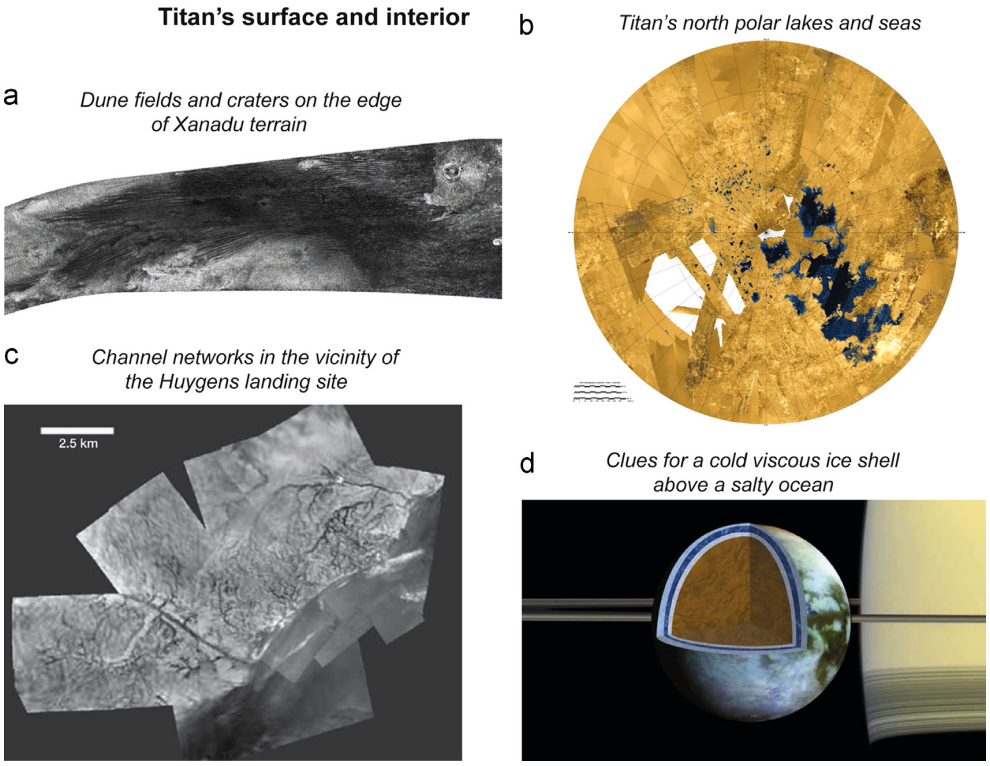

Fig. 2. (a) Radar image from Cassini illustrating three of Titan's major surface fetters: dunes, craters and enigmatic Xanadu (credit: NASA/JPL-Caltech/ASI); (b) colorized mosaic of radar images showing Titan's northern land of lakes and seas (credit: NASA/JPL-Caltech/ASI/USGS; (c) channel networks observed by the DISR camera on Huygens during its descent on January 14, 2005 (Tomasko et al., 2005); (d) interior structure of Titan with a salty ocean below a rigid ice shell with varying thickness, constrained from gravity and shape data (Mitri et al., 2014) (credit: NASA/JPL-Caltech/SSI/University of Arizona/University of Nantes).

else is being explored in a temporary state. A better understanding and more data on the chemistry of Titan's atmosphere and its interaction with the surface will enable us to solve this question.

Competition between absorbed ultraviolet and emitted infrared radiation creates Titan's pronounced Earth-like stratopause, which is not present on Mars or Venus, making Titan especially relevant for comparison with Earth. Although the single Huygens atmospheric profile suggests waves could be important above 500 km (Fulchignoni et al., 2005), there are serious gaps in our knowledge that Cassini will not be able to address. We have little information for the altitude ranges 0–100 km and 500–950 km. These regions are important because many of Titan's trace species condense around 100 km, whereas the 500–950 km region links the bulk neutral atmosphere to photochemical source regions. Additionally the location of the homopause on Titan has long been an issue of debate and has major implications for atmospheric escape rate (Strobel, 2009). Thermospheric temperatures strongly influence escape and are important for determining how the system as a whole operates and how or if equilibrium is maintained. Furthermore, a currently inaccessible region below 200 km within the winter polar vortex is a potential site for exotic chemistry on nitrile/hydrocarbon ices and could have parallels with Earth's Antarctic polar chemistry and polar stratospheric clouds (Flasar et al., 2005).

2.1.4. *Complex chemistry and haze formation*

A mission to Titan is the most effective way to study complex organic, inorganic and ionic chemistry at all altitudes, from formation of complex hydrocarbon species high in the atmosphere down through the bulk atmosphere. Currently formation of complex molecules, ions, and haze is poorly constrained. The present lack of constraints on the aerosol chemical composition precludes clear benchmarks for further synthetic organic solid studies in the laboratory (Cable et al., 2012; Gautier et al., 2014; Sebree et al., 2014; Westlake et al., 2014). A mission dedicated to Titan is essential to determine haze composition, how its formation in the ionosphere links to other levels, if its composition changes with altitude, how it affects climate, and its role in the methane cycle and surface composition, morphology and alteration.

Titan's atmosphere is rich in organic compounds sourced from a highly active photochemical cycle that begins in the ionosphere (~1000 km) and influences the entire atmospheric column (Lavvas et al., 2008). Discovery of the extent of the chemical complexity of Titan's ionosphere was one of Cassini's major breakthroughs and encompasses neutral species, positive ions, and negative ions (Coates et al., 2007; Waite et al., 2007, Fig. 3a and b). Cassini found unexpected negative ions up to 13,800 u/q (Coates et al., 2007; Coates, 2009) and positive ions up to ~1000 u (Waite et al., 2007; Crary et al., 2009; Coates et al., 2010), implying that linked neutral–cation–anion chemistry could play a key role in haze formation (Lavvas et al., 2013). Some amount of nitrogen inclusion occurs in these compounds, but it is unclear how far into the chemical chains nitrogen prevails. Ion structures are at present unconstrained and could be chains, rings or even fullerenes, which may play a role transporting oxygen to the surface (Sittler et al., 2009). Furthermore, although Cassini's instruments have not yet detected molecules more complex than benzene (C_6H_6) below 500 km, recent laboratory work by Gudipati et al. (2013) showed that complex chemistry may be important throughout the entire atmospheric column, including both upper and lower atmospheric regions (Fig. 3c).

Retour à la table des matières : p. v

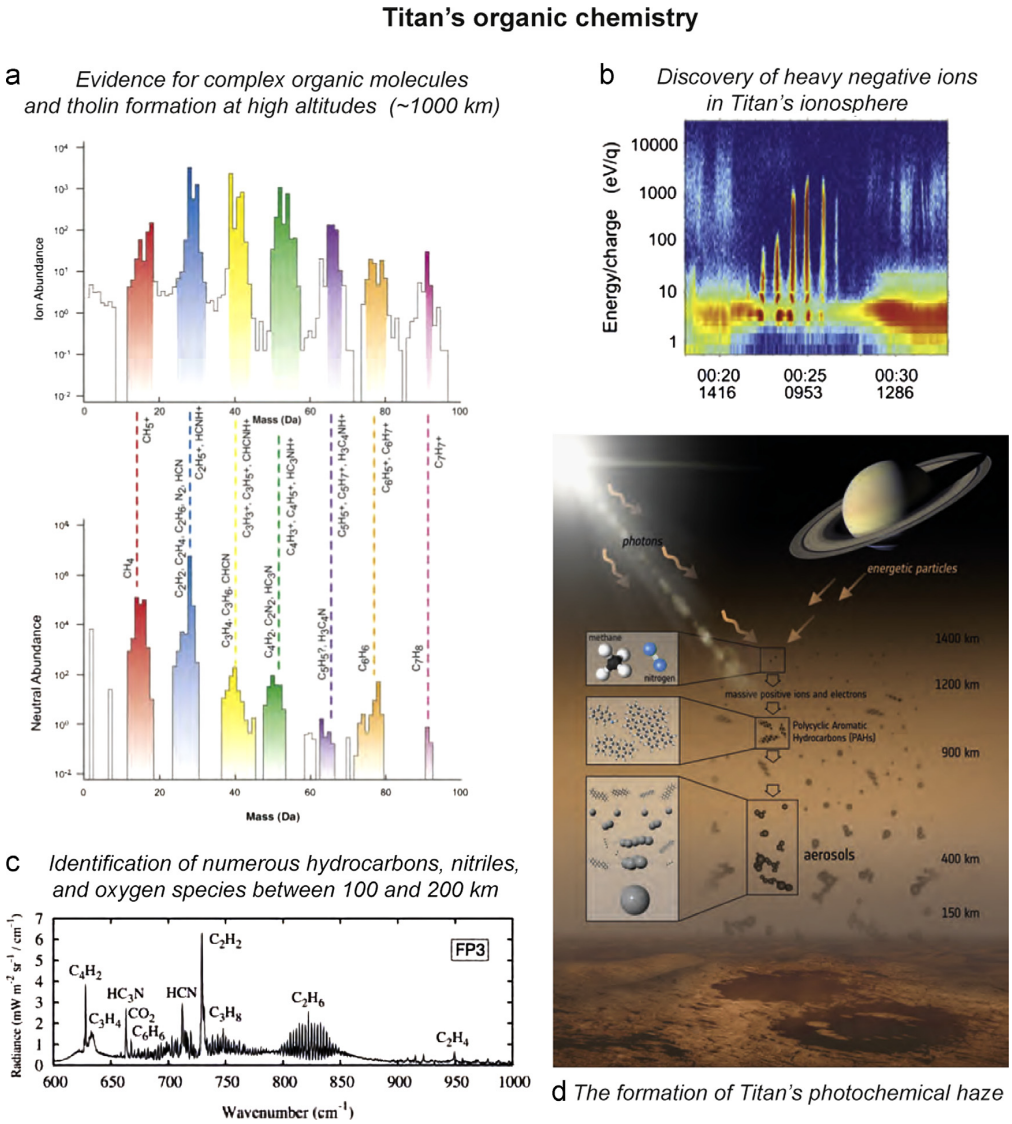

Fig. 3. (a) Detection of organic neutrals and positive ions containing up to seven carbons by the INMS on Cassini (Waite et al., 2007); (b) detection of heavy negative ions, with mass per charge as high as 10,000 u/q (Coates et al., 2007); (c) average CIRS limb spectra taken between January 2005 and January 2007 at altitudes between 100 and 200 km and latitudes between 55 and 90°N (Bézard et al., 2014); (d) illustration of the various steps that lead to the formation of organic aerosols on Titan (credit: ESA/ATG media lab).

2.2. Titan's geology

Titan's dense atmosphere is opaque at most visible and near-infrared wavelengths and the surface is only visible using reflected sunlight at specific windows in the near infrared and at RADAR wavelengths. Prior to Cassini's arrival at Saturn in 2004, bright and dark features were observed in near-infrared images acquired by the Hubble Space Telescope and Earth-based telescopes (e.g. Coustenis et al., 2005). But the lack of spatial resolution precluded any geological interpretation. Observations performed by the Cassini RADAR, the Visual and Infrared Mapping Spectrometer (VIMS), and the Imaging Science Subsystem (ISS), have revealed a remarkably diverse Earth-like surface in terms of landforms and geologic features, indicating that Titan shares many characteristics with the Earth (e.g. Jaumann et al., 2009; Stephan et al., 2013, Fig. 2). Titan's landscapes are shaped by a variety of surficial processes including impact cratering, aeolian, fluvial and lacustrine processes, and also endogenic processes including cryovolcanism and tectonism.

2.2.1. Impact craters

A remarkable characteristic of Titan's surface is the relative paucity of impact craters – one of the many attributes it shares with the Earth – which indicates a relatively young and active surface (Jaumann et al., 2009; Wood et al., 2010; Neish and Lorenz, 2012). Wood et al. (2010) and Neish and Lorenz (2012) list a total of 60 possible impact craters using Cassini RADAR data (currently covering ~33% of the surface) ranging from 3 to 445 km in diameter. Titan's craters appear in some ways morphologically different from those on airless icy satellites, perhaps due to effects of the atmosphere or subsurface liquids (Neish and Lorenz, 2014).

Retour à la table des matières : p. v

Soderblom et al. (2010), for example, report an apparent fluidized-ejecta blanket, similar in morphology to the bright crater outflows of Venus. With so few preserved craters, the age of Titan's surface remains uncertain and depends both on the cratering chronology model used and the sample set selected; estimates range from ~200 Ma to ~1 Ga, depending on which crater scaling function is used (e.g. Neish and Lorenz, 2012).

2.2.2. Aeolian features and processes

Aeolian activity on Titan has proven to be one of the major forces at work, as is especially apparent at low latitudes. Almost half the terrain within 30° of the equator is covered in dark (presumably organic-rich) streaks or dunes (e.g. Lorenz et al., 2006; Radebaugh et al., 2008, Fig. 2a). In a few of the best-imaged regions, these dunes are hundreds of kilometres long and ~150 m high. Almost all appear to be linear dunes, a type common in the Arabian, Sahara, and Namib deserts on Earth, but rare on Mars. These types of dunes typically form in long-lived bidirectional wind regimes. A tidal wind origin has been proposed for Titan, but seasonal wind changes may also play a role. While it has not been demonstrated that these dunes are presently active, they are certainly young relative to other geologic features (cf. Radebaugh et al., 2008). Interestingly, dune morphologies suggest westerly surface winds, which seems a priori at odds with the Huygens wind measurements (cf. Bird et al., 2005; Tomasko et al., 2005).

2.2.3. Fluvial features and processes

Fluvial surface modification was evident at the Huygens landing site (Tomasko et al., 2005; Lorenz et al., 2008b; Jaumann et al., 2008, 2009, Fig. 2c). Not only were steeply incised channels a few kilometres long and ~30 m across observed in the nearby bright highland (Perron et al., 2006; Jaumann et al., 2008), but the view from the probe after landing showed rounded cobbles characteristic of transport in a low-viscosity fluid (Tomasko et al., 2005). Radar-bright channels have been observed at low and mid-latitudes (Lorenz et al., 2008b; Langhans et al., 2012), while channels incised to depths of several hundred meters are exposed elsewhere. At high latitudes radar-dark, meandering channels suggest a lower-energy environment where deposition of fine-grained sediment occurs. Whether formation of these larger channels – some of which exceed a kilometre in width – and the large-scale flow features near the landing site (Soderblom et al., 2007; Jaumann et al., 2009) requires a different climate regime remains to be determined. The flow of methane rivers in an unsaturated atmosphere on Titan is analogous to the problem of ephemeral water flow on Mars and terrestrial deserts: determining whether the rivers dry out, freeze solid, or drain into subsurface alkanifers or ephemeral lakes and seas requires measurement of presently unknown meteorological factors.

2.2.4. Lacustrine features and processes

Extremely radar-dark features at Titan's high latitudes are consistent with liquid-filled lakes and seas ranging in size from less than 10 km^2 to at least 100,000 km^2 (Stofan et al., 2007, Fig. 2b). A specular reflection observed in VIMS data also indicates surface liquids (Stephan et al., 2010; Soderblom et al., 2012). Although ethane has been detected as a component of the liquid (Brown et al., 2008), the composition remains largely uncertain (Cordier et al., 2012). The most recent radar analyses indicate that the lakes have a very smooth surface (Zebker et al., 2014) and are remarkably transparent (Mastrogiuseppe et al., 2014), suggesting that they are mostly composed of methane. Empty lakebeds have been detected (Stofan et al., 2007; Hayes et al., 2008) and the existence of evaporite deposits is suspected (Barnes et al., 2011). The morphology of boundaries between some lakes and their surroundings resembles a terrain flooded by liquids, with the dark material appearing to flood valleys between brighter hilly terrain and in some cases occupying networks of channels that feed into or out of the lakes. Other lakes (e.g., many of the smaller lakes at high northern latitudes and possibly Ontario Lacus in the south) appear to be formed by dissolution (e.g. Cornet et al., 2012). The Huygens landing site is littered with 1–10-cm-scale mostly rounded pebbles, implying they were tumbled and deposited by liquids feeding into a now dry lake bed from dendritic valley systems seen in the Huygens DISR images (Keller et al., 2008). Systematically determining the depths of the lakes, similar to what have been tentatively done with *Cassini* (e.g. Ventura et al., 2012; Mastrogiuseppe et al., 2014), is of high importance, both to constrain the total amount of liquid they contain, and to understand the underlying geological processes and "methanological" cycling that formed them.

2.2.5. Endogenic activity

Cryovolcanism is a process of particular interest at Titan, especially because of the astrobiological potential of liquid water erupting onto photochemically produced organic compound deposits, solid and liquid, accumulated at the surface through time (e.g. Fortes and Grindrod, 2006; Poch et al., 2012). Radiogenic heating in Titan's interior, possibly augmented by tidal heating, can provide enough heat to drive a substantial resurfacing rate (e.g. Tobie et al., 2006). Kinetically, cryovolcanism is much easier in the Saturnian system, where ammonia can facilitate the generation and rise of cryofluids through an ice crust, than in the Galilean satellites (e.g. Fortes et al., 2007). Several candidate sites of cryovolcanism have been identified in Cassini near-infrared VIMS and RADAR data (e.g. Lopes et al., 2013; Sohl et al., 2014). Evidence for active volcanism, however, is still debated (cf. Moore and Pappalardo, 2011), and the role of cryovolcanism on Titan is an important factor for understanding exchange processes between atmosphere, surface and interior. It thus needs further scrutiny.

The role tectonism plays on Titan is also not well understood. A number of large-scale linear features are seen optically (Porco et al., 2005). Some features on Titan are parts of the landscape morphology correlated to tectonics that are/were subsequently subjected to exogenous processes, surficial and/or atmospheric (Solomonidou et al., 2013). Such features include mountains (e.g. Radebaugh et al., 2007), ridges (e.g. Mitri et al., 2010), faults (e.g. Radebaugh et al., 2011), and canyons (e.g. Lopes et al., 2010). Radar imagery of some of these features has not helped in their interpretation and is not yet sufficiently widespread to evaluate tectonic patterns, although some linear mountain ranges (e.g. Radebaugh et al., 2007) have been detected, several forming a chevron pattern near the equator. Near-infrared imagery by Cassini VIMS has also shown long ridges (e.g. Soderblom et al., 2007; Jaumann et al., 2009). An outstanding mystery is the nature of the large bright terrain Xanadu and its adjoining counterpart Tsegihi. These areas are distinct optically, and they have unusual radar properties. SAR imagery shows Xanadu to be extremely rugged, and appeared to be an ancient large-scale feature reshaped by fluvial process (e.g. Langhans et al., 2013). However, processes at its origin still remain unclear.

2.2.6. Evidence for a global internal ocean on Titan

A series of geophysical measurements (gravity field, Iess et al., 2012; electric field, Béghin et al., 2012; obliquity, Baland et al., 2011, 2014; and shape, Nimmo and Bills, 2010; Mitri et al., 2014) performed by Cassini–Huygens indicate the presence of a global water ocean, likely salt-rich, a few 10 s to > 100 km below the surface (Fig. 2d). Measured tidal fluctuations in the gravity field are consistent with the existence of a decoupling water layer

Retour à la table des matières : p. v

below the ice shell (Iess et al., 2012). The interpretation of gravity and topography data indicates that the thickness of the ice shell above the ocean should vary with latitude and longitude, implying that the ice shell is thermally conductive and has a high viscosity at present (Hemingway et al., 2013; Lefevre et al., 2014; Mitri et al., 2014). Moreover, the observed elevated tidal Love number and obliquity imply a dense ocean (Baland et al., 2014), which is consistent with a cold and salty ocean. Such an ocean, with an elevated concentration of ionic solutes, may also explain the electric field perturbation observed by Huygens and interpreted as a Schumann resonance (Béghin et al., 2012). The salt enrichment as well as the ^{40}Ar atmospheric abundance (Niemann et al., 2010) suggests an efficient leaching process and prolonged water–rock interactions. The chemical exchanges associated with water–rock interactions may be quantified by accurately measuring the ratio between radiogenic and non-radiogenic isotopes in noble gases (Ar, Ne, Kr, Xe) in Titan's atmosphere (Tobie et al., 2012). Further tidal monitoring from gravity, topography and rotation data along with magnetic and electric field measurements would provide key constraints on the physical properties of the ocean (depth, density, electric conductivity) as well as the ice shell (thickness, viscosity structure).

3. Science goal B: Enceladus as an active cryovolcanic moon

The detection of jets of water vapor and ice particles emanating from the south polar terrain of Enceladus is one of the major discoveries of the Cassini–Huygens mission (Fig. 4). This surprising activity has been studied by a suite of instruments onboard the Cassini spacecraft, analyzing the plume structure and the composition of the vapor and icy grain components (also called the dust in the following), their mass ratio, the speed and size distributions of the constituents, the interaction with the Saturnian corotational plasma, as well as the replenishment of the magnetosphere and E ring region with fresh plasma and dust particles. Science goal B seeks to further characterize the present-day activity of Enceladus, to understand what processes power it and how it affects the Saturnian environment.

Although geyser-like plumes and transient water vapor activity have been reported on Triton (Soderblom et al., 1990) and on Europa (Roth et al., 2014) respectively, Enceladus is the only icy world in the Solar System proven to have current endogenic activity. Triton's geysers are believed to be solar-driven (Brown et al., 1990; Kirk et al., 1990) and the origin of the transient water vapor emission above Europa's south pole are still unknown (Roth et al., 2014). The cryovolcanic activity of Enceladus offers a unique possibility to sample fresh material emerging from subsurface liquid water and to understand how exchanges with the interior controls surface activity. It provides us with an opportunity to study today, phenomena that may have been important in the past throughout the outer Solar System, when tidal effects and/or higher radiogenic heat fluxes could have powered eruptions, melting, and aqueous chemistry in a number of icy bodies.

3.1. Enceladus' plume activity

3.1.1. Plume characteristics

About 200 kg/s of vapor is ejected from Enceladus' south pole at speeds exceeding 500 m/s (Hansen et al., 2008), which is well above the escape velocity of 240 m/s. The gas is emitted in a broad, vertically extended plume with embedded, collimated and supersonic jets (Waite et al., 2006; Hansen et al., 2008, 2011). The dust plume also exhibits a broad component and localized jets (Porco et al., 2014, Fig. 4a), but it has a relatively small scale-height (Porco et al., 2006; Spahn et al., 2006; Schmidt et al., 2008), corresponding to slower mean ejection speeds on the order of 100 m/s. Schmidt et al. (2008) infer a dust production rate of 5–10% of the vapor production, although later photometric studies indicate a more massive dust plume (Hedman et al., 2009; Ingersoll and Ewald, 2011). A precise determination of the dust-to-vapor ratio, and variability therein, is now crucial to better understand the physical mechanisms responsible for the activity.

In contrast to the gas plume, only a small fraction (1–5%) of ejected icy dust exceeds the escape velocity of Enceladus and feeds the E ring. Most grains fall back on the surface in a characteristic global "snow" pattern (Kempf et al., 2010; Schenk et al., 2011). The size distribution of this dust was constrained from in situ measurements (Spahn et al., 2006) and infrared spectroscopy (Hedman et al., 2009) to roughly follow a power law (exponent -4), extending from the submicron range up to a few microns. Estimating accurately, both the fraction of particles falling back to the surface and the thickness of surface deposit, will provide essential information on the duration of plume activity.

3.1.2. Gas and grain composition

In situ measurements by Cassini INMS (Waite et al., 2006, 2009) showed that plume gas consists primarily of water vapor and about ~5–10% other volatiles (Fig. 4b). The main volatile species are CO_2, NH_3 and a mixture of organic gases (Waite et al., 2009). Amongst the latter are lightweight molecules like methane, acetylene and propane, but recent measurements also indicate even higher molecular weight compounds with masses exceeding 100 u. and aromatic organics (Waite et al., 2011). A molecule with mass of 28 u., which could be attributed to N_2, CO or C_2H_4, was also identified, but due to the lack of resolution, the ratio $CO/N_2/C_2H_4$ cannot be constrained. This information is, however, essential in establishing the origin of the volatiles.

Analyzing the composition of particles in the E ring and directly in the plume with Cassini CDA, Postberg et al. (2009, 2011) found that nearly all grains contain at least small amounts of sodium (roughly on ppm level), while other grains show much larger fractions of sodium and potassium salts like NaCl, $NaHCO_3$ and KCl (Fig. 4c). The conclusion was that these salt-rich grains (~ 0.5–2% by mass of salts) must directly disperse from salt water. Moreover, the composition inferred by CDA matches the prediction of Zolotov (2007) for the composition of a subsurface ocean that is, or was, in contact with a pristine rocky core. Nanometre-sized silicate inclusions in E ring ice grains (Hsu et al., 2011) further support this finding. As with the gas phase, the presence of organic compounds is also conjectured for the icy solids (Hillier et al., 2007; Postberg et al., 2008), but their precise nature is currently unconstrained.

In the plume, salt-rich particles were found to be more abundant close to jet sources. Postberg et al. (2011) concluded that these must be larger grains, ejected at lower speeds. As a consequence, the overwhelming part of the dust mass ejected into the plume is salt-rich whereas the small and fast salt-poor grains dominate (by number) the dust fraction that escapes into the E ring. A third type of dust particle was observed by Cassini's plasma instrument (Jones et al., 2009). To be detectable by this instrument, the grains must not be larger than a few nanometres, if singly charged. The locations where these small particles are detected are closely associated with the strongest jets in the plume. Precise determination of the different particle populations and their correlation with the jets is crucial to better understand the source of the jets and their interaction with the Saturnian environment.

3.1.3. Plume interaction with the magnetosphere

Enceladus is the main source of material in Saturn's magnetosphere, playing a similar role to Io in the Jovian system. On one

Retour à la table des matières : p. v

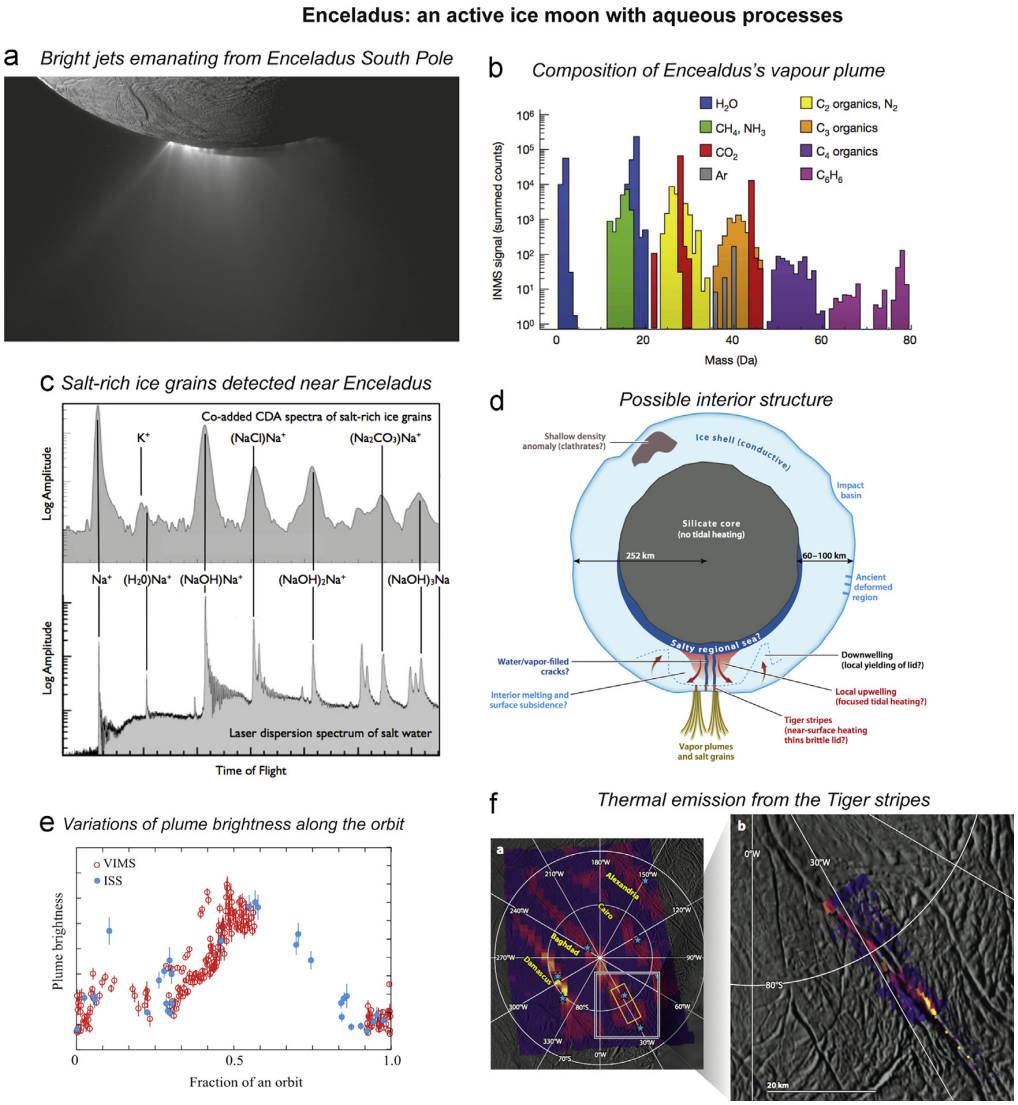

Fig. 4. (a) Cassini/ISS images showing eruption activity over the South Pole of Enceladus (Porco et al., 2014); (b) composition of Enceladus' vapor plume determined by the mass spectrometer INMS onboard Cassini (Waite et al., 2009); (c) comparison between co-added Cassini/CDA spectra of salt-rich water ice grains detected near Enceladus and a spectrum of laser-dispersed salty water provided proof for a subsurface water reservoir (Postberg et al., 2009, 2011); (d) diagram showing a possible interior structure of Enceladus (Spencer and Nimmo, 2013); (e) variation in brightness of Enceladus' plume, as a function of the moon's orbital position, observed by ISS (blue dots) (Nimmo et al., 2014) and VIMS (red dots) (Hedman et al., 2013) (credit: NASA/JPL-Caltech/Space Science Institute); (f) thermal emission at 10–17 μm from the tiger stripes as mapped by Cassini, superposed on a map based on visible-wavelength images (Spencer and Nimmo, 2013) (credit: NASA/JPL/GSFC/SwRI/Sapce Science Institute) (For interpretation of the references to color in this figure caption, the reader is referred to the web version of this paper.).

hand, the gas plume constitutes an obstacle for the corotational Kronian plasma. The deflected plasma forms a system of currents that lead to measurable deviations in the planetary dipolar magnetic field and the corotational electric field (Dougherty et al., 2006; Kriegel et al., 2009, 2011; Jia et al., 2010) and charge exchange collisions lead to an effective deceleration of the corotational plasma. On the other hand, the plume gas feeds a neutral torus around the orbit of Enceladus (Burger et al., 2007; Fleshman et al., 2010). Electron impacts and photoionization ionize neutrals in the plume and torus, thus replenishing the magnetospheric plasma (Tokar et al., 2006, 2008, 2009; Fleshman et al., 2010). The possible importance of dust-charging processes for the electromagnetic field close to the plume has been emphasized (Simon et al., 2011; Kriegel et al., 2011), and the presence of a dusty plasma was conjectured for the plume (Wahlund et al., 2009; Shafiq et al., 2011). Such conclusions are subject to controversial debate and a future mission provides a unique opportunity to verify and quantify the related processes and settle these issues.

3.1.4. *Plume source and surface activity*

Qualitatively, a consistent picture based on the presence of liquid water on Enceladus seems to emerge. Only in this way can the elevated salinity of the dust particles be understood (Postberg et al., 2009, 2011). Salt-rich particles could form by direct dispersion from liquid, possibly when bubbles of exsolved gases burst at the liquid's surface (Matson et al., 2012). This scenario could also resolve the problem with the large dust/vapor ratio (Ingersoll and Ewald, 2011) and the observation of fairly large (and massive) particles in the lower parts of the plume (Hedman et al., 2009).

Retour à la table des matières : p. v

Additional mass could condense on these particles when they are transported upwards in the supersaturated vents below the ice crust. In contrast, salt-poor (Postberg et al., 2009, 2011) and nano-sized grains (Jones et al., 2009) might form by direct homogeneous condensation from the gas phase (Schmidt et al., 2008). Water vapor in the plume would then directly evaporate from liquid. Some non-water volatile compounds in the plume gas (Waite et al., 2006, 2009; Hansen et al., 2011) could be released at a quasi-steady rate from the warm ice close to the liquid, or in de-pressurized zones close to the cracks.

Although recent observations by Cassini/VIMS and ISS indicate variability in the jet activity (Hedman et al., 2013; Nimmo et al., 2014), this activity is not yet fully characterized and the origin of the time variations are not fully understood. Stellar occultations from UVIS indicate little or no variability of the vapor production rate over a time-span of 5 years (Hansen et al., 2011), which appears in contradiction with the jet observations. Moreover, when viewed at different Enceladus' orbital true anomalies, the small observed changes appear to contradict the predictions of tidally driven eruption models (Hurford et al., 2012), while variability in plume brightness seen by VIMS seems consistent with such models (Hedman et al., 2013; Nimmo et al., 2014). Generally, limited spatial and temporal resolution of remote Cassini observations as well as the uncertain phase-function of the plume hamper the determination of possible variations with orbital true anomaly. Multiple, dedicated close flybys by a future spacecraft performed at different orbital true anomalies will permit an accurate determination of correlations between eruption activity and tidal cycles, as well as comparison with activity observed by Cassini.

3.1.5. *Evidence for subsurface salt-water reservoirs on Enceladus*

The detection of salt-rich ice grains in the plume (Postberg et al., 2011) clearly indicates the existence of a subsurface salt-water reservoir on Enceladus (Fig. 4). The presence of a liquid water reservoir is also supported by the gravity measurements performed by Cassini (Iess et al., 2014), as well as by models of tidal deformation (e.g. Nimmo et al., 2007; Tobie et al., 2008) (Fig. 4d). The low K/Na ratio in salt-bearing ice grains (Postberg et al., 2009) further indicates that water–rock interactions at the origin of the salt enrichment occurred at relatively low temperature (Zolotov, 2007; Zolotov et al., 2011). Such enrichment suggests efficient leaching processes and prolonged water–rock interactions. The involved chemical exchanges may be quantified by measuring accurately the ratio between radiogenic and non-radiogenic isotopes in noble gases (Ar, Ne, Kr, Xe) in Enceladus' plume and by determining more precisely the composition of organics, salts, and other minerals contained in sampled ice grains. The size and composition of the internal ocean – if any – must also be addressed. Monitoring tides and rotation (via measurements of altimetry, gravity, surface tracking) as well as magnetic signals may provide essential information on the ocean extent, density and electric conductivity, thus constraining its composition.

3.1.6. *Geodynamical evolution of Enceladus*

Enceladus' icy surface reveals a wide variety of tectonic structures that record a long history of tectonic deformation (Spencer et al., 2009). Ancient tectonically modified plains identified outside the active south-polar region (Crow-Willard and Pappalardo, 2010) suggest a complex geological history with multiple episodes of enhanced activity. Long-wavelength topography, as well as heterogeneity in crater distribution and tectonic activity, probably reflect strong temporal and spatial variations in ice shell thermal structure (Schenk and McKinnon, 2009; Kirchoff and Schenk, 2009). As indicated by the huge heat flow emitted from the Tiger stripes (Spencer and Nimmo, 2013, Fig. 4f), tidal interaction dominates the moon's evolution. Variations of endogenic activity are expected due to coupling with the orbital evolution. However, it is still unknown how activity varies on geological timescales. Surface and sub-surface mapping of Enceladus will permit a better understanding of its long-term evolution.

4. Science goal C: chemistry of Titan and Enceladus – clues for the origin of life

Both Titan and Enceladus possess several, if not all, of the key components for habitability: internal liquid water, organic material, energy sources, and a stable environment. Complex organics discovered in Titan's upper atmosphere indicate that a very rich organic chemistry is occurring on Titan (Fig. 3a and b). How these organic compounds formed, and how they evolve once at the surface and buried in the subsurface remain open questions. Organic compounds are also strongly indicated in Enceladus' plume, though not precisely identified. The presence of salt water as a plume source further increases the astrobiological potential of Enceladus. Titan and Enceladus offer an opportunity to study analogous prebiotic processes that may have led to the emergence of life on Earth. Goal C seeks to determine the degree of chemical complexity on the two moons, to analyse chemical processes that may have prebiotic implications.

4.1. *Similarities of Titan and Enceladus with the early earth*

Retracing the processes that allowed the emergence of life on Earth around 4 Ga ago is a difficult challenge since most traces of the environmental conditions at that time have been erased. It is, therefore, crucial for astrobiologists to find extraterrestrial planetary bodies with similarities to our planet, providing a way to study some of the processes that occurred on the primitive Earth, when prebiotic chemistry was active. Although Titan is much colder than the Earth, and has formed in a different environment, it nevertheless presents – perhaps more than any other object in the Solar System – striking analogies with our planet. A major example is Titan's atmosphere, which is composed of the same main constituent, nitrogen, and has a similar structure with a surface pressure of 1.5 bar. Methane's complex cycle on Titan mimics that of water on the Earth and generates, with nitrogen, a large inventory of organic molecules leading to an intense prebiotic chemistry, such as hydrogen cyanide (HCN) and cyanoacetylene (HC_3N) (Raulin et al., 2012). Moreover, Titan is the only planetary body, other than the Earth with long-standing bodies of liquid on its surface, albeit hydrocarbons instead of water. The degree of complexity that can be reached from organic chemistry in the absence of permanent liquid water bodies on Titan's surface, however, has yet to be determined.

Analogies also concern potential habitats. Although quite speculative, Titan lakes could harbor very exotic life (McKay and Smith, 2005; Schulze-Makuch and Grinspoon, 2005), using energy provided by the reduction of hydrocarbons into methane, cell membranes made of reversed vesicles (Norman and Fortes, 2011) and no liquid water. Another place is the likely internal liquid water reservoir mixed with some ammonia. Models of Titan's formation even suggest that, initially, this subsurface ocean was in direct contact with the atmosphere and with the internal bedrock (e.g. Tobie et al., 2006; Lunine et al., 2009), offering interesting analogies with the primitive Earth, and the potential implication of hydrothermal vents in terrestrial-like prebiotic chemistry. It cannot be excluded that life may have emerged in this environment and may have been able to adapt and persist since the current conditions are not incompatible with life as we know it on Earth (Fortes, 2000). Thus, it seems essential to confirm the presence

Retour à la table des matières : p. v

of this ocean and determine some of its properties. With the likely presence of subsurface salt-water reservoirs, Enceladus also offers interesting analogies with terrestrial oceans and subglacial lakes. The co-existence of organic compounds, salts, liquid water and energy sources on this small moon provides all necessary ingredients for the emergence of life by chemoautotrophic pathways (McKay et al., 2008) – a generally held model for the origin of life on Earth in deep sea vents. In this model, life on Earth began in deep sea hot springs where chemical energy was available from a mix of H, S, and Fe compounds. The fact that the branches of the tree of life that are closest to the common ancestor are thermophilic has been used to argue a thermophilic origin of life – although other explanations are possible. In situ sampling of the plume provides a unique opportunity to search for the specific molecules associated with such systems, including H_2, H_2S, FeS, etc., and to study processes analogous to those involved with the origin of life on Earth.

4.2. Origin and evolution of volatile compounds on Titan and Enceladus

A preliminary requirement for assessment of the astrobiological potential of Titan and Enceladus is to constrain the origin(s) of volatile compounds and to determine how their inventory evolved since satellite accretion. The present-day composition of Titan's atmosphere, as revealed by Cassini–Huygens, results from a combination of complex processes including internal outgassing, photochemistry, escape and surface interactions. The detection of a significant amount of ^{40}Ar (the decay product of ^{40}K) by Cassini–Huygens (Niemann et al., 2005, 2010; Waite et al., 2005) indicated that a few per cent of the initial inventory was outgassed from the interior. The chemical exchanges with the surface and the interior as well as the initial composition, however, still remain unconstrained (e.g. Tobie et al., 2014). In contrast, the analysis of Enceladus' plumes provides a unique opportunity to observe eruptive processes in real time and to constrain the composition of the building blocks of the Saturnian system (Waite et al., 2009). Comparison between Titan and Enceladus thus enables us to differentiate what was inherited during formation from what was acquired during their evolution.

The isotopic ratios in different gas compounds observed on Titan and Enceladus constitute crucial constraints to assess their origin and evolution. Cassini–Huygens and ground-based measurements provided isotopic ratios of H, C, N, and O in N_2, CO, CH_4, HCN and C_2 hydrocarbons at various altitudes in Titan's atmosphere (e.g. Mandt et al., 2012; Nixon et al., 2012). The measured $^{15}N/^{14}N$ ratio is enigmatic because it is about 60% higher than the terrestrial value (Niemann et al., 2010), suggesting an abnormally high fractionation. In contrast, $^{13}C/^{12}C$ in methane implies little to no fractionation, suggesting that methane has been present in the atmosphere for less than a billion years (Mandt et al., 2012). In the absence of a proper initial reference value, however, it is impossible to retrieve information on fractionation processes with confidence. Precise isotopic ratios in the photochemical by-products of CH_4 and N_2 on Titan are also lacking. Except for D/H in H_2O on Enceladus (with large error bars Waite et al., 2009), no information is yet available for the isotopic ratio in Enceladus' plume gas. Simultaneous precise determination of isotopic ratios in N, H, C and O-bearing species in Enceladus' plume and Titan's atmosphere will permit a better determination of the initial reference ratio and a quantification of the fractionation process due to atmospheric escape and photochemistry.

In situ sampling of the plasma and energetic particle environment surrounding Titan is also required to provide a better understanding of present escape. Saturn's magnetospheric plasma consists of primarily of water group ions (O^+, OH^+, H_2O^+), H_2^+, protons, and electrons near Titan (Thomsen et al., 2010). These ions impact Titan's thermosphere primarily heating the thermosphere, but also ionizing the local gas (Westlake et al., 2011; Shah et al., 2009; Smith et al., 2009). The oxygen and water group ions in the 1–100 keV range are most efficient at heating the thermosphere (Shah et al., 2009), while protons deposit their energy below the homopause (Smith et al., 2009). Energetic electrons (up to a few keV) impact the thermosphere primarily near 1200 km. There are two complimentary methods for determining the energy input into Titan's upper atmosphere, both of which were flown on Cassini: in situ measurements of upstream ions with energy and composition determination, and remote sensing of the atmospheric interaction through energetic neutral atom (ENA) detection. In situ measurement upstream and near Titan will identify the composition and energetics of Saturn's magnetospheric flow near Titan, with a sufficient fidelity magnetic field model derived from measurements the particles can be propagated into the thermosphere to determine the energy deposition. Remote ENA observations give the global energy deposition in Titan's thermosphere, and can also sense the structure and the extent of the exosphere (Brandt et al., 2012).

4.3. Titan complex prebiotic-like chemistry

In Titan's atmosphere, the coupling between CH_4 and N_2 chemistries produces many organics in the gas and particulate phases, especially hydrocarbons, nitriles and complex refractory organics (Fig. 3d). The latter seem to be well modeled by the solid products, commonly called the “tholins”, formed in laboratory simulation (e.g. Cable et al., 2012). Water and oxygen ions coming from a magnetospheric source linked to Enceladus plumes are also involved in this atmospheric chemistry (e.g. Sittler et al., 2009). Could these water-oxygen compounds then be locked up into aerosols? Several organic compounds have already been detected in Titan's stratosphere, including hydrocarbons and nitriles (Coustenis et al., 2007, 2010; Teanby et al., 2009a, Fig. 3c). Direct analysis of the ionosphere by the INMS instrument during the closest Cassini flybys of Titan shows the presence of many organic species at very high altitudes (1100–1300 km): the INMS and CAPS measurements strongly suggest that high-molecular-weight species (up to several 1000 u.) are present in the ionosphere (Waite et al., 2007, Fig. 3a and b). This unexpected discovery revolutionizes the understanding of the organic processes occurring in Titan's atmosphere, indicating that ionospheric chemistry plays a key role in the formation of complex organic compounds in Titan's environment. It is essential to determine ionosphere ion and neutral composition with sufficient mass range and resolution to study a wide range of organically relevant compounds. A mass range extending from 10 to about 10,000 u., with a mass resolution ($m/\delta m$) of at least 10,000, is necessary to determine with no ambiguity the elemental composition (in C, H, O and N) for a wide range of organic compounds. Isotopic knowledge for these compounds would require even greater mass resolution, generally 30,000.

The presence of water vapor and benzene has been unambiguously confirmed by the CIRS instrument, which also detected isotopomers of several organics (Nixon et al., 2008; Coustenis et al., 2010). The GCMS data collected during the descent of the Huygens probe show that the middle and lower stratosphere and the troposphere are poor in volatile organic species, with the exception of methane (Niemann et al., 2005, 2010). Condensation of such species on aerosol particles is a probable explanation for these atmospheric characteristics. The Huygens ACP instrument carried out the first in situ chemical analysis of these particles. The results show that they are made of nitrogen-rich refractory organics, which release HCN and NH_3 during pyrolysis, supporting the tholin hypothesis (Israël et al., 2005; Coll et al., 2013). These measurements suggest that the aerosol

Retour à la table des matières : p. v

particles are made of a refractory organic nucleus, covered with condensed volatile compounds. However, neither the nature and abundances of the condensates nor the elemental composition and the molecular structure of the refractory part of the aerosols have been determined. Moreover, the chirality of its complex organic part is unknown.

The nitrogen content of the aerosols means they are of immediate astrobiological interest following their production in the upper atmosphere (Hörst et al., 2012). Once deposited on Titan's surface, aerosols and their complex organic content produced by atmospheric chemistry may also follow a chemical evolution of astrobiological interest. Laboratory experiments show that, once in contact with liquid water, tholins can release many compounds of biological importance, such as amino acids and purines (Poch et al., 2012). Such processes could be particularly favorable if liquid water is brought to the surface by cryovolcanism (Lopes et al., 2007) or cratering events (Artemieva and Lunine, 2003). Thus one can envision the possible presence of such compounds on Titan's surface or near subsurface. Long-term chemical evolution is impossible to mimic experimentally in the laboratory. It is, therefore, crucial to be able to perform a detailed chemical analysis (at the elemental, molecular, isotopic and chiral levels) of the various types of surface zones, particularly those where cryovolcanism and impact ejecta (or melt sheets) are or have been present.

4.4. Enceladus' prebiotic aqueous processes

The jets emanating from Enceladus' south pole are probably the most accessible samples from an extra-terrestrial liquid water environment in the Solar System. In addition to water ice, jets include CO_2 and several organics such as methane, propane, acetylene, and even higher molecular weight compounds with masses exceeding 100 u., present in the gas and ice grains (Waite et al., 2009). Most of the erupted ice grains contain significant amounts of sodium and potassium salts (about 1%) indicating that salt water plays an important part as a plume source (Postberg et al., 2009, 2011), which suggests contact with Enceladus' rocky core. The ice grains also carry tiny silicate particles that may have previously floated in the liquid (Hsu et al., 2011). The total heat emission at the south polar Tiger Stripes is at least 5 GW (possibly up to 15 GW, Howett et al., 2011), and in some of the hot spots where jets emanate, the surface temperatures are estimated to exceed 200 K (Spencer et al., 2011). Such enormous heat output, associated with liquid water in contact with rocks, favors prebiotic processes, providing both an energy source and mineral surfaces for catalyzing chemical reactions.

The low molecular weight organics detected by Cassini may be just one part of a suite of organics present in the plume and on the surface. Studies of the nature of these organics could tell us whether or not they are biogenic. The molecular species likely to be produced by such a prebiotic or biotic chemistry – such as amino acids, heterocyclic bases, lipidic compounds and sugars – could be detected in the plume of Enceladus using in situ techniques. It is also crucial to confirm the presence of liquid water reservoirs and to constrain their composition, both by remote sensing and in situ measurements.

4.5. Summary of science questions, investigations and key measurements relevant for Goals A, B and C

Tables 1–3 summarize the different key questions and the corresponding investigations that should be addressed by a future Large-class mission for the three main science goals. The measurements, both from orbit and in situ from a balloon, required to address these scientific objectives are listed in Tables 4–6. Further details on the mission concepts and relevant instruments are provided in Section 7.

5. Mission concept

5.1. Previous mission concepts for post-Cassini–Huygens exploration of Titan and Enceladus

Future exploration of the Saturnian system with a focus on Titan and Enceladus has been considered for quite some time, almost since the first years of the Cassini–Huygens mission. Early discoveries by Cassini–Huygens at Titan and Enceladus (discussed

Table 1
Summary of science questions, investigations and key measurements relevant for Goal A.

A: Titan as an Earth-like system	Saturn–Titan Orbiter	Titan Balloon
How does Titan's methane cycle vary with season?	Cloud distribution, lake changes [A-1, A-2]	Rain, surface evaporation, detailed cloud activity [A-12, A-13]
How does Titan's global circulation vary with season?	Cloud tracking, Doppler and thermal winds [A-2, A-3]	Balloon tracking, tropospheric winds [A-14]
What is Titan's atmospheric temperature structure and how does this influence atmospheric escape, photochemistry, and haze production?	In situ upper atmosphere, remote sensing, occultations [A-3, A-4, A-5]	Tropospheric temperatures, condensation processes [A-12]
How are hazes distributed globally and seasonally? What causes the detached haze layer?	Imaging, spectroscopy, middle atmosphere distribution/composition [A-2, A-4]	Tropospheric hazes distribution and composition [A-13]
What is the composition of Titan's atmosphere? How does it change over seasonal timescales?	Global spectroscopy, in situ upper atmosphere [A-3, A-4]	High precision in situ gas and isotopes [A-12]
How old is Titan's surface? What erosional processes are currently active on Titan?	High resolution imaging of craters, aeolian, fluvial and glacial features, surface changes [A-6, A-7, A-8, A-9]	Very high resolution surface imaging: morphology and activity [A-15, A-16, A-17, A-18]
What are the properties of Titan's lakes (composition, waves)? How do they vary over seasonal and geological timescales?	Distribution, seasonal change, lake depths [A-1, A-8, A-9]	Shoreline imaging, lake clouds, dry lakebeds [A-15, A-16, A-17]
What is the composition of Titan's surface and how does it interact with the atmosphere and subsurface?	High-resolution global spectroscopy, hydrocarbon deposits [A-6, A-7, A-9]	Very high spatial resolution spectroscopy, deposits [A-16, A-17]
Are cryovolcanic and tectonic processes currently active on Titan? Have these endogenic processes been active in the past?	Cryovolcanic and tectonic features [A-6, A-7, A-8, A-9]	Very high spatial resolution imaging: morphology, activity [A-15, A-16, A-17, A-18]
What is the origin of Titan's atmosphere? How has it evolved since its formation? What is the resupply process of methane?	Isotopic ratio, noble gas, atmospheric escape [A-4]	Isotopic ratios, noble gases [A-1, A-18]
What is Titan's internal structure? What are the properties of any internal ocean and of the icy shell?	Gravity, topography, spin state, magnetic field [A-10, A-11]	Electric field [A-19]

Retour à la table des matières : p. v

Table 2
Summary of science questions, investigations and key measurements relevant for Goal B.

B: Enceladus as an active cryovolcanic moon	Saturn–Titan Orbiter	Titan Balloon
What is the composition of Enceladus' plume and what implications does this have for origin of the Saturn system icy moons?	In situ gas and ice grain sampling, occultations: organic compounds, noble gases, isotopic ratios [B-1, B-2, B-3]	–
What are the characteristics of the plume source region and origin of the plume salts?	Thermal/visible imaging, in situ ice grain sampling, subsurface sounding, time variability [B-2, B-3, B-9, B-10]	–
What dust–plasma interactions occur within the plume? How does the plume interact with Saturn's magnetosphere?	In situ sampling, occultation, magnetic field, plasma [B-1, B-2, B-3, B-13]	–
What processes drive the surface and plume activities and is this a long-lived or transient phenomenon?	Heat flow, tectonic morphology and distribution, change in plume activity [B-4, B-5, B-6, B-7, B-8, B-9, B-10]	–
What are the internal structure and properties of any internal ocean? How is this coupled to the ice shell and the rocky core?	Gravity, topography, spin state, magnetic field, orbital dynamics [B-11, B-12, B-13]	–

Table 3
Summary of science questions, investigations and key measurements relevant for Goal C.

C: Chemistry of Titan and Enceladus – clues to the origin of life	Saturn–Titan Orbiter	Titan Balloon
What are the compositions of the heavy ions and neutrals found in Titan's upper atmosphere?	In situ mass spectrometry [C-1]	–
What is the composition of Titan's haze? Are there variations in composition with altitude, latitude and/or season?	Spectroscopy/in situ of haze forming and intermediate regions [C-2]	In situ analysis of aerosols in the troposphere [C-10]
How do organic compounds evolve on Titan's surface? Do these compounds interact with liquid water in cryovolcanic or impact sites?	Global spectroscopy, subsurface sounding [C-3, C-4, C-5]	Very high spatial resolution spectral imaging, surface sampling, subsurface sounding [C-11, C-12, C-13, C-14]
What is the nature of Enceladus' chemistry? Does the plume contain complex molecules of astrobiological interest?	in situ gas and grain sampling, surface mapping [C-6, C-7, C-8]	–
Do water reservoirs exist at shallow depths on Enceladus? How does/did liquid water interact with rocky and/or organic material on Enceladus?	Surface spectral-mapping, geophysics, in situ gas and grain sampling [C-6, C-9]	–

Table 4
Measurement requirements to address the science questions of Goal A.
Goal A: Titan as an Earth-like system

Saturn–Titan Orbiter	Titan Balloon
A-1. Detect seasonally driven surface changes in the methane hydrological cycle, in particular lake-extent	A-12. Determine profiles of T, P, CH_4, C_2H_6 and other organic molecule mole fraction
A-2. Map the formation and dissipation of clouds, and determine their altitude.	A-13. Track cloud motions and determine particle size and properties of clouds and haze
A-3. Determine temperature, wind fields and the abundances of the gaseous + solid constituents in the stratosphere and agnostosphere (500–950 km) versus altitude and latitude, with a goal of detecting seasonally driven changes.	A-14. Determine wind directions in the troposphere and the interaction with the surface in dune fields
A-4. Collect molecular species (ion and neutral) from one pole to the equator, with an altitude goal of 600 km for in situ orbiter measurements at certain points, covering lower altitudes with remote techniques	
A-5. Determine exchange of energy and escape of major volatile species, including H_2, methane and N_2, by comprehensive longitudinal sampling	
A-6. Map at least 80% of the surface to 50 m resolution, in one near-infrared band	A-15. Acquire regional geological maps at 2.5 m resolution and measure regional topography.
A-7. Map the spatial distribution of simple hydrocarbons and important geologic materials	
A-8. Determine the topography by altimetry over 80% of the surface with 10 m vertical resolution	
A-9. Perform the sub-surface sounding (lakes, dunes, crustal layering) with 10-m vertical resolution	A-17. Perform subsurface sounding (with vertical resolution <10 m)
	A-18. Search for methane source and possible cryovolcanic activity
A-10. Determine Titan's gravity field, and its time-variation, with an accuracy of 10^{-9} m s^{-2} at an altitude of 1500 km, and to degree and order 6	
A-11. Characterize magnetic induction and magnetospheric interactions	A-19. Determine electric and magnetic perturbations

above) demonstrated the need for further exploration of the two satellites with a dedicated orbiter, and a balloon for in situ exploration of Titan, with advanced instrumentation specifically adapted for the environments revealed by Cassini–Huygens, and possibly at different seasonal periods. To place our proposed mission concept in this context, previously proposed mission concepts are briefly outlined below.

The Titan explorer (Lorenz et al., 2008a) and the Titan and Enceladus Mission (TandEM Coustenis et al., 2009) concepts had been selected respectively by NASA and ESA for studies before they were merged into the joint large (Flagship) Titan and Saturn System Mission (TSSM) concept, which was extensively studied in 2008 (TSSM report, Reh et al., 2008a,b). TSSM aimed at an in-depth long-term exploration of Titan's atmospheric and surface environment and in situ measurements in one of the Titan's lakes with goals to explore Titan as an Earth-like System, to examine Titan's organic inventory and to explore Enceladus and the coupling and interaction of the two moons with Saturn's magnetosphere. To achieve these goals, a

Retour à la table des matières : p. v

Table 5
Measurement requirements to address the science questions of Goal B.
B: Enceladus as an active cryovolcanic moon

Saturn–Titan Orbiter	Titan Balloon
B-1. Determine the spatial distribution, and possible time variations, of gas compounds in the plume, from in situ sampling and occultation, with at least $M/\Delta M \sim 10,000$ and a detection limit at least 1000-x lower than Cassini	–
B-2. Determine density, as well as velocity and size distribution of the ice grains and their spatial and temporal variations with at least 0.5 km spatial resolution	–
B-3. Determine the mass spectra of ice grains from 1 u. to 500 u. with at least 10-x higher mass resolution and 100-x better spatial resolution than Cassini	–
B-4. Map surface features at global scale with at least 0.5 km spatial resolution.	–
B-5. Map surface composition (water ice, frost, non-water compounds) at 1 km spatial resolution at global scale, and down to 300 m spatial resolution on regional scales	–
B-6. Map surface features at 1 m spatial resolution for selected candidate locations, in particular around the identified jet sources	–
B-7. Acquire regional topography maps of Enceladus' surface with a spatial resolution up to 0.1 km and a vertical resolution of ~10 m	–
B-8. Map the surface temperature distribution in active regions with a precision of 1 K and a spatial resolution of 100 m	–
B-9. Sound the subsurface up to 5 km in depth, at 10 m vertical resolution over the active south pole region	–
B-10. Monitor possible time variations in activity of the jet sources	–
B-11. Determine degree-two gravity field and harmonic amplitudes at precisions of 10-7 of Enceladus' surface gravity	–
B-12. Monitor time variations of the gravity field, spin state and magnetic field	-
B-13. Measure global plasma and magnetic field structure in the vicinity of Enceladus	–

Table 6
Measurement requirements to address the science questions of Goal C.
C: Chemistry of Titan and Enceladus – clues to the origin of life

Saturn–Titan Orbiter	Titan Balloon
C-1. Perform chemical analysis of the ions and neutral, including heavy species (up to several 1000 u.) in Titan's upper atmosphere	
C-2. Perform chemical analysis of the haze particles in Titan's upper atmosphere: search for variations with latitude, altitude and time	C-10. Perform chemical analysis of the haze particles throughout the descent, and determine spatial and temporal variations in the troposphere
C-3. Determine the isotopic composition in major C, H, N, O-bearing species in Titan's atmosphere and Enceladus' plume	C-11. Measure noble gases and C, H, O, N isotopes in gas phases and aerosols
C-4. Quantify the different isotopes of noble gases (Ar, Ne, Kr, Xe) in Titan's atmosphere and Enceladus' plume	
C-5. Determine the infrared spectra of Titan's surface: search for organics of astrobiological interest, and potential correlation with cryovolcanism or impact sites	C-12. Determine the location and the composition of complex organics with a few meter resolution C-13. Identify ammonia, sulfate, inorganic salts and compounds containing phosphorous and other potentially reactive inorganic agents C-14. Determine the thickness of organic deposit (liquid and solid) from subsurface sounding
C-6. Determine the nature of organics and salts contained in the icy grains of Enceladus' plume	
C-7. Search for organics of astrobiological interest in the plume and on the surface near the jet sources	
C-8. Perform chiral analysis of organic compounds and search for potential enantiomeric excess	
C-9. Search for near-surface water reservoir on Enceladus	

dedicated orbiter would have carried two in situ elements: the Titan montgolfière (hot air balloon) and the Titan Lake Lander, each of which would provide complementary data and analyses directly in the atmosphere and on the surface of Titan, and sound its interior. During the Saturn Tour phase, multiple flybys of Enceladus (and possibly of other moons) in addition to Titan would have been performed. The mission would have been launched in the 2023–2025 timeframe on a trajectory using Solar Electric Propulsion (SEP), as well as gravity assists, to arrive ~9 years later for a 4-year mission in the Saturn system. Soon after arrival at Saturn, the montgolfière and Lake Lander would have been delivered to Titan. The three TSSM elements would have operated as follows:

- The orbiter, powered by MMRTGs (Multi-Mission Radioisotope Thermal Generators), would have performed seven close-up Enceladus flybys and then enter into orbit around Titan for 2 years of dedicated observations.
- The montgolfière would have studied both Titan's atmosphere and surface from above the equator at low altitude (~ 10 km) for at least 6 months using MMRTGs.
- The Lake Lander would have performed the first extraterrestrial oceanographic experiment by landing in one of the Titan's seas, the Kraken Mare, located at approximately 75°N.

This mission was ranked second in the final decision by the agencies and was not considered for further study. It has, however, inspired several other proposed concepts for smaller size missions:

- Titan Aerial Explorer (TAE) was an M3 candidate for ESA's Cosmic Vision call (Lunine et al., 2011). TAE was a pressurized balloon, which was planned to fly in the lower atmosphere of Titan at an altitude of 8 km for 3–6 months over Titan's equatorial latitudes, with direct to Earth transmission and no need for an orbiter to relay data.
- The Aerial Vehicle for in situ and Airborne Titan Reconnaissance (AVIATR) was an alternative idea to the Titan balloon. In Titan's low gravity and a dense atmosphere, an ASRG (Advanced Stirling Radioisotope Generator) powered airplane could fly more easily than on Earth and could sample directly

Retour à la table des matières : p. v

the atmosphere over large swaths of Titan's surface (Barnes et al., 2012).

- The Titan Mare Explorer (TiME), a Discovery candidate, was a probe focusing on exploring Titan's lakes by landing in and floating across Ligeia mare. This lander was designed to study the chemical composition, wave and geological characteristics of the lakes (Stofan et al., 2010). A similar idea was the Titan Lake Probe, which included a submarine concept (Waite et al., 2010).
- The Journey to Enceladus and Titan (JET) was a Discovery candidate Saturn orbiter with only two instruments and radio science that would explore the plume of Enceladus and the atmosphere and surface of Titan (Sotin et al., 2011).

5.2. Mission concept involving a Saturn–Titan-Orbiter and a Titan-Balloon for the exploration of Titan and Enceladus

The mission concept described below was proposed in response to the ESA call for the definition of the science themes of the next L-class mission (L2/L3), after the L1 JUICE mission. This mission concept is inspired from the ambitious TSSM concept, which included three elements (one orbiter and two in situ elements as mentioned above). We describe here a mission concept involving only two elements (Saturn–Titan Orbiter and Titan Balloon, Fig. 5). Note that a mission concept involving an orbiter and a lake probe is described in a companion paper by Mitri et al., 2014).

5.2.1. Mission scenario and elements

For the L2 and L3 launch opportunities, the duration of the cruise from Earth to Saturn were estimated at 8–10 years. Following the mission scenario of TSSM, on arrival at Saturn, the Saturn–Titan orbiter would deliver the Titan balloon, perform a Saturn Tour Phase of about 2 years with multiple flybys of Titan and Enceladus (and possibly of other moons), and finally be captured around Titan at the end of the Saturn Tour Phase in an elliptical orbit (700 km periapsis to 15,000 km apoapsis) followed by a 2-month aero-breaking phase. This aero-breaking phase would enable the exploration of a poorly known, but chemically critical, part of the atmosphere (700–800 km), with in situ atmospheric sampling at altitudes much lower than possible with Cassini. Following the aero-breaking phase, the orbiter would be placed into a circular 1500 km, near-polar orbit, for the orbital science phase. This orbit allows detailed mapping of all latitudes with high temporal resolutions. The resulting complete global coverage would provide a substantial increase in our understanding of Titan's climatic system and allow global access to all types of surface terrain, atmospheric phenomena, and upper atmosphere interactions.

The Saturn Tour Phase would be optimized for Enceladus science via numerous flybys targeted over Enceladus' southern plumes and geological features, or potentially other ancient active regions elsewhere on the moon. Additionally, the Saturn Tour Phase would allow direct in situ study of the possible transport of (organic) material between Enceladus and Titan, and indirectly to other parts of the Saturnian system.

The Titan balloon would be deployed during the first Titan flyby. Data would be transmitted to the orbiter via a steerable high gain antenna, for relay to Earth. Direct-to-Earth transmission may also be considered, which would be more convenient during the Saturn Tour Phase. A balloon provides an ideal platform for studying Titan's lower atmosphere in detail (e.g. Lorenz et al., 2008b). Penetrating the thick atmosphere to sound the troposphere and surface from orbit is extremely difficult otherwise. The balloon would be able to sample multiple altitudes in the 1–10 km range and by using Titan's winds and global circulation pattern could systematically cover many different latitudes and terrain types. Extremely high-resolution surface imaging could be performed, and the chemical composition of the aerosols and atmospheric gases could be directly sampled. Such measurements would be invaluable for interpreting orbital data, studying evolution of the atmosphere, and determining haze composition and the extent of the complex organic chemistry. Titan's low gravity and thick atmosphere make it an ideal candidate for a balloon-based mission.

5.2.2. Strawman instrument payload

Table 7 presents a tentative payload that would address the required measurements presented in Tables 4–6 for the science goals A, B, and C. The proposed instruments will benefit from the heritage of previously successful missions such as Cassini–Huygens as well as new missions currently under study (such as JUICE).

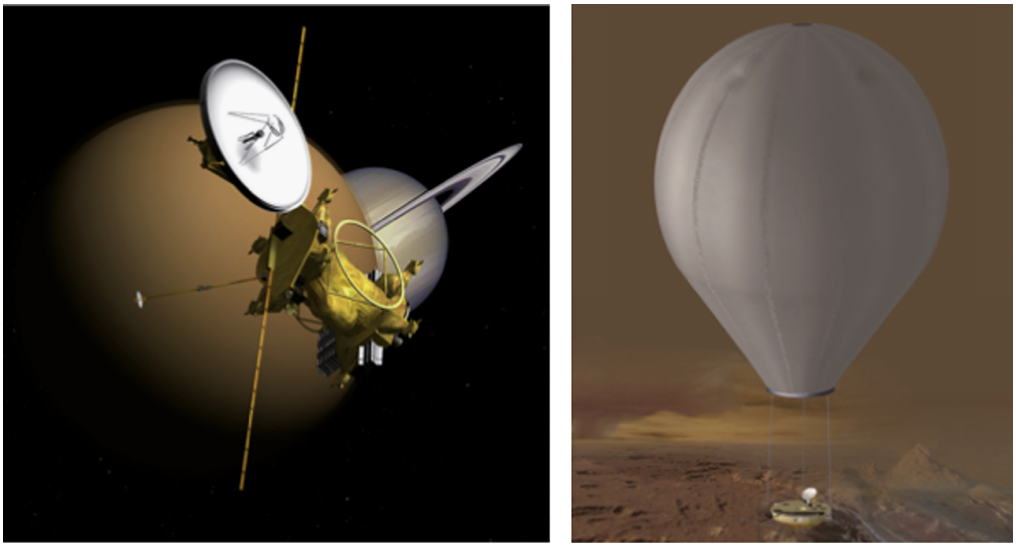

Fig. 5. Concepts of orbiter and hot air balloon considered for TSSM (Reh et al., 2009a).

Retour à la table des matières : p. v

5.2.3. Critical issues and technological developments

Beyond Jupiter, a critical issue concerns the power source. At Saturn, solar power is very low and a long-term exploration mission as proposed here requires the use of radioisotope power sources. In the TSSM concept, MMRTGs or ASRGs using ^{238}Pu were considered and were to be provided by NASA. The developments of ASRGs have now been abandoned by NASA and the amount of available ^{238}Pu is now reduced. Within Europe, the radioisotope ^{241}Am is considered a feasible alternative to ^{238}Pu and can provide a heat source for small-scale radioisotope thermoelectric generators (RTGs) and radioisotope heating units (RHUs) (Tinsley et al., 2011). About 1000 kg of ^{241}Am exists in an isotopically pure state within stored civil plutonium at reprocessing sites within the UK and France. A study is underway to design a process that will chemically separate ^{241}Am (Sarsfield et al., 2012). The development of ^{241}Am-based RTGs is under consideration by ESA and the first RTGs at high TRL may be available in about one decade.

Following the TSSM pre-selection in 2008, a feasibility study by CNES and JPL was initiated in order to optimize the design of a hot air balloon under Titan's conditions. The assessment was based on ^{238}Pu-RTGs, which, in addition to providing electric power, were the heat source for generating buoyancy of the balloon. The possible use of ^{241}Am-RTGs, which provide 20% less decay heat per unit mass, will require further assessment of the feasibility. A pressurized air balloon, as proposed in the TAE project, may also be considered as an alternative. A detailed comparison between the different approaches will be needed to determine the best option for in situ exploration of Titan's atmosphere. Instrumenting the balloon heat shield with abasic seismometer and possibly other lightweight instruments that would sit at the surface after landing was also considered in TSSM. Such options would require further study to evaluate their feasibility and utility. International collaboration, in the same spirit that what was done during the TSSM study, will be crucial to assess the feasibility of such mission and to develop the different elements needed to make such a mission successful.

6. Conclusion and perspectives

Titan and Enceladus are two extraordinary planetary objects, which the Cassini–Huygens mission have just started to unveil. In situ investigations of the two moons from orbit, and of Titan from an aerial platform, will provide a unique opportunity to solve several key questions that will remain unanswered by the Cassini–Huygens mission:

- What is the chemical composition of Titan's aerosols?
- What are the dynamics of Titan's troposphere, and how does it affect the surface evolution?
- How do organic compounds evolve on Titan's surface, in lakes and in ice-rich regions?
- What processes drive the surface and plume activities on Enceladus?
- Does the plume contain complex molecules of astrobiological interest?

Most of these key questions can be addressed by the suite of instruments and measurements in the proposed mission concept. Sampling of Enceladus' plumes and remote sensing observations during successive close flybys before insertion around Titan will provide key data on the plume composition and its sources. For Titan, the orbiter will provide a global coverage which is essential to map the surface as well as the atmosphere dynamics and composition, and it will allow a direct sampling of the upper atmosphere during aerobreaking phases. The Titan balloon will provide crucial information inaccessible from the orbit by monitoring the troposphere dynamics and composition (aerosol and gas). It will be an ideal platform to acquire very high resolution images, offering spectacular views of the surface with unprecedented details all around the equatorial band, not only at a single location like Huygens. This mission concept will, however, address only partially the questions of lake and surface composition as no direct sampling of the surface is proposed. The composition will be addressed only from remote sensing data. Detailed determination of the lake composition requires a dedicated probe as described in Mitri et al., (2014). Ideally, a mission concept involving two in situ elements in addition to an orbiter, provided by several space agencies as proposed for TSSM, will be needed to fully address the main science questions highlighted here.

Although Titan, Enceladus and the Saturn system were not chosen as the science theme for the next ESA L-class missions (after JUICE), strong support from the scientific community clearly showed that the exploration of these two moons is a high-priority challenge in the future exploration of the Solar system. Many ideas for future exploration missions are now blooming. Although some key objectives may be addressed by medium-size “reconnaissance” missions (Discovery-class, Medium-class missions), an in-depth exploration of these moons will require a large and ambitious mission, involving a strong international cooperation in the same spirit that led to the highly successful Cassini–Huygens mission. A major goal for the next decade is to prepare for such an ambitious project by continuing to strengthen international collaboration among scientists and by convincing space agencies that international cooperation is the best way forward for future exploration of Titan and Enceladus, and more generally of the Outer Solar System.

To prepare for future exploration of Titan and Enceladus, a series of studies involving observations, instrumental development, laboratory experiments and theoretical modeling are needed. For Titan, a major objective for the future is to fully characterize the chemical composition and structure of atmospheric aerosols, and if possible at different altitudes. This requires the development of devices for collecting and analyzing aerosols from an aerial platform. Laboratory experiments on organic materials analogous to Titan's aerosols are needed to prepare

Table 7
Tentative instrument payload to address the three mission Goals A, B and C. The checkmarks indicate for each instrument the goal it can address.

Saturn–Titan Orbiter	A	B	C	Titan Balloon	A	B	C
1. High-resolution imager (2, 2.7, 5–6 μm) and Spectrometer (0.85–2.4/4.8–5.8 μm)	✓	✓	✓	1. Visual imaging system (two wide angle stereo cameras and one narrow angle camera)	✓		✓
2. Penetrating radar and altimeter (> 20 MHz)	✓	✓	✓	2. Imaging spectrometer (1–5.6 ~ μm)	✓		✓
3. Thermal Infrared Spectrometer (7–333 μm)	✓	✓	✓	3. Atmospheric structure instrument and meteorological package	✓		
4. High resolution mass spectrometer (up to 10,000 u.)	✓	✓	✓	4. Electric environment package	✓		✓
5. Icy grain and organic dust analyzer	✓	✓	✓	5. Radar sounder (> 150 MHz)	✓		✓
6. Plasma suite	✓	✓	✓	6. Gas chromatograph mass spectrometer (1–600 u.)	✓		✓
7. Magnetometer	✓	✓	✓	7. Radio science using spacecraft telecom system	✓		✓
8. Radio Science Experiment	✓	✓	✓	8. Magnetometer	✓		✓
9. Sub-millimetre heterodyne	✓	✓	✓				
10. UV spectrometer	✓	✓	✓				

Retour à la table des matières : p. v

for their future in situ analysis and to anticipate the best instrumental strategy to determine their complex composition. More generally, laboratory studies on materials analogous to what is expected on Titan's surface (solid and liquid organics, hydrates, ices) are needed to determine their spectral, dielectric, thermo-mechanical properties, as well as their possible interactions with the atmosphere, through wind transport and evaporation/condensation/dissolution processes. Spectroscopic measurements of complex atmospheric gaseous and condensed ice-phase organics are also lacking, and will be essential for implementation of remote sensing measurements of their global distribution. Such measurements will allow evolution pathways to Titan's aerosols to be further constrained. Even though not directly mentioned in the present mission concept, possible collection of surface samples and onboard analysis could be envisioned. Here again, different analytical techniques should be tested and validated. Modeling of the atmosphere structure and dynamics, especially in the troposphere, for future balloon navigations is required. In addition a better understanding of the upper part of the atmosphere is needed to enable the potential future aero-sampling from an orbiter.

For Enceladus, one of the major objectives is to detect complex molecules in both the gas and the solid phase of the plume. Measurements performed by Cassini/INMS (Waite et al., 2011) indicated that, for elevated flyby velocities, collision processes with the instrument chamber can dissociate organic macromolecules and affect the determination of plume composition. Future investigations are needed to understand how complex organics may be sampled and analyzed during close flybys. Modeling efforts are also needed to better understand the connection between the jet and surface activities and to identify measurements that will allow the identification of the controlling mechanisms.

Support from national agencies will be essential in developing the new generation of highly capable instrumentation, as well as in pursuing experimental and modeling efforts initiated with Cassini-Huygens, in order to be ready for the next rendezvous with Titan and Enceladus.

Acknowledgments

The research leading to these results has received funding from the European Research Council under the European Community's Seventh Framework Programme (FP7/2007–2013 Grant agreement no. 259285), UK Science and Technology Facilities Council, Leverhulme Trust and CNES.

Appendix A. Supplementary data

Supplementary data associated with this article can be found in the online version at http://dx.doi.org/10.1016/j.pss.2014.10.002.

References

Achterberg, R.K., Conrath, B.J., Gierasch, P.J., Flasar, F.M., Nixon, C.A., 2008. Observation of a tilt of Titan's middle-atmospheric superrotation. Icarus 197, 549–555.
Artemieva, N., Lunine, J., 2003. Cratering on Titan: impact melt, ejecta, and the fate of surface organics. Icarus 164, 471–480.
Baland, R.M., Tobie, G., Lefèvre, A., Van Hoolst, T., 2014. Titan's internal structure inferred from its gravity field, shape, and rotation state. Icarus 237, 29–41.
Baland, R.M., van Hoolst, T., Yseboodt, M., Karatekin, Ö., 2011. Titan's obliquity as evidence of a subsurface ocean? Astron. Astrophys. 530, A141.
Barnes, J.W., Bow, J., Schwartz, J., Brown, R.H., Soderblom, J.M., Hayes, A.G., Vixie, G., Le Mouélic, S., Rodriguez, S., Sotin, C., Jaumann, R., Stephan, K., Soderblom, L.A., Clark, R.N., Buratti, B.J., Baines, K.H., Nicholson, P.D., 2011. Organic sedimentary deposits in Titan's dry lakebeds: probable evaporite. Icarus 216, 136–140.
Barnes, J.W., Lemke, L., Foch, R., McKay, C.P., Beyer, R.A., Radebaugh, J., Atkinson, D.H., Lorenz, R.D., Le Mouélic, S., Rodriguez, S., Gundlach, J., Giannini, F., Bain, S., Flasar, F.M., Hurford, T., Anderson, C.M., Merrison, J., Ádámkovics, M., Kattenhorn, S.A., Mitchell, J., Burr, D.M., Colaprete, A., Schaller, E., Friedson, A.J., Edgett, K.S., Coradini, A., Adriani, A., Sayanagi, K.M., Malaska, M.J., Morabito, D., Reh, K., 2012. AVIATR—aerial vehicle for in-situ and airborne Titan Reconnaissance. A Titan airplane mission concept. Exp. Astron. 33, 55–127.
Béghin, C., Randriamboarison, O., Hamelin, M., Karkoschka, E., Sotin, C., Whitten, R.C., Berthelier, J.J., Grard, R., Simões, F., 2012. Analytic theory of Titan's Schumann resonance: constraints on ionospheric conductivity and buried water ocean. Icarus 218, 1028–1042.
Bell, J.M., Hunter Waite, J., Westlake, J.H., Bougher, S.W., Ridley, A.J., Perryman, R., Mandt, K., 2014. Developing a self-consistent description of Titan's upper atmosphere without hydrodynamic escape. J. Geophys. Res. (Space Phys.) 119, 4957–4972.
Bézard, B., Yelle, R.V., Nixon, C.A., 2014. The composition of Titans atmosphere. In: Müller-Wodarg, I., Griffith, C.A., Lellouch, E., Cravens, T.E. (Eds.), Titan: Interior, Surface, Atmosphere, and Space Environment. Cambridge University Press, Cambridge, pp. 158–189.
Bird, M.K., Allison, M., Asmar, S.W., Atkinson, D.H., Avruch, I.M., Dutta-Roy, R., Dzierma, Y., Edenhofer, P., Folkner, W.M., Gurvits, L.I., Johnston, D.V., Plettemeier, D., Pogrebenko, S.V., Preston, R.A., Tyler, G.L., 2005. The vertical profile of winds on Titan. Nature 438, 800–802.
Brandt, P.C., Dialynas, K., Dandouras, I., Mitchell, D.G., Garnier, P., Krimigis, S.M., 2012. The distribution of Titańs high-altitude (out to 50,000 km) exosphere from energetic neutral atom (ena) measurements by Cassini/inca. Plan. Space Sci. 60, 107–114.
Brown, R.H., Johnson, T.V., Kirk, R.L., Soderblom, L.A., 1990. Energy sources for Triton's geyser-like plumes. Science 250, 431–435.
Brown, R.H., Soderblom, L.A., Soderblom, J.M., Clark, R.N., Jaumann, R., Barnes, J.W., Sotin, C., Buratti, B., Baines, K.H., Nicholson, P.D., 2008. The identification of liquid ethane in Titan's Ontario Lacus. Nature 454, 607–610.
Burger, M.H., Sittler, E.C., Johnson, R.E., Smith, H.T., Tucker, O.J., Shematovich, V.I., 2007. Understanding the escape of water from Enceladus. J. Geophys. Res. 112, 6219.
Cable, M.L., Hörst, S.M., Hodyss, R., Beauchamp, P.M., Smith, M.A., Willis, P.A., 2012. Titan tholins: simulating Titan organic chemistry in the Cassini–Huygens era. Chem. Rev. 112, 1882–1909.
Coates, A.J., 2009. Interaction of Titan's ionosphere with Saturn's magnetosphere. Phil. Trans. R. Soc. Lond. A 367, 773–788.
Coates, A.J., Crary, F.J., Lewis, G.R., Young, D.T., Waite, J.H., Sittler, E.C., 2007. Discovery of heavy negative ions in Titan's ionosphere. Geophys. Res. Lett. 34, 22103.
Coates, A.J., Wellbrock, A., Lewis, G.R., Jones, G.H., Young, D.T., Crary, F.J., Waite, J.H., Johnson, R.E., Hill, T.W., Sittler Jr., E.C., 2010. Negative ions at Titan and Enceladus: recent results. Faraday Discuss. 147, 293–305.
Coll, P., Navarro-González, R., Szopa, C., Poch, O., Ramírez, S.I., Coscia, D., Raulin, F., Cabane, M., Buch, A., Israël, G., 2013. Can laboratory tholins mimic the chemistry producing Titan's aerosols? A review in light of ACP experimental results. Plan. Space Sci. 77, 91–103.
Cordier, D., Mousis, O., Lunine, J.I., Lebonnois, S., Rannou, P., Lavvas, P., Lobo, L.Q., Ferreira, A.G.M., 2012. Titan's lakes chemical composition: sources of uncertainties and variability. Plan. Space Sci. 61, 99–107.
Cornet, T., Bourgeois, O., Le Mouélic, S., Rodriguez, S., Lopez Gonzalez, T., Sotin, C., Tobie, G., Fleurant, C., Barnes, J.W., Brown, R.H., Baines, K.H., Buratti, B.J., Clark, R.N., Nicholson, P.D., 2012. Geomorphological significance of Ontario lacus on titan: integrated interpretation of Cassini vims, iss and radar data and comparison with the etosha pan (namibia). Icarus 218, 788–806.
Cours, T., Burgalat, J., Rannou, P., Rodriguez, S., Brahic, A., West, R.A., 2011. Dual origin of aerosols in Titan's detached Haze layer. Astrophys. J. Lett. 741, L32.
Coustenis, A., Achterberg, R.K., Conrath, B.J., Jennings, D.E., Marten, A., Gautier, D., Nixon, C.A., Flasar, F.M., Teanby, N.A., Bézard, B., Samuelson, R.E., Carlson, R.C., Lellouch, E., Bjoraker, G.L., Romani, P.N., Taylor, F.W., Irwin, P.G.J., Fouchet, T., Hubert, A., Orton, G.S., Kunde, V.G., Vinatier, S., Mondellini, J., Abbas, M.M., Courtin, R., 2007. The composition of Titan's stratosphere from Cassini/CIRS mid-infrared spectra. Icarus 189, 35–62.
Coustenis, A., Atreya, S.K., Balint, T., Brown, R.H., Dougherty, M.K., Ferri, F., Fulchignoni, M., Gautier, D., Gowen, R.A., Griffith, C.A., Gurvits, L.I., Jaumann, R., Langevin, Y., Leese, M.R., Lunine, J.I., McKay, C.P., Moussas, X., Müller-Wodarg, I., Neubauer, F., Owen, T.C., Raulin, F., Sittler, E.C., Sohl, F., Sotin, C., Tobie, G., Tokano, T., Turtle, E.P., Wahlund, J.E., Waite, J.H., Baines, K.H., Blamont, J., Coates, A.J., Dandouras, I., Krimigis, T., Lellouch, E., Lorenz, R.D., Morse, A., Porco, C.C., Hirtzig, M., Saur, J., Spilker, T., Zarnecki, J.C., Choi, E., Achilleos, N., Amils, R., Annan, P., Atkinson, D.H., Bénilan, Y., Bertucci, C., Bézard, B., Bjoraker, G.L., Blanc, M., Boireau, L., Bouman, J., Cabane, M., Capria, M.T., Chassefière, E., Coll, P., Combes, M., Cooper, J.F., Coradini, A., Crary, F., Cravens, T., Daglis, I.A., de Angelis, E., de Bergh, C., de Pater, I., Dunford, C., Durry, G., Dutuit, O., Fairbrother, D., Flasar, F.M., Fortes, A.D., Frampton, R., Fujimoto, M., Galand, M., Grasset, O., Grott, M., Haltigin, T., Herique, A., Hersant, F., Hussmann, H., Ip, W., Johnson, R., Kallio, E., Kempf, S., Knapmeyer, M., Kofman, W., Koop, R., Kostiuk, T., Krupp, N., Küppers, M., Lammer, H., Lara, L.M., Lavvas, P., Le Mouélic, S., Lebonnois, S., Ledvina, S., Li, J., Livengood, T.A., Lopes, R.M., Lopez-Moreno, J.J., Luz, D., Mahaffy, P.R., Mall, U., Martinez-Frias, J., Marty, B., McCord, T., Menor Salvan, C., Milillo, A., Mitchell, D.G., Modolo, R., Mousis, O., Nakamura, M., Neish, C.D., Nixon, C.A., Nna Mvondo, D., Orton, G., Paetzold, M., Pitman, J., Pogrebenko, S., Pollard, W., Prieto-Ballesteros, O., Rannou, P., Reh, K., Richter, L., Robb, F.T., Rodrigo, R., Rodriguez, S., Romani, P., Ruiz Bermejo, M., Sarris, E.T., Schenk, P., Schmitt, B., Schmitz, N., Schulze-Makuch, D., Schwingenschuh, K., Selig, A., Sicardy, B., Soderblom, L., Spilker, L.J., Stam, D., Steele, A., Stephan, K., Strobel, D.F., Szego, K., Szopa, C., Thissen, R., Tomasko, M.G., Toublanc, D., Vali, H., Vardavas, I., Vuitton, V., West, R.A., Yelle, R., Young, E.F., 2009. TandEM: Titan and Enceladus mission. Exp. Astron. 23, 893–946.

Retour à la table des matières : p. v

Coustenis, A., Hirtzig, M., Gendron, E., Drossart, P., Lai, O., Combes, M., Negrão, A., 2005. Maps of Titan's surface from 1 to 2.5 μm. Icarus 177, 89–105.

Coustenis, A., Jennings, D.E., Nixon, C.A., Achterberg, R.K., Lavvas, P., Vinatier, S., Teanby, N.A., Bjoraker, G.L., Carlson, R.C., Piani, L., Bampasidis, G., Flasar, F.M., Romani, P.N., 2010. Titan trace gaseous composition from CIRS at the end of the Cassini–Huygens prime mission. Icarus 207, 461–476.

Crary, F.J., Magee, B.A., Mandt, K., Waite, J.H., Westlake, J., Young, D.T., 2009. Heavy ions, temperatures and winds in Titan's ionosphere: combined Cassini CAPS and INMS observations. Plan. Space Sci. 57, 1847–1856.

Crow-Willard, E.N., Pappalardo, R.T., 2010. Global geological mapping of Enceladus. In: Lunar and Planetary Institute Science Conference Abstracts, p. 2715.

Dougherty, M.K., Khurana, K.K., Neubauer, F.M., Russell, C.T., Saur, J., Leisner, J.S., Burton, M.E., 2006. Identification of a dynamic atmosphere at Enceladus with the Cassini magnetometer. Science 311, 1406–1409.

Flasar, F.M., Achterberg, R.K., Conrath, B.J., Gierasch, P.J., Kunde, V.G., Nixon, C.A., Bjoraker, G.L., Jennings, D.E., Romani, P.N., Simon-Miller, A.A., Bézard, B., Coustenis, A., Irwin, P.G.J., Teanby, N.A., Brasunas, J., Pearl, J.C., Segura, M.E., Carlson, R.C., Mamoutkine, A., Schinder, P.J., Barucci, A., Courtin, R., Fouchet, T., Gautier, D., Lellouch, E., Marten, A., Prangé, R., Vinatier, S., Strobel, D.F., Calcutt, S.B., Read, P.L., Taylor, F.W., Bowles, N., Samuelson, R.E., Orton, G.S., Spilker, L.J., Owen, T.C., Spencer, J.R., Showalter, M.R., Ferrari, C., Abbas, M.M., Raulin, F., Edgington, S., Ade, P., Wishnow, E.H., 2005. Titan's atmospheric temperatures, winds, and composition. Science 308, 975–978.

Flasar, F.M., Baines, K.H., Bird, M.K., Tokano, T., West, R.A., 2009. Atmospheric dynamics and meteorology. In: Brown, R.H., Lebreton, J.P., Waite, J.H. (Eds.), Titan from Cassini–Huygens. Springer, New York, pp. 323–352.

Fleshman, B.L., Delamere, P.A., Bagenal, F., 2010. Modeling the Enceladus plume–plasma interaction. Geophys. Res. Lett. 37, 3202.

Fortes, A.D., 2000. Exobiological implications of a possible ammonia–water ocean inside Titan. Icarus 146, 444–452.

Fortes, A.D., Grindrod, P.M., 2006. Modelling of possible mud volcanism on Titan. Icarus 182, 550–558.

Fortes, A.D., Grindrod, P.M., Trickett, S.K., Vočadlo, L., 2007. Ammonium sulfate on Titan: possible origin and role in cryovolcanism. Icarus 188, 139–153.

Fulchignoni, M., Ferri, F., Angrilli, F., Ball, A.J., Bar-Nun, A., Barucci, M.A., Bettanini, C., Bianchini, G., Borucki, W., Colombatti, G., Coradini, M., Coustenis, A., Debei, S., Falkner, P., Fanti, G., Flamini, E., Gaborit, V., Grard, R., Hamelin, M., Harri, A.M., Hathi, B., Jernej, I., Leese, M.R., Lehto, A., Lion Stoppato, P.F., López-Moreno, J.J., Mäkinen, T., McDonnell, J.A.M., McKay, C.P., Molina-Cuberos, G., Neubauer, F.M., Pirronello, V., Rodrigo, R., Saggin, B., Schwingenschuh, K., Seiff, A., Simões, F., Svedhem, H., Tokano, T., Towner, M.C., Trautner, R., Withers, P., Zarnecki, J.C., 2005. In situ measurements of the physical characteristics of Titan's environment. Nature 438, 785–791.

Gautier, T., Carrasco, N., Schmitz-Afonso, I., Touboul, D., Szopa, C., Buch, A., Pernot, P., 2014. Nitrogen incorporation in Titan's tholins inferred by high resolution orbitrap mass spectrometry and gas chromatography–mass spectrometry. Earth Planet. Sci. Lett. 404, 33–42.

Gudipati, M.S., Jacovi, R., Couturier-Tamburelli, I., Lignell, A., Allen, M., 2013. Photochemical activity of Titan's low-altitude condensed haze. Nat. Commun. 4, 1–8.

Hansen, C.J., Esposito, L.W., Stewart, A.I.F., Meinke, B., Wallis, B., Colwell, J.E., Hendrix, A.R., Larsen, K., Pryor, W., Tian, F., 2008. Water vapour jets inside the plume of gas leaving Enceladus. Nature 456, 477–479.

Hansen, C.J., Shemansky, D.E., Esposito, L.W., Stewart, A.I.F., Lewis, B.R., Colwell, J.E., Hendrix, A.R., West, R.A., Waite Jr., J.H., Teolis, B., Magee, B.A., 2011. The composition and structure of the Enceladus plume. Geophys. Res. Lett. 38, 11202.

Hayes, A., Aharonson, O., Callahan, P., Elachi, C., Gim, Y., Kirk, R., Lewis, K., Lopes, R., Lorenz, R., Lunine, J., Mitchell, K., Mitri, G., Stofan, E., Wall, S., 2008. Hydrocarbon lakes on Titan: distribution and interaction with a porous regolith. Geophys. Res. Lett. 35, 9204.

Hedman, M.M., Gosmeyer, C.M., Nicholson, P.D., Sotin, C., Brown, R.H., Clark, R.N., Baines, K.H., Buratti, B.J., Showalter, M.R., 2013. An observed correlation between plume activity and tidal stresses on Enceladus. Nature 500, 182–184.

Hedman, M.M., Nicholson, P.D., Showalter, M.R., Brown, R.H., Buratti, B.J., Clark, R.N., 2009. Spectral observations of the Enceladus plume with Cassini–Vims. Astrophys. J. 693, 1749–1762.

Hemingway, D., Nimmo, F., Zebker, H., Iess, L., 2013. A rigid and weathered ice shell on Titan. Nature 500, 550–552.

Hillier, J.K., Green, S.F., McBride, N., Schwanethal, J.P., Postberg, F., Srama, R., Kempf, S., Moragas-Klostermeyer, G., McDonnell, J.A.M., Grün, E., 2007. The composition of Saturn's E ring. Mon. Not. R. Astron. Soc. 377, 1588–1596.

Hinson, D.P., Tyler, G.L., 1983. Internal gravity-waves in Titan's atmosphere observed by Voyager radio occultation. Icarus 54, 337–352.

Hörst, S.M., Yelle, R.V., Buch, A., Carrasco, N., Cernogora, G., Dutuit, O., Quirico, E., Sciamma-O'Brien, E., Smith, M.A., Somogyi, Á., Szopa, C., Thissen, R., Vuitton, V., 2012. Formation of amino acids and nucleotide bases in a Titan atmosphere simulation experiment. Astrobiology 12, 809–817.

Howett, C.J.A., Spencer, J.R., Pearl, J., Segura, M., 2011. High heat flow from Enceladus' south polar region measured using 10–600 cm^{-1} Cassini/CIRS data. J. Geophys. Res. 116, 3003.

Hsu, H.W., Kempf, S., Postberg, F., Trieloff, M., Burton, M., Roy, M., Moragas-Klostermeyer, G., Srama, R., 2011. Cassini dust stream particle measurements during the first three orbits at Saturn. J. Geophys. Res. 116, 8213.

Hurford, T.A., Helfenstein, P., Spitale, J.N., 2012. Tidal control of jet eruptions on Enceladus as observed by Cassini ISS between 2005 and 2007. Icarus 220, 896–903.

Iess, L., Jacobson, R.A., Ducci, M., Stevenson, D.J., Lunine, J.I., Armstrong, J.W., Asmar, S.W., Racioppa, P., Rappaport, N.J., Tortora, P., 2012. The tides of Titan. Science 337, 457–459.

Iess, L., Stevenson, D.J., Parisi, M., Hemingway, D., Jacobson, R.A., Lunine, J.I., Nimmo, F., Armstrong, J.W., Asmar, S.W., Ducci, M., Tortora, P., 2014. The gravity field and interior structure of Enceladus. Science 344, 78–80.

Ingersoll, A.P., Ewald, S.P., 2011. Total particulate mass in Enceladus plumes and mass of Saturn's E ring inferred from Cassini ISS images. Icarus 216, 492–506.

Israël, G., Szopa, C., Raulin, F., Cabane, M., Niemann, H.B., Atreya, S.K., Bauer, S.J., Brun, J.F., Chassefière, E., Coll, P., Condé, E., Coscia, D., Hauchecorne, A., Millian, P., Nguyen, M.J., Owen, T., Riedler, W., Samuelson, R.E., Siguier, J.M., Steller, M., Sternberg, R., Vidal-Madjar, C., 2005. Complex organic matter in Titan's atmospheric aerosols from in situ pyrolysis and analysis. Nature 438, 796–799.

Jaumann, R., Brown, R.H., Stephan, K., Barnes, J.W., Soderblom, L.A., Sotin, C., Le Mouélic, S., Clark, R.N., Soderblom, J., Buratti, B.J., Wagner, R., McCord, T.B., Rodriguez, S., Baines, K.H., Cruikshank, D.P., Nicholson, P.D., Griffith, C.A., Langhans, M., Lorenz, R.D., 2008. Fluvial erosion and post-erosional processes on Titan. Icarus 197, 526–538.

Jaumann, R., Kirk, R.L., Lorenz, R.D., Lopes, R.M.C., Stofan, E., Turtle, E.P., Keller, H.U., Wood, C.A., Sotin, C., Soderblom, L.A., Tomasko, M., 2009. Geology and surface processes on Titan. In: Brown, R.H., Lebreton, J.P., Waite, J.H. (Eds.), Titan from Cassini–Huygens. Springer, New York, pp. 75–140.

Jia, Y.D., Russell, C.T., Khurana, K.K., Leisner, J.S., Ma, Y.J., Dougherty, M.K., 2010. Time-varying magnetospheric environment near Enceladus as seen by the Cassini magnetometer. Geophys. Res. Lett. 37, 9203.

Jones, G.H., Arridge, C.S., Coates, A.J., Lewis, G.R., Kanani, S., Wellbrock, A., Young, D.T., Crary, F.J., Tokar, R.L., Wilson, R.J., Hill, T.W., Johnson, R.E., Mitchell, D.G., Schmidt, J., Kempf, S., Beckmann, U., Russell, C.T., Jia, Y.D., Dougherty, M.K., Waite, J.H., Magee, B.A., 2009. Fine jet structure of electrically charged grains in Enceladus' plume. Geophys. Res. Lett. 36, 16204.

Keller, H.U., Grieger, B., Küppers, M., Schröder, S.E., Skorov, Y.V., Tomasko, M.G., 2008. The properties of Titan's surface at the Huygens landing site from DISR observations. Plan. & Space Sci. 56, 728–752.

Kempf, S., Beckmann, U., Schmidt, J., 2010. How the Enceladus dust plume feeds Saturn's E ring. Icarus 206, 446–457.

Kirchoff, M.R., Schenk, P., 2009. Crater modification and geologic activity in Enceladus' heavily cratered plains: evidence from the impact crater distribution. Icarus 202, 656–668.

Kirk, R.L., Soderblom, L.A., Brown, R.H., 1990. Subsurface energy storage and transport for solar-powered geysers on Triton. Science 250, 424–429.

Kriegel, H., Simon, S., Motschmann, U., Saur, J., Neubauer, F.M., Persoon, A.M., Dougherty, M.K., Gurnett, D.A., 2011. Influence of negatively charged plume grains on the structure of Enceladus' Alfvén wings: hybrid simulations versus Cassini Magnetometer data. J. Geophys. Res. 116, 10223.

Kriegel, H., Simon, S., Müller, J., Motschmann, U., Saur, J., Glassmeier, K.H., Dougherty, M.K., 2009. The plasma interaction of Enceladus: 3D hybrid simulations and comparison with Cassini MAG data. Plan. Space Sci. 57, 2113–2122.

Langhans, M., Lunine, J.I., Mitri, G., 2013. Titan's Xanadu region: geomorphology and formation scenario. Icarus 223, 796–803.

Langhans, M.H., Jaumann, R., Stephan, K., Brown, R.H., Buratti, B.J., Clark, R.N., Baines, K.H., Nicholson, P.D., Lorenz, R.D., Soderblom, L.A., Soderblom, J.M., Sotin, C., Barnes, J.W., Nelson, R., 2012. Titan's fluvial valleys: morphology, distribution, and spectral properties. Plan. Space Sci. 60, 34–51.

Lavvas, P., Yelle, R.V., Koskinen, T., Bazin, A., Vuitton, V., Vigren, E., Galand, M., Wellbrock, A., Coates, A.J., Wahlund, J.E., Crary, F.J., Snowden, D., 2013. Aerosol growth in Titan's ionosphere. Proc. Natl. Acad. Sci. 110, 2729–2734.

Lavvas, P.P., Coustenis, A., Vardavas, I.M., 2008. Coupling photochemistry with haze formation in Titan's atmosphere, Part I: model description. Plan. Space Sci. 56, 27–66.

Le Mouélic, S., Rannou, P., Rodriguez, S., Sotin, C., Griffith, C.A., Le Corre, L., Barnes, J.W., Brown, R.H., Baines, K.H., Buratti, B.J., Clark, R.N., Nicholson, P.D., Tobie, G., 2012. Dissipation of Titan's north polar cloud at northern spring equinox. Plan. Space Sci. 60, 86–92.

Lefevre, A., Tobie, G., Choblet, G., Čadek, O., 2014. Structure and dynamics of titan's outer icy shell constrained from Cassini data. Icarus 237, 16–28.

Lopes, R.M.C., Kirk, R.L., Mitchell, K.L., Legall, A., Barnes, J.W., Hayes, A., Kargel, J., Wye, L., Radebaugh, J., Stofan, E.R., Janssen, M.A., Neish, C.D., Wall, S.D., Wood, C.A., Lunine, J.I., Malaska, M.J., 2013. Cryovolcanism on Titan: new results from Cassini RADAR and VIMS. J. Geophys. Res. 118, 416–435.

Lopes, R.M.C., Mitchell, K.L., Stofan, E.R., Lunine, J.I., Lorenz, R., Paganelli, F., Kirk, R.L., Wood, C.A., Wall, S.D., Robshaw, L.E., Fortes, A.D., Neish, C.D., Radebaugh, J., Reffet, E., Ostro, S.J., Elachi, C., Allison, M.D., Anderson, Y., Boehmer, R., Boubin, G., Callahan, P., Encrenaz, P., Flamini, E., Francescetti, G., Gim, Y., Hamilton, G., Hensley, S., Janssen, M.A., Johnson, W.T.K., Kelleher, K., Muhleman, D.O., Ori, G., Orosei, R., Picardi, G., Posa, F., Roth, L.E., Seu, R., Shaffer, S., Soderblom, L.A., Stiles, B., Vetrella, S., West, R.D., Wye, L., Zebker, H.A., 2007. Cryovolcanic features on Titan's surface as revealed by the Cassini Titan Radar Mapper. Icarus 186, 395–412.

Lopes, R.M.C., Stofan, E.R., Peckyno, R., Radebaugh, J., Mitchell, K.L., Mitri, G., Wood, C.A., Kirk, R.L., Wall, S.D., Lunine, J.I., Hayes, A., Lorenz, R., Farr, T., Wye, L., Craig, J., Ollerenshaw, R.J., Janssen, M., Legall, A., Paganelli, F., West, R., Stiles, B., Callahan, P., Anderson, Y., Valora, P., Soderblom, L., The Cassini Radar Team, 2010. Distribution and interplay of geologic processes on Titan from Cassini radar data. Icarus 205, 540–558.

Lorenz, R.D., Leary, J.C., Lockwood, M.K., Waite, J.H., 2008a. Titan explorer: a NASA flagship mission concept. In: El-Genk, M.S. (Ed.), Space Technology and Applications International Forum—STAIF 2008, pp. 380–387.

Retour à la table des matières : p. v

Lorenz, R.D., Lopes, R.M., Paganelli, F., Lunine, J.I., Kirk, R.L., Mitchell, K.L., Soderblom, L.A., Stofan, E.R., Ori, G., Myers, M., Miyamoto, H., Radebaugh, J., Stiles, B., Wall, S.D., Wood, C.A., The Cassini Radar Team, 2008. Fluvial channels on Titan: initial Cassini RADAR observations. Plan. Space Sci. 56, 1132–1144.
Lorenz, R.D., Wall, S., Radebaugh, J., Boubin, G., Reffet, E., Janssen, M., Stofan, E., Lopes, R., Kirk, R., Elachi, C., Lunine, J., Mitchell, K., Paganelli, F., Soderblom, L., Wood, C., Wye, L., Zebker, H., Anderson, Y., Ostro, S., Allison, M., Boehmer, R., Callahan, P., Encrenaz, P., Ori, G.G., Francescetti, G., Gim, Y., Hamilton, G., Hensley, S., Johnson, W., Kelleher, K., Muhleman, D., Picardi, G., Posa, F., Roth, L., Seu, R., Shaffer, S., Stiles, B., Vetrella, S., Flamini, E., West, R., 2006. The sand seas of Titan: Cassini RADAR observations of longitudinal dunes. Science 312, 724–727.
Lunine, J., Choukroun, M., Stevenson, D., Tobie, G., 2009. The origin and evolution of Titan. In: Brown, R.H., Lebreton, J.P., Waite, J.H. (Eds.), Titan from Cassini–Huygens. Springer, New York, pp. 35–60.
Lunine, J.I., Reh, K., Sotin, C., Couzin, P., Vargas, A., 2011. Titan aerial explorer: a mission to circumnavigate Titan. In: Lunar and Planetary Institute Science Conference Abstracts, p. 1230.
Mandt, K.E., Waite, J.H., Teolis, B., Magee, B.A., Bell, J., Westlake, J.H., Nixon, C.A., Mousis, O., Lunine, J.I., 2012. The $^{12}C/^{13}C$ ratio on Titan from Cassini INMS measurements and implications for the evolution of methane. Astrophys. J. 749, 160.
Mastrogiuseppe, M., Poggiali, V., Hayes, A., Lorenz, R., Lunine, J., Picardi, G., Seu, R., Flamini, E., Mitri, G., Notarnicola, C., Paillou, P., Zebker, H., 2014. The bathymetry of a Titan sea. Geophys. Res. Lett. 41, 1432–1437.
Matson, D.L., Castillo-Rogez, J.C., Davies, A.G., Johnson, T.V., 2012. Enceladus: a hypothesis for bringing both heat and chemicals to the surface. Icarus 221, 53–62.
McKay, C.P., Porco Carolyn, C., Altheide, T., Davis, W.L., Kral, T.A., 2008. The possible origin and persistence of life on Enceladus and detection of biomarkers in the plume. Astrobiology 8, 909–919.
McKay, C.P., Smith, H.D., 2005. Possibilities for methanogenic life in liquid methane on the surface of Titan. Icarus 178, 274–276.
Mitchell, J.L., Ádámkovics, M., Caballero, R., Turtle, E.P., 2011. Locally enhanced precipitation organized by planetary-scale waves on Titan. Nat. Geosci. 4, 589–592.
Mitri, G., Bland, M.T., Showman, A.P., Radebaugh, J., Stiles, B., Lopes, R.M.C., Lunine, J.I., Pappalardo, R.T., 2010. Mountains on Titan: modeling and observations. J. Geophys. Res. 115, 10002.
Mitri, G., Meriggiola, R., Hayes, A., Lefevre, A., Tobie, G., Genova, A., Lunine, J.I., Zebker, H., 2014. Shape, topography, gravity anomalies and tidal deformation of Titan. Icarus 236, 169–177.
Moore, J.M., Pappalardo, R.T., 2011. Titan: an exogenic world?. Icarus 212, 790–806.
Neish, C.D., Lorenz, R.D., 2012. Titan's global crater population: a new assessment. Plan. Space Sci. 60, 26–33.
Neish, C.D., Lorenz, R.D., 2014. Elevation distribution of Titan's craters suggests extensive wetlands. Icarus 228, 27–34.
Niemann, H.B., Atreya, S.K., Bauer, S.J., Carignan, G.R., Demick, J.E., Frost, R.L., Gautier, D., Haberman, J.A., Harpold, D.N., Hunten, D.M., Israel, G., Lunine, J.I., Kasprzak, W.T., Owen, T.C., Paulkovich, M., Raulin, F., Raaen, E., Way, S.H., 2005. The abundances of constituents of Titan's atmosphere from the GCMS instrument on the Huygens probe. Nature 438, 779–784.
Niemann, H.B., Atreya, S.K., Demick, J.E., Gautier, D., Haberman, J.A., Harpold, D.N., Kasprzak, W.T., Lunine, J.I., Owen, T.C., Raulin, F., 2010. Composition of Titan's lower atmosphere and simple surface volatiles as measured by the Cassini-Huygens probe gas chromatograph mass spectrometer experiment. J. Geophys. Res. 115, 12006.
Nimmo, F., Bills, B.G., 2010. Shell thickness variations and the long-wavelength topography of Titan. Icarus 208, 896–904.
Nimmo, F., Porco, C., Mitchell, C., 2014. Tidally modulated eruptions on Enceladus: Cassini ISS observations and models. Astron. J. 148, 46.
Nimmo, F., Spencer, J.R., Pappalardo, R.T., Mullen, M.E., 2007. Shear heating as the origin of the plumes and heat flux on Enceladus. Nature 447, 289–291.
Nixon, C.A., Achterberg, R.K., Vinatier, S., Bézard, B., Coustenis, A., Irwin, P.G.J., Teanby, N.A., de Kok, R., Romani, P.N., Jennings, D.E., Bjoraker, G.L., Flasar, F.M., 2008. The presup12C/^{13}C isotopic ratio in Titan hydrocarbons from Cassini/CIRS infrared spectra. Icarus 195, 778–791.
Nixon, C.A., Temelso, B., Vinatier, S., Teanby, N.A., Bézard, B., Achterberg, R.K., Mandt, K.E., Sherrill, C.D., Irwin, P.G.J., Jennings, D.E., Romani, P.N., Coustenis, A., Flasar, F.M., 2012. Isotopic ratios in Titan's Methane: measurements and modeling. Astrophys. J. 749, 159.
Norman, L.H., Fortes, A.D., 2011. Is there life on … Titan? Astron. Geophys. 52, 39–42.
Perron, J.T., Lamb, M.P., Koven, C.D., Fung, I.Y., Yager, E., Ádámkovics, M., 2006. Valley formation and methane precipitation rates on Titan. J. Geophys. Res. 111, 11001.
Poch, O., Coll, P., Buch, A., Ramírez, S.I., Raulin, F., 2012. Production yields of organics of astrobiological interest from H_2O-NH_3 hydrolysis of Titan's tholins. Plan. Space Sci. 61, 114–123.
Porco, C., DiNino, D., Nimmo, F., 2014. How the Geysers, tidal stresses, and thermal emission across the South Polar Terrain of Enceladus are related. Astron. J. 148, 45.
Porco, C.C., Baker, E., Barbara, J., Beurle, K., Brahic, A., Burns, J.A., Charnoz, S., Cooper, N., Dawson, D.D., Del Genio, A.D., Denk, T., Dones, L., Dyudina, U., Evans, M.W., Fussner, S., Giese, B., Grazier, K., Helfenstein, P., Ingersoll, A.P., Jacobson, R.A., Johnson, T.V., McEwen, A., Murray, C.D., Neukum, G., Owen, W.M., Perry, J., Roatsch, T., Spitale, J., Squyres, S., Thomas, P., Tiscareno, M., Turtle, E.P., Vasavada, A.R., Veverka, J., Wagner, R., West, R., 2005. Imaging of Titan from the Cassini spacecraft. Nature 434, 159–168.
Porco, C.C., Helfenstein, P., Thomas, P.C., Ingersoll, A.P., Wisdom, J., West, R., Neukum, G., Denk, T., Wagner, R., Roatsch, T., Kieffer, S., Turtle, E., McEwen, A., Johnson, T.V., Rathbun, J., Veverka, J., Wilson, D., Perry, J., Spitale, J., Brahic, A., Burns, J.A., Del Genio, A.D., Dones, L., Murray, C.D., Squyres, S., 2006. Cassini observes the active South Pole of Enceladus. Science 311, 1393–1401.
Postberg, F., Kempf, S., Hillier, J.K., Srama, R., Green, S.F., McBride, N., Grün, E., 2008. The E-ring in the vicinity of Enceladus. II. Probing the moon's interior—the composition of E-ring particles. Icarus 193, 438–454.
Postberg, F., Kempf, S., Schmidt, J., Brilliantov, N., Beinsen, A., Abel, B., Buck, U., Srama, R., 2009. Sodium salts in E-ring ice grains from an ocean below the surface of Enceladus. Nature 459, 1098–1101.
Postberg, F., Schmidt, J., Hillier, J., Kempf, S., Srama, R., 2011. A salt-water reservoir as the source of a compositionally stratified plume on Enceladus. Nature 474, 620–622.
Radebaugh, J., Lorenz, R.D., Kirk, R.L., Lunine, J.I., Stofan, E.R., Lopes, R.M.C., Wall, S.D., the Cassini Radar Team, 2007. Mountains on Titan observed by Cassini Radar. Icarus 192, 77–91.
Radebaugh, J., Lorenz, R.D., Lunine, J.I., Wall, S.D., Boubin, G., Reffet, E., Kirk, R.L., Lopes, R.M., Stofan, E.R., Soderblom, L., Allison, M., Janssen, M., Paillou, P., Callahan, P., Spencer, C., the Cassini Radar Team, 2008. Dunes on Titan observed by Cassini Radar. Icarus 194, 690–703.
Radebaugh, J., Lorenz, R.D., Wall, S.D., Kirk, R.L., Wood, C.A., Lunine, J.I., Stofan, E.R., Lopes, R.M.C., Valora, P., Farr, T.G., Hayes, A., Stiles, B., Mitri, G., Zebker, H., Janssen, M., Wye, L., LeGall, A., Mitchell, K.L., Paganelli, F., West, R.D., Schaller, E.L., Cassini Radar Team, 2011. Regional geomorphology and history of Titan's Xanadu province. Icarus 211, 672–685.
Raulin, F., Brassé, C., Poch, O., Coll, P., 2012. Prebiotic-like chemistry on Titan. Chem. Soc. Rev. 41, 5380–5393.
Reh, F., Erd, C., Matson, D., Coustenis, A., Lunine, J., Lebreton, J.P., The TSSM Joint Definition Team, 2009a. Tssm Final Report on the NASA Contribution to a Joint Mission with ESA, 3 November 2008, jpl d-48148. NASA Task Order, NMO710851.
Reh, F., Erd, C., Matson, D., Coustenis, A., Lunine, J., Lebreton, J.P., The TSSM Joint Definition Team, 2009b. Tssm NASA/ESA Joint Summary Report, 15 November 2008, esa-sre (2008) 3, jpl d-48442. NASA Task Order, NMO710851.
Rodriguez, S., Le Mouélic, S., Rannou, P., Sotin, C., Brown, R.H., Barnes, J.W., Griffith, C.A., Burgalat, J., Baines, K.H., Buratti, B.J., Clark, R.N., Nicholson, P.D., 2011. Titan's cloud seasonal activity from winter to spring with Cassini/VIMS. Icarus 216, 89–110.
Rodriguez, S., Le Mouélic, S., Rannou, P., Tobie, G., Baines, K.H., Barnes, J.W., Griffith, C.A., Hirtzig, M., Pitman, K.M., Sotin, C., Brown, R.H., Buratti, B.J., Clark, R.N., Nicholson, P.D., 2009. Global circulation as the main source of cloud activity on Titan. Nature 459, 678–682.
Roman, M.T., West, R.A., Banfield, D.J., Gierasch, P.J., Achterberg, R.K., Nixon, C.A., Thomas, P.C., 2009. Determining a tilt in Titan's north–south albedo asymmetry from Cassini images. Icarus 203, 242–249.
Roth, L., Saur, J., Retherford, K.D., Strobel, D.F., Feldman, P.D., McGrath, M.A., Nimmo, F., 2014. Transient water vapor at Europa's south pole. Science 343, 171–174.
Sarsfield, M., Bell, K., Maher, C., Carrott, M., Gregson, C., Brown, J., Woodhead, D., Baker, S., Cordingley, L., Taylor, R., Tinsley, T., Rice, T., 2012. A European radioisotope production facility for power sources in space. In: European Nuclear Conference, Manchester, pp. 4–8 (Non-power Industrial Applications).
Schenk, P., Hamilton, D.P., Johnson, R.E., McKinnon, W.B., Paranicas, C., Schmidt, J., Showalter, M.R., 2011. Plasma, plumes and rings: Saturn system dynamics as recorded in global color patterns on its midsize icy satellites. Icarus 211, 740–757.
Schenk, P.M., McKinnon, W.B., 2009. One-hundred-km-scale basins on Enceladus: evidence for an active ice shell. Geophys. Res. Lett. 36, 16202.
Schmidt, J., Brilliantov, N., Spahn, F., Kempf, S., 2008. Slow dust in Enceladus' plume from condensation and wall collisions in tiger stripe fractures. Nature 451, 685–688.
Schulze-Makuch, D., Grinspoon, D.H., 2005. Biologically enhanced energy and carbon cycling on Titan? Astrobiology 5, 560–567.
Sebree, J.A., Trainer, M.G., Loeffler, M.J., Anderson, C.M., 2014. Titan aerosol analog absorption features produced from aromatics in the far infrared. Icarus 236, 146–152.
Shafiq, M., Wahlund, J.E., Morooka, M.W., Kurth, W.S., Farrell, W.M., 2011. Characteristics of the dust–plasma interaction near Enceladus' South Pole. Plan. Space Sci. 59, 17–25.
Shah, M.B., Latimer, C.J., Montenegro, E.C., Tucker, O.J., Johnson, R.E., Smith, H.T., 2009. The Implantation and Interactions of O^+ in Titan's atmosphere: laboratory measurements of collision-induced dissociation of N_2 and modeling of positive ion formation. Astrophys. J. 703, 1947–1954.
Simon, S., Saur, J., Kriegel, H., Neubauer, F.M., Motschmann, U., Dougherty, M.K., 2011. Influence of negatively charged plume grains and hemisphere coupling currents on the structure of Enceladus' Alfvén wings: analytical modeling of Cassini magnetometer observations. J. Geophys. Res. 116, 4221.
Sittler, E.C., Ali, A., Cooper, J.F., Hartle, R.E., Johnson, R.E., Coates, A.J., Young, D.T., 2009. Heavy ion formation in Titan's ionosphere: magnetospheric introduction of free oxygen and a source of Titan's aerosols?. Plan. Space Sci. 57, 1547–1557.
Smith, H.T., Mitchell, D.G., Johnson, R.E., Paranicas, C.P., 2009. Investigation of energetic proton penetration in Titan's atmosphere using the Cassini INCA instrument. Plan. Space Sci. 57, 1538–1546.
Snowden, D., Yelle, R.V., 2014. The thermal structure of Titan's upper atmosphere, II: energetics. Icarus 228, 64–77.

Retour à la table des matières : p. v

Snowden, D., Yelle, R.V., Cui, J., Wahlund, J.E., Edberg, N.J.T., Ågren, K., 2013. The thermal structure of Titan's upper atmosphere, I: temperature profiles from Cassini INMS observations. Icarus 226, 552–582.

Soderblom, J.M., Barnes, J.W., Soderblom, L.A., Brown, R.H., Griffith, C.A., Nicholson, P.D., Stephan, K., Jaumann, R., Sotin, C., Baines, K.H., Buratti, B.J., Clark, R.N., 2012. Modeling specular reflections from hydrocarbon lakes on Titan. Icarus 220, 744–751.

Soderblom, J.M., Brown, R.H., Soderblom, L.A., Barnes, J.W., Jaumann, R., Mouélic, S.L., Sotin, C., Stephan, K., Baines, K.H., Buratti, B.J., Clark, R.N., Nicholson, P.D., 2010. Geology of the Selk crater region on Titan from Cassini VIMS observations. Icarus 208, 905–912.

Soderblom, L.A., Becker, T.L., Kieffer, S.W., Brown, R.H., Hansen, C.J., Johnson, T.V., Kirk, R.L., Shoemaker, E.M., Cook, A.F., 1990. Triton's geyser-like plumes—discovery and basic characterization. Science 250, 410–415.

Soderblom, L.A., Tomasko, M.G., Archinal, B.A., Becker, T.L., Bushroe, M.W., Cook, D.A., Doose, L.R., Galuszka, D.M., Hare, T.M., Howington-Kraus, E., Karkoschka, E., Kirk, R. L., Lunine, J.I., McFarlane, E.A., Redding, B.L., Rizk, B., Rosiek, M.R., See, C., Smith, P. H., 2007. Topography and geomorphology of the Huygens landing site on Titan. Plan. Space Sci. 55, 2015–2024.

Sohl, F., Solomonidou, A., Wagner, F.W., Coustenis, A., Hussmann, H., Schulze-Makuch, D., 2014. Structural and tidal models of Titan and inferences on cryovolcanism. J. Geophys. Res. 119, 1013–1036.

Solomonidou, A., Bampasidis, G., Hirtzig, M., Coustenis, A., Kyriakopoulos, K., St. Seymour, K., Bratsolis, E., Moussas, X., 2013. Morphotectonic features on Titan and their possible origin. Plan. Space Sci. 77, 104–117.

Sotin, C., Altwegg, K., Brown, R.H., Hand, K., Lunine, J.I., Soderblom, J., Spencer, J., Tortora, P., JET Team, 2011. JET: journey to Enceladus and Titan. In: Lunar and Planetary Institute Science Conference Abstracts, p. 1326.

Spahn, F., Schmidt, J., Albers, N., Hörning, M., Makuch, M., Seiß, M., Kempf, S., Srama, R., Dikarev, V., Helfert, S., Moragas-Klostermeyer, G., Krivov, A.V., Sremčević, M., Tuzzolino, A.J., Economou, T., Grün, E., 2006. Cassini dust measurements at Enceladus and implications for the origin of the E ring. Science 311, 1416–1418.

Spencer, J.R., Barr, A.C., Esposito, L.W., Helfenstein, P., Ingersoll, A.P., Jaumann, R., McKay, C.P., Nimmo, F., Waite, J.H., 2009. Enceladus: an active cryovolcanic satellite. In: Dougherty, M.K., Esposito, L.W., Krimigis, S.M. (Eds.), Saturn from Cassini–Huygens. Springer, New York, pp. 683–724.

Spencer, J.R., Howett, C.J.A., Verbiscer, A.J., Hurford, T.A., Segura, M.E., Pearl, J.C., 2011. High-resolution observations of thermal emission from the south pole of Enceladus. In: Lunar and Planetary Institute Science Conference Abstracts, p. 2553.

Spencer, J.R., Nimmo, F., 2013. Enceladus: an active ice world in the saturn system. Ann. Rev. Earth Planet. Sci. 41, 693–717.

Stephan, K., Jaumann, R., Brown, R.H., Soderblom, J.M., Soderblom, L.A., Barnes, J.W., Sotin, C., Griffith, C.A., Kirk, R.L., Baines, K.H., Buratti, B.J., Clark, R.N., Lytle, D.M., Nelson, R.M., Nicholson, P.D., 2010. Specular reflection on Titan: liquids in Kraken Mare. Geophys. Res. Lett. 37, 7104.

Stephan, K., Jaumann, R., Wagner, R., 2013. Geology of icy bodies. In: Gudipati, M.S., Castillo-Rogez, J. (Eds.), The Science of Solar System Ices. Springer, New York, pp. 279–367.

Stofan, E.R., Elachi, C., Lunine, J.I., Lorenz, R.D., Stiles, B., Mitchell, K.L., Ostro, S., Soderblom, L., Wood, C., Zebker, H., Wall, S., Janssen, M., Kirk, R., Lopes, R., Paganelli, F., Radebaugh, J., Wye, L., Anderson, Y., Allison, M., Boehmer, R., Callahan, P., Encrenaz, P., Flamini, E., Francescetti, G., Gim, Y., Hamilton, G., Hensley, S., Johnson, W.T.K., Kelleher, K., Muhleman, D., Paillou, P., Picardi, G., Posa, F., Roth, L., Seu, R., Shaffer, S., Vetrella, S., West, R., 2007. The lakes of Titan. Nature 445, 61–64.

Stofan, E.R., Lunine, J.I., Lorenz, R.D., Aharonson, O., Bierhaus, E., Clark, B., Griffith, C., Harri, A.M., Karkoschka, E., Kirk, R., Kantsiper, B., Mahaffy, P., Newman, C., Ravine, M., Trainer, M., Waite, H., Zarnecki, J., 2010. Exploring the seas of Titan: the Titan Mare Explorer (TiME) Mission. In: Lunar and Planetary Institute Science Conference Abstracts, p. 1236.

Strobel, D.F., 2009. Titan's hydrodynamically escaping atmosphere: escape rates and the structure of the exobase region. Icarus 202, 632–641.

Teanby, N.A., Irwin, P.G.J., de Kok, R., Jolly, A., Bézard, B., Nixon, C.A., Calcutt, S.B., 2009a. Titan's stratospheric C_2N_2, C_3H_4, and C_4H_2 abundances from Cassini/CIRS far-infrared spectra. Icarus 202, 620–631.

Teanby, N.A., Irwin, P.G.J., de Kok, R., Nixon, C.A., 2009b. Dynamical implications of seasonal and spatial variations in Titan's stratospheric composition. Phil. Trans. R. Soc. Lond. A 367, 697–711.

Teanby, N.A., Irwin, P.G.J., de Kok, R., 2010a. Compositional evidence for Titan's stratospheric tilt. Plan. Space Sci. 58, 792–800.

Teanby, N.A., Irwin, P.G.J., de Kok, R., Nixon, C.A., 2010b. Seasonal changes in Titan's polar trace gas abundance observed by Cassini. Astrophys. J. 724, L84–L89.

Teanby, N.A., Irwin, P.G.J., Nixon, C.A., de Kok, R., Vinatier, S., Coustenis, A., Sefton-Nash, E., Calcutt, S.B., Flasar, F.M., 2012. Active upper-atmosphere chemistry and dynamics from polar circulation reversal on Titan. Nature 491, 732–735.

Teanby, N.A., de Kok, R., Irwin, P.G.J., Osprey, S., Vinatier, S., Gierasch, P.J., Read, P.L., Flasar, F.M., Conrath, B.J., Achterberg, R.K., Bezard, B., Nixon, C.A., Calcutt, S.B., 2008. Titan's winter polar vortex structure revealed by chemical tracers. J. Geophys. Res. 113, E12003.

Thomsen, M.F., Reisenfeld, D.B., Delapp, D.M., Tokar, R.L., Young, D.T., Crary, F.J., Sittler, E.C., McGraw, M.A., Williams, J.D., 2010. Survey of ion plasma parameters in Saturn's magnetosphere. J. Geophys. Res. 115, 10220.

Tinsley, T., Sarsfield, M., Rice, T., 2011. Alternative radioisotopes for heat and power sources. J. Br. Interplan. Soc. 64, 49–53.

Tobie, G., Gautier, D., Hersant, F., 2012. Titan's bulk composition constrained by Cassini–Huygens: implication for internal outgassing. Astrophys. J. 752, 125.

Tobie, G., Lunine, J.I., Monteux, J., Mousis, O., Nimmo, F., 2014. The origin and evolution of Titan. In: Müller-Wodarg, I., Griffith, C.A., Lellouch, E., Cravens, T.E. (Eds.), Titan: Interior, Surface, Atmosphere, and Space Environment. Cambridge University Press, Cambridge, pp. 29–62.

Tobie, G., Lunine, J.I., Sotin, C., 2006. Episodic outgassing as the origin of atmospheric methane on Titan. Nature 440, 61–64.

Tobie, G., Čadek, O., Sotin, C., 2008. Solid tidal friction above a liquid water reservoir as the origin of the south pole hotspot on Enceladus. Icarus 196, 642–652.

Tokar, R.L., Johnson, R.E., Hill, T.W., Pontius, D.H., Kurth, W.S., Crary, F.J., Young, D.T., Thomsen, M.F., Reisenfeld, D.B., Coates, A.J., Lewis, G.R., Sittler, E.C., Gurnett, D.A., 2006. The interaction of the atmosphere of Enceladus with Saturn's plasma. Science 311, 1409–1412.

Tokar, R.L., Johnson, R.E., Thomsen, M.F., Wilson, R.J., Young, D.T., Crary, F.J., Coates, A.J., Jones, G.H., Paty, C.S., 2009. Cassini detection of Enceladus' cold water-group plume ionosphere. Geophys. Res. Lett. 36, 13203.

Tokar, R.L., Wilson, R.J., Johnson, R.E., Henderson, M.G., Thomsen, M.F., Cowee, M.M., Sittler, E.C., Young, D.T., Crary, F.J., McAndrews, H.J., Smith, H.T., 2008. Cassini detection of water-group pick-up ions in the Enceladus torus. Geophys. Res. Lett. 35, 14202.

Tomasko, M.G., Archinal, B., Becker, T., Bézard, B., Bushroe, M., Combes, M., Cook, D., Coustenis, A., de Bergh, C., Dafoe, L.E., Doose, L., Douté, S., Eibl, A., Engel, S., Gliem, F., Grieger, B., Holso, K., Howington-Kraus, E., Karkoschka, E., Keller, H.U., Kirk, R., Kramm, R., Küppers, M., Lanagan, P., Lellouch, E., Lemmon, M., Lunine, J., McFarlane, E., Moores, J., Prout, G.M., Rizk, B., Rosiek, M., Rueffer, P., Schröder, S.E., Schmitt, B., See, C., Smith, P., Soderblom, L., Thomas, N., West, R., 2005. Rain, winds and haze during the Huygens probe's descent to Titan's surface. Nature 438, 765–778.

Turtle, E.P., Perry, J.E., Hayes, A.G., Lorenz, R.D., Barnes, J.W., McEwen, A.S., West, R.A., Del Genio, A.D., Barbara, J.M., Lunine, J.I., Schaller, E.L., Ray, T.L., Lopes, R.M.C., Stofan, E.R., 2011. Rapid and extensive surface changes near Titan's equator: evidence of April showers. Science 331, 1414–1417.

Ventura, B., Notarnicola, C., Casarano, D., Posa, F., Hayes, A.G., Wye, L., 2012. Electromagnetic models and inversion techniques for Titan's Ontario Lacus depth estimation from Cassini RADAR data. Icarus 221, 960–969.

Wahlund, J.E., André, M., Eriksson, A.I.E., Lundberg, M., Morooka, M.W., Shafiq, M., Averkamp, T.F., Gurnett, D.A., Hospodarsky, G.B., Kurth, W.S., Jacobsen, K.S., Pedersen, A., Farrell, W., Ratynskaia, S., Piskunov, N., 2009. Detection of dusty plasma near the E-ring of Saturn. Plan. Space Sci. 57, 1795–1806.

Waite, J.H., Brockwell, T., Elliot, J., Reh, K., Spencer, J., Outer Planets Satellites Decadal Subpanel, 2010. Titan lake probe: the ongoing NASA decadal study preliminary report. In: EGU General Assembly Conference Abstracts, p. 14762.

Waite, J.H., Combi, M.R., Ip, W.H., Cravens, T.E., McNutt, R.L., Kasprzak, W., Yelle, R., Luhmann, J., Niemann, H., Gell, D., Magee, B., Fletcher, G., Lunine, J., Tseng, W.L., 2006. Cassini ion and neutral mass spectrometer: Enceladus plume composition and structure. Science 311, 1419–1422.

Waite, J.H., Magee, B., Brockwell, T., 2011. The effect of flyby velocity on the composition of the Enceladus gas torus as measured by Cassini INMS. In: Lunar and Planetary Institute Science Conference Abstracts, p. 2818.

Waite, J.H., Niemann, H., Yelle, R.V., Kasprzak, W.T., Cravens, T.E., Luhmann, J.G., McNutt, R.L., Ip, W.H., Gell, D., De La Haye, V., Müller-Wordag, I., Magee, B., Borggren, N., Ledvina, S., Fletcher, G., Walter, E., Miller, R., Scherer, S., Thorpe, R., Xu, J., Block, B., Arnett, K., 2005. Ion neutral mass spectrometer results from the first Flyby of Titan. Science 308, 982–986.

Waite, J.H., Young, D.T., Cravens, T.E., Coates, A.J., Crary, F.J., Magee, B., Westlake, J., 2007. The process of Tholin formation in Titan's upper atmosphere. Science 316, 870.

Waite Jr., J.H., Lewis, W.S., Magee, B.A., Lunine, J.I., McKinnon, W.B., Glein, C.R., Mousis, O., Young, D.T., Brockwell, T., Westlake, J., Nguyen, M.J., Teolis, B.D., Niemann, H.B., McNutt, R.L., Perry, M., Ip, W.H., 2009. Liquid water on Enceladus from observations of ammonia and ^{40}Ar in the plume. Nature 460, 487–490.

West, R.A., Balloch, J., Dumont, P., Lavvas, P., Lorenz, R., Rannou, P., Ray, T., Turtle, E.P., 2011. The evolution of Titan's detached haze layer near equinox in 2009. Geophys. Res. Lett. 38, 6204.

Westlake, J.H., Bell, J.M., Waite Jr., J.H., Johnson, R.E., Luhmann, J.G., Mandt, K.E., Magee, B.A., Rymer, A.M., 2011. Titan's thermospheric response to various plasma environments. J. Geophys. Res. 116, 3318.

Westlake, J.H., Waite, J.H., Carrasco, N., Richard, M., Cravens, T., 2014. The role of ion-molecule reactions in the growth of heavy ions in Titan's ionosphere. J. Geophys. Res. 119, 5951–5963.

Wood, C.A., Lorenz, R., Kirk, R., Lopes, R., Mitchell, K., Stofan, E., Cassini Radar Team, 2010. Impact craters on Titan. Icarus 206, 334–344.

Yelle, R.V., Cui, J., Müller-Wodarg, I.C.F., 2008. Methane escape from Titan's atmosphere. J. Geophys. Res. 113, 10003.

Yung, Y.L., Allen, M., Pinto, J.P., 1984. Photochemistry of the atmosphere of Titan—comparison between model and observations. Astrophys. J. Suppl. 55, 465–506.

Zebker, H., Hayes, A., Janssen, M., Le Gall, A., Lorenz, R., Wye, L., 2014. Surface of Ligeia Mare, Titan, from Cassini altimeter and radiometer analysis. Geophys. Res. Lett. 41, 308–313.

Zolotov, M.Y., 2007. An oceanic composition on early and today's Enceladus. Geophys. Res. Lett. 34, 23203.

Zolotov, M.Y., Tobie, G., Postberg, F., Magee, B., Waite, J.H., Esposito, L., 2011. Chemical and phase composition of Enceladus: insights from Cassini data. In: EPSC-DPS Joint Meeting 2011, p. 1330.

Retour à la table des matières : p. v

4.8 Article sur l'évaporation des lacs

Earth and Planetary Science Letters 410 (2015) 75–83

Contents lists available at ScienceDirect

Earth and Planetary Science Letters

www.elsevier.com/locate/epsl

Experimental constraints on the composition and dynamics of Titan's polar lakes

A. Luspay-Kuti [a,b,*], V.F. Chevrier [b], D. Cordier [c], E.G. Rivera-Valentin [d], S. Singh [b], A. Wagner [b], F.C. Wasiak [b]

[a] Space Science & Engineering Division, Southwest Research Institute, 6220 Culebra Rd., San Antonio, TX 78238, USA
[b] Arkansas Center for Space and Planetary Sciences, STON F47, 346 1/2 N. Arkansas Ave., University of Arkansas, Fayetteville, AR 72701, USA
[c] Université de Franche-Comté, Institut UTINAM, CNRS/INSU, UMR 6213, Besancon Cedex, France
[d] Arecibo Observatory (USRA), National Astronomy and Ionosphere Center, Arecibo, PR 00612, USA

ARTICLE INFO

Article history:
Received 10 December 2013
Received in revised form 4 September 2014
Accepted 4 November 2014
Available online xxxx
Editor: C. Sotin

Keywords:
Titan
evaporation rate
hydrocarbon lakes
experimental
lake composition

ABSTRACT

Titan's polar lakes are thought to be predominantly composed of liquid ethane and methane; however, little is known on the ratio of these hydrocarbons in the lakes, and the stability and dynamics of these mixtures. Here we provide the first experimental constraints under Titan surface conditions of liquid hydrocarbon mixture evaporation. Our results are relevant to Titan's polar temperatures and pressures (∼92 K and 1.5 bar), and cover a wide range of methane–ethane compositions. We show that evaporation is negligible for pure ethane, but increases nearly linearly with increasing methane concentration. Early dissolution of N_2 results in ternary mixtures evaporating, which is modeled by a 'hybrid' thermodynamic equilibrium approach combining Perturbed-Chain Statistical Associating Fluid Theory with a diffusion and buoyancy-driven mass flux model. The approach follows the experimental evaporation rate measurements presented in this study, and allows for the calculation of the corresponding liquid methane–ethane–nitrogen ratios. Such results along with *Cassini* inferred lake evaporation rates can be used to estimate the composition of Titan's polar liquids, and may have implications on their origin. Our results suggest that Ontario Lacus is predominantly composed of ethane (>50–80 mol%), indicating it may be a residual lake following extensive seasonal methane evaporation, and/or might be in contact with a subsurface liquid reservoir.

© 2014 Elsevier B.V. All rights reserved.

1. Introduction

One of the landmark discoveries of the *Cassini–Huygens* mission to date is the existence of stable liquid bodies on Titan's surface. *Cassini* Synthetic Aperture Radar (SAR) images showed several lake-like features in the north polar region of Titan (Stofan et al., 2007). RADAR microwave radiometry provided further evidence, suggesting these radar-dark features are in fact liquid filled basins with a dielectric constant consistent with an ethane–methane mixture (Janssen et al., 2009). Thus far, hundreds of these hydrocarbon lakes and seas have been identified, mainly confined to the colder and presumably more humid polar regions, with more observed lakes in the north (Aharonson et al., 2009). There is evidence for tropical liquids as well, possibly supplied by occasional heavy rainfall events (Turtle et al., 2011) and/or underground aquifers (Griffith et al., 2012).

While the lakes are thought to be dominated by ethane and methane, there is little direct evidence on the exact amount of these components in the liquid phase. Brown et al. (2008) reported on spectral features observed by the Visible and Infrared Mapping Spectrometer (VIMS) in Ontario Lacus that were interpreted as liquid ethane. Alternatively, Moriconi et al. (2010) suggest the same absorption feature might be in the region surrounding the lake, and could be associated with damp sediments of ethane, propane, methane and possibly other minor hydrocarbons, indicative of retreat due to evaporation. While the presence of ethane in Ontario Lacus does not rule out the presence of methane in the lake, direct surface detection of liquid methane is essentially impossible due to the strong atmospheric absorption of methane. There is, though, a variety of thermodynamic and geochemical models aimed at determining lake composition. Cordier et al. (2009) considered the lakes as non-ideal solutions in thermodynamic equilibrium with the atmosphere and calculated the ethane and methane mole percent to be 76–79% and 6–11%, respectively (Cordier et al., 2013b). Their model based on Regular Solution Theory predicts negligible amounts (∼0.4–0.6%) of dissolved nitrogen in the mixture.

* Corresponding author.
E-mail address: aluspaykuti@swri.edu (A. Luspay-Kuti).

http://dx.doi.org/10.1016/j.epsl.2014.11.023
0012-821X/© 2014 Elsevier B.V. All rights reserved.

Glein and Shock (2013) estimate 15.5% ethane, 68.1% methane, and 14.8% N_2 in their modified van Laar model, while Tan et al. (2013) calculate 53.2-8.3% C_2H_6, 31.8–68.4% CH_4, and 6.9–22% N_2 for the equator and poles, respectively. The discrepancy in the various model results may be due to the absence of extended datasets at Titan relevant cryogenic temperatures and pressures.

Because methane is thought to be the primary participant in the hydrological cycle on Titan (Lunine and Atreya, 2008), accurate evaporation rates are crucial for general circulation models, as well as to predict the stability of polar lakes. Luspay-Kuti et al. (2012) reported an average evaporation flux of $(3.1 \pm 0.6) \times 10^{-4}$ kg m^{-2} s^{-1} from experimental simulations for pure CH_4 in a N_2 atmosphere, with a gravity-corrected value for Titan of $(1.6 \pm 0.3) \times 10^{-4}$ kg s^{-1}m^{-2} for ∼94 K, 1.5 bar, and $\sim 2 \times 10^{-2}$ CH_4 mole fraction in the simulated atmosphere. While that study focused on evaporation of methane at equatorial temperature conditions, it does not directly represent the poles in composition.

Here we present experimental measurements on the evaporation rate of two major components of the polar lakes under Titan relevant temperature and pressure conditions for a variety of methane–ethane compositions. We also propose a model to describe mixture evaporation and liquid composition, and discuss the implications of our experimental results to Titan's lakes.

2. Laboratory simulations

We used an experimental facility specifically designed for simulating Titan surface conditions (Wasiak et al., 2013). It consists of a larger, stainless steel host chamber (Andromeda), with a smaller unit (Temperature Control Box (TCB)) located inside. Temperatures relevant to Titan are reproduced via liquid nitrogen flow through coils positioned on both the inside and outside of the TCB and within the condenser, while a 1.5 bar atmosphere is maintained with pressurized N_2. A schematic of the chamber is shown in Fig. 1.

The same simulation chamber has been used to measure pure CH_4 evaporation rates in a N_2 atmosphere with ∼20% methane relative humidity (Luspay-Kuti et al., 2012). As a continuation of that work, before simulating CH_4–C_2H_6 mixtures we ran controlled experiments on pure C_2H_6 as follows: once the required temperature and pressure conditions were achieved, we introduced ethane gas into the condenser, maintained at ∼110 K, then poured the condensed liquid into a Petri dish connected to a scale with a readability of 0.01 g. Mass loss over time was then recorded for the determination of the evaporation rate of ethane. For simulating mixtures of methane and ethane, the previous step is followed by introducing methane on top of ethane once the temperature in the condenser reaches ∼95 K. Using gas injection times and fluxes, we can control liquid masses of these different hydrocarbons based on the desired concentrations to be simulated. The samples are then allowed to mix without being stirred. The liquid and gas temperatures were measured via K type thermocouples placed at the bottom of the Petri dish, and 1 inch above it, respectively. While the chamber used in the current study was the same facility described in Luspay-Kuti et al. (2012), some experimental details, such as the cooling procedure via liquid N_2, were slightly modified, which can result in an overall higher methane relative humidity compared to the conditions in Luspay-Kuti et al. (2012).

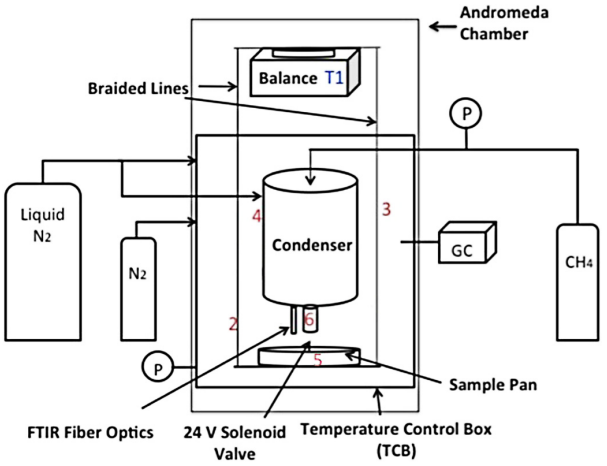

Fig. 1. Schematic diagram of the Titan simulation facility and its various components. The locations of the thermocouples are indicated with numbers. Image modified from Luspay-Kuti et al. (2012), Wasiak et al. (2013).

3. Experimental evaporation rates

The results and details for each simulation performed are summarized in Table 1. Figs. 2 and 3 show typical experimental data

Table 1
Experimentally determined evaporation rates of mixtures with various initial liquid methane mole fractions ($x_{CH_4,ini}$(exp)). The temperature values are averaged over the duration of evaporation for each individual run. The gas temperature of the simulated atmosphere was measured an inch above the liquid layer (thermocouple #2 in Fig. 1), and the temperature of the liquid was taken in the bottom of the Petri dish (thermocouple #5 in Fig. 1).

CH_4 mole fraction	Evaporation rate $\times 10^{-4}$ (kg m^{-2} s^{-1})	Standard error $\times 10^{-5}$ (kg m^{-2} s^{-1})	Average gas temperature (K)	Average liquid temperature (K)	CH_4 relative humidity	Duration of 'plateau' (s)
0.21	0.339	0.179	92.7 ± 0.3	93.4 ± 0.6	17%	n/a
0.23	0.282	0.049	91.9 ± 3.8	93.3 ± 2.3	20%	n/a
0.33	0.395	1.011	93.6 ± 1.4	95.8 ± 1.6	25%	n/a
0.44	0.621	0.199	93.3 ± 0.9	92.9 ± 0.5	25%	n/a
0.46	0.734	0.08	93.6 ± 0.7	92.9 ± 0.6	25%	n/a
0.49	0.621	0.294	93 ± 0.1	91.8 ± 0.2	28%	n/a
0.51	0.96	0.092	93.6 ± 0.4	91.6 ± 0.1	30%	n/a
0.53	1.243	0.207	92.4 ± 1.6	91.1 ± 0.9	30%	n/a
0.53	1.13	1.489	91.5 ± 0.3	90.9 ± 0.8	28%	n/a
0.63	1.525	0.233	89.7 ± 0.6	86.5 ± 0.1	30%	n/a
0.66	1.017	0.19	94.2 ± 0.6	n/a	28%	n/a
0.68	0.791	0.033	93.6 ± 2.7	92 ± 1.5	30%	n/a
0.68	1.412	0.116	90.8 ± 0.2	n/a	35%	n/a
0.74	1.243	0.187	90.9 ± 0.1	90.5 ± 0.2	33%	580
0.8	1.525	0.07	94.45 ± 0.2	92.9 ± 0.1	33%	840
0.85	2.034	0.047	91.9 ± 0.3	90.5 ± 0.6	35%	1100
0.86	1.921	0.06	93.7 ± 3.2	89.8 ± 0.8	40%	1560
0.86	1.469	0.047	n/a	n/a	39%	1700

Retour à la table des matières : p. v

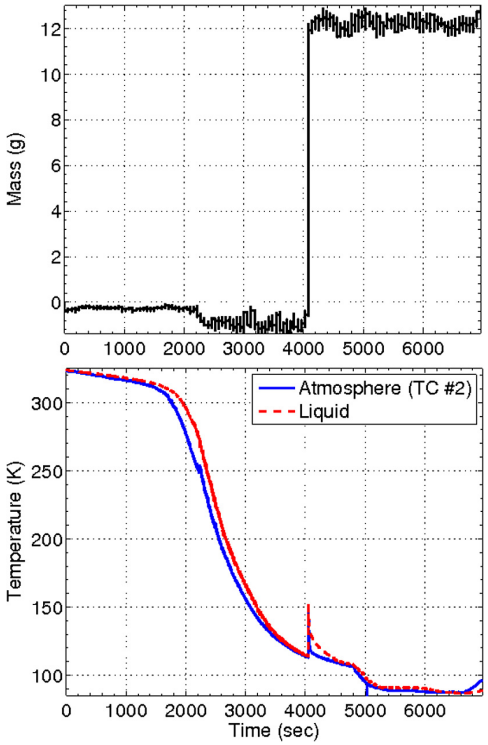

Fig. 2. Mass as a function of time for pure C_2H_6 and the corresponding atmospheric and liquid temperatures.

of mass loss over time of pure liquid ethane and ethane–methane mixtures at three different initial concentrations, as well as the corresponding temperatures in the liquid, and the gas an inch above the liquid layer (Figs. 2 and 3, bottom panels). The sudden ethane mass increase at 4000 s indicates the introduction of the liquid sample from the condenser into the Titan chamber (Fig. 2). Small mass fluctuations in the early stages of the experiments are due to instrumental sensitivity to the drastic temperature and pressure changes. The steps visible in the mixture curves in Fig. 3 correspond to the pour of different hydrocarbons into the Petri dish, also indicated by the distinctive 'spikes' in the temperature profiles. In the case of 85 mol% CH_4 (Fig. 3a), ∼8 g of ethane was condensed at 3000 s, followed by methane condensation two times: first at ∼3800 s, then at ∼4900 s. A total mass of ∼20 g of methane–ethane mixture was then evaporated at 91 K, with a liquid temperature of 90 K. In the case of the mixture with 68 mol% methane (Fig. 3b), roughly 10 g of liquid ethane and ∼11 g methane were introduced into the chamber, and at 23 mol% methane (Fig. 3c), ∼35 g ethane was condensed stepwise, followed by ∼5 g methane poured on top of the liquid C_2H_6.

The mass versus time curves exhibit a different trend after the initial condensation peaks. In the case of pure ethane, the condensed ∼12 g does not decrease over the entire course of the simulation (∼1 h in Fig. 2), in contrast with the mixture samples. On all occasions, the mixtures show time-dependent mass loss.

Evaporation rates are determined by a least-squares fit line to the nearly-linear portion of the mass loss curves, which corresponds to steady-state evaporation in the experiments. The slope of the regression line is then used to determine the evaporation rate with corresponding uncertainties to a 95% confidence. We studied CH_4 mole fractions ranging from 0.21 to 0.86, referring to the initial CH_4 mole fractions at the time of condensation, determined by the condensed mass (hereon: $x_{CH_4,ini}(exp)$) (Fig. 7a below).

The data at lower mole fractions do not show significant variation with values between $\sim 3 \times 10^{-5}$ and 4×10^{-5} $kg\,m^{-2}\,s^{-1}$; however, above $x_{CH_4,ini}(exp) = 0.33$ we observe a linear increase of evaporation rates with CH_4 mole fraction. The maximum measured evaporation rate occurs at $x_{CH_4,ini}(exp) = 0.85$ with a value

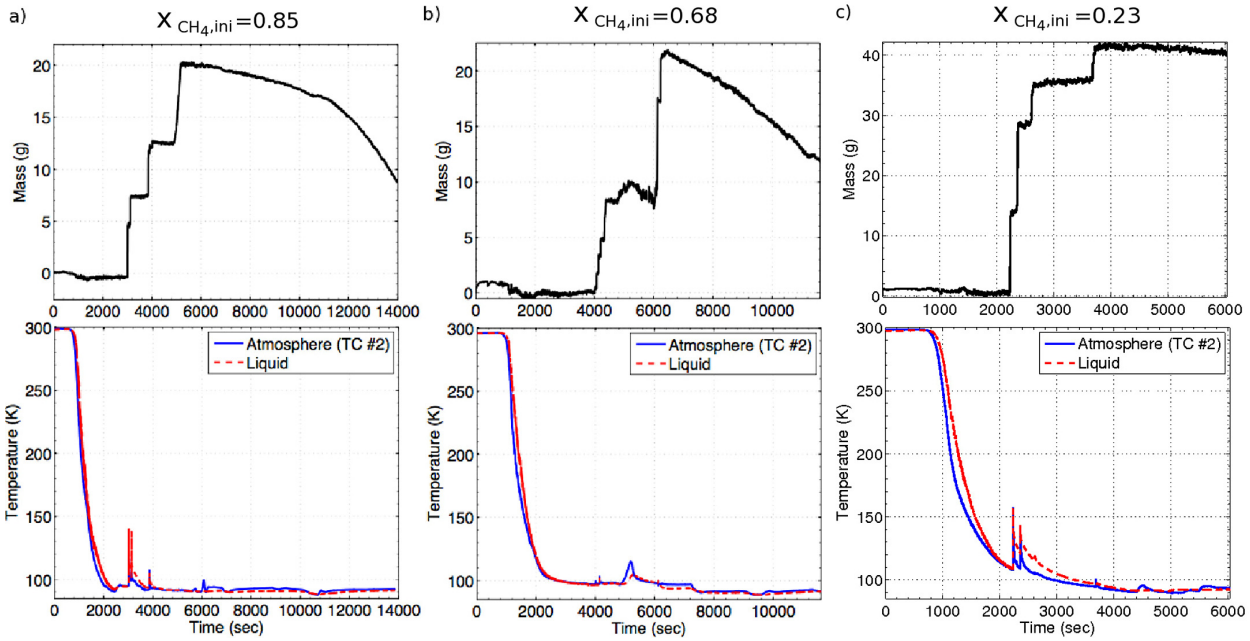

Fig. 3. Mass loss over time for CH_4–C_2H_6 mixtures of 85% (a), 65% (b) and 23% (c) initial CH_4. Corresponding temperatures of the chamber atmosphere (thermocouple #2) and that of the liquid (thermocouple #5) are shown under each mass curve. The steps before the maximum mass and the peaks in temperature correspond to C_2H_6 and CH_4 condensation. Liquid temperatures are defined after condensation only, as before they refer to the temperature measured in the empty sample pan.

Retour à la table des matières : p. v

of $\sim 2 \times 10^{-4}$ kg m^{-2} s^{-1}, about an order of magnitude higher than the lowest values. Overall, a linear trend fits the mixture data well, as shown in Fig. 7a. The slope of the line is $(2.28 \pm 0.4) \times 10^{-4}$ to a 95% confidence, with an R^2 value of 0.81. Previously measured evaporation rates for pure methane in a nitrogen atmosphere are also indicated in Fig. 7a for comparison, with an average flux of $(3.1 \pm 0.6) \times 10^{-4}$ kg m^{-2} s^{-1} (Luspay-Kuti et al., 2012). Mixture values are systematically below this assumed methane–nitrogen liquid evaporation rate, with our current maximum rate (for $x_{CH_4,ini}(exp) \approx 0.85$) nearly 1.5 times lower than for pure methane. While the presence of ethane is expected to lower the evaporation rate relative to pure methane, extrapolation of the linear fit to $x_{CH_4,ini} = 1$ still results in a break compared to the values measured by Luspay-Kuti et al. (2012) for their assumed methane–nitrogen mixtures. This may be due to the higher methane relative humidity in the current study. The evaporation rate of pure ethane in our experiments is below the level of measurable significance (0.2 g) after ~4000–11 000 s of evaporation. Based on the limitations in our detection, that gives an upper limit for ethane evaporation on the order of $\sim 10^{-6}$ kg m^{-2} s^{-1}.

4. Theoretical approach

Previously, pure CH_4 evaporation inside the Titan simulation chamber was described as primarily driven by two major effects: diffusion and buoyancy (Luspay-Kuti et al., 2012), using the equation developed by Ingersoll (1970), and modified for Titan conditions. Under these effects, the mass flux is described as:

$$J = 0.17 D_{CH_4/N_2} \Delta\eta \left(\frac{\frac{\Delta\rho}{\rho_{surf}} g}{\nu^2} \right)^{\frac{1}{3}} \quad (1)$$

where D_{CH_4/N_2} is the diffusion coefficient of CH_4 gas in nitrogen (Poling et al., 2007), $\Delta\eta = \rho_{CH_4,surf} - \rho_{CH_4,atm}$ is the methane concentration gradient between the liquid surface and the ambient atmosphere, $\Delta\rho = \rho_{atm} - \rho_{surf}$ is the difference between the density of the ambient gas and the gas at the liquid surface (contact layer), g is the gravitational acceleration at the surface of the Earth, and ν is the kinematic viscosity of methane (Crane Co., 1982). Molecules from the liquid diffuse into a thin contact layer at the liquid–gas interface until thermodynamic equilibrium in the layer is reached. At the same time, methane is being removed from this contact layer as a result of mass flux driven by the concentration difference between the contact layer and the overlying ambient atmosphere ($\Delta\eta$), and by buoyancy ($(\Delta\rho/\rho_{surf})g$). Buoyancy is controlled by the total density (or, the mole fractions) of the CH_4–N_2 gas mixture in the ambient atmosphere (ρ_{atm}), and in the contact layer (ρ_{surf}) in Eq. (1). An illustration of the components in this framework is shown in Fig. 4. The approach described here was shown to match the experimental data presented in Luspay-Kuti et al. (2012) for an assumed CH_4–N_2 liquid with calculated mole fractions of ~0.84 and 0.16, respectively.

In the case of a two-component system, such as pure methane in a nitrogen atmosphere, at a fixed temperature and pressure, both the liquid and the vapor compositions will be determined by thermodynamics, according to the Gibbs phase rule. To validate the use of Eq. (1), we have compared the methane mole fraction value in the thin contact layer resulting from purely thermodynamic considerations ($y_{CH_4,surf}$(thermo)) to those deduced by the use of the experimental flux values ($y_{CH_4,surf}$(exp)) reported by Luspay-Kuti et al. (2012). For the experimental temperature and pressure conditions used in Luspay-Kuti et al. (2012), we obtain a value of $y_{CH_4,surf}$(thermo) = 0.11, as shown in the CH_4–N_2 phase diagram in Fig. 5, while an evaporative flux of $\sim 3 \times 10^{-4}$ kg m^{-2} s^{-1} (Luspay-Kuti et al., 2012) results in a methane mole fraction of $y_{CH_4,surf}$(exp) ~ 0.08 in the contact layer right above the liquid. Despite the uncertainties in the calculation of the diffusion coefficient, kinematic viscosity, etc., these values are similar; therefore, validating the use of a diffusion/buoyancy driven evaporation approach described by Eq. (1) for Titan-relevant hydrocarbons. Therefore, we adopt the same evaporation theory, and combine it with an up-to-date thermodynamic equilibrium model called Perturbed-Chain Statistical Associating Fluid Theory (hereafter: PC-SAFT) to investigate the experimental mixture evaporation data.

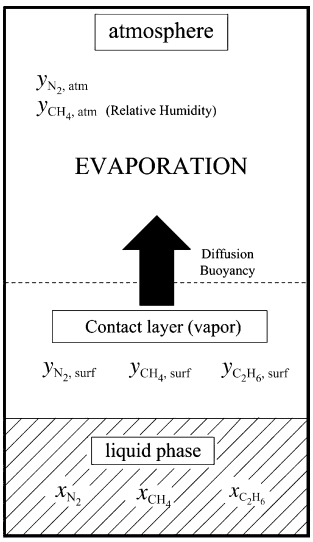

Fig. 4. Schematic of evaporation in the diffusion-buoyancy framework used in this study. x denotes the liquid phase mole fractions, while gas phase mole fractions are donated by y. The subscript 'surf' refers to parameters in the contact layer right above the liquid. Parameters in the ambient gas (atmosphere) are given the subscript 'atm'. E.g., the mole fraction of methane in the atmosphere (gas above the contact layer), which gives the relative humidity, is denoted by y_{atm,CH_4}.

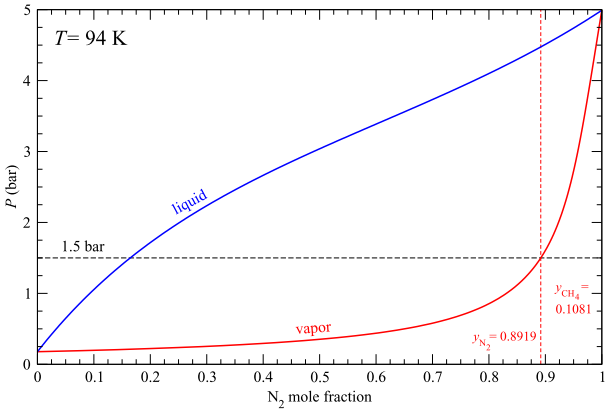

Fig. 5. Binary diagram for a CH_4–N_2 system at 94 K. As determined by the pressure of 1.5 bar (black dashed line), the nitrogen–methane composition of the vapor phase in the contact layer right above the liquid surface is $y_{N_2} = 0.89$; therefore, $y_{CH_4} = 0.11$ (red dashed line). The curves have been obtained using the PC-SAFT theory (Section 4), with parameters from Tan et al. (2013). (For interpretation of the references to color in this figure legend, the reader is referred to the web version of this article.)

4.1. Nitrogen dissolution

Even though the samples condensed in the experiments are composed of methane and ethane only, N_2 from the simulated

Retour à la table des matières : p. v

atmosphere will dissolve into this binary mixture. Hence, we are dealing with ternary mixtures of liquid CH_4–C_2H_6–N_2, rather than binaries. Although the condensed masses, and therefore initial mole fractions in the liquid, are known at the start of the experiment, nitrogen dissolution will change their relative concentrations over time. For that reason, the $x_{CH_4,ini}(exp)$ values do not reflect absolute concentrations, but should be taken as points of reference.

A possible manifestation of nitrogen dissolution in the experimental mass profiles may be the nearly horizontal section that is observable in some cases right after condensation, but before the onset of steady-state evaporation (e.g. Fig. 3a), and was referred to as 'plateau' in Luspay-Kuti et al. (2012). During this time, mass loss is negligible. While the 'plateau' section has been previously interpreted as ongoing heat transfer between the liquid and the overlying atmosphere (Luspay-Kuti et al., 2012), nitrogen dissolution might be a more realistic explanation. In this scenario, dissolving N_2 from the simulated atmosphere might be offsetting the early evaporation of methane, keeping the mass nearly constant. To explore the possibility of N_2 dissolution over heat transfer, we estimated the time it takes to attain thermal equilibrium in the experiments, as well as the time scale of nitrogen diffusion. The thermal relaxation time scale of the liquid is given by Cordier et al. (2012):

$$\tau_{th} \sim e^2/\chi \tag{2}$$

where e is the liquid depth and χ is the thermal diffusivity given by $\chi = \kappa/\rho C_P$ (Landau and Lifshitz, 1987), κ is the thermal conductivity ($W\,m^{-1}\,K^{-1}$), ρ is the density of the liquid ($kg\,m^{-3}$), and C_P ($J\,kg^{-1}\,K^{-1}$) is the specific heat capacity at constant pressure ($J\,kg^{-1}\,K^{-1}$). Using values listed by Lorenz et al. (2010), for a 3 mm deep liquid layer we obtain $\tau_{th} \sim 60$ s for pure methane, and $\tau_{th} \sim 50$ s for pure ethane at 92 K, suggesting that the system in both extremes attains thermal equilibrium very quickly. At the same time, nitrogen diffusion into liquid methane of the same depth would take 1300 s, and is estimated by:

$$\tau_{diff} \sim e^2/D_{N_2-CH_4}, \tag{3}$$

where $D_{N_2-CH_4}$ is the diffusion coefficient of N_2 into liquid CH_4. This is more than a factor of 20 longer than the estimated thermal relaxation time scale, and is on the order of magnitude of the duration of the plateaus. The fact that $\tau_{diff} \gg \tau_{th}$ implies that the plateau may be dominated by the dissolution of N_2 into the liquid sample. Preliminary analysis shows the length of the plateau-like feature might increase with increasing methane content in the liquid mixture (Table 1), which makes possible thermal effects, or the formation of a methane saturated laminar layer in the experimental chamber less likely.

4.2. Liquid composition

Though direct measurement of the liquid sample composition is not possible in our simulations, knowledge of the mole fractions of each constituent in the liquid is necessary in order to calculate the methane density, and the total density in the contact layer (appearing in the terms $\Delta\eta$, and $\Delta\rho/\rho_{surf}$, respectively, in Eq. (1)). The liquid phase composition determines the composition of the vapor phase in the contact layer via Raoult's law:

$$P_{i,surf} = y_{i,surf} P_{surf} = \gamma_i x_i P_i^{sat}, \tag{4}$$

where $P_{i,surf}$ is the partial pressure of species i, $y_{i,surf}$ is its gas phase mole fraction in the contact layer, P_{surf} is the total pressure in the contact layer, x_i and γ_i are the liquid phase mole fraction and activity coefficient of species i, respectively, and P_i^{sat} is the saturation vapor pressure of pure component i. In the lack of direct compositional measurements, we use the experimental data presented here, together with Eq. (1) to estimate the methane–ethane–nitrogen liquid concentration.

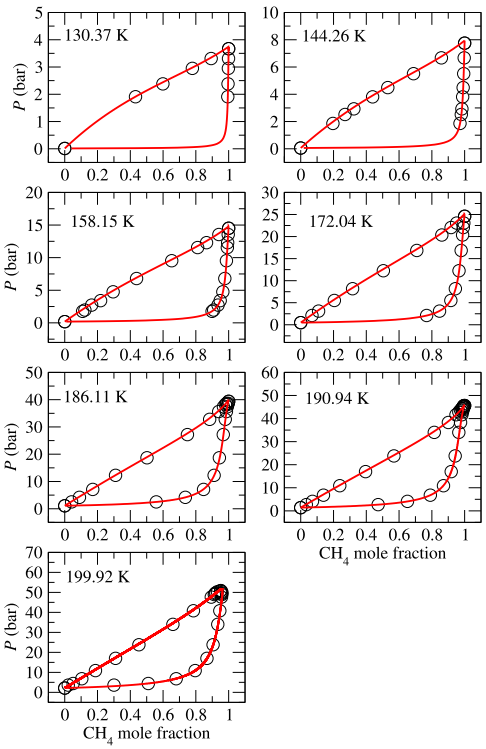

Fig. 6. Phase diagrams of CH_4–C_2H_6 mixtures at various temperatures. Circles: experimental data from Wichterle and Kobayashi (1972). Red curves: PC-SAFT model used in this study. (For interpretation of the references to color in this figure legend, the reader is referred to the web version of this article.)

Mass flux values in the model are determined by the best-fit regression line to the existing experimental data points through

$$E_{model} = \left(\beta x_{CH_4,ini}(exp) + b\right) \times 10^{-4}, \tag{5}$$

where $\beta = 2.28$ is the slope of the regression line, and $b = -0.26$. Then, the vapor-phase methane mole fractions in the contact layer ($y_{CH_4,surf}(model)$) corresponding to the E_{model} evaporation rate values ($E_{model} = J$; Eq. (5)) are found via a 1D Newton–Raphson algorithm for a given temperature, pressure, and methane relative humidity in the ambient simulated atmosphere. Thermodynamic equilibrium is then considered between the liquid phase and the contact layer through a PC-SAFT approach to derive the vapor-phase mole fractions of N_2 and C_2H_6 in the contact layer, and thus, the CH_4–C_2H_6–N_2 mole fractions in the liquid. PC-SAFT is a modified SAFT equation of state (Gross and Sadowski, 2001), and is widely used in chemical engineering with great success. It has recently been introduced to planetary applications by Tan et al. (2013), with optimized values of segment number m, segment diameter σ, and segment energy parameter ϵ/k for the cryogenic context of Titan's thermochemistry. Based on the theory developed by Gross and Sadowski (2001), using the parameters published in Tan et al. (2013), we constructed an original PC-SAFT implementation that consists of a set of FORTRAN 2008 object-oriented subroutines. Similarly to Tan et al. (2013), our PC-SAFT implementation provides a perfect match with thermodynamic N_2–CH_4 and N_2–C_2H_6 binary mixture data (Parrish and Hiza, 1995; Sprow and Prausnitz, 1966; Stryjek et al., 1974,

Retour à la table des matières : p. v

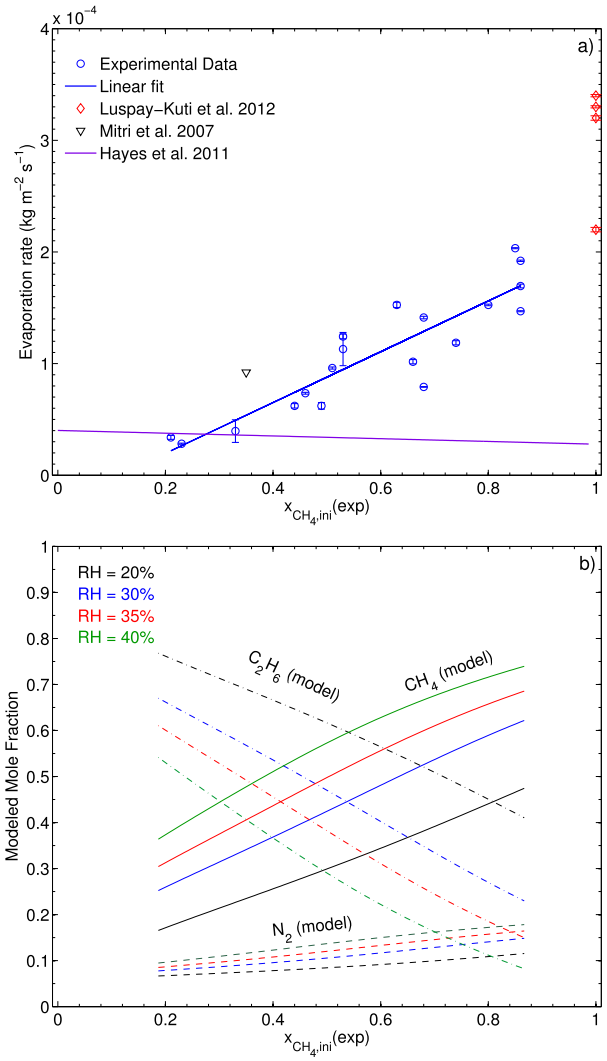

Fig. 7. a) Experimental evaporation rate as a function of initial methane mole fraction (blue circles), and linear fit to the data points (blue line). The red diamonds indicate experimental results of pure CH_4 evaporation in a N_2 atmosphere (Luspay-Kuti et al., 2012). Evaporation rates from Mitri et al. (2007) and Hayes et al. (2011) are also shown after correcting for gravity. (b) Modeled composition of the simulated hydrocarbon liquids. Solid: CH_4, dashed: N_2, dash–dot: C_2H_6. The x axis shows the initial methane mole fractions determined from the mass of condensed methane and ethane in the experiments ($x_{CH_4,ini}(exp)$), while the y axis refers to the calculated mole fraction from the combined PC-SAFT/diffusion-buoyancy model. The different colors correspond to different methane relative humidity values. (For interpretation of the references to color in this figure legend, the reader is referred to the web version of this article.)

Chang and Lu, 1967; Wilson, 1975). Furthermore, we validated our model with CH_4–C_2H_6 binary mixture data available in the literature (Wichterle and Kobayashi, 1972); the comparison between the PC-SAFT output and these data at various temperatures is shown in Fig. 6. Based on the excellent match, we consider our implementation of PC-SAFT reliable. With the method described in this section, the model follows the experimentally determined evaporation rate values by principle, and can be used to construct estimates for the ternary liquid composition.

The derived liquid phase chemical composition from our PC-SAFT/diffusion-buoyancy model compared to the initial methane mole fraction given by the condensed methane–ethane mass in the chamber ($x_{CH_4,ini}(exp)$) is shown in Fig. 7b. Based on these results, the amount of nitrogen that dissolves in the methane–ethane liquid increases with increasing methane concentration, and varies between 5–18 mol%. This is in agreement with our preliminary experimental results on the increasing plateau length with methane content in the mixture. These results suggest that ethane is a non-player in N_2 dissolution. Indeed, N_2 **is** ∼5500 times more soluble in CH_4 than in C_2H_6 at 100 K and 1 bar (Battino et al., 1984). While these values are slightly different than the temperature and pressure conditions in our simulations, they are representative of the expected solubilities.

4.3. Relative humidity

Relative humidity is a key component in deriving liquid composition. For a given evaporation rate, the calculated liquid phase mole fraction ratios vary notably based on methane relative humidity (Fig. 7b). While the mole fraction of methane in the simulated atmosphere was not directly measured in the experiments, several considerations can be made that help constrain the humidity posteriori for each experiment. The break between the linear fit extrapolated to $x_{CH_4,ini}(exp) = 1$ and the evaporation rates measured by Luspay-Kuti et al. (2012) in Fig. 7a indicates a reduced evaporation rate under the conditions the current samples were run. Because the methane mole fraction equals 1, the lower extrapolated evaporation rate cannot be explained by the presence of ethane. The most viable explanation is a higher relative humidity than the experiments in Luspay-Kuti et al. (2012), which was ∼20%. This hypothesis is also in agreement with the minor modifications in the experimental setup compared to that in Luspay-Kuti et al. (2012), mentioned in Section 2.

To estimate the relative humidity for each simulation, we assume that ethane mole fractions remain roughly the same before and after nitrogen dissolution, and are not affected by the possible preferential loss of methane, and diffusion of N_2 into the liquid in the early stages of the simulations (see discussion in Section 4.1). In this case, the initial $x_{C_2H_6}(exp)$ determined by the condensed masses of ethane and methane will equal the modeled $x_{C_2H_6}(model)$ ethane mole fractions. This is a reasonable assumption considering that ethane does not evaporate over the time scales of our experiments (Section 3), neither does it play a role in nitrogen diffusion. Based on that, approximation of relative humidity is possible using the initial hydrocarbon mass ratios through the following relationship ('m' is the mass of condensed hydrocarbons in the chamber, while 'M' is the molar mass):

$$\frac{m_{C_2H_6}}{m_{CH_4}} = \frac{x_{C_2H_6}(exp) M_{C_2H_6}}{x_{CH_4,ini}(exp) M_{CH_4}} \tag{6}$$

by finding $x_{C_2H_6}(exp)$ $(= x_{C_2H_6}(model))$, and matching that to the best-fit relative humidity value on the y-axis of Fig. 7b. For instance, for a mass ratio of 5 g/15 g = 0.33 ($x_{CH_4,ini}(exp) = 0.85$), $x_{C_2H_6}(exp) = 0.33 x_{CH_4,ini}(exp) \frac{M_{CH_4}}{M_{C_2H_6}} = 0.15$ from Eq. (6), which favors the value corresponding to a methane relative humidity of roughly 35%. It is important to emphasize that while the ethane mole fraction is assumed to be constant, the methane mole fraction will change compared to the initial value obtained from the condensed mass ratios ($x_{CH_4,ini}(exp) \neq x_{CH_4}(model)$) due to nitrogen dissolution, and simultaneous preferential methane loss preceding steady-state evaporation. The appropriate methane, and nitrogen mole fractions are calculated by our model described in this study (Fig. 7b). The humidity values determined for each experiment in this manner generally vary between ∼25 and 35%, and are summarized in Table 1.

Retour à la table des matières : p. v

Table 2
Calculated or measured evaporation rates in the literature.

Model	Non-radiative flux ($W m^{-2}$)	Mass flux ($kg m^{-2} s^{-1}$)	Evaporation rate ($m yr^{-1}$)	Notes
McKay et al. (1991)	0.037	7.24×10^{-8}	0.0052	Pure CH_4
Mitri et al. (2007)	20	1.58×10^{-4}	11.02	Pure CH_4
Mitri et al. (2007)	20	4.75×10^{-5}	3.3	CH_4:C_2H_6:N_2 0.35:0.60:0.05
Mitchell et al. (2008)	2	3.91×10^{-6}	0.28	Pure CH_4
Tokano et al. (2009)	n/a	10^{-5}	3	Pure CH_4
Hayes et al. (2011)	n/a	n/a	1 ± 0.6	Ontario Lacus
Williams et al. (2012)	0.7	1.37×10^{-6}	0.1	Pure CH_4
Williams et al. (2012)	0.7	n/a	0.0069	CH_4:C_2H_6:N_2 0.44:0.34:0.22
Luspay-Kuti et al. (2012)	n/a	$(1.6 \pm 0.3) \times 10^{-4}$	11	CH_4:N_2 ~ 0.84:0.16

4.4. Implications for Titan

4.4.1. Lake evaporation

Our experimentally determined evaporation rates vary between 1 $m yr^{-1}$ and 11 $m yr^{-1}$ over a wide range of concentrations (Table 1), when translated to change in liquid depth. The top value of 11 $m yr^{-1}$ refers to liquid methane in a simulated N_2 atmosphere (Luspay-Kuti et al., 2012). At the same time, there are various other predictions on the evaporation rate of Titan's hydrocarbon lakes in the literature. Estimates come from local or general circulation models (GCMs) that provide the non-radiative fluxes at the surface available for evaporation, and span a wide range of values. Evaporation rates from previous studies, along with results of the present work are summarized in Table 2. The pre-*Cassini* model of McKay et al. (1991) estimates the non-radiative fluxes available at the surface are ~0.037 $W m^{-2}$, which would result in a pure methane mass flux of 7.2×10^{-8} $kg m^{-2} s^{-1}$, and a depth decrease of 5.2×10^{-3} $m yr^{-1}$. Several later models used this evaporative flux value to provide constraints on lake evaporation (Griffith et al., 2008; Graves et al., 2008). Williams et al. (2012) also followed the approach of McKay et al. (1991), though they estimated surface energy fluxes by incorporating direct measurements by the *Huygens* probe, and limited their model to the *Huygens* landing site. The resulting value of 0.7 $W m^{-2}$ is about 20 times larger than derived by McKay et al. (1991), and would result in a liquid depth change of 0.1 $m yr^{-1}$ for pure methane, and 6.9×10^{-3} $m yr^{-1}$ for a ternary liquid with mole fractions of 0.44 CH_4, 0.34 C_2H_6, and 0.22 N_2. The general circulation model of Mitchell (2008) predicts an evaporative flux of 2 $W m^{-2}$ available near the equator, which leads to a pure methane evaporation rate of 3.91×10^{-6} $kg m^{-2} s^{-1}$, or 0.28 $m yr^{-1}$. Recently, Schneider et al. (2012) used their 3-dimensional coupled surface–atmosphere model to predict polar CH_4 loss from late summer to winter of 0.2 $m yr^{-1}$. Mitri et al. (2007) balanced the sensible and latent heat fluxes for lakes in equilibrium, and obtained 20 $W m^{-2}$, a significantly higher value than the aforementioned models. Their evaporation rate depends linearly on the methane mole fraction, deviation from atmospheric saturation, and surface wind speed, and varies between 0.3 and 11 $m yr^{-1}$ (pure CH_4 case). For a lake with molar concentrations of 35%, 60% and 5% CH_4, C_2H_6 and N_2, respectively, the predicted depth decrease is ~3 $m yr^{-1}$. Tokano (2009) deduces a value of the same magnitude, for pure methane though. He also notes that the evaporation of a mixed lake (40% CH_4, 40% C_2H_6, 20% N_2) will be controlled by methane and nitrogen, and all CH_4 from the lake would evaporate in ~350 Titan days, roughly 15 Earth years. To date, the only evaporation rate value inferred from observations refers to Ontario Lacus, and is estimated to be 1 $m yr^{-1}$ (Hayes et al., 2011).

Overall, the laboratory evaporation data presented here are significantly higher than most model predictions, but are comparable to the results of Mitri et al. (2007) and Hayes et al. (2011). The results are shown in Fig. 7a after correcting for the gravity difference between Titan and Earth. The evaporation rate from Mitri et al. (2007) is just slightly higher than our experimental value for the appropriate CH_4 mole fraction ($E = 9.2 \times 10^{-5}$ $kg m^{-2} s^{-1}$ at $x_{CH_4} = 0.35$ vs. 4×10^{-5} $kg m^{-2} s^{-1}$ at $x_{CH_4} = 0.33$). One of the reasons might be that we do not simulate the effect of wind, which reduces humidity, hence increases the evaporation rate. Shear effects are most probably negligible for evaporation compared to the effect of the latter, as was experimentally shown previously for sublimation of H_2O ice on Mars (Chittenden et al., 2008).

We also note the possibility of layering of the simulated liquids, even though our data do not indicate stratification. In the lack of convection within the liquid, which we do not observe, diffusion would be the only means of generating partial stratification. Based on our calculations, the order of magnitude for ethane diffusion in liquid methane is ~500 s, an order of magnitude lower than the typical time-scale of evaporation in our simulations. Therefore, should diffusion play any role in the experiments, it would only be minor during the steady state evaporation episode in the experiments.

The inconsistency between most model results and the experimental data presented here may be indicative of the role of additional mechanisms compared to models limited by heat balance. Luspay-Kuti et al. (2012) point out the good match between their experimental results and the diffusion and passive convection driven evaporation model may suggest a combined effect of the two drive lake evaporation on Titan. The results presented in this study further support mass loss through diffusion and buoyancy, indicating these processes could indeed significantly contribute to evaporation on Titan.

4.5. Lake composition

The evaporation rate of Ontario Lacus inferred from observed shoreline recession (Hayes et al., 2011) enables us to estimate the composition of this southern lake based on the laboratory measurements and model presented in the current study. As seen in Fig. 7a, the evaporation rate from observed shoreline changes (Hayes et al., 2011) is most consistent with our data between $x_{CH_4,ini}(exp) = 0.20$ and 0.33. At the same time, methane mole fractions higher than $x_{CH_4,ini} = 0.33$ show higher evaporation rates than those deduced for Ontario Lacus (Hayes et al., 2011). Based on Fig. 7b, the lower limit bound by the experimental data and the appropriate relative humidity corresponds to a CH_4–C_2H_6–N_2 mixture of ~16%–77%–7%, while the upper limit correlates with 30%-61%–9%, respectively. Given the uncertainties in the model and the determined relative humidity, we estimate the composition of Ontario Lacus to be 15–30% CH_4, 50–80% C_2H_6, and 5–10% N_2. The upper bound for the ethane content is limited by the evaporation rate of the lowest methane concentration mixture that was experimentally measured, hence, it might even exceed the value provided here.

In the same manner, our dataset along with future Cassini observations of shoreline recessions may be used to estimate the methane–ethane–nitrogen concentration of any polar lake.

Retour à la table des matières : p. v

5. Conclusions

We performed laboratory simulations under temperature and pressure conditions relevant to Titan's poles on C_2H_6–CH_4 liquid mixtures. A linear relationship has been found between methane concentration and evaporation rate. Methane–ethane mixtures exhibit an initial N_2 dissolution from the simulated atmosphere with increasing methane concentration. To account for nitrogen dissolution and calculate the ternary composition of the evaporating liquids, a thermodynamic equilibrium model that follows the experimentally determined evaporation rates has been developed, using a PC-SAFT (Gross and Sadowski, 2001; Tan et al., 2013) approach combined with a diffusion and buoyancy-driven evaporation model for Titan conditions (Luspay-Kuti et al., 2012). The evaporation rates determined in our experiments are generally higher than previous, purely theoretical estimates. This implies a role of additional mechanisms not considered in former models. We showed that mass flux due to diffusion and buoyancy is a valid approach to describe liquid hydrocarbon mixture evaporation rates, hence, might be an important contributor to evaporation on Titan as well.

Evaporation rates derived from Cassini observations together with the laboratory measurements and model detailed in this study may provide estimates on polar liquid composition. Here we present the first, semi-direct estimation of the chemical composition of the southern lake Ontario Lacus. Our results imply that Ontario Lacus is enriched in ethane (>50–80%), and possibly other heavier hydrocarbons, perhaps as a result of seasonal effects. This may indicate it might have incurred extensive methane evaporation. In addition, the ethane-dominated lake composition may suggest origin, or replenishment from a subsurface liquid reservoir, as predicted by Mousis et al. (2014). We note, though, that the large uncertainties in the detection of the shoreline recession of Ontario Lacus by Cassini instruments make our method an approximation. Indeed, this is assuming the observed recession is due to evaporation Hayes et al. (2011). These results, though, do not imply that all lakes on Titan are ethane-rich. Northern lakes are predicted to be dominated by methane, which would increase their evaporation rates. A methane-dominated composition would imply replenishment by rainfall rather than contact with possible subsurface springs (Mousis et al., 2014). Hence, their stability over seasonal and longer time scales may change depending on the rate of methane precipitation over the seasons.

While we do not observe any ethane evaporation over the duration of our experiments (1–5 h), some evaporation of C_2H_6 might still occur on Titan. The instrumental limitation on the detectable changes in mass in our experimental protocol indicates an ethane evaporation rate lower than $\sim 10^{-6}\,\mathrm{kg\,m^{-2}\,s^{-1}}$. If ethane evaporation is bound by its low saturation pressure, it would be $\sim 10^{-3}$–10^{-4} times slower than pure methane evaporation. This is in agreement with the value provided by Tokano (2009) for pure ethane evaporation rate of $10^{-8}\ \mathrm{kg\,m^{-2}\,s^{-1}}$. Additional effects not considered here, such as drag force or heat balance may contribute to possible ethane loss from the lakes. Alternatively, higher humidity values (of methane and/or ethane) at the poles might reduce evaporation rates and result in a slightly different composition. Furthermore, we note that models predict propane to be present in the lakes with non-negligible mole fractions (Cordier et al., 2009; Tan et al., 2013; Glein and Shock, 2013), and its behavior would be expected to be similar to that of ethane (Cordier et al., 2013a).

As of currently, no shoreline recession has been detected for the northern polar lakes of Titan (Sotin et al., 2012). Yet, as the Saturn system moves further into spring and summer, possible increased evaporation and better viewing conditions might reveal changes linked to evaporation. These future Cassini observations along with our experimental data will provide valuable estimates on the composition and dynamics, as well as the source of Titan's polar lakes.

Acknowledgements

This work was funded by the NASA Outer Planet Research Program #NNX10AE10G. DC acknowledges financial support from the Observatoire des Sciences de l'Univers THETA Franche-Comté-Bourgogne, France. The authors would also like to thank two anonymous reviewers for improving the quality of the paper with their valuable comments.

References

Aharonson, O., Hayes, A.G., Lunine, J.I., Lorenz, R.D., Allison, M.D., Elachi, C., 2009. An asymmetric distribution of lakes on Titan as a possible consequence of orbital forcing. Nat. Geosci. 2, 851–854.
Battino, R., Rettich, T.R., Tominaga, T., 1984. The solubility of nitrogen and air in liquids. J. Phys. Chem. Ref. Data 13, 563. Jan.
Brown, R.H., Soderblom, L.A., Soderblom, J.M., Clark, R.N., Jaumann, R., Barnes, J.W., Sotin, C., Buratti, B., Baines, K.H., Nicholson, P.D., 2008. The identification of liquid ethane in Titan's Ontario Lacus. Nature 454, 607–610.
Chang, S., Lu, B., 1967. Vapor–liquid equilibriums in the nitrogen–methane–ethane system. Chem. Eng. Prog. Symp. Ser. 63, 81.
Chittenden, J.D., Chevrier, V., Roe, L.A., Bryson, K., Pilgrim, R., Sears, D.W.G., 2008. Experimental study of the effect of wind on the stability of water ice on Mars. Icarus 196, 477–487.
Cordier, D., Barnes, J.W., Ferreira, A.G., 2013a. On the chemical composition of Titan's dry lakebed evaporites. Icarus 226, 1431–1437.
Cordier, D., Mousis, O., Lunine, J.I., Lavvas, P., Vuitton, V., 2013b. Erratum: "An estimate of the chemical composition of Titan's lakes" [Astrophys. J. Lett. 707 (2009) L128]. Astrophys. J. Lett. 768, L23. Astrophys. J. Lett. 768 (2009) L23.
Cordier, D., Mousis, O., Lunine, J.I., Lavvas, P., Vuitton, V., 2009. An estimate of the chemical composition of Titan's lakes. Astrophys. J. Lett. 707, L128–L131.
Cordier, D., Mousis, O., Lunine, J.I., Lebonnois, S., Rannou, P., Lavvas, P., Lobo, L.Q., Ferreira, A.G.M., 2012. Titan's lakes chemical composition: sources of uncertainties and variability. Planet. Space Sci. 61, 99–107.
Crane Co., 1982. Flow of fluids through valves, fittings and pipe. Technical paper No. 410M, 21st printing. Crane Co., 300 Park Ave. New York.
Glein, C.R., Shock, E.L., 2013. A geochemical model of non-ideal solutions in the methane–ethane–propane–nitrogen–acetylene system on Titan. Geochim. Cosmochim. Acta 115, 217–240.
Graves, S.D.B., McKay, C.P., Griffith, C.A., Ferri, F., Fulchignoni, M., 2008. Rain and hail can reach the surface of Titan. Planet. Space Sci. 56, 346–357.
Griffith, C.A., Lora, J.M., Turner, J., Penteado, P.F., Brown, R.H., Tomasko, M.G., Doose, L., See, C., 2012. Possible tropical lakes on Titan from observations of dark terrain. Nature 486, 237–239.
Griffith, C.A., McKay, C.P., Ferri, F., 2008. Titan's tropical storms in an evolving atmosphere. Astrophys. J. Lett. 687, L41–L44.
Gross, J., Sadowski, G., 2001. Perturbed-chain SAFT: an equation of state based on a perturbation theory for chain molecules. Ind. Eng. Chem. Res. 40, 1244–1260.
Hayes, A.G., Aharonson, O., Lunine, J.I., Kirk, R.L., Zebker, H.A., Wye, L.C., Lorenz, R.D., Turtle, E.P., Paillou, P., Mitri, G., Wall, S.D., Stofan, E.R., Mitchell, K.L., Elachi, C., 2011. Transient surface liquid in Titan's polar regions from Cassini. Icarus 211, 655–671.
Ingersoll, A.P., 1970. Mars: occurrence of liquid water. Science 168, 972–973.
Janssen, M.A., Lorenz, R.D., West, R., Paganelli, F., Lopes, R.M., Kirk, R.L., Elachi, C., Wall, S.D., Johnson, W.T.K., Anderson, Y., Boehmer, R.A., Callahan, P., Gim, Y., Hamilton, G.A., Kelleher, K.D., Roth, L., Stiles, B., Le Gall, A., Cassini RADAR Team, 2009. Titan's surface at 2.2-cm wavelength imaged by the Cassini RADAR radiometer: calibration and first results. Icarus 200, 222–239.
Landau, L.D., Lifshitz, E.M., 1987. Fluid Mechanics (Course of Theoretical Physics), 2nd edition. Butterworth–Heinemann.
Lorenz, R.D., Newman, C., Lunine, J.I., 2010. Threshold of wave generation on Titan's lakes and seas: effect of viscosity and implications for Cassini observations. Icarus 207, 932–937.
Lunine, J., Atreya, S., 2008. The methane cycle on Titan. Nat. Geosci. 1, 335.
Luspay-Kuti, A., Chevrier, V.F., Wasiak, F.C., Roe, L.A., Welivitiya, W.D.D.P., Cornet, T., Singh, S., Rivera-Valentin, E.G., 2012. Experimental simulations of CH_4 evaporation on Titan. Geophys. Res. Lett. 39, 23203.
McKay, C.P., Pollack, J.B., Courtin, R., 1991. The greenhouse and antigreenhouse effects on Titan. Science 253, 1118–1121.
Mitchell, J.L., 2008. The drying of Titan's dunes: Titan's methane hydrology and its impact on atmospheric circulation. J. Geophys. Res., Planets 113, 8015.
Mitri, G., Showman, A.P., Lunine, J.I., Lorenz, R.D., 2007. Hydrocarbon lakes on Titan. Icarus 186, 385–394.
Moriconi, M.L., Lunine, J.I., Adriani, A., D'Aversa, E., Negrão, A., Filacchione, G., Coradini, A., 2010. Characterization of Titan's Ontario Lacus region from Cassini/VIMS observations. Icarus 210, 823–831.
Mousis, O., Choukroun, M., Lunine, J.I., Sotin, C., 2014. Equilibrium composition between liquid and clathrate reservoirs on Titan. Icarus 239, 39–45.

Retour à la table des matières : p. v

Parrish, W., Hiza, M., 1995. Liquid–vapor equilibria in the nitrogen–methane system between 95 and 120 K. In: Timmerhaus, K. (Ed.), Adv. Cryog. Eng., vol. 19. Springer, US, pp. 300–308.
Poling, B.E., Prausnitz, J.M., O'Connell, J., 2007. The Properties of Gases and Liquids, 5th edition. McGraw-Hill Professional, Englewood Cliffs.
Schneider, T., Graves, S.D.B., Schaller, E.L., Brown, M.E., 2012. Polar methane accumulation and rainstorms on Titan from simulations of the methane cycle. Nature 481, 58–61.
Sotin, C., Lawrence, K.J., Reinhardt, B., Barnes, J.W., Brown, R.H., Hayes, A.G., Le Mouélic, S., Rodriguez, S., Soderblom, J.M., Soderblom, L.A., Baines, K.H., Buratti, B.J., Clark, R.N., Jaumann, R., Nicholson, P.D., Stephan, K., 2012. Observations of Titan's Northern lakes at 5 μm: implications for the organic cycle and geology. Icarus 221, 768–786.
Sprow, F.B., Prausnitz, J.M., 1966. Vapor–liquid equilibria for five cryogenic mixtures. AIChE J. 12 (4), 780–784.
Stofan, E.R., Elachi, C., Lunine, J.I., Lorenz, R.D., Stiles, B., Mitchell, K.L., Ostro, S., Soderblom, L., Wood, C., Zebker, H., Wall, S., Janssen, M., Kirk, R., Lopes, R., Paganelli, F., Radebaugh, J., Wye, L., Anderson, Y., Allison, M., Boehmer, R., Callahan, P., Encrenaz, P., Flamini, E., Francescetti, G., Gim, Y., Hamilton, G., Hensley, S., Johnson, W.T.K., Kelleher, K., Muhleman, D., Paillou, P., Picardi, G., Posa, F., Roth, L., Seu, R., Shaffer, S., Vetrella, S., West, R., 2007. The lakes of Titan. Nature 445, 61–64.
Stryjek, R., Chappelear, P.S., Kobayashi, R., 1974. Low-temperature vapor–liquid equilibriums of nitrogen–ethane system. J. Chem. Eng. Data 19 (4), 340–343.
Tan, S.P., Kargel, J.S., Marion, G.M., 2013. Titan's atmosphere and surface liquid: new calculation using statistical associating fluid theory. Icarus 222, 53–72.
Tokano, T., 2009. Limnological structure of Titan's hydrocarbon lakes and its astrobiological implication. Astrobiology 9, 147–164.
Turtle, E.P., Perry, J.E., Hayes, A.G., Lorenz, R.D., Barnes, J.W., McEwen, A.S., West, R.A., Del Genio, A.D., Barbara, J.M., Lunine, J.I., Schaller, E.L., Ray, T.L., Lopes, R.M.C., Stofan, E.R., 2011. Rapid and extensive surface changes near Titan's equator: evidence of April showers. Science 331, 1414.
Wasiak, F.C., Luspay-Kuti, A., Welivitiya, W.D.D.P., Roe, L.A., Chevrier, V.F., Blackburn, D.G., Cornet, T., 2013. A facility for simulating Titan's environment. Adv. Space Res. 51, 1213–1220.
Wichterle, I., Kobayashi, R., 1972. Vapor–liquid equilibrium of methane–ethane system at low temperatures and high pressures. J. Chem. Eng. Data 17 (1), 9–12.
Williams, K.E., McKay, C.P., Persson, F., 2012. The surface energy balance at the Huygens landing site and the moist surface conditions on Titan. Planet. Space Sci. 60, 376–385.
Wilson, G., 1975. Vapor–liquid equilibria of nitrogen, methane, ethane, and propane binary mixtures at temperatures from total pressure measurements. In: Adv. Cryog. Eng., vol. 20. Plenum Press, New York, p. 164.

Retour à la table des matières : p. v

4.9 Article sur la formation des dépressions lacustres

AGU PUBLICATIONS

JGR

Journal of Geophysical Research: Planets

RESEARCH ARTICLE

10.1002/2014JE004738

Dissolution on Titan and on Earth: Toward the age of Titan's karstic landscapes

Thomas Cornet[1], Daniel Cordier[2], Tangui Le Bahers[3], Olivier Bourgeois[4], Cyril Fleurant[5], Stéphane Le Mouélic[4], and Nicolas Altobelli[1]

[1]European Space Agency (ESA), European Space Astronomy Centre (ESAC), Villanueva de la Canada, Spain, [2]Institut UTINAM, CNRS/INSU, Université de Franche-Comté, Besançon Cedex, France, [3]Laboratoire de Chimie UMR 5182, Université de Lyon, Université Claude Bernard Lyon 1, ENS Lyon, Lyon, France, [4]LPG Nantes, UMR 6112, CNRS, OSUNA, Université de Nantes, 2 rue de la Houssinière, Nantes, France, [5]LETG - UMR CNRS 6554, Université d'Angers, UFR Sciences, Angers, France,

Key Points:
- Titan's lacustrine depressions result from the dissolution of the surface
- Denudation rates allow to infer dissolution timescales on Earth and Titan
- Titan's depressions developed in less than a few hundred million years

Correspondence to:
T. Cornet,
tcornet@sciops.esa.int

Citation:
Cornet, T., D. Cordier, T. Le Bahers, O. Bourgeois, C. Fleurant, S. Le Mouélic, and N. Altobelli (2015), Dissolution on Titan and on Earth: Toward the age of Titan's karstic landscapes, *J. Geophys. Res. Planets*, *120*, doi:10.1002/2014JE004738.

Received 3 OCT 2014
Accepted 19 APR 2015
Accepted article online 25 APR 2015

Abstract Titan's polar surface is dotted with hundreds of lacustrine depressions. Based on the hypothesis that they are karstic in origin, we aim at determining the efficiency of surface dissolution as a landshaping process on Titan, in a comparative planetology perspective with the Earth as reference. Our approach is based on the calculation of solutional denudation rates and allow inference of formation timescales for topographic depressions developed by chemical erosion on both planetary bodies. The model depends on the solubility of solids in liquids, the density of solids and liquids, and the average annual net rainfall rates. We compute and compare the denudation rates of pure solid organics in liquid hydrocarbons and of minerals in liquid water over Titan and Earth timescales. We then investigate the denudation rates of a superficial organic layer in liquid methane over one Titan year. At this timescale, such a layer on Titan would behave like salts or carbonates on Earth depending on its composition, which means that dissolution processes would likely occur but would be 30 times slower on Titan compared to the Earth due to the seasonality of precipitation. Assuming an average depth of 100 m for Titan's lacustrine depressions, these could have developed in a few tens of millions of years at polar latitudes higher than 70°N and S, and a few hundreds of million years at lower polar latitudes. The ages determined are consistent with the youth of the surface (<1 Gyr) and the repartition of dissolution-related landforms on Titan.

1. Introduction

Along with the Earth, Saturn's icy moon Titan is the only planetary body of the entire solar system that possesses lakes and seas [*Lopes et al.*, 2007; *Stofan et al.*, 2007; *Hayes et al.*, 2008]. Some of these lakes and seas are currently covered by liquids, while others are not [*Hayes et al.*, 2008]. Most are located in the polar regions [*Hayes et al.*, 2008; *Aharonson et al.*, 2009], although a few occurrences have been reported at lower latitudes [*Moore and Howard*, 2010; *Vixie et al.*, 2012]. The currently filled lakes and seas are located poleward of 70° of latitude in both hemispheres whereas most empty depressions are located at lower latitudes (Figure 1) [*Hayes et al.*, 2008; *Aharonson et al.*, 2009].

Altogether, empty depressions, lakes, seas, and fluvial channels argue for the presence of an active "hydrological" cycle on Titan similar to that of the Earth, with exchanges between the subsurface (ground liquids), the surface (lakes, seas, and fluvial channels), and Titan's methane-rich atmosphere, where convective clouds and sporadic intense rainstorms have been imaged by the Cassini spacecraft instruments [*Turtle et al.*, 2011a]. Methane, rather than water as on Earth, probably dominates the cycle on Titan [*Lunine et al.*, 2008] and thus constitutes one of the main components of the surface liquid bodies observed in the polar regions [*Glein and Shock*, 2013; *Tan et al.*, 2013]. Ethane, the main photodissociation product of methane [*Atreya*, 2007], is also implied in Titan's lakes chemistry, as predicted by several thermodynamical models [*Lunine et al.*, 1983; *Raulin*, 1987; *Dubouloz et al.*, 1989; *Cordier et al.*, 2009; *Tan et al.*, 2013; *Cordier et al.*, 2013a; *Glein and Shock*, 2013], or as identified in Ontario Lacus thanks to the Cassini Visual and Infrared Mapping Spectrometer (VIMS) instrument [*Brown et al.*, 2008].

Titan's lakes are located in topographic depressions carved into the ground by geological processes that are poorly understood to date. The origin of the liquid would be related to precipitation, surface runoff, and underground circulation, leading to the accumulation of liquids in local topographic depressions.

©2015. American Geophysical Union. All Rights Reserved.

Retour à la table des matières : p. v

Journal of Geophysical Research: Planets 10.1002/2014JE004738

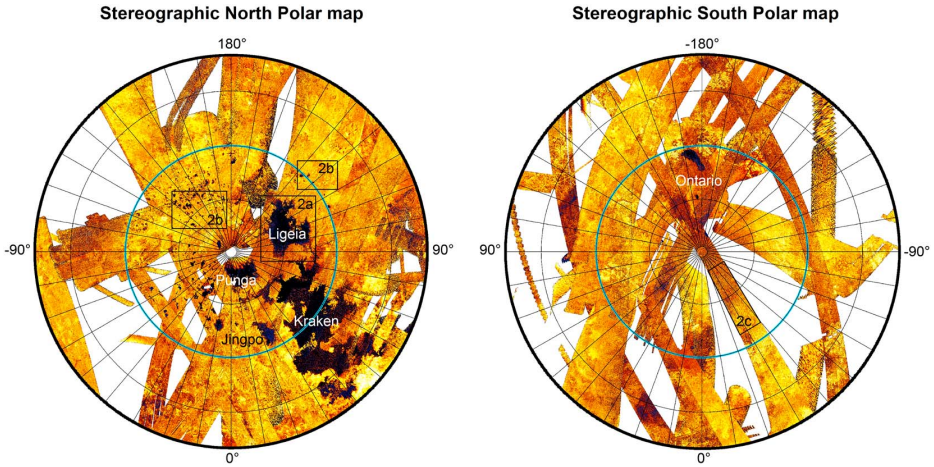

Figure 1. RADAR Synthetic Aperture Radar (SAR) mosaic of the TA (2004) to T95 (2013) flybys in north and south polar stereographic projections (down to 55° latitudes). All current lakes observed to date are located above 70° in latitude (blue circles).

In the present work, we aim to constrain the origin and the age of these depressions. Section 2 first provides a brief overview of their geology and a discussion of their possible origin based on their morphological characteristics and from considerations about Titan's surface composition and climate. Based on this discussion, we propose a new quantitative model, whereby the depressions have formed by the dissolution of a surface geological layer over geological timescales, such as in karstic landscapes on Earth.

In terrestrial karstic landscapes, the maximum quantity of mineral that can be dissolved per year, namely the solutional denudation rate, can be computed using a simple thermodynamics-climatic model presented in section 3. The denudation rate depends on the nature of the surface material (solubility and density of the minerals) and on the climate conditions (precipitation, evaporation, and surface temperature). Using this simple model, it is possible to determine theoretical timescales for the formation of specific karstic landforms on Earth, which are compared to relative or absolute age determinations in section 4.

We apply the same model to Titan's surface in section 5. Section 5.1 is dedicated to the comparative study of denudation rates of pure solid organics in pure liquid methane, ethane, and propane and of common soluble minerals (halite, gypsum, anhydrite, calcite, and dolomite), cornerstones of karstic landscapes development on Earth, in liquid water over terrestrial timescales. Section 5.2 describes the computation of denudation rates of pure solids and of mixed organic surface layers in liquid methane over Titan timescales by using the methane precipitation rates extracted from the Global Circulation Model (GCM) of *Schneider et al.* [2012]. Based on these denudation rates, we compute the timescales needed to develop the typical 100 m deep topographic depressions observed in the polar regions of Titan (section 6) and compare them to timescales estimated from other observations (e.g., crater counting and dune formation).

2. Geology of Titan's Lacustrine Depressions

2.1. Geomorphological Settings

Seas and lacustrine depressions strongly differ in shape (Figure 2). On the one hand, seas are large (several hundred kilometers in width) and deep (from 150 to 300–400 m in depth) [*Lorenz et al.*, 2008, 2014; *Mastrogiuseppe et al.*, 2014]. They possess dendritic contours and are connected to fluvial channels (e.g., Ligeia Mare, Figure 2a) [*Stofan et al.*, 2007; *Sotin et al.*, 2012; *Wasiak et al.*, 2013]. They seem to develop in areas associated with reliefs, which constitute some parts of their coastlines.

On the other hand, Titan's lacustrine depressions (Figure 2b) develop in relatively flat areas. They lie between 300 and 800 m above the level of the northern seas [*Stiles et al.*, 2009; *Kirk et al.*, 2012]. They are typically rounded or lobate in shape, and some of them seem to be interconnected [*Bourgeois et al.*, 2008]. Their widths vary from a few tens of kilometers, such as for most of Titan's lacunae, up to a few hundred kilometers, such as Ontario Lacus or Jingpo Lacus. Their depths have been tentatively estimated to range from a few meters

Retour à la table des matières : p. v

AGU Journal of Geophysical Research: Planets 10.1002/2014JE004738

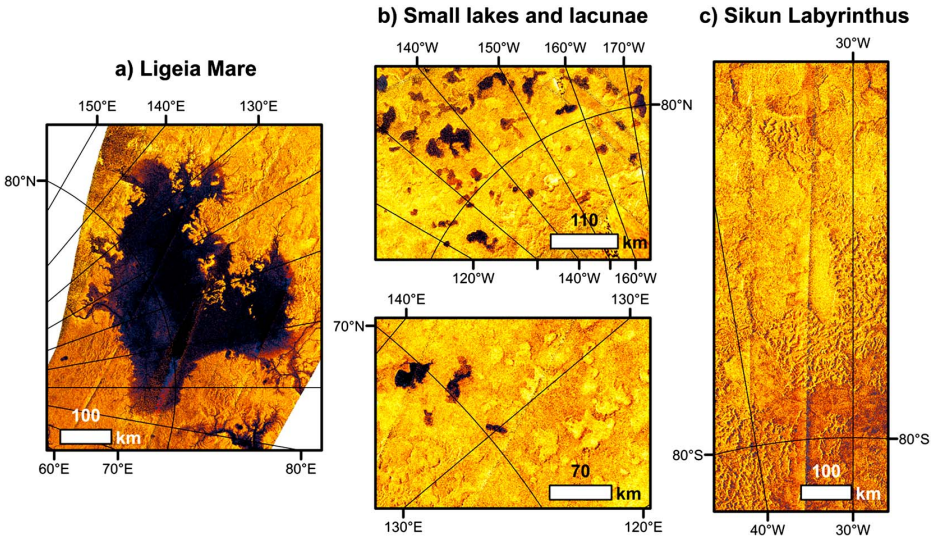

Figure 2. RADAR SAR views of (a) Titan's second largest sea Ligeia Mare, (b) empty and liquid-covered lacustrine depressions, and (c) the heavily dissected terrains of Sikun Labyrinthus. Ligeia Mare clearly differs in size and shape from the smaller lacustrine depressions, which suggests a different formation mechanism. Lacustrine depressions and labyrinthic terrains pertain to the class of features potentially related to the dissolution of the surface.

to 100–300 m [*Hayes et al.*, 2008; *Kirk and Howington-Kraus*, 2008; *Stiles et al.*, 2009; *Lorenz et al.*, 2013], with "steep"-sided walls [*Mitchell et al.*, 2007; *Bourgeois et al.*, 2008; *Kirk and Howington-Kraus*, 2008; *Hayes et al.*, 2008]. The liquid-covered depressions would lie 250 m below the floor of the empty depressions [*Kirk et al.*, 2007], which could be indicative of the presence of an alkanofer in the subsurface, analog to terrestrial aquifers, filling or not the depressions depending on their base level [*Hayes et al.*, 2008; *Cornet et al.*, 2012]. The depressions sometimes possess a raised rim, ranging from a few hundred meters up to 600 m in height [*Kirk et al.*, 2007; *Kirk and Howington-Kraus*, 2008]. All these numbers are likely subject to modification following future improvements in depth-deriving techniques.

2.2. Geological Origin of the Depressions

The geological origin of the topographic depressions and how they are fed by liquids are still debated. The geometric analysis of the lakes by *Sharma and Byrne* [2010, 2011] led to the conclusion that, unlike on Earth, the formation mechanism of the lacustrine depressions cannot be derived from the analysis of their coastline shapes. Recently, *Black et al.* [2012] and *Tewelde et al.* [2013] showed that mechanical erosion due to fluvial activity would have a minor influence in landscape evolution on Titan. Given this context, several hypotheses are being explored to understand how Titan's lakes have formed. These include (1) cryovolcanic origin [*Mitchell et al.*, 2007; *Wood et al.*, 2007], forming topographic depressions in which lakes can exist, such as in terrestrial calderas [*Acocella*, 2007] or maars [*Lorenz*, 1986]; (2) thermokarstic origin [*Kargel et al.*, 2007; *Mitchell et al.*, 2007; *Harrisson*, 2012], where the cyclic destabilization of a methane frozen ground would form topographic depressions, such as in periglacial areas on Earth where the permafrost cyclically freezes and thaws and forms thermokarst lakes, pingos, or alases [*French*, 2007]; and (3) solutional origin [*Mitchell et al.*, 2007; *Bourgeois et al.*, 2008; *Mitchell*, 2008; *Mitchell and Malaska*, 2011; *Malaska et al.*, 2011; *Barnes et al.*, 2011; *Cornet et al.*, 2012], where processes analogous to terrestrial karstic dissolution create topographic depressions, such as terrestrial sinkholes/dolines, playas, and pans under various climates [*Shaw and Thomas*, 2000; *Ford and Williams*, 2007].

On the one hand, the general lack of unequivocal cryovolcanic features on Titan tends to limit the likelihood of the cryovolcanic hypothesis [*Moore and Pappalardo*, 2011]. A methane-based permafrost would be difficult to form on Titan due to the presence of nitrogen in the atmosphere [*Lorenz and Lunine*, 2002; *Heintz and Bich*, 2009]. Its putative cyclic destabilization would also be challenging, given the tiny temperature variations between summer and winter, day and night, and equator and poles [*Jennings et al.*, 2009; *Lora et al.*, 2011; *Cottini et al.*, 2012] over all timescales [*Aharonson et al.*, 2009; *Lora et al.*, 2011]. On the other hand, solid organics have been shown to be quite soluble in liquid hydrocarbons under Titan's surface conditions [*Lunine et al.*,

AGU Journal of Geophysical Research: Planets 10.1002/2014JE004738

Table 1. Production Rates (in Molecules/cm^2/s) of Simple Solid Organics in Titan's Atmosphere Derived From Several Photochemical Models[a]

	Y84	T95	L96	W04	L08	K09
C_2H_6	5.80×10^9	1.50×10^{10}	1.41×10^9	1.60×10^9	4.10×10^9	1.16×10^9
C_3H_8	1.40×10^8	5.40×10^8	3.14×10^7	3.30×10^7	3.70×10^8	2.17×10^8
C_4H_{10}	2.30×10^7	8.80×10^7		3.00×10^7		7.02×10^5
C_2H_2	1.20×10^9	1.10×10^9	9.28×10^8	3.70×10^8	3.20×10^8	3.22×10^8
C_2H_4				9.30×10^7	6.00×10^7	
C_3H_4						2.64×10^6
C_4H_4						1.57×10^4
C_4H_6				6.50×10^4		1.71×10^7
C_6H_6				4.60×10^5	2.10×10^5	1.08×10^6
HCN	2.00×10^8	1.00×10^8	8.00×10^7	2.10×10^6	3.20×10^8	1.54×10^8
HC_3N	1.70×10^7		3.73×10^7	1.30×10^7	9.20×10^6	1.26×10^7
C_2N_2	1.20×10^7		2.89×10^4	2.00×10^6	2.60×10^4	3.52×10^6
C_4N_2			7.20×10^6	9.70×10^5	1.90×10^6	
CH_3CN			6.61×10^5	3.40×10^4	1.70×10^7	1.27×10^7
C_2H_3CN				1.60×10^7	2.80×10^5	1.62×10^7
C_2H_5CN						8.00×10^5

[a]Not reported here is the production rate of tholins, estimated by *Cabane et al.* [1992], *Rannou et al.* [2003], and *Krasnopolsky* [2009] to be between 0.2 and 7 kg/cm^2/GEyr (giga Earth year). The list of compound names is available in Appendix A. Y84: *Yung et al.* [1984], T95: *Toublanc et al.* [1995], L96: *Lara et al.* [1996], W04: *Wilson and Atreya* [2004], L08: *Lavvas et al.* [2008a, 2008b], K09: *Krasnopolsky* [2009].

1983; *Raulin*, 1987; *Dubouloz et al.*, 1989; *Cordier et al.*, 2009, 2013a, 2013b; *Glein and Shock*, 2013; *Tan et al.*, 2013], provided that they are available at the surface. The observation of bright terrain around present lakes and inside of empty depressions, analogs of terrestrial evaporites produced by the evaporitic crystallization of dissolved solids, also strengthens this hypothesis [*Barnes et al.*, 2011; *MacKenzie et al.*, 2014].

On Earth, dissolution-related landforms are not restricted to sinkholes/dolines, pans, or playa, which characterize relatively young karsts [*Ford and Williams*, 2007]. Spectacular instances of reliefs nibbled by dissolution, known as cone/cockpit karsts, fluvio karsts, or tower karsts, exist under temperate to tropical/equatorial climates, such as in China [*Xuewen and Weihai*, 2006; *Waltham*, 2008], Indonesia [*Ford and Williams*, 2007], or the Caribbeans [*Fleurant et al.*, 2008; *Lyew-Ayee*, 2010]. The observation of possible mature karst-like terrains in Sikun Labyrinthus (Figure 2c) by *Malaska et al.* [2010], similar to these terrestrial karstic landforms also gives further credence to the hypothesis that lacustrine depressions on Titan are karstic in origin.

2.3. Composition of Titan's Solid Surface

Titan's surface can be divided into five main spectral units identified by the Cassini/VIMS instrument: bright terrain, dark equatorial dune fields, or dark brown units, blue units, 5 μm bright units, and the dark lakes [*Barnes et al.*, 2007; *Stephan et al.*, 2009]. In the polar regions, the solid surface appears dominantly as bright terrain, lakes, and patches identified as the 5 μm bright unit in VIMS data [*Barnes et al.*, 2011; *Sotin et al.*, 2012; *MacKenzie et al.*, 2014]. The spectral characteristics of the VIMS 5 μm bright unit seen inside and around some polar (and equatorial) lacustrine depressions indicate the presence of various hydrocarbons and nitriles [*Clark et al.*, 2010; *Moriconi et al.*, 2010] and are not compatible with the presence of water ice [*Barnes et al.*, 2009].

The origin of the organic materials is probably linked to the atmospheric photochemistry, which results in the formation of various hydrocarbons and nitriles [*Lavvas et al.*, 2008a, 2008b; *Krasnopolsky*, 2009] detected by Cassini [*Cui et al.*, 2009; *Magee et al.*, 2009; *Clark et al.*, 2010; *Coustenis et al.*, 2010; *Vinatier et al.*, 2010; *Cottini et al.*, 2012]. Table 1 gives the estimated fluxes of some produced organics, as derived from several models. Most of these compounds could condense as solids and sediment onto the surface over geological timescales [*Atreya*, 2007; *Malaska et al.*, 2011]. Most of them would be relatively soluble in liquid alkanes [*Raulin*, 1987; *Dubouloz et al.*, 1989; *Cordier et al.*, 2009, 2013a; *Glein and Shock*, 2013; *Tan et al.*, 2013].

Retour à la table des matières : p. v

AGU Journal of Geophysical Research: Planets 10.1002/2014JE004738

It is therefore reasonable to assume that a superficial soluble layer, composed of organic products, exists at the surface of Titan. Episodic dissolution of this layer would be responsible for the development of karst-like depressions and labyrinthic terrains [*Bourgeois et al.*, 2008; *Malaska et al.*, 2010, 2011; *Mitchell and Malaska*, 2011; *Cornet et al.*, 2012]. Evaporitic crystallization could also occur after episodes of dissolution in the liquids, forming evaporite-like deposits [*Barnes et al.*, 2011; *Cornet et al.*, 2012; *Cordier et al.*, 2013b; *MacKenzie et al.*, 2014].

3. Solutional Denudation Rates on Earth

On Earth, karstic landforms develop thanks to the dissolution of carbonate (calcite and dolomite) and evaporite (gypsum, anhydrite and halite) minerals under the action of groundwater and rainfall percolating through pore space and fractures present in rocks. The mineral solubilities vary as a function of the environmental conditions (amount of rain and partial pressure of carbon dioxide) [*Ford and Williams*, 2007]. Karstic landforms like dolines or sinkholes are often located under temperate to humid climates in carbonates (though gypsum or halite karsts also exist on Earth). They reach depths of up to a few hundred meters [*Ford and Williams*, 2007]. Karsto-evaporitic landforms like pans are located under semiarid to arid climates. They reach depths of up to a few tens of meters [*Goudie and Wells*, 1995; *Bowen and Johnson*, 2012]. Evaporitic landforms like playas are located under arid climates. They are characterized by their extreme flatness and can occur in any kind of topographic depression [*Shaw and Thomas*, 2000].

Denudation rates (hereafter *DR*) in terrestrial karstic landscapes are primarily constrained by geological (age and physicochemical nature of rocks) and climate (net precipitation rates evolution) analyses. For many limestone-dominated areas (the majority of karst areas), it is commonly assumed that dissolution features are mainly created in the epikarstic zone located in the top few meters below the surface [*White*, 1984; *Ford and Williams*, 2007]. Classically, in karstic terrains, the chemical/solutional denudation rate *DR* (in meters per Earth year or m/Eyr) is related to the rock physicochemical properties and the climate by the following equation [*White*, 1984; *Tucker et al.*, 2001; *Ford and Williams*, 2007; *Fleurant et al.*, 2008]:

$$DR = \rho_w \frac{M_{\text{calcite}}}{\rho_{\text{calcite}}} \tau\, m_{\text{Ca}} \qquad \text{(m/Eyr)}, \tag{1}$$

where ρ_w is the mass density of liquid water ($\simeq$ 1000 kg/m^3), M_{calcite} is the molar mass of calcite (in kg/mol), ρ_{calcite} is the mass density of calcite (in kg/m^3), τ is the mean annual net precipitation rate (in m/yr), equivalent to the sum of runoff and infiltration or the difference between precipitation and evapotranspiration over long timescales [*White*, 2012], and m_{Ca} is the equilibrium molality of calcite (Ca^{2+} cations, in mol/kg), assuming an instantaneous dissolution. Following this equation, denudation rates depend linearly on the climate precipitation regime and on the molality of dissolved materials.

Molality calculations are provided in Appendix B for various soluble minerals, based on two thermodynamic hypotheses: an Ideal Solution Theory (IST, no preferential interactions between molecules) and an Electrolyte Solution Theory (EST, preferential interactions between molecules). We incorporated the effect of CO_2 gas dissolved in water, which acidifies water due to a series of intermediate reactions (one of which producing carbonic acid) and increases the dissolution rates of carbonates (calcite and dolomite, see Appendix B for more details). The partial pressure of CO_2 (hereafter P_{CO_2}, in atm) under different climates can be computed as follows [*Ford and Williams*, 2007]:

$$\log P_{CO_2} = -3.47 + 2.09\,(1 - e^{-0.00172\,AET}), \tag{2}$$

where *AET* is the mean annual evapotranspiration rate in mm/Eyr. Applying the above formula gives $P_{CO_2} < 3$ matm for arid areas, $3 < P_{CO_2} < 12$ matm for temperate areas and $P_{CO_2} > 12$ matm for tropical or equatorial climates. The resulting typical values of denudation rates on Earth for common soluble minerals in liquid water are given in Table 2. Depending on the climatic conditions, denudation rates of salts are on the order of a few hundred µm to a few centimeters per Earth year, whereas denudation rates of carbonates are on the order of a few µm to a few hundred µm per Earth year. Note that chemical erosion is just one of the landshaping processes on Earth. Other mechanisms, such as mechanical erosion, would tend to increase the total denudation rate of a surface [*Fleurant et al.*, 2008]. The dissolved solids can take part in the crystallization

AGU Journal of Geophysical Research: Planets 10.1002/2014JE004738

Table 2. Solutional Denudation Rates in mm/Eyr for Terrestrial Minerals at 298.15 K and Under Various Climatic Conditions (CO_2 Content and Precipitation Rates)[a]

Name	τ = 30 cm/Eyr	τ = 1 m/Eyr
	Dissolution by Dissociation	
Halite	50.643	167.122
Gyspum	0.504	1.662
Anhydrite	0.224	0.740
Calcite	8.55×10^{-4}	2.82×10^{-3}
Dolomite	7.84×10^{-4}	2.59×10^{-3}
	Acid Dissolution	
Calcite, P_{CO_2} = 0.33 matm	0.006	0.020
Dolomite, P_{CO_2} = 0.33 matm	0.005	0.017
Calcite, P_{CO_2} = 0.01 atm	0.020	0.066
Dolomite, P_{CO_2} = 0.01 atm	0.017	0.057
Calcite, P_{CO_2} = 0.11 atm	0.047	0.156
Dolomite, P_{CO_2} = 0.11 atm	0.040	0.132

[a]All values correspond to the EST hypothesis except those for halite (IST).

of soluble deposits at the surface (e.g., calcretes or salt crusts in arid environments) or in the subsurface (e.g., cements), when they saturate the liquids. They do not necessarily crystallize at the location where they dissolved [*Ford and Williams*, 2007].

4. Denudation Rates to Determine Ages of Terrestrial Karstic Landscapes

Using the denudation rates, theoretical timescales for the development of dissolution landforms of a given depth can be inferred. We test hereafter this hypothesis on terrestrial instances by comparing ages determined from the denudation rates and ages determined from relative or absolute chronology. For carbonates, the partial pressure of CO_2 is computed based on the MOD16 Global Evapotranspiration Product of the University of Montana/Environmental Systems Research Institute Mapping Center. The notation GEyrs, MEyrs, and kEyrs will refer to timescales expressed, respectively, in giga Earth years (10^9 years), million Earth years (10^6 years), and kilo Earth years (10^3 years) in the following sections.

4.1. Example Under a Hyperarid Climate: The Caves of the Mount Sedom Diapir (Israel)

Mount Sedom is a 11×1.5 km salt diapir located in Israel, 250 m above the level of the Dead sea, under a hyperarid climate [*Frumkin*, 1994, 1996]. It is composed of a Pliocene-Pleistocene (<7 MEyrs) halite basis covered by a 5–50 m thick layer composed of anhydrite and sandstones. Several sinkholes and caves exist in Mount Sedom [*Frumkin*, 1994].

In this part of Israel, the present-day hyperarid climate leads to average rainfall rates of 50 mm/Eyr, of which 10–15 mm/Eyr constitutes the average effective rainfall rate (τ). Gvishim and Mishquafaim Caves are, respectively, 60 m and 20 m deep caves and are essentially carved into halite in the northern part of Mount Sedom. Radioisotopic age measurements in several caves of Mount Sedom give an Holocene age, about 8 kEyrs (and around 3.2–3.4 kEyrs from age measurements performed in Mishquafaim Cave) [*Frumkin*, 1996].

Assuming that underground dissolution is somewhat connected to the rainfall percolating through anhydrite and reaching halite, the denudation rates computed with our model (equation (1)) over this region are $DR \simeq 1.69 - 2.53$ mm/Eyr. The timescales required to form these caves would be between 23.7 and 35.5 kEyrs for Gvishim Cave, and between 7.9 and 11.8 kEyrs for Mishquafaim Cave, longer than those estimated from radioisotopic measurements.

However, it should be noted that Mount Sedom experiences a rather deep dissolution, the load of dissolved solids in the underground liquid water flowing in its caves being up to 3 times that of surface runoff [*Frumkin*, 1994]. Therefore, considering that the denudation rate should be 3 times greater, we find timescales of development between 7.9 and 11.8 kEyrs for Gvishim Cave and between 2.6 and 3.9 kEyrs for Mishquafaim Cave, in better agreement with age measurements.

4.2. Example Under a Semiarid Climate: The Etosha Super-Pan (Namibia)

The Etosha Pan, located in Namibia under a semiarid climate, is a flat 120×60 km karsto-evaporitic depression that has already been suggested as a potential analog for Titan's lacustrine depressions [*Bourgeois et al.*, 2008; *Cornet et al.*, 2012]. The depression is about 15 to 20 m deep at most and has been carved into the carbonate layer essentially composed of calcretes and dolocretes lying on top a middle Tertiary-Quaternary detritical

Retour à la table des matières : p. v

AGU Journal of Geophysical Research: Planets 10.1002/2014JE004738

sedimentary sequence that covers the Owambo basin [*Buch and Rose*, 1996; *Hipondoka*, 2005]. This sedimentary sequence is believed to have accumulated under a semiarid climate, relatively similar to the current one. The age of the calcrete layer is not known precisely, but its formation is believed to have started during the Miocene/Pliocene transition about 7 MEyrs ago [*Buch*, 1997; *Buch and Trippner*, 1997], or even later during the late Pliocene, 4 MEyrs ago [*Miller et al.*, 2010]. The Etosha Pan is believed to have developed at the expense of the calcrete layer since 2 MEyrs [*Miller et al.*, 2010].

In the Owambo sedimentary basin, $AET \simeq 350$ mm/Eyr, yielding $P_{CO_2} = 3$ matm. Precipitation rates during the summer rainy season reach up to 500 mm/Eyr, which leads to $\tau = 150$ mm/Eyr at most. These conditions lead to $DR = 6.5$ µm/Eyr in a substratum composed of calcite (calcrete) and $DR = 5.6$ µm/Eyr in a substratum composed of dolomite (dolocrete). These denudation rates give an approximate age for the Etosha Pan of about 2.31–3.08 MEyrs in calcretes and 2.68 to 3.57 MEyrs in dolocretes. These ages are consistent with ages estimated from geological observations (< 4 MEyrs).

4.3. Example Under a Temperate Climate: The Doline of Crveno Jezero (Croatia)

Crveno Jezero is a 350 m wide collapse doline located in the Dinaric Karst of Croatia, under a presently Mediterranean temperate climate. This part of the Dinaric Karst is essentially composed of limestones and dolomites that have been deposited during the Mesozoic (Triassic to Cretaceous), when the area was covered by shallow marine carbonate shelves [*Vlahovic et al.*, 2002; *Mihevc et al.*, 2010]. The cliffs forming the doline are up to 250 m in height. The bottom of the depression is covered by a lake, named Red Lake, about 250 m deep. The total depth of the doline is therefore about 500 m [*Garasic*, 2001, 2012].

Although the formation process of the collapse dolines in the area is still not completely understood, especially in terms of the relative importance and timing of the collapse compared to the dissolution in the development of the structure, the uplift linked to the formation of the Alps (Eocene–Oligocene) led to the exposure of these carbonates and their subsequent karstification since at least Oligo-Miocene times (last 30 MEyrs) [*Sket*, 2012]. At some point, dissolution occurred to form an underground cave; then the load of the capping rocks exceeded their cohesion, leading to the brutal or progressive collapse of the cap in the empty space beneath. The timescale calculated for the doline formation therefore constitutes a higher estimate. Age determinations in the northern Dinaric caves have been performed and show that karstification would be older than 4 to 5 MEyrs [*Zupan Hajna*, 2012]. Crveno Jezero thus developed between 4 and 30 MEyrs ago.

In this region of Croatia, $AET \simeq 500$ mm/Eyr, which leads to $P_{CO_2} = 5.44$ matm. Annual mean precipitation rates are about 1100 mm/Eyr [*Mihevc et al.*, 2010], leading to $\tau = 600$ mm/Eyr. These parameters give $DR = 31.8$ µm/Eyr in limestones dominated by calcite ($DR = 27.5$ µm/Eyr in limestones dominated by dolomite). The time required to dissolve 500 m of calcite under these present conditions would be around 15.7 MEyrs (18.2 MEyrs in dolomite). It is likely that cap rocks fell into the cave, leading to a younger age (1 m of calcite and dolomite dissolve in about 31 and 36 kEyrs, respectively). However, the age determined by our method is still consistent with the geological records.

4.4. Example Under a Tropical Climate: The Xiaozhai Tiankeng (China)

The Xiaozhai Tiankeng is a 600 m wide collapse doline located in the Chongqing province of China, under a tropical climate. The depth of this doline is evaluated between 511 and 662 m depending on the location [*Xuewen and Weihai*, 2006; *Ford and Williams*, 2007]. It is organized into two major collapse structures, an upper 320 m deep structure and a lower 342 m deep shaft. The tiankeng developed into Triassic limestones in a karst drainage basin. It results from various surface and subsurface processes such as dissolution, fluid flows, and collapse. Tiankengs of China would have formed during the late Pleistocene (last 128,000 Eyrs) [*Xuewen and Weihai*, 2006] under an equatorial monsoonal climate similar to nowadays, emplaced 14 MEyrs ago [*Wang and Li*, 2009].

In the area, annual precipitation rates are about 1500 mm/Eyr, for an annual evapotranspiration rate of about 800 mm/Eyr, which leads to $P_{CO_2} = 0.0123$ atm and $\tau = 700$ mm/Eyr. Under these conditions, $DR = 49.6$ µm/Eyr (calcite) or $DR = 42.6$ µm/Eyr (dolomite) and the timescale to form the Xiaozhai Tiankeng would be between 10.3 and 13.3 MEyrs (calcite) and 12.0 and 15.5 MEyrs (dolomite), considerably longer timescales than those estimated from geological records. However, such a difference is to be expected, since the formation of gigantic tiankengs are subject to complex interconnected surface processes not taken into account in these simple calculations (collapse and underground circulation of water). This illustrates the limits of our method, generally overestimating the ages of karstic features when they do not result from dissolution only.

AGU Journal of Geophysical Research: Planets 10.1002/2014JE004738

5. Denudation Rates on Titan

Equation (1) has to be adapted for Titan. From thermodynamics, we compute molar volumes ($V_{m,i}$ in m^3/mol, see Appendix C) and mole fractions at saturation ($X_{i,sat}$, see Appendix B) instead of mass densities and molalities. We considered the Ideal and the nonideal Regular Solutions Theories (IST and RST, respectively) and ensured that our results are consistent with experimentally determined solubilities. The RST has been developed to determine the solubility of nonpolar to slightly polar molecules, such as simple hydrocarbons or carbon dioxide, in nonpolar solvents. It is less likely to be appropriate for polar molecules such as nitriles/tholins and water ice. We therefore always provide a comparison between the IST and the RST in order to assess the uncertainty of the calculation by using the RST for polar molecules (see also Appendix B). However, we consider the RST, which provides our lowest and more realistic solubilities (at least for hydrocarbons), as the most suited model for the study. We assume that dissolution is instantaneous, which is not unreasonable given the rapid saturation of solid hydrocarbons in liquid ethane inferred from recent dissolution experiments [*Malaska and Hodyss*, 2014], compared to the long geological timescales considered in our work. For a binary solute-solvent system, equation (1) becomes

$$DR_i = \frac{X_{i,\mathrm{sat}}}{1 - X_{i,\mathrm{sat}}} \tau \frac{V^S_{\mathrm{m},i}}{V^L_{\mathrm{m,solv}}} \quad \text{(m/Eyr)}, \tag{3}$$

where $V^S_{\mathrm{m},i}$ and $V^L_{\mathrm{m,\,solv}}$ are the molar volumes of the solid (crystallized) phase and of the liquid phase, respectively.

5.1. Comparison Between Titan and the Earth Over Terrestrial Timescales

In order to compare the behavior of Titan's solids in Titan's liquids with that of minerals in liquid water on Earth, we computed Titan's and Earth's denudation rates over Earth timescales by varying the precipitation rate between 0 and 2 m/Eyr. This range of precipitation rates encompasses the expected range on Titan (up to 1.2–1.3 m/Eyr during the rainy season [*Schneider et al.*, 2012]). It also covers the precipitation range between arid and tropical climates on Earth. This comparison is illustrated in Figures 3 (for hydrocarbons and carbon dioxide ice) and 4 (for nitriles and water ice), for which we fixed Titan's temperature to 91.5 K (the surface temperature during the rainy season according to *Schneider et al.* [2012]) and Earth's temperature to 298.15 K (with a partial pressure of carbon dioxide equal to 0.33 matm).

All organic compounds except $C_{11}H_{11}N$ would behave like common mineral salts (halite, gypsum, or anhydrite) according to the IST, which means that they would experience dissolution rates in the range of hundred µm to a few centimeters over one Eyr. According to the RST and assuming that the liquid is methane, C_2H_4 would behave like halite (centimeter-scale dissolution); C_4H_{10} and C_4H_4 like gypsum (hundred µm to millimeter-scale dissolution); C_2H_2, C_3H_4, C_4H_6, and CO_2 like carbonates (up to hundred µm-scale dissolution). C_6H_6 and nitriles would be less soluble in methane than calcite is in pure liquid water, with the least soluble nitriles being $C_{11}H_{11}N$, HCN, and CH_3CN. As expected, water ice is completely insoluble according to the RST, developed for nonpolar molecules.

The denudation rates of all organic compounds are higher in ethane and propane than in methane. Nitriles and C_6H_6, which are poorly soluble in methane, are quite soluble in ethane and propane (except $C_{11}H_{11}N$, HCN, and CH_3CN still under the calcite level) and reach denudation rates similar to those of carbonates or even gypsum. C_2H_2 and C_3H_4 would behave like carbonates (in ethane) or gypsum (in propane). C_4H_4 and C_4H_6 behave like salts in those liquids and are even more soluble than gypsum. C_4H_{10} and C_2H_4 are halite-like materials, extremely soluble in ethane and propane. Therefore, the likelihood of developing dissolution landforms in a hydrocarbon-dominated substrate, by analogy with the Earth, is high.

5.2. Present Denudation Rates on Titan Over a Titan Year

5.2.1. Net Precipitation Rates on Titan

Computing denudation rates over Titan timescales requires us to define the evolution of the net precipitation over one Titan year (1 Tyr $\simeq$ 29.5 Earth years). Titan's climate is primarily defined by a rainy warm "summer" season and a cold dry "winter" season, both spanning about 10 Earth years. Southern summers are shorter and more intense than those in the north [*Aharonson et al.*, 2009]. Precipitation occurs as sporadic and intense rainstorms during summer, when cloud formation is observed [*Roe et al.*, 2002; *Schaller et al.*, 2006, 2009; *Rodriguez et al.*, 2009, 2011; *Turtle et al.*, 2011a, 2011b].

Retour à la table des matières : p. v

AGU Journal of Geophysical Research: Planets 10.1002/2014JE004738

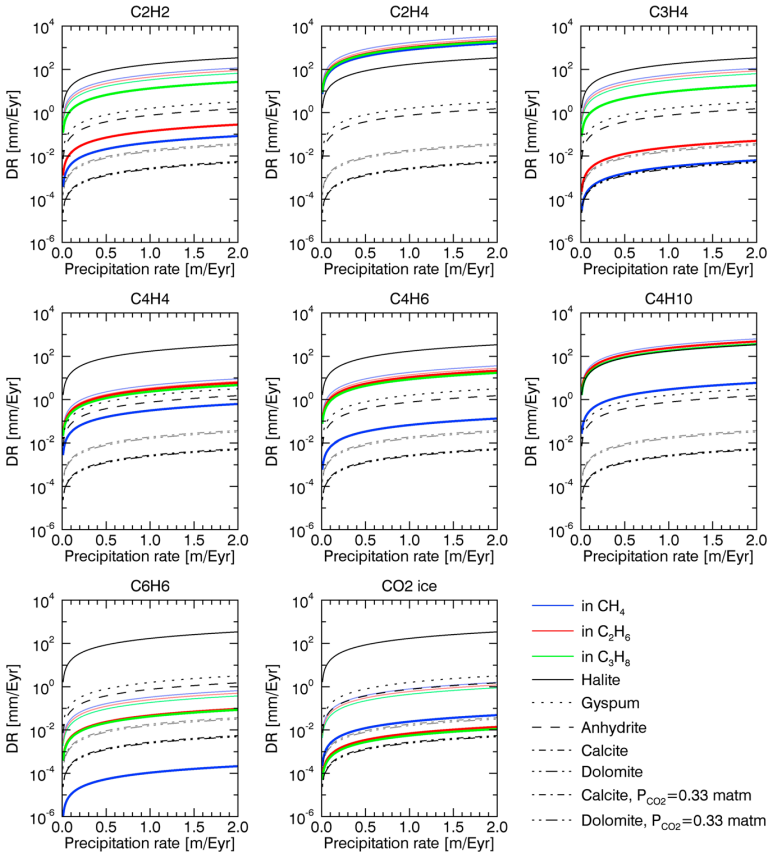

Figure 3. Denudation rates (in mm/Eyr) of nonpolar to slightly polar molecules (hydrocarbons and carbon dioxide ice) in Titan's liquids at 91.5 K (light curves: IST, bold curves: RST) compared to those of Earth's minerals in liquid water at 298.15 K (EST). The partial pressure of carbon dioxide for acid dissolution is set to 0.33 matm.

A few Global Circulation Models (GCM) attempt to describe, at least qualitatively, the methane cycle on Titan [e.g., *Rannou et al.*, 2006; *Mitchell*, 2008; *Tokano*, 2009; *Schneider et al.*, 2012]. Usually, net accumulation of rain is predicted at high latitudes >60° during summer, in agreement with the presence of lakes, whereas middle to low latitudes experience net evaporation, in agreement with the absence of lakes and the presence of deserts. Quantitatively, the model predictions are subject to debate since they depend on their physics (e.g., cloud microphysics, size of the methane reservoir, and radiative transfer scheme). Still, they remain our best estimates about Titan's climate.

During the summer season, the model of *Rannou et al.* [2006] predicts net precipitation rates of methane lower than 1 cm/Eyr at 70° latitude and up to 1 m/Eyr poleward of 70°, equivalent of a few μm to 2.7 mm/Earth day (Eday), respectively. The model of *Mitchell* [2008] predicts precipitation rates of about 2 mm/Earth day (Eday) in the polar regions and along an "Intertropical Convergence Zone" (ITCZ), nearly moving "pole to pole." The intermediate and moist models of *Mitchell et al.* [2009] predict precipitation roughly varying between 2 and 4 mm/Eday at the poles and along the ITCZ. These rates are consistent with those estimated in *Mitchell et al.* [2011] in order to reproduce the tropical storms seen in 2010 [*Turtle et al.*, 2011a] and with those estimated by the model of *Schneider et al.* [2012]. The model of *Tokano* [2009] also predicts similar precipitation rates (800 to 1600 kg/m^2 in half a Titan year, equivalent to precipitations between 3 and 6 mm/Eday).

Here we use the methane net precipitation rates extracted from the GCM of *Schneider et al.* [2012] to compute the present-day denudation rate on Titan. Figure 5 represents the mean net precipitation rates at various polar latitudes. High latitudes > 80° would be quite humid ($\tau = 7 - 8$ m/Tyr). Lower latitudes would be

Journal of Geophysical Research: Planets 10.1002/2014JE004738

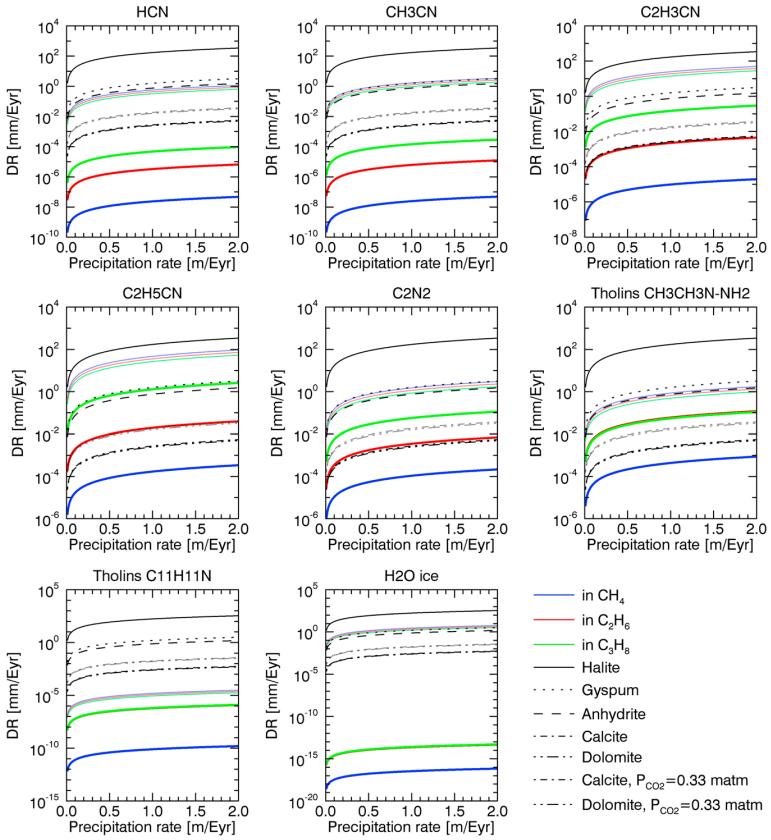

Figure 4. Same as Figure 3 but for polar molecules (nitriles and water ice).

less humid (τ=3 – 3.6 m/Tyr at 70°, decreasing to τ=0.4 – 1.6 m/Tyr at 60°). Southern low latitudes would be much drier than northern latitudes over a Titan year as a result of sparser but more intense rainstorms.

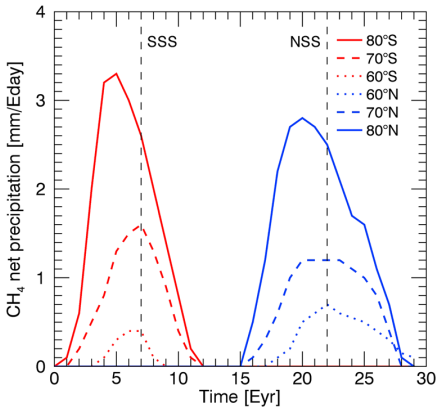

Figure 5. Net precipitation rates in mm/Earth day (Eday) at high southern and northern latitudes from *Schneider et al.* [2012] over a Titan year (29.5 Eyrs). SSS and NSS: southern and northern summer solstices.

5.2.2. Case of Pure Compounds

Figure 6 illustrates the denudation rates of a surface composed of pure organic compounds exposed to methane rains at several southern and northern polar latitudes according to the IST and RST hypotheses. Ethane and propane are not shown since the model of *Schneider et al.* [2012] only considers methane, but the behavior of Titan's solids in these liquids is already discussed in section 5.1.

Over one Titan year, the denudation rates are the highest at high latitudes and the lowest at low southern latitudes. According to the IST, all compounds would experience dissolution on the order of a few millimeters to a few meters at almost all latitudes (salt-like material), except $C_{11}H_{11}N$, the denudation rate of which would be a few hundred nanometers. The dissolution of $C_2H_8N_2$, CO_2, HCN, and C_6H_6 at 60°S, however, would be on the order of several hundred µm (carbonate-like material).

Retour à la table des matières : p. v

AGU Journal of Geophysical Research: Planets 10.1002/2014JE004738

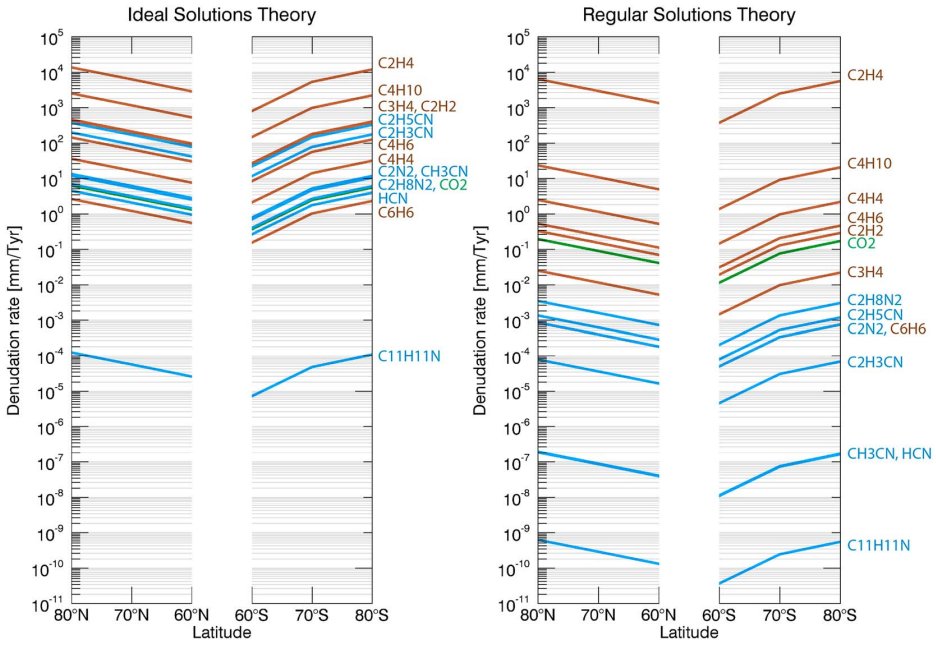

Figure 6. Denudation rates (in mm/Tyr) of Titan's surface solids in liquid methane according to the methane net precipitation rates of *Schneider et al.* [2012] over an entire Titan year for the IST and RST hypotheses. In brown are represented simple hydrocarbons, in blue the nitriles, and in green carbon dioxide.

According to the RST, C_2H_4 and C_4H_{10} denudation rates are between a few millimeters up to a few meters per Titan year (salt-like materials). The dissolution of C_4H_4, C_4H_6, C_2H_2, CO_2, and C_3H_4 is µm to hundred µm scale over a Titan year (carbonate-like materials). The denudation rates of nitriles and C_6H_6 are between 10^{-7}–10^{-10} mm/Tyr (for HCN, CH_3CN, and $C_{11}H_{11}N$) and a few µm/Tyr (carbonate to siliceous-like materials).

At high latitudes $> 70°$, we do not see much differences between the northern and the southern denudation rates, as expected from the similarities in precipitation rate between the two poles shown in Figure 5. At low southern latitudes, net precipitation rates are too low over one Titan year to allow a rapid and significant dissolution. Interestingly, Ontario Lacus and Sikun Labyrinthus, two landforms compared with terrestrial karsto-evaporitic and karstic landforms [*Malaska et al.*, 2010; *Cornet et al.*, 2012], are observed at latitudes greater than 70°S, and no other well-developed dissolution-related landforms are seen at lower southern latitudes.

Therefore, if Titan's surface is composed of pure hydrocarbons, dissolution processes are likely to occur but the formation of a karstic-like landscapes would be roughly 30 times slower on Titan than on Earth due to Titan's seasonality in precipitation. Of course, this latter consideration depends on the actual composition of the surface, which is unlikely to be pure, and of the accuracy of the climate model used.

5.2.3. Case of a Mixed Surface Layer

We now assume the presence of a surface layer, the composition of which is proportional to the accumulation rates at the surface (h_i) of solids coming from the atmosphere, calculated in the same way as *Malaska et al.* [2011] did

$$h_i = p_i \, V^S_{\mathrm{m},i}/N_A \qquad \text{(m/Eyr)}, \tag{4}$$

where p_i is the production rate of molecules (in molecules/m^2/Eyr) listed in Table 1, $V^S_{\mathrm{m},i}$ is the molar volume of the solid (or subcooled liquid if the former is not known, in m^3/mol), and N_A is the Avogadro number ($\simeq 6.022\times10^{23}$ mol^{-1}). The composition of the mixed organic layer is then determined as percentages (f_i) of each organic compound in the layer (so that $f_i = h_i/\sum_i h_i$). This method allows us to consider the volume occupied by each molecule, which is important especially for tholins because these contribute up to 20% on

AGU Journal of Geophysical Research: Planets 10.1002/2014JE004738

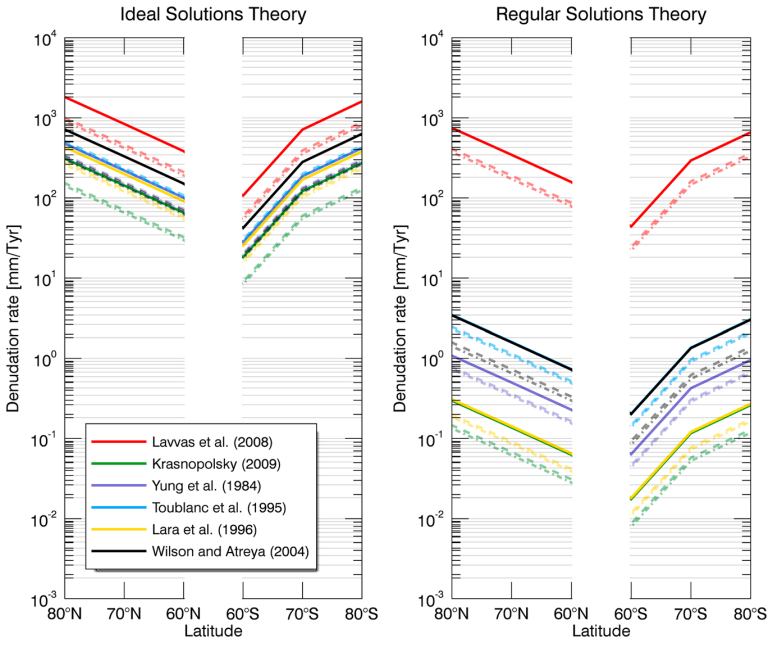

Figure 7. Denudation rates (in mm/Tyr) of Titan's surface solids in liquid methane according to the *Schneider et al.* [2012] model net precipitation rates over an entire Titan year at various latitudes and for different surface layer compositions established from photochemical models, including (dashed lines) or not (solid lines) the influence of tholins (dashed line: with $C_2N_8N_2$; dash-dotted line: with $C_{11}H_{11}N$).

average to the total production rates of molecules, but they build up to $\simeq$ 50% of the total thickness of the surface deposits due to their higher molar volumes compared to those of simple hydrocarbons or nitriles.

We consider three cases for the surface composition: without tholins and with $C_2H_8N_2$ or $C_{11}H_{11}N$ as tholins. Tholins production rate is that mentioned in *Cabane et al.* [1992]. Methane precipitation rates are those of *Schneider et al.* [2012]. The denudation rates for these mixed organic layers (DR_{mix}) are computed in a linear mixing model scheme where

$$DR_{mix} = \sum_i f_i \, DR_i \qquad \text{(m/Eyr)}. \tag{5}$$

Figure 7 gives the repartition of denudation as a function of latitude and photochemical models at the end of a Titan year. According to the IST, the denudation rate of all mixed layers would be on the order of a few centimeters to a few meters over a Titan year (salt-like layers). According to the RST, the organic layer originating from the *Lavvas et al.* [2008b] model would be the most soluble (dissolution rates of a few centimeters to a few decimeters per Titan year, salt-like layer). The organic layers originating from the other models would be more carbonate-like layers over a Titan year (dissolution rates of a few tens of µm to a few millimeters per Titan year), whether tholins are included or not. The lowest solubility of all mixed layers is reached using a *Krasnopolsky* [2009]-type composition. Over a Titan year, the likelihood of developing dissolution-related landforms is therefore nonnegligible, even if the surface is not composed of pure soluble simple solids. These mixed organic layers would behave like carbonate or salty terrestrial layers over a Titan year.

6. Discussion: How Old Are Titan's Karstic Landscapes?

Despite the strong assumptions of the method described in section 4 to infer timescales of formation of terrestrial karstic landforms (we consider only chemical erosion at equilibrium without significant climate changes over the past few MEyrs), the resulting ages are consistent with ages determined by relative or absolute chronology or constitute upper limits. Therefore, the determination of the age of the lacustrine depressions on Titan probably result in maximum timescales of development. Titan's climate is believed to have remained

Retour à la table des matières : p. v

AGU Journal of Geophysical Research: Planets 10.1002/2014JE004738

Table 3. Timescales Required to Dissolve 100 m of a Surface Organic Layer (Composition Given by Photochemistry in the Atmosphere) in Liquid Methane According to the Precipitation Rates of *Schneider et al.* [2012]

	IST		RST	
Latitude	Minimum (kEyrs)	Maximum (kEyrs)	Minimum (kEyrs)	Maximum (MEyrs)
80°N	1.6	20.9	3.9	22.1
70°N	3.5	45.2	8.5	47.8
60°N	7.7	99.0	18.7	104.6
60°S	27.6	354.9	67.1	375.1
70°S	4.1	53.2	10.1	56.2
80°S	1.8	23.7	4.5	25.0

quite stable over the recent past, with a small periodic insolation variation of ± 2 W/m^2 at the poles during the last MEyr, for the current low insolation at the north pole [*Aharonson et al.*, 2009]. This probably brings some stability to the calculations.

By applying our simple model, we compute the timescales needed to form a 100 m deep depression by dissolution of a superficial mixed organic layer under the current climate conditions evaluated by *Schneider et al.* [2012]. These are shown in Table 3 and Figure 8. We compute our formation timescales using both the IST and the RST since the solubility of polar molecules is not well constrained by the RST and could get closer to that computed using the IST. However, we consider timescales evaluated using the RST as our references since they present the most conservative values for the age of the lacustrine depressions.

Independent of the thermodynamic theory considered, Titan's lacustrine depressions would be young. Among all the compositions tested, the time needed to carve a 100 m deep depression by dissolution under current climate conditions at latitudes poleward of 70° would be between a few kEyrs (IST) and 56 MEyrs (RST). At 60°N, a 100 m deep depression would be created in 7.7 kEyrs (IST) to 104.6 MEyrs (RST) while the same depression would be created in 27.6 kEyrs (IST) to 375.1 MEyrs (RST) at 60°S. This strong difference between the two hemispheres could explain why Titan's south polar regions are deprived of well-developed lacustrine depressions compared to the north.

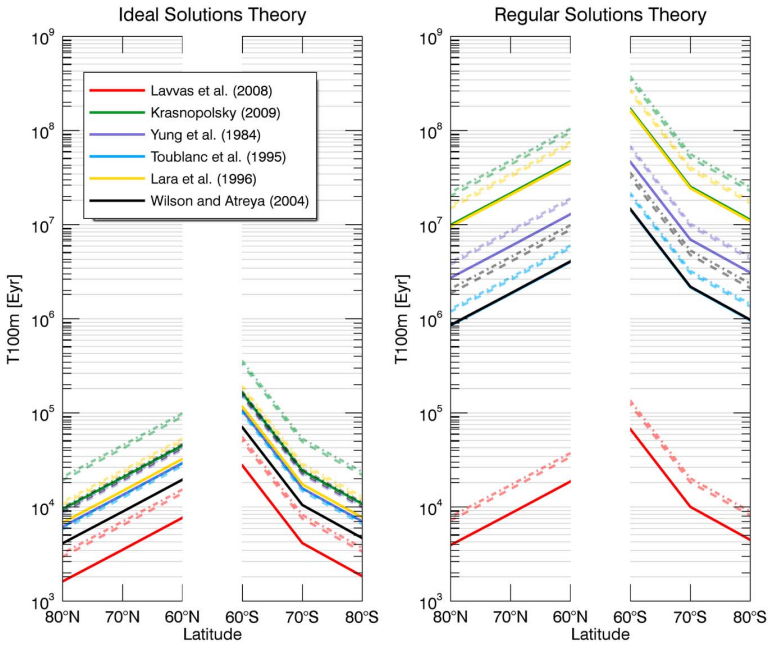

Figure 8. Same as Figure 7 but for the timescales of formation (in Eyr) of 100 m deep depressions on Titan.

Retour à la table des matières : p. v

AGU Journal of Geophysical Research: Planets 10.1002/2014JE004738

It should be noted that the hypothesized timescale difference between the northern and the southern low latitudes results from an extrapolation of Titan's current climate to the past. *Aharonson et al.* [2009] showed that Croll-Milankovich-like cycle with periods of 45 (and 270) kEyrs could exist on Titan, resulting in a N-S reversal in insolation and likely subsequent climate conditions. Over geological timescales, the N-S differences in denudation rates and timescales estimated at these latitudes could be smoothed by these cycles. However, as noted earlier, we made the same extrapolation for the Earth, whose climate dramatically changed over time, without obtaining unreasonable formation timescales.

In any case, all these timescales are consistent with the youth of Titan's surface as determined from (1) crater counting (0.3–1.2 GEyrs, *Neish and Lorenz* [2012]), (2) dune sediment inventory (50–730 MEyrs, *Sotin et al.* [2012] and *Rodriguez et al.* [2014]), (3) the flattening of the poles due to the substitution of methane by ethane in clathrates (500 MEyrs if restricted to the poles or 0.3–1.7 GEyrs if not, *Choukroun and Sotin*) [2012], and the possible methane outgassing event (1.7–2.7 GEyrs, *Tobie et al.* [2006]).

In summary, the morphology of Titan's lacustrine depressions suggests that dissolution occurs on Titan. The denudation rates of pure organic compounds and a mixed organic layer as compared to those of soluble minerals on Earth also supports this hypothesis. The timescales needed to dissolve various amounts of material as compared to the timescales of development of karstic landforms on Earth are also quite consistent in the sense that karstic landscapes are usually relatively young landscapes. Finally, the latitudinal repartition of denudation rates and timescales of dissolution is consistent with the latitudinal repartition of the possible dissolution-related landforms at the surface of Titan. The surface dissolution scenario for the origin of Titan's lakes appears very likely and Titan's lakes could be among the youngest features of the moon.

7. Conclusion

Titan's lakes result from the filling of topographic depressions by surface or subsurface liquids. Their morphology led to analogies with terrestrial landforms of various origins (volcanic, thermokarstic, karstic, evaporitic, or karsto-evaporitic). The karstic/karsto-evaporitic dissolution scenario seems to be the most relevant, given the nature of surface materials on Titan and its climate. We constrained the timescales needed for the formation of Titan's depressions by dissolution, on the basis of the current knowledge on the development of terrestrial karsts.

We computed solutional denudation rates from the theory developed by *White* [1984]. This simple theory needs three parameters: the solubilities and the densities of solids and liquids at a given temperature and a climatic parameter linked to the net precipitation rates onto the surface. We computed the solubilities of terrestrial minerals in liquid water at 25°C and tested the model by computing the denudation rates and timescales of formation of several terrestrial examples of karstic landforms.

We then applied the same model to Titan. We computed the solubilities of Titan's surface organic compounds in pure liquid methane, ethane, and propane at 91.5 K using different thermodynamic theories. We evaluated the molar volumes of liquid and solid Titan's surface compounds at 91.5 K, and we used the results of the recent GCM of *Schneider et al.* [2012] as input for the precipitation rates of methane on Titan, which allowed us to compute denudation rates at several latitudes. Denudation rates have then been computed for pure organic compounds at Earth and Titan timescales and have been compared to those determined for soluble minerals on Earth. We also computed denudation rates for three different compositions of the surface organic layer. Over one Titan year, these mixed layers of organic compounds behave like terrestrial salts or carbonates, which indicates their high susceptibility to dissolution, though these processes would be 30 times slower on Titan than on Earth due to the seasonality (rainfall occurs only during Titan's summer).

We computed theoretical timescales for the formation of 100 m deep depressions in mixed organic layers under present climatic conditions. As with dissolution landforms on Earth, Titan's depressions would be young. At high polar latitudes, we found that the timescales of development for depressions are relatively short (on the order of 50 MEyrs at maximum to carve 100 m) and consistent with the young age of Titan's surface. These timescales are consistent with the existence of numerous lacustrine depressions and dissected landscapes at these latitudes. At southern low latitudes, the computed timescales are as long as 375 MEyrs due to the low precipitation rates. This low propensity to develop depressions by dissolution is consistent with their relative absence/bare formation at low latitudes. Over geological timescales greater than those of Titan's

Retour à la table des matières : p. v

AGU Journal of Geophysical Research: Planets 10.1002/2014JE004738

Croll-Milankovitch cycles (45 and 270 kEyrs), this difference would probably be strongly attenuated. However, climate model predictions are not presently available over geologic timescales, and the present-day seasonal climate variations are the best that can be currently constrained.

The results of these simple calculations are consistent with the hypothesis that Titan's depressions most likely originate from surface dissolution. Theoretical timescales for the formation of these landforms are consistent with the other age estimates of Titan's surface. Future works could include the effects of rain in equilibrium with the nitrogen, ethane, and propane atmospheric gases in the raindrop composition (e.g., *Graves et al.* [2008] or *Glein and Shock* [2013]). Experimental constraints on the solubility of gases and solids in liquids thanks to recent technical developments for Titan experiments [*Luspay-Kuti et al.*, 2012, 2014; *Malaska and Hodyss*, 2014; *Chevrier et al.*, 2014; *Leitner et al.*, 2014; *Singh et al.*, 2014] would also be of extreme importance for such work. Finally, the influence of other landshaping mechanisms such as collapse or subsurface fluid flows, which play a significant role in the development of some karstic landforms on Earth, could also be implemented.

Appendix A: List of Compound Names for Titan

CH_4: methane (liquid)
C_2H_6: ethane (liquid)
C_3H_8: propane (liquid)
C_4H_{10}: n-butane
C_2H_2: acetylene
C_2H_4: ethylene
C_3H_4: methyl-acetylene
C_4H_4: vinyl-acetylene
C_4H_6: 1-3 butadiene
C_6H_6: benzene
HCN: hydrogen cyanide
C_2N_2: cyanogen
CH_3CN: acetonitrile
C_2H_3CN: acrylonitrile
C_2H_5CN: propionitrile
$C_2H_8N_2$: 1-1 dimethyl-hydrazine (tholins-like)
$C_{11}H_{11}N$: quinoline (tholins-like)
H_2O: water ice Ih
CO_2: carbon dioxide ice

Appendix B: Solubility of Solids on Earth and Titan

B1. Dissolution Processes on Earth

Dissolution occurs in karstic to evaporitic areas on Earth, where the dominant minerals are calcite, dolomite, halite, anhydrite, or gypsum. Basic aqueous reactions of congruent dissolution for these common soluble minerals (i.e., all components of the minerals dissolve entirely) are summarized below:

$$CaCO_3 + H_2O + CO_2 \iff Ca^{2+} + 2HCO_3^-$$
$$CaMg(CO_3)_2 + 2H_2O + 2CO_2 \iff Ca^{2+} + Mg^{2+} + 4HCO_3^-$$
$$CaSO_4.2H_2O \iff Ca^{2+} + SO_4^{2-} + 2H_2O$$
$$CaSO_4 + H_2O \iff Ca^{2+} + SO_4^{2-} + H_2O$$
$$NaCl + H_2O \iff Na^+ + Cl^- + H_2O.$$

Halite (NaCl), gypsum ($CaSO_4.2H_2O$), and anhydrite ($CaSO_4$) dissolve by pure dissociation, and calcite ($CaCO_3$) and dolomite ($CaMg(CO_3)_2$) dissolve by dissociation and acid dissolution, i.e., with the help of the CO_2 gas dissolved in water [*Langmuir*, 1997; *Ford and Williams*, 2007; *Brezonik and Arnold*, 2011].

AGU Journal of Geophysical Research: Planets 10.1002/2014JE004738

Table B1. Thermodynamic and Physical Parameters of Minerals, Water, and Ions Considered in the Dissolution Reactions, Collected From the Literature [*Lide*, 2010; *Langmuir*, 1997; *Ford and Williams*, 2007; *Brezonik and Arnold*, 2011; *White*, 2013]

Name	Formula	M_i (g/mol)	z_i	a_i (Å)	b_i (kg/mol)	$\Delta_f G_i^\circ$ (kJ/mol)	$\Delta_f H_i^\circ$ (kJ/mol)
			Minerals				
Calcite	$CaCO_3$	100.087	0	-	-	−1129.1	−1207.6
Dolomite	$CaMg(CO_3)_2$	184.401	0	-	-	−2161.7	−2324.5
Gypsum	$CaSO_4.2H_2O$	172.171	0	-	-	−1797.2	−2022.6
Anhydrite	$CaSO_4$	136.141	0	-	-	−1321.7	−1434.1
Halite	NaCl	58.443	0	-	-	−384.1	−411.2
			Aqueous Species				
Chlore	Cl^-	35.460	−1	3.71	0.01	−131.3	−167.2
Sodium	Na^+	22.990	+1	4.32	0.06	−261.9	−240.1
Hydroxyl	OH^-	17.007	−1	10.65	0.21	−157.3	−230
Hydrogen	H^+	1.008	+1	4.78	0.24	0	0
Calcium	Ca^{2+}	40.080	+2	4.86	0.15	−553.54	−542.83
Magnesium	Mg^{2+}	24.320	+2	5.46	0.22	−454.8	−466.8
Sulfate	SO_4^{2-}	96.060	−2	5	−0.04	−744.6	−909.2
Carbonate	CO_3^{2-}	60.010	−2	5.4	0	−527.9	−677.1
Bicarbonate	$HCO3^-$	61.020	−1	5.4	0	−586.8	−692
Carbonic acid	H_2CO_3	62.025	0	-	-	−623.2	-699.7
			Solvent and Gas				
Water	H_2O	18.015	0	-	-	−237.18	−285.83
Carbon dioxide	CO_2	44.010	0	-	-	−394.4	−393.51

The physical and thermodynamic parameters needed to compute solubilities are given in Table B1. Ideal and nonideal electrolyte theories are considered. We also consider the acid dissolution of carbonate minerals.

B1.1. Pure Dissociation of Minerals: Halite, Anhydrite and Gypsum

For a given chemical reaction implying *A* and *B* and producing *C* and *D*, with their respective stoichiometric numbers *a*, *b*, *c*, and *d*, the law of mass action gives

$$aA + bB \iff cC + dD, \tag{B1}$$

where one can define a thermodynamical equilibrium constant (or thermodynamic solubility product) for the reaction K_{eq} (often written pK_{eq}, with $pK_{eq} = -\log K_{eq}$), so that

$$K_{eq} = \frac{(C)^c\,(D)^d}{(A)^a\,(B)^b} = \frac{(m_C\Gamma_C)^c\,(m_D\Gamma_D)^d}{(m_A\Gamma_A)^a\,(m_B\Gamma_B)^b}, \tag{B2}$$

where (i) denotes the activity of the ith compound, being the product of an activity coefficient Γ_i and a molality m_i (in mol/kg of solvent). For liquids and solids reacting together (or being produced) during a congruent dissolution reaction, the activity is set to unity. The equilibrium constant can be derived from thermodynamics at standard state ($T = 25°C$ and $P = 1$ atm) using the Gibbs-Helmholtz equation:

$$\Delta_r G^\circ = -R\,T\,\ln K_{eq} = -2.303\,R\,T\,\log K_{eq} \qquad \text{(J/mol)}, \tag{B3}$$

where $\Delta_r G^\circ$ is the standard Gibbs free energy of reaction (in J/mol), calculated using the Hess' law:

$$\Delta_r G^\circ = \sum_{\text{products}} n_i\,\Delta_f G_i^\circ - \sum_{\text{reactants}} n_j\,\Delta_f G_j^\circ \qquad \text{(J/mol)}, \tag{B4}$$

with $\Delta_f G^\circ$ being the standard Gibbs free energy of formation of each species (in J/mol) and n their stoichiometric numbers. Following the same principle, we compute the standard enthalpy of reaction $\Delta_r H^\circ$ (J/mol) from the individual enthalpies of formation $\Delta_f H^\circ$ (in J/mol). The standard enthalpy of reaction is then used to

Retour à la table des matières : p. v

AGU Journal of Geophysical Research: Planets 10.1002/2014JE004738

Table B2. Thermodynamic Constants of Dissociation and Dissolution Reactions in Standard Conditions (at 25°C and 1 atm)

Reaction	Equations	$\Delta_r G°$ (kJ/mol)	$\Delta_r H°$ (kJ/mol)	K_{eq}	pK_{eq}	Equilibrium Constant Expression
Pure Dissociation Reactions for Minerals						
Gypsum dissociation	$CaSO_4{\cdot}2H_2O \Longleftrightarrow Ca^{2+} + SO_4^{2-} + 2H_2O$	24.70	−1.09	4.71×10^{-5}	4.327	$K_{gd} = (Ca^{2+})(SO_4^{2-})$
Anhydrite dissociation	$CaSO_4 \Longleftrightarrow Ca^{2+} + SO_4^{2-}$	23.56	−17.93	7.46×10^{-5}	4.128	$K_{ad} = (Ca^{2+})(SO_4^{2-})$
Halite dissociation	$NaCl \Longleftrightarrow Na^{+} + Cl^{-}$	−9.10	3.90	39.29	−1.594	$K_{hd} = (Na^{+})(Cl^{-})$
Calcite dissociation	$CaCO_3 \Longleftrightarrow Ca^{2+} + CO_3^{2-}$	47.36	−12.53	5.05×10^{-9}	8.297	$K_{cd} = (Ca^{2+})(CO_3^{2-})$
Dolomite dissociation	$CaMg(CO_3)_2 \Longleftrightarrow Ca^{2+} + Mg^{2+} + 2CO_3^{2-}$	97.56	−39.33	8.10×10^{-18}	17.092	$K_{dd} = (Ca^{2+})(Mg^{2+})(CO_3^{2-})^2$
Secondary Dissociation Reactions and Dissolution Reactions for Carbonates Dissolution						
CO_2 dissolution	$CO_2 + H_2O \Longleftrightarrow H_2CO_3^{\circ}$	8.38	−20.36	3.40×10^{-2}	1.468	$K_{CO_2} = (H_2CO_3^{\circ})/P_{CO_2}$
Carbonic acid dissociation	$H_2CO_3^{\circ} \Longleftrightarrow H^{+} + HCO_3^{-}$	36.40	7.70	4.20×10^{-7}	6.377	$K_1 = (H^{+})(HCO_3^{-})/(H_2CO_3^{\circ})$
Bicarbonate dissociation	$H^{+} + CO_3^{2-} \Longleftrightarrow HCO_3^{-}$	58.90	14.90	4.80×10^{-11}	10.319	$K_2 = (HCO_3^{-})/(H^{+})(CO_3^{2-})$
Calcite dissolution	$CaCO_3 + H_2O + CO_2 \Longleftrightarrow Ca^{2+} + 2\,HCO_3^{-}$	33.24	−40.09	1.50×10^{-6}	5.823	$K_{cal} = (Ca^{2+})(HCO_3^{-})^2/P_{CO_2}$
Dolomite dissolution	$CaMg(CO_3)_2 + 2H_2O + 2CO_2 \Longleftrightarrow Ca^{2+} + Mg^{2+} + 4\,HCO_3^{-}$	69.32	−94.45	7.17×10^{-13}	12.144	$K_{dol} = (Ca^{2+})(Mg^{2+})(HCO_3^{-})^4/P_{CO_2}^2$

Retour à la table des matières : p. v

AGU Journal of Geophysical Research: Planets 10.1002/2014JE004738

Table B3. Molalities (in mol/kg of Solvent) of Minerals in Water at 25°C According to the Ideal and the Electrolyte Solutions Theories[a]

Name	IST	EST
	Dissolution by Dissociation	
Halite	6.27	6.27
Gyspum	8.63×10^{-3}	2.26×10^{-2}
Anhydrite	6.86×10^{-3}	1.62×10^{-2}
Calcite	7.10×10^{-5}	7.72×10^{-5}
Dolomite	3.77×10^{-5}	4.11×10^{-5}
	Acid Dissolution	
Calcite, $P_{CO_2} = 0.33$ matm	4.99×10^{-4}	5.42×10^{-4}
Dolomite, $P_{CO_2} = 0.33$ matm	2.59×10^{-4}	2.76×10^{-4}
Calcite, $P_{CO_2} = 0.01$ atm	1.55×10^{-3}	1.80×10^{-3}
Dolomite, $P_{CO_2} = 0.01$ atm	8.09×10^{-4}	8.99×10^{-4}
Calcite, $P_{CO_2} = 0.11$ atm	3.46×10^{-3}	4.28×10^{-3}
Dolomite, $P_{CO_2} = 0.11$ atm	1.80×10^{-3}	2.09×10^{-3}

[a] $P_{CO_2} = 0.33$ matm refers to normal dry air [*Langmuir*, 1997] while $P_{CO_2} = 0.01$ atm more refers to tropical climate environments [*Fleurant et al.*, 2008], which actually could even reach considerable CO_2 content in the soils of up to $P_{CO_2} = 0.11$ atm [*Ford and Williams*, 2007].

compute the equilibrium constants at temperatures that differ from standard conditions using the Van't Hoff equation [*Langmuir*, 1997] as follows:

$$\ln \frac{K_{T2}}{K_{T1}} = \frac{\Delta_r H_i^\circ}{R} \left(\frac{1}{T_1} - \frac{1}{T_2} \right), \tag{B5}$$

where K_{T1} and K_{T2} are the equilibrium constant of a given chemical reaction at two different temperatures T_1 and T_2 (in K) (the subscript 1 is used to indicate the reference state, 25°C in this case). Table B2 gathers the thermodynamic parameters for all the considered dissolution reactions. It also displays each equilibrium constant equation for common terrestrial minerals.

B1.2. Acid Dissolution of Carbonates: Calcite and Dolomite

For calcium and magnesium carbonates, a set of reactions happens, not only involving the mineral dissociation itself (K_{cd} or K_{dd}) but also including the carbon dioxide gas dissolution in water (K_{CO_2}), which produces carbonic acid that acidifies water. Then, carbonic acid rapidly dissociates into bicarbonate ions (K_1), which are also created by the association of protons H^+ and carbonate ions (K_2). The thermodynamic properties of these intermediate reactions to the dissolution of calcite and dolomite are summarized in Table B2. The activity of carbon dioxide is approximately equal to its partial pressure (P_{CO_2}, see *Langmuir* [1997] and *Ford and Williams* [2007]) so that, for calcite acid dissolution, one can write

$$K_{cal} = \frac{(Ca^{2+})\,(HCO_3^-)^2}{P_{CO_2}} = \frac{K_1\, K_{CO_2}\, K_{cd}}{K_2}, \tag{B6}$$

and for dolomite acid dissolution:

$$K_{dol} = \frac{(Ca^{2+})\,(Mg^{2+})\,(HCO_3^-)^4}{P_{CO_2}^2} = \frac{K_1^2\, K_{CO_2}^2\, K_{dd}}{K_2^2}. \tag{B7}$$

Assuming a given partial pressure of carbon dioxide, one can compute the activity, molality, and mole fraction at saturation of calcite and dolomite in water. The molality of CO_2 in the system is calculated thanks to the Henry law ($m_{CO_2} = k_H(T)\, P_{CO_2}$, $K_H(T)$ being Henry's law constant, varying with temperature). We performed the calculations for three values of P_{CO_2} at 25°C: $P_{CO_2} = 0.33$ matm, which represents the normal dry air [*Langmuir*, 1997] that could be quite analogous to atmospheric conditions in arid/semiarid areas, and $P_{CO_2} = 0.01$–0.11 atm, which represents values encountered in more humid areas such as under equatorial/tropical climates [*Ford and Williams*, 2007; *Fleurant et al.*, 2008].

B1.3. Activity Coefficients for Electrolyte Solutions

We infer the molalities m_i and activities (i) of ions in solution from K_{eq} at different temperatures under an Ideal (IST, $\Gamma_i = 1$) and a nonideal Electrolyte (EST, $\Gamma_i \neq 1$) Solution Theory. For the EST, the activity coefficients Γ_i are calculated by iteration using the extended Debye-Hückel equation as modified by *Truesdell and Jones* [1974]:

$$\log \Gamma_i = -A\, z_i^2 \left(\frac{\sqrt{I}}{1 + B\, a_i \sqrt{I}} \right) + b_i\, I, \tag{B8}$$

where I is the molal ionic strength of the solution, defined as follows:

$$I = \frac{1}{2} \sum_{i=1}^{n} m_i\, z_i^2 \qquad \text{(mol/kg)}, \tag{B9}$$

Retour à la table des matières : p. v

AGU Journal of Geophysical Research: Planets 10.1002/2014JE004738

Table B4. Melting and Boiling Points Thermodynamic Constants of Titanian Materials[a]

Formula	T_m (K)	$\Delta_m H°$ (kJ/mol)	T_b (K)	$\Delta_v H°$ (kJ/mol)
CH_4	90.680	0.940	111.670	8.190
C_2H_6	90.360	0.582	184.570	14.690
C_3H_8	85.460	3.500	232.040	19.040
C_4H_{10}	134.850	4.660	272.660	22.440
C_2H_2	192.450	4.105	188.450	16.674
C_2H_4	104.000	3.350	169.380	13.530
C_3H_4	170.450	5.349	249.950	22.185
C_4H_4	227.600	7.687	278.250	22.470
C_4H_6	164.240	7.980	268.740	22.470
C_6H_6	278.640	9.870	353.240	30.720
HCN	259.860	8.406	298.850	26.896
C_2N_2	245.320	8.110	252.100	23.330
CH_3CN	229.330	8.160	354.800	29.750
C_2H_3CN	189.670	6.230	350.450	32.600
C_2H_5CN	207.150	5.030	350.500	31.810
$C_2H_8N_2$	215.950	10.070	337.050	28.477
$C_{11}H_{11}N$	326.650	20.418	538.855	50.005
H_2O	273.150	6.010	373.200	40.650
CO_2	216.592	9.020	194.600	15.326

[a]Data gathered from *Lide* [2010] and *Yaws* [1996]. The melting properties of $C_{11}H_{11}N$ have been taken in *Chirico et al.* [2007].

where z_i is the charge of i and a_i and b_i are the two parameters of the *Truesdell and Jones* [1974] equation (a modified hydrated radius, in Å, and a purely empirical parameter, respectively). A and B are two variables depending on the temperature T (in °C), defined as follows [*Ford and Williams*, 2007]:

$$A = 0.4883 + 8.074 \times 10^{-4}\, T \qquad \text{(B10)}$$

$$B = 0.3241 + 1.6 \times 10^{-4}\, T. \qquad \text{(B11)}$$

Results from these calculations are given in Table B3. The calculation of activity coefficients has a relatively minor impact in the change of molality for carbonates, while a clear difference can be seen for salts (anhydrite and gypsum). The presence of CO_2 in the carbonate-water system greatly increases the amount of dissolved carbonates, until reaching solubilities roughly similar to those of gypsum and anhydrite. The EST molalities has been used for all minerals except for halite, which possesses a ionic strength too strong to be computed using our Debye-Hückel equation.

B2. Solubility of Titan's Solids

The solubility of Titan's solids in pure liquid hydrocarbons is calculated according to the Van't Hoff equation:

$$\ln \Gamma_i X_{i,\text{sat}} = \frac{\Delta_m H_i^\circ}{R}\left(\frac{1}{T_{m,i}} - \frac{1}{T}\right), \qquad \text{(B12)}$$

where Γ_i is the activity coefficient of the solute, $X_{i,\text{sat}}$ its mole fraction at saturation, $\Delta_m H_i^\circ$ its enthalpy of melting (in J/mol) evaluated at $T_{m,i}$, its melting temperature (in K), which differs from the temperature of the solution T (K), and R is the ideal gas constant. Melting properties of Titan compounds are given in Table B4.

We consider the case of the Ideal Solutions Theory (IST), for which $X_{i,\text{sat}}$ is calculated by assuming $\Gamma_i = 1$ (all the molecules share the same affinity with each other), and the case of the Regular Solutions Theory (RST) of *Preston and Prausnitz* [1970] for which $\Gamma_i \neq 1$ (molecules have preferential affinity with one or the other). The latter approach has already been used in several publications dealing with the lakes and seas composition [*Raulin*, 1987; *Dubouloz et al.*, 1989; *Cordier et al.*, 2009, 2013b].

The RST requires to compute Γ_i's. Assuming the subscripts 1 for the solvent and 2 for the solute, the RST gives

$$\ln \Gamma_2 = \frac{(\delta_1 - \delta_2)^2 + 2\, l_{12}\delta_1\delta_2}{R\,T}\, V_{m,2}^L\, \phi_1^2, \qquad \text{(B13)}$$

where $V_{m,2}^L$ is the subcooled liquid molar volume of the solute (in m^3/mol), l_{12} is the empirical interaction parameter between the solvent and the solute taken from various sources (e.g. *Preston and Prausnitz* [1970] and *Szczepaniec-Cieciak et al.* [1978]), ϕ_1 is the volume fraction of the liquid, computed as follows:

$$\phi_1 = \frac{(1 - X_2)\, V_{m,1}^L}{(1 - X_2)\, V_{m,1}^L + X_2\, V_{m,2}^L}, \qquad \text{(B14)}$$

and δ_1 and δ_2 are the Hildebrand solubility parameters of the solvent and the solute, respectively, (in $(J/m^3)^{1/2}$ computed from their enthalpy of vaporization $\Delta_v H_i$ (J/mol), as follows:

$$\delta_i^2 = \frac{\Delta_v H_i - R\,T}{V_{m,i}^L} \qquad ((J/m^3)^{1/2}), \qquad \text{(B15)}$$

Retour à la table des matières : p. v

AGU Journal of Geophysical Research: Planets 10.1002/2014JE004738

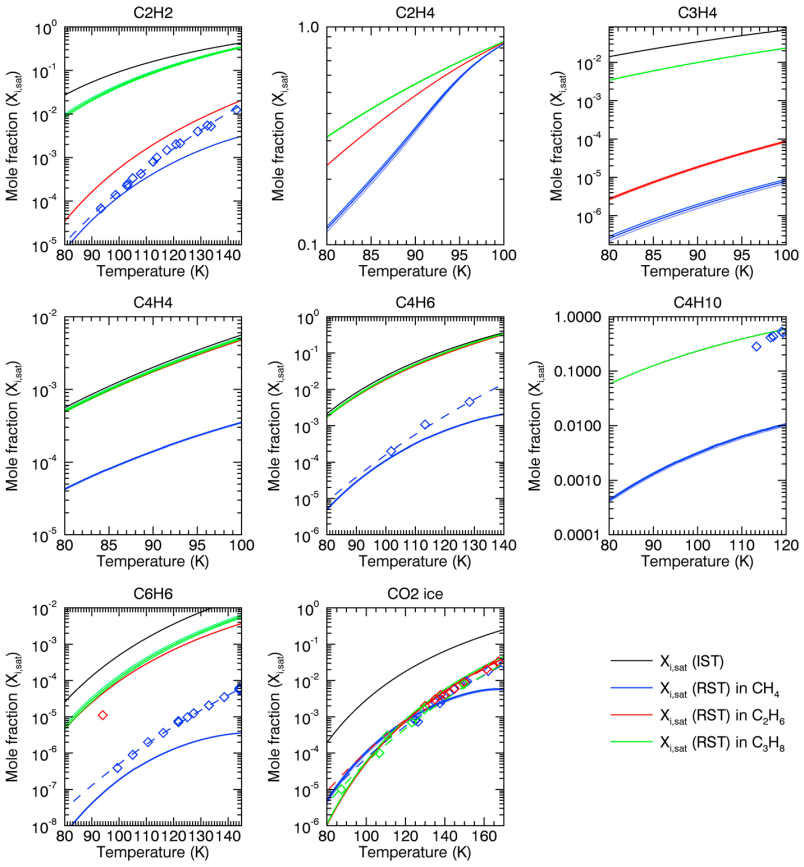

Figure B1. Saturation mole fraction of Titan's "nonpolar solids" (hydrocarbons and carbon dioxide ice) in Titan's liquids computed using the RST and IST, and different Rackett equations (see section C1). The darkest curves represent $X_{i,\mathrm{sat}}$ evaluated by equation (C3) with the Z_{RA} parameter. Diamonds are experimental values collected for C_4H_{10} [*Brew*, 1977; *Kuebler and McKinley*, 1975], C_2H_2 [*Neumann and Mann*, 1969], C_4H_6 [*Preston et al.*, 1971], C_6H_6 [*von Szalghary*, 1972; *Luks et al.*, 1981; *Kuebler and McKinley*, 1995; *Malaska and Hodyss*, 2014], and CO_2 [*Clark and Din*, 1953; *Davis et al.*, 1962; *Cheung and Zander*, 1968; *Preston et al.*, 1971] in the corresponding liquids. Dashed lines are empirical power fits of the experimental points (with $R^2 > 0.98$).

where $\Delta_v H_i$ is taken in the literature at the boiling point temperature T_b (Table B4) for each compound and extrapolated down to lower temperatures using the Watson equation [*Poling et al.*, 2007]:

$$\Delta_v H_{i,T} = \Delta_v H_{i,Tb} \left(\frac{1 - T/T_c}{1 - T_b/T_c} \right)^{0.38} \quad \text{(J/mol)}. \tag{B16}$$

The solubilities are given for a wide range of temperatures in Figures B1 (nonpolar molecules) and B2 (polar molecules), on top of which we also reported experimental data points gathered from the literature, fitted by an empirical power law ($R^2 > 0.98$) in order to extrapolate the experimental values at low temperatures for comparison.

The IST hypothesis provides a first estimate of the solubility, as seen in Figures B1 and B2. It does not consider the different behavior of the solutes in the different solvents but presents the advantage of not depending on approximate calculations of the activity coefficients of each species. According to this theory, all simple hydrocarbons would thus be rather solubles at low temperatures, the least soluble being nitriles and C_6H_6.

The RST hypothesis provides a second estimate and shows that solids are less soluble in methane than in ethane and propane. Whatever the liquid, simple nitriles generally show an increase in solubility with a higher

Retour à la table des matières : p. v

AGU Journal of Geophysical Research: Planets 10.1002/2014JE004738

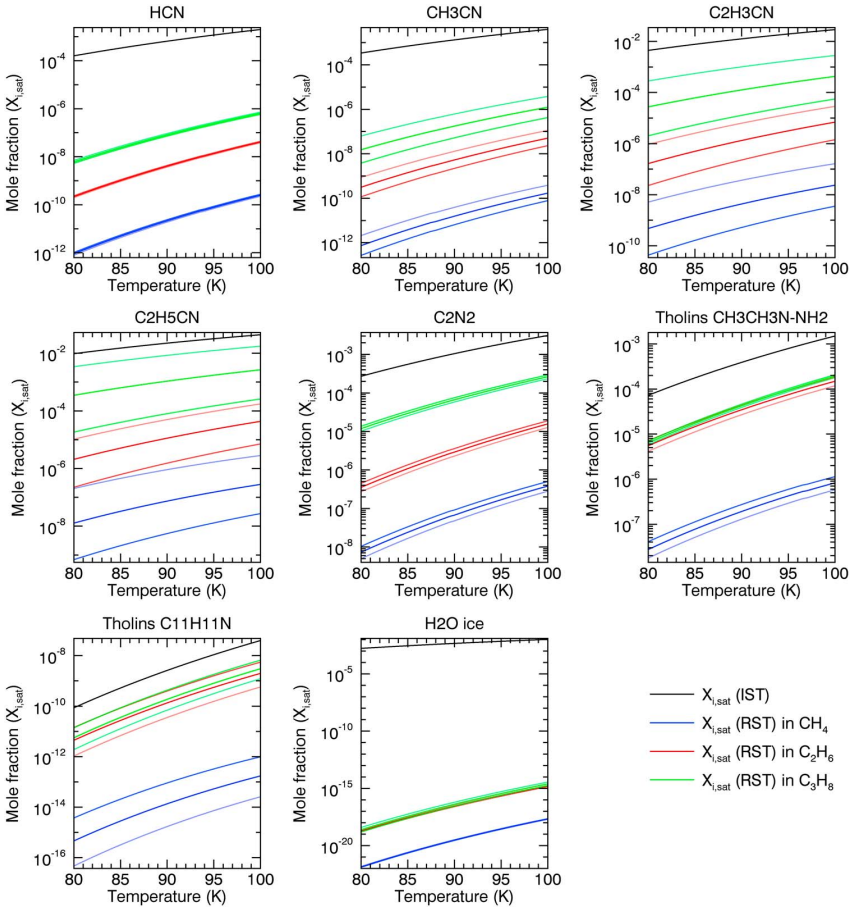

Figure B2. Same as Figure B1 but for Titan's polar solids (nitriles and water ice).

number of C atoms in their carbon chain. C_2H_4, C_4H_{10}, and C_2H_2 are the most soluble compounds again, joined by C_4H_4, C_4H_6, CO_2, C_3H_4, and finally C_6H_6. Nitriles are the least soluble compounds. At cryogenic temperatures (<100 K), the simulated solubilities are in good agreement with the power fits of experimental data (with the exception of n-butane, which shows a higher solubility in experiments). It is also worth noting that recent solubility experiments of benzene in liquid ethane have been performed at 94 K by *Malaska and Hodyss* [2014]. The $X_{i,sat}$ for benzene in ethane they determined experimentally ($1.11 \pm 0.09 \times 10^{-5}$) is also quite close to our theoretical value computed using the RST at 94 K (4.42×10^{-5}), though slightly lower. This difference is probably due to the dissolution of nitrogen into liquid ethane during the experiment, which tends to lower the solubility of benzene. Benzene also reached saturation so quickly in liquid ethane (in less than 2 h) [*Malaska and Hodyss*, 2014], compared to the timescales considered in the present work, that dissolution can be assumed instantaneous. Finally, as expected, the solubility of water ice is unconstrained given the considerable range between IST and RST estimates (about a factor of 10^{17}) but is probably low.

Solubilities calculated using the IST and RST are also given at 91.5 K in Table B5 along with those gathered from our empirical fits of experimental data and the literature. The fits of experimental data are quite consistent with our RST values. Previous studies document the solubility of pure solids in liquid mixtures in equilibrium with the atmosphere (thus composed of methane, ethane, propane, and/or nitrogen) at various temperatures. Direct comparisons are therefore tentative, since the liquid composition, temperatures, and the thermodynamic parameters sources are heterogeneous. Nitrogen tends to decrease the solubility of solids in liquids while ethane and propane tend to increase it. It should be noted that the solubility of hydrocarbons is quite

AGU Journal of Geophysical Research: Planets 10.1002/2014JE004738

Table B5. Saturation Mole Fractions of Titan's Solids in Pure Liquid Methane, Ethane, and Propane at 91.5 K Evaluated Using the Ideal Solutions and Regular Solutions Theories Compared With Our Fits at 91.5 K of Experimental Data and With Values Taken From the Literature[a]

	X_i (IST)		X_i (RST)		Experiments		R87 (RST)		D89 (RST)	C13 (IST)	G13 (MVL)	T13 (PC-SAFT)	
Formula	91.5 K		91.5 K		91.5 K		94 K		92.5 K	90 K	90.7 K	90 K	93.7 K
CH_4	-	1.00	-	-	1.00	8.60×10^{-1}	-	7.30×10^{-2}	-	6.81×10^{-1}	6.84×10^{-1}	3.18×10^{-1}	
C_2H_6	-	-	1.00	-	-	-	9.70×10^{-1}	9.09×10^{-1}	-	1.55×10^{-1}	8.30×10^{-2}	5.32×10^{-1}	
C_3H_8	-	-	-	1.00	-	-	-		-	1.55×10^{-2}	7.80×10^{-3}	7.20×10^{-2}	
N_2	-	-	-	-	-	1.40×10^{-1}	3.00×10^{-2}	1.80×10^{-2}	-	1.48×10^{-1}	2.21×10^{-1}	6.89×10^{-2}	
C_4H_{10}	1.40×10^{-1}	1.51×10^{-3}	1.39×10^{-1}	1.40×10^{-1}	-	-	-	-	1.22×10^{-1}	-	-	-	
C_2H_2	5.90×10^{-2}	4.48×10^{-5}	2.00×10^{-4}	2.45×10^{-2}	5.72×10^{-5}	1.81×10^{-4}	6.93×10^{-4}	4.10×10^{-4}	5.40×10^{-2}	2.20×10^{-4}	3.40×10^{-3}	7.70×10^{-3}	
C_2H_4	5.89×10^{-1}	4.02×10^{-1}	5.33×10^{-1}	5.88×10^{-1}	-	1.81×10^{-3}	4.62×10^{-2}	-	-	-	-	-	
C_3H_4	3.85×10^{-2}	2.25×10^{-6}	2.36×10^{-5}	1.14×10^{-2}	-	7.26×10^{-6}	1.39×10^{-4}	5.00×10^{-5}	-	-	-	-	
C_4H_4	2.38×10^{-3}	1.64×10^{-4}	2.05×10^{-3}	2.16×10^{-3}	-	-	-	-	-	-	-	-	
C_4H_6	9.60×10^{-3}	3.57×10^{-5}	7.57×10^{-3}	8.06×10^{-3}	4.85×10^{-5}	3.27×10^{-5}	2.77×10^{-4}	-	-	-	-	-	
C_6H_6	1.64×10^{-4}	5.32×10^{-8}	3.11×10^{-5}	3.76×10^{-5}	1.59×10^{-7}	3.63×10^{-7}	9.24×10^{-6}	-	2.20×10^{-4}	-	-	-	
HCN	7.78×10^{-4}	3.25×10^{-11}	5.90×10^{-9}	1.14×10^{-7}	-	7.26×10^{-7}	2.31×10^{-5}	8.50×10^{-6}	6.46×10^{-4}	-	-	-	
C_2N_2	1.25×10^{-3}	8.96×10^{-8}	3.83×10^{-6}	8.30×10^{-5}	-	1.09×10^{-7}	2.77×10^{-6}	1.40×10^{-6}	-	-	-	-	
CH_3CN	1.59×10^{-3}	2.31×10^{-11}	7.64×10^{-9}	2.42×10^{-7}	-	2.18×10^{-6}	2.77×10^{-5}	6.30×10^{-5}	3.73×10^{-3}	-	-	-	
C_2H_3CN	1.44×10^{-2}	5.75×10^{-9}	1.74×10^{-6}	1.54×10^{-4}	-	-	-	2.20×10^{-5}	-	-	-	-	
C_2H_5CN	2.49×10^{-2}	9.28×10^{-8}	1.41×10^{-5}	1.25×10^{-3}	-	2.18×10^{-6}	3.70×10^{-5}	8.90×10^{-5}	-	-	-	-	
$C_2H_8N_2$	4.87×10^{-4}	2.46×10^{-7}	4.41×10^{-5}	5.44×10^{-5}	-	-	-	-	-	-	-	-	
$C_{11}H_{11}N$	4.07×10^{-9}	2.08×10^{-14}	2.09×10^{-10}	2.94×10^{-10}	-	-	-	-	-	-	-	-	
H_2O	5.23×10^{-3}	6.17×10^{-20}	5.50×10^{-17}	7.98×10^{-17}	-	1.81×10^{-15}	3.24×10^{-12}	-	-	-	-	-	
CO_2	1.06×10^{-3}	3.29×10^{-5}	1.23×10^{-5}	1.32×10^{-5}	2.68×10^{-5}	7.26×10^{-5}	3.24×10^{-5}	1.20×10^{-5}	8.72×10^{-4}	-	-	-	

[a]R87: *Raulin* [1987] (graphical reading), D89: *Dubouloz et al.* [1989], C13: *Cordier et al.* [2013b], G13: *Glein and Shock* [2013], T13: *Tan et al.* [2013].

Retour à la table des matières : p. v

AGU Journal of Geophysical Research: Planets 10.1002/2014JE004738

Table C1. Critical Properties of Titanian Materials [*Lide*, 2010][a]

Formula	M (g/mol)	T_c (K)	P_c (MPa)	V_c (cm^3/mol)	Z_{RA}	Z_c
CH_4	16.043	190.564	4.599	98.600	0.289	0.286
C_2H_6	30.069	305.320	4.872	145.500	0.281	0.279
C_3H_8	44.096	369.830	4.248	203.000	0.277	0.280
C_4H_{10}	58.122	425.160	3.787	255.000	0.273	0.273
C_2H_2	26.037	308.300	6.138	112.200	0.271	0.269
C_2H_4	28.053	282.340	5.041	131.000	0.282	0.281
C_3H_4	40.064	402.000	5.630	163.500	0.272	0.275
C_4H_4	52.075	455.600	4.860	218.710	0.282	0.281
C_4H_6	54.091	425.000	4.320	221.000	0.271	0.270
C_6H_6	78.112	562.050	4.895	256.000	0.270	0.268
HCN	27.026	456.700	5.390	139.000	0.197	0.197
C_2N_2	53.034	399.900	6.303	144.520	0.266	0.274
CH_3CN	41.042	545.500	4.850	171.000	0.199	0.183
C_2H_3CN	53.063	536.000	4.559	214.061	0.261	0.219
C_2H_5CN	55.079	561.300	4.260	229.000	0.263	0.209
$C_2H_8N_2$	60.098	522.200	5.400	218.241	0.265	0.271
$C_{11}H_{11}N$	157.212	775.100	3.353	514.500	0.247	0.268
H_2O	18.015	647.140	22.064	56.000	0.233	0.230
CO_2	40.010	304.130	7.375	94.000	0.272	0.274

[a]The Rackett parameters (Z_{RA}) have been gathered from the *CHemical and Engineering Research Information Center* database (http://www.cheric.org/research/kdb/hcprop/cmpsrch.php) and from *Infotherm* (http://www.infotherm.com/servlet/infothermSearch). The compressibility factors (Z_c) have been calculated for comparison with Z_{RA}. The critical properties of cyanogen and our tholins analogs (1-1 dimethyl-hydrazine $C_2H_8N_2$, as suggested in *Cordier et al.* [2013b], based on the experiments of *Quirico et al.* [2008], and quinoline $C_{11}H_{11}N$, as suggested by *Coll et al.* [1995]) have been collected in *Yaws* [1996].

in agreement between our study and others [*Raulin*, 1987; *Dubouloz et al.*, 1989; *Glein and Shock*, 2013] but the solubility of nitriles appears lower in our simulations than in previous ones [*Raulin*, 1987; *Dubouloz et al.*, 1989; *Cordier et al.*, 2013a], for which they lie between our IST and RST estimates.

Appendix C: Molar Volumes of Solvents and Solutes

If the density of a compound at a given temperature (T) is known from experimental data, it is straightforward to derive its molar volume $V_{m,i}(T)$, as follows:

$$V_{m,i}(T) = M_i/\rho_i(T) \qquad (m^3/mol). \tag{C1}$$

This is the case for water ice [*Loerting et al.*, 2011] and minerals [*Lide*, 2010]. However, experimentally determined densities for solids and liquids at the very low temperatures relevant to Titan are rather rare. We describe two complimentary techniques to evaluate the molar volumes of solids and liquids.

C1. Subcooled Liquid Molar Volumes

We first evaluate molar volumes at a given temperature T using the Rackett equation [*Spencer and Danner*, 1972; *Poling et al.*, 2007]. This method is designed to estimate the saturated subcooled liquid molar volumes of pure hydrocarbons and organic solvents ($V^L_{m,i}$).

$$V^L_{m,i} = \frac{R\,T_{c,i}}{P_{c,i}} Z_{c,i}^{\,[1+(1-T_{r,i})^{2/7}]} \qquad (m^3/mol). \tag{C2}$$

AGU Journal of Geophysical Research: Planets 10.1002/2014JE004738

Table C2. Estimated Subcooled Liquid Molar Volumes (in cm^3/mol) and Associated Mass Densities for Our Best Molar Volume Estimates (in g/cm^3, for Equation (C3) With Z_{RA}) for Titan's Solids and Liquids, Evaluated Using the Rackett Equations and Parameters at 91.5 K

Formula	Equation (C2) (Z_{RA})	Equation (C2) (Z_c)	Equation (C3) (Z_{RA})	Equation (C3) (Z_c)	2σ (Z_{RA})	ρ
CH_4	35.557	34.928	35.212	34.928	0.517	0.456
C_2H_6	46.520	45.968	46.229	45.968	0.456	0.650
C_3H_8	61.390	62.865	62.153	62.865	1.219	0.710
C_4H_{10}	75.882	75.978	75.932	75.978	0.080	0.766
C_2H_2	34.753	34.185	34.453	34.185	0.469	0.756
C_2H_4	42.344	42.147	42.240	42.147	0.162	0.664
C_3H_4	48.267	49.354	48.828	49.354	0.898	0.821
C_4H_4	67.280	66.398	66.824	66.398	0.729	0.779
C_4H_6	65.652	65.175	65.405	65.175	0.394	0.827
C_6H_6	74.256	73.269	73.748	73.269	0.817	1.059
HCN	30.232	30.323	30.279	30.323	0.075	0.893
C_2N_2	41.034	43.436	42.263	43.436	1.987	1.255
CH_3CN	40.219	34.105	36.956	34.105	5.041	1.111
C_2H_3CN	71.655	50.733	60.016	50.733	17.199	0.884
C_2H_5CN	81.023	51.731	64.373	51.731	24.046	0.856
$C_2H_8N_2$	60.828	63.522	62.197	63.522	2.230	0.966
$C_{11}H_{11}N$	123.135	144.275	133.476	144.275	17.564	1.178
H_2O	14.087	13.692	13.884	13.692	0.327	1.298
CO_2	28.789	29.225	29.017	29.225	0.360	1.379

R is the ideal gas constant (= 8.3144621 J/mol/K), T_c and P_c are the critical temperature (in K) and pressure (in Pa or J/m^3), respectively, Z_c is the critical compressibility factor, similar to the Rackett parameter ($Z_{RA} = 0.29056–0.08775\omega$, ω being the accentric factor, see *Poling et al.* [2007] for more details), and T_r the reduced temperature ($T_{r,i} = T/T_{c,i}$). All these parameters are given in Table C1. An alternative form of this equation is given by

$$V^L_{m,i} = V_{c,i} Z_{c,i}^{(1-T_{r,i})^{2/7}} \quad (m^3/mol). \tag{C3}$$

We investigated uncertainties in the molar volumes computed using the Rackett equations (C2) and (C3), with the two different parameters (Z_{RA}, taken from database or computed using the accentric factor, and Z_c, computed from the ideal gas equation at the critical point). The results are reported in Table C2 and Figures C1

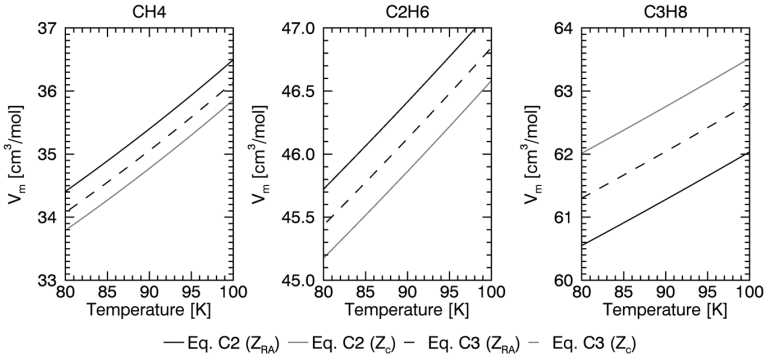

Figure C1. Differences in the calculated molar volumes of Titan's liquids due to the use of different Rackett equations and compressibility factors.

Retour à la table des matières : p. v

AGU Journal of Geophysical Research: Planets 10.1002/2014JE004738

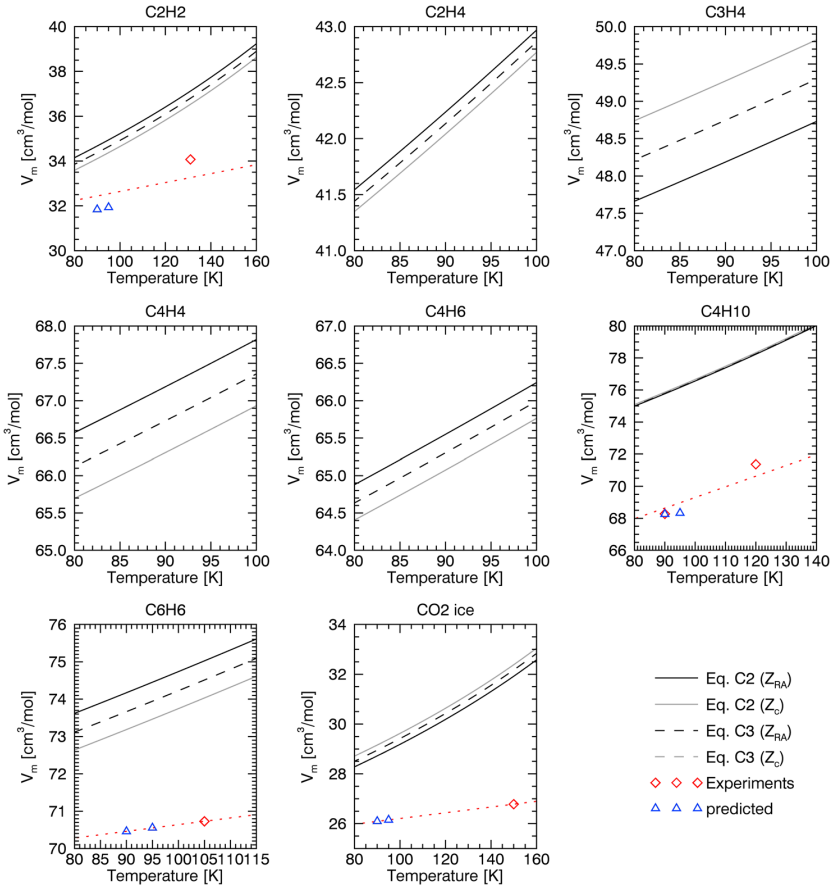

Figure C2. Same as Figure C1 but for "nonpolar" solids (hydrocarbons and carbon dioxide ice). Red and blue diamonds are experimental and predicted values, respectively. Sources: C_4H_{10} [*Refson and Pawley*, 1986], C_2H_2 [*McMullan et al.*, 1992], C_6H_6 [*Craven et al.*, 1993], and CO_2 [*Simon and Peters*, 1980].

(liquids), C2 (nonpolar solids), and C3 (polar solids). Differences in molar volumes are only significant for nitriles, going up to $2\sigma < 24$ cm^3/mol for propionitrile. To reduce possible over or underestimates for nitriles molar volumes and solubilities, we use equation (C3) with Z_{RA}, which is our "intermediate" case and also the most accurate estimates of $V^L_{m,i}$ [*Poling et al.*, 2007].

C2. Titan's Solids Molar Volumes

The solid molar volumes were determined from crystal structures available in the literature [*Dulmage and Lipscomb*, 1951; *Dietrich et al.*, 1975; *Simon and Peters*, 1980; *Refson and Pawley*, 1986; *Antson et al.*, 1987; *Etters and Kuchta*, 1989; *McMullan et al.*, 1992; *Craven et al.*, 1993]. The CH_3CN, HCN, C_4H_{10}, and C_2H_2 have a temperature dependent polymorphism. For each of these compounds, the selected crystal structure corresponds to the one observed at the temperature of Titan's surface (i.e., 90–95 K). Except for CH_3CN, the cell volume was experimentally determined for different temperatures. A second-order polynomial was used to fit the cell volume as a function of the temperature to extrapolate them at Titan's temperatures (90–95 K).

Since the pressure on Titan (around 1.5 bar) is not the same as on Earth (1 bar) where the crystal cell volume were determined, we checked the influence pressure on molar volumes by calculations based on the Density Functional Theory using the Vienna Ab-initio Simulation Package (VASP) 5.3 package. Cell volumes of each compound were optimized using vdW-DF2 [*Lee et al.*, 2010; *Klimeš et al.*, 2011] functional involving a nonlocal kernel for the electronic correlation energy calculation. This functional allows to reproduce dispersion interactions (such as Van der Waals interactions) which are major intermolecular interaction encountered

AGU Journal of Geophysical Research: Planets 10.1002/2014JE004738

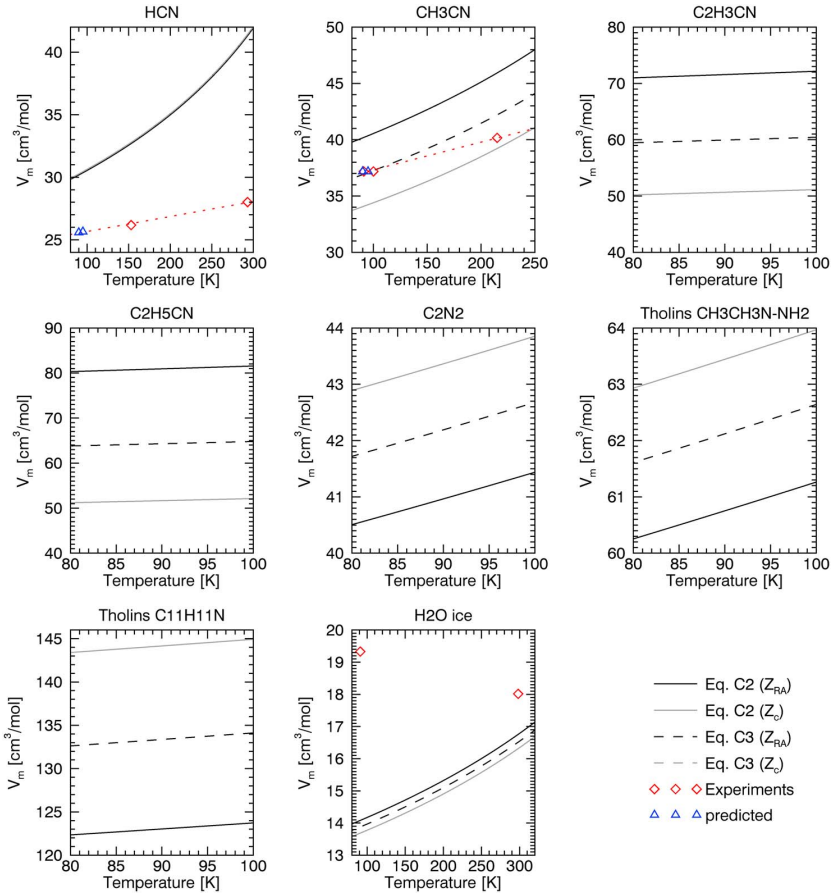

Figure C3. Same as Figure C2 but for polar solids (nitriles and water ice). Sources: HCN [*Dulmage and Lipscomb*, 1951], CH_3CN [*Barrow*, 1981; *Antson et al.*, 1987], and H_2O [*Loerting et al.*, 2011].

in molecular crystals. The E_{ncut} value, defining the basis set size, was fixed to 800 eV in order to suppress Pulay's stress. The *k*-points sampling was done with a 12 × 12 × 12 Monkhorst-Pack grid. The core electrons were described with the projector-augmented plane wave approach. Calculations were performed with and without static pressure (set to 100 bar) to compare cell volumes. The larger variation was observed for C_4H_{10}, with

Table C3. Subcooled Liquid Molar Volumes (in cm^3/mol) and Associated Mass Densities (in g/cm^3) of Titan's Solids Estimated Using the Rackett Equation (C3) With Z_{RA} at 91.5 K Compared to the Solid Molar Volumes (in cm^3/mol) and Associated Mass Densities (in g/cm^3) Computed From an Empirical Linear Fit Between Predictions of the Model and Experimental Data for Some Titanian Materials

Name	Formula	V_m^L (Equation (C3), Z_{RA})	V_m^S (fit)	2σ	ρ^L	ρ^S
n-butane	C_4H_{10}	75.932	68.737	7.195	0.766	0.846
Acetylene	C_2H_2	34.453	32.471	1.982	0.756	0.802
Benzene	C_6H_6	73.748	70.487	3.261	1.059	1.108
Hydrogen cyanide	HCN	30.279	25.562	4.717	0.893	1.057
Acetonitrile	CH_3CN	36.956	37.122	0.166	1.111	1.106
Water ice Ih	H_2O	13.884	19.329	5.446	1.298	0.932
Carbon dioxide ice	CO_2	29.017	26.109	2.909	1.379	1.532

AGU Journal of Geophysical Research: Planets 10.1002/2014JE004738

a volume decrease of 0.44% upon pressure. This is reasonably low to conclude that cell volumes measured on Earth (P = 1 bar) should be very similar to the ones on Titan (P = 1.5 bar).

We reported in Figures C2 and C3 the predicted crystalline molar volumes on top of the experimental and Rackett values (individual values also given in Table C3). Overall, we get a quite good agreement between all these estimates. We estimate the solid molar volumes at 91.5 K using a simple empirical linear fit between experimental and predicted points. The Rackett method is used to give an approximate molar volume for the solids for which we do not have experimental data.

Acknowledgments
The Cassini/RADAR SAR imaging data sets are provided through the NASA Planetary Data System Imaging Node portal (http://pds-imaging.jpl.nasa.gov/volumes/radar.html). Terrestrial annual evapotranspiration data taken from the Numerical Terradynamic Simulation Group (NTSG) database (http://ntsg.umt.edu/project/mod16) and precipitation data taken from the WorldClim database (http://www.worldclim.org/current) have been used in this study. The authors want to thank François Raulin and Sébastien Rodriguez for their helpful discussions, Axel Lefèvre and Manuel Giraud for their contribution in the Cassini SAR data processing, and Tim Rawle for the careful proofreading of the manuscript. The authors would like to acknowledge two anonymous reviewers for their work on the preliminary version of the manuscript, as well as the Editor and Associate Editor for useful comments. T.C. is funded by the ESA Postdoctoral Research Fellowship Programme in Space Science.

References

Acocella, V. (2007), Understanding caldera structure and development: An overview of analogue models compared to natural calderas, *Earth Sci. Rev.*, *85*(3–4), 125–160, doi:10.1016/j.earscirev.2007.08.004.
Aharonson, O., A. G. Hayes, J. I. Lunine, R. D. Lorenz, M. D. Allison, and C. Elachi (2009), An asymmetric distribution of lakes on Titan as a possible consequence of orbital forcing, *Nat. Geosci.*, *2*, 851–854, doi:10.1038/ngeo698.
Antson, O., K. Tilli, and N. Andersen (1987), Neutron powder diffraction study of deuterated b-acetonitrile, *Acta Crystallogr., Sect. B: Struct. Sci.*, *43*, 296–301, doi:10.1107/S0108768187097866.
Atreya, S. K. (2007), Titan's organic factory, *Science*, *316*(5826), 843–845, doi:10.1126/science.1141869.
Barnes, J. W., R. H. Brown, L. Soderblom, B. J. Buratti, C. Sotin, S. Rodriguez, S. Le Mouélic, K. H. Baines, R. Clark, and P. Nicholson (2007), Global-scale surface variations on Titan seen from Cassini/VIMS, *Icarus*, *186*(1), 242–258, doi:10.1016/j.icarus.2006.08.021.
Barnes, J. W., et al. (2009), Shoreline features of Titan's Ontario Lacus from Cassini/VIMS observations, *Icarus*, *201*(1), 217–225, doi:10.1016/j.icarus.2008.12.028.
Barnes, J. W., et al. (2011), Organic sedimentary deposits in Titan's dry lakebeds: Probable evaporite, *Icarus*, *216*(1), 136–140, doi:10.1016/j.icarus.2011.08.022.
Barrow, M. (1981), A-acetonitrile at 215 K, *Acta Crystallogr., Sect. B: Struct. Sci.*, *37*, 2239–2242, doi:10.1107/S0567740881008510.
Black, B. A., J. T. Perron, D. M. Burr, and S. A. Drummond (2012), Estimating erosional exhumation on Titan from drainage network morphology, *J. Geophys. Res.*, *117*, E08006, doi:10.1029/2012JE004085.
Bourgeois, O., T. Lopez, S. Le Mouélic, C. Fleurant, G. Tobie, L. Le Corre, L. Le Deit, C. Sotin, and Y. Bodeur (2008), A surface dissolution/precipitation model for the development of lakes on Titan, based on an arid terrestrial analogue: The Pans and Calcretes of Etosha, *Lunar Planet. Sci. Conf. 39th*, p. 1733.
Bowen, M. W., and W. C. Johnson (2012), Late Quaternary environmental reconstructions of playa-lunette system evolution on the central High Plains of Kansas, United States, *Geol. Soc. Am. Bull.*, *124*(1), 146–161, doi:10.1130/B30382.1.
Brew, T. C. L. (1977), A study on the solubility of heavy hydrocarbons in liquid methane and methane containing mixtures, Master's thesis, Univ. of Ottawa, Canada.
Brezonik, P., and W. Arnold (2011), *Water Chemistry: An Introduction to the Chemistry of Natural and Engineered Aquatic Systems*, 809 pp., Oxford Univ. Press, New York.
Brown, R. H., L. A. Soderblom, J. M. Soderblom, R. N. Clark, R. Jaumann, J. W. Barnes, C. Sotin, B. Buratti, K. H. Baines, and P. D. Nicholson (2008), The identification of liquid ethane in Titan's Ontario Lacus, *Nature*, *454*, 607–610, doi:10.1038/nature07100.
Buch, M. W. (1997), Etosha Pan—The third largest lake in the world?, *Madoqua*, *20*(1), 49–64.
Buch, M. W., and D. Rose (1996), Mineralogy and geochemistry of the sediments of the Etosha Pan Region in northern Namibia: A reconstruction of the depositional environment, *J. Afr. Earth. Sci.*, *22*(3), 355–378, doi:10.1016/0899-5362(96)00020-6.
Buch, M. W., and C. Trippner (1997), Overview of the geological and geomorphological evolution of the Etosha region, Northern Namibia, *Madoqua*, *20*(1), 65–74.
Cabane, M., E. Chassefière, and G. Israel (1992), Formation and growth of photochemical aerosols in Titan's atmosphere, *Icarus*, *96*(2), 176–189, doi:10.1016/0019-1035(92)90071-E.
Cheung, H., and E. H. Zander (1968), Solubility of carbon dioxide and hydrogen sulfide in liquid hydrocarbons at cryogenic temperatures, *Chem. Eng. Prog.*, *64*(88), 33–34.
Chevrier, V., S. Singh, D. Nna-Mvondo, D. Mège, M. Leitner, and A. Wagner (2014), Solubility and detection of simple and complex organics in Titan's liquid hydrocarbons, in *Titan Through Time—3rd Workshop*, pp. 14–15.
Chirico, R. D., R. D. J. III, and W. V. Steele (2007), Thermodynamic properties of methylquinolines: Experimental results for 2,6-dimethylquinoline and mutual validation between experiments and computational methods for methylquinolines, *J. Chem. Thermodyn.*, *39*(5), 698–711, doi:10.1016/j.jct.2006.10.012.
Choukroun, M., and C. Sotin (2012), Is Titan's shape caused by its meteorology and carbon cycle?, *Geophys. Res. Lett.*, *39*, L04201, doi:10.1029/2011GL050747.
Clark, A. M., and F. Din (1953), Equilibria between solid, liquid and gaseous phases at low temperatures. The system carbon dioxide + ethane + ethylene, *Discuss. Faraday Soc.*, *15*, 202–207.
Clark, R. N., et al. (2010), Detection and mapping of hydrocarbon deposits on Titan, *J. Geophys. Res.*, *115*, E10005, doi:10.1029/2009WR008896.
Coll, P., D. Cosia, M.-C. Gazeau, E. de Vanssay, J.-C. Guillemin, and F. Raulin (1995), Organic chemistry in Titan's atmosphere: New data from laboratory simulations at low temperature, *Adv. Space Res.*, *16*(2), 93–103, doi:10.1016/02731177(95)00197-M.
Cordier, D., O. Mousis, J. I. Lunine, P. Lavvas, and V. Vuitton (2009), An estimate of the chemical composition of Titan's lakes, *Astrophys. J.*, *707*, L128–L131, doi:10.1088/0004-637X/707/2/L128.
Cordier, D., O. Mousis, J. I. Lunine, P. Lavvas, and V. Vuitton (2013a), Erratum: An estimate of the chemical composition of Titan's lakes, *Astrophys. J. Lett.*, *768*, L23, doi:10.1088/2041-8205/768/1/L23.
Cordier, D., J. Barnes, and A. Ferreira (2013b), On the chemical composition of Titan's dry lakebed evaporites, *Icarus*, *226*(2), 1431–1437, doi:10.1016/j.icarus.2013.07.026.
Cornet, T., et al. (2012), Geomorphological significance of Ontario Lacus on Titan: Integrated interpretation of Cassini VIMS, ISS and RADAR data and comparison with the Etosha Pan (Namibia), *Icarus*, *218*(2), 788–806, doi:10.1016/j.icarus.2012.01.013.
Cottini, V., et al. (2012), Water vapor in Titan's stratosphere from Cassini CIRS far-infrared spectra, *Icarus*, *220*(2), 855–862, doi:10.1016/j.icarus.2012.06.014.
Coustenis, A., et al. (2010), Titan trace gaseous composition from CIRS at the end of the Cassini-Huygens prime mission, *Icarus*, *207*(1), 461–476, doi:10.1016/j.icarus.2009.11.027.

AGU Journal of Geophysical Research: Planets 10.1002/2014JE004738

Craven, C., P. Hatton, C. Howard, and G. Pawley (1993), The structure and dynamics of solid benzene. I. A neutron powder diffraction study of deuterated benzene from 4 K to the melting point, *J. Chem. Phys.*, *98*, 8236–8243.
Cui, J., et al. (2009), Analysis of Titan's neutral upper atmosphere from Cassini Ion Neutral Mass Spectrometer measurements, *Icarus*, *200*(2), 581–615, doi:10.1016/j.icarus.2008.12.005.
Davis, J. A., N. Rodewald, and F. Kurata (1962), Solid-liquid-vapor phase behavior of the methane-carbon dioxide system, *AIChE J.*, *8*(4), 537–539, doi:10.1002/aic.690080423.
Dietrich, O., G. Mackenzie, and G. Pawley (1975), The structural phase transition in solid DCN, *J. Phys. C: Solid State Phys.*, *8*, L98, doi:10.1088/0022-3719/8/7/002.
Dubouloz, N., F. Raulin, E. Lellouch, and D. Gautier (1989), Titan's hypothesized ocean properties: The influence of surface temperature and atmospheric composition uncertainties, *Icarus*, *82*(1), 81–96, doi:10.1016/0019-1035(89)90025-0.
Dulmage, W., and W. Lipscomb (1951), The crystal structures of hydrogen cyanide, HCN, *Acta Crystallogr.*, *4*, 330–334, doi:10.1107/S0365110X51001070.
Etters, R., and B. Kuchta (1989), Static and dynamic properties of solid CO2 at various temperatures and pressures, *J. Chem. Phys.*, *90*, 4537–4551, doi:10.1063/1.456640.
Fleurant, C., G. Tucker, and H. Viles (2008), A cockpit karst evolution model, in *Landscape Evolution: Denudation, Climate and Tectonics Over Different Time and Space Scales*, vol. 296, edited by Gallagher, K., S. J. Jones, and J. Wainwright, pp. 47–62, Geol. Soc. of London, doi: 10.1144/SP296.4.
Ford, D., and P. Williams (2007), *Karst Hydrogeology and Geomorphology*, 562 pp., John Wiley, Chichester, West Sussex, England.
French, H. M. (2007), *The Periglacial Environment*, 3rd ed., 458 pp., John Wiley, Chichester, West Sussex, England.
Frumkin, A. (1994), Hydrology and denudation rates of halite karst, *J. Hydrol.*, *162*, 171–189, doi:10.1016/0022-1694(94)90010-8.
Frumkin, A. (1996), Uplift rate relative to base-levels of a salt diapir (Dead Sea Basin, Israel) as indicated by cave levels, *Geol. Soc. Spec. Publ.*, *100*, 41–47, doi:10.1144/GSL.SP.1996.100.01.04.
Garasic, M. (2001), New speleohydrogeological research of Crveno jezero (Red Lake) near Imotski in Dinaric Karst Area (Croatia, Europe)—International speleodiving expedition "Crveno jezero 98', *13th International Congress of Speleology, 4th Speleological Congress of Latin América and Caribbean, 26th Brazilian Congress of Speleology*, pp. 555–559.
Garasic, M. (2012), Crveno Jezero—The biggest sinkhole in Dinaric Karst (Croatia), in *EGU General Assembly Conference Abstracts*, edited by A. Abbasi, and N. Giesen, pp. 7132–7134.
Glein, C. R., and E. L. Shock (2013), A geochemical model of non-ideal solutions in the methane-ethane-propane-nitrogen-acetylene system on Titan, *Geochim. Cosmochim. Acta*, *115*, 217–240, doi:10.1016/j.gca.2013.03.030.
Goudie, A. S., and G. L. Wells (1995), The nature, distribution and formation of pans in arid zones, *Earth Sci. Rev.*, *38*, 1–69, doi:10.1016/0012-8252(94)00066-6.
Graves, S. D. B., C. P. McKay, C. A. Griffith, F. Ferri, and M. Fulchigoni (2008), Rain and hail can reach the surface of Titan, *Planet. Space Sci.*, *56*, 346–357, doi:10.1016/j.pss.2007.11.001.
Harrisson, K. P. (2012), Thermokarst processes in Titan's lakes: Comparison with terrestrial data, *Lunar Planet. Sci. Conf. 43rd*, pp. 2271–2272.
Hayes, A., et al. (2008), Hydrocarbon lakes on Titan: Distribution and interaction with an isotropic porous regolith, *Geophys. Res. Lett.*, *35*, L09204, doi:10.1029/2008GL033409.
Heintz, A., and E. Bich (2009), Thermodynamics in an icy world: The atmosphere and internal structure of Saturn's moon Titan, *Pure Appl. Chem.*, *81*(10), 1903–1920, doi:10.1351/PAC-CON-08-10-04.
Hipondoka, M. H. T. (2005), The development and evolution of Etosha Pan, Namibia, PhD thesis, 154 pp., Univ. of Wurzburg, Germany.
Jennings, D. E., et al. (2009), Titan's surface brightness temperatures, *Astrophys. J. Lett.*, *691*(2), L103–L105, doi:10.1088/0004-637X/691/2/L103.
Kargel, J. S., R. Furfaro, C. C. Hays, R. M. C. Lopes, J. I. Lunine, K. L. Mitchell, S. D. Wall, and Cassini RADAR Team (2007), Titan's GOO-sphere: Glacial, permafrost, evaporite, and other familiar processes involving exotic materials, *Lunar Planet. Sci. Conf. 38th*, pp. 1992–1993.
Kirk, R. L., and E. Howington-Kraus (2008), Radargrammetry on three planets, *Int. Arch. Photogramm. Remote Sens.*, *37*(B4), 973–980.
Kirk, R. L., E. Howington-Kraus, K. L. Mitchell, S. Hensley, B. W. Stiles, and Cassini RADAR Team (2007), First stereoscopic radar images of Titan, *Lunar Planet. Sci. Conf. 38th*, pp. 1427–1428.
Kirk, R. L., et al. (2012), Topographic mapping of Titan: Latest results, *Lunar Planet. Sci. Conf. 43rd*, pp. 2759–2760.
Klimeš, J., D. R. Bowler, and A. Michaelides (2011), Van Der Waals density functionals applied to solids, *Phys. Rev. B*, *83*, 195131, doi:10.1103/PhysRevB.83.195131.
Krasnopolsky, V. A. (2009), A photochemical model of Titan's atmosphere and ionosphere, *Icarus*, *201*(1), 226–256, doi:10.1016/j.icarus.2008.12.038.
Kuebler, G. P., and G. McKinley (1975), Solubility of solid n-butane and n-pentane in liquid methane, in *Advances in Cryogenic Engineering*, vol. 21, pp. 509–515, Springer, doi:10.1007/978-1-4757-0208-8_60.
Kuebler, G. P., and G. McKinley (1995), Solubility of solid benzene, toluene, n-hexane, n-heptane, in liquid methane, in *Advances in Cryogenic Engineering*, vol. 19, pp. 320–326, Springer, doi:10.1007/978-1-4613-9847-9_39.
Langmuir, D. (1997), *Aqueous Environmental Geochemistry*, 618 pp., Prentice Hall, Upper Saddle River, N. J.
Lara, L. M., E. Lellouch, J. J. López-Moreno, and R. Rodrigo (1996), Vertical distribution of Titan's atmospheric neutral constituents, *J. Geophys. Res.*, *101*(E10), 23,161–23,283, doi:10.1029/96JE02036.
Lavvas, P. P., A. Coustenis, and I. M. Vardavas (2008a), Coupling photochemistry with haze formation in Titan's atmosphere, Part I: Model description, *Planet. Space Sci.*, *56*(1), 27–66, doi:10.1016/j.pss.2007.05.026.
Lavvas, P. P., A. Coustenis, and I. M. Vardavas (2008b), Coupling photochemistry with haze formation in Titan's atmosphere, Part II: Results and validation with Cassini/Huygens data, *Planet. Space Sci.*, *56*(1), 67–99, doi:10.1016/j.pss.2007.05.027.
Lee, K., E. D. Murray, L. Kong, B. I. Lundqvist, and D. C. Langreth (2010), Higher-accuracy Van der Waals density functional, *Phys. Rev. B*, *82*, 081101, doi:10.1103/PhysRevB.82.081101.
Leitner, M., S. Singh, and V. F. Chevrier (2014), Solubility and detectability of acetonitrile in Titan lakes, *Lunar Planet. Sci. Conf. 45th*, p. 2658.
Lide, D. (2010), *CRC Handbook of CHemistry and Physics*, 90th ed. (CD-ROM version 2010), CRC Press/Taylor and Francis, Boca Raton, Fla.
Loerting, T., M. Bauer, I. Kohl, K. Watschinger, K. Winkel, and E. Mayer (2011), Cryoflotation: Densities of amorphous and crystalline ices, *J. Phys. Chem. B*, *115*, 14,167–14,175, doi:10.1021/jp204752w.
Lopes, R. M. C., et al. (2007), The lakes and seas of Titan, *Eos Trans. AGU*, *88*(51), 569–576, doi:10.1029/2007EO510001.
Lora, J. M., P. J. Goodman, J. L. Russell, and J. I. Lunine (2011), Insolation in Titan's troposphere, *Icarus*, *216*(1), 116–119, doi:10.1016/j.icarus.2011.08.017.
Lorenz, R. D., and J. I. Lunine (2002), Titan's snowline, *Icarus*, *158*(2), 557–559, doi:10.1006/icar.2002.6880.
Lorenz, R. D., et al. (2008), Titan's inventory of organic surface materials, *Geophys. Res. Lett.*, *35*, L02206, doi:10.1029/2007GL03118.
Lorenz, R. D., et al. (2013), A global topographic map of Titan, *Icarus*, *225*(1), 367–377, doi:10.1016/j.icarus.2013.04.002.

AGU Journal of Geophysical Research: Planets 10.1002/2014JE004738

Lorenz, R. D., et al. (2014), A Radar map of Titan seas: Tidal dissipation and ocean mixing through the throat of Kraken, *Icarus*, *237*, 9–15, doi:10.1016/j.icarus.2014.04.005.
Lorenz, V. (1986), On the growth of maars and diatremes and its relevance to the formation of tuff rings, *Bull. Volcanol.*, *48*, 265–274, doi:10.1007/BF01081755.
Luks, K. D., J. D. Hottovy, and J. P. Kohn (1981), Three-phase solid-liquid-vapor equilibriums in the binary hydrocarbon systems methane-n-hexane and methane-benzene, *J. Chem. Eng. Data*, *26*(4), 402–403, doi:10.1021/je00026a016.
Lunine, J. I., D. J. Stevenson, and Y. L. Yung (1983), Ethane ocean on Titan, *Science*, *222*(4629), 1229–1230, doi:10.1126/science.222.4629.1229.
Lunine, J. I., et al. (2008), Titan's diverse landscapes as evidenced by Cassini Radar's third and fourth looks at Titan, *Icarus*, *195*(1), 415–433, doi:10.1016/j.icarus.2007.12.022.
Luspay-Kuti, A., V. F. Chevrier, F. C. Wasiak, L. A. Roe, W. D. D. P. Welivitiya, T. Cornet, S. Singh, and E. G. Rivera-Valentin (2012), Experimental simulations of CH_4 evaporation on Titan, *Geophys. Res. Lett.*, *39*, L23808, doi:10.1029/2012GL054003.
Luspay-Kuti, A., V. F. Chevrier, D. Cordier, E. G. Rivera-Valentin, S. Singh, A. Wagner, and F. Wasiak (2014), Experimental constraints on the composition and dynamics of Titan's polar lakes, *Earth Planet. Sci. Lett.*, *410*, 75–83, doi:10.1016/j.epsl.2014.11.023.
Lyew-Ayee, P. (2010), *The Cockpit Country of Jamaïca: An Island Within an Island*, pp. 69–77, Springer, Dordrecht, Heidelberg, London, and New York, doi:10.1007/978-90-481-3055-9_8.
MacKenzie, S. M., et al. (2014), Evidence of Titan's climate history from evaporite distribution, *Icarus*, *243*, 191–207, doi:10.1016/j.icarus.2014.08.022.
Magee, B. A., J. H. Waite, K. E. Mandt, J. Westlake, J. Bell, and D. A. Gell (2009), INMS-derived composition of Titan's upper atmosphere: Analysis methods and model comparison, *Planet. Space Sci.*, *57*(14–15), 1895–1916, doi:10.1016/j.pss.2009.06.016.
Malaska, M., J. Radebaugh, R. Lorenz, K. Mitchell, T. Farr, and E. Stofan (2010), Identification of karst-like terrain on Titan from valley analysis, *Lunar Planet. Sci. Conf. 41st*, pp. 1544–1545.
Malaska, M., J. Radebaugh, K. Mitchell, R. Lopes, S. Wall, and R. Lorenz (2011), Surface dissolution model for Titan karst, in *First International Planetary Cave Research Workshop*, pp. 8018–8019.
Malaska, M. J., and R. Hodyss (2014), Dissolution of benzene, naphthalene, and biphenyl in a simulated Titan lake, *Icarus*, *242*, 74–81, doi:10.1016/j.icarus.2014.07.022.
Mastrogiuseppe, M., et al. (2014), The bathymetry of a Titan sea, *Geophys. Res. Lett.*, *41*, 1432–1437, doi:10.1002/2013GL058618.
McMullan, R., A. Kvick, and P. Popelier (1992), Structures of cubic and orthorhombic phases of acetylene by single-crystal neutron diffraction, *Acta Crystallogr., Sect. B: Struct. Sci*, *48*, 726–731, doi:10.1107/S0108768192004774.
Mihevc, A., M. Prelovsek, and N. Zupan Hajna (Eds.) (2010), *Introduction to the Dinaric Karst*, 72 pp., Karst Res. Inst., ZRC SAZU, Postojna, Slovenia.
Miller, R. M., M. Pickford, and B. Senut (2010), The geology, palaeontology and evolution of the Etosha Pan, Namibia: Implications for terminal Kalahari deposition, *S. Afr. J. Geol.*, *113*(3), 307–334, doi:10.2113/gssajg.113.307.
Mitchell, J. L. (2008), The drying of Titan's dunes: Titan's methane hydrology and its impact on atmospheric circulation, *J. Geophys. Res.*, *113*, E08015, doi:10.1029/2007JE003017.
Mitchell, J. L., R. T. Pierrehumbert, D. M. Frierson, and R. Caballero (2009), The impact of methane thermodynamics on seasonal convection and circulation in a model Titan atmosphere, *Icarus*, *203*(1), 250–264, doi:10.1016/j.icarus.2009.03.043.
Mitchell, J. L., M. Ádámkovics, R. Caballero, and E. P. Turtle (2011), Locally enhanced precipitation organized by planetary-scale waves on Titan, *Nat. Geosci.*, *4*, 589–592, doi:10.1038/ngeo1219.
Mitchell, K. L., and M. Malaska (2011), Karst on Titan, in *First International Planetary Cave Research Workshop*, pp. 8021–8022.
Mitchell, K. L., J. S. Kargel, C. A. Wood, J. Radebaugh, R. M. C. Lopes, J. I. Lunine, E. R. Stofan, R. L. Kirk, and Cassini RADAR Team (2007), Titan's crater lakes: Caldera vs. karst?, *Lunar Planet. Sci. Conf. 38th*, pp. 2061–2064.
Moore, J. M., and A. D. Howard (2010), Are the basins of Titan's Hotei Regio and Tui Regio sites of former low latitude seas?, *Geophys. Res. Lett.*, *37*, L22205, doi:10.1029/2010GL045234.
Moore, J. M., and R. T. Pappalardo (2011), Titan: An exogenic world?, *Icarus*, *212*(2), 790–806, doi:10.1016/j.icarus.2011.01.019.
Moriconi, M. L., J. I. Lunine, A. Adriani, E. D'Aversa, A. Negrao, G. Filacchione, and A. Coradini (2010), Characterization of Titan's Ontario Lacus region from Cassini/VIMS observations, *Icarus*, *210*(2), 823–831, doi:10.1016/j.icarus.2010.07.023.
Neish, C. D., and R. D. Lorenz (2012), Titan's global crater population: A new assessment, *Planet. Space Sci.*, *60*(1), 26–33, doi:10.1016/j.pss.2011.02.016.
Neumann, A., and R. Mann (1969), Die Löslichkeit von festem Acetylen in flüssigen Methan/Äthylen-Mischungen, *Chem. Ing. Tech.*, *41*(12), 708–711, doi:10.1002/cite.330411204.
Poling, B. E., J. M. Prausnitz, and J. P. O'Connell (2007), *The Properties of Gases and Liquids*, 5th ed., McGraw-Hill Prof., Englewood Cliffs, N. J.
Preston, G. T., and J. M. Prausnitz (1970), Thermodynamics of solid solubility in cryogenic solvents, *Ind. Eng. Chem. Process Des. Dev.*, *9*(2), 264–271, doi:10.1021/i260034a017.
Preston, G. T., E. W. Funk, and J. M. Prausnitz (1971), Solubilities of hydrocarbons and carbon dioxide in liquid methane and in liquid argon, *J. Phys. Chem.*, *75*(15), 2345–2352.
Quirico, E., et al. (2008), New experimental constraints on the composition and structure of tholins, *Icarus*, *198*(1), 218–231, doi:10.1016/j.icarus.2008.07.012.
Rannou, P., C. P. McKay, and R. D. Lorenz (2003), A model of Titan's haze of fractal aerosols constrained by multiple observations, *Planet. Space Sci.*, *51*(14–15), 963–976, doi:10.1016/j.pss.2003.05.008.
Rannou, P., F. Montmessin, F. Hourdin, and S. Lebonnois (2006), The latitudinal distribution of clouds on Titan, *Science*, *311*, 201–205, doi:10.1126/science.1118424.
Raulin, F. (1987), Organic chemistry in the oceans of Titan, *Adv. Space Res.*, *7*(5), 571–581, doi:10.1016/0273-1177(87)90358-9.
Refson, K., and G. Pawley (1986), The structure and orientational disorder in solid n-butane by neutron powder diffraction, *Acta Crystallogr., Sect. B: Struct. Sci.*, *42*, 402–410, doi:10.1107/S010876818609804X.
Rodriguez, S., et al. (2009), Global circulation as the main source of cloud activity on Titan, *Nature*, *459*, 678–682, doi:10.1038/nature08014.
Rodriguez, S., et al. (2011), Titan's cloud seasonal activity from winter to spring with Cassini/VIMS, *Icarus*, *216*(1), 89–110, doi:10.1016/j.icarus.2011.07.031.
Rodriguez, S., et al. (2014), Global mapping and characterization of Titan's dune fields with Cassini: Correlation between {RADAR} and {VIMS} observations, *Icarus*, *230*, 168–179, doi:10.1016/j.icarus.2013.11.017.
Roe, H. G., I. de Pater, B. A. Macintosh, S. G. Gibbard, C. E. Max, and C. P. McKay (2002), Titan's atmosphere in late southern spring observed with adaptive optics on the W. M. Keck II 10-meter telescope, *Icarus*, *157*(1), 254–258, doi:10.1006/icar.2002.6831.
Schaller, E. L., M. E. Brown, H. G. Roe, and A. H. Bouchez (2006), A large cloud outburst at Titan's south pole, *Icarus*, *182*(1), 224–229, doi:10.1016/j.icarus.2005.12.021.

AGU Journal of Geophysical Research: Planets 10.1002/2014JE004738

Schaller, E. L., H. G. Roe, T. Schneider, and M. E. Brown (2009), Storms in the tropics of Titan, *Nature*, *460*(7257), 873–875, doi:10.1038/nature08193.

Schneider, T., S. D. B. Graves, E. L. Schaller, and M. E. Brown (2012), Polar methane accumulation and rainstorms on Titan from simulations of the methane cycle, *Nature*, *481*, 58–61, doi:10.1038/nature10666.

Sharma, P., and S. Byrne (2010), Constraints on Titan's topography through fractal analysis of shorelines, *Icarus*, *209*, 723–737, doi:10.1016/j.icarus.2010.04.023.

Sharma, P., and S. Byrne (2011), Comparison of Titan's north polar lakes with terrestrial analogs, *Geophys. Res. Lett.*, *38*, L24203, doi:10.1029/2011GL049577.

Shaw, P. A., and D. S. G. Thomas (2000), Pans, playas and salt lakes, in *Arid Zone Geomorphology: Process, Form and Change in Drylands*, edited by D. S. G. Thomas, 2nd ed., chap. 15, pp. 293–317, John Wiley, England.

Simon, A., and K. Peters (1980), Single-crystal refinement of the structure of carbon dioxide, *Acta Crystallogr., Sect. B: Struct. Sci*, *36*, 2750–2751, doi:10.1107/S0567740880009879.

Singh, S., V. F. Chevrier, A. Wagner, M. Leitner, M. Gainor, L. Roe, T. Cornet, and J.-P. Combe (2014), Solubility of acetylene in liquid hydrocarbons under Titan surface conditions, *Lunar Planet. Sci. Conf. 45th*, p. 2850.

Sket, B. (2012), Diversity patterns in the Dinaric Karst, in *Encyclopedia of Caves*, edited by W. B. White, and D. C. Cluver, pp. 228–238, Elsevier Inc., Amsterdam.

Sotin, C., et al. (2012), Observations of Titan's northern lakes at 5 microns: Implications for the organic cycle and geology, *Icarus*, *221*(2), 768–786, doi:10.1016/j.icarus.2012.08.017.

Spencer, C. F., and R. P. Danner (1972), Improved equation for prediction of saturated liquid density, *J. Chem. Eng. Data*, *17*, 236–241, doi:10.1021/je60053a012.

Stephan, K. et al. (2009), Titan from Cassini-Huygens, in *Mapping Products of Titan's Surface*, edited by R. H. Brown, J.-P. Lebreton, and J. H. Waite, pp. 489–510, Springer, Netherlands, doi:10.1007/978-1-4020-9215-2.

Stiles, B. W., et al. (2009), Determining Titan surface topography from Cassini SAR data, *Icarus*, *202*(2), 584–598, doi:10.1016/j.icarus.2009.03.032.

Stofan, E. R., et al. (2007), The lakes of Titan, *Nature*, *445*, 61–64, doi:10.1038/nature05438.

Szczepaniec-Cieciak, E., B. Dabrowska, J. M. Lagan, and Z. Wojtaszek (1978), Estimation of the solubility of solidified substances in liquid methane by the Preston-Prausnitz method, *Cryogenics*, *18*(10), 591–600, doi:10.1016/0011-2275(78)90186-8.

Tan, S. P., J. S. Kargel, and G. M. Marion (2013), Titan's atmosphere and surface liquid: New calculation using statistical associating fluid theory, *Icarus*, *222*(1), 53–72, doi:10.1016/j.icarus.2012.10.032.

Tewelde, Y., J. T. Perron, P. Ford, S. Miller, and B. Black (2013), Estimates of fluvial erosion on titan from sinuosity of lake shorelines, *J. Geophys. Res. Planets*, *118*, 2198–2212, doi:10.1002/jgre.20153.

Tobie, G., J. I. Lunine, and C. Sotin (2006), Episodic outgassing as the origin of atmospheric methane on Titan, *Nature*, *440*(7080), 61–64, doi:10.1038/nature04497.

Tokano, T. (2009), Impact of seas/lakes on polar meteorology of Titan: Simulation by a coupled GCM-Sea model, *Icarus*, *204*(2), 619–636, doi:10.1016/j.icarus.2009.07.032.

Toublanc, D., J. P. Parisot, J. Brillet, D. Gautier, F. Raulin, and C. P. McKay (1995), Photochemical modeling of Titan's atmosphere, *Icarus*, *113*(1), 2–26, doi:10.1006/icar.1995.1002.

Truesdell, A., and B. Jones (1974), WATEQ, a computer program for calculating chemical equilibria of natural waters, *J. Res. U.S. Geol. Surv.*, *2*, 233–248.

Tucker, G. E., S. T. Lancaster, N. M. Gasparini, and R. L. Bras (2001), The Channel-Hillslope Integrated Landscape Development (CHILD) model, in *Landscape Erosion and Evolution Modeling*, edited by R. S. Harmon, and W. W. Doe III, pp. 349–388, Springer.

Turtle, E. P., et al. (2011a), Rapid and extensive surface changes near Titan's equator: Evidence of April showers, *Science*, *331*, 1414–1417, doi:10.1126/science.1201063.

Turtle, E. P., A. D. Del Genio, J. M. Barbara, J. E. Perry, E. L. Schaller, A. S. McEwen, R. A. West, and T. L. Ray (2011b), Seasonal changes in Titan's meteorology, *Geophys. Res. Lett.*, *38*, L03203, doi:10.1029/2010GL046266.

Vinatier, S., et al. (2010), Analysis of Cassini/CIRS limb spectra of Titan acquired during the nominal mission: I. Hydrocarbons, nitriles and CO2 vertical mixing ratio profiles, *Icarus*, *205*(2), 559–570, doi:10.1016/j.icarus.2009.08.013.

Vixie, G., J. W. Barnes, B. Jackson, and P. Wilson (2012), Temperate lakes discovered on Titan, *Lunar Planet. Sci. Conf. 43rd*, p. 2766.

Vlahovic, I., J. Tisljar, I. Velic, and D. Maticec (2002), The Karst Dinarides are composed of relics of a single Mesozoic platform: Facts and consequences, *Geol. Croat.*, *55*(2), 171–183.

von Szalghary, W.-D. (1972), Löslichkeit von festem benzol in flüssigen Kohlenwasserstoffen, *Kältetechnik-Klimatisierung*, *24*, 145–149.

Waltham, T. (2008), Fengcong, fenglin, cone karst and tower karst, *Cave Karst Sci.*, *35*, 77–88.

Wang, P., and Q. Li (2009), Monsoons: Pre-quaternary, in *Encyclopedia of Paleoclimatology and Ancient Environments*, edited by V. Gornitz, pp. 583–589, Springer, Netherlands.

Wasiak, F. C., D. Androes, D. G. Blackburn, J. A. Tullis, J. Dixon, and V. F. Chevrier (2013), A geological characterization of Ligeia Mare in the northern polar region of Titan, *Planet. Space Sci.*, *84*, 141–147, doi:10.1016/j.pss.2013.05.007.

White, W. B. (1984), Rate processes: Chemical kinetics and karst landform development, in *Groundwater as a Geomorphic Agent*, pp. 227–248, Allen and Unwin, Inc, Boston, Mass.

White, W. B. (2012), Hydrogeology of karst aquifers, in *Encyclopedia of Caves*, 2nd edn., pp. 383–391, Elsevier, Amsterdam.

White, W. M. (2013), *Geochemistry*, 672 pp., John Wiley, New York.

Wilson, E. H., and S. K. Atreya (2004), Current state of modeling the photochemistry of Titan's mutually dependent atmosphere and ionosphere, *J. Geophys. Res.*, *109*, E06002, doi:10.1029/2003JE002181.

Wood, C. A., K. L. Mitchell, R. M. C. Lopes, J. Radebaugh, E. Stofan, J. Lunine, and Cassini RADAR Team (2007), Volcanic calderas in the north polar region of Titan, *Lunar Planet. Sci. Conf. 38th*, pp. 1454–1455.

Xuewen, Z., and C. Weihai (2006), Tiankengs in the karst of China, *Speleogenesis Evol. Karst Aquifers*, *4*(1), 1–18.

Journal of Geophysical Research: Planets 10.1002/2014JE004738

Yaws, C. L. (1996), Appendix D—Critical properties and acentric factor for inorganic compounds and elements inorganic compounds and elements, in *Handbook of Thermodynamic Diagrams*, vol. 4, pp. 351–356, Gulf Prof. Publ., doi:10.1016/B978-0-88415-860-8.50036-2.
Yung, Y. L., M. Allen, and J. P. Pinto (1984), Photochemistry of the atmosphere of Titan: Comparison between model and observations, *Astrophys. J.*, *55*, 465–506, doi:10.1086/190963.
Zupan Hajna, N. (2012), Dinaric Karst: Geography and geology, in *Encyclopedia of Caves*, 2nd edn., pp. 195–203, Elsevier, Amsterdam.

4.10 Article sur la vitesse du son comme contrainte sur la composition chimique

MNRAS 459, 2008–2013 (2016) doi:10.1093/mnras/stw732
Advance Access publication 2016 March 30

How speed-of-sound measurements could bring constraints on the composition of Titan's seas

D. Cordier*

Groupe de Spectrométrie Moléculaire et Atmosphérique, UMR 6089, Campus Moulin de la Housse, BP 1039, Université de Reims Champagne-Ardenne, F-51687 Reims, France

Accepted 2016 March 24. Received 2016 March 24; in original form 2016 January 18

ABSTRACT

The hydrocarbon seas of Titan, discovered by the *Cassini/Huygens* mission are among the most mysterious and interesting features of this moon. In the future, a possible dedicated planetary probe will certainly measure the speed of sound in this cryogenic liquid, as was planned in the case of *Huygens* landing in a sea. Previous theoretical studies of such acoustic measurements were based on simple models, leading in some cases to unphysical situations. Employed in a vast body of chemical engineering works, the state-of-the-art perturbed-chain statistical associating fluid theory (PC-SAFT) model has been recently introduced in studies aimed at Titan. Here, I revisit the issue of the speed of sound in Titan's liquids, in light of this theory. I describe, in detail, the derivation of the speed of sound from the chosen equation of state and the potential limitations of the approach. To make estimations of the composition of a ternary liquid mixture N_2:CH_4:C_2H_6 from speed-of-sound measurements an original inversion algorithm is proposed. It is shown that 50 measures between 90 and 100 K are enough to ensure an accuracy of the derived compositions of better than 10 per cent. The influence of the possible presence of propane is also investigated.

Key words: instrumentation: miscellaneous – methods: numerical – techniques: miscellaneous – planets and satellites: individual: Titan.

1 INTRODUCTION

Among a multitude of fascinating features, Titan, the main satellite of Saturn, is – with the Earth – the only body of the Solar system bearing stable liquid phases at its surface. These hydrocarbon seas and lakes remain largely mysterious; they appear amazingly flat (Zebker et al. 2014), with unexplained reflectivity events (Hofgartner et al. 2014), while their precise chemical composition is not well known. Only the presence of ethane has been detected (Brown et al. 2008) and estimations performed with numerical models disagree (Tan, Kargel & Marion 2013; Glein & Shock 2013; Cordier et al. 2009, 2013). Given their important role as a reservoir in the hydrocarbon cycle, and because of their high exobiological potential (McKay & Smith 2005; Schulze-Makuch & Grinspoon 2005; Lunine 2010), these lakes/seas would be very interesting targets for an *in situ* exploration. Already mission concepts have been studied: for instance, the *Titan Mare Explorer* (*TiME*) project (see Stofan et al. 2011) proposes a sea surface exploration with a boat, while Lorenz et al. (2015) suggest a submarine. Both proposals incorporate an instrument that exploits the properties of sound propagation in liquids.

* E-mail: daniel.cordier@univ-reims.fr

The idea of instruments based on acoustic measurements has been investigated and implemented for Mars. Originally aimed at thunder detection, sound sensors have been deployed at the surface of Venus (Ksanfomaliti et al. 1982; Ksanfomaliti, Goroshkova & Khondryev 1986). Finally, Lorenz (1999) has discussed what could be learned about the atmospheres of the outer planets using acoustic properties. In the context of Titan, the *Huygens* probe was equipped with an instrument called the Acoustic Properties Investigation (API), belonging to the Surface Science Package, which consisted of two units: API-V (velocity of sound) and API-S (sounding) (Svedhem et al. 2004). Even if this instrument also had capabilities for performing analysis in the atmosphere, it was mainly aimed at liquid-phase investigations. Since *Huygens* landed in a dry region, no measurements were carried out in Titan's surface liquid. However, acoustic data collected during the descent allowed Hagermann et al. (2007) to derive constraints on the composition of the atmosphere.

Hagermann et al. (2005) carried out conceptual work of how the measurements, acquired by *Huygens*' instruments in a cryogenic liquid could give information regarding its composition. Among other physical quantities, they considered the speed of sound. Faced with a lack of published speed-of-sound measurements, particularly for the hydrocarbon mixtures, they used an equation of fit. They validated the latter by comparison with the results given by the equation of state (hereafter EoS) published by Peng & Robinson (1976). They

© 2016 The Author
Published by Oxford University Press on behalf of the Royal Astronomical Society

Downloaded from http://mnras.oxfordjournals.org/ at University of Otago on April 28, 2016

Retour à la table des matières : p. v

also employed data from the National Institute of Standards and Technology (NIST14). However, they did not give a full derivation of the computed speed of sound. In the context of depth sounding, Arvelo & Lorenz (2013) performed computations based on the speed of sound in cryogenic liquids. Their work also involves the NIST14 data base. Unfortunately, the obtained velocities exhibit discontinuities that are certainly not physical (see fig. 3 of Arvelo & Lorenz 2013). In addition, these authors assumed that their adopted linear fit can be extrapolated to temperatures higher than 92.5 K. For all these reasons, I decided to explore the question of the speed of sound in cryogenic liquids and to revisit its sensitivity to chemical composition. I have chosen to use the up-to-date, Helmholtz energy based theory, the perturbed-chain statistical associating fluid theory (PC-SAFT), which has successfully been used in countless works of chemical engineering, and introduced in Titan research field by Tan et al. (2013). On average, PC-SAFT is more accurate than all other EoS, and particularly Peng–Robinson cubic EoS (see, for instance, Diamantonis et al. 2013; Annesini, Gironi & Guerani 2014). Focusing on the speed-of-sound dependency with chemical composition, I describe the concept of a very simple instrument, similar to the API-V, but including an active temperature control of the probed liquid. In this paper, I emphasize the required accuracy and the necessary number of velocity of sound measurements, in a way that is as quantitative as possible. In addition, the exact derivation of the speed of sound from PC-SAFT quantities is presented in detail. The system is not thought to compete with an instrument that is as accurate as a mass spectrometer, but it would be very useful in the case of a failure of such a high-precision sensor. In Section 2, I discuss the principle of speed-of-sound measurements. Section 3 is devoted to the thermodynamical computations and model description. In Section 4, the inversion algorithm is described and the sensibility of results to experimental conditions is discussed. Final remarks and conclusions are made in Section 5.

2 PRINCIPLE OF THE MEASUREMENTS

If the bulk composition of Titan's lakes contains only three compounds, a characterization of the composition can be achieved if we know the mole fraction of nitrogen x_{N_2} and the ratio $r_{46} = x_{CH_4}/x_{C_2H_6}$, where x_{CH_4} and $x_{C_2H_6}$ are the mole fractions of methane and ethane, respectively. As shown, in principle, by Hagermann et al. (2005), an appropriate set of physical property measurements can be used as an indicator of the chemical composition of the considered liquids. Following this idea, the measurements of two independent values of the speed of sound u in a liquid could be used – at least formally – to determine the values of x_{N_2} and r_{46}. These measurements could be performed for two different temperatures, and a more extended set of measurements will bring stronger constraints on the composition. If u_1 and u_2 are the determined sound velocity at temperatures T_1 and T_2, respectively, one has to solve the following set of equations:

$$u(x_{N_2}, x_{CH_4}, x_{C_2H_6}, T_1) = u_1;$$
$$u(x_{N_2}, x_{CH_4}, x_{C_2H_6}, T_2) = u_2. \quad (1)$$

This assumes that the liquid mixture does not evaporate at a temperature in the range $[T_1, T_2]$. Moreover, the liquid has to be isolated from any vapour phase such as the local atmosphere. With more than two measurements, systems similar to equation (1), each corresponding to a couple $(T_i, T_j)_{i \neq j}$, can be resolved. The composition is then obtained by averaging the inferred mole fractions. In the framework of this approach, a law $u(x_i, T)$ has to be determined

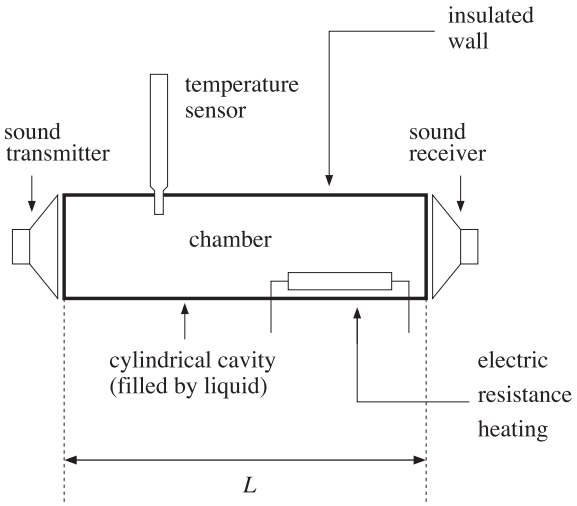

Figure 1. Sketch of the device that could be used to measure the speed of sound in the liquid of one of Titan's lakes. The temperature control of the liquid is ensured by means of temperature sensors and an electric heating system.

during the preparation of the space mission, by theoretical works and/or laboratory calibrations. One might conceive of a run of measurements in a passive mode (i.e. taking advantage of the natural variations of the surface temperature of the sea). Unfortunately, the expected amplitude of climatic temperature variations is of the order of a few kelvins by Titan's year (29.5 Earth years); these circumstances make these variations unusable for our purpose. Thus, an active system of temperature control is needed. A device inspired by the Kundt's tube (Kundt 1866) could be employed. Although it would be equipped by valves, such a system has the great advantage of a small number of mobile mechanical pieces. The Kundt's device is sketched in Fig. 1. Enclosing the tube (which can also be called a 'chamber of measurement'), an insulating wall prevents too high a heat flux towards the ambient liquid, and stabilizes the temperature when acoustic experiments are conducted. The probed liquid is heated by an electrical resistor, whereas a device and/or a dedicated procedure ensure the homogeneity of the temperature in the chamber. The measurement can be done by determining the time taken by an ultrasonic pulse to travel the length of the tube between the emitter and the receiver. This is the operating principle achieved by API-V *Huygens* or 'SOSO' (*TiME*). I emphasize that the tube could also be used in a way similar to what Kundt has done. Indeed, the tube is a cylindrical resonant cavity (of length L). The natural frequencies f_n of such a cavity obey the simple law given by

$$f_n = n \frac{u}{2L} \quad (2)$$

(see Feynman, Leighton & Sands 1963). For a fixed cavity length L, the determination of only two consecutive resonant frequencies gives the speed of sound: $u = 2L(f_{n+1} - f_n)$. The measurement of a travel time is then replaced by a detection of resonance frequencies. The larger the sample of acquired data is, the more precise the value of the speed u is. An electronic unit dedicated to frequency generation and a signal receiver processing are required to complete the system. In addition, the liquid heating could be easily done with the help of an electrical resistor, while temperature measurements would be monitored by means of thermocouples. The global

Downloaded from http://mnras.oxfordjournals.org/ at University of Otago on April 28, 2016

Retour à la table des matières : p. v

performances (e.g. number of measurements per unit of time) determine the actual accuracy achieved for the law $u(T)$.

In the next section, I discuss the precision needed for speed-of-sound determinations (or equivalently for frequencies) to obtain results useful for liquid composition. Concerning the range of temperature that would be used, I propose the interval from 90 to 100 K. Indeed, the ground temperature of Titan's polar regions has been estimated to be ∼90 K based on near-surface brightness temperature measurements (Jennings et al. 2009). In addition, methane has its boiling point at 111.2 K. It is surely technically easier to heat the liquid of a lake up to 100 K than to cool it down to 80 K, a temperature at which the fluid might solidify.

3 ESTIMATION OF THE SPEED OF SOUND IN A TERNARY MIXTURE OF NITROGEN, METHANE AND ETHANE

The speed of sound in a given substance is computed from its thermodynamic properties using the general equation (see, for instance, Diamantonis & Economou 2011)

$$u = \sqrt{\frac{C_P}{C_V}\left(\frac{\partial P}{\partial \rho}\right)_T} \tag{3}$$

where C_P and C_V are the isobaric and isochoric specific heat, respectively, P is the pressure, ρ is the density and T is the temperature. This equation can be easily derived from first principles and classical thermodynamics equations (e.g. Lobo & Ferreira 2006). The Helmholtz free energy is generally used in statistical thermodynamics to express EoS, as most properties of interest can be obtained by proper differentiation of this. With PC-SAFT, the total Helmholtz energy – denoted A – can be written as a sum

$$A = A^{(\mathrm{id})} + A^{(\mathrm{res})} \tag{4}$$

in which $A^{(\mathrm{id})}$ represents the Helmholtz energy of the corresponding ideal gas and and $A^{(\mathrm{res})}$ is the residual contribution that accounts for intermolecular interactions. In the PC-SAFT framework, molecules are conceived to be chains comprised of freely jointed spherical segments. Intersegment and intermolecular potentials are introduced and the theory provides the resulting Helmholtz energy of the macroscopic system. A reader who is interested in the nature of the terms included in $A^{(\mathrm{res})}$ is invited to consult the vast body of literature devoted to the basis of PC-SAFT. The foundations of this theory were originally published by Gross & Sadowski (2001). A good introduction to PC-SAFT can be found in Soo (2011). This theory has been extensively tested in the context of cryogenic liquids by Tan et al. (2013), and it has also been proved that it reproduces laboratory data, particularly isotherms and binary diagrams, with a very satisfying degree of accuracy. However, despite its great performances, PC-SAFT, similarly to the theories applied by Cordier et al. (2009) and Glein & Shock (2013), includes free parameters that have to be adjusted. However, theories belonging to the SAFT family have the advantage that they rely on a strong statistical physics basis. Moreover, I have checked that PC-SAFT reproduces the reference ternary mixture (N_2, CH_4, C_2H_6) of Gabis (1991) provided as supplementary data by Glein & Shock (2013).

In the framework of this EoS, each considered species is characterized by the three parameters of PC-SAFT: the segment diameter σ, the depth of the potential ϵ/k_B and the number of segments per chain m. The values of these parameters have all been given in Tan et al. (2013); Cordier et al. (2016). Beside this, the binary interaction parameters k_{ij} are also taken in this article. Equation (3) can be rewritten as

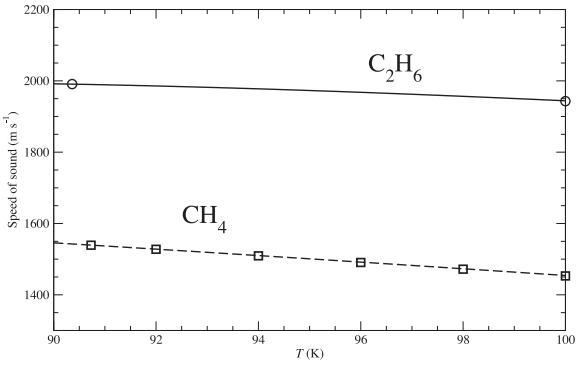

Figure 2. Comparison between experimental determination of the speed of sound (symbols) for CH_4 and C_2H_6 and the outputs of our model. Squares denote experimental data from Setzmann & Wagner (1991), and circles denote data taken from Younglove & Ely (1987).

$$u = \sqrt{\frac{C_P}{C_V}\frac{1}{k_T \rho}}, \tag{5}$$

where $k_T^{-1} = \rho(\partial P/\partial \rho)_T$. The density ρ and the derivative $(\partial P/\partial \rho)_T$ are provided by PC-SAFT, whereas the non-ideal isobaric heat capacity of the mixture C_P is derived using the relation

$$C_P - C_V = \frac{T\,\alpha^2}{k_T\,\rho}\,\bar{M}, \tag{6}$$

where $\alpha = k_T(\partial P/\partial T)_V$ is also computed with PC-SAFT. Here, $\bar{M}$ represents the average molar mass of the mixture. The isochoric heat capacity C_V is given by (see Diamantonis & Economou 2011, equation 19)

$$C_V = \underbrace{-T\left[\frac{\partial^2 A^{(\mathrm{id})}}{\partial T^2}\right]_V}_{=C_V^{(\mathrm{id})}} - T\left[\frac{\partial^2 A^{(\mathrm{res})}}{\partial T^2}\right]_V. \tag{7}$$

The term denoted $C_V^{(\mathrm{id})}$ is the isochoric heat capacity of the corresponding ideal gas. I made a series of tests to evaluate this term. Among them, I used the group-contribution method developed by Joback and Reid (Joback 1984; Joback & Reid 1987) and summarized in Poling, Prausnitz & O'Connell (2007). This approach consists of an approximate estimation of the requested thermodynamical quantities. Unfortunately, doing so did not yield speeds of sound in very good agreement with the tabulated experimental data. As a consequence, I found that adjusting the individual heat capacities $C_{P,i}^{(\mathrm{id})}$, by fitting the individual velocity of sound data, gives much better results. This isochoric $C_{V,i}^{(\mathrm{id})}$ is derived from $C_{P,i}^{(\mathrm{id})}$ thanks to Mayer's law; while C_V comes from equation (7), equation (6) provides C_P. A comparison between the model outputs and experimental data is presented in Fig. 2. The agreement for methane speed of sound (Setzmann & Wagner 1991) and also for ethane data (Younglove & Ely 1987) appears to be very good. I have also been able to reproduce the velocity of sound in liquid nitrogen at 77 K (859 m s^{-1}; Zuckerwar & Mazel 1985). In Fig. 3, the calculated speed of sound for temperatures between 90 and 100 K, is plotted for ranges of mole fractions that cover the plausible abundances of Titan's seas. As can be seen in Figs 3(a)

Downloaded from http://mnras.oxfordjournals.org/ at University of Otago on April 28, 2016

Retour à la table des matières : p. v

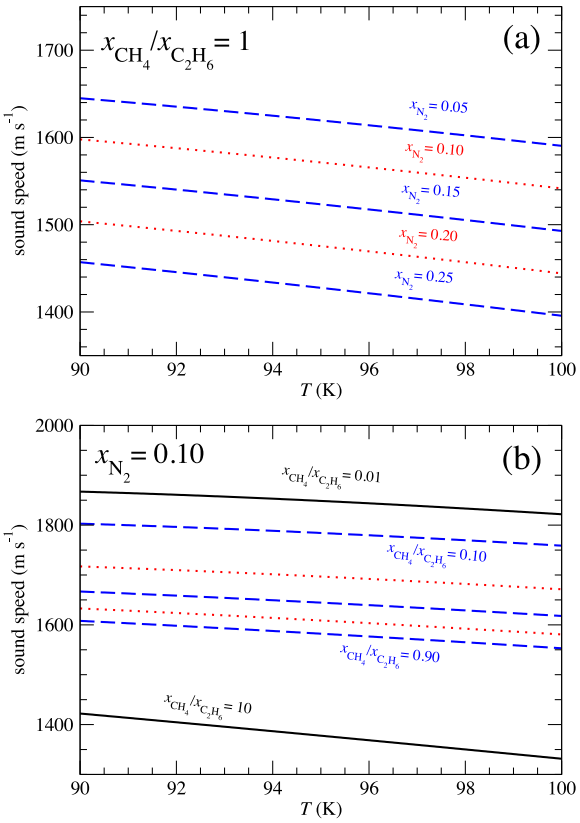

Figure 3. The calculated speed of sound as a function of temperature in the considered ternary mixture. (a) The ratio $r_{46} = x_{CH_4}/x_{C_2H_6}$ is fixed at 1 while the nitrogen mole fraction x_{N_2} takes the values 0.05, 0.10, 0.15, 0.20 and 0.25. (b) The mole fraction of nitrogen is set to 0.10 while the ratio $r_{46} = x_{CH_4}/x_{C_2H_6}$ takes the values 0.01, 0.10, 0.30, 0.50, 0.70, 0.90 and 10. For all calculations, the pressure has been fixed at 1.5 bar, which is the observed value on Titan's surface (Niemann et al. 2005).

and (b), u always decreases when T increases. It is noticeable that the amplitude of these variations, between the boundaries of the considered interval, is roughly ∼50–60 m s^{-1}. This implies an accuracy of measurements of a few per cent, if we want to capture the variations of u with temperature. The curves in Fig. 3 do not exhibit local extrema; this is a useful (and expected) feature from the perspective of data inversion. Finally, we can remark that, not surprisingly, the computed speed of sound becomes higher when the average molar mass increases.

4 DATA INVERSION

One major goal of this discussion is to assess the possibility of deriving chemical composition information from acoustic velocity. Thus, I have simulated a chemical composition extraction for a lake from artificial acoustic measurements. The samples were constructed using a finite number of sound velocities, computed with the model, for a list of N temperatures in the range of interest (i.e. 90–100 K). In general, an inverse problem, like the one we are facing here, can be treated in different ways (Aster, Borchers & Thurber 2012). In a first attempt, I have tried to minimize a likelihood function based on χ^2. However, a very bad convergence was observed. Instead, I built pre-computed tables of speeds of sound depending on three

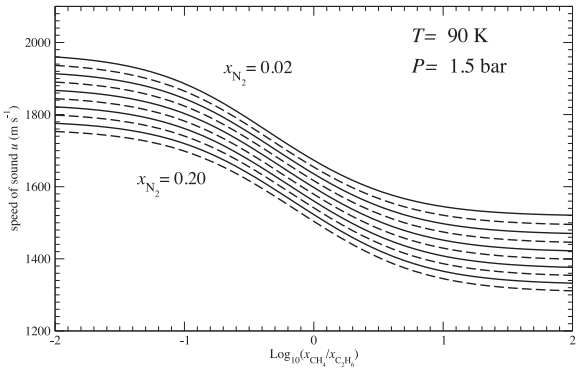

Figure 4. Tabulated speed of sound versus ratio $x_{CH_4}/x_{C_2H_6}$ at $T = 90$ K and $P = 1.5$ bar, for mole fraction of nitrogen $x_{N_2} = 2 \times 10^{-2}$, 4×10^{-2}, 6×10^{-2}, 8×10^{-2}, 1×10^{-1}, 1.2×10^{-1}, 1.4×10^{-1}, 1.6×10^{-1}, 1.8×10^{-1} and 2×10^{-1}.

parameters: the temperature T, the nitrogen mole fraction x_{N_2} and the ratio $r_{46} = x_{CH_4}/x_{C_2H_6}$. The data inversion is performed using the following algorithm.

(i) For each 'experimental' temperature T_i, the value of the ratio r_{46} is searched by solving the equation $u_{exp} = u_{Table}$, for each value of x_{N_2} implemented in the multidimensional table. In Fig. 4, I have displayed examples of curves giving u versus $\log_{10}(r_{46})$ for a temperature fixed at 90 K and a nitrogen mole fraction ranging from 0.02 to 0.20. This way, one builds a set of curves providing $x_{N_2}^{(T)}$ as a function of the ratio r_{46}.

(ii) In a second step, for each couple of temperature values $(T_i, T_j)_{i \neq j}$, the coordinates of the intersection point of the curves $x_{N_2}^{(T_i)}(r_{46})$ and $x_{N_2}^{(T_j)}(r_{46})$ are determined using a root-finding method. It should be noted that, in an ideal situation, all the curves have to intersect strictly at the same point $(r_{46}|_0, x_{N_2}|_0)$ characterizing the chemical composition of the studied liquid. In practice, this is not the case, due to numerical errors, and above all because of experimental uncertainties, the derived points are scattered around an average position. The barycentre of these points represents the observed chemical composition, while the scattering offers information on uncertainties associated with this derivation.

Here, the uncertainties were estimated by computing the difference between the 'true' composition used at the time of the look-up table construction, and the abundances inferred with our inversion algorithm. It is valuable to estimate the sensitivity of the results (i.e. derived values of the composition of the liquid) to the uncertainties on the measured speed of sound. In order to mimic the instrumental errors, I added a random signal to velocity values, originally computed with the thermodynamical model. Subsequently, the analysis of these surrogate samples is done by the use of the algorithm described above. Thus, I applied artificial speed errors Δu_i uniformly distributed between $-\Delta u_{max}$ and $+\Delta u_{max}$, where Δu_{max} is an arbitrary chosen value, representing the maximum error allowed in the numerical test. As already noticed in Section 3, the accuracy of the speed of sound in the considered liquid must be much lower than ∼50–60 m s^{-1} for a typical value of speed around 1500 m s^{-1}. Then the required instrumental precision should be a priori better than ∼50 m s^{-1}. In Fig. 5, we have reported the results of two simulations: the first based on a set of $N = 10$ values of temperature uniformly distributed between 90 and 100 K, and the second consisting of $N = 50$ values. In this figure, the errors on nitrogen

Downloaded from http://mnras.oxfordjournals.org/ at University of Otago on April 28, 2016

Retour à la table des matières : p. v

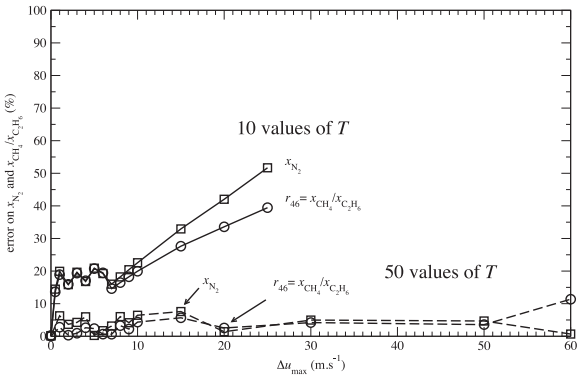

Figure 5. Results of simulations of experimental data inversion. Two sets of experimental data have been analysed: the first set contains speeds of sound for 10 values of temperature uniformly distributed between 90 and 100 K, and the second set consists of 50 values. In order to mimic instrumental errors on speed-of-sound measurements, a random signal has been added to the data, originally computed using my PC-SAFT-based thermodynamic model. This signal consists of randomly chosen speed-of-sound contributions uniformly distributed between $-\Delta u_{max}$ and $+\Delta u_{max}$, where Δu_{max} is the maximum measurement error allowed in the simulation. This plot represents the error on chemical composition determination as a function of Δu_{max}.

mole fraction and errors on the ratio $r_{46} = x_{CH_4}/x_{C_2H_6}$ were plotted as functions of the value of the maximum error Δu_{max}. Both simulations were carried out using an initial true chemical composition corresponding to $x_{N_2} = 0.10$ and $x_{CH_4}/x_{C_2H_6} = 0.50$. As we can see, for $N = 10$ the errors are relatively stable around ∼20 per cent for Δu_{max} up to ∼10 m s^{-1}; beyond this value, the errors increase regularly, and finally the algorithm no longer converges properly for $\Delta u_{max} \sim 25$ m s^{-1}. This numerical experiment corresponds to a temperature control at a 1-K level, which appears feasible. As a corollary, in that case, the speed-of-sound measurements have to be done with an absolute accuracy better than 10 m s^{-1}, which corresponds to a relative precision better than 10^{-2}. In Fig. 5, the $N = 50$ numerical experiment shows clearly that, for a given Δu_{max}, the increase of the number of measurements yields to an appreciable improvement in the chemical composition determination. In addition, the results of the inversion remain acceptable (errors remain below ∼10 per cent) up to $\Delta u_{max} \sim 60$ m s^{-1}. Nonetheless, the number of measurements of $N = 50$ requires a temperature control of the liquid at the level of ∼0.2 K, which is more difficult to achieve than a ∼1-K level. This gives an idea of the precision needed on the temperature control. The dependency on N is anticipated as the final step of the inversion algorithm consists of an average. During the design stage of the instrument, a compromise will have to be found between temperature control and the accuracy of speed-of-sound determinations.

I have also checked that the errors on temperature have a negligible influence. For instance, in the case of a sample of 10 measurements between 90 and 100 K, randomly distributed errors on T with a maximum of ±0.2 K lead to errors on speed of sound below 0.8 m s^{-1} while a maximum error of ±0.5 K produces speed uncertainties no larger than 2 m s^{-1}, a value well below the Δu_{max} values considered above. This demonstrates that, if the temperature accuracy required by a number of independent measurements can be guaranteed (e.g. better than 1 K for 10 measurements between 90 and 100 K), then the effects of the inaccuracies in the temperature measurements on the results are negligible compared to the uncertainties in the speed-of-sound measurements.

Finally, photochemical models of Titan's atmosphere show that propane could be produced (Lavvas, Coustenis & Vardavas 2008a,b). Thus, I introduced some amount of propane in the case where Δu_{max} is fixed at 30 m s^{-1}. The chemical composition of the experimental sample (e.g. $x_{CH_4} = 0.30$, $x_{N_2} = 0.10$ and $x_{C_2H_6} = 0.60$) is replaced by $x_{CH_4} = 0.30$, $x_{N_2} = 0.10$, $x_{C_2H_6} = 0.55$ and $x_{C_3H_8} = 0.05$. These data are then used in the algorithm, which assumes a sample composed only by the ternary mixture (CH_4, N_2, C_2H_6). I found that, even with such a small amount of propane, the derived abundances of N_2 and the ratio r_{46} are substantially affected: the error on x_{N_2} is around 20 per cent (instead of ∼5 per cent without C_3H_8) while r_{46} presents an error of about 100 per cent. This numerical test emphasizes the sensibility of the velocity of sound to composition. Obviously, to overcome this issue, the best solution is to introduce the measurement of another independent physical quantity.

5 CONCLUSIONS

In this work, I have shown that the use of a realistic model, based on PC-SAFT, prevents the appearance of unphysical situations, such as a speed-of-sound discontinuity, already noticed in previous published papers (Hagermann et al. 2005; Arvelo & Lorenz 2013). However, even such sophisticated models need to be constrained by empirical data. Consequently, new laboratory measurements of sound speeds would be greatly useful, particularly in the case of mixtures. The simultaneous measurements of refractive index, density, thermal conductivity, electromagnetic permittivity and speed of sound required by the method of Hagermann et al. is not easy to achieve and requires a complex set of sensors.

Alternatively, the dynamic method proposed here, whereby the speed of sound is measured at different temperatures, provides a better composition estimation with an accuracy comparable to that of the measured physical quantities (i.e. a few per cent), here the speed of sound. Indeed, with only 50 temperature measurements, I have shown that the errors in derived composition remain below 10 per cent. I have also emphasized that the method employed by Hagermann et al. (2005) implicitly assumes the existence of a device implementing a temperature control by heating, as they need thermal conductivity determinations. This fact suggest that the two approaches could be combined in a future mission concept.

ACKNOWLEDGEMENTS

I acknowledge Dr Ralph Lorenz for scientific discussions. I thank the anonymous reviewer for remarks and comments that have improved the clarity of the paper. I also warmly thank my colleague Panayotis Lavvas for reading and improving my text.

REFERENCES

Annesini M. C., Gironi F., Guerani W., 2014, Chemical Engineering Transactions, 38, 67
Arvelo J., Lorenz R. D., 2013, J. Acoust. Soc. Am., 134, 4335
Aster R. C., Borchers B., Thurber C. H., 2012, Parameter Estimation and Inverse Problems, 2nd edn. Elsevier, Amsterdam
Brown R. H. et al., 2008, Nature, 454, 607
Cordier D., Mousis O., Lunine J. I., Lavvas P., Vuitton V., 2009, ApJ, 707, L128
Cordier D., Mousis O., Lunine J. I., Lavvas P., Vuitton V., 2013, ApJ, 768, L23

Downloaded from http://mnras.oxfordjournals.org/ at University of Otago on April 28, 2016

Retour à la table des matières : p. v

Cordier D., Cornet T., Barnes J. W., MacKenzie S. M., Le Bahers T., Nna-Mvondo D., Rannou P., Ferreira A. G., 2016, Icarus, 270, 41
Diamantonis N. I., Economou I. G., 2011, Energy & Fuels, 25, 3334
Diamantonis N. I., Boulougouris G. C., Mansoor E., Tsangaris D. M., Economou I. G., 2013, Ind. Eng. Chem. Res., 52, 3933–3942
Feynman R., Leighton R. B., Sands M. L., 1963, The Feynman Lectures on Physics. Addison-Wesley, Reading, MA
Gabis D. H., 1991, PhD thesis, Cornell Univ
Glein C. R., Shock E. L., 2013, Geochim. Cosmochim. Acta, 115, 217
Gross J., Sadowski G., 2001, Ind. Eng. Chem. Res., 40, 1244
Hagermann A., Zarnecki J. C., Towner M. C., Rosenberg P. D., Lorenz R. D., Leese M. R., Hathi B., Ball A. J., 2005, MNRAS, 359, 637
Hagermann A. et al., 2007, Icarus, 189, 538
Hofgartner J. D. et al., 2014, Nature Geoscience, 7, 493
Jennings D. E. et al., 2009, ApJ, 691, L103
Joback K. G., 1984, PhD thesis, Massachusetts Institute of Technology
Joback K. G., Reid R. C., 1987, Chem. Eng. Comm., 57, 233
Ksanfomaliti L. V., Goroshkova N. V., Naraeva M. K., Suvorov A. P., Khondryev V. K., Yabrova L. V., 1982, Sov. Astron. Lett., 8, 227
Ksanfomaliti L. V., Goroshkova N. V., Khondryev V. K., 1986, Wind velocity near the surface of Venus from acoustic measurements, Technical report
Kundt A., 1866, Annalen der Physik, 127, 497
Lavvas P. P., Coustenis A., Vardavas I. M., 2008a, Planet. Space Sci., 56, 27
Lavvas P. P., Coustenis A., Vardavas I. M., 2008b, Planet. Space Sci., 56, 67
Lobo L. Q., Ferreira A. G., 2006, Termodinâmica e propriedades termofísicas – Volume 1. Imprensa da Universidade de Coimbra
Lorenz R. D., 1999, Planet. Space Sci., 47, 67
Lorenz R. D. et al., 2015, in 46th Lunar and Planetary Science Conference, LPI Contribution No. 1832. Lunar and Planetary Institute, Houston, TX, p. 1259
Lunine J. I., 2010, Faraday Discussions, 147, 405
McKay C. P., Smith H. D., 2005, Icarus, 178, 274
Niemann H. B. et al., 2005, Nature, 438, 779
Peng D. Y., Robinson D. B., 1976, Ind. Eng. Chem. Fundam., 15, 59
Poling B. E., Prausnitz J. M., O'Connell J., 2007, The Properties of Gases and Liquids, 5th edn. McGraw-Hill Professional, Englewood Cliffs, NJ
Schulze-Makuch D., Grinspoon D. H., 2005, Astrobiology, 5, 560
Setzmann U., Wagner W., 1991, J. Phys. Chem. Ref. Data, 20, 1062
Soo C.-B., 2011, PhD thesis, MINES ParisTech
Stofan E. R. et al., 2011, in EPSC-DPS Joint Meeting 2011. p. 909
Svedhem H., Lebreton J.-P., Zarnecki J., Hathi B., 2004, in Wilson A., ed., ESA Special Publication Vol. 544, Planetary Probe Atmospheric Entry and Descent Trajectory Analysis and Science. ESA Publications Division, Noordwijk, p. 221
Tan S. P., Kargel J. S., Marion G. M., 2013, Icarus, 222, 53
Younglove B. A., Ely J. F., 1987, J. Phys. Chem. Ref. Data, 16, 577
Zebker H., Hayes A., Janssen M., Le Gall A., Lorenz R., Wye L., 2014, Geophys. Res. Lett., 41, 308
Zuckerwar A. J., Mazel D. S., 1985, NASA Technical Paper 2464

This paper has been typeset from a TEX/LATEX file prepared by the author.

Downloaded from http://mnras.oxfordjournals.org/ at University of Otago on April 28, 2016

Retour à la table des matières : p. v

4.11 Article sur l'apparition de bulles de N_2 dans au fond des lacs

nature astronomy

ARTICLES

PUBLISHED: 10 APRIL 2017 | VOLUME: 1 | ARTICLE NUMBER: 0102

Bubble streams in Titan's seas as a product of liquid $N_2 + CH_4 + C_2H_6$ cryogenic mixture

Daniel Cordier[1]*, Fernando García-Sánchez[2], Daimler N. Justo-García[3] and Gérard Liger-Belair[1]

Titan, Saturn's largest moon, is the only extraterrestrial body known to support stable liquid on its surface, in the form of seas and lakes that dot the polar regions. Many indications suggest that the liquid should be composed of a mixture of nitrogen, methane and ethane. Recent observations by Cassini's Radio Detection and Ranging (RADAR) instrument of Titan's large sea, called Ligeia Mare, have shown unexplained and ephemeral bright features, possibly due to rising bubbles. Here we report that our numerical model, when combined with experimental data found in the literature, shows that Ligeia Mare's bed is a favourable place for nitrogen exsolution. This process could produce centimetre-sized and RADAR-detectable bubbles.

Titan, the main satellite of the giant planet Saturn, is the only moon in the Solar System that has a dense atmosphere. Among many unique features, this gaseous envelope, mainly composed of nitrogen and methane, harbours a 'hydrological' cycle of methane. In addition, the complex photochemistry of its atmosphere produces a wide variety of organic species, with ethane being its main product in terms of quantity[1,2]. The Radio Detection and Ranging (RADAR) instrument, onboard the Cassini spacecraft, allowed the discovery of dark features partially covering Titan's polar regions. Long suspected to be there[3,4], they are interpreted as seas or lakes of liquid hydrocarbons[5]. Although their exact chemical composition is not known, the lower atmosphere contains around 5% of CH_4 and 95% of N_2. Together with C_2H_6, produced by photochemistry, these species should be the main components of Titan's seas[6–8]. Titan's maritime environments exhibit an absence of ocean waves[9], but strange transient RADAR over-brightness events have been reported in two places at the surface of the northern sea, Ligeia Mare. To explain these episodes, the formation of gas bubbles has been proposed together with potential suspended or floating solids[10,11]. In this work, we focus on thermodynamic instabilities that can lead to exsolution of N_2, and consequently feed streams of bubbles, which can explain the events observed by RADAR.

Liquid–liquid–vapour equilibria for hydrocarbon mixtures

The most straightforward equilibrium between phases of a N_2+CH_4+C_2H_6 ternary system is a liquid–vapour equilibrium (LVE). However, liquid–liquid–vapour equilibria (LLVE) do occur under certain conditions in ternary and liquefied natural gas systems, including liquid phase inversion[12]. LLVE consist in the coexistence of two liquids, of different compositions, with a vapour. In the laboratory, LLVEs have been observed under cryogenic conditions for systems comparable to Titan's liquid phases: nitrogen + methane + (ethane, propane or *n*-butane)[12–16].

At the Huygens landsite, in Titan's tropical regions, the temperature[17] was 93.65 ± 0.25 K. Using the Composite Infrared Spectrometer instrument aboard Cassini, Titan's atmospheric temperature has been retrieved as a function of latitude, for the lowest 1 km. The average temperature of the northern polar region, during mid-northern spring, has been found[18] to be around 91 K. However, the question of the specific temperature at the surface of Ligeia Mare remains open, as the thermal properties of the liquid could differ from those of the surrounding land. Moreover, the behaviour of temperature with depth is not well constrained. Most estimations rely only on numerical simulations that depend on many parameters, such as the light extinction coefficient of the sea[19,20]. Nevertheless, all models agree with a temperature cooling of a few degrees between the surface and the sea bottom[20,21]. We therefore adopted a characteristic range of Ligeia Mare temperatures from 80 to 90 K.

Titan's ground pressure, measured *in situ* by the Huygens probe, is close to $P_0 = 1.5$ bar and should not vary significantly over the satellite surface[17]. As the maximum depths of Ligeia Mare have been determined[19,22,23] to be between ~100 m and ~200 m, we estimated the pressure at these depths. As a first approximation, liquids can be considered as incompressible. In that case, the pressure P at a given depth z within a Titan's sea follows the law

$$P = P_0 + \overline{\rho}\, g_{\mathrm{Titan}}\, z \qquad (1)$$

where $\overline{\rho}$ represents the mean density of the liquid between the considered depth and the surface, and g_{Titan} denotes the gravity. Values for the density of liquid CH_4, C_2H_6 or N_2 can be found in the literature[24,25]: for instance, at 1 bar, $\rho_{CH_4} = 451.8\,\mathrm{kg\,m^{-3}}$, $\rho_{C_2H_6} = 651.6\,\mathrm{kg\,m^{-3}}$ and $\rho_{N_2} \approx 800\,\mathrm{kg\,m^{-3}}$. We checked that these values are only weakly dependent on pressure: for example, at 10 bar, $\rho_{CH_4} = 452.1\,\mathrm{kg\,m^{-3}}$ and $\rho_{C_2H_6} = 651.8\,\mathrm{kg\,m^{-3}}$. Using these numbers at 10 bar, we found $P_{100} \approx 2.1$ bar at 100 m (and $P_{200} = 2.7$ bar at 200 m) for pure methane layers. For layers composed exclusively of ethane, the pressure at 100 m reaches $P_{100} = 2.4$ bar ($P_{200} = 3.3$ bar). Owing to the higher density of N_2 ($870\,\mathrm{kg\,m^{-3}}$ at its triple point $T_t = 63$ K, probably $\sim 800\,\mathrm{kg\,m^{-3}}$ at ~90 K), adding some nitrogen would increase the mean density of the mixture and thus the pressure at 100 or 200 m. If we focus on the heaviest hydrocarbon under consideration, ethane, and if we assume a nitrogen mean abundance of 40% (in mole fraction), which represents a very high solubility of N_2, we found $P_{100} = 2.5$ bar and $P_{200} = 3.5$ bar. In addition to these estimations, we developed a more sophisticated model based on the law of hydrostatics and the equation of state (EoS) PC-SAFT[7,26]

[1]Groupe de Spectrométrie Moléculaire et Atmosphérique — UMR CNRS 7331 Campus Moulin de la Housse — BP 1039, Université de Reims Champagne-Ardenne 51687 Reims, France. [2]Engineering Management of Additional Recovery, Mexican Petroleum Institute, Eje Central Lázaro Cárdenas Norte 152, 07730 Mexico City, Mexico. [3]Department of Chemical and Petroleum Engineering, ESIQIE, National Polytechnic Institute. Unidad Profesional Adolfo López Mateos, 07738 Mexico City, Mexico. *e-mail: daniel.cordier@univ-reims.fr

© 2017 Macmillan Publishers Limited, part of Springer Nature. All rights reserved.

(see Methods). In this way, the compressibility of the fluid was taken into account. We also investigated the influence of temperature in the range 80–90 K. With this model, we arrived at the same conclusion: the pressure at 100–200 m should be in the range 2–3.5 bar.

Stability analysis of the ternary system $N_2 + CH_4 + C_2H_6$

The most relevant laboratory experiments[14] on LLVEs were acquired at 94.3 K under a pressure between 4.2 and 4.55 bar. These conditions are inconsistent with Ligeia Mare's expected bathymetry and temperature profile. We therefore investigated the stability of the $N_2 + CH_4 + C_2H_6$ system at a lower pressure and cooler temperature. To do so, we used a numerical method of phase stability analysis that was originally introduced for the gas and oil industry.

First, we investigated whether the lake's surface could be the location of phase-splitting events: that is, the appearance of two liquids of distinct compositions, in equilibrium with the atmosphere. For a temperature and pressure appropriate for Titan's surface (90 K and 1.5 bar), we found that on varying the mole fraction of nitrogen, the binary system $N_2 + CH_4$ does not undergo any demixing; it remains either in vapour or in a vapour–liquid equilibrium. The same results were obtained for $N_2 + C_2H_6$. For the ternary mixture $N_2 + CH_4 + C_2H_6$, we followed two distinct scenarios, to maximize the range of parameter space explored: (1) we fixed the N_2 abundance of the entire system (that is, including the vapour and the liquid(s)) and only varied the abundances of CH_4 from 0.05 to 0.001 (with ethane making up the remainder) in mole fraction; and (2) we fixed the overall composition of CH_4 and gradually changed the mole fraction of N_2 from 0.95 to 0.90. All cases resulted in a simple liquid–vapour equilibrium. The vapour, representing Titan's atmosphere, was always strongly dominated by nitrogen. In the light of these results, we can safely conclude that, under the expected polar ground conditions, Titan's sea surface is thermodynamically stable and should not split into two liquids.

Next, we searched for LLVE conditions relevant to environments below the sea surface (pressure up to ~3.5 bar and temperature possibly down to ~80–85 K). Our results are summarized in Fig. 1. For all three temperatures considered, we found LLVE. In all cases, these three-phase equilibria consist of two liquids in coexistence with a vapour phase composed almost exclusively of nitrogen (open squares in Fig. 1). The existence of this almost pure nitrogen vapour requires the exsolution of some of the nitrogen contained in the liquid before the occurrence of the LLVE. One liquid is a nitrogen-rich phase (filled squares in Fig. 1); the other is enriched in ethane (open circles in Fig. 1). We have also evaluated the densities of the phases involved in our study. A set of values corresponding to a specific LLVE is presented in the inset to Fig. 1. The higher density of the nitrogen-rich liquid is a trend confirmed for all the LLVEs that we found. Low temperature and high pressure both favour the occurrence of phase splitting that results in a LLVE. At $T = 90$ K, the temperature at the surface of the sea or slightly below, a LLVE appears at pressures as low as ~2.7 bar. These conditions allow LLVEs to occur at depths between 130 and 170 m, compatible with Ligeia Mare's bathymetry. Clearly, the temperatures lower than 90 K, caused for instance by infrared absorption in layers near the surface, would favour phase splitting at much shallower depths in the range 20–30 m (Fig. 1a,b). The temperature strongly influences the depth required to obtain a pressure high enough to reach conditions for exsolution.

Implications for Titan

A sea with a homogeneous composition that matches that required for the occurrence of a LLVE at a specific depth is an improbable scenario. In addition, such a case would imply nitrogen degassing through the whole extent of the system. Instead, we propose a scenario in which the sea is vertically stratified with ethane-enriched bottom layers and methane-rich upper layers, the latter

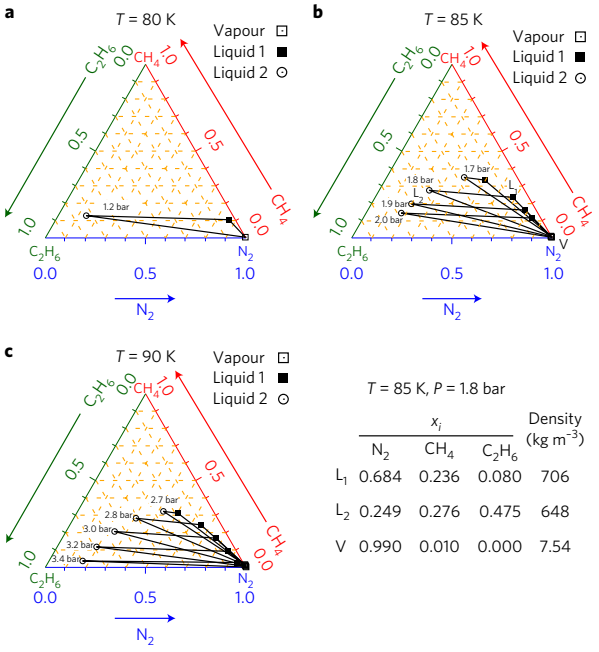

Figure 1 | The behaviour of a ternary mixture, $N_2 + CH_4 + C_2H_6$, at three temperature values relevant to the subsurface environment of Titan's sea. **a**–**c**, Assumed temperatures are $T = 80$ K (**a**), $T = 85$ K (**b**) and $T = 90$ K (**c**). Each set of circles, filled squares and open squares represents a liquid–liquid–vapour equilibrium (LLVE) for a given pressure. While the LLVE shown in **a** at $T = 80$ K demonstrates that, at low enough temperatures, LLVE can be produced at pressures even lower than the surface pressure, panels **b** and **c** provide estimates of the lowest pressures at which LLVE occur at $T = 85$ K and $T = 90$ K, respectively ~1.7 bar and ~2.7 bar. The table provides composition (in terms of mole fraction x_i) and densities of fluids involved in the LLVE corresponding to $T = 85$ K and $P = 1.8$ bar (see panel **b**). Tabulated results for the other ternary diagrams can be found in Supplementary Tables 1–3. L_1, liquid 1; L_2, liquid 2; V, vapour.

containing more dissolved nitrogen. This is supported by the higher density of ethane-rich mixtures and the larger solubility of nitrogen in methane than in ethane[7]. In addition, surface layers are in contact with the nitrogen-rich atmosphere, a situation that favours the dissolution of nitrogen. In addition, given Ligeia Mare's surface area of several thousand square kilometres, local episodes of evaporation and precipitation of methane can lead to a horizontal gradient of compound abundances[20]. Three-dimensional modelling of ocean circulation with a modified version of the Bergen Ocean Model suggests the existence of maritime streams produced by tides or wind, or generated by solar heating[20,27]. We propose that the vertical sea circulation feeds the lowest sea layers locally with methane- and nitrogen-enriched liquid. Depending on how exactly the composition has been altered at the surface (by local rain, evaporation or nitrogen dissolution), this downward flow can meet the deep ethane-rich layers, thus fulfilling the composition, pressure and temperature required for the occurrence of a LLVE.

Our thermodynamical modelling informs us only about which equilibria are possible under given conditions, and is unable to predict either the amounts of matter involved or the kinetics of the described process. Nevertheless, in our scenario, circumstances favourable to LLVE are ephemeral: the composition of liquid sinking from the surface has a composition that varies with time, first

© 2017 Macmillan Publishers Limited, part of Springer Nature. All rights reserved.

Retour à la table des matières : p. v

because of weather over the sea, and second because of mixing during downward flow.

Once the phase-splitting begins, at a specific depth, droplets of the denser (nitrogen-rich) liquid tend to sink while the lighter (ethane-rich) ones rise toward the surface. Of course, this phase-separation process naturally tends to stop the formation of a LLVE, by the exhaustion of one or several required constituents. Both kinds of droplets mentioned should redissolve into the ambient liquid during their descent or ascent, because the pressure and temperature move away from those required for a LLVE. It is worth noting that buoyancy-driven bubbles of almost pure N_2 rapidly rise through the upper nitrogen-rich layers to the surface, and for this reason probably do not redissolve into surrounding liquid. This scenario matches the Ligeia Mare observations of RADAR over-brightness events. It is also striking that the locations of the Transient Features Ligeia 1 (TFL1) and TFL2[11], superimposed on the depth map[23], indicate places at the boundaries of sea areas deeper than ~100 m. Moreover, bubbles are probably not observed at the surface directly above their formation site, owing to their own stochastic movement and to sea circulation. The break-up diameter of buoyancy-driven gas bubbles, which has to be understood as a maximum diameter, can be estimated as

$$d_{\mathrm{breakup}} \approx 8\sqrt{\frac{\gamma}{g_{\mathrm{Titan}}\Delta\rho}} \qquad (2)$$

where γ is the surface tension of the liquid, g_{Titan} stands for the Titan's surface gravity, and $\Delta\rho = \rho_{\mathrm{liq}} - \rho_{\mathrm{gas}}$, with ρ_{liq} and ρ_{gas} being, respectively, the density of the surrounding liquid and the gas contained in the bubbles[28]. Using surface tensions from the Dortmund Data Bank (http://www.ddbst.com), and for a 0.4:0.4:0.2 mixture of CH_4, C_2H_6 and N_2, a composition that could be typical of the upper layers of liquid, $\gamma_{\mathrm{mix}} \approx 2\times10^{-2}\,\mathrm{N\,m^{-1}}$ at 90 K; $\Delta\rho$ is estimated at a few bars for the same mixture, thanks to PC-SAFT. This yields $d_{\mathrm{breakup}} \approx 4.6$ cm, approximately twice the RADAR wavelength (2.2 cm). It should be noted that a composition based only on CH_4 and N_2 in the ratio 1:1, which is probably an extreme situation, also leads to a d_{breakup} of a few centimetres. Such large bubbles can magnify the Cassini RADAR backscattering, allowing easy detection, as is suspected to occur for pebbles in dry river beds[29] or evaporites[30] on Titan. In comparison, predicted sea current speeds (a few cm s^{-1}) can lift only sediment particles well below 1 cm in size[20], which would not be detectable with the Cassini RADAR.

At its specific site of occurrence, the LLVE demixing should perturb the local circulation of fluids. The densest liquid will sink below the lightest, while vapour rises to the surfaces. This phase separation also tends to stop the process, as it changes the local composition. Unfortunately, our approach cannot determine the amount of matter involved in the different phases, so we cannot quantify the influence on circulation and the magnitude of degassing.

We have focused on Ligeia because the 'Magic Islands' (the nicknames for TFL1 and TFL2) were observed in this sea. But our argument can be applied to other seas such as Kraken and Punga. However, the existence of depths between 100 and 200 m is a crucial point. We can reasonably expect that such depths exist under the surface of Kraken, but for Punga this is much more questionable: the bathymetry is not yet available, and Punga could be substantially shallower than Ligeia and Kraken, as suggested by its smaller size. As nitrogen exsolution in the deepest parts of Titan's seas could represent a potential hazard for *in situ* exploration[31,32], future laboratory experiments, specifically designed to study these ternary equilibria, would be useful. As a priority, the existence of LLVEs found in past experiments must be confirmed by modern measurements[33,34]. These investigations could then easily be extended to pressures of a few bars higher than Titan's surface pressure, and to temperatures a few degrees below ~90 K. In this way, our numerical stability analysis could be reinforced. Concerning the sea circulation, 3D models including a full treatment of the chemical composition, with the possibility of LLVEs, would be welcome. But, as the data used as inputs to such models, and especially the topography of the sea beds, are still poorly known, the last word will come from a submarine exploration of Titan.

Methods

To evaluate the pressure at the bottom of Titan's seas, we used the well-known equation

$$\frac{\partial P}{\partial z} = -\rho g_{\mathrm{Titan}} \qquad (3)$$

where z is the depth, ρ the density and g_{Titan} the gravity at the ground surface of Titan. The density depends on the pressure P, the temperature T and the mole fractions of the species N_2, CH_4 and C_2H_6 being considered. The PC-SAFT EoS[26], widely used in the chemical engineering community, was used to determine the density ρ. In the PC-SAFT EoS, the molecules are conceived to be chains composed of spherical segments, in which the pair potential for the segment of a chain is given by a modified square-well potential[35]. Non-associating molecules are characterized by three pure-component parameters: the temperature-independent segment diameter σ, the potential depth ε/k_B, and the number of segments per chain m. The PC-SAFT EoS, expressed in terms of the Helmholtz energy for a multicomponent mixture of non-associating chains, consists of a hard-chain reference contribution and a perturbation contribution to account for the attractive interactions. The three pure-component parameters of N_2, CH_4 and C_2H_6 were taken from the literature[26]. For mixtures, the PC-SAFT EoS uses classical van der Waals one-fluid mixing rules for the perturbation term. In these mixing rules, the parameters for a pair of unlike segments are obtained through conventional Lorentz–Betherlot combining rules, where one binary interaction parameter k_{ij} is introduced to correct the segment–segment interactions of unlike chains. The binary interaction parameters used in all the phase equilibrium calculations for the PC-SAFT EoS are: 0.0307 for $N_2 + CH_4$, 0.0458 for $N_2 + C_2H_6$ and −0.0058 for $CH_4 + C_2H_6$, and these were also taken from the literature[36,37].

For the stability analysis, the technique used relies on the above-mentioned PC-SAFT EoS and uses an efficient computational procedure for solving the isothermal multiphase problem. Initially, the system is assumed to be monophasic. A stability test allows us to check whether the system is stable. If stability is reached, the procedure is stopped. If not, it provides an estimation of the composition of an additional phase to take into account for the equilibrium calculation. The number of phases is then increased by one, and equilibrium is reached by minimizing the Gibbs energy. The procedure is continued until a stable solution is found[13]. This approach has been validated by comparison with many laboratory measurements involving ternary mixtures. For instance, very good agreement is found with mixtures of liquid methane and nitrogen with *n*-pentane, *n*-hexane or *n*-heptane at various temperatures[38]. In addition, in the specific context of this work, we have paid great attention to the reproduction of laboratory data[14] for the system $N_2 + CH_4 + C_2H_6$ at 94.3 K and ~4 bar.

Data availability. The data that support the plots within this paper and other findings of this study are available from the corresponding author upon reasonable request.

Received 15 October 2016; accepted 7 March 2017; published 10 April 2017

References

1. Yung, Y. L., Allen, M. & Pinto, J. P. Photochemistry of the atmosphere of Titan. Comparison between model and observations. *Astrophys. J. Suppl. Ser.* **55,** 465–506 (1984).
2. Krasnopolsky, V. A. A photochemical model of Titan's atmosphere and ionosphere. *Icarus* **201,** 226–256 (2009).
3. Flasar, F. M. Oceans on Titan? *Science* **221,** 55–57 (1983).
4. Lunine, J. I., Stevenson, D. J. & Yung, Y. L. Ethane ocean on Titan. *Science* **222,** 1229–1230 (1983).
5. Stofan, E. R. *et al.* The lakes of Titan. *Nature* **445,** 61–64 (2007).
6. Cordier, D., Mousis, O., Lunine, J. I., Lavvas, P. & Vuitton, V. An estimate of the chemical composition of Titan's lakes. *Astrophys. J. Lett.* **707,** L128–L131 (2009).
7. Tan, S. P., Kargel, J. S. & Marion, G. M. Titan's atmosphere and surface liquid: new calculation using statistical associating fluid theory. *Icarus* **222,** 53–72 (2013).
8. Brown, R. H. *et al.* The identification of liquid ethane in Titan's Ontario Lacus. *Nature* **454,** 607–610 (2008).
9. Zebker, H. *et al.* Surface of Ligeia Mare, Titan, from Cassini altimeter and radiometer analysis. *Geophys. Res. Lett.* **41,** 308–313 (2014).

© 2017 Macmillan Publishers Limited, part of Springer Nature. All rights reserved.

Retour à la table des matières : p. v

10. Hofgartner, J. D. *et al.* Transient features in a Titan sea. *Nat. Geosci.* **7,** 493–496 (2014).
11. Hofgartner, J. D. *et al.* Titan's 'Magic Islands': transient features in a hydrocarbon sea. *Icarus* **271,** 338–349 (2016).
12. Lu, B. C. Y., Yu, P. & Poon, D. P. L. Liquid phase inversion. *Nature* **225,** 1128–1129 (1970).
13. Ramírez-Jiménez, E., Justo-García, D. N., García-Sánchez, F. & Stateva, R. P. VLL equilibria and critical end points calculation of nitrogen-containing LNG systems: application of SRK and PC-SAFT equations of state. *Ind. Eng. Chem. Res.* **51,** 9409–9418 (2012).
14. Yu, P. *A Study of Liquid–Liquid–Vapor Equilibria at Low Temperatures.* PhD thesis, Univ. Ottawa (1972).
15. Merrill, R. C., Luks, K. D. & Kohn, J. P. Three-phase liquid–liquid–vapor equilibria in the methane + *n*-butane + nitrogen system. *Adv. Cryog. Eng.* **29,** 949–955 (1984).
16. Llave, F. M., Luks, K. D. & Kohn, J. P. Three-phase liquid–liquid–vapor equilibria in the nitrogen + methane + ethane and nitrogen + propane systems. *J. Chem. Eng. Data* **32,** 14–17 (1987).
17. Fulchignoni, M. *et al. In situ* measurements of the physical characteristics of Titan's environment. *Nature* **438,** 785–791 (2005).
18. Jennings, D. E. *et al.* Surface temperatures on Titan during northern winter and spring. *Astrophys. J.* **816,** L17 (2016).
19. Le Gall, A. *et al.* Composition, seasonal change, and bathymetry of Ligeia Mare, Titan, derived from its microwave thermal emission. *J. Geophys. Res. (Planets)* **121,** 233–251 (2016).
20. Tokano, T. & Lorenz, R. D. Sun-stirred Kraken Mare: circulation in Titan's seas induced by solar heating and methane precipitation. *Icarus* **270,** 67–84 (2016).
21. Tokano, T. Limnological structure of Titan's hydrocarbon lakes and its astrobiological implication. *Astrobiology* **9,** 147–164 (2009).
22. Mastrogiuseppe, M. *et al.* The bathymetry of a Titan sea. *Geophys. Res. Lett.* **41,** 1432–1437 (2014).
23. Hayes, A. G. The lakes and seas of Titan. *Annu. Rev. Earth Planet. Sci.* **44,** 57–83 (2016).
24. Younglove, B. A. & Ely, J. F. Thermophysical properties of fluids. II. Methane, ethane, propane, isobutane, and normal butane. *J. Phys. Chem. Ref. Data* **16,** 577–798 (1987).
25. *CRC Handbook of Chemistry and Physics* (ed. Lide, D. P.) (CRC, 1974).
26. Gross J. & Sadowski, G. Perturbed-chain SAFT: an equation of state based on a perturbation theory for chain molecules. *Ind. Eng. Chem. Res.* **40,** 1244–1260 (2001).
27. Tokano, T., Lorenz, R. D. & Van Hoolst, T. Numerical simulation of tides and oceanic angular momentum of Titan's hydrocarbon seas. *Icarus* **242,** 188–201 (2014).
28. Clift, R., Grace, J. R. & Weber, M. E. *Bubbles, Drops and Particles* (Academic, 1978).
29. Le Gall, A. *et al.* Radar-bright channels on Titan. *Icarus* **207,** 948–958 (2010).
30. Cordier, D. *et al.* Structure of Titan's evaporites. *Icarus* **270,** 41–56 (2016).
31. Hartwig, J. W. *et al.* Exploring the depths of Kraken Mare — power, thermal analysis, and ballast control for the Saturn Titan submarine. *Cryogenics* **74,** 31–46 (2016).
32. Lorenz, R. D. *et al.* Titan submarine: vehicle design and operations concept for the exploration of the hydrocarbon seas of Saturn's giant moon. In *Lunar and Planetary Science Conference, Lunar and Planetary Institute Technical Report* **46,** 1259 (2015).
33. Hollyday, G. *et al.* Fitting nitrogen solubility lab data for modeling Titan's lakes and seas. In *Lunar and Planetary Science Conference, Lunar and Planetary Institute Technical Report* **47,** 2292 (2016).
34. Farnsworth, K., McMahon, Z., Laxton, D., Chevrier, V. & Soderblom, J. M. Experimental study of the effects of freezing on liquid hydrocarbons on the surface of Titan. In *Lunar and Planetary Science Conference, Lunar and Planetary Institute Technical Report* **48,** 1974 (2017).
35. Chen, S. & Kreglewski, A. Applications of the augmented van der Waals theory of fluids. I. Pure fluids. *Ber. Bunsenges. Phys. Chem.* **81,** 1048–1052 (1977).
36. García-Sánchez, F., Eliosa-Jiménez, G., Silva-Oliver, G. & Vázquez-Román, R. Vapor–liquid equilibria of nitrogen-hydrocarbon systems using the PC-SAFT equation of state. *Fluid Phase Equilib.* **217,** 241–253 (2004).
37. Justo-García, D. N., García-Sánchez, F., Díaz-Ramírez, N. L. & Romero-Martínez, A. Calculation of critical points for multicomponent mixtures containing hydrocarbon and nonhydrocarbon components with the PC-SAFT equation of state. *Fluid Phase Equilib.* **265,** 192–204 (2008).
38. Justo-García, D. N., García-Sánchez, F., Stateva, R. P. & García-Flores, B. E. Modeling of the multiphase behavior of nitrogen-containing systems at low temperatures with equations of state. *J. Chem. Eng. Data* **54,** 2689–2695 (2009).

Author contributions

D.C. wrote the paper and performed PC-SAFT computations, F.G.-S. and D.N.J.-G. made the stability analysis of the N_2 + CH_4 + C_2H_6 mixtures, and G.L.-B. provided expertise on the physics of bubbles and effervescence.

Additional information

Supplementary information is available for this paper.

Reprints and permissions information is available at www.nature.com/reprints.

Correspondence and requests for materials should be addressed to D.C.

How to cite this article: Cordier, D. *et al.* Bubble streams in Titan's seas as a product of liquid N_2+ CH_4+ C_2H_6 cryogenic mixture. *Nat. Astron.* **1,** 0102 (2017).

Publisher's note: Springer Nature remains neutral with regard to jurisdictional claims in published maps and institutional affiliations.

Competing interests

The authors declare no competing financial interests.

© 2017 Macmillan Publishers Limited, part of Springer Nature. All rights reserved.

Retour à la table des matières : p. v

4.12 Article sur la solubilité de l'acétylène et l'éthylène dans le méthane et l'éthane liquide

Available online at www.sciencedirect.com

ScienceDirect

Geochimica et Cosmochimica Acta 208 (2017) 86–101

Geochimica et Cosmochimica Acta

www.elsevier.com/locate/gca

Experimental determination of acetylene and ethylene solubility in liquid methane and ethane: Implications to Titan's surface

S. Singh [a,b,*], J.-Ph. Combe [b], D. Cordier [c], A. Wagner [a], V.F. Chevrier [a], Z. McMahon [a]

[a] Arkansas Center for Space and Planetary Sciences, University of Arkansas, 346 ½ Arkansas Ave, Fayetteville, AR 72701, United States
[b] Bear Fight Institute, 22 Fiddlers Rd, Winthrop, WA 98862, United States
[c] Groupe de Spectrométrie Moléculaire et Atmosphérique, UMR 6089, Campus Moulin de la Housse, BP 1039, Université de Reims Champagne-Ardenne, 51687 Reims, France

Received 18 November 2015; accepted in revised form 1 March 2017; Available online 9 March 2017

Abstract

In this study, the solubility of acetylene (or ethyne, C_2H_2) and ethylene (or ethene, C_2H_4) in liquid methane (CH_4) and ethane (C_2H_6) has been experimentally determined at Titan surface temperature (90 K) and pressure (1.5 bars). As predicted by theoretical models, the solubilities of acetylene and ethylene are very large at Titan temperature and these species are most likely to be abundantly present in the lakes and as evaporites on the shores or dry lake beds. Our results indicate the solubility of 4.9×10^{-2} mole fraction for acetylene in methane and 48×10^{-2} mole fraction in ethane; for ethylene, 5.6×10^{-1} mole fraction in methane and 4.8×10^{-1} mole fraction in ethane. Assuming the mole fractions from atmospheric models in the lower stratosphere and equilibrium with the surface, we determined that the lakes on Titan that cover ~400,000 km^2 are not saturated. The liquid lakes on Titan act as an important reservoir for both acetylene and ethylene. Assuming difference of methane and ethane content in the lakes at different latitudes, the difference in solubility in liquid methane and ethane, solutes in lakes may change with the temporal evolution (such as; evaporation and condensation) over seasons and geological time scales.
© 2017 Elsevier Ltd. All rights reserved.

Keywords: Titan; Solubility; Acetylene; Ethylene; Infrared spectroscopy; Planetary surfaces; Atmosphere

1. INTRODUCTION

Since the arrival of the *Cassini-Huygens* mission in the Saturn system in 2004, strong evidence of the presence of liquid bodies has been found on Titan's surface near the poles (Lopes et al., 2007; Stofan et al., 2007; Hayes et al., 2008). Titan possesses a thick atmosphere mainly composed of 95% nitrogen and <5% methane, and experiences an active methane cycle similar to the water cycle on Earth (Lorenz and Lunine, 1997; Hayes et al., 2008). This cycle allows retaining potential liquid hydrocarbons on Titan's surface (Lorenz et al., 2001; Atreya et al., 2006). Although predicted to exist as large oceans (Lunine et al., 1983; Raulin, 1987), free surface liquids have been discovered and interpreted as lakes and seas of various sizes and shapes (Lopes et al., 2007; Stofan et al., 2007; Hayes et al., 2008; Stephan et al., 2010). The observed lake morphologies in *Cassini*'s data is comparable with some terrestrial landforms encountered in semiarid regions, which suggests that the lakes lie in a depression formed by dissolution of a surface soluble porous layer (Bourgeois et al., 2008; Cornet

* Corresponding author at: Arkansas Center for Space and Planetary Sciences, University of Arkansas, 346 ½ Arkansas Ave, Fayetteville, AR 72701, United States.
E-mail address: ssingh@bearfightinstitute.com (S. Singh).

http://dx.doi.org/10.1016/j.gca.2017.03.007
0016-7037/© 2017 Elsevier Ltd. All rights reserved.

et al., 2015). For example, in the Namibian analog, this layer is constituted of calcretes, a rock that is soluble on geological timescales. Indeed, the data acquired during the landing of *Huygens* probe in January 2005 seems to argue of a porous and damp surface and are therefore consistent with this hypothesis (Zarnecki et al., 2005; Lorenz et al., 2006). Photochemical and thermodynamic models (Dubouloz et al., 1989; Cordier et al., 2009), as well as the potential detection of hydrocarbon compounds on Titan's surface (Clark et al., 2010), brought indication about the potential solutes existing in Titan's lakes and as evaporites on the surface.

1.1. Titan's global settings

Atmosphere: Titan's atmosphere is composed of 95% of nitrogen, methane is the second most abundant component, having mixing ratio of 4.92% at near surface (Niemann et al., 2005) and less than 1% of minor species such as dihydrogen (Owen and Niemann, 2009), carbon monoxide (Dekok et al., 2007) argon (Niemann et al., 2005) and ethane (Cordier et al., 2009). The atmosphere of Titan is photochemically active, producing acetylene, ethylene, propane, and benzene as minor components (Mitri et al., 2007; Lavvas et al., 2008a, 2008b; Coustenis and Hirtzig, 2009) that act as solutes.

Surface: Titan surface temperature is comprised between 93.65 k measured at the *Huygens* landing site (HLS) (Niemann et al., 2005; Tomasko et al., 2008) and 90.5–91.7 K interval inferred from the Composite Infra-Red Spectrometer (CIRS) and the radiometer data at the Titan's poles (Janssen et al., 2009; Jennings et al., 2009; Cottini et al., 2012). The measured surface pressure at the HLS is 1.46 bar (Niemann et al., 2005). The pressure and temperature at the surface lie near the triple point of methane and ethane states (90 K), which suggest both are stable and act as solvents. Titan's surface consists of high-albedo terrains with predominantly high elevation, and low-lying terrains or lower albedo. Exceptions in albedo exist, such as Tui Regio, which is a low-altitude area with high albedo (MacKenzie et al., 2014). Interpretations suggest that the high albedo of the largest highlands region is due to the reflected light of ices (possible solutes) washed down slopes by flash floods instigated by methane/ethane rainfall. Rainfall has been suggested as a cleansing mechanism that might render elevated terrain optically brighter than lowlands (Griffith et al., 1991; Smith et al., 1996). If Titan's bright terrain highlands are made of solid compounds such as acetylene and ethylene, they can easily dissolute in the liquid methane and ethane and transport to the liquid reservoirs at lowlands.

According to photochemical models (Yung and DeMore, 1999; Lavvas et al., 2008a, 2008b), three organic compounds are expected to be in liquid form on Titan's surface: methane, ethane, and to a lesser extent, propane. Several others, such as acetylene and ethylene, are expected to exist in solid phase and are produced abundantly in the atmosphere (Roe et al., 2004). Acetylene and ethylene are the next most abundant hydrocarbons after ethane. Their formation is initiated in the upper atmosphere directly from the products of methane photolysis. In the lower atmosphere, acetylene recycles back to ethylene, hence both acetylene and ethylene are abundant in the atmosphere. The model of Cordier et al. (2009) tends to argue for a lake composition dominated by ethane (more than 70%), propane (7–10%), and methane (5–10%) in which some solid compounds can be dissolved if thermodynamic equilibrium between the lake and the atmosphere is assumed. Tan et al. (2013) and Glein and Shock (2013) present new geochemical models estimating the liquid compositions at the Titan's surface. The equatorial surface liquid is predicted to be dominated by ethane, methane, propane, and nitrogen with mole percent of 53%, 32%, 7%, and 7% respectively (Tan et al., 2013). However, these well-established models tend to argue the need of more information and laboratory experiments to accurately estimate the liquid composition.

Luspay-Kuti et al. (2012, 2015), estimates the lake composition of Ontario Lacus to be ~70–30% of ethane to methane, the major lake in Titan's southern hemisphere. Whereas, northern lakes are thought to be more methane-rich reaching up to 90–10% methane to ethane concentration (Luspay-Kuit et al., 2012, 2015). Depending on the solubility rates of Titan's solids in liquid methane and ethane, we should be able to estimate the amounts of solutes that are present on Titan. A solubility measurement under Titan's conditions in the lab will provide constraints for the atmospheric models and test the limits of these models. In this study, we propose estimations of solubility values of acetylene and ethylene in liquid methane and ethane from experimental measurements under Titan surface conditions.

1.2. Acetylene

Acetylene is known to be one of the end products of methane photolysis in laboratory experiments (Smith and Raulin, 1999; Vuitton et al., 2006; Lavvas et al., 2008a, 2008b). Its photochemistry also plays an important role in the atmosphere of Titan, and is predicted in Titan's lakes as a major component (Cordier et al., 2009, 2013; Glein and Shock, 2013; Tan et al., 2013). Acetylene is the second largest compound after ethane produced in the atmosphere, models predict a net creation of acetylene approximately 125–2000 times greater than other compound produced (Wilson, 2004), and may settle and exist under its solid form at the surface (Cordier et al., 2009, 2013). It has been suggested that over the geological time scale, a solid layer of acetylene a few hundreds of meters thick would have formed on the surface of Titan (Owen and Niemann, 2009). Although, being so abundant in the atmosphere with the stratospheric mixing ratio of a mole fraction of about 3.7×10^{-6} (Coustenis et al., 2010), evidence of acetylene at the surface is still lacking on bright terrains. However, Singh et al. (2016) reports the evidence of acetylene on the low albedo region near equator. Since acetylene is assumed to be abundant on Titan, it is also thought to be highly soluble in Titan liquids (methane and ethane). Several models have previously attempted to determine the solubility of acetylene in methane and ethane (Cordier et al., 2009; Glein and Shock, 2013). Depending on the

Retour à la table des matières : p. v

mole fraction determined by the photochemical models, acetylene is found to be the main compounds in lakes formed on the surface of Titan. With all the numerical models, available to determine the solubility values, laboratory experiments are needed to set constraints and provide solubility limits for future models. Here, we present experimentally determined solubility of solid acetylene in liquid methane and ethane under conditions of pressure, temperature and chemistry relevant for the surface of Titan.

1.3. Ethylene

Roe et al. (2004) observes a significant accumulation of ethylene in the south polar stratosphere near latitudes south of 60° S. Ethylene is thought to be among one of several chemical species that varies in abundances as a function of latitudes (Coustenis et al., 1989) and shows polar enrichments, which may be due to seasonally varying chemistry. Roe et al. (2004) suggests the extent of the south polar ethylene abundance of ~20 times more than equatorial abundance. According to Roe et al. (2004), ethylene accumulation retreated to latitudes above 50° N, whereas there is significant accumulation of ethylene in the south polar stratosphere and it does not extend further than 60° S. Overall, from these measurements we can estimate that there is plenty of ethylene in the Polar Regions and probably on the surface. A majority of the lakes lie at the poles of Titan and thus ethylene could also be one of the main constituents dissolved in the lakes, assuming ethylene reaches the surface of Titan.

On the other hand, the first complete model of the post *Cassini-Huygens* era is the one by Lavvas et al. (2008a, 2008b). Even though the model includes recent *Cassini-Huygens* measurements, it underestimates the abundance of ethylene (1.5×10^{-7}) in the stratosphere, which implies a bias in underestimating the likelihood of presence of ethylene on the surface. An attempt made by Cordier et al. (2009, 2012, 2013) to estimate the composition of lakes did not include ethylene as a constituent of the lake. In this study, assuming ethylene is somewhat present at the surface and the atmospheric mixing ratio, we determined the solubility of ethylene in liquid methane and ethane. Using these solubility values, we can estimate the amount of ethylene present in north and south polar lakes.

2. EXPERIMENTS

We performed the solubility experiments using the Andromeda chamber at University of Arkansas that is designed to simulate the Titan surface conditions (Wasiak et al., 2013). The Titan simulation chamber is a stainless-steel cylinder (height of 2.08 m, diameter of 0.61 m) sealed with a vacuum pump at the bottom and a lid at the top (the lid can be removed to perform maintenance) (Fig. 1). The outer cylindrical chamber accommodates the Titan module, which consists of the Temperature Control Box (TCB). The experiments are performed within the TCB that contains a condenser to prepare the liquid and solid samples. The Titan module also contains a FTIR (*Fourier-Transform Infra-Red Spectrometer*) fiber optic probe (bi-directional, conical beam), a balance to measure the mass of the sample, five thermocouples, two endoscopes for visual observation of samples, pressurized gas lines, and electronic connectors. The chamber is internally equipped

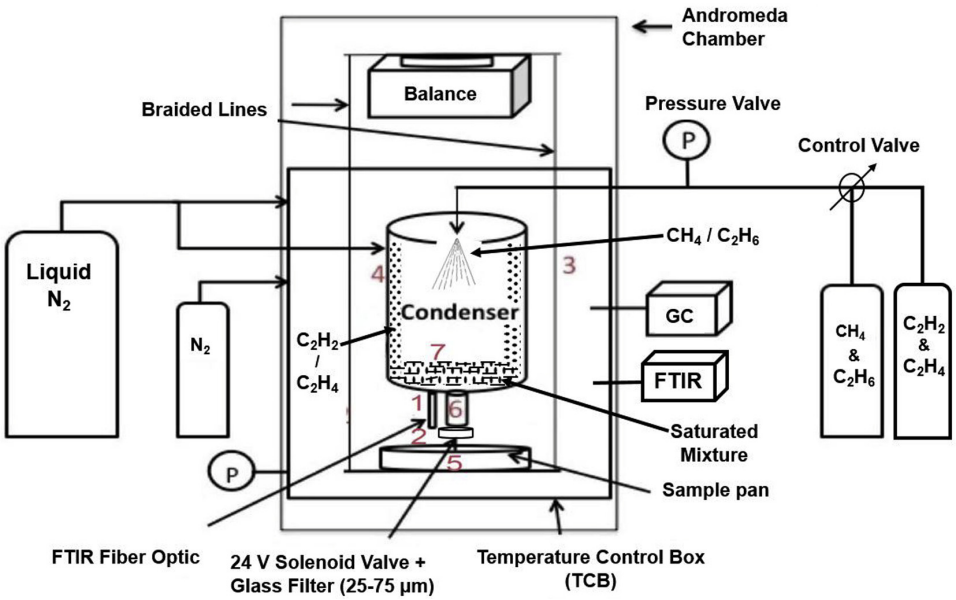

Fig. 1. A schematic of Andromeda chamber at University of Arkansas. Numbers in the TCB corresponds to the thermocouples at different locations. Where, 1 is fiber probe temperature, 2 is atmosphere above the sample, 3 & 4 records the upper atmosphere of the TCB, 5 is the sample temperature, 6 & 7 records the temperature inside the condenser.

Retour à la table des matières : p. v

with pressure coils to maintain the pressure of 1.5 bar with continuous supply of N_2. Inside the Titan module, the TCB is equipped with Liquid Nitrogen (LN_2) cooling coils that allow the module to reach temperatures relevant to the surface of Titan (90–94 K). The temperature is controlled by varying the flow of LN_2 flowing through the coils.

To perform solubility experiments, we start with purging the entire chamber with N_2 to remove contaminants prior to the experiment. We also carefully exchange the atmosphere during the experiments and maintain a 1.5 bar pressure via pressure valves. We also purge the condenser independently with N_2 by opening the solenoid valve and valves to the exhaust, to remove any contaminants from previous experiments. Once the chamber is fully purged for ~20 min, we start the LN_2 flow through the external coils around TCB. Once the TCB reaches a low enough temperature (typically below 150 K), we start the LN_2 flow through the condenser using independent, specifically dedicated coils. Thermocouples located at different locations in the Titan module help us maintain and control the LN_2 flow. Five thermocouples allow continuous recording of temperatures during the experiment: one is fixed at the bottom of the Petri dish (sample temperature), one is attached and fixed right above the Petri dish (~2 cm) that monitors the atmosphere, one is attached to the FTIR probe (atmosphere ~3 cm above the petri dish) and two are located at the top of the TCB (~15–20 cm above the sample). These thermocouples allow a precise characterization of the thermal profile in the TCB. In addition to these temperatures, the mass is continuously recorded. Finally, the FTIR probe allows reflectance spectra (wavelength 1–2.5 μm) of the sample to be taken at various time intervals, while the endoscopes allow direct imaging of the sample.

Different samples condense at different temperatures; before allowing the hydrocarbons to enter the condenser, we make sure that the condenser temperature is within the right range to condense the sample of interest. Once Titan relevant temperature (90–94 K) is reached, and the condenser has the appropriate temperature, the sample is introduced in gas form into the condenser, and then converted into solid, before being poured into the Petri dish. This reduces the risk of clogging the valve, as the sample condenses on the walls of the condenser directly from the gas phase. After condensing the sample, we decrease the temperature to the condensation temperature of methane (~95 K) or ethane (~120 K). Methane and ethane condense as liquid from the gas phase, allowing them to dissolve the sample. The amount of time allowed for dissolution is dependent on the timescales for saturation to be reached, which can only be determined by repeated experiments with increasing times. The solenoid valve is then opened to pour the solution into the petri dish through a fritted glass filter (25–75 μm diameter) placed between the solenoid valve and the Petri dish to allow removal of residual solid particles from the condenser (Fig. 1).

To monitor the total mass of the sample, the Petri dish (15 cm diameter, 1.5 cm deep) where the sample is poured into is suspended via nylon wires to a balance scale (precision of 0.01 g) located outside and above the TCB. This precaution is necessary because the electronics of the balance is not designed to function at cryogenic temperatures. The bottom of the petri dish is covered with a reference white target (Spectralon® from LabSphere) made of a fluoropolymer which diffuses light isotropically (Lambertian surface) and which reflectance is close to 100%. A reference spectrum is acquired at the beginning of each experiment. The amount of individual mass of acetylene and methane/ethane is unknown in the total mass of the solution. Knowing individual mass of each compound in the solution is necessary to calculate the solubility. This is done by Spectral Mixture Analysis (SMA) of infrared spectra of the samples.

2.1. Calculation of solubility from Spectral Mixture Analysis (SMA, e.g. Adams et al., 1986)

In order to retrieve the mass of individual components in a mixture from infrared spectra, it is necessary to measure the mass and spectra of pure components (also referred to as spectral endmembers). In this study, for acetylene, methane, and ethane spectra are characterized by several absorption bands. Their position in wavelength, width and symmetry are diagnostic of the type of molecular bonds and, by extension, of molecular species. The depths of those absorption bands increase as a function of the sample depth (or mass). The rate of this increase depends on the photon's path length through the sample. In our experimental setting, the light source is above the Petri dish and all the samples are translucent. As a consequence, the sample diffuses photons to the bottom of the Petri dish into various directions, the reference white target diffuses photons back through the sample, and the sample diffuses photons towards the FTIR fiber optic probe. This complex distribution pattern of photon fluxes and directions is determined by technical constraints of the experiment. It results in a relationship between spectra and masses that is unique to our system, therefore we have to acquire spectra for several masses of each molecular species used as a solvent in our mixtures. Because of the high volatility of liquid acetylene, we could not build its corresponding lookup table.

The mixture sample has two unknowns (the mass of each component), and two knowns (the total mass and the infrared spectrum). In order to determine the proportion of each component from the spectrum, we modeled the reflectance spectrum of a mixture R_M by a linear combination of the spectral endmembers R_n:

$$R_M(\lambda) = r(\lambda) + \sum_{n=1}^{N} a_n R_n(\lambda), \quad (1)$$

where N is the number of spectral endmembers, a is the modeled weighing coefficient of the spectra, and r the model residual.

The modeled weighing coefficients of the spectra are sensitive to the quantity of each component, but they are not proportions. In order to calculate masses from the weighing coefficients, we built a lookup table by modeling the spectrum of each pure component with a given mass, by spectra of the same component with different masses (Fig. 2). Modeling the spectrum of a large-mass sample with the spectrum of small-mass sample results in a weighing coeffi-

Retour à la table des matières : p. v

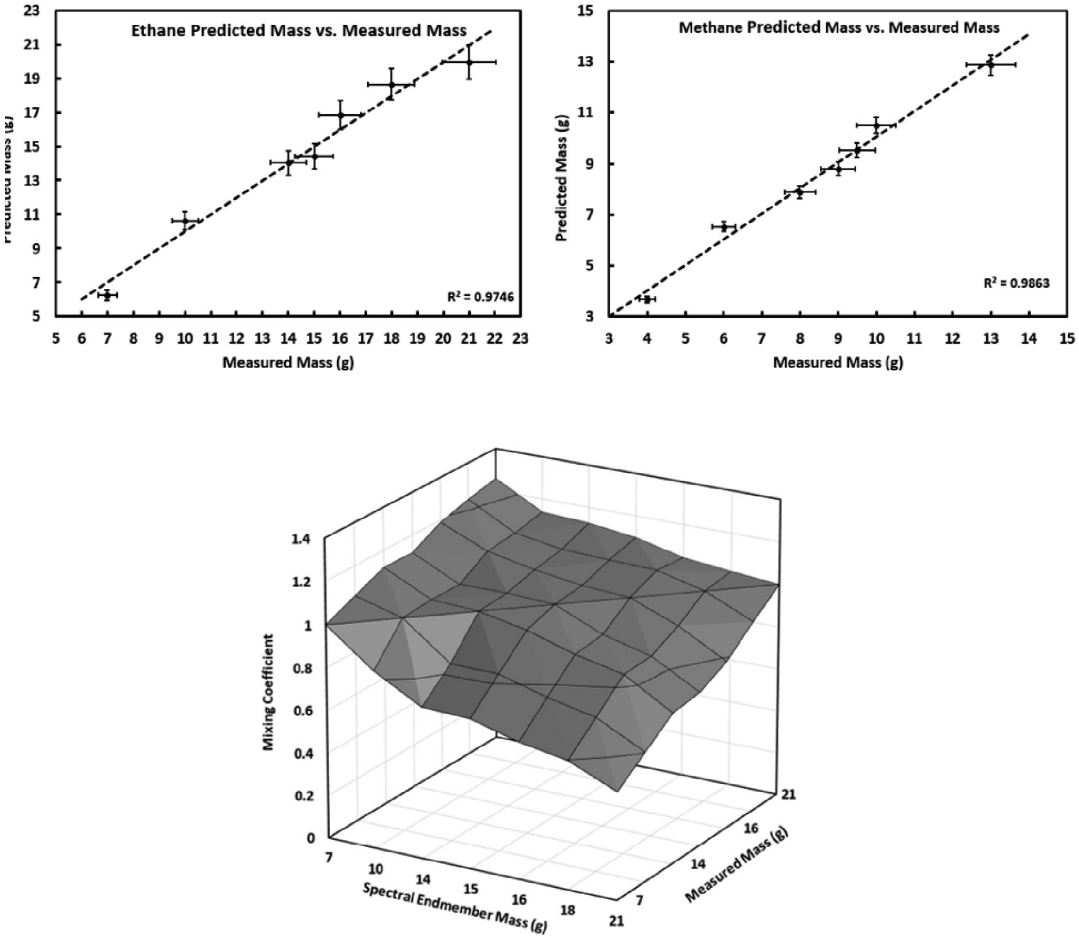

Fig. 2. (Top) Predicted mass by MELSUM vs. measured mass in the lab. (Bottom) A calibration curve showing the linear dependence between the weighing coefficient, predicted mass, and measure mass.

cient greater than one; the opposite scenario leads to values lower than one. The quality of fit improves as the spectral endmember and the modeled spectrum correspond to sample masses that are close to each other. Each series is fitted by a linear relationship of mass as a function of weighing coefficient.

In order to calculate weighing coefficients from the equation above, we are using the Multiple-Endmember Linear Spectral Unmixing Model (MELSUM, Combe et al., 2008), which relies on the least square inversion of the system $\boldsymbol{Y} = \boldsymbol{AX}$, where $\boldsymbol{Y}$ is a vector containing the unknown spectrum, $\boldsymbol{A}$ is $\boldsymbol{N} \times \boldsymbol{M}$ matrix filled with the endmembers spectra (the input spectral library, with N the number of endmembers and M the number of spectral channels), and $\boldsymbol{X}$ is a vector containing the coefficients of each component of the input library. The solution of this linear system is given by $\mathbf{X} = (\mathbf{A}^{\mathbf{t}}\mathbf{A})^{-1}\ \mathbf{A}^{\mathbf{t}}\ \mathbf{Y}$. MELSUM automatically selects the best linear combination of spectral endmembers from the reference library. It also provides strictly positive weighing coefficient values, which is not the default property of the least-square inversion. This tool allows the user to fix the maximum number of spectral endmembers used to model a mixture.

2.2. Calibration of MELSUM-derived spectral weighing coefficients to calculate mass

The principle of this step is to use spectra of samples of known mass to model spectra of samples of unknown mass with a linear combination of one sample spectrum, an offset and a residual. Two different sets of calibration were performed for methane and ethane. To calibrate MELSUM we built a spectral library of one pure component (methane or ethane) from spectral measurements made with various amounts (mass in the Petri dish). Then, for each mass, the corresponding spectrum is modeled with MELSUM

Retour à la table des matières : p. v

by spectra from samples of different masses. Model residuals provide information on the best fit data. The weighing coefficient corresponding to the best model can be used to determine the mass of the endmember in the unknown spectra.

In our experiments, methane is in contact with 1.5 bar of N_2 at all times, N_2 is mixed when CH_4 is in contact with the chamber atmosphere, in our previous experiments Luspay-Kuti et al. (2012) estimated the time for the mixture to equilibrate to be only 10 s, and that the mole fractions of N_2 and CH_4 in the condensed liquid are 0.16 and 0.84, respectively (Luspay-Kuti et al., 2012). The dissolution of N_2 is consistent in all the methane experiments performed under the same thermodynamic conditions. However, the solubility of N_2 in methane is highly dependent on the temperature (Farnsworth et al., 2016). Thus, it is extremely important to perform all the experiments under same thermodynamic conditions. The conditions used in experiments of pure methane and ethane were also used to perform solubility experiments and were used to calibrate MELSUM. Since the nitrogen dissolution stays consistent in all the methane experiments, we used this binary mixture for calibration.

In any mixture with ethane or methane, the data summarized in Fig. 2 can be used to determine the mass m_x corresponding to each weighing coefficient α_x compared to a standard mass of a compound m_0 and its associated weighing coefficient α_0, following the relationship $m_x = m_0 \times \alpha_x/\alpha_0$. For example, using the spectrum for 1 g of methane, we modeled the spectrum for 2 g, and the corresponding weighing coefficient value is 2.2. When we apply MELSUM on sample spectra of unknown masses, if the best fit is obtained with the endmember spectrum of 1 g of methane and a weighing coefficient α_x, it means the mass of methane is 2 g $\times$ α_x/2.2. Best fits can be obtained both for weighing coefficients less than 1 (when modeling a sample spectrum which mass is higher than the mass of the endmember spectrum sample) or greater than 1 (when modeling a sample spectrum which mass is lower than the mass of the endmember spectrum sample). The quality of fit is higher when the mass of the unknown sample is close to the mass of the sample of the endmember spectrum; this is why it is important to build a spectral library with as many values of mass as possible.

Fig. 2 illustrates the results of predicted mass by MELSUM with the measured mass in the lab and a proof that the technique described above can predict methane and ethane mass up to 97% confidence. Using the weighing coefficient, spectral endmember mass, and measured mass relation in any mixture with ethane or methane we can determine the corresponding mass from the weighing coefficient. Then we subtract the mass of solvent derived from calibration curves from the total mass that we know from measurements with the balance. The mass difference is the mass of the dissolved compound, allowing us to determine the solubility. The technique described above is only applicable to the compounds that do not interact at molecular levels such as a mixture of liquid methane and ethane. Any compound that modifies the original solvent or solute molecule will change the spectrum shape and the positioning of absorption bands. In our case, the experimental data shows that when methane and ethane interact with acetylene or ethylene, the shape and position of absorption bands does not change and thus this technique can be used to identify the quantity of individual compound in the solution.

3. RESULTS

In our previous work, we determined a significant increase in reflectivity of acetylene from the solid phase to liquid phase (Singh et al., 2015). We also observed a shift in the major absorption band at 1.56 μm to longer wavelength (Fig. 3). On the surface of Titan, ethylene will be solid and we collected pure ethylene spectra in different phases and determined no change or repositioning of absorption bands; the overall reflectivity is the only factor that seems to change. The reflectivity ratio (R_{solid}/R_{liquid}) is 1.63 under Titan surface conditions (Fig. 3). A shift in the 1.55 μm was noticed to longer wavelength during the phase change from liquid to solid (Singh et al., 2015). Thus, preliminary work on determining changes in absorption bands during phase change is important. However, knowing the reflectivity ratio of ethylene also serves purpose in *Cassini* VIMS data. Ethylene ice will appear bright and liquid ethylene will appear dark in VIMS data. In future, if ethylene is identified on the surface reflectivity ratio will be helpful in determining the phase it exists on Titan.

3.1. Solubility of acetylene in methane and ethane

Fig. 4 (right) shows the near infrared (NIR) spectra of acetylene (green), methane (blue), and the mixture spectra of the dissolution of C_2H_2 in pure methane (red) ranging from 1 to 2.2 μm. We have identified several absorption bands of acetylene and methane at 90 K in our previous work (Singh et al., 2015, 2016). Acetylene has two important absorption bands within the range (1–2.2 μm) of our experiments; they lie within VIMS atmospheric windows at 1.55 μm and a negative slope at 2.0 μm. Methane has several absorption bands at 1.19, 1.33, and three sharp bands at 1.66, 1.71, 1.79 μm. In the mixture spectra, methane absorption bands are dominant with minor traces of dissolved acetylene with absorption bands at 1.55 and 2.0 μm. The acetylene signature in the mixture spectra is barely visible and the band depth of the absorption bands relates to the quantity of acetylene present in the solution. From the mixture spectra, it clearly indicates that acetylene is present in very little quantity as compared to methane.

In a similar type of experiment, Fig. 4 (left) shows the NIR spectra of ethane (blue), acetylene (green) and the mixture spectra of the dissolution of acetylene in pure ethane (red) ranging from 1 to 2.2 μm. Ethane has numerous absorption bands over the same wavelength range as methane. Ethane also has three distinctive absorption bands at 2.0 μm that are not present in the methane spectra. As a result, in the dissolution spectra of ethane and acetylene, only a single absorption band of acetylene is identified at 1.5 μm. The negative slope at 2.0 μm of acetylene is overlapped with the three distinctive absorption bands of ethane. In comparison to acetylene absorption band in methane at 1.55 μm, acetylene absorption band is significantly larger in ethane mixture within the same time range

Retour à la table des matières : p. v

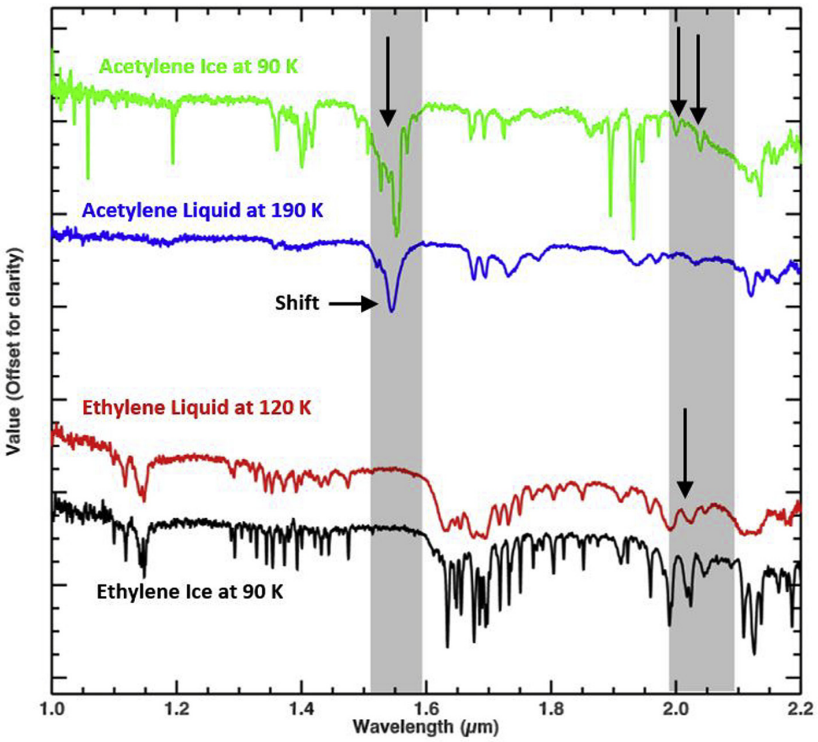

Fig. 3. Comparison between liquid and solid phase of acetylene and ethylene. Shaded region represent two Cassini VIMS atmospheric windows at 1.56 and 2.0 μm.

allowed for dissolution. The band depth of the absorption bands clearly indicates that the amount of acetylene present in the ethane mixture is significantly larger than in the methane mixture, which implies that acetylene is significantly more soluble in ethane than in methane.

MELSUM results are presented in Fig. 5. They show a comparison between the unknown mixture spectral data (red) and the linear mixing modeled spectra (green dotted). Blue and magenta color corresponds to the spectra of endmember of methane and acetylene and ethane and acetylene respectively in Fig. 4 which have been selected by the model, multiplied by their weighing coefficient. It shows how much a given endmember contributes to the final modeled spectra. The residual value is given in the dashed line with very minimal value of 0.02. The value of weighing coefficient of known methane endmember is 0.95 and for acetylene is 0.05. When using these weighing coefficients, we extracted the mass of methane to 9.2 g from calibrated curve (Fig. 2 top), which is then subtracted from the total mass obtained by balance and gives us the mass of acetylene of 0.8 g. The value of weighing coefficient of known ethane endmember is 0.84 and for acetylene is 0.16. From the calibration curves, the estimated mass of ethane in the solution is 10 g, and the mass of acetylene is 8 g.

At 90 K, the solubility of acetylene in liquid methane is 4.9×10^{-2} mole fraction and is 48.0×10^{-2} mole fraction in liquid ethane. The solubility of acetylene in methane and ethane is consistent with previous work that calculated the solubility of acetylene, based on numerical models and Peter Prestuian method (Szczepaniec-Cięciak et al., 1978). Acetylene is nearly 10 times more soluble in liquid ethane as in liquid methane. The large difference between the solubility of acetylene in methane and ethane can be explained by the value of Hildebrand solubility parameter. The value of this parameter represents a measure of the molecular cohesion energy of the pure compound (Cordier et al., 2009). It depends on the nature and the strength of the intermolecular forces between molecules of the same species. Two components presenting close Hildebrand solubility parameter $(cal/cm^3)^{1/2}$ are likely to be highly soluble. The value of Hildebrand parameter for methane (CH_4), ethane (C_2H_6), and acetylene (C_2H_2) at 92.5 K are 7.23, 9.07, and 11.11, respectively (Dubouloz et al., 1989). This implies that acetylene should be more soluble in ethane than in methane, as observed in our laboratory work.

3.2. Solubility of ethylene in methane and ethane

In a separate set of experiments, we determined ethylene solubility in liquid methane and ethane. Fig. 6 presents raw NIR spectra from binary system experiment for methane-ethylene, and ethane-ethylene, respectively. From the FTIR data, the ethylene spectra have numerous absorption bands over the entire NIR range allowed in our experiments from

Retour à la table des matières : p. v

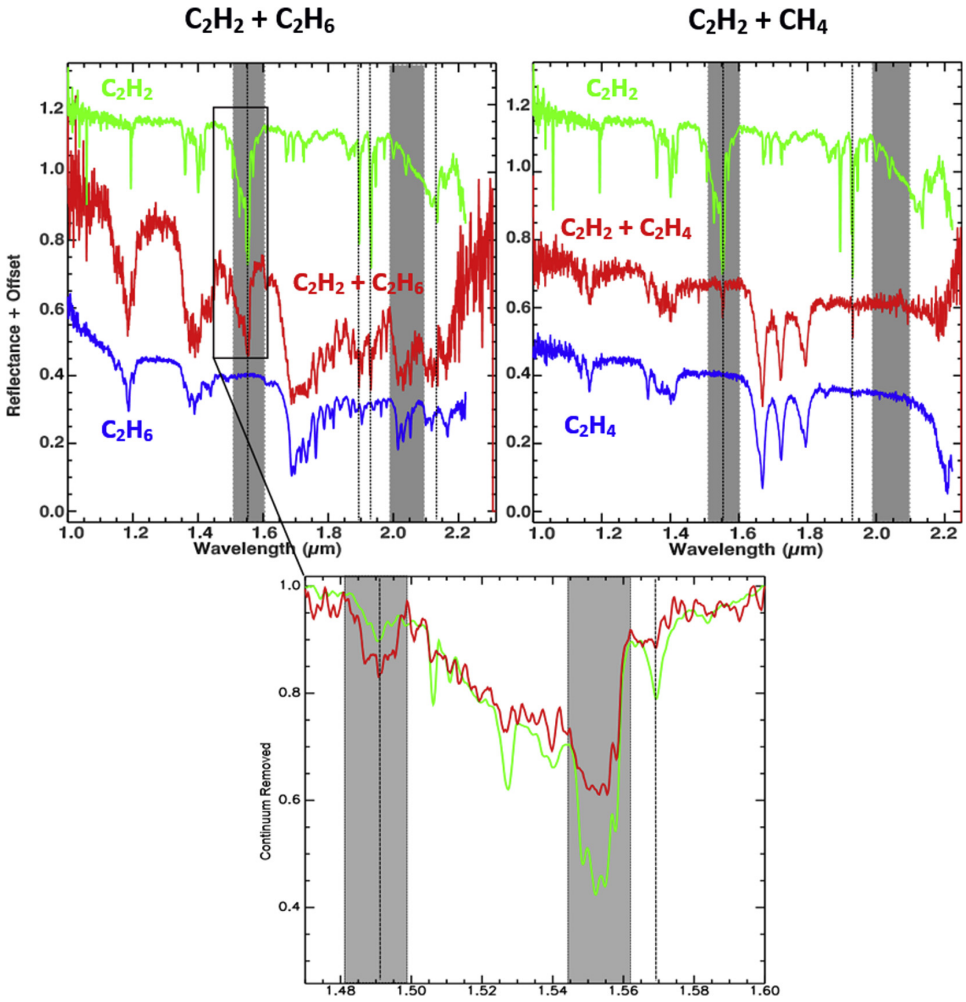

Fig. 4. Right: NIR spectra of pure acetylene (green) and pure methane (blue) compared to the NIR spectra of the mixture of methane and acetylene (red). Left: NIR spectra of pure acetylene (green) and pure ethane (blue) compared to the NIR spectra of the mixture of methane and acetylene (red) (left) indication of large absorption band at 1.55 μm. Thin dotted line shows the identified absorption bands of acetylene in mixture spectrum, shaded region are two Cassini VIMS atmospheric windows at 1.6 and 2.0 μm. Bottom Panel. (For interpretation of the references to colour in this figure legend, the reader is referred to the web version of this article.)

1 to 2.2 μm. As discussed above, both methane and ethane have several distinctive absorption bands in the same range (Fig. 6 magenta and red, respectively), most of the absorption bands produced by methane and ethane are overlapped by ethylene (green) except at few wavelengths. The NIR spectra for the binary system methane –ethylene (Fig. 6 (left), blue) and ethane –ethylene (Fig. 6 (right), blue) shows the absorption bands produce by the mixtures.

The results from MELSUM for ethylene in two liquids can be seen in Fig. 7. Blue and magenta color corresponds to the spectra of endmember of methane and ethylene and ethane and ethylene in Fig. 6, which have been retained by the model, multiplying by their weighing coefficient. It shows the amount endmember contributes to the final modeled spectra. The residual value is given in the black line with the very minimal value close to zero. The value of weighing coefficient of known methane endmember is 0.48 and for ethylene is 0.83. When used these weighing coefficients we extracted the mass of methane to 4 g from calibrated curve (Fig. 2), which is then subtracted from the total mass obtained by balance and gives us the mass of ethylene of 9 g. The value of weighing coefficient of known ethane endmember is 0.71 and for ethylene is 0.54. The extracted mass for ethane is 9 g from the predictive mass curve and the mass of acetylene is derived as 6 g in the solution.

The experimental value of the solubility of ethylene in liquid methane at 90 K is 5.6×10^{-1} in mole fraction and the solubility of ethylene in liquid ethane at 90 K is 4.8×10^{-1} in mole fraction. The value of ethylene in

Retour à la table des matières : p. v

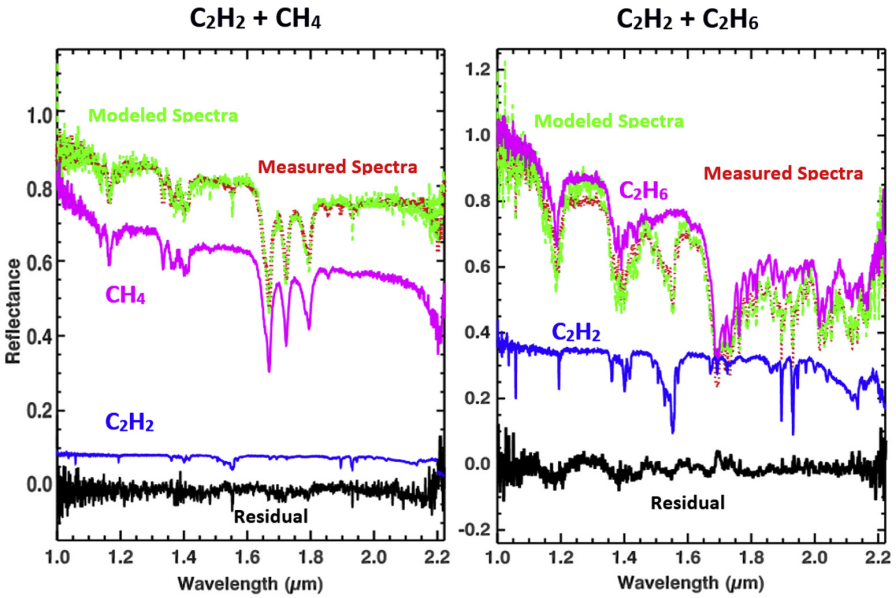

Fig. 5. Results from MELSUM. Left: Unknown spectrum of methane + acetylene (red) is modeled with MELSUM (green dotted) by using endmember of methane (magenta) and acetylene (blue). Residual from the modeled spectrum and unknown spectrum is displayed in black with a value of ~0. Right: Same as left but with ethane + acetylene mixture. Ethane endmember is shown in magenta color. (For interpretation of the references to colour in this figure legend, the reader is referred to the web version of this article.)

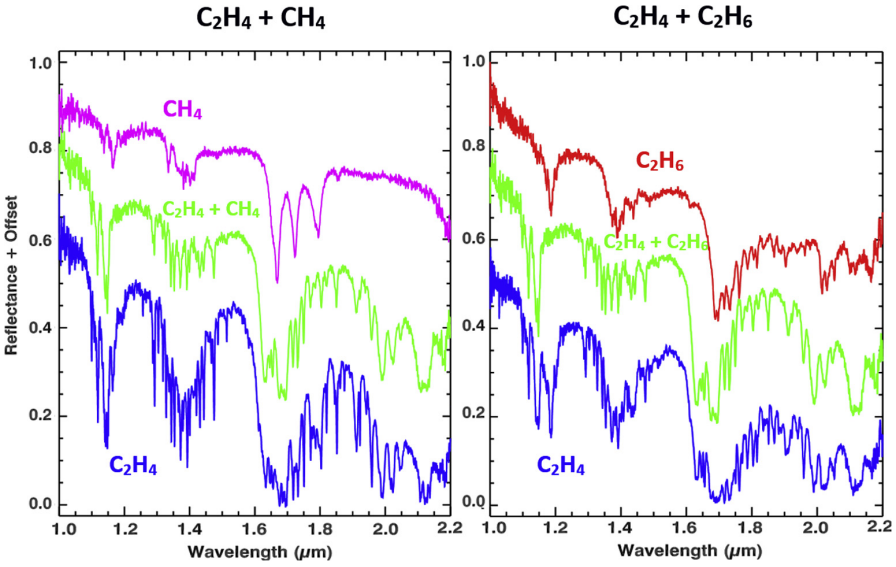

Fig. 6. Left: NIR spectra of pure ethylene (green) and pure methane (magenta) compared to the NIR spectra of the mixture of methane and acetylene (blue). Right: NIR spectra of pure ethylene (green) and pure ethane (red) compared to the NIR spectra of the mixture of methane and acetylene (blue). (For interpretation of the references to colour in this figure legend, the reader is referred to the web version of this article.)

methane and ethane is consistent with previous work that calculated solubility based on a non-ideal solution (Szczepaniec-Cięciak et al., 1978). By comparing solubility of ethylene in two liquids at the same temperature, it appears that ethylene is nearly equally soluble in both methane and ethane. The difference between the solubilities can be explained with the close value of hildebrand/solubility parameter. Hildebrand parameter for methane (CH_4),

Retour à la table des matières : p. v

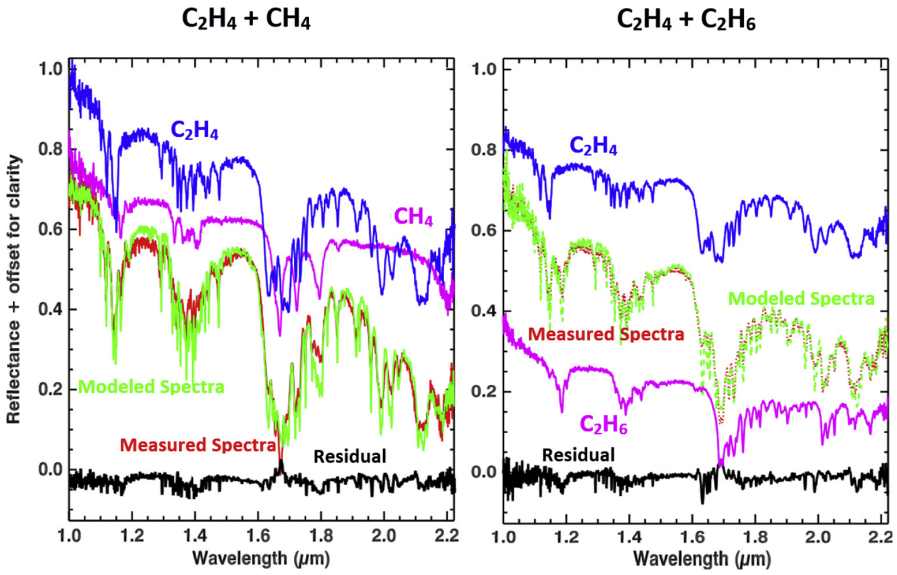

Fig. 7. Results from MELSUM. Left: Unknown spectrum of methane + acetylene (red) is modeled with MELSUM (green dotted) by using endmember of methane (magenta) and acetylene (blue). Residual from the modeled spectrum and unknown spectrum is displayed in black with a value of ~0. Right: same as left but with ethane + acetylene mixture. Ethane endmember is shown in magenta color. (For interpretation of the references to colour in this figure legend, the reader is referred to the web version of this article.)

ethane (C_2H_6), and acetylene (C_2H_2) at 92.5 K are 7.23, 9.07, and 11.11, respectively (Dubouloz et al., 1989). The solubility parameter for ethylene was calculated to be 8.0 $(cal/cm^3)^{1/2}$, which is close to the solubility parameter of both methane (7.23) and ethane (9.07). Therefore, ethylene is somewhat equally soluble in both methane and ethane, as we have observed.

Difference in solubility values from that in literature: we would like to discuss the differences in the solubility measurements of acetylene in liquid methane measured by Neumann and Mann (1969) and our measured values. Neumann and Mann (1969) measured the solubility of acetylene in liquid methane to be 6.8×10^{-5} mole fractions, while our results found a value of 4.9×10^{-2}. As clearly noticed there are three orders of magnitude in difference, this difference in the values can be explained by the difference in experimental setup. Neumann and Mann (1969) conducted experiments using 99.95% pure methane and no data is available for acetylene. In our study, we used 99.99% methane and industrial grade acetylene (95%) with added impurities of acetone (5%) from Airgas. Also, our experiments were conducted at 1.5 bar N_2 atmosphere. Since, N_2 is highly soluble in methane at 100 K at 1 bar (Battino et al., 1984), our previous work Chevrier et al. (2015) observes that in our experiments ~34% of N_2 will dissolve in methane. We suspect the large difference in the solubility is caused due to the involvement of N_2 into the system. However, Stevenson et al. (2015) built a model that estimates the solubility of acetylene in CH_4–N_2 (90–10%) system of 1.03×10^{-2}, which is indeed in accord with our experiential values. Stevenson et al. (2015) uses the model parameters estimated by Szczepaniec-Cięciak et al. (1978) which calculated the solubility of acetylene in liquid methane using Preston-Prausnitz method of 5.8×10^{-2}. Again, these estimated values are in accord with the solubility values measured in this study. Our measurements conclude that if N_2 dissolution is taken into account it significantly increases the solubility of acetylene in liquid methane.

4. DERIVATION OF INTERACTION COEFFICIENTS (K_{IJ})

Similar to what has been done in Cordier et al. (2013) and Cordier et al. (2016), we have performed theoretical solubility estimations by solving the equation

$$\ln \Gamma_i X_{i,sat} = -\frac{\Delta H_{i,m}}{R T_{i,m}} \left(\frac{T_{i,m}}{T} - 1 \right) \quad (2)$$

where $X_{i,sat}$ is the mole fraction of the compound i at saturation and Γ_i is the activity co-efficient of the considered species. $T_{i,m}$ and $\Delta H_{i,m}$ are melting temperature and enthalpy of melting respectively. The temperature of the system is denoted T, and R is the gas constant. This relation can be found, for instance, in the textbook by Poling et al. (2001). The physical meaning of Eq. (2) is that a thermodynamic equilibrium between the considered precipitated solid i and the liquid solution - Eq. (2) is nothing more than an equality of chemical potential.

Here, the activity coefficient Γ_i that appears in Eq. (2) is computed with the help of PC-SAFT 1 (Gross and Sadowski, 2001). This approach is widely used in chemical engineering and has been successfully introduced in planetology by Tan et al. (2013) and Luspay-Kuti et al. (2015).

Retour à la table des matières : p. v

For this application to solid-liquid equilibrium (SLE), the activity coefficient is written as the ratio Γ_i $\Gamma_i = \varnothing_i^L/\varnothing_i^{L0}$, where $\varnothing_i^L$ is the fugacity coefficient of the species i and $\varnothing_i^{L0}$ is the fugacity coefficient of the pure subcooled liquid of the same compound. The PC-SAFT is extended to mixtures using the Berthelot-Lorentz combining rule for the dispersive energy, resulting in a single binary parameter k_{ij}. The values of all these k_{ij}'s are determined by comparison with experimental results and are shown in Table 1.

5. DISCUSSION

Cassini spacecraft revealed the existence of several different lakes in the Polar Regions of Titan. Lakes cover an area of 400,000 km^2 (Hayes et al., 2008; Sotin et al., 2012) and include small lakes of 1–10 km wide with circular steep-sided depressions, and medium lakes 20–50 km wide. Some of the depressions are completely filled with material that appears dark in radar measurements, which are therefore interpreted as a liquid. Other depressions appear to reflect more radar energy than surrounding areas, which is consistent with empty or partially filled depressions, implying the presence of solid particles after the liquid is evaporated from the lakes (Hayes et al., 2008). Solid particles that remain in the dry lakebed are interpreted as evaporites of solid hydrocarbons dissolved in the lakes; acetylene and ethylene are the most probable evaporite candidates (Cordier et al., 2016). depressions also include fluvial channels carved into the solid surface by liquid runoff implying a superficial soluble layer. The solubility of acetylene and ethylene in liquid methane and ethane provide a limit to the estimation of the amount of acetylene and ethylene present in the lakes and evaporite deposits in dry lakes. However, other candidates such as benzene, argon, and naphthalene which are also soluble in methane and ethane can also be present in the evaporite-rich area. The experiments to determine the solubility of benzene, naphthalene, and biphenyl in liquid ethane have recently been reported by Malaska and Hodyss (2014).

The atmospheric mixing ratio of acetylene at lower stratosphere (~120 km) is 2.2×10^{-6} mole fractions at 54° S also consistent with the measurements by the GCMS instrument on the Huygens probe and 5.2×10^{-6} mole fractions at 69° N measured from 2006–2007 *Cassini* data by Vinatier et al. (2010). The values measured by the Ion and Neutral Mass Spectrometer (INMS) instrument at 1100 km is 2.82×10^{-4} (Waite et al., 2005) and at 300 km is 5.0×10^{-6} (Vinatier et al., 2007). For ethylene, the atmospheric mixing ratio of ethylene at lower stratosphere (~120 km) is 1.4×10^{-7} mole fractions at 54° S and 2.7×10^{-7} mole fractions at 69° N measured from 2006–2007 *Cassini* data by Vinatier et al. (2010). The values measured by the Ion and Neutral Mass Spectrometer (INMS) instrument at 1100 km is 1.0×10^{-3} (Waite et al., 2005) and at 300 km is 3.0×10^{-7} (Vinatier et al., 2007). The values are surely an upper limit as we assume that the atmospheric mole fraction at the ground is similar to that at 120 km and the acetylene and ethylene flux is distributing evenly across the Titan surface. The GCMS instrument on the Huygens probe could only detect acetylene at a mole fraction of 2.2×10^{-6} in the troposphere (Niemann et al., 2010), but could not detect the ethylene as it was below the detection threshold on the instrument. We use these values in our model, but it should be clearly noted that the values used are suspected to decrease close to the surface.

Using a model constructed by Hodyss et al. (2013) similar to the model used by Cordier et al. (2009) based on the assumption that the lakes are in equilibrium with the atmosphere, we can predict the composition of lakes for comparison with acetylene and ethylene values at saturation. The atmospheric abundance of acetylene and ethylene at 120 km, suggests that acetylene and ethylene could be concentrated in the lakes at mole fractions of 5.32 and 3.9×10^{-3}, respectively. The geochemical models such as Tan et al. (2013) and Glein and Shock (2013) clearly indicate that the atmospheric mole fraction changes with the altitude. Both acetylene and ethylene abundance will decrease close to the surface due to condensation and other chemical reaction. We use the lower stratospheric values to estimate the upper limit of the solutes in the lakes directly dissolved from the atmosphere.

From the solubility values of our experiments, we can calculate the amount of acetylene and ethylene dissolved in the lakes of Titan for different depths. A simple model

Table 1
The interaction coefficient (K_{ij}) values derived from experimental solubilities obtained by using PC-SAFT model. These results are not to be understood/considered as pure theoretical predictions.

Temperature (T) = 90 K
Pressure (P) = 1.5 bar

Solvent (i)	Solute (j)	Solubility value (mole fraction)	K_{ij}	References
CH_4	C_2H_4	0.320000	0.012	Tan et al. (2013)
CH_4	C_2H_4	0.420000	0.000	No interaction
CH_4	C_2H_4	0.560000	−0.034	This study
C_2H_6	C_2H_4	0.495000	0.010	Tan et al. (2013)
C_2H_6	C_2H_4	0.480000	0.012	This study
CH_4	C_2H_2	0.049000	−0.081	This study
CH_4	C_2H_2	0.000048	0.115	Neumann and Mann (1969)
CH_4	C_2H_2	0.000082	0.100	Tan et al. (2013)
C_2H_6	C_2H_2	0.000520	0.105	Tan et al. (2013)
C_2H_6	C_2H_2	0.480000	−0.140	This study

Retour à la table des matières : p. v

was adapted from Hodyss et al. (2013) where the volume of lakes can be approximated by knowing the surface area (S_{lakes}) of the lakes and the average depth (d_{lakes}). Titan's total surface of lakes covers ~400,000 km^2 (Stofan et al., 2007; Hayes et al., 2008; Sotin et al., 2012). Knowing all these parameters, we can calculate the total number of moles of hydrocarbons (N_{hydro}) as:

$$N_{hydro} = \frac{m_{hydro}}{M_{hydro}} = \frac{\rho_{hydro} V_{hydro}}{M_{hydro}} = \frac{\rho_{hydro} S_{hydro} d_{lakes}}{M_{hydro}} \quad (3)$$

where m_{hydro} is the mass of hydrocarbon contained in the lakes, M_{hydro} is their molar mass, and ρ_{hydro} is the liquid hydrocarbon density at Titan's conditions. The mass of acetylene and ethylene dissolved in the lakes was calculated as follows:

$$m_x = M_x N_x = M_x X_x N_{hydro}$$
$$m_x = M_x X_x \frac{\rho_{hydro} S_{hydro} d_{lakes}}{M_{hydro}} \quad (4)$$

where N_x is the number of moles of acetylene or ethylene dissolved in the lakes and M_x is the molar mass. The values of the parameters used in the calculation are as follows: the typical density of the lakes $\rho_{hydro} = 584$ kg m^{-3}, M_x for acetylene = 26 g/mol, M_x for ethylene = 28 g/mol, $S_{lakes} = 4.2 \times 10^{11}$ m^2. We assume that lakes are mainly composed of a mixture of methane and ethane, therefore from Luspay-Kuti et al. (2015) we assume a 65% ethane - 35% methane composition for the lake mixture. This assumption matches well those expected from *Cassini* data (Hayes et al., 2011) with a molar mass of $M_{hydro} = 25.1$ g/mol.

With all the parameters fixed, we calculated the mass of acetylene dissolved in the lakes as a function of their depth. We computed the dissolved mass calculation for several molar fractions of acetylene in the lakes: (1) 4.9×10^{-2}, the saturation value measured in liquid methane; (2) 48×10^{-2}, the saturation value measured in liquid ethane; (3) 5.8×10^{-2}, based on the solubility value in methane by Szczepaniec-Cięciak et al. (1978); (4) 2.0×10^{-2}, based on the model assuming 85% methane and 15% nitrogen mixture by Stevenson et al. (2015); 95) 1.16×10^{-2}, based on the model of Cordier et al. (2012); (6) 6.8×10^{-4}, based on Preston and Praustnitz method by Neumann and Mann (1969); (7) 1.8×10^{-2}, based on MVL model by Glein and Shock (2013). The results of the calculations are shown in Fig. 8. The amount of acetylene dissolved in the lakes is directly proportional to the lake depth. The increase in lake depth or more liquid in the lakes will result in high solubility of acetylene considering molar fractions of acetylene in both methane and ethane are provided by previous studies and derived from our experimental saturation measurements. Depending on the liquid composition, acetylene will dissolve almost an order of magnitude more in ethane-rich lakes than methane-rich lakes.

For ethylene, the dissolved mass in the lake is also plotted as a function of lake depth (Fig. 9). We computed the dissolved mass calculations for different molar fractions of ethylene in the lakes. As mentioned above, ethylene has been ignored in major atmospheric models that suggest

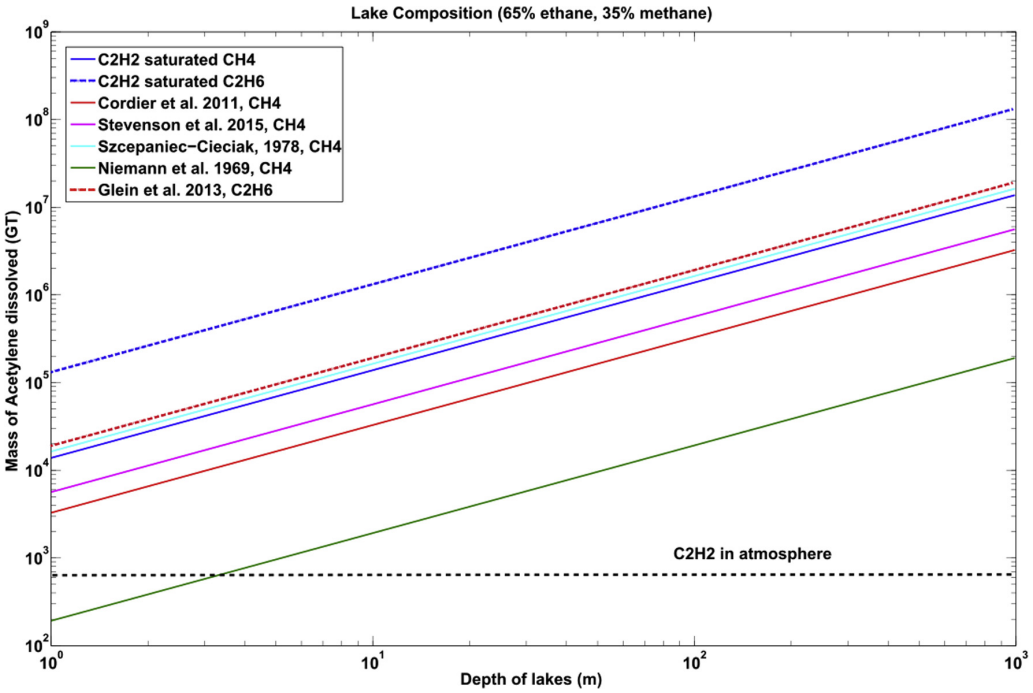

Fig. 8. Mass of acetylene dissolved in liquid as a function of depth of lakes compared to several theoretical values in the literature. The thick black dashed line indicates the amount of acetylene present in the atmosphere.

Retour à la table des matières : p. v

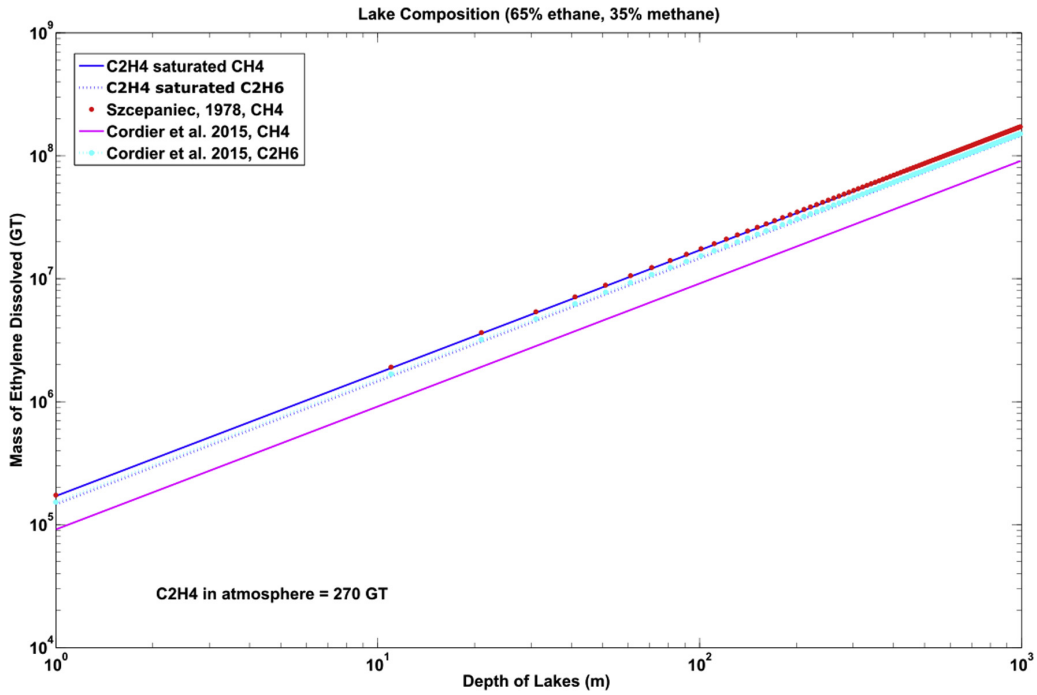

Fig. 9. Mass of ethylene dissolved in liquid as a function of depth of lakes compared to the theoretical values.

that ethylene is destroyed in the lower stratosphere (Lavvas et al., 2008a, 2008b). Despite the fact that ethylene is considered not rich on the surface it may still be dissolved directly from the atmosphere in the lakes as a major component (Cordier et al., 2013). We consider several available molar fraction values on ethylene in methane and ethane: (1) 5.6×10^{-1}, the saturation value measured in methane; (2) 4.8×10^{-1}, the saturation value measured in ethane; (3) 5.74×10^{-1}, based on the solubility value in methane by Szczepaniec-Cięciak et al. (1978); (4) 5.0×10^{-1}, based on the model by Cordier et al. (2016) in liquid ethane; (5) 3.0×10^{-1}, based on the model by Cordier et al. (2016) in liquid methane. All these values are in accord with the solubility value of ethylene measured in this study.

The calculations are shown in Figs. 8 and 9 and imply the following: First, assuming the lakes are in equilibrium with the atmosphere, the value of 6.8×10^{-4} mole fractions (Neumann and Mann, 1969) of acetylene imply that lakes 1–5 m deep are saturated with acetylene and will dissolve equivalent of entire Titan's atmospheric acetylene. Second, the solubility values from this study implies that small lakes and even small hydrocarbon liquid pockets trapped within the crust could also be an important reservoir of acetylene and ethylene. Third, our Solubility values imply, that no lakes on Titan will be saturated with acetylene or ethylene because there is not enough acetylene or ethylene present in the atmosphere. Fourth, large solubility of acetylene in liquid hydrocarbons measured in this study implies that deeper lakes would be rich in acetylene and ethylene allowing the dissolution from the atmosphere and via surface processes. (5) These calculations suggest that the temporal evolution of the lakes (evaporation, and condensation) over a season and geologic history on Titan may influence the atmospheric abundance of soluble volatiles. The soluble volatiles may play an important role in shaping the Titan surface and contribute to its hydrocarbon cycle. (6) We assume that acetylene or ethylene dissolve directly from the atmosphere when in equilibrium with lakes, however, if acetylene or ethylene is present on the surface, geological processes such as surface erosion will also contribute to the addition of acetylene and ethylene into the lakes; therefore, if those surface processes exist, deeper lakes could be saturated.

5.1. Formation of acetylene/ethylene top layer evaporites

Barnes et al. (2011) interpreted spatially-coherent, bright units at 5 μm in Cassini VIMS observation as surface units that originated from evaporation of the solvent yielding to the saturation of the dissolved solutes. If this idea is correct, the observed bright region at 5 μm may relate to an evaporitic top layer. Previously, Titan has been geomorphologically identified as evaporitic and evaporite candidates cover ~1% of Titan's surface (Mackenzie et al., 2014). According to Cordier et al. (2013) the top layers of the evaporites should be composed of the most soluble species; however, the chemical composition of these possible evaporites is still unknown. The only solutes species undergoing enrichment in the surface evaporites layer were the solutes with high solubility's and have high overall initial abundance in lakes.

According to calculations by Cordier et al. (2013) of the chemical composition of the lake evaporites, acetylene tops the candidate list, whereas ethylene was not considered in

Retour à la table des matières : p. v

the model. Our, measurement of high acetylene solubility in liquid methane and ethane reinforce this conclusion about acetylene as a good candidate for the composition of the top layer of evaporite. Since ethylene has high solubility and assuming the ethylene dissolves in the lakes when in equilibrium with the atmosphere, it could also have a major role in the composition of the top layer of evaporate. Hypothetically, ethylene can be present on the surface in dry lake beds and near evaporite deposits. Cordier et al. (2013) predict ~50% increase in the formation of acetylene evaporites in the top layer when a methane-poor solvent case was considered. These results are consistent with our lab measurements as acetylene is ~10 times more soluble in ethane. Ethane rich lakes have almost an order of magnitude higher potential to dissolve acetylene.

6. CONCLUSIONS

In this study, we have measured the solubilities of acetylene and ethylene in liquid methane and ethane. Theoretically, acetylene is expected to be more soluble in ethane than in methane, although there have been large differences between numerical models that predict the solubility of acetylene in liquid methane and ethane. Models predict a range of acetylene solubility increase by a factor from ~3 to ~300 in ethane than in methane. Our results indicate that acetylene is ~10 times more soluble in ethane than in methane. Ethylene, on the other hand, has similar solubility's in both liquid methane and ethane. Our results also indicate that ethylene is almost an order of magnitude more soluble in liquid hydrocarbons than acetylene. These values are in accordance with theoretical values predicted and derived from various models.

The dissolution rate of acetylene and ethylene in methane and ethane implies that large lakes on Titan are not saturated. However, the calculations also suggest that the evolution of lakes over seasons and geological time scale may influence the overall abundance of acetylene and ethylene in the lakes, at the surface, and in the atmosphere. The high solubility values also indicate that lakes contain several orders of magnitude less acetylene and ethylene than their saturation values. The solubility values only estimate the amount of acetylene and ethylene present in lakes by using the measurements of the mixing ratio from the atmosphere. Future measurement by *Cassini* and other planned *in situ* missions could provide further insights into the abundance of these solutes in the lakes and their abundance at the surface.

ACKNOWLEDGMENTS

This work was funded by NASA Outer Planet Research Program #NNX10AE10G and NASA Cassini subcontract # 1416996.

REFERENCES

Adams J. B., Smith M. O. and Johnson P. E. (1986) Spectral mixture modeling: a new analysis of rock and soil types at the Viking Lander 1 site. *J. Geophys. Res.: Solid Earth (1978–2012)* **91**, 8098–8112.

Atreya S. K., Adams E. Y., Niemann H. B., Demick-Montelara J. E., Owen T. C., Fulchignoni M., Ferri F. and Wilson E. H. (2006) Titan's methane cycle. *Planet. Space Sci.* **54**, 1177–1187. http://dx.doi.org/10.1016/j.pss.2006.05.028.

Barnes J. W., Bow J., Schwartz J., Brown R. H., Soderblom J. M., Hayes A. G., Vixie G., Mouélic S. L., Rodriguez S., Sotin C., Jaumann R., Stephan K., Soderblom L. A., Clark R. N., Buratti B. J., Baines K. H. and Nicholson P. D. (2011) Organic sedimentary deposits in Titan's dry lakebeds: probable evaporite. *Icarus* **216**, 136–140. http://dx.doi.org/10.1016/j.icarus.2011.08.022.

Battino R., Rettich T. R. and Tominaga T. (1984) The solubility of nitrogen and air in liquids. *J. Phys. Chem. Ref. Data* **13**, 563–600.

Bourgeois, O., Lopez, T., Le Mouélic, S., Fleurant, C., Tobie, G., Le Corre, L., Le Deit, L., Sotin, C., Bodeur, Y., (2008). A surface dissolution/precipitation model for the development of lakes on titan, based on an arid terrestrial analogue: the pans and calcretes of etosha (Namibia). In: Lunar and Planetary Science Conference, Lunar and Planetary Science Conference. p. 1733.

Chevrier, V. F., Luspay-Kuti, A., Singh, S., (2015). Experimental study of nitrogen dissolution in methane-ethane mixtures under titan surface conditions. In: Lunar and Planetary Science Conference, Lunar and Planetary Science Conference. p. 2763.

Clark R. N., Curchin J. M., Barnes J. W., Jaumann R., Soderblom L., Cruikshank D. P., Brown R. H., Rodriguez S., Lunine J., Stephan K., Hoefen T. M., Le Mouélic S., Sotin C., Baines K. H., Buratti B. J. and Nicholson P. D. (2010) Detection and mapping of hydrocarbon deposits on Titan. *J. Geophys. Res.: Planets* **115**. http://dx.doi.org/10.1029/2009JE003369.

Combe J.-P., Mouélic S. L., Sotin C., Gendrin A., Mustard J. F., Deit L. L., Launeau P., Bibring J.-P., Gondet B., Langevin Y. and Pinet P. (2008) Analysis of OMEGA/mars express data hyperspectral data using a multiple-endmember linear spectral unmixing model (MELSUM): methodology and first results. *Planet. Space Sci.* **56**, 951–975. http://dx.doi.org/10.1016/j.pss.2007.12.007.

Cordier D., Mousis O., Lunine J. I., Lavvas P. and Vuitton V. (2009) An estimate of the chemical composition of Titan's lakes. *Astrophys. J. Lett.* **707**, L128.

Cordier D., Mousis O., Lunine J. I., Lebonnois S., Rannou P., Lavvas P., Lobo L. Q. and Ferreira A. G. M. (2012) Titan's lakes chemical composition: sources of uncertainties and variability. *Planet. Space Sci.* **61**, 99–107. http://dx.doi.org/10.1016/j.pss.2011.05.009.

Cordier D., Barnes J. W. and Ferreira A. G. (2013) On the chemical composition of Titan's dry lakebed evaporites. *Icarus* **226**, 1431–1437.

Cordier D., Cornet T., Barnes J. W., MacKenzie S. M., Le Bahers T., Nna-Mvondo D. and Ellipsis Ferreira A. G. (2016) Structure of Titan's evaporites. *Icarus* **270**, 41–56. http://dx.doi.org/10.1016/j.icarus.2015.12.034.

Cornet T., Cordier D., Bahers T. L., Bourgeois O., Fleurant C., Mouélic S. L. and Altobelli N. (2015) Dissolution on titan and on earth: toward the age of Titan's karstic landscapes. *J. Geophys. Res.: Planets* **120**, 1044–1074. http://dx.doi.org/10.1002/2014JE004738.

Cottini V., Nixon C. A., Jennings D. E., de Kok R., Teanby N. A., Irwin P. G. J. and Flasar F. M. (2012) Spatial and temporal variations in Titan's surf ace temperatures from Cassini CIRS observations. *Planet. Space Sci.* **60**(1), 62–71. http://dx.doi.org/10.1016/j.pss.2011.03.015.

Coustenis A., Bézard B. and Gautier D. (1989) Titan's atmosphere from voyager infrared observations: I. The gas composition of Titan's equatorial region. *Icarus* **80**, 54–76. http://dx.doi.org/10.1016/0019-1035(89)90161-9.

Retour à la table des matières : p. v

Coustenis A. and Hirtzig M. (2009) Cassini-Huygens results on Titan's surface. *Res. Astron. Astrophys.* **9**, 249.

Coustenis A., Jennings D. E., Nixon C. A., Achterberg R. K., Lavvas P., Vinatier S., Teanby N. A., Bjoraker G. L., Carlson R. C., Piani L., Bampasidis G., Flasar F. M. and Romani P. N. (2010) Titan trace gaseous composition from CIRS at the end of the Cassini-Huygens prime mission. *Icarus* **207**, 461–476. http://dx.doi.org/10.1016/j.icarus.2009.11.027.

Dekok R., Irwin P., Teanby N., Nixon C., Jennings D., Fletcher L., Howett C., Calcutt S., Bowles N. and Flasar F. (2007) Characteristics of Titan's stratospheric aerosols and condensate clouds from Cassini CIRS far-infrared spectra. *Icarus* **191**, 223–235. http://dx.doi.org/10.1016/j.icarus.2007.04.003.

Dubouloz N., Raulin F., Lellouch E. and Gautier D. (1989) Titan's hypothesized ocean properties: the influence of surface temperature and atmospheric composition uncertainties. *Icarus* **82**, 81–96. http://dx.doi.org/10.1016/0019-1035(89)90025-0.

Farnsworth, K., McMahon, Z., Laxton, D., Chevrier, V., Luspay-Kuti, A., Singh, S., (2016). Experimental study of nitrogen dissolution in methane-ethane mixtures under titan surface conditions. In: Lunar and Planetary Science Conference, Lunar and Planetary Inst. Technical Report. p. 2380.

Glein C. R. and Shock E. L. (2013) A geochemical model of non-ideal solutions in the methane–ethane–propane–nitrogen–acetylene system on Titan. *Geochim. Cosmochim. Acta* **115**, 217–240. http://dx.doi.org/10.1016/j.gca.2013.03.030.

Griffith C. A., Owen T. and Wagener R. (1991) Titan's surface and troposphere, investigated with ground-based, near-infrared observations. *Icarus* **93**, 362–378. http://dx.doi.org/10.1016/0019-1035(91)90219-J.

Gross J. and Sadowski G. (2001) Perturbed-chain SAFT: an equation of state based on a perturbation theory for chain molecules. *Ind. Eng. Chem. Res.* **40**, 1244–1260. http://dx.doi.org/10.1021/ie0003887.

Hayes A., Aharonson O., Callahan P., Elachi C., Gim Y., Kirk R., Lewis K., Lopes R., Lorenz R., Lunine J., Mitchell K., Mitri G., Stofan E. and Wall S. (2008) Hydrocarbon lakes on Titan: distribution and interaction with a porous regolith. *Geophys. Res. Lett.* **35**. http://dx.doi.org/10.1029/2008GL033409.

Hayes A. G., Aharonson O., Lunine J. I., Kirk R. L., Zebker H. A., Wye L. C., Lorenz R. D., Turtle E. P., Paillou P., Mitri G., Wall S. D., Stofan E. R., Mitchell K. L. and Elachi C. (2011) Transient surface liquid in Titan's polar regions from Cassini. *Icarus* **211**, 655–671. http://dx.doi.org/10.1016/j.icarus.2010.08.017.

Hodyss R., Choukroun M., Sotin C. and Beauchamp P. (2013) The solubility of ^{40}Ar and ^{84}Kr in liquid hydrocarbons: implications for Titan's geological evolution: ^{40}Ar solubility in liquid hydrocarbons. *Geophys. Res. Lett.* **40**, 2935–2940. http://dx.doi.org/10.1002/grl.50630.

Janssen M. A., Lorenz R. D., West R., Paganelli F., Lopes R. M., Kirk R. L., Elachi C., Wall S. D., Johnson W. T. K., Anderson Y., Boehmer R. A., Callahan P., Gim Y., Hamilton G. A., Kelleher K. D., Roth L., Stiles B. and Le Gall A. (2009) Titan's surface at 2.2-cm wavelength imaged by the Cassini RADAR radiometer: calibration and first results. *Icarus* **200**, 222–239. http://dx.doi.org/10.1016/j.icarus.2008.10.017.

Jennings D. E., Flasar F. M., Kunde V. G., Samuelson R. E., Pearl J. C., Nixon C. A., Carlson R. C., Mamoutkine A. A., Brasunas J. C., Guandique E., Achterberg R. K., Bjoraker G. L., Romani P. N., Segura M. E., Albright S. A., Elliott M. H., Tingley J. S., Calcutt S., Coustenis A. and Courtin R. (2009) Titan's surface brightness temperatures. *Astrophys. J.* **691**, L103–L105. http://dx.doi.org/10.1088/0004-637X/691/2/L103.

Lavvas P. P., Coustenis A. and Vardavas I. M. (2008a) Coupling photochemistry with haze formation in Titan's atmosphere, Part II: Results and validation with Cassini/Huygens data. *Planet. Space Sci.* **56**, 67–99. http://dx.doi.org/10.1016/j.pss.2007.05.027.

Lavvas P. P., Coustenis A. and Vardavas I. M. (2008b) Coupling photochemistry with haze formation in Titan's atmosphere, Part I: Model description. *Planet. Space Sci.* **56**, 27–66. http://dx.doi.org/10.1016/j.pss.2007.05.026.

Lopes R. M. C., Mitchell K. L., Stofan E. R., Lunine J. I., Lorenz R., Paganelli F., Kirk R. L., Wood C. A., Wall S. D., Robshaw L. E., Fortes A. D., Neish C. D., Radebaugh J., Reffet E., Ostro S. J., Elachi C., Allison M. D., Anderson Y., Boehmer R., Boubin G., Callahan P., Encrenaz P., Flamini E., Francescetti G., Gim Y., Hamilton G., Hensley S., Janssen M. A., Johnson W. T. K., Kelleher K., Muhleman D. O., Ori G., Orosei R., Picardi G., Posa F., Roth L. E., Seu R., Shaffer S., Soderblom L. A., Stiles B., Vetrella S., West R. D., Wye L. and Zebker H. A. (2007) Cryovolcanic features on Titan's surface as revealed by the Cassini Titan Radar Mapper. *Icarus* **186**, 395–412. http://dx.doi.org/10.1016/j.icarus.2006.09.006.

Lorenz R. D. and Lunine J. I. (1997) Titan's surface reviewed: the nature of bright and dark terrain. *Planet. Space Sci.* **45**, 981–992. http://dx.doi.org/10.1016/S0032-0633(97)00087-1.

Lorenz R. D., Young E. F. and Lemmon M. T. (2001) Titan's smile and collar: HST observations of seasonal change 1994–2000. *Geophys. Res. Lett.* **28**, 4453–4456. http://dx.doi.org/10.1029/2001GL013728.

Lorenz R. D., Niemann H. B., Harpold D. N., Way S. H. and Zarnecki J. C. (2006) Titan's damp ground: constraints on titan surface thermal properties from the temperature evolution of the Huygens GCMS inlet. *Meteorit. Planet. Sci.* **41**, 1705–1714.

Lunine J. I., Stevenson D. J. and Yung Y. L. (1983) Ethane Ocean on titan. *Science* **222**, 1229–1230. http://dx.doi.org/10.1126/science.222.4629.1229.

Luspay-Kuti A., Chevrier V. F., Wasiak F. C., Roe L. A., Welivitiya W. D. D. P., Cornet T., Singh S. and Rivera-Valentin E. G. (2012) Experimental simulations of CH_4 evaporation on titan: CH_4 evaporation on titian. *Geophys. Res. Lett.* **39**. http://dx.doi.org/10.1029/2012GL054003.

Luspay-Kuti A., Chevrier V. F., Cordier D., Rivera-Valentin E. G., Singh S., Wagner A. and Wasiak F. C. (2015) Experimental constraints on the composition and dynamics of Titan's polar lakes. *Earth Planet. Sci. Lett.* **410**, 75–83. http://dx.doi.org/10.1016/j.epsl.2014.11.023.

MacKenzie S. M., Barnes J. W., Sotin C., Soderblom J. M., Le Mouélic S., Rodriguez S., Baines K. H., Buratti B. J., Clark R. N., Nicholson P. D. and McCord T. B. (2014) Evidence of Titan's climate history from evaporite distribution. *Icarus* **243**, 191–207. http://dx.doi.org/10.1016/j.icarus.2014.08.022.

Malaska M. J. and Hodyss R. (2014) Dissolution of benzene, naphthalene, and biphenyl in a simulated Titan lake. *Icarus* **242**, 74–81. http://dx.doi.org/10.1016/j.icarus.2014.07.022.

Mitri G., Showman A. P., Lunine J. I. and Lorenz R. D. (2007) Hydrocarbon lakes on Titan. *Icarus* **186**, 385–394. http://dx.doi.org/10.1016/j.icarus.2006.09.004.

Neumann A. and Mann R. (1969) Die Löslichkeit von festem Acetylen in flüssigen Methan/Äthylen-Mischungen. *Chem. Ing. Tec.* **41**, 708–711.

Niemann H. B., Atreya S. K., Bauer S. J., Carignan G. R., Demick J. E., Frost R. L., Gautier D., Haberman J. A., Harpold D. N., Hunten D. M., Israel G., Lunine J. I., Kasprzak W. T., Owen T. C., Paulkovich M., Raulin F., Raaen E. and Way S. H. (2005) The abundances of constituents of Titan's atmosphere from the GCMS instrument on the Huygens probe. *Nature* **438**, 779–784. http://dx.doi.org/10.1038/nature04122.

Niemann H. B., Atreya S. K., Demick J. E., Gautier D., Haberman J. A., Harpold D. N., Kasprzak W. T., Lunine J. I., Owen T. C. and Raulin F. (2010) Composition of Titan's lower atmosphere

Retour à la table des matières : p. v

and simple surface volatiles as measured by the Cassini-Huygens probe gas chromatograph mass spectrometer experiment. *J. Geophys. Res.* **115**, E12006. http://dx.doi.org/10.1029/2010JE003659.

Owen T. and Niemann H. (2009) The origin of Titan's atmosphere: some recent advances. *Philos. Trans. R. Soc. A: Math., Phys. Eng. Sci.* **367**, 607–615. http://dx.doi.org/10.1098/rsta.2008.0247.

Poling B. E., Prausnitz J. M. and O'connell J. P., et al. (2001) *The Properties of Gases and Liquids*. McGraw-Hill, New York.

Raulin F. (1987) Organic chemistry in the oceans of Titan. *Adv. Space Res.* **7**, 71–81. http://dx.doi.org/10.1016/0273-1177(87)90358-9.

Roe H. G., de Pater I. and McKay C. P. (2004) Seasonal variation of Titan's stratospheric ethylene (C_2H_4) observed. *Icarus* **169**, 440–461. http://dx.doi.org/10.1016/j.icarus.2004.01.002.

Singh S., Cornet T., Chevrier V. F., Combe J.-P., McCord T. B., Roe L. A., Mouélic S. L., Menn E. L. and Wasiak F. C. (2015) Near-infrared spectra of liquid/solid acetylene under Titan relevant conditions and implications for Cassini/VIMS detections. *Icarus*. http://dx.doi.org/10.1016/j.icarus.2015.11.002.

Singh S., McCord T. B., Combe J.-P., Rodriguez S., Cornet T., Mouélic S. L., Clark R. N., Maltagliati L. and Chevrier V. F. (2016) Acetylene on titan's surface. *Astrophy. J.* **828**(2016), 55. http://dx.doi.org/10.3847/0004-637X/828/1/55.

Smith P. H., Lemmon M. T., Lorenz R. D., Sromovsky L. A., Caldwell J. J. and Allison M. D. (1996) Titan's surface, revealed by HST imaging. *Icarus* **119**, 336–349.

Smith N. S. and Raulin F. (1999) Modeling of methane photolysis in the reducing atmospheres of the outer solar system. *J. Geophys. Res.: Planets* **104**, 1873–1876. http://dx.doi.org/10.1029/1998JE900027.

Sotin C., Lawrence K. J., Reinhardt B., Barnes J. W., Brown R. H., Hayes A. G., Mouélic S. L., Rodriguez S., Soderblom J. M., Soderblom L. A., Baines K. H., Buratti B. J., Clark R. N., Jaumann R., Nicholson P. D. and Stephan K. (2012) Observations of Titan's Northern lakes at 5 μm: implications for the organic cycle and geology. *Icarus* **221**, 768–786. http://dx.doi.org/10.1016/j.icarus.2012.08.017.

Stephan K., Jaumann R., Brown R. H., Soderblom J. M., Soderblom L. A., Barnes J. W., Sotin C., Griffith C. A., Kirk R. L., Baines K. H., Buratti B. J., Clark R. N., Lytle D. M., Nelson R. M. and Nicholson P. D. (2010) Specular reflection on titan: liquids in kraken mare: specular reflection on titan. *Geophys. Res. Lett.* **37**. http://dx.doi.org/10.1029/2009GL042312.

Stevenson J. M., Fouad W. A., Shalloway D., Usher D., Lunine J., Chapman W. G. and Clancy P. (2015) Solvation of nitrogen compounds in Titan's seas, precipitates, and atmosphere. *Icarus* **256**, 1–12. http://dx.doi.org/10.1016/j.icarus.2015.04.019.

Stofan E. R., Elachi C., Lunine J. I., Lorenz R. D., Stiles B., Mitchell K. L., Ostro S., Soderblom L., Wood C., Zebker H., Wall S., Janssen M., Kirk R., Lopes R., Paganelli F., Radebaugh J., Wye L., Anderson Y., Allison M., Boehmer R., Callahan P., Encrenaz P., Flamini E., Francescetti G., Gim Y., Hamilton G., Hensley S., Johnson W. T. K., Kelleher K., Muhleman D., Paillou P., Picardi G., Posa F., Roth L., Seu R., Shaffer S., Vetrella S. and West R. (2007) The lakes of Titan. *Nature* **445**, 61–64. http://dx.doi.org/10.1038/nature05438.

Szczepaniec-Cięciak E., Dąbrowska B., Łagan J. M. and Wojtaszek Z. (1978) Estimation of the solubility of solidified substances in liquid methane by the preston-prausnitz method. *Cryogenics* **18**, 591–600. http://dx.doi.org/10.1016/0011-2275(78)90186-8.

Tan S. P., Kargel J. S. and Marion G. M. (2013) Titan's atmosphere and surface liquid: new calculation using statistical associating fluid theory. *Icarus* **222**, 53–72. http://dx.doi.org/10.1016/j.icarus.2012.10.032.

Tomasko M. G., Bézard B., Doose L., Engel S., Karkoschka E. and Vinatier S. (2008) Heat balance in Titan's atmosphere. *Planet. Space Sci.* **56**, 648–659. http://dx.doi.org/10.1016/j.pss.2007.10.012.

Vinatier S., Bézard B., Fouchet T., Teanby N. A., de Kok R., Irwin P. G. J., Conrath B. J., Nixon C. A., Romani P. N., Flasar F. M. and Coustenis A. (2007) Vertical abundance profiles of hydrocarbons in Titan's atmosphere at 15 S and 80 N retrieved from Cassini/CIRS spectra. *Icarus* **188**, 120–138. http://dx.doi.org/10.1016/j.icarus.2006.10.031.

Vinatier S., Bézard B., de Kok R., Anderson C. M., Samuelson R. E., Nixon C. A., Mamoutkine A., Carlson R. C., Jennings D. E., Guandique E. A., Bjoraker G. L., Flasar F. M. and Kunde V. G. (2010) Analysis of Cassini/CIRS limb spectra of Titan acquired during the nominal mission II: aerosol extinction profiles in the 600–1420 cm^{-1} spectral range. *Icarus* **210**, 852–866. http://dx.doi.org/10.1016/j.icarus.2010.06.024.

Vuitton V., Yelle R. V. and Anicich V. G. (2006) The nitrogen chemistry of Titan's upper atmosphere revealed. *Astrophys. J. Lett.* **647**, L175.

Waite J. H., Niemann H., Yelle R. V., Kasprzak W. T., Cravens T. E., Luhmann J. G., McNutt R. L., Ip W.-H., Gell D. and De La Haye V., et al. (2005) Ion neutral mass spectrometer results from the first flyby of Titan. *Science* **308**, 982–986.

Wasiak F. C., Luspay-Kuti A., Welivitiya W. D. D. P., Roe L. A., Chevrier V. F., Blackburn D. G. and Cornet T. (2013) A facility for simulating Titan's environment. *Adv. Space Res.* **51**, 1213–1220. http://dx.doi.org/10.1016/j.asr.2012.10.020.

Wilson E. H. (2004) Current state of modeling the photochemistry of Titan's mutually dependent atmosphere and ionosphere. *J. Geophys. Res.* **109**. http://dx.doi.org/10.1029/2003JE002181.

Yung Y. L. and DeMore W. D. (1999) *Photochemistry of Atmospheres, 456 pp*. Oxford University Press, New York.

Zarnecki J. C., Leese M. R., Hathi B., Ball A. J., Hagermann A., Towner M. C., Lorenz R. D., McDonnell J. A. M., Green S. F., Patel M. R., Ringrose T. J., Rosenberg P. D., Atkinson K. R., Paton M. D., Banaszkiewicz M., Clark B. C., Ferri F., Fulchignoni M., Ghafoor N. A. L., Kargl G., Svedhem H., Delderfield J., Grande M., Parker D. J., Challenor P. G. and Geake J. E. (2005) A soft solid surface on Titan as revealed by the Huygens surface science package. *Nature* **438**, 792–795. http://dx.doi.org/10.1038/nature04211.

Retour à la table des matières : p. v

4.13 Article sur la solubilité de l'éthylène et d'autres molécules dans l'argon liquide

Article

Applied Spectroscopy

Applied Spectroscopy
0(0) 1–8
© The Author(s) 2017
Reprints and permissions:
sagepub.co.uk/journalsPermissions.nav
DOI: 10.1177/0003702817702387
journals.sagepub.com/home/asp
SAGE

C–H Infrared Absorption and Solubility of Ethylene, Propyne, 2-methyl-2-butene, and 2-methyl-1, 3-butadiene (Isoprene) in Liquid Argon Solutions

Parashu R. Nyaupane[1], Helena Diez-y-Riega[1], Daniel Cordier[2], and Carlos E. Manzanares[1]

Abstract

The solubility of ethylene ($H_2C{=}CH_2$), propyne ($CH_3{-}C{\equiv}C{-}H$), 2-methyl-2-butene ($CH_3{-}CH{=}C(CH_3)_2$), and isoprene or 2-methyl-1, 3-butadiene ($H_2C{=}C(CH_3){-}CH{=}CH_2$) in liquid argon has been measured using mid-infrared and near-infrared (NIR) absorption. Spectra were recorded in the C–H infrared (IR) region. Spectra were obtained at increasing solution composition until the magnitude of the integrated absorption band reached a maximum value, indicating a saturated solution. The approximate experimental solubilities are: (600 ± 100) ppm at 92 K for ethylene, (22 ± 9) ppm at 100 K for propyne, (9 ± 5) ppm at 100 K for 2-methyl-2-butene, and (12 ± 2) ppm at 86 K for isoprene. The experimental solubility values at the corresponding temperature were used with solubility parameters of two separate models: the perturbed-chain statistical associating fluid theory (PC-SAFT) and the regular solution theory. Solvent–solute interaction parameters k_{12} (PC-SAFT) and ι_{12} (RST) were obtained for each solute in the presence of argon as the solvent. Data from experimental measurements are important for more realistic simulations of solubility of solids in cryogenic liquids.

Keywords

Solubility, infrared spectroscopy, unsaturated hydrocarbons, liquid argon, cryogenic

Date received: 17 January 2017; accepted: 21 February 2017

Introduction

The concentration of a compound in a saturated solution of a cryogenic solvent at a given temperature (solubility) is an important consideration in the design of heat exchangers and transport systems for cryogenic liquids.[1] The solubility of many organic molecules in cryogenic solvents have been discussed in the literature.[2,3] The spectroscopy of molecules in cryogenic solvents is an excellent technique to detect solute absorption bands. Generally, if the solvents used are noble gases or nitrogen they are transparent to infrared (IR), near-infrared (NIR), and visible electromagnetic radiation so there are no interfering solvent bands. Another advantage of the spectroscopic method is that in the rare occasions where the signal saturation occurs at high concentrations, it is not necessary to reduce the length of the cell used. For example, with a 5–10 cm length cell, if the solubility of the sample is less than 10 ppm (mole fraction) a fundamental IR absorption can be used to detect the solute, but if the solubility is 1000 ppm or higher, a weaker first overtone absorption of the solute will also be good for detection. In addition to solubility determinations, spectroscopic studies in cryogenic liquids at low temperatures produce simplification of the spectrum because of the collapse of the rotational distribution. Overlapping vibrational bands are resolved and visualization of hidden bands is then possible.

In our laboratory, the solubility of unsaturated hydrocarbons in cryogenic solutions has been determined by preparing solutions in liquid argon of increasing hydrocarbon

[1]Department of Chemistry & Biochemistry, Baylor University, Waco, TX, USA
[2]Groupe de Spectrométrie Moléculaire et Atmosphérique, Université de Reims Champagne-Ardenne, Reims, France

Corresponding author:
Carlos E. Manzanares, Department of Chemistry & Biochemistry, Baylor University, 101 Bagby Avenue, Baylor Sciences Building E-216, Waco, TX 76706, USA.
Email: Carlos_Manzanares@baylor.edu

composition and obtaining the absorption between 2000 cm^{-1} and 8000 cm^{-1}. In general, the integrated absorption of the selected C–H band increases in magnitude until it reaches a plateau that indicates that solute saturation has occurred. By observing absorption bands in the fundamental and overtone regions, it is possible to do the study selecting an overtone region even if the sample concentration is too large to saturate the absorption of the fundamental transition. This method of solubility determination has been successfully done with solutions of increasing concentrations of benzene in liquid methane or ethane as solvents.[4] The problem is that the mid-IR and NIR absorptions of the solvent (ethane or methane) interfere with the weak absorption bands of the solute at very low concentrations. For cases like this, the preferred spectroscopic region is between 200 nm and 900 nm. Electronic transitions of benzene produce absorption bands between 200 and 300 nm, completely separated from the solvent bands that appear only as C–H vibrational overtone transitions in the 600–900 nm region. Experimental determinations of solubility in cryogenic solvents are becoming important for more realistic simulations of the chemical composition, chemical reactions, and erosion processes that occur in the atmosphere and surface of satellites and planets of our outer solar system.[5–7] Experimental determination of solubility of solids in very dilute solutions at low temperatures is prone to technical difficulties. For this reason, some of the existing data need to be re-evaluated.

Experimental

A Thermo Nicolet (Nexus 670) Fourier transform infrared (FT-IR) spectrophotometer was used to obtain mid-IR and NIR spectra in the range of 2000–8000 cm^{-1}. The beamsplitter (XT-KBr), the deuterated triglycine sulfate detector with KBr window (DTGS–KBr), and the Ever-glow white light source were used to obtain the spectra over the entire range of wavenumbers. A cryostat, APD Cryogenics Helitran Model LT-3-110 system was used to achieve liquid argon temperature (80–100 K). The sample cell is made of a 5 cm (path length) brass block. The cell was equipped with silicon end windows (14 mm diameter) which were sealed with indium O rings and fastened to the cell with flanges. The cell was fastened to the cryostat cold head and suspended in a metal vacuum chamber which was fitted with two KBr windows parallel to and in line with the ones of the cell. The vacuum chamber was placed inside of the sample compartment of the FT-IR spectrometer and was aligned with the IR beam. Thermal isolation of the cell was achieved by evacuating ($<10^{-4}$ Torr) the metal chamber. The cell was connected to the external gas handling system through a small section of stainless steel tubing. Liquid nitrogen was used as coolant. A Scientific Instruments 9650 temperature controller and indicator was used to control the cell temperature. This unit feeds power to the heater resistance on the cryostat cold head and can hold and reproduce any dialed temperature from 300 to 2 K. For measuring the temperature of the cell, a sensor was attached to the middle of the cell body. The background data of empty cell at room temperature were collected with certain resolution and number of scans. The sample was introduced into the cell at room temperature and the pressure was measured with a capacitance manometer. The IR absorption spectrum was recorded (2000–8000 cm^{-1}). The cell was evacuated, closed, and cooled down to about 87 K. The argon gas was introduced into the cell through a gas handling manifold using a back pressure of about 25 psi and it immediately started condensing in the cell. After the cell was full and the temperature of the cell stabilized at desired value, the background data of liquid argon at that specific temperature were collected. The cell was then warmed up to room temperature, evacuated, filled with certain amount sample, closed, and cooled down to about 87 K. The argon gas was pressurized into the cell through the manifold using the same treatment and back pressure as for background data collecting. The immediate condensation of argon gas caused turbulence inside the cell that allowed the sample to dissolve without additional stirring. When the desired temperature of the cell was stabilized and the solution reached equilibrium (usually within 1 h), the IR spectrum was registered. The resolution and number of scans were 1 cm^{-1} and 200, respectively.

The concentrations of sample in solution were calculated as mole fraction (X_2) of the solute, using the ratio of molar densities

$$X_2 = \frac{n_2}{n_1 + n_2} = \frac{n_2/V}{n_{total}/V} \tag{1}$$

For very dilute solutions $(n_{total}/\mathrm{V}) \approx (n_1/V) = \rho_1$ is essentially the solvent molar density. Assuming the ideal gas approximation, the mole fraction (ppm) is calculated as:

$$X_2 = \frac{(P_2/RT_2)}{\rho_1(T)} \times 10^6 \tag{2}$$

where P_2 is the pressure (atm) of the sample in the cell at room temperature T_2, R is the gas constant 0.082 (L atm/mol K) and $\rho_1(T)$ is the density (mol/L) of liquid argon at the temperature T of the experiment $(\rho_1(86\mathrm{K}) = 35.3, \rho_1(92\mathrm{K}) = 34.5, \rho_1(100\mathrm{K}) = 32.9)$. The compounds: ethylene (C_2H_4) with a purity of 99.99 % was obtained from Matheson, propyne (C_3H_4) with a purity of 97% was obtained from Aldrich, 2-methyl-2-butene (C_5H_{10}) with a purity of 96% was obtained from Wiley organics, and 2-methyl-1,3-butadiene (C_5H_8) with a purity of 96% was obtained from Wiley organics. All of them were used without further purification. Argon gas with a purity of 99.9995% was ordered from Matheson.

Retour à la table des matières : p. v

Results

Ethylene absorption spectra of homogeneous solutions in liquid argon were recorded at 92 K. The maximum absorbance in the region of 2800–3100 cm^{-1} was above the limit for the instrument (Abs. = 10) at mole fractions above 100 ppm. For solubility determinations of ethylene, it was better to detect a weaker absorption in an overtone region. Each solution was prepared and several spectra were taken during 4 h to make sure that intensities of the bands did not change and the concentration of the sample in solution was under equilibrium conditions. Figure 1 (top) shows the C–H stretching bands of ethylene as a function of the wavenumber (5800–6300 cm^{-1}) for four different concentrations. The assignment of the bands has been given in a previous publication.[8] The strongest band in the spectra at 6143 cm^{-1} has been assigned as the combination band $\nu_5 + \nu_9$ of C_2H_4. The integrated absorbance of the band was obtained for seven different concentrations. A plot of integrated absorbance as a function of the mole fraction (ppm) is shown in Figure 1 (bottom). It is shown that the integrated absorbance reaches a saturated value for concentrations above 1000 ppm. For unsaturated solutions, the integrated absorbance increases linearly with mole fraction while for saturated solutions the integrated absorbance is approximately constant. The intersection of the two straight lines was taken as the solubility at the temperature of the experiment. The approximate solubility is (600 ± 100) ppm at 92 K.

Propyne absorption spectra of homogeneous solutions in liquid argon were recorded at 100 K. After each solution was prepared, several spectra were taken to make sure that intensities of the bands did not change and the

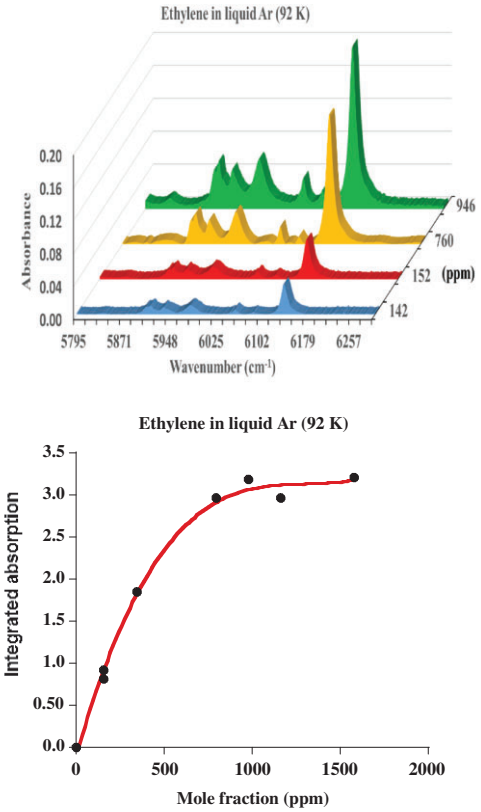

Figure 1. (Top) Absorption around the combination band ($\nu_5 + \nu_9$) of ethylene ($H_2C{=}CH_2$) in liquefied argon solution for several concentrations (mole fraction) at 92 K. (Bottom) Integrated absorbance of the region of 5800–6300 cm^{-1} as a function of the mole fraction in liquid argon.

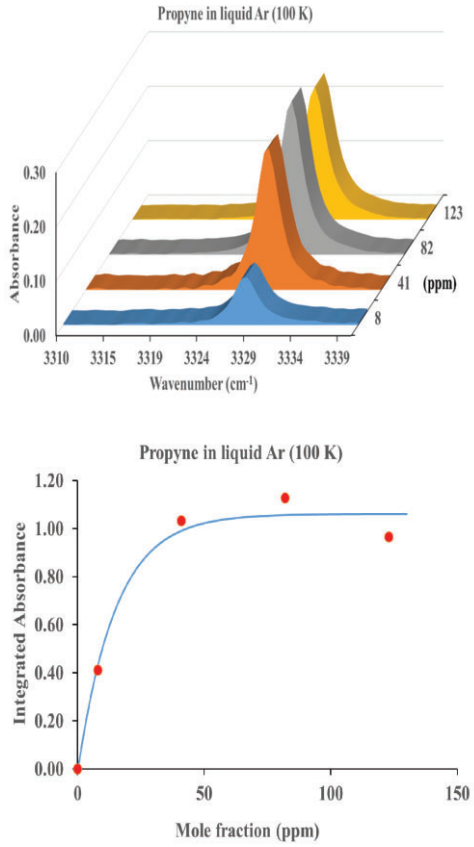

Figure 2. (Top) Fundamental C–H (acetylenic) absorption of propyne ($H{-}C{\equiv}C{-}CH_3$) in liquefied argon solution for several concentrations (mole fraction) at 100 K. (Bottom) Integrated absorbance of propyne as a function of the mole fraction in liquid argon.

Retour à la table des matières : p. v

concentration of the sample in solution was under equilibrium conditions. Figure 2 (top) shows the ≡C–H stretching band of propyne as a function of the wavenumber (3310–3340 cm^{-1}) for four different concentrations. The band in the spectra at 3329 cm^{-1} has been assigned as the C–H acetylenic (ν_1) of CH_3CC–H. The total integrated absorbance of the band was obtained for four different concentrations. A plot of integrated absorbance as a function of the mole fraction (ppm) is shown in Figure 2 (bottom). The approximate solubility is (22 ± 9) ppm at 100 K.

Recorded at 100 K, 2-methyl-2-butene absorption spectra of homogeneous solutions in liquid argon. The sample in solution was under equilibrium conditions. Figure 3 (top) shows the C–H stretching region of the spectrum of 2-methyl-2-butene (2800–3100 cm^{-1}) for five different concentrations. The bands in the spectra correspond to saturated and unsaturated C–H absorptions. The structure of 2-methyl-2-butene is CH_3–C=C(CH_3)$_2$. The total integrated absorbance of the entire band was obtained for six different concentrations. A plot of integrated absorbance as a function of the mole fraction (ppm) is shown in Figure 3 (bottom). The approximate solubility is (9 ± 5) ppm at 100 K.

Isoprene or 2-methyl-1,3-butadiene absorption spectra of homogeneous solutions in liquid argon were recorded at 86 K. The intensity of the bands did not change under equilibrium conditions. Figure 4 (top) shows the C–H absorption bands of isoprene as a function of the wavenumber (2800–3140 cm^{-1}) for three different concentrations. The bands in the spectra correspond to saturated and unsaturated C–H absorptions. The total integrated absorbance of the entire band was obtained for four different concentrations. A plot of integrated absorbance as a function of the mole fraction (ppm) is shown in Figure 4 (bottom). The approximate solubility is (12 ± 2) ppm at 86 K.

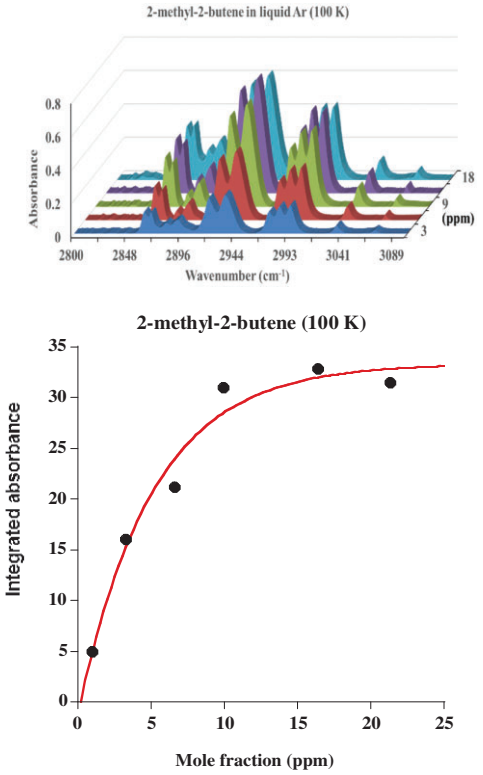

Figure 3. (Top) Fundamental C–H transition spectra of 2-methyl-2-butene (CH_3–C=C(CH_3)$_2$), dissolved in liquid argon for several concentrations (mole fraction) at 100 K. (Bottom) Integrated absorbance of 2-methyl-2-butene as a function of the mole fraction in liquid argon.

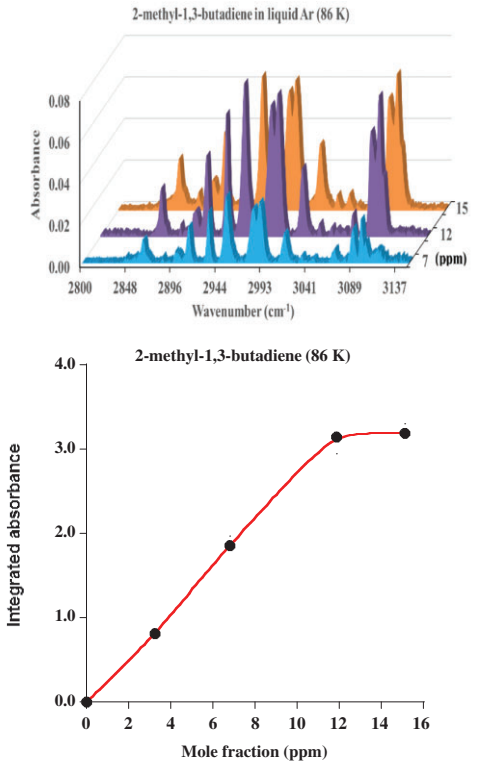

Figure 4. (Top) Fundamental C–H transition spectra of 2-methyl-1,3-butadiene dissolved in liquid argon for several concentrations (mole fraction) at 86 K. (Bottom) Integrated absorbance of 2-methyl-1,3-butadiene (2800–3140 cm^{-1}) as a function of the mole fraction in liquid argon.

Retour à la table des matières : p. v

Discussion

Thermodynamic Model of Solubility (PC-SAFT)

In order to evaluate the experimental solubilities with a theoretical model, we have adopted an approach similar to the one used by Cordier et al.[6,7] This method assumes a thermodynamic equilibrium between the solid phase of the considered species (2) and the quantity of matter, of the same compound, dissolved, here in liquid argon (1). The theoretical transcription of such an equilibrium is written as the equation:

$$ln\Gamma_2 X_{2,sat} = -\left(\frac{H_{2,m}}{RT_{2,m}}\right)\left(\frac{T_{2,m}}{T} - 1\right) \quad (3)$$

where $X_{2,sat}$ is the mole fraction of the solute (2) at saturation, Γ_2 is the activity coefficient, $T_{2,m}$ is the melting temperature and $(\Delta H_{2,m})$ is the enthalpy of melting of the considered species. The temperature of the system is denoted as T, and $R = 8.314$ J/mol K is the gas constant. This relation can be found in the textbook by Poling et al.[9] In Cordier et al.[6,7] the validity of Eq. 3 is discussed. The activity coefficient (Γ_2) that takes into account the effect of the solvent is calculated in the frame of the perturbed-chain statistical associating fluid theory (PC-SAFT)[10] which has been proven to be one of the most powerful equation of state for the liquid and vapor states. This theory has been used in many calculations related to thermodynamics of solutions. For this application to solid–liquid equilibrium, the activity coefficient is written as the ratio $\Gamma_2 = \Phi_2^L/\Phi_2^{Lo}$ where Φ_2^L is the fugacity coefficient of the solute (2) and Φ_2^{Lo} is the fugacity coefficient of the pure subcooled liquid solute. In the frame of the PC-SAFT, molecules are considered as "chains" of segments where each molecule is characterized by its pure component parameters: the number of segments m, the segment diameter σ (Å) and the energy of interaction ε/k_B (K). The PC-SAFT is extended to mixtures using the Berthelot-Lorentz combining rule for the dispersive energy, resulting in a single binary parameter k_{12}. The value of the parameters m, σ, and ε/k_B were estimated using the group contribution method developed by Tihic et al.[11] except in the case of C_2H_4 that was obtained from Tan et al.[5] who used the NIST database. The corresponding values are given in Table 1. The experimental solubilities were reproduced by adjusting the interaction parameter k_{12}. The interaction parameters obtained are valid only for the temperature used for the determination, since, the parameter is temperature dependent.

Regular Solution Theory

In the regular solution theory (RST) or Preston–Prausnitz solubility model,[9,12] the solubility term $(ln\Gamma_2 X_{2,sat})$ is calculated using Eq. 3 with the values for $(\Delta H_{2,m})$ and $T_{2,m}$ for the molecules from Yaws.[13] The activity coefficient is given by:

$$\ln \Gamma_2 = \frac{V_2\phi_1^2}{RT}((\delta_1 - \delta_2)^2 + 2l_{12}\delta_1\delta_2) \quad (4)$$

The molar volume of the solute is V_2, the volume fraction of the solvent in solution is ϕ_1, the solubility parameters are δ_1 (solvent) and δ_2 (solute). The term $\iota_{12}$is an interaction constant characteristic of a solvent–solute pair. Instead of calculating solubility parameters (δi) from the molar enthalpy of vaporization (ΔH^V), the temperature T and the liquid volume (V^L) of the component i (1 or 2) the method used by Preston–Prausnitz[12] is adopted. In order to find the reduced molar volumes of the solvent and solute, the reduced volume (V_R) surface corresponding to the table (A-1) given Preston and Prausnitz[12] was fitted to a two-dimensional (2D) polynomial with the variables: reduced temperature (T_R) and Pitzer's acentric factor (w).[13] The polynomial is:

$$\begin{aligned} V_R(T_R, w) = {} & 0.3236 + 0.1762T_R - 0.1564w \\ & - 0.3896T_R^2 + 0.004791T_Rw + 0.03122w^2 \\ & + 0.4611T_R^3 + 0.1839T_R^2w \\ & - 0.1408T_Rw^2 + 0.02778w^3 \end{aligned} \quad (5)$$

Once the reduced volumes are calculated for solvent and solute, the molar volumes V_1 and V_2 from $V_i = (V_R{}^*V_C)_i$ (i = 1 or 2) are obtained. Similarly, in order to find the reduced solubility parameters of the solvent and solute, the reduced solubility (δ_R) surface corresponding to

Table 1. Individual PC-SAFT parameters and derived interaction parameters from experimental solubilities.

Compound	Temperature (K)	$\Delta H_{2,m}$ (J/mol)	$T_{2,m}$ (K)	Molar mass (g/mol)	m	σ (Å)	ε/k_B (K)	Solubility	k_{12}
C_2H_4	92	3349.2	104.0	28.05	1.6018	3.4029	176.57	~600	0.197
C_3H_4	100	5348.0	170.4	40.06	1.8167	3.4710	229.66	~22	0.143
C_5H_{10}	100	7579.0	139.4	70.13	2.4470	3.7800	243.90	~9	0.119
C_5H_8 (isoprene)	86	4928.1	127.2	68.12	2.4160	3.7470	242.19	~12	0.096

Retour à la table des matières : p. v

Table 2. Interaction parameter (ι_{12}) calculated from experimental solubilities, molar volumes (V_i), and solubility parameters (δ_i). Molar volumes and solubility parameters were obtained from acentric factors (w), reduced volumes (V_R), and reduced temperatures (T_R) obtained from Eqs. 5 and 6.

T (K)	92		100		100		86	
Solvent (1)	Ar	—	Ar	—	Ar	—	Ar	—
Solute (2)	—	C_2H_4	—	C_3H_4	—	C_5H_{10}	—	C_5H_8
T_C (K)	150.7	282.3	150.7	402.4	150.7	470	150.7	478.6
P_C (atm)	48.0	51.1	48.0	57.0	48.0	34.7	48.0	42.5
V_C (cm^3/mol)	75.2	131	75.2	163.5	75.2	292	75.2	260.5
w	–0.002	0.086	–0.002	0.212	–0.002	0.287	–0.002	0.230
T_R	0.61	0.32	0.66	0.25	0.66	0.21	0.57	0.18
V_R	0.3909	0.3442	0.4029	0.3201	0.4029	0.3065	0.3830	0.3116
V_1 (cm^3/mol)	29.40	—	30.30	—	30.30	—	28.80	—
V_2 (cm^3/mol)	—	45.09	—	52.33	—	89.50	—	81.17
δ_R	0.98	1.28	0.94	1.49	0.94	1.59	1.01	1.55
δ_1 $(cal/cm^3)^{1/2}$	6.79	—	6.51	—	6.51	—	7.00	—
δ_2 $(cal/cm^3)^{1/2}$	—	9.15	—	11.25	—	9.37	—	10.1
ι_{12}	0.18		0.06		0.10		0.07	
$X_2^{(calc.)}$ ppm	~600		~19		~8		~12	
$X_2^{(exp.)}$ ppm	600 ± 100		22 ± 9		9 ± 5		12 ± 2	

Table 2 given Preston and Prausnitz[12] was fitted to a 2D polynomial with the variables: reduced temperature (T_R) and Pitzer's acentric factor (w).[13] The polynomial is:

$$\delta_R(T_R,w) = 1.3 + 2.01w - 0.561T_R - 2.009w^2 - 0.9183wT_R + 0.4607T_R^2 + 0.06944w^3 + 3.102w^2T_R - 1.054wT_R^2 - 0.6481T_R^3 \quad (6)$$

Once the reduced solubility parameters are calculated for solvent and solute, the solubility parameters δ_1 and δ_2 from $\delta_i = (\delta_R{}^*(P_c)^{1/2})_i$ are obtained. Table 2 gives the values of critical constants and calculated parameters for the solutions of argon with the solute molecules at the temperature of the experiment. Table 2 shows the interaction parameter (ι_{12}) that reproduces the experimental solubility of each solution.

Comparison with Other Methods and Results

A summary of our results in liquid Ar compared with results with other solvents and techniques at similar temperatures is presented in Table 3. Different methods of analysis require the initial preparation of a saturated solution in equilibrium with the crystals of solute (static analytic method) followed by separation of an amount of solution (filtrate). Analysis of the filtrate by evaporation is sometimes used to determine the solute concentration in the original solution. The saturated solution can also be analyzed by spectroscopic methods (IR or ultraviolet) or by chromatography. Another method is the analytic–optical method (or visual), where the solute–solvent mixture is prepared in the gas phase and deposited as a liquid in a transparent cell. If a solid solute is observed in the liquid, the temperature is increased until the solid disappears indicating solubility at the registered final temperature. The solubility of C_2H_4 in liquid O_2 has been reported using different methods.[1] Filtration was employed to measure the solubility in mole fraction and (temperature) from 0.00065 (69 K) to 0.1743 (101 K).[14] The visual method was used to get the solubility 0.0013 (77.3 K)[15] and 0.0275 (90 K).[16] Using IR absorption detection, the solubility was reported as 0.0340 (90 K).[17] Solubilities in liquid nitrogen in the range of 0.0039 (77.4 K) to 0.0059 (80.1 K) have been obtained using IR spectroscopy for detection.[17,18]

The solubility of propyne in liquid Ar has been reported in the range of 2.3×10^{-6} (90 K) to 8.5×10^{-6} (100 K).[19] The value at 100 K is approximately 2.6 times smaller than the one reported here. Our reported value of solubility for 2-methyl-1,3-butadiene (isoprene) in liquid Ar (12×10^{-6}) at 86 K is eight times larger than the one reported by Kurdziel et al.[20] at 87 K (1.56×10^{-6}) using the filtration method. The difference is probably due to the fact that the filtration method requires more steps beginning with separation of the saturated solution from the precipitate solute, followed by evaporation of the solvent to obtain the amount of sample. Our unsaturated and saturated solutions are prepared and measured directly on the cell.

Retour à la table des matières : p. v

Table 3. Experimental solubilities of the unsaturated hydrocarbons in cryogenic liquids.

Solute	Temperature (K)	Liquid Solvent	Mole fraction	Method (Ref.)
Ethylene	77 K	N_2	3.9×10^{-03}	IR[17,18]
	80 K	N_2	5.9×10^{-03}	IR[17,18]
	90 K	O_2	3.4×10^{-02}	IR[17]
	92 K	Ar	$(600 \pm 100) \times 10^{-06}$	This work
Propyne	100 K	Ar	8.5×10^{-06}	IR[19]
	100 K	Ar	$(22 \pm 9) \times 10^{-06}$	This work
2-methyl-2-butene	100 K	Ar	$(9 \pm 5) \times 10^{-06}$	This work
2-methyl-1,3- butadiene (Isoprene)	77 K	N_2	$(1.56 \pm 0.36) \times 10^{-07}$	Filtration[20]
	87 K	Ar	$(1.41 \pm 0.27) \times 10^{-06}$	Filtration[20]
	86 K	Ar	$(12 \pm 2) \times 10^{-06}$	This work

The PC-SAFT and the RST models use the same Eq. 3 to calculate the activity coefficient of the solute in the saturated solution. The difference between the two theories begins with the calculation of the activity coefficient. The RST provides good preliminary results for binary solutions of non-polar components. By including an interaction parameter (l_{12}), the real behavior for solutions is taken into account. In this paper, the two polynomial equations (Eqs. 5 and 6) that reproduce the values in tables given by Preston and Prausnitz[12] are presented in order to facilitate calculations of the solubility parameters $\delta_1$and δ_2. The SRT model has been used in our laboratory to estimate concentrations of solutes in saturated solutions of cryogenic solvents before experiments are done. The equation of state PC-SAFT is derived from statistical physics. Solvent and solutes are represented by parameters related to their individual molecular properties. It has been proven to be a more realistic representation for the liquid and vapor states and it is also an excellent method for the simulation of multicomponent solutions. Both methods (PC-SAFT and RST) require a temperature dependent interaction parameter k_{ij} (PC-SAFT) and l_{ij} (RST) that is usually derived from experimental data.

Conclusion

In our laboratory, the solubility of four unsaturated hydrocarbons in cryogenic solutions has been determined by preparing solutions in liquid argon of increasing hydrocarbon composition and obtaining the absorption between 2000 cm^{-1} and 8000 cm^{-1}. In general, the integrated absorption of the selected C–H band increases in magnitude until it reaches a plateau that indicates that solute saturation has occurred. This method allows for the observation of the transition from unsaturated to saturated solution. An advantage of observing absorption bands that include fundamental and overtone regions is that in occasions where signal saturation (large absorbance) occurs at high concentrations, it is not necessary to change the length of the cell used. For solubility determinations using a 5 or 10 cm length cell, if the solubility of the sample is less than 100 ppm (mole fraction) a fundamental IR absorption can be selected to detect the solute, but if the solubility is larger than 100 ppm, a weaker first overtone absorption of the solute will also be good for detection. The solubility of C_2H_4 in liquid Ar is in the same order of magnitude as the solubilities in liquid N_2 at similar temperatures. In the case of propyne, our solubility is 2.6 times higher than the comparison value. Isoprene in liquid Ar is almost one order of magnitude higher than the value measured using the filtration method. The calculated values of the binary parameter k_{12} from PC-SAFT could be used in solubility simulations of unsaturated hydrocarbons dissolved in liquefied gases at low temperatures.

Conflict of Interest

The authors report there are no conflicts of interest.

Funding

This study was supported by funds from the Baylor University Research Committee and the Vice Provost for Research.

References

1. V. De Stefani, A. Baba-Ahmed, D. Richon. "A Review of Experimental Methods for Solid Solubility Determination in Cryogenic Systems". Cryogenics. 2004. 44: 631–641.
2. M.O. Bulanin, G. Ya. Zelikina. "Phase Equilibria and Spectral Analysis of Cryosystems". In: R.J.H. Clark, R.E. Hester (eds) Molecular Cryospectroscopy. New York: John Wiley & Sons, 1995, pp.21–34.
3. Ya. M. Kimelfeld. "Spectroscopy of Molecules and Molecular Complexes Dissolved in Liquefied Gases: Structure and Reactivity". Russ. Chem. Rev. 1988. 57: 730–743.
4. H. Diez-y-Riega, D. Camejo, A.E. Rodriguez, C.E. Manzanares. "Unsaturated Hydrocarbons in the Lakes of Titan: Benzene Solubility in Liquid Ethane and Methane at Cryogenic Temperatures". Planet. Space Sci. 2014. 99: 28–35.
5. S.P. Tan, J.S. Kargel, G.M. Marion. "Titan's Atmosphere and Surface Liquid: New Calculation Using Statistical Associating Fluid Theory". Icarus. 2013. 222: 53–72.

Retour à la table des matières : p. v

6. D. Cordier, J.W. Barnes, A.G. Ferreira. "On the Chemical Composition of Titan's Dry Lakebed Evaporites". Icarus. 2013. 226: 1431–1437.
7. D. Cordier, T. Cornet, J.W. Barnes, S.M. Mackenzie, T. Le Bahers, et al. "Structure of Titan's Evaporites". Icarus. 2016. 270: 41–56.
8. A. Brock, N. Mina-Camilde, C.E. Manzanares. "Vibrational Spectroscopy of C-H Bonds of C_2H_4 Liquid and C_2H_4 in Liquid Argon Solutions". J. Phys. Chem. 1994. 98: 4800–4808.
9. B.E. Poling, J.M. Prausnitz, J. O'Connell. The Properties of Gases and Liquids, 5th ed. New York: McGraw-Hill Education, 2007.
10. J. Gross, G. Sadowski. "Perturbed-Chain SAFT: An Equation of State Based on a Perturbation Theory for Chain Molecules". Ind. Eng. Chem. Res. 2001. 40: 1244–1260.
11. A. Tihic, G.M. Kontogeorgis, N. von Solms, M.L. Michelsen, L. Constantinou. "A Predictive Group-Contribution Simplified PC-SAFT Equation of State: Application to Polymer Systems". Ind. Eng. Chem. Res. 2008. 47: 5092–5101.
12. G.T. Preston, J.M. Prausnitz. "Thermodynamics of Solid Solubility in Cryogenic Solvents". Ind. Eng. Chem. Process Des. Develop. 1970. 9: 264–271.
13. C.L. Yaws. Thermophysical Properties of Chemicals and Hydrocarbons, 2nd ed. New York: Elsevier, 2014.
14. N.M. Tsin. "Solubility of Ethylene and Propylene in Liquid Nitrogen and Liquid Oxygen". Zh. Fiz. Khim. 14: 1940418–421.
15. C. McKinley, F. Himmelberger. "The Role of Air Contaminants in Formulating Oxygen Plant Safety Principles". Chem. Eng. Progr. 1957. 53: 112–118.
16. C. McKinley, E.S. Wang. "Hydrocarbon-Oxygen Systems Solubilities". In: T.D. Timmerhaus (ed.) Advances in Cryogenic Engineering. Volume 4, New York: Plenum, 1960, pp.11–25.
17. R.J.H. Clark, R.E. Hester. Molecular Cryospectroscopy. New York: John Wiley & Sons Ltd, 1995. Tables A8, A9, p. 237.
18. E. Szczepaniec-Cieciak, V.A. Kondaurov, S.M. Melikova. "The Solubility of Light Olefins in Liquid Nitrogen: Part 2". Cryogenics. 1979. 19: 649–651.
19. R.G. Amamchyan. "A Study of Phase Equilibria at Low Temperatures by Infrared Spectroscopy. 2: Diacetylene and Acetylene Homologues in Liquid Argon". Zhur. Fiz. Khim. 1974. 48: 2678–2679.
20. M. Kurdziel, E. Szczepaniec-Cieciak, M. Watorczyk, B. Dabrowska. "Solubility of Solid 2-Methyl-1,3-butadiene (Isoprene) in Liquid Argon and Nitrogen at the Standard Boiling Points of the Solvents". J. Solution Chem. 2004. 33: 453–464.

Retour à la table des matières : p. v

4.14 Article sur la nucléation, la croissance et la signature RADAR des bulles

The Astrophysical Journal, 859:26 (9pp), 2018 May 20 https://doi.org/10.3847/1538-4357/aabc10
© 2018. The American Astronomical Society. All rights reserved.

Bubbles in Titan's Seas: Nucleation, Growth, and RADAR Signature

Daniel Cordier and Gérard Liger-Belair
Groupe de Spectrométrie Moléculaire et Atmosphérique, UMR CNRS 7331, Campus Moulin de la Housse, BP 1039, Université de Reims Champagne-Ardenne, F-51687 Reims, France; daniel.cordier@univ-reims.fr
Received 2018 January 29; revised 2018 April 2; accepted 2018 April 3; published 2018 May 18

Abstract

In the polar regions of Titan, the main satellite of Saturn, hydrocarbon seas have been discovered by the *Cassini–Huygens* mission. RADAR observations have revealed surprising and transient bright areas over the Ligeia Mare surface. As suggested by recent research, bubbles could explain these strange features. However, the nucleation and growth of such bubbles, together with their RADAR reflectivity, have never been investigated. All of these aspects are critical to an actual observation. We have thus applied the classical nucleation theory to our context, and we developed a specific radiative transfer model that is appropriate for bubble streams in cryogenic liquids. According to our results, the sea bed appears to be the most plausible place for the generation of bubbles, leading to a signal comparable to observations. This conclusion is supported by thermodynamic arguments and by RADAR properties of a bubbly column. The latter are also valid in the case of bubble plumes, due to gas leaking from the sea floor.

Key words: planets and satellites: surfaces – radiative transfer – waves

1. Introduction

In 1655, the Dutch astronomer Christiaan Huygens turned his telescope toward Saturn with the intention of studying its rings. However, to his surprise, besides the rings, he also observed an object that has since been known as the largest moon of Saturn: Titan. More than three centuries after this discovery, Titan still offers surprises. For instance, after the arrival of *Cassini/Huygens* in the Saturn system, hundreds of lakes and seas of hydrocarbons were detected in Titan's polar regions (Stofan et al. 2007). One of the northern seas, Ligeia Mare, has shown a strange property: ephemeral RADAR bright areas, nicknamed "Magic Islands," which appear and disappear from one flyby to another (Hofgartner et al. 2014, 2016). Several ideas have been proposed to explain these transient features. Up to now, only scenarios based on streams of bubbles, due the nitrogen exsolution, seem to posses a firm physical basis (Cordier et al. 2017; Malaska et al. 2017a). Indeed, Titan's seas are probably composed of methane and some ethane, in which atmospheric nitrogen can easily dissolve. The existence of such bubbly plumes is not extravagant, since bubbles of methane megaplumes are observed in Earth's oceans (Leifer et al. 2015, 2017). To be efficient RADAR waves reflectors, bubbles must be of a size roughly the same as the RADAR wavelength, i.e., 2.2 cm. Here, we focus our purpose on bubble nucleation and growth, and on bubble plume reflectivity. This paper is divided into four sections: the first and the second are devoted to the production and evolution of nitrogen bubbles, whereas the third concerns the RADAR signature of the bubble streams. We conclude in the last section.

2. Homogeneous Nucleation of Nitrogen Bubbles

For the sake of simplicity and because this is the most plausible place for a temperature rise to trigger bubbling, we begin our reasoning by considering the surface of Titan's hydrocarbon sea. Then, the relevant thermodynamic conditions are a temperature within the range of 90–95 K and a total pressure around 1.5 bar (Cordier et al. 2017). Generally speaking, there are two ways for bubbles to nucleate and grow within a liquid (Brennen 1995). When homogeneous nucleation occurs, the vapor molecules may come together by collisions, forming embryonic bubbles. Depending on local fluctuations, the vapor deposits around these embryos and allows some bubbles to grow irreversibly. In the case of heterogeneous nucleation, the vapor molecules add on an existing solid substance, foreign in composition to the vapor. In our context, this solid material could be formed by particles in suspension into the liquid phase. The modern theory of homogeneous nucleation goes back to the early twentieth century (Volmer & Weber 1926; Zeldovich 1943), its results are now well established (Brennen 1995). From this experimental and theoretical corpus, evidence has been provided to show that an embryo of a bubble has to overcome a "free energy barrier" to grow during the nucleation process. This barrier is well represented by a bubble critical radius r_c. Bubbles containing gas, with a radius $r_b < r_c$, tend to redissolve into the liquid phase, whereas embryonic bubbles reaching r_c can grow to a much larger size. The critical radius (in m) is governed by Laplace's equation (Brennen 1995)

$$P_B - P_L = \frac{2\sigma}{r_c}, \quad (1)$$

where P_B is the pressure (Pa) inside the bubble, P_L represents the pressure into the surrounding liquid, and σ stands for the surface tension (Nm^{-1}). Figure 1 reports a liquid–vapor equilibria for the system N_2–CH_4 which is relevant, in first approximation, for Ligeia Mare. Two temperatures are considered: 91 and 95 K, corresponding to a couple of sets of measurements. If we restrict our reasoning to the 95 K case, a liquid under 1.5 bar could be in equilibrium with a vapor at a maximum pressure of ~5.4 bar, composed almost exclusively of nitrogen in that case ($x_{N_2} \sim 1$). From the difference in pressure $P_B - P_L \simeq 3.9$ bar, we are able to estimate the corresponding critical radius. According to surface tension values gathered in Table 1, a cryogenic liquid containing around 20% of N_2 and 80% of CH_4 has a surface tension of

Retour à la table des matières : p. v

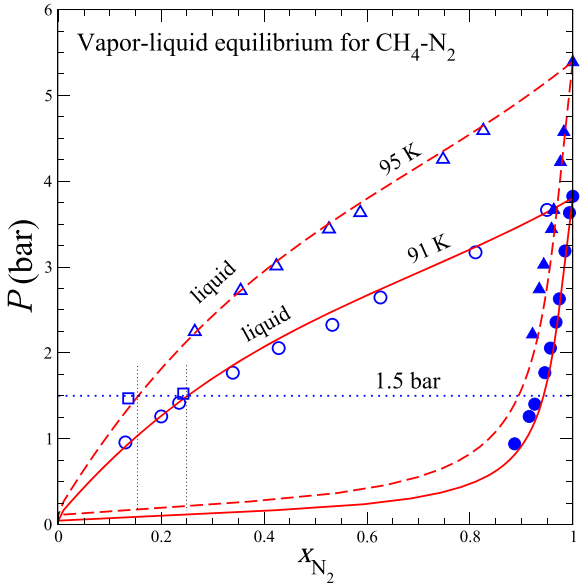

Figure 1. Comparison between experimental data for the binary system N_2–CH_4 and our PC-SAFT based model (Cordier et al. 2017), for two temperatures: 91 K (circles) and 95 K (triangles). Laboratory measurements, already used by Tan et al. (2013), come from various sources: Sprow & Prausnitz (1966) for 91 K and Parrish & Hiza (1974) for 95 K (triangles). Squares represent N_2 dissolution data from recent work (Malaska et al. 2017a), respectively, at 89 ± 0.5 K and 95 ± 0.5 K. The pressure $P = 1.5$ bar represents the value determined by *Huygens* at ground level.

Table 1
Surface Tensions of the Main Constituents of the Liquid Filling Titan's Seas[a]

Species	N_2	CH_4	C_2H_6
γ(N m^{-1})	6×10^{-3}	1.7×10^{-2}	3.15×10^{-2}

Note. These data have been provided by the dortmund data bank.
[a] http://www.ddbst.com.

$\sigma \sim 1.5 \times 10^{-2}$ N m^{-1}. This leads to the critical radius $r_c \simeq 10^{-7}$ m. In principle, other possibilities are conceivable, involving a pressure P_B determined between ~5.4 bar and the liquid pressure of 1.5 bar. Clearly, as P_B gets closer to P_L, the critical radius diverges, taking arbitrary large values. However, the net energy required to form a bubble of radius r_c is given by (Brennen 1995)

$$W = \underbrace{4\pi r_c^2 \sigma}_{\text{(A)}} - \underbrace{\frac{4}{3}\pi r_c^3 (P_B - P_L)}_{\text{(B)}} = \frac{4}{3}\pi r_c^2 \sigma. \quad (2)$$

The physical meaning of terms in Equation (2) are the following: (A) represents the energy stored in the surface of the bubble, while (B) accounts for the work done by the liquid during the bubble inflation. It can be shown (Brennen 1995) that the probability of formation of a microbubble of radius r_c is proportional to $\exp -W/k_B T$, with k_B the Boltzmann constant. This consideration clearly favors the above mentioned embryonic ($r_c \simeq 10^{-7}$ m) bubbles of pure nitrogen ($x_{N_2} \simeq 1$), since these small bubbles have a probability of formation much larger than that of bigger bubbles. The theory also provides the homogeneous nucleation rate J_{nuc}^{hom} (m^{-3} s^{-1}), i.e., the mean

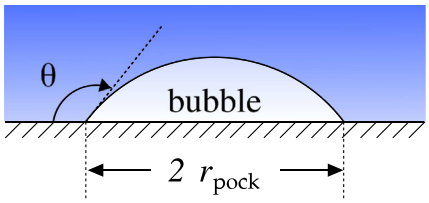

Figure 2. Heterogeneous nucleation on a flat surface, r_{pock} is the typical maximum dimension of the gas pocket. The contact angle at the liquid–vapor–solid intersection is denoted θ.

number of bubbles reaching the critical radius, per unit of volume of liquid, per unit of time (Brennen 1995)

$$J_{nuc}^{hom} = N_{N_2}^{*} \left(\frac{2\sigma}{\pi m_{N_2}} \right)^{1/2} \exp - \frac{W}{k_B T}, \quad (3)$$

where $N_{N_2}^{*}$ (m^{-3}) is the number of nitrogen molecules, per unit of volume, in the liquid phase, and m_{N_2} (kg) represents the mass of a single N_2 molecule. For the mixture under consideration, we found $N_{N_2}^{*} \sim 3.4 \times 10^{27}$ m^{-3}, with an extremely low nucleation rate

$$\log_{10} J_{nuc}^{hom} \sim -2 \times 10^5. \quad (4)$$

For a system like Ligeia Mare, which contains roughly 10^{13} m^3 of liquid, the time required for the formation of a single bubble is much longer than the age of the universe. These estimations unequivocally rule out homogeneous nucleation, as an efficient bubble formation mechanism, in Titan's sea. Neither higher pressures nor the presence of ethane changes this conclusion. At the bottom of a sea, like Ligeia Mare, the pressure is evaluated to be around 3 bars (Cordier et al. 2017), this higher liquid pressure only decreases the difference $P_B - P_L$ (in Figure 1, 1.5 bar is replaced by 3.0 bar) and the nucleation rate is not significantly affected. The presence of some amount of ethane, for instance a mole fraction of the order of 0.20–0.30 changes only marginally the values of $N_{N_2}^{*}$, while only slightly modifying the surface tension in Equation (3).

3. Heterogeneous Nucleation and Bubble Growth

Alternatively to homogeneous nucleation, heterogeneous nucleation may occur in Titan's seas. It is well known, as a general fact, that heterogeneous nucleation is faster than homogeneous nucleation (Vehkamäki 2006; Sánchez-Lavega 2010). The presence of a different interface reduces the height of the Gibbs free energy barrier. This is true for all types of phase transitions: vapor to liquid, liquid to vapor, liquid to solid, etc. In Titan's seas, the possible presence of solids may trigger heterogeneous nucleation of nitrogen bubbles. This kind of material could cover the sea bottom or could be present under the form of suspended particles. The size of a bubble leaving a solid substrate, under the influence of buoyancy forces, can be roughly estimated for a contact angle (see Figure 2) around 90°, a value that represents the boundary between the low wettability and the high wettability domains. The radius r_{hetero} of the hemispherical vapor nucleus, leaving its solid horizontal substrate, is given by (de Gennes

Retour à la table des matières : p. v

et al. 2004)

$$r_{\text{hetero}} \simeq \sqrt{\frac{3\sigma}{\rho g_{\text{Titan}}}}. \quad (5)$$

If, for example, we consider a 0.8:0.2 mixture of CH_4 and N_2, a composition that could be typical of the upper layers of liquid, the surface tension should be $\sigma \simeq 10^{-2}\,\text{N m}^{-1}$ at 90 K (see Table 1), with a density $\rho \simeq 520\,\text{kg m}^{-3}$. These numbers lead to $r_{\text{hetero}} \simeq 7 \times 10^{-3}$ m, i.e., a diameter of about ∼1.4 cm. If the nucleation occurs at the sea bed, during the rise to the free surface, bubbles will undergo an inflation caused by the pressure drop. Using the law of ideal gases and adopting a pressure of ∼3 bars at the sea bottom (Cordier et al. 2017), together with a surface pressure of 1.5 bar, leads to a radius/diameter enhancement factor of $2^{1/3} \simeq 1.3$, corresponding to bubbles at the surface with a radius of 1.8 cm. This estimation is more or less comparable to the *Cassini* RADAR instrument wavelength of 2.2 cm. Other mechanisms, particularly bubble coalescence, could also contribute to bubble size evolution, they will be discussed in the following. It is striking that the video provided by the NASA press release (Malaska et al. 2017b), associated with the Malaska and co-authors article (Malaska et al. 2017a), precisely shows bubbles leaving a solid substrate, which is much larger than bubbles.

Heterogeneous nucleation could also occur on suspended solid particles. To produce centimeter-sized bubbles at the moment of solid substrate detachment, solids of similar sizes are required. However, such relatively large particles could explain, by themselves, the occurrence of "Magic Islands," without the need for bubble production, since these preexisting large solids could be good RADAR reflectors (Hofgartner et al. 2016). In addition, while we know plausible formation processes for bubbles, the presence of solids remains entirely speculative. Therefore, the formation of centimeter-sized bubbles, via a purely heterogeneous process is much more plausible at the sea bed than anywhere else. Nonetheless, the existence of suspended sediments, small enough to be undetectable to the RADAR, cannot be ruled out. Solid particles, much smaller than the RADAR wavelength may produce embryonic gas pockets, which could grow during their ascent along a column of liquid. Two distinct growth mechanisms could be at work in such a situation: growth by nitrogen diffusion through the bubble surface or the coalescence of bubbles due to stochastic encounters, within their rising stream. The first possibility requires a liquid supersaturated in dissolved nitrogen over the entire column, while the second needs a population of bubbles showing a number of bubbles per unit of volume that is high enough. We study these two alternative scenarios in the following sections.

3.1. Bubble Growth by Diffusion

Let us imagine, as suggested by Malaska and co-authors (Malaska et al. 2017a), a scenario according to which a methane–nitrogen Titan lake is quickly heated from ∼90 to 95 K, i.e., fast enough to avoid any degassing. This operation should leave a liquid supersaturated in N_2. In such a situation, from data plotted in Figure 1, we conclude that the mole fraction in N_2 should be around 0.25 instead of 0.15, just before the evaporation starts. These mole fractions are, respectively, equivalent to $7 \times 10^3\,\text{mol m}^{-3}$ and $4.2 \times 10^3\,\text{mol m}^{-3}$, leading to a strong supersaturation of $\Delta c_{N_2} = 2.8 \times 10^3\,\text{mol m}^{-3}$. If homogeneous nucleation appears very unlikely, small sediment particles may generate gas bubbles similar in size to these solid heterogeneities. We have developed a model, that provides the bubble evolution during their rise, through layers of liquid hydrocarbons supersaturated in nitrogen. This model, based on the well accepted theory of bubbles (Clift et al. 1978), takes into account the bubbles expansion due to the pressure drop together with their growth produced by the diffusion of N_2 from the supersaturated liquid to the bubble interior. The details of the model are described in the Appendix. Our simulations have shown strikingly that the final bubble radius R_s, i.e., obtained at the surface of the sea, does not depend on the initial bubble radius R_0, but only on the depth H_0 at which the embryonic bubble is assumed to start its rise. This property is explained by the dependence of rising velocity U_b on bubble radius: $U_b \propto \sqrt{r_b}$. Under this circumstance, smaller bubbles are the slowest; thus, they have more time to let diffusion feed their interior with nitrogen. Numerically, we found that a depth of $H_0 \sim 0.5$ m is a minimum to get a radius of $R_s \sim 1.1$ cm at the surface. The rise along such a relatively small height requires only $\tau_{\text{rise}} \sim 9$ s. It is clear that, if tiny sediment particles have a volumic number density that is high enough, the considered layers of liquid would reach the thermodynamic equilibrium of the atmosphere in a few seconds. Therefore, we have to compare τ_{rise} with the thermal relaxation time τ_{therm} of such layers. In the literature (Cordier et al. 2012), we found that τ_{therm} should be of the order of 2 Titan days[1] for $H_0 = 1$ m. Since $\tau_{\text{therm}} \propto H_0^2$, a depth of $H_0 = 0.5$ m leads to $\tau_{\text{therm}} \sim 10^6$ s. These numbers suggest that nitrogen exsolution, by bubble transport to the surface, should be much faster than thermal relaxation. In such a case, any modest temperature increase at the sea surface would produce an immediate release of nitrogen in the form of tiny bubbles. As a consequence, the liquid layers closest to the atmosphere would quickly lose their supersaturation. This way, embryonic bubbles, produced in deeper layers, would rise through nonsupersaturated zones, a thermodynamic state that inhibits growth by diffusion. Finally, even if tiny sediment particles are numerous enough to trigger a quantitative nitrogen dissolution, under the form of small bubbles, the mechanism of growth to RADAR visible bubbles should be rapidly blocked by "de-supersaturation" of the top liquid layers. Of course, larger values for H_0 make the situation worse.

A similar desaturation would occur in the case of cosmic rays reaching the surface, even though Titan's dense atmosphere is heavily shielded and the overall cosmic-ray flux is low (Molina-Cuberos et al. 1999). Let us now consider the growth by bubble coalescence.

3.2. Bubble Growth by Coalescence

In the previous sections, we have neglected all possible interactions between bubbles. The features of observed "Magic Islands" suggest the existence of plumes containing a rather large volume density of bubbles. Within a dense population, the probability of the encounters becomes appreciable. When two bubbles collide, they may coalesce, forming a bigger bubble. This effect substantially enhances the diameter of bubbles reaching the surface, after having undergone one or several instances of coalescence during the rise. The simplest effect, producing bubble collisions, originates in the difference

[1] One Titan day corresponds to 15 terrestrial days.

Retour à la table des matières : p. v

Table 2
Rising Terminal Velocities $U_{b,i}$ for Three Radius Values

Bubble Radius r_{bi} (m)	10^{-4}	10^{-3}	10^{-2}
$U_{b,i}$ (m s^{-1})	7.8×10^{-3}	2.5×10^{-2}	7.8×10^{-2}
τ_{100} (s)	1.3×10^{4}	4.1×10^{3}	1.3×10^{3}

Note. The Titan's gravity is $g = 1.352$ m s^{-2}, the rising time τ_{100} is computed for an initial depth of $H_0 = 100$ m.

in rise velocities of bubbles of different sizes. The subsequent buoyancy-driven collision rates θ_{ij}^{B} (m^{-3} s^{-1}) is given by the literature (Prince & Blanch 1990; Friedlander 2000)

$$\theta_{ij}^{\mathrm{B}} = n_i n_j S_{ij} (U_{b,i} - U_{b,j}), \tag{6}$$

where n_i and n_j (m^{-3}) are the concentration of bubbles of radius $r_{b,i}$ and $r_{b,j}$ (m), and $S_{ij} = \pi (r_{b,i} + r_{b,j})^2/4$ (m^2). Here $U_{b,k}$ is the rise velocity of the particle k. During its ascent, a given bubble i quickly reaches its terminal velocity $U_{b,i} = 2\sqrt{g_{\mathrm{Titan}} r_{b,i}}/3$ (m s^{-1}) (Clift et al. 1978). By moving through the liquid, bubbles generate their own, small-scale turbulence, and this expression of $U_{b,i}$ (also used in the model described in the Appendix) implicitly assumes a turbulent close neighborhood. However, as a first approach, we consider this velocity as an average value and we will take typical radius values in order to get the velocity difference term in Equation (6), unequal to zero. We have gathered in Table 2 estimations of rising velocities and rising timescale τ_{100} for a 100 m deep sea, using those radius typical values, i.e., 10^{-4}, 10^{-3}, and 10^{-2} m. Since the goal is to obtain a final bubble with a radius larger than 1 cm, and since big bubbles rise faster than small ones (see Table 2), we consider a typical example of a "test bubble" of 1 mm, riding through a population of 0.1 mm in radius bubbles. If the differential dh is the elementary depth variation for our "1 mm bubble" during the duration dt, the average number of coalescence events undergone by our "1 mm test bubble" is

$$d^2 N_c = \theta_{ij}^{\mathrm{B}} dt\ dh\ s, \tag{7}$$

where s represents the cross section of the considered column of liquid, we took $s = 1$ m^2 for convenience. By integrating Equation (7) over time and depth, with θ_{ij}^{B} assumed approximately constant over the entire column, we get

$$N_c \simeq \theta_{ij}^{\mathrm{B}} \tau_{100}\ s H_0. \tag{8}$$

If coalescence is the only mechanism at work, a simple calculation, based on the conservation of the total quantity of gas contained in bubbles, shows that $N_c \sim 10^6$ bubbles, with a radius of 0.1 mm, are needed to make one final 1 cm in radius bubble. This result can be used to estimate the required order of magnitude of θ_{ij}^{B}, thanks to Equation (8), we found $\theta_{ij}^{\mathrm{B}} \sim 1$ coalescences m^{-3} s^{-1}, over the column of $H_0 = 100$ m. For one single 1 mm sized bubble (i.e., $n_i = 1$) rising along the column, we can evaluate the required number density of 0.1 mm bubbles, needed to get a final centimeter-sized bubbles. For that purpose, Equation (6) is used, together with values available in Table 2, to finally obtain $n_j \sim 10^8$ bubbles per m^3 along the entire column (with $r_{b,j} \sim 10^{-4}$ m). Polydisperse bubble populations may be simply generated by sea floor composition heterogeneities, or caused by stochastic fluctuations in bubble/substrate uncoupling. Clearly, buoyancy-driven bubble coalescence appears to be an efficient mechanism that could produce centimeter-sized bubbles in bubble trajectory ends, within the sea top layers.

This concentration represents 100 bubbles per cm^3, i.e., a total volume of gas of 4.2×10^{-4} cm^3, per cm^3 of liquid. The number appears reasonable since it corresponds only to a small fraction of the volume of liquid. In this scenario, bubbles are formed at the sea bed, with a nonuniform distribution in size. The first bundles of bubbles, leaving the depths of the sea, settle all the sea levels. The following generations of bubbles pass through this bubbly medium. As big bubbles are faster than small ones, similarly to our example, big bubbles (e.g. with $r_{b,i} \sim 10^{-3}$ m) aggregate small ones (e.g., with $r_{bi} \sim 10^{-4}$ m).

Collisions induced only by different rising velocities assume a gentle turbulent field, mainly localized in the immediate vicinity of bubbles. In massive bubble streams, a strong turbulent field may appear. Under such a regime, the turbulent collision rate θ_{ij}^{T} (see Equation (9)) no longer depends on differences of individual velocities. Instead, it can be estimated with (Prince & Blanch 1990)

$$\theta_{ij}^{\mathrm{T}} = 0.089 \pi n_i n_j (d_{bi} + d_{bj})^2 \epsilon^{1/3} (d_{bi}^{2/3} + d_{bj}^{2/3})^{1/2}, \tag{9}$$

where d_b is the bubble diameter and ϵ is the energy dissipation per unit of mass and unit of time (J kg^{-1} s^{-1}). Compared to buoyancy-driven collision, in that case, even bubbles of the same size can coalesce. The factor ϵ can be estimated using $k_d = \epsilon^{1/4}/2\nu^{3/4}$, where k_d (m^{-1}) is the wave number of turbulent eddies and ν is the liquid kinetic viscosity (Batchelor 1953). Eddies most affecting bubbles have wave numbers roughly similar to $1/r_b$. Density and viscosity of liquid methane, together with an assumed radius of 10^{-3} m, yields $\epsilon \sim 0.4$ J kg^{-1} s^{-1}. Assuming a population of millimeter-sized bubbles, basic computations show that we need a number of $N_c = 10^3$ of such bubbles to build up a centimeter-sized final bubble by successive coalescences. For a sea depth of $H_0 = 100$ m, corresponding to $\tau_{100} \sim 10^3$ s for a millimeter-sized particle, we found the required turbulent collision rate to be of the order of $\theta_{ij}^{\mathrm{T}} \sim 10^{-2}$ m^{-3} s^{-1}. We can then derive the minimum bubbles density $n_j \sim 10^5$ m^{-3}. This represents one single millimeter-sized bubble for 10 cm^3, which is a pretty modest concentration. Here, the volume of gas is also, incidentally, equal to 4.2×10^{-4} cm^3 per cm^3 of liquid.

As we can see, both coalescence mechanisms, are able to produce bubbles big enough to be detectable at the Ligeia Mare surface. This conclusion is true if the number of bubbles initially produced is sufficiently large and if they start their journey to the surface from a depth of the order of ~100 m. These two coalescence processes may be at work in nature, depending on the size distribution and volumic density by number of bubble populations, initially nucleated at the seabed. We emphasize that the turbulence-driven collision rate could dominate if gases are injected in the liquid through hypothetical sea bottom vents. In that case, high ϵ values could be reached, causing a large collision rate. Finally, we stress that break-up radius (Clift et al. 1978; Cordier et al. 2017) $r_{\mathrm{bk}} \simeq 4\sqrt{\sigma/(\rho\ g)}$

Retour à la table des matières : p. v

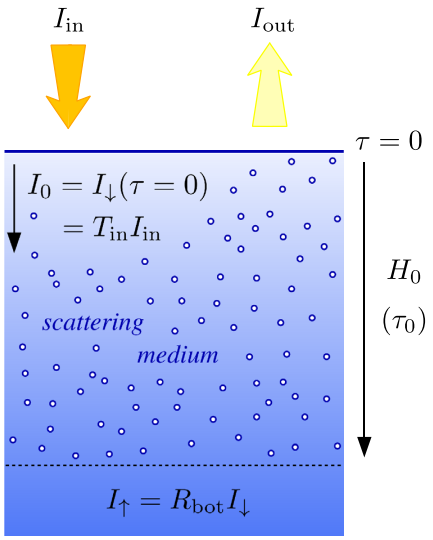

Figure 3. Sketch of the liquid column containing bubbles. $I_{\rm in}$ is the incident RADAR photons flux, while $I_{\rm out}$ is the signal returning back to the emitter. The total height of the column is denoted H_0 corresponding to the optical depth τ_0. The bottom of the column, filled by bubbles, does not necessarily correspond to the sea bed.

cannot be overcome by any mechanism. This remains an absolute upper limit, of the order of ∼2.3 cm (∼4.6 cm in diameter; Cordier et al. 2017), for bubble size.

4. Bubble RADAR Signature

Throughout the discussion, the criterion used to decide whether or not bubbles could be RADAR detectable is based on their size. Objects possessing a diameter comparable to the wavelength (i.e., 2.16 cm) have been considered to have a measurable effect. This approach is relevant in first approximation, but it is—by essence—not quantitative, and it neglects effects like multiple scattering, which may be important in the context. Previous works (Hofgartner et al. 2016) have estimated the possible single scattering albedo of a population of relatively small bubbles ($r_b \sim 10^{-3}$ m), i.e., using the Rayleigh scattering theory (Bohren & Huffman 2014). For larger reflectors, i.e., with sizes comparable to the wavelength, the Mie scattering theory is required (Mie 1908). We then built a model in which a column of liquid is filled by bubbles, with a total height denoted H_0, corresponding to the "optical" depth τ_0 (see Figure 3). The geometry is simplified: the flux of energy $I_{\rm in}$ coming from the spacecraft arrives at the sea-atmosphere interface with a normal incidence. This approximation is perfectly relevant in our case, since during T92 and T104 observations, the incident angles were respectively 6.°0 and 11.°5 (Hofgartner et al. 2016). The effects of the polarization, and the absorption, are neglected as suggested by previous works (Hofgartner et al. 2016). In that frame, using a two-stream radiative transfer model (Bohren & Huffman 2014), accounting for multiscattering by principle, the energy fluxes, through the liquid, in downward and upward directions are, respectively,

$$I_\downarrow = D + C(1 - \tau^*) \tag{10}$$

$$I_\uparrow = D - C(1 + \tau^*) \tag{11}$$

where τ^* is the optical depth corrected by the asymmetry factor g_b of bubbles: $\tau^* = (1 - g_b)\tau$. The asymmetry factor is computed in the frame of Mie's theory. The coefficients D and C are given as functions of $I_0 = I_{\downarrow,\tau=0}$, and τ_0^* the total optical depth of the column (see Figure 3), we have

$$C = \frac{(1 - R_{\rm bot})I_0}{2 + (1 - R_{\rm bot})\tau_0^*} \tag{12}$$

$$D = \frac{2 + (1 - R_{\rm bot})(\tau_0^* - 1)}{2 + (1 - R_{\rm bot})\tau_0^*} I_0, \tag{13}$$

where $R_{\rm bot}$ represents the reflectance at the bottom of the column, or equivalently at the sea floor. The uncorrected total optical depth τ_0, of the column of the liquid, is provided by

$$\tau_0 = \int_0^{H_0} \beta \, dz \tag{14}$$

in which $1/\beta$ represents the radar photon's mean-free path; β is a function of the number density n_b (bubbles m^{-3}) and of the bubbles Mie's cross section $\sigma_{\rm Mie}$: $\beta = n_b \, \sigma_{\rm Mie}$. The flux leaving the sea and returning to the RADAR is $I_{\rm out} = (1 - R_{\rm in})I_{\uparrow,\tau=0}$; here, the reflectance $R_{\rm in}$ of the interface sea atmosphere is assumed to take into account the effect of the rugosity (Grima et al. 2017), which is usually, except in the occurrence of a "Magic Island" event, measured to be very small (Wye et al. 2009; Stephan et al. 2010; Barnes et al. 2011; Zebker et al. 2014; Grima et al. 2017).

In order to quantify the RADAR signature of bubbles, we compare the reflected flux with and without the presence of bubbles. For that purpose, we introduce the quantity $R_{\rm bubb} = I_{\rm out}/I_{\rm in}$, which has to be compared to the "clear sea," i.e., without bubbles, global reflectance given by $R_{\rm cs} = R_{\rm bot} T_{\rm in}^2 + R_{\rm in}$, where $T_{\rm in} = 1 - R_{\rm in}$. For that purpose, we denote Bubble Radar Signal Amplification (BRSA) as the ratio $R_{\rm bubb}/R_{\rm cs}$.

As a first approach, we have chosen to neglect the upward flux of RADAR photons at the bottom of the column: $I_\uparrow(\tau_0) = 0$. Below the bubbly column, the microwave photons are considered to be lost. In other words, the reflectance at the bottom of the column is taken equal to zero: $R_{\rm bot} = 0$. Taking the methane permittivity (Mitchell et al. 2015) $\epsilon_r(CH_4) = 1.72$ as a reference, we have explored the influences of the bubble radius r_b, of the number of bubbles per unit of volume n_b and of the column height H_0, results are gathered in Figure 4. Not surprisingly, large bubble radii favor a strong backscattering (Figure 4(a)). Similar effects are found for the influence of the number of bubbles per unit of volume n_b (Figure 4(b)) and the total height H_0 of the bubbly column (Figure 4(c)). The dielectric permittivity of the liquid also has its influence. Taking the permittivity of pure liquid nitrogen: $\epsilon_r(N_2) = 1.55$ (Hosking et al. 1993), we found a BRSA higher than values obtained with CH_4 permittivity (see Figure 4, panels (a), (b), and (c)). In contrast, a simulation with liquid ethane permittivity, $\epsilon_r(C_2H_6) = 2.00$ (Mitchell et al. 2015), yields to a reduction of the BRSA. Perhaps surprisingly, a low liquid permittivity favors the bubble stream RADAR reflection. The chemical composition of Titan is still not firmly known, but we emphasize that, accidentally, the mean value of nitrogen and ethane respective permittivities is very close to the methane individual value. Consequently, a sea with a composition in N_2:CH_4:C_2H_6 around 0.20: 0.40: 0.20 will show a permittivity close to the

Retour à la table des matières : p. v

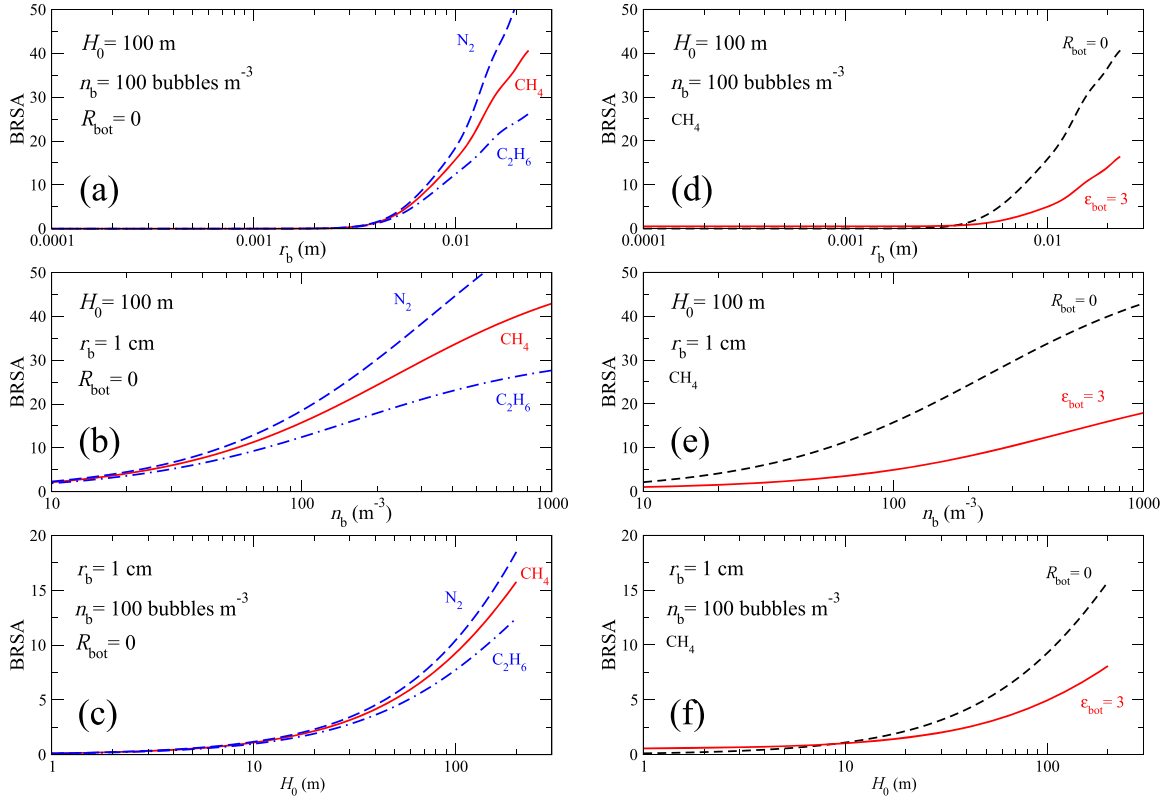

Figure 4. Influence of bubble stream parameters on RADAR Signal Amplification (BRSA). (a) Influence bubble radius r_b, the simulation is stopped at the bubble break-up radius $r_{breakup} \sim 2.3$ cm (Cordier et al. 2017). While the solid red curve has been computed using the methane permittivity $\epsilon_r = 1.72$ (Mitchell et al. 2015), dashed and dotted–dashed blue lines correspond, respectively, to liquid nitrogen ($\epsilon_r = 1.55$; Hosking et al. 1993) and ethane ($\epsilon_r = 2.00$; Mitchell et al. 2015). (b) Influence of volume density n_b of bubbles. (c) Influence of the total height of the column H_0 (see Figure 3), the considered range of H_0 has been limited to 0–200 m, since the bathymetry of Ligeia Mare shows a maximum depth around 200 m (Hayes 2016). In panels (d), (e), and (f), we report computations including a non-zero reflectance of the sea floor; its permittivity is $\epsilon_{bot} = 3$, which is probably a very high value (corresponding to $R_{bot} \simeq 2\%$). In these panels, the methane $R_{bot} = 0$ curve is recalled for comparison.

pure liquid methane value $\epsilon_r(CH_4) = 1.72$ (Mitchell et al. 2015). In Hofgartner et al. (2016), the Normalized Radar Cross Section (NRCS) along the flyby tracks is reported in their Figures 4 and 5. In these figures, the NRCS "peaks" corresponding to T92 and T104 transient feature events offer the opportunity to estimate the ratio of the quantity of radar photons backscattered with the presence of a "Magic Island" and without such a structure. The height of NRCS "peaks," measured to be between ∼6 and ∼9.5 in dB, leads to ratios ranging between ∼6 and ∼10. This means that radar reflectors present at Ligeia Mare, during "Magic Island" episodes, enhance the local reflectivity by a factor in the interval 6–10. Panel (c) in Figure 6 of the same reference, gives another opportunity to evaluate the "reflectivity enhancement" during Ligeia Mare overbrightness events. A quick comparison of NRCS predicted by the sea floor model plotted in this figure and actual measurements performed during T92 and T104, leads to energy ratios magnified by a factor of ∼10–16. If we keep a factor around ∼10, which corresponds to what we call BRSA, the Ligeia Mare "Magic Islands" can be easily explained by a column of $H_0 \sim 100$ m, containing around 100 centimetric bubbles per cubic meters, if sea floor reflectance can be neglected.

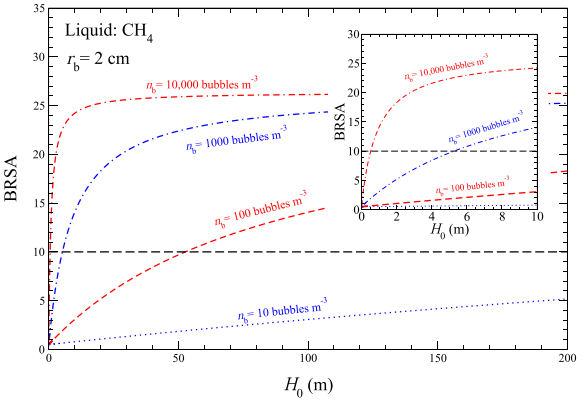

Figure 5. Bubbles Radar Signal Amplification (BRSA) for a column of liquid methane, harboring bubbles with a radius of 2 cm, as a function of the total height H_0 of the column. Several volume densities of bubbles are considered: $n_b = 10$, 100, 1000, and 10,000 bubbles m^{-3}. The explanation of Ligeia Mare "Magic Island" requires BRSA ∼ 10. The panel inserted on the right-hand side is a magnification of the main figure in the region of the origin.

Retour à la table des matières : p. v

Unfortunately, the hypothesis of the seabed zero-reflectivity is an oversimplification. Actually, the sea floor partly re-emits the incident RADAR beam energy. This property has been utilized to derived Ligeia Mare bathymetry (Hayes 2016). For that purpose, two distinct echoes in altimetry tracks (Hayes 2016) have been detected (Hayes 2016), one caused by the surface and the second produced by energy back-scattered by the sea bottom. Thus, we have compared published values of NRCS (Hayes 2016) of these echoes; we found a difference in dB around 30, which leads to a ratio in energy of about $\sim 10^3$. The flux coming from the deepest part of the sea is obviously the weakest, suggesting a quite low reflectance of the sea bottom. Using RADAR observation, and their models, Hofgartner and co-authors (Hofgartner et al. 2016) propose a sea floor dielectric constant around $\epsilon_{r,\mathrm{seafloor}} = 1.99$, but the actual value is not well constrained since the real nature of the seabed is not known. Titan belongs to the so-called "icy moons;" therefore, water ice is recognized to be a major component of Titan's geological layers (Baland et al. 2014). If we assume a sea floor composed by pure water ice, its microwaves permittivity should be around $\epsilon_{r,\mathrm{ice}} = 3$ (Bradford et al. 2009). The actual value depends on the porosity of the ice and on the nature of the material mixed within it. Adopting $\epsilon_{r,\mathrm{ice}} = 3$ for the seabed, which has to be understood as a high value (Le Gall et al. 2016), we computed the corresponding BRSAs. They are compared to their counterparts computed with a bottom zero-reflectivity; results are plotted in panels (d), (e), and (f) of Figure 4. These simulations demonstrate that a non-zero bottom reflectivity ($R_{\mathrm{bot}} \neq 0$) damps the BRSAs, i.e., the ratios $R_{\mathrm{bubb}}/R_{\mathrm{cs}}$. This behavior is caused by the addition of the term $R_{\mathrm{bot}} T_{\mathrm{in}}^2$ in the expression of R_{cs}. Nonetheless, as we can see in Figure 4, even with a relatively large value for R_{bot} ($\epsilon_{r,\mathrm{seafloor}} = 3$ corresponds to $R_{\mathrm{bot}} \sim 2\%$), reasonable combinations of r_b, n_b, and H_0 can be found, with a resulting BRSA around $\sim$10, a value that explains the observed Ligeia Mare "Magic Island." For instance, a column of $H_0 = 100$ m, containing $n_b = 100$ bubbles m^{-3} with $r_b = 2$ cm has a BRSA of $\sim$14. If we adopt a bubble radius close to the maximum value allowed by bubble physics, i.e., $r_b = 2$ cm, which is approximately the break-up radius, we can search for the minimum height H_0 required to get a BRSA around $\sim$10. This is done in Figure 5, in which several values for n_b are assumed. Since with $r_b = 2$ cm, one cannot include more than $\sim$10,000 bubbles within one cubic meter, $n_b = 10{,}000$ bubbles m^{-3} represents a geometrical maximum. As we can see, even with $r_b = 2$ cm and $n_b = 10{,}000$ bubbles m^{-3}, we need $H_0 \sim 0.5$ m to reach BRSA$\sim$10. According to the discussion conducted in Section 3.1, it appears impossible to form centimetric bubbles due to heating starting at the sea surface. One more time, a scenario based on a bubble production in the depth of Ligeia Mare looks more plausible than a pure surface phenomenon. Indeed, Figure 5 tells us that a few tens of meters, with a relatively modest number of bubbles per cubic meters, produced the required value for the BRSA.

5. Conclusion

In this work, we have demonstrated that the homogeneous nucleation of small bubbles of N_2 is impossible under the conditions of the Titan surface. Heterogeneous nucleation, i.e., involving a solid substrate, is much easier. Such substrates could be found at the seabed or under the form of small sediment particles suspended in the liquid. However, in that case, a growth mechanism has to be at work to obtain bubbles large enough to be efficient RADAR reflectors. While the growth by diffusion in nitrogen supersaturated layers appears to be very difficult, if not impossible; the growth by coalescence, along a bubbly column has been found to be a powerful process to get large bubbles. In this case, such a column must have a height that is more or less comparable to Ligeia Mare depth. We also developed a model of reflection of the RADAR wave by a stream of bubbles in Titan's sea. This approach also favors streams of bubbles with a vertical extension of several tens of meters.

In short, to explain the "Magic Islands," one scenario, based on bubbles, has the best plausibility if it implies that bubbles are released or formed in the depths of the sea.

Our understanding of the problem of bubble stream RADAR reflectivity has been greatly helped by discussions with Dr. Jason Hofgartner of the Jet Propulsion Laboratory; it is our pleasure to acknowledge our indebtedness to him. We also thank the anonymous reviewer, who led us to significantly clarify our manuscript.

Appendix A
Model of Bubble Ascension and Growth

In a column of liquid, the gas bubbles have a vertical upward motion due to buoyancy forces, the liquid flowing around bubbles rapidly reaches a high Reynolds number. In such a situation, the bubble velocity U_b (m s^{-1}) can be estimated with (Clift et al. 1978)

$$U_b = \frac{2}{3}\sqrt{\frac{ga\Delta\rho}{\rho}} \tag{15}$$

since, during their ascent to the free surface, the bubbles distort, the parameter a represents a characteristic length of bubble geometry. For the sake of simplicity, we adopted the approximation $a \simeq r_b$, with r_b the bubble "radius" or typical size. In addition, we have $\Delta\rho = \rho_{\mathrm{liq}} - \rho_{\mathrm{gas}} \simeq \rho_{\mathrm{liq}}$, then $\Delta\rho/\rho \sim 1$, leading to

$$U_b \simeq \frac{2}{3}\sqrt{g_{\mathrm{Titan}} r_b}. \tag{16}$$

We emphasize that, before adopting the velocity given by Equation (15), we performed tests using the so-called "Levich velocity"

$$U \simeq \frac{\rho g_{\mathrm{Titan}} r_b^2}{9\eta_{\mathrm{liq}}}, \tag{17}$$

where η_{liq} is the viscosity of the liquid, for which velocity is valid for relatively moderate Reynolds numbers, i.e., $50 \lesssim Re \lesssim 200$ (Clift et al. 1978). In that case, the Reynolds numbers, obtained in our simulation, quickly reached $\sim 10^3$, to finally increase to $\sim 10^5$ near the surface, far beyond the validity of Equation (17). We, then, turned to Equation (15) to get more consistent numerical simulations. The initial depth of $H_0 \sim 0.50$ m, found to get centimeter-sized bubbles at the surface, has to be understood as a minimum. Indeed, in the early times of the ascent, the Reynolds numbers were below $\sim$200 and Levich's form should have been employed during this stage, leading to larger H_0 values.

Retour à la table des matières : p. v

In the case of the fluid sphere, for high Reynolds numbers, the Sherwood number and the Peclet number are linked through the equation (Clift et al. 1978)

$$\mathrm{Sh} = \frac{2}{\sqrt{\pi}}\mathrm{Pe}^{1/2}. \quad (18)$$

We recall that

$$\mathrm{Sh} = \frac{kl}{D}, \quad (19)$$

where k is the convective mass transfer rate (m s^{-1}), l is a characteristic length (m), and D is the molecular diffusion coefficient (m^2 s^{-1}), in our context $D \sim D_{N_2-CH_4}$. The Peclet number is given by

$$\mathrm{Pe} = \frac{Ul}{D}. \quad (20)$$

Using the above equation and taking $l \sim r_b$, we can express that the convective mass transfer rate are linked through the equation (Clift et al. 1978)

$$k = \sqrt{\frac{2}{\pi}}\sqrt{\frac{D_{N_2-CH_4}U_b}{r_b}}. \quad (21)$$

Here, the N_2 bubble content, noted as n (mol) is driven by the equation

$$\frac{dn}{dt} = k\ 4\pi r_b^2\ \Delta c_{N_2}. \quad (22)$$

This equation can be easily reformulated as

$$\frac{dn}{dh} = -\sqrt{\frac{2}{\pi}}\left(\frac{D_{N_2-CH_4}}{r_b U_b}\right)^{1/2} 4\pi r_b^2\ \Delta c_{N_2}, \quad (23)$$

where h (m) is the depth at which the bubble is located at a particular moment. For convenience, we have considered time as a function of h, which has been chosen as our independent variable. Thus, $t(h)$ follows the law

$$\frac{dt}{dh} = -\frac{1}{U_b}. \quad (24)$$

The external bubble pressure P_e is ruled by the hydrostatic law $P_e(h) = P_0 + \rho g_{\mathrm{Titan}} h$, where P_0 represents the atmospheric pressure at the sea surface, leading to

$$\frac{dP_e}{dh} = \rho g_{\mathrm{Titan}}. \quad (25)$$

With P_i as the internal pressure of bubbles, assumed spherical, we can write the ideal gas law

$$P_i(h) \times \frac{4}{3}\pi r_b^3 = n(h) R_{\mathrm{gas}} T \quad (26)$$

with R_{gas} as the gas constant. The pressures P_e and P_i are linked by Laplace's equation

$$P_i = P_e + \frac{2\sigma}{r_b}; \quad (27)$$

from this, we can easily derive the equation governing the evolution of the bubble radius

$$\frac{dr_b}{dh} = -\frac{R_{\mathrm{gas}}T}{P_i}\sqrt{\frac{2}{\pi}}\left(\frac{D_{N_2-CH_4}}{r_b U_b}\right)^{1/2}\Delta c_{N_2} - \frac{\rho g_{\mathrm{Titan}} r_b}{3P_i}. \quad (28)$$

In summary, we have four unknowns: $n(h)$, $t(h)$, $P_e(h)$, and $r_b(h)$, which are found by numerically integrating (Nougier 1987) the system of four Equations: (23)–(25) and (28). Assuming an isothermal column of liquid, at temperature T, showing a uniform supersaturation Δc_{N_2} in dissolved N_2, these equations are solved adopting a starting depth H_0 and an initial radius R_0 for bubbles.

Appendix B
Diffusion Coefficient of Nitrogen in Liquid Methane

The N_2 molecules, initially in the vicinity of a given microbubble, can migrate toward the bubble interior under the influence of thermal agitation. The literature proposes several methods to estimate the diffusion coefficient $D_{N_2-CH_4}$ of the nitrogen molecule through liquid methane (Poling et al. 2007). Among these methods, the Wilke–Chang technique (Wilke & Chang 1955) is widely used. It is based on correlations and provides diffusion coefficient D^0_{A-B} of a compound A in a compound B, at infinite dissolution, i.e., when the mole fraction of A is very small. For our system, one can write

$$D^0_{N_2-CH_4} = \frac{7.4 \times 10^{-11}(\Phi M_{CH_4})^{1/2} T}{\eta_{CH_4} V_{N_2}^{0.6}}, \quad (29)$$

with $D^0_{N_2-CH_4}$ in cm^2 s^{-1}, Φ is an adimensional coefficient around unity, M_{CH_4} is the molecular weight (g mol^{-1}) of methane, η_{CH_4} is the dynamic viscosity of liquid methane (Pa s), and V_{N_2} is the molar volume of solute N_2 at its normal boiling temperature (cm^3 mol^{-1}). The molecular weight has the well-known value $M_{CH_4} = 16.04$ g mol^{-1}, the viscosity is provided by the literature (Hellemans et al. 1970) $\eta_{CH_4} \simeq 1.7 \times 10^{-3}$ Pa s and the molar volume $V_{N_2} = 35$ cm^3 mol^{-1} (Lide 1974). At $T = 95$ K, these numbers lead to $D^0_{N_2-CH_4} \simeq 2 \times 10^{-6}$ cm^2 s^{-1}. This determination is comparable to those published for other simple molecules in the liquid state (Poling et al. 2007).

Liquid methane, in equilibrium with a vapor dominated by nitrogen, such as in the case of Titan, should contain an amount of dissolved nitrogen around 0.15 in mole fraction (see Figure 1). Then the assumption of infinite dissolution is not valid in our context. Fortunately, empirical corrections are available and the diffusion coefficient D_{AB} can be derived from coefficients D^0_{AB} and D^0_{BA} obtained in the frame of the hypothesis of infinite dissolution. For instance, one may use (Poling et al. 2007)

$$D_{AB} = (D^0_{BA}x_A + D^0_{AB}x_B)\,\alpha, \quad (30)$$

where $x_{A(B)}$ are the respective mole fraction and α is a thermodynamic coefficient, which is not too different from unity. Using an approach similar to the one previously done for nitrogen, we computed an estimation for the diffusion coefficient of methane in liquid nitrogen, in the case of large dissolution, $D^0_{CH_4-N_2} \simeq 4 \times 10^{-5}$ cm^2 s^{-1}, using $\eta_{N_2} \sim 10^{-4}$ Pa s (Forster 1963). Our final estimation for the diffusion coefficient of N_2 in liquid CH_4 is $D_{N_2-CH_4} \simeq 10^{-5}$ cm^2 s^{-1}.

Retour à la table des matières : p. v

References

Baland, R.-M., Tobie, G., Lefèvre, A., & Van Hoolst, T. 2014, Icar, 237, 29
Barnes, J. W., Soderblom, J. M., Brown, R. H., et al. 2011, Icar, 211, 722
Batchelor, G. K. 1953, The Theory of Homogeneous Turbulence (Cambridge: Cambridge Univ. Press)
Bohren, C. F., & Huffman, D. R. 2014, Absorption and Scattering of Light by Small Particles (2nd ed.; Weinheim: Wiley-VCH)
Bradford, J. H., Harper, J. T., & Brown, J. 2009, WRR, 45, W08403
Brennen, C. E. 1995, Cavitation and Bubble Dynamics (Oxford: Oxford Univ. Press)
Clift, R., Grace, J. R., & Weber, M. E. 1978, Bubbles, Drops and Particles (New York: Academic)
Cordier, D., García-Sánchez, F., Justo-García, D. N., & Liger-Belair, G. 2017, NatAs, 1, 0102
Cordier, D., Mousis, O., Lunine, J. I., et al. 2012, P&SS, 61, 99
de Gennes, P.-G., Brochard-Wyart, F., & Quéré, D. 2004, Capillarity and Wetting Phenomena: Drops, Bubbles, Pearls, Waves (New York: Springer)
Forster, S. 1963, Cryo, 3, 176
Friedlander, S. K. 2000, Smoke, Dust and Haze: Fundamentals of Aerosol Dynamics (2nd ed.; Oxford: Oxford Univ. Press)
Grima, C., Mastrogiuseppe, M., Hayes, A. G., et al. 2017, E&PSL, 474, 20
Hayes, A. G. 2016, AREPS, 44, 57
Hellemans, J., Zink, H., & Van Paemel, O. 1970, Phy, 46, 395
Hofgartner, J. D., Hayes, A. G., Lunine, J. I., et al. 2014, NatGe, 7, 493
Hofgartner, J. D., Hayes, A. G., Lunine, J. I., et al. 2016, Icar, 271, 338
Hosking, M. W., Tonkin, B. A., Proykova, Y. G., et al. 1993, SuScT, 6, 549
Le Gall, A., Malaska, M. J., Lorenz, R. D., et al. 2016, JGR, 121, 233
Leifer, I., Chernykh, D., Shakhova, N., & Semiletov, I. 2017, TCry, 11, 1333
Leifer, I., Solomon, E., von Deimling, J. S., et al. 2015, MarPG, 68, 806
Lide, D. P. (ed.) 1974, CRC Handbook of Chemistry and Physics (74th ed.; Boca Raton, FL: CRC Press)
Malaska, M. J., Hodyss, R., Lunine, J. I., et al. 2017a, Icar, 289, 94
Malaska, M. J., Hodyss, R., Lunine, J. I., et al. 2017b, Experiments Show Titan Lakes May Fizz with Nitrogen, https://www.nasa.gov/feature/jpl/experiments-show-titan-lakes-may-fizz-with-nitrogen
Mie, G. 1908, AnP, 330, 377
Mitchell, K. L., Barmatz, M. B., Jamieson, C. S., Lorenz, R. D., & Lunine, J. I. 2015, GeoRL, 42, 1340
Molina-Cuberos, G. J., López-Moreno, J. J., Rodrigo, R., Lara, L. M., & O'Brien, K. 1999, P&SS, 47, 1347
Nougier, J. P. 1987, Méthodes de Calcul Numérique (Paris: Masson)
Parrish, W. R., & Hiza, M. J. 1974, Adv. Cryog. Eng., 19, 300
Poling, B. E., Prausnitz, J. M., & O'Connell, J. 2007, The Properties of Gases and Liquids (5th ed.; Englewood Cliffs, NJ: McGraw-Hill Professional)
Prince, M. J., & Blanch, H. W. 1990, AIChE, 36, 1485
Sánchez-Lavega, A. 2010, An Introduction to Planetary Atmospheres (Boca Raton, FL: CRC Press)
Sprow, F. B., & Prausnitz, J. M. 1966, AIChE, 12, 780
Stephan, K., Jaumann, R., Brown, R. H., et al. 2010, GeoRL, 37, 7104
Stofan, E. R., Elachi, C., Lunine, J. I., et al. 2007, Natur, 445, 61
Tan, S. P., Kargel, J. S., & Marion, G. M. 2013, Icar, 222, 53
Vehkamäki, H. 2006, Classical Nucleation Theory in Multicomponent Systems (Berlin: Springer)
Volmer, M., & Weber, A. 1926, ZPC, 119, 277
Wilke, C. R., & Chang, P. 1955, AIChE, 1, 264
Wye, L. C., Zebker, H. A., & Lorenz, R. D. 2009, GeoRL, 36, L16201
Zebker, H., Hayes, A., Janssen, M., et al. 2014, GeoRL, 41, 308
Zeldovich, J. B. 1943, Acta Physicochim. URSS, 18, 1

Retour à la table des matières : p. v

Retour à la table des matières : p. v

Chapitre 5

Articles : atmosphère de Titan

5.1 Article sur le D/H dans l'atmosphère de Titan

The Astrophysical Journal, 689: L61–L64, 2008 December 10
© 2008. The American Astronomical Society. All rights reserved. Printed in U.S.A.

PHOTOCHEMICAL ENRICHMENT OF DEUTERIUM IN TITAN'S ATMOSPHERE: NEW INSIGHTS FROM *CASSINI-HUYGENS*

Daniel Cordier,[1,2] Olivier Mousis,[3,4] Jonathan I. Lunine,[3] Audrey Moudens,[1] and Véronique Vuitton[3,5]
Received 2008 July 31; accepted 2008 October 13; published 2008 November 14

ABSTRACT

Cassini-Huygens data are used to reexamine the potential sources of the D/H enhancement over solar, measured in methane, in Titan's atmosphere. Assuming that the system is closed with respect to carbon, the use of constraints from the *Huygens* probe for the determination of the current mass of atmospheric methane and the most up-to-date determination of D/H from *Cassini* CIRS infrared spectra allow us to show that photochemical enrichment of deuterium is not sufficient to be the sole mechanism yielding the measured D/H value. A possible fractionation between CH_3D and CH_4 during the escape process may slightly enhance the deuterium enrichment, but is not sufficient to explain the observed D/H value over the range of escape values proposed in the literature. Hence, alternative mechanisms such as a primordial deuterium enrichment must be combined with the photochemical enrichment in Titan's atmosphere in order to explain its current D/H value.

Subject headings: planets and satellites: formation — planets and satellites: individual (Titan)

1. INTRODUCTION

The interpretation of the D/H ratio measured in methane in the atmosphere of Titan is not straightforward. All measurements indicate values substantially higher than the protosolar value, namely the value in the hydrogen of the solar nebula, but less than the values in water in the Earth's oceans (SMOW[6]) and in comets (Bézard et al. 2007). There is no general agreement on the cause of the enhancement. Indeed, methane on Titan could have originated in the molecular cloud or interstellar medium with a high D/H value. Deuterium in methane would have then isotopically exchanged with molecular hydrogen in the gas phase at the time of entrapment in solids condensed in Saturn's formation zone (Mousis et al. 2002) to obtain the D/H value observed in Titan.

On the other hand, Titan could have been accreted from solids condensed in an initially hot and dense Saturn subnebula. In this picture, the methane incorporated in Titan would result from CO and CO_2 gas-phase conversions (Prinn & Fegley 1981) and would present an almost solar D/H ratio at the time of its trapping in solids ultimately accreted by the satellite (Lunine et al. 1999; Mousis et al. 2002). Pinto et al. (1986) and Lunine et al. (1999) argued that, because the initial methane reservoir on Titan was likely larger than what is seen today in the atmosphere of Titan, the observed D/H enhancement could be the result of photochemical enrichment of deuterium through that isotope's preferential retention during methane photolysis (Pinto et al. 1986; Lunine et al. 1999). The D/H ratio acquired by the atmospheric methane of Titan would be progressively enriched with time via photolysis, until it reaches the value observed today.

Here we reinvestigate the hypothesis of photochemical enrichment of deuterium in the atmosphere of Titan, in light of a number of recent *Cassini-Huygens* measurements. Pinto et al. (1986) and Lunine et al. (1999) estimated the current mass of methane in the atmosphere of the satellite by assuming that its molar fraction is uniform, whatever the altitude. In contrast, we use the methane mole fraction and density atmospheric profiles resulting from data collected by the Gas Chromatograph Mass Spectrometer (GCMS) and *Huygens* Atmospheric Structure Instrument (HASI) on board the *Huygens* probe during its descent in Titan's atmosphere to better constrain the actual mass of methane. *Cassini* data also have provided new constraints on the vertical mixing in the atmosphere of Titan, leading Yelle et al. (2008) to derive the existence of a CH_4 escape flux which is about one third the photolytic destruction rate of CH_4. Here we investigate the influence of this prodigious escape on the total fractionation between CH_3D and CH_4.

Moreover, we utilize the most recent determination of D/H obtained by Bézard et al. (2007) from *Cassini* CIRS infrared spectra, which indicates values of $1.32^{+0.15}_{-0.11} \times 10^{-4}$, substantially higher than those employed by Lunine et al. (1999) [$(7.75 \pm 2.25) \times 10^{-5}$; Orton 1992]. Since the determination of Bézard et al. (2007) was obtained by fitting simultaneously the ν_6 bands of both $^{13}CH_3D$ and $^{12}CH_3D$ and the ν_4 band of CH_4 from precise information on the CH_4 mixing ratio and temperature profile in the stratosphere available from the *Huygens* descent and limb-viewing Composite Infrared Spectrometer (CIRS) measurements, we believe that this measurement is more reliable than the previous ones.

All these revisions, together with the use of updated rate coefficients for methane loss derived from a recent photochemical model (Vuitton et al. 2008), allow us to show that the photochemical enrichment of deuterium is not efficient enough in the atmosphere of Titan to explain its current D/H value, even if the current atmospheric reservoir of methane is postulated to exist over 4.5 Gyr. We conclude that the D/H ratio in methane initially trapped in Titan was already higher than the protosolar value prior to its release in the atmosphere.

2. ISOTOPIC ENRICHMENT MODEL

Our photochemical enrichment model is derived from the formalisms of Pinto et al. (1986) and Lunine et al. (1999). We determine the deuterium enrichment that occurred following the ultimate outgassing event that gave existence to the current

[1] Institut de Physique de Rennes, CNRS, UMR 6251, Université de Rennes 1, Campus de Beaulieu, 35042 Rennes, France.
[2] Ecole Nationale Supérieure de Chimie de Rennes, Campus de Beaulieu, 35700 Rennes, France; daniel.cordier@ensc-rennes.fr.
[3] Lunar and Planetary Laboratory, University of Arizona, Tucson, AZ.
[4] Université de Franche-Comté, Institut UTINAM, CNRS/INSU, UMR 6213, Observatoire des Sciences de l'Univers de Besançon Cedex, France.
[5] Université Joseph Fourier, Laboratoire de Planétologie de Grenoble, CNRS/INSU, France.
[6] Standard Mean Ocean Water.

Retour à la table des matières : p. v

atmospheric methane of Titan. This event might have started 4.5 Gyr ago at the epoch of core overturn, giving birth to a reservoir of methane dense enough to allow its survival up until now. On the other hand, the current reservoir of methane might also have resulted from a much more recent outgassing event, as late as ~0.6 Gyr ago based on evolution models (Tobie et al. 2006) which are consistent with the surface cratering record (Lorenz et al. 2007). We assume that the system (atmosphere and subsurface from which the methane outgasses) is open with respect to the dissociated hydrogen (either deuterium or protium) which is lost to space, and to carbon only when methane loss is considered in the upper atmosphere of Titan.

We define R as the ratio of the total mass of methane expelled from the interior of Titan (and constituting the initial reservoir) to the current atmospheric mass of methane. Let $N_1(t)$ and $N_2(t)$ be the respective total column abundances of CH_4 and CH_3D on Titan at time t. With the condition $N_1 \gg N_2$, the evolution of $N_1(t)$ and $N_2(t)$ is given by

$$\frac{dN_1}{dt} = -\frac{N_1(t)}{N_1(t)+N_2(t)}F - \frac{N_1(t)}{N_1(t)+N_2(t)}\Phi \simeq -(F+\Phi), \quad (1)$$

$$\frac{dN_2}{dt} = -q\frac{N_2(t)}{N_1(t)+N_2(t)}F - l\frac{N_2(t)}{N_1(t)+N_2(t)}\Phi \simeq -(qF+l\Phi)\frac{N_2(t)}{N_1(t)}, \quad (2)$$

where F is the net photolytic destruction rate of CH_4 and Φ the methane escape rate. The parameter q corresponds to the ratio of k_2 over k_1, namely the respective rates for CH_3D and CH_4 destruction, and ranges between 0.8 and 0.88 from consideration of the chemical kinetics of deuterated species (Lunine et al. 1999). The value of the free parameter l ranges between 0 and 1, representing a possible fractionation between CH_3D and CH_4 during the escape process.

The integration of equations (1) and (2) leads to the following expression for R:

$$\log R = \frac{1}{1-(qF+l\Phi)/(F+\Phi)}\log f, \quad (3)$$

where f is defined as the ratio of D/H observed in Titan's current atmospheric methane to protosolar D/H [$(D/H)_\odot = (2.35 \pm 0.3) \times 10^{-5}$; Mousis et al. 2002].

Alternatively, R can be expressed as follows (Lunine et al. 1999):

$$R = \frac{x^{(s)}_{CH_4}P^{(s)}/g + m_{CH_4}(F+\Phi)\tau}{x^{(s)}_{CH_4}P^{(s)}/g} \simeq \frac{g m_{CH_4}(F+\Phi)\tau}{x^{(s)}_{CH_4}P^{(s)}}, \quad (4)$$

where g is the Titan's surface gravity, m_{CH_4} the mass of a methane molecule, $x^{(s)}_{CH_4}$ the methane surface mole fraction ($x^{(s)}_{CH_4} = 4.9 \times 10^{-2}$; Niemann et al. 2005), and $P^{(s)}$ the pressure at the surface of Titan. The time elapsed since the formation of the initial methane reservoir up to now is τ. Since the term

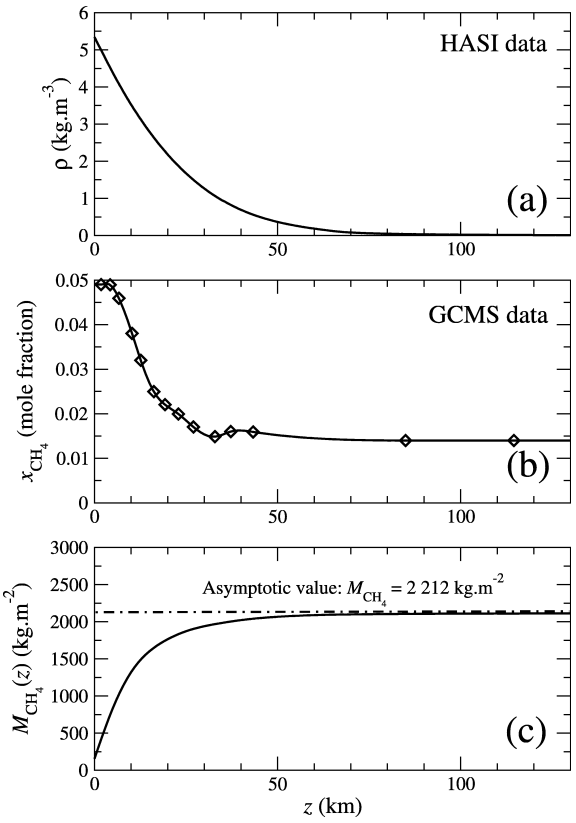

FIG. 1.—(*a*) Density ρ of Titan's atmosphere as a function of the altitude z derived from the HASI data (Fulchignoni et al. 2005). (*b*) Methane mole fraction x_{CH_4} as a function of the altitude derived from the GCMS data (Niemann et al. 2005). Diamonds show the in situ measurements and the solid line corresponds to the values interpolated with the spline technique. (*c*) Cumulative mass of methane in Titan's atmosphere as a function of the altitude.

$x^{(s)}_{CH_4}P^{(s)}/g$ corresponds to the total mass of methane per unit of area, R can be written as

$$R = \frac{m_{CH_4}(F+\Phi)\tau}{M_{CH_4}}, \quad (5)$$

where M_{CH_4} is the cumulative mass of atmospheric methane per unit area.

We adopt here $F = 6.9 \times 10^{13}$ molecules m^{-2} s^{-1}, a value derived from the photochemical model of Vuitton et al. (2008). In addition, when the escape of CH_4 is considered in our calculations, we set $\Phi = 2.8 \times 10^{13}$ m^{-2} s^{-1}, namely the value of CH_4 escape derived by Yelle et al. (2008) from *Cassini* INMS measurements. Otherwise, Φ is set to 0 and the deuterium enrichment is calculated in a way similar to the work of Pinto et al. (1986) and Lunine et al. (1999).

Huygens probe data allow us to accurately determine the value of M_{CH_4}. Indeed, knowing the atmospheric density and methane mole fraction profiles (see Figs. 1*a* and 1*b*), one can write

$$M_{CH_4} = \int_{z=0}^{z=H} X_{CH_4}(z)\rho(z)dz, \quad (6)$$

Retour à la table des matières : p. v

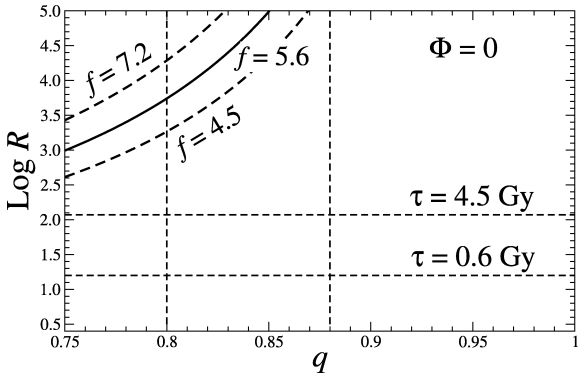

FIG. 2.—Fractionation of deuterium in methane photochemistry with $\Phi = 0$. *Top left*: Plotted is R as a function of q (see eq. [3]). Three curves are shown, corresponding to different present-day deuterium enrichments measured in methane by *Cassini* CIRS (see text). *Bottom*: The two horizontal lines represent values that would be acquired by R for two different values of τ (see eq. [5]). The two vertical lines represent limits on plausible values of q.

where X_{CH_4} is the methane mass fraction, $\rho(z)$ the density profile, and z the altitude. H is the altitude above which M_{CH_4} has no significant change. Figure 1*c* shows that $M_{CH_4} \simeq 2112$ kg m^{-2} is asymptotically reached when the altitude exceeds ~70 km. This determination is substantially lower than the value of ~5338 kg m^{-2} derived from Lunine et al. (1999). This discrepancy results from the use by Lunine et al. (1999) (as well as by Pinto et al. 1986) of a uniform methane mole fraction in the atmosphere of Titan whatever the altitude, in the absence of available in situ measurements.

3. RESULTS

We consider two different cases of photochemical enrichment. In the first case, the CH_4 escape from the upper atmosphere of Titan is neglected. In the second, this escape and a consequent additional fractionation between CH_3D and CH_4 are included.

Figure 2 summarizes the results for deuterium enrichment via photodissociation calculated with equation (3) assuming that $\Phi = 0$, and shows the initial methane reservoir R (normalized to the present one) against q. Three cases of present-day deuterium enrichment in the atmospheric methane of Titan are represented: the solid curve corresponds to the nominal value reported by Bézard et al. (2007) ($f = 5.6$) and the dashed curves to the extreme values ($f = 4.5$–7.2) obtained when uncertainties are taken into account. We assume in all our calculations that the D/H ratio in the methane initially acquired by Titan during its accretion is protosolar.

Note that a smaller value of q yields greater fractionation for a given amount of methane photolysis, because it corresponds to deuterium being more tightly bound (Lunine et al. 1999). Therefore, for a given deuterium enrichment, smaller values of q allow the initial methane reservoir of Titan to be smaller than in the case required for higher values of q. The two horizontal lines represent values that would be acquired by R if the actual methane reservoir were to exist since 0.6 or 4.5 Gyr ago, respectively (see eq. [5]). Figure 2 shows that the initial reservoir of Titan's atmospheric methane was ~16 times more massive than the current one if it was formed 0.6 Gyr ago, provided that F remained fixed to its current value throughout the existence of this reservoir. If methane were present in the atmosphere of Titan since 4.5 Gyr ago, the initial reservoir was ~126 times more massive than the current one.

TABLE 1
DEUTERIUM ENRICHMENT EXPECTED IN THE METHANE OF TITAN'S CURRENT ATMOSPHERE

Φ (m^{-2} s^{-1})	τ (Gyr)	$q = 0.8$	$q = 0.88$
0	0.6	1.7	1.4
	4.5	2.6	1.8
2.8×10^{13}	0.6	1.6	1.3
	4.5	2.1	1.5

Table 1 summarizes the deuterium enrichments via photolysis in the atmospheric methane calculated for the adopted limits on plausible values of q and the two different values of τ, in the case $\Phi = 0$. This table shows that, assuming a protosolar D/H in the methane originally released into the surface-atmosphere system, the photochemical enrichment is not efficient enough to allow the atmospheric D/H to reach the observed enrichment, even if the reservoir is postulated to have existed since 4.5 Gyr. A higher D/H ratio than the protosolar value must be advocated in the methane of Titan prior its outgassing, in order to explain the observed enrichment. Depending on the adopted value for q, the range of initial deuterium enrichments f_0 needed by the initial methane reservoir to allow photolysis to reach the nominal value of Bézard et al. (2007) is between 3.2 and 4.0 for $\tau = 0.6$ Gyr, and between 2.2 and 3.2 for $\tau = 4.5$ Gyr.

Figure 3 shows the results for deuterium enrichment via photodissociation calculated with equation (3) assuming that $\Phi = 2.8 \times 10^{13}$ m^{-2} s^{-1}, and shows R against q. The two upper left curves have been determined for $f = 5.6$ in equation (3), namely the nominal value reported by Bézard et al. (2007). The solid curve corresponds to the case where no fractionation occurs between CH_3D and CH_4 during methane escape, while the dot-dot-dashed curve assumes there is fractionation. A word of caution must be given here. We have arbitrarily set the escape rate equal to the CH_4/CH_3D molar ratio ($l = 16/17$) in order to quantify the influence of a possible fractionation between these two species. This is an order-of-magnitude estimate because the escape mechanism of methane remains unclear (Yelle et al. 2008). As a result, the fractionation may behave differently. Figure 3 shows that, despite the higher values of R ob-

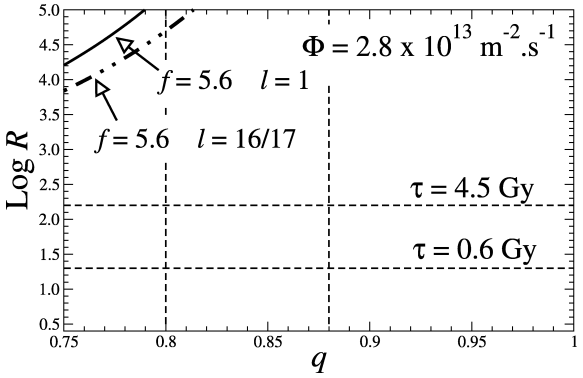

FIG. 3.—Same as Fig. 2, but with $\Phi = 2.8 \times 10^{13}$ m^{-2} s^{-1}. *Top left*: Both curves show R as a function of q in the case of $f = 5.6$. The solid curve corresponds to the case where no fractionation is assumed during the methane escape ($l = 1$). The dot-dot-dashed curve corresponds to the case where a fractionation between CH_3D and CH_4 occurs.

Retour à la table des matières : p. v

tained with the methane loss in the upper atmosphere of Titan ($R \simeq 22$ for $\tau = 0.6$ Gyr and $R \simeq 166$ for $\tau = 4.5$ Gyr), the discrepancy between the values of $R(q)$ and $R(\tau)$ increases when compared with Figure 2, even if a fractionation between CH_3D and CH_4 is taken into account. This translates into a lower photochemical enrichment than when methane escape is neglected (see Table 1). The range of f_0 needed by the initial methane reservoir to allow the matching of photolysis with the nominal value of Bézard et al. (2007) is consequently higher than without methane escape. Here f_0 is between 3.6 and 4.3 for $\tau = 0.6$ Gyr, and between 2.7 and 3.6 for $\tau = 4.5$ Gyr, depending on the adopted value of q and with no fractionation. If the fractionation between CH_3D and CH_4 is considered, the range of f_0 values is slightly lower, but still higher than the one inferred in the case of no methane escape.

4. DISCUSSION

Our results differ from those obtained by Lunine et al. (1999) who concluded that the deuterium enrichment via photolysis was efficient enough to explain the current D/H value observed in Titan's atmosphere even if the methane incorporated in the forming satellite had acquired only a slightly supersolar D/H. By considering the *Cassini-Huygens* data, we show that the minimum value required for f_0 is higher than in Lunine et al. (1999), even when the escape of methane and a possible fractionation between CH_3D and CH_4 are included. Therefore, additional mechanisms must be considered in order to explain the D/H value observed in Titan's methane.

One possibility is isotopic thermal exchange of molecular hydrogen with CH_3D in the gas phase of the solar nebula. In this case, CH_3D might have originated from highly deuterium-enriched ices that vaporized when entering the nebula (Mousis et al. 2002). During the cooling of the nebula, methane was trapped in crystalline ices around 10 AU, perhaps clathrates formed at ~ 60 K, and incorporated into planetesimals that were preserved in the Saturnian subnebula because the latter was too cold to fully vaporize the ices (Mousis et al. 2002; Alibert & Mousis 2007). Subsequent to outgassing, additional enrichment in D/H would have occurred by the photochemical and escape mechanisms quantified here.

Atreya et al. (2006) have argued that methane formed in Titan's interior by reaction of CO and CO_2 with water and rock, in which case the D/H ratio in methane outgassed to the atmosphere would have been determined by that in the water, modified by fractionation associated with these so-called "serpentinization" reactions. Our results show that such a model for methane's origin must be able to produce a substantially supersolar value of D/H in the outgassed methane. Computation of the D/H fractionation associated with serpentinization depends on the details of the temperature in Titan's interior, the original D/H in the water, and possibly on the composition of the silicate buffer. It is unlikely to be large in view of the requisite high temperatures (well above the water melting point) in Titan's interior. Thus, for this case, the considerations we made above for primordial methane would have to be invoked instead for the water, namely, that it was significantly enriched in D/H in the planetesimals that formed Saturn's largest moon. Finally, because the original appearance of methane in Titan's atmosphere could have been quite early, some 4.5 billion years ago, its origin might be tightly connected to the formation of the N_2 atmosphere from the dissociation of primordial NH_3. Hence, important amounts of H and H_2 could be present in the ancient atmosphere, leading to the possibility of additional fractionation between CH_4 and CH_3D via the following reversible equations $CH_4 + HD \rightleftharpoons CH_3D + H_2$ and $C + CH_3 = H + CH_2D$ (see Lee et al. [2001] for a list of reactions forming back CH_4 and CH_3D from CH_3). However, it is difficult to quantify the influence of these reactions on the final CH_3D/CH_4 ratio because the existence of a H_2-rich primordial atmosphere remains uncertain.

This work was supported in part by the CNES and NASA's *Cassini* program. We thank F. Ferri and M. Fulchignoni for providing us with the atmospheric density profile of Titan as measured by the *Huygens* probe.

REFERENCES

Alibert, Y., & Mousis, O. 2007, A&A, 465, 1051
Atreya, S. K., Adams, E. Y., Niemann, H. B., Demick-Montelara, J. E., Owen, T. C., Fulchignoni, M., Ferri, F., & Wilson, E. H. 2006, Planet. Space Sci., 54, 1177
Bézard, B., Nixon, C. A., Kleiner, I., & Jennings, D. E. 2007, Icarus, 191, 397
Fulchignoni, M., et al. 2005, Nature, 438, 785
Lee, A. Y. T., et al. 2001, ApJ, 551, L93
Lorenz, R. D., et al. 2007, Geophys. Res. Lett., 34, 7204
Lunine, J. I., Yung, Y. L., & Lorenz, R. D. 1999, Planet. Space Sci., 47, 1291
Mousis, O., Gautier, D., & Coustenis, A. 2002, Icarus, 159, 156
Niemann, H. B., et al. 2005, Nature, 438, 779
Orton, G. S. 1992, in Symposium on Titan (ESA SP-338; Noordwijk: ESA), 81
Pinto, J. P., Lunine, J. I., Kim, S.-J., & Yung, Y. L. 1986, Nature, 319, 388
Prinn, R. G., & Fegley, B., Jr. 1981, ApJ, 249, 308
Tobie, G., Lunine, J. I., & Sotin, C. 2006, Nature, 440, 61
Vuitton, V., Yelle, R. V., & Cui, J. 2008, J. Geophys. Res. Planets, 113, 5007
Yelle, R. V., Cui, J., & Müller-Wodarg, I. 2008, J. Geophys. Res., in press

Retour à la table des matières : p. v

5.2 Article sur l'évolution des isotopes dans l'atmosphère de Titan

Planetary and Space Science 57 (2009) 1917–1930

Contents lists available at ScienceDirect

Planetary and Space Science

journal homepage: www.elsevier.com/locate/pss

Isotopic evolution of the major constituents of Titan's atmosphere based on Cassini data

Kathleen E. Mandt [a,*], J. Hunter Waite Jr.[a], William Lewis [a], Brian Magee [a], Jared Bell [a], Jonathan Lunine [b], Olivier Mousis [b,c], Daniel Cordier [d,e]

[a] Space Science and Engineering Division, Southwest Research Institute, 6220 Culebra Road, San Antonio, TX 78228, USA
[b] Lunar and Planetary Laboratory, University of Arizona, 1629 East University Boulevard, Tucson, AZ 85721, USA
[c] Institut UTINAM, CNRS-UMR 6213, Observatoire de Besançon, BP 1615, 25010 Besançon Cedex, France
[d] Institut de Physique de Rennes, CNRS, UMR 6251, Université de Rennes 1, Campus de Beaulieu, 35042 Rennes, France
[e] Ecole Nationale Supérieure de Chimie de Rennes, Campus de Beaulieu, 35700 Rennes, France

ARTICLE INFO

Article history:
Received 21 November 2008
Received in revised form
2 June 2009
Accepted 10 June 2009
Available online 16 June 2009

Keywords:
Titan
Atmospheric evolution
Isotopes
Atmospheric escape

ABSTRACT

Using Cassini ion neutral mass spectrometer stable isotope observations, we have developed a comprehensive method for modeling the time-evolution of the stable isotopic ratios in Titan's major constituents, N_2, CH_4 and H_2. Our model provides constraints on the initial $^{14}N/^{15}N$ ratio in N_2, the time scale for the outgassing of methane from the interior, and the initial D/H ratio in methane. Over geologic time scales, the isotopes are fractionated by diffusion, atmospheric escape and photochemistry. Diffusion and escape preferentially remove the lighter isotopes for all constituents. Photolysis of methane also removes the lighter isotopes, while photolysis of nitrogen preferentially removes the heavier isotopes. We have found the following: (1) even taking past hydrodynamic escape into consideration, the initial $^{14}N/^{15}N$ ratio in N_2 cannot have changed much from its current value as the result of atmospheric processes. This is due to the large amount of N_2 that must be fractionated. High-rate loss processes, such as hydrodynamic escape, are inefficient fractionators and take a very long time to change the isotopic ratio. On the other hand, low-rate loss processes are efficient fractionators, but also take a very long time to influence a large inventory. (2) The current inventory of methane represents the remnant of methane that, constrained by the $^{12}C/^{13}C$ ratio, began outgassing from the interior more than 60 million years ago, resulting in a total inventory of 3–4 times the current inventory cycling through the system during this time period. Methane production is likely to be ongoing. (3) The initial D/H in methane was found to be $6.96–11.3 \times 10^{-5}$.

© 2009 Elsevier Ltd. All rights reserved.

1. Introduction

Titan, Saturn's largest satellite, has a thick nitrogen atmosphere with 1.4% methane in the upper atmosphere and 0.1–0.3% molecular hydrogen (Niemann et al., 2005). The mixing ratio of methane increases near the surface to 5%, but this does not affect the upper atmosphere because the methane is suppressed by condensation at higher altitudes in the troposphere. The stable isotopes of these major constituents provide a basis for mapping the evolution of Titan's atmosphere over geologic time scales. Similar calculations have been carried out for Venus to determine the amount of water lost over geologic time (Donahue et al., 1997) and at Mars to study the evolution of water, carbon dioxide (Jakosky, 1991; Jakosky et al., 1994) and the nitrogen cycle (Manning et al., 2008). Various efforts have been made to measure the stable isotopic ratios in Titan's atmosphere (e.g. Waite et al., 2005; Niemann et al., 2005; Bezard et al., 2007; Nixon et al., 2008), listed in Table 1, and work has been done to evaluate the implications of these measurements (Lunine et al., 1999; Liang et al., 2007; Cordier et al., 2008). We have developed a model that combines the methods of Hunten (1982), Hunten et al. (1989) and Donahue et al. (1997) and expands them for multiple fractionating processes to outline the evolution of the stable isotopic ratios in the major constituents over geologic time scales based on the known fractionating processes at work in Titan's atmosphere.

The $^{14}N/^{15}N$ ratio in N_2 is highly enriched compared to terrestrial values. A commonly suggested explanation for this is that up to 30 times the current inventory of N_2 escaped from the atmosphere hydrodynamically in the distant past due to higher solar extreme ultraviolet (EUV) flux (Lunine et al., 1999; Penz et al., 2005). To determine if past hydrodynamic escape can reasonably explain this extreme enrichment, we evaluated the

* Corresponding author. Tel.: +1 210 557 1605.
E-mail address: kmandt@swri.edu (K.E. Mandt).

0032-0633/$ - see front matter © 2009 Elsevier Ltd. All rights reserved.
doi:10.1016/j.pss.2009.06.005

Retour à la table des matières : p. v

Table 1
List of most recently measured isotopic ratios in Titan's atmosphere.

Isotope	Ratio	Source
$^{14}N/^{15}N$ ratio in N_2	147.5 ± 7.5	INMS extrapolated to surface
	167	Owen and Niemann (2009)
	188 ± 16	INMS extrapolated to surface (Waite et al., 2005)
Initial $^{12}C/^{13}C$ in CH_4	$89.01^{+4.45}_{-2.67}$	Alexander et al. (2007); Martins et al. (2008)
Current $^{12}C/^{13}C$ ratio in CH_4	76.6 ± 2.7	Nixon et al. (2008)
	82.3 ± 1.0	Niemann et al. (2005)
	81	INMS extrapolated to surface (Waite et al., 2005)
D/H in CH_4	$1.32 \pm 0.15 \times 10^{-4}$	Bezard et al. (2007)
D/H in H_2	$\sim 2.64 \times 10^{-4}$	Owen and Niemann (2009)

$^{14}N/^{15}N$ ratio in N_2 over time for two periods in Titan's history: a hydrodynamic escape period and a period reflecting current processes. The current processes affecting fractionation of N_2 are fairly well constrained, so the main question is the possible role that past hydrodynamic escape played in attaining the current ratio. From the model, we were able to derive a limited range of values for the initial $^{14}N/^{15}N$ ratio in N_2.

The presence of methane in the atmosphere is a source of curiosity, because the inventory currently in the atmosphere would be destroyed in ~50 million years. It is unknown how long the methane has been present, how much was initially outgassed, or if methane continues to be outgassed from the interior. Tobie et al. (2006) suggest that there have been three major methane outgassing periods since the initial formation of Titan: one major outgassing at core overturn immediately after formation, a second period of outgassing lasting from 2 to 2.6 Gigayears (Gyr) after solar system formation began, and the most recent period that began 350–1350 million years ago (mya). In our model, the most recent outgassing would then be the source of the current inventory of methane in Titan's atmosphere. Fortes et al. (2007) put forth a different model and argue that methane has been constantly outgassing since the initial formation of Titan.

After methane outgassing began, whether at Titan's formation or periodically over geological time scales, the $^{12}C/^{13}C$ and D/H isotopic ratios in methane evolved as a result of fractionating processes that occur in the atmosphere: diffusion, atmospheric escape and photochemistry. Titan's photochemistry is modestly constrained by models of the atmosphere (e.g. Wilson and Atreya, 2004; Nixon et al., 2008). Atmospheric escape is not so well understood, and some question as to its role in Titan's atmospheric evolution exists. A fit of a one-dimensional diffusion model to altitude profiles measured by the Cassini ion neutral mass spectrometer (INMS) predicts high escape rates of methane (Yelle et al., 2008) due to hydrodynamic escape (Strobel, 2008), while other models using the same data have found low escape rates attributed to sputtering (de la Haye et al., 2007a). Direct Monte Carlo simulations support a much lower loss rate (Tucker and Johnson, 2009), as do magnetospheric plasma composition measurements by Cassini (Sittler et al., 2008; Hamilton et al., 2008). Our model of isotopic evolution of the carbon ratios in methane is able to describe the atmospheric evolutionary implications of the high and low escape rates for the history of Titan's atmosphere.

The H_2 in Titan's upper atmosphere is believed to be produced by methane photochemistry, although the possibility of a surface source cannot be ruled out. H_2 produced by the methane photochemistry escapes rapidly because of its small mass and the weak gravity of Titan, and is permanently lost from the system. GCMS measured the D/H in H_2 at the surface to be ~2 times the D/H in methane, though work is still in progress to derive an exact value (Owen and Niemann, 2009).

Jeans escape is expected to be effective for H_2 because of its low mass. On the other hand, fitting a one-dimensional diffusion model to INMS altitude profiles, Cui et al. (2008) reported an escape rate ~3 times higher than that for Jeans escape, implying "slow" hydrodynamic escape of H_2 along with the methane (Strobel, 2008). Escape rates found by the three-dimensional Titan Global Ionosphere–Thermosphere Model (T-GITM) (Bell et al., 2009) are in the same range as those of Cui et al. (2008) whether methane is escaping hydrodynamically or not.

2. Data

Data from 16 passes of the Cassini spacecraft through the atmosphere of Titan to a depth below 1000 km in altitude were used to provide altitude profiles of the isotopic ratios of the major constituents for this analysis. Signal found in mass channels 2, 3, 16, 17, 28 and 29 are used to calculate densities of H_2, HD, CH_4, $^{13}CH_4$, N_2 and $^{14}N^{15}N$, respectively. These species contribute the overwhelming majority of signal to the listed mass channels. Some corrections of the raw data are necessary to correct for instrument effects and result in analytical uncertainties in the calculated isotopic ratios. These corrections include saturation of the high-sensitivity detector, high-pressure background effects, and signal contamination from ammonia and thruster exhaust (Magee et al., 2009). Saturation of the low-sensitivity detector affects calculations of both the N and C isotopic ratios; effects are apparent in mass 28 below 1300 km as well as masses 29 and 16 below 1100 km. Altitude profiles of $^{14}N/^{15}N$ are limited to values observed above 1100 km due to the excessive nature of saturation in the region below. Ammonia present in the INMS antechamber distorts the signal at masses 16 and 17. Removal of this contamination, thus, affects the calculation of $^{12}C/^{13}C$. Such distortion is much more prominent during the outbound portion of a Titan pass, and we thus limit our data to that observed during inbound.

These data cover a wide range of latitudes and locations of Titan within Saturn's magnetosphere, and thus represent a reasonable global average for our investigation of long-term processes in the atmosphere. Altitude profiles of the isotopic ratios measured by INMS provide excellent constraints on the efficiency of diffusive fractionation of molecular nitrogen and methane.

3. Model

The model we have developed for the isotopic evolution of Titan's main atmospheric constituents is based on fractionation models presented by Hunten (1982), Hunten et al. (1989) and Donahue et al. (1997). The Hunten (1982), Hunten et al. (1989) model determines the change in the isotopic ratio with increasing altitude, described by the fractionation factor for diffusive separation. It also uses the Rayleigh distillation relationship to calculate the inventory required to fractionate the isotopes by diffusion and escape. The Donahue et al. (1997) model provides a method for evaluating the time-evolution of the isotopic ratios due to differential escape. Our model employs the equations developed by Hunten (1982), Hunten et al. (1989) and Donahue et al. (1997) and expands them to allow for multiple fractionation processes, providing a comprehensive description of the evolution

Retour à la table des matières : p. v

of Titan's isotopic ratios over geologic time scales. The equations used in our model are presented in Appendix A.

3.1. Fractionation

Isotopic fractionation occurs through a variety of processes. The degree of fractionation for each process is represented by the variable f. A value for f of 1 means no fractionation, less than 1 denotes retention of the heavier isotope, and greater than 1 indicates that the lighter isotope is preferentially retained. In the atmosphere of Titan, these processes can be broken down into three specific categories: diffusion (subscript d), escape (subscript e) and chemical (subscript c) processes. Each of these categories will be addressed below.

3.1.1. Diffusive fractionation

In the region of the atmosphere between the homopause and the exobase, the isotopic ratio is expected to become lighter with increasing altitude due to diffusive processes that dominate in this region. If an atmospheric constituent is escaping, the isotopic ratio of the escaping constituent is lighter than the isotopic ratio below the homopause. This effect over geologic time scales results in an evolution of the isotopic ratio below the homopause to a heavier value. The fractionation factor due to this process is

$$f_d = \frac{R(z_{exo})}{R(z_0)} \tag{1}$$

where R is the isotopic ratio, z_{exo} and z_0 the altitudes of the exobase and homopause, respectively.

Diffusive fractionation for an atmosphere in hydrostatic equilibrium was derived by Hunten et al. (1989) based on diffusion models

$$f_d = e^{(-\Delta z/H_d)} \tag{2}$$

where $H_d = kT/((m_2-m_1)g)$ and Δz is the difference between the altitude of the homopause and the exobase. If significant atmospheric escape is occurring, the altitude profile of the escaping species and its isotope will be altered and the effect of diffusive fractionation will be reduced. In this case, Eq. (2) is not valid and diffusive fractionation effects can only be determined if the isotopic ratio is known below the homopause and at the exobase (using Eq. (1)). All diffusive fractionation factors used in this model are derived with Eq. (1).

3.1.2. Escape fractionation

Fractionation due to differential escape from the atmosphere was given by Donahue et al. (1997)

$$f_e = \frac{F_2}{F_1} * \frac{1}{R} \tag{3}$$

where F_i is the escape flux rate.

Our model evaluates two types of escape for Titan: non-thermal escape by sputtering and hydrodynamic escape.

Various non-thermal processes play a role in atmospheric escape and may contribute to isotopic fractionation. However, the recent work by de la Haye et al. (2007a,b) on Titan's corona demonstrates that sputtering results in escape fluxes an order of magnitude greater than those produced by exothermic chemistry. Therefore, in our model we include only the sputtering-induced escape of the lighter isotope (n_1), which has diffusively separated from the heavier isotope (n_2) below the exobase. Whether sputtering results in additional isotopic fractionation at Titan is not known and is assumed in our model to be zero.

Hydrodynamic escape is an outflow of the atmosphere due to a bulk velocity. The theory on hydrodynamic escape was first developed by Parker (1963). In hydrodynamic escape, energy is deposited in the upper atmosphere through solar EUV, magnetospheric electrons and protons, and upper atmospheric chemistry. This energy flux heats the upper atmosphere and results in an expansion similar to what occurs in comets. As the atmosphere expands, it reaches a point where the thermal energy is great enough to drive escape. Jeans escape is a type of escape that describes the loss of only the molecules at the extreme energetic end of the Maxwellian distribution, but in the case of hydrodynamic escape the entire Maxwellian is depleted more rapidly than it is replenished. Hydrodynamic escape only occurs at high temperatures, where the thermal energy and escape energy are approximately equal: $kT \sim 1/2 m v_{esc}^2$ (Chassefiére and Leblanc, 2004). On Titan this temperature is 530 K for H_2, 4250 K for CH_4 and 15,000 K for N_2.

The N_2 isotopic ratio measured in Titan's atmosphere indicates a significant ^{15}N enrichment compared with Earth and represents a value not commonly found throughout the solar system. The $^{14}N/^{15}N$ ratio in Mars' atmosphere shows a comparable enrichment in ^{15}N which has been attributed to fractionation by escape (e.g. Manning et al., 2008). According to conventional theory, the nitrogen isotopes on Titan are highly fractionated because a large amount of the initial N_2 in the atmosphere escaped hydrodynamically under the more extreme solar EUV radiation of the early solar system, leaving more of the isotopically heavy N_2 behind (Penz et al., 2005). According to standard theories of solar system evolution, the hydrodynamic escape of inner planets' atmospheres began some time around the end of formation of the planets, ~100 million years after the formation of the solar system, and ended at most 1 billion years later (Chassefiére, 1996). Although Titan has only 37% the surface gravity of Mars, we can use a Mars-like scenario to set an upper bound for fractionation due to hydrodynamic escape because the energy reaching Titan is only 1% of the energy reaching Mars. This represents an energy-limited regime for the purpose of our model. Hydrodynamic escape driven by solar EUV changes as a function of time (Chassefiére, 1996)

$$F(t) = F(t_0) * \left(\frac{t}{t_0}\right)^{-a} \tag{4}$$

where a is believed to be $\sim\frac{5}{6}$ and t_0 represents the time when hydrodynamic escape ceased ($\sim 10^9$ years). For a given escape rate, the energy required to drive hydrodynamic escape can be approximated by (Chassefiére, 1996)

$$\Phi = \frac{GMmF(t_0)}{r} \tag{5}$$

where r is the level at which the energy is deposited.

Recent modeling has suggested that escape of methane and molecular hydrogen from Titan is much greater than can be explained by Jeans escape or sputtering. Fits of diffusion equations to INMS altitude profiles of hydrogen (Cui et al., 2008) and methane (Yelle et al., 2008) suggest that methane is escaping at its diffusion-limited rate (Yelle et al., 2008) and hydrogen escape is ~3 times greater than the Jeans escape rate. A hydrodynamic escape model, similar to that represented in Eq. (5), applied to Titan found similar mass loss rates (Strobel, 2008), suggesting that hydrodynamic escape may be the mechanism driving the enhanced escape.

Mass fractionation of the isotopes during hydrodynamic escape is described by the equations of Hunten et al. (1987). Hydrodynamically escaping particles create a drag force on heavier species in the atmosphere and decrease the fractionation efficiency. Derived from diffusion equations for a two-component atmosphere, mass fractionation during hydrodynamic escape is

$$f_e = \frac{(m_c - m_2)}{(m_c - m_1)} \tag{6}$$

Retour à la table des matières : p. v

where $m_c = m_1+(kTF_1/b_1gX_1)$, X_1 is the mixing ratio of the lighter isotope and b_1/n_{atmos} the binary diffusion coefficient. For derivation of these fractionation factors see Appendix A.

3.1.3. Chemical fractionation

Chemistry within an atmosphere such as Titan's causes a net loss of molecular nitrogen and methane by breaking up the molecules which recombine to form larger molecules and eventually aerosols. These aerosols are deposited on the surface and the initial nitrogen and methane are assumed to be permanently lost from the system.

Nitrogen is fractionated due to a shielding effect in the atmosphere resulting in preferential photodissociation of $^{15}N^{14}N$ over $^{14}N^{14}N$ at some altitudes below the homopause, which is later incorporated into HCN, the major nitrile resulting from the dissociated molecular nitrogen (Liang et al., 2007). The fractionation factor resulting from this process is found by

$$f_c = \frac{R_{\text{product}}}{R_{\text{reactant}}} \tag{7}$$

The $^{12}C/^{13}C$ ratio in more complex molecules (containing more than one carbon atom) was recently observed to have an enrichment in the lighter isotope relative to the $^{12}C/^{13}C$ ratio in methane (Nixon et al. 2008). This enrichment is possibly due to a kinetic isotope effect (KIE) in which ^{12}C reactions occur 1.04 times faster than ^{13}C reactions.

3.2. Inventories required for fractionation

Both Hunten et al. (1989) and Donahue et al. (1997) use the Rayleigh distillation relationship to determine the total inventory required for fractionation from an initial isotopic ratio to the current ratio by the various fractionating processes discussed above

$$\frac{n_1^0}{n_1} = \left(\frac{R}{R_0}\right)^{(1/(1-f))} \tag{8}$$

In this case, the f represents the total fractionation by all combined processes. Calculating the combined fractionation effects is complicated, and discussed in Appendix A. Inventories are measured in terms of the current atmospheric inventory. In the case of methane, we include the liquid methane in the surface lakes assuming that free exchange occurs between the lakes and the atmosphere. Any production over time adds to the total inventory represented in Eq. (8).

3.3. Isotopic ratios over time

Donahue et al. (1997) used a differential equation for both isotopes to evaluate the time-evolution of the isotopic ratio

$$\frac{dn}{dt} = P - L$$

where n is the column density, P the column-integrated production rate and L the column-integrated loss rate. We used the same method to determine individual equations for each of the isotopic ratios that our model evaluates. We divided the evolution of nitrogen into two time periods: hydrodynamic escape starting with the formation time of Titan and ending at 1 Gyr after solar system formation started, and a second period starting at the end of the hydrodynamic escape period and continuing to today. The methane equations ((16A) and (17A) in Appendix A) allow for a production rate, an energy-limited photochemical loss rate and either density-dependent or energy-limed escape loss rates. The equations for hydrogen ((18A) and (19A) in Appendix A) are coupled with the methane equations, because the production rate for hydrogen depends on methane's photochemical loss rate. All of these equations are listed in Appendix A in Table 1A.

3.4. Application to modeling the isotopic ratios

Once we derived the equations for the column densities as a function of time, we developed a model of the evolution of the isotopes based on what was known about Titan. Model inputs included:

- the isotopic ratios as measured by Cassini composite infrared spectrometer (CIRS) and INMS and Huygens gas chromatograph mass spectrometer (GCMS) and the initial carbon isotopic ratio as determined from a wide range of samples throughout the solar system as referenced in Table 1;
- the maximum possible time scale for hydrodynamic escape to influence the nitrogen isotopes;
- the fractionation factors and the loss rates as listed in Tables 2 and 3 and
- the binary diffusion coefficient of N_2 from Massman (1998) to determine the critical mass values for past hydrodynamic escape.

3.4.1. $^{14}N/^{15}N$ Evolution

Letting the current parameters (time, density, ratio, etc.) be represented by the subscript *b*, the parameters at the time when nitrogen hydrodynamic escape ended be represented by subscript

Table 2
Published methane loss and hydrogen production rates used to evaluate the loss and production rates for methane and hydrogen.

Source	CH_4 loss	H_2 production	H_2 escape	C/H[a] aerosol	C/H[b] thermosphere
Yung et al. (1984)	1.5×10^{10}		7.2×10^{9}		
Toublanc et al. (1995)	1.3×10^{10}		1.0×10^{10}		
Wilson and Atreya (2004)	4.9×10^{9}	3.2×10^{9}			
Lebonnois et al. (2003)	3.4×10^{10}	7.5×10^{9}	1.5×10^{10}		
Lavvas et al. (2008)	1.4×10^{10}	8.5×10^{9}		1.3	
Sekine et al. (2008)			$9.6–10.4\times10^{9}$	0.62–0.64	1.5
Magee et al. (2009)					1.5
Input for this model	1×10^{10}	7.5×10^{9} chemistry 6.2×10^{9} surface	1.37×10^{10}		

All rates are given in $cm^{-2}\,s^{-1}$.

[a] This is the carbon to hydrogen ratio of the aerosols that are the end product of the methane photochemistry in Titan's atmosphere.

[b] This is the carbon to hydrogen ratio of the minor species produced early in the photochemistry process in the upper atmosphere where molecular hydrogen production is greatest.

Retour à la table des matières : p. v

Table 3
Results for the $^{12}C/^{13}C$ and D/H analysis based on the two methane escape scenarios.

	Hydrodynamic	Sputtering and jeans escape
CH_4 escape flux ($cm^{-2}\,s^{-1}$)	$2–3.5\times10^{9}$	$2.8\pm2.1\times10^{7}$
CH_4 escape limited by	Energy	Density
H_2 escape flux ($cm^{-2}\,s^{-1}$)	$1.37\pm0.01\times10^{10}$	4×10^{9}
Total $^{12}C/^{13}C$ escape fractionation factor	0.685 ± 0.044	
$^{12}C/^{13}C$ CH_4 chemical fractionation factor	0.961	
D/H CH_4 chemical fractionation factor	0.84	
Total D/H escape fractionation factor for H_2	0.442 ± 0.006	
Time scale (mya)	59.5 ± 4.8	183 ± 15
Total inventory	3.47 ± 0.28	4.25 ± 0.36
Initial methane D/H	$1.05\pm0.08\times10^{-4}$	$8.73\pm0.74\times10^{-5}$
Predicted H_2 D/H	4.0 ± 0.1	$3.4\pm0.4\times10^{-4}$

c, and solving for the density of isotopically light nitrogen at the time when hydrodynamic escape ended gives

$$n_c = \frac{n_b - (L_c/K_e)(e^{-K_e t_b} - 1)}{e^{-K_e t_b}}$$

where L_c is the chemical loss rate and $K_e = F_e/n$. This assumes that the current escape due to sputtering is linearly dependent on the amount of N_2 available to remove from the atmosphere.

The same type of equation is solved for the heavier isotope based on the current isotopic ratio to give the ratio at the end of the hydrodynamic escape regime

$$R_c = \frac{R_b[n_b - ((f_c L_c)/(f_e K_e))(e^{-f_e K_e t_b} - 1)]}{n_b - (L_c/K_e)(e^{-K_e t_b} - 1)}\left(\frac{e^{-K_e t_b}}{e^{-f_e K_e t_b}}\right)$$

The initial nitrogen density, at the time when hydrodynamic escape began is the density at t_c plus the escape rate (Eq. (4)) integrated from t_0 to t_c. The initial isotopic ratio is found by determining the hydrodynamic escape fractionation as a function of time and solving the integral in the equation for the nitrogen hydrodynamic escape period at time t_0. This solves for the unknowns in the other nitrogen equations, (Appendix A Eqs. (12A)–(14A)), to map out the evolution of the isotopes over time for both the hydrodynamic period and the current regime period.

3.4.2. Evolution of methane's isotopes

The initial isotopic ratio for $^{12}C/^{13}C$ is limited to a small range, δ^{13} −30‰ to 50‰, based on values measured throughout the solar system (Alexander et al., 2007; Martins et al., 2008), so we solved for $^{12}C/^{13}C$ first. As with nitrogen, the initial density at the onset of outgassing for methane lost due to photochemistry and sputtering was found by

$$n_0 = \frac{n_b - ((P_1 - L_c)/K_e)(1 - e^{-K_e t_b})}{e^{-K_e t_b}} \quad (9)$$

The same approach was taken for methane lost due to photochemistry and hydrodynamic escape, but treating the hydrodynamic escape rate as energy limited.

Substituting Eq. (9) into the equations for the evolution of methane (see Eqs. (16A) and (17A) in Appendix A) at time t_b and dividing the heavy isotope density by the lighter isotope density gives the current isotopic ratio. Since this value is known, a solution for t_b and n_0 is found based on the current isotopic ratio. The value of time t_b represents the length of time since the start of methane outgassing from the interior, and n_0 is the amount of the initial major outgassing. This must be instantaneous on geological time scales.

The Rayleigh distillation Eq. (8), was then used to determine the relationship between the total fractionation factor for all the various processes, the total inventory cycled through the system, and the current and initial isotopic ratios.

The fractionation factor for the system as a whole changes as a function of time and is therefore difficult to estimate. The total fractionation factor for the system can be found through Eq. (8), since the current density and initial and current isotopic ratios are known, and the total inventory can be found through

$$n_1^0 = n_0 + Pt_b$$

This solves for all the unknowns in the methane evolution equations allowing the evolution of the isotopes to be mapped.

The initial D/H in methane is not known, but can be solved based on current measurements of the D/H in methane and what we have learned about methane from $^{12}C/^{13}C$. The initial D/H is

$$R_0 = R_b\left[\frac{((P - L_c)/K_e))(1 - e^{-K_e t_b}) + n_0 e^{-K_e t_b}}{((P - f_c L_c)/(f_e K_e))(1 - e^{-f_e K_e t_b}) + n_0 e^{-f_e K_e t_b}}\right]$$

where f_c for CH_3D (Lunine et al., 1999) is not the same as for $^{13}CH_4$.

4. Results and discussion

In this section, we summarize the model input parameters and the results for each of the major constituents. We used the model to investigate: (1) whether past hydrodynamic escape of nitrogen can explain the extreme enrichment in the heavy isotope and (2) what impact the two different escape rates proposed for methane have on the isotopic ratios.

4.1. Molecular nitrogen

INMS data for nitrogen show fractionation (Fig. 1) between 1100 km and the exobase. Data below 1100 km are excluded due to detector saturation effects. To determine the isotopic ratio below the homopause, the data are fit to the T-GITM for multiple scenarios in which methane is escaping hydrodynamically and when it is not (Bell et al., 2009). The fit of the model, indicates that R below the homopause is 147.5 ± 7.5. This shows enrichment over terrestrial values of δ^{15} 902 ± 7‰. GCMS measurements indicate a higher ratio, around 167 (Owen and Niemann, 2009), so the mean value with error bars including both ratios, 155 ± 15, was used for this modeling. The difference in the two results may be due to poor understanding of the total altitude profile of the isotopic ratio below 1000 km, where atmospheric shielding effects result in a preferential photodissociation of the heavier isotope over the lighter (Liang et al., 2007). Until further constraints are available, large error bars are necessary. The $^{14}N/^{15}N$ ratio at the exobase is 245 ± 15, giving a total diffusive fractionation factor of 0.633 ± 0.062.

De la Haye et al. (2007a) found that nitrogen is sputtering at a rate greater than by other non-thermal processes (de la Haye et al., 2007b). It is unknown if there is any additional fractionation due to sputtering. Photodissociation of N_2 fractionates the isotopes because photons with wavelengths that dissociate $^{14}N^{15}N$ can penetrate deeper into the atmosphere than those that dissociated $^{14}N^{14}N$ (Liang et al., 2007). The primary nitrile produced by photodissociation of N_2 is HCN, and the net effect of this fractionation is observed in the difference between the isotopic ratio of N_2, ~155 and its product HCN, 85 ± 25. For this reason, a chemical fractionation factor of 1.88 ± 0.58 was used in the model based on the $^{14}N/^{15}N$ ratios of N_2 and its product HCN (Eq. (7)). Because this chemical fractionation depends on the

Retour à la table des matières : p. v

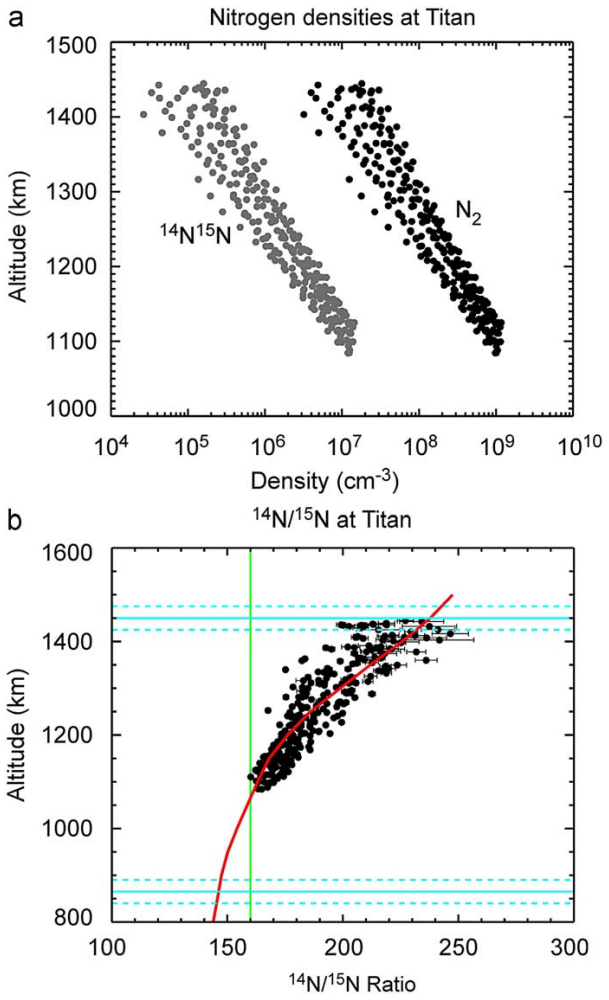

Fig. 1. (a) Altitude profile of INMS measurements of $^{14}N^{14}N$ (black) and $^{15}N^{14}N$ (gray). (b) Altitude profile of INMS measurements for the $^{14}N/^{15}N$ ratio showing the fit of T-GITM (red) to determine the ratio below the homopause and the GCMS value (green) for comparison. The exobase and homopause are represented by the cyan lines.

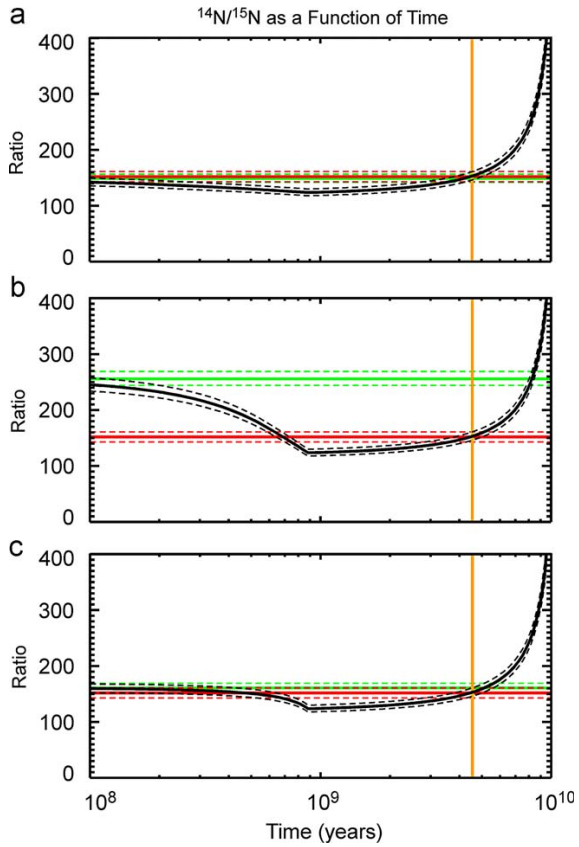

Fig. 2. $^{14}N/^{15}N$ isotopic ratio (black line with dashed error bars) as a function of time based on initial hydrodynamic escape then transitioning to the current regime of sputtering and chemical fractionation of HCN/N_2. The source ratio is shown in green and the INMS/GCMS measured value is shown in red. The orange line represents the approximate age of the solar system and is the maximum time period over which fractionation could take place. Initial $^{14}N/^{15}N$ ratios and hydrodynamic escape rates at the end of the hydrodynamic regime are: (a) 149, $1\times10^{9}\,cm^{-2}\,s^{-1}$, (b) 256, $1\times10^{10}\,cm^{-2}\,s^{-1}$ and (c) 161, $1\times10^{11}\,cm^{-2}\,s^{-1}$.

presence of methane in the atmosphere it would not be effective in cases described by Tobie et al. (2006), where methane has disappeared from the atmosphere. In this case, the atmosphere would likely collapse to a thin layer of nitrogen (Lorenz et al., 1997) and both fractionating loss processes – escape and photochemistry – would cease.

The results of entering the nitrogen fractionation factors into Eqs. (12A)–(15A), assuming zero production and solving for the initial isotopic ratio, are shown in Fig. 2 for three possible t_0 values of the hydrodynamic flux (see Eq. (4)). The model suggests that it is impossible over the history of the solar system for the ratio to have changed from terrestrial values of 272 to the current value, even if hydrodynamic escape is included (see Fig. 3). There are two reasons for this: hydrodynamic escape does not fractionate very efficiently, and from the time hydrodynamic escape ended to the present the isotopic ratio has become less fractionated from the terrestrial value due to photochemistry.

The maximum possible value for the initial ratio assuming that hydrodynamic escape occurred for the longest time possible is 254. The initial ratio depends directly on the escape rate at the end of the hydrodynamic escape period and peaks when the escape rate is $1.4\times10^{10}\,cm^{-2}\,s^{-1}$. A rough calculation can be made as to what the escape rate at that time period may have been based on Eqs. (4) and (5). Since the current solar EUV flux at Titan is $99.32\,erg\,m^{-2}\,s^{-1}$, the escape rate at the end of hydrodynamic escape would have been $2.16\times10^{10}\,cm^{-2}\,s^{-1}$. This value is greater than the rate at the peak initial ratio and gives an initial isotopic ratio of ~227. A more detailed energy-evaluation is the next step we intend to take in this analysis. The main conclusion is that initial ratio is limited to less than 254.

Penz et al. (2005) found that past EUV-driven escape could remove 30 times the current atmospheric inventory of N_2, but base their fractionation of the isotopes on enhanced diffusive fractionation due to an increased distance between the exobase and homopause during the escape process. A problem with this approach is that diffusive fractionation is invalid as described by Eq. (2) based on the requirement of hydrostatic equilibrium. A hydrodynamically escaping atmosphere is not in hydrostatic equilibrium, it is in an outward expanding motion. For this reason, the fractionation during hydrodynamic escape is best represented by Eq. (6), as we have used in our model where the

Retour à la table des matières : p. v

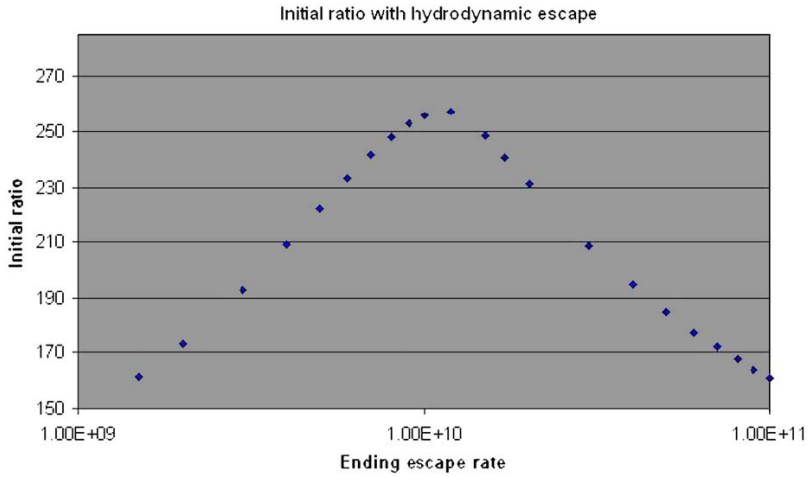

Fig. 3. Illustration of the influence that the ending hydrodynamic escape rate has on the initial ratio of $^{14}N/^{15}N$. The initial ratio peaks at a value of 254 when the ending escape rate is $1.4 \times 10^{10}\,cm^{-2}\,s^{-1}$.

altered altitude profile due to hydrodynamic escape is properly accounted for.

Since molecular nitrogen is the bulk constituent of the atmosphere (98%) it is difficult for any atmospheric process to change the isotopic ratio of nitrogen over the lifetime of the solar system. Large loss processes provide weak fractionation, and small loss processes provide strong fractionation. Neither large nor small escape rates can account for the fractionation of N_2 compared with terrestrial values, so processes other than escape must have led to the enrichment of the $^{14}N/^{15}N$ ratio in N_2.

The fact that the initial $^{14}N/^{15}N$ ratio in Titan is significantly lower than the terrestrial value suggests strongly that the nitrogen sources are different for the two bodies. Earth's nitrogen was originally incorporated in silicate phases (Mather et al., 2004); the current terrestrial atmospheric $^{14}N/^{15}N$ ratio is well within the range of values measured in interplanetary dust particles (Wieler et al., 2006). In the case of Titan, it is difficult to explain the highly enriched $^{14}N/^{15}N$ ratio with any measured phase of molecular nitrogen in primordial materials, suggesting that the molecular nitrogen came from a distinct chemical source.

It has been proposed that Titan's molecular nitrogen came from primordial ammonia initially acquired by the satellite during its accretion (Atreya et al., 1978; Mousis et al., 2009). The ammonia was possibly incorporated in the form of ammonia hydrate in icy planetesimals accreted by Titan and in turn could have been derived from interstellar ices. The conversion of ammonia to the N_2 atmosphere could have produced some fractionation, but the degree of fractionation is difficult to determine at this time. It has been shown that ion-molecule chemistry in dense interstellar and/or protostellar material could create very low $^{14}N/^{15}N$ ratios in the ammonia ice that is produced in these environments (Charnley and Rodgers, 2002). Hence, the accretion in Titan of ammonia of interstellar origin may account for the initial ^{15}N enrichment (relative to the terrestrial value) needed by the initial atmospheric nitrogen reservoir to explain the current observed $^{14}N/^{15}N$ ratio. Cometary measurements of the $^{14}N/^{15}N$ ratio in NH_3 have not been made, but $^{14}N/^{15}N$ ratio values for CN in comets 122P/1995 S1 (de Vico) and 153P/2002 C1 (Ikeya–Zhang) are in the range seen at Titan (Jehin et al., 2004).

4.2. Methane and molecular hydrogen

To understand the evolution of methane at Titan, we must consider both the $^{12}C/^{13}C$ and D/H ratios.

4.2.1. $^{12}C/^{13}C$

CIRS and GCMS have measured close, but differing values for the $^{12}C/^{13}C$ ratio in methane: 76.6 ± 2.7 (Nixon et al., 2008) and 82.3 ± 1.0 (Niemann et al., 2005), respectively. These values represent enrichments of δ^{13} 162‰ and δ^{13} 81.5‰ over terrestrial values. The range seen throughout the solar system is δ^{13} −30‰ to 50‰ (Alexander et al., 2007; Martins et al., 2008), suggesting a net fractionation of the carbon isotopes of methane in Titan's atmosphere from what the primordial value likely was. In this analysis, the current $^{12}C/^{13}C$ ratio was set at 78.75 ± 4.85 to include both measurements and their error bars.

Two distinct escape rates for CH_4 that differ by two orders of magnitude have been reported: $2.8 \pm 2.1 \times 10^7\,cm^{-2}\,s^{-1}$ as a result of sputtering (de la Haye et al., 2007a) and $2–3.5 \times 10^9\,cm^{-2}\,s^{-1}$ (Yelle et al., 2008) as a result of hydrodynamic escape (Strobel, 2008). A difference of two orders of magnitude in the loss rate can have significant implication for the long-term evolution of the atmosphere. To determine the effect of diffusive fractionation, the $^{12}C/^{13}C$ ratio at the exobase was found using T-GITM and the values from INMS in the upper atmosphere (Fig. 4) as was the case for N_2. The fit of T-GITM to the data was done for multiple scenarios of methane escape as outlined in Bell et al. (2009) to determine the appropriate error bars for the fractionation factor. The fractionation factor is 0.685 ± 0.044.

In addition to escape, photochemistry has a significant impact on the methane inventory and, consequentially, the isotopic ratio over geological time scales. Nixon et al. (2008) show a trend of increasing $^{12}C/^{13}C$ with higher order hydrocarbons, suggesting that some chemical fractionation occurs. The fractionation factor for this process is probably due to a KIE as described in Section 3.1.3 has a value of 0.961.

Since sputtering and hydrodynamic escape rates differ by two orders of magnitude, the total methane reservoir (i.e. the total amount of methane released from the interior), n_1^0/n_1, and timescale for a hydrodynamic escape scenario will be quite different from those for a sputtering scenario. The two time scales

Retour à la table des matières : p. v

can be compared to recent models of Titan's interior evolution (Tobie et al., 2006; Fortes et al., 2007) to determine the interior evolution implications for each escape rate.

4.2.2. D/H in CH_4 and H_2

The current D/H for methane cannot be determined with INMS data due to the small fraction of CH_3D in the same mass channel as $^{13}CH_4$. The value given by CIRS (Bezard et al., 2007) is $1.32 \pm 0.15 \times 10^{-4}$. The diffusive/escape fractionation factors for CH_3D/CH_4 will be the same as was measured for the $^{12}C/^{13}C$ ratios. The chemical fractionation factor is expected to be different due to the stronger bond between the carbon and deuterium molecules compared to carbon and hydrogen. Lunine et al. (1999) estimated this fractionation factor to be 0.84 ± 0.04.

D/H ratios throughout the solar system vary widely, and a source ratio for the methane in Titan is difficult to estimate. The total methane reservoir for CH_3D/CH_4 will be the same as that found for the $^{12}C/^{13}C$ ratios. Knowing the reservoir size and the total fractionation of CH_3D/CH_4, we were able to solve for the initial D/H in methane.

The production of H_2 in the upper atmosphere is tightly coupled to the loss of methane, though uncertainty exists as to the exact percentage of methane loss that represents H_2 production (see Table 2). In order for H_2 to be in equilibrium, the production rate must equal the loss rate. In this analysis, the production was assumed to be ~75% of the methane chemical loss rate and the remaining production was presumed to be from the possible enriched surface source (Owen and Niemann, 2009).

As in the case of methane and nitrogen, differential escape of H_2 and HD will over time increase the isotopic ratio. Using T-GITM, we found a fractionation factor for H_2 escape of 0.442 ± 0.006 (Eq. (3)).

When modeling the isotopic ratios over time, two scenarios were investigated: (1) hydrodynamic escape of methane and (2) methane loss through sputtering.

4.2.3. CH_4 and H_2 loss scenarios

Different loss mechanisms have been proposed for the escape of CH_4 from Titan. Our model allows us to assess the implications of the proposed mechanisms for the evolution of the atmosphere. All results are summarized in Tables 3 and 4.

4.2.3.1. Hydrodynamic escape. The evolution of the CH_4 and H_2 isotopic ratios as a function of time is shown in Figs. 5a, 5c and 6a and 6b for the hydrodynamic scenario. In this scenario, the value of the production rate through methane outgassing from the interior has no effect on the time scale because all loss rates are constant. This factor limits the total period of the most recent methane outgassing episode to the last 59.5 ± 4.8 million years. The initial D/H in methane is $1.05 \pm 0.08 \times 10^{-4}$, and the current D/H in hydrogen by this scenario would be $4.0 \pm 0.10 \times 10^{-4}$. The total inventory of methane required to be outgassed from the interior and cycle through the various fractionating processes is 3.47 ± 0.28 times the current inventory.

If the isotopic ratio is in steady state, the production rate required to bring the steady-state ratio to the current ratio is 2.2 times the photochemical loss rate. However, any time scale beyond 59.5 ± 4.8 million years would result in a massive current inventory of CH_4 (see Fig. 5d). On the other hand, if the CH_4 inventory is assumed to be in steady state, where the production equals the loss, then the isotopes cannot ever reach steady state

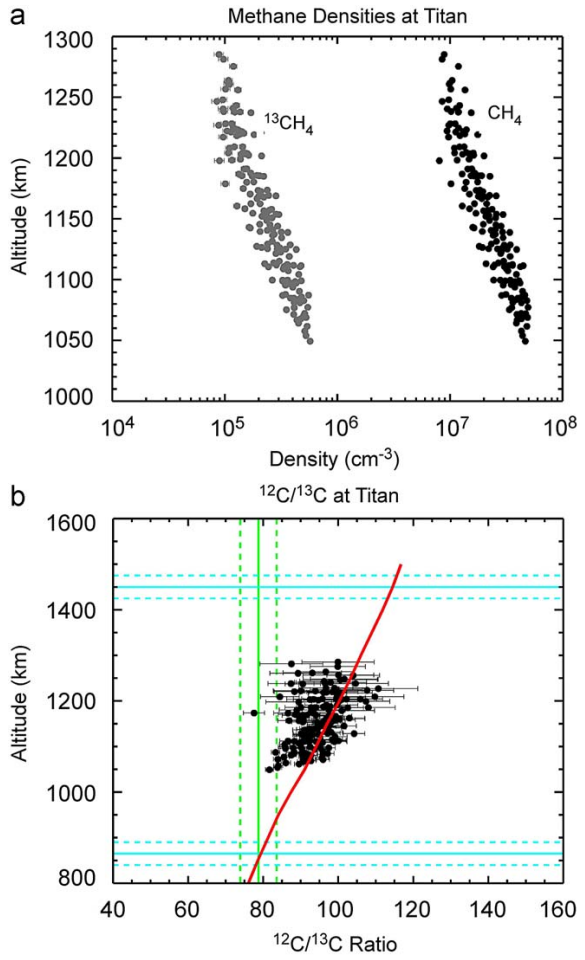

Fig. 4. (a) Altitude profile of INMS measurements of $^{12}CH_4$ (black) and $^{13}CH_4$ (gray). (b) Altitude profile of INMS measurements for the $^{12}C/^{13}C$ ratio showing the fit of T-GITM (red) to determine the ratio at the exobase and the CIRS value (green) for reference. The exobase and homopause are represented by the cyan lines.

Table 4
A comparison of our two scenarios for methane volatile evolution with the surface organic inventory in GT Carbon as estimated by Lorenz et al. (2008).

	Sand dune inventories	Isotopic model: hydrodynamic escape	Isotopic model: sputtering
Total surface lake and atmospheric reservoir passing through the system	Not addressed	497,000±40,000	1,254,000±810,000
Present day surface lake and atmospheric reservoir	376,000–520,000		
Permanently lost to complex organics	160,000–640,000	312,000±25,000	955,000±80,000
Sediments on surface due to haze production according to the mass flux of Lavvas et al. (2009)	Not addressed	57,100±4600	183,700±15,100
Lost to the magnetosphere	Not addressed	41,500±3300	4200±2700

Retour à la table des matières : p. v

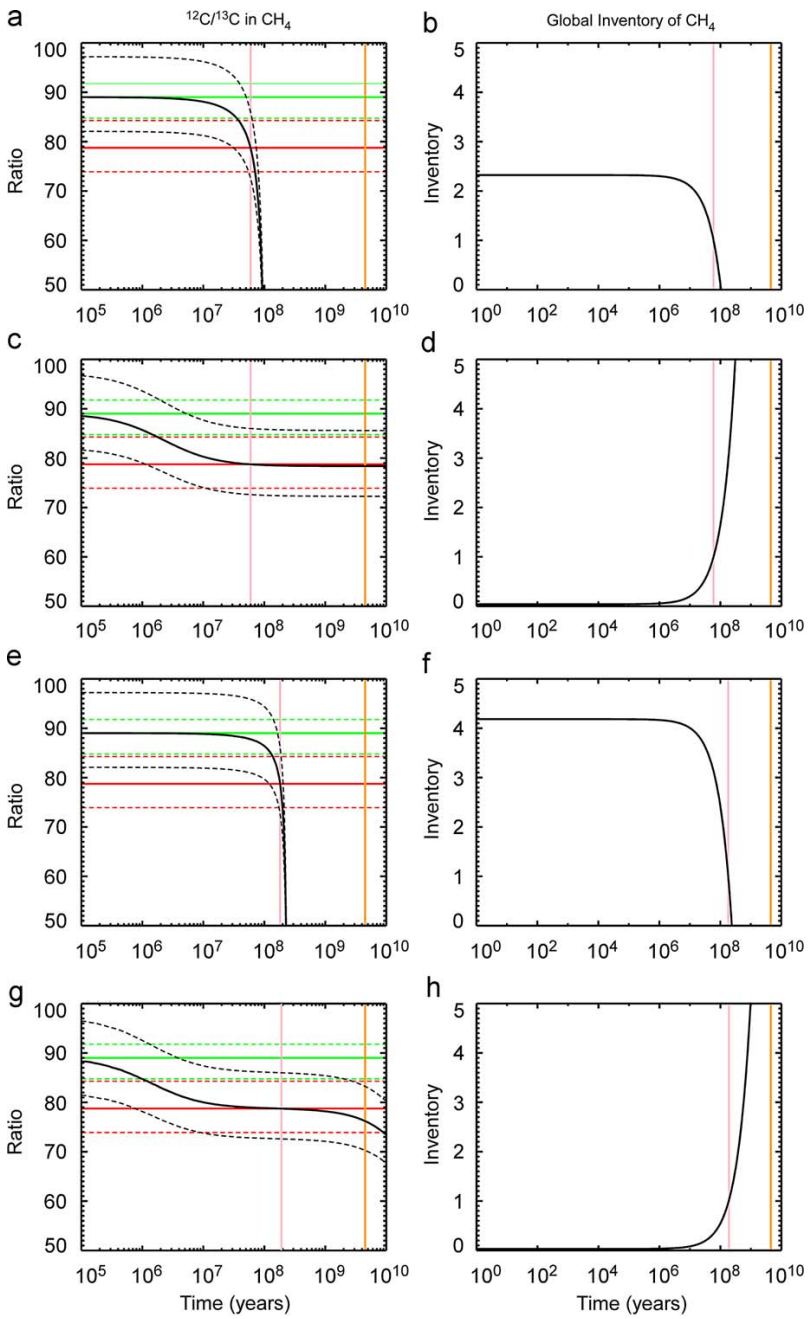

Fig. 5. $^{12}C/^{13}C$ isotopic ratio (a, c, e and g: black line with dashed error bars) and methane inventory in terms of the current inventory (b, d, f and h: black line) as a function of time for the two methane loss scenarios. The green lines represent the initial isotopic ratio and the red lines are the CIRS/GCMS measurement. The pink line shows the length of time required to fractionate the isotopes to the CIRS/GCMS value and the orange line gives the lifetime of the solar system. (a) and (b) Hydrodynamic escape with no production; (c) and (d) hydrodynamic escape with maximum production; (e) and (f) sputtering of methane with no production; and (g) and (h) Sputtering of methane with maximum production.

and would continue to decrease. This effectively limits the time scale to 59.5 ± 4.8 million years. Recent interior modeling shows either initial outgassing around 350–1350 mya (Tobie et al., 2006) or an ongoing production rate for the entire history of Titan (Fortes et al., 2007). A time scale limit of 59.5 ± 4.8 million years is inconsistent with both of these models.

In the hydrodynamic scenario, a total of $41{,}500 \pm 3300$ GT of carbon is lost to space while $312{,}000 \pm 25{,}000$ GT is permanently deposited onto the surface. Table 4 shows a comparison of these values to inventories of dunes on the surface of Titan (Lorenz et al., 2008).

4.2.3.2. Sputtering of CH_4 and jeans escape of H_2. Figs. 5e, 5g, 6c and 6d show the evolution of the CH_4 and H_2 densities and isotopic ratios as a function of time for the scenario, where CH_4 escapes due to sputtering. In this scenario, a total inventory of 4.25 ± 0.36

Retour à la table des matières : p. v

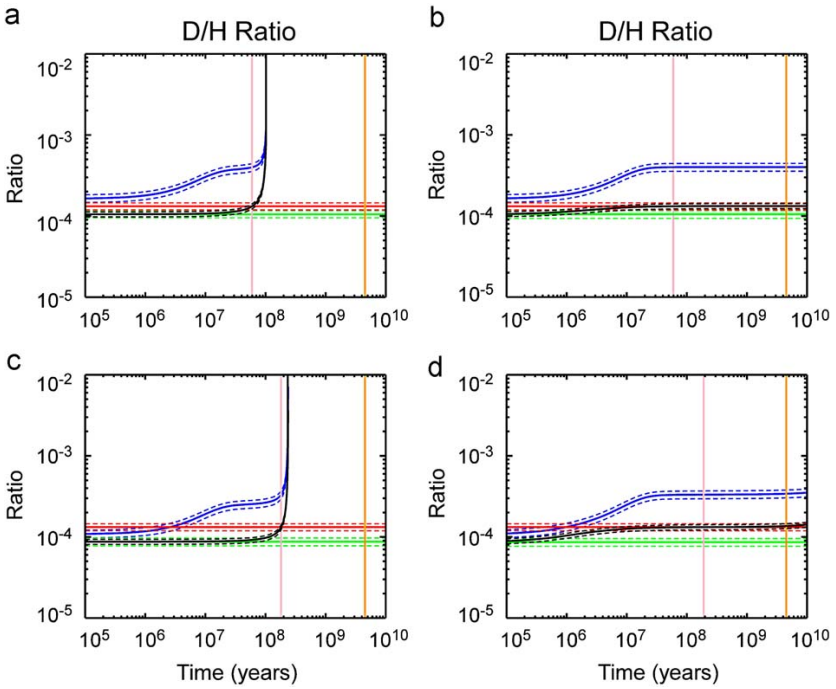

Fig. 6. D/H in CH_4 (black line with dashed error bars) and H_2 (blue line with dashed error bars) as a function of time for the two methane loss scenarios with zero and maximum production. The green lines represent the initial isotopic ratio, and the red lines are the CIRS measurement. The pink line shows the length of time required to fractionate the isotopes to the CIRS value and the orange line gives the lifetime of the solar system. The initial D/H in CH_4 is constrained by the fractionation influencing the $^{12}C/^{13}C$ isotopic ratio. (a) Hydrodynamic escape with zero production; (b) hydrodynamic escape with maximum production; (c) sputtering of methane with zero production and (d) sputtering of methane with maximum production.

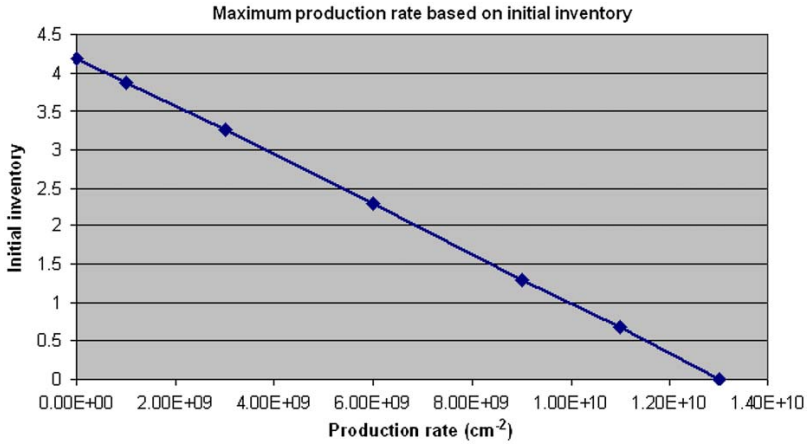

Fig. 7. The amount of methane that must be outgassed instantaneously on geological time scales at the onset of methane fractionation is linearly dependent on the ongoing production rate since outgassing began.

times the current inventory of methane has been outgassed from the interior over the past 183 ± 15 million years. This time scale is also less than that proposed by Tobie et al. (2006) for the most recent methane outgassing period.

The initial inventory at the onset of the most recent methane outgassing period is dependent upon the value of any ongoing production rate (i.e. cryovolcanic release, etc.). For zero production, the initial inventory is 4.25 times the current inventory. Allowing for ongoing production decreases the initial inventory linearly to zero, with a maximum production rate equal to 130% of the photochemical loss rate (see Fig. 7). Inventories of 4.2 times the current inventory require a massive initial outgassing from the interior on very short geologic time scales that may not be realistic without obvious surface structures providing evidence of such an event. More data on surface structures are needed to constrain the ongoing production rate if any exists. If the

Retour à la table des matières : p. v

outgassing is ongoing at the maximum possible rate, the isotopes fractionate slowly enough that they remain within the error bars of the values measured by CIRS and GCMS over the lifetime of the solar system. This should mean that both interior models (Tobie et al., 2006; Fortes et al., 2007) could agree with the isotopic measurements if escape of methane is limited to the sputtering rate, but as Fig. 5h shows the inventory increases rapidly with time just like in the hydrodynamic scenario. Initial inventory estimates outlined in Fig. 7 suggest that production (i.e. cryovolcanic release, etc.) is ongoing. Like in the hydrodynamic scenario, a steady-state inventory (production equals loss) of CH_4 would lead to a constantly decreasing isotopic ratio, effectively limiting the time scale to 183 ± 15 million years.

Only 4200 ± 2700 GT carbon is lost to space, while $955{,}000 \pm 80{,}000$ GT is permanently deposited onto the surface. According to Table 4, the total carbon deposited on the surface is greater than current estimates of surface dune material. The excess material is probably not sculpted into dunes but spread across the surface of Titan (Elachi et al., 2005).

The D/H in H_2 would be $3.4 \pm 0.4 \times 10^{-4}$. The initial D/H in methane was $8.73 \pm 0.74 \times 10^{-5}$, about three times the protosolar value. This value is in agreement with the one found by the preliminary work of Cordier et al. (2008).

4.2.3.3. Implications of the results of the two distinct scenarios. The error bars for each of the result parameters reflects each parameter's sensitivity to variations in the input fractionation factors and isotopic ratios. The result parameters' sensitivity to loss rates is highlighted by the difference between the results for the two scenarios as summarized in Table 3. Variations in the loss rates, therefore, have a much greater impact on the end result than the fractionation factors or the input isotopic ratios (all of which have fairly wide error bars to begin with).

Both scenarios produce an initial D/H in methane that is much greater than the protosolar value. This need for an initially high D/H ratio in the atmospheric methane reservoir has implications for the origin of the material of Titan. In particular, such a high initial ratio supports the idea that Titan was formed from solids produced in the primitive solar nebula and not in Saturn's subnebula itself. Indeed, the initially high D/H ratio in Titan's methane would result from the isotopic thermal exchange of molecular hydrogen with CH_3D in the gas phase of the solar nebula. In this case, CH_3D might have originated from highly deuterium-enriched ISM ices that vaporized when entering the nebula (Mousis et al., 2002), reducing the highly enriched ratio to the initial value that is still enriched over protosolar ratios. During the cooling of the nebula, the methane was then trapped in crystalline ices around 10 AU, perhaps in clathrates formed at about 60 K, and incorporated into planetesimals that were preserved in the Saturnian subnebula because the latter was too cold to fully vaporize the ices (Mousis et al., 2009). Such a model would be consistent with the origin of nitrogen as well in that it argues against heavy chemical reprocessing in a warm disk around Saturn.

Alternatively, Atreya et al. (2006) have argued that methane could be formed in Titan's interior by reactions of CO and CO_2 with water and rock. In this case, the D/H ratio in methane outgassed to the atmosphere would have been determined by that in the water, modified by fractionation associated with these "serpentinization" reactions. However, preliminary calculations show that it is impossible to derive by serpentinization the initially high D/H ratio in CH_4 in Titan from a SMOW or higher D/H ratio in the bulk water of the satellite (Mousis et al., 2009). Under these conditions, it is unlikely that the methane of Titan was produced in its interior.

5. Conclusion

By modeling the evolution of the stable isotopic ratios, based on the currently available observational data and using the parameters described in the previous sections, we conclude the following:

1. Fractionation of the atmosphere's bulk constituent is very difficult. Small escape rates are more efficient at fractionating the isotopes, but take a very long time to be effective due to the amount of inventory to influence. Large escape rates provide very weak fractionation and also take a very long time to influence the inventory because of the lack of effective fractionation. Therefore, the initial isotopic ratio could not have changed much over the lifetime of Titan as a result of atmospheric processes. A highly enriched initial isotopic ratio could be explained by ion-molecule chemistry in dense interstellar and/or protostellar material producing ammonia ice with very low $^{14}N/^{15}N$ ratios (Charnley and Rodgers, 2002). This ammonia was incorporated in the form of ammonia hydrate in icy planetesimals accreted by Titan (Atreya et al., 1978; Mousis et al., 2009) and was later the source of the molecular nitrogen atmosphere (Atreya et al., 1978; Mousis et al., 2009).
2. Because current fractionation of the nitrogen isotopes depends directly on the presence of methane in the atmosphere, fractionating loss processes – escape and photochemistry – would cease during periods when methane may be absent. In this case, the atmosphere would likely collapse to a thin layer of nitrogen (Lorenz et al., 1997).
3. Isotopic evolution of the $^{12}C/^{13}C$ ratio in hydrodynamically escaping methane suggests that the current inventory of methane represents that which began outgassing from the interior 59.5 ± 4.8 million years ago, that $312{,}000 \pm 25{,}000$ GT of carbon has been deposited on the surface, and that $41{,}500 \pm 3300$ GT of carbon has been lost to space.
4. In the case of methane that is sputtering, isotopic evolution of the $^{12}C/^{13}C$ ratio suggests that the current inventory of methane represents that which began outgassing from the interior 183 ± 15 million years ago, that $955{,}000 \pm 80{,}000$ GT of carbon has been deposited on the surface, and that 4200 ± 2700 GT of carbon has been lost to space.
5. To start the process of methane outgassing with a reasonable inventory of methane, production is expected to be ongoing.
6. Ongoing production of methane from the surface as suggested by the Fortes et al. (2007) interior model requires current methane inventories orders of magnitude greater than exist to agree with the isotopic ratio measurements.
7. The initial D/H in methane was $1.05 \pm 0.08 \times 10^{-4}$ for hydrodynamically escaping methane or $8.73 \pm 0.74 \times 10^{-5}$ for sputtering methane. This is an enrichment of 3–4 times the protosolar value. This initially high D/H ratio in the atmospheric methane reservoir supports the idea that Titan was formed from solids initially produced in the primitive solar nebula and not in Saturn's subnebula itself. Such a model would be consistent as well with the origin of nitrogen in that it argues against heavy chemical reprocessing in a warm disk around Saturn.

These results could have important implications for our understanding of how Titan formed and the dynamics of the Saturnian subnebula. The $^{14}N/^{15}N$ ratio is particularly relevant to these questions, and an energy-limited flux evaluation for past hydrodynamic escape could further constrain the initial ratio.

Retour à la table des matières : p. v

Acknowledgements

The INMS team at Southwest Research Institute acknowledges funding of this work through JPL Subcontract no. 1283095 under NASA task order to JPL NMO710023. The authors would like to thank Tobias Owen, Roger Yelle, Ralph Lorenz and an anonymous reviewer for their helpful feedback on the model. Encouragement and support from the greater INMS operations and science team community has played an important role in the evolution of the authors' model development and science results.

Appendix A

A.1. Fractionation factors

A simple model for diffusive fractionation in an isothermal atmosphere was devised by Hunten (1982) and Hunten et al. (1989) based on how the density of a species diffusively changes as a function of altitude

$$n(z) = n(z_0)e^{(-\Delta z/H)}$$

n is the density of the gas, z the altitude, z_0 the homopause altitude and $H = kT/mg$ the scale height, where T is the temperature in degrees Kelvin, k Boltzmann's constant, m the atomic mass of the gas and g gravitational acceleration: MG/r^2.

The isotopic ratio as a function of altitude can be determined by dividing the density of the heavier species (n_2), by that of the lighter species (n_1)

$$\frac{n_2(z)}{n_1(z)} = R(z) = R(z_0)e^{(-\Delta z/H_d)} \tag{1A}$$

where $H_d = kT/((m_2-m_1)g)$ and Δz is the difference between the altitude of the homopause and the exobase. The diffusive fractionation factor, y_d, for an escaping species that is in hydrostatic equilibrium below the exobase is defined by Hunten et al. (1989) as

$$y_d = e^{(\Delta z/H_d)} - 1 \tag{2A}$$

where Δz represents the distance between the homopause and the exobase.

Combining Eqs. (1A) and (2A) gives

$$y_d = \frac{R(z_0)}{R(z_{exo})} - 1$$

The ratio of the total reservoir of the light species cycled through the fractionating process to the remaining reservoir (i.e. current reservoir) is determined through the Rayleigh distillation relationship based on the fractionation factor (Hunten et al., 1989)

$$\frac{n_1^0}{n_1} = \left(\frac{R}{R_0}\right)^{((1+y)/y)} \tag{3A}$$

where R is the isotopic ratio (heavy/light) in the homosphere and R_0 the original isotopic ratio. The total reservoir represents the initial inventory and any inventory produced over the effective time scale. Donahue et al. (1997) use a slightly different form of this equation

$$\frac{n_1^0}{n_1} = \left(\frac{R}{R_0}\right)^{(1/(1-f))} \tag{4A}$$

Donahue et al. (1997) and Hunten et al. (1989) treat the exponent differently, reflecting their differing definitions of the fractionation factor. The relationship between the y used by Hunten et al. (1989) and the f used by Donahue et al. (1997) can be found using Eqs. (3A) and (4A)

$$f = \frac{1}{1+y} \tag{5A}$$

Therefore, diffusive fractionation in the form of f is

$$f_d = \frac{R(z_{exo})}{R(z_0)} \tag{6A}$$

This is the definition of the fractionation factor that we use in our model. If significant escape is occurring, the diffusive fractionation factor cannot be represented by Eq. (1A). Direct measurements of the ratio below the homopause and at the exobase are required in this case to determine the correct diffusive fractionation factor using Eq. (6A).

A.2. Atmospheric escape

The equations used for evaluating atmospheric escape are as follows. The equation to describe Jeans escape is (Yung and DeMore, 1999)

$$F_i = \frac{n_{critical}v_{thermal}}{2\sqrt{\pi}}(1+\lambda)e^{-\lambda}; \quad K_i = \frac{v_{thermal}}{2\sqrt{\pi}}(1+\lambda)e^{-\lambda}$$

where $v = \sqrt{2kT_{critical}/m_i}$ and $n_{critical}$ is the number density of the escaping gas at the critical level. Dividing the Jeans escape rate for the heavier isotope by the lighter isotope and cancelling out the densities gives the fractionation factor

$$f_e = \sqrt{\frac{m_1}{m_2}}\left[e^{(\lambda_1-\lambda_2)}\left(\frac{1+\lambda_2}{1+\lambda_1}\right)\right]$$

A component of the atmosphere is limited from escaping at too high a rate by diffusion in the lower atmosphere. Rates above this flux result in negative mixing ratios at high altitudes. Diffusion-limited flux is defined as

$$F_i = b_i X_i\left[\frac{(m_a - m_i)MG}{kTr^2}\right]$$

where m_a is the atmospheric mean mass and b_1/n_{atmos} is the binary diffusion coefficient. If both a species and its isotope have attained their diffusion-limited rates, mass fractionation is a function of the binary diffusion coefficients and the atmospheric mean mass

$$f_l = \frac{b_2(m_a - m_2)}{b_1(m_a - m_1)}$$

If hydrodynamic escape has not reached diffusion-limited rates, mass fractionation is described by the equations of Hunten et al. (1987). Hydrodynamically escaping particles create a drag force on heavier species in the atmosphere and decrease the fractionation efficiency. Derived from diffusion equations for a two-component atmosphere, the drag force created by this escape flux induces an escape flux on minor species in the atmosphere of

$$F_2 = \frac{X_2}{X_1}F_1\left(\frac{m_c - m_2}{m_c - m_1}\right)$$

where $m_c = m_1 + (kTF_1/b_1gX_1)$. Dividing the escape rates and cancelling out the mixing ratios gives mass fractionation during hydrodynamic escape

$$f_h = \frac{(m_c - m_2)}{(m_c - m_1)}$$

A.3. Time-evolution of densities and isotopic ratios

The column density of a constituent in the atmosphere changes as a function of time as

$$\frac{dn}{dt} = P - L \tag{7A}$$

Retour à la table des matières : p. v

where n represents column density, t represents time, and P and L represent the various production and loss processes for the constituent.

Donahue et al. (1997) found for a single loss process of escape fractionating according to

$$f_e = \frac{F_2}{F_1} * \frac{1}{R}$$

that Eq. (7A) for both the light and heavy isotopes is

$$\frac{dn_1}{dt} = P_1 - K_e n_1 \tag{8A}$$

$$\frac{dn_2}{dt} = R_s P_1 - f_e K_e n_2 \tag{9A}$$

where $K_e = F/n$.

Eqs. (8A) and (9A) are easily solved first-order differential equations that can be used to find an equation for the density of each isotope as a function of time. The isotopic ratio, $n_2(t)/n_1(t)$, as a function of time is

$$R(t) = \frac{((R_s P_1)/(f_e K_e))(1 - e^{-f_c K_e t}) + R_0 n_0 e^{-f_c K_e t}}{(P_1/K_e)(1 - e^{-K_e t}) + n_0 e^{-K_e t}} \tag{10A}$$

Eventually, after enough time passes the exponential terms go to zero and the ratio will reach a steady-state value of

$$R_{ss} = \frac{R_s}{f_e} \tag{11A}$$

Eqs. (8A)–(11A) only allow for one form of fractionation to operate on the inventory. We determined dn/dt for each species, allowing for more than one fractionating loss process and integrated to find the density as a function of time. The fractionating loss processes include energy-limited (e.g. the photochemical, Lorenz et al., 1997) loss rates that are constant with time and density-dependent loss rates that change over time.

The combination of a constant loss process with density-dependent loss processes meant that the total fractionation occurring as a result of the multiple processes also changed over time, complicating evaluation of the inventories through Eq. (4A). If a production rate exists, the isotopes reach a steady state that is a function of the production rate as the exponentials go to zero over large time scales. Table 1A lists the equations used for deriving each time-evolution equation.

Nitrogen is divided into two time periods: hydrodynamic escape starting with the formation time of Titan and ending at 1 Gyr after solar system formation started, and the second period starting at the end of the hydrodynamic escape period and continuing to today. Eqs. (12A) and (14A) are able to characterize the nitrogen isotopic ratio during hydrodynamic escape based on Eqs. (4) and (6) in Section 3. The integral for Eq. (14A) must be solved with caution as the fractionation depends on the critical mass. If the critical mass is below 29 amu then the fractionation is 0 and none of the isotope is removed from the atmosphere, but direct calculation of the integral can easily include negative fractionation factors and throw the results off. The second period for nitrogen, Eqs. (13A) and (15A), includes sputtering loss as measured by INMS as a density-dependent loss process and photochemical loss as an energy-limited loss process (Lorenz et al., 1997). Nitrogen is not believed to have a production rate, and thus cannot reach a steady-state value.

The methane Eqs. (16A) and (17A), allow for a production rate, an energy-limited photochemical loss rate and an escape rate. In the case of hydrodynamic escape, the loss rate is energy limited but it is density-dependent for sputtering. Hydrodynamic escape eventually reaches a steady-state value that is dependent on the production rate

$$R_{ss} = \frac{R_s(P - f_c L_c - f_e F_e)}{(P - L_c - F_e)}$$

The sputtering equations can reach a steady-state value with a large production rate over an extended period of time represented by

$$R_{ss} = \frac{R_s K_e (P - f_c L_c)}{f_e K_e (P - L_c)}$$

The equations for hydrogen (18A) and (19A) are coupled with the methane equations, because the production rate for hydrogen depends on methane's photochemical loss rate. H_2 production is assumed to be 75% of the chemical loss rate of CH_4 though much uncertainty remains at this time. The remainder of the necessary production comes from a surface inventory with an isotopic ratio equal to the GCMS value. Even though the production of H_2 is

Table 1A
List of equations for tracking the isotopic ratio as a function of time for each of the species.

Species	Equations		#
N_2	$dn_1/dt = -F_e(t_c/t)^{5/6}$ $n_1(t) = n_0 - 6F_e t_c^{5/6} t^{1/6}$	$10^8 y \le t \le 10^9 y$	(12A)
	$dn_1/dt = -K_e n_1 - L_c$ $n_1(t) = (L_c/K_e)(e^{-K_e t} - 1) + n_0 e^{-K_e t}$	$10^9 y \le t \le now$	(13A)
$^{15}N^{14}N$	$dn_2/dt = -f_e(t) F_e(t_c/t)^{5/6}(n_2(t)/n_1(t))$ $n_2(t) = R_0 n_0 e^{\int((f_e(t_0)F_e(t_0)/n_0) - (f_e(t)F_e(t)/n_1(t)))\,dt}$	$10^8 y \le t \le 10^9 y$	(14A)
	$dn_2/dt = -f_e K_e n_1 - f_c L_c$ $n_2(t) = ((f_c L_c)/(f_e K_e))(e^{-f_e K_e t} - 1) + R_0 n_0 e^{-f_e K_e t}$	$10^9 y \le t \le now$	(15A)
CH_4	Hydrodynamic escape $dn_1/dt = P_1 - F_e - L_c$ $n_1(t) = n_0 + t(P_1 - F_e - L_c)$	Sputtering $dn_1/dt = P_1 - K_e n_1 - L_c$ $n_1(t) = ((P_1 - L_c)/K_e)(1 - e^{-K_e t}) + n_0 e^{-K_e t}$	(16A)
$^{13}CH_4$	$dn_2/dt = R_s(P_1 - f_e F_e - f_c L)$ $n_2(t) = R_0 n_0 + R_s t(P_1 - f_e F_e - f_c L)$	$dn_2/dt = R_s(P_1 - f_c L) - f_e K_e n_2$ $n_2(t) = ((R_s(P_1 - L_c))/(f_e K_e))(1 - e^{-f_e K_e t}) + R_0 n_0 e^{-f_e K_e t}$	(17A)
H_2	$dn_1/dt = P_1 + P_2 - K_e n_1$ $n_1(t) = ((P_1 + P_2)/K_e)(1 - e^{-K_e t})$		(18A)
HD	$dn_2/dt = R_{CH4} P_1 + R_s P_2 - f_e K_e n_1$ $n_2(t) = ((R_{CH4} P_1 + R_s P_2)/(f_e K_e))(1 - e^{-f_e K_e t})$		(19A)

Retour à la table des matières : p. v

energy limited like the photochemical loss rate of CH_4, the escape rate should be approximated as a linear function of the density. The reason for this is that H_2 escapes at the same rate that it is produced, so the escape rate is a function of the amount of H_2 available to be removed from the atmosphere.

References

Alexander, C.M.O.D., Fogel, M., Yabuta, H., Cody, G.D., 2007. The origin and evolution of chondrites recorded in the elemental and isotopic compositions of their macromolecular organic matter. Geochim. Cosmochim. Acta 71, 4380–4403.

Atreya, S.K., Donahue, T.M., Kuhn, W.R., 1978. Evolution of a nitrogen atmosphere on Titan. Science 201, 611–613.

Atreya, S.K., Adams, E.Y., Niemann, H.B., Demick-Montelara, J.E., Owen, T.C., Fulchignoni, M., Ferri, F., Wilson, E.H., 2006. Titan's methane cycle. Planet. Space Sci. 54, 1177–1187.

Bell, J., Bougher, S.W., Waite, Jr., J.H., Ridley, A.J., Magee, B., Bar-Nun, A., Mandt, K., Westlake, J., Toth, G., de la Haye, V., 2009. Simulating The Global Mean Structure of Titan's Upper Atmosphere Using the Titan Global Ionospher-e–Thermosphere Model, Planetary and Space Science, in preparation.

Bezard, B., Nixon, C., Kleiner, I., Jennings, D., 2007. Detection of $^{13}CH_3D$ on Titan. Icarus 191, 397–400.

Charnley, S.B., Rodgers, S.D., 2002. The end of interstellar chemistry as the origin of nitrogen in comets and meteorites. Astrophys. J. 569, L133–L137.

Chassefiére, E., 1996. Hydrodynamic escape of oxygen from primitive atmospheres: applications to the cases of Venus and Mars. Icarus 124, 537–552.

Chassefiére, E., Leblanc, F., 2004. Mars atmospheric escape and evolution; interaction with the solar wind. Planet. Space Sci. 52, 1039–1058.

Cordier, D., Mousis, O., Lunine, J.I., Moudens, A., Vuitton, V., 2008. Photochemical enrichment of deuterium in Titan's atmosphere: new insights from Cassini-Huygens. The Astrophysical Journal Letters 689, L61–L64.

Cui, J., Yelle, R.V., Volk, K., 2008. Distribution and escape of molecular hydrogen in Titan's thermosphere and exosphere. J. Geophys. Res. 113, E10004.

De La Haye, V., Waite, J.H., Johnson, R.E., Yelle, R.V., Cravens, T.E., Luhmann, J.G., Kasprzak, W.T., Gell, D.A., Magee, B., Leblanc, F., Michael, M., Jurac, S., Robertson, I.P., 2007a. Cassini ion and neutral mass spectometer data in Titan's upper atmosphere and exosphere: observation of a suprathermal corona. J. Geophys. Res. 112, A07309.

De La Haye, V., Waite, J.H., Cravens, T.E., Johnson, R.E., Lebonnois, S., Robertson, I.P., 2007b. Titan's corona: the contribution of exothermic chemistry. Icarus 191, 236–250.

Donahue, T.M., Grinspoon, D.H., Hartle, R.E., Hodges Jr., R.R., 1997. Ion/neutral escape of hydrogen and deuterium: evolution of water. In: Bougher, S.W., Hunten, D.M., Phillips, R.J. (Eds.), Venus II. University of Arizona Press, Tucson, pp. 385–414.

Elachi, C., Wall, S., Allison, M., Anderson, Y., Boehmer, R., Callahan, P., Encrenaz, P., Flamini, E., Franceschetti, G., Gim, Y., Hamilton, G., Hensley, S., Janssen, M., Johnson, W., Kelleher, K., Kirk, R., Lopes, R., Lorenz, R., Lunine, J., Muhleman, D., Ostro, S., Paganelli, F., Picardi, G., Posa, F., Roth, L., Seu, R., Shaffer, S., Soderblom, L., Stiles, B., Stofan, E., Vetrella, S., West, R., Wood, C., Wye, L., Zebker, H., 2005. Cassini Radar views the surface of Titan. Science 308, 970–974.

Fortes, A.D., Grindrod, P.M., Trickett, S.K., Vocadlo, L., 2007. Ammonium sulfate on Titan: possible origin and role in cryovolcanism. Icarus 188, 139–153.

Hamilton, D.C., Difabio, R.D., Christon, S.P., Krimigis, S.M., Mitchell, D.G., Dandouras, I., 2008. Suprathermal Heavy Ion Composition in Saturn's Magnetosphere, AGU Fall Meeting Abstracts, A2

Hunten, D.M., Pepin, R.O., Walker, J.C.G., 1987. Mass fractionation in hydrodynamic escape. Icarus 69 (3), 532–549.

Hunten, D.M., 1982. Thermal and nonthermal escape mechanisms for terrestrial bodies. Planet. Space Sci. 30 (8), 773–783.

Hunten, D.M., Donahue, T.M., Walker, J.C.G., Kasting, J.F., 1989. In: Atreya, S.K., Pollack, J.B., Matthews, M.S. (Eds.), Origin and Evolution of Planetary and Satellite Atmospheres. University of Arizona Press, Tucson, pp. 386–422.

Jakosky, B.M., 1991. Mars volatile evolution: evidence from stable isotopes. Icarus 94, 14–31.

Jakosky, B.M., Pepin, R.O., Johnson, R.E., Fox, J.L., 1994. Mars atmospheric loss and isotopic fractionation by solar-wind induced sputtering and photochemical escape. Icarus 111, 271–288.

Jehin, E., Manfroid, J., Cochran, A.L., Arpigny, C., et al., 2004. The anomalous $^{14}N/^{15}N$ ratio in comets 122P/1995 S1 (De Vico) and 153P/2002 C1 (Ikeya–Zhang), ApJ 613, L161

Lavvas, P.P., Coustenis, A., Vardavas, I.M., 2008. Coupling photochemistry with haze formation in Titan's atmosphere, Part II: results and validation with Cassini/Huygens data. Planet. Space Sci. 56, 67–99.

Lavvas, P.P., Yelle, R.V., Vuitton, V., 2009. The detached haze layer in Titan's mesosphere. Icarus 201 (2).

Lebonnois, S., Bakes, E.L.O., McKay, C.P., 2003. Atomic and molecular hydrogen budget in Titan's atmosphere. Icarus 161, 474–485.

Liang, M., Heays, A.N., Lewis, B.R., Gibson, S.T., Yung, Y.L., 2007. Source of nitrogen isotope anomaly in HCN in the atmosphere of Titan. Astrophys. J. 664, L115–L118.

Lorenz, R.D., McKay, C.P., Lunine, J.I., 1997. Photochemically driven collapse of Titan's atmosphere. Science 275, 642–645.

Lorenz, R.D., Mitchell, K.L., Kirk, R.L., Hayes, A.G., Aharonson, O., Zebker, H.A., Paillou, P., Radebaugh, J., Lunine, J.I., Janssen, M.A., Wall, S.D., Lopes, R.M., Stiles, B., Ostro, S., Mitri, G., Stofan, E.R., 2008. Titan's inventory of organic surface materials. Geophys. Res. Lett. 35, L02206.

Lunine, J.I., Yung, Y.L., Lorenz, R.D., 1999. On the volatile inventory of Titan from isotopic abundances in nitrogen and methane. Planet. Space Sci. 47, 1291–1303.

Magee, B.A., Waite Jr., J.H., Mandt, K.E., Bell, J., Westlake, J., Gell, D.A., de la Haye, V., 2009. INMS derived composition of Titan's upper atmosphere: analysis methods and model comparison. Planet. Space Sci., in preparation.

Manning, C.V., McKay, C.P., Zahnle, K.J., 2008. The nitrogen cycle on Mars: impact decomposition of near-surface nitrates as a source for a nitrogen steady state. Icarus.

Martins, Z., Alexander, C.M.O.D., Orzechowska, G.E., Fogel, M.L., Ehrenfreund, P., 2008. Indigenous amino acids in primitive CR meteorites. Meteoritics and Planetary Science 42, 2125–2136.

Massman, W.J., 1998. A review of the molecular diffusivities of H_{20}, CO_2, CH_4, CO, O_3, SO_2, NH_3, N_{20}, NO AND NO_2 in air, O_2 and N_2 near STP. Atmos. Environ. 32, 1111–1127.

Mather, T.A., Pyle, D.M., Allen, A.G., 2004. Volcanic source for fixed nitrogen in the early Earth's atmosphere. Geology 32 (10), 905–908.

Mousis, O., Gautier, D., Coustenis, A., 2002. The D/H ratio in methane in Titan: origin and history. Icarus 159, 156–165.

Mousis, O., Lunine, J.I., Thomas, C., Pasek, M., Marboeuf, U., Alibert, Y., Ballenegger, V., Cordier, D., Ellinger, Y., Pauzat, F., Picaud, S., 2009. Clathration of volatiles in the solar nebula and implications for the origin of Titan's atmosphere. J. Astrophys 691, 1780–1786.

Niemann, H.B., et al., 2005. The abundances of constituents of Titan's atmosphere from the GCMS instrument on the Huygens probe. Nature 438 (8), 779–784.

Nixon, C.A., Achterberg, R.K., Vinatier, S., Bézard, B., Coustenis, A., Irwin, P.G.J., Teanby, N.A., de Kok, R., Romani, P.N., Jennings, D.E., Bjoraker, G.L., Flasar, F.M., 2008. The $^{12}C/^{13}C$ isotopic ratio in Titan hydrocarbons from Cassini/CIRS infrared spectra. Icarus 9.

Owen, T., Niemann, H., 2009. The origin of Titan's atmosphere: some recent advances. Philisophical Trans. R. Soc., Ser. A 367, 607–615.

Parker, E.N., 1963. Interplanetary Dynamical Processes. Wiley, New York, pp. 41–51.

Penz, T., Lammer, H., Kulikov, Y.N., Biernat, H.K., 2005. The influence of the solar particle radiation environment on Titan's atmosphere evolution. Adv. Sp. Res. 36, 241–250.

Sekine, Y., Lebonnois, S., Imanaka, H., Matsui, T., Bakes, E.L.O., McKay, C.P., Khare, B.N., Sugita, S., 2008. The role of organic haze in Titan's atmospheric chemistry II. Effect of heterogeneous reaction to the hydrogen budget and chemical composition of the atmosphere. Icarus 194, 201–211.

Sittler, E.C., Hartle, R.E., Cooper, J.F., Johnson, R.E., Smith, H.T., Shappirio, M.D., Simpson, D.J., 2008. Methane group ions in Saturn's outer magnetosphere. Bull. Am. Astron. Soc. 40, 448.

Strobel, D.F., 2008. Titan's hydrodynamically escaping atmosphere. Icarus 193, 588–594.

Tobie, G., Lunine, J.I., Sotin, C., 2006. Episodic outgassing as the origin of atmospheric methane on Titan. Nature 440, 61–64.

Toublanc, D., Parisot, J.P., Brillet, J., Gautier, D., Raulin, F., McKay, C.P., 1995. Photochemical modeling of Titan's atmosphere. Icarus 113 (1), 2–26.

Tucker, O.J., Johnson, R.E., 2009. Thermally driven atmospheric escape: Monte Carlo simulations for Titan's atmosphere. Planet. Space Sci., in press.

Waite Jr., J.H., Niemann, H., Yelle, R.V., Kasprzak, W.T., Cravens, T.E., Luhmann, J.G., McNutt, R.L., Ip, W.-H., Gell, D., de la Haye, V., Mueller-Wordag, I., McGee, B., Borggren, N., Ledvina, S., Fletcher, G., Walter, E., Miller, R., Scherer, S., Thorpe, R., Xu, J., Block, B., Arnett, K., 2005. Ion Neutral Mass Spectrometer (INMS) results from the first flyby of Titan. Science 308 (5724), 982–986.

Wieler, R., Busemann, H., Franchi, I.A., 2006. Trapping and modification processes of noble gases and nitrogen in meteorites and their parent bodies. Meteorites and the Early Solar System II 499–521.

Wilson, E.H., Atreya, S.K., 2004. Current state of modeling the photochemistry of Titan's mutually dependent atmosphere and ionosphere. J. Geophys. Res. 109, E06002.

Yelle, R.V., Cui, J., Mueller-Wodarg, I.C.F., 2008. Methane escape from Titan's atmosphere. J. Geophys. Res. 113, E10003.

Yung, Y.L., Allen, M., Pinto, J.P., 1984. Photochemistry of the atmosphere of Titan – Comparison between model and observations. Astrophysical Journal (Supplement Series 1) 55, 465–506.

Yung, Y.L., DeMore, W.B., 1999. Photochemistry of Planetary Atmospheres. Oxford University Press, New York, p. 9.

Retour à la table des matières : p. v

5.3 Article sur la croissance des anions dans l'atmosphère de Titan

Icarus 227 (2014) 123–131

Contents lists available at ScienceDirect

Icarus

journal homepage: www.elsevier.com/locate/icarus

Low temperature reaction kinetics of CN^- + HC_3N and implications for the growth of anions in Titan's atmosphere

Ludovic Biennier [a,*], Sophie Carles [a], Daniel Cordier [b], Jean-Claude Guillemin [c], Sébastien D. Le Picard [a], Alexandre Faure [d]

[a] Institut de Physique de Rennes, Département de Physique Moléculaire, Astrophysique de Laboratoire, UMR CNRS 6251, Université de Rennes 1, Campus de Beaulieu, 35042 Rennes Cedex, France
[b] Université de Franche-Comté, Institut UTINAM, CNRS/INSU, UMR 6213, 25030 Besançon Cedex, France
[c] Ecole Nationale Supérieure de Chimie de Rennes, UMR CNRS 6226, 11, Allée de Beaulieu, 35708 Rennes Cedex 7, France
[d] UJF-Grenoble 1/CNRS-INSU, Institut de Planétologie et d'Astrophysique de Grenoble (IPAG), UMR 5274, Grenoble F-38041, France

ARTICLE INFO

Article history:
Received 21 June 2013
Revised 2 September 2013
Accepted 3 September 2013
Available online 21 September 2013

Keywords:
Titan, atmosphere
Atmospheres, chemistry
Ionospheres

ABSTRACT

The Cassini–Huygens probe has uncovered the existence of a profusion of negatively charged molecular species in the upper atmosphere of Titan (~950 km). The presence of large amounts of anions was unexpected and the chemical pathways leading to their formation mostly unknown. The investigation of the negative ion chemistry appears therefore to be a key factor for modeling Titan's upper atmosphere. We present here the first low temperature experimental kinetic study involving CN^-, proposed by Vuitton et al. (2009) to be one of the negative ions detected by the CAPS-ELS instrument onboard the Cassini spacecraft. The temperature dependence of the rate coefficient of the reaction CN^- + HC_3N, was explored over the 49–294 K temperature range in uniform supersonic flows using the CRESU technique. We find that the kinetics of this reaction is fast ($k \gtrsim 4 \times 10^{-9}$ cm^3 molecule^{-1} s^{-1}) and presents a weak negative temperature dependence which, considering the experimental error bars, agrees with long-range based capture theory. We also observe that C_3N^- + HCN represents the main exit channel demonstrating that the studied reaction participates efficiently to the chemical growth of negative ions in the atmosphere of Titan.

© 2013 Elsevier Inc. All rights reserved.

1. Introduction

Negative ions have been discovered in various astrophysical environments during the last decade. So far, six anions have been detected in the gas phase in the interstellar medium through radio-astronomy on the basis of laboratory spectra: C_4H^-, C_6H^-, C_8H^-, CN^-, C_3N^- and C_5N^- (Cernicharo et al., 2007; McCarthy et al., 2006; Remijan et al., 2007; Brunken et al., 2007; Agundez et al., 2010; Thaddeus et al., 2008; Cernicharo et al., 2008). Latest research suggests that carbon chain anions are relatively abundant in a variety of interstellar objects and that their presence correlates with the abundance of their neutral counterparts (Cordiner et al., 2011). Closer to us, the presence of numerous negative ions has also been revealed in Titan's upper atmosphere by the Electron Spectrometer sensor of the Cassini Plasma Spectrometer (CAPS-ELS) on-board the Cassini spacecraft (Waite et al., 2007; Coates et al., 2007). Heavy ions up to 13,800 amu/q have been detected at the altitude of 950 km. Despite the low resolution of the spectrum ($\Delta m/m \sim 17\%$), three peaks at 22 ± 4, 44 ± 8 and 82 ± 14 amu/q can be distinguished on the low-mass side and were attributed to CN^-, C_3N^-/C_4H^- and C_5N^- by Vuitton et al. (2009) with the help of an ionospheric photochemical model. It is worth noting however, that most of the anion–molecule reactions present in the model have not been studied, especially below room temperature. It is therefore necessary to acquire laboratory data on the kinetics of elementary reactions involving anions including their branching ratios in relevant physical conditions in order to improve the accuracy of the predicted abundances of the molecular species. More experimental work has been performed on reactions involving neutral and positively charged ions. For instance, a critical review of the main processes involving nitrogen species, including N^+, N_2^+, N^{++} and N_2^{++}, relevant for Titan's atmosphere was recently published by Dutuit et al. (2013). Several studies (Waite et al., 2007; Vuitton et al., 2007, 2009; Krasnopolsky, 2009; Zabka et al., 2012) have also highlighted the importance of positive and negative ion-neutral chemistry in the molecular growth in the upper atmosphere of Titan. A recent experimental work by Zabka et al. (2012) showed that in the multiple collision regime, negative ion chemistry could lead to the formation of large anions. Using a model coupling aerosol microphysics and photochemistry, Lavvas et al. (2013) established that the formation of aerosols is directly related to ion processes

* Corresponding author.
E-mail address: ludovic.biennier@univ-rennes1.fr (L. Biennier).

0019-1035/$ - see front matter © 2013 Elsevier Inc. All rights reserved.
http://dx.doi.org/10.1016/j.icarus.2013.09.004

Retour à la table des matières : p. v

in Titan's upper atmosphere, revealing the fundamental role of ion chemistry and the consequent importance of determining accurately the kinetics of the chemical reactions involved.

The dense atmosphere of Titan has revealed a rich organic chemistry initiated by the dissociation and ionization of N_2 (composing 90–98% of the atmosphere) and CH_4 (1–6%) by energetic solar photons combined with Saturn magnetospheric electrons (Niemann et al., 2005; Waite et al., 2005, 2007). Decades of astronomical observations have led to the identification of a wealth of hydrocarbons and nitrogen-bearing species. Among those molecular compounds, acetylene C_2H_2 and polyynes such as di-acetylene C_4H_2 have been detected and their abundance established (Coustenis et al., 2007; Waite et al., 2005, 2007). Larger polyynes such as C_6H_2 and C_8H_2 are also likely to be present. All these compounds are suspected to play a major role in molecular growth. In addition to HCN, a large variety of nitriles are generated such as CH_3CN (Marten et al., 2002), HC_3N, C_2N_2 (see Coustenis et al., 2010, and references therein) and – in the condensed form – C_4N_2 inferred from earlier Voyager infrared observations (Coustenis et al., 1989). Even though nitriles and hydrocarbon molecules occur only in trace amounts, they are of particular importance because they are considered to be key ingredients and building blocks to form Titan's organic, aerosol-particle based haze layers which blacken the surface (Wilson and Atreya, 2003). The aerosol composition is yet unknown but Cassini's Composite Infrared Spectrometer (CIRS) far infrared observations uncovered a correlation between the haze and HC_3N abundance that could then represents a good tracer (Jennings et al., 2012).

According to the model proposed by Vuitton et al. (2009), CN^- and C_3N^- are the most abundant ions around 1000 km, while C_5N^- becomes prominent below 850 km. CN^- is mainly produced by dissociative attachment of supra-thermal electrons on HCN and HC_3N and is essentially destroyed by associative detachment with H and CH_3 and through reaction with HC_3N. Interestingly, HC_3N is assumed to play a role both in the production and the destruction of CN^-. Reactions between these charged species and neutral molecules are expected to be involved in the growth of anions by triggering a chain of polymerization reactions. It is therefore important to understand the mechanisms involved, which can be better inferred by comparing kinetics experimental measurements to theoretical predictions. Apart from recent studies focusing on the reactions of C_mN^- (m = 1–6) with H atoms (Snow et al., 2009; Yang et al., 2011) and of CN^- with cyanoacetylene (Carles et al., 2011; Zabka et al., 2012), little is known about the reactivity of CN-bearing anions, and to our knowledge, no kinetics measurements involving these compounds exist below room temperature. More generally, only a handful of laboratory studies have indeed investigated the temperature dependence of the rate coefficients of reactions involving anions below 200 K. Three different types of experiments can be distinguished. The first one is based on a temperature variable radiofrequency ion trap. This technique, capable of cooling molecular ions to below 10 K in all degrees of molecular freedom, was successfully used to measure the reaction of $NH_2^- + H_2$ down to 8 K (Otto et al., 2008). The second method employs a liquid nitrogen cooled selected ion flow tube (SIFT) and can measure reactions down to 88 K. It has been used to investigate the associative detachment reactions of $O^- + NO$, $S^- + CO$ and $S^- + O_2$ and the rate coefficients and branching ratios for the reactions of $O^- + C_2H_2$ and $O^- + C_2H_4$ (Viggiano and Paulson, 1983). The third approach makes use of supersonic uniform flows providing wall-less reactors down to very low temperatures, in which molecules can easily be introduced at very high degrees of supersaturation. The method hence called CRESU, a French acronym for Cinétique de Réaction en Ecoulement Supersonique Uniforme, was used to measure the kinetics of the reaction of Cl^- with CH_3Br down to 23 K (Le Garrec et al., 1997).

We present here the first low temperature kinetics study involving CN^-, reacting with HC_3N, one of the most abundant nitrogen-bearing molecule in Titan's ionosphere around 1000 km (Vuitton et al., 2009). The temperature dependence of the rate coefficient of this reaction was measured from 49 to 294 K using the CRESU technique. The temperature dependence of the reaction was well reproduced theoretically using the infinite-order sudden (IOS) approximation combined with the capture theory (Clary, 1990). Charged products were also experimentally identified, allowing us to provide some insights into the growth of anions in the cold upper atmosphere of Titan.

2. Laboratory experiments

2.1. Experimental apparatus

The kinetics of reaction of CN^- anions with cyanoacetylene, HC_3N, is explored using the CRESU technique, which has been described in details elsewhere (Rowe et al., 1984). Only specific features are provided hereafter. Fig. 1 displays a schematic diagram of the experimental setup. An axially and radially symmetric uniform supersonic beam is generated by the isentropic expansion of a buffer gas (helium in the present experiments) through a Laval nozzle. Upstream of this nozzle, helium is continuously introduced into a reservoir by a calibrated mass flow controller at a typical flow rate of 50–100 slm (standard $l\,min^{-1}$). Downstream, in the main chamber, the supersonic expansion generated by the nozzle is maintained by a 24,000 $m^3\,h^{-1}$ capacity pumping system. The design of the nozzle, as well as the pressures in the reservoir (a few tens of mbar) and in the main chamber (a few tenths of mbar), set the temperature of the supersonic flow. The velocity (several 10^4 cm s^{-1}), the density (typically 10^{16}–10^{17} molecule cm^{-3}) and the low temperature of the supersonic flow are kept uniform over several tens of centimeters corresponding to hydrodynamic times of about 100–1000 μs. All other neutral gases necessary for the study of the title reaction are introduced in small amount into the reservoir by means of calibrated mass flow controllers. Due to the relatively high density of the flow, frequent collisions occur ensuring thermal equilibrium for all the molecular species present in the supersonic expansion.

An electron beam, produced by an electron gun (12 kV, 200 μA), crosses the supersonic neutral flow at 90°, downstream of the nozzle, generating a low density plasma, consisting primarily of buffer gas cations (He^+ here) and electrons ($[e^-] \sim 10^8$–10^9 cm^{-3}). Downstream along the axis of the supersonic flow, a movable quadrupole mass spectrometer (0–200 amu/q) coupled with a Langmuir probe (a loop of 25 μm diameter gold plated tungsten wire and 8.84 ± 0.05 mm long) allows to measure the ion signal and the electron density in the supersonic flow by skimming out a central portion of the flow.

One of the main difficulties of the present experiments is to generate CN^- ions rapidly and abundantly. To achieve this, negative ions are produced by dissociative electron attachment of cyanogen bromide BrCN vapors (Sigma Aldrich) previously diluted in helium (2% mole fraction) and injected into the reservoir. The exit channels for this reaction are (Bruning et al., 1996):

$$BrCN + e^-(\leqslant 0.5eV) \rightarrow Br + CN^- \quad (1)$$

$$\rightarrow Br^- + CN \quad (2)$$

As one can see on a typical ion spectrum recorded at a reaction time of 75 μs in a 157.5 K supersonic He flow (Fig. 2), the first exit channel clearly dominates the reaction. This is consistent with low energy electron attachment studies which determined a large cross section of 5.05×10^{-14} cm^2 for that exit channel at 0 eV (Alajajian et al., 1988).

Retour à la table des matières : p. v

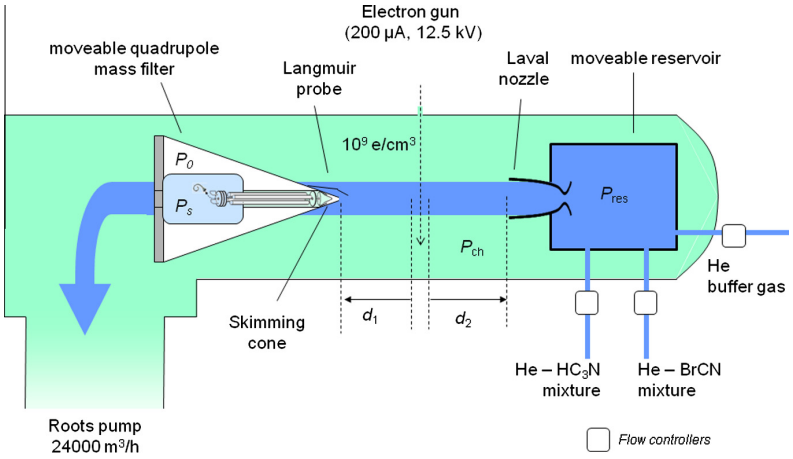

Fig. 1. Diagram of the CRESU apparatus showing the retractable Laval nozzle, the ionization region and the moveable quadrupole mass spectrometer/Langmuir probe assembly.

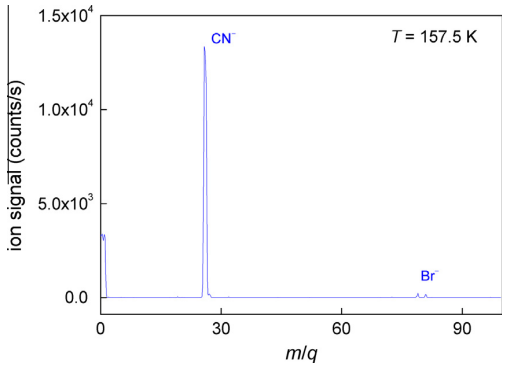

Fig. 2. Negative ion mass spectrum of a 157.5 K supersonic He flow seeded with small amounts of BrCN and recorded after a reaction time of t = 75 µs.

In order to optimize the CN^- production, the distance d_2 between the exit of the nozzle and the electron beam is kept short (~1 cm). The density of CN^-, formed by electron attachment and mainly consumed by chemical reaction with the co-reactant (HC_3N here) also introduced in the flow through the reservoir, as well as the density of all ions produced, are monitored by moving the mass spectrometer along the supersonic expansion.

In all experiments, the cyanoacetylene is introduced in large excess compared to the amount of CN^- formed, in order to perform the kinetics experiments under pseudo-first-order conditions. The cyanoacetylene sample is synthesized following the procedure of Miller and Lemmon (1967). Methylpropiolate, $HCC–CO_2CH_3$ reacts with dry ammonia NH_3, to give propiolamide $HCC–CONH_2$. In the second step of the reaction, the amide is dehydrated with phosphorous pentoxide dispersed in sea sand to give cyanoacetylene (propiolonitrile), selectively trapped at 153 K. A yield of 67% is obtained on a preparative scale of about 10 g. After that, HC_3N vapors are diluted in helium at the percent level. Typical number densities and purities of all the species present in the supersonic flow are reported in Table 1.

2.2. Kinetic experimental procedure

Contrary to many kinetic experiments performed in fast flow reactors, the CN^- ions are not produced here instantaneously. As a consequence, the analysis of the ion signal must take into account a source term in addition to usual sink terms. The experimental data-set consists in mass spectrometer ion counts for the anion CN^-, as a function of time and recorded at a given temperature T associated with a specific Laval nozzle and an initial cyanoacetylene density $[HC_3N]$. In order to retrieve the reaction rate, we solve the following system of differential equations:

Table 1
Typical number densities of the species in the supersonic uniform flow.

Species	Density (molecule cm^{-3})	Purity
He	6×10^{16}–13×10^{16}	99.995%
HC_3N	1×10^{11}–8×10^{12}	⩾98%[a]
BrCN	1×10^{11}–15×10^{11}	97%
e^-	10^8–10^9	
CN^-	10^8	

[a] See CheikhSidEly et al. (2013).

$$\frac{dCN^-}{dt} = -k_1[HC_3N]\ CN^- - \left(\frac{D}{\Lambda^2} + k_3[X]\right)\ CN^- + k_2[BrCN]\ [e^-] \quad (3)$$

$$\frac{d[e^-]}{dt} = -k_2[BrCN]\ [e^-] \quad (4)$$

where CN^- represents the scaled ion signal, [BrCN] and $[e^-]$ the cyanobromide and electron densities in the supersonic uniform beam in molecule cm^{-3}, [X] the impurities in the carrier gas, k_1 the global reaction rate of the $CN^- + HC_3N$ reaction, k_2 the dissociative attachment rate, k_3 the rate of the reaction of CN^- + X, D the molecular diffusion rate, and Λ the characteristic diffusion length.

The concentration of cyanogen bromide [BrCN] is assumed to be constant throughout the entire dataset for temperatures ⩾49 K and for a given value of $[HC_3N]$ concentration. The dissociative attachment rate coefficient k_2, together with the initial electron density $[e^-]$ are treated as free adjustable parameters. In this manner, slow fluctuations of cyanogen bromide injection and of electron gun current emission and incorrect scaling of the CN^- ion count are in fact included in the obtained $[e^-]$'s and k_2's. They should then be regarded as "effective" coefficients. We emphasize that k_2's and $[e^-]$'s have no equivalent roles since only the k_2's contribute to the time constant of the electron variations, while $[e^-]$'s have no contribution to that. The starting time of the reaction, t_0 which represents in a spatial framework, the intersection of the electron beam with the supersonic flow is also treated as a free

Retour à la table des matières : p. v

parameter. Short times below a few tens of μs (meaning short distances between the tip of the mass spectrometer and the electron beam) are not accessible experimentally. The effect of molecular diffusion is included through the sink term $-D/\Lambda^2\,CN^-$. Simple order of magnitude calculations (See Appendix) show that molecular diffusion plays a significant role only in room temperature experiments. Obviously, the concentration of CN anions at the starting time t_0 is assumed to be zero.

For a given temperature T, we build a χ^2 function taking into account the full set of data, i.e. embracing all the [HC_3N] values. This way, if n is the number of different HC_3N concentrations at a given temperature, and if we denote by m_i the number of CN^- measurements for the ith value of [HC_3N], we write by definition

$$\chi^2(T) = \frac{1}{n}\sum_{i=1}^{n}\frac{1}{m_i}\sum_{j=1}^{m_i}\left\{CN^-(t_j)_{exp} - CN^-(t_j)_{calc}\right\}^2 \quad (5)$$

where CN^-_{exp} and CN^-_{calc} are respectively the experimental and simulated abundances of the CN^- ion. With the adopted definition of $\chi^2(T)$, a perfect adjustment of calculated abundances to experimental ones corresponds to $\chi^2(T) = 0$ which has no physical sense for measurements with error bars. The theoretical values CN^-_{calc} come from the integration of the system of differential equations relevant for the kinetics involved in our experiments.

The parameters having the best physical meaning are those obtained by minimizing $\chi^2(T)$ considered as our likelihood function. To do so, we employed a classical "descent method" which converges reasonably quickly in our context and has the advantage of being very robust (Snyman, 2005).

In order to estimate the uncertainty associated with the results, we developed an approach in which all the parameters (i.e. k_2's and [e^-]'s) except k_1 have been fixed to their best fit values. Varying the value of k_1 (typically in the range of ±30% and ±20%) we have plotted examples of corresponding curves in Figs. 3 and 4. As can be seen, the ion counts lie between the curves corresponding to the ±20% levels, with the exception of the ambient temperature case (Fig. 3) for which the range +50% to −20% seems to be more relevant. Table 2 summarizes the adopted uncertainties. We also computed a 'fit quality parameter' (denoted Δ^*), defined by Eq. (6), which can be interpreted as the average relative difference between experimental data and fitted curves. The Δ^*'s reported in Table 2 shows the highest uncertainty at 294 K.

$$\Delta^* = \frac{1}{n}\sum_{i=1}^{n}\frac{1}{m_i}\sum_{j=1}^{m_i}\frac{\sqrt{\left\{CN^-_{exp}(t_j) - CN^-_{calc}(t_j)\right\}^2}}{CN^-_{exp}(t_j)} \quad (6)$$

Besides that, we have also performed Monte-Carlo simulations in which several surrogate datasets have been generated in order to mimic experimental errors and/or fluctuations (due, for instance, to turbulent flow around the sublimating BrCN solid sample). The results obtained with this method are fully consistent with the parameter variation approach.

Finally, the derived reaction rate coefficient k_1 versus temperature is plotted in Fig. 5.

2.3. Reaction products

The mass spectrometry analysis reveals that C_3N^- is the only ion produced by the $CN^- + HC_3N$ reaction over the whole 49–294 K temperature range. The current mass spectrometer is not configured to detect the smallest ion, H^-, but its production is unlikely. The much lower electron affinity of H (0.75 eV) than that of CN sets a strong constraint on the enthalpy of formation of the co-product. The parallel evolution of the CN^- and C_3N^- populations at 71.6 K is displayed on Fig. 6 for different densities of HC_3N. As soon as CN^- is formed, it can readily react with cyanoacetylene to give C_3N^- through proton exchange:

$$CN^- + HC_3N \rightarrow C_3N^- + HCN \quad (7)$$

The current results agree with observations made at room temperature in a flowing afterglow (Carles et al., 2011) and in a quadrupole tandem mass spectrometer (Zabka et al., 2012). They are also in line with a growing electron affinity from CN (3.862 ± 0.004 eV) to C_3N (4.305 ± 0.001 eV) as determined by photoelectron spectroscopic studies (Bradforth et al., 1993; Yen et al., 2009). In order to investigate further the thermodynamics of the reaction, we performed quantum chemistry calculations using the Gaussian 09 suite of programs (Frisch et al., 2009). The structures were optimized using a hybrid B3LYP functional in connection with an augmented cc-pVTZ basis set. The calculations, corrected by zero point vibration energies, give an enthalpy for reaction (7) of −10.25 kJ mol^{-1}. The exothermicity of the reaction, although small, supports this picture.

Negative ions can also undergo associative detachment. In this process, the negative ion and the neutral molecule associate to form a complex, which is stabilized by the ejection of an electron:

$$A^- + B \rightarrow (AB^-)^* \rightarrow AB + e^- \quad (8)$$

Such reactions can occur when the energy to detach the electron is less than the energy to break the bond (Drake, 2006). The co-reactant B is usually a radical species and AB a stable neutral molecule. Our apparatus is not designed to make these measurements which would imply either (1) an ionization source within the mass spectrometer chamber to detect the neutral products or (2) an electron ultra-sensitive detector. The sensitivity of the existing Langmuir probe does not allow us to perform measurements of electron densities below 10^7 cm^{-3}. We cannot therefore experimentally prove or rule out the existence of a minor associative detachment channel. This information cannot either be easily inferred from monitoring simultaneously the CN^- and C_3N^- ions because the sink terms for C_3N^- are not well defined.

However, quantum chemistry calculations give enthalpies of reactions $\geqslant$ 131 kJ mol^{-1} for $CN^- + HC_3N \rightarrow CN\,(HC_3N) + e^-$, hence bringing decisive evidence of the absence of an associative detachment channel. We can therefore affirm that the branching to the C_3N^- + HCN channel is ∼100%.

In some experimental conditions, we also observed that the maximum of the signal of $C_3N^-(t)$ could be above the maximum of $CN^-(t)$, depending on the initial density of HC_3N introduced and on the temperature of the flow. This can be explained by examining the potential sources of C_3N^- under our experimental conditions: the first source term is well identified and corresponds to the proton exchange of HC_3N with CN^-. The second one arises from dissociative electron attachment to the cyanoacetylene molecule or to clusters of cyanoacetylene potentially formed in the supersonic expansion, especially at the lowest temperatures and for the highest densities of HC_3N used. Dissociative electron attachment to cyanoacetylene HC_3N has been investigated over the 0–12 eV range (Graupner et al., 2006). Negative ions are formed in two main bands with maxima at ∼1.6 eV (C_3N^-) and ∼5.3 eV (C_3N^-, CN^-, C_2H^- and C_2^-). In our experiment, secondary electrons produced by the electron gun are relatively cold even though not in complete thermal equilibrium with the bath neutral gas (Goulay et al., 2004). Therefore, the detection of negative ions, such as C_3N^-, is not expected in the sole presence of cyanoacetylene HC_3N. This is indeed the case at room temperature. However, mass spectra recorded at low temperatures and for large initial amounts of HC_3N (see Fig. 7) uncover many peaks which have been identified on the basis of the work of Zabka et al. (2012). Note that these negative ions disappear when even traces of BrCN are injected, at the benefit of CN^- as the reaction (1) dominates the electron loss kinetics. These mass spectra clearly reveal that HC_3N

Retour à la table des matières : p. v

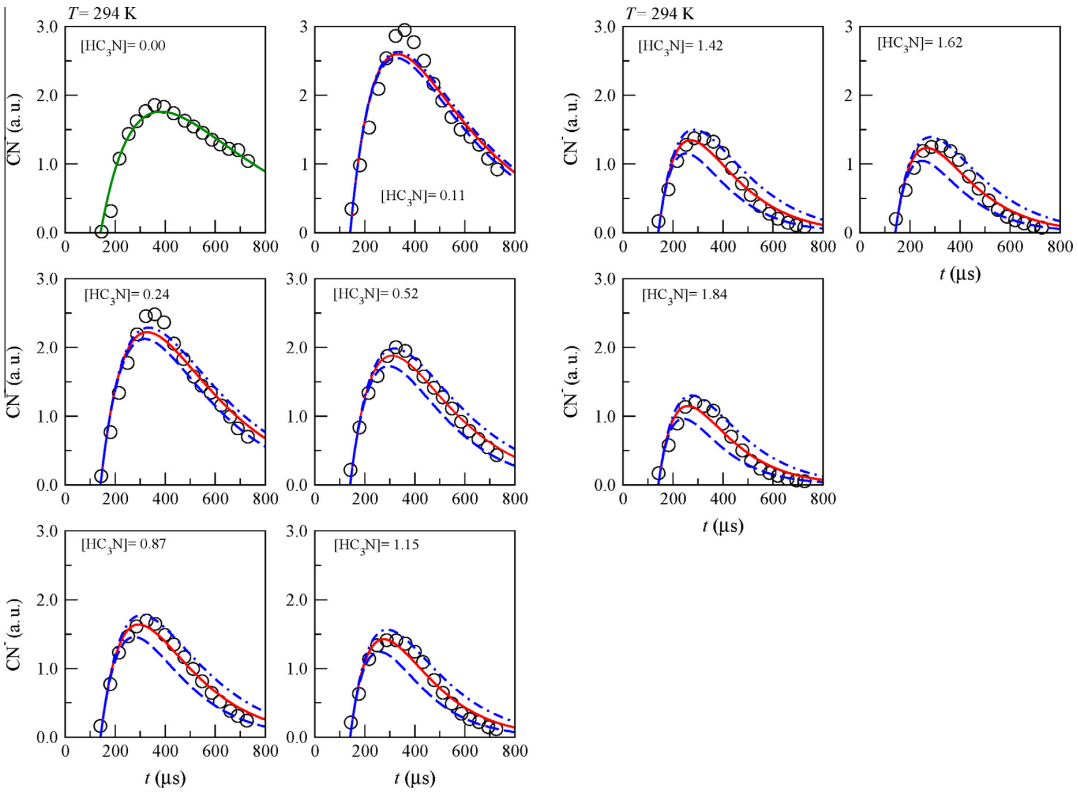

Fig. 3. Experimental CN^- ion signal – proportional to the ion counts per second (open circles) at $T = 294$ K in presence of various initial number density (in 10^{12} molecule cm^{-3}), best fit values (red full line), −20% and +50% (dashed and dot-dashed lines). The losses caused by molecular diffusion and reactions with impurities are determined by fitting the CN^- ion signal in absence of co-reactant (upper left panel). (For interpretation of the references to color in this figure legend, the reader is referred to the web version of this article.)

clusters could form in the cold supersonic flow with a size distribution tightly depending on the initial density of cyanoacetylene and on the temperature. They then attach electrons to produce a wide variety of anions that either stabilize into $(HC_3N)_{m-1}C_3N^-$, fragment, or grow further. This channel represents a small but significant source of C_3N^-. All the experiments were performed therefore using HC_3N densities at least four orders of magnitude lower than the density of buffer gas (see Table 1). The presence of a significant amount of HC_3N clusters below 49 K however, could not be avoided, precluding any kinetics measurement under this temperature. For temperatures lower than 49 K, $(BrCN)_m$ clusters can also be formed and attach electrons, hence delaying the formation of CN^- ions.

3. Temperature dependence

In contrast to cations, very few studies have investigated the temperature dependence of reactions involving anions. In all published results, however, a negative temperature dependence of the rate coefficients was observed. For such reactions, Faure et al. (2010) have shown that the rates at very low temperature can be estimated by using a semiempirical model based on the long-range (classical) capture theory. Only the long-range ion-induced dipole and ion–dipole interaction terms were considered. The basic requirement for this model to apply is that the measured rate coefficient at 300 K is above 10^{-11} cm^3 s^{-1}. The reaction rate is then simply assumed to approach the capture limit at very low temperature (∼10 K). Full details can be found in Faure et al. (2010).

In the present case, the rate coefficient is well above the Langevin rate ($k_L \sim 1.3 \times 10^{-9}$ cm^3 s^{-1}) at room temperature, suggesting that the rate is already close to the capture limit and that the ion–dipole term is very important. The dipole moment of HC_3N is indeed very large (3.7 D). Several studies have shown that the contribution of the ion–dipole interaction is difficult to estimate (see Faure et al. (2010) and references therein). In the case of HC_3N, the rotational constant is small, $B \sim 0.15$ cm^{-1}, and it corresponds to a long rotational period of $\sim 1/(2B) = 110$ ps. From the measured rate coefficient, one can estimate an interaction time[1] of $t_{int} \lesssim 15$ ps for temperatures above 50 K. As a result, the interaction time is much shorter than the rotational period of the molecule over the whole experimental temperature range. In such condition, the infinite-order-sudden (IOS) approximation is expected to be valid. If this approximation is combined with the long-range capture theory, the rate coefficient for a reaction of an ion with a polar molecule is simply (Clary, 1990):

$$k(T) = 2\pi q\left(\frac{\alpha}{\mu}\right)^{1/2} + 0.25\pi q\mu_D\left(\frac{8}{\pi k_B \mu T}\right)^{1/2}, \quad (9)$$

where q is the charge of the ion, α is the polarizability of the neutral, μ is the reduced mass, μ_D is the dipole moment of the neutral molecule and k_B is the Boltzmann constant. It should be noted that this IOS approach corresponds exactly to the popular average-dipole-orientation (ADO) theory where the dimensionless coefficient C is

[1] The interaction time can be defined as $t_{int} \sim b/v_{th}$ where v_{th} is the thermal velocity and b is the effective impact parameter defined from the rate coefficient as $k = \pi b^2 v_{th}$.

Retour à la table des matières : p. v

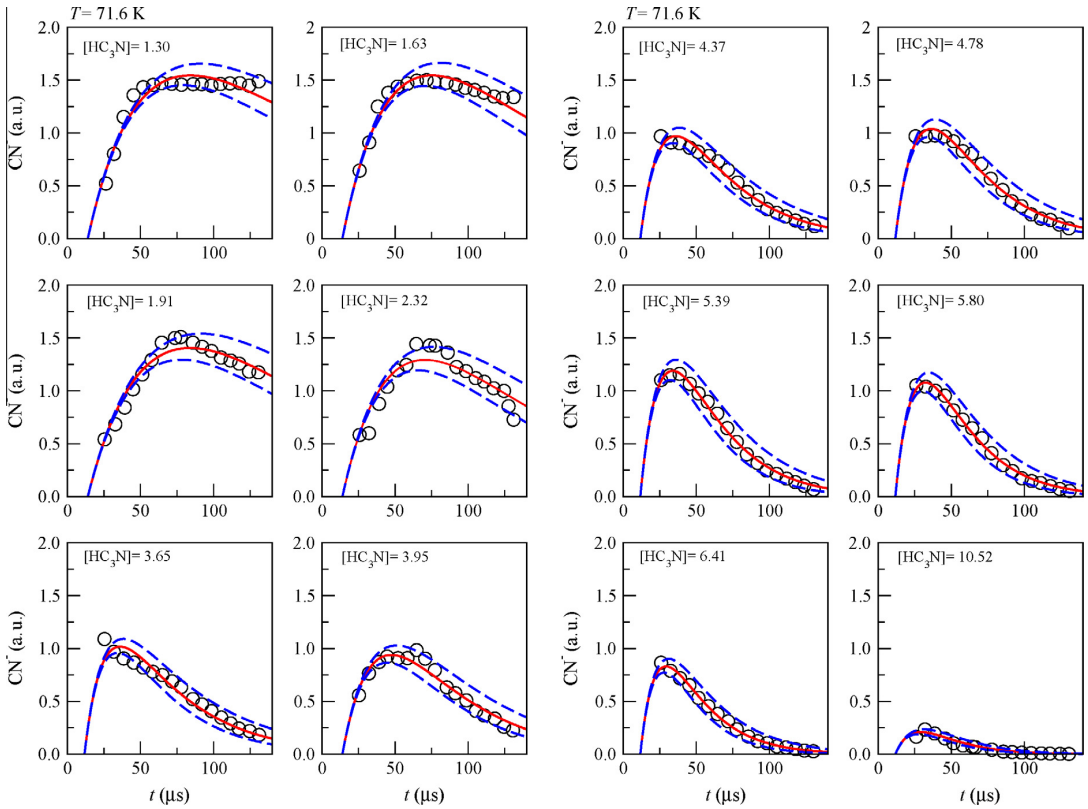

Fig. 4. Experimental CN^- ion signal – proportional to the ion counts per second (open circles) at $T = 71.6$ K in presence of various initial [HC_3N] number density (in 10^{12} molecule cm^{-3}), best fit values (red full line), ±20% (dashed lines). (For interpretation of the references to color in this figure legend, the reader is referred to the web version of this article.)

Table 2
Rate coefficients for the reaction of CN^- with cyanoacetylene, HC_3N over the 49–294 K temperature range. Δ^* is the average relative difference between experimental data and fitted curves, as defined by Eq. (6). The fourth column displays the error estimated using the Monte-Carlo method mentioned in the text.

T (K)	k_1 (cm^3 $molecules^{-1}$ s^{-1})	Δ^*	Monte-Carlo error	Adopted uncertainties
49.1	4.5×10^{-9}	18.0%	∼18%	±20%
71.6	6.0×10^{-9}	9.7%	∼11%	±20%
123.0	4.7×10^{-9}	21.0%	∼13%	±20%
157.5	6.4×10^{-9}	8.9%	∼21%	±20%
294	3.8×10^{-9}	26.0%	∼+45%	+50%/−20%

set to 0.25 (see e.g. Clary et al. (1985)). In contrast, the "locked dipole" approximation corresponds to $C = 1$.

The IOS rate coefficients for the $CN^- + HC_3N$ reaction are reported in Fig. 5. The agreement with the CRESU data is very satisfactory. In particular, the IOS rate coefficients are found to agree within experimental error bars at 71.6, 123.0 and 294 K. This good agreement between the experiment and the IOS calculation suggests that the long-range ion–dipole interaction is simply averaged over the orientation angles of the colliding partners, as expected. In other words, the HC_3N dipole has no time to align with the incoming charge of CN^-, even at the lowest temperature. We note that this is in contrast with the results observed for other, lighter, neutral polar targets. For instance, in the case of HCN ($B \sim 1.48$ cm^{-1}) reacting with H_3^+, the IOS and ADO theories were found to underestimate the rate coefficient at low temperature by large factors (Clary et al., 1985). In such case, the locked dipole approximation provides better results in the low temperature regime because the shorter rotational period allows dipole alignment. The parameterized trajectory theory of Su and Chesnavich (1982) was also employed. The temperature dependence is found in rather good agreement with the IOS results. We note, however, that the rate coefficients derived from the IOS theory are in better agreement with the experimental data in the low temperature regime, where the ion–dipole contribution is crucial.

To summarize, both the magnitude and temperature dependence of the $CN^- + HC_3N$ reaction rate coefficient are reproduced by the IOS theory, indicating that the reaction proceeds at the capture rate over the whole experimental temperature range, without any barrier (other than the centrifugal barrier), and with the ion–dipole term being dominant and simply averaged over the orientation angles.

4. Implications for the chemistry of Titan's ionosphere

The investigation of the reactivity of small negative ions is essential to understand their presence in the upper atmosphere of Titan. Advances have been essentially made through the development of

Retour à la table des matières : p. v

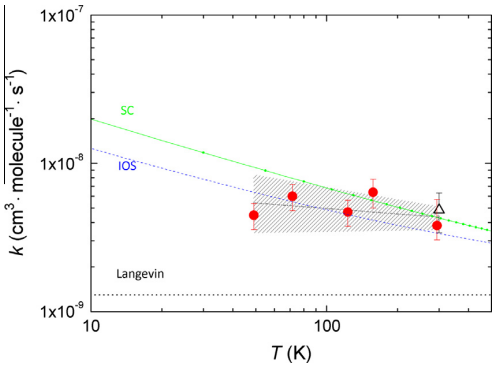

Fig. 5. Rate coefficients for the reaction of CN^- with cyanoacetylene, HC_3N over the 49–294 K temperature range. The filled circles represent the current work. The empty triangle corresponds to the value measured at room temperature in a flowing afterglow (Carles et al., 2011). The rate coefficient is calculated using the IOS approximation combined with the capture theory (dash line) and the Langevin model (dotted line). The results from the parametrized trajectory theory from Su and Chesnavich (1982) are also shown (line with small full circles). The fit of the data is displayed (short dash dot line) over the 49–294 K range with a shaded area which corresponds to the associated uncertainty.

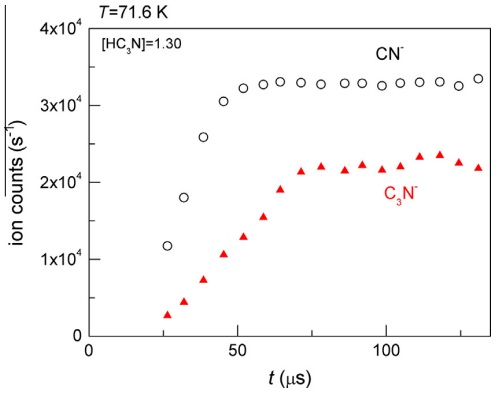

Fig. 6. Ion population vs. reaction time at 71.6 K in presence of an initial $[HC_3N]$ concentration of 1.30×10^{12} molecule cm^{-3}.

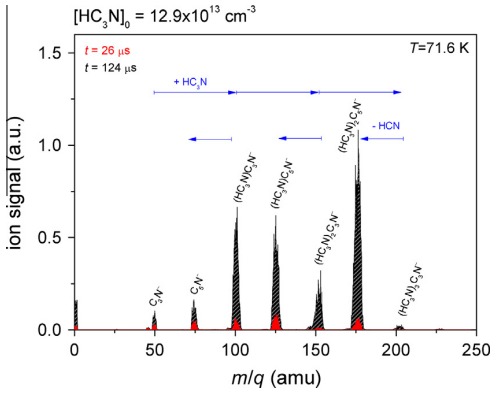

Fig. 7. Negative ion mass spectra of a 71.6 K supersonic He flow in the sole presence of HC_3N with an initial density of 12.9×10^{12} molecule cm^{-3}. The spectra have been recorded after reaction times of $t = 26$ μs and 124 μs.

an ionospheric chemical network (Vuitton et al., 2009), constrained by *in situ* measurements of the abundance of neutrals, ions and electrons. The ionospheric photo-chemical model takes into account production and loss processes that include photo-ionization, photo-detachment, energetic electron impact, and chemical reactions between ions and neutral species over the 700–1200 km altitude range. However, the kinetics and the exit channels of some of the processes considered remain poorly known as well as the density of radical species such as H, CH_3, CN, and C_3N.

According to the model of Vuitton et al. (2009), the CN^- ion is produced mainly by dissociative attachment of supra-thermal electrons onto HCN and HC_3N. More marginally, it is generated by the reaction of C_mH^- + HCN. Yet, no measurement is available for that ion–molecule reaction for which a Langevin rate has been adopted.

Then CN^- is essentially lost by reacting with HC_3N, H and CH_3. The reaction of CN^- with H and CH_3 is assumed to proceed through associative detachment. In a recent work, Yang et al. (2011) determined a rate of 6.3×10^{-10} cm^3 molecule s^{-1} for the CN^- + H reaction at room temperature using a flowing afterglow-selected ion flow tube, hence confirming previously available data (Ferguson and Fehsenfeld, 1969; Fehsenfeld et al., 1973). Through ab initio theoretical calculations, they established that the addition of H atom to the carbon atom of CN^- is barrierless, and the products (HCN + e^-) are exothermic (−139.3 kJ mol^{-1}).

According to the semi-empirical capture model of Faure et al. (2010), the temperature dependence of the rate coefficient of the CN^- + H reaction is, here also, small over the 160–200 K range considered, validating the adoption of a constant rate coefficient in the model. Nevertheless, this is not the case of the CN^- + CH_3 reaction for which no measurement has been reported so far.

This experimental study shows that the CN^- + HC_3N reaction is faster than the commonly used Langevin rate by a factor $\gtrsim 3$ with a weak negative temperature dependence. We also show that the dominant channel forms C_3N^- and HCN. Our kinetics results validate the rate coefficient adopted in the model of Vuitton et al. (2009), in which the value calculated from Su and Chesnavich (1982) at 300 K was used with no temperature dependence applied. Over the 49–294 K range, we suggest using the following temperature dependence equation of the rate coefficient in chemical models:

$$k(T) = (4.3 \pm 0.8) \times 10^{-9} \times \left(\frac{T}{298\ \mathrm{K}}\right)^{-0.12\pm0.15} \mathrm{cm^3\ molecule^{-1}\ s^{-1}} \quad (10)$$

Our measurements confirm therefore the importance of this reaction both for the loss of CN^- and for the production of C_3N^-. The C_3N^- negative ion is indeed mainly generated through the CN^- + HC_3N reaction, remotely followed by electron attachment onto neutral C_3N and by the C_mH^- + HC_3N reaction (Vuitton et al., 2009).

Beyond its interest for determining more accurately the abundance of CN^- in the atmosphere of Titan, this study is key to understanding the initial steps of aerosol formation which remain elusive. In a recent study Lavvas et al. (2013) demonstrated that the formation of aerosols in Titan's upper atmosphere was directly linked to ion processes. Their model couples the aerosol microphysics and the photochemistry in a self-consistent manner. They assume that the ionosphere initially contained one type of positive ion ($m^+ \sim 30$ amu), one type of negative ion ($m^- \sim 50$ amu) and electrons. As a consequence, the model cannot provide any insights into the first steps of aerosols formation or their chemical composition. The experimental study by Zabka et al. (2012) showed that in a multiple collision regime, the reaction of CN^- anion with cyanoacetylene could lead efficiently to the formation of heavy ions $(HC_3N)_m \cdot C_pN^-$. These results were obtained in physical

Retour à la table des matières : p. v

conditions (i.e. temperature, pressure, reaction time) that are different from those of Titan's atmosphere. Low temperature measurements are therefore necessary to confirm the importance of these processes. A kinetics study of reactions involving the C_3N^- anion is in progress in our laboratory, using the same methodology, in order to both determine accurate rate coefficients to be included in photochemical models and better understand the molecular growth through anion–molecule reactions at low temperature.

5. Conclusions

We have explored the kinetics of the $CN^- + HC_3N$ reaction over the 49–294 K temperature range using the CRESU apparatus. Only a handful of anion–molecule reactions have been investigated so far down to low temperatures. We used here a methodology, which could prove very helpful in other experiments, employing dissociative attachment for generating negative ions from a neutral molecular precursor. Lower temperatures could not be investigated because the negative ion production seems to slow down with the temperature and because of the competition with dissociative attachment to clusters.

The rate coefficient of the $CN^- + HC_3N$ reaction shows a very weak negative temperature dependence over the temperature range of this study (49–294 K). Considering the experimental error bars, our measurements agree reasonably with the infinite-order sudden (IOS) approximation combined with the capture theory suggesting that this reaction is barrierless and dominated by the capture rate with the ion dipole term being dominant. The analysis of the mass spectra shows that C_3N^- is the only primary ion product of the $CN^- + HC_3N$ reaction over the whole range of temperature.

The reaction investigated is one of the first steps towards the formation of larger ions in Titan's ionosphere, whose importance has been shown in the growth of molecules and aerosols at lower altitudes. Further low temperature studies involving other anions, starting with C_3N^- are planned.

Finally, these kinetics measurements should also be taken into account in chemical models of astrophysical objects such as the evolved carbon-rich asymptotic giant branch star IRC +10216, in the envelope of which, CN^- (Agundez et al., 2010), C_3N^- (Thaddeus et al., 2008) and HC_3N (Morris et al., 1975) have all been identified. Our understanding of the chemistry of negative ions is far from complete in these environments as well, as highlighted for instance by the poor agreement between the calculated and observed spatial distribution of CN^- in the envelope of IRC +10216 (Agundez et al., 2010).

Acknowledgments

We express our gratitude to Bertrand Rowe and Jonathan Courbe for the design of the moveable quadrupole mass spectrometer. We warmly thank Daniel Travers for the elaboration of the data acquisition. This work benefited from many discussions with our collaborators Christian Alcaraz, Claire Romanzin, Véronique Vuitton and Roland Thissen. We also thank Jean-Christophe Loison for his help on thermochemistry calculations. This research was supported by the CNRS-INSU Programme de Physique et Chimie du Milieu Interstellaire and the CNRS-INSU Programme National de Planétologie. J.-C.G. thanks the Centre National d'Etudes Spatiales (CNES) for financial support. S.L.-P. thanks the Institut Universitaire de France (IUF) for financial support.

Appendix A

The molecular diffusion of the CN ions becomes significant when the time-scale τ_{diff} attributed to this phenomenon is comparable to the experiment time-scale τ_{exp} (here of the order of ~140 μs for all temperatures except 294 K where $\tau_{exp} \sim 800$ μs). The diffusion coefficient D_{AB} of a molecular species A diffusing in a gas composed of molecules of type B, can be written as Poling et al. (2007)

$$D_{AB} = \frac{0.00266\ T^{3/2}}{P M_{AB}^{1/2} \sigma_{AB}^2 \Omega_D} \quad (11)$$

where P is the pressure, M_{AB} the reduced mass, σ_{AB} the collision cross section and Ω_D the collision integral which can be computed with the Neufeld et al. (1972) interpolation formula (see Poling et al., 2007, p. 11.6) employing the following Lennard–Jones' parameters: $\epsilon_{He}/k = 10.22$ K and $\epsilon_{CN^-}/k \simeq \epsilon_{CO}/k = 91.7$ K; $\sigma_{He} = 2.566$ Å and $\sigma_{CN^-} \simeq \sigma_{CO} = 3.59$ Å (see Appendix B p. B.1 of Poling et al., 2007).

In a first approximation, the characteristic diffusion length, $\Lambda \sim 0.5$ cm, is given by the size of the transverse electron beam crossing the CRESU flow. A dimensional analysis (see for instance Gibbings, 2011) leads to define τ_{diff} as the molecular diffusion time-scale

$$\tau_{diff} = \frac{\Lambda^2}{D_{AB}} \quad (12)$$

The results of the calculations reported in Table A.1 show that $\tau_{diff} \ll \tau_{exp}$ except for $T = 294$ K where $\tau_{diff} \sim \tau_{exp}$. Then, it can be safely concluded that molecular diffusion plays no significant role for temperatures below 294 K.

Table A.1
Evaluation of molecular diffusion time-scale under temperatures and pressures generated by the different Laval nozzles.

T (K)	P (mbar)	Ω_D	D_{AB} (cm^2 s^{-1})	τ_{diff} (μs)
49.1	0.76	1.17	41.35	6045
71.6	0.66	1.02	95.90	2608
123.0	2.27	0.88	72.58	3445
157.5	3.06	0.84	82.18	3042
294	2.60	0.75	277.46	901

References

Agundez, M. et al., 2010. Astronomical identification of CN^-, the smallest observed molecular anion. Astron. Astrophys. 517, L2, 5 pp.
Alajajian, S.H., Bernius, M.T., Chutjian, A., 1988. Electron attachment lineshapes, cross sections and rate constants at ultra-low energies in several halomethyl and haloethyl molecules. J. Phys. B: Atomic Mol. Opt. Phys. 21, 4021–4034.
Bradforth, S.E., Kim, E.H., Arnold, D.W., Neumark, D.M., 1993. Photoelectron spectroscopy of CN^-, NCO^-, and NCS^-. J. Chem. Phys. 98, 800–810.
Bruning, F., Hahndorf, I., Stamatovic, A., Illenberger, E., 1996. Electron attachment to XCN (X = Br,Cl). Competition between X^- and CN^- formation. J. Phys. Chem. 100, 19740–19746.
Brunken, S., Gupta, H., Gottlieb, C.A., McCarthy, M.C., Thaddeus, P., 2007. Detection of the carbon chain negative ion C_8H^- in TMC-1. Astrophys. J. 664, L43–L46 (Part 2).
Carles, S., Adjali, F., Monnerie, C., Guillemin, J.C., Le Garrec, J.L., 2011. Kinetic studies at room temperature of the cyanide anion CN^- with cyanoacetylene (HC_3N) reaction. Icarus 211, 901–905.
Cernicharo, J., Guelin, M., Agundez, M., Kawaguchi, K., McCarthy, M., Thaddeus, P., 2007. Astronomical detection of C_4H^-, the second interstellar anion. Astron. Astrophys. 467, L37–L40.
Cernicharo, J., Guélin, M., Agundez, M., McCarthy, M.C., Thaddeus, P., 2008. Detection of C_5N^- and Vibrationally Excited C_6H in IRC +10216. Astrophys. J. Lett. 688, L83–L86.
CheikhSidEly, S., Morales, S., Guillemin, J.C., Klippenstein, S.J., Sims, I., 2013. Low temperature rate coefficients for the reaction $CN + HC_3N$. J. Phys. Chem. A, in press.
Clary, D.C., 1990. Fast chemical reactions: Theory challenges experiment. Ann. Rev. Phys. Chem. 41, 61–90.
Clary, D.C., Smith, D., Adams, N.G., 1985. Temperature dependence of rate coefficients for reactions of ions with dipolar molecules. Chem. Phys. Lett. 119, 320–326.
Coates, A.J., Crary, F.J., Lewis, G.R., Young, D.T., Waite Jr., J.H., Sittler Jr., E.C., 2007. Discovery of heavy negative ions in Titan's ionosphere. Geophys. Res. Lett. 34, 9.
Cordiner, M.A., Charnley, S.B., Buckle, J.V., Walsh, C., Millar, T.J., 2011. Discovery of interstellar anions in cepheus and auriga. Astrophys. J. Lett. 730, L18, 5 pp.

Retour à la table des matières : p. v

Coustenis, A., Achterberg, R.K., Conrath, B.J., Jennings, D.E., Marten, A., Gautier, D., Nixon, C.A., Flasar, F.M., Teanby, N.A., Bzard, B., Samuelson, R.E., Carlson, R.C., Lellouch, E., Bjoraker, G.L., Romani, P.N., Taylor, F.W., Irwin, P.G.J., Fouchet, T., Hubert, A., Orton, G.S., Kunde, V.G., Vinatier, S., Mondellini, J., Abbas, M.M., Courtin, R., 2007. The composition of Titan's stratosphere from Cassini/CIRS mid-infrared spectra. Icarus 189, 35–62.

Coustenis, A., Bézard, B., Gautier, D., 1989. Titan's atmosphere from voyager infrared observations: I. The gas composition of Titan's equatorial region. Icarus 80, 54–76.

Coustenis, A., Jennings, D.E., Nixon, C.A., Achterberg, R.K., Lavvas, P., Vinatier, S., Teanby, N.A., Bjoraker, G.L., Carlson, R.C., Piani, L., Bampasidis, G., Flasar, F.M., Romani, P.N., 2010. Titan trace gaseous composition from CIRS at the end of the Cassini–Huygens prime mission. Icarus 207, 461–476.

Drake, G.F., 2006. Springer Handbook of Atomic, Molecular, and Optical Physics.

Dutuit, O. et al., 2013. Critical review of N, N^+, N_2^+, N^{++}, and N_2^{++} main production processes and reactions of relevance to Titan's atmosphere. Astrophys. J. Suppl. Ser. 204, 20, 45 pp.

Faure, A., Vuitton, V., Thissen, R., Wiesenfeld, L., Dutuit, O., 2010. Fast ion–molecule reactions in planetary atmospheres: A semiempirical capture approach. Farad. Discuss. 147, 337–348.

Fehsenfeld, F.C., Howard, C.J., Ferguson, E.E., 1973. Thermal energy reactions of negative ions with H atoms in the gas phase. J. Chem. Phys. 58, 5841–5842.

Ferguson, E., Fehsenfeld, F.C., Schmeltekopf, A.L., 1969. Ion–Molecule Reaction Rates Measured in a Discharge Afterglow. American Chemical Society. Advances in Chemistry, vol. 80, pp. 83–91 (Chapter 6).

Frisch, M.J., et al., Gaussian 09 Revision A.1. "Gaussian Inc., Wallingford, CT, 2009.

Gibbings, J.C., 2011. Dimensional Analysis. Springer.

Goulay, F., Rebrion-Rowe, C., Carles, S., Le Garrec, J., Rowe, B., 2004. Electron attachment on HI and DI in a uniform supersonic flow: Thermalization of the electrons. J. Chem. Phys. 121, 1303–1308.

Graupner, K., Merrigan, T., Field, T., Youngs, T., Marr, P., 2006. Dissociative electron attachment to HCCCN. New J. Phys. 8, 117, 17 pp.

Jennings, D.E. et al., 2012. Seasonal disappearance of far-infrared haze in Titan's stratosphere. Astrophys. J. Lett. 754, L3, 4 pp.

Krasnopolsky, V.A., 2009. A photochemical model of Titan's atmosphere and ionosphere. Icarus 201, 226–256.

Lavvas, P. et al., 2013. Aerosol growth in Titan's ionosphere. Proc. National Acad. Sci. 110, 2729–2734.

Le Garrec, J.L., Rowe, B.R., Queffelec, J.L., Mitchell, J.B.A., Clary, D.C., 1997. Temperature dependence of the rate constant for the $Cl^- + CH_3Br$ reaction down to 23 K. J. Chem. Phys. 107, 1021–1024.

Marten, A., Hidayat, T., Biraud, Y., Moreno, R., 2002. New millimeter heterodyne observations of Titan: Vertical distributions of nitriles HCN, HC_3N, CH_3CN, and the isotopic ratio $^{15}N/^{14}N$ in its atmosphere. Icarus 158, 532–544.

McCarthy, M.C., Gottlieb, C.A., Gupta, H., Thaddeus, P., 2006. Laboratory and astronomical identification of the negative molecular ion C_6H^-. Astrophys. J. 652, L141–L144 (Part 2).

Miller, F.A., Lemmon, D.H., 1967. Infrared and Raman spectra of dicyanodiacetylene N≡C–C≡C≡C–C≡N. Spectrochim. Acta Part A – Mol. Spectrosc. A 23, 1415–1423.

Morris, M., Gilmore, W., Palmer, P., Turner, B.E., Zuckerman, B., 1975. Detection of interstellar SiS and a study of the IRC +10216 molecular envelope. Astrophy. J. Lett. 199, L47–L51.

Niemann, H.B. et al., 2005. The abundances of constituents of Titan's atmosphere from the GCMS instrument on the Huygens probe. Nature 438, 779–784.

Neufeld, Philip D., Janzen, A.R., Aziz, R.A., 1972. Empirical Equations to Calculate 16 of the Transport Collision Integrals $\Omega^{(l,s)^*}$ for the Lennard Jones (12-6) Potential. J. Chem. Phys. 57, 1100.

Otto, R., Mikosch, J., Trippel, S., Weidemller, M., Wester, R., 2008. Nonstandard behavior of a negative ion reaction at very low temperatures. Phys. Rev. Lett. 101, 063201, 4 pp.

Poling, B.E., Prausnitz, J.M., O'Connell, J., 2007. The Properties of Gases and Liquids. fifth ed.. McGraw-Hill Professional,, Englewood Cliffs.

Remijan, A.J., Hollis, J.M., Lovas, F.J., Cordiner, M.A., Millar, T.J., Markwick-Kemper, A.J., Jewell, P.R., 2007. Detection of C_8H^- and comparison with C_8H toward IRC +10216. Astrophys. J. 664, L47–L50 (Part 2).

Rowe, B.R., Dupeyrat, G., Marquette, J.B., Gaucherel, P., 1984. Study of the reactions $N_2^+ + 2N_2) \rightarrow N_4^+ + N_2$ and $O_2^+ + 2O_2 \rightarrow O_4^+ + O_2$ from 20 to 160 K by the CRESU technique. J. Chem Phys. 80, 4915–4921.

Snow, T.P., Stepanovic, M., Betts, N.B., Eichelberger, B.R., Martinez, O., Bierbaum, V.M., 2009. Formation of gas-phase glycine and cyanoacetylene via associative detachment reactions. Astrobiology 9, 1001–1005.

Snyman, J.A., 2005. Practical Mathematical Optimization – An Introduction to Basic Optimization Theory and Classical and New Gradient-Based Algorithms. Springer, New York, USA.

Su, T., Chesnavich, W.J., 1982. Parametrization of the ion–polar molecule collision rate constant by trajectory calculations. J. Chem. Phys. 76, 5183–5185.

Thaddeus, P. et al., 2008. Laboratory and astronomical detection of the negative molecular ion C_3N^-. Astrophys. . 677, 1132–1139.

Viggiano, A.A., Paulson, J.F., 1983. Temperature dependence of associative detachment reactions. J. Chem. Phys. 79, 2241–2245.

Vuitton, V. et al., 2009. Negative ion chemistry in Titan's upper atmosphere. Planet. Space Sci. 57, 1558–1572.

Vuitton, V., Yelle, R.V., McEwan, M.J., 2007. Ion chemistry and N-containing molecules in Titan's upper atmosphere. Icarus 191, 722–742.

Waite, J.H. et al., 2005. Ion neutral mass spectrometer results from the first flyby of Titan. Science 308, 982–986.

Waite, J.H., Young, D.T., Cravens, T.E., Coates, A.J., Crary, F.J., Magee, B., Westlake, J., 2007. The process of Tholin formation in titan's upper atmosphere. Science 316, 870–875.

Wilson, E.H., Atreya, S.K., 2003. Chemical sources of haze formation in Titan's atmosphere. Planet. Space Sci. 51, 1017–1033.

Yang, Z., Cole, C.A., Martinez Jr., O., Carpenter, M.Y., Snow, T.P., Bierbaum, V.M., 2011. Experimental and theoretical studies of reactions between H atoms and nitrogen-containing carbanions. Astrophys. J. 739, 19, 10 pp.

Yen, T.A., Garand, E., Shreve, A.T., Neumark, D.M., 2009. Anion photoelectron spectroscopy of C_3N^- and C_5N^-. J. Phys. Chem. A 114, 3215–3220.

Zabka, J., Romanzin, C., Alcaraz, C., Polasek, M., 2012. Anion chemistry on Titan: A possible route to large N-bearing hydrocarbons. Icarus 219, 161–167.

Retour à la table des matières : p. v

Deuxième partie

Origine du système solaire

Chapitre 6

Modélisation des disques proto-planétaires : généralités

« *To do high, real good physics work you do need absolutely solid lenghts of time, so that when you're putting ideas together which are vague and hard to remember, it's very much like building a house of cards and each of the cards is shaky, and if you forget one of them the whole thing collapses again.* »

— Richard Feynman, *The Pleasure of Finding Things Out*, p. 19, Basic Books, 1999.

Sommaire

6.1 Préambule **236**
6.2 Introduction **238**
6.3 Une modélisation de l'évolution temporelle d'un disque protoplanétaire **240**
6.4 Structure verticale d'un disque d'accrétion **242**
6.5 Evolution temporelle d'un disque protoplanétaire **246**
6.6 Références **247**

6.1 Préambule

La question de l'origine du système solaire, comme plus généralement celle des systèmes planétaires, est un champ de recherche scientifique extrêmement vaste. De nombreux pans de la physique et de la chimie sont mobilisés ; ils peuvent relevés de domaines aussi divers que la mécanique des fluides, du transfert radiatif ou de la photochimie. Faire une liste exhaustive des disciplines impliquées est pratiquement impossible. Les problèmes encore ouverts sont pléthore, on citera en exemple celui de la fameuse «barrière du mètre», tant sa résolution est cruciale à notre compréhension des premiers temps du système solaire. En effet, dans les années 70, Stuart Weidenschilling, dans un article resté célèbre [WEIDENSCHILLING, 1977], montre que pour des distances héliocentriques inférieures à 7 UA, les planétésimaux, dont la taille est de l'ordre de 1 mètres, ont une durée de vie inférieure à 1000 ans, ce qui interdit la formation de Jupiter et de toutes les planètes internes. L'état actuel du système solaire, après une évolution de plus de 4 milliards d'années, montre que la Nature a mis en œuvre des mécanismes de contournement de cette apparente barrière. Encore maintenant, les processus proposés afin que cette «barrière du mètre» soit passée, ne font pas consensus.
Comme celles ayant pour objet cette «barrière du mètre», les études concernant l'origine du système solaire font appel, très couramment, à la notion de «nébuleuse primordiale», également appelée «nébuleuse proto-solaire ou proto-planétaire». Ce concept a été introduit par Pierre Simon de Laplace, à la fin du 18e siècle dans son livre «*Exposition du système du monde*». Ceux qui me connaissent savent mon goût pour les livres anciens portant sur la physique et l'astronomie. Il se trouve que je possède un exemplaire de la 5^{e} édition du livre de Laplace (voir Fig. 6.1). L'ouvrage de Laplace est très souvent cité comme la première source proposant l'idée d'une «nébuleuse primordiale». J'ai souhaité retrouver, dans ce livre, le passage relatant l'hypothèse de l'auteur au sujet de l'origine du système solaire, le voici :

> [...] *Enfin, on ne voit point dans l'hypothèse de Buffon, pourquoi les orbes de plus de cent comètes déjà observées, sont tous fort élongés ; cette hypothèse est donc très éloignée de satisfaire aux phénomènes précédens. Voyons s'il est possible de s'élever à leur véritable cause.*
> *Quelle que soit sa nature, puisqu'elle a produit ou dirigé les mouvemens des planètes, il faut qu'elle ait embrassé tous ces corps : et vu la distance prodigieuse qui les sépare, elle ne peut avoir été qu'un fluide d'une immense étendue.* [...]. *Dans l'état primitif où nous supposons le soleil, il ressemblait aux nébuleuses que le télescope nous montre composées d'un noyau plus ou moins brillant, entouré d'une nébulosité qui, en se condensant à la surface du noyau, le transforme en étoile.* [...] *on peut donc conjecturer que les planètes ont été formées à ses limites successives, par condensation des zones de vapeurs, qu'elle a dû en se refroidissant, abandonner dans le plan de son équateur.*
>
> – M. le Marquis de Laplace,
> «*Exposition du système du monde*», cinquième édition,
> Bachelier, libraire, Paris, 1824

Comme on le voit, il y a déjà là l'idée d'appliquer à notre système ce qui est suggéré par les nébuleuses observées dans le ciel, et celle du lien entre les comètes et les âges les plus primitifs de notre système planétaire. Le texte de Laplace, pour un lecteur moderne, est très descriptif, et présente très peu de formalisme ou de calculs.
Aujourd'hui, à l'époque des ordinateurs omniprésents, et omnipotents, le comportement d'un disque proto-solaire peut être calculé, ce qui permet de dépasser largement les discussions purement conceptuelles. Dans le cadre de mon intégration à l'équipe de l'Observatoire de Besançon,

Retour à la table des matières : p. v

FIGURE 6.1 – Mon exemplaire de la 5e édition de l'«*Exposition du système du monde*» de Laplace, posé sur le «*Cours de mécanique de la seconde division — Comprenant la Statique et les premiers principes de la Dynamique*» (Ecole Polytechnique) de Poisson (sans date ni éditeur).

j'ai donc écrit un code simulant le comportement d'une nébuleuse proto-planétaire, *i.e.* fournissant au cours du temps, et en fonction de la distance au Soleil, les différentes grandeurs physiques rendant compte des propriétés de cette nébuleuse : densité surfacique de matière, température, épaisseur, etc. Les applications possibles sont très variées : l'ajout de chimie ou thermophysique permet d'aborder les questions de distribution des espèces chimiques dans le système solaire, les phénomènes de transports et d'agrégation des solides peuvent être abordés, etc.
Afin de construire un modèle de disque proto-planétaire, de nombreuses approches sont envisageables, tout dépend de la classe de problème qu'on souhaite traiter. Dans ce domaine, une source de grandes difficultés est apportée par la turbulence du milieu gazeux et le couplage du plasma avec le champ magnétique. Certains travaux se concentrent sur ces aspects magnétohydrodynamiques [FLOCK et collab., 2011; FROMANG, 2010; FROMANG et collab., 2013, 2011], d'autres contournent le problème en adoptant une paramétrisation des effets du mélange turbulent [ALIBERT et collab., 2005; PAPALOIZOU et TERQUEM, 1999]. Cette dernière approche correspond à des modèles dits «modèles α», du nom du paramètre introduit par SHAKURA et SUNYAEV [1973] dans un formalisme très proche de celui de la théorie de la longueur de mélange (MLT : Mixing Length Theory) employé en physique stellaire [BIERMANN, 1951; BÖHM-VITENSE, 1958; PRANDTL, 1952; SCHWARZSCHILD, 1906; VITENSE, 1953]. Le présent chapitre est une présentation générale des modèles, dits «modèles α» ; dénommés également «1 + 1D» car ils combinent deux dimensions spatiales, l'une correspondant à la distance au Soleil dans le plan médian de la nébuleuse, l'autre comptée suivant la perpendiculaire à ce plan. Le terme «2D» n'est pas adopté ici, car les calculs suivant les deux dimensions se font de manière indépendante. Bien qu'ils soient présents dans la littérature, ces «modèles α, 1 + 1D» semblent n'être décrits, dans tous leurs détails numériques, nulle part. J'ai donc souhaiter profiter de l'écriture de ce manuscrit d'Habilitation à Diriger des Recherches pour publier la méthode numérique que j'ai mise au point, afin qu'elle ne soit pas perdue. En effet, bien que n'occupant pas tout mon temps de recherche, ces travaux physico-numériques se sont étalés sur plusieurs années.

Après la lecture du présent chapitre, le lecteur ayant peu d'appétence pour les problèmes numériques pourra directement poursuivre son chemin au chapitre dédié aux applications, et possibles développements de mon modèle de disque proto-planétaire *EvAD*[1]. La présentation géné-

1. *Ev*olutionary *A*ccretion *D*isk.

rale, qui va suivre, ne satisfait sans doute pas aux canons d'un texte scientifique de recherche. En effet, assez peu de références sont citées, ceci est du à son origine : c'est une adaptation d'un texte que j'avais proposé aux épreuves de TIPE [2] en 2015. Son avantage est, naturellement, de pouvoir être lu par un lectorat assez large.

6.2 Introduction

La question de l'origine de la Terre, et plus généralement celle du système solaire, a toujours suscité beaucoup d'intérêt. Notre planète a été considérée comme le centre de l'Univers jusqu'au XVIe siècle. Ce statut a ensuite évolué avec l'avènement de l'héliocentrisme, promu par Johannes Kepler et Nicolas Copernic. Plus tard, les découvertes, par Galilée, des satellites de Jupiter et des phases de Vénus, ont amené la Terre au rang d'une planète parmi d'autres dans le système solaire.

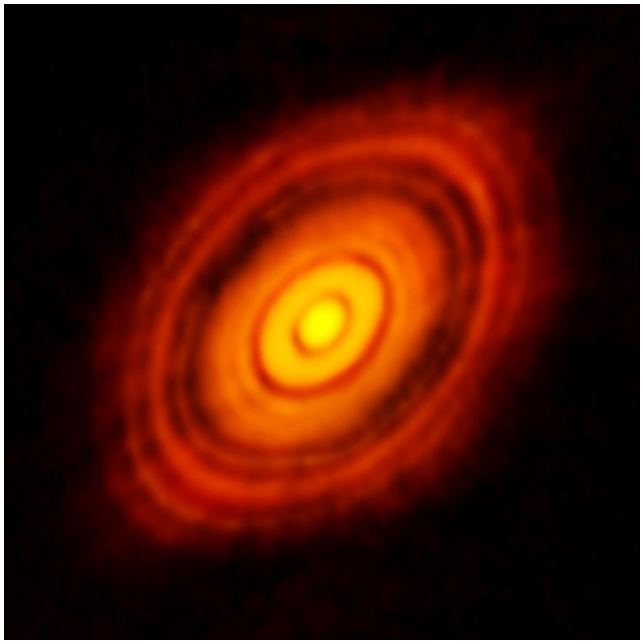

FIGURE 6.2 – Vue du disque protoplanétaire présent autour de HL Tauri, étoile similaire au Soleil et située à une distance d'environ 450 années-lumière. La ligne de visée est à peu près perpendiculaire au plan du disque. L'image, faite dans les domaines submillimétriques-millimétriques montre des anneaux sombres qui pourraient être les «sillages» de planètes en cours de formation et accrétant de la matière. Crédit : ALMA (NRAO/ESO/NAOJ), C. Brogan, B. Saxton (NRAO/AUI/NSF) [CARRASCO-GONZÁLEZ et collab., 2016].

Au cours de l'Histoire, de nombreux systèmes, principalement mystiques ou philosophiques, ont été avancés. En 1644, René Descartes fait une tentative reposant sur ce qui pourrait être considéré comme des prémices de lois physiques. En effet, il propose que le système solaire, et même l'Univers dans sa globalité, soient animés par un ensemble de «vortex». Cette théorie, qui péchait par la pauvreté de ses fondements formels, fut vite supplantée par la révolution newtonienne. Les lois découvertes empiriquement par Képler, et expliquées par la mécanique de Newton, permettent alors une percée scientifique sans précédent.
Si la théorie du système solaire, tel qu'il était observé, avait alors fait un grand pas en avant, son mode de formation restait encore très mystérieux. Au XVIIIe siècle, deux scenarii ont été opposés : l'un, élaboré par le naturaliste Georges Buffon, supposait un arrachement de matière au Soleil, par effet de marée, lors du passage de comètes. Cette matière allait ensuite donner naissance aux planètes. Le deuxième scénario, soutenu par Pierre-Simon de Laplace, repose sur l'existence d'une

2. Epreuves de Travail d'Initiative Personnelle Encadré aux concours d'entrée aux Grandes Ecoles d'Ingénieur.

nébuleuse primordiale, formée d'un disque de gaz et de poussières en rotation autour du Soleil, et dont le refroidissement progressif aurait donné naissance au cortège des planètes que nous connaissons. Cette hypothèse, également promue par Immanuel Kant et Friedrich Herschel, permettait d'expliquer les observations disponibles à l'époque. Ce concept de «nébuleuse primitive», qui n'est autre qu'un disque d'accrétion protoplanétaire, a fini par s'imposer et sous-tend toutes les études concernant l'origine du système solaire.

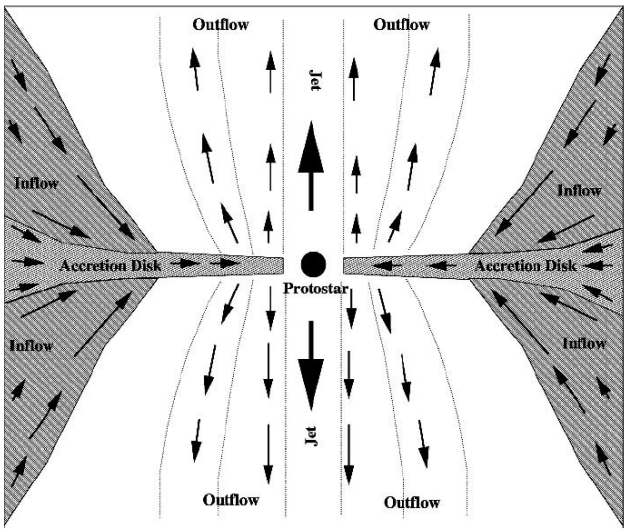

FIGURE 6.3 – Schématisation d'une vue en coupe d'un disque protoplanétaire. Au travers du disque, la matière est transportée («inflow» et «accrétion») vers l'étoile («protostar» : étoile en formation), sur laquelle elle tombe ou est éjectée vers le milieu interstellaire («outflow» et «jet»). Reproduction de la Fig. 1.3 de SCHULZ [2012].

Les disques d'accrétion protoplanétaires sont observés autour d'un très grand nombre d'étoiles jeunes (dites de type «T Tauri», du nom de l'une d'entre elles). Ils sont composés de gaz et de poussières, ces dernières représentant quelques pourcents de la masse totale. La phase gazeuse est, tout comme le Soleil, composée essentiellement d'hydrogène et d'hélium. La figure 6.2 représente le disque observé, dans le domaine radio, autour de l'étoile HL Tauri. Au sein de ce type d'objet, la matière est globalement transportée des régions les plus externes vers celles plus centrales. Le gaz et les grains de poussière sont ensuite accrétés sur l'étoile ou éjectés vers le milieu interstellaire. Le schéma de la figure 6.3 résume les phénomènes impliqués. L'éjection de matière, dans la partie centrale, est produite par le fort couplage entre le plasma du disque et le champ magnétique généré par l'étoile. En outre, le proto-soleil irradie la «surface» externe du disque dans les domaines UV et rayons X. Cette irradiation produit également une perte de masse, justement nommée «photoévaporation», qui est toujours l'objet de discussions scientifiques.

Le système, composé d'une étoile et de son disque, est formé lors de l'effondrement d'un nuage moléculaire. Ce dernier, beaucoup plus grand, est l'objet d'instabilités gravitationnelles qui finissent par le disloquer. Du fait des phénomènes de transport dont ils sont le siège, les disques circumstellaires évoluent dans le temps, pour *in fine*, après plusieurs millions d'années, conduire à l'apparition d'un système planétaire.

Les disques d'accrétion sont des systèmes très largement répandus dans l'Univers, et ne sont pas l'exclusivité des étoiles jeunes. En effet, les différents types de galaxies spirales peuvent être considérés comme des disques d'accrétion, les trous noirs –qui sont des objets particulièrement exotiques– comportent également des disques où la physique est extrême. Enfin, les cortèges satellitaires et/ou les systèmes d'anneaux que possèdent certaines planètes peuvent être considérés

comme les vestiges d'un disque d'accrétion.

6.3 Une modélisation de l'évolution temporelle d'un disque protoplanétaire

Comme déjà mentionné, un disque d'accrétion est constitué principalement de gaz, l'ensemble étant en rotation autour de l'étoile centrale. Cette rotation est quasi-képlerienne, et possède donc une vitesse angulaire peu différente de :

$$\Omega = \frac{\sqrt{GM_\star}}{r^{3/2}} \tag{6.1}$$

où G est la constante de la gravité, $M_\star$ la masse de l'étoile et r la distance au centre de masse du système. Du fait de la symétrie cylindrique, ce centre de masse se trouve au centre de l'étoile.

La dépendance de Ω vis-à-vis de r, entraîne un cisaillement entre les anneaux de matière contigus. Cet effet, combiné avec des instabilités magnéto-rotationnelles, est à l'origine de la turbulence qui prend naissance dans le disque. Un transport radial de matière est alors induit, et amène le gaz et les poussières vers l'étoile. La vitesse d'accrétion v_{acc} (m s^{-1}) peut être estimée par [LYNDEN-BELL et PRINGLE, 1974] :

$$v_{acc} = -\frac{3}{\Sigma\sqrt{r}}\frac{\partial}{\partial r}\left(\Sigma\nu\sqrt{r}\right) \tag{6.2}$$

avec Σ (kg m^{-2}) la densité surfacique de matière sur le disque, et ν la viscosité cinématique (m^2 s^{-1}) du gaz turbulent. On reviendra dans la suite sur la signification physique de ν. Si l'épaisseur du disque est 2H, la densité Σ peut alors être calculée comme :

$$\Sigma = 2\int_{z=0}^{z=+H} \rho\, dz \tag{6.3}$$

avec ρ la masse volumique (kg m^{-3}) du gaz et z l'altitude au-dessus du plan médian, en supposant que ce dernier est plan de symétrie du système. Si on combine l'équation (6.2) avec l'équation de continuité, écrite en coordonnées cylindriques, on obtient :

$$\frac{\partial\Sigma}{\partial t} = \frac{3}{r}\frac{\partial}{\partial r}\left\{r^{1/2}\frac{\partial}{\partial r}\left(\Sigma\nu r^{1/2}\right)\right\} \tag{6.4}$$

équation qui gouverne le comportement spatio-temporel du disque, ceci si on connaît ν. Cette équation est une équation aux dérivées partielles, deux variables indépendantes interviennent : t et r, du deuxième ordre. De plus, elle est non-linéaire car ν, qui contient ici toutes les propriétés de la matière, dépend de r, mais aussi de Σ. Dans le cas général, il n'y a pas de solution analytique à cette équation, on doit donc avoir recours à des méthodes numériques. L'aspect non-linéaire apporte ici une vraie difficulté car les méthodes classiques de type Crank-Nicolson [NOUGIER, 1987] s'applique aux cas linéaires. Un schéma explicite pourrait permettre de contourner le problème, mais il demande des pas de temps extrêmement petits, qui peuvent mener à des temps de calculs prohibitifs.

L'équation (6.4) est formellement très proche d'une équation de diffusion [BIRNSTIEL, 2011] ; en effet si on pose $x = 2\sqrt{r}$ et $u = \Sigma\sqrt{r}$, elle devient :

$$\frac{\partial u}{\partial t} = D\frac{\partial^2 u}{\partial x^2} \tag{6.5}$$

avec $D = 12\nu/x^2$, en faisant l'hypothèse d'une viscosité constante. Le temps de vie visqueux t_{visc} du disque peut alors être estimé en posant :

$$t_{visc} = \frac{x^2}{D} \simeq \frac{r^2}{\nu} \tag{6.6}$$

En prenant pour la distance r une valeur typique du système solaire, à savoir $r \sim 10$ UA[3], on a une température T ~ 100 K et une masse volumique du gaz (essentiellement H_2) $\rho_m = 10^{-6}$ kg m^{-3} sur le plan médian de la nébuleuse. Pour un gaz parfait, la viscosité dynamique η (Pa s) est donnée par

$$\eta = \frac{1}{3\sqrt{2}} \frac{m\bar{v}}{\sigma} \tag{6.7}$$

où m est la masse d'une molécule, $\bar{v}$ la vitesse moyenne des molécules et $\sigma \sim 10^{-20}$ m^2 la section efficace de collision des molécules. Sachant que

$$\bar{v} = \sqrt{\frac{8 k_B T}{\pi m}} \tag{6.8}$$

où $k_B = 1{,}38 \times 10^{-23}$ J K^{-1} est la constante de Boltzmann, on en déduit que la viscosité cinématique moléculaire est de l'ordre de $\nu = \eta/\rho \sim 80$ m^2 s^{-1}. On obtient alors $t_{visc} \sim 10^{22}$ s, soit plus de 10^5 milliards d'années. Cette valeur est très supérieure à l'âge du système solaire (~ 4,5 milliards d'années) et même à celui de l'Univers (~ 13,8 milliards d'années).

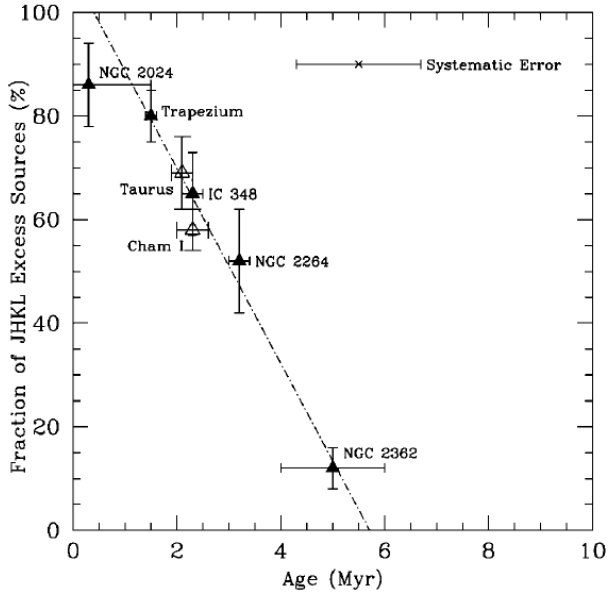

FIGURE 6.4 – Pour un échantillon d'amas d'étoiles (NGC 2024, Trapezium, ...) l'excès de luminosité dans les bandes de longueur d'onde JHKL est mesuré, en ordonnée la fraction d'étoiles avec une valeur donnée de cet excès est représentée. En abscisse, l'âge de l'amas est reporté, toutes les étoiles appartenant au même amas sont censées avoir l'âge en question. L'excès en luminosité JHKL est un indicateur d'existence d'une grande quantité de poussières, et donc d'un disque d'accrétion. L'unité de temps «Myr» correspond à un million d'années. Reproduction de la Fig. 1 de HAISCH et collab. [2001].

La viscosité est une grandeur qui quantifie le transfert de quantité de mouvement dans un fluide. Clairement, la viscosité d'origine moléculaire, utilisée dans l'évaluation précédente, ne convient pas dans le cas des disques d'accrétion protoplanétaires. La durée de vie typique de ce type d'objet peut être évaluée grâce aux observations. La figure 6.4 montre la fréquence de présence de disques d'accrétion circumstellaires dans des amas d'étoiles, ceci en fonction de l'âge de l'amas [HAISCH et collab., 2001]. Il apparaît que l'âge des disques ne peut excéder quelques millions d'années, d'autres travaux confirment cette tendance [PASCUCCI et TACHIBANA, 2010].

3. Unité Astronomique : distance moyenne au centre de masse du système solaire.

En fait, la viscosité moléculaire n'est pas directement responsable du transport dans les disques, la turbulence qui s'y développe y est beaucoup plus efficace. C'est pourquoi on a introduit une «viscosité turbulente», dont on note $< \nu_{turb} >$ la valeur moyenne sur l'épaisseur d'un disque. Cette quantité rend compte du transport de quantité de mouvement à des échelles beaucoup plus grandes que celles impliquées par la viscosité moléculaire : on ne considère plus les collisions entre molécules, mais les «collisions» entre «tourbillons» de l'écoulement turbulent.

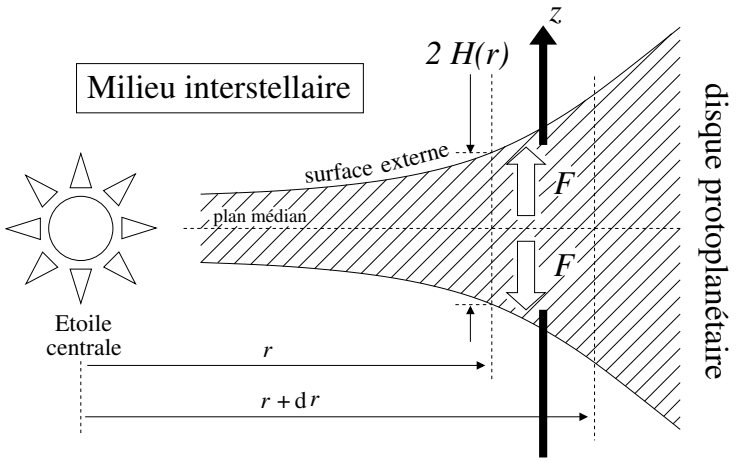

FIGURE 6.5 – Schéma d'une vue en coupe d'un disque protoplanétaire.

Le mouvement turbulent se manifeste dans toute une gamme d'échelles allant du centimètre à plusieurs kilomètres. Cependant, réaliser des simulations numériques du comportement d'un disque protoplanétaire, dans tous ses détails, et en particulier en menant une résolution multi-échelle des équations de Navier-Stokes n'est pas envisageable ; ceci, même avec la puissance de calcul atteinte aujourd'hui par les ordinateurs. C'est pourquoi, dès les années soixante-dix, le «formalisme α» déjà mentionné, a été introduit [SHAKURA et SUNYAEV, 1973]. Celui-ci repose sur un raisonnement d'analyse dimensionnelle. On considère un «tourbillon» typique d'un écoulement turbulent, si son diamètre est de l'ordre de L (m) et sa vitesse de retournement [4] v (m s^{-1}), la viscosité (cinématique) turbulente ν_{turb} qu'on lui associe, peut alors être estimée en posant le produit :

$$\nu_{turb} \sim \mathrm{L} \times v \tag{6.9}$$

On remarquera que ν_{turb} est bien homogène à une viscosité cinématique (m^2 s^{-1}). Dans la construction de ce «formalisme α», on choisit pour L l'échelle de hauteur de pression H_P, qui est la distance caractéristique sur laquelle la pression varie dans le disque, et $\alpha \times c_s$ pour v, avec c_s la vitesse du son. Le paramètre α est libre, il donne son nom au modèle. Malheureusement, on n'a pas pu déterminer de valeur précise et universelle de α, les estimations disponibles varient sur un ordre de grandeur entre $\sim 10^{-3}$ et $\sim 10^{-2}$. Cependant, pour une valeur fixée de α on peut calculer la viscosité turbulente ν_{turb} et sa valeur moyennée sur l'épaisseur locale du disque $< \nu_{turb} >$. En remplaçant ν dans l'équation d'évolution (6.4), on est alors capable –au moins en principe– de simuler l'évolution temporelle du disque modélisé. Ceci requiert cependant le calcul de la structure verticale, préalable dont on va étudier la construction dans le paragraphe suivant.

6.4 Structure verticale d'un disque d'accrétion

Dans un repère ayant pour origine l'étoile centrale et muni de coordonnées cylindriques, on découpe virtuellement le disque en anneaux élémentaires et concentriques, chacun d'eux étant

4. si on assimile un «tourbillon» à un mouvement circulaire de la matière, cette vitesse est la vitesse typique d'un volume élémentaire de gaz appartenant à un «tourbillon».

délimité par les cercles de rayons respectifs r et $r + \mathrm{d}r$. En conséquence de la symétrie cylindrique du système, la physique de l'intérieur d'un anneau est ramenée à celle d'une colonne de gaz de demi-hauteur $\mathrm{H}(r)$ (voir figure 6.5). Les lois qu'on va alors appliquer sont au nombre de trois : (1) l'équilibre hydrostatique, (2) la conservation de l'énergie, et (3) une loi similaire à celle de Fourier pour rendre compte du transfert radiatif d'énergie.

Si on admet que le disque est géométriquement fin, soit $r \gg \mathrm{H}(r)$ en tout point, l'équilibre hydrostatique peut alors s'écrire très simplement :

$$\frac{1}{\rho}\frac{\partial \mathrm{P}}{\partial z} = -\Omega^2 z \tag{6.10}$$

avec P la pression et ρ la masse volumique. On note z l'altitude (algébrique) comptée à partir du plan médian du système (voir figure 6.5). La vitesse angulaire Ω a déjà été définie par l'équation (9.2), le terme $-\Omega^2 z$ provient de la composante verticale de l'attraction gravitationnelle exercée par l'étoile.

On appelle F le flux vertical d'énergie radiative (*i.e.* sous forme de photons, F s'exprime en $\mathrm{W\,m^{-2}}$), la conservation de l'énergie s'exprime de la façon suivante :

$$\frac{\partial \mathrm{F}}{\partial z} = \frac{9}{4}\rho \nu_{\mathrm{turb}} \Omega^2 \tag{6.11}$$

En effet, la friction associée aux mouvements turbulents dégrade *in fine* l'énergie cinétique en chaleur, ceci dans chaque portion de colonne comprise entre les altitudes z et $z + \mathrm{d}z$.

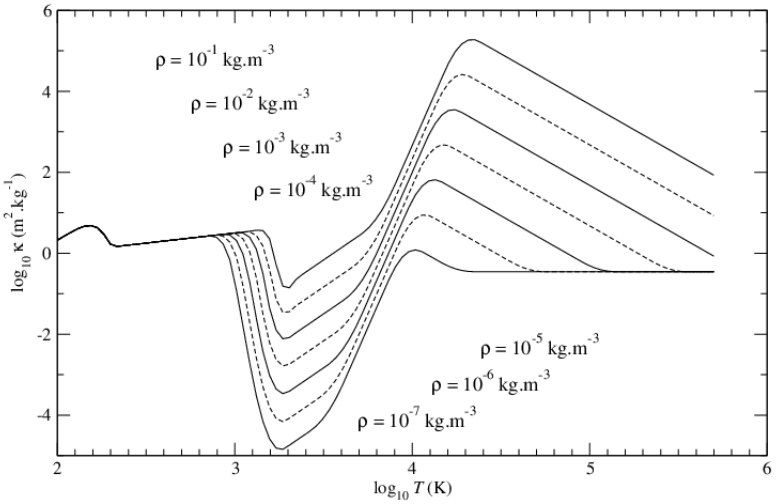

FIGURE 6.6 – Comportement de l'opacité κ (échelle logarithmique) en fonction de la température T, ceci pour plusieurs valeurs de la masse volumique ρ. Ces courbes ont été tracées à partir des formules d'interpolation données par BELL et LIN [1994].

La distribution verticale de la température T est imposée par une loi où le gradient de température $\partial \mathrm{T}/\partial z$ est proportionnel au flux de photons F, on a donc :

$$\frac{\partial \mathrm{T}}{\partial z} = -\underbrace{\frac{3\kappa\rho}{16\sigma \mathrm{T}^3}}_{(1)} \mathrm{F} \tag{6.12}$$

L'inverse du terme (1) joue un rôle analogue à celui de la conductivité thermique intervenant dans la loi de Fourier. Dans cette expression σ est la constante de Stefan-Boltzmann ($\sigma = 5{,}67 \times$

10^{-8} W m^{-2} K^{-4}) et κ, nommée opacité (m^2 kg^{-1}), représente l'absorption de photons produite par le gaz et les poussières en présence.

Divers phénomènes contribuent à l'opacité κ : les grains de poussière, l'absorption par les molécules, la diffusion par les atomes d'hydrogène ou les électrons libres, etc. Les valeurs de κ sont calculées grâce à des modèles dédiés, elles sont ensuite fournies sous forme de tables ou de formules approchées. La figure 6.6 donne un exemple de comportement de κ en fonction de la température et de la masse volumique. On a donc un système différentiel de trois équations : (6.10), (6.11) et (6.12) ; dont les fonctions inconnues sont P, F et T. Implicitement, pour faire le lien entre P, T et ρ, on doit se munir d'une équation d'état ; c'est ce qui est fait en adoptant l'équation d'état des gaz parfaits.
La résolution du système ne peut être menée que si on se dote de conditions aux limites pour les grandeurs inconnues. On peut montrer que la pression à la «surface» externe du disque est :

$$\mathrm{P}_s = \frac{\Omega^2 \mathrm{H} \tau_{ab}}{\kappa_s} \tag{6.13}$$

où τ_{ab} est l'épaisseur optique au-dessus du disque, c'est une constante usuellement prise égale à 10^{-2}. L'opacité à la surface κ_s, ne dépend que de la température de surface T_s. Cette dernière est déterminée en résolvant :

$$\underbrace{2\sigma(\mathrm{T}_s^4 - \mathrm{T}_b^4)}_{(1)} - \underbrace{\frac{9\alpha k \mathrm{T}_s}{8\mu m_\mathrm{H} \kappa_s}\Omega}_{(2)} - \underbrace{\frac{3}{8\pi}\dot{\mathrm{M}}_\mathrm{st}\Omega^2}_{(3)} = 0 \tag{6.14}$$

La température du milieu interstellaire, dans lequel est immergé le disque, est T_b (usuellement ~ 10 K). On note k la constante de Boltzmann, m_H représente la masse d'un atome d'hydrogène et le produit $\mu \times m_\mathrm{H}$ est la masse moléculaire moyenne. L'équation (6.14) est une équation de conservation de l'énergie : le terme (1) est le bilan radiatif à la surface du disque, alors que les termes (2) et (3) représentent l'énergie produite par la turbulence à l'intérieur du disque. Le paramètre $\dot{\mathrm{M}}_\mathrm{st}$ (kg $^{-1}$) est libre, il représente le taux d'accrétion vers l'étoile d'un disque en régime permanent («st» pour «steady»).

Pour des valeurs fixées de α et $\dot{\mathrm{M}}_\mathrm{st}$, on peut donc résoudre l'équation (6.14) ; on obtient donc finalement T_s et P_s. Connaissant les valeurs de P, F et T en surface on peut ainsi intégrer le système d'équations qui régit la structure verticale. Cependant, il reste un problème important : la hauteur $\mathrm{H}(r)$ est jusque là inconnue. Par symétrie on doit avoir $\mathrm{F}(z=0)=0$, on exploite donc cette propriété en cherchant, par une méthode itérative, la valeur de H qui assure cette condition sur le plan médian.

Pour chaque jeu de paramètres $(\alpha, \dot{\mathrm{M}}_\mathrm{st}, r)$ on est donc en mesure de calculer les propriétés de la structure verticale d'un disque en intégrant les équations (6.10), (6.11) et (6.12). Pour chacun de ces triplets $(\alpha, \dot{\mathrm{M}}_\mathrm{st}, r)$ on peut alors déduire une valeur de Σ et de $< \nu_\mathrm{turb} >$. On construit alors des tables donnant Σ et $< \nu_\mathrm{turb} >$ en fonction de $(\alpha, \dot{\mathrm{M}}_\mathrm{st}, r)$. Lors de la résolution de l'équation d'évolution (6.4) ; ces tables sont utilisées afin d'obtenir $< \nu_\mathrm{turb} >$, un algorithme d'interpolation permet de tirer $< \nu_\mathrm{turb} >$ en fonction de Σ et r, à α fixé. La figure 6.7 montre les variations de P, F et T dans l'épaisseur d'un disque pour $r = 0.1$ UA, $\alpha = 10^{-3}$ et $\dot{\mathrm{M}}_\mathrm{st} = 10^{-9}$ masse solaire par an.

Retour à la table des matières : p. v

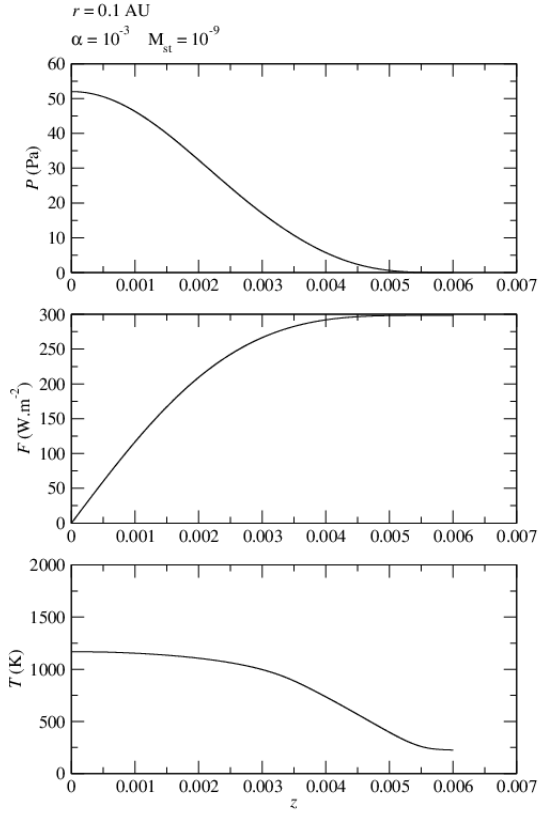

FIGURE 6.7 – Structure verticale d'un disque d'accrétion protoplanétaire simulé en adoptant $\alpha = 10^{-3}$ et $\dot{M}_{st} = 10^{-9}$ masse solaire par an. On a ici les variations de la pression P, du flux radiatif F et de la température T en fonction de l'altitude z exprimée en unité astronomique.

On pourra noter que dans le formalisme exposé jusqu'ici, et qui correspond à ce qui a été utilisé par PAPALOIZOU et TERQUEM [1999], le seul paramètre rendant compte d'une interaction entre le disque proto-planétaire et l'étoile centrale, est la masse de cette dernière $M_\star$ qui apparaît dans l'expression de la fréquence képlerienne Ω. L'irradiation du disque par l'étoile peut être prise en compte en utilisant une version modifiée de l'équation 6.14

$$2\sigma\left(T_s^4 - T_{birr}^4\right) - \frac{9\alpha k T_s}{8\mu m_H \kappa_s} - \frac{3}{8\pi}\dot{M}_{st}\Omega^2 = 0 \tag{6.15}$$

où T_{birr} est donnée par

$$T_{birr}^4 = T_b^4 + T_{irr}^4 \tag{6.16}$$

avec $T_b = 10$ K, la température du milieu interstellaire, et T_{irr} donnée par

$$T_{irr} = T_{eff}(t) \left[\underbrace{\frac{2}{3\pi}\left(\frac{R_\star(t)}{r}\right)^3}_{(1)} + \underbrace{\frac{1}{2}\left(\frac{R_\star(t)}{r}\right)^2 \left(\frac{H_p(t)}{r}\right)\left(\frac{d\ln H_p(t)}{d\ln r} - 1\right)}_{(2)} \right]^{1/4} \tag{6.17}$$

où T_{eff} et $R_\star$ sont respectivement la température et le rayon de l'étoile à un instant donné. L'échelle de hauteur de pression H_p est assimilée à l'épaisseur du disque à un moment donné. Ceci ouvre

la voie à des modèles de disques proto-planétaires «co-évoluant» avec leur étoile centrale, c'est ce qui est fait dans CORDIER et collab. [2016] (voir page 274).

6.5 Evolution temporelle d'un disque protoplanétaire

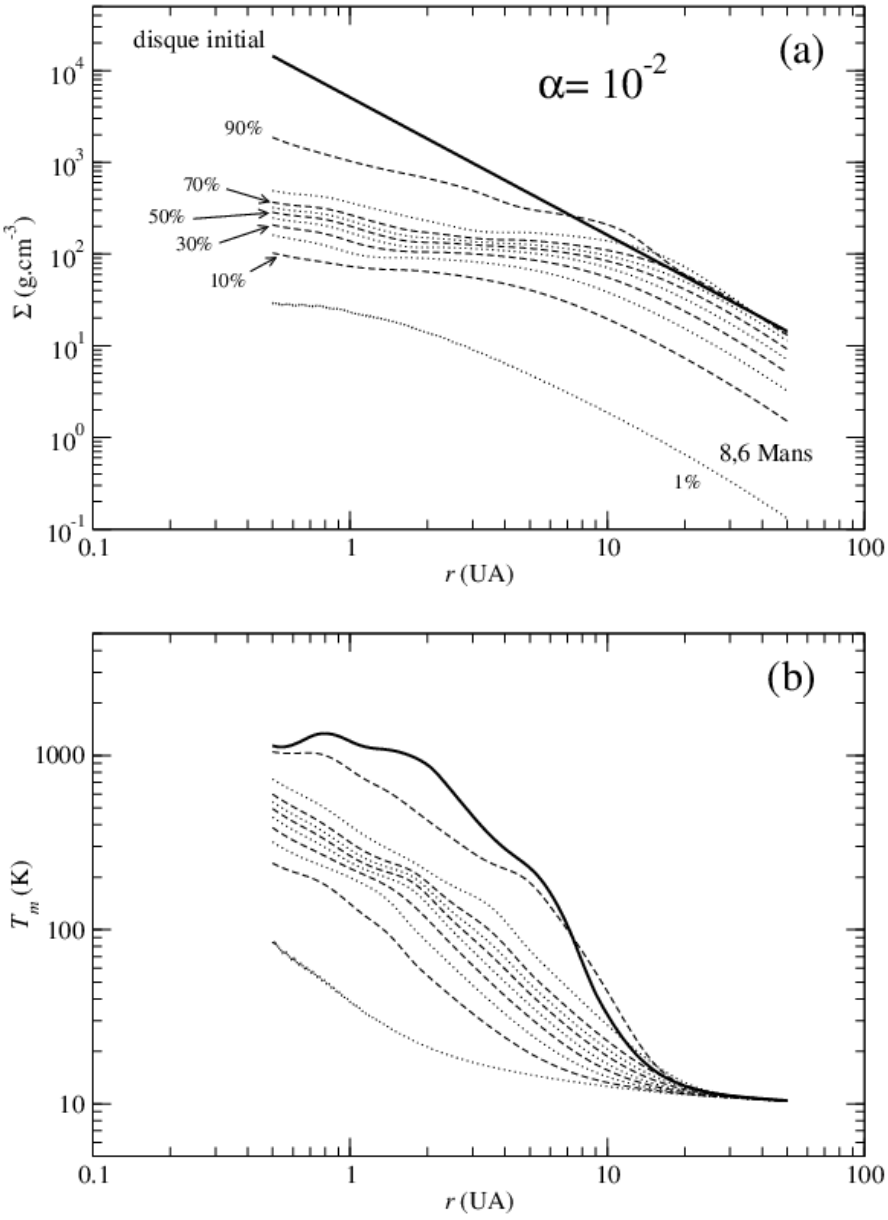

FIGURE 6.8 – Evolution temporelle d'un modèle de disque d'accrétion calculé en adoptant $\alpha = 10^{-2}$. Le temps de vie obtenu est de 8,6 millions d'années (méga-ans, «Mans» sur la figure). (a) Evolution de la densité surfacique de matière Σ en fonction de la distance r au centre du système (r en unité astronomique). (b) Evolution de la température sur le plan médian T_m (en K) en fonction de r. Les pourcentages représentent la masse du disque en fonction de sa masse initiale, on a tracé une courbe tous les 10%.

En adoptant un état initial où la matière est distribuée radialement suivant une loi du type $\Sigma \propto r^{-3/2}$ [HAYASHI, 1981] et pour une masse totale de 3 MMSN[5], on a calculé l'évolution d'un

5. Minimum Mass Solar Nebula : masse minimum pour la nébuleuse solaire.

disque pour deux valeurs de α : 10^{-2} et 10^{-3}. Le comportement de la densité massique surfacique Σ et celui de la température sur le plan médian T_m, ont été reportés sur la figure 6.8. L'évolution a été stoppée lorsque la masse totale a atteint 1% de la masse initiale du disque, ce qui correspond approximativement au contenu en poussières. La durée totale de l'évolution est de 102,4 millions d'années pour $\alpha = 10^{-3}$ et 8,6 millions d'années pour $\alpha = 10^{-2}$. Comme on le voit, l'utilisation de $< v_{turb} >$ au lieu de la viscosité moléculaire permet d'approcher des valeurs beaucoup plus réalistes pour la durée de vie d'un disque.

Pour réduire encore l'âge finalement obtenu, on doit inclure d'autres phénomènes physiques, notamment la photoévaporation induite par l'irradiation solaire. En effet le chauffage, par le Soleil, des parties les plus externes du disque entraîne un échappement de matière vers le milieu interstellaire. Cette perte de masse se traduit par un raccourcissement significatif du temps de vie de la nébuleuse. Le traitement rigoureux de cet échappement demanderait de recourir à la prise en compte d'une hydrodynamique extrêmement exigeante en termes de ressources de calcul. Une approche simplifiée est cependant envisageable. Au-delà d'une certaine distance (par exemple 5 UA) la masse perdue par photoévaporation, par unité de surface de disque et par unité de temps, est supposée suivre une loi de la forme λ/r avec λ un paramètre ajustable. En supposant par exemple une photoévaporation correspondant à une perte totale (*i.e.* intégrée sur toute la surface) de 10^{-9} masse solaire par année, on obtient –en reprenant $\alpha = 10^{-2}$– un temps de vie de 5.3 millions d'années, cette fois parfaitement compatible avec les observations comme celles indiquées par la figure 6.4. La dispersion en âge constatée sur cette figure peut venir d'une dispersion en masse totale initiale des disques. Par exemple, en supposant une masse initiale de 1 MMSN on obtient un âge final de 9,0 millions d'années, alors qu'en prenant 10 MMSN on a 7,8 millions d'années, ceci en conservant $\alpha = 10^{-2}$ et sans tenir compte de la photoévaporation.

6.6 Références

ALIBERT, Y., C. MORDASINI, W. BENZ et C. WINISDOERFFER. 2005, «Models of giant planet formation with migration and disc evolution», *A&A*, vol. 434, doi: 10.1051/0004-6361:20042032, p. 343–353. 237

BELL, K. R. et D. N. C. LIN. 1994, «Using FU Orionis outbursts to constrain self-regulated protostellar disk models», *ApJ*, vol. 427, doi: 10.1086/174206, p. 987–1004. 243

BIERMANN, L. 1951, *Z. Astrophys.*, vol. 28, p. 304. 237

BIRNSTIEL, T. 2011, *The Evolution of Gas and Dust in Protoplanetary Accretion Disks*, thèse de doctorat, PhD Thesis, 2011. 240

BÖHM-VITENSE, E. 1958, *Zs. f. Ap.*, vol. 46, p. 108. 237

CARRASCO-GONZÁLEZ, C., T. HENNING, C. J. CHANDLER, H. LINZ, L. PÉREZ, L. F. RODRÍGUEZ, R. GALVÁN-MADRID, G. ANGLADA, T. BIRNSTIEL, R. VAN BOEKEL, M. FLOCK, H. KLAHR, E. MACIAS, K. MENTEN, M. OSORIO, L. TESTI, J. M. TORRELLES et Z. ZHU. 2016, «The VLA View of the HL Tau Disk : Disk Mass, Grain Evolution, and Early Planet Formation», *ApJL*, vol. 821, doi: 10.3847/2041-8205/821/1/L16, L16. 238

CORDIER, D., P. G. PRADA MORONI et E. TOGNELLI. 2016, «Dust photophoretic transport around a T Tauri star : Implications for comets composition», *Icarus*, vol. 268, doi: 10.1016/j.icarus.2015.11.037, p. 281–294. 246

FLOCK, M., N. DZYURKEVICH, H. KLAHR, N. J. TURNER et T. HENNING. 2011, «Turbulence and Steady Flows in Three-dimensional Global Stratified Magnetohydrodynamic Simulations of Accretion Disks», *ApJ*, vol. 735, doi: 10.1088/0004-637X/735/2/122, 122. 237

FROMANG, S. 2010, «MHD simulations of the magnetorotational instability in a shearing box with zero net flux : the case Pm = 4», *A&A*, vol. 514, doi: 10.1051/0004-6361/201014284, L5. 237

FROMANG, S., H. LATTER, G. LESUR et G. I. OGILVIE. 2013, «Local outflows from turbulent accretion disks», *A&A*, vol. 552, doi: 10.1051/0004-6361/201220016, A71. 237

FROMANG, S., W. LYRA et F. MASSET. 2011, «Meridional circulation in turbulent protoplanetary disks», *A&A*, vol. 534, doi: 10.1051/0004-6361/201016068, A107. 237

HAISCH, K. E., JR., E. A. LADA et C. J. LADA. 2001, «Disk Frequencies and Lifetimes in Young Clusters», *ApJ*, vol. 553, doi: 10.1086/320685, p. L153–L156. 241

HAYASHI, C. 1981, «Structure of the Solar Nebula, Growth and Decay of Magnetic Fields and Effects of Magnetic and Turbulent Viscosities on the Nebula», *Progress of Theoretical Physics Supplement*, vol. 70, doi: 10.1143/PTPS.70.35, p. 35–53. 246

LYNDEN-BELL, D. et J. E. PRINGLE. 1974, «The evolution of viscous discs and the origin of the nebular variables.», *MNRAS*, vol. 168, p. 603–637. 240

NOUGIER, J. P. 1987, *Méthodes de calcul numérique*, Masson, Paris, ISBN 978-2-225-81086-2. 240

PAPALOIZOU, J. C. B. et C. TERQUEM. 1999, «Critical Protoplanetary Core Masses in Protoplanetary Disks and the Formation of Short-Period Giant Planets», *ApJ*, vol. 521, doi: 10.1086/307581, p. 823–838. 237, 245

PASCUCCI, I. et S. TACHIBANA. 2010, *The Clearing of Protoplanetary Disks and of the Protosolar Nebula*, p. 263–298. 241

PRANDTL, L., éd.. 1952, *Essential of Fluid Dynamics*, London : Blakie. 237

SCHULZ, N. S. 2012, *The Formation and Early Evolution of Stars – From Dust to Stars and Planets*, 2e éd., Springer-Verlag, Berlin-Heidelberg, ISBN 978-3-642-44168-4, doi: 10.1007/978-3-642-23926-7. 239

SCHWARZSCHILD, K. 1906, *Gott. Nach.*, vol. 1, p. 41. 237

SHAKURA, N. I. et R. A. SUNYAEV. 1973, *A&A*, vol. 24, p. 337–355. 237, 242

VITENSE, E. 1953, *Zs. f. Ap.*, vol. 32, p. 135. 237

WEIDENSCHILLING, S. J. 1977, «Aerodynamics of solid bodies in the solar nebula», *MNRAS*, vol. 180, doi: 10.1093/mnras/180.1.57, p. 57–70. 236

Chapitre 7

Equation d'évolution d'un disque α et méthode numérique de résolution

Sommaire

7.1 Une très brève introduction 249
7.2 L'équation d'évolution et les conditions aux limites 249
7.2.1 L'équation d'évolution du disque 249
7.2.2 Conditions aux limites 252
7.3 Discrétisation de l'équation d'évolution 253
7.3.1 Construction du système à résoudre 253
7.3.2 Résumé 256
7.3.3 Méthode de résolution numérique 256
7.4 Références 257

7.1 Une très brève introduction

Dans ce chapitre, comme dans le suivant (chapitre 8) je décris en détail les méthodes numériques employées pour construire mon modèle de disque protoplanétaire, je n'ai trouvé aucune référence dans la littérature où une description fine de ce type de technique est donnée. Le présent chapitre est consacré à l'intégration numérique de l'équation d'évolution spatio-temporelle du disque, alors que le suivant concerne l'intégration du système d'équation de la structure verticale. L'implémentation de ces méthodes a été faite en `FORTRAN 2008`, et j'ai donné le petit nom d'*EvAD*[1] au programme, qui représente actuellement environ 36 000 lignes de code.

7.2 L'équation d'évolution et les conditions aux limites

7.2.1 L'équation d'évolution du disque

Comme on l'a vu au chapitre précédent, l'équation d'évolution temporelle d'un disque d'accrétion protoplanétaire peut s'écrire sous la forme :

$$\frac{\partial \Sigma}{\partial t} = \frac{3}{r}\frac{\partial}{\partial r}\left\{\sqrt{r}\frac{\partial}{\partial r}\left(\Sigma \nu \sqrt{r}\right)\right\} \tag{7.1}$$

où la densité surfacique de masse $\Sigma(r,t)$ (kg m^{-2}) est la fonction inconnue. Dans le cas le plus général la viscosité turbulente ν (m^2 s^{-1}) n'est pas une constante mais dépend de Σ et r : $\nu = \nu(r,\Sigma(t))$. Cette équation établie par Lynden-Bell et Pringle [1974], est reprise dans de nombreuses publications, nous allons ici rappeler les étapes de sa démonstration. Les principaux ingrédients physiques sur lesquels elle repose sont :

1. *Ev*olutionary *A*ccretion *D*isk

— le théorème du moment cinétique
— la conservation de la matière
— le fait d'avoir un disque en rotation képlérienne.

Dans les manuels de physique français, le théorème du moment cinétique s'écrit souvent sous la forme :

$$\frac{\mathrm{D}\vec{\sigma_o}}{\mathrm{D}t} = \vec{\mathcal{M}}_{\vec{F}/O} \tag{7.2}$$

avec $\vec{\sigma_o}$ le moment cinétique par rapport au point O :

$$\vec{\sigma_o} = \vec{OM} \wedge \vec{p} \tag{7.3}$$

avec $\vec{p}$ la quantité de mouvement et $\vec{\mathcal{M}}_{\vec{F}/O}$ le moment des forces exercées au point M. Dans le cas d'un disque d'accrétion, en le considérant plan et en rotation (képlérienne) circulaire autour de l'étoile située à l'origine O ; on peut écrire en projection suivant l'axe Oz perpendiculaire au plan du disque :

$$\sigma_o = r\,(\delta m\, r\,\Omega) \tag{7.4}$$

où δm est la masse de matière comprise entre les cercles de rayons respectifs r et $r+\delta r$, Ω est la vitesse angulaire de la matière située à la distance r. Dans leur article de 1974, Lynden-Bell et Pringle pose :

$$h = \Omega r^2 \tag{7.5}$$

Le membre de gauche du théorème du moment cinétique (7.2) s'écrit alors :

$$\frac{\mathrm{D}\vec{\sigma_o}}{\mathrm{D}t} = \frac{\mathrm{D}}{\mathrm{D}t}\left(\delta m\,\Omega\, r^2\right) = \delta m\,\frac{\mathrm{D}h}{\mathrm{D}t} \tag{7.6}$$

comme :

$$\delta m = 2\pi\, r\,\delta r\,\Sigma \tag{7.7}$$

on a alors :

$$\frac{\mathrm{D}\vec{\sigma_o}}{\mathrm{D}t} = 2\pi r \times \delta r \times \Sigma \times \frac{\mathrm{D}}{\mathrm{D}t}(\Omega r^2) \tag{7.8}$$

Nous allons maintenant évaluer le moment des forces de frottement visqueux subies par la matière contenue entre les distances r et $r+\delta r$, quantité que Lynden-Bell et Pringle notent g. En sommant sur un périmètre $2\pi r$, on a le moment total :

$$g = r\,(2\pi r)\,(-\Sigma \nu r \frac{\mathrm{d}\Omega}{\mathrm{d}r}) \tag{7.9}$$

Cette relation s'appliquant aux cercles de rayons r et $r+\delta r$; cercles délimitant la couronne contenant la masse δm de matière ; le moment total des forces appliquées est alors :

$$-\,\delta r\,\frac{\partial g}{\partial r} \tag{7.10}$$

En injectant cette relation dans le théorème du moment cinétique (7.2), et en utilisant (7.8), il vient :

$$2\pi r\,\delta r\,\Sigma\,\frac{\mathrm{D}}{\mathrm{D}t}(\Omega r^2) = -\delta r\,\frac{\partial g}{\partial r} \tag{7.11}$$

On montre, dans les cours d'introduction à la mécanique des fluides, que la dérivées totale $\mathrm{D}/\mathrm{D}t$ est :

$$\frac{\mathrm{D}}{\mathrm{D}t} = \frac{\partial}{\partial t} + (\vec{v}\,.\,\vec{\nabla}) \tag{7.12}$$

où $\vec{v}$ est la vitesse d'écoulement du fluide et $\vec{\nabla}$ l'opérateur nabla. Dans le cas d'un écoulement radial, cette relation devient :

$$\frac{\mathrm{D}}{\mathrm{D}t} = \frac{\partial}{\partial t} + v_r \times \frac{\partial}{\partial r} \tag{7.13}$$

si on considère le disque comme étant en rotation képlérienne, Ω est indépendante du temps, on a alors :

$$\frac{\mathrm{D}}{\mathrm{D}t}(\Omega r^2) = v_r \frac{\partial}{\partial r}(\Omega r^2) \tag{7.14}$$

cependant dans le cas képlérien :

$$\Omega = \frac{\sqrt{\mathrm{GM}_\star}}{r^{3/2}} \tag{7.15}$$

d'où :

$$\frac{\partial}{\partial r}(\Omega r^2) = \frac{\sqrt{\mathrm{GM}_\star}}{2\sqrt{r}} \tag{7.16}$$

le théorème du moment cinétique conduit alors à :

$$2\pi r\,\delta r\,\Sigma \frac{\sqrt{\mathrm{GM}_\star}}{2\sqrt{r}} v_r = -\delta r \frac{\partial g}{\partial r} \tag{7.17}$$

or :

$$\frac{\partial g}{\partial r} = -\frac{\partial}{\partial r}\left(2\pi r^3 \nu \Sigma \frac{\mathrm{d}\Omega}{\mathrm{d}r}\right) \tag{7.18}$$

où :

$$\frac{\mathrm{d}\Omega}{\mathrm{d}r} = -\frac{3}{2}\frac{\sqrt{\mathrm{GM}_\star}}{r^{5/2}} \tag{7.19}$$

ainsi :

$$\frac{\partial g}{\partial r} = 3\pi\sqrt{\mathrm{GM}_\star}\frac{\partial}{\partial r}\left(\Sigma\nu\sqrt{r}\right) \tag{7.20}$$

en injectant ceci dans (7.17) :

$$2\pi r\Sigma\frac{\sqrt{\mathrm{GM}_\star}}{2\sqrt{r}} v_r = -3\pi\sqrt{\mathrm{GM}_\star}\frac{\partial}{\partial r}(\Sigma\nu\sqrt{r}) \tag{7.21}$$

d'où la vitesse d'accrétion vers l'étoile :

$$\boxed{v_r = -\frac{3}{\Sigma\sqrt{r}}\frac{\partial}{\partial r}\left(\Sigma\nu\sqrt{r}\right)} \tag{7.22}$$

Cette expression est très importante, il s'agit de la vitesse d'écoulement du gaz, à une distance héliocentrique r et un instant donné t. Le signe moins indique que la matière se déplace vers l'étoile centrale.

On applique à présent la conservation de la matière sous la forme de l'équation de continuité :

$$\mathrm{Div}(\delta m\,\vec{v}) = -\frac{\partial\,\delta m}{\partial t} \tag{7.23}$$

où δm est toujours la masse contenue entre les cercles de rayons r et $r+\delta r$:

$$\delta m = 2\pi r\,\delta r\Sigma \tag{7.24}$$

on a alors suivant la direction radiale :

$$\frac{\partial}{\partial r}(r\Sigma v_r) = -\frac{\partial}{\partial t}(r\Sigma) \tag{7.25}$$

soit encore :

$$\frac{\partial\Sigma}{\partial t} = \frac{1}{r}\frac{\partial}{\partial r}\left(r\Sigma\frac{3}{\Sigma\sqrt{r}}\frac{\partial}{\partial r}(\Sigma\nu\sqrt{r})\right) \tag{7.26}$$

finalement :

$$\boxed{\frac{\partial\Sigma}{\partial t} = \frac{3}{r}\frac{\partial}{\partial r}\left\{\sqrt{r}\frac{\partial}{\partial r}\{\Sigma\nu\sqrt{r}\}\right\}} \tag{7.27}$$

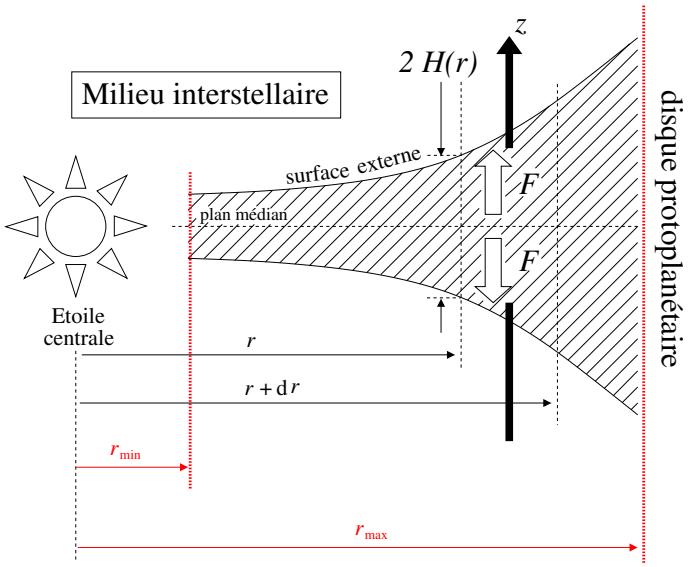

FIGURE 7.1 – Vue schématique d'une coupe verticale d'un disque protoplanétaire, la matière se distribue entre deux distances héliocentriques : $r_{\min}$ et $r_{\max}$, des valeurs typiques de $r_{\min}$ et $r_{\max}$ sont typiquement 0.1 AU et 50 AU.

On trouve bien l'équation d'évolution (6.4) présentée page 240 dans le chapitre précédent. Les effets de la dimension verticale, *i.e.* perpendiculairement au plan du disque, tout comme ceux des propriétés de la matière (composition chimique, opacité et équation d'état) sont globalement représentés par la viscosité turbulente ν. Des expressions plus sophistiquées existent, par exemple celle utilisée par ALIBERT et collab. [2005] :

$$\frac{\partial \Sigma}{\partial t} = \frac{3}{r}\frac{\partial}{\partial r}\left\{\sqrt{r}\,\frac{\partial}{\partial r}\left\{\Sigma \nu \sqrt{r}\right\} + \Lambda(r)\right\} + \dot{\Sigma}_w(r) + \dot{Q}_{\text{planet}}(r) \tag{7.28}$$

avec $\Lambda(r)$ un terme de transfert de moment cinétique entre les planètes et le disque, $\dot{\Sigma}_w(r)$ représente les pertes de matière dues à la photo-évaporation [VERAS et ARMITAGE, 2004], et $\dot{Q}_{\text{planet}}(r)$ est une second terme de perte de masse, causée cette fois par l'accrétion sur les planètes. Sauf mention contraire, dans la suite nous considérerons seulement l'équation la plus simple, à savoir (7.27) qui contient l'essentiel de la physique.

7.2.2 Conditions aux limites

Pour résoudre (7.27) on a naturellement besoin de deux conditions aux limites, on peut choisir :

- une condition limite interne, *i.e.* en $r = r_{\min}$ voir Fig. 7.1, qui traduit le fait que le couple de friction exercé par le gaz contenu dans le disque à $r < r_{\min}$ est nul, ceci pour la très bonne raison qu'il n'y a pas de matière en $r < r_{\min}$. Cette condition est nommé en anglais «zero torque condition», elle se traduit par :

$$\boxed{\left(r\,\frac{\partial(\Sigma\nu)}{\partial r}\right)_{r=r_{\min}} = 0} \tag{7.29}$$

cependant :

$$\begin{aligned} u &= \sqrt{r}\frac{\partial f}{\partial r} \\ &= \sqrt{r}\,\frac{\partial}{\partial r}\left(\Sigma\nu\sqrt{r}\right) \\ &= \sqrt{r}\left(\frac{\partial(\Sigma\nu)}{\partial r}\sqrt{r}+\Sigma\nu\,\frac{1}{2\sqrt{r}}\right) \\ &= \sqrt{r}\,\frac{\partial(\Sigma\nu)}{\partial r}+\frac{1}{2}\Sigma\nu \end{aligned}$$

à la limite interne $r = r_{\min}$ on a donc :

$$\boxed{u_{r=r_{\min}} = \frac{1}{2}(\Sigma\nu)_{r=r_{\min}}} \tag{7.30}$$

- une condition limite externe, *i.e.* en $r = r_{\max}$ voir Fig. 7.1, pour laquelle la vitesse d'accrétion est nulle, ce qui revient à considérer que le disque n'est pas alimenter en matière par l'«extérieur», *i.e.* par le interstellaire qui lui a donné naissance ; cette condition s'écrit simplement :

$$\boxed{\left(\frac{\partial}{\partial r}\left[\Sigma\nu\sqrt{r}\right]\right)_{r=r_{\max}} = 0} \tag{7.31}$$

D'autres choix sont bien sûr possibles, mais correspondent à un disque qu'on alimente en matière avec un flux choisi de façon arbitraire. Dans ce texte, on se restreint aux disques isolés de l'extérieur en termes d'apport de matière. Avec notre changement de fonction inconnue, l'équation (7.31) devient :

$$\boxed{u_{r=r_{\max}} = 0} \tag{7.32}$$

7.3 Discrétisation de l'équation d'évolution

7.3.1 Construction du système à résoudre

Comme on vient de la voir, l'équation à résoudre est (7.27) :

$$\frac{\partial\Sigma}{\partial t} = \frac{3}{r}\frac{\partial}{\partial r}\left\{\sqrt{r}\,\frac{\partial}{\partial r}\left\{\Sigma\nu\sqrt{r}\right\}\right\} \tag{7.33}$$

face à ce type d'équation, le premier réflexe est peut être de développer le membre de droite, ce qui donne :

$$\frac{\partial\Sigma}{\partial t} = 3\nu\frac{\partial^2\Sigma}{\partial r^2}+3\left(2\frac{\partial\nu}{\partial r}+\frac{3}{2}\frac{\nu}{r}\right)\frac{\partial\Sigma}{\partial r}+3\left(\frac{\partial^2\nu}{\partial r^2}+\frac{3}{2r}\frac{\partial\nu}{\partial r}\right)\Sigma \tag{7.34}$$

Cette équation fait malheureusement apparaître des dérivées premières, et seconde de la viscosité ν. Cette dernière, sera calculée indépendamment, puis tabulée. L'utilisation des valeurs de ν, lors de la résolution de (7.33), se fera alors par interpolation de tables, ce qui peut poser des problèmes dans le calcul des dérivées de ν, en particulier dans celui des dérivées secondes. Afin de contourner ce problème, j'ai introduit un double changement de fonction inconnue, en posant :

$$f = \Sigma\nu\sqrt{r} \tag{7.35}$$

puis :

$$u = \sqrt{r}\frac{\partial}{\partial r}f \tag{7.36}$$

l'équation à résoudre devient alors :

$$\frac{\partial\Sigma}{\partial t} = \frac{3}{r}\frac{\partial u}{\partial r} \tag{7.37}$$

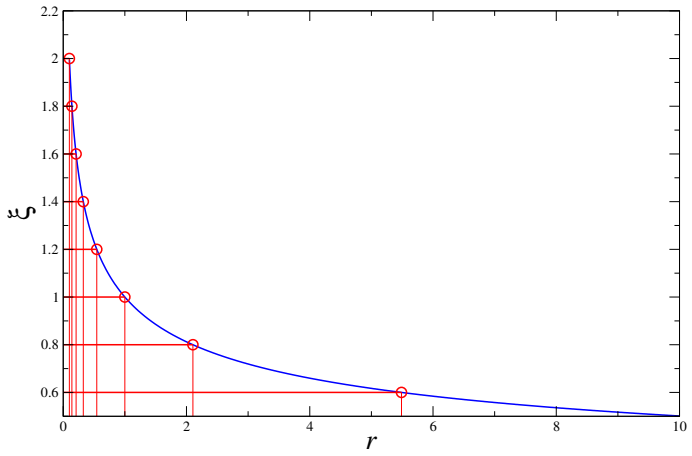

FIGURE 7.2 – Illustration de la répartition des points auxquels on applique l'équation (7.33), une fois cette dernière discrétisée. Sur cette exemple $p = 0.3$, on constate bien qu'ayant un pas constant en ξ (0.2 sur cet exemple) on obtient une distribution non-uniforme des valeurs de r correspondantes, avec une «concentration» aux petites valeurs de r.

et ne présente plus aucune dérivée de ν.

Avec les différences finies, on peut les dérivées premières qui interviennent dans notre problème de la façon suivante :

$$\left.\frac{\partial g}{\partial r}\right|_i \simeq \left.\frac{\partial \xi}{\partial r}\right|_i \frac{g_{i+1} - g_{i-1}}{2\Delta\xi} \tag{7.38}$$

avec g une des fonctions qui nous intéresse, *i.e.* f ou u. On a de plus réalisé un changement de variable en introduisant ξ qui permet d'avoir une distribution non-uniforme en r, ceci à partir d'une distribution uniforme en ξ. Dans notre cas, la densité surfacique de masse Σ montre des variations très fortes dans les régions proches de l'étoile centrale, alors qu'elles sont beaucoup plus modestes lorsqu'on s'éloigne. On peut donc choisir une fonction du type :

$$\xi = r^{-p} \tag{7.39}$$

En choisissant, par exemple, $p = 1/3$ on placera alors beaucoup de points proche de l'étoile, et moins aux grandes distances stellocentriques. Ce changement de variable permet de concentrer les efforts de calculs aux endroits où il y en a le plus besoin, il est également suggéré par les variations de Σ dans la distribution initiale de masse, classiquement adoptée à partir des résultats de HAYASHI [1981] pour lesquels on a $\Sigma \propto r^{-3/2}$ (voir Fig. 7.2).

Le domaine d'intégration spatiale (représenté par la variable r ou son équivalent ξ) est divisé en (N − 1) intervalles délimités par N «interfaces», la largeur de chacun de ces intervalles est Δξ qui est une constante choisie suffisamment petite pour assurer la précision et la stabilité du calcul. De façon analogue, les différents instants, *i.e.* les différents âges du disque, sont espacés d'une durée Δt, qui peut éventuellement varier au cours du calcul : en cas de non-convergence lors de l'intégration spatial, Δt peut être diminuée, dans le cas contraire on peut l'augmenter afin de gagner du temps de calcul. L'indice représentant le temps est nommé k, celui lié à l'espace est i, notre approche est résumée sur la Fig. 7.3.

On applique maintenant la formule des différences finies à l'équation à résoudre, *i.e.* (7.33), ce qui conduit à :

$$\frac{\Sigma_i^{(k+1)} - \Sigma_i^{(k)}}{\Delta t} = (1-\theta)\,\frac{3}{r_i}\left.\frac{\partial \xi}{\partial r}\right|_i \frac{u_{i+1}^{(k)} - u_{i-1}^{(k)}}{2\Delta\xi} + \theta\,\frac{3}{r_i}\left.\frac{\partial \xi}{\partial r}\right|_i \frac{u_{i+1}^{(k+1)} - u_{i-1}^{(k+1)}}{2\Delta\xi} \tag{7.40}$$

avec θ un paramètre numérique, de valeur comprise entre 0 et 1, qu'on peut appeler «paramètre d'implicité». En effet, pour θ = 0 le schéma (7.40) est totalement explicite puisque toutes les valeurs

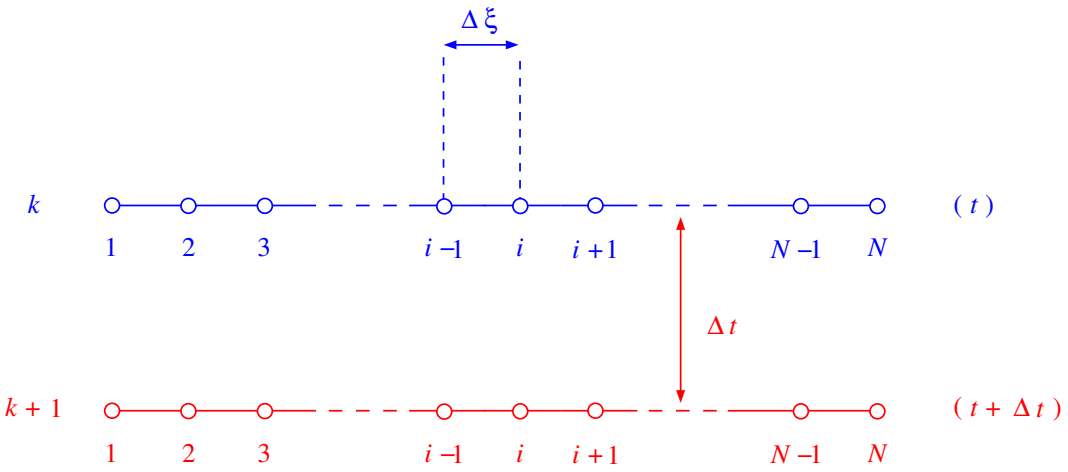

FIGURE 7.3 – Schématisation de la discrétisation adaptée pour notre modèle de disque proto-planétaire, l'indice i représente l'espace (variable r ou ξ)), alors que l'indice k représente le temps (t). Les inconnues de notre système sont les valeurs de la densité surface de masse Σ au temps $t+\Delta t$, soit avec notre notation : les $\Sigma_i^{(k+1)}$ avec $i = 1,\ldots,\mathrm{N}$ où N est le nombre de points considérés. Au temps t, toutes les valeurs de Σ sont supposées connues, *i.e.* il s'agit des $\Sigma_i^{(k)}$ avec $i = 1,\ldots,\mathrm{N}$.

de $\Sigma_i^{(k+1)}$ (*i.e.* au temps $t+\Delta t$) se déduisent explicitement des celles au temps t : les $\Sigma_i^{(k)}$. A contrario, lorsque $\theta = 1$, les valeurs des $\Sigma_i^{(k+1)}$ sont définies implicitement et s'obtiennent en résolvant le jeu d'équations. Mes expériences numériques ont montré qu'un schéma explicite, ou même semi-implicite (*i.e.* avec $\theta = 1/2$) conduisaient immanquablement à des instabilités numériques qui ne permettaient pas d'intégrer le système. J'ai donc retenu un schéma purement implicite ($\theta = 1$) :

$$\frac{\Sigma_i^{(k+1)} - \Sigma_i^{(k)}}{\Delta t} = \frac{3}{r_i} \left.\frac{\partial \xi}{\partial r}\right|_i \frac{u_{i+1}^{(k+1)} - u_{i-1}^{(k+1)}}{2\Delta\xi} \tag{7.41}$$

Si on se reporte à la Fig. 7.3, on voit que (7.41) est centrée sur les points repérés par les cercles, ceci quelque soit l'instant t. On constate également que cette équation (7.41) ne peut s'appliquer qu'en $\mathrm{N}-2$ points, *i.e.* pour $i = 2,\ldots,\mathrm{N}-1$.

A ce stade, le nombre d'équations est $\mathrm{N}-2$, alors que le nombre d'inconnues est N : ce sont les $\Sigma_i^{(k+1)}$ pour $i = 1,\ldots,\mathrm{N}$. Il nous faut donc prendre en compte 2 équations supplémentaires qui vont être fournies par les conditions aux limites introduites dans le paragraphe 7.2.2.

Pour mémoire, la condition limite interne s'écrit :

$$u_{r=r_{\min}} = \frac{1}{2}(\Sigma\nu)_{r=r_{\min}} \tag{7.42}$$

ce qui avec notre notation se traduit par :

$$u_1^{(k+1)} = \frac{1}{2}(\Sigma\nu)_1^{(k+1)} \tag{7.43}$$

qui sera utilisée dans le schéma implicite, centré en $1+\frac{1}{2}$ cette fois-ci :

$$\frac{\Sigma_1^{(k+1)} - \Sigma_1^{(k)}}{\Delta t} = \frac{3}{r_1} \left.\frac{\partial \xi}{\partial r}\right|_1 \frac{u_2^{(k+1)} - u_1^{(k+1)}}{\Delta\xi} \tag{7.44}$$

On rappelle maintenant la condition limite externe (7.32)

$$u_{r=r_{\max}} = 0 \tag{7.45}$$

qui se traduit, avec la notation en cours, par :

$$u_{\mathrm{N}}^{(k+1)} = 0 \tag{7.46}$$

ce qui donne, en utilisant un schéma centré en $\mathrm{N}-\frac{1}{2}$:

$$\frac{\Sigma_{\mathrm{N}}^{(k+1)} - \Sigma_{\mathrm{N}}^{(k)}}{\Delta t} = \frac{3}{r_{\mathrm{N}}} \left.\frac{\partial \xi}{\partial r}\right|_{\mathrm{N}} \frac{u_{\mathrm{N}}^{(k+1)} - u_{\mathrm{N-1}}^{(k+1)}}{\Delta \xi} \tag{7.47}$$

$$= -\frac{3}{r_{\mathrm{N}}} \left.\frac{\partial \xi}{\partial r}\right|_{\mathrm{N}} \frac{u_{\mathrm{N-1}}^{(k+1)}}{\Delta \xi} \tag{7.48}$$

7.3.2 Résumé

Le système à résoudre est :

- Pour $i = 1$ on a la condition limite interne :

$$\mathrm{F}_1 = \frac{\Sigma_1^{(k+1)} - \Sigma_1^{(k)}}{\Delta t} - \frac{3}{r_1} \left.\frac{\partial \xi}{\partial r}\right|_1 \frac{1}{\Delta \xi} (u_2^{(k+1)} - \frac{1}{2} (\Sigma \nu)_1^{(k+1)}) \tag{7.49}$$

- Pour $i = 2, \ldots, \mathrm{N}-1$:

$$\mathrm{F}_i = \frac{\Sigma_i^{(k+1)} - \Sigma_i^{(k)}}{\Delta t} - \frac{3}{r_i} \left.\frac{\partial \xi}{\partial r}\right|_i \frac{u_{i+1}^{(k+1)} - u_{i-1}^{(k+1)}}{2\Delta \xi} \tag{7.50}$$

- Pour $i = \mathrm{N}$ on a la condition limite externe :

$$\mathrm{F}_{\mathrm{N}} = \frac{\Sigma_{\mathrm{N}}^{(k+1)} - \Sigma_{\mathrm{N}}^{(k)}}{\Delta t} + \frac{3}{r_{\mathrm{N}}} \left.\frac{\partial \xi}{\partial r}\right|_{\mathrm{N}} \frac{u_{\mathrm{N-1}}^{(k+1)}}{\Delta \xi} \tag{7.51}$$

Le système (7.3.2), (7.50) et (7.51) comporte N équations : $\mathrm{F}_i = 0$ pour $i = 1, \ldots, \mathrm{N}$, ainsi que N inconnues : les $\Sigma_i^{(k+1)}$ pour $i = 1, \ldots, \mathrm{N}$, il est donc soluble.

7.3.3 Méthode de résolution numérique

Comme on le sait, le système (7.3.2), (7.50) et (7.51) est non-linéaire : la viscosité turbulente ν dépend de la solution Σ. La méthode classique pour résoudre un tel système est l'algorithme de Newton-Raphson [Press et collab., 1992; Wikipedia, 2018], on linéarise en fait le système d'origine en écrivant :

$$\mathrm{J_F}\left(\Sigma_{i,m}^{(k+1)}\right)\left(\Sigma_{i,m+1}^{(k+1)} - \Sigma_{i,m}^{(k+1)}\right) = -\mathrm{F}\left(\Sigma_{i,m}^{(k+1)}\right) \tag{7.52}$$

avec $[\mathrm{J_F}]$ la matrice jacobienne associée aux équations F_i, un élément de ce jacobien s'écrit :

$$\mathrm{J_{F},}i,j,m = \frac{\partial \mathrm{F}_{i,m}}{\partial \Sigma_{j,m}^{(k+1)}} \tag{7.53}$$

avec dans (7.52) comme dans (7.53), l'indice m repérant l'itération de l'algorithme de Newton-Raphson.

A partir d'une solution initiale $\Sigma_{i,1}^{(k+1)}$, le système linéaire (7.52) est résolu par une méthode d'algèbre linéaire (voir plus avant), ce qui permet d'avoir les corrections $\Sigma_{i,2}^{(k+1)} - \Sigma_{i,1}^{(k+1)}$, et ainsi d'obtenir une deuxième estimation de la solution composée des $\Sigma_{i,2}^{(k+1)}$. Cette dernière est utilisée pour construire un nouveau système (7.52), sa résolution conduisant à une nouvelle solution $\Sigma_{i,3}^{(k+1)}$. Les itérations sont ainsi poursuivi jusqu'à obtention de solutions, qui ont des différences relatives maximales en dessous d'une valeur déterminée à l'avance (usuellement 10^{-4}) et qui constitue le critère de convergence de l'algorithme.

Une propriété intéressante du jacobien $[J_F]$ est d'être une matrice bande, avec 2 «sous-diagonales» et 2 «sur-diagonale», ce genre de matrice se prête facilement aux méthodes de résolution de l'algèbre linéaire. Le système (7.52) est résolu grâce à la sous-routine «DGBSV_F95» disponible dans la bibliothèque LAPACK[2] [ANDERSON et collab., 1999].

Comme on le voit, la construction du jacobien $[J_F]$ requière la connaissance des dérivées des $u_i^{(k+1)}$. Si on allège l'écriture en omettant les exposants $(k+1)$, on a alors :

$$u_i = \sqrt{r_i}\left.\frac{\partial\xi}{\partial r}\right|_i \frac{f_{i+1}-f_{i-1}}{2\Delta\xi} \tag{7.54}$$

$$= \sqrt{r_i}\left.\frac{\partial\xi}{\partial r}\right|_i \frac{\Sigma_{i+1}\nu_{i+1}\sqrt{r_{i+1}}-\Sigma_{i-1}\nu_{i-1}\sqrt{r_{i-1}}}{2\Delta\xi} \tag{7.55}$$

on aura donc besoin des dérivées $\partial\nu/\partial\Sigma$, leur fourniture est donc dans le cahier des charges du sous-programme délivrant la viscosité turbulente ν.

7.4 Références

ALIBERT, Y., C. MORDASINI, W. BENZ et C. WINISDOERFFER. 2005, «Models of giant planet formation with migration and disc evolution», *A&A*, vol. 434, doi: 10.1051/0004-6361:20042032, p. 343–353. 252

ANDERSON, E., Z. BAI, C. BISCHOF, S. BLACKFORD, J. DEMMEL, J. DONGARRA, J. DU CROZ, A. GREENBAUM, S. HAMMARLING, A. MCKENNEY et D. SORENSEN. 1999, *LAPACK Users' Guide*, 3e éd., Society for Industrial and Applied Mathematics, Philadelphia, PA, ISBN 0-89871-447-8 (paperback). 257

HAYASHI, C. 1981, «Structure of the Solar Nebula, Growth and Decay of Magnetic Fields and Effects of Magnetic and Turbulent Viscosities on the Nebula», *Progress of Theoretical Physics Supplement*, vol. 70, doi: 10.1143/PTPS.70.35, p. 35–53. 254

LYNDEN-BELL, D. et J. E. PRINGLE. 1974, «The evolution of viscous discs and the origin of the nebular variables.», *MNRAS*, vol. 168, p. 603–637. 249

PRESS, W., S. TEUKOLSKY, W. VETTERLING et B. FLANNERY. 1992, *Numerical Recipes in Fortran 77*, Cambridge University Press. 256

VERAS, D. et P. J. ARMITAGE. 2004, «Outward migration of extrasolar planets to large orbital radii», *MNRAS*, vol. 347, doi: 10.1111/j.1365-2966.2004.07239.x, p. 613–624. 252

WIKIPEDIA, T. F. E. 2018, «Newton's method», https://en.wikipedia.org/wiki/Newton23-April-2018]. 256

2. Linear Algebra PACKage : http://www.netlib.org/lapack/

Retour à la table des matières : p. v

Chapitre 8

Intégration verticale

Sommaire

8.1 Le système d'équations et son intégration 259
8.2 Interpolation des valeurs de < ν > 261
8.3 Validation du programme 262
8.4 Résultats 263
8.5 Références 268

8.1 Le système d'équations et son intégration

le système d'équations gouvernant la structure verticale du disque en une valeur de r donnée est [FRANK et collab., 1992; HURÉ, 2000; PAPALOIZOU et TERQUEM, 1999] :

- l'équilibre hydrostatique, qui est l'effet de la composante verticale de la force d'attraction gravitationnelle vers l'étoile :

$$\frac{1}{\rho}\frac{\partial P}{\partial z} = -\Omega^2 z \tag{8.1}$$

  avec ρ la masse volumique, z l'altitude au-dessus (en dessous pour les valeurs négatives) du plan médian et P la pressions. On remarquera que comme Ω^2 varie en r^{-3}, le gradient vertical de pression diminue lorsque r augmente.

- la dissipation de l'énergie mécanique en chaleur :

$$\frac{\partial F}{\partial z} = \frac{9}{4}\rho\nu\Omega^2 \tag{8.2}$$

  avec F le flux vertical d'énergie et ν la viscosité turbulente.

- le transport d'énergie, issue sous forme radiative :

$$\frac{\partial T}{\partial z} = -\frac{3\kappa\rho}{16\sigma T^3}F \tag{8.3}$$

  On peut remarquer qu'une possible amélioration de cette formulation pourrait être la prise en compte de la convection, cela avec une approche de type Mixing Length Theory.

à ces équations s'ajoute les conditions limites à la surface externe du disque, *i.e.* à sa jonction avec le milieu interstellaire, pour le flux d'énergie on a [PAPALOIZOU et TERQUEM, 1999] :

$$F_s = \frac{3}{8\pi}\dot{M}_{st}\Omega^2 \tag{8.4}$$

avec le taux d'accrétion vers l'étoile $\dot{M}_{st}$ qui est un paramètre libre, on a : $\dot{M}_{st}3\pi < \nu > \Sigma$ où $\Sigma = \int_{-H}^{+H}\rho dz$, H représentant la demi-épaisseur du disque à un endroit donné. On définit alors le viscosité turbulente moyenne, qui sera ensuite utilisée lors de l'intégration de l'équation d'évolution

$< \nu >= \int_{-H}^{+H} \rho \nu dz/\Sigma$. La pression à la surface est fournie par :

$$P_s = \frac{\Omega^2 H \tau_{ab}}{\kappa_s} \tag{8.5}$$

où τ_{ab} est l'épaisseur optique de l'«atmosphère» du disque.

Finalement, pour une valeur du paramètre α fixée, la température à la surface est obtenue en résolvant l'équation :

$$2\sigma(T_s^4 - T_{birr}^4) - \frac{9\alpha k_B T_s}{8\mu m_H \kappa_s} - \frac{3}{8\pi}\dot{M}_{st}\Omega^2 = 0 \tag{8.6}$$

où $T_{birr}^4 = T_b^4 + T_{irr}^4$, T_b est la température du milieu interstellaire, T_{irr}^4 est obtenue grâce à l'équation (6.17) déjà mentionnée page 245. Outre la masse de l'étoile présente dans l'expression de Ω, T_{irr} permet de faire le lien entre l'étoile et le disque, cette fois via un processus d'irradiation. L'étoile évoluant au cours du temps, T_{irr} est une fonction du temps.

Encore une fois très peu de détails sont présentés dans la littérature concernant les méthodes numériques utilisées pour intégrer le système (8.1), (8.2) et (8.3). Certains auteurs indiquent utiliser une méthode de relaxation [D'ALESSIO et collab., 1998; HAMEURY et collab., 1998; MILSOM et collab., 1994], *i.e.* une méthode de la famille de ce que j'ai mis au point pour l'intégration de l'évolution temporelle.

D'autres travaux mentionnent une méthode de tir [LIN et PAPALOIZOU, 1980; MEYER et MEYER-HOFMEISTER, 1982; MINESHIGE et OSAKI, 1983; PAPALOIZOU et TERQUEM, 1999; RÓŻAŃSKA et collab., 1999], c'est ce genre de méthode que j'ai adopté en utilisant un algorithme de Runge-Kutta d'ordre 5 [PRESS et collab., 1992] pour intégrer le système depuis la surface externe jusqu'au plan médian.

A la suite de HURÉ [2000], j'ai adopté le changement de fonctions suivant :

$$u = \ln \rho \tag{8.7}$$

$$v = \frac{F}{\sigma T_s^4} \tag{8.8}$$

$$w = \ln T \tag{8.9}$$

qui présente plusieurs avantages :

- ce choix réduit la raideur du système à intégrer.
- il interdit également, par construction, les valeurs négatives pour ρ et T, ce qui évite l'exploration de ces domaines négatifs lors de l'exécution de l'algorithme d'intégration.

Le système d'équations à intégrer est donc effectivement :

$$\frac{\partial u}{\partial z} = -\frac{\mu m_H \Omega^2}{k_B} z \exp(-w) + \frac{3\kappa T_s^4}{16} v \exp(u - 4w) \tag{8.10}$$

$$\frac{\partial v}{\partial z} = \frac{9\alpha\Omega k_B}{4\sigma T_s^4 \mu m_H} \exp(u + w) \tag{8.11}$$

$$\frac{\partial w}{\partial z} = -\frac{3\kappa T_s^4}{16} v \exp(u - 4w) \tag{8.12}$$

Pour un jeu donné de paramètres, à savoir (α, $\dot{M}_{st}$, r), on intègre le système en utilisant comme valeurs de départ P_s, F_s et T_s, cependant la demi-épaisseur H du disque, à la distance héliocentrique r, est inconnue. On cherche donc à obtenir sur la plan médian un flux d'énergie nulle (condition dictée par la symétrie) :

$$F_{r=0} = 0 \tag{8.13}$$

pour se faire on résout cette équation $F_{r=0}(H) = 0$ par une méthode de dichotomie [NOUGIER, 1987], spécialement aménagée afin de contourner la difficulté créée par les valeurs négatives de $F_{r=0}$ qui apparaissent lors des itérations. Concernant le pas d'intégration, une gestion semi-automatique a été mise en place. Cependant, la valeur de départ peut être prise aux alentours de H/10000.

Finalement, on obtient des tables qui donnent la viscosité turbulente $< \nu >$ en fonction de r, et des paramètres α et $\dot{M}_{st}$; ces tables forment une relation du type :

$$< \nu >=< \nu > (r, \dot{M}_{st}, \alpha) \tag{8.14}$$

Cette relation dépend également d'autres paramètres, comme la masse de l'étoile et sa luminosité si on considère le disque comme étant irradié. Le problème suivant consiste en l'interpolation des valeurs de $< \nu >$ afin qu'elles soient utilisables lors de la résolution de l'équation d'évolution.

8.2 Interpolation des valeurs de $< \nu >$

Le but de ce paragraphe est de montrer comment passer d'une loi :

$$< \nu >=< \nu >_{(r,\dot{M}_{st},\alpha)} \tag{8.15}$$

à une loi :

$$< \nu >=< \nu >_{(r,\Sigma,\alpha)} \tag{8.16}$$

sachant que l'algorithme d'intégration de l'équation d'évolution a besoin de $< \nu >=< \nu > (r, \Sigma)$ (α est une constante du calcul), et qu'en un point donné r du disque, la valeur de $\dot{M}_{st}$ est inconnue.

L'interpolation est effectuée selon les étapes suivantes :

1. On cherche la valeur de $\dot{M}_{st}$, qu'on notera $\dot{M}_{st,0}$, correspondant à la valeur de densité Σ_0 donnée en entrée ; pour cela on procède de la façon suivante :
   (a) à valeur de r fixée (et implicitement α fixée), on construit une table $\Sigma = \Sigma(\dot{M}_{st})$.
   (b) de cette relation on tire $\dot{M}_{st,0}$, correspondant à la valeur de densité surfacique Σ_0 donnée en entrée.
2. ensuite la valeur de $\dot{M}_{st,0}$ trouvée permet de faire les interpolations successives :
   (a) pour chaque valeur de $\dot{M}_{st}$, on interpole en r afin d'obtenir $< \nu >$ pour r (interpolation à l'aide de splines).
   (b) la table des $< \nu >$ en fonction des $\dot{M}_{st}$ permet finalement d'obtenir $< \nu >$ pour les valeurs de r et Σ données en entrée.

Lors de ce processus d'interpolation, on en profite également pour calculer diverses autres quantités comme la pression, la température et la masse volumique de la matière sur le plan médian, et à la surface externe.

8.3 Validation du programme

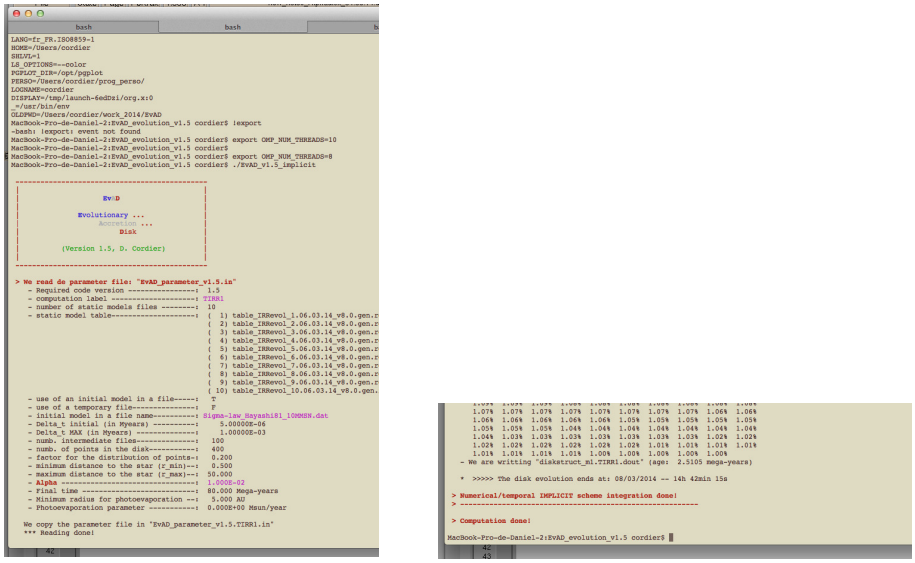

FIGURE 8.1 – Pour le plaisir : une copie d'écran des sorties d'EvAD lors du calcul de la première «co-évolution» disque-étoile de Pré-Main Sequence. Ici $\alpha = 10^{-2}$ et le temps de vie du disque obtenu est 2.51 mega-years.

Le modèle de structure verticale, précédemment décrit, a été comparé avec les résultats de PAPALOIZOU et TERQUEM [1999], ceci en lisant des valeurs sur les Fig. 2 ($\alpha = 10^{-2}$) et Fig. 3 ($\alpha = 10^{-3}$), ces comparaisons ont été reportées sur les Fig. 8.2 et Fig. 8.3. Comme on peut le voir l'accord est très bon. Ces comparaisons portent sur H la demi-épaisseur du disque, Σ la densité surfacique de masse, ainsi que sur T_m la température sur le plan médian.

D'autres comparaisons ont également été faites, en utilisant cette fois la Fig. 1 de PAPALOIZOU et TERQUEM [1999]. Ces comparaisons peuvent être trouvées sur la Fig. 8.4, encore une fois on peut constater que l'accord entre les deux implémentations de modèles de disque α.

Pour ce qui de la validation du modèle complet, i.e. comprenant l'évolution temporelle du disque, je n'ai pas trouvé dans la littérature de loi $\Sigma(r, t)$ grâce auxquelles j'aurais pu faire de comparaisons directes, comme celles qu'on vient de mentionner. Cependant les résultats obtenus, en particulier les temps de dissipation du disque semblent tout à fait compatibles avec les données observationnelles et ce qui peut être lu dans la littérature. En effet, les viscosités turbulentes obtenues sont de l'ordre de $< \nu > \sim 10^{11}$ m^2 s^{-1} (valeur typique), ce qui conduit à des échelles de temps de dissipation visqueuse :

$$\tau_{vis} \sim \frac{r^2}{< \nu >} \tag{8.17}$$

de l'ordre du million d'années, pour des distances de l'ordre de quelques unités astronomiques. Un exemple de simulation est donné sur la Fig. 8.5, le critère d'arrêt du calcul est une masse finale valant 1% de la masse initiale. Ce «1%» n'est pas totalement arbitraire car il correspond grossièrement à la matière, potentiellement solide, présente dans le disque, et de ce fait ayant éventuellement échappé à l'entraînement vers l'étoile centrale.

Finalement, j'ajouterais que le code a été complètement écrit en FORTRAN 2008 et parallélisé grâce à la bibliothèque OPENMP [1], et il se compile très facile avec `gfortran`. Ces spécificités lui

1. Open Multi-Processing, http://www.openmp.org/.

confère une grande portabilité, de ce fait j'ai pu l'exécuter sur un *Raspberry Pi 2*, sur un *MacBook Pro*, sur le cluster de l'Institut UTINAM de Besançon, sur un PC/Dell sous Debian, ainsi que sur le supercalculateur rémois `ROMEO`.

8.4 Résultats

Le code d'évolution de disque protoplanétaire est au cœur de l'article CORDIER et collab. [2016] (voir page 274) sur le transport de poussières par photophorèse, depuis les régions proches du proto-Soleil, vers les zones de formation des comètes.

Ce travail couple des résultats de physique stellaire, en l'occurrence des trajets évolutifs produits par une équipe italienne, avec le modèle *EvAD*. Nous avons mis en évidence l'effet de irradiation du disque qui ne rend plus obligatoire la prise en compte de la photoévaporation pour obtenir un temps de dissipation réaliste. CORDIER et collab. [2016] montrent aussi le rôle crucial de la conductivité thermique des poussières.

De nombreux développements sont possibles sur ces questions de transport photophorétique, en particulier une prise en compte plus cohérente de l'opacité du plasma de la nébuleuse.

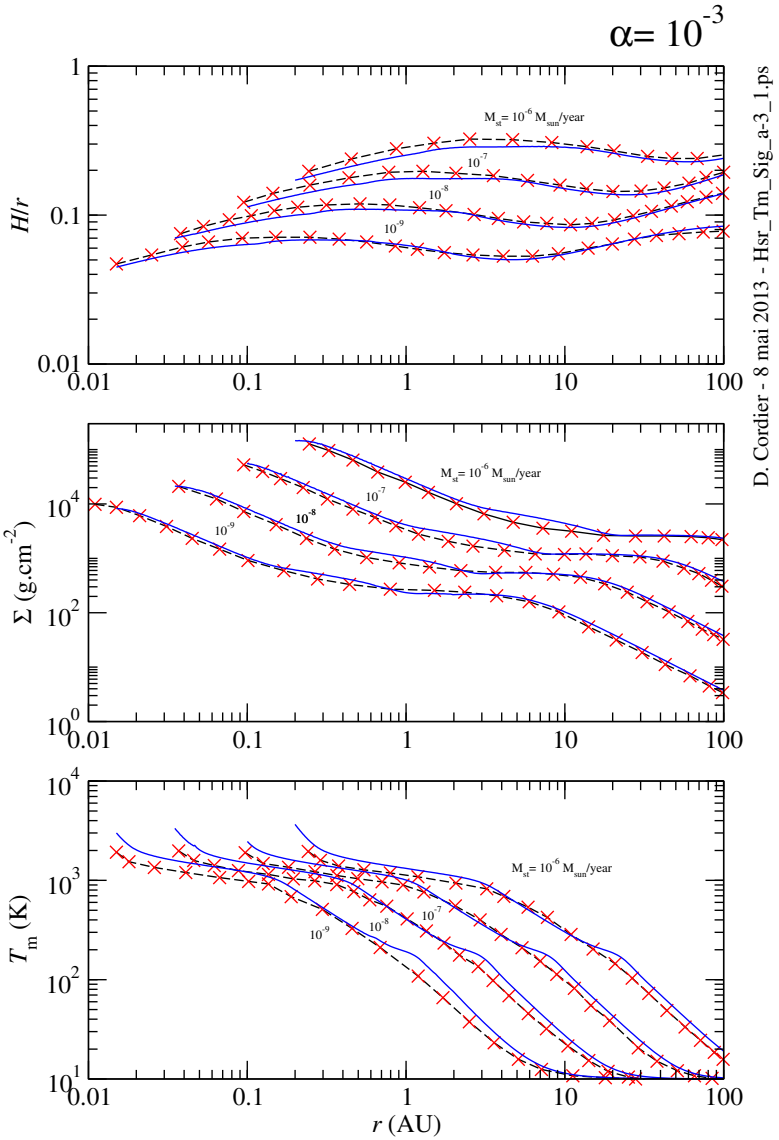

FIGURE 8.2 – Comparaison de l'intégration des équations de la structure verticale, faite suivant la méthode décrite dans le présent document, avec les résultats publiés par PAPALOIZOU et TERQUEM [1999], ici pour $\alpha = 10^{-3}$. Mon calcul est représenté par la courbe bleue, alors que les données de PAPALOIZOU et TERQUEM [1999] sont symbolisées par les croix rouges. Les grandeurs comparées sont la demi-épaisseur du disque H, la densité surfacique Σ ainsi que le température sur le plan médian T_m, ceci en fonction de la distance à l'étoile r.

Retour à la table des matières : p. v

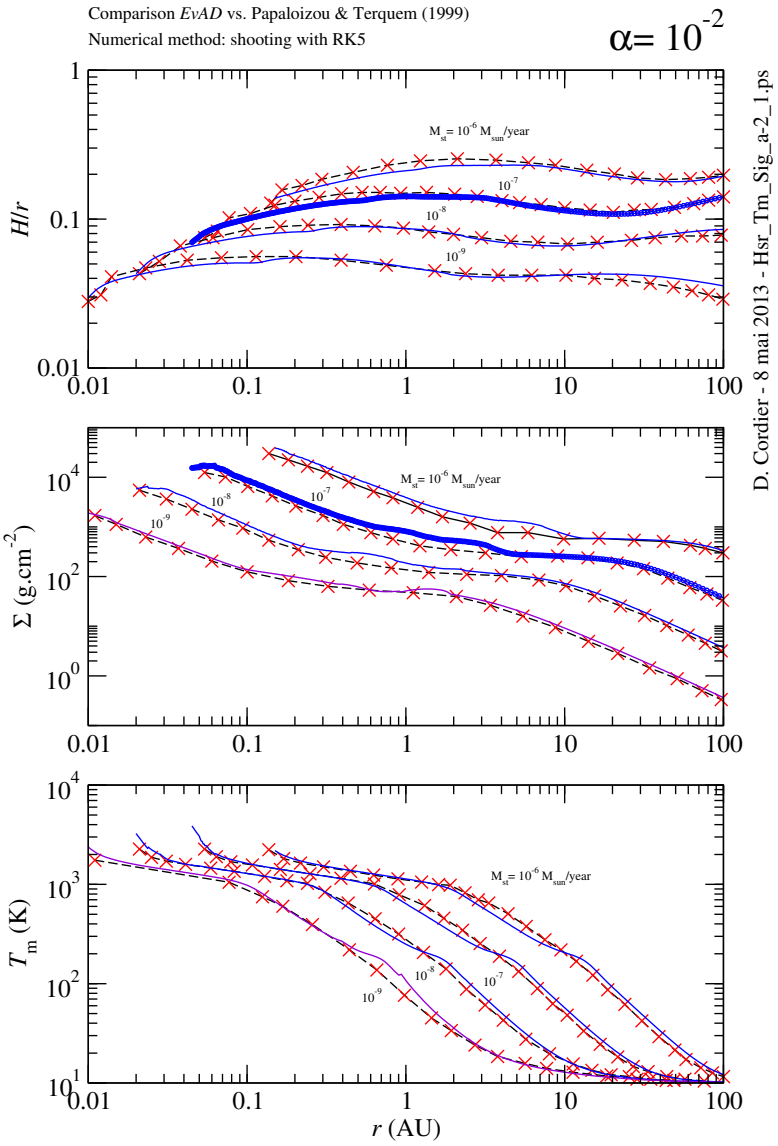

FIGURE 8.3 – Comparaison de l'intégration des équations de la structure verticale, faite suivant la méthode décrite dans le présent document, avec les résultats publiés par PAPALOIZOU et TERQUEM [1999], ici pour $\alpha = 10^{-2}$. Mon calcul est représenté par la courbe bleue, alors que les données de PAPALOIZOU et TERQUEM [1999] sont symbolisées par les croix rouges. Les grandeurs comparées sont la demi-épaisseur du disque H, la densité surfacique Σ ainsi que le température sur le plan médian T_m, ceci en fonction de la distance à l'étoile r.

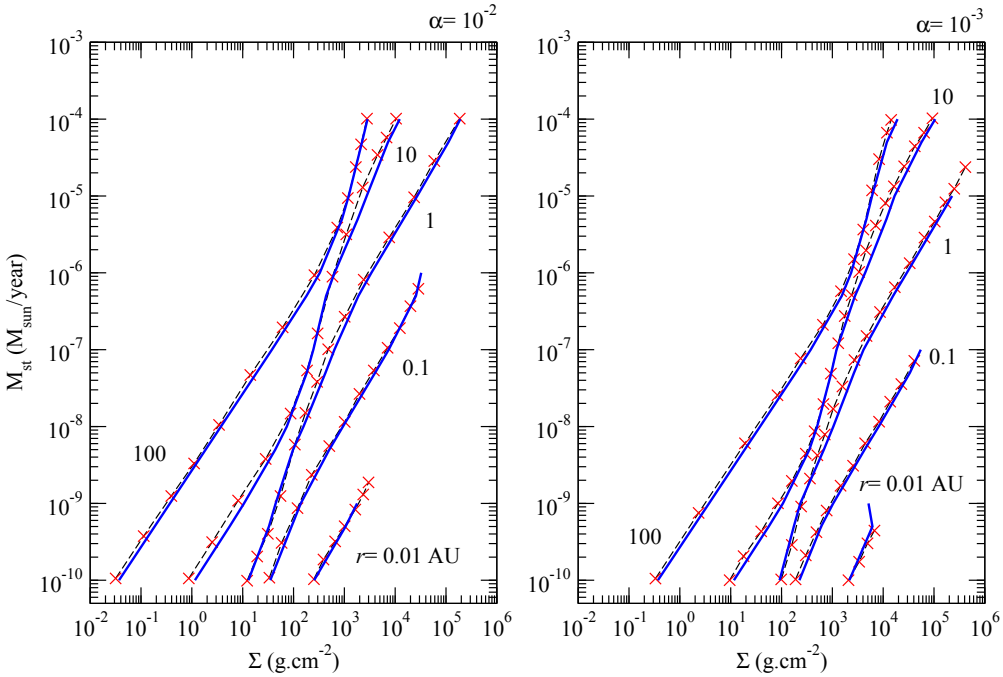

FIGURE 8.4 – Comparaison des données de la Fig. .1 de PAPALOIZOU et TERQUEM [1999] avec mes calculs. $\dot{M}_{st}$ en fonction de Σ pour plusieurs distances r. Mon calcul est représenté par la courbe bleue, alors que les données de PAPALOIZOU et TERQUEM [1999] sont symbolisées par les croix rouges.

Retour à la table des matières : p. v

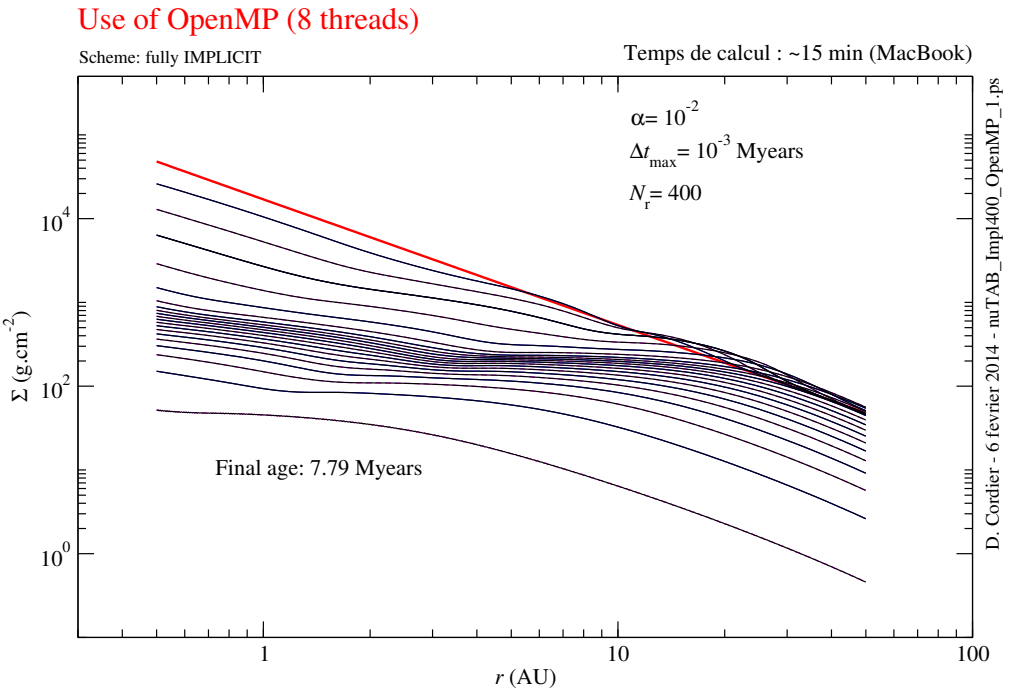

FIGURE 8.5 – Un exemple d'évolution temporelle d'un disque pour lequel $\alpha = 10^{-2}$. La matière est initialement répartie entre 0.2 et 50 AU, ceci suivant la loi de HAYASHI [1981] (représentée par la droite rouge). La pas de temps maximal est $\Delta t = 10^{-3}$ million d'années et le nombre de points «spatiaux» est ici de 400. L'évolution commence par la loi en rouge (distribution initiale de matière, puis au fur et à mesure que la matière est accrétée sur l'étoile,

Retour à la table des matières : p. v

8.5 Références

CORDIER, D., P. G. PRADA MORONI et E. TOGNELLI. 2016, «Dust photophoretic transport around a T Tauri star : Implications for comets composition», *Icarus*, vol. 268, doi: 10.1016/j.icarus.2015.11.037, p. 281–294. 263

D'ALESSIO, P., J. CANTÖ, N. CALVET et S. LIZANO. 1998, «Accretion Disks around Young Objects. I. The Detailed Vertical Structure», *ApJ*, vol. 500, doi: 10.1086/305702, p. 411–427. 260

FRANK, J., A. KING et D. RAINE. 1992, *Accretion power in astrophysics*, Cambridge Uni. Press., San Diego. 259

HAMEURY, J.-M., K. MENOU, G. DUBUS, J.-P. LASOTA et J.-M. HURE. 1998, «Accretion disc outbursts : a new version of an old model», *MNRAS*, vol. 298, doi: 10.1046/j.1365-8711.1998.01773.x, p. 1048–1060. 260

HAYASHI, C. 1981, «Structure of the Solar Nebula, Growth and Decay of Magnetic Fields and Effects of Magnetic and Turbulent Viscosities on the Nebula», *Progress of Theoretical Physics Supplement*, vol. 70, doi: 10.1143/PTPS.70.35, p. 35–53. 267

HURÉ, J.-M. 2000, «On the transition to self-gravity in low mass AGN and YSO accretion discs», *A&A*, vol. 358, p. 378–394. 259, 260

LIN, D. N. C. et J. PAPALOIZOU. 1980, «On the structure and evolution of the primordial solar nebula», vol. 191, p. 37–48. 260

MEYER, F. et E. MEYER-HOFMEISTER. 1982, «Vertical structure of accretion disks», *A&A*, vol. 106, p. 34–42. 260

MILSOM, J. A., X. CHEN et R. E. TAAM. 1994, «The vertical structure and stability of accretion disks surrounding black holes and neutron stars», *ApJ*, vol. 421, doi: 10.1086/173680, p. 668–676. 260

MINESHIGE, S. et Y. OSAKI. 1983, «Disk-instability model for outbursts of dwarf novae Time-dependent formulation and one-zone model», *Publ. Astron. Soc. Jpn.*, vol. 35, p. 377–396. 260

NOUGIER, J. P. 1987, *Méthodes de calcul numérique*, Masson, Paris, ISBN 978-2-225-81086-2. 261

PAPALOIZOU, J. C. B. et C. TERQUEM. 1999, «Critical Protoplanetary Core Masses in Protoplanetary Disks and the Formation of Short-Period Giant Planets», *ApJ*, vol. 521, doi: 10.1086/307581, p. 823–838. 259, 260, 262, 264, 265, 266

PRESS, W., S. TEUKOLSKY, W. VETTERLING et B. FLANNERY. 1992, *Numerical Recipes in Fortran 77*, Cambridge University Press. 260

RÓŻAŃSKA, A., B. CZERNY, P. T. ŻYCKI et G. POJMAŃSKI. 1999, «Vertical structure of accretion discs with hot coronae in active galactic nuclei», vol. 305, doi: 10.1046/j.1365-8711.1999.02425.x, p. 481–491. 260

Chapitre 9

Origine du système solaire : projet scientifique

Ma mutation, en 2015, de l'Institut UTINAM de Besançon vers la GSMA à Reims, m'a éloigné des problématiques attachées à l'origine du système solaire. Néanmoins, je souhaiterais prolonger l'utilisation du code *EvAD*[1] décrit ci-avant aux chapitres 6, 8 et 7. En effet, ce programme, qui m'a demandé au gros travail de développement a été uniquement utilisé dans Cordier et collab. [2016] (voir page 274). Bien sûr, mon temps de travail reste un facteur très limitant pour ce genre de projet. Cependant, dans les années à venir, des opportunités se présenteront peut être à l'occasion d'une collaboration ou de la disponibilité d'un étudiant.

Bien que les idées d'études ne manquent pas au sujet des tout premiers temps des systèmes planétaires, deux types de questions me tiennent à cœur :

1. l'influence de la masse de l'étoile centrale sur le «temps de vie» de la nébuleuse primitive.

2. l'influence du traitement du transfert radiatif sur le comportement de cette nébuleuse, cette physique étant particulièrement simplifiée dans l'état actuel d'*EvAD*.

Concernant la première question, des observations [Ribas et collab., 2015] tendent à montrer que l'évolution des disques protoplanétaires dépend de la masse de l'étoile centrale, et que cette évolution est d'autant plus rapide que l'étoile est massive. Il serait donc intéressant d'étudier si *EvAD* est capable de reproduire ce genre de tendance. En effet, la dynamique du disque simulé par *EvAD* dépend de la masse de l'étoile via l'équation de l'équilibre hydrostatique :

$$\frac{1}{\rho}\frac{\partial P}{\partial z} = -\Omega^2 z \tag{9.1}$$

(voir l'équation 8.1 page 259), où Ω est la vitesse de rotation angulaire képlerienne :

$$\Omega = \frac{\sqrt{GM_\star}}{r^{3/2}} \tag{9.2}$$

(voir l'équation 9.2 page 269), expression dans laquelle apparaît la masse de l'étoile $M_\star$. Pour mener à bien cette étude, il faut calculer des tables de viscosité turbulente $< \nu >$ pour différentes valeurs de $M_\star$. Dans le cas où on considère le disque comme irradié, ce qui est le modèle le plus réaliste, on doit tenir compte de l'évolution de l'étoile sur son trajet évolutif, ceci pour différentes valeurs du paramètre α (voir chapitres 8 et 7). En 2016 j'ai commencé cet important travail de simulation, mais malheureusement j'ai rencontré des problèmes numériques que je n'ai pas pris le

1. *Ev*olutionary *A*ccretion *D*isk

temps de résoudre depuis. J'ai cependant déjà une idée d'un nouvel algorithme d'intégration verticale gommant les inconvénients de celui décrit au chapitre 8. Cet algorithme prend r (la distance à l'étoile) et Σ (la densité surfacique de masse au point considéré) comme paramètres, éliminant de la sorte $\dot{M}_{st}$ qui posait des difficultés lors de l'interpolation des tables. Du point de vue strictement numérique, il s'agit d'une méthode de relaxation avec une distribution non-uniforme des nœuds du calcul.
Pour ce qui est des données observationnelles, j'avais commencé, en 2016, à interagir avec Àlvaro Ribas, post-doc à la Boston University, qui m'avait fourni ces données. Au-delà de la reproduction du comportement montré par ces résultats empiriques, la rapidité d'évolution d'un disque protoplanétaire comme fonction de la masse de l'étoile est un aspect certainement très important si on veut expliquer la relative rareté des «Jupiter chauds» autour des étoiles de masse élevée [*i.e.* $M_\star > 1.5\,M_\odot$, voir Fig. 6 de RIBAS et collab., 2015].

Dans $E\nu AD$, l'énergie mécanique, dissipée en chaleur via la turbulence, est rayonnée vers l'extérieur du disque. Ce transfert de photons est représenté par l'équation 8.3 (voir page 259 du chapitre 8), qu'on rappelle ici :

$$\frac{\partial T}{\partial z} = -\frac{3\kappa\rho}{16\sigma T^3}F \tag{9.3}$$

L'interaction rayonnement-matière est prise en compte dans le modèle via la valeur de l'opacité κ. Cette quantité clef a été jusqu'à présent estimée à partir de formules d'interpolation [voir BELL et LIN, 1994] reposant sur des valeurs d'opacités uniquement valable à la métallicité [2] solaire. Il serait donc particulièrement intéressant d'explorer la dépendance du comportement d'un disque vis-à-vis de la composition chimique élémentaire du système protostellaire. Ce problème est crucial pour la formation des cortèges planétaires, car plus la métallicité sera élevée, plus la quantité de matériaux disponibles pour former des planètes sera importante. Ici encore l'utilisation de table adaptée, de valeurs de κ, ceci pour en déduire des tables de viscosité turbulente $< \nu >$ est nécessaire, cela représente une quantité de travail conséquente. Jusqu'à présent, dans la littérature traitant des disques protoplanétaires, la question de la cohérence entre la valeur de κ et la composition du disque n'a pas été considérée sérieusement, ceci en raison de la difficulté du problème.

Enfin, j'aimerais beaucoup aborder le fameux problème de l'homochiralité des molécules du vivant. En effet, 19 des 20 acides aminés naturels sont des énantiomères L alors que les sucres naturels sont des énantiomères D [BONNER, 1995]. De nombreux travaux ont été publiés sur cette fascinante question [voir par exemple les références dans FLAMANT, 2016], et j'aimerais étudier l'effet éventuel de la polarisation des photons solaires diffusés par la nébuleuse elle-même. Une idée voisine a déjà été exploité [BAILEY et collab., 1998] dans le contexte des régions de formation stellaire. En utilisant une approche langragienne dans le suivi des grains de poussières, comme l'ont fait CIESLA et SANDFORD [2012], on pourrait calculer le taux de polarisation des photons reçus par les poussières, à la surface desquelles une chimie pré-biotique pourrait avoir eu lieu.

Ces deux derniers sujets sont très proches des problématiques du GSMA concernant les atmosphères planétaires. En effet, un disque protoplanétaire n'est pas, par la physique mise en jeu, très différent d'une atmosphère : il s'agit d'une masse de gaz et de poussières (pour les atmosphères emploie le terme d'«aérosols») subissant une irradiation et un champ de gravité.

9.1 Références

BAILEY, J., A. CHRYSOSTOMOU, J. H. HOUGH, T. M. GLEDHILL, A. MCCALL, S. CLARK, F. MENARD et M. TAMURA. 1998, «Circular Polarization in Star-Formation Regions : Implications for Biomolecular Homochirality», *Science*, vol. 281, doi: 10.1126/science.281.5377.672, p. 672. 270

2. Fraction massique des éléments plus lourds que l'hélium.

BELL, K. R. et D. N. C. LIN. 1994, «Using FU Orionis outbursts to constrain self-regulated protostellar disk models», *ApJ*, vol. 427, doi: 10.1086/174206, p. 987–1004. 270

BONNER, W. A. 1995, «Chirality and life», *Origins of Life and Evolution of the Biosphere*, vol. 25, n° 1, doi: 10.1007/BF01581581, p. 175–190, ISSN 1573-0875. URL https://doi.org/10.1007/BF01581581. 270

CIESLA, F. J. et S. A. SANDFORD. 2012, «Organic Synthesis via Irradiation and Warming of Ice Grains in the Solar Nebula», *Science*, vol. 336, doi: 10.1126/science.1217291, p. 452–454. 270

CORDIER, D., P. G. PRADA MORONI et E. TOGNELLI. 2016, «Dust photophoretic transport around a T Tauri star : Implications for comets composition», *Icarus*, vol. 268, doi: 10.1016/j.icarus.2015.11.037, p. 281–294. 269

FLAMANT, F., éd.. 2016, *La science insolite de l'asymétrie — De la ola au neutrino*, Edition du Seuil – Science ouverte, Paris. 270

RIBAS, Á., H. BOUY et B. MERÍN. 2015, «Protoplanetary disk lifetimes vs. stellar mass and possible implications for giant planet populations», *A&A*, vol. 576, doi: 10.1051/0004-6361/201424846, A52. 269, 270

Retour à la table des matières : p. v

Chapitre 10

Articles : origine du système solaire

10.1 Article sur le transport par photophorèse au voisinage d'une T Tauri

Icarus 268 (2016) 281–294

Contents lists available at ScienceDirect

Icarus

journal homepage: www.journals.elsevier.com/icarus

Dust photophoretic transport around a T Tauri star: Implications for comets composition

D. Cordier [a,b,*], P.G. Prada Moroni [c,e], E. Tognelli [d,e]

[a] Groupe de Spectrométrie Moléculaire et Atmosphérique, UMR 6089, Campus Moulin de la Housse, BP 1039 Université de Reims Champagne-Ardenne 51687 Reims, France
[b] Université de Franche-Comté, Institut UTINAM, CNRS/INSU, UMR 6213, 25030 Besançon Cedex, France
[c] Physics Department "E. Fermi", University of Pisa, Largo B. Pontecorvo 3, I-56127 Pisa, Italy
[d] Department of Physics, University of Roma Tor Vergata, Via della Ricerca Scientifica 1, 00133 Roma, Italy
[e] INFN, Largo B. Pontecorvo 3, I-56127 Pisa, Italy

ARTICLE INFO

Article history:
Received 25 November 2014
Revised 13 November 2015
Accepted 27 November 2015
Available online 22 December 2015

Keywords:
Comets, composition
Comets, dust
Comets, origin
Solar Nebula

ABSTRACT

There is a growing body of evidences for the presence of crystalline material in comets. These crystals are believed to have been annealed in the inner part of the proto-solar Nebula, while comets should have been formed in the outer regions. Several transport processes have been proposed to reconcile these two facts; among them a migration driven by photophoresis. The primarily goal of this work is to assess whether disk irradiation by a Pre-Main Sequence star would influence the photophoretic transport. To do so, we have implemented an evolving 1+1D model of an accretion disk, including advanced numerical techniques, undergoing a time-dependent irradiation, consistent with the evolution of the proto-Sun along the Pre-Main Sequence. The photophoresis is described using a formalism introduced in several previous works. Adopting the opacity prescription used in these former studies, we find that the disk irradiation enhances the photophoretic transport: the assumption of a disk central hole of several astronomical units in radius is no longer strictly required, whereas the need for an *ad hoc* introduction of photoevaporation is reduced. However, we show that a residual trail of small particles could annihilate the photophoretic driven transport via their effect on the opacity. We have also confirmed that the thermal conductivity of transported aggregates is a crucial parameter which could limit or even suppress the photophoretic migration and generate several segregation effects.

© 2015 Elsevier Inc. All rights reserved.

1. Introduction

As reported by Tielens et al. (2005) the interstellar medium (hereafter ISM) is very poor in crystalline solids. For instance, Kemper et al. (2004) well reproduce the interstellar absorption band using a mixture composed of ∼15.1% of amorphous pyroxene and ∼84.9% of amorphous olivine by mass, leading to a crystalline fraction of the interstellar silicates around 0.2%. The proto-solar Nebula is supposed to have been formed from material coming from the ISM. As a consequence, the primordial dust in the Solar System should be composed of amorphous solids except grains which have undergone either a thermal annealing in high temperature regions (*i.e.* around 1000–1500 K) close to the star (*i.e.* $r \lesssim 1$–2 AU) or a sequence starting by a vaporization or a melting and finishing by a re-condensation. Besides this, comets are presumed to have formed in the cold outer part of the solar Nebula along the lines of the scenario recalled below.

The dissipation of the early gaseous and dusty protoplanetary disk is presumed to have left a disk of icy planetesimals beyond ∼5 AU. The Edgeworth–Kuiper Belt (hereafter KB) and the Oort Cloud (hereafter OC) are the remains of this disk and are the well accepted two main cometary reservoirs (Mumma and Charnley, 2011). A corpus of studies, based on dynamics, show that icy asteroids originally located between ∼5 AU and ∼30 AU have either participated to the formation of giant planets or have been ejected far away because of the planet migration. The majority of the KB objects have probably been accreted at their current distances (*i.e.* $\gtrsim 30$ AU); but as suggested by results of the Nice model, an orbital resonance of Saturn and Jupiter may have partially filled the KB with objects initially located between ∼15 AU and ∼30 AU (Tsiganis et al., 2005). Furthermore, the planetesimals of the inner part of the primordial disk (*i.e.* located in the interval ∼5–15 AU) have been likely ejected and finally participated to the formation of the outer regions of the KB and the OC. In summary, the crystals

* Corresponding author at: Groupe de Spectrométrie Moléculaire et Atmosphérique, UMR 6089, Campus Moulin de la Housse, BP 1039 Université de Reims Champagne-Ardenne 51687 Reims, France.
E-mail address: daniel.cordier@univ-reims.fr (D. Cordier).

http://dx.doi.org/10.1016/j.icarus.2015.11.037
0019-1035/© 2015 Elsevier Inc. All rights reserved.

Retour à la table des matières : p. v

have been incorporated into icy planetesimals when they occupied zones from ∼5 AU to ∼30 AU and beyond; prior to be scattered to the KB and OC. Of course, the transport processes studied in this paper should deposit crystalline dusts at least around 5 AU, but the deeper the penetration beyond 5 AU will be, the more credible the proposed mechanism will be. The formation of the comets is also believed to have occurred early during the Solar System formation. For instance Weidenschilling (1997) showed that the formation of comets could have been completed in $\sim 2 \times 10^5$ years.

Campins and Ryan (1989) have found that crystalline olivine is a major component of the silicates in Comet Halley and Wooden et al. (1999, 2000) detected crystalline silicates in Hale-Bopp observations. *Stardust* samples of Comet 81P/Wild 2 include large single mineral crystals and X-ray microscopic analysis leads to a crystal mass fraction $f_{\rm cryst}$ larger than ∼50% (Zolensky et al., 2006; Ogliore et al., 2009; Brownlee et al., 2006). More generally, comets have a ratio $f_{\rm cryst}$ exceeding ∼20% (Kelley and Wooden, 2009; Lindsay et al., 2013). This discrepancy between the crystallinity of the ISM grains and the of cometary grains one is the mark of a radial transport process and/or a specific physical phenomenon occurring in the accretion disk. Several transport processes have been proposed to explain the presence of these refractory material in comets: annealing by shock waves in the outer solar Nebula (Harker and Desch, 2002), radial mixing by turbulent diffusion (Gail, 2001; Wehrstedt and Gail, 2002; Bockelée-Morvan et al., 2002; Cuzzi et al., 2003) or mixing in a marginally gravitationally unstable (MGU) disk (see the series of papers by Boss and co-authors: Boss, 2008 could be a starting point), transport by photophoresis (Krauss and Wurm, 2005; Wurm and Krauss, 2006; Krauss et al., 2007; Mousis et al., 2007; Moudens et al., 2011). Some authors (Ciesla, 2007; Keller and Gail, 2004) built models including the vertical disk structure and found a radial outflow of dust grains due to pressure gradients within the protoplanetary disk. The X-wind mechanism, which has been advocated for the redistribution of CAIs throughout the Nebula (Shu et al., 1996), could have also brought a contribution.

In this paper, we focus on photophoretic process for which we employ a 1+1D accretion disk undergoing a time-dependent irradiation. Indeed, the proto-Sun, at the epoch during which it was surrounded by a disk of gas and dust, was evolving through the so-called T Tauri phase. The stars belonging to the T Tauri class, are known to possess an accretion disk and are evolving along the Pre-Main Sequence (hereafter PMS) tracks where their luminosity could be much higher than that of the Sun. This high luminosity could have an important influence on photophoresis and might change the disk structure or its dynamics by irradiation. This is why we were interested in modeling an accretion disk evolving consistently with a proto-Sun. It is of particular interest to assess if the assumption of the existence of a central gap (as hypothesized in previous works, see Moudens et al., 2011) in the disk is still required. It should be noticed that Turner et al. (2012) have taken into account the PMS luminosity of the proto-Sun in the context of Jupiter formation.

The presence of crystals in comets is not the only issue for which photophoresis is supposed to play a role, Teiser and Dodson-Robinson (2013) have proposed that photophoresis could accelerate the giant planets formation and Wurm et al. (2013) have investigated the involvement of this effect in the formation of Mercury-like planets and in the metal depletion in chondrites. Detailed theoretical and experimental studies on chondrules photophoretic properties have been also conducted (Wurm et al., 2010; Loesche et al., 2013).

Concerning the photophoretic transport itself we have essentially adopted the approach described in Krauss et al. (2007) and Moudens et al. (2011), as recalled in Section 2. The main features of our disk model are presented in the same section, and additional details are given in Appendix A. Section 3 is devoted to our results, while in Section 4 we discuss some aspects of the problem such as the influence of aggregate properties, in particular that of thermal conductivity as suggested by Krauss et al. (2007), and the role of gas–dust opacity. Conclusions can be found in Section 5.

2. Description of the model

We have developed an original implementation of a 1+1D irradiated protoplanetary accretion disk model based on the equation introduced by Lynden-Bell and Pringle (1974) and Pringle (1981)

$$\frac{\partial \Sigma}{\partial t} = \frac{3}{r}\frac{\partial}{\partial r}\left\{ r^{1/2}\frac{\partial}{\partial r}\langle \nu \rangle \Sigma r^{1/2} \right\} + \dot{\Sigma}_w(r) \tag{1}$$

which governs the secular variations of the disk surface density Σ (kg m^{-2}) as a function of the heliocentric distance r. The numerical method employed to solve Eq. (1) is described in Appendix A.2. The average turbulent viscosity $\langle \nu \rangle$ (m^2 s^{-1}), depending on a free parameter α, is computed in the frame of the Shakura and Sunyaev (1973) formalism – after the integration of the vertical structure equations (see Appendix A.1 for details). Our disk model is based on a generalization of the method introduced by Papaloizou and Terquem (1999) (hereafter PT99) and Alibert et al. (2005). The photoevaporation $\dot{\Sigma}_w(r)$ is provided by the simple prescription published by Veras and Armitage (2004): $\dot{\Sigma}_w(r) = 0$ for $r \leqslant R_g$ and $\dot{\Sigma}_w(r) = \lambda_{\rm evap}/r$ for $r > R_g$, where R_g is taken to be 5 AU and $\lambda_{\rm evap}$ is an adjustable parameter. A rigorous treatment of the radiative transfer in all its complexity is beyond the scope of the present work, and represents probably a physical and numerical challenge. Instead, the effect of the irradiation by the central star has been taken into account by modifying the temperature boundary condition at the disk external surface. This way, the temperature at this surface, denoted T_s, is given by $T_s^4 = T_b^4 + T_{\rm irr}^4$ where T_b is the background temperature (usually $T_b = 10$ K) and $T_{\rm irr}$ comes from the following equation, derived in Hueso and Guillot (2005),

$$T_{\rm irr} = T_{\rm eff}(t)\left[\underbrace{\frac{2}{3\pi}\left(\frac{R_\star(t)}{r}\right)^3}_{(1)} + \underbrace{\frac{1}{2}\left(\frac{R_\star(t)}{r}\right)^2 \left(\frac{H_p(t)}{r}\right)\left(\frac{{\rm dln}H_p(t)}{{\rm dln}r} - 1\right)}_{(2)} \right]^{1/4} \tag{2}$$

where $R_\star(t)$ and $T_{\rm eff}(t)$ are respectively the stellar radius and effective temperature at the age t; $H_p(t)$ represents the disk pressure height at the heliocentric distance r and at time t. This prescription has also been adopted by Fouchet et al. (2012) who have emphasized its significance that we recall here: the term (1) corresponds to the radiative flux that would be intercepted by a flat disk, the term (2) is an estimation for the effect of the disk flaring. Following Fouchet et al. (2012) and Hueso and Guillot (2005) we fixed ${\rm dln}H_p/{\rm dln}r$ at its equilibrium value, namely 9/7. In order to validate our model, we have performed several tests. For instance, we have verified that we reproduce the mid-plane temperature T_m, the surface density Σ and the shape factor H/r obtained by PT99 (see *e.g.* Figs. 2 and 3 in PT99). We also obtained a good agreement between our computations and the PT99 ones for the accretion rate $\dot{M}_{st}$ ($M_\odot$ yr^{-1}) as a function of Σ for various turbulence parameters α and distances r to the Sun. In their study, PT99 did not take into account the effect of irradiation. Notice that, this is why we verified that our computations are compatible with results found by D'Alessio et al. (1998), even if the treatment of the irradiation is not exactly the same. This way, following the same procedure adopted by Fouchet et al. (2012), we also verified that our compu-

Retour à la table des matières : p. v

tations are compatible with results found by D'Alessio et al. (1998), who used a more sophisticated approach concerning irradiation.

Both stars and protoplanetary disks change with time. The stars evolve under the influence of gravitation and nuclear reactions, while disks lose their mass either by accreting on the star and/or evaporating to the interstellar space. Thus, we have decided to include both evolutions in a model in which the proto-Sun and the disk interact via irradiation.

Young Main Sequence stars may exhibit a debris disk, that has a very tenuous or even non-existent gaseous component (Ollivier et al., 2009). In contrast, T Tauri stars have their spectroscopic features (as the excess UV or IR radiation) well explained by the presence of a surrounding, optically thick, gaseous accretion disk (Lynden-Bell and Pringle, 1974). The objects of this class are Pre-Main Sequence stars, located in the Hertzsprung-Russell diagram between the "birthline" and the early Main Sequence, where the stellar luminosity is provided by the hydrogen burning in their core with the secondary elements at equilibrium. The "birthline" is a line in the HR diagram corresponding to a threshold below which stars become visible to the observer, they therefore begin their quasi-static contraction and move to the Main Sequence. We have adopted a PMS evolutionary track computed by Tognelli et al. (2011) who have employed the well-tested and developed stellar evolutionary code FRANEC[1] (Degl'Innocenti et al., 2008) together with up-to-date input physics (Tognelli et al., 2012; Dell'Omodarme et al., 2012).

The starting time t_0 of the evolution of our accretion disk has been taken where the "birthline" (from Stahler and Palla, 2004) intersects the proto-solar PMS stellar track.

The solar models have been calibrated on the present solar luminosity ($L_\odot$), radius ($R_\odot$), for the surface chemical composition ($Z/X_{ph,\odot}$, see Asplund et al., 2005). We used an iterative procedure that consists in varying the initial helium abundance (Y), metallicity (Z), and mixing length parameter ($\alpha_{\rm MLT}$), in order to reproduce at the age of the Sun ($t_\odot$) the present $L_\odot, R_\odot$, and $(Z/X)_{ph,\odot}$ within a tolerance of, at most, 10^{-4}. Then, we obtained for the proto-Sun the initial helium and metal mass fraction $Y = 0.2533$, $Z = 0.01377$, and $\alpha_{\rm MLT} = 1.68$ (see Fig. 1). In their study of samples of stars belonging to six young stellar clusters, Haisch et al. (2001) have measured the JHKL infrared excess fractions of stars. For each cluster, these ratios can be regarded as the fractions of stars surrounded by a disk. For the selected clusters, age determinations are available in the literature. This way, Haisch et al. (2001) have shown that, not surprisingly, the fraction of stars accompanied by a disk decreases with age and should be negligible for an age around ∼6 Myr (hereafter 1 Myr = 10^6 years). This limitation is confirmed by Pascucci and Tachibana (2010) and references therein. According to these works, protoplanetary disks older than ∼6 Myr should not exist or be very rare. Our 1+1D disk model requires the pre-computation of tables of turbulent viscosity $\langle\nu\rangle$ depending on various parameters among which the luminosity of the star $L_\star$ and its effective temperature $T_{\rm eff}$. Consequently, along the PMS track we took a set of couples $(L_\star, T_{\rm eff})$ corresponding to ages $t \lesssim 16$ Myr with $t = 0$ at the "birthline". Hence, for each t, tables of mean viscosity were constructed using $(L_\star(t), T_{\rm eff}(t))$ or equivalently $(R_\star(t), T_{\rm eff}(t))$ and playing with a set of parameters values: $\alpha = 10^{-3}$ and 10^{-2}; $\dot{M}_{st}$ ranging from 10^{-12} $M_\odot$ yr^{-1} to 10^{-4} $M_\odot$ yr^{-1}; and $0.05 \leqslant r \leqslant 50$ AU. A dedicated subroutine allows interpolation in mentioned tables of $\langle\nu\rangle_{t,\Sigma,r}$.

The dust grains transported through the disk are aggregates of small particles (Brownlee, 1978; Greenberg, 1985; Meakin and Donn, 1988; Blum et al., 2000) and are very approximately considered

[1] Frascati Raphson Newton Evolutionary Code.

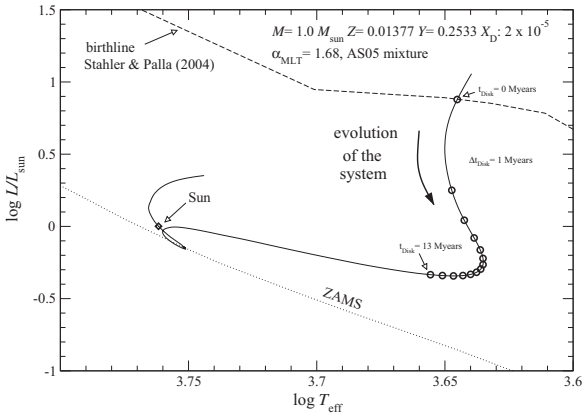

Fig. 1. Solid line: Pre-Main Sequence evolutionary track computed by Tognelli et al. (2011), chosen parameters are representative for the Sun: $Z = 0.01377$ and $Y = 0.2533$ are respectively the initial heavy elements and the helium mass fractions, $\alpha_{\rm MLT} = 1.68$ is the solar calibrated Mixing Length Theory parameter and $X_{\rm D}$ denotes the initial mass fraction of deuterium. This stellar track has been computed with the mixture of heavy elements provided by Asplund et al. (2005) (labeled AS05). Dashed line: the stellar "birthline" from Stahler and Palla (2004). Dotted line: the ZAMS. Circles are displayed each 1 Myr and the Sun position on the track has been marked with a diamond.

as spherules of radius a. Hereafter, the terms "particles", "grains" and "aggregates" will be synonyms; while "monomer" will be reserved for the components of aggregates.

Following the approach developed by Krauss and Wurm (2005) and Krauss et al. (2007) we assume that the gas flow conditions are described by the Knudsen number, K_n, which is defined as $K_n = l/a$, where l is the mean free path of the gas molecules.

An expression of the photophoretic force F_{ph}, valid for free molecular regime ($K_n > 1$) and for continuum regime ($K_n \leqslant 1$), has been proposed by Beresnev et al. (1993) (see their Eq. (31))

$$F_{ph} = \frac{\pi}{3} a^2 I(r,t) J_1 \left(\frac{\pi m_g}{2kT}\right)^{1/2} \frac{\alpha_E \psi_1}{\alpha_E + 15\Lambda Kn(1-\alpha_E)/4 + \alpha_E \Lambda \psi_2} \qquad (3)$$

We are not going to recall the expression of each term of Eq. (3), instead we invite the interested reader to consult previous works (Beresnev et al., 1993; Krauss et al., 2007; Moudens et al., 2011). Nonetheless, we specify some important points. First of all, given that the collision/scattering cross section of molecules is not known, the free mean path l is estimated from the value of the dynamic viscosity η provided by $\eta = \eta_0\sqrt{T/T_0}$ (see Krauss et al., 2007) with $\eta_0 = 8.4 \times 10^{-6}$ Pa s, T the temperature and $T_0 = 280$ K. Since the viscosity η for a dilute gas is also given by $\eta = nm\bar{v}l/3$ (with n the number of molecules per unit of volume and m the average mass of these molecules, Reif, 1967), we compute $l = 3\eta/\rho_m\bar{v}$ where ρ_m is the mid-plane density and $\bar{v}$ the thermal velocity of gas molecules.

The parameter Λ that appears in Eq. (3) measures the thermal relaxation of aggregates, we have (see Krauss et al., 2007) $\Lambda = \lambda_{\rm eff}/\lambda_g$, with λ_g the thermal conductivity of gas and $\lambda_{\rm eff}$ the effective thermal conductivity given by the following expression,

$$\lambda_{\rm eff} = \lambda_p + 4\epsilon\sigma T^3 a \qquad (4)$$

where ϵ is the emissivity (assumed to be 1) and λ_p is the heat conductivity of aggregates. As usual, σ denotes the Stefan–Boltzmann constant. Although minerals, in massive and not porous form, have thermal conductivity around ∼10 W m^{-1} K^{-1} (see for instance Horai and Simmons, 1969), aggregates – due to their porosity – are believed worse thermal conductors than massive dust grains.

Retour à la table des matières : p. v

In their experimental investigations of laboratory analogs, Krause et al. (2011) found thermal conductivity ranging from 0.002 to 0.02 $W\,m^{-1}\,K^{-1}$. We have fixed λ_p to $10^{-3}\,W\,m^{-1}\,K^{-1}$ in order to facilitate comparisons with earlier researches having adopted this value (Mousis et al., 2007; Moudens et al., 2011; Krauss and Wurm, 2005). Nevertheless, in Section 4 we will explore the influence of λ_p. The density of dust particles have been fixed to $\rho_p = 500\,kg\,m^{-3}$; this value has been adopted by Mousis et al. (2007) and Moudens et al. (2011). This density value is based on an olivine density of $3300\,kg\,m^{-3}$ (Mousis et al., 2007), and on an aggregates filling factor of 15% (Blum and Schräpler, 2004). The influence of ρ_p is briefly discussed in Section 4.2. The photophoretic force (see Eq. (3)) is not the only one taken into account; the force F_{res} due to residual gravity (Weidenschilling, 1977a) and the radiative pressure force are also considered. These forces are respectively provided by

$$F_{res} = \frac{m_p}{\rho_g}\frac{dP}{dr} \tag{5}$$

$$F_{rad} = \pi a^2 \frac{I(r,t)}{c_{light}} \tag{6}$$

where m_p is the mass of an aggregate, ρ_g and P are the density and the pressure of the gas; $I(r,t)$ represents the radiative flux ($W\,m^{-2}$) at time t, at the location of the test particle. The speed of light is noted c_{light}. The radiative flux $I(r,t)$, as it appears in Eqs. (3) and (6) is derived from the star luminosity $L_\star(t)$. Similarly to the previous works (Mousis et al., 2007; Moudens et al., 2011), we have hypothesized the existence of an inner gap of radius r_{gap}, optically thin enough for particles to see the proto-Sun, but still containing the gas content of the disk structure. This assumption is supported by an increasing number of observational evidences. For instance, D'Alessio et al. (2005) show that observations of the Pre-Main Sequence star CoKu Tau/4 suggest the presence of an accretion disk with an inner hole cleared of small dust grains. The infrared imaging survey, conducted by Sicilia-Aguilar et al. (2006) with the Spitzer Space Telescope, indicates that around 10% of the stars of their sample, owning a disk, exhibit spectral features explained by the existence of an optically thin inner disk. In addition, Pontoppidan et al. (2008) studied three disks, and detected an inner gap depleted in dust particles but containing gas. Up to now, it is not clear which physical mechanism could be the origin of such inner cavities or gaps in protoplanetary disks (see for instance Thalmann et al., 2010). This is the reason why we have only postulated their existence. The model is sketched in Fig. 2. The radiative transfer along the line of sight between particles and proto-Sun is treated in a very simplified way. Firstly, neglecting the absorption by the gas, the radiative flux I_{geom} ($W\,m^{-2}$) is evaluated at the distance r reached by particles at the time t

$$I_{geom}(r,t) = \frac{L_\star(t)}{4\pi r^2} \tag{7}$$

this reflects the sphericity of stellar emissions. In a second step, the equation

$$dI = -\kappa_R\,\rho_m(r,t)\,I(r,t)\,dr \tag{8}$$

is integrated at fixed t from r_{gap} to r_p using the boundary condition $I(r_{gap},t) = I_{geom}(r_p,t)$; in this manner the effect of gas absorption is combined with the pure geometrical decrease. The opacity κ_R is due to Rayleigh's scattering for which Mousis et al. (2007) derived

$$\kappa_R(T_{eff}) = 3.96\times10^{-19}\,T_{eff}^4(t) \tag{9}$$

($cm^2\,g^{-1}$). It has to be emphasize that, using Eq. (9), the disk is assumed to have been cleared of dust by the photophoretic transport between r_{gap} and $r_p(t)$ (see Fig. 2). We also point out that the

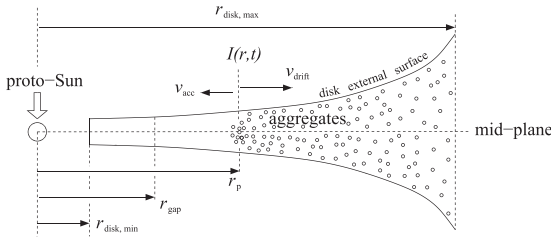

Fig. 2. Sketch of the photophoretic transport model discussed in this paper. The disk structure has been computed between $r_{disk,min} = 0.5$ AU and $r_{disk,max} = 50$ AU. The existence of an inner gap of radius $r_{gap} \geqslant r_{disk,min}$ is hypothesized.

employment of the opacity law provided by Bell and Lin (1994) (see Appendix A.1) is not more relevant, since it assumes the absence of dust depletion caused by the photophoretic transport. With an overestimated contribution of dust grains, Bell and Lin (1994) opacity law yields to the annihilation of the photoretic migration. Thus, the approach adopted here is clearly an idealized situation and the derived results have to be considered as maximized effects. We will come back to this opacity issue in a dedicated section of the discussion. The use of Eq. (9) means that the effect of the thermal radiation field of the gas itself and the effect of the photon multi-scattering have also been neglected. Finally, the aggregates are drifted (in the gas frame) in the radial direction with the velocity (see Fig. 2)

$$v_{drift} = \frac{F_{ph} + F_{rad} + F_{res}}{m_p}\,\tau \tag{10}$$

where τ, the coupling time of particles with gas, is provided by

$$\tau = \frac{m_p}{6\pi\eta a}\,C_c \tag{11}$$

The correction factor C_c is expressed as a function of the Knudsen number K_n (Cunningham, 1910; Hutchins et al., 1995)

$$C_c = 1 + K_n\,(1.231 + 0.47\,e^{-1.178/K_n}) \tag{12}$$

In protoplanetary disks, the mid-plane temperature decreases with the distance to the central star. This is why we have checked that the thermophoretic force given by Young (2011), and recalled in Lutro (2012), remains negligible compared to the forces contributing to Eq. (7). For a given age of the disk, the distance r_p reached by particles is obtained by integrating the difference between the drift velocity v_{drift} and the accretion velocity v_{acc}, we have

$$r_p = \int_0^{age} (v_{drift} - v_{acc})\,dt \tag{13}$$

More rigourously than Moudens et al. (2011), we derived v_{acc} from the disk model, that provides naturally the speed of the gas which is falling to the star (see Fig. 2)

$$v_{acc} = -\frac{3}{\Sigma\sqrt{r}}\frac{\partial}{\partial r}\left(\Sigma\langle v\rangle\sqrt{r}\right) \tag{14}$$

(Lynden-Bell and Pringle, 1974).

3. Results

The concept of the Minimum Mass of Solar Nebula (hereafter MMSN) dates back to the end of the seventies (Weidenschilling, 1977b; Hayashi, 1981), and the initial total mass of the solar Nebula is now expected to be approximately a few MMSN (*e.g.* Crida, 2009 found ~10 MMSN). We have chosen 3 MMSN as a typical value, that allows easy comparison with past investigations

Retour à la table des matières : p. v

(Moudens et al., 2011). The proto-planetary disks are believed to be the place of turbulent mixing produced by magneto-rotational instabilities (Balbus and Hawley, 1998) and the associated α-parameter introduced by Shakura and Sunyaev (1973) has admitted values within the interval 10^{-2}–10^{-3}; we have selected $\alpha = 7 \times 10^{-3}$ as our nominal value which also facilitates comparisons. The literature reported the observation of accretion disks having a central hole with a radius of ∼1–2 AU (see for instance Besla and Wu, 2007; Pontoppidan et al., 2008; Hughes et al., 2010; Thalmann et al., 2010); for this reason we first assumed the existence of such an inner gap of radius $r_{gap} = 2$ AU. This strong hypothesis, already made by Mousis et al. (2007) and Moudens et al. (2011), favors clearly the transport driven by photophoresis since it decreases the radiative flux attenuation between the proto-Sun and the dust grains.

The results of our first calculations can be seen in Fig. 3a, they are very similar to those plotted in Fig. 4 of Moudens et al. (2011); for which equivalent parameters and hypothesis have been chosen. We recall that, in this case, the lifetime of the protoplanetary disk has been adjusted to 6 Myr (see Haisch et al., 2001; Pascucci and Tachibana, 2010) by tuning the photoevaporation parameter λ_{evap}. In Moudens et al.'s work the disk is not irradiated, and the solar luminosity was provided by Pietrinferni et al. (2004) for the Sun at the ZAMS.[2] For each simulation of a disk evolution, we stopped the calculation when the total mass of the disk reached ∼1% of its initial mass. This criterion will be applied in all simulations discussed in the rest of the present work.

In Fig. 3(b) an identical disk structure is kept but the photophoresis force is computed in a slightly different way: the solar luminosity is no longer taken constant at its ZAMS value, but instead it follows the luminosity variations along the PMS tracks plotted in Fig. 1. In addition, the gas opacity which depends on the stellar effective temperature T_{eff} (see Eq. (9)), is computed consistently. Not surprisingly, the aggregates are very efficiently pushed outwards, because the luminosity at the birthline is about 10 times larger than that at the ZAMS. Interestingly, particles with a radius of $a = 10^{-5}$ m reach ∼10 AU after ∼0.3 Myr and do not move further away even after 6 Myr.

Keeping fixed the inner gap at 2 AU, and letting unchanged all the other parameters, we adopted a protoplanetary disk model computed with a time-dependent stellar luminosity given by the already mentioned PMS track. The subsequent positions of the aggregates are represented in Fig. 3c. It is clearly visible that the use of an irradiated disk damps the particle movement. This behavior could be caused either by a higher accretion velocity or by smaller forces. In order to disentangle the various effects, we have focused our analysis on the movement of particles of radius 10^{-4} m, which appear to be typical at the examination of Fig. 3b and c. The panel (a) of Fig. 4 indicates that the accretion velocity undergone by the considered particle, along its path in the disk mid-plane, is larger (in absolute value) when the disk structure is irradiated. Beside this, we have checked that during the period of interest, *i.e.* before ∼1.5 Myr, the photophoretic force has the dominant contribution to the drift velocity (see Eq. (7)). To catch the effect of the disk structure, we have normalized the photophoretic force by the received flux of light (see Eq. (3)). The resulting ratio F_{ph}/I is either not significantly different or slightly higher, respectively when irradiation is accounted or when it is not (see Fig. 4b). Therefore, the larger accretion velocity appears to weaken the efficiency of the photophoretic force during the T Tauri phase of the Sun. We emphasized that this irradiated disk model is dissipated at the age of 4.32 Myr. Therefore, the photoevaporation has not been needed to get a lifetime compatible with astronomical observations. Indeed, with non-irradiated disks the photoevaporation rate was adjusted to get a disk lifetime of 6 Myr. With an initial mass of 3 MMSN, $\alpha = 7 \times 10^{-3}$ and no photoevaporation, the disk is dissipated in 12.6 Myr. A photoevaporation rate of $\dot{M}_w = 1.425 \times 10^{-9}$ $M_\odot$ yr^{-1} is therefore required to reduce the dissipation time to 6 Myr. In fact, we found that for $r \gtrsim 15$ AU, irradiation increases significantly (*i.e.* by a factor up to ∼4) the mean turbulent viscosity $\langle \nu \rangle = \int_{-H}^{+H} \rho \nu \, dz / \Sigma$, where ν is computed in the frame of the Shakura and Sunyaev's (1973) formalism: $\nu = \alpha c_s^2 / \Omega$ (Ω being the Kepler's frequency and c_s the speed of sound). For an ideal gas: $c_s^2 = P/\rho \propto T$; at relatively large distances for the star (*i.e.* beyond ∼15–20 AU), the radiative flux rises the temperature in the thickness of the disk, leading to the observed increase in $\langle \nu \rangle$, and consequently to the shorter dissipation times. We stress that this fact is consistent with the larger observed ν_{acc} (see Fig. 4a). Table 1 summarizes the obtained lifetimes for initial masses of 1, 3 and 10 MMSN, and α parameter ranging between 10^{-3} and 10^{-2}. As we can see, for simulations corresponding to α higher than $\sim 6 \times 10^{-3}$ the lifetimes are compatible with observations. Obviously, this does not mean that photoevaporation does not exist (see for instance Owen, 2006) but rather that our improved models are in better agreement with astronomical observations, and do not required systematically large assumed photoevaporation rates. As it can be noticed in Table 1, the computed lifetimes seem to depend slightly on the initial mass, this behavior is due to the chosen criterion for stopping the simulation (*i.e.* the total mass decreased to 1% of its initial value): for the largest initial masses the mass accretion rates are the highest causing a criterion satisfied earlier. Finally, the inner gap radius has been reduced from 2 AU to 0.55 AU. In order to ease comparisons with previous works, all our reference disk structures have been computed between 0.50 and 50 AU (determined the edge of the KB around ∼50 AU Allen et al., 2001). The inner boundary of 0.55 AU has been chosen instead of 0.50 AU so that to avoid numerical difficulties caused by the finite-differences calculation of derivatives with respect to r. As it could be expected (see Fig. 3d), the distances r_p are in average lower than those computed in the previous case where $r_{gap} = 2$ AU, this is clearly the consequence of a stronger light absorption along the line of sight: since the difference $r_p - r_{gap}$ (see Fig. 2) is larger, the flux of photons received by a given aggregate becomes fainter, thus producing weaker photophoretic and radiative forces. Remarkably, dust particles with radius larger than 10^{-4} m can be found up to 20–30 AU from the proto-Sun and consequently could participate to the formation of icy planetesimals within the KB.

In Table 2 we have gathered the maximum distances reached by dust aggregates when the initial mass of the Nebula ranges between 1 MMSN and 10 MMSN. Clearly, a low mass Nebula favors large distances for small particles. We would like to stress that this is not only because small particles ($\sim 10^{-4}$–10^{-5} m) get to outer regions that larger aggregates could not be found in cometary material: indeed aggregation/coagulation processes could form relatively big grains using small ones as building blocks (Güttler et al., 2010; Zsom et al., 2010; Blum et al., 2014). Alternatively, the opposite process could occur: fragmentation could produce small particles from relatively large ones.

We have also performed irradiated disk simulations with $\alpha = 10^{-2}$ and $\alpha = 10^{-3}$; limiting – when necessary – the age to 6 Myr, by adjusting the photoevaporation parameter. The results were essentially similar to those obtained at $\alpha = 7 \times 10^{-3}$ (displayed in Table 2).

The inner limit of the disk structure (*i.e.* the above mentioned 0.5 AU) may appear somewhat arbitrary. Nonetheless, even in

[2] Zero Age Main Sequence.

Retour à la table des matières : p. v

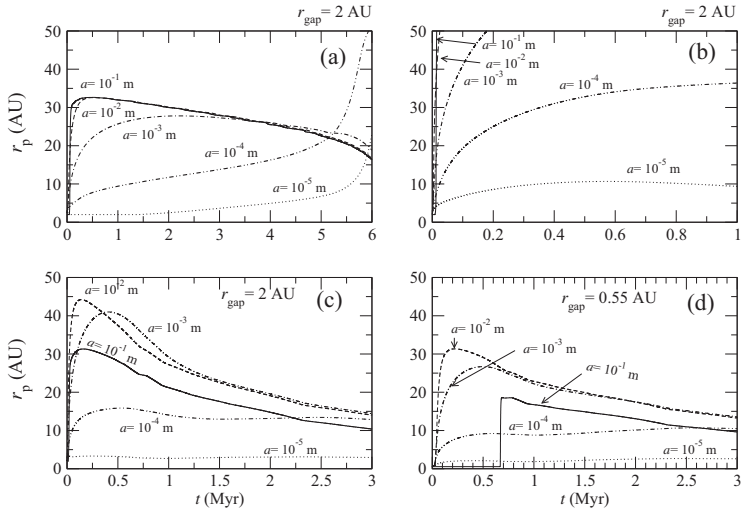

Fig. 3. In this figure we have displayed the heliocentric distance r_p (AU) reached by aggregates of differents radius a ranging from 10^{-5} m to 10^{-1} m, as a function of time t (Myr). In all represented computations, the initial mass of the simulated proto-solar Nebula has been fixed to 3 MMSN and the turbulent viscosity parameter is $\alpha = 7 \times 10^{-3}$. (a) The disk structure is not irradiated and the Sun luminosity is constant, fixed at the ZAMS value. An inner gap with a radius of 2 AU is assumed to occupy the central part of the disk. (b) The disk is still not irradiated, the Nebula structure is the same as in panel (a). However, time-dependent effective temperature $T_{\rm eff}(t)$ and the luminosity $L_\star(t)$ have been used for the photophoretic and radiative forces estimations. (c) The disk evolution is simulated taking into account the irradiation by the star evolving along its PMS track, the forces acting upon the particles are computed consistently, an inner gap of 2 AU is still assumed. (d) The same simulation as the one represented in panel (c) but the hypothesis of the existence of an inner gap has been abandoned; the inner gap radius of 0.55 AU corresponds practically to a very reduced gap.

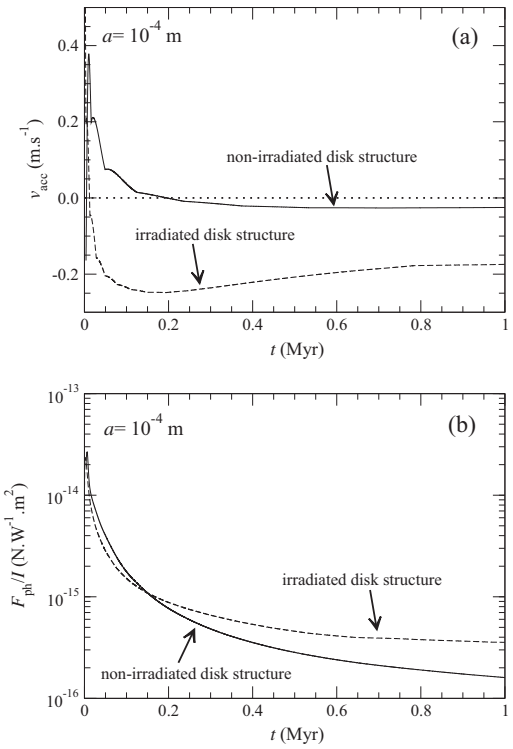

Fig. 4. (a) The gas accretion velocity $v_{\rm acc}$ (see Eq. (14)) undergone by a dust particle along its "trajectory" through the disk mid-plane. Two cases are distinguished: a non-irradiated disk (solid line), an irradiated disk (dashed line). (b) The photophoretic force F_{ph} divided by the radiative flux I as it is seen by a test particle during its migration in the Nebula. Both examples correspond to a particle size of $a = 10^{-4}$ m, a Nebula initial mass of 3 MMSN and a turbulent viscosity parameter $\alpha = 7 \times 10^{-3}$.

Table 1
Lifetimes (in Myr) of the disk model as a function of the initial mass (in MMSN) and the turbulent mixing parameter α. All these simulations were performed without photoevaporation but they include the time-dependent irradiation by the PMS Sun.

α						
Mass (in MMSN)	10^{-3}	2×10^{-3}	4×10^{-3}	6×10^{-3}	8×10^{-3}	10^{-2}
1	16.4	10.7	7.9	5.8	4.0	3.0
3	15.7	10.4	7.7	5.3	3.7	2.8
10	15.1	10.0	7.4	4.8	3.3	2.5

Table 2
Maximum heliocentric distances (in AU) reached by aggregates of radius a ranging between 10^{-1} and 10^{-5} m. The disk is irradiated and $\alpha = 7 \times 10^{-3}$.

a (m)	10^{-1}	10^{-2}	10^{-3}	10^{-4}	10^{-5}
1 MMSN	15	27.5	28	23	50
3 MMSN	19	32	27	10	5
10 MMSN	17	30.5	19	8	2

the case of T Tauri stars which have not developed an extended inner hole (*i.e.* up to distances of several AU) the accretion disk is truncated in the vicinity of the star. Indeed, T Tauri stars are known to be magnetically very active; *e.g.*, Zeeman broadening measurements have revealed surface field in the range of 1–3 kG. Such strong magnetic fields are at the origin of "jets" that eject material to the interstellar medium, and also produce a magnetospheric accretion in which the disk matter is channeled onto the star along magnetic field lines (Ferreira et al., 2006; Bouvier et al., 2007) out of the mid-plane, leaving it optically thin. Although, this quantity is the subject of star-to-star substantial variations, the radius of this magnetospheric accretion zone can be reasonably estimated to be around ∼0.1 AU. We, then, computed a specific set of evolving disk structures using $r_{\rm gap} = 0.10$ AU. Keeping other parameters unchanged compared to those used for the simulations reported in Fig. 3d, we obtained only aggregates with radius of $a = 10^{-3}$ m

Retour à la table des matières : p. v

and $a = 10^{-2}$ m reaching heliocentric distances slightly larger than ~6 AU while the other dust particles remain closer to the star within 5 AU. These outputs shows, one more time, that the existence of an inner hole, optically thin and having an expansion beyond ~0.5 AU, is a determining factor for the efficiency of the photophoretic transport of dust in protoplanetary disks.

4. Discussion

4.1. The kinetics of the grains annealing in an irradiated disk

The problem of the existence of crystals in comets raises naturally the question of the kinetics of thermal annealing of silicate grains that originate from the interstellar medium. Indeed, this lattice structure transformation cannot be instantaneous; in addition, one can wonder if grains at relatively low temperature could be annealed in timescale compatible with disk lifetime. If the process could occur at large heliocentric distances with a duration $\lesssim$6 Myr, then the transport of grain from regions in the vicinity of the proto-Sun, to larger distances would be no longer needed. Lenzuni et al. (1995) gave the typical duration t for converting an amorphous domain to a crystalline domain: $t = \nu^{-1} e^{D/k_B T_a}$, where ν is the characteristic vibrational frequency of silicate, D is the activation energy of repositioning atoms within the lattice structure, T_a the temperature and k_B the Boltzmann's constant. Lenzuni et al. (1995) gave also the typical values $\nu \sim 2.5 \times 10^{13}$ s^{-1} and $D/k_B \sim 41{,}000$ K, which leads to $t \sim 5$ Myr for $T_a = 645$ K and 23 Myr for $T_a = 630$ K. We have checked in our models of irradiated disks that the mid-plane temperature T_m remains always below ~100 K disk life-long for distances larger than a few AU. As a consequence, amorphous grains cannot be annealed, by gas temperature, at distances compatible with comets formation during the disk lifetime, even if the disk is irradiated. Concerning the production of crystals by vaporization/recondensation, the temperatures required to vaporized silicates (*i.e.* $T \leqslant 1500$ K) are never reached in our models in the external Solar System. As a consequence, the remaining possibility is an evaporation/condensation sequence in high temperature regions – *i.e.* those close to the proto-Sun – during the early phases of the disk evolution.

4.2. The influence of monomers density

In this work, each dust particle is an agglomerate of smaller grains. In real accretion disks, these "elementary grains" may show a distribution in size, shape and composition. Here, like in previous ones, the aggregates have been represented by a radius (*i.e.* a typical size), a thermal conductivity (whose influence is discussed in Section 4.3) and a density that determines the mass of each aggregate. This density is a function of the assumed aggregate porosity and of the average density of monomers. Blum and Schräpler (2004) conducted laboratory experiments consisting of random ballistic deposition of monodisperse SiO_2 spheres with 1.5 µm diameter and found an – already mentioned – volume filling factor of 0.15. More recently, Zsom et al. (2010) using sophisticated Monte-Carlo simulations, based on a detailed modelization of collisions, derived filling factors around 0.30. This leads to a higher dust particle density, of the order of 1000 kg m^{-3} rather than 500 kg m^{-3} previously employed. By replacing 500 kg m^{-3} with 1000 kg m^{-3}, for a non-irradiated model of an initial mass of 3 MMSN and evolving for 6 Myr (this model is comparable to the one plotted in Fig. 3a which has been computed taking 500 kg m^{-3}) we obtained a maximum distance reached by aggregates that decreases, due to the larger inertia of particles. Not surprisingly, a dependence with respect to the dust particle size has been found: the larger the particle is (*i.e.* large radius a), and the lower is the maximum distance reached. For instance, for radii a in the range 10^{-1}–10^{-2} m the distance reduction is of the order of 15%, while it falls to ~10% for $a = 10^{-3}$ m, and becomes negligible for $a = 10^{-5}$ m. Compared to the other sources of uncertainties, particularly those regarding the actual thermal conductivity of aggregates, the effect of dust monomer density does not appear to be the dominant one (*i.e.* when replacing our fiducial value of 500 kg m^{-3} by 1000 kg m^{-3}).

4.3. The influence of thermal conductivity and porosity of aggregates

The thermal conductivity of aggregates λ_p remains poorly constrained, and could depend on many parameters: the temperature, the exact nature of the bulk material, the porosity, the shape and the size distribution of the monomers, the number and the size of contact areas between monomers, the lattice structure of the monomers, etc. The heat conductivity is a crucial quantity in the context of photophoresis: high values should diminish the effect of photophoresis because they facilitate the uniformization of the temperature over the "surface" of each particle. In contrast to this, if aggregates are bad thermal conductors the photophoretic effect is expected to be very efficient. So far, we used the value $\lambda_p = 10^{-3}$ W m^{-1} K^{-1} which is the same adopted by Mousis et al. (2007) and Moudens et al. (2011); although this is an extreme value, it has been adopted by these authors without any well referenced justification. Surprisingly, Krauss et al. (2007) (who have several authors in common with Mousis et al., 2007; Moudens et al., 2011) have worked with $\lambda_p = 10^{-2}$ W m^{-1} K^{-1} and have suggested that the precise influence of λ_p should be explored. The value used by Krauss et al. (2007) comes from Presley and Christensen (1997) who have not reported value as low as 10^{-3} W m^{-1} K^{-1} for relevant materials. In addition, von Borstel and Blum (2012), who found thermal conductivities around 10^{-1} W m^{-1} K^{-1}, mentioned that results published by Moudens et al. (2011) should be quantitatively affected by a higher heat conductivity. For all these reasons, detailed investigations about the importance of thermal conductivity are needed.

Krause et al. (2011) conducted laboratory experiments with aggregate analogs composed by monodisperse spherical monomers. Their samples of 1.5 µm-sized SiO_2 particles were prepared following several specific protocoles which led to various values of the porosity. This way, Krause et al. (2011) obtained a range of thermal conductivity that lies between 0.002 and 0.02 W m^{-1} K^{-1}. Gundlach and Blum (2012), in their work on the heat transport in porous surface dust layers, found values compatible with such a range. We should notice that the lowest value of Gundlach and Blum (2012), *i.e.* 0.002 W m^{-1} K^{-1}, is close the one that we have used. For an irradiated disk model of 3 MMSN computed with $\alpha = 7 \times 10^{-3}$, the use of $\lambda_p = 0.02$ W m^{-1} K^{-1} yields to a maximum heliocentric distance reached by particles around 10 AU (corresponding to $a = 10^{-2}$ m). This result has to be compared to what it is depicted in Fig. 3d and thus illustrates the high sensitivity of photophoresis with respect to thermal conductivity.

Krause et al. (2011) were able to derive an empirical law providing the thermal conductivity of their analogs as a function of the volume filling factor, or equivalently of the porosity Π. This relationship can be expressed as

$$\lambda_p = 0.000514 \exp(7.91\,(1 - \Pi)) \qquad (15)$$

(in W m^{-1} K^{-1}). Straightforwardly, the density of the composite material can be written $\rho_p = (1 - \Pi)\,\rho_{\text{olivine}} + \Pi\,\rho_{\text{gas}}$, where ρ_{olivine} represents the density of monomers of non-porous olivine, we have found $\rho_{\text{olivine}} \sim 4 \times 10^3$ kg m^{-3} (Kogel et al., 2006), ρ_{gas} is the local density of the gas. In summary, Eq. (15) together with the above

Retour à la table des matières : p. v

mentioned expression of ρ_p offers the possibility of an exploration of the combined effects of thermal conductivity and of the density, for several values of the porosity. Fig. 5 displays results of two of such simulations performed respectively with $\Pi = 0.90$ and $\Pi = 0.50$. The work of Zsom et al. (2010), who found $\Pi \sim 0.60$ in the mid-plan at 1 AU, favors the latter value. With the set of physical inputs involved there, *i.e.* an irradiated disk computed from an initial mass of 3 MMSN, using a turbulent viscosity parameter $\alpha = 7 \times 10^{-3}$ and with a small (*i.e.* 0.55 AU in radius) assumed inner gap, the aggregates with $\Pi = 90\%$ are transported, to probable comets formation zone, but a relatively strong gradient in porosity is obtained. Only the smallest aggregates did not exceed 5 AU (see Fig. 5a). In this frame, a "mild porosity" around 50% should annihilate any substantial photophoretic driven migration (see Fig. 5b). Of course, if one reintroduces a hypothesized larger inner gap, optically thin, a lower porosity would be permitted. In actual accretion disk, the ambient gas fills the empty spaces within the aggregates. The thermal conductivity of the gas, which depends on the local thermodynamic conditions, should affect the effective conductivity of the whole aggregate. Because the presence of gases would have contributed to the measured conductivity, Krause et al. (2011) have operated under high vacuum conditions, setting the pressure within their chamber around 10^{-5} mbar (*i.e.* around 10^{-3} Pa). Then, their measurements have not to be taken at face, but rather have to be corrected by the effect of the gas incorporated in the porous structures. In the context of ceramic materials, Russell (1935) has derived the effective thermal conductivity of a dry porous material taking into account the properties of its component gas and of the solid. A uniform distribution of pores in a cubic lattice and a parallel heat flow are assumed, the convection across the pores is neglected. Russell found

$$\frac{\lambda_s}{\lambda_p} = 1 - \Pi^{1/3} + \frac{\Pi^{1/3}}{(\lambda_{gas}/\lambda_s)\Pi^{2/3} + 1 - \Pi^{2/3}} \quad (16)$$

In this formalism λ_p is the conductivity of the composite material (here the aggregate), λ_{gas} and λ_s respectively the gas conductivity and the one of the solid (here olivine). Unfortunately, we found that Eq. (16) is not in agreement with Krause et al. (2011) results, even when the contribution of gas is neglected. Nevertheless, we have computed the gas heat conductivity along the particles tracks, we obtained values around a few 10^{-2} W m^{-1} K^{-1}, as a consequence the effective conductivity of aggregates for porosity as high as 90% should be close to $\sim 10^{-2}$ W m^{-1} K^{-1} and the photophoretic migration through the disk mid-plane should be considerably reduced.

Another aspect of the issue discussed here relates to the thermal conductivity of the bulk material of the dust particles. Krause et al. (2011) have employed amorphous silica in their experiments. In the case of solid vitreous SiO_2, the heat conductivity remains in the interval 0.85–1.30 W m^{-1} K^{-1} depending on the temperature (Haynes, 2015). However, actual aggregates are very likely mainly made of olivine. The thermal conductivity of olivine could be estimated by mean of Eq. (12) published in the article by Xu et al. (2004) and parameters values provided therein. By doing this, we found a conductivity around 3.7 W m^{-1} K^{-1}. Thus, aggregates made of olivine could be expected to exhibit a higher heat conductivity than those built from amorphous monomers of SiO_2.

All these arguments, together with the properties of the turbulence do not support far migrations of dust particles, but favor transport by photophoresis limited to maximum distances between ~5 AU and ~30 AU accompanied by several segregation processes on porosity, chemical nature and size; processes which will be difficult to disentangle.

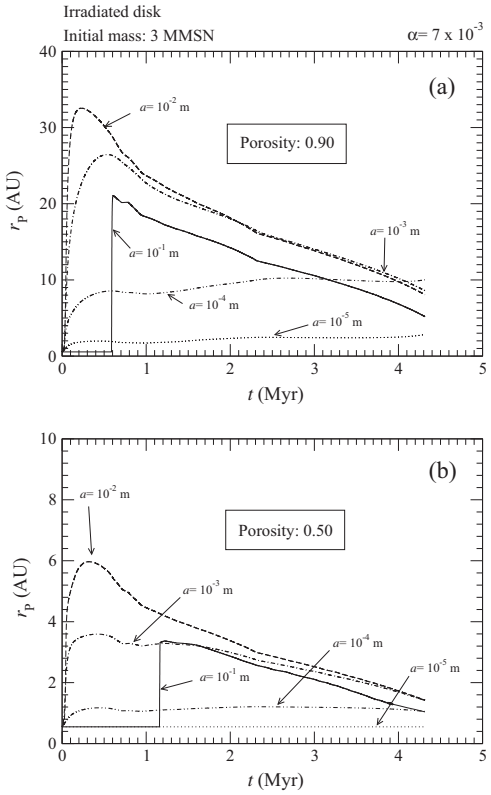

Fig. 5. (a) Heliocentric distances r_p reached by particles of various sizes a, in an irradiated disk similar to one used in Fig. 3(d); the thermal conductivity has been given by Eq. (15) for a porosity $\Pi = 0.90$, the density of aggregates has been estimated consistently. (b) The same as in panel (a), but taking $\Pi = 0.50$.

The emissivity ϵ is also a thermodynamic parameter. We have checked that it has no noticeable influence on the maximum heliocentric distances reached by grains. Decreasing the value of ϵ (we made test with $\epsilon = 0.5$ and $\epsilon = 0.1$) increases by a tiny amount the efficiency of photophoresis.

If thermal effects reduce or impede dust migration driven by photophoresis in the disk mid-plane, we could examine whether more favorable conditions may be found within other zones of the Nebula. This is what it will be discussed in Section 4.5.

4.4. The influence of the opacity

As it can be seen in Fig. 3, regardless of considered scenario, the velocity of migration of "test particles" strongly depends on their size. The tendency is that small particles move slower than bigger ones. For the computation of the trajectories, the employed prescription – also used in previous published works – assumes the existence of the dust-free space between the inner boundary of the disk and the position of the "test particles" r_p (see Fig. 2). This simplifying hypothesis allows the use of the opacity law given by Eq. (9) that accounts only for the gas Rayleigh's scattering, which is valid in the absence of dust grains. In observed accretion disk, as in the ISM, the populations of grains are not monodisperse but rather follow a size distribution (see for instance Apai and Lauretta, 2010 and references therein). As it has been noticed, the transport of the largest grains is faster than that of small particles, then some amount of small aggregates should remain along the line of sight between the Sun and the largest dust grains.

Retour à la table des matières : p. v

Unfortunately, the small grains are the most numerous as the distribution of the grains size is believed to follow a powerlaw a^{-n} with $n \sim 3$, and consequently they produce a dominant contribution to the opacity. Indeed, in Fig. 6 one can compare the opacity laws (Cuzzi et al., 2014) resulting from an aggregates sizes distribution spanning from 1 to 10 μm and another with radii between 1 μm and 1 cm. Clearly, the population dominated by the smallest particles produces the highest opacity.

For our purpose, the relevant distribution in size is the one with radii between 1 μm and 1 cm. As we can see in Fig. 6 the corresponding opacity lies between 10^{-2} and 2×10^{-1} cm^2 g^{-1}. These values have to be compared with an estimation made using Eq. (9). Using this latter formula, we obtained an opacity of the order of $\sim 1.4 \times 10^{-4}$ cm^2 g^{-1} for an effective temperature of the proto-Sun around 4400 K. It demonstrates that the opacity of the gas alone is order of magnitudes lower than what we find if a residual amount of dust is left. As a conclusion, if large particles (for instance with a radius $a \sim 1$ cm) are pushed away by some transport mechanism, then the small ones remaining on the optical path have an effect on the opacity strong enough to annihilate any force produced by photophoresis and/or radiation pressure. Hence, two alternatives would be possible: (1) all the grains are displaced at the same velocity, which is that of the smallest aggregates, or (2) the biggest particles are transported over a fraction of AU, the residual population of smaller grains coagulate and re-establish a distribution of sizes containing a fraction of large dusts but with a global mass of solids diminished. The process could then repeat and extend itself, tending to a dust-free gas in the disk mid-plane.

Concerning the first scenario, the comets formation zone could be provided in crystal only if the smallest aggregates reach a far enough distance during the lifetime of the protoplanetary disk. In our approach, this could occur in the case of a non-irradiated disk (see Fig. 3a) which is not the most realistic model. Unfortunately, when the irradiation is taken into account, particles with radius as small as 10^{-5} m seem to stay at few AU from the Sun. In this situation, the second scenario could be invoked. In that case, the coagulation process has to be fast enough; such a scenario looks plausible since Ormel et al. (2007) found that aggregates can grow to radii up to ~10 cm in a few thousand years. The depletion in solids created locally by the short-range migration of the biggest grains yields to a more transparent medium by decreasing the opacity (see dash-dotted curve in Fig. 6). The proposed mechanism, which differs from that described in studies like Krauss and Wurm (2005) – who did not take into account the feedback on opacity – has to be studied in details in future researches. In-depth investigations of this scenario could decide if the net effect lets the grains piling up at the inner edge of the disk or if this solid material could be efficiently swept out from inner regions. The answer is not straightforward. For instance, we have noticed that a high porosity of aggregates (which favors the photophoresis by producing low thermal conductivities) is an unfavorable factor by enhancing the opacity. In addition, to crown it all, the thermal conductivity of grains seems to depend on their size (see Presley and Christensen, 1997). Beside these effects, in future investigations, one has to include coagulation/fragmentation and the detailed evolution of the aggregates population over time, together with their influence on the opacity, has to be consistently followed.

Throughout this paragraph, the physical processes were assumed to take place in the disk plane of symmetry, which is supposed to embed the majority of dust grains. Of course, the mid-plane of the disk is also the optically thickest region and the material becomes progressively optically thinner and thinner moving outwards. For instance, we have estimated the optical depth τ_{10} at ~10 AU at the "external surface", and we have made comparison with its mid-plane counterpart. Using (Cuzzi et al., 2014) opacities

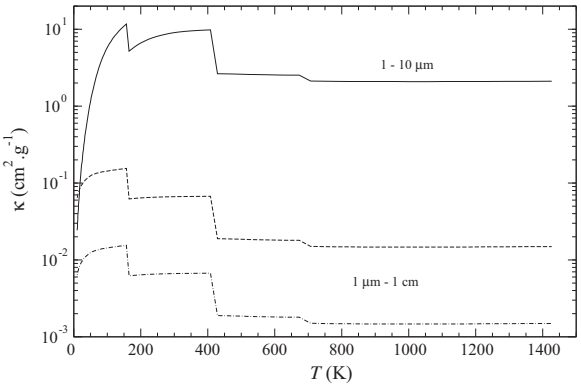

Fig. 6. The opacity κ of a gas–dust mixture relevant for a protoplanetary disk (Cuzzi et al., 2014). A dust-to-gas mass ratio of 0.014 and a power law distribution in size are assumed for all curves. Solid line: the range of sizes spans from 1 to 10 μm, dashed line: the interval of radii is 1 μm to 1 cm. The dash-dotted curve corresponds to a 1 μm to 1 cm but with a total mass fraction of solids divided by ten compared to 0.014.

(that include the effect of dust) we got τ_{10} ranging between ~35 and more than 100 at the mid-plane, while τ_{10} never exceeded ~0.6 during the same disk lifetime of 6 Myr, when evaluated at the "external surface". Then, even if the disk mid-plane stays very opaque, transport induced by stellar photon flux could occur through other optically thinner regions.

4.5. About a possible off mid-plane transport

As mentioned above, we have mainly assumed that particles were transported through the disk mid-plane. In real accretion disks, dust particles are not confined in the mid-plane, but they rather explore the entire thickness of the disk between the mid-plane and the external surface (see Fig. 2). As the surface is less dense and cooler compared to that at the mid-plane, we can expect quite different drift velocities. In fact, a less dense matter is more transparent and thus favors a larger effect of the radiation pressure. Concerning the photophoretic force, the net effect is more uncertain: a less opaque gas should cause an easier heating of particles (that favors the photophoretic effect, if this heating is restricted to one "side" of each particle) while the scarcity of molecules available for photophoresis would be a limiting factor. Throughout this paragraph, one has to keep in mind that the dust grains are probably much more abundant in the disk mid-plane than at the external surface, for instance in the steady-state regime the vertical distribution of grains follows a gaussian law (see for instance Birnstiel, 2011). Nonetheless, the determination of the actual vertical distribution in our context is, by far, beyond the primarily scope of the present paper.

Concerning the transport of particles at the external surface of the disk, one can argue that irradiation by the stellar wind and/or by energetic galactic cosmic rays, could damage their lattice and subsequently produces an irradiation-induced amorphization (see for instance Famá et al. (2010) for a discussion concerning the water ice or Le Guillou et al. (2013) for an experimental study of the effect of electron irradiation of kerogens). Nevertheless, the small cross-section of dust particles could prevent this effect. In future works, a more in depth discussion is needed about this aspect.

For the sake of simplicity, the radiation attenuation will be computed as if the external surface was flat. The adopted disk model is a 3 MMSN irradiated disk, computed with $\alpha = 7 \times 10^{-3}$. Concerning the computation of the photophoretic force we keep

Retour à la table des matières : p. v

our "standard" value for the involved parameters; particularly, the thermal conductivity λ_p is set to 10^{-3} W m^{-1} K^{-1}. As the accretion velocity v_{acc} (see Eq. (14)) is a vertically averaged quantity, we did not compute the trajectory of aggregates by using Eq. (13) that requires a local expression of v_{acc}, relevant for the considered surface. We then calculated only the drift velocity v_{drift} and found very high values. They are much higher than v_{acc} (to be considered as a typical value) and even higher than the speed of sound. This large velocity makes no physical sense by itself, this is the reason why we have searched what caused such very high values. To do so, we have computed the quantities contributing to v_{drift} (*i.e.* $F_{res}, F_{rad}, \ldots$) at all points along the upper surface layer; this, for two disk ages of the early evolution. All these quantities were computed using the local pressure and temperature (*i.e.* those at the external surface). In Fig. 7 we have represented the velocity v_{drift} for the adopted initial disk model (corresponding age: 0.00 Myr) and at the time when about 10% of the initial mass has been accreted (*i.e.* age: $\simeq 1.3 \times 10^{-2}$ Myr). The choice of these two ages is relevant for our purpose since they will bracket the early evolution of the system. The aggregate radius a has been fixed to 10^{-3} m for these simulations. As can be seen in Fig. 7, at $t = 1.3 \times 10^{-2}$ Myr and $r \sim 1$ AU the velocity v_{drift} at the external surface (see Fig. 7b) is roughly 4 orders of magnitude larger than the corresponding value at the mid-plane (see Fig. 7a). To go further, we have plotted the forces $|F_{res}|$ (in general $F_{res} < 0$ because P decreases when r increases), F_{rad} and F_{ph} (see respectively Eqs. (5), (6) and (3)) together with the coupling time of particles with gas (see Eq. (11)) in Fig. 8. The same disk model is employed, all these quantities have been computed respectively at the external surface (right hand side of Fig. 8) and at the disk mid-plane (left hand side of Fig. 8); and respectively for $t = 0.0$ Myr and $t = 1.3 \times 10^{-2}$ Myr. It can be noticed that at mid-plane the force of residual gravity $|F_{res}|$ is the largest at the beginning of the disk evolution. After a few times, it turns out that the photophoretic force F_{ph} dominates other contributions. At the external surface, the force due to the residual gravity is lower than at the disk mid-plane; all the three forces have a similar order of magnitude (*i.e.* $\sim 10^{-11}$ N) although the radiative pressure force dominates slightly the others. The major difference between situations at external surface and mid-plane consists in the role played by F_{rad} at the surface. Table 3 gives precise value of forces at 2 AU from the proto-Sun. We can remark that the photophoretic force does not undergo a large change between the two locations: the effect of the higher radiative flux at the surface seems to be compensated by the increasing scarcity of gas molecules contributing to the photophoresis. Finally, the global resulting force (*i.e.* given by the sum $F_{res} + F_{rad} + F_{ph}$) appears to be not so different at disk mid-plane and at external surface (*i.e.* it ranges between $\sim 10^{-11}$–10^{-10} for our test particle). As a consequence, the quantitatively significant difference between mid-plane and external surface comes from factor of 10^4 in gas-grain coupling time τ (see Fig. 8 panels (g) and (h) for $r \sim 2$ AU). This ratio of 4 orders of magnitude is due to local thermodynamic conditions. We recall that $\tau \propto C_c/\eta$ (see Eqs. (11) and (12)) in a low density environment. Moreover, in low density regions η becomes very low implying large $1/\eta$ values, while the Knudsen's number K_n tends to be very large, and for $K_n \gg 1$ we have $C_c \simeq 1.701\, K_n$, so that C_c also increases. The net result is a strong rise of τ. The physical meaning of these large value of τ is a weak coupling between the aggregates and the gas.

In summary, at the external boundary of the dense region of the protoplanetary disk the photophoretic force may not be the dominant force, particularly if the thermal conductivity λ_p is much higher than 10^{-3} W m^{-1} K^{-1}. The fact that the aggregates particles are weakly coupled to the gas allows any small force to generate a transport process. In such circumstances, particles can sediment, be pushed outward by stellar wind bursts, taken away by photoevaporation, etc. A study of such transport processes is far beyond the scope of the present paper and required a minimum modelization of the disk's "atmosphere".

5. Conclusion and perspectives

The 1+1D disk model used here implements the classical α-viscosity prescription that allows a description of the physical evolution of the disk as it undergoes mass and angular momentum transport. To this standard approach, we have added time-dependent irradiation which is consistent with the evolution of the proto-Sun along the Pre-Main Sequence phase. Since this phase corresponds to the T Tauri period of our star, which is known to be contemporary of the existence of a circumstellar dusty and gaseous accretion disk, our model represents a noticeable improvement of the proto-solar Nebula modeling. This is particularly true in our context, in which we examine the influence of proto-Sun radiation on the transport of dust driven by photophoresis.

By adopting the same prescription used in previous works for the opacity of the gas, we have found that the high luminosity of the Sun considered in its T Tauri phase favors the migration of dust grains to the outer parts of the protoplanetary disk. However, the effect is not as high as if the irradiation would not change the disk properties. Indeed, the irradiation enhances the computed turbulent viscosity which in turn increases the accretion velocity. Consequently, the particles are slowed down whereas the disk lifetime is reduced. This latter effect reduces the need for an *ad hoc* photoevaporation in order to get ages in agreement with astronomical observations. Unfortunately, since the dust particles have migration velocities that depend on their size, a trail of small grains should be left along the line of sight. The smallest aggregates show an important contribution to the gas–dust opacity. This leads to a strong extinction which could eliminate the photophoretic effect. This point is one of our most important results and, models involving a consistent treatment of the opacity as a function of dust content, are highly desirable. Noticeably, external optically thin disk regions could provide an environment favorable to stellar photons driven transport processes. In such a case, the net quantity of dust delivered to the comets formation zone could not ba large enough to explain the observations, because of the vertical stratification of grain distribution.

Besides this, using gas temperature distribution provided by our model, we confirm that amorphous grains cannot be annealed into regions beyond ~1–2 AU, due to arguments based on phase transition kinetics at gas temperature. More importantly, we have identified the heat conductivity of aggregates as a crucial parameter. Using realistic estimations and published experimental results for the thermal conductivity, we have shown that the photophoretic strength can be considerably reduced and could yield to situations in which photophoretic migration through the mid-plane could be marginal even if the disk is irradiated by a bright PMS star.

Laboratory experimentations conducted by van Eymeren and Wurm (2012) on ice aggregates, trapped in a cell under the combined effects of photophoresis and thermophoresis, show that rotation induced by photophoretic forces does not change the strength of photophoresis force, but ignores the influence of a turbulent flow. Krauss et al. (2007) and Moudens et al. (2011) have discussed, respectively the possible effects of the turbulence and of the particles rotation. However, they considered turbulence and rotation as independent processes. Krauss et al. (2007), who discussed turbulence as a factor affecting the mean radial motion of dusts, concluded that turbulence essentially does not prevent

Retour à la table des matières : p. v

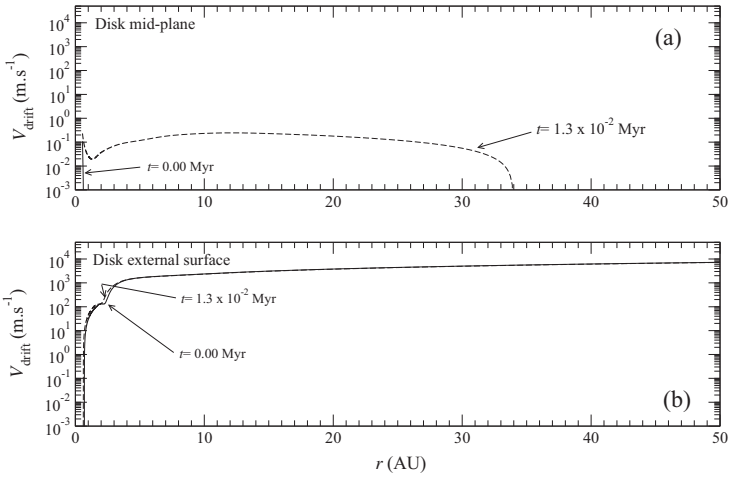

Fig. 7. The drift velocity computed: (a) in the disk mid-plane, (b) at the external surface, for the initial disk model (i.e. at $t = 0.00$ Myr) represented by a solid line and at $t = 1.3 \times 10^{-2}$ Myr (corresponding to a disk mass of about ∼90% of the initial mass) shown by a dashed line, in this case the lines are almost merged. All these computation were done assuming a particle radius of 10^{-3} m. For these tests the adopted thermal conductivity is our "standard" value, i.e. 10^{-3} W m^{-1} K^{-1}.

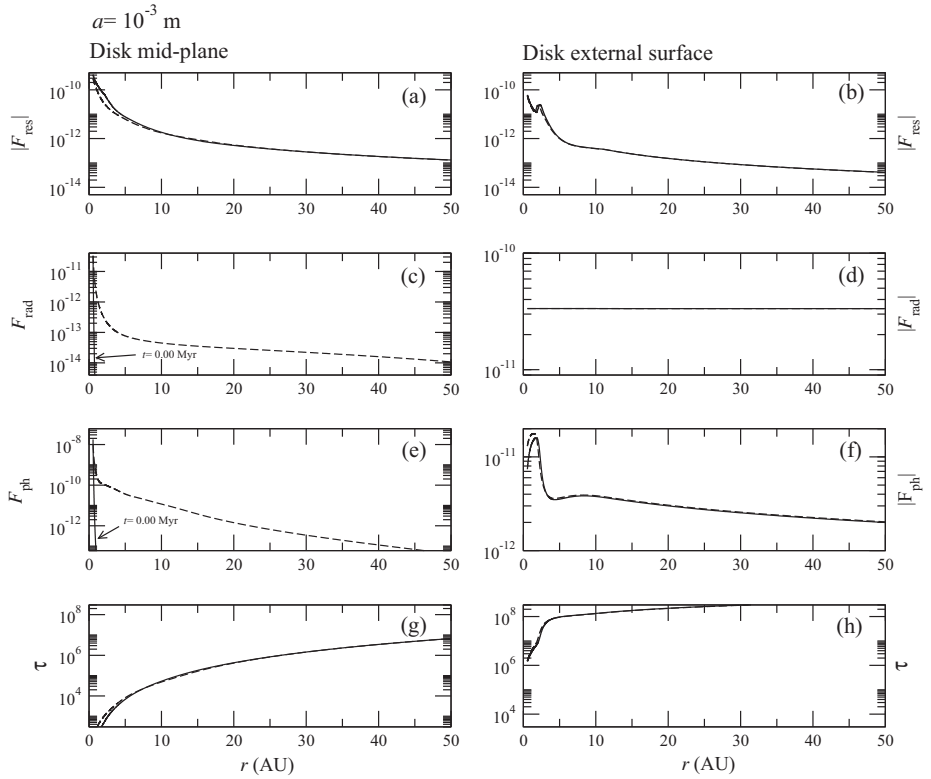

Fig. 8. Comparison of forces and gas-coupling time at mid-plane and at the external surface. In all panels a solid line has been used to represent quantities related to $t = 0.0$ Myr while a dashed one has been drawn for $t = 1.3 \times 10^{-2}$ Myr. The assumed particle radius is in all cases 10^{-3} m. In all panels, except in (c) and (e) the two curves merge each other. For these computations we kept the thermal conductivity of aggregates monomers at our "standard" value, *i.e.* 10^{-3} W m^{-1} K^{-1}.

the outward migration. Moudens et al. (2011) have looked to the influence of rotation of particles on themselves, induced for instance by particle to particle collisions. We have to keep in mind that dusts are embedded in a gaseous environment, to which they are strongly coupled (at least in the mid-plane). Following a simple picture, a turbulent flow is made of a cascade of eddies, with a distribution of sizes and lifetimes. In such a flow, aggregates can meet eddies with rotational motion in a plane that contains the radial direction. In this configuration, if the thermal relaxation timescale of the particle is larger than the overturning timescale of the turbulent eddy, the temperature distribution at the surface of the particle could be uniformized, leading to the removal of

Retour à la table des matières : p. v

Table 3
Forces (in newtons) acting on a particle of radius 10^{-3} m located at 2 AU from the central star. The notation $x \cdot yz \times 10^{-n} = x \cdot yz(-n)$ is used. The times t_0 and t_1 are respectively the initial time and $t = 1.3 \times 10^{-2}$ Myr.

	$\lvert F_{\rm res}\rvert$		$F_{\rm rad}$		$F_{\rm ph}$	
	t_0	t_1	t_0	t_1	t_0	t_1
Mid-plane	6.8 (−11)	3.0 (−11)	1.3 (−18)	3.2 (−13)	1.6 (−16)	1.1 (−10)
Ext. surface	1.6 (−11)	2.3 (−11)	3.3 (−11)	3.4 (−11)	1.5 (−11)	1.2 (−11)

any photophoretic force. The global effect on dust migration through the disk depends on the intrinsic properties of dust (thermal properties and aerodynamics drag) and on statistical properties of the involved turbulent flow. The net result will be a convolution of the statistical distribution of grains properties (bulk material nature, porosity, size, etc.) and of the properties of the cascade of turbulent eddies.

In a first approach, the influence of the turbulence on dust trajectories could also be investigated using a particle-tracking technics as already employed in other contexts by Supulver and Lin (2000) or Ciesla and Sandford (2012). Thanks to this method, applied in a 2D or better a 3D geometry, we could follow the trajectories of particles within the disk and even those that could be launched upwards, pushed outward by the radiation pressure and possibly fall back onto the Nebula at different locations. A similar scenario has been already studied by Wurm and Haack (2009) in their investigations concerning the outward transport of CAIs during FU-Orionis events. The vertical transport of grains, caused by convection and thermophoresis could be also included together with the existence of a quiet "dead zone" in which the turbulent activity should be very low.

Acknowledgments

We acknowledge Ulysse Marboeuf, together with James Owen and Philippe Rousselot for scientific discussion. We also warmly thank Pierre Morel for useful advices concerning numerical aspects, and we are grateful to Panayotis Lavvas for his scientific comments and for reading the manuscript. We express our grateful thanks to Jeff Cuzzi who provided us his opacity code. Simulations have been executed on computers from the Utinam Institute of the Université de Franche-Comté, supported by the Région de Franche-Comté and Institut des Sciences de l'Univers (INSU). We thank Sékou Diakité who help us to parallelize the *EvAD* source code and to deal with the UTINAM Institute cluster. Finally, we thank the anonymous Reviewers who improved the clarity of the paper with their remarks and comments.

Appendix A. Description of the disk model

Our model of accretion disk is basically based on a generalized version of the procedure originally published by Papaloizou and Terquem (1999). More specifically, this is a 1+1D model for which the turbulence is treated in the frame of the well known α formalism (Shakura and Sunyaev, 1973). During its temporal evolution, the disk is irradiated by the star which also evolves along its Pre-Main Sequence evolutionary track. Both static model and disk temporal evolution programs have been implemented from scratch in `FORTRAN 2008`, and parallelized using Open Multi-Processing (OpenMP[3]). We have nicknamed the whole package *EvAD*.[4] The following sections provide a detailed description of our model.

[3] http://openmp.org.
[4] *Ev*olutionary *A*ccretion *D*isk.

A.1. Vertical structure

The vertical structure of the disk is governed by the equations (see Papaloizou and Terquem, 1999; Huré, 2000) (already labeled PT99), Frank et al. (1992)

$$\frac{1}{\rho}\frac{\partial P}{\partial z} = -\Omega^2 z \tag{A.1}$$

$$\frac{\partial F}{\partial z} = \frac{9}{4}\rho \nu \Omega^2 \tag{A.2}$$

$$\frac{\partial T}{\partial z} = -\frac{3\kappa\rho}{16\sigma T^3}F \tag{A.3}$$

where P, F and T are respectively the pressure, the vertical radiative flux and the temperature; z represents the altitude above the mid-plane and Ω is the keplerian angular velocity. The density is denoted ρ while κ is the opacity of the disk's material taken in Bell and Lin (1994). Following PT99 the boundary condition at the external disk surface are given by

$$F_s = \frac{3}{8\pi}\dot{M}_{\rm st}\,\Omega^2 \tag{A.4}$$

where $\dot{M}_{\rm st} = 3\pi\langle\nu\rangle\Sigma$ with $\Sigma = \int_{-H}^{+H}\rho\,{\rm d}z$ (the disk surface mass density) and $\langle\nu\rangle = \int_{-H}^{+H}\rho\,\nu\,{\rm d}z/\Sigma$ the vertically averaged viscosity. The pressure at external surface is

$$P_s = \frac{\Omega^2 H \tau_{ab}}{\kappa_s} \tag{A.5}$$

where H is the disk mid-height, τ_{ab} is the optical depth above the disk (following PT99, we have taken $\tau_{ab} = 10^{-2}$) and κ_s is the opacity at the external surface. The temperature T_s can be obtained by solving for given values of α and $\dot{M}_{\rm st}$

$$2\sigma(T_s^4 - T_{\rm birr}^4) - \frac{9\alpha k T_s}{8\mu m_H \kappa_s} - \frac{3}{8\pi}\dot{M}_{\rm st}\Omega^2 = 0 \tag{A.6}$$

where $T_{\rm birr}$ is given by

$$T_{\rm birr}^4 = T_b^4 + T_{\rm irr}^4 \tag{A.7}$$

where $T_{\rm irr}$ is given by Eq. (2), T_b is the background temperature, *i.e.* the temperature of the medium in which the disk is immersed. We have chosen $T_b = 10$ K. The mid-height of the disk being not known a priori, we have to solve a Two Boundary Value Problems (TBVP). While some authors work with relaxation algorithms (Cannizzo, 1992; Milsom et al., 1994; D'Alessio et al., 1998; Hameury et al., 1998); we have prefered an algorithm based on shooting methods (Lin and Papaloizou, 1980; Meyer and Meyer-Hofmeister, 1982; Mineshige and Osaki, 1983; Smak, 1984; Mineshige et al., 1990; Różańska et al., 1999; Papaloizou and Terquem, 1999) turning our TBVP into an Initial Values Problems (IVP): the equations of the vertical structure are integrated from the surface of the disk to the mid-plan. The 5th-order Runge–Kutta method with adaptive step length described in Press et al. (1992), already used in previous other works (see Papaloizou and Terquem, 1999; Alibert et al., 2005; Dodson-Robinson et al., 2009), has been employed to perform

Retour à la table des matières : p. v

the vertical integration. To reduce the effects of the stiffness of the set of equations, we have opted for – after several tests – the set of variables $u = \ln(\rho)$, $v = F/\sigma/T_s^4$ and $w = \ln(T)$ (also adopted by Huré (2000)). The equation $F(z = 0) = 0$ is then solved by a root finding method. Finally, the vertically averaged turbulent viscosity $\langle \nu \rangle = \int_{-H}^{+H} \rho \nu \, dz/\Sigma$ is tabulated as a function of disk surface density $\Sigma = \int_{-H}^{+H} \rho \, dz$, the steady state accretion rate $\dot{M}_{st} = 3\pi \langle \nu \rangle \Sigma$, the turbulent viscosity parameter α and the age of the system t (*i.e.* providing $T_{eff}(t)$ and $R_\star(t)$ which are directly involved in the calculation. During the integration of Eq. (1), these pre-built tables are interpolated"on-the-fly" by a dedicated routine involving advanced B-splines technics (de Boor, 1985).

A.2. Secular evolution

The temporal evolution of the disk is governed by Eq. (1), combined with boundary conditions similar to those used by Alibert et al. (2005), which is a non-linear equation ($\langle \nu \rangle$ depends on the solution Σ). Unfortunately, there is no standard numerical method for such equation. Although explicit finite difference method is often used (*e.g.* Papaloizou et al., 1983; Ruden and Lin, 1986; Nakamoto and Nakagawa, 1994; Jin and Sui, 2010) the time-step must meet the Courant–Friedrichs–Lewy condition (see Courant et al., 1928) that limits the value of the time-step to small values. Instead of an explicit finite difference scheme, we have chosen a fully implicit scheme which has the great advantage of being unconditionally stable at least in the case of linear equations. The obtained set of non-linear finite difference equations is solved using a multidimensional Newton–Raphson algorithm.[5] Our approach is similar to the methods used by Eggleton (1971) and Hameury et al. (1998), respectively in the contexts of stellar structure or accretion disc outburst. We used a decentralized finite difference formula

$$\left.\frac{\partial f}{\partial r}\right|_i \simeq \left.\frac{\partial \xi}{\partial r}\right|_i \frac{f_{i+1} - f_{i-1}}{2\Delta\xi} \tag{A.8}$$

where ξ is a chosen function of r. The initial distribution of matter being of the form $\Sigma_0 \propto r^{-3/2}$; we have found convenient to adopt a function like $\xi(r) = r^p$ where p is an adjustable real parameter that tunes the distribution of points through the disk. Finally, the evolution equation has been rewritten using $f = \Sigma \langle \nu \rangle \sqrt{r}$ and $u = \sqrt{r}\partial f/\partial r$.

References

Alibert, Y. et al., 2005. Models of giant planet formation with migration and disc evolution. Astron. Astrophys. 434 (April), 343–353.

Allen, R.L., Bernstein, G.M., Malhotra, R., 2001. The edge of the Solar System. Astrophys. J. Lett. 549 (March), L241–L244.

Apai, A., Lauretta, D.S. (Eds.), 2010. Protoplanetary Dust – Astrochemical and Cosmochemical Perspective, second ed. Cambridge University Press.

Asplund, M., Grevesse, N., Sauval, A.J., 2005. The solar chemical composition. In: Barnes III, T.G., Bash, F.N. (Eds.), Cosmic Abundances as Records of Stellar Evolution and Nucleosynthesis. Astronomical Society of the Pacific Conference Series, vol. 336, p. 25.

Balbus, S.A., Hawley, J.F., 1998. Instability, turbulence, and enhanced transport in accretion disks. Rev. Modern Phys. 70 (January), 1–53.

Bell, K.R., Lin, D.N.C., 1994. Using FU orionis outbursts to constrain self-regulated protostellar disk models. Astrophys. J. 427 (June), 987–1004.

Beresnev, S., Chernyak, V., Fomyagin, G., 1993. Phys. Fluids 5, 2043–2047.

Besla, G., Wu, Y., 2007. Formation of narrow dust rings in circumstellar debris disks. Astrophys. J. 655 (January), 528–540.

Birnstiel, T., 2011. The Evolution of Gas and Dust in Protoplanetary Accretion Disks. Ph.D. Thesis.

Blum, J., Schräpler, R., 2004. Structure and mechanical properties of high-porosity macroscopic agglomerates formed by random ballistic deposition. Phys. Rev. Lett. 93 (11), 115503-1–115503-4.

Blum, J. et al., 2000. Growth and form of planetary seedlings: Results from a microgravity aggregation experiment. Phys. Rev. Lett. 85 (September), 2426–2429.

Blum, J. et al., 2014. Comets formed in solar-Nebula instabilities! – An experimental and modeling attempt to relate the activity of comets to their formation process. Icarus 235 (June), 156–169.

Bockelée-Morvan, D. et al., 2002. Turbulent radial mixing in the solar Nebula as the source of crystalline silicates in comets. Astron. Astrophys. 384 (March), 1107–1118.

Boss, A.P., 2008. Mixing in the solar Nebula: Implications for isotopic heterogeneity and large-scale transport of refractory grains. Earth Planet. Sci. Lett. 268 (April), 102–109.

Bouvier, J. et al., 2007. Magnetospheric accretion in classical T Tauri stars. Protostars Planets V, 479–494.

Brownlee, D.E., 1978. Microparticle studies by sampling techniques. In: McDonnell, J. (Ed.), Cosmic Dust. John Wiley & Sons, pp. 295–336.

Brownlee, D. et al., 2006. Comet 81P/Wild 2 under a microscope. Science 314 (December), 1711–1716.

Campins, H., Ryan, E.V., 1989. The identification of crystalline olivine in cometary silicates. Astrophys. J. 341 (June), 1059–1066.

Cannizzo, J.K., 1992. Accretion disks in active galactic nuclei – Vertically explicit models. Astrophys. J. 385 (January), 94–107.

Ciesla, F.J., 2007. Outward transport of high-temperature materials around the midplane of the solar Nebula. Science 318 (October), 613–615.

Ciesla, F.J., Sandford, S.A., 2012. Organic synthesis via irradiation and warming of ice grains in the solar Nebula. Science 336 (April), 452–454.

Courant, R., Friedrichs, K., Lewy, H., 1928. ber die partiellen Differenzengleichungen der mathematischen Physik. Math. Ann. 100, 32–74.

Crida, A., 2009. Minimum mass solar Nebulae and planetary migration. Astrophys. J. 698 (June), 606–614.

Cunningham, J., 1910. Proc. R. Soc. London Ser. A 83, 357–365.

Cuzzi, J.N., Davis, S.S., Dobrovolskis, A.R., 2003. Blowing in the wind. II. Creation and redistribution of refractory inclusions in a turbulent protoplanetary Nebula. Icarus 166 (December), 385–402.

Cuzzi, J.N., Estrada, P.R., Davis, S.S., 2014. Utilitarian opacity model for aggregate particles in protoplanetary Nebulae and exoplanet atmospheres. Astrophys. J. Ser. 210 (February), 21–38.

D'Alessio, P. et al., 1998. Accretion disks around young objects. I. The detailed vertical structure. Astrophys. J. 500 (June), 411–427.

D'Alessio, P. et al., 2005. The truncated disk of CoKu Tau/4. Astrophys. J. 621 (March), 461–472.

de Boor, C., 1985. A Practical Guide to Splines. third ed. Springer.

Degl'Innocenti, S. et al., 2008. The FRANEC stellar evolutionary code. Astrophys. Space Sci. 316 (August), 25–30.

Dell'Omodarme, M. et al., 2012. The pisa stellar evolution data base for low-mass stars. Astron. Astrophys. 540 (April), A26 (1–12).

Dodson-Robinson, S.E. et al., 2009. Ice lines, planetesimal composition and solid surface density in the solar Nebula. Icarus 200 (April), 672–693.

Eggleton, P.P., 1971. The evolution of low mass stars. Mon. Not. R. Astron. Soc. 151, 351–364.

Famá, M. et al., 2010. Radiation-induced amorphization of crystalline ice. Icarus 207 (May), 314–319.

Ferreira, J., Dougados, C., Cabrit, S., 2006. Which jet launching mechanism(s) in T Tauri stars? Astron. Astrophys. 453 (July), 785–796.

Fouchet, L. et al., 2012. Effects of disk irradiation on planet population synthesis. Astron. Astrophys. 540 (April), A107 (1–7).

Frank, J., King, A., Raine, D., 1992. Accretion Power in Astrophysics. Cambridge Uni. Press, San Diego.

Gail, H.-P., 2001. Radial mixing in protoplanetary accretion disks. I. Stationary disc models with annealing and carbon combustion. Astron. Astrophys. 378 (October), 192–213.

Greenberg, J.M., 1985. The chemical and physical evolution of interstellar dust. Phys. Scr. Vol. T 11, 14–26.

Gundlach, B., Blum, J., 2012. Outgassing of icy bodies in the Solar System – II: Heat transport in dry, porous surface dust layers. Icarus 219 (June), 618–629.

Güttler, C. et al., 2010. The outcome of protoplanetary dust growth: Pebbles, boulders, or planetesimals?. I. Mapping the zoo of laboratory collision experiments. Astron. Astrophys. 513 (April), A56 (1–16).

Haisch Jr., K.E., Lada, E.A., Lada, C.J., 2001. Disk frequencies and lifetimes in young clusters. Astrophys. J. 553 (June), L153–L156.

Hameury, J.-M. et al., 1998. Accretion disc outbursts: A new version of an old model. Mon. Not. Roy. Astron. Soc. 298 (August), 1048–1060.

Harker, D.E., Desch, S.J., 2002. Annealing of silicate dust by Nebular shocks at 10 AU. Astrophys. J. Lett. 565 (February), L109–L112.

Hayashi, C., 1981. Structure of the solar Nebula, growth and decay of magnetic fields and effects of magnetic and turbulent viscosities on the Nebula. Prog. Theoret. Phys. Suppl. 70, 35–53.

Horai, K., Simmons, G., 1969. Earth Planet. Sci. Lett. 6, 359–368.

Hueso, R., Guillot, T., 2005. Evolution of protoplanetary disks: Constraints from DM Tauri and GM Aurigae. Astron. Astrophys. 442 (November), 703–725.

Hughes, A.M. et al., 2010. Structure and composition of two transitional circumstellar disks in Corona Australis. Astron. J. 140 (September), 887–896.

Huré, J.-M., 2000. On the transition to self-gravity in low mass AGN and YSO accretion discs. Astron. Astrophys. 358 (June), 378–394.

Hutchins, D.K., Harper, M.H., Felder, R.L., 1995. Aerosol Sci. Technol. 22, 202–218.

[5] http://en.wikipedia.org/wiki/Newton%27s_method.

Retour à la table des matières : p. v

Jin, L., Sui, N., 2010. The evolution of the solar Nebula I. Evolution of the global properties and planet masses. Astrophys. J. 710 (February), 1179–1194.

Keller, C., Gail, H.-P., 2004. Radial mixing in protoplanetary accretion disks. VI. Mixing by large-scale radial flows. Astron. Astrophys. 415 (March), 1177–1185.

Kelley, M.S., Wooden, D.H., 2009. The composition of dust in Jupiter-family comets inferred from infrared spectroscopy. Planet. Space Sci. 57 (August), 1133–1145.

Kemper, F., Vriend, W.J., Tielens, A.G.G.M., 2004. The absence of crystalline silicates in the diffuse interstellar medium. Astrophys. J. 609 (July), 826–837.

Kogel, J.E. et al., 2006. Industrial Minerals & Rocks (Book-CD Set), seventh ed. Society for Mining, Metallurgy, and Exploration, Englewood, CO 80112.

Krause, M. et al., 2011. Thermal conductivity measurements of porous dust aggregates: I. Technique, model and first results. Icarus 214 (July), 286–296.

Krauss, O., Wurm, G., 2005. Photophoresis and the pile-up of dust in young circumstellar disks. Astrophys. J. 630 (September), 1088–1092.

Krauss, O. et al., 2007. The photophoretic sweeping of dust in transient protoplanetary disks. Astron. Astrophys. 462 (February), 977–987.

Le Guillou, C. et al., 2013. Amorphization and D/H fractionation of kerogens during experimental electron irradiation: Comparison with chondritic organic matter. Icarus 226 (September), 101–110.

Lenzuni, P., Gail, H.-P., Henning, T., 1995. Dust evaporation in protostellar cores. Astrophys. J. 447 (July), 848–862.

Haynes, W.M. (Ed.), 2015. CRC Handbook of Chemistry and Physics, 96 ed. CRC Press, Boca Raton, FL, 2677 p. ISBN: 9781482260977.

Lin, D.N.C., Papaloizou, J., 1980. On the structure and evolution of the primordial solar Nebula. Mon. Not. Roy. Astron. Soc. 191 (April), 37–48.

Lindsay, S.S. et al., 2013. Absorption efficiencies of forsterite. I. Discrete dipole approximation explorations in grain shape and size. Astrophys. J. 766 (March), 54–78.

Loesche, C. et al., 2013. Photophoretic Strength on Chondrules. 1. Modeling. Astrophys. J. 778 (December), 101–110.

Lutro, H.F., 2012. The Effect of Thermophoresis on the Particle Deposition on a Cylinder. Ph.D. Thesis, NTNU – Trondheim – Norwegian University of Science and Technology.

Lynden-Bell, D., Pringle, J.E., 1974. The evolution of viscous discs and the origin of the Nebular variables. Mon. Not. R. Astron. Soc. 168 (September), 603–637.

Meakin, P., Donn, B., 1988. Aerodynamic properties of fractal grains – Implications for the primordial solar Nebula. Astrophys. J. 329 (June), L39–L41.

Meyer, F., Meyer-Hofmeister, E., 1982. Vertical structure of accretion disks. Astron. Astrophys. 106 (February), 34–42.

Milsom, J.A., Chen, X., Taam, R.E., 1994. The vertical structure and stability of accretion disks surrounding black holes and neutron stars. Astrophys. J. 421 (February), 668–676.

Mineshige, S., Osaki, Y., 1983. Disk-instability model for outbursts of dwarf novae. Time-dependent formulation and one-zone model. Publ. Astron. Soc. Jpn. 35, 377–396.

Mineshige, S., Tuchman, Y., Wheeler, J.C., 1990. Structure and evolution of irradiated accretion disks. II. Dynamical evolution of a thermally unstable torus. Astrophys. J. 359 (August), 176–185.

Moudens, A. et al., 2011. Photophoretic transport of hot minerals in the solar Nebula. Astron. Astrophys. 531 (July), A106 (1–11).

Mousis, O. et al., 2007. Photophoresis as a source of hot minerals in comets. Astron. Astrophys. 466 (May), L9–L12.

Mumma, M.J., Charnley, S.B., 2011. The chemical composition of comets – Emerging taxonomies and natal heritage. Annu. Rev. Astron. Astrophys. 49 (September), 471–524.

Nakamoto, T., Nakagawa, Y., 1994. Formation, early evolution, and gravitational stability of protoplanetary disks. Astrophys. J. 421 (February), 640–650.

Ogliore, R.C. et al., 2009. Nebular mixing constrained by the Stardust samples. Meteorit. Planet. Sci. 44 (November), 1675–1681.

Ollivier, M. et al., 2009. Planetary Systems – Detection, Formation and Habitability of Extrasolar Planets, third ed. Springer-Verlag, Berlin, Heidelberg.

Ormel, C.W., Spaans, M., Tielens, A.G.G.M., 2007. Dust coagulation in protoplanetary disks: Porosity matters. Astron. Astrophys. 461 (January), 215–232.

Owen, T.C., 2006. The origin of nitrogen atmospheres on Earth and Titan. American Geophysical Union (Fall). Abstracts A5+.

Papaloizou, J.C.B., Terquem, C., 1999. Critical protoplanetary core masses in protoplanetary disks and the formation of short-period giant planets. Astrophys. J. 521 (August), 823–838.

Papaloizou, J., Faulkner, J., Lin, D.N.C., 1983. On the evolution of accretion disc flow in cataclysmic variables. II – The existence and nature of the collective relaxation oscillations in dwarf nova systems. Mon. Not. Roy. Astron. Soc. 205 (November), 487–513.

Pascucci, I., Tachibana, S., 2010. The clearing of protoplanetary disks and of the protosolar Nebula. In: Apai, D.A., Lauretta, D.S. (Eds.), Protoplanetary Dust: Astrophysical and Cosmochemical Perspectives. SAO/NASA Astrophysics Data System, pp. 263–298, http://cdsads.u-strasbg.fr/abs/2010pdac.book..263P.

Pietrinferni, A. et al., 2004. A large stellar evolution database for population synthesis studies. I. Scaled solar models and isochrones. Astrophys. J. 612 (September), 168–190.

Pontoppidan, K.M. et al., 2008. Spectroastrometric imaging of molecular gas within protoplanetary disk gaps. Astrophys. J. 684 (September), 1323–1329.

Presley, M.A., Christensen, P.R., 1997. Thermal conductivity measurements of particulate materials 1. A review. J. Geophys. Res. 102 (March), 6535–6550.

Press, W. et al., 1992. Numerical Recipes in Fortran 77. Cambridge University Press.

Pringle, J.E., 1981. Accretion discs in astrophysics. Annu. Rev. Astron. Astrophys. 19, 137–162.

Reif, F., 1967. Berkeley Physics Course: Statistical Physics. Berkeley Physics Course. McGraw-Hill.

Różańska, A. et al., 1999. Vertical structure of accretion discs with hot coronae in active galactic nuclei. Mon. Not. Roy. Astron. Soc. 305 (May), 481–491.

Ruden, S.P., Lin, D.N.C., 1986. The global evolution of the primordial solar Nebula. Astrophys. J. 308 (September), 883–901.

Russell, H.W., 1935. J. Am. Ceram. Soc. 18, 1–5.

Shakura, N.I., Sunyaev, R.A., 1973. Black holes in binary systems. Observational appearance. Astron. Astrophys. 24, 337–355.

Shu, F.H., Shang, H., Lee, T., 1996. Toward an astrophysical theory of chondrites. Science 271 (March), 1545–1552.

Sicilia-Aguilar, A. et al., 2006. Disk evolution in Cep OB2: Results from the Spitzer Space Telescope. Astrophys. J. 638 (February), 897–919.

Smak, J., 1984. Accretion in cataclysmic binaries. IV – Accretion disks in dwarf novae. Acta Astron. 34, 161–189.

Stahler, S.W., Palla, F., 2004. The Formation of Stars. Wiley Edition, New York.

Supulver, K.D., Lin, D.N.C., 2000. Formation of icy planetesimals in a turbulent solar Nebula. Icarus 146 (August), 525–540.

Teiser, J., Dodson-Robinson, S.E., 2013. Photophoresis boosts giant planet formation. Astron. Astrophys. 555 (July), A98 (1–5).

Thalmann, C. et al., 2010. Imaging of a transitional disk gap in reflected light: Indications of planet formation around the young solar analog LkCa 15. Astrophys. J. Lett. 718 (August), L87–L91.

Tielens, A.G.G.M., Waters, L.B.F.M., Bernatowicz, T.J., 2005. Origin and evolution of dust in circumstellar and interstellar environments. In: Krot, A.N., Scott, E.R.D., Reipurth, B. (Eds.), Chondrites and the Protoplanetary Disk. Astronomical Society of the Pacific Conference Series, vol. 341, p. 605.

Tognelli, E., Degl'Innocenti, S., Prada Moroni, P.G., 2012. ^{7}Li surface abundance in Pre-Main Sequence stars. Testing theory against clusters and binary systems. Astron. Astrophys. 548 (December), A41 (1–10).

Tognelli, E., Prada Moroni, P.G., Degl'Innocenti, S., 2011. The Pisa Pre-Main Sequence tracks and isochrones. A database covering a wide range of Z, Y, mass, and age values. Astron. Astrophys. 533 (September), A109 (1–20).

Tsiganis, K. et al., 2005. Origin of the orbital architecture of the giant planets of the Solar System. Nature 435 (May), 459–461.

Turner, N.J. et al., 2012. A hot gap around Jupiter's orbit in the solar Nebula. Astrophys. J. 748 (April), 92–100.

van Eymeren, J., Wurm, G., 2012. The implications of particle rotation on the effect of photophoresis. Mon. Not. R. Astron. Soc. 420 (February), 183–186.

Veras, D., Armitage, P.J., 2004. Outward migration of extrasolar planets to large orbital radii. Mon. Not. R. Astron. Soc. 347 (January), 613–624.

von Borstel, I., Blum, J., 2012. Photophoresis of dust aggregates in protoplanetary disks. Astron. Astrophys. 548 (December), A96 (1–13).

Wehrstedt, M., Gail, H.-P., 2002. Radial mixing in protoplanetary accretion disks. II. Time dependent disk models with annealing and carbon combustion. Astron. Astrophys. 385 (April), 181–204.

Weidenschilling, S.J., 1977a. The distribution of mass in the planetary system and solar Nebula. Astrophys. Space Sci. 51 (September), 153–158.

Weidenschilling, S.J., 1977b. The distribution of mass in the planetary system and solar Nebula. Astrophys. Space Sci. 51 (September), 153–158.

Weidenschilling, S.J., 1997. The origin of comets in the solar Nebula: A unified model. Icarus 127 (June), 290–306.

Wooden, D.H. et al., 1999. Silicate mineralogy of the dust in the inner coma of Comet C/1995 01 (Hale-Bopp) pre- and postperihelion. Astrophys. J. 517 (June), 1034–1058.

Wooden, D.H. et al., 2000. Mg-rich silicate crystals in Comet Hale-Bopp: ISM relics or solar Nebula condensates? Icarus 143 (January), 126–137.

Wurm, G., Haack, H., 2009. Outward transport of CAIs during FU-Orionis events. Meteorit. Planet. Sci. 44 (July), 689–699.

Wurm, G., Krauss, O., 2006. Concentration and sorting of chondrules and CAIs in the late solar Nebula. Icarus 180 (February), 487–495.

Wurm, G. et al., 2010. Experiments on the photophoretic motion of chondrules and dust aggregates – Indications for the transport of matter in protoplanetary disks. Icarus 208 (July), 482–491.

Wurm, G., Trieloff, M., Rauer, H., 2013. Photophoretic separation of metals and silicates: The formation of mercury-like planets and metal depletion in chondrites. Astrophys. J. 769 (May), 78–84.

Xu, Y. et al., 2004. Thermal diffusivity and conductivity of olivine, wadsleyite and ringwoodite to 20 GPa and 1373 K. Phys. Earth Planet. Interiors 143, 321–336.

Young, J.B., 2011. Thermophoresis of a spherical particle: Reassessment, clarification, and new analysis. Aerosol Sci. Technol. 45, 927–948.

Zolensky, M.E. et al., 2006. Mineralogy and petrology of Comet 81P/Wild 2 nucleus samples. Science 314 (December), 1735–1739.

Zsom, A. et al., 2010. The outcome of protoplanetary dust growth: Pebbles, boulders, or planetesimals? II. Introducing the bouncing barrier. Astron. Astrophys. 513 (April), A57 (1–22).

Retour à la table des matières : p. v

10.2 Article sur le transport par photophorèse

Astronomy & Astrophysics manuscript no. phot_editor
June 1, 2018
© ESO 2018

Photophoretic transport of hot minerals in the solar nebula

A. Moudens[1,2], O. Mousis[2], J.-M. Petit[2], G. Wurm[3], D. Cordier[1,4] and S. Charnoz[5]

[1] Institut de Physique de Rennes, CNRS, UMR 6251, Université de Rennes 1, Campus de Beaulieu, 35042 Rennes, France
[2] Institut UTINAM, CNRS-UMR 6213, Observatoire de Besançon, BP 1615, 25010 Besançon Cedex, France
e-mail: olivier.mousis@obs-besancon.fr
[3] Faculty of Physics, University of Duisburg-Essen, Lotharstr. 1, 47048 Duisburg, Germany
[4] Ecole Nationale Supérieure de Chimie de Rennes, CNRS, UMR 6226, Avenue du Général Leclerc, CS 50837, 35708 Rennes Cedex 7, France
[5] Equipe AIM, Université Paris Diderot/CEA/CNRS, CEA/SAp, Centre de l'Orme Les Merisiers, 91191 Gif-Sur-Yvette Cedex, France

Received ??; accepted ??

arXiv:1105.6259v1 [astro-ph.EP] 31 May 2011

ABSTRACT

Context. Hot temperature minerals have been detected in a large number of comets and were also identified in the samples of Comet Wild 2 that were returned by the Stardust mission. Meanwhile, observations of the distribution of hot minerals in young stellar systems suggest that these materials were produced in the inner part of the primordial nebula and have been transported outward in the formation zone of comets.
Aims. We investigate the possibility that photophoresis provides a viable mechanism to transport high-temperature materials from the inner solar system to the regions in which the comets were forming.
Methods. We use a grid of time-dependent disk models of the solar nebula to quantify the distance range at which hot minerals can be transported from the inner part of the disk toward its outer regions as a function of their size (10^{-5} to 10^{-1} m) and density (500 and 1000 kg m^{-3}). These models will also yield information on the disk properties (radius of the inner gap, initial mass, and lifetime of the disk). The particles considered here are in the form of aggregates that presumably were assembled from hot mineral individual grains ranging down to submicron sizes and formed by condensation within the hottest portion of the solar nebula. Our particle-transport model includes the photophoresis, radiation pressure, and gas drag.
Results. Depending on the postulated disk parameters and the density of particles, 10^{-2} to 10^{-1} m aggregates can reach heliocentric distances up to ~35 AU in the primordial nebula over very short timescales (no more than a few hundred thousand years). 10^{-3} m particles follow the same trajectory as the larger ones but their maximum migration distance does not exceed ~26 AU and is reached at later epochs in the disks. On the other hand, 10^{-5} to 10^{-4} m aggregates are continuously pushed outward during the evolution of the solar nebula. Depending on the adopted disk parameters, these particles can reach the outer edge of the nebula well before its dissipation.
Conclusions. Our simulations suggest that irrespective of the employed solar nebula model, photophoresis is a mechanism that can explain the presence of hot temperature minerals in the formation region of comets. Comets probably had the time to trap the dust transported from the inner solar system either in their interior during accretion or in the form of shells surrounding their surface if they ended their growth before the particles reached their formation location.

Key words. planetary systems – protoplanetary disks – comets: general – comets: individual (81P/Wild 2) – Kuiper Belt: general – Oort Cloud

1. Introduction

Hot-temperature minerals have been detected in a large number of comets (Campins & Ryan 1989; Crovisier et al. 2000; Sitko et al. 2004; Wooden et al. 2000, 2004, 2010) and were also identified in the samples of Comet 81P/Wild 2 that were returned by the Stardust mission (Brownlee et al. 2006). These minerals include crystalline silicates that presumably condensed in the 1200–1400 K temperature range in the solar nebula (Hanner 1999) and calcium, aluminum-rich inclusions (CAIs), which are the record of a very hot (1400–1500 K) stage of nebular evolution because they are composed of the first minerals to condense from a gas of solar composition (Grossman 1972; Jones et al. 2000). On the other hand, observations of young stellar systems show that the abundance of crystalline silicates is much higher in the inner disk than in the outer disk, but that even the outer disks show more crystalline silicates than the interstellar medium (Tielens et al. 2005). These observations then suggest that crystalline silicates, and probably also CAIs, were produced in the inner part of the primordial nebula and have been transported outward in the formation zone of comets.

A number of mechanisms has been invoked to account for the origin of these high-temperature minerals in comets. It has been proposed that shock waves in the outer solar nebula could anneal the amorphous silicates to crystallinity in situ prior to their incorporation in comets (Harker & Desch 2002). However, the isotopic composition, minor element composition, and even the range of Fe/Si ratios measured in the dust that was returned by the Stardust spacecraft from Comet 81P/Wild 2 appear to be inconsistent with an origin by annealing of interstellar silicates in the primordial nebula (Brownlee et al. 2006). An alternative possiblity is the radial mixing induced by turbulence which is responsible for the angular momentum transport within the primitive nebula (Shakura & Sunyaev 1973). This turbulence favors the rapid diffusion of the different gaseous compounds and gas-coupled solids throughout the nebula. One-dimensional

Retour à la table des matières : p. v

(vertically averaged) diffusive transport of particles in the disk (Bockelée-Morvan et al. 2002) or through its surrounding layers (Ciesla 2007, 2009) has therefore been proposed to account for the presence of hot temperature minerals in the formation zone of comets. It is uncertain however whether turbulent transport suffices to explain the observations, or whether alternative physical processes are also needed. On the other hand, Hughes & Armitage (2010) recently studied the outward transport of particles in the nebula via a combination of advection (inward drift of particles though interaction with gas) and turbulent diffusion in an evolving disk. These authors found that the advection of solids within the gas flow significantly reduces the outward transport efficiency for larger particles (typically a few millimeters), thereby limiting the extent of mixing uniformity that is achievable within the disk via turbulent diffusion.

An alternative transport mechanism to turbulent diffusion whose effects have been investigated in the last years in the solar nebula is photophoresis (Krauss & Wurm 2005; Wurm & Krauss 2006; Krauss et al. 2007; Mousis et al. 2007; Wurm et al. 2010). This effect is based on a radiation-induced temperature gradient on the surface of a particle and the consequential nonuniform interaction with surrounding gas. When the existence of an inner gap is postulated in the disk, this latter becomes optically thin enough for particles to see the proto-Sun, but still has a reasonable gas content, which enables the photophoretic force to push dust grains outward (Mousis et al. 2007). This process provides a mechanism to transport high-temperature material from the inner solar system to the regions in which the comets were forming. Eventually, the dust driven outward in this manner will reach a region where the gas pressure and irradiation are so low that the combined outward forces of radiation pressure and photophoresis can only balance the inward drift of particles.

In this work, we use a grid of time dependent models of the solar nebula to quantify the distance range at which particles (i.e hot minerals) can be transported from the inner part of the disk toward its outer regions as a function of their size and density as well as of the disk properties (radius of the inner gap, initial mass, and lifetime of the disk). The grid of models used here allows us to consider the full range of thermodynamic conditions that might have taken place during the solar nebula's evolution. The particles considered in our model are in the form of hot mineral aggregates with sizes ranging between 10^{-5} and 10^{-1} m. The trajectories of particles with lower sizes are generally influenced by radiation pressure while those of particles with larger sizes begin to be mostly affected by gas drag. The aggregates are presumed to have been assembled from hot mineral individual grains ranging down to submicron sizes. We consider that these hot minerals have formed by condensation within the hottest portion of the solar nebula, well inside 1 AU (Chick & Cassen 1997). We also show that the determination of the dust size distribution within rings observed in young circumstellar disks and their position relative to the parent star is likely to bring some constraint on the lifetime and eventually the initial mass of the disk from which they originate.

Section 2 is devoted to the description of our modeling approach, detailing the particle transport and solar nebula models employed in this work. In Section 3 we detail the disk and particle parameters employed in our different models. In Section 4 we present and analyze the trajectories of particles determined in the frame of these models. In Section 5 we show that calculations of particle trajectories induced by photophoresis can be used as a tool to determine some physical parameters of circumstellar disks. Section 6 is devoted to the discussion of the assumptions of our model.

2. Model

2.1. The photophoretic force

Any particle embedded in gas and heterogeneously heated by light feels a photophoretic force, which usually pushes it away from the light source (Krauss & Wurm 2005; Wurm & Krauss 2006). The force is strongly pressure-dependent and can be stronger than radiation pressure and the gravity of the Sun by orders of magnitude in the solar nebula. This mechanism induces the migration of particles ranging from micron to centimeter sized in the solar nebula under the combined action of photophoresis, radiation pressure, and gas drag, provided that the disk is sufficiently transparent (Mousis et al. 2007).

Following the approach developed by Krauss et al. (2007), we assume here that the disk's gas flow conditions are described by the Knudsen number, Kn, which is defined as $Kn = l/a$, where l is the mean free path of the gas molecules and a is the radius of the particle. If the mean free path of the gas molecules is large compared to the considered particle sizes, i.e., for $Kn > 1$, then the gas flow is in the free molecular flow regime. In the contrary case, the gas flow is in the continuum regime. In these conditions, the photophoretic force F_{ph} on a spherical particle, valid for both flow regimes, can be expressed as follows (Beresnev et al. 1993):

$$F_{ph} = \frac{\pi}{3} a^2 I J_1 \left(\frac{\pi m_g}{2kT}\right)^{1/2} \frac{\alpha_E \psi_1}{\alpha_E + 15\Lambda Kn(1-\alpha_E)/4 + \alpha_E \Lambda \psi_2}, \quad (1)$$

where I is the light flux (power incident per area), m_g is the average mass of the gas molecules (3.89×10^{-27}kg), T is the gas temperature, and k the Boltzmann constant. J_1 is the asymmetry factor that contains the relevant information on the distribution of heat sources over the particle's surface upon irradiation. In the following calculations, we assume $J_1 = 0.5$, which corresponds to the case where the incident light is completely absorbed on the illuminated side of the particle. The energy accommodation coefficient α_E is the fraction of incident gas molecules that accommodate to the local temperature on the particle surface and, thus, contribute to the photophoretic effect. Here, we assume complete accommodation, i.e, $\alpha_E = 1$.

The thermal relaxation properties of the particle are summarized in the heat exchange parameter $\Lambda = \lambda_{eff}/\lambda_g$, where λ_g is the thermal conductivity of the gas and λ_{eff} the effective thermal conductivity of the particle. For λ_g, we adopt values for molecular hydrogen for temperatures above 150K (as tabulated by Incropera & DeWitt 2002). On the other hand, because helium has a higher thermal conductivity than hydrogen for lower temperatures, we assume that this species determines the thermal conductivity of the gas and use values taken from the compilation of Bich et al. (1990). The expression of Λ includes the conduction of heat through the particle and the thermal emission from the particle's surface, according to

$$\lambda_{eff} = \lambda_p + 4\epsilon\sigma T^3 a. \quad (2)$$

where λ_p is the thermal conductivity of the particle supposed here to be 10^{-3} W m^{-1} K^{-1} (Mousis et al. 2007), ϵ its emissivity assumed to be 1, and σ the Stefan-Boltzmann constant. On the other hand, the functions ψ_1 and ψ_2 in Eq. (1) depend only on Kn in the form

$$\psi_1 = \frac{Kn}{Kn+(5\pi/18)}\left(1 + \frac{2\pi^{1/2}Kn}{5Kn^2+\pi^{1/2}Kn+\pi/4}\right),$$
$$\psi_2 = \left(\frac{1}{2} + \frac{15}{4}Kn\right)\left(1 - \frac{1.21\pi^{1/2}Kn}{100Kn^2+\pi/4}\right). \quad (3)$$

Retour à la table des matières : p. v

As noted by Krauss et al. (2007), an additional photophoretic force arises if the accommodation coefficients vary over the surface of the dust grain (Cheremisin et al. 2005), but we restrict the treatment to the "classical" photophoretic force as given in Eq. (1). In the present work, we assume that Eq. (1) is valid for all parts of the solar nebula and all particles.

2.2. Balistic transport

In a protoplanetary disk where the gas pressure (in the midplane) decreases with distance from the star, the gas is supported by a pressure gradient and rotates slower than the Keplerian velocity (Weidenschilling 1977). Solid particles are only stable on a Keplerian orbit. Therefore, interaction with the gas leads to an inward drift of solids toward the star. For particles that couple to the gas flow on timescales short compared to an orbital period, the problem reduces to a one-dimensional (radial) calculation. The inward drift is then induced by the fraction of gravity (residual gravity), which is not balanced by the circular motion with the sub-Keplerian gas velocity. The force, F_{res}, acting on a particle of mass m_p due to residual gravity is given as

$$F_{res} = \frac{m_p}{\rho_g}\frac{dp}{dr}, \tag{4}$$

where ρ_g is the density and p the pressure of the gas.

In addition, radiation pressure has also to be considered for at least micron-sized particles (Krauss & Wurm 2005). The radiation pressure force can then be expressed as follow:

$$F_{rad} = \pi a^2 \frac{I}{c_{light}}, \tag{5}$$

where c_{light} is the speed of light. The sum of the outward forces (Eq. (1) and Eq. (5)) and the inward force (Eq. (4)) gives the drift force F_{drift}. We treat the problem as being purely radial here because we are mostly interested in the small particles. These small particles couple to the gas on timescales much shorter than the orbital timescale, which justifies the radial treatment as outlined in Wurm & Krauss (2006). The radial drift velocity with respect to the nebula is then estimated to be

$$v_{dr} = \frac{F_{ph} + F_{rad} + F_{res}}{m_p}\tau, \tag{6}$$

where τ is the gas grain coupling time and m_p the mass of the considered particle.

As larger dust aggregates drift outward, they pass from a region where the continuum flow regime is valid to a region where the free molecular flow regime applies. Hence, as with the photophoretic force, we have to consider an equation describing the gas grain friction time in both regimes. It is given by

$$\tau = \frac{m_p}{6\pi\eta a}C_c, \tag{7}$$

where η is the dynamic viscosity of the gas. This assumes Stokes friction, which is justified because the Reynolds numbers for the drift of particles smaller than 10 cm are well below 1. The Cunningham correction factor, C_c, accounts for the transition between the different flow regimes (Cunningham 1910) and is given as (Hutchins 1995)

$$C_c = 1 + Kn\left(1.231 + 0.47e^{-1.178/Kn}\right). \tag{8}$$

To close the set of equations, we need to determine the dynamic viscosity η and the mean free path l. In the framework of the classical kinetic theory for dilute gases (see e.g. Reif 1972), these quantities are given by

$$\eta = \frac{1}{3}nm_g\sqrt{\frac{8kT}{m_g\pi}}l \tag{9}$$

and

$$l = \frac{1}{\sqrt{2}n\sigma} \tag{10}$$

where n is the molecule number density in the gas, and σ the collisional cross section of the gas molecules. The latter is very difficult to obtain. It is easier to find the value of the dynamic viscosity at a given temperature for H_2 and then use the functional form of η in Eq. 9 to determine its value at any temperature. We use $\eta_0 = 9.0 \times 10^{-6}$ Pa s at $T_0 = 300$ K (Lide 2007). Finally, inverting Eq. 9, one obtains the mean free path.

We note in passing that Beresnev et al. (1993) used a normalising factor of 1/2 in Eq. 9 instead of the 1/3 that applies for three-dimensional gases, and this may slightly modify the numerical constants in Eq. 1. However, the change is likely smaller than the uncertainties because of all the approximations made to solve the conservation equations in their model.

Our description of the radial transport of particles in the disk includes their drag back toward the central star by the infalling nebula flow that moves at the velocity of v_{ac}. In our disk model, the accretion speed ranges from a few tens of cm/s in the inner part to below one cm/s at larger distance in the early stages and substantially decreases later on. In the simplified solar nebula model presented in Section 2.3, the accretion velocity is estimated to be

$$v_{ac} = \frac{r}{2t_{vis}}, \tag{11}$$

where r is the distance from the Sun, $t_{vis} = \frac{1}{3\alpha}\frac{r^2}{H^2}\frac{1}{\Omega}$ is the typical local viscous time, H is the local height of the nebula, Ω is the local Keplerian frequency given by $\Omega^2 = GM_\odot/r^3$ and α is the viscosity parameter of the disk described in Section 2.3. Finally, the position of particles is integrated from the inner edge of the disk at time $t = 0$ to a position $r(t_{disk})$ at the age of the disk t_{disk} via

$$r(t_{disk}) = \int_0^{t_{disk}} \left(v_{dr}(r(t), t) - v_{ac}(r(t), t)\right) dt. \tag{12}$$

2.3. The protoplanetary disk

The structure and evolution of the protoplanetary disk is modeled as a non irradiated, 1+1D turbulent disk, following the method originally presented in Papaloizou & Terquem (1999) and also developed by Alibert et al. (2005). The diffusion equation (see Lynden-Bell & Pringle 1974; Papaloizou & Lin 1995) describing the evolution of the gas surface density Σ is consequently solved as a function of time t and distance r to the star:

$$\frac{d\Sigma}{dt} = \frac{3}{r}\frac{\partial}{\partial r}\left[r^{1/2}\frac{\partial}{\partial r}\nu\Sigma r^{1/2}\right] + \dot{\Sigma}_w(r), \tag{13}$$

where Σ is the surface density of mass in the gas phase in the nebula and ν the mean (vertically averaged) turbulent viscosity. Compared to the original equation, the photo-evaporation

Retour à la table des matières : p. v

term, $\dot{\Sigma}_w(r)$, was added and is taken to be the same as in Veras & Armitage (2004). The mean turbulent viscosity is determined from the calculation of the vertical structure of the nebula: for each radius, r, the vertical structure is calculated by solving the equation for hydrostatic equilibrium together with the energy equation and the diffusion equation for the radiative flux (see Papaloizou & Terquem 1999). The local turbulent viscosity (as opposed to that averaged in the vertical direction) is computed using the standard Shakura & Sunyaev (1973) formalism: $\nu = \alpha C_s^2/\Omega$, where α is a free parameter and C_s the local speed of sound determined by the equation of state. Using this procedure, we derived the midplane pressure and temperature as well as the mean turbulent viscosity as a function of r and Σ. These laws are finally used to solve the diffusion equation (Eq. (13)) and to calculate the pressure- and temperature-dependant forces on dust grains. Figure 1 represents the temperature, pressure and surface density profiles in the midplane of the disk characterized by a mass of 0.03 $M_\odot$ and a lifetime of 6 Myr (see Sec. 3 for fore details) at different epochs of its evolution.

Following the approach of Mousis et al. (2007), we consider that the disk is not optically thin and that Rayleigh scattering from molecular hydrogen is the dominant dimming effect in the nebula (Mayer & Duschl 2005) for temperatures below 1500 K and at wavelengths shorter than a few μm. This condition is fulfilled only after 10^5 yr and beyond 0.5 AU in all the solar nebula models used in our calculations. For H_2, i.e, the dominant molecule, the Rayleigh scattering cross section is $\sigma(\lambda) = 8.49 \times 10^{-45}/\lambda^4 (\mathrm{cm}^2)$ (Vardya 1962). Assuming the illuminating light follows a black body spectrum, the Planck mean cross section as a function of the black body temperature T_B is found to be $\sigma(T_B) = 1.54 \times 10^{-42}\ T_B^4\ (\mathrm{cm}^2)$ (Dalgarno & Williams 1962). Note that, in our case, T_B is not the temperature of the nebula, but rather the effective temperature of the illuminating source, the Sun. With a disk's mean molar mass of 2.34 g/mol, the mass absorption coefficient is found to be $\sigma_m(T_B) = 3.96 \times 10^{-19}\ T_B^4\ (\mathrm{cm}^2/\mathrm{g})$. The effective temperature and the luminosity of the early Sun were taken from the ZAMS (Zero Age Main Sequence) model computed by Pietrinferni et al. (2004), which is available in the BaSTI database (http://albione.oa-teramo.inaf.it). We chose the parameters relevant for the Sun, i.e, a solar mixture of heavy elements, no overshooting, a metallicity Z= 0.0198, and a helium content Y= 0.273 (Z and Y together in the mass fraction). In this model, the surface temperature of the early Sun is 5652 K and its initial luminosity is 2.716×10^{26} W. We derived $\sigma_m(5770) = 4.0 \times 10^{-4}$ (cm^2/g) from the adopted effective temperature of the early Sun. Light becomes extinguished close to the star as a result of the high gas density, while the outer regions play only a minor role in the extinction.

3. Choice of parameters

We constructed a grid of nine disk models encompassing the range of thermodynamic conditions that might have taken place during the solar nebula's evolution. The three initial disk masses were fixed to 0.01, 0.03 and 0.1 $M_\odot$ respectively, with 0.01 $M_\odot$ corresponding to the minimum mass solar nebula (hereafter MMSN) defined by Hayashi (1981). The initial mass of each disk is integrated between 0.25 and 50 AU and the initial gas surface density is given by a power law $\Sigma \propto r^{-3/2}$, with an initial value taken to be $\Sigma(5.2\mathrm{AU})$ = 100, 300, and 1000 $\mathrm{g\,cm^{-2}}$ at 5.2 AU for disk masses of 0.01, 0.03 and 0.1 $M_\odot$, respectively. Here, the lifetime of the disk is governed both by viscosity and photoevaporation by the Sun or nearby stars. On the other hand, the viscosity parameter rules the accretion velocity of the disk (Eq. 12) but this latter is found to be low compared to the velocities due to photophoresis and gas drag for particles larger than 10^{-4} m (see Fig. 2 for an example of particle velocities due to photophoresis, radiation pressure, residual gravity and accretion flow along their trajectories in the nebula). Here the viscosity parameter is fixed to 7×10^{-3}, i.e, a value adopted in works aiming at synthesizing different populations of planets around other stars (Mordasini et al. 2009a, 2009b) and the photoevaporation rate is varied to obtain the appropriate disk lifetimes (1, 3, and 6 Myr for each selected mass). In each case, the lifetime corresponds to the time taken for the mass of the disk (integrated until 50 AU) to decrease to 1% of its initial value.

Mousis et al. (2007) have calculated the optical depth of the disk at 30 AU as a function of time. They found that even at late epochs, only ∼0.1% of the Sun's radiation is available in this region. As a result, these authors found that the high extinction induced by H_2 Rayleigh scattering limits the outward transport of particles only to very short heliocentric distances (typically a few AU) when they are released from the innermost regions. On the other hand, particle transport can be enhanced at larger heliocentric distances when a gap is formed in the inner disk. In particular, there is a growing body of observational evidence for the existence of disks whose inner few AU are cleared or are strongly depleted of gas (D'Alessio et al. 2005; Sicilia-Aguilar et al. 2006; Espaillat et al. 2008; Pontoppidan et al. 2008; Thalmann et al. 2010). For this reason, and similar to Mousis et al. (2007), we assume here the presence of 1 and 2 AU inner gaps within the nebula during the course of its viscous evolution. Gaps are prescribed in a way independent of the structure of the disk models used in this work and their sizes remain constant with time. As shown in Sect. 4, such an inner hole is large enough to leave a reasonable fraction of the incoming light to let photophoresis work even in the outer solar system.

Particles considered in our simulations have sizes ranging between 10^{-5} and 10^{-1}m and are assumed to be spherical and composed of olivine, with a variable porosity. Density of aggregates is varied between 500 and 1000 $\mathrm{kg\,m^{-3}}$. The first value corresponds to the random deposition of irregular olivine particles with density of 3300 $\mathrm{kg\,m^{-3}}$, with a 15% filling factor (Blum & Schräpler 2004). The second value corresponds to the average density measured in cometary interplanetary dust particles (Joswiak et al. 2007). We do not consider particles with sizes lower than 10^{-5} m because their path in the nebula is essentially controlled by radiation pressure. Moreover, for objects larger than about 1 m, the radial treatment we apply does no longer hold because the gas grain friction times become comparable to the orbital period.

4. Outward transport of hot temperature aggregates

All our calculations are based on the assumption that the disk opacity is essentially caused by Rayleigh scattering and not to dust, implying that the dust size distribution in the nebula is dominated by large particles instead of small particles. In the contrary case, smallest aggregates (here 10^{-5} m) would create a prominent opacity in the disk, implying that larger aggregates could only migrate outward in the wake of the small ones.

Figures 3–6 represent the trajectories of 10^{-5} to 10^{-1} m aggregates in the solar nebula that were computed using the defined particle densities and a set of six disk models that are expected to encompass the range of plausible thermodynamic conditions within the solar nebula (disk masses of 1 MMSN, 3 MMSN, 10 MMSN with lifetimes of 1 or 6 Myr). At the beginning of each

Retour à la table des matières : p. v

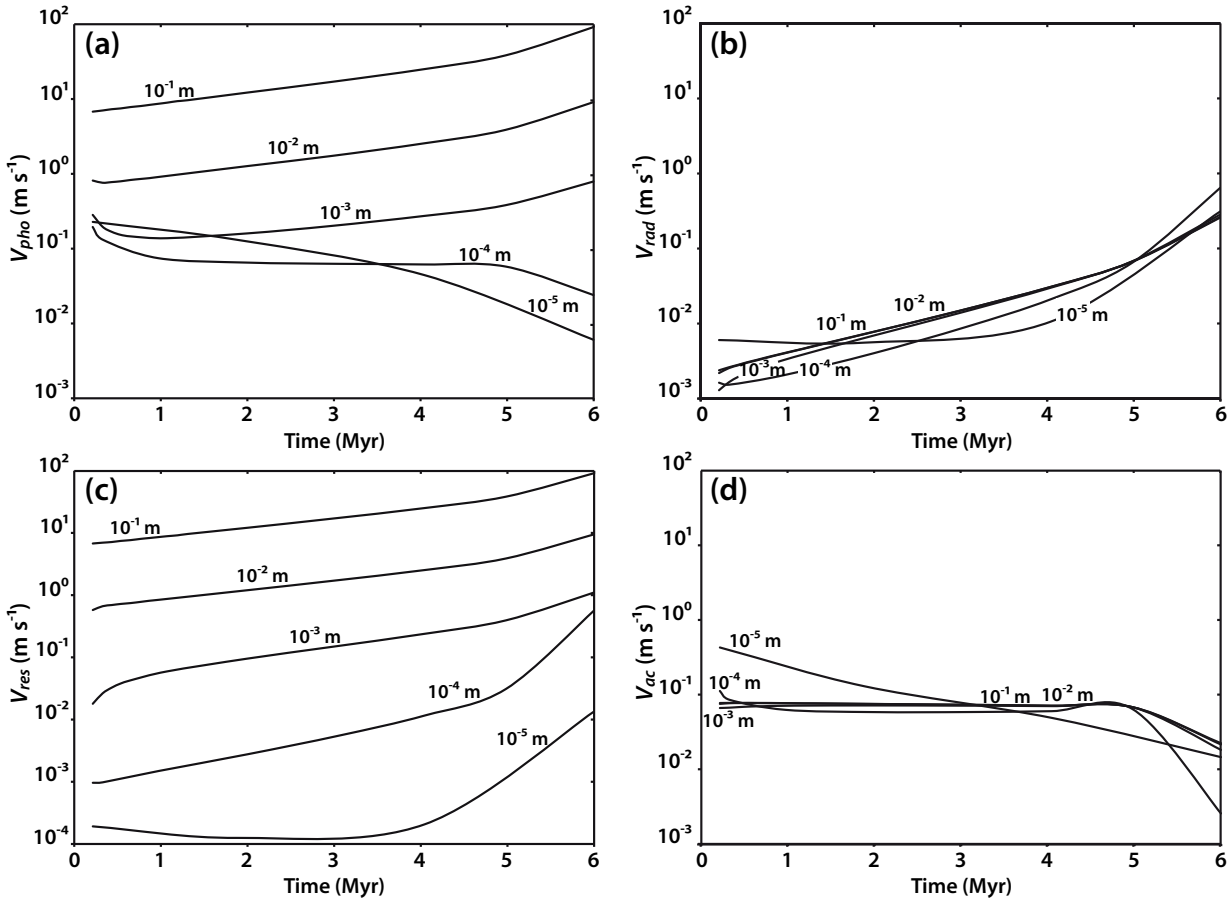

Fig. 2. Velocities of particles due to photophoresis (a), radiation pressure (b), residual gravity (c), and accretion flow (d) represented as a function of time and size in the midplane of the disk characterized by a mass of 0.03 $M_{\odot}$ and a lifetime of 6 Myr. The density of particles is 500 kg m^{-3} and the radius of the inner gap is 2 AU. Position of larger particles essentially corresponds to the balance between photophoresis and residual gravity velocities. When the disk opacity is prominent, i.e., at early epochs, the position of smaller particles is mainly driven by the balance between photophoresis and accretion flow velocities. At later epochs, the position of these particles becomes ruled by the balance between all velocities.

computation, the particles start their migration within the disk from the outer edge of the inner gap.

Figure 3 shows that 10^{-2}–10^{-1} m particles with densities of 500 kg m^{-3} that migrate within a disk with a 1 AU inner gap can reach heliocentric distances ranging between ~24 and 28.1 AU, depending on the choice of the initial mass and lifetime of the nebula. Each of these positions corresponds to an equilibrium reached at the position where the outward drift of aggregates just balances the accretion flow and in no more than a few hundred thousand years. With time, the location of these particles slightly rebounds toward the Sun until the dissipation of the disk. The figure also shows that 10^{-3} m particles follow the same trajectory as the larger ones but their equilibrium position is reached at lower heliocentric distance (~20–22.8 AU) and at later epochs in disks owning similar input parameters. Interestingly enough, the position of smaller aggregates (10^{-5}–10^{-4} m) continuously progresses outward during the evolution of the disks. 10^{-5} m particles can even be pushed beyond the outer edge (~50 AU) of the nebula if one selects a low-mass disk (1 MMSN) with a long lifetime (6 Myr). This is because of the strong decrease of the gas density and opacity in this model that enables the radiation pressure to push the particles at higher heliocentric distance.

Figure 4 represents the trajectories of the same particles as in Fig. 3, but for disk models with inner gaps fixed to 2 AU. Because the Rayleigh scattering through H_2 is strongly diminished here, all particles reach higher heliocentric distances than in the cases considered in Fig. 3, but for similar migration timescales. Thus, 10^{-2}–10^{-1} m particles reach heliocentric distances as high as ~27–35.1 AU, depending on the adopted parameters of the disk. In similar conditions, 10^{-3} m particles are also able to reach the ~23.9–26.3 AU distance range within the nebula. Moreover, 10^{-5} and even 10^{-4} m particles reach the edge of the nebula for low mass (1 MMSN) and long lifetime (6 Myr) disk.

Figures 5 and 6 show the trajectories of 10^{-5} to 10^{-1} m aggregates with densities of 1000 kg m^{-3} within disk models with

Retour à la table des matières : p. v

inner gaps of 1 and 2 AU, respectively. Migration timescales remain similar to the previous cases: larger particles migrate very rapidly toward a maximum heliocentric distance while smaller ones continuously drift outward during the evolution of the disk. Because (i) the inward drift linearly depends on the mass of the aggregate (see Eq. 4) and (ii) the radial drift velocity v_{dr} is inversely proportional to this quantity (see Eq. 6), all particles here migrate at lower heliocentric distances than in cases of disks based on similar parameters. Indeed, 10^{-2}–10^{-1} m particles do not exceed ∼20.2–23.6 AU (∼22.7–29.7 AU) in the case of disks with 1 AU (2 AU) inner gaps. The maximum migration distance reached by intermediary size particles (10^{-3} m) becomes ∼20 AU (∼23.3 AU) in the case of disks with 1 AU (2 AU) inner gaps. In every case, the maximum migration distance of 10^{-4} m particles is several AU smaller than those of same size particles with densities of 500 kg m^{-3}. Now only 10^{-5} m particles reach the outer edge of the nebula for low mass (1 MMSN) and long lifetime (6 Myr) disk, irrespective of the gap size.

5. Probing the dissipation of circumstellar disks

Particle transport through the combination of photophoresis and radiation pressure has been invoked to explain the presence of ring-shaped dust distributions in young circumstellar disks such as the one around HR 4796A (Krauss & Wurm 2005). Here we show that in some cases, the determination of the dust size distribution within rings and their position relative to the parent star is likely to bring some constraints on the lifetime and eventually on the initial mass of the circumplanetary disk from which they originate. Indeed, Figure 7 represents the settling distances reached by particles of different sizes and with densities of 500 kg m^{-3} at the end of the solar nebula evolution. The figure shows, for example, that ring-like structures essentially composed of 10^{-5} m particles and located in the ∼1.8–12 AU (3–21 AU) distance range from the star could have formed in disks with 1 AU (2 AU) inner gap, which have short or intermediary lifetimes (here 1–3 Myr), irrespective of the initial disk's mass. In addition, same size particles located at long distance to the star, i.e., ∼50 AU (upper limit owing to the truncation of our model) or farther, could have formed in disks with long lifetimes (6 Myr) and low initial masses (1 MMSN), irrespective of the size of the inner gap. To a lesser extent, one can also identify in Fig. 7 a relationship between the position (in the 15–25 AU range) of ring-like structures dominated by the settling of 10^{-3} to 10^{-1} m particles and the disk's lifetime and inner gap size.

6. Discussion

6.1. Disk's structure and evolution

One could argue that the existence of an inner gap at early epochs within the nebula remains questionable. Indeed, gaps are often found in disks (i.e., transition disks) that are millions of years old. In this context, a significant offset might exist between the times of the different models used in this work and the chronology of the solar system formation and evolution that is testified by meteorite measurements or by the age of disks as inferred from luminosity studies of protostars. For these reasons, the less massive disk models used in this work that are associated to inner gaps correspond to cases that are the most consistent with the structure of transition disks. Moreover, our calculations are based on the assumption that the nebula is essentially devoid of dust, i.e., that the dust opacity is negligible. Indeed, if we assume that the smallest aggregates (10^{-5} m) have created a prominent opacity in the nebula, larger aggregates could only follow the small ones and reach the formation zone of comets toward the end of the disk evolution.

Despite these caveats, the use of a set of disk models covering the whole range of plausible thermodynamic conditions that took place in the primordial nebula allows us to show that hot-temperature minerals can drift up to heliocentric distances reaching ∼34 AU for the largest particles and 50 AU or beyond for the smallest ones provided that i) the existence of an inner gap is postulated within the nebula and ii) the opacity of the smallest dust particles remains negligible inside the photophoretic transport front. These simulations suggest that, irrespective of the employed solar nebula model, photophoresis is a mechanism that can explain the presence of hot-temperature minerals at early epochs of the disk's evolution in the formation region of comets (from 10 to 30 AU according to the different scenarios – see, e.g., Horner et al. 2007 for a review). Because comets have presumably accreted within a few hundred thousand years (Weidenschilling 1997), i.e., a timescale shorter than the one probably required to form an inner gap in the disk and to allow the photophoretic transport of particles formed close to the Sun, they probably had the time to essentially trap the dust transported from the inner solar system in the form of shell surrounding their surface if their accretion ended before particles reached their formation location. Because photophoresis works heterogeneously, depending on the individual properties of a dust aggregate (composition, size, thermal and optical properties), one would expect the bulk of comets to be laden with particles of size and/or composition that would vary as a function of their accretion distance in the solar nebula. It is important to note that our calculations were made with the typical values of 0.5 and 1 for the asymmetry factor J_1 and the emissivity ϵ. Assuming lower but still reasonable values for these parameters would not alter our conclusions. For example, if one assumes $J_1 = 0.4$ and $\epsilon = 0.8$ in the disk model characterized by a mass of 3 MMSN and a lifetime of 6 Myr, 10^{-1}–10^{-2} m particles still migrate up to ∼ 25.4–25.9 AU (29.5–30 AU) and 10^{-5}–10^{-4} m particles up to ∼ 11–23.8 AU (18.5–33.3 AU) in the nebula owning a 1 AU (2 AU) inner gap.

6.2. Role of turbulence

The influence of turbulence on the particle motion has also to be considered in comparison to photophoresis. Two different cases have to be discussed. In the first case, the disk has an inner clear region and an optically thick outer region where opacity is provided by dust grains. In principle photophoresis is capable of moving the edge between optically thin and thick parts outward, thus clearing the disk inside-out from solids (see Krauss et al. 2007 for details). In this scenario, turbulent inward diffusion might counteract the outward motion of the edge. However, Krauss et al. (2007) discuss that turbulence will not prevent the outward motion of the edge. The edge will finally reach a lower heliocentric distance than in a similar situation where turbulence is negligible. The position of the edge will depend on the effective inward transport of particles by the turbulence. The second case would be more like the situation discussed in this paper. In a disk where solid particles are treated as test particles and opacity is essentially generated by the gas (Rayleigh scattering) and not by dust extinction, turbulence is not an issue. It only broadens any ring-like particle concentration because photophoresis is a

Retour à la table des matières : p. v

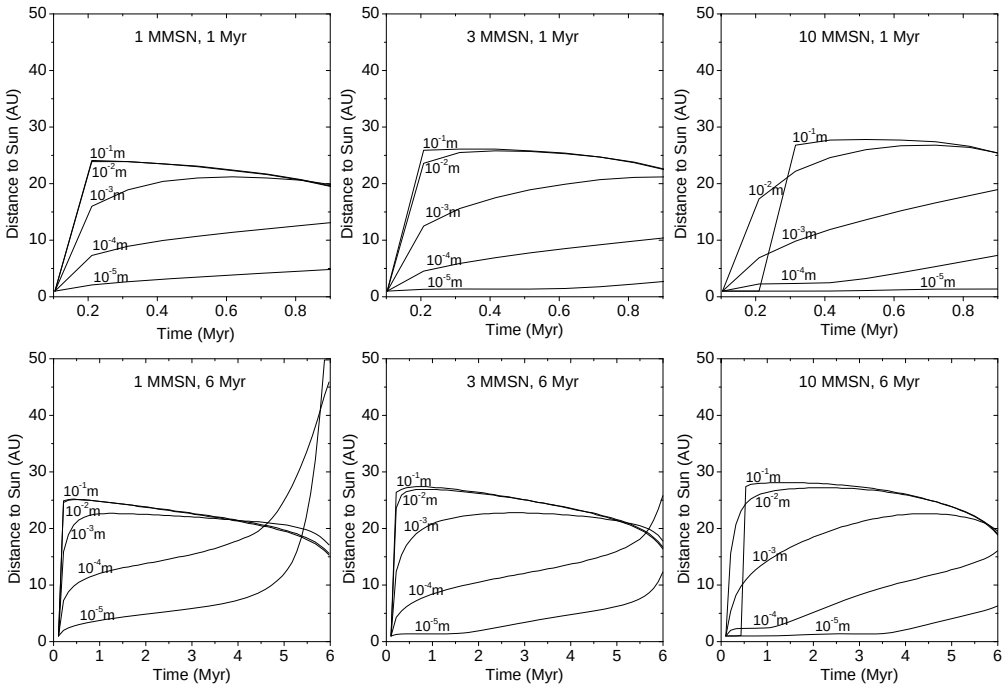

Fig. 3. Position of particles of size 10^{-5} to 10^{-1} m, as a function of time for disks with masses of 1, 3, or 10 MMSN and lifetimes of 1 or 6 Myr. The density of particles is 500 kg m^{-3} and the radius of the inner gap is 1 AU.

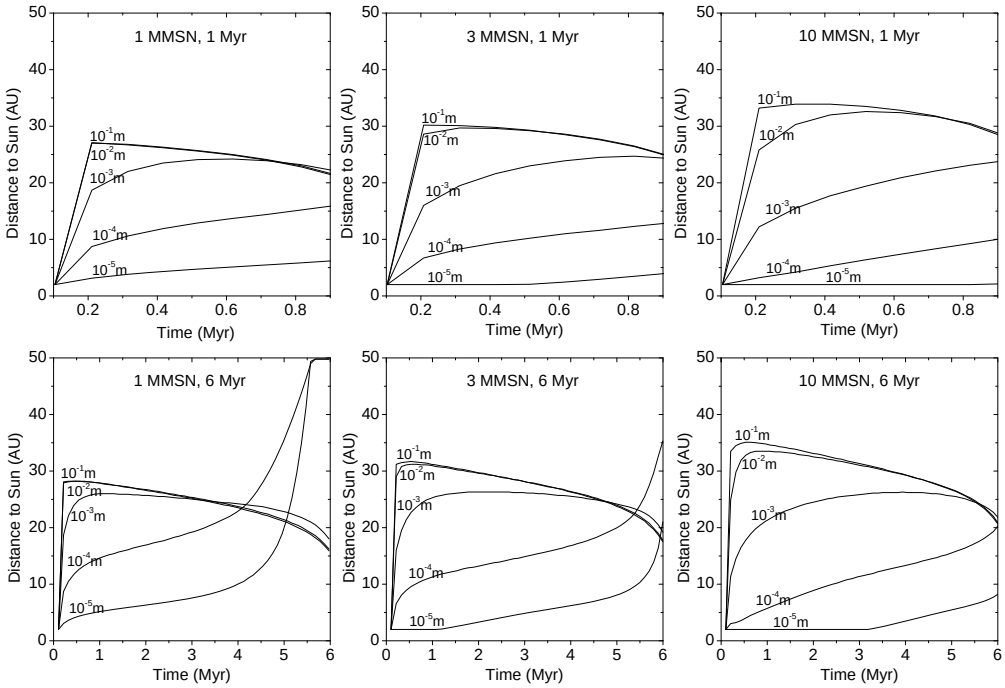

Fig. 4. Same as in Fig. 3, but for an inner gap radius of 2 AU.

Retour à la table des matières : p. v

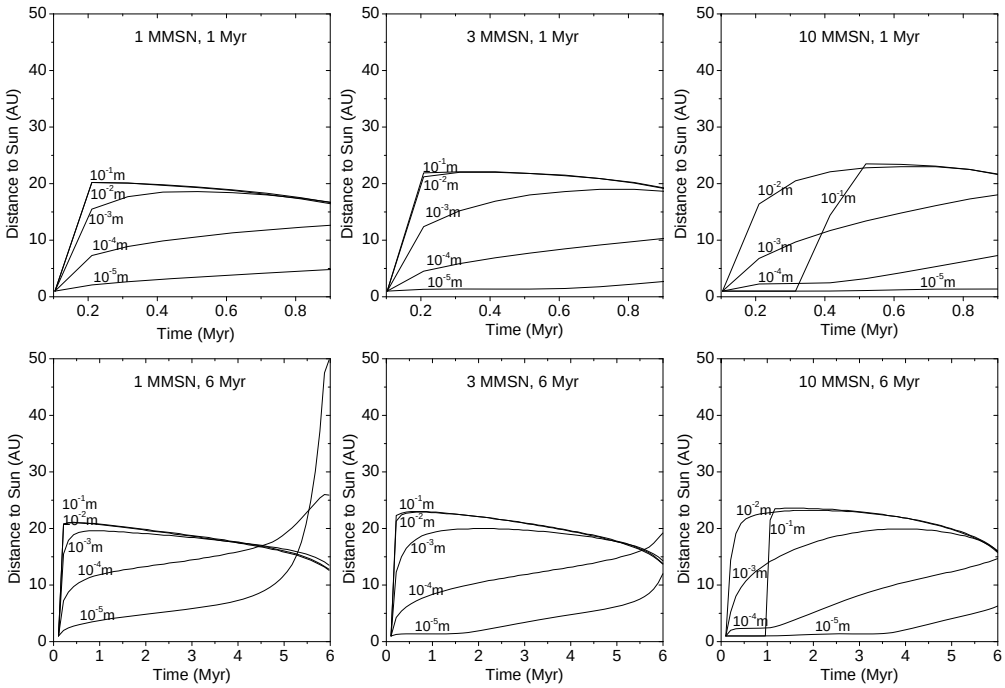

Fig. 5. Position of particles of size 10^{-5} to 10^{-1} m, as a function of time for disks with masses of 1, 3, or 10 MMSN and lifetimes of 1 or 6 Myr. The density of particles is 1000 kg m^{-3} and the radius of the inner gap is 1 AU.

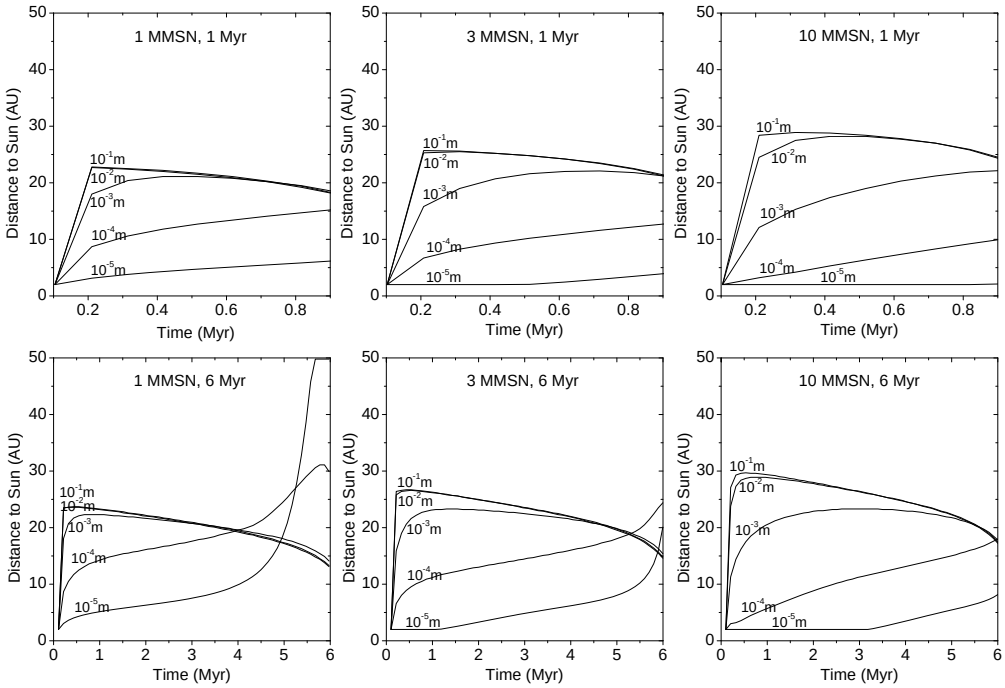

Fig. 6. Same as in Fig. 5 but for an inner gap radius of 2 AU.

Retour à la table des matières : p. v

directed force while turbulence is diffusive and acts statistically in both directions.

6.3. Influence of particle rotation

Particle rotation is an interesting topic for photophoretic forces. Photophoresis depends on the fact that a temperature gradient is established across the particle. Usually, an illuminated particle is warmer on the bright side than on the dark side. This temperature gradient always needs a certain time to adjust to changes in the illumination. Therefore, if the particle rotates, the temperature gradient might be different from the simple case where the particle is considered at rest. Rotations might be divided into two classes.

The first class corresponds to rotations around the direction of the incident radiation. This rotation does not change the front and back side of the particle. The temperature gradient in a reference frame fixed to the particle always stays the same. While the main component of photophoresis will still point away from the light source, the subtleties of particle morphology and composition will induce sideward components of photophoresis as well. If a particle only rotates around the direction of light, the sideward motion will oscillate but the component along the direction of light will remain constant.

The second class corresponds to rotations around axes perpendicular to the direction of light. These rotations change front and back of the particle. For slow rotations, the temperature gradient can follow the rotation. For somewhat faster spin the gradient lags behind, meaning that the cold side will trail into the warm side and vice versa. In total this results in a certain temperature gradient directed in a direction perpendicular to the direction of light. On a given orbit, these directed forces along the orbit can accelerate or slow down the particle and make it drif inward or outward. This is a photophoretic analog to the Yarkovsky effect, which works by radiation pressure, but the photophoretic effect can be several orders of magnitudes larger. This rotation would change the calculations given here one way or the other. Wurm et al. (2010) present first experimental evidence showing this effect in microgravity experiments for rotating particles.

However, this second class of rotations can only occur temporarily and is not of general importance. To see this, we remind the reader that the idea of photophoresis is founded on the fact that particles in protoplanetary disks are embedded in a gaseous environment. This point might explicitly be noted in view of particle rotation. This simple fact is important because it implies a fundamental difference to particles in the current solar system where particles move in vacuum. While a particle in the solar system retains any arbitrary rotation state for a long time, random rotation of small particles in protoplanetary disks is rapidly damped away. For example, if a particle rotates through collisions with other particles, this rotation is gone on the order of one gas-grain friction time, which for bodies smaller than a meter is much shorter than the orbital timescale. Typical values for dust particles in the inner disk would be on the order of seconds, depending on the model and specific location in detail. Therefore, to retain a rotation, a constant torque around a given axis has to be applied to the particle. There are only two effects that can lead to torques:

1. Particle motion with respect to the gas, i.e., radial drift. In analogy to particles in Earth's atmosphere (like snowflakes), particle rotation will be around the drift axis. For the small particles considered here, this relative motion can be regarded as purely radial and transversal motion is not important (Weidenschilling 1977). A windmill might be an appropriate visualization for this.
2. Radiation-induced torques. In principle this might be regarded in analogy to gas drag (assuming photons instead of gas molecules) and any rotation is around the direction of illumination.

In both cases, a torque around another axis might initially be present but this will align the particles and only the systematic torques around the drift direction or radiation direction pertain. In both cases a potential rotation axis is oriented toward the star. This will always adjust during the orbit. This rotation does not change the front and back side and does not influence radial photophoresis. Details with quantitative estimates can be found in Krauss et al. (2007).

6.4. Prospects

A more realistic description of the disk's structure requires one to account for irradiation by the Sun at the disk atmosphere's surface (D'Alessio et al. 1998; Hueso & Guillot 2005; Garaud & Lin 2007; Cabral et al. 2010). Comparisons between irradiated and non irradiated models show that, for similar disk parameters, the midplane temperature in the outer part of the disk becomes substantially higher (up to a few dozen of K) in the first series of cases (Garaud & Lin 2007; Cabral et al. 2010). In order to estimate the influence of irradiation on photophoretic transport, we need to know not only the temperature profile, but also the pressure and volume density in the midplane of the disk. As a first attempt, we increased the temperature by 30 K or up to 100 K for any initial temperature lower than 100 K in our nominal disk model, to mimic the difference in temperature caused by irradiation. The trajectories of larger particles (10^{-3}–10^{-1} m) remain almost similar to those plotted in Figs. 3–6, except for the maximum distances that are 2 to 5 AU closer to the Sun. The trajectories of small particles (10^{-5} m) are more affected by the temperature difference because their maximum migration distance is about half that shown in Figs. 3–6. Modifying the midplane density to keep the product $T \times \rho$ constant roughly doubles the effect. However, both the photophoretic force and gas drag depend on the gas pressure and density and a fully consistent irradiated disk model will be needed to investigate the real influence of irradiation on the trajectories of transported particles.

An interesting evolution of this work would also be to consider explicitly the motion of dust particles in both radial and vertical directions. Indeed, the disk's upper layers are more transparent than those close to the midplane (because of dust sedimentation), and are therefore a perfect place for photophoresis to be effective in the earliest phase of the disk's evolution and prior to the "transition disk" phase. At this epoch turbulence driven by active magnetorotational instability (MRI) may even be a useful ingredient because it would help a fraction of particles to be maintained above the photosphere and be transported outward thanks to both photophoeresis and radiation pressure. Indeed, computations of turbulence in MRI disks (Turner et al. 2010) have shown that turbulence is increasingly effective with scale-height, and consequently, may help to maintain particles high above. This may be a potentially interesting mechanism that would help photoporesis to be effective even in the youngest ages of the disk.

Acknowledgements. We thank Y. Alibert for having supplied us the thermodynamic data of his disk model. O.M. and J.-M. P. acknowledge the support of

Retour à la table des matières : p. v

CNES. G.W. acknowledges support by the DFG (SPP 1385). We acknowledge an anonymous Referee whose useful comments allowed us to strenghten our manuscript.

References

Alibert, Y., Mordasini, C., Benz, W., & Winisdoerffer, C. 2005, A&A, 434, 343
Beresnev, S., Chernyak, V., & Fomyagin, G. 1993, Physics of Fluids, 5, 2043
Bich, E., Millat, J., & Vogel, E. 1990, J. Phys. Chem. Ref. Data, 19, 1289
Blum, J., Wurm, G., Kempf, S., & Henning, T. 1996, Icarus, 124, 441
Blum, J., & Schräpler, R. 2004, Physical Review Letters, 93, 115503
Bockelée-Morvan, D., Gautier, D., Hersant, F., Huré, J.-M., & Robert, F. 2002, A&A, 384, 1107
Brownlee, D., et al. 2006, Science, 314, 1711
Cabral, N., Fouchet, L., Alibert, Y., Mordasini, C., & Benz, W. 2010, SF2A-2010: Proceedings of the Annual meeting of the French Society of Astronomy and Astrophysics, 281
Campins, H., & Ryan, E. V. 1989, ApJ, 341, 1059
Cheremisin, A. A., Vassilyev, Y. V., & Horvath, H. 2005, Aerosol Sci., 36, 1277
Chick, K. M., & Cassen, P. 1997, ApJ, 477, 398
Ciesla, F. J. 2009, Meteoritics and Planetary Science, 44, 1663
Ciesla, F. J. 2007, ApJ, 654, L159
Ciesla, F. J. 2010, ApJ, 723, 514
Crovisier, J., et al. 2000, Thermal Emission Spectroscopy and Analysis of Dust, Disks, and Regoliths, 196, 109
Cunningham, E. 1910, Proceedings of the Royal Society of London Series a-Containing Papers of a Mathematical and Physical Character, 83(563), 357
D'Alessio, P., et al. 2005, ApJ, 621, 461
D'Alessio, P., Canto, J., Calvet, N., & Lizano, S. 1998, ApJ, 500, 411
Dalgarno, A., & Williams, D. A. 1962, ApJ, 136, 690
Espaillat, C., Calvet, N., Luhman, K. L., Muzerolle, J., & D'Alessio, P. 2008, ApJ, 682, L125
Garaud, P., & Lin, D. N. C. 2007, ApJ, 654, 606
Grossman, L. 1972, Geochim. Cosmochim. Acta, 36, 597
Hanner, M. S. 1999, Space Sci. Rev., 90, 99
Harker, D. E., & Desch, S. J. 2002, ApJ, 565, L109
Hayashi C., 1981, PThPS, 70, 35
Horner, J., Mousis, O., & Hersant, F. 2007, Earth Moon and Planets, 100, 43
Hueso, R., & Guillot, T. 2005, A&A, 442, 703
Hughes, A. L. H., & Armitage, P. J. 2010, ApJ, 719, 1633
Hutchins, D. K., Harper, M. H., & Felder, R. L. 1995, Aerosol Science and Technology, 22(2), 202
Incropera, F. P., & DeWitt, D. P. 2002, Heat and Mass Transfer (John Wiley & Sons)
Jones, R. H., Lee, T., Connolly, H. C., Jr., Love, S. G., & Shang, H. 2000, Protostars and Planets IV, 927
Joswiak, D. J., Brownlee, D. E., Pepin, R. O., & Schlutter, D. J. 2007, Dust in Planetary Systems, 643, 141
Koike, C., & Tsuchiyama, A. 1992, MNRAS, 255, 248
Krauss, O., Wurm, G., Mousis, O., Petit, J.-M., Horner, J., & Alibert, Y. 2007, A&A, 462, 977
Krauss, O., & Wurm, G. 2005, ApJ, 630, 1088
Lide, D. R. 2007, CRC Handbook of chemistry and physics : a ready-reference book of chemical and physical data, 88th ed., by David R. Lide. Boca Raton: CRC Press, ISBN 0849304881, 2007
Lynden-Bell, D., & Pringle, J. E. 1974, MNRAS, 168, 603
Mayer, M., & Duschl, W. J. 2005, MNRAS, 358, 614
Mordasini, C., Alibert, Y., & Benz, W. 2009a, A&A, 501, 1139
Mordasini, C., Alibert, Y., Benz, W., & Naef, D. 2009b, A&A, 501, 1161
Mousis, O., Petit, J.-M., Wurm, G., Krauss, O., Alibert, Y., & Horner, J. 2007, A&A, 466, L9
Papaloizou, J. C. B., & Terquem, C. 1999, ApJ, 521, 823
Papaloizou, J. C. B., & Lin, D. N. C. 1995, ARA&A, 33, 505
Pietrinferni, A., Cassisi, S., Salaris, M., & Castelli, F. 2004, ApJ, 612, 168
Pontoppidan, K. M., Blake, G. A., van Dishoeck, E. F., Smette, A., Ireland, M. J., & Brown, J. 2008, ApJ, 684, 1323
Reif, F. 1972, Cours de Physique de Berkeley (vol. 5), Armand Colin, Dunod, 398 pp
Sicilia-Aguilar, A., et al. 2006, ApJ, 638, 897
Shakura, N. I., & Sunyaev, R. A. 1973, A&A, 24, 337
Sitko, M. L., Lynch, D. K., Russell, R. W., & Hanner, M. S. 2004, ApJ, 612, 576
Tielens, A. G. G. M., Waters, L. B. F. M., & Bernatowicz, T. J. 2005, Chondrites and the Protoplanetary Disk, 341, 605
Thalmann, C., et al. 2010, ApJ, 718, L87
Turner, N. J., Carballido, A., & Sano, T. 2010, ApJ, 708, 188
Vardya, M. S. 1962, ApJ, 135, 303
Veras, D., & Armitage, P. J. 2004, MNRAS, 347, 613
Wurm, G., & Krauss, O. 2006, Icarus, 180, 487
Weidenschilling, S. J. 1997, Icarus, 127, 290
Weidenschilling, S. J. 1977, MNRAS, 180, 57
Wooden, D. H., Lindsay, S. S., Harker, D. E., Kelley, M. S., Woodward, C. E., Richard, D. T., Kolokolova, L., & Moreno, F. 2010, Bulletin of the American Astronomical Society, 42, 960
Wooden, D. H., Woodward, C. E., & Harker, D. E. 2004, ApJ, 612, L77
Wooden, D. H., Butner, H. M., Harker, D. E., & Woodward, C. E. 2000, Icarus, 143, 126
Wurm, G., Teiser, J., Bischoff, A., Haack, H., & Roszjar, J. 2010, Icarus, 208, 482

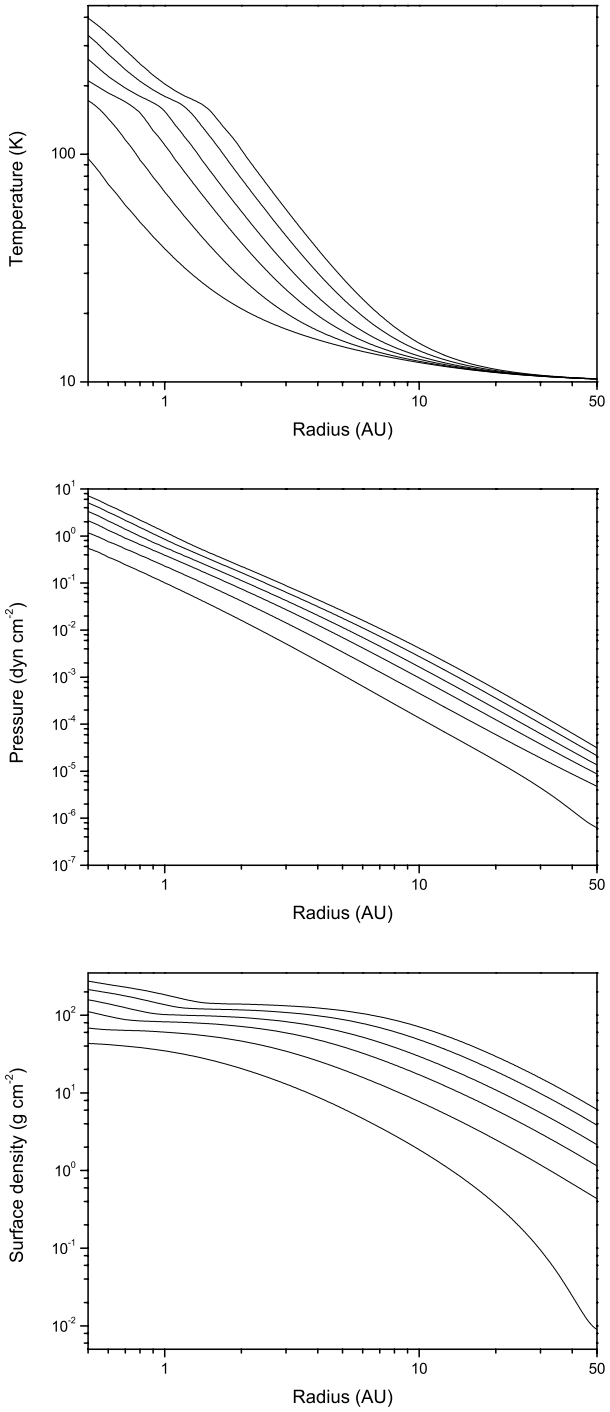

Fig. 1. Temperature, pressure and surface density profiles in the midplane of the disk characterized by a mass of 0.03 $M_{\odot}$ and a lifetime of 6 Myr. From top to bottom in each panel, times are 1, 2, 3, 4, 5, and 6 Myr.

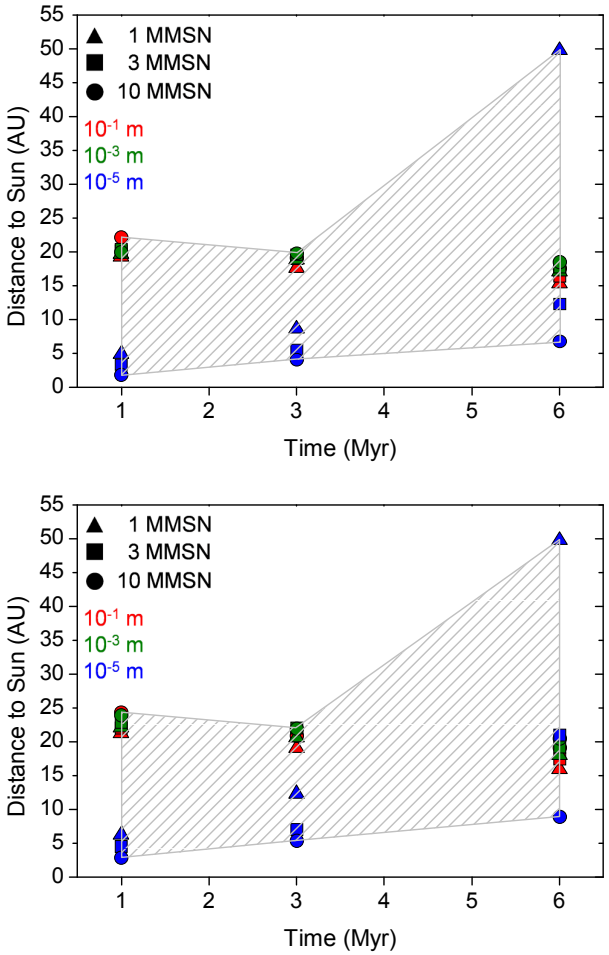

Fig. 7. Heliocentric distance reached by aggregates at the end of the solar nebula evolution as a function of the disk parameters and of the particle sizes. Density of all particles is 500 kg m^{-3} and the inner gap of the disk is 1 AU (top) and 2 AU (bottom).

Retour à la table des matières : p. v

10.3 Article sur l'origine du méthane de Titan

Icarus 204 (2009) 749–751

Contents lists available at ScienceDirect

Icarus

journal homepage: www.elsevier.com/locate/icarus

Note

A primordial origin for the atmospheric methane of Saturn's moon Titan

Olivier Mousis [a,b,*], Jonathan I. Lunine [a], Matthew Pasek [a], Daniel Cordier [c,d], J. Hunter Waite Jr. [e], Kathleen E. Mandt [e], William S. Lewis [e], Mai-Julie Nguyen [e]

[a] Lunar and Planetary Laboratory, University of Arizona, Tucson, AZ 85721, USA
[b] Université de Franche-Comté, Institut UTINAM, CNRS/INSU, UMR 6213, Observatoire des Sciences de l'Univers de Besancon, France
[c] Université de Rennes 1, Institut de Physique de Rennes, CNRS, UMR 6251, France
[d] Ecole Nationale Supérieure de Chimie de Rennes, CNRS, UMR 6226, 35708 Rennes Codex 7, France
[e] Space Science and Engineering Division, Southwest Research Institute, San Antonio, TX 78228, USA

ARTICLE INFO

Article history:
Received 10 June 2009
Revised 30 July 2009
Accepted 30 July 2009
Available online 7 August 2009

Keywords:
Saturn, Satellites
Satellites, Composition
Satellites, Formation
Satellites, Atmospheres

ABSTRACT

The origin of Titan's atmospheric methane is a key issue for understanding the origin of the saturnian satellite system. It has been proposed that serpentinization reactions in Titan's interior could lead to the formation of the observed methane. Meanwhile, alternative scenarios suggest that methane was incorporated in Titan's planetesimals before its formation. Here, we point out that serpentinization reactions in Titan's interior are not able to reproduce the deuterium over hydrogen (D/H) ratio observed at present in methane in its atmosphere, and would require a maximum D/H ratio in Titan's water ice 30% lower than the value likely acquired by the satellite during its formation, based on Cassini observations at Enceladus. Alternatively, production of methane in Titan's interior via radiolytic reactions with water can be envisaged but the associated production rates remain uncertain. On the other hand, a mechanism that easily explains the presence of large amounts of methane trapped in Titan in a way consistent with its measured atmospheric D/H ratio is its direct capture in the satellite's planetesimals at the time of their formation in the solar nebula. In this case, the mass of methane trapped in Titan's interior can be up to ~1300 times the current mass of atmospheric methane.

© 2009 Elsevier Inc. All rights reserved.

1. Introduction

Deuterium is a sensitive indicator of the origin and evolution of planetary atmospheres. Current deuterium over hydrogen ratios (D/H) measured in the atmospheres of Venus and Mars suggest that these planets were wetter in ancient times than they are at present (Lécuyer et al., 2000; Krasnopolsky et al., 1998). In the case of Titan, any scenario describing a possible origin for the observed methane has to account for its present high D/H atmospheric ratio of $1.32^{+0.15}_{-0.11} \times 10^{-4}$ (Bézard et al., 2007), which represents an enrichment of 4.5–7.2 times the protosolar value (Cordier et al., 2008). It has been proposed that this observed D/H enhancement could be the result of photochemical enrichment of deuterium through that isotope's preferential retention during methane's photolysis (Pinto et al., 1986; Lunine et al., 1999). However, Cassini–Huygens data have been recently used to reexamine this possibility and it was shown that the photochemical enrichment of deuterium is not sufficient to explain the measured D/H value (Cordier et al., 2008; Mandt et al., in press). A possible fractionation between CH_3D and CH_4 during the escape process may slightly enhance the deuterium enrichment by a factor of at most 2.6 times the protosolar value (Cordier et al., 2008), but is not sufficient to explain the observed D/H enhancement over the range of escape values proposed in the literature (Cordier et al., 2008; Mandt et al., in press). This suggests that D/H in methane is already substantially oversolar when released into the atmosphere of Titan.

Here, we examine the impact of the D/H value in methane on the proposed formation of methane in the interior of Titan from carbon dioxide or carbon grains via the hydrothermal alteration of peridotite (Moody, 1976; Atreya et al., 2006; Oze and Sharma, 2007). In this scenario, the H_2 produced during the so-called "serpentinization" process in Titan would react with carbon grains or CO_2 to produce the methane (Atreya et al., 2006; Oze and Sharma, 2007). Our calculations suggest that, were the atmospheric methane of Titan produced solely by serpentinization reactions in its interior, the D/H ratio in the primordial water reservoir would not be consistent with the value inferred from the recent Cassini INMS measurement of the D/H ratio in the H_2O grains embedded in the Enceladus' plume (Waite et al., 2009). We then discuss the alternative mechanisms that could explain the presence of methane in Titan's atmosphere in agreement with its measured D/H ratio.

2. Serpentinization reactions in Titan

In terrestrial oceans, hydrothermal fluids and seawater interact with rock and promote the formation of significant concentration of H_2. This process involves peridotite, such as olivine [$(Mg, Fe)_2SiO_4$] and pyroxene [$(Mg, Fe)SiO_3$], whose hydratation leads primarily to the formation of molecular hydrogen [$H_{2(aq)}$], together with serpentine [$(Mg, Fe)_3Si_2O_5(OH)_4$], Mg-brucite [$Mg(OH)_2$] and magnetite [Fe_3O_4]. Key geochemical reactions are (Moody, 1976; Atreya et al., 2006):

$$6Fe_2SiO_4 + 7H_2O \rightarrow H_{2(aq)} + 3Fe_3Si_2O_5(OH)_4 + Fe_3O_4,$$
$$2Mg_2SiO_4 + 3H_2O \rightarrow Mg_3Si_2O_5(OH)_4 + Mg(OH)_2,$$

followed by

$$2Fe_3Si_2O_5(OH)_4 + 6Mg(OH)_2 \rightarrow 2H_{2(aq)} + 2Mg_3Si_2O_5(OH)_4 + 2Fe_3O_4 + 4H_2O.$$

On Titan, the subcrustal liquid water ocean would constitute the free-water reservoir susceptible to interaction with rocks assumed to constitute the core of the body (Tobie et al., 2006). Serpentinization of Titan's core may have happened during the early history of the satellite when all the ice was molten, or may have happened over geological history as liquid water circulates through the outer parts of the warm rocky core. Because the core of the cooling Titan was cut off early on from the ocean by a growing layer of high-pressure ice whose thickness at present is several hundred kilometers (Tobie et al., 2006), H_2 may more likely have been

* Corresponding author. Address: Université de Franche-Comté, Institut UTINAM, CNRS/INSU, UMR 6213, Observatoire des Sciences de l'Univers de Besancon, France. Fax: +33 381 666 921.
E-mail address: olivier.mousis@obs-besancon.fr (O. Mousis).

0019-1035/$ - see front matter © 2009 Elsevier Inc. All rights reserved.
doi:10.1016/j.icarus.2009.07.040

produced at early epochs of the satellite's evolution. CH_4 would then be formed from the reaction of H_2 with CO or CO_2 via Fischer–Tropsch-type synthesis (Anderson, 1984; Matson et al., 2007) or from the heating of graphite- or carbonate-bearing rocks in presence of H_2 (Giardini and Salotti, 1968; McCollom, 2003). The methane produced would then saturate the deep ocean (Tobie et al., 2006; Fortes et al., 2007), and would be transported towards the surface of Titan via ammonia–water pockets which erupt through the ice shell and lead to cryovolcanism (Mitri et al., 2008). Alternatively, the methane coming from the saturated ocean could diffuse through the solid icy shell to the surface or could be stored in clathrates formed at the ocean–ice shell interface that would be destabilized and melt by ascent of hot thermal plumes (Tobie et al., 2006).

3. *D*/*H* ratio in the produced methane

During serpentinization reactions, residual water is deuterium-enriched at the expense of the initial reservoir of free-water. The fractionation factor, α_{r-w}, between OH-bearing minerals and water is then (Lécuyer et al., 2000):

$$\alpha_{r-w} = \frac{R_r^f}{R_w^f}, \tag{1}$$

where R_r^f and R_w^f are the D/H ratios in the OH-bearing minerals and the residual water, respectively.

The effect on the D/H ratio of the residual water of a D/H fractionation between the initial water and hydrated peridotite can be readily tested with the following mass balance equation that describes a batch equilibrium mechanism of both hydration and isotopic fractionation between given masses of rock and water:

$$M_w^i X_w^i R_w^i + M_r^i X_r^i R_r^i = M_w^f X_w^f R_w^f + M_r^f X_r^f R_r^f, \tag{2}$$

where M is the mass, X the mass fractions of hydrogen in water ($X_w^i = X_w^f = 1/9$) or rock ($X_r^f = 4/277$), R the D/H ratios before hydration reactions (i) and at batch equilibrium (f). If we insert Eq. (1) into Eq. (2) and neglect the likely small amount of water in primordial peridotite of Titan ($X_r^i = 0$), Eq. (2) becomes:

$$R_w^i = \frac{\left(\frac{M_w^f X_w^f}{\alpha_{r-w}} + M_r^f X_r^f\right) R_r^f}{M_w^i X_w^i}. \tag{3}$$

Here, we postulate that the D/H ratio in the methane initially released from the interior is that acquired by hydrated rocks once equilibrium is reached during serpentinization reactions. The D/H ratio acquired by hydrated rocks would then be preserved in the hydrogen produced from the alteration of peridotite and used in the recombination of CH_4.

The initial mass M_w^i of the free-water reservoir is expected to range between 1.79×10^{22} and 6.73×10^{22} kg. These values correspond, respectively, to the current and initial masses of the liquid water ocean (Grasset and Pargamin, 2005), whose volume has decreased with time during the cooling of Titan (Tobie et al., 2006). Assuming that methane has been present continuously in the atmosphere of Titan since 4.5 Gyr and destroyed over Titan's history at the current photolytic destruction rate of 6.9×10^{13} molecules m^{-2} s^{-1} (Vuitton et al., 2008), the total mass of expelled methane is $\sim 2.17 \times 10^{19}$ kg. Assuming that the hydrogen from the methane is derived from serpentinization reactions only, the equivalent mass of produced H_2 is then $\sim 5.42 \times 10^{18}$ kg. Depending on the composition of peridotite, key geochemical reactions (Moody, 1976; Charlou et al., 2002) suggest that 4.5 moles of serpentine [$Mg_3Si_2O_5(OH)_4$] are produced per mole of H_2 released during serpentinization reactions. Hence, the maximum mass of serpentine M_r^f is then 3.38×10^{21} kg, namely about 5% of Titan's rock mass, over 4.5 Gyr, including 10 wt.% of H_2O extracted from the free-water reservoir (Lécuyer et al., 2000). Because $M_w^i \simeq M_w^f \gg M_r^f$ and $X_w^i \gg X_r^f$, Eq. (3) can be simplified as follows:

$$R_w^i \simeq \frac{R_r^f}{\alpha_{r-w}}. \tag{4}$$

Eq. (4) is of the form of Eq. (1) but concerns R_w^i rather than R_w^f. It remains valid independent of the production timescale of methane in the interior of Titan because the mass of hydrated rocks is still small compared to that of the free-water. Note that assuming an episodic methane outgassing would have led us to a lower estimate of the maximum mass of formed serpentine, hence leading to no change in this condition. We consider two extreme values, 0.95 and 1.03, of the hydrogen fractionation α_{r-w} between serpentine and the free-water reservoir in the literature based on laboratory and field data made at temperatures ranging between 298 and 773 K (Wenner and Taylor, 1973; Sakai and Tsutsumi, 1978; Vennemann and O'Neil, 1996). Finally, we consider two different cases for the value of R_r^f. In the first case, we neglect the effect of deuterium photochemical enrichment in the atmosphere of Titan and we consider that R_r^f is equal to 1.32×10^{-4}, namely the nominal D/H ratio measured by Cassini in Titan's atmosphere (Bézard et al., 2007). In the second case, we consider the influence of photochemistry that might have enriched the primordial D/H ratio in methane by a maximum factor of 2.6 (Cordier et al., 2008) and then set R_r^f equal to 5.08×10^{-5}.

Table 1 shows the range of values of R_w^i needed in the primordial water reservoir to explain the D/H ratio observed in the atmospheric methane of Titan. When neglecting the possibility of photochemical enrichment of deuterium in Titan's methane, the values of R_w^i are about 10–20% lower than that corresponding to Standard Mean Ocean Water (V-SMOW) ($D/H = 1.56 \times 10^{-4}$ (Craig, 1961)). The discrepancy becomes even higher when using values of R_r^f that take into account the possibility of deuterium enrichment in Titan's methane. In this case, the required values of R_w^i are more than 60% lower than the V-SMOW value. Moreover, the values of R_w^i calculated with Eq. (4) are upper estimates because we make the assumption that the mass of the free-water reservoir in contact with rocks, i.e. that of the liquid water ocean, remains constant during serpentinization in Titan. However, the progressive cooling of the satellite implies the shrinking of the water reservoir available for isotopic exchange with rocks, and consequently significant reduction of M_w^f compared to M_w^i. Assuming that the mass of the free-water reservoir has decreased from 6.73×10^{22} to 1.79×10^{22} kg during the serpentinization process and using Eq. (3), the values of R_w^i range now between 1.34×10^{-5} and 3.80×10^{-5}. Therefore, in all cases evaluated, the initial D/H in the primordial water of Titan's interior is lower than V-SMOW.

Table 1
Values of R_w^i calculated as a function of the D/H ratio adopted in the methane outgassing from the interior of Titan and for two extreme values of the hydrogen fractionation factor α_{r-w} between serpentine and water (see text).

	$\alpha_{r-w} = 0.95$	$\alpha_{r-w} = 1.03$
$R_r^f = 5.08 \times 10^{-5}$	5.36×10^{-5}	4.92×10^{-5}
$R_r^f = 1.32 \times 10^{-4}$	1.39×10^{-4}	1.28×10^{-4}

4. Discussion

It is unlikely that the D/H ratio in the primordial water ice accreted by Titan could be as low as the V-SMOW value. Indeed, the INMS instrument aboard the Cassini spacecraft has recently measured D/H in water in the icy grains embedded in the vapor plumes of Enceladus (Waite et al., 2009). It shows that the D/H ratio in the water ice expelled from Enceladus is about $2.9^{+1.5}_{-0.7} \times 10^{-4}$, a value close to that measured in comets (Bockelée-Morvan et al., 2004). This implies that the planetesimals accreted by Enceladus were initially produced in the outer solar nebula prior to having being embedded in Saturn's subnebula. Indeed, the D/H ratio of icy planetesimals condensed in an initially dense and warm Saturn's subnebula should be lower than the measured value because an isotopic exchange would have occurred between H_2 and H_2O in the gas phase of the subdisk, thus decreasing the degree of deuteration acquired by water in the solar nebula (Horner et al., 2008). Since the temperature and pressure conditions are expected to have decreased with increasing distance from Saturn when the latter was surrounded by satellite-forming material (Alibert and Mousis, 2007; Barr and Canup, 2008), then the planetesimals accreted by Titan were also formed in the outer solar nebula (not in Saturn's subnebula) and should have the same D/H ratio in water as is in the building blocks of Enceladus. This value is then in conflict with the one required by the hypothesis that serpentinization reactions occurred in Titan's interior. Even when error bars are taken into account, the maximum D/H ratio (1.55×10^{-4}) possessed by primordial water ice – if CH_4 comes entirely from serpentinization reactions – should be at least 30% lower than the minimum value (2.2×10^{-4}) of the D/H ratio measured at Enceladus by the INMS instrument aboard Cassini.

A word of caution must be given about our estimate of the D/H ratio in methane produced via serpentinization reactions. Our calculations are based on the assumption that no D-fractionation occurred between the produced H_2 and the formed serpentine, and during the production of CH_4 from H_2 and other C-bearing compounds. We have also assumed that no D-fractionation has occurred during the transport of CH_4 towards the surface of the satellite. Unfortunately, except recent laboratory work that shows an extremely light D-fractionation when CH_4 is trapped in clathrates (the difference in $\delta(D)$[1] is lower than 10‰ (Hachikubo et al., 2008)), all the other points still remain unconstrained.

Interestingly enough, substantial quantities of abiogenically produced CH_4 have been observed on Earth within Precambrian rocks of the Canadian Shield, the Fennoscandian Shield and the Witwatersrand basin in South Africa Lollar et al. (1993), Lollar et al. (2008). These samples have been found to be deuterium impoverished compared to the V-SMOW value ($\delta(D)_{CH_4}$ up to −450‰). However, the observed amplitude of D-fractionation must be tempered by the fact that ground waters are already D-depleted, even if the magnitude of this depletion is lower[2] than that observed for CH_4. In fact, the exact mechanism that led to the formation of these D-depleted CH_4 collected samples on Earth is not yet firmly established. Serpentinization has been invoked but, as mentioned above, there is no laboratory experiment

[1] $\delta(D) = \left(\frac{(D/H)_{sample}}{(D/H)_{standard}} - 1\right) \times 1000$, where D is deuterium, and the standard is V-SMOW (Craig, 1961).

[2] An inventory of the $\delta(D)$ values in water in the main terrestrial reservoirs is given in Table 1 of Lécuyer et al. (1998). $\delta(D)$ can be up to −80‰ in the mantle or up to −400‰ in the ice sheets.

Retour à la table des matières : p. v

that shows the fractionation effects induced by this process on the produced H_2. An alternative mechanism, which works experimentally and can explain the most *D*-light CH_4 samples collected on Earth, is the production of H_2 from radiolytic reaction with H_2O, due to the decay of radioactive elements (U, Th, K, etc.) (Lin et al., 2005). The $\delta(D)$ of H_2 produced by radiolysis in laboratory can be up to $-500‰$ and is then compatible with the observed *D*/*H* ratio in Titan's atmospheric methane. However, it is difficult to quantify the production rate of radiolytic H_2 in the interior of Titan and compare it to the mass of H_2 needed to form the atmospheric CH_4. Indeed, the production rate of radiolytic H_2 on Earth depends on the concentration of radiogenic elements measured in the rocks and also on the porosity of the mineral matrix (Lin et al., 2005). In particular, the presence of an open porosity in the matrix favors the circulation of free-water and increases the efficiency of radiolysis. In the case of Titan, the porosity of the core must be almost zero due to the high pressure (tens of kilobars) exerted by the surrounding layers. Also, the concentration of radiogenic elements in the mineral matrix in Titan's core is unknown.

On the other hand, a mechanism that easily explains the presence of large amounts of methane trapped in Titan's interior is its direct capture in the building blocks of the satellite at the time of their formation in the solar nebula. Indeed, the CH_4/H_2O mass ratio in the planetesimals produced in Saturn's feeding zone has been estimated to be $\sim 2.2–3.4 \times 10^{-3}$ (Mousis et al., 2009a). The mass of methane thus trapped in Titan's interior is $\sim 1.5–2.3 \times 10^{20}$ kg and corresponds to ~852–1307 times the current mass of atmospheric methane determined with the data from the Huygens Atmospheric Structure Instrument (Cordier et al., 2008). Moreover, it has been shown that the *D*/*H* ratio in the methane acquired in this way could be consistent with the implications of existing atmospheric measurements (Mousis et al., 2002; Cordier et al., 2008; Mandt et al., in press). Because methane falling into the solar nebula from the interstellar medium was highly enriched in deuterium when compared with the infalling molecular hydrogen, a reversible gas phase isotopic exchange between these two nebular components led to a slow but steady reduction in the deuterium fraction of the methane (Mousis et al., 2002). Once the temperature of the nebula dropped, methane condensed or was clathrated by the available crystalline water ice in the feeding zone of Saturn, halting the reaction and fixing the *D*/*H* value acquired in the gas phase (Mousis et al., 2002). These ices agglomerated in the feeding zone of Saturn and formed the building blocks of Titan in the Saturn's subnebula. As methane was released over time into the atmosphere of Titan, a progressive photochemical enrichment of deuterium may have occurred, the magnitude of which is dependant on the time elapsed since the last major outgassing from the interior as well as the nature (episodic or continuous) of the outgassing (Cordier et al., 2008; Mandt et al., in press).

This scenario is robust because it does not preclude processes such as the partial devolatilization of planetesimals during their migration within Saturn's subnebula that would explain Titan's observed CO and noble gas deficiencies (Alibert and Mousis, 2007; Mousis, 2009b). Moreover, since Enceladus is expected to be formed from the same building blocks as Titan and should also contain large amounts of methane originating from the solar nebula, the measurement of the *D*/*H* ratio in the CH_4 found in its plumes could provide the initial *D*/*H* ratio acquired by primordial methane at the time of its trapping in the solar nebula, and thus information on the efficiency of the deuterium photochemical enrichment that occurred in Titan's atmosphere.

Acknowledgments

This work was supported in part by the French Centre National d'Etudes Spatiales. Support from the Cassini project is also gratefully acknowledged. We acknowledge Barbara Sherwood Lollar for helpful discussions about her work. Many thanks to Ralf Jaumann and an anonymous Referee whose comments have helped us to improve our manuscript.

References

Alibert, Y., Mousis, O., 2007. Formation of Titan in Saturn's subnebula: Constraints from Huygens probe measurements. Astron. Astrophys. 465, 1051–1060.
Anderson, R.B., 1984. The Fischer–Tropsch Synthesis. Academic Press, London.
Atreya, S.K., Adams, E.Y., Niemann, H.B., Demick-Montelara, J.E., Owen, T.C., Fulchignoni, M., Ferri, F., Wilson, E.H., 2006. Titan's methane cycle. Planet. Space Sci. 54, 1177–1187.
Barr, A.C., Canup, R.M., 2008. Constraints on gas giant satellite formation from the interior states of partially differentiated satellites. Icarus 198, 163–177.
Bézard, B., Nixon, C.A., Kleiner, I., Jennings, D.E., 2007. Detection of $^{13}CH_3D$ on Titan. Icarus 191, 397–400.
Bockelée-Morvan, D., Crovisier, J., Mumma, M.J., Weaver, H.A., 2004. The composition of cometary volatiles. Comets II, 391–423.
Charlou, J.-L., Donval, J.-P., Fouquet, Y., Jean-Baptiste, P., Holm, N., 2002. Geochemistry of high H_2 and CH_4 vent fluids issuing from ultramafic rocks at the rainbow hydrothermal field (36°14′N, MAR). Chem. Geol. 191, 345–359.
Cordier, D., Mousis, O., Lunine, J.I., Moudens, A., Vuitton, V., 2008. Photochemical enrichment of deuterium in Titan's atmosphere: New insights from Cassini-Huygens. Astrophys. J. 689, L61–L64.
Craig, H., 1961. Standard for reporting concentrations of deuterium and oxygen-18 in natural waters. Science 133, 1833–1834.
Fortes, A.D., Grindrod, P.M., Trickett, S.K., Vočadlo, L., 2007. Ammonium sulfate on Titan: Possible origin and role in cryovolcanism. Icarus 188, 139–153.
Giardini, A.A., Salotti, C.A., 1968. Synthesis of graphite and hydrocarbons by reaction between calcite and hydrogen. Science 159, 317–319.
Grasset, O., Pargamin, J., 2005. The ammonia water system at high pressures: Implications for the methane of Titan. Planet. Space Sci. 53, 371–384.
Hachikubo, A., Ozeki, T., Kosaka, T., Sakagami, H., Minami, H., Nunokawa, Y., Takahashi, N., Shoji, H., 2008. Isotopic fractionation of guest gas at the formation of methane and ethane hydrates. In: Proceedings of the 6th International Conference on Gas Hydrates (ICGH 2008), Vancouver, Canada, 5351.
Horner, J., Mousis, O., Alibert, Y., Lunine, J.I., Blanc, M., 2008. Constraints from deuterium on the formation of icy bodies in the jovian system and beyond. Planet. Space Sci. 56, 1585–1595.
Krasnopolsky, V.∼A., Mumma, M.∼J., Randall Gladstone, G., 1998. Detection of atomic deuterium in the upper atmosphere of Mars. Science 280, 1576–1580.
Lécuyer, C., Gillet, P., Robert, F., 1998. The hydrogen isotope composition of seawater and the global water cycle. Chem. Geol. 145, 249–261.
Lécuyer, C., Simon, L., Guy, F., 2000. Comparison of carbon, nitrogen and water budgets on Venus and the Earth. Earth Planet. Sci. Lett. 181, 33–40.
Lin, L.-H., Slater, G.F., Sherwood Lollar, B., Lacrampe-Couloume, G., Onstott, T.C., 2005. The yield and isotopic composition of radiolytic H_2, a potential energy source for the deep subsurface biosphere. Geochim. Cosmochim. Acta 69, 893–903.
Lunine, J.I., Yung, Y.L., Lorenz, R.D., 1999. On the volatile inventory of Titan from isotopic abundances in nitrogen and methane. Planet. Space Sci. 47, 1291–1303.
Mandt, K.E., Waite Jr., J.H., Lewis, W., Magee, B., Bell, J., Lunine, J.I., Mousis, O., Cordier, D., in press. Isotopic evolution of the major constituents of Titan's atmosphere based on Cassini data. Planet. Space Sci., doi:10.1016/j.pss.2009.06.005.
Matson, D.L., Castillo, J.C., Lunine, J., Johnson, T.V., 2007. Enceladus' plume: Compositional evidence for a hot interior. Icarus 187, 569–573.
McCollom, T.M., 2003. Formation of meteorite hydrocarbons from thermal decomposition of siderite ($FeCO_3$). Geochim. Cosmochim. Acta 67, 311–317.
Mitri, G., Showman, A.P., Lunine, J.I., Lopes, R.M.C., 2008. Resurfacing of Titan by ammonia-water cryomagma. Icarus 196, 216–224.
Moody, J., 1976. Serpentinization: A review. Lithos 9, 125–138.
Mousis, O., and 10 colleagues, 2009b. Clathration of volatiles in the solar nebula and implications for the origin of Titan's atmosphere. Astrophys. J. 691, 1780–1786.
Mousis, O., Gautier, D., Coustenis, A., 2002. The *D*/*H* ratio in methane in Titan: Origin and history. Icarus 159, 156–165.
Mousis, O., Marboeuf, U., Lunine, J.I., Alibert, Y., Fletcher, L.N., Orton, G.S., Pauzat, F., Ellinger, Y., 2009a. Determination of the minimum masses of heavy elements in the envelopes of Jupiter and Saturn. Astrophys. J. 696, 1348–1354.
Oze, C., Sharma, M., 2007. Serpentinization and the inorganic synthesis of H_2 in planetary surfaces. Icarus 186, 557–561.
Pinto, J.P., Lunine, J.I., Kim, S.-J., Yung, Y.L., 1986. *D* to *H* ratio and the origin and evolution of Titan's atmosphere. Nature 319, 388–390.
Sakai, H., Tsutsumi, M., 1978. *D*/*H* fractionation factors between serpentine and water at 100–500°C and 2000 bar water pressure, and the *D*/*H* ratios of natural serpentines. Earth Planet. Sci. Lett. 40, 231–242.
Sherwood Lollar, B., Frape, S.K., Weise, S.M., Fritz, P., Macko, S.A., Welhan, J.A., 1993. Abiogenic methanogenesis in crystalline rocks. Geochim. Cosmochim. Acta 57, 5087–5097.
Sherwood Lollar, B., Lacrampe-Couloume, G., Voglesonger, K., Onstott, T.C., Pratt, L.M., Slater, G.F., 2008. Isotopic signatures of CH_4 and higher hydrocarbon gases from Precambrian Shield sites: A model for abiogenic polymerization of hydrocarbons. Geochim. Cosmochim. Acta 72, 4778–4795.
Tobie, G., Lunine, J.I., Sotin, C., 2006. Episodic outgassing as the origin of atmospheric methane on Titan. Nature 440, 61–64.
Vennemann, T.W., O'Neil, J.R., 1996. Hydrogen isotope exchange reactions between hydrous minerals and molecular hydrogen: I. A new approach for the determination of hydrogen isotope fractionation at moderate temperatures. Geochim. Cosmochim. Acta 60, 2437–2451.
Vuitton, V., Yelle, R.V., Cui, J., 2008. Formation and distribution of benzene on Titan. J. Geophys. Res. (Planets) 113, 5007.
Waite, Jr., H.J., Lewis, W.S., Magee, B.A., Lunine, J.I., McKinnon, W.B., Glein, C.R., Mousis, O., Young, D.T., Brockwell, T., Westlake, J., Nguyen, M.-J., Teolis, B.D., Niemann, H.B., McNutt, Jr., R.L., Perry, M., Ip, W.-H., 2009. Liquid water on Enceladus from observations of ammonia and 40Ar in the plume. Nature 460, 487–490.
Wenner, D.B., Taylor Jr., H.P., 1973. Oxygen and hydrogen isotope studies of the serpentinization of ultramafic rocks in oceanic environments and continental ophiolite complexes. Am. J. Sci. 273, 207–239.

Retour à la table des matières : p. v

10.4 Article sur l'origine du méthane d'Encelade

The Astrophysical Journal, 701:L39–L42, 2009 August 10 doi:10.1088/0004-637X/701/1/L39
© 2009. The American Astronomical Society. All rights reserved. Printed in the U.S.A.

FORMATION CONDITIONS OF ENCELADUS AND ORIGIN OF ITS METHANE RESERVOIR

O. Mousis[1,2], J. I. Lunine[1], J. H. Waite, Jr.[3], B. Magee[3], W. S. Lewis[3], K. E. Mandt[3], D. Marquer[4], and D. Cordier[5,6]
[1] Lunar and Planetary Laboratory, University of Arizona, Tucson, AZ, USA
[2] Université de Franche-Comté, Institut UTINAM, CNRS/INSU, UMR 6213, 25030 Besançon Cedex, France; mousis@lpl.arizona.edu
[3] Center for Excellence in Analytical Mass Spectroscopy, Southwest Research Institute, San Antonio, Texas, USA
[4] Université de Franche-Comté, Chrono-Environnement, CNRS/INSU, UMR 6249, 25030 Besançon Cedex, France
[5] Institut de Physique de Rennes, CNRS, UMR 6251, Université de Rennes 1, Campus de Beaulieu, 35042 Rennes, France
[6] Ecole Nationale Supérieure de Chimie de Rennes, Campus de Beaulieu, 35700 Rennes, France
Received 2009 April 3; accepted 2009 June 22; published 2009 July 24

ABSTRACT

We describe a formation scenario of Enceladus constrained by the deuterium-to-hydrogen ratio (D/H) in the gas plumes as measured by the Cassini Ion and Neutral Mass Spectrometer. We propose that, similarly to Titan, Enceladus formed from icy planetesimals that were partly devolatilized during their migration within the Kronian subnebula. In our scenario, at least primordial Ar, CO, and N_2 were devolatilized from planetesimals during their drift within the subnebula, due to the increasing temperature and pressure conditions of the gas phase. The origin of methane is still uncertain since it might have been either trapped in the planetesimals of Enceladus during their formation in the solar nebula or produced via serpentinization reactions in the satellite's interior. If the methane of Enceladus originates from the solar nebula, then its D/H ratio should range between $\sim 4.7 \times 10^{-5}$ and 1.5×10^{-4}. Moreover, Xe/H_2O and Kr/H_2O ratios are predicted to be equal to $\sim 7 \times 10^{-7}$ and 7×10^{-6}, respectively, in the satellite's interior. On the other hand, if the methane of Enceladus results from serpentinization reactions, then its D/H ratio should range between $\sim 2.1 \times 10^{-4}$ and 4.5×10^{-4}. In this case, Kr/H_2O should not exceed $\sim 10^{-10}$ and Xe/H_2O should range between $\sim 1 \times 10^{-7}$ and 7×10^{-7} in the satellite's interior. Future spacecraft missions, such as *Titan Saturn System Mission*, will have the capability to provide new insight into the origin of Enceladus by testing these observational predictions.

Key words: planets and satellites: formation – planets and satellites: individual (Enceladus)

1. INTRODUCTION

The composition of the gas plume emanating from Enceladus' southern pole has been measured five times by the Ion and Neutral Mass Spectrometer (INMS) instrument aboard the *Cassini* spacecraft. From these data, Waite et al. (2009) inferred that the composition of the plume is dominated by H_2O vapor, a few percent of CO_2, CH_4, NH_3, H_2S, and organic compounds ranging from C_2H_2 to C_6H_6. Signatures of possible CO, N_2, and H_2 are seen but the presence of such species cannot be confirmed from the data alone. ^{40}Ar has also been detected and is probably the decay product of ^{40}K (Waite et al. 2009).

Among the compounds observed by the INMS instrument, at least H_2O, NH_3, H_2S, and CO_2 are expected to be primordial (Waite et al. 2009). Indeed, the possible presence of N_2 can be explained as a result from the thermal decomposition of NH_3 in the interior of Enceladus (Matson et al. 2007). The measured CO is likely the product of fragmentation of primordial CO_2 during collection by the INMS (Waite et al. 2009). Moreover, the origin of CH_4 and high-order hydrocarbons is uncertain because these compounds might have been trapped by the building blocks[7] of Enceladus at the time of their formation (Waite et al. 2009) or might also result from hydrothermal reactions in the interior of the satellite (Matson et al. 2007).

In the present work, we propose that Enceladus formed from icy planetesimals initially produced in the solar nebula that, once embedded in the subnebula of Saturn, have been partly devolatilized due to the increasing gas temperature and pressure conditions during their migration inward within the subdisk. The idea of a solar nebula origin for the building blocks of Enceladus is supported by the recent deuterium-to-hydrogen (D/H) measurement in H_2O in the satellite's plume ($D/H = 2.9^{+1.5}_{-0.7} \times 10^{-4}$), which is close to the cometary value (Waite et al. 2009). Furthermore, the hypothesis of a partial devolatilization of planetesimals in Saturn's subnebula has already been formulated in order to account for the origin of Titan and the composition of its current atmosphere (Alibert & Mousis 2007; Mousis et al. 2009b). Thus, in the case of Titan, it has been proposed that H_2O, NH_3, CO_2, and CH_4 remained trapped in the building blocks of the satellite during their migration within the subnebula, while CO and N_2 were devolatilized. Since Enceladus orbits Saturn at a closer distance than Titan, and because the gas temperature and pressure conditions increase within the subdisk with decreasing distance from Saturn (Mousis et al. 2002; Alibert & Mousis 2007), the devolatilization of its planetesimals should be greater than Titan's.

Here, we aim to provide observational tests that may allow characterization of the importance of the devolatilization undergone by the building blocks of Enceladus during their migration within Saturn's subnebula. Our attention is focused on the origin of CH_4, which is directly tied to the magnitude of this devolatilization. We show that the fractions of Kr and Xe trapped in the interior of Enceladus will vary as a function of the CH_4 origin, i.e., trapping in the solar nebula or production via serpentinization reactions in the interior of Enceladus. These noble gases have the ability to be incorporated in H_2S- and CH_4-dominated clathrates initially trapped in the building blocks of Enceladus at the time of their formation. Moreover, we demonstrate that the resulting D/H ratio in CH_4 differs as a function of its source. The future investigation of these predictions will place important constraints on the devolatilization process that the building blocks of Enceladus might have undergone in Saturn's subnebula and on the origin of the methane detected in the satellite.

[7] Building blocks designate the planetesimals that accreted together to form Enceladus.

Retour à la table des matières : p. v

Table 1
Gas Phase Abundances in the Solar Nebula

Species X	(X/H_2)	Species X	(X/H_2)
O	1.16×10^{-3}	N_2	4.05×10^{-5}
C	5.82×10^{-4}	NH_3	4.05×10^{-5}
N	1.60×10^{-4}	CO	2.21×10^{-4}
S	3.66×10^{-5}	CO_2	3.16×10^{-5}
Ar	8.43×10^{-6}	CH_3OH	6.31×10^{-6}
Kr	4.54×10^{-9}	CH_4	3.16×10^{-6}
Xe	4.44×10^{-10}	H_2S	1.83×10^{-5}
H_2O	4.43×10^{-4}		

Notes. Elemental abundances derive from Lodders (2003). Molecular abundances result from the distribution of elements between refractory and volatile components.

2. FORMATION OF ENCELADUS' BUILDING BLOCKS

We briefly recall the formation conditions of planetesimals in Saturn's feeding zone as detailed in Mousis et al. (2009b). We assume that the gas phase abundances of all elements are solar and that they are distributed between refractory and volatile components, with $CO:CO_2:CH_3OH:CH_4 = 70:10:2:1$, $H_2S:H_2 = 0.5 \times (S:H_2)_\odot$ and $N_2:NH_3 = 1:1$ in the nebula gas phase (see Table 1 for the list of the gas-phase abundances of the main volatile compounds).

The process by which volatiles are trapped in icy planetesimals, illustrated in Figure 1, is calculated using the stability curves of hydrates, clathrates, and pure condensates, and the thermodynamic path detailing the evolution of temperature and pressure at 9.5 AU in the solar nebula, corresponding to the position of Saturn. The cooling curve intercepts the equilibrium curves of the different ices at particular temperatures and pressures. For each ice considered, the domain of stability is the region located below its corresponding equilibrium curve. The clathration process stops when no more crystalline water ice is available to trap the volatile species. As a result of the assumed solar gas-phase abundance for oxygen, ices formed in the outer solar nebula are composed of a mix of clathrates, hydrates, and pure condensates which are, except for CO_2 and CH_3OH,[8] produced at temperatures ranging between 20 and 50 K. Once formed, the different ices agglomerated and incorporated into the growing planetesimals. Figure 1 illustrates the case where the efficiency of clathration is only of ∼25%. Here, either only a part of the clathrates cages have been filled by guest molecules, either the diffusion of clathrated layers through the planetesimals was too slow to enclathrate most of the ice, or the poor trapping efficiency was the combination of these two processes. In this case, only NH_3, H_2S, Xe, and CH_4 form NH_3-H_2O hydrates and H_2S-5.75H_2O, Xe-5.75H_2O, and CH_4-5.75H_2O clathrates. Due to the deficiency in accessible water in icy planetesimals, all CO, Ar, Kr, and N_2 form pure condensates in the feeding zone of Saturn.

3. NOBLE GASES TRAPPING IN ENCELADUS AS A FUNCTION OF METHANE INCORPORATION

We investigate the fraction of noble gases that can be incorporated in Enceladus at the time of its formation, provided that Ar, Kr, and Xe were in solar abundances in the initial gas phase of Saturn's feeding zone. These results can be useful to constrain the formation of Enceladus because the nature of the trapped species in the interior of the satellite will depend on the temperature at which its building blocks have been devolatilized within the subdisk.

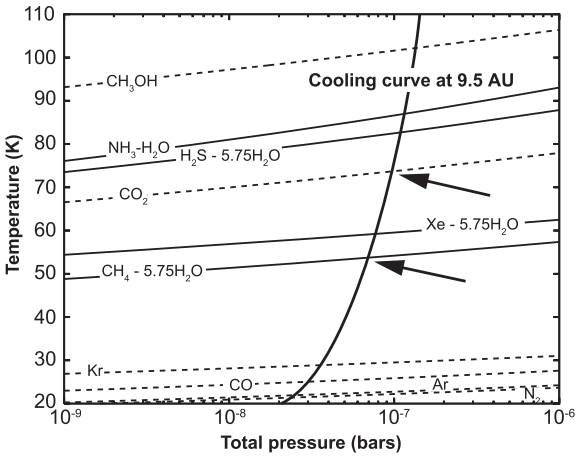

Figure 1. Formation sequence of the different ices in Saturn's feeding zone. Equilibrium curves of ammonia monohydrate, clathrates (solid lines), and pure condensates (dotted lines), and cooling curve of the solar nebula at the heliocentric distance of 9.5 AU, assuming a clathration efficiency of 25%. The bottom and top arrows designate, respectively, the maximum temperatures at which the building blocks of Enceladus can be heated during their migration within the Saturn's subnebula if methane observed in the plumes is primordial or if it is produced in the satellite.

Mousis et al. (2009b) have calculated the relative abundances of guests that can be incorporated in H_2S-, Xe-, and CH_4-dominated clathrates at the temperature and pressure formation conditions in the solar nebula reported in Figure 1. They have followed the method described by Lunine & Stevenson (1985) and Thomas et al. (2008), which uses classical statistical mechanics to relate the macroscopic thermodynamic properties of clathrates to the molecular structure and interaction energies. Table 2 represents the fraction F_i of volatiles incorporated in these clathrates relative to their initial fraction available in the nebula gas. These calculations show that CO, N_2, and Ar are poorly trapped in clathrates because their relative abundances in these structures are orders-of-magnitude lower than those found in the solar nebula. On the other hand, substantial amounts of Xe and Kr are trapped in H_2S- and CH_4-dominated clathrates, respectively. In particular, because the Kr/CH_4 ratio is larger in CH_4-dominated clathrate than in the solar nebula ($F_{Kr} > 1$), most of Kr is incorporated in this clathrate, thus preventing the formation of its pure condensate at lower temperature.

Two different maximum devolatilization temperatures can be envisaged for the building blocks of Enceladus. In the first case, similarly to Titan we assume that the methane detected in the plumes is primordial. This corresponds to the hypothesis that the devolatilization temperature of planetesimals never exceeded ∼50 K during their drift within the subdisk. In the second case, we assume that methane is not primordial and has been produced in the interior of the satellite. Here, the maximum devolatilization temperature is then of ∼75 K because a higher value would not be compatible with the presence of primordial CO_2 in Enceladus (see Figure 1).

In the first case, since most of Xe is trapped as a Xe-dominated clathrate in the building blocks of Enceladus, the corresponding

[8] CO_2 is the only species that crystallizes at a higher temperature than its associated clathrate in the solar nebula. Moreover, we consider only the formation of CH_3OH pure ice because no experimental data concerning the equilibrium curve of its associated clathrate have been reported in the literature.

Retour à la table des matières : p. v

Table 2
Abundance of Volatile *i* in Clathrate Relative to Initial Abundance in the Nebula (from Mousis et al. 2009b)

Clathrate	Species	f_i	F_i
H_2S-dominated	CO_2	3.12×10^{-6}	1.81×10^{-6}
	Xe	4.36×10^{-6}	0.18
	CH_4	5.45×10^{-6}	3.16×10^{-5}
	CO	2.13×10^{-7}	1.76×10^{-8}
	Kr	3.57×10^{-9}	1.43×10^{-5}
	Ar	8.74×10^{-9}	1.90×10^{-8}
	N_2	4.04×10^{-7}	1.83×10^{-7}
Xe-dominated	CH_4	7.28×10^{-2}	1.02×10^{-5}
	CO	5.18×10^{-5}	1.04×10^{-10}
	Kr	7.82×10^{-6}	7.65×10^{-7}
	Ar	1.08×10^{-6}	5.69×10^{-11}
	N_2	6.68×10^{-4}	7.32×10^{-9}
CH_4-dominated	CO	1.74×10^{-3}	2.49×10^{-5}
	Kr	1.67×10^{-3}	1.16
	Ar	6.43×10^{-5}	2.41×10^{-5}
	N_2	3.94×10^{-3}	3.07×10^{-4}

Notes. f_i is defined as the molar ratio of *i* to X in X-dominated clathrate and F_i is the ratio of f_i to the initial ratio (*i* to *X*) in the solar nebula. Calculations are performed at temperature and pressure conditions given by the intersection of the cooling curve at 9.5 AU and the stability curves of the considered clathrates (see Figure 1). Only the species that are not yet condensed or trapped prior the epoch of clathrate formation are considered in our calculations.

Xe/H_2O ratio in the satellite is given by (Mousis & Gautier 2004):

$$y_X = \frac{x_X}{x_{H_2O}} \frac{\Sigma(9.5AU; T_X, P_X)}{\Sigma(9.5AU; T_{H_2O}, P_{H_2O})}, \quad (1)$$

where x_X and x_{H_2O} are the molar mixing ratios of species X and H_2O with respect to H_2 in the nebula, respectively. $\Sigma(9.5AU; T_X, P_X)$ and $\Sigma(9.5AU; T_{H_2O}, P_{H_2O})$ are the surface density of the nebula at the current heliocentric distance of Saturn at the formation epoch of X-dominated clathrate, and at the epoch of condensation of water, respectively. These values are 1146.9 g cm^{-2}, 829.1 g cm^{-2}, 688.2 g cm^{-2}, 659.2 g cm^{-2} for water, H_2S-, Xe-, and CH_4-dominated clathrates, respectively. On the other hand, the remaining fraction of Xe and essentially all Kr are trapped in H_2S- and CH_4-dominated clathrates, respectively. The corresponding fractions relative to water are then given by:

$$z_i = f_i \times y_X, \quad (2)$$

where f_i is the molar ratio of *i* to X in X-dominated clathrate given in Table 2. From Equations (1) and (2), we infer that Xe/H_2O and Kr/H_2O ratios are respectively equal to $\sim 7 \times 10^{-7}$ and 7×10^{-6} in Enceladus if methane is primordial. In the second case, Kr/H_2O should not be higher than $\sim 10^{-10}$ in Enceladus because CH_4-dominated clathrates have been dissociated during the migration of the planetesimals within the subdisk. On the other hand, depending on the value of the devolatilization temperature of planetesimals, which translates into the preservation or not of the Xe-dominated clathrates, the Xe/H_2O ratio in Enceladus should range between $\sim 1 \times 10^{-7}$ and 7×10^{-7}.

4. WHAT IF SERPENTINIZATION WERE THE SOURCE OF METHANE OBSERVED IN ENCELADUS?

We examine the possibility that CH_4 is the result of serpentinization reactions, as proposed by Atreya et al. (2006) in the case of Titan. We first estimate the D/H value in the methane of Enceladus, assuming it was produced in its interior from the association of CO_2 or carbon grains with the H_2 formed during the hydrothermal alteration of peridotite (Moody 1976; Atreya et al. 2006; Oze & Sharma 2007), and we compare this value to the one acquired by methane if it had originated from the solar nebula.

Table 3
D/H Ratio in Methane as a Function of its Postulated Origin

Origin	Range of D/H Values
Serpentinization reactions	2.1×10^{-4}–4.5×10^{-4}
Solar nebula	4.7×10^{-5}[a]–1.5×10^{-4}

Notes.
[a] Minimum D/H ratio acquired by the primordial methane of Titan in case of strong photochemical enrichment in the atmosphere (see the text).

In terrestrial oceans, hydrothermal fluids and seawater interact with peridotite via the following summary reaction (Moody 1976; Atreya et al. 2006):

$$\text{peridotite(olivine/pyroxene)} + \text{water} \rightarrow \text{serpentine} + \text{brucite} + \text{magnetite} + \text{hydrogen}. \quad (3)$$

With a bulk density of 1610 kg m^{-3}, thermal evolution models suggest that Enceladus is most likely a differentiated body with a large rocky core surrounded by a water ice shell that may be liquid at depth (Schubert et al. 2007). In our calculations, we assume that this liquid layer constitutes the water reservoir that is in contact with peridotite during serpentinization reactions. Under these conditions, residual water is deuterium-enriched at the expense of the initial reservoir of free water and the fractionation factor, α, between OH-bearing minerals and water is then (Lécuyer et al. 2000):

$$\alpha_{r-w} = \frac{R_r^f}{R_w^f}. \quad (4)$$

The effect on the D/H ratio of the residual water of a D/H fractionation between the initial water and hydrated peridotite can be readily tested with the following mass balance equation that describes a batch equilibrium mechanism of both hydration and isotopic fractionation between given masses of rock and water (Lécuyer et al. 2000):

$$M_w^i X_w^i R_w^i + M_r^i X_r^i R_r^i = M_w^f X_w^f R_w^f + M_r^f X_r^f R_r^f, \quad (5)$$

where M is the mass, X the mass fractions of hydrogen in water ($X_w^i = X_w^f = 1/9$) or rock ($X_r^f = 4/277$), R the D/H ratios before hydration reactions (*i*) and at batch equilibrium (*f*). If we neglect the amount of water incorporated in primordial peridotites of Enceladus ($X_r^i = 0$) and postulate that $M_w^i \simeq M_w^f$ and $M_w^f.X_w^f \gg M_r^f.X_r^f$, which is a reasonable assumption,[9] then Equation (5) can be expressed as

$$R_r^f \simeq \alpha_{r-w} R_w^i. \quad (6)$$

[9] The CH_4/H_2O volume ratio observed in the plumes is $\sim$0.5% during the E2 encounter (Waite et al. 2006) and is representative of the value existing in the hypothetical internal ocean (Waite et al. 2009). Assuming that all H_2 involved in the formation of CH_4 results from the reaction of peridotite and water, the fraction of used water is only of $\sim$1% and the term $M_w^f.X_w^f$ is more than 11 times greater than the term $M_r^f.X_r^f$.

Retour à la table des matières : p. v

We consider two extreme values, 0.95 and 1.03, of the hydrogen fractionation α_{r-w} between the serpentine and the free-water reservoir in the literature based on laboratory and field data made at temperatures ranging between 298 and 773 K (Vennemann & O'Neil 1996). We also postulate that the D/H ratio in the methane initially released from the interior is that acquired by hydrated rocks once equilibrium is reached during serpentinization reactions. Hence, the D/H ratio acquired by hydrated rocks would be preserved in the H_2 produced from the alteration of peridotite and used in the recombination of CH_4.

Table 3 summarizes the range of predicted values for D/H in CH_4 produced within Enceladus, assuming that D/H ratio in the primordial water reservoir is the value measured by *Cassini* (Waite et al. 2009). This value is compared to the one acquired by methane if it was initially incorporated by the building blocks of Enceladus during their formation in the nebula. In this case, since it was established that the methane of Titan originates from the solar nebula (Mousis et al. 2009a) and since the building blocks of the two satellites share a common origin, the D/H ratio in Enceladus' methane should range between the minimum D/H ratio initially acquired by Titan if a significant photochemical enrichment of deuterium occurred during the evolution of its atmosphere (Cordier et al. 2008) and the value observed today in Titan by *Cassini* (Bézard et al. 2007). From these values, we infer that the D/H ratio in CH_4 produced by serpentinization should be enriched by a factor of 1.4–9.6 relative to D/H in methane originating from the nebula.

5. DISCUSSION

A word of caution must be given about our estimate of the D/H ratio in CH_4 produced via serpentinization. It is based on the idea that no D-fractionation occurred between the produced H_2 and serpentine, and between the produced CH_4 and H_2. Unfortunately, these points are still not well established in the literature and future laboratory work is required to assess their validity.

Recent INMS measurements during the 2008 October 9 encounter with the best signal quality to date have shown no clear sign of Kr in the Enceladus' plume. Instrument sensitivity and observed signal to noise constrain the determination of Kr/H_2O to an upper limit of $< 10^{-5}$. However, subsequent encounters with Enceladus' plume may enhance the signal-to-noise to a level at which Kr can be identified without ambiguity. On the other hand, the INMS instrument is unable to directly measure Xe as its observable mass range is capped at 100 D. As noted in Waite et al. (2009), the measured H_2 in recent encounters is most likely a product of H_2O interactions with the instrument's antechamber walls due to the high spacecraft velocity relative to the plume. Therefore, the amount of endogenous H_2 and its D/H ratio remains undetermined. Future *Cassini* encounters are currently planned at slower spacecraft speed that may allow separate assessments of H_2 in the plume from that synthesized inside the INMS instrument. In this case, determinations of D/H in H_2 during the Cassini mission remain a remote possibility that could tell if this species is produced by serpentinization reactions. Measurement of D/H in CH_4 cannot be made with INMS due to overlapping signals of several species in this portion of the mass spectrum. This measurement requires an instrument with mass resolution ($M/\Delta M$) greater than 6000 and, thus, must wait for a future spacecraft mission, such as *Titan Saturn System Mission* actually studied by NASA and ESA.

Support from the *Cassini* project is gratefully acknowledged.

REFERENCES

Alibert, Y., & Mousis, O. 2007, A&A, 465, 1051
Atreya, S. K., Adams, E. Y., Niemann, H. B., Demick-Montelara, J. E., Owen, T. C., Fulchignoni, M., Ferri, F., & Wilson, E. H. 2006, Planet. Space Sci., 54, 1177
Bézard, B., Nixon, C. A., Kleiner, I., & Jennings, D. E. 2007, Icarus, 191, 397
Cordier, D., Mousis, O., Lunine, J. I., Moudens, A., & Vuitton, V. 2008, ApJ, 689, L61
Lécuyer, C., Simon, L., & Guy, F. 2000, Earth Planet. Sci. Lett., 181, 33
Lodders, K. 2003, ApJ, 591, 1220
Lunine, J. I., & Stevenson, D. J. 1985, ApJS, 58, 493
Matson, D. L., Castillo, J. C., Lunine, J., & Johnson, T. V. 2007, Icarus, 187, 56
Moody, J. 1976, Lithos, 9, 125
Mousis, O., & Gautier, D. 2004, Planet. Space Sci., 52, 361
Mousis, O., Gautier, D., & Bockelée-Morvan, D. 2002, Icarus, 156, 162
Mousis, O., Lunine, J. I., Pasek, M., Cordier, D., Waite, J. H., Mandt, K. E., Lewis, W. S., & Nguyen, M.-J. 2009a, Icarus, submitted
Mousis, O., et al. 2009b, ApJ, 691, 1780
Oze, C., & Sharma, M. 2007, Icarus, 186, 557
Schubert, G., Anderson, J. D., Travis, B. J., & Palguta, J. 2007, Icarus, 188, 345
Thomas, C., Picaud, S., Mousis, O., & Ballenegger, V. 2008, Planet. Space Sci., 56, 1607
Vennemann, T. W., & O'Neil, J. R. 1996, Geochim. Cosmochim. Acta, 60, 2437
Waite, J. H., et al. 2006, Science, 311, 1419
Waite, J. H., et al. 2009, Nature, in press

Retour à la table des matières : p. v

10.5 Article sur la clathration dans la nébuleuse primordiale et l'origine de l'atmosphère de Titan

The Astrophysical Journal, 691:1780–1786, 2009 February 1 doi:10.1088/0004-637X/691/2/1780
© 2009. The American Astronomical Society. All rights reserved. Printed in the U.S.A.

CLATHRATION OF VOLATILES IN THE SOLAR NEBULA AND IMPLICATIONS FOR THE ORIGIN OF TITAN'S ATMOSPHERE

Olivier Mousis[1,2], Jonathan I. Lunine[1], Caroline Thomas[2], Matthew Pasek[1], Ulysse Marboeuf[2], Yann Alibert[2], Vincent Ballenegger[2], Daniel Cordier[3,4], Yves Ellinger[5], Françoise Pauzat[5], and Sylvain Picaud[2]
[1] Lunar and Planetary Laboratory, University of Arizona, Tucson, AZ, USA; olivier.mousis@obs-besancon.fr
[2] Université de Franche-Comté, Institut UTINAM, CNRS/INSU, UMR 6213, 25030 Besançon Cedex, France
[3] Institut de Physique de Rennes, CNRS, UMR 6251, Université de Rennes 1, Campus de Beaulieu, 35042 Rennes, France
[4] École Nationale Supérieure de Chimie de Rennes, Campus de Beaulieu, 35700 Rennes, France
[5] Université Pierre et Marie Curie, Laboratoire de Chimie Théorique, CNRS/INSU, UMR 7616, 75252 Paris Cedex 05, France
Received 2008 January 28; accepted 2008 September 23; published 2009 February 12

ABSTRACT

We describe a scenario of Titan's formation matching the constraints imposed by its current atmospheric composition. Assuming that the abundances of all elements, including oxygen, are solar in the outer nebula, we show that the icy planetesimals were agglomerated in the feeding zone of Saturn from a mixture of clathrates with multiple guest species, so-called stochiometric hydrates such as ammonia hydrate, and pure condensates. We also use a statistical thermodynamic approach to constrain the composition of multiple guest clathrates formed in the solar nebula. We then infer that krypton and xenon, that are expected to condense in the 20–30 K temperature range in the solar nebula, are trapped in clathrates at higher temperatures than 50 K. Once formed, these ices either were accreted by Saturn or remained embedded in its surrounding subnebula until they found their way into the regular satellites growing around Saturn. In order to explain the carbon monoxide and primordial argon deficiencies of Titan's atmosphere, we suggest that the satellite was formed from icy planetesimals initially produced in the solar nebula and that were partially devolatilized at a temperature not exceeding ∼50 K during their migration within Saturn's subnebula. The observed deficiencies of Titan's atmosphere in krypton and xenon could result from other processes that may have occurred both prior to or after the completion of Titan. Thus, krypton and xenon may have been sequestrated in the form of XH_3^+ complexes in the solar nebula gas phase, causing the formation of noble gas-poor planetesimals ultimately accreted by Titan. Alternatively, krypton and xenon may have also been trapped efficiently in clathrates located on the satellite's surface or in its atmospheric haze. We finally discuss the subsequent observations that would allow us to determine which of these processes is the most likely.

Key words: planets and satellites: formation – planets and satellites: individual (Titan)

1. INTRODUCTION

The exploration of Saturn's satellite system by the *Cassini–Huygens* spacecraft has forced a reappraisal of existing models for the origin of Titan. Indeed, a puzzling feature of the atmosphere of Titan is that no primordial noble gases other than argon were detected by the Gas Chromatograph Mass Spectrometer (GCMS) aboard the *Huygens* probe during its descent to Titan's surface on 2005 January 14. The observed argon includes primordial ^{36}Ar (the main isotope) and the radiogenic isotope ^{40}Ar, which is a decay product of ^{40}K (Niemann et al. 2005). In any case, with a ^{36}Ar/^{14}N lower than the solar value by more than five orders of magnitude (Niemann et al. 2005), a very tight constraint is imposed on the origin of the bulk constituent of Titan's atmosphere, N_2 (Owen 1982). The other primordial noble gases Kr and Xe (and ^{38}Ar) were not detected by the GCMS instrument down to upper limits of 10 parts per billion relative to nitrogen (Niemann et al. 2005). These latter nondetections are striking given the detection of noble gases in the atmospheres of telluric planets, as well as in the atmosphere of Jupiter where their abundances are found to be oversolar (Owen et al. 1999). Moreover, the measurements made by the GCMS aboard the *Huygens* probe have confirmed what was previously known from Voyager and ground-based observations: that the atmosphere of Titan is dominated by N_2 and CH_4, with a low CO:CH_4 ratio (CO:$CH_4 \sim 10^{-3}$; Gautier & Raulin 1997). This last value is also a strong constraint on the composition because CO is believed to have been more abundant than CH_4 in the solar nebula (Prinn & Fegley 1981), a result indirectly confirmed by studies of the densities of Kuiper Belt and former Kuiper Belt objects (Johnson & Lunine 2005).

It has been proposed that Titan's atmospheric molecular nitrogen results from ammonia photolysis or shock chemistry early in Titan's history (Atreya et al. 1978; McKay et al. 1988), implying that this species is probably not primordial. In addition, the high CH_3D:CH_4 ratio measured in the satellite's atmosphere (D:H $= 1.32^{+0.15}_{-0.11} \times 10^{-4}$; Bézard et al. 2007) implies that this compound is likely to have been incorporated in solids produced in the solar nebula prior to having been accreted by Titan. Thus, CH_3D originated from interstellar methane highly D-enriched ices that vaporized when entering the solar nebula. Deuterated methane then isotopically exchanged with molecular hydrogen in the gas phase prior to its trapping in solids formed in the nebula (Mousis et al. 2002). The high deuterium enrichment acquired by methane in the satellite's atmosphere excludes its production from the gas phase conversion of carbon monoxide in a dense and warm subnebula, as was first suggested by Prinn & Fegley (1981). Indeed, in this case the deuterium enrichment of methane produced from carbon monoxide in Saturn's subnebula would be almost solar (Mousis et al. 2002). It would then be impossible to explain the measured value from atmospheric photochemistry only (Cordier et al. 2008). Note that it has alternatively been suggested that the atmospheric methane of Titan could be produced from serpentinization in its interior (Atreya et al. 2006), but there is as yet no isotopic test of this process that has been proposed. Identification of abundant

Retour à la table des matières : p. v

carbon dioxide in fresh volcanic deposits might favor production of hydrocarbons via serpentinization in the interior, and some evidence for such deposits has been argued from Cassini Visible and Infrared Mapping Spectrometer (VIMS) data (Hayne et al. 2008), but the extent of such deposits remains to be quantified.

Recently, in order to explain the deficiencies of CO, N_2, Ar, and Kr in Titan, Alibert & Mousis (2007, hereafter AM07) proposed that the satellite formed in a Saturn's subnebula is warm enough to partly devolatilize the planetesimals captured from the solar nebula itself. Indeed, following AM07, the migration of planetesimals in a balmy subnebula would allow an efficient devolatilization of most volatile species (CO, N_2, Ar, and Kr) whose clathration temperatures are low, whereas H_2O, NH_3, H_2S, CO_2, Xe, and CH_4 would remain incorporated in solids. However, since Xe was expected to remain trapped in planetesimals, the scenario proposed by AM07 could not explain in a self-consistent way the observed deficiency of this noble gas in Titan's atmosphere.

Moreover, because AM07 did not consider the possibility of multiple guest trapping when they determined the clathration sequence in the solar nebula, their predictions about the incorporation conditions of the different volatiles could be strongly modified by this effect. Indeed, it has been shown in the literature (Lunine & Stevenson 1985; Osegovic & Max 2005; Thomas et al. 2007, 2008) that minor compounds can deeply affect the composition of clathrates formed from a given gas phase. As a result, the validity of the Titan's formation scenario proposed by AM07 can be questioned if the multiple guest trapping of volatiles is considered during the clathration sequence in the solar nebula.

In addition, AM07 made the ad hoc hypothesis that the oxygen abundance was "oversolar" in the feeding zone of Saturn in order to provide enough water to allow the full clathration of volatiles during the cooling of the nebula. This assumption was supported by the work of Hersant et al. (2001) who estimated that Jupiter was formed at temperatures higher than ∼40–50 K in the solar nebula. Hence, because hydrates and clathrates generally form at higher temperatures than pure condensates, the accretion of these ices was thus required during the formation of Jupiter in order to explain the volatile enrichments observed in its atmosphere (Gautier et al. 2001a, 2001b). The fact that both Jupiter and Saturn might have accreted planetesimals formed at similar locations during their growth and migration within the solar nebula (Alibert et al. 2005b) thus led AM07 to consider the same gas phase composition in the two giant planets feeding zones. However, Hersant et al. (2001) only used an evolutionary solar nebula model to derive the disk's temperature at the time when the mass of Jupiter's feeding zone was equal to that of the gas in its current envelope, and did not include the influence of protoplanet formation on the structure of the disk. Recent giant planet core accretion formation models that include migration, disk evolution, such as those proposed by Alibert et al. (2004, 2005b), have shown that the nebula's temperature can be as low as ∼10–20 K at the end of Jupiter's formation. This implies that, during their formation, both Jupiter and Saturn can accrete pure condensates produced at lower temperatures than those required for clathration. As a result, no extra water is required in the nebula to allow all the volatiles to be trapped in clathrates, and the oversolar oxygen abundance condition in the nebula can be relaxed.

In this paper, we reinvestigate the scenario of Titan's formation initially proposed by AM07 in order to match the constraints derived from its atmospheric composition. We assume that the abundance of all elements, including oxygen, are solar in the outer nebula, implying that the icy planetesimals were agglomerated in the feeding zone of Saturn from a mixture of clathrates with multiple guest species, hydrates such as ammonia hydrate, and pure condensates. In addition, we use a statistical thermodynamic approach to constrain the composition of clathrates formed in the solar nebula. We then infer that krypton and xenon, that are expected to condense in the 20–30 K temperature range in the solar nebula, are trapped in clathrates at higher temperatures than 50 K. Once formed, these ices either were accreted by Saturn or remained embedded in Saturn's surrounding subnebula until they found their way into the regular satellites growing around Saturn. In order to explain the carbon monoxide and primordial argon deficiencies of Titan's atmosphere, we suggest that the satellite was formed from icy planetesimals initially produced in the solar nebula and that were partially devolatilized at a temperature not exceeding ∼50 K during their migration within Saturn's subnebula. On the other hand, the observed deficiencies of Titan's atmosphere in krypton and xenon must result from other processes that occurred both prior to or after the completion of Titan.

In Section 2, we determine the formation sequence of the different ices produced in the outer solar nebula and then examine the relative propensities among the different volatiles for trapping in clathrates produced in Saturn's feeding zone assuming solar abundances for all elements. In Section 3, we propose that carbon monoxide and argon were only devolatilized from planetesimals, due to the increasing gas temperature and pressure conditions they encountered during their migration inward in the Saturn's subnebula. We then explore the different mechanisms that may explain the deficiency of Titan's atmosphere in krypton and xenon. Section 4 is devoted to discussion.

2. FORMATION OF ICY PLANETESIMALS IN SATURN'S FEEDING ZONE

In this Section, we first describe the formation sequence of the different ices produced in the outer solar nebula. We then examine the relative propensities among the different volatiles for trapping in clathrates produced in Saturn's feeding zone at temperatures greater than ∼50 K. Once formed, these ices will add to the composition of the planetesimals that will be either accreted by Saturn or embedded in its surrounding subnebula from which the regular satellite system has formed.

2.1. Initial Gas Phase Composition

In order to define the gas phase composition in the feeding zone of Saturn, we assume that the abundances of all elements are solar (Lodders 2003; see Table 1) and consider both refractory and volatile components. Refractory components include rocks and organics. According to Lodders (2003), rocks contain ∼23% of the total oxygen in the nebula. The fractional abundance of organic carbon is assumed to be 55% of total carbon (Pollack et al. 1994), and the ratio of C:O:N included in organics is supposed to be 1:0.5:0.12 (Jessberger et al. 1988). We then assume that the remaining O, C, and N exist only under the form of H_2O, CO, CO_2, CH_3OH, CH_4, N_2, and NH_3. Hence, once the gas phase abundances of elements are defined, the abundances of CO, CO_2, CH_3OH, CH_4, N_2, and NH_3 are determined from the adopted $CO:CO_2:CH_3OH:CH_4$, and $N_2:NH_3$ gas phase molecular ratios, and from the C:O:N relative abundances set in organics. Finally, once the abundances of these molecules are fixed, the remaining O gives the abundance of H_2O.

Retour à la table des matières : p. v

Table 1
Gas Phase Abundances in the Solar Nebula

Species X	(X/H_2)	Species X	(X/H_2)
O	1.16×10^{-3}	N_2	4.05×10^{-5}
C	5.82×10^{-4}	NH_3	4.05×10^{-5}
N	1.60×10^{-4}	CO	2.21×10^{-4}
S	3.66×10^{-5}	CO_2	3.16×10^{-5}
Ar	8.43×10^{-6}	CH_3OH	6.31×10^{-6}
Kr	4.54×10^{-9}	CH_4	3.16×10^{-6}
Xe	4.44×10^{-10}	H_2S	1.83×10^{-5}
H_2O	4.43×10^{-4}		

Notes. Elemental abundances derive from Lodders (2003). Molecular abundances result from the distribution of elements between refractory and volatile components (see the text).

We then set $CO:CO_2:CH_3OH:CH_4 = 70:10:2:1$ in the gas phase of the disk, values that are consistent with the interstellar medium (ISM) measurements considering the contributions of both gas and solid phases in the lines of sight (Frerking et al. 1982; Ohishi et al. 1992; Ehrenfreund & Schutte 2000; Gibb et al. 2000). In addition, S is assumed to exist in the form of H_2S, with $H_2S:H_2 = 0.5 \times (S:H_2)_\odot$, and other refractory sulfide components (Pasek et al. 2005). We also consider $N_2:NH_3 = 1:1$ in the nebula gas-phase. This value is compatible with thermochemical calculations in the solar nebula that take into account catalytic effects of Fe grains on the kinetics of N_2 to NH_3 conversion (Fegley 2000).

2.2. Formation of Ices in Saturn's Feeding Zone

The process by which volatiles are trapped in icy planetesimals, illustrated in Figures 1 and 2, is calculated using the stability curves of hydrates, clathrates and pure condensates, and the thermodynamic path detailing the evolution of temperature and pressure at 9.5 AU in the solar nebula, corresponding to the actual position of Saturn. This thermodynamic path (hereafter cooling curve) results from the determination of the disk vertical structure which, in turn, derives from the turbulent model used in this work. While a full description of our turbulent model of the accretion disk can be found in Papaloizou & Terquem (1999) and Alibert et al. (2005a), we simply provide here a concise outline of the underlying assumptions.

Assuming cylindrical symmetry in the protoplanetary disk, the vertical structure along the z-axis at a given radial distance r is calculated by solving a system of three equations, namely, the equation for hydrostatic equilibrium, the energy conservation, and the diffusion equation for the radiative flux (Equations (1)–(3) in Alibert et al. 2005a, respectively). The system variables are the local pressure $P(r, z)$, temperature $T(r, z)$, density $\rho(r, z)$, and viscosity $\nu(r, z)$. Following Shakura & Sunyaev (1973), the turbulent viscosity ν is expressed in terms of Keplerian rotation frequency Ω and sound velocity C_s, as $\nu = \alpha C_s^2/\Omega$, where α is a parameter characterizing the turbulence in the disk. For the model we use here, the α parameter is equal to 2×10^{-3}, and the total evaporation rate is of the order of $10^{-8}\ M_\odot\ \mathrm{year}^{-1}$. At the beginning of the calculation, the gas surface density is given by a power law, $\Sigma \propto r^{-3/2}$, normalized to have $\Sigma = 600\ \mathrm{g\ cm}^{-2}$ at the current day position of Jupiter. This disk model was used in Alibert et al. (2005b) in order to calculate formation models of Jupiter and Saturn.

The stability curves of hydrates and clathrates derive from the Lunine & Stevenson (1985) compilation of published experimental work, in which data are available at relatively low temperatures and pressures. On the other hand, the stability curves of pure condensates used in our calculations derive from the compilation of laboratory data given in the CRC Handbook of Chemistry and Physics (Lide 2002). The cooling curve intercepts the stability curves of the different ices at particular temperatures and pressures. For each ice considered, the domain of stability is the region located below its corresponding stability curve. The clathration process stops when no more crystalline water ice is available to trap the volatile species. Note that, in the pressure conditions of the solar nebula, CO_2 is the only species that crystallizes at a higher temperature than its associated clathrate. We then assume that solid CO_2 is the only existing condensed form of CO_2 in this environment. In addition, we have considered only the formation of pure ice of CH_3OH in our calculations since, to our best knowledge, no experimental data concerning the stability curve of its associated clathrate have been reported in the literature. As a result of the assumed

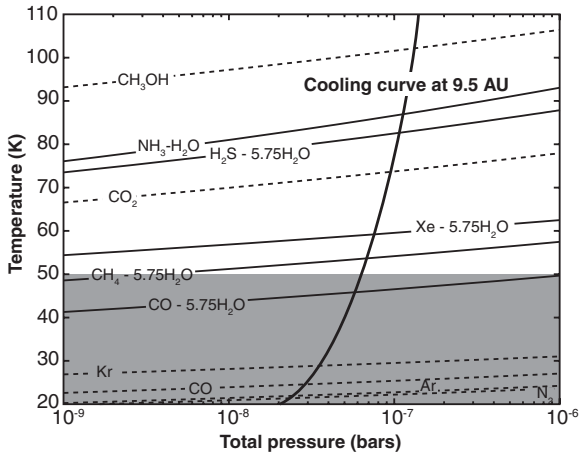

Figure 1. Stability curves of hydrate (NH_3–H_2O), clathrates (X–5.75H_2O) (solid lines), and pure condensates (dotted lines), and cooling curve of the solar nebula at the heliocentric distance of 9.5 AU, assuming a full efficiency of clathration. Species remain in the gas phase above the stability curves. Below, they are trapped as clathrates or simply condense. The gray area characterizes the different ices assumed to be heated during their migration and accretion in Saturn's subnebula to form proto-Titan.

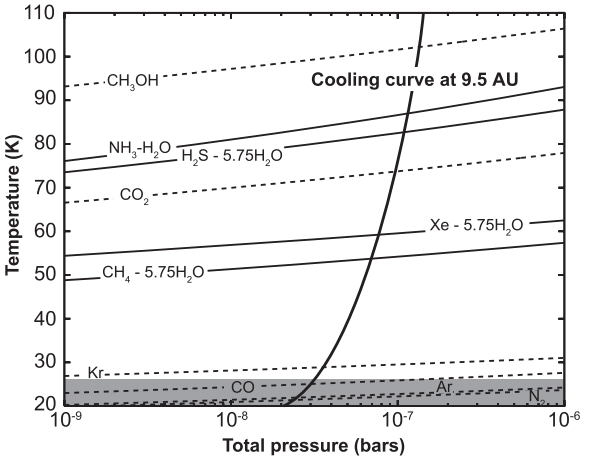

Figure 2. Same as Figure 1, but with a clathration efficiency of ∼25%.

Retour à la table des matières : p. v

solar gas phase abundance for oxygen, ices formed in the outer solar nebula are composed of a mix of clathrates, hydrates, and pure condensates which are, except for CO_2 and CH_3OH, produced at temperatures ranging between 20 and 50 K. Once formed, the different ices agglomerated and incorporated into the growing planetesimals.

Because the efficiency of clathration remains unknown in the solar nebula, we explore here two opposite cases of trapping efficiencies of volatiles. Figure 1 illustrates the case where the efficiency of clathration is total, implying that guest molecules had the time to diffuse through porous water-ice planetesimals in the solar nebula. This situation is plausible if we consider that collisions between planetesimals have exposed essentially all the ice to the gas over timescales shorter or equal to planetesimals lifetimes in the nebula (Lunine & Stevenson 1985). In this case, NH_3, H_2S, Xe, CH_4, and ∼60% of CO form NH_3-H_2O hydrate and H_2S-5.75H_2O, Xe-5.75H_2O, CH_4-5.75H_2O, and CO-5.75H_2O clathrates with the available water. The remaining CO, as well as N_2, Kr, and Ar, whose clathration normally occurs at lower temperatures, remains in the gas phase until the nebula cools enough to allow the formation of pure condensates.

Figure 2 illustrates the case where the efficiency of clathration is only ∼25%. Here, either only a part of the clathrates cages have been filled by guest molecules, either the diffusion of clathrated layers through the planetesimals was to slow to enclathrate most of the ice, or the poor trapping efficiency was the combination of these two processes. In this case, only NH_3, H_2S, Xe, and CH_4 form NH_3-H_2O hydrate and H_2S-5.75H_2O, Xe-5.75H_2O, and CH_4-5.75H_2O clathrates. Due to the deficiency in accessible water in icy planetesimals, all CO, Kr, and N_2 form pure condensates in the solar nebula.

In both cases, i.e., high and poor clathration efficiencies, the abundances of volatiles observed in the envelopes of Jupiter and Saturn can be reproduced in a way consistent with their internal structure models, provided that the formation of the two planets ended at ∼20 K in the solar nebula (Mousis & Marboeuf 2006).[6] As discussed in Section 3.1, these two formation sequences of the different ices in the feeding zone of Saturn are compatible with the scenario of partial devolatilization of planetesimals accreted by Titan proposed by AM07.

2.3. Multiple Guest Trapping in Clathrates

Here, we calculate the relative abundances of guests that can be incorporated in H_2S-, Xe-, and CH_4 dominated clathrates at the time of their formation at temperatures greater than ∼50 K in the solar nebula. In our calculations, any volatile already trapped or condensed at a higher temperature than that of the considered clathrate is excluded from the coexisting gas phase composition. We follow the method described by Lunine & Stevenson (1985) and Thomas et al. (2007, 2008) which uses classical statistical mechanics to relate the macroscopic thermodynamic properties of clathrates to the molecular structure and interaction energies. It is based on the original ideas of van der Waals & Platteeuw (1959) for clathrate formation, which assume that trapping of guest molecules into cages corresponds to the three-dimensional generalization of ideal localized adsorption. In this model, the occupancy fraction of a guest molecule K for a given type t of cage (t = small or large) can be written as

$$y_{K,t} = \frac{C_{K,t} P_K}{1 + \sum_J C_{J,t} P_J}, \quad (1)$$

where the sum in the denominator includes all the species which are present in the initial gas phase. $C_{K,t}$ is the Langmuir constant of species K in the cage of type t, and P_K is the partial pressure of species K. This partial pressure is given by $P_K = x_K \times P$, with x_K the molar fraction of species K in the initial gas phase given in Table 1, and P the total H_2 pressure. The Langmuir constants are in turn determined by integrating the molecular potential within the cavity as

$$C_{K,t} = \frac{4\pi}{k_B T} \int_0^{R_c} \exp\left(-\frac{w(r)}{k_B T}\right) r^2 dr, \quad (2)$$

where R_c represents the radius of the cavity assumed to be spherical, and $w(r)$ is the spherically averaged Kihara potential representing the interactions between the guest molecules and the H_2O molecules forming the surrounding cage. Following McKoy & Sinanoğlu (1963), this potential $w(r)$ can be written for a spherical guest molecule, as

$$w(r) = 2z\epsilon \frac{\sigma^{12}}{R_c^{11} r}\left(\delta^{10}(r) + \frac{a}{R_c}\delta^{11}(r)\right) - \frac{\sigma^6}{R_c^5 r}\left(\delta^4(r) + \frac{a}{R_c}\delta^5(r)\right), \quad (3)$$

with

$$\delta^N(r) = \frac{1}{N}\left[\left(1 - \frac{r}{R_c} - \frac{a}{R_c}\right)^{-N} - \left(1 + \frac{r}{R_c} - \frac{a}{R_c}\right)^{-N}\right]. \quad (4)$$

In Equation (3), z is the coordination number of the cell. These parameters, which depend on the structure of the clathrate and on the type of the cage (small or large), are given in Table 2. The Kihara parameters a, σ, and ϵ for the molecule–water interactions, given in Table 3, have been taken from Diaz Peña et al. (1982) for CO and from Parrish & Prausnitz (1972a, 1972b) for all the other molecules of interest.

Finally, the relative abundance f_K of a guest molecule K in a clathrate can be calculated with respect to the whole set of species considered in the system as

$$f_K = \frac{b_s y_{K,s} + b_\ell y_{K,\ell}}{b_s \sum_J y_{J,s} + b_\ell \sum_J y_{J,\ell}}, \quad (5)$$

Table 2
Parameters for the Cavities

Clathrate Structure	I		II	
Cavity Type	small	large	small	large
R_c (Å)	3.975	4.300	3.910	4.730
b	2	6	16	8
z	20	24	20	28

Notes. R_c is the radius of the cavity (values taken from Parrish & Prausnitz 1972a, 1972b). b represents the number of small (b_s) or large (b_ℓ) cages per unit cell for a given structure of clathrate (I or II), z is the coordination number in a cavity.

[6] If Jupiter and Saturn were formed at $T \geqslant 50$ K in the solar nebula, only hydrates and clathrates, and not pure condensates, would be accreted in their interiors. This assumption has been used by Hersant et al. (2008) to predict an oversolar abundance of Xe in the envelope of Saturn, and solar abundances for Ar and Kr.

Retour à la table des matières : p. v

Table 3
Parameters for the Kihara Potential

Ref	Molecule	σ(Å)	ϵ/k_B(K)	a(Å)
(a)	H_2S	3.1558	205.85	0.36
(a)	CO_2	2.9681	169.09	0.36
(a)	CH_4	3.2398	153.17	0.300
(a)	N_2	3.2199	127.95	0.350
(a)	Xe	3.1906	201.34	0.280
(a)	Ar	2.9434	170.50	0.184
(a)	Kr	2.9739	198.34	0.230
(b)	CO	3.101	134.95	0.284

Notes. σ is the Lennard–Jones diameter, ϵ is the depth of the potential well, and a is the radius of the impenetrable core. These parameters derive from the works of (a) Parrish & Prausnitz (1972a, 1972b) and (b) Diaz Peña et al. (1982).

where b_s and b_l are the number of small and large cages per unit cell respectively, for the considered clathrate structure.

Table 4 gives the fraction of volatiles incorporated in H_2S-, Xe-, and CH_4-dominated clathrates relative to their initial fraction available in the nebula gas (F_i). Our calculations show that CO, N_2, and Ar are poorly trapped in clathrates. Indeed, their relative abundances in these structures are orders of magnitude lower than those found in the solar nebula. On the other hand, we note that substantial amounts of Xe and Kr are trapped in H_2S- and CH_4-dominated clathrates, respectively. About 18% of available Xe is incorporated in H_2S-dominated clathrate prior to the formation of Xe-dominated clathrate at lower temperature. Because the Kr/CH_4 ratio is larger in CH_4-dominated clathrate than in the solar nebula ($F_{Kr} > 1$), we infer that all Kr is incorporated in this clathrate, thus preventing the formation of its pure condensate at lower temperature.

3. IMPLICATIONS FOR THE ORIGIN OF TITAN'S ATMOSPHERE

3.1. Partial Devolatilization of Titan's Planetesimals in Saturn's Subnebula

In order to explain the formation of Titan, we assume that it was formed in a low surface density circum-Saturnian accretion disk, resulting from the reduced gas inflow characterizing the last stages of the planet's growth and refer the reader to the work of AM07 for a full description of the thermodynamic structure of the subnebula. In particular, using time-dependent accretion disk models, AM07 have shown that the evolution of the Saturn's subnebula is divided in two phases. During the first phase, the subnebula is fed through its outer edge by gas and gas-coupled solids originating from the protoplanetary disk. When the solar nebula disappears, the subnebula enters its second phase of evolution. The mass flux through the outer edge stops, and the subnebula expands outward due to viscosity. In order to yield Titan from the Saturn's accretion disk, we assume that solid material has been supplied essentially by the direct transport of gas-coupled solids into the disk with the gas inflow during the first phase of the subnebula's evolution or by capture of heliocentrically orbiting solids as they pass through the disk (Canup & Ward 2002, 2006). AM07 have proposed that once embedded in the subnebula, solids originating from Saturn's feeding zone could have been altered if they encountered gas temperature and pressure conditions high enough to generate a loss of volatiles during their migration, and if they remained relatively porous, which seems a reasonable assumption. While more calculations,

Table 4
Abundance of Volatile i in Clathrate Relative to Initial Abundance in the Nebula

Clathrate	Species	f_i	F_i
H_2S-dominated	CO_2	3.12×10^{-6}	1.81×10^{-6}
	Xe	4.36×10^{-6}	0.18
	CH_4	5.45×10^{-6}	3.16×10^{-5}
	CO	2.13×10^{-7}	1.76×10^{-8}
	Kr	3.57×10^{-9}	1.43×10^{-5}
	Ar	8.74×10^{-9}	1.90×10^{-8}
	N_2	4.04×10^{-7}	1.83×10^{-7}
Xe-dominated	CH_4	7.28×10^{-2}	1.02×10^{-5}
	CO	5.18×10^{-5}	1.04×10^{-10}
	Kr	7.82×10^{-6}	7.65×10^{-7}
	Ar	1.08×10^{-6}	5.69×10^{-11}
	N_2	6.68×10^{-4}	7.32×10^{-9}
CH_4-dominated	CO	1.74×10^{-3}	2.49×10^{-5}
	Kr	1.67×10^{-3}	1.16
	Ar	6.43×10^{-5}	2.41×10^{-5}
	N_2	3.94×10^{-3}	3.07×10^{-4}

Notes. f_i is defined as the molar ratio of i to X in X-dominated clathrate and F_i is the ratio of f_i to the initial ratio (i to X) in the solar nebula. Calculations are performed at temperature and pressure conditions given by the intersection of the cooling curve at 9.5 AU and the stability curves of the considered clathrates (see Figures 1 and 2). Only the species that are not yet condensed or trapped prior to the epoch of clathrate formation are considered in our calculations.

taking into account migration of captured planetesimals, as well as their thermal evolution and devolatilization in an evolving subnebula, are necessary to quantitatively test the scenario of AM07, we favor this mechanism to explain the carbon monoxide and argon deficiencies in the atmosphere of Titan. Indeed, as Figures 1 and 2 show, if planetesimals ultimately accreted by Titan experienced intrinsic temperatures of ∼50 K during their migration in Saturn's subnebula, they are expected to release most of their CO, Ar, and N_2. However, more volatile compounds than CH_4 form pure condensates when the clathration efficiency is poor in the feeding zone of Saturn, and the gap between the devolatilization temperatures of CH_4-dominated clathrate and these ices is much larger than in the case of full clathration ($\Delta T \simeq 30$ K instead of 8 K). Hence the hypothesis of poor clathration efficiency requires a less vigorous thermal control of planetesimals during their migration within Saturn's subnebula.

Note that, in our scenario of partial devolatilization, a higher sublimation temperature of planetesimals is excluded since it would imply the dissociation of methane clathrate from solids accreted by Titan, a result in conflict with the large abundance of methane in the satellite's atmosphere. On the other hand, since Kr and Xe are incorporated at higher temperatures than ∼50 K in clathrates produced in the nebula, they cannot be eliminated via this partial devolatilization mechanism only.

3.2. Mechanisms of Noble Gas Trapping

In this section, we discuss the processes of noble gas trapping which might have occurred either in the solar nebula gas phase before the formation of ices that were ultimately accreted by Titan, or at the satellite's surface or atmosphere during its postaccretion evolution. Each of these processes may explain the deficiencies of Kr and Xe observed in the atmosphere of Titan.

It has been thus proposed that the presence of H_3^+ ion in the outer solar nebula may induce the trapping of Ar, Xe, and Kr in

Retour à la table des matières : p. v

the form of stable complexes XH_3^+ (with X = Ar, Kr, and Xe; Pauzat & Ellinger 2007; Mousis et al. 2008). The efficiency of this trapping is ruled by the abundance profile of H_3^+, which is poorly constrained in the primordial nebula. Assuming that the gas of the solar nebula is ionized by cosmic rays at a rate of 1×10^{-15} s^{-1}, which is considered as an upper limit, Mousis et al. (2008) calculated that the abundance of H_3^+ in the 3 to 30 AU midplane region of the nebula is about 1×10^{-12} relative to H_2, at most. Such a low concentration of H_3^+ implies a poor noble gas sequestration since the solar abundances of Xe, Kr, and Ar hold between about 10×10^{-10} and 10×10^{-6}, relative to H_2 (see e.g., Table 1). On the other hand, there is evidence that the solar nebula has been exposed to additional sources of energetic particles. This is testified by the presence of radionuclides with half-lives less than 1 Myr in the calcium-aluminum–rich inclusions in meteorites (see e.g., McKeegan & Davis 2003) which could be due to the irradiation of energetic particles from the young Sun (Lee et al. 1998; Gounelle et al. 2001, 2006) or to the presence of a nearby supernova during the solar system formation (Busso et al. 2003; Tachibana & Huss 2003). If this hypothesis is correct, one associated effect might be an augmentation of the cosmic ionization rate in the disk by several orders of magnitude. As a result, given the noble gases abundances in the solar nebula, Kr and Xe could be relatively easily trapped, in regions where H_3^+ is at least $\sim 1 \times 10^{-9}$ times the H_2. From these considerations, Mousis et al. (2008) suggested that the H_3^+ abundance in the 10–30 AU region of the solar nebula was indeed effectively large enough to make possible at least the efficient trapping of Xe and Kr, and limited trapping of Ar. Therefore, once formed, these complexes would remain stable, even at low temperature, and their presence in the outer nebula gas phase could have as one implication the formation of Kr and Xe-poor bodies that are then delivered to Titan.

Alternatively, it has been shown that if large amounts of Kr and Xe were initially present in Titan's atmosphere, they could have been efficiently trapped as clathrates by crystalline water ice located on the satellite's surface (Osegovic & Max 2005; Thomas et al. 2007, 2008). Indeed, by considering several initial gas phase compositions, including different sets of noble gases abundances that may be representative of Titan's early atmosphere, Thomas et al. (2007, 2008) showed that the trapping efficiency of clathrates is high enough to significantly decrease the atmospheric concentrations of Xe and, to a lesser extent, of Kr, irrespective of the initial gas phase composition, provided that these clathrates are abundant enough at the surface of Titan. In these conditions, Thomas et al. (2007) calculated that the total sink of Xe or Kr in clathrates would represent a layer at the surface of Titan whose equivalent thickness would not exceed ~50 cm. In addition, from laboratory experiments, Jacovi & Bar-Nun (2008) recently proposed that the noble gases of Titan could be removed by their trapping in its atmospheric haze. Hence, these two proposed mechanisms, i.e., trapping in clathrates located on the surface or in the atmospheric haze, could act as sinks of Xe and Kr in the atmosphere of Titan.

4. DISCUSSION

Taking into account the constraints derived from the current composition of Titan's atmosphere, and from precise calculations of multiple guest trapping in clathrates formed in the solar nebula, we propose a formation scenario in which the satellite accreted from solids initially produced in the solar nebula. Based on the conclusions of AM07, we postulate that during their drift in Saturn's subnebula, and prior to their accretion by the forming Titan, these solids encountered gas temperature and pressure conditions high enough to generate a loss via sublimation of most of their carbon monoxide and argon, but low enough to retain the incorporated methane, ammonia, krypton, and xenon. Interestingly enough, our model predicts that if all CO and Ar pure condensates where devolatilized from planetesimals ultimately accreted by Titan, small amounts of these species remained essentially trapped in CH_4-dominated clathrates, and subsequently in the satellite, with $CO/CH_4 \sim 1.7 \times 10^{-3}$ and $Ar/CH_4 \sim 6.4 \times 10^{-5}$ (see e.g., Table 4), in good agreement with the abundances of CO and ^{36}Ar observed in Titan's atmosphere.

A plausible gas phase composition was adopted for the primordial nebula, but the conclusions derived from our model are not affected by the choice of other molecular ratios. Indeed, whatever the range of $CO:CO_2:CH_3OH:CH_4$ and $N_2:NH_3$ initial gas phase molecular ratios adopted in the solar nebula, the stability curves of CO, N_2, and Ar ices produced in this environment still remain at lower temperatures than that of CH_4 clathrate. Hence, independent of the initial gas phase composition, icy planetesimals migrating within Saturn's subnebula are still first depleted in carbon monoxide, nitrogen, and argon when they experience progressive heating. Moreover, our Titan formation scenario is not influenced by the possible inward migration of Saturn (Alibert et al. 2005b) during its formation within the nebula since the composition of planetesimals remains almost constant, independent of the formation distance in the disk, provided that there was a homogeneous gas phase in the solar nebula (Marboeuf et al. 2008).

Because more volatile compounds than CH_4 form pure condensates when the clathration efficiency is assumed to be poor in the feeding zone of Saturn, and since the gap between the devolatilization temperatures of CH_4-dominated clathrate and these ices is much larger than in the case of full clathration, a less vigorous thermal control of planetesimals is required during their migration within Saturn's subnebula. This suggests that the efficiency of clathration may have been limited in the outer solar nebula.

In situ measurements by a future probe of Kr and Xe abundances in Saturn's atmosphere could constrain the origin of their deficiency in Titan. If the abundances of Kr and Xe are detected in solar proportions in Saturn, this would support the hypothesis of an efficient sequestration of these species by H_3^+ in the primitive nebula gas phase prior to the formation of solids. Note that the H_3^+ abundance is expected to increase with the growing heliocentric distance in the primitive nebula (Mousis et al. 2008). Hence, independent of Saturn's case, the greater than solar abundances of these noble gases measured by the *Galileo* probe in Jupiter's atmosphere (Owen et al. 1999) can be explained by the low H_3^+ concentration at the time of formation and location of its building blocks (Mousis et al. 2008). On the other hand, if the abundances of these noble gases are measured to be greater than solar in Saturn, this would favor the hypothesis of a Kr and Xe sequestration that occurred at a later epoch than that of the planetesimals formation in the giant planet's feeding zone. In this case, the future sampling of the material constituting the dunes of Titan, which is likely to derive from the stratospheric photolysis products (Jacovi & Bar-Nun 2008), would give information on the potential trapping of noble gases by haze. Similarly, the sampling of the icy surface of Titan would allow the amount of noble gases possibly incorporated in clathrates to be quantified.

Retour à la table des matières : p. v

Because the temperature and pressure conditions increase within the subnebula at diminishing distances to Saturn (AM07), the planetesimals accreted by regular satellites interior of the orbit of Titan should have experienced the same or more devolatilization process during their migration. We predict that these satellites are depleted in primordial carbon monoxide and nitrogen, similar to Titan. Note that the INMS instrument aboard the *Cassini* spacecraft has detected 91 ± 3% H_2O, 4 ± 1% N_2 or CO,[7] 3.2 ± 0.6% CO_2, 1.6 ± 0.4% CH_4 and other minor compounds in the plumes of Enceladus (Waite et al. 2006; Hansen et al. 2006). The detection of CO or N_2 in the plumes may appear in conflict with our predictions but it has been proposed that N_2 could be the result of thermal processing of primordial NH_3 in the hot interior of Enceladus (Matson et al. 2007) or produced from the irradiation of solid ammonia on the surface of the satellite (Zheng et al. 2008). Moreover, it has been experimentally shown that UV irradiation of carbon grains embedded in water ice or of CH_4-containing icy mixtures could lead to the formation of CO and CO_2 molecules at low temperature (Mennella et al. 2006; Baratta et al. 2003). Therefore, all these processes suggest that the observed N_2 or CO may not be primordial in the plumes of Enceladus, in agreement with our Titan's formation scenario. A key measurement in Enceladus would be then the detection of argon since our scenario also predicts a strong depletion of this noble gas in satellites interior of Titan. More constraints on the composition of Enceladus will be placed by the extended *Cassini* mission, through further flybys closer to and within its active geysers.

This work was supported in part by the French Centre National d'Etudes Spatiales. Supports from the PID program "Origines des Planètes et de la Vie" of the CNRS, and the *Cassini* project, are also gratefully acknowledged.

REFERENCES

Alibert, Y., Mordasini, C., & Benz, W. 2004, A&A, 417, L25
Alibert, Y., Mordasini, C., Benz, W., & Winisdoerffer, C. 2005a, A&A, 434, 343
Alibert, Y., & Mousis, O. 2007, A&A, 465, 1051 (AM07)
Alibert, Y., Mousis, O., Mordasini, C., & Benz, W. 2005b, ApJ, 626, L57
Atreya, S. K., Adams, E. Y., Niemann, H. B., Demick-Montelara, J. E., Owen, T. C., Fulchignoni, M., Ferri, F., & Wilson, E. H. 2006, Planet. Space Sci., 54, 1177
Atreya, S. K., Donahue, T. M., & Kuhn, W. R. 1978, Science, 201, 611
Baratta, G. A., Domingo, M., Ferini, G., Leto, G., Palumbo, M. E., Satorre, M. A., & Strazzulla, G. 2003, Nucl. Instrum. Methods Phys. Res. B, 209, 283
Bézard, B., Nixon, C. A., Kleiner, I., & Jennings, D. E. 2007, Icarus, 191, 397
Busso, M., Gallino, R., & Wasserburg, G. J. 2003, Publ. Astron. Soc. Aust., 20, 356
Canup, R. M., & Ward, W. R. 2002, AJ, 124, 3404
Canup, R. M., & Ward, W. R. 2006, Nature, 441, 834
Cordier, D., Mousis, O., Lunine, J. I., Moudens, A., & Vuitton, V. 2008, ApJ, 689, L61
Diaz Peña, M., Pando, C., & Renuncio, J. A. R. 1982, J. Chem. Phys., 76, 325
Ehrenfreund, P., & Schutte, W. A. 2000, Adv. Space Res., 25, 2177
Fegley, B. J. 2000, Space Sci. Rev., 92, 177
Frerking, M. A., Langer, W. D., & Wilson, R. W. 1982, ApJ, 262, 590
Gautier, D., Hersant, F., Mousis, O., & Lunine, J. I. 2001a, ApJ, 550, L227
Gautier, D., Hersant, F., Mousis, O., & Lunine, J. I. 2001b, ApJ, 559, L183
Gautier, D., & Raulin, F. 1997, ESA Spec. Publ., 1177, 359
Gibb, E. L., et al. 2000, ApJ, 536, 347
Gounelle, M., Shu, F. H., Shang, H., Glassgold, A. E., Rehm, K. E., & Lee, T. 2001, ApJ, 548, 1051
Gounelle, M., Shu, F. H., Shang, H., Glassgold, A. E., Rehm, K. E., & Lee, T. 2006, ApJ, 640, 1163
Hansen, C. J., Esposito, L., Stewart, A. I. F., Colwell, J., Hendrix, A., Pryor, W., Shemansky, D., & West, R. 2006, Science, 311, 1422
Hayne, P., McCord, T. B., Combe, J. Ph., Barnes, J.W., & Hansen, G. B. 2008, LPSC, 39 abstr. 2010.
Hersant, F., Gautier, D., & Huré, J.-M. 2001, ApJ, 554, 391
Hersant, F., Gautier, D., Tobie, G., & Lunine, J. I. 2008, Planet. Space Sci., 56, 1103
Jacovi, R., & Bar-Nun, A. 2008, Icarus, 196, 302
Jessberger, E. K., Christoforidis, A., & Kissel, J. 1988, Nature, 332, 691
Johnson, T. V., & Lunine, J. I. 2005, Nature, 435, 69
Lee, T., Shu, F. H., Shang, H., Glassgold, A. E., & Rehm, K. E. 1998, ApJ, 506, 898
Lide, D. R. 2002, in CRC Handbook of Chemistry and Physics: A Ready-reference Book of Chemical and Physical Data, ed. David R. Lide (83rd ed.; Boca Raton: CRC Press)
Lodders, K. 2003, ApJ, 591, 1220
Lunine, J. I., & Stevenson, D. J. 1985, ApJS, 58, 493
Marboeuf, U., Mousis, O., Ehrenreich, D., Alibert, Y., Cassan, A., Wakelam, V., & Beaulieu, J.-P. 2008, ApJ, 681, 1624
Matson, D. L., Castillo, J. C., Lunine, J., & Johnson, T. V. 2007, Icarus, 187, 569
McKay, C. P., Scattergood, T. W., Pollack, J. B., Borucki, W. J., & van Ghyseghem, H. T. 1988, Nature, 332, 520
McKeegan, K. D., & Davis, A. M. 2003, Treatise on Geochemistry, 1, 431
McKoy, V., & Sinanoğlu, O. 1963, J. Chem. Phys., 38 (12), 2946
Mennella, V., Baratta, G. A., Palumbo, M. E., & Bergin, E. A. 2006, ApJ, 643, 923
Mousis, O., Gautier, D., & Coustenis, A. 2002, Icarus, 159, 156
Mousis, O., & Marboeuf, U. 2006, Bull. Amer. Astron. Soc., 38, 507
Mousis, O., Pauzat, F., Ellinger, Y., & Ceccarelli, C. 2008, ApJ, 673, 637
Niemann, H. B., et al. 2005, Nature, 438, 779
Ohishi, M., Irvine, W. M., & Kaifu, N. 1992, Astrochem. Cosm. Phenom., 150, 171
Osegovic, J. P., & Max, M. D. 2005, J. Geophys. Res. (Planets), 110, 8004
Owen, T. C. 1982, Planet. Space Sci., 39, 833
Owen, T., Mahaffy, P., Niemann, H. B., Atreya, S., Donahue, T., Bar-Nun, A., & de Pater, I. 1999, Nature, 402, 269
Papaloizou, J. C. B., & Terquem, C. 1999, ApJ, 521, 823
Parrish, W. R., & Prausnitz, J. M. 1972a, Industrial and Engineering Chemistry: Process Design and Development, 11, 26
Parrish, W. R., & Prausnitz, J. M. 1972b, Industrial and Engineering Chemistry: Process Design and Development, 11, 462
Pasek, M. A., Milsom, J. A., Ciesla, F. J., Lauretta, D. S., Sharp, C. M., & Lunine, J. I. 2005, Icarus, 175, 1
Pauzat, F., & Ellinger, Y. 2007, J. Chem. Phys., 127, 014308
Pollack, J. B., Hollenbach, D., Beckwith, S., Simonelli, D. P., Roush, T., & Fong, W. 1994, ApJ, 421, 615
Prinn, R. G., & Fegley, B., Jr. 1981, ApJ, 249, 308
Shakura, N. I., & Syunyaev, R. A. 1973, A&A, 24, 337
Tachibana, S., & Huss, G. R. 2003, Lunar Planet. Inst. Conf. Abstr., 34, 1737
Thomas, C., Mousis, O., Ballenegger, V., & Picaud, S. 2007, A&A, 474, L17
Thomas, C., Picaud, S., Mousis, O., & Ballenegger, V. 2008, P&SS, 56, 1607
van der Waals, J. H., & Platteeuw, J. C. 1959, Adv. Chem. Phys., 2, 1
Waite, J. H., et al. 2006, Science, 311, 1419
Zheng, W., Jewitt, D., Osamura, Y., & Kaiser, R. I. 2008, ApJ, 674, 1242

[7] The resolution of the INMS instrument is too low to bring firm constraints on the nature of the observed species (Waite et al. 2006).

Retour à la table des matières : p. v

View Article Online / Journal Homepage / Table of Contents for this issue

PAPER www.rsc.org/faraday_d | Faraday Discussions

10.6 Article sur la clathration des volatiles dans la nébuleuse primordiale

Volatile inventories in clathrate hydrates formed in the primordial nebula

Olivier Mousis,*[ab] Jonathan I. Lunine,[c] Sylvain Picaud[d] and Daniel Cordier[ef]

Received 26th February 2010, Accepted 18th March 2010
DOI: 10.1039/c003658g

Published on 12 July 2010. Downloaded by Université de Reims Champagne-Ardenne on 08/12/2014 15:36:10.

The examination of ambient thermodynamic conditions suggests that clathrate hydrates could exist in the Martian permafrost, on the surface and in the interior of Titan, as well as in other icy satellites. Clathrate hydrates are probably formed in a significant fraction of planetesimals in the solar system. Thus, these crystalline solids may have been accreted in comets, in the forming giant planets and in their surrounding satellite systems. In this work, we use a statistical thermodynamic model to investigate the composition of clathrate hydrates that may have formed in the primordial nebula. In our approach, we consider the formation sequence of the different ices occurring during the cooling of the nebula, a reasonable idealization of the process by which volatiles are trapped in planetesimals. We then determine the fractional occupancies of guests in each clathrate hydrate formed at a given temperature. The major ingredient of our model is the description of the guest–clathrate hydrate interaction by a spherically averaged Kihara potential with a nominal set of parameters, most of which are fitted to experimental equilibrium data. Our model allows us to find that Kr, Ar and N_2 can be efficiently encaged in clathrate hydrates formed at temperatures higher than ~48.5 K in the primitive nebula, instead of forming pure condensates below 30 K. However, we find at the same time that the determination of the relative abundances of guest species incorporated in these clathrate hydrates strongly depends on the choice of the parameters of the Kihara potential and also on the adopted size of cages. Indeed, by testing different potential parameters, we have noted that even minor dispersions between the different existing sets can lead to non-negligible variations in the determination of the volatiles trapped in clathrate hydrates formed in the primordial nebula. However, these variations are not found to be strong enough to reverse the relative abundances between the different volatiles in the clathrate hydrates themselves. On the other hand, if contraction or expansion of the cages due to temperature variations are imposed in our model, the Ar and Kr mole fractions can be modified up to several orders of magnitude in clathrate hydrates. Moreover, mole fractions of other molecules such as N_2 or CO are also subject to strong changes with the variation of the size of the cages. Our results may affect the predictions of the composition of the planetesimals

[a]*Université de Franche-Comté, Institut UTINAM, CNRS/INSU, UMR 6213, France*
[b]*Université européenne de Bretagne, Université de Rennes 1, Institut de Physique de Rennes, CNRS, UMR 6251, France. E-mail: olivier.mousis@obs-besancon.fr*
[c]*Dipartimento di Fisica, Università degli Studi di Roma "Tor Vergata", Rome, Italy*
[d]*Université de Franche-Comté, Institut UTINAM, CNRS/INSU, UMR 6213, France*
[e]*Ecole Nationale Supérieure de Chimie de Rennes, CNRS, UMR 6226, France*
[f]*Université européenne de Bretagne, Université de Rennes 1, Institut de Physique de Rennes, CNRS, UMR 6251, France*

Retour à la table des matières : p. v

View Article Online

Published on 12 July 2010. Downloaded by Université de Reims Champagne-Ardenne on 08/12/2014 15:36:10.

formed in the outer solar system. In particular, the volatile abundances calculated in the giant planets' atmospheres should be altered because these quantities are proportional to the mass of accreted and vaporized icy planetesimals. For similar reasons, the estimates of the volatile budgets accreted by icy satellites and comets may also be altered by our calculations. For instance, under some conditions, our calculations predict that the abundance of argon in the atmosphere of Titan should be higher than the value measured by Huygens. Moreover, the Ar abundance in comets could be higher than the value predicted by models invoking the incorporation of volatiles in the form of clathrate hydrates in these bodies.

1 Introduction

Clathrate hydrates (hereafter clathrates) were discovered in 1810 by Sir Humphrey Davy. Initially considered as laboratory curiosities, it is only from the 1930s that the study of their formation conditions became of significant interest because of the clogging pipelines during transportation of gas under cold conditions. Clathrates are crystalline solids which look like ice and form when water molecules constitute a cage-like structure around small "guest molecules". The most common guest molecules in terrestrial clathrates are methane (the most abundant), ethane, propane, butane, nitrogen, carbon dioxide and hydrogen sulfide. Water crystallizes in the cubic system in clathrates, rather than in the hexagonal structure of normal ice. Several different clathrate structures are known, the two most common ones being named "structure I" and "structure II". In structure I, the unit cell is formed of 46 water molecules and can incorporate up to 8 guest molecules. In structure II, the unit cell consists of 136 water molecules and can incorporate at most 24 guest molecules.

The thermodynamic conditions prevailing in many bodies of the solar system suggest that clathrates could also exist in the Martian permafrost,[1–3] on the surface and in the interior of Titan as well as in other icy satellites.[4–8] Moreover, it has been suggested that the activity observed in some cometary nuclei results from the dissociation of these crystalline structures.[9] Generally speaking, clathrates probably participated in the formation of planetesimals in the solar system. Indeed, formation scenarios of the protoplanetary nebula invoke two main reservoirs of ices that took part in the production of icy planetesimals. The first reservoir, located within 30 Astronomical Units (AU) of the Sun, contains ices (mostly water ice) originating from the Interstellar Medium (ISM) which, due to their proximity to the Sun, were initially vaporized.[10] With time, the decrease of temperature and pressure conditions allowed the water in this reservoir to condense at $\sim$150 K (for a total gas pressure of $\sim 10^{-7}$ bar) in the form of microscopic crystalline ice.[11] It is then considered that a substantial fraction of the volatile species were trapped as clathrates as long as free water ice was available within $\sim$30 AU in the outer solar nebula.[12] On the other hand, the remaining volatiles that have not been enclathrated due to the lack of available water ice have probably formed pure condensates at lower temperatures in this part of the nebula.[13,14] The other reservoir, located at larger heliocentric distances, is composed of ices originating from ISM that did not vaporize when entering into the disk. In this reservoir, water ice was essentially in the amorphous form and the other volatiles remained trapped in the amorphous matrix.[15,16] Consequently, icy planetesimals formed at heliocentric distances below 30 AU mainly agglomerated from clathrates while, in contrast, those produced at higher heliocentric distances (*i.e.* in the cold outer part of the solar nebula) are expected to be formed from primordial amorphous ice originating from ISM. Thus, clathrates may have been accreted in comets, in the forming giant planets and in their surrounding satellite systems.[4,12–14,17–24]

 This journal is © The Royal Society of Chemistry 2010

Retour à la table des matières : p. v

View Article Online

Published on 12 July 2010. Downloaded by Université de Reims Champagne-Ardenne on 08/12/2014 15:36:10.

During the twentieth century, many theoretical and experimental studies allowed characterization of the crystalline structures of the most common clathrates. Meanwhile, a classification has been established to identify the nature of the clathrate and the form of occupation of the trapped molecules (single clathrate, multiple guest clathrates, *etc*). From the knowledge of the structure of clathrates, predictive rigorous methods have been developed to determine their thermodynamic properties. In particular, van der Waals & Platteeuw[25] laid the foundations of a statistical thermodynamics model to determine the properties of clathrates. This method is an excellent modern example of the use of statistical thermodynamics to predict macroscopic quantities such as temperature and pressure, using the microscopic properties like potential interactions. This approach, used today in industry and science, has saved substantial experimental effort for the determination of: (i) the equilibrium pressure of a clathrate formed from various mixtures; and (ii) the mole fraction of the different species trapped in the clathrate from a given fluid phase.

In the present work, we use a statistical thermodynamic model derived from the approach of van der Waals & Platteeuw in order to investigate the composition of clathrates that may have formed in the solar nebula. Indeed, many works published in the last decade and detailing the formation conditions of ices in the solar nebula have neglected the possibility of multiple guest trapping in clathrates.[14,17,18,20,24,26,27] In our approach, we consider the formation sequence of the different ices occurring during the cooling of the solar nebula and that is usually used to describe the process by which volatiles are trapped in planetesimals[14,17,18,20,24,26,27] (see Fig. 1). We then determine the fractional occupancies of guests in each clathrate formed at a given temperature. Similarly to papers following the approach of van der Waals & Platteeuw, our model is based on the use of intermolecular potentials, which themselves depend on parameters describing the interaction between the molecule and the cage, called "Kihara parameters". Because the models are extremely sensitive to the choice of these parameters, and because different sets of data exist in the literature,[28–34] we

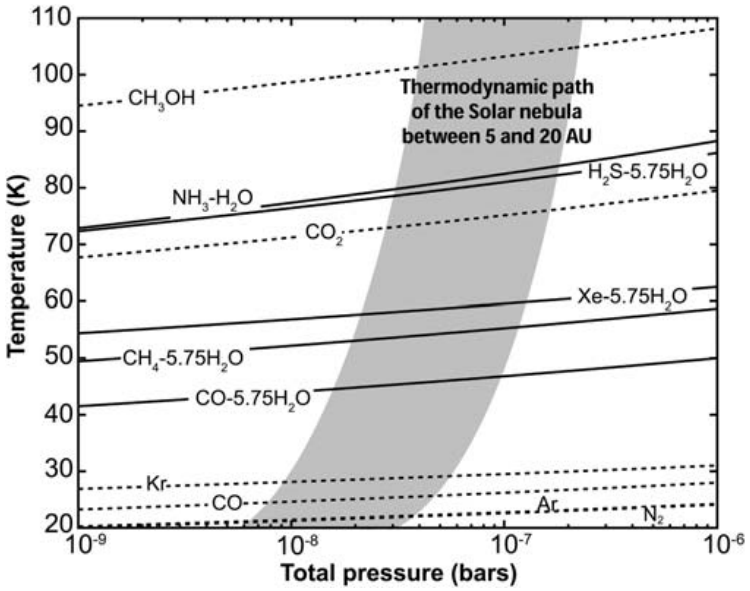

Fig. 1 Equilibrium curves of NH_3–H_2O hydrate, H_2S, Xe, CH_4 and CO clathrates (solid lines), CH_3OH, CO_2, Kr, CO, Ar and N_2 pure condensates (dotted lines), and the thermodynamic path followed by the solar nebula between 5 and 20 AU as a function of time, respectively, assuming a full efficiency of clathration. Abundances of various elements are solar, with $CO : CO_2 : CH_3OH : CH_4 = 70 : 10 : 2 : 1$, $H_2S : H_2 = 0.5 \times (S/H_2)_\odot$, and $N_2 : NH_3 = 10 : 1$ in the gas phase of the disk. Species remain in the gas phase above the stability curves. Below, they are trapped as clathrates or simply condense.

Retour à la table des matières : p. v

View Article Online

Published on 12 July 2010. Downloaded by Université de Reims Champagne-Ardenne on 08/12/2014 15:36:10.

examine the influence of the interaction potential parameters on our calculations. Moreover, it has been shown that the size of the clathrate cages depends on their formation temperature.[35–37] This also led us to investigate the influence of the size of cages on the resulting composition of clathrates formed in the low pressure and temperature conditions of the nebula.

The paper is organized as follows. In Section 2, we briefly depict the formation sequence of the different ices, including clathrates, in the outer solar nebula. In Section 3, we describe the statistical model based on the work of van der Waals and Platteeuw, and used to calculate the precise composition of clathrates. In Section 4, we define an optimal set of Kihara parameters used in our statistical model in order to calculate the nominal fractional occupancies of the different guests incorporated in clathrates formed in the solar nebula. Section 5 is devoted to the investigation of the influence of the potential parameters and structural characteristics (*i.e.* size of cages) of clathrates on our calculations of the fractional occupancies. In Section 6, we discuss the implications of our calculations for the composition of the outer solar system. In particular, we focus our attention on the volatile abundances in the atmosphere of Saturn, the issue of the measured argon deficiency in Titan and the prediction of the noble gas content in comets. Section 7 is devoted to the summary and discussion of our results.

2 Formation of clathrates in the primordial nebula

In the present work, we focus our attention on the formation sequence of the different ices produced in the giant-planets formation-zone in the primordial nebula. Once formed, these ices will add to the composition of the planetesimals accreted by the giant planets and their surrounding satellites during their growth. The composition of the initial gas phase of the disk is defined as follows: we assume that the abundances of all elements, including oxygen, are protosolar[38] and that O, C, and N exist only under the form of H_2O, CO, CO_2, CH_3OH, CH_4, N_2, and NH_3. The abundances of CO, CO_2, CH_3OH, CH_4, N_2 and NH_3 are then determined from the adopted $CO : CO_2 : CH_3OH : CH_4$ and $N_2 : NH_3$ gas phase molecular ratios. Once the abundances of these molecules are fixed, the remaining O gives the abundance of H_2O. Concerning the distribution of elements in the main volatile molecules, we set $CO : CO_2 : CH_3OH : CH_4 = 70 : 10 : 2 : 1$ in the gas phase of the disk, values that are consistent with the ISM measurements considering the contributions of both gas and solid phases in the lines of sight.[39–42] In addition, S is assumed to exist in the form of H_2S, with $H_2S : H_2 = 0.5 \times (S/H_2)_{\odot}$,† and other refractory sulfide components.[43] We also consider $N_2 : NH_3 = 10 : 1$ in the nebula gas-phase, a value compatible with thermochemical models of the solar nebula[44] and with observations of cometary comae.[27] In the following, we adopt these mixing ratios as our nominal model of the solar nebula gas phase composition (see Table 1).

The process by which volatiles are trapped in icy planetesimals, illustrated in Fig. 1, is calculated using the stability curves of stochiometric hydrates, clathrates and pure condensates, and the thermodynamic path (hereafter cooling curve) detailing the evolution of temperature and pressure between 5 and 20 AU roughly corresponding to the formation locations of the giant planets in the solar nebula.‡ We refer the reader to the works of Papaloizou & Terquem[48] and Alibert *et al.*[49] for a full description of the turbulent model of accretion disk used here. The stability

† $(S/H_2)_{\odot}$ means the solar abundance of S relative to H_2. $\odot$ is the astronomical symbol for the Sun.

‡ Recent models of giant planet formation show that instead of forming at 20 and 30 AU, *i.e.* their current orbits, Uranus and Neptune underwent most of their growth among proto-Jupiter and proto-Saturn and were scattered outward when Jupiter acquired its massive gas envelope, and subsequently evolved toward their present orbits.[45–47]

 This journal is © The Royal Society of Chemistry 2010

Retour à la table des matières : p. v

View Article Online

Published on 12 July 2010. Downloaded by Université de Reims Champagne-Ardenne on 08/12/2014 15:36:10.

Table 1 Gas phase abundances in the solar nebula.[a]

Species X	(X : H_2)	Species X	(X : H_2)
O	1.16×10^{-3}	N_2	7.62×10^{-5}
C	5.82×10^{-4}	NH_3	7.62×10^{-6}
N	1.60×10^{-4}	CO	4.91×10^{-4}
S	3.66×10^{-5}	CO_2	7.01×10^{-5}
Ar	8.43×10^{-6}	CH_3OH	1.40×10^{-5}
Kr	4.54×10^{-9}	CH_4	7.01×10^{-6}
Xe	4.44×10^{-10}	H_2S	1.83×10^{-5}
H_2O	5.15×10^{-4}		

[a] Elemental abundances derive from Lodders (2003). Molecular abundances result from the distribution of elements following the approach given in the text.

curves of hydrates and clathrates derive from Lunine & Stevenson's compilation[4] of published experimental work, in which data are available at relatively low temperatures and pressures. On the other hand, the stability curves of pure condensates used in our calculations derive from the compilation of laboratory data given in the CRC *Handbook of Chemistry and Physics*.[50] The cooling curve intercepts the stability curves of the different ices at particular temperatures and pressures. For each ice considered, the domain of stability is the region located below its corresponding stability curve. The clathration process stops when no more crystalline water ice is available to trap the volatile species. Note that, in the pressure conditions of the solar nebula, CO_2 is the only species that crystallizes at a higher temperature than its associated clathrate. We then assume that solid CO_2 is the only existing condensed form of CO_2 in this environment. In addition, we have considered only the formation of pure ice of CH_3OH in our calculations since, to the best of our knowledge, no experimental data concerning the stability curve of its associated clathrate have been reported in the literature.

In this study, we assume that the clathration efficiency is total, implying that guest molecules had the time to diffuse through porous water-ice solids before their growth into planetesimals and their accretion by proto-planets or proto-satellites. This statement remains plausible only if collisions between planetesimals have exposed essentially all the ice to the gas over time scales shorter or equal to planetesimals' lifetimes in the nebula.[4] In this case, NH_3, H_2S, Xe, CH_4 and ~38.6% of CO form NH_3–H_2O hydrate and H_2S, Xe, CH_4 and CO clathrates with the available water in the outer nebula. The remaining CO, as well as N_2, Kr, and Ar, whose clathration normally occurs at lower temperatures, remain in the gas phase until the nebula cools enough to allow the formation of pure condensates. Note that, because we assume that the gas phase composition of the disk does not vary with the heliocentric distance, the calculated clathration conditions remain the same in the 5–20 AU range of the nebula, as shown recently by Marboeuf *et al.*[51] in the case of their study of the composition of ices produced in protoplanetary disks. Once crystallized, these ices will agglomerate and form planetesimals large enough to decouple from the nebular gas and will be accreted by the forming planets and satellites.

3 The statistical–thermodynamic model

To calculate the relative abundances of guest species incorporated in a clathrate from a coexisting gas of specified composition at given temperature and pressure, we follow the method described by Lunine & Stevenson[4] and Thomas *et al.*[3,7,52] which uses classical statistical mechanics to relate the macroscopic thermodynamic properties of clathrates to the molecular structure and interaction energies. It is

Retour à la table des matières : p. v

View Article Online

Published on 12 July 2010. Downloaded by Université de Reims Champagne-Ardenne on 08/12/2014 15:36:10.

based on the original ideas of van der Waals & Platteeuw for clathrate formation, which assume that trapping of guest molecules into cages corresponds to the three-dimensional generalization of ideal localized adsorption. This approach is based on four key assumptions:[4,31]

1. The host molecules contribution to the free energy is independent of the clathrate occupancy. This assumption implies in particular that the guest species do not distort the cages.
2. (a) The cages are singly occupied. (b) Guest molecules rotate freely within the cage.
3. Guest molecules do not interact with each other.
4. Classical statistics is valid, *i.e.*, quantum effects are negligible.

In this formalism, the fractional occupancy of a guest molecule K for a given type t (t = small or large) of cage can be written as

$$y_{K,t} = \frac{C_{K,t} P_K}{1 + \sum_J C_{J,t} P_J} \tag{1}$$

where the sum in the denominator includes all the species which are present in the initial gas phase. $C_{K,t}$ is the Langmuir constant of species K in the cage of type t, and P_K is the partial pressure of species K. This partial pressure is given by $P_K = x_K \times P$ (we assume that the sample behaves as an ideal gas), with x_K the mole fraction of species K in the initial gas phase given in Table 1, and P the total gas pressure, which is dominated by H_2.

The Langmuir constant depends on the strength of the interaction between each guest species and each type of cage, and can be determined by integrating the molecular potential within the cavity as

$$C_{K,t} = \frac{4\pi}{k_B T} \int_0^{R_c} \exp\left(- \frac{w_{K,t}(r)}{k_B T} \right) r^2 dr \tag{2}$$

where R_c represents the radius of the cavity assumed to be spherical, k_B the Boltzmann constant, and $w_{K,t}(r)$ is the spherically averaged Kihara potential representing the interactions between the guest molecules K and the H_2O molecules forming the surrounding cage t. This potential $w(r)$ can be written for a spherical guest molecule, as[53]

$$w(r) = 2z\varepsilon \left[\frac{\sigma^{12}}{R_c^{11} r} \left(\delta^{10}(r) + \frac{a}{R_c} \delta^{11}(r) \right) - \frac{\sigma^6}{R_c^5 r} \left(\delta^4(r) + \frac{a}{R_c} \delta^5(r) \right) \right] \tag{3}$$

with

$$\delta^N(r) = \frac{1}{N} \left[\left(1 - \frac{r}{R_c} - \frac{a}{R_c} \right)^{-N} - \left(1 + \frac{r}{R_c} - \frac{a}{R_c} \right)^{-N} \right] \tag{4}$$

In eqn (3), z is the coordination number of the cell. This parameter, which depends on the structure of the clathrate (I or II) and on the type of the cage (small or large), is given in Table 2. The Kihara parameters a, σ and ϵ for the molecule–water interactions employed in this work have been taken from Diaz Peña *et al.*[30] for CO and from Parrish & Prausnitz[28,29] or from Sloan & Koh[34] for all the other molecules of interest (see Table 3).

Finally, the mole fraction f_K of a guest molecule K in a clathrate can be calculated with respect to the whole set of species considered in the system as

$$f_K = \frac{b_s y_{K,s} + b_\ell y_{K,\ell}}{b_s \sum_J y_{J,s} + b_\ell \sum_J y_{J,\ell}} \tag{5}$$

where b_s and b_ℓ are the number of small and large cages per unit cell respectively, for the clathrate structure under consideration, and with $\sum_K f_K = 1$.

 This journal is © The Royal Society of Chemistry 2010

Retour à la table des matières : p. v

View Article Online

Published on 12 July 2010. Downloaded by Université de Reims Champagne-Ardenne on 08/12/2014 15:36:10.

Table 2 Parameters for the cavities[28,29,a]

Clathrate structure	I		II	
Cavity type	Small	Large	Small	Large
R_c/Å	3.975	4.300	3.910	4.730
b	2	6	16	8
z	20	24	20	28

[a] R_c is the radius of the cavity. b represents the number of small (b_s) or large (b_ℓ) cages per unit cell for a given structure of clathrate (I or II), z is the coordination number in a cavity.

Table 3 Two different sets for the Kihara potential[a]

Set	Ref.	Molecule	σ/Å	(ϵ/k_B)/K	a/Å
(1)	PP72	H_2S	3.1558	205.85	0.36
	PP72 + SK08	CO_2	2.9681	169.09	0.6805
	PP72	CH_4	3.2398	153.17	0.300
	PP72	N_2	3.2199	127.95	0.350
	PP72	Xe	3.1906	201.34	0.280
	PP72	Ar	2.9434	170.50	0.184
	PP72	Kr	2.9739	198.34	0.230
	DP82	CO	3.101	134.95	0.284
(2)	SK08	H_2S	3.10000	212.047	0.3600
	SK08	CO_2	2.97638	175.405	0.6805
	SK08	CH_4	3.14393	155.593	0.3834
	SK08	N_2	3.13512	127.426	0.3526
	SK08	Xe	3.32968	193.708	0.2357
	PP72	Ar	2.9434	170.50	0.184
	PP72	Kr	2.9739	198.34	0.230
	DP82	CO	3.101	134.95	0.284

[a] σ is the Lennard-Jones diameter, ϵ is the depth of the potential well, and a is the radius of the impenetrable core. PP72, DP82 and SK08 correspond to the data taken from Parrish & Prausnitz,[28,29] Diaz Peña *et al.*[30] and Sloan & Koh,[34] respectively.

4 Predicted clathrate hydrates occupancies in the primordial nebula

We calculate here the relative abundances of guests that can be incorporated in H_2S, Xe, CH_4 and CO clathrates at the time of their formation in the solar nebula. As far as we know, the two most complete sets of Kihara parameters available in the literature concerning astrophysical molecules are those published by Parrish & Prausnitz and Diaz Peña *et al.* The parameters given by Parrish & Prausnitz have been obtained by comparing calculated chemical potentials based on the structural data of the clathrate cages with experimental results based on clathrate dissociation pressure data. These parameters have been used in recent work that aimed at investigating the composition of clathrates that may exist at the surfaces of Titan and Mars.[2,3,7,52] On the other hand, the parameters given by Diaz Peña *et al.* have been fitted to experimentally measured interaction virial coefficients for binary mixtures. These parameters have been used to quantify the trapping by clathrates of gases contained in volatiles observed in comets.[54] Thomas *et al.*[52] did a comprehensive comparison between these two sets of data and concluded that the

Retour à la table des matières : p. v

View Article Online

Published on 12 July 2010. Downloaded by Université de Reims Champagne-Ardenne on 08/12/2014 15:36:10.

parameters given by Parrish & Prausnitz are the most reliable because they have been self-consistently determined on experimentally measured clathrate properties and also because the results are similar to those obtained from other recent compilations (such as that of Sloan & Koh) whose molecules of astrophysical interest are listed in set (2) of Table 3). For these reasons, we have used the potential and structural parameters given by Parrish & Prausnitz for H_2S, CH_4, N_2, Xe, Ar and Kr in our nominal calculations. However, in the case of CO, we have used the Kirara parameters from Diaz Peña *et al.* because these data are absent from the compilation of Parrish & Prausnitz. Finally, Thomas *et al.*[3] found that, for common molecules, the parameters from Parrish and Prausnitz are very similar to those published in recent compilations also obtained from the fit of Langmuir constants to simple clathrate formation experimental data,[31–33] except for the value of the parameter *a* for CO_2 (the radius of the impenetrable core), which is almost twice larger in the recent sets of parameters than in Parrish and Prausnitz's parameters. Following the conclusions of Thomas *et al.*,[3] we have used the CO_2 Kirara parameters from Parrish & Prausnitz, except for the suspicious a_{CO_2} value, which has been replaced by the one given by Sloan & Koh. Set (1) of Table 3 enumerates the list of Kihara parameters for various molecules considered in our system and used in our nominal calculations.

In our calculations, any volatile already trapped or condensed at a higher temperature than the formation temperature of the clathrate under consideration is excluded from the coexisting gas phase composition. This implies that CO_2, Xe, CH_4, CO, Kr, Ar and N_2 are considered as possible guests in the case of H_2S clathrate. On the other hand, only N_2, Ar, Kr can become guests in CO clathrate. Fig. 2 represents the mole fraction *f* (eqn (5)) of volatiles encaged in structure I and structure II clathrates *a priori* dominated by H_2S, Xe, CH_4 and CO and formed in the primordial nebula. Interestingly enough, this Figure shows that, contrary to H_2S, Xe and CH_4, which remain the dominating guest species in the clathrates considered, CO becomes a minor compound in the clathrate that is expected to be dominated by this molecule. Indeed, whatever the structure considered, Kr and N_2 become more

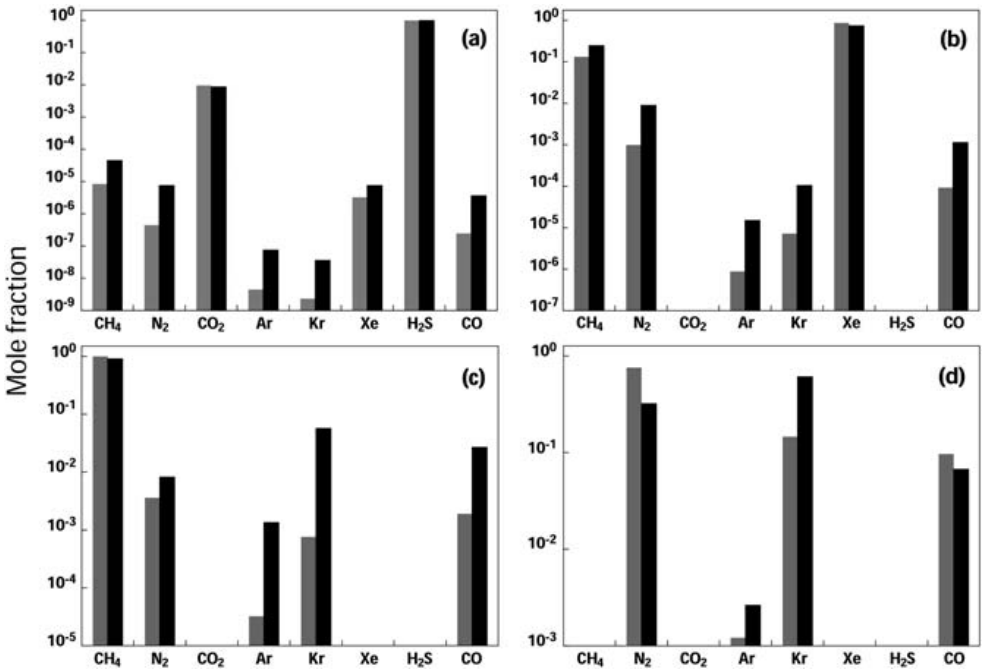

Fig. 2 Mole fraction of volatiles encaged in H_2S (a), Xe (b), CH_4 (c) and CO (d) clathrates. Grey and dark bars correspond to structure I and structure II clathrates, respectively.

 This journal is © The Royal Society of Chemistry 2010

Retour à la table des matières : p. v

View Article Online

Published on 12 July 2010. Downloaded by Université de Reims Champagne-Ardenne on 08/12/2014 15:36:10.

abundant than CO in this clathrate, irrespective of their initial abundances in the gas phase of the nebula. This behavior results from the fact that the interaction potential between CO and the water molecules forming the surrounding cages is weaker than those involving the other species.

Table 4 gives the temperature and pressure formation conditions of these clathrates in the nebula and the relative abundance f_K* defined as the ratio of K/X in X clathrate (where X = H_2S, Xe, CH_4 or CO). Fig. 3 represents the abundance ratio F_K* which is defined as the ratio of K/X in X clathrate (*i.e.* f_K*) to K/X in the initial nebula gas phase. A guest K which incorporates completely into a given clathrate displays a F_K* value of 1 or greater, provided that there is enough water in the nebula available for clathration. This Figure shows that volatile species such as Kr, Ar or N_2 that are expected to form pure condensates below 30 K in the primitive nebula can be efficiently encaged in clathrates formed at higher temperature (~48.5 K and above). Indeed, irrespective of the particular structure, and depending on the amount of water available for clathration, these three volatiles can be efficiently trapped in CO clathrate at $T = 48.5$ K in the primitive nebula (panel (d) of Fig. 3). Kr can also be efficiently enclathrated at at $T = 55.5$ K in CH_4 clathrate (panel (c) of Fig. 3). Generally speaking, Fig. 3 illustrates the fact that some volatiles can be efficiently trapped at relatively high temperature in multiple guest clathrates compared to the temperatures at which they are expected to condense or to form single guest clathrates in the primordial nebula. It is important to note that the present results strongly depend on the choice of the initial gas phase conditions and on the amount of water ice available for clathration in the formation zone of planetesimals.

Table 4 Relative abundance f* of volatiles encaged in structure I and structure II clathrates.[a]

Clathrate	Species	Structure I f_K*	Structure II
H_2S	CO_2	9.67×10^{-3}	8.74×10^{-3}
$T = 82.3$ K	Xe	3.28×10^{-6}	7.58×10^{-6}
$P = 1.7 \times 10^{-7}$ bar	CH_4	8.46×10^{-6}	4.51×10^{-5}
	CO	2.47×10^{-7}	3.66×10^{-6}
	Kr	2.35×10^{-9}	3.63×10^{-8}
	Ar	4.48×10^{-9}	7.54×10^{-8}
	N_2	4.50×10^{-7}	7.62×10^{-6}
Xe	CH_4	1.52×10^{-1}	3.32×10^{-1}
$T = 59.8$ K	CO	1.07×10^{-4}	1.52×10^{-3}
$P = 1.2 \times 10^{-7}$ bar	Kr	8.30×10^{-6}	1.41×10^{-4}
	Ar	1.01×10^{-6}	2.02×10^{-5}
	N_2	1.13×10^{-3}	1.20×10^{-2}
CH_4	CO	1.91×10^{-3}	2.95×10^{-2}
$T = 55.3$ K	Kr	7.64×10^{-4}	6.27×10^{-2}
$P = 1.1 \times 10^{-7}$ bar	Ar	3.24×10^{-5}	1.48×10^{-3}
	N_2	3.62×10^{-3}	9.01×10^{-3}
CO	Kr	1.51	9.08
$T = 47.0$ K	Ar	1.25×10^{-2}	3.90×10^{-2}
$P = 1.0 \times 10^{-7}$ bar	N_2	7.84	4.78

[a] f_K* is defined as the relative abundance of guest K to X in X clathrate (where X = H_2S, Xe, CH_4 or CO). Values of T and P correspond to the temperature and pressure of the H_2-dominated gas at which the cooling curve (here at 5 AU) intercepts the equilibrium curves of the considered clathrates (see Fig. 1) Only the species that are not yet condensed or trapped prior the epoch of clathrate formation are considered in our calculations.

Retour à la table des matières : p. v

View Article Online

Published on 12 July 2010. Downloaded by Université de Reims Champagne-Ardenne on 08/12/2014 15:36:10.

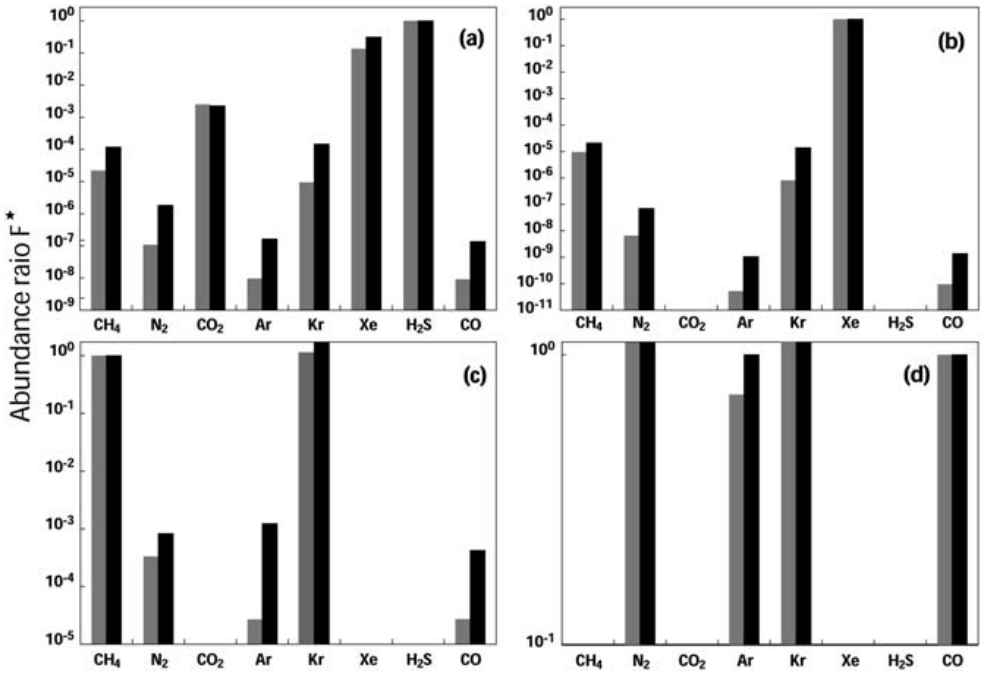

Fig. 3 Abundance ratio F_K* is defined as the ratio of K/X in X clathrate (*i.e.* f_K*) to K/X in the initial nebula gas phase (where X = H_2S (a), Xe (b), CH_4 (c) and CO (d)). Grey and dark bars correspond to structure I and structure II clathrates, respectively.

5 Sensitivity to parameters

The determination of the relative abundances of guest species incorporated in clathrates formed in the primitive nebula, and more generally in clathrates formed in any thermodynamic condition, strongly depends on their structural characteristics (*i.e.* size of the cages) and also on the parameters of the Kihara potential. Here, we investigate the influence of these structural characteristics and potential parameters on the fractional occupancies of guests in clathrates formed in the nebula.

5.1 Influence of the interaction potential parameters

It has been recently shown that, perturbing the σ and ϵ Kihara parameters taken from a given compilation in the 1–10% range, leads to strong variations of the values of the Langmuir constants and thus of the fractional occupancies of enclathrated molecules.[55] In the present case, in order to investigate the sensitivity of the composition of clathrates formed in the nebula to the variation of Kihara parameters, we have tested a second compilation of parameters close to our nominal set of values taken from Parrish & Prausnitz (set 1 of Table 3) but which derives from Sloan & Koh for H_2S, CO_2, CH_4, N_2 and Xe. Because we did not find any Kihara parameter for Ar, Kr and CO in the recent published compilations, we have adopted the same values as in our nominal set for these molecules (see set 2 of Table 3). As a result, the two sets of Kihara parameters used in our comparison are almost identical since several volatiles share the same data and the dispersion of data between other compounds is narrow. Two comparisons, represented in Fig. 4, have been made in the cases of Xe and CH_4 clathrates produced in the primordial nebula. In both cases, calculations have been performed for structure I and II clathrates. Despite the similarity of the potential parameters used, one can note dispersions up to more than one order of magnitude in the resulting mole fractions (eqn (5)) for a given volatile encaged in the same clathrate. We then conclude that even minor dispersions between the different existing sets of Kihara parameters can lead to large variations

 This journal is © The Royal Society of Chemistry 2010

Retour à la table des matières : p. v

View Article Online

Published on 12 July 2010. Downloaded by Université de Reims Champagne-Ardenne on 08/12/2014 15:36:10.

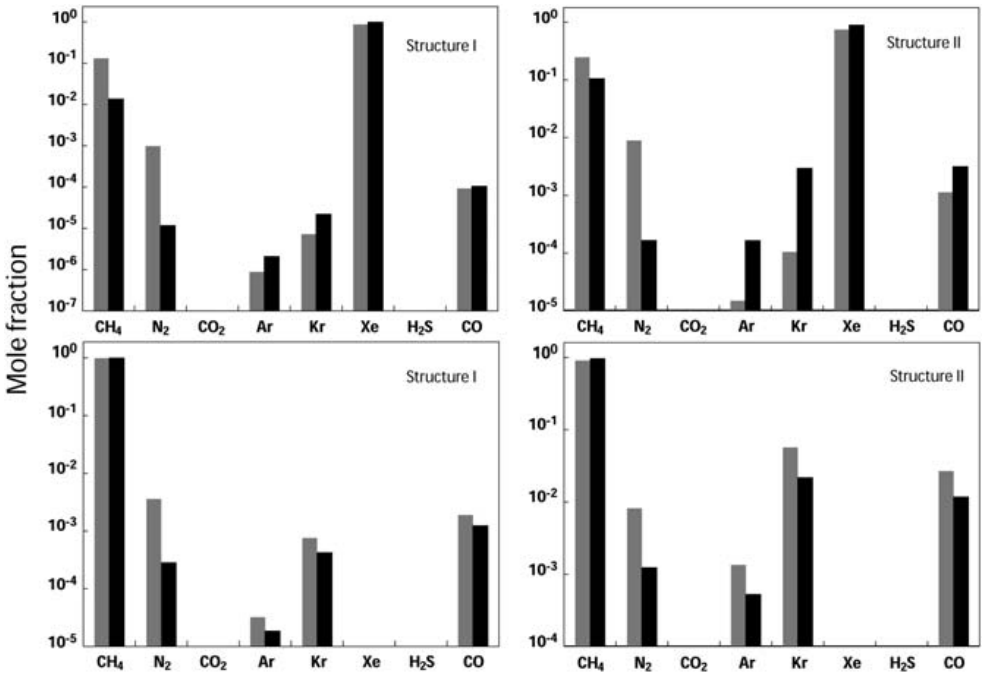

Fig. 4 Mole fraction of volatiles encaged in structure I and structure II clathrates dominated by Xe (top panels) and CH_4 (bottom panels). Grey and dark bars correspond to sets (1) and (2) of parameters of the Kihara potential given in Table 3, respectively.

into the determination of the volatiles trapping in clathrates formed in the primordial nebula. However, these variations were not found to be strong enough to modify the relative trapping efficiencies between the different volatiles in the clathrates considered here.

5.2 Influence of cage variations

In the present work, we have adopted the structural parameters of clathrates given by Parrish & Prausnitz and shown in Table 2. Up to now, we have assumed that the size of the cages R_c is unaffected by the trapping conditions of the different guests in the primordial nebula. However, laboratory measurements have shown that the size of the cages could increase with temperature and also with the size of the incorporated guest species.[35–37,56] We have thus investigated the influence of variations of the cage sizes on the mole fractions of guests encaged in clathrates by modifying by up to $\pm 5\%$ the values of R_c given in Table 2. This large variation is consistent with typical thermal expansion or contraction measured in the temperature range 90–270 K.[35–37,56] Note that because clathration of volatiles occurs at lower temperature in the nebula, slightly larger variations of the cage sizes may be expected.

The evolution of the mole fractions of all guests in structure I clathrates formed in the primitive nebula is given in Fig. 5 as a function of the size of the cages, at clathration temperatures and pressures given in Table 4. This Figure shows that the contraction or expansion of the cages clearly affects the mole fractions of some volatiles in clathrates and that the magnitude of these changes strongly depends on the interaction parameters between the guest species and the cages. Indeed, irrespective of the clathrate considered, Fig. 5 shows that the mole fractions of Ar and Kr can vary up to several orders of magnitude by changing the size of the cages in the range considered. Moreover, depending on the particular clathrate, mole fractions of other molecules such as N_2 or CO are also subject to strong changes with the variation of the size of the cages. Similar trends have been revealed by performing calculations for clathrates of structure II. Our calculations confirm that the trapping propensity

Retour à la table des matières : p. v

View Article Online

Published on 12 July 2010. Downloaded by Université de Reims Champagne-Ardenne on 08/12/2014 15:36:10.

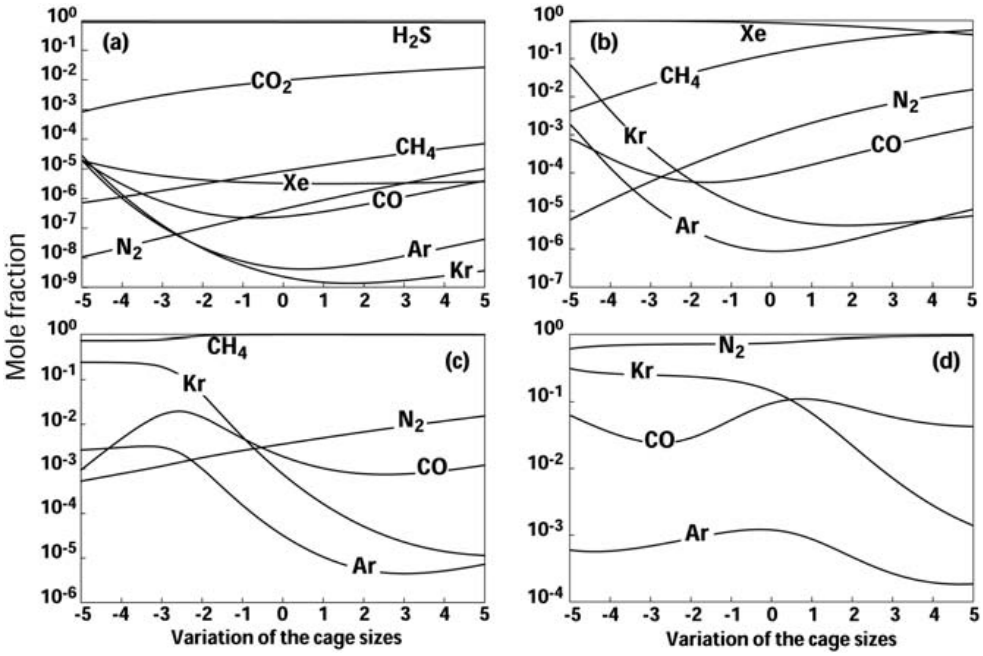

Fig. 5 Mole fraction of volatiles encaged in structure I clathrates dominated by H_2S (a), Xe (b), CH_4 (c) and CO (d) as a function of the cage sizes.

of a given molecule in clathrates is related rather sensitively to the shape of its intermolecular potential, which is determined from the adopted Kihara parameters and also from the adopted size of the cages (see eqn (3)). This is to be expected given that the Kihara parameters enter exponentially into the statistical partition function which determines the probability of occupancy. The tradeoff between the attractive part of the potential and the repulsive part is a function of the guest molecule shape and size, as well as the size of the cage, and given that clathrate structures feature two cage sizes, it is not easy to predict what happens to the relative incorporation of a molecule as cages shrink or expand thanks to temperature. The statistical mechanical model is therefore essential for predictive purposes.

Fig. 5 suggests that thermal variations of the cages need to be taken into account in particular if these variations are greater than a few percent. Similar conclusions have been obtained by Thomas *et al.*[52] in their study of clathrate formation and composition at the surface–atmosphere interface of Titan. As discussed in the following Section, these results may affect the predictions of the composition of the bodies formed in the outer solar system. On the other hand, variations with temperature are often not well constrained due to the small number of specific systems that have been studied, such as for example the pure methane clathrate for which the variations of the cages have been found to be small (~0.3%) between 83 and 173 K(37). In the present study, several species are encaged in the same clathrate and the temperature range of interest is lower than those considered in experiments. For these reasons, it is difficult to infer variation laws describing the expansion/contraction of clathrates at temperatures relevant for the solar nebula.

6 Implications for the composition of the outer solar system

Our calculations of the multiple guest trapping in clathrates formed in the primordial nebula have implications for the formation and composition models of the giant planets, their surrounding satellites and also comets. Indeed, the fact that several compounds expected to be trapped or condensed at low temperature are incorporated at relatively higher temperature in clathrates in the nebula modifies the

 This journal is © The Royal Society of Chemistry 2010

Retour à la table des matières : p. v

View Article Online

Published on 12 July 2010. Downloaded by Université de Reims Champagne-Ardenne on 08/12/2014 15:36:10.

predictions of the composition of the icy planetesimals from which these bodies were presumably formed relative to what is obtained from simple condensation models. A few examples are discussed here.

6.1 Volatile enrichments in Saturn

Measurements by the mass spectrometer aboard the Galileo probe have shown that the abundances of C, N, S, Ar, Kr and Xe are all enriched by similar amounts with respect to their solar abundances in the atmosphere of Jupiter.[15,57,58] Similarly, recent Cassini CIRS observations have also confirmed what was inferred from previous measurements, that C is substantially enriched in the atmosphere of Saturn.[59,60] In order to interpret these volatile enrichments, it has been proposed that the main volatile compounds initially existing in the solar nebula gas phase were essentially trapped by crystalline water ice in the form of clathrates or hydrates in the feeding zones of Jupiter and Saturn.[14,17–19,24,26,27] These ices then agglomerated and formed planetesimals that were ultimately accreted by the forming Jupiter and Saturn. This is then the fraction of these icy planetesimals that vaporized when entering the envelopes of the two growing planets which engendered the observed volatile enrichments.

On the other hand, our statistical model allows us to infer that multiple guest clathrates were more likely formed than single clathrates in the solar nebula, implying substantial changes in the presumed composition of the planetesimals formed from these ices. As a result, the volatile enrichments calculated in the giant planets' atmospheres should also be altered because these quantities are proportional to the mass of accreted and vaporized icy planetesimals. Indeed, for instance, a recent interpretation of the carbon abundance in the atmosphere of Saturn is based on the hypothesis that the giant planet never formed at a disk temperature below 30 K,[27] implying that the planetesimals accreted by the giant planet were impoverished in Ar, Kr, CO and N_2 (*i.e.* volatiles whose condensation curves are located below 30 K in the nebula – see Fig. 1). However, our nominal calculations predict that Kr can be entirely trapped in CH_4-dominated clathrates at ~55 K in the nebula, provided that there is enough water available for clathration at this temperature in the feeding zone of Saturn. In this scenario, the trapping of Kr at higher temperature in the planetesimals accreted by Saturn implies that the atmospheric abundance of this noble gas should also be enhanced by an amount similar to that of carbon compared to solar (at least ~9 times solar[14,60]), instead of being predicted in solar abundance in Saturn's envelope.[27] However, this conclusion is valid only for the structural characteristics and the Kihara parameters adopted in our nominal calculations. As shown in Fig. 5, any expansion of the cage sizes during the formation of CH_4-dominated clathrate in the solar nebula could strongly reduce the trapping efficiency of Kr in this clathrate and thus decrease its resulting enhancement in the atmosphere of Saturn.

6.2 The argon deficiency in Titan

A puzzling feature of the atmosphere of Titan is that no primordial noble gases other than argon were detected by the Gas Chromatograph Mass Spectrometer (GCMS) aboard the Huygens probe during its descent to Titan's surface on January 14, 2005. The observed argon includes primordial ^{36}Ar, *i.e.* the main isotope, and the radiogenic isotope ^{40}Ar, which is a decay product of ^{40}K.[61] In any case, the $^{36}Ar/^{14}N$ is lower than the solar value by more than five orders of magnitude.[61] The other primordial noble gases Kr and Xe (and ^{38}Ar) were not detected by the GCMS instrument down to upper limits of 10 parts per billion relative to nitrogen.[61] The Kr and Xe deficiencies could simply be explained by the presence of clathrates on the surface of Titan that would have efficiently incorporated these noble gases.[7,52] On the other hand, in order to interpret the Ar deficiency in the atmosphere of Titan, it has been

Retour à la table des matières : p. v

View Article Online

Published on 12 July 2010. Downloaded by Université de Reims Champagne-Ardenne on 08/12/2014 15:36:10.

proposed that the satellite was formed from icy planetesimals initially produced in the solar nebula and that were partially devolatilized at a temperature not exceeding ~50 K during their migration within Saturn's subnebula.[13] In this case, because Ar is poorly trapped in clathrates formed above ~50 K in the nebula, only tiny amounts of this compound would have been incorporated in the building blocks of the forming Titan, in agreement with the observations. In particular, our nominal model predicts that this noble gas would remain essentially trapped in CH_4-dominated clathrate,§ and subsequently in the satellite, with $Ar : CH_4$ of 2.7×10^{-5} (see Fig. 3), in good match with the abundances of ^{36}Ar observed in Titan's atmosphere. However, this statement remains valid only if one considers our nominal calculations of multiple guest trapping in clathrates formed in the feeding zone of Saturn. Indeed, Fig. 5 shows that the trapping of Ar can strongly increase by a factor of more than 300 in CH_4-dominated clathrate formed in the solar nebula if the size of the cages decreases by a few percent. In this case, the amount of argon predicted by our calculations in the atmosphere of Titan would be higher than the value measured by Huygens or an alternative scenario must be invoked to explain its apparent depletion.

6.3 Noble gas content in comets

It has been proposed that the composition of volatiles observed in comets could be explained on the basis of their trapping in the form of clathrates in the primordial nebula.[54] In this model, the key parameter to explain the volatile content observed in comets is the amount of water ice available in the region of the nebula where the clathration took place. The mass of available water is then varied between the amount needed to trap the whole mass of volatiles present in the nebula (high-mass ice scenario) and that which is just required to enclathrate volatiles at temperatures above ~50 K in the nebula (low-mass ice scenario). In this model, the case of argon is interesting because its relative abundance in comets is found to be very small ($Ar : H_2O \sim 10^{-8}$) when the low-mass ice scenario is considered. On the other hand, if enough water ice is present, $Ar : H_2O$ jumps to potentially detectable values ($Ar : H_2O \sim 10^{-4}$–10^{-3}). However, as in the case of Titan described above, taking into account the uncertainties of our calculations (in particular on the cage sizes), substantial amounts of Ar can be trapped in CH_4-dominated clathrates. In this case, we find $Ar : H_2O \sim 10^{-5}$–10^{-4} in the low-mass ice scenario, a value which is close to the one determined in the case of the high-mass ice scenario. Our estimate for the low-mass ice scenario implies then that it is difficult to consider the measurement of the abundance of argon in comets as a key test to constrain the mass of water ice that was available in the nebula for forming comets.

7 Summary and discussion

In this paper, we have calculated the relative abundances of guest species that can be incorporated in clathrates formed in the gas phase and thermodynamic conditions of the primordial nebula. We have assumed that the clathration efficiency is total in the primitive nebula, implying that guest molecules had the time to diffuse through porous water-ice solids before their growth into planetesimals and their accretion by proto-planets or proto-satellites. This statement remains plausible only if collisions between planetesimals have exposed essentially all the ice to the gas over time scales shorter or equal to planetesimals lifetimes in the nebula.[4] However, it is important to note that the efficiency of collisions between planetesimals to expose all the "fresh" ice over such a time scale still remains questionable and that we have no evidence that clathration was important in the primordial nebula.

§ The amount of Ar found in Xe and H_2S-dominated clathrates is negligible.

 This journal is © The Royal Society of Chemistry 2010

Retour à la table des matières : p. v

View Article Online

Published on 12 July 2010. Downloaded by Université de Reims Champagne-Ardenne on 08/12/2014 15:36:10.

The results presented here derive from the usual statistical model based on the van der Waals and Platteeuw approach, generalized by Parrish & Prausnitz for the calculations of dissociation pressures of multiple guest clathrates. The major ingredient of our model is the description of the guest–clathrate interaction by a spherically averaged Kihara potential with a nominal set of parameters, most of which being fitted on experimental equilibrium data. Our model allows us to find that Kr, Ar and N_2 can be efficiently encaged in clathrates formed at temperatures higher than ~48.5 K, the temperature of CO clathrate, in the primitive nebula, instead of forming pure condensates below 30 K. However, we find at the same time that the determination of the relative abundances of guest species incorporated in these clathrates strongly depends on the choice of the parameters of the Kihara potential and also on their adopted structural characteristics. Indeed, testing different potential parameters, we have noted that even minor dispersions between the different existing sets can lead to non-negligible variations in the determination of the volatiles trapped in clathrates formed in the primordial nebula. However, these variations are not found to be strong enough to reverse the relative abundances between the different volatiles in the considered clathrates. Moreover, we have found that the contraction or expansion of the cages, due to temperature variations, can alter the mole fractions of some volatile molecules up to several orders of magnitude in clathrates. On the other hand, due to the lack of laboratory experiments describing properly the variation of the size of cages as a function of temperature for molecules of astrophysical interest, it is actually difficult to quantify the influence of this parameter on the composition of planetesimals formed in the nebula. The determination of specific laws describing the variation with temperature of the size of cages is important because it could help to constrain the thermodynamic conditions encountered by planetesimals during their formation in the primordial nebula. Indeed, given a sufficient number of species whose abundances are determined in a particular object, our statistical mechanical model could be used to predict the composition and temperature (through the thermal expansion/contraction of the ice which affects cage size) of the planetesimals from which the object formed and hence the composition of bodies issued from the same family. Such a measurement will be achievable by the Rosetta spacecraft mission towards Comet 67P/Churyumov-Gerasimenko or by the next generation of missions designed to investigate the outer solar system.

Our results alter the predictions of the composition of the planetesimals formed in the outer solar system. In particular, the volatile abundances calculated in the giant planets' atmospheres should be recalculated because these quantities are proportional to the mass of accreted and vaporized icy planetesimals. For the same reasons, the estimates of the volatile budgets accreted by icy satellites and comets must be reconsidered based on our calculations. For instance, our calculations predict that the abundance of argon in the atmosphere of Titan might for some initial conditions be higher than the value measured by Huygens because substantial amounts of this volatile may be trapped in the satellite's building blocks during their formation. Similarly to the case of Titan, if comets were agglomerated from clathrates in the nebula, then the Ar abundance in these bodies should still remain potentially detectable, irrespective of their formation temperature (~50 K and below) because substantial amounts of this volatile are expected to be trapped in CH_4-dominated clathrate at ~55.5 K.

It is important to note that the validity of the statistical model to determine the composition of clathrates in the nebula probably meets some limitations. In particular, the transferability of the Kihara parameters to temperatures and pressures beyond the range for which they have been fitted is uncertain.[62,63] Moreover, inconsistencies have been evidenced between Kihara parameters derived from different sets of experimental data.[64] In these conditions, supplementary measurements of the equilibrium pressure of clathrates at low temperature would be needed in order to obtain a set of Kihara parameters consistent with the low temperature and pressure conditions of the nebula. Moreover, it has been claimed in the literature that

Retour à la table des matières : p. v

View Article Online

Published on 12 July 2010. Downloaded by Université de Reims Champagne-Ardenne on 08/12/2014 15:36:10.

Kihara potential may not accurately describe the interaction between guest and water molecules.[65] Recent works have thus been based on an atom–atom description of the intermolecular guest–clathrate interactions, in which effective parameters for these interactions have been fitted from results of *ab initio* quantum mechanical methods.[65–67] However, the accuracy of this atom–atom approach is strongly dependent on the ingredients of the fit, which can be the number of water molecules considered in the *ab initio* calculations, the number of sites chosen to represent the interacting molecules, the level of accuracy of the quantum methods used… It is then unfortunately very difficult to discriminate which approach (atom–atom or spherically averaged) is the most accurate.

References

1 B. K. Chastain and V. Chevrier, *Planet. Space Sci.*, 2007, **55**, 1246.
2 T. D. Swindle, C. Thomas, O. Mousis, J. I. Lunine and S. Picaud, *Icarus*, 2009, **203**, 66.
3 C. Thomas, O. Mousis, S. Picaud and V. Ballenegger, *Planet. Space Sci.*, 2009, **57**, 42.
4 J. I. Lunine and D. J. Stevenson, *Astrophys. J. Suppl.*, 1985, **58**, 493.
5 K. P. Hand, C. F. Chyba, R. W. Carlson and J. F. Cooper, *Astrobiology*, 2006, **6**, 463.
6 G. Tobie, J. I. Lunine and C. Sotin, *Nature*, 2006, **440**, 61.
7 C. Thomas, O. Mousis, V. Ballenegger and S. Picaud, *Astron. Astrophys.*, 2007, **474**, L17.
8 O. Mousis and B. Schmitt, *Astrophys. J.*, 2008, **677**, L67.
9 U. Marboeuf, O. Mousis, J.-M. Petit and B. Schmitt, *Astrophys. J.*, 2010, **708**, 812.
10 K. M. Chick and P. Cassen, *Astrophys. J.*, 1997, **477**, 398.
11 A. Kouchi, T. Yamamoto, T. Kozasa, T. Kuroda and J. M. Greenberg, *Astron. Astrophys.*, 1994, **290**, 1009.
12 O. Mousis, D. Gautier, D. Bockelée-Morvan, F. Robert, B. Dubrulle and A. Drouart, *Icarus*, 2000, **148**, 513.
13 O. Mousis, J. I. Lunine, C. Thomas, M. Pasek, U. Marboeuf, Y. Alibert, V. Ballenegger, D. Cordier, Y. Ellinger, F. Pauzat and S. Picaud, *Astrophys. J.*, 2009, **691**, 1780.
14 O. Mousis, U. Marboeuf, J. I. Lunine, Y. Alibert, L. N. Fletcher, G. S. Orton, F. Pauzat and Y. Ellinger, *Astrophys. J.*, 2009, **696**, 1348.
15 T. Owen, P. Mahaffy, H. B. Niemann, S. Atreya, T. Donahue, A. Bar-Nun and I. de Pater, *Nature*, 1999, **402**, 269.
16 G. Notesco and A. Bar-Nun, *Icarus*, 2005, **175**, 546.
17 D. Gautier, F. Hersant, O. Mousis and J. I. Lunine, *Astrophys. J.*, 2001, **550**, L227.
18 D. Gautier, F. Hersant, O. Mousis and J. I. Lunine, *Astrophys. J.*, 2001, **559**, L183.
19 Y. Alibert, O. Mousis and W. Benz, *Astrophys. J.*, 2005, **622**, L145.
20 Y. Alibert and O. Mousis, *Astron. Astrophys.*, 2007, **465**, 1051.
21 O. Mousis, *Astron. Astrophys.*, 2004, **413**, 373.
22 O. Mousis and D. Gautier, *Planet. Space Sci.*, 2004, **52**, 361.
23 O. Mousis and Y. Alibert, *Astron. Astrophys.*, 2006, **448**, 771.
24 O. Mousis, Y. Alibert and W. Benz, *Astron. Astrophys.*, 2006, **449**, 411.
25 J. H. van der Waals and J. C. Platteeuw, *Adv. Chem. Phys.*, 1959, **2**, 1.
26 F. Hersant, D. Gautier and J. I. Lunine, *Planet. Space Sci.*, 2004, **52**, 623.
27 F. Hersant, D. Gautier, G. Tobie and J. I. Lunine, *Planet. Space Sci.*, 2008, **56**, 1103.
28 W. R. Parrish and J. M. Prausnitz, *Ind. Eng. Chem. Process Des. Dev.*, 1972, **11**(1), 26.
29 W. R. Parrish and J. M. Prausnitz, *Ind. Eng. Chem. Process Des. Dev.*, 1972, **11**(3), 462.
30 M. Diaz Peña, C. Pando and J. A. R. Renuncio, *J. Chem. Phys.*, 1982, **76**, 325.
31 E. D. Sloan, *Clathrate Hydrates of Natural Gases*, 2nd ed.; Marcel Decker, Inc.: New York, 1998.
32 M. Jager, High pressure studies of hydrate phase inhibition using Raman spectroscopy. Ph.D. Thesis, 2001.
33 S. P. Kang, H. Lee, C. S. Lee and W. M. Sung, *Fluid Phase Equilib.*, 2001, **185**, 101.
34 E. D. Sloan and C. A. Koh, *Clathrate Hydrates of Natural Gases*, 3rd ed.; CRC Press, Taylor & Francis Group, Boca Raton, 2008.
35 V. P. Shpakov, J. S. Tse, C. A. Tulk, B. Kvamme and V. R. Belosludov, *Chem. Phys. Lett.*, 1998, **282**(2), 107.
36 V. R. Belosludov, T. M. Inerbaev, O. S. Subbotin, R. V. Belosludov, J. Kudoh and Y. Kawazoe, *J. Supramol. Chem.*, 2002, **2**(4–5), 453.
37 S. Takeya, M. Kida, H. Minami, H. Sakagami, A. Hachikubo, N. Takahashi and et al, *Chem. Eng. Sci.*, 2006, **61**(8), 2670.
38 K. Lodders, *Astrophys. J.*, 2003, **591**, 1220.
39 M. A. Frerking, W. D. Langer and R. W. Wilson, *Astrophys. J.*, 1982, **262**, 590.

 This journal is © The Royal Society of Chemistry 2010

Retour à la table des matières : p. v

View Article Online

Published on 12 July 2010. Downloaded by Université de Reims Champagne-Ardenne on 08/12/2014 15:36:10.

40 M. Ohishi, W. M. Irvine and N. Kaifu, *Astrochem. Cosmic Phenom.*, 1992, **150**, 171.
41 P. Ehrenfreund and W. A. Schutte, *Adv. Space Res.*, 2000, **25**, 2177.
42 E. L. Gibb, *et al.*, *Astrophys. J.*, 2000, **536**, 347.
43 M. A. Pasek, J. A. Milsom, F. J. Ciesla, D. S. Lauretta, C. M. Sharp and J. I. Lunine, *Icarus*, 2005, **175**, 1.
44 J. S. Lewis and R. G. Prinn, *Astrophys. J.*, 1980, **238**, 357.
45 E. W. Thommes, M. J. Duncan and H. F. Levison, *Astron. J.*, 2002, **123**, 2862.
46 K. Tsiganis, R. Gomes, A. Morbidelli and H. F. Levison, *Nature*, 2005, **435**, 459.
47 P. S. Lykawka, J. Horner, B. W. Jones and T. Mukai, *Mon. Not. R. Astron. Soc.*, 2009, **398**, 1715.
48 J. C. B. Papaloizou and C. Terquem, *Astrophys. J.*, 1999, **521**, 823.
49 Y. Alibert, C. Mordasini, W. Benz and C. Winisdoerffer, *Astron. Astrophys.*, 2005, **434**, 343.
50 D. R. Lide, *CRC Handbook of Chemistry and Physics: A Ready-Reference Book of Chemical and Physical Data*, 83rd edn, Boca Raton, CRC Press, ISBN 0849304830, 2002.
51 U. Marboeuf, O. Mousis, D. Ehrenreich, Y. Alibert, A. Cassan, V. Wakelam and J.-P. Beaulieu, *Astrophys. J.*, 2008, **681**, 1624.
52 C. Thomas, S. Picaud, O. Mousis and V. Ballenegger, *Planet. Space Sci.*, 2008, **56**, 1607.
53 V. McKoy and O. Sinanoğlu, *J. Chem. Phys.*, 1963, **38**(12), 2946.
54 N. Iro, D. Gautier, F. Hersant, D. Bockelée-Morvan and J. I. Lunine, *Icarus*, 2003, **161**, 511.
55 N. I. Papadimitriou, I. N. Tsimpanogiannis, A. G. Yiotis, T. A. Steriotis and A. K. Stubos, in *Physics and Chemistry of Ice. Proceedings of the 11th International Conference on the Physics and Chemistry of Ice*, ed. W. Kuhs, 2007, vol. 311, p. 475.
56 K. C. Hester, Z. Huo, A. L. Ballard, C. A. Koh, K. T. Miller and E. D. Sloan, *J. Phys. Chem. B*, 2007, **111**, 8830.
57 P. R. Mahaffy, H. B. Niemann, A. Alpert, S. K. Atreya, J. Demick, T. M. Donahue, D. N. Harpold and T. C. Owen, *J. Geophys. Res.*, 2000, **105**, 15061.
58 M. H. Wong, P. R. Mahaffy, S. K. Atreya, H. B. Niemann and T. C. Owen, *Icarus*, 2004, **171**, 153.
59 F. M. Flasar, *et al.*, *Science*, 2005, **308**, 975.
60 L. N. Fletcher, G. S. Orton, N. A. Teanby, P. G. J. Irwin and G. L. Bjoraker, *Icarus*, 2009, **199**, 351.
61 H. B. Niemann and et al, *Nature*, 2005, **438**, 779.
62 A. L. Ballard and E. D. Sloan, *Chem. Eng. Sci.*, 2000, **55**, 5773.
63 M. A. Clarke and P. R. Bishnoi, *Fluid Phase Equilib.*, 2003, **211**, 51.
64 L. S. Tee, S. Gotoh and W. E. Stewart, *Ind. Eng. Chem. Fundam.*, 1966, **5**, 363.
65 R. Sun and Z. Duan, *Geochim. Cosmochim. Acta*, 2005, **69**, 4411.
66 J. B. Klauda and S. I. Sandler, *J. Phys. Chem. B*, 2002, **106**, 5722.
67 J. B. Klauda and S. I. Sandler, *Chem. Eng. Sci.*, 2003, **58**, 24.

Retour à la table des matières : p. v

Retour à la table des matières : p. v

Troisième partie

Le champagne

Chapitre 11

La physico-chimie du champagne : approche transdisciplinaire

« *Champagne Is Always The Answer.* »

— Auteur indéterminé, *Internet*,
... mais ici c'est plutôt la question.

Sommaire

11.1 Bleu et blanc au-dessus d'une bouteille 333
11.2 Projet scientifique pétillant 336
11.2.1 La cinématique d'un bouchon de champagne 336
11.2.2 L'oscillation des bulles du champagne 338
11.2.3 Les instabilités de Kelvin–Helmholtz 338
11.2.4 La physique des panaches de mousse 340
11.3 Références 341

11.1 Bleu et blanc au-dessus d'une bouteille

Les expériences conduites par Gérard Liger-Belair et Jacques Honvault laissent voir un comportement surprenant : la «brume», apparaissant lors du débouchage d'une bouteille de champagne, a des propriétés qui dépendent de la température de stockage de la bouteille. Pour une température relativement basse, *i.e.* 6°C, seul un panache blanc, optiquement épais, se manisfeste au-dessus du goulot (*cf.* Fig 11.1.a). A 12°C (*cf.* Fig 11.1.b) une brume bleutée apparaît, après ~ 2µs dans l'espace de tête, alors qu'un panache blanc, similaire au précédent, est également présent. Finalement, à la température initiale de 20°C (*cf.* Fig 11.1.c), seul un «brouillard» bleu se forme dans l'espace de tête, pour ensuite gagner l'extérieur de la bouteille. Ces images posent donc beaucoup de questions auxquelles nous avons tenté de répondre dans l'article LIGER-BELAIR et collab. [2017] qui est visible à la section 12.1.

Dans l'espace de tête, avant débouchage, on a du CO_2 avec des traces d'eau et d'éthanol. La pression initiale varie notablement avec la température de la bouteille, allant d'environ 4,5 bar pour une bouteille à 6°C, à une pression de l'ordre de 7,5 bar pour une température de 20° (voir Fig. 3 de l'article en section 12.1). La détente adiabatique provoquée par l'ouverture de la bouteille fait chuter la température selon l'expression bien connue, issue de la loi de Laplace :

$$T_f = T \times \left(\frac{P_0}{P_{CB}} \right)^{\frac{\gamma-1}{\gamma}} \tag{11.1}$$

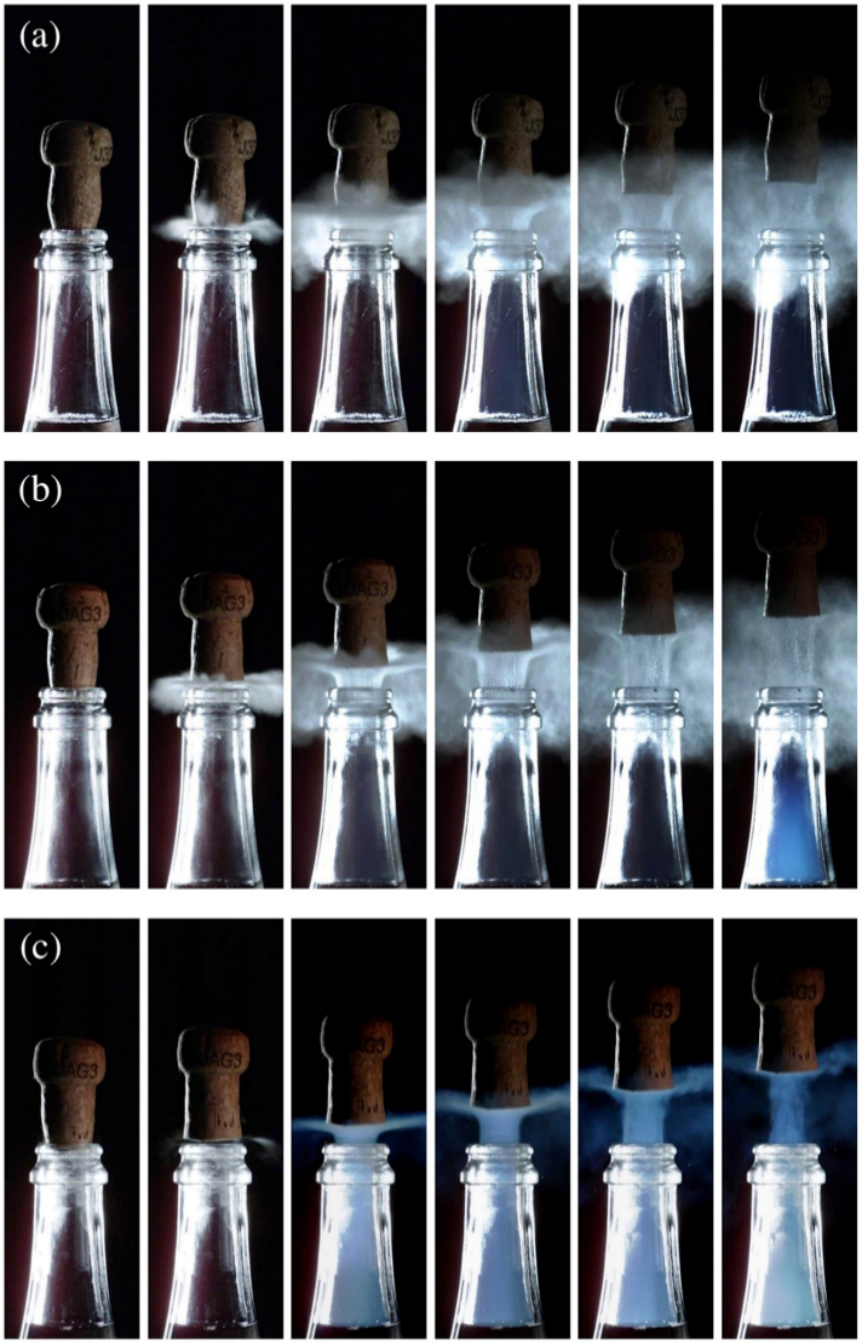

FIGURE 11.1 – Débouchage spontané d'une bouteille de champagne, ceci pour trois températures de stockage de la bouteille : (a) 6°C, (b) 12°C et (c) 20°C. Pour chaque température, le temps entre chaque cliché est de 400 µs, une séquence a donc une durée totale de 2,4 ms.

avec T_f la température à l'issue de la détente, P_0 et T la pression atmosphérique et la température intiale, et P_{CB} la pression intiale dans l'espace de tête. Pour une température intiale de 6°C, la température immédiatement après la détente est de −75°C. Dans le cas d'une température de stockage de 20° on obtient, de façon un peu contre-intuitive, une température finale de −90°C. Bien sûr, le gaz se mélangeant à l'air environnant est rapidement réchauffé, mais pendant les quelques millisecondes suivant l'ouverture, les températures sont très basses. Les différentes pressions de vapeur impliquées : celles de l'eau ou du CO_2, pour un équilibre liquide-vapeur ou solide-vapeur, dépendent fortement de la température. Dans tous les cas, les estimations numériques (voir Table 1, article en section 12.1) indiquent une très forte sursaturation en eau après la détente, ce qui

explique le panache blanc au-dessus de la bonteille. En effet, l'air humide se mélangeant au CO_2, cela provoque la condensationde l'eau. Pour renforcer l'argument VOLMER et MÖLLMANN [2012] ont fait des expériences dans une atmosphère sèche où l'absence de panache montre sans ambiguïté le rôle de l'eau. Le cas du CO_2 est moins tranché : la saturation du CO_2-gaz est seulement de 0.92 pour une bouteille initialement à 6°C. Cette saturation passe à 1.44 pour une température de stockage de 12°C, elle est finalement de 2.53 pour une bouteille à 20°C. On a donc là l'explication de la formation d'un «brouillard» dans l'espace de tête, correspondant à la formation de cristaux de CO_2.
La théorie classique de la nucléation donne le taux de nucléation homogène :

$$J_{hom} = N_G \frac{\rho_V}{\rho_S} \left(\frac{2\sigma}{\pi m}\right)^{1/2} \exp\left(-\frac{\Delta G^*}{k_B T}\right) \tag{11.2}$$

qui fournit le nombre de site de nucléation homogène dépassant le rayon critique par unité de volume et de temps ($cm^{-3}\ s^{-1}$). Pour l'eau on a des valeurs de J_{hom} allant de 10^{18} à $10^{20}\ cm^{-3}\ s^{-1}$, ceci quand la température de la bouteille passe de 6°C à 20°C. Dans le cas du CO_2, la valeur de J_{hom} reste pratiquement nulle. Ceci indique que l'eau présente dans l'espace de tête, bien qu'en faible quantité, doit cristalliser, produisant ainsi des sites favorables à une nucléation hétérogène du CO_2. Pourquoi n'est-ce pas seulement l'eau qui cristallise ? Parce que la sursaturation en vapeur d'eau, pour un équilibre solide-vapeur, passe de ~ 40 à ~ 3.5 pour une température de bouteille croissant de 6°C à 20°C. Si les cristaux d'eau, seuls, étaient responsables de la lueur bleutée observée, le phénomène devrait être présent à 6°C et disparaître à 20°C, hors c'est le contraire qui est constaté. Comme on a, dans le même temps, une augmentation de la sursaturation du CO_2 de 0.92 à 2.53, on a certainement la formation de microcristaux de CO_2, autour de germes de glace d'eau.

Abordons maintenant la question de la couleur du «brouillard» de l'espace de tête. Ce bleu est très caractéristique de la diffusion de Rayleigh (Lord Rayleigh, alias John William Strutt) [STRUTT, 1871a,b, 1881, 1899]. Pour des particules sphériques, de rayon a et d'indice optique n, la section efficace de diffusion Rayleigh σ_R (m^2) est donnée par [SÁNCHEZ-LAVEGA, 2010] :

$$\sigma_R = \frac{128\pi^5 a^6}{3\lambda^4} \left(\frac{n^2-1}{n^2+2}\right)^2 \tag{11.3}$$

si on évalue σ_R pour une taille de particule correspondant au rayon critique de nucléation r^* de CO_2 (voir l'article pour l'expression de r^*), on obtient $\sigma_R \sim 1.7 \times 10^{-23}\ m^2$, ceci pour une longueur d'onde de 0.4 µm. Cette valeur est à comparer avec la section efficace de diffusion Rayleigh de l'air, qu'on trouve également dans SÁNCHEZ-LAVEGA [2010], on obtient alors $\sigma_R(\text{air}) \sim 1.7 \times 10^{-30}\ m^2$, ce rapport de 7 ordres de grandeur montre la très grande efficacité des microcristaux de CO_2 à diffuser la lumière dans le bleu, ce qui explique les observations.

Finalement, la disparition du panache blanc au-dessus du goulot, ceci pour la bouteille à 20°C, peut être expliqué par la chaleur latente de sublimation du CO_2. En effet, la variation d'énergie interne liée à la détente est $\Delta U \simeq 24$ J. L'enthalpie de sublimation de CO_2 est $\Delta H_{sub}^{CO_2} \sim 26\ kJ\ mol^{-1}$. Dans le cas de la bouteille à 20°C, 8×10^{-3} mol de CO_2 subit la détente, il suffit que ~ 10% de cette quantité de CO_2 gèle pour absorber totalement les 24 J de la détente, rendant totalement impossible la condensation de l'eau en sortie de bouteille. Bien sûr, dans l'expérience, seule le gel d'une quantité de CO_2 nécessaire pour que l'eau de l'air ne soit pas sursaturée est requise pour faire disparaître le nuage blanc observé à 6°C et 12°C.

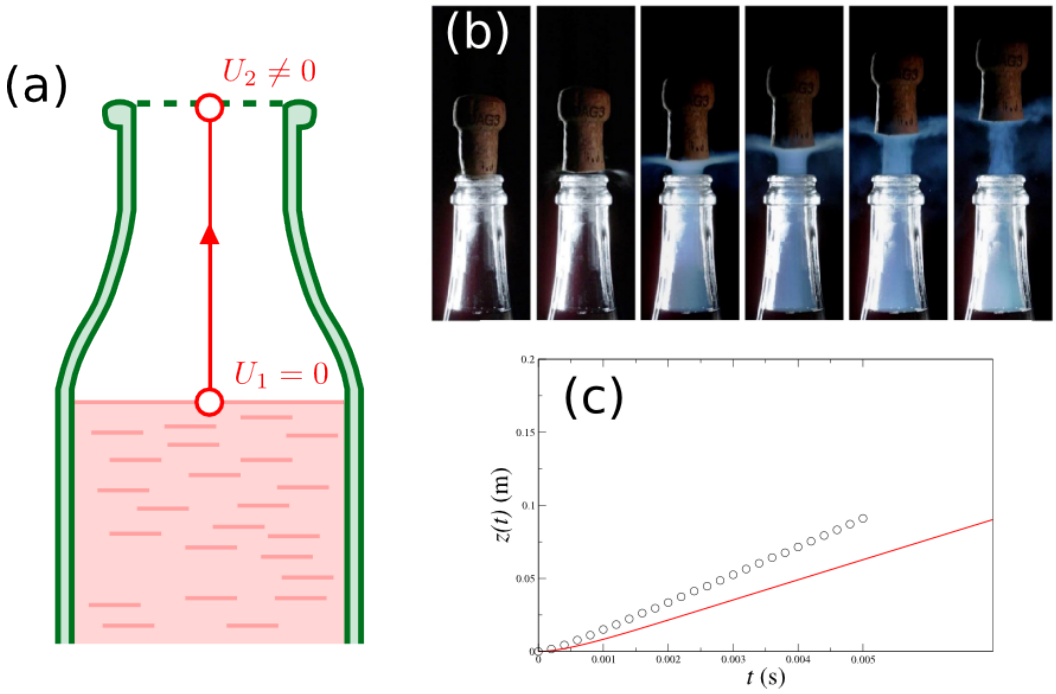

FIGURE 11.2 – (a) Schéma de l'intérieur d'une bouteille. (b) Un exemple de film montrant le mouvement du bouchon lorsqu'il est propulsé par la pression de la bouteille seule. Les clichés ont été réalisés à des intervalles de 400 µs, pour une bouteille initiallement à 20°C. (c) Comparaison entre les données expérimentales du mouvement du bouchon : altitude atteinte en fonction du temps (cercles), et le modèle décrit dans ces lignes (trait continu).

11.2 Projet scientifique pétillant

11.2.1 La cinématique d'un bouchon de champagne

Lorsqu'on laisse, livrée à elle même, une bouteille de champagne, libérée de son muselet, le bouchon finit toujours par partir à grande vitesse. C'est ce genre de phénomène qui est montré sur la série d'images de la Fig. 11.2 (b). On peut construire une première modélisation en estimant la vitesse d'éjection U_2 du CO_2 à la sortie de la bouteille, ceci en utilisant le théorème de Bernoulli le long d'une ligne de courant comme celle spécifiée sur la Fig. 11.2 (a). La vitesse d'écoulement à la surface du liquide U_1 est nulle, la pression est $P(t)$, alors que le goulot est à la pression atmosphérique. On a alors grâce à Bernoulli :

$$P_0 + \frac{1}{2}\rho U_2^2 = P(t) \tag{11.4}$$

d'où on tire la vitesse U_2 d'éjection du gaz :

$$U_2 = \sqrt{\frac{2RT(P(t) - P_0)}{P M_{CO_2}}} \tag{11.5}$$

En adoptant, par commodité, la notation U au lieu de U_2, la conservation de la matière permet d'avoir la variation du volume total V du CO_2 qui se détend pendant la durée dt :

$$dV = S_g U \, dt \tag{11.6}$$

avec S_g la section droite du goulot. Le dernier ingrédient physique à prendre en compte est la loi de Laplace qui régit les détentes adiabatiques ici :

$$P V^\gamma = P_{CB} V_g^\gamma \tag{11.7}$$

où P_{CB} est la pression initiale dans la bouteille et V_g le volume de l'espace de tête. La différentiation de l'équation (11.7) combinée avec les équations (11.5), (11.6) et différentes écritures de la loi de Laplace conduisent à l'équation donnant la variation temporelle de la pression P :

$$\frac{dP}{dt} = -\gamma P_{CB}^{-1/\gamma} V_g^{-1} P^{\frac{\gamma+1}{\gamma}} S_g \sqrt{\frac{2RT_0 P_{CB}^{\frac{1-\gamma}{\gamma}}}{M_{CO_2}}} \sqrt{(P-P_0)P^{-1/\gamma}} \tag{11.8}$$

à cette dernière on ajoute l'équation du mouvement du bouchon :

$$m_B \frac{dU}{dt} = S_B(P-P_0) - m_B g - \frac{1}{2} C_D \rho_{air} S_B U^2 \tag{11.9}$$

le système d'équations formé par (11.8) et (11.9) est complété par $dz/dt = U$, avec z l'altitude du bouchon à un instant t donné. Ce système, non-linéaire, de trois équations, s'intègre facilement numériquement.

La Fig. 11.2 (c) montre la trajectoire d'un bouchon, calculée numériquement. De façon assez surprenante, la trajectoire simulée se trouve en-dessous des points expérimentaux, alors qu'on pouvait s'attendre au contraire ! En effet, le fait d'utiliser le terme en $S_B(P-P_0)$ dans l'équation (11.9), comme force motrice du bouchon, implique une détente du volume de CO_2 sous la forme d'un cyclindre au-dessus du goulot. Cette hypothèse aurait du maximiser l'effet de la poussée du gaz sur le bouchon. On peut cependant pousser plus loin la critique de ce modèle de «première

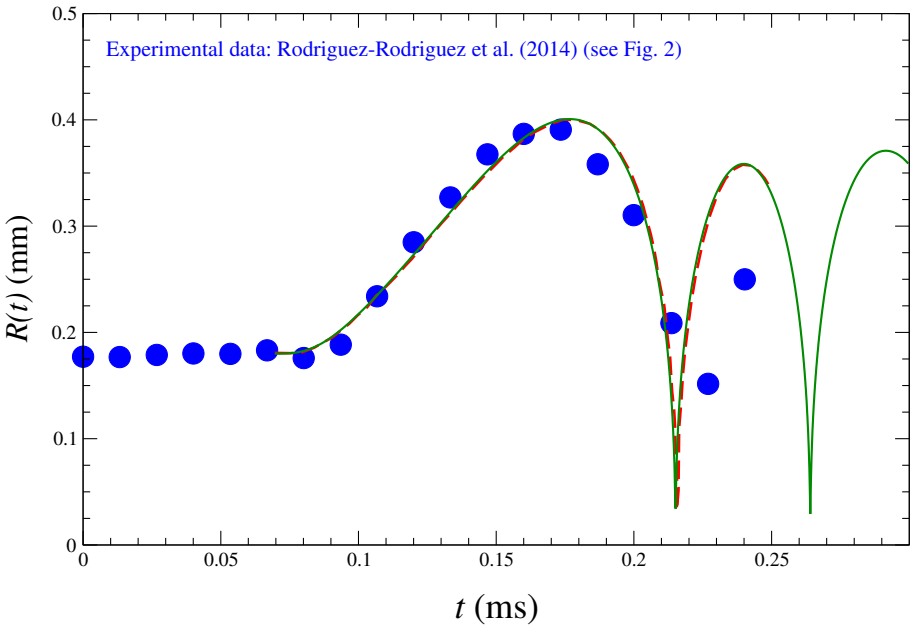

FIGURE 11.3 – Oscillations de bulles de bière. Comparaison entre les données expérimentales (les points bleux) de RODRÍGUEZ-RODRÍGUEZ et collab. [2014] et l'intégration numérique de l'équation de Rayleigh-Plesset. La ligne rouge en tirets est l'intégration réalisée par RODRÍGUEZ-RODRÍGUEZ et collab. [2014], celle en trait plein vert correspond aux calculs que j'ai mené.

approche». L'équation (11.4) suppose l'existence d'un gradient de pression dans le volume de l'espace de tête : P est la pression à la surface du liquide, alors que l'équation de Laplace (11.7) considère que tout le volume subissant la détente adiabatique est à pression uniforme. Cette contradiction interne au modèle est peut être à l'origine du désaccord surprenant qu'on constate sur le Fig. 11.2 (c).

La solution à ce problème viendra sans doute d'une résolution de l'équation de Navier-Stokes, appliquée au moins dans l'espace de tête. Cette résolution est envisageable par intégration de

l'équation de Navier-Stokes, mais aussi en utilisant la SPH (Smooth Particles Hydrodynamics) [MONAGHAN, 1992; PRABHU RAMACHANDRAN, 2016] ou la LBM (Lattice Boltzmann Method) [**?**]. La poussée sur le bouchon pourrait être ainsi traitée beaucoup plus simplement qu'avec une approche basée sur une intégration d'équations différentielles. En effet, le bouchon présente pour le fluide, ici le CO_2 éjecté, une condition limite qui évolue au cours du temps. Dans le livre LIU et LIU [2003], l'exemple de «shock tube problem» traité à partir de la page 94 est très similaire au débouchage d'une bouteille, et pourra donc servir de source d'inspiration.

11.2.2 L'oscillation des bulles du champagne

Les bulles de gaz dans un liquide, sont des objets élastiques susceptibles de subir des oscillations de leur forme. L'écart à la sphéricité peut être plus ou moins important suivant les situations. Dans certains cas, l'amplitude des déformations peut être comparable à la taille de la bulle, ce qui conduit souvent à la fragmentation de cette dernière. Dans le cas le plus général, ces déformations sont tridimensionnelles.
Pour les bulles les plus petites, *i.e.* dont la taille est petite devant le rayon de «breakup» [CLIFT et collab., 1978] :

$$r_{\text{breakup}} \sim 4\sqrt{\frac{\sigma}{g\Delta\rho}} \tag{11.10}$$

avec g l'accélération de la pesanteur, σ la tension superficielle et $\Delta\rho$ la différence de masse volumique entre le gaz et le liquide ; les oscillations sont souvent monodimentionnelle, dans les directions radiales. Dans ce cas, l'équation de Rayleigh-Plesset [LORD RAYLEIGH, 1917; PLESSET, 1949] régit le comportement, au cours du temps, du rayon r d'une bulle de gaz dans un environnement liquide incompressible :

$$r\frac{\mathrm{d}^2 r}{\mathrm{d}r^2} + \frac{3}{2}\left(\frac{\mathrm{d}r}{\mathrm{d}t}\right)^2 + \frac{4\nu_L}{r}\frac{\mathrm{d}r}{\mathrm{d}t} + \frac{2\sigma}{\rho_L r} + \frac{\Delta P(t)}{\rho_L} = 0 \tag{11.11}$$

avec ν_L et ρ_L respectivement la viscosité cinématique ($m^2\ s^{-1}$) du liquide environnant, et sa masse volumique (kg m^{-3}). Gérard Liger-Belair et Jacques Honvault ont effectué des prises de données vidéo, où les oscillations des bulles de champagne sont clairement visibles. Une étude du comportement de ces bulles est évidemment intéressante, et c'est ce que je projette de mener, en collaboration étroite avec Gérard Liger-Belair, dans un proche avenir. Un système similaire a déjà été étudié par RODRÍGUEZ-RODRÍGUEZ et collab. [2014], en l'espèce, la dynamique des bulles de la bière, ceci dans le cadre de la fameuse expérience de comptoir du «beer tapping» qui voit le contenu d'une canette se déverser après un choc sur le récipient.

L'intégration de l'équation de Rayleigh-Plesset peut se faire par des méthodes assez classiques permettant de traiter le cas d'équations très raides. Alors que RODRÍGUEZ-RODRÍGUEZ et collab. [2014] ne sont pas particulièrement explicites sur la méthode numérique utilisée, DHARMAVARAM NARENDRANATH [2016] évoque une méthode dite «LSODA» qui est en fait une routine du package ODEPACK [HINDMARSH, 1983]. LSODA est un programme écrit par Alan Hindmarsh et Linda Petzold, son appellation doit être basé sur LSODE (Livermore Solver for Ordinary Differential Equations) et Adams, car LSODA utilise la méthode d'Adams pour les systèmes non-raides, et bascule automatiquement vers une méthode BDF (Backward differentiation formula) pour les systèmes raides [PETZOLD, 1983]. Sur la Fig. 11.3 une première d'intégration, réalisée avec LSODA, est comparé avec les résultats expérimentaux et l'intégration issus des travaux de RODRÍGUEZ-RODRÍGUEZ et collab. [2014]. Comme on peut le voir, l'accord est très bon, un outil est donc en place pour pouvoir aller plus loin dans l'étude du comportement dynamique des bulles de champagne.

11.2.3 Les instabilités de Kelvin–Helmholtz

L'instabilité de Kelvin-Helmoltz [LORD KELVIN, 1871; VON HELMHOLTZ, 1868] est une instabilité hydrodynamique qui peut apparaître lorsqu'existe un fort gradient de vitesse d'écoulement

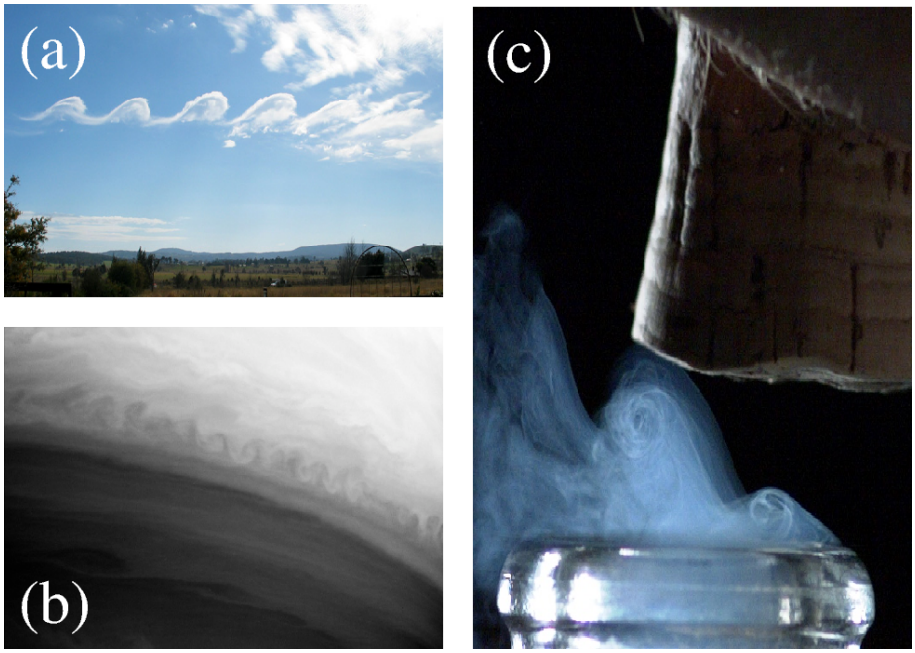

FIGURE 11.4 – (a) Des instabilités de Kelvin-Helmholtz au-dessus du Mont Duval en Australie https://en.wikipedia.org/wiki/Kelvin-Helmholtz_instability. (b) Instabilité de Kelvin-Helmoltz dans l'atmosphère de Saturne, ce cliché a été pris avec la *Narrow Angle Camera* de l'instrument ISS de la sonde Cassini le 9 octobre 2004 (https://photojournal.jpl.nasa.gov/catalog/PIA06502). (c) Un exemple d'instabilités de Kelvin-Helmoltz mises en évidence lors d'un débouchage (cliché : Jacques Honvault).

dans un ou des fluides. Au niveau du gradient apparaissent des sortes de «vagues» comme celles matérialisées par la condensation de l'eau dans les nuages de la Fig. 11.4 (a). Des instabilités de Kelvin-Helmoltz ont été mises en évidence dans de nombreux contextes : celui de l'atmosphère terrestre ou celles des planètes géantes (voir Fig. 11.4 a, b), dans les profondeurs océaniques ou dans certains milieux plasmas [MATSUOKA, 2014].

Lors du débouchage d'une bouteille de champagne, le bouchon étant maintenu à la main, de façon à créer un écoulement latéral du CO_2 expulsé, on obtient des volutes très similaires à ce qui est communément observé pour les instabilités de Kelvin-Helmoltz (voir Fig. 11.4). Dans ce cas, le CO_2 s'échappe à grande vitesse du goulot, tout en rencontrant l'air environnement, initialement immobile. La vitesse d'échappement $v_{\mathrm{esc,CO_2}}$ peut être estimée à l'aide d'une formule issue de l'analyse dimensionnelle du système :

$$v_{\mathrm{esc,CO_2}} \sim \sqrt{\frac{\Delta P}{\rho_{\mathrm{CO_2}}}} \tag{11.12}$$

avec ΔP la différence de pression entre l'intérieur de la bouteille avant ouverture et l'air ambiant. La masse volumique du CO_2 est notée $\rho_{\mathrm{CO_2}}$. Une application numérique conduit à :

$$v_{\mathrm{esc,CO_2}} \sim 200\,\mathrm{m\,s^{-1}} \tag{11.13}$$

La longueur d'onde critique λ_{crit} en dessous de laquelle des instabilités de Kelvin-Helmoltz peuvent apparaître peut être estimée grâce à [ARABI et collab., 2015] :

$$k_{\mathrm{crit}} > g\,\frac{\rho_1-\rho_2}{\rho_1+\rho_2}\,\frac{(\rho_1+\rho_2)^2}{4\rho_1\rho_1\,v_{\mathrm{esc,CO_2}}^2} \tag{11.14}$$

avec ρ_1 la masse volumique de l'air et ρ_2 celle du CO_2. Le nombre d'onde est k_{crit} duquel on tire la longueur d'onde : $\lambda_{\mathrm{crit}} = 2\pi/k_{\mathrm{crit}}$. Des valeurs numériques mènent à :

$$\lambda_{\mathrm{crit}} \sim 1.3\times10^4\,\mathrm{m} \tag{11.15}$$

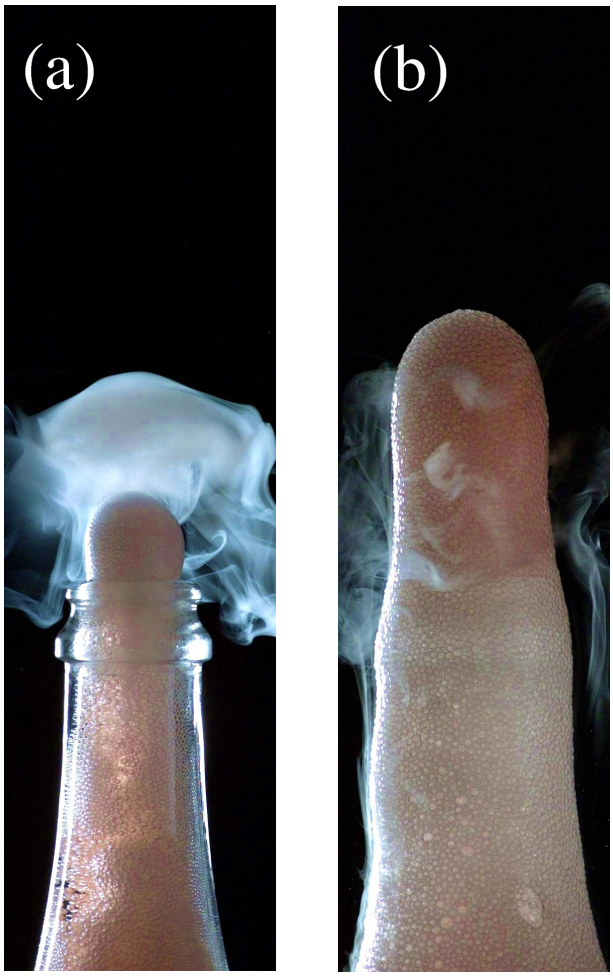

FIGURE 11.5 – Panache de mousse lors du gerbage d'une bouteille (cliché : Jacques Honvault).

ce qui est très supérieur à la taille caractéristiques, de l'ordre du centimètre, des volutes observées sur Fig. 11.4 (c). On en conclut que les instabilités de Kelvin-Helmoltz peuvent exister lors du débouchage d'une bouteille de champagne.

Pour aller plus loin dans l'analyse du phénomène, une première modélisation analytique ou semi-analytique peut être envisagée [ARABI et collab., 2015]. Ensuite, suivant les informations qui auront pu être tirées de cette approche, une modélisation numérique, éventuellement basée sur la SPH ou la LBM pourrait être utilisée.

11.2.4 La physique des panaches de mousse

Lors de l'élaboration [1] du champagne, une étape consiste à retirer un dépôt formé dans le col de la bouteille. Cette opération s'appelle le dégorgement est nécessite, quelque soit la technique utilisée, l'ouverture de la bouteille. Bien que délicate, cette étape se passe le plus souvent sans encombre. Il arrive néanmoins que, pour des raisons qui sont encore mal comprises, la bouteille gerbe. Dans ce cas, de la mousse se forme massivement et sort de la bouteille entraînant ainsi une grande partie de son contenu. Ce phénomène nuisible s'appelle le gerbage, et ce n'est pas tant le volume de vin perdu qui importe mais plutôt le ralentissement, voire la mise à l'arrêt, de la ligne de production, dont certaines débitent plus de 14 000 bouteilles par heure. La Fig. 11.5 montre un début de gerbage avec une colonne de mousse s'élevant à la sortie de la bouteille. La question du

1. On n'emploie surtout pas le mot «fabrication» au sujet du champagne, sous peine de s'attirer les foudres des gens de la profession !

Retour à la table des matières : p. v

gerbage est un problème industriel auquel Gérard Liger-Belair s'intéresse depuis de nombreuses années, et à la compréhension duquel je tenterai d'apporter ma contribution.

L'étude du gerbage peut être scindée en deux thèmes : (1) l'origine du phénomène, (2) les propriétés physiques du panache de mousse, et son évolution une fois le processus amorcé. Concernant le premier point une voie intéressante est sans doute de chercher des mécanismes menant à un emballement de la production de bulles, pour le deuxième point une modélisation des propriétés hydrodynamiques de la mousse, tout comme celle de ses propriétés optiques seraient sans doute très intéressantes.

L'aspect hydrodynamique pourra être traité en SPH ou LBM, tandis que une approche de type Monte-Carlo devrait permettre de rendre des propriétés optiques de l'écoulement de mousse.

11.3 Références

ARABI, S., S. DOUBLET, F. HAFFNER, L. GHEERBRANT, S. ROUSSEL et F. TÉTARD. 2015, *Kelvin-Helmholtz Instabilities*, mémoire de maîtrise. 339, 340

CLIFT, R., J. R. GRACE et M. E. WEBER. 1978, *Bubbles, Drops and particles*, Academic Press, New York, San Fransisco, London. 338

DHARMAVARAM NARENDRANATH, A. 2016, «Solution to the one-dimensional Rayleigh-Plesset equation by the Differential Transform method», *ArXiv e-prints*. 338

HINDMARSH, A. C. 1983, «A. C. Hindmarsh, "ODEPACK, A Systematized Collection of ODE Solvers," in Scientific Computing, R. S. Stepleman et al. (eds.), North-Holland, Amsterdam, 1983 (vol. 1 of IMACS Transactions on Scientific Computation), pp. 55-64.», URL http://www.llnl.gov/CASC/nsde/pubs/u88007.pdf. 338

LIGER-BELAIR, G., D. CORDIER, J. HONVAULT et C. CYLINDRE. 2017, «Unveiling CO 2 heterogeneous freezing plumes during champagne cork popping», *Sci. Rep.*, vol. 7, doi: 10.1038/s41598-017-10702-6, p. 10 938. 333

LIU, G. R. et M. B. LIU. 2003, *Smoothed Particle Hydrodynamics – A Meshfree Particle Method*, 1re éd., World Scientific Publishing, 5 Toh Tuck Link, Singapore 596224, ISBN 981-238-456-1. 338

LORD KELVIN, W. 1871, «Hydrokinetic solutions and observations», *Philos. Mag.*, vol. 42, p. 362–377. 338

LORD RAYLEIGH, O. F. 1917, «VIII. On the pressure developed in a liquid during the collapse of a spherical cavity», *The London, Edinburgh, and Dublin Philosophical Magazine and Journal of Science*, vol. 34, no 200, doi: 10.1080/14786440808635681, p. 94–98. URL https://doi.org/10.1080/14786440808635681. 338

MATSUOKA, C. 2014, «Kelvin-Helmholtz Instability and Roll-up», *Scholarpedia*, vol. 9, doi: 10.4249/scholarpedia.11821, p. 11 821. 339

MONAGHAN, J. J. 1992, «Smoothed particle hydrodynamics», *Annu. Rev. Astron. Astrophys.*, vol. 30, doi: 10.1146/annurev.aa.30.090192.002551, p. 543–574. 338

PETZOLD, L. R. 1983, «Automatic Selection of Methods for Solving Stiff and Nonstiff Systems of Ordinary Differential Equations», *Siam J. Sci. Stat. Comput.*, vol. 4, p. 136–148. 338

PLESSET, M. 1949, «The dynamics of cavitation bubbles», *ASME J. Appl. Mech.*, vol. 16, p. 228–231. 338

PRABHU RAMACHANDRAN. 2016, «PySPH : a reproducible and high-performance framework for smoothed particle hydrodynamics», dans *Proceedings of the 15th Python in Science Conference*, édité par Sebastian Benthall et Scott Rostrup, p. 122 – 129. URL http://conference.scipy.org/proceedings/scipy2016/prabhu_ramachandran_pysph.html. 338

RODRÍGUEZ-RODRÍGUEZ, J., A. CASADO-CHACÓN et D. FUSTER. 2014, «Physics of Beer Tapping», *Phys. Rev. Lett.*, vol. 113, doi: 10.1103/PhysRevLett.113.214501, p. 214 501. URL https://link.aps.org/doi/10.1103/PhysRevLett.113.214501. 337, 338

SÁNCHEZ-LAVEGA, A. 2010, *An Introduction to Planetary Atmospheres*, CRC Press. 335

STRUTT, J. 1871a, «On the light from the sky, its polarization and colour», *Philos. Mag.*, vol. 41, p. 107–120. 335

STRUTT, J. 1871b, «On the scattering of light by small particles», *Philos. Mag.*, vol. 41, p. 447–454. 335

STRUTT, J. 1881, «On the electromagnetic theory of light», *Philos. Mag.*, vol. 12, p. 81–101. 335

STRUTT, J. 1899, «On the transmission of light through an atmosphere containing small particles in suspension, and on the origin of the blue of the sky», *Philos. Mag.*, vol. 47, p. 375–394. 335

VOLMER, M. et K.-P. MÖLLMANN. 2012, «Vapour pressure and adiabatic cooling from champagne : Slow-motion visualization of gas thermodynamics», *Phys. Educ.*, vol. 45, p. 608–615. 335

VON HELMHOLTZ, H. 1868, «Über discontinuierliche Flüssigkeits-Bewegungen (On the discontinuous movements of fluids)», vol. 23, p. 215–228. 338

Chapitre 12

Articles : le champagne

12.1 Article la lueur bleue lors du débouchage

www.nature.com/scientificreports

SCIENTIFIC REPORTS

OPEN

Unveiling CO_2 heterogeneous freezing plumes during champagne cork popping

Received: 30 May 2017
Accepted: 11 August 2017
Published online: 14 September 2017

Gérard Liger-Belair[1], Daniel Cordier[1], Jacques Honvault[2] & Clara Cilindre[1]

Cork popping from clear transparent bottles of champagne stored at different temperatures (namely, 6, 12, and 20 °C) was filmed through high-speed video imaging in the visible light spectrum. During the cork popping process, a plume mainly composed of gaseous CO_2 with traces of water vapour freely expands out of the bottleneck through ambient air. Most interestingly, for the bottles stored at 20 °C, the characteristic grey-white cloud of fog classically observed above the bottlenecks of champagne stored at lower temperatures simply disappeared. It is replaced by a more evanescent plume, surprisingly blue, starting from the bottleneck. We suggest that heterogeneous freezing of CO_2 occurs on ice water clusters homogeneously nucleated in the bottlenecks, depending on the saturation ratio experienced by gas-phase CO_2 after adiabatic expansion (indeed highly bottle temperature dependent). Moreover, and as observed for the bottles stored at 20 °C, we show that the freezing of only a small portion of all the available CO_2 is able to pump the energy released through adiabatic expansion, thus completely inhibiting the condensation of water vapour found in air packages adjacent to the gas volume gushing out of the bottleneck.

Uncorking a bottle is indeed the first action preceding champagne tasting, and even if it is far safer and advised to uncork a bottle of champagne with a subdued sigh, anyone of us has certainly already experienced popping the cork with a bang[1,2]. From a strictly physicochemical point of view, Champagne wines are multicomponent hydroalcoholic systems, with a density close to unity, a surface tension close to 50 mN m^{-1} (indeed highly ethanol-dependent), and a viscosity about 50% higher than that of pure water (also mainly due to the presence of 12–13% v/v ethanol)[3]. Moreover, Champagne and sparkling wines elaborated through the same traditional method hold a concentration of dissolved carbon dioxide (CO_2) formed together with ethanol during a second fermentation process (called *prise de mousse*) promoted by adding yeasts and a certain amount of sugar in the sealed bottles. It is an application of Henry's law which states that the concentration of dissolved CO_2 in the liquid phase is proportional to the partial pressure of gas-phase CO_2 above the solution, in the bottleneck. Nevertheless, the solubility of CO_2 in the liquid phase being strongly temperature-dependent, the partial pressure of gas-phase CO_2 in the bottleneck is therefore also strongly temperature-dependent. During the cork popping process, a plume mainly composed of gaseous CO_2 with traces of water vapour freely expands out of the bottleneck through ambient air. Recently, the cloud of gaseous CO_2 expanding out of the bottleneck while cork popping, was made visible through high-speed infrared imaging[4]. Differences according to the bottle's temperature were clearly observed concerning both the volume of gas-phase CO_2 gushing out of the bottleneck, and its overall dynamics. Results were discussed by considering that gases under pressure in the bottleneck experience adiabatic expansion while cork popping. Observations of the cork popping process were already conducted in visible light with green bottles of sparkling wine stored at a single temperature on the order of 10 °C, and therefore at a single corresponding pressure in the order of only 5 bar[5]. Condensation of water vapour above the bottleneck was clearly observed during the cork popping process, thus revealing the rapid cooling of ambient air packages adjacent to the flow of gas gushing out of the bottleneck. Nevertheless, the opacity of classical dark green opaque glass bottles used in the previous set of experiments forbade the visualization of condensation processes in the bottlenecks[5,6].

[1]Equipe Effervescence, Champagne et Applications (GSMA - UMR CNRS 7331), Université de Reims Champagne-Ardenne, UFR Sciences Exactes et Naturelles, BP 1039, 51687, Reims Cedex 2, France. [2]Engineering Art, 17 rue Bel Air, 60110, Amblainville, France. Correspondence and requests for materials should be addressed to G.L.-B. (email: gerard.liger-belair@univ-reims.fr)

Retour à la table des matières : p. v

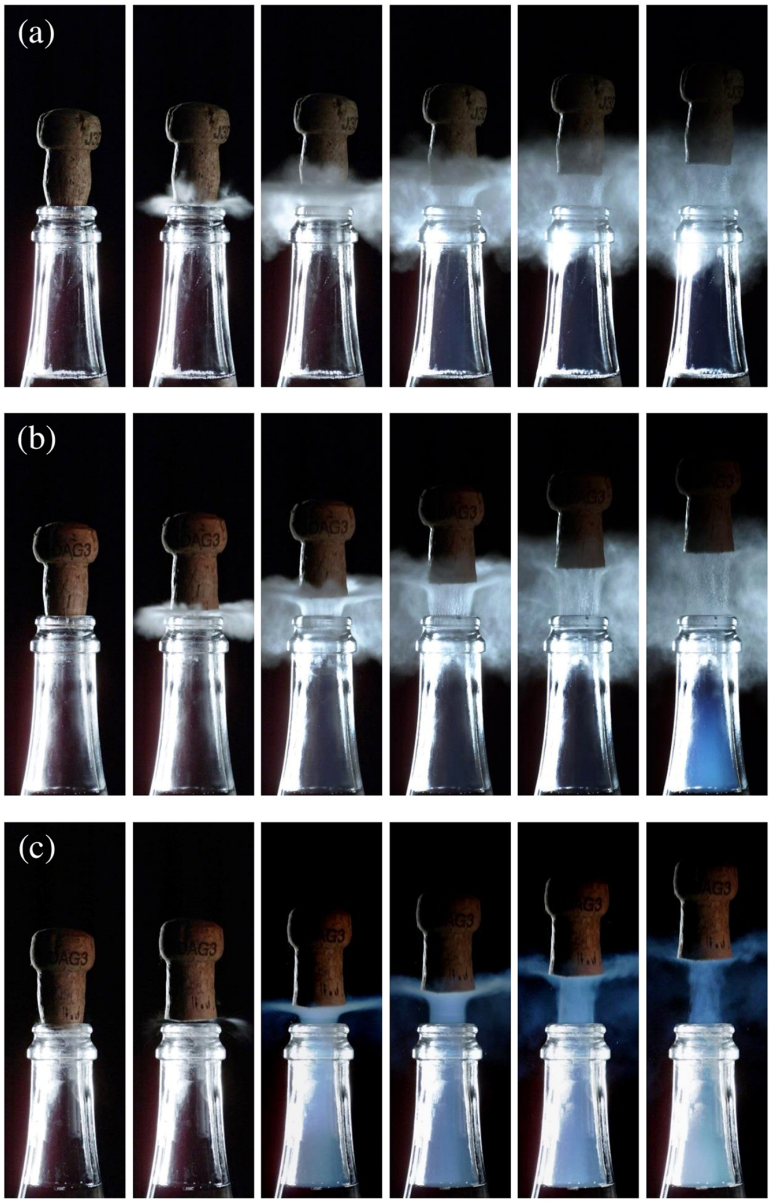

Figure 1. Time sequences showing the cork popping process from bottles stored at three different temperatures, namely 6 °C (**a**) 12 °C (**b**) and 20 °C (**c**). The time interval between each frame is 400 µs.

Here high-speed video imaging was used to visualize cork popping, and especially the condensation processes following the adiabatic expansion of the gas mixture found in the bottlenecks of transparent champagne bottles stored at different temperatures. The bottle temperature was found to be a key parameter concerning the condensation processes that can occur above, and inside the bottlenecks. After adiabatic expansion of the gas mixture, and on the basis of the respective saturation ratios and corresponding homogeneous nucleation rates of the gas species initially present in the bottleneck before cork popping (mainly composed of gas-phase CO_2 with traces of water and ethanol vapours), a scenario was proposed that explains our visually appealing observations.

Results

Time-sequences displayed in Figs 1 and 2 illustrate champagne cork popping as seen through high-speed video imaging, for bottles stored at 6 °C, 12 °C, and 20 °C, respectively. As already observed previously, the cork popping process is characterized by the formation of a cloud of fog above the bottlenecks[2,5,6]. Contrary to popular belief, this cloud of fog is not formed by gas-phase CO_2 gushing out of the bottleneck, indeed invisible in the visible

Retour à la table des matières : p. v

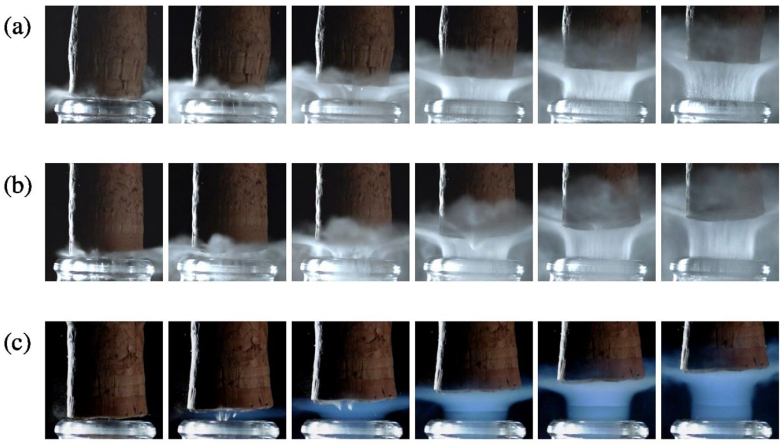

Figure 2. Close-up time sequences showing details of the cork popping process just above the bottlenecks of bottles stored at three different temperatures, namely 6 °C (**a**), 12 °C (**b**), and 20 °C (**c**). The time interval between each frame is 167 µs.

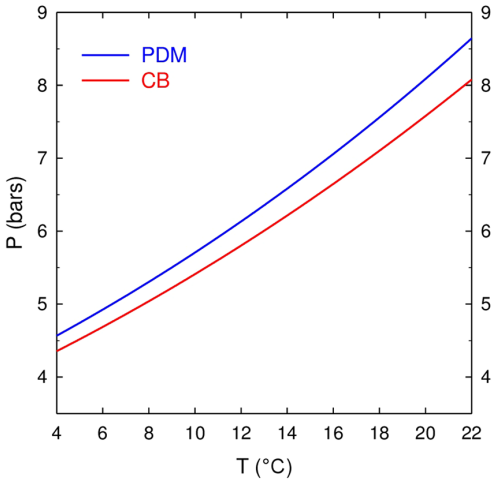

Figure 3. Partial pressure of gas-phase CO_2 inside the sealed bottle as a function of champagne temperature, as determined through equations (13) and (15). The blue line corresponds to the gas-phase CO_2 pressure reached after the *prise de mousse* in the bottles sealed with a cap, namely $P_{PDM}^{CO_2}$, whereas the red line corresponds to the equilibrium gas-phase CO_2 pressure reached after the disgorging process in the corked bottles ready for cork popping, namely $P_{CB}^{CO_2}$.

light spectrum, and made visible only through infrared imaging[4]. The commonly accepted idea is that the gas mixture trapped in the headspace under the cork experiences a drop of pressure while cork popping, from the pressure inside the bottle before uncorking - strongly temperature dependent, as seen in Fig. 3 - to the ambient pressure close to 1 bar. Details about the temperature dependence of the pressure found inside the corked bottles can be found in the Methods section. Assuming adiabatic expansion, a corresponding huge drop of temperature experienced by the gas mixture gushing out of the bottleneck therefore also inevitably cools adjacent air packages (before thermal equilibrium at room temperature is re-established again), thus causing the condensation of water vapour found in ambient air. High-speed time-sequences showing the cork popping process at 6 and 12 °C, as displayed in Fig. 1a,b, clearly show a grey-white cloud of fog right above the bottlenecks. The grey-white colour is characteristic of Mie scattering (i.e., the scattering of light by particles with typical sizes larger than the wavelength), well known to be at the origin of cloud colour in the sky[7]. It is worth noting that these very characteristic grey-white plumes occurred only outside the bottleneck. Actually, a previous set of experimental observations in dry atmosphere clearly showed the absence of such a white plume above the bottleneck of freshly uncorked bottles of champagne[5], thus supporting the idea that the condensation of the water vapour found in ambient air is indeed responsible for such a grey-white fog right above the bottlenecks.

Retour à la table des matières : p. v

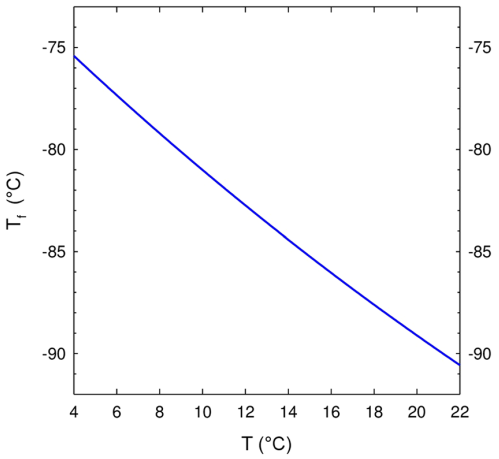

Figure 4. Final temperature T_f reached by the gas mixture (mostly composed of gas-phase CO_2) gushing out of the bottleneck after adiabatic expansion, as a function of the initial storage temperature T of champagne.

Most interestingly, bottles stored at 20 °C showed a very different behaviour. The characteristic grey-white cloud of fog observed above the bottlenecks of champagne stored at 6, and 12 °C (rather isotropically oriented), simply disappears, and is replaced by an even more evanescent plume, vertically oriented, starting from inside the bottleneck, and surprisingly blue (see Figs 1c and 2c). Blue haze is indeed characteristic of processes controlled by Rayleigh scattering (i.e., the scattering of light by particles with typical sizes much smaller than the wavelength). Contrary to the grey-white fog forming exclusively right above the bottlenecks, the blue haze accompanying the cork popping process starts inside the bottlenecks, and therefore in a region almost exclusively composed of gaseous CO_2. Otherwise, it is interesting to mention that blue haze can also be observed in the bottlenecks of champagne stored at 12 °C (about 2 ms after the grey-white fog has formed above the bottlenecks – see Fig. 1b), whereas for bottles stored at 20 °C, blue haze appears more rapidly (about 0.8 ms after cork popping – see Fig. 1c). Moreover, it is noteworthy to mention that blue haze has never been observed inside the bottleneck during the cork popping process of bottles stored at 6 °C.

The same scenario was strictly observed for each bottle belonging to a given batch of bottles stored at a given temperature. We are logically tempted to wonder why such striking differences were observed regarding the dependence with the initial bottle temperature of both the colour, and the overall dynamics of condensation processes that accompany the cork popping process.

Discussion

A discussion based on adiabatic expansion. Adiabatic expansion and its drop of temperature while cork popping, is undoubtedly the mechanism behind the condensation processes observed above and within the bottlenecks. The drop of temperature experienced by the gas mixture gushing out of the bottleneck while cork popping classically obeys the following equation:

$$T_f = T \times \left(\frac{P_0}{P_{CB}}\right)^{\frac{\gamma-1}{\gamma}} \tag{1}$$

with T and P_{CB} being the temperature and pressure of gas phase before cork popping (in the sealed bottle), T_f and P_0 being the final temperature and pressure of gas phase after adiabatic expansion, and γ being the ratio of specific heats of the gas phase experiencing adiabatic expansion (mainly composed of gaseous CO_2 and being equal to 1.3)[8].

By combining equations (1) and (15) (which provides the initial pressure of gas-phase CO_2 within the sealed bottle, before cork popping), and by replacing each and every parameter by its numerical value, the final temperature T_f reached by the gas mixture after adiabatic expansion and cooling may therefore be determined as a function of the initial temperature T of champagne in the sealed bottles (i.e., before cork popping). Very clearly, and rather counter-intuitively, the higher the initial temperature of champagne before cork popping, the lower the final temperature T_f reached by the gas mixture after adiabatic cooling, as seen in Fig. 4. By rapidly mixing with adjacent air packages above the bottleneck, holding water vapour with a partial pressure $P_{vap} \approx 0.02$ bar (see the Methods section), ambient air close to the bottleneck cools down. With such a huge drop of temperature of several tens of °C for gas phase expanding out of the bottlenecks, it is no wonder that the temperature of the resulting gas mixture near the bottlenecks falls well beyond the water dew point. It means that locally, and during a very short period of time, ambient air close to the cork popping holds much more water vapour than it can withstand thermodynamically speaking, resulting in the condensation or even freezing of water vapour, as described in the article by Vollmer and Möllman[5].

Retour à la table des matières : p. v

Storage temperature of bottles (in K)	279	285	293
Pressure of gas-phase CO_2 in the sealed bottle, $P_{CB}^{CO_2}$ (in bar)	4.7	5.8	7.5
Pressure of water vapor in the sealed bottle, $P_{CB}^{H_2O}$ (in bar)	0.0093	0.0140	0.0233
Temperature reached by the gas mixture in the bottleneck after adiabatic expansion, T_f (in K)	195.7	191.3	183.2
Pressure of gas-phase CO_2 in the bottleneck after adiabatic expansion, $P_{vap}^{CO_2}$ (in bar)	1	1	1
Pressure of water vapor in the bottleneck after adiabatic expansion, $P_{vap}^{H_2O}$ (in bar)	0.0020	0.0024	0.0031
Saturated vapor pressure of gas-phase CO_2 after adiabatic expansion, $P_{sat}^{CO_2}$ (in bar)	1.09	0.70	0.39
Saturated vapor pressure of ice water after adiabatic expansion, $P_{sat}^{H_2O}$ (in Pa)	0.084	0.034	0.011
Saturation ratio of gas-phase CO_2 after adiabatic expansion, S_{CO_2}	0.92	1.44	2.53
Saturation ratio of water vapor after adiabatic expansion, S_{H_2O}	2 376	7 023	27 400

Table 1. Pertinent parameters of the CO_2/H_2O gas mixture found in the bottlenecks, before (in the corked bottles), and after adiabatic expansion.

Homogeneous versus heterogeneous nucleation. In the following, focus is made on the gas mixture trapped in the bottlenecks, before, and after adiabatic expansion. Before cork popping, in the sealed bottle, the gas mixture trapped within the bottleneck is indeed mostly composed of gas-phase CO_2 with only traces of water vapour, as detailed in the Methods section. In the sealed bottle, the strongly temperature-dependent partial pressure of gas-phase CO_2 is accurately determined through equation (15), whereas the partial pressure of water vapour (being considered as the saturated vapour pressure corresponding to the temperature of storage of the bottle) is given in equation (17). In the range of temperatures between 6 and 20 °C, the partial pressure of gas-phase CO_2 in the sealed bottles ranges between approximately 4.5 and 7.5 bar (see Fig. 3), whereas the partial pressure of water vapour ranges between about 9×10^{-3}, and 2.3×10^{-2} bar. After adiabatic expansion, the pressure within the bottleneck falls to atmospheric pressure (close to 1 bar). CO_2 being the major component of the gas mixture in the bottleneck, its partial pressure therefore falls close to 1 bar, whatever the bottle temperature, whereas the partial pressure of water vapour falls between about 2×10^{-3}, and 3×10^{-3} bar, depending on the bottle temperature. Moreover, after adiabatic expansion, the huge drop of temperature experienced by the gas mixture found in the bottleneck has some serious effects on the respective saturated vapour pressures of both CO_2, and water. In the range of very low temperatures reached by the gas mixture after adiabatic expansion (comprised between −76 and −89 °C, depending on the initial temperature of storage before corking), the saturated vapour pressure of CO_2 $P_{sat}^{CO_2}$ is approached through Antoine equation with the appropriate coefficients given in equation (18)[9]. Likewise, in this range of temperatures, the vapour pressure of ice water $P_{sat}^{H_2O}$ was found to obey the relationship displayed in equation (19)[10].

With the knowledge of the respective gas phase partial pressures of both CO_2 and water combined with their corresponding saturated vapour pressures, the saturation ratios of both CO_2 and water (i.e., $S_{H_2O} = P_{vap}^{H_2O}/P_{sat}^{H_2O}$, and $S_{CO_2} = P_{vap}^{CO_2}/P_{sat}^{CO_2}$), can be determined in the bottleneck after adiabatic expansion. Depending on the temperature of bottle storage, the saturation ratios of both water and CO_2 are displayed in Table 1, together with the final temperature reached by the gas mixture in the bottlenecks after adiabatic expansion. Whatever the storage temperature of bottles, the saturation ratio of water vapour reached after adiabatic expansion is huge ($S_{H_2O} >> 1$). Phase change from water vapour to ice water is therefore thermodynamically favourable. The situation is different for gas-phase CO_2. For bottles stored at 6 °C, after adiabatic expansion, the saturation ratio of gas-phase CO_2 remains lower than unity. CO_2 is therefore simply unable to undergo a phase change, from gas to dry ice. Nevertheless, for bottles stored at 12 and 20 °C, the saturation ratio of gas-phase CO_2 goes beyond 1, thus making the bottlenecks a favourable place to freeze gas-phase CO_2. Actually, as the gas mixture is locally supersaturated with water vapour or gas-phase CO_2 after adiabatic expansion, the Gibbs free energy term regarding the transfer of molecules from the vapour phase (whether water vapour or gaseous CO_2) to the solid phase (whether ice water or dry ice) in the form of a cluster of radius r is negative. Following the classical nucleation theory (CNT), the nucleation energy barrier ΔG^* to overcome, and the corresponding critical radius r^* needed for a cluster to spontaneously grow through condensation of water vapour or CO_2 both express as follows[11,12]:

Retour à la table des matières : p. v

Storage temperature of bottles (in K)	279	285	293
Saturation ratio of gas-phase CO_2 after adiabatic expansion, S_{CO_2}	0.92	1.44	2.53
Saturation ratio of water vapor after adiabatic expansion, S_{H_2O}	2 376	7 023	27 400
Critical radius for water clusters after adiabatic expansion, $r^*_{H_2O}$ (in m)	2.9×10^{-10}	2.6×10^{-10}	2.3×10^{-10}
Critical radius for CO_2 clusters after adiabatic expansion, $r^*_{CO_2}$ (in m)	/	7.7×10^{-9}	3.1×10^{-9}
Nucleation energy barrier for water clusters after adiabatic expansion, $\Delta G^*_{H_2O}$ (in J)	3.4×10^{-20}	2.8×10^{-20}	2.2×10^{-20}
Nucleation energy barrier for CO_2 clusters after adiabatic expansion, $\Delta G^*_{CO_2}$ (in J)	/	2.0×10^{-17}	3.3×10^{-18}
Molecular concentration of water vapor in the bottleneck after adiabatic expansion, $N_G^{H_2O}$ (in molecules cm^{-3})	7.4×10^{16}	9.2×10^{16}	1.2×10^{17}
Molecular concentration of gas-phase CO_2 after adiabatic expansion, $N_G^{CO_2}$ (in molecules cm^{-3})	3.7×10^{19}	3.8×10^{19}	3.9×10^{19}
Homogeneous nucleation rate for water clusters after adiabatic expansion, $J_{hom}^{H_2O}$ (in $cm^{-3}\ s^{-1}$)	8×10^{17}	10^{19}	10^{20}
Homogeneous nucleation rate for CO_2 clusters after adiabatic expansion, $J_{hom}^{CO_2}$ (in $cm^{-3}\ s^{-1}$)	/	≈0	≈0

Table 2. Based on the classical nucleation theory (CNT), critical radii, nucleation energy barriers, and corresponding homogeneous nucleation rates of both water and CO_2 after adiabatic expansion. To evaluate the critical radii, homogeneous nucleation energy barriers, and nucleation rates of both ice water and dry ice CO_2 clusters, their respective surface energy, and density were used (i.e., $\sigma_{H_2O} \approx 0.106\ J\ m^{-2}$, $\sigma_{CO_2} \approx 0.08\ J\ m^{-2}$, $\rho_{H_2O} \approx 920\ kg\ m^{-3}$, and $\rho_{CO_2} \approx 1600\ kg\ m^{-3}$ [29]).

$$\begin{cases} \Delta G^* = \dfrac{16\pi\sigma^3\nu_S^2}{3(k_B T\ \ln S)^2} \\ r^* = \dfrac{2\sigma\nu_S}{k_B T\ \ln S} \end{cases} \quad (2)$$

with σ being the corresponding surface energy of ice water or dry ice CO_2, ν_S being the corresponding volume of a single molecule in the solid phase, and k_B being the Boltzmann constant.

According to the CNT, the steady state nucleation rate for homogeneous nucleation J_{hom}, defined as the number of clusters that grow past the critical radius r^* per unit volume and per unit time, can be written as[13]:

$$J_{hom} = N_G \frac{\rho_V}{\rho_S}\left(\frac{2\sigma}{\pi m}\right)^{1/2} \exp\left(-\frac{\Delta G^*}{k_B T}\right) \quad (3)$$

with the exponential pre-factor being typically determined from gas-kinetic considerations, m being the mass of a single molecule, ρ_V being the density of the corresponding specie in the gas mixture (water vapour or gas-phase CO_2), ρ_S being the density of the solid phase (ice water or dry ice) in the clusters, and N_G being the molecular concentration of the corresponding specie in the gas mixture (i.e., $P_{vap}^{H_2O/CO_2}/k_B T$, in m^{-3}).

As far as homogeneous nucleation is concerned in the bottlenecks after adiabatic expansion, critical radii, nucleation energy barriers, molecular concentrations, and nucleation rates of both water and CO_2 are presented in Table 2, depending on the initial temperature of bottle storage. Whatever the bottle storage temperature, homogeneous nucleation of ice water clusters is very likely to occur in the bottleneck after adiabatic expansion, given their huge nucleation rates ranging from $\approx 10^{18}\ cm^{-3}\ s^{-1}$ (for bottles stored at 6 °C) to $\approx 10^{20}\ cm^{-3}\ s^{-1}$ (for bottles stored at 20 °C). Inversely, and despite the fact that bottles stored at 12 and 20 °C show saturation ratios significantly higher than 1 for gas-phase CO_2 after adiabatic expansion, freezing of CO_2 through homogeneous nucleation remains undoubtedly thermodynamically forbidden, because $J_{hom}^{CO_2} \approx 0$ in both cases. It is indeed well-known that significant amount of homogeneous nucleation requires much higher saturation ratios than those experienced for gas-phase CO_2 after adiabatic expansion[11,12]. Compared to homogeneous nucleation, heterogeneous nucleation requires relatively low saturation ratios, but foreign particles or aerosols are needed in the system to initiate the process of phase change by condensing molecules on the pre-existing nuclei. It is nevertheless very unlikely that floating particles, which could promote the freezing of gas-phase CO_2 through heterogeneous

Retour à la table des matières : p. v

nucleation after adiabatic expansion, pre-exist in the sealed champagne bottlenecks. If eventually present in the bottleneck immediately after corking the bottle, such particles would have been progressively immersed or wetted on the glass wall during the period of aging, before cork popping. However, even in the absence of foreign particles or aerosols pre-existing in a supersaturated condensable environment, heterogeneous nucleation remains possible. Heterogeneous condensation caused by the presence of multiple gaseous species was already described in the literature, particularly in operational rocket plume exhausts that typically consist of mixtures of simple gaseous species[13,14]. Initial nuclei can be created out of the more easily condensable trace species through homogeneous nucleation, followed by heterogeneous condensation of the less condensable species. In rocket plume exhausts that typically consist of mixtures of simple gaseous species such as N_2, O_2, Ar, and CO_2, condensation can occur when plume temperatures decrease during the expansion process[15–18]. Condensation phenomena with the formation of particles within the plumes can even harm sensitive surfaces of a spacecraft[19,20]. In the article by Li *et al.*[13], simulations of homogeneous and heterogeneous condensations were performed to study freely expanding mixtures of CO_2 and N_2 condensation plumes. A pure N_2 expanding flow was found to not produce any clusters, whereas in a mixture consisting of 5% CO_2 and 95% N_2, under the same expansion conditions, heterogeneous condensation of N_2 molecules on homogeneously condensed CO_2 nuclei was reported.

At a smaller scale indeed, we believe that champagne bottlenecks could be viewed as small rocket nozzles. By drawing a parallel between the gas mixture freely expanding during the champagne cork popping process, and condensation phenomena observed in freely expanding condensation plumes, we therefore propose the following scenario. After adiabatic expansion of the gas mixture following the cork popping process of champagne bottles, clusters of ice water appear in the bottlenecks through homogeneous nucleation due to the very high saturation ratio experienced by water vapour, whatever the storage temperature of bottles. For bottles stored at 6 °C, the saturation ratio of gas-phase CO_2 nevertheless remains lower than 1, thus simply forbidding the freezing of CO_2 (whether through homo- or heterogeneous nucleation). The amount of water vapour being very low in the bottlenecks, the bottleneck remains optically transparent. For bottles stored at 12 and 20 °C, the saturation ratio of gas-phase CO_2 is significantly higher than 1, thus enabling the freezing of gas-phase CO_2 (through heterogeneous nucleation only) on ice water cluster nuclei. Blue haze is therefore attributed to the freezing of gas-phase CO_2 on ice water nuclei much smaller than the wavelength of light. Moreover, heterogeneous freezing of gas-phase CO_2 on ice water nuclei starts earlier, and with a much stronger effect for the bottles stored at 20 °C showing the highest saturation ratio (as clearly observed in Fig. 1b,c).

Rayleigh scattering. Blue haze is typical of Rayleigh scattering, which describes the elastic scattering of light by spherical particles much smaller than the wavelength of light. At the wavelength λ, for spherical particles with radii a, and with a refractive index n, the Rayleigh scattering cross-section σ_R is given by the following relationship[7]:

$$\sigma_R = \frac{128\pi^5 a^6}{3\lambda^4}\left(\frac{n^2-1}{n^2+2}\right)^2 \tag{4}$$

At the wavelength $\lambda \approx 0.4\,\mu m$ (which corresponds to the blue region of the visible light spectrum), dry ice CO_2 has a refractive index $n \approx 1.35$[21]. Therefore, considering a in the latter equation as being the critical radius for dry ice CO_2 clusters after adiabatic expansion for bottles stored at 20 °C (see Table 2) yields to a cross-section $\sigma_R \approx 1.7 \times 10^{-23}\,m^2$. This result has to be compared to the Rayleigh scattering cross-section of ambient air surrounding the bottlenecks during our observations. Indeed, and similarly to the Earth atmosphere, ambient air in the laboratory does also scatter light. By keeping the wavelength $\lambda \approx 0.4\,\mu m$, and by using an equation provided by the literature for atmospheric scattering[7], the cross-section for ambient air was found to be $\sigma_{air} \approx 1.7 \times 10^{-30}\,m^2$ (i.e., seven orders of magnitude lower than the scattering cross-section of dry ice CO_2 clusters). Therefore, despite the fact that the number of CO_2 clusters per unit volume is still unknown, this huge ratio of order of 10^7 between σ_R and σ_{air} tells us that even a modest number of dry ice CO_2 condensation nuclei would be enough to produce a much stronger scattering in the blue than ambient air (as observed during the cork popping of bottles stored at 20 °C, where gas-phase CO_2 is strongly suspected to freeze in the bottlenecks). We therefore conclude that this characteristic blue haze is the signature of a partial and transient freezing of gas-phase CO_2 initially present in the bottleneck before cork popping. After adiabatic expansion, the progressive growth in size of dry ice CO_2 clusters can even be evidenced by observing the change in colour of the condensation cloud found in the bottleneck of bottles stored at 20 °C, as shown in the time sequence displayed in Fig. 5. It is worth noting that the cloud colour progressively changes from deep blue to white-grey, which pleads in favour of a transition between Rayleigh scattering by nuclei much smaller than the wavelength of ambient light, and Mie scattering as the size of nuclei becomes comparable and larger than the wavelength of light.

Inhibition of water vapour condensation above the bottlenecks. As already mentioned earlier, the grey-white plume above the bottlenecks (clearly observed for bottles stored at 6 and 12 °C) is the signature of the condensation of water vapour naturally present in ambient air[2,5,6]. The other striking feature revealed by our experiments is the complete disappearance of this grey-white plume above the bottleneck of champagne stored at 20 °C, while the blue haze starts early within the bottleneck, as exemplified in Fig. 6. It is worth noting that the energy required to condense water vapour is brought by the change of internal energy ΔU of the gas mixture initially found in the bottlenecks. The first law of thermodynamics states that $\Delta U = Q + W$, where Q denotes the exchange of heat during the process, and W relates to the work of expansion of the gas mixture gushing out of the bottleneck. For adiabatic processes, $Q = 0$, so that the gas mixture experiences a drop of its internal energy determined by the following relationship:

Retour à la table des matières : p. v

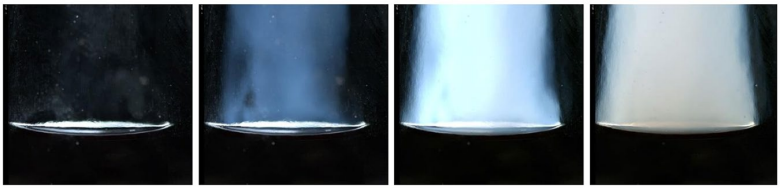

Figure 5. After adiabatic expansion, in the bottleneck of bottles stored at 20 °C, the progressive growth in size of dry ice CO_2 clusters can also be evidenced by observing the change in colour experienced by the condensation cloud, which progressively changes from deep blue to grey-white. The time interval between each frame is 83 µs.

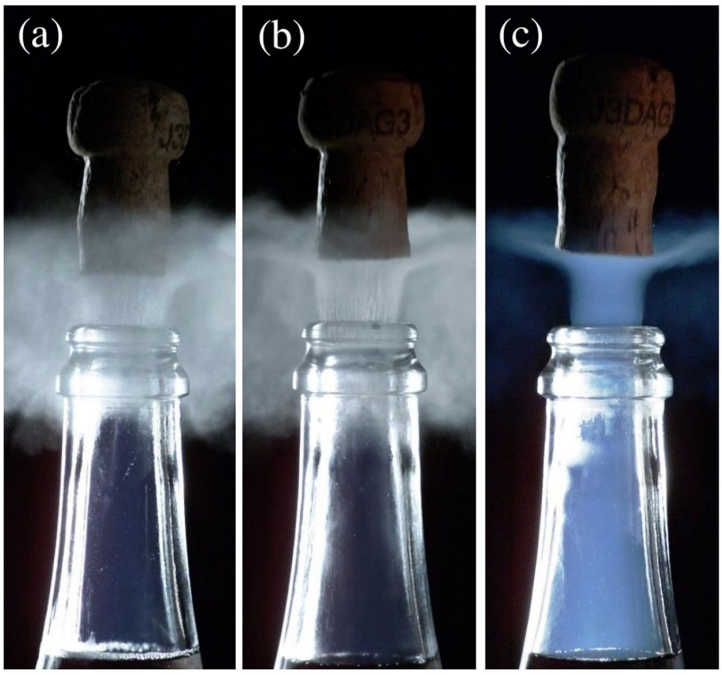

Figure 6. Three snapshots, taken 1.2 ms after the cork popping process, showing the condensation of water vapour above the bottlenecks of bottles stored at 6 °C (**a**), 12 °C (**b**), and the deep blue CO_2 freezing plume gushing from the bottleneck of the bottle stored at 20 °C (**c**), respectively. In frame (**c**), the grey-white cloud of condensation droplets found in air packages adjacent to the gas volume gushing out of the bottleneck disappeared.

$$\Delta U = \int_{V_G}^{V_f} P dV \tag{5}$$

with P being the pressure of the gas mixture freely expanding during adiabatic expansion, V_G being the volume of the gas mixture in the sealed bottle before cork popping, and V_f being the volume of the gas mixture after adiabatic expansion.

Adiabatic expansion keeping the product PV^γ as constant, the latter equation therefore transforms as follows:

$$\Delta U = P_{CB} V_G^\gamma \int_{V_G}^{V_f} \frac{dV}{V^\gamma} \tag{6}$$

with P_{CB} being the strongly temperature dependent pressure of gas-phase CO_2 in the corked bottle.

Integrating equation (6) between the initial stage in the corked bottle, and the final stage after adiabatic expansion, and developing, leads to the following relationship, function of both the initial pressure, and the volume of gas phase in the corked bottle:

Retour à la table des matières : p. v

$$\Delta U = \frac{P_{CB}V_G}{(\gamma - 1)}\left[1 - \left(\frac{P_{CB}}{P_0}\right)^{\frac{1-\gamma}{\gamma}}\right] \quad (7)$$

By application of the latter equation to the bottles stored at 6 °C, and with a pressure in the sealed bottles in the order of 4.5 bar, the decrease in internal energy of the gas mixture after adiabatic expansion is in the order of $\Delta U \approx 11$ J. A fraction of this energy is used to cool adjacent air packages from about 20 °C to the dew point temperature (around 14.5 °C for ambient air with RH ≈ 70%). Then another fraction of this energy is required to force phase change by condensing a portion of water vapour in the form of liquid droplets, and thus forming the very characteristic grey-white cloud of fog above the bottleneck. By application of the latter equation to the bottles stored at 20 °C, and with a pressure in the sealed bottles in the order of 7.5 bar, the decrease in internal energy of the gas mixture after adiabatic expansion becomes in the order of $\Delta U \approx 24$ J. Actually, because the saturation ratio of gas-phase CO_2 becomes in the order of 2.5 after adiabatic expansion, a fraction of gas-phase CO_2 is believed to be able to experience gas phase and transform into dry ice CO_2 (through heterogeneous nucleation on ice water cluster nuclei, as proposed earlier). But since the latent heat of sublimation of dry ice CO_2 is high (with $\Delta H_{sub}^{CO_2} \approx 26$ kJ mol^{-1} [22]), phase change of even a small portion of CO_2 from gas phase to dry ice will pump the loss of internal energy $\Delta U \approx 24$ J released through adiabatic expansion. For bottles stored at 20 °C, about 8×10^{-3} mol of gas-phase CO_2 experience adiabatic expansion. It is worth noting that the deposition of only about 9×10^{-4} mol of gas-phase CO_2 requires an energy of $Q \approx 24$ J. Therefore, the phase change from gas phase to dry ice of only a small volume fraction of all the available CO_2 (in the order of 0.1) is able to pump all the available energy released through adiabatic expansion. Finally, the freezing of only about 10% of the gas-phase CO_2 found in the bottleneck can forbid the condensation of water vapour found in air packages adjacent to the gas volume gushing out of the bottleneck, as observed during the cork popping process of bottles stored at 20 °C.

Conclusion

Initially under pressure in the bottleneck, a gas mixture mainly composed of gas-phase CO_2 with traces of water vapour freely expands during cork popping. The commonly accepted idea behind champagne cork popping was that the gas mixture gushing from the bottleneck experiences adiabatic expansion, and therefore cools adjacent air packages, thus causing condensation of water vapour found in ambient air in the form of a characteristic grey-white cloud of fog. Nevertheless, based on this set of experiments, the situation has appeared really more complex and subtle. We pointed out the key role of bottle temperature. Most interestingly, for the bottles stored at 20 °C, the characteristic grey-white cloud of fog classically observed above the bottlenecks of bottles stored at lower temperatures completely disappeared. It was replaced by a more evanescent plume, surprisingly blue, starting from inside the bottleneck. Depending on the strongly bottle temperature dependent saturation ratio experienced by gas-phase CO_2 after adiabatic expansion, it was emphasized that blue haze is the signature of a partial and transient heterogeneous freezing of gas-phase CO_2 on ice water clusters homogeneously nucleated in the bottlenecks.

Materials and Methods

Batch of champagne bottles. A single batch of champagne rosé (from Champagne Vranken Pommery, Marne, France), elaborated with a blend of chardonnay and pinot noir base wines (vintage 2008), was used for this set of experiments. In March 2010, the blended wine was put in standard 75 cL clear transparent bottles, along with yeasts and sugar to promote its second fermentation (or *prise de mousse*). A classical amount of 24 g L^{-1} of sugar was added in the blend to promote the *prise de mousse*[3]. Bottles were then hermetically sealed with a crown cap. The key metabolic process behind the production of gaseous CO_2 in the sealed bottles is alcoholic fermentation (i.e., the conversion of sugars into ethanol and gaseous carbon dioxide by yeast), displayed hereafter.

$$C_6H_{12}O_6 \rightarrow 2\ CH_3CH_2OH + 2\ CO_2 \quad (8)$$

Following equation (8) with 24 g L^{-1} of sugar added in the blend, leads to the production of 9 g of CO_2 (i.e., 0.2 mole) in every bottle of this batch during the *prise de mousse*.

Batch of cork stoppers. After a long period of aging of 42 months following the *prise de mousse*, bottles were then disgorged (in order to remove the sediment of dead yeast cells), and corked with traditional natural cork stopper from a same batch of corks (provided by Amorim & Irmãos, Portugal). Each cork stopper is composed of two well-distinct different parts: (i) a upper part composed of agglomerated cork granules, and (ii) a lower part, into contact with the wine, made of two massive cork disks stuck together. The mass of each cork is about 10 ± 0.1 g. It is also worth noting that, into every bottle of this batch, the volume of the headspace under the cork is precisely equal to 25 mL. To examine the role of temperature on champagne cork popping, three storage temperatures were chosen in a reasonable range of temperatures likely to be encountered by bottles during champagne making or even by standard consumers (namely, 6, 12, and 20 °C, respectively). 72 hours before each set of experiments, bottles were stored at the desired temperature.

Temperature dependence of gas phase pressure in the corked bottles. The capacity of CO_2 to get dissolved in champagne is ruled by Henry's law equilibrium, which states that the concentration c of dissolved CO_2 in the liquid phase is proportional to the partial pressure of gas-phase CO_2 denoted P:

Retour à la table des matières : p. v

$$c = k_H P \tag{9}$$

with k_H being the strongly temperature-dependent Henry's law constant of gas-phase CO_2 in the liquid phase (i.e., its solubility)[23,24].

Thermodynamically speaking, the temperature-dependence of Henry's law constant can be conveniently expressed with a van't Hoff like equation as follows:

$$k_H(T) = k_{298\mathrm{K}} \exp\left[-\frac{\Delta H_{\mathrm{diss}}}{R}\left(\frac{1}{T} - \frac{1}{298}\right)\right] \tag{10}$$

with ΔH_{diss} being the dissolution enthalpy of CO_2 molecules in the liquid phase, and R being the ideal gas constant ($8.31\,\mathrm{J\,K^{-1}mol^{-1}}$). The best fit of $k_H(T)$ with a previous set of experimental data was found with $k_{298\mathrm{K}} \approx 1.21\,\mathrm{g\,L^{-1}bar^{-1}}$, and $\Delta H_{\mathrm{diss}} \approx 24.8\,\mathrm{kJ\ mol^{-1}}$ [25].

In the sealed bottle, the volume V_G of gas phase in the headspace cohabits with a volume V_L of champagne (i.e., the liquid phase). For the sake of simplicity, we suppose that both volumes remain constant during the *prise de mousse* (i.e., we neglect the minute changes of the liquid volume due to the progressive dissolution of CO_2). In the pressure range of interest (a few bars), we may safely suppose that the gas phase is ruled by the ideal gas law. Thus,

$$PV_G = n_G RT \tag{11}$$

with T being the champagne temperature (in K), and n_G being the mole number of gas-phase CO_2 in the headspace.

Moreover, in the bottle hermetically sealed, the total number of moles of carbon dioxide n_T is a conserved quantity that decomposes into n_G moles in the gaseous phase and n_L moles in the liquid phase. Therefore,

$$n_T = n_G + n_L \tag{12}$$

By combining equations (9), (11) and (12), the following relationship was determined for the pressure of gas-phase CO_2 in the sealed bottle after the *prise de mousse* was achieved:

$$P_{PDM} \approx \frac{n_T RT}{V_G + k_H RTV_L} \tag{13}$$

with P_{PDM} being expressed in Pa, and k_H being conveniently expressed in $\mathrm{mol\ m^{-3}\ Pa^{-1}}$.

After the *prise de mousse*, bottles aged in a cool cellar for 42 months. Bottles were then disgorged, which consists in opening the bottles in order to remove the dead yeast cells, and re-corking them with the traditional cork stoppers described above. During the disgorging process, a bit of CO_2 is inevitably lost at this step as gas-phase CO_2 escapes from the bottleneck under the action of pressure when opening the bottle. The partial pressure of gas-phase CO_2 therefore falls. The thermodynamic equilibrium of CO_2 is broken, but the bottle is then quickly re-corked with a traditional cork stopper. Dissolved and gas-phase CO_2 therefore quickly recover Henry's equilibrium in the corked bottle. The newly defined total number of CO_2 moles in the re-corked bottle, namely n_T^{CB}, finally becomes equivalent to:

$$n_T^{CB} = n_T - n_G \approx n_T - \frac{P_{PDM} V_G}{RT} \tag{14}$$

The newly recovered equilibrium pressure of gas-phase CO_2 is therefore accessed by replacing n_T in equation (13) with the newly defined total number of CO_2 moles in the corked bottle n_T^{CB}, defined in equation (14). Finally, and after developing, the newly recovered equilibrium pressure of gas-phase CO_2 can be expressed as:

$$P_{CB} \approx \frac{n_T k_H (RT)^2 V_L}{(V_G + k_H RTV_L)^2} \tag{15}$$

For standard champagne bottles with $V_L = 75$ cL, a gaseous volume in the headspace of $V_G = 25$ mL, and a total number of CO_2 moles trapped per bottle of $n_T \approx 0.2$ mole (after a *prise de mousse* promoted with $24\,\mathrm{g\,L^{-1}}$ of sugar), the temperature dependence of both gas-phase CO_2 pressures P_{PDM}, and P_{CB}, as given in equations (13) and (15), respectively, is displayed in Fig. 3. The disgorging step has therefore a slight but significant impact on the final pressure found within the corked bottle (especially near ambient temperatures), and has therefore to be taken into account in every problematic dealing with pressure dependence phenomena. It was indeed wrongly neglected in previous studies dedicated to thermodynamic equilibrium of CO_2 within the sealed bottles[4,26].

High-speed video device. A digital high-speed cinema camera (Phantom Flex - Vision Research, USA) was used for this set of experiments on the visualization of phenomena accompanying champagne cork popping. Classically, the maximum filming rate of the Phantom Flex digital camera increases as its resolution decreases, with for example up to 2.570 frames per second (fps) at a resolution of 1920×1080 pixels, 5.350 fps at 1280×720, and 10.750 fps at 640×480. Generally speaking, powerful illumination is required to get satisfying high frame rate moving time sequences. A 5000 W lamp using tungsten filaments, and powered by direct current (DC), was placed behind the corked bottleneck. It is worth noting that, in addition to a powerful illumination, DC is needed to eliminate the so-called flicker phenomenon. Actually, when powered by 60 Hz alternating current

Retour à la table des matières : p. v

(AC) electricity, the lamp tungsten filament intensity can slightly vary with the same frequency, thus altering time sequences above a 120 fps frame rate. To get synchronized with the split-second timing of cork popping, the shooting of the camera was post-triggered by using a simple microphone recording the "bang" done by the fast traveling cork popping out of the bottleneck. The powerful lamp, which acts as a source of heat, was switched on just before filming the cork popping process, and switched off immediately after recording the sequence.

Relative humidity in ambient air. Temperature and hygrometry of ambient air were supplied with a digital coupled Thermo-Hygrometer (2212TM, IHM, France). Our cork popping experiments were done in a controlled temperature room (at 20 ± 2 °C), where the relative humidity (RH) slightly varied throughout the day, but was very close to 70%. At a given temperature T, RH is defined as follows:

$$\mathrm{RH} = S \times 100 = \frac{P_{\mathrm{vap}}}{P_{\mathrm{sat}}(T)} \times 100 \tag{16}$$

with S being the saturation water vapour ratio, P_{vap} being the partial pressure of water vapour in air, and $P_{\mathrm{sat}}(T)$ being the strongly temperature-dependent saturated vapour pressure.

In ambient air, $P_{\mathrm{sat}}(T)$ is correctly approached through the Clausius-Clapeyron equation defined as follows, provided that water vapour behaves as an ideal gas, and that the specific latent heat of water evaporation L_{vap} remains reasonably constant in this range of temperatures[27]:

$$P_{\mathrm{sat}}(T) = P_0 \exp\left[\frac{ML_{\mathrm{vap}}}{R}\left(\frac{1}{373} - \frac{1}{T}\right)\right] \tag{17}$$

with P_0 being the ambient pressure (close to 1 bar), M being the molar mass of water (0.018 kg mol^{-1}), and L_{vap} being the specific latent heat of water evaporation at 20 °C ($\approx 2.47 \times 10^6$ J kg^{-1})[28].

Therefore, by combining RH $\approx$ 70% (at $T \approx 20$ °C) with equations (16) and (17) enabled to retrieve the partial pressure of water vapor in ambient air as $P_{\mathrm{vap}} \approx 0.02$ bar during the day our cork popping experiments were done.

Temperature dependence of ice water and dry ice CO_2 saturated vapor pressures. The relationship between the saturated vapor pressure of gas-phase CO_2 $P_{\mathrm{sat}}^{\mathrm{CO_2}}$, and temperature T is provided by Antoine equation as follows[9]:

$$\log_{10}(P_{\mathrm{sat}}^{\mathrm{CO_2}}) = A - \frac{B}{T + C} \tag{18}$$

with $P_{\mathrm{sat}}^{\mathrm{CO_2}}$ being expressed in bar, T being expressed in K, and the coefficients A, B, and C being provided by the NIST database[28]. In the range of temperatures between 154 and 196 K (i.e., between −119 and −77 °C), that covers the range of temperatures reached by the gas mixture gushing out of the bottleneck after adiabatic expansion, Antoine coefficients A, B, and C are 6.81228, 1301.679, and −3.494, respectively[28].

Likewise, in this range of temperatures, the vapor pressure of ice water $P_{\mathrm{sat}}^{\mathrm{H_2O}}$ was found to obey the following relationship[10]:

$$P_{\mathrm{sat}}^{\mathrm{H_2O}} = \exp\left(28.868 - \frac{6132.9}{T}\right) \tag{19}$$

with $P_{\mathrm{sat}}^{\mathrm{H_2O}}$ being expressed in Pa, and T being expressed in K.

References

1. Archer, D. & Galloway, N. Champagne-cork injury to the eye. *Lancet* **2**, 487–489 (1967).
2. Batt, R. Pop! Goes the champagne bottle cork. *J. Chem. Educ.* **48**, 71 (1971).
3. Liger-Belair, G. Effervescence in champagne and sparkling wines: From grape harvest to bubble rise. *Eur. Phys. J. Special Topics* **226**, 3–116 (2017).
4. Liger-Belair, G., Bourget, M., Cilindre, C., Pron, H. & Polidori, G. Champagne cork popping revisited through high-speed infrared imaging: The role temperature. *J. Food Eng.* **116**, 78–85 (2013).
5. Volmer, M. & Möllmann, K.-P. Vapour pressure and adiabatic cooling from champagne: Slow-motion visualization of gas thermodynamics. *Phys. Educ.* **45**, 608–615 (2012).
6. Liger-Belair, G., Polidori, G. & Jeandet, P. Recent advances in the science of champagne bubbles. *Chem. Soc. Rev.* **37**, 2490–2511 (2008).
7. Sanchez-Lavega A. *An Introduction to Planetary Atmospheres* (CRC Press, 2011).
8. Speight J. G. *Lange's Handbook of Chemistry* (McGraw-Hill, 2017).
9. Giauque, W. F. & Egan, C. J. *Carbon dioxide. The heat capacity and vapor pressure of the solid. The heat of sublimation. Thermodynamic and spectroscopic values of the entropy. J. Chem. Phys.* **5**, 45–54 (1937).
10. Marti, J. & Mauersberger, K. A survey and new measurements of ice vapor pressure at temperatures between 170 and 250 K. *Geophys. Res. Lett.* **20**, 363–366 (1993).
11. Abraham F. F. *Homogeneous Nucleation Theory* (Academic Press, 1974).
12. Zhang, R., Khalizov, A., Wang, L., Hu, M. & Xu, W. Nucleation and growth of nanoparticles in the atmosphere. *Chem. Rev.* **112**, 1957–2011 (2012).
13. Li, Z., Zhong, J. & Levin, D. A. Modeling of CO_2 homogeneous and heterogeneous condensation plumes. *J. Phys. Chem. C* **114**, 5276–5286 (2010).
14. Wyslouzil, B. E., Heath, C. H., Cheung, J. L. & Wilemski, G. Binary condensation in a supersonic nozzle. *J. Chem. Phys.* **113**, 7317–7329 (2000).

Retour à la table des matières : p. v

15. Hagena, O. F. & Obert, W. Cluster formation in expanding supersonic jets: Effect of pressure, temperature, nozzle size, and test gas. *J. Chem. Phys.* **56**, 1793–1802 (1972).
16. Lamanna, G., Poppel, J. & Dongen, M. E. H. Experimental determinations of droplet size and density field in condensing flows. *Exp. Fluids* **32**, 381–395 (2002).
17. Ramos, A., Fernández, J. M., Tejeda, G. & Montero, S. Quantitative study of cluster growth in free-jet expansions of CO_2 by Rayleigh and Raman scattering. *Phys. Rev. A* **72**, 3204–3210 (2005).
18. Zhong, J., Zeifman, M. I. & Levin, D. A. Kinetic model of condensation in a free argon expanding jet. *J. Thermophys. Heat Transfer* **20**, 41–51 (2006).
19. Harvey, G. Thruster residues on returned Mir solar panel. *Proc. SPIE* **4096**, 41–46 (2000).
20. Alexeenko, A. A., Wadsworth, D. C., Gimelshein, S. F. & Ketsdever, A. D. Numerical modeling of ISS thruster plume induced contamination environment. *Proc. SPIE* **5526**, 125 (2004).
21. Warren, C. G. Optical constants of carbon dioxide ice. *Appl. Opt.* **25**, 2650–2674 (1974).
22. Ambrose, D. The vapour pressures and critical temperatures of acetylene and carbon dioxide. *Trans. Faraday Soc.* **52**, 772–781 (1956).
23. Carroll, J. J. & Mather, A. E. The system carbon dioxide/water and the Krichevsky-Kasarnovsky equation. *J. Sol. Chem.* **21**, 607–621 (1992).
24. Diamond, L. W. & Akinfief, N. N. Solubility of CO_2 in water from 1.5 to 100 °C and from 0.1 to 100 MPa: Evaluation of literature data and thermodynamic modelling. *Fluid Phase Equilib.* **208**, 265–290 (2003).
25. Liger-Belair, G. The physics and chemistry behind the bubbling properties of champagne and sparkling wines: A state-of-the-art review. *J. Agric. Food Chem.* **53**, 2788–2802 (2005).
26. Vreme, A., Pouligny, B., Nadal, F. & Liger-Belair, G. Does shaking increase the pressure inside a bottle of champagne? *J. Colloid Interface Sci.* **439**, 42–53 (2015).
27. Stowe, K. An *Introduction to Thermodynamics and Statistical Mechanics* (Cambridge University Press, 2007).
28. Provided by the NIST database (http://webbook.nist.gov/chemistry).
29. Määttänen, A. *et al.* Nucleation studies in the Martian atmosphere. *J. Geophys. Res.* **110**, E02002 (2005).

Acknowledgements

We acknowledge Thierry Gasco, chef de cave from Champagne Pommery, for kindly providing us with the batch of champagne rosé used in this set of experiments. The authors also acknowledge the Association Recherche Œnologique Champagne et Université (AROCU), and especially President Jean-Pierre Dargent, for supporting our research.

Author Contributions

G.L.-B., J.H., and C.C. designed and performed research. G.L.-B., D.C. and C.C. analyzed data. G.L.-B. and D.C. wrote the paper. All authors discussed the results and commented on the manuscript at all stages.

Additional Information

Competing Interests: The authors declare that they have no competing interests.

Publisher's note: Springer Nature remains neutral with regard to jurisdictional claims in published maps and institutional affiliations.

Open Access This article is licensed under a Creative Commons Attribution 4.0 International License, which permits use, sharing, adaptation, distribution and reproduction in any medium or format, as long as you give appropriate credit to the original author(s) and the source, provide a link to the Creative Commons license, and indicate if changes were made. The images or other third party material in this article are included in the article's Creative Commons license, unless indicated otherwise in a credit line to the material. If material is not included in the article's Creative Commons license and your intended use is not permitted by statutory regulation or exceeds the permitted use, you will need to obtain permission directly from the copyright holder. To view a copy of this license, visit http://creativecommons.org/licenses/by/4.0/.

© The Author(s) 2017

Retour à la table des matières : p. v

Retour à la table des matières : p. v

Quatrième partie

Physique stellaire

Chapitre 13

La physique stellaire

« *You'd look pretty simple from ten parsecs too.* »

Attribué à Fred Hoyle (1955),
en réponse à une personne se demandant pourquoi on ne
comprend apparemment pas une chose aussi simple qu'une étoile,
citation reprise de HANSEN et collab. [2004].

Alors que j'étais professeur agrégé à l'*Ecole Nationale Supérieure de Chimie de Rennes*, ma rencontre avec Yveline Lebreton (maintenant au LESIA/Observatoire de Paris) a été l'occasion de débuter une thèse en physique stellaire [CORDIER, 2000]. Ce travail co-dirigé par MarieJo Goupil, et sous la direction officielle d'Annie Baglin, portait sur les étoiles de type céphéide, importantes dans la détermination des distances intergalactiques.
A cette occasion j'ai participé au développement du code de structure interne et d'évolution stellaire `CESAM`[1] [MOREL et LEBRETON, 2008]. Concernant les populations de céphéides du Petit Nuage de Magellan nos résultats ont suggéré un effet de sélection dû aux caractéristiques de l'évolution de ces étoiles [CORDIER et collab., 2003] (voir page 374). Les modèles d'évolution stellaire dépendent de données physiques, comme l'opacité et l'équation d'état du plasma ; ils dépendent également de paramètres, dont l'un est particulièrement important : celui d'«overshooting», qui détermine l'extension exacte du mélange convectif dans le cœur de l'étoile, quand celui-ci est sujet à un tel brassage. Cette extension conditionne la quantité totale, sur la séquence principale, d'hydrogène qui sera consommé. Ceci fixe la durée de séjour de l'étoile en question dans cette phase. Des simulations basées sur `CESAM`, complétées par ceux d'un code de synthèse de populations stellaires (développés par mes soins) a permis de contraindre la valeur de ce paramètre d'«overshooting» CORDIER et collab. [2002] (voir page 362) et d'étudier son éventuelle dépendance avec la composition chimique.
L'Italie est dotée de fortes équipes dans le domaine de la physique stellaire, j'ai donc collaboré un temps avec Santi Cassisi de l'Observatoire de Teramo [CORDIER et collab., 2007; KING et collab., 2012; MANZATO et collab., 2008] (voir à partir de la page 385).

Mon implication dans le domaine de la physique stellaire s'est arrêté lors de mon détachement au CNRS, époque à laquelle je me suis tourné vers la planétologie. Cependant, je profite encore de certains acquis associés à cette période : mon étude du transport de poussières par photopho-

1. Code d'Evolution Stellaire Adaptatif et Modulaire

rèse CORDIER et collab. [2016] utilise des résultats de simulations d'évolutions stellaires ; sur le plan numérique des algorithmes de Newton-Raphson ou de Monte-Carlo ont été utilisés dans mes modèles de thermodynamique et dans le modèle de disque protoplanétaire *EvAD*.

13.1 Références

CORDIER, D. 2000, *Les étoiles de type céphéide : tests pour la théorie de la structure interne stellaire*, Theses, Université Rennes 1. URL https://tel.archives-ouvertes.fr/tel-00549139. 359

CORDIER, D., M. J. GOUPIL et Y. LEBRETON. 2003, «The faint Cepheids of the Small Magellanic Cloud : An evolutionary selection effect ?», *A&A*, vol. 409, doi: 10.1051/0004-6361:20031185, p. 491–501. 359

CORDIER, D., Y. LEBRETON, M.-J. GOUPIL, T. LEJEUNE, J.-P. BEAULIEU et F. ARENOU. 2002, «Convective core mixing : A metallicity dependence ?», *A&A*, vol. 392, doi: 10.1051/0004-6361:20020934, p. 169–180. 359

CORDIER, D., A. PIETRINFERNI, S. CASSISI et M. SALARIS. 2007, «A Large Stellar Evolution Database for Population Synthesis Studies. III. Inclusion of the Full Asymptotic Giant Branch Phase and Web Tools for Stellar Population Analyses», *AJ*, vol. 133, doi: 10.1086/509870, p. 468–478. 359

CORDIER, D., P. G. PRADA MORONI et E. TOGNELLI. 2016, «Dust photophoretic transport around a T Tauri star : Implications for comets composition», *Icarus*, vol. 268, doi: 10.1016/j.icarus.2015.11.037, p. 281–294. 360

HANSEN, C. J., S. D. KAWALER et V. TRIMBLE, éd.. 2004, *Stellar Interiors – Physical Principles, Structure, and Evolution*, Springer, New-York. 359

KING, I. R., L. R. BEDIN, S. CASSISI, A. P. MILONE, A. BELLINI, G. PIOTTO, J. ANDERSON, A. PIETRINFERNI et D. CORDIER. 2012, «Hubble Space Telescope Observations of an Outer Field in Omega Centauri : A Definitive Helium Abundance», *AJ*, vol. 144, doi: 10.1088/0004-6256/144/1/5, 5. 359

MANZATO, P., A. PIETRINFERNI, F. GASPARO, G. TAFFONI et D. CORDIER. 2008, «BaSTI, a Bridge between Grid and Virtual Observatory Part 1 : BaSTI inside the VO», *Publ. Astron. Soc. Pac.*, vol. 120, doi: 10.1086/591294, p. 922. 359

MOREL, P. et Y. LEBRETON. 2008, «CESAM : a free code for stellar evolution calculations», *Astrophys. Space Sci.*, vol. 316, doi: 10.1007/s10509-007-9663-9, p. 61–73. 359

Chapitre 14

Articles : physique stellaire

14.1 Article sur la variation de l'overshooting en fonction de la métallicité

A&A 392, 169–180 (2002)
DOI: 10.1051/0004-6361:20020934
© ESO 2002

Astronomy & Astrophysics

Convective core mixing: A metallicity dependence?

D. Cordier[1,2], Y. Lebreton[1], M.-J. Goupil[1], T. Lejeune[3], J.-P. Beaulieu[4], and F. Arenou[1]

[1] DASGAL, CNRS UMR 8632, Observatoire de Paris-Meudon, DASGAL, 92195 Meudon Principal Cedex, France
[2] École Nationale Supérieure de Chimie de Rennes, Campus de Beaulieu, 35700 Rennes, France
[3] Observatorio Astronomico, Universidade de Coimbra, Santa Clara 3040 Coimbra, Portugal
[4] I.A.P., 98bis boulevard Arago, 75014 Paris, France

Received 5 March 2002 / Accepted 6 June 2002

Abstract. The main purpose of this paper is to investigate the possible existence of a metallicity dependence of the overshooting from main sequence star turbulent cores. We focus on objects with masses in the range ~2.5 $M_\odot$–~25 $M_\odot$. Evolutionary time scale ratios are compared with star number ratios on the main sequence. Star populations are synthesized using grids of evolutionary tracks computed with various overshooting amounts. Observational material is provided by the large and homogeneous photometric database of the OGLE 2 project for the Magellanic clouds. Attention is paid to the study of uncertainties: distance modulus, intergalactic and interstellar reddening, IMF slope and average binarity rate. Rotation and the chemical composition gradient are also considered. The result for the overshooting distance is $l_{\rm over}^{\rm SMC} = 0.40^{+0.12}_{-0.06}$ H_p ($Z_0 = 0.004$) and $l_{\rm over}^{\rm LMC} = 0.10^{+0.17}_{-0.10}$ H_p ($Z_0 = 0.008$) suggesting a possible dependence of the extent of the mixed central regions with metallicity within the considered mass range. Unfortunately it is not yet possible to fully disentangle the effects of mass and chemical composition.

Key words. convection – stars: evolution, interiors

1. Introduction

Extensive convective phenomena occur in the cores of main sequence stars with masses above about 1.2 $M_\odot$ (for galactic chemical composition). In standard models, convection is crudely modeled with the well-known Mixing Length Theory of Böhm-Vitense (1958) (hereafter MLT) and the core extension is determined according to the Schwarzschild criterion. The Schwarzschild limit is the value of the radius where the buoyancy force vanishes. However, inertia of the convective elements leads to an extra mixing above the Schwarzschild limit, called "overshooting" and is usually expressed as a fraction of the pressure scale height. Several theoretical works (for a review see Zahn 1991) give arguments in favor of such additional mixing. Many laboratory experiments show evidence for overshooting (see Massaguer 1990). Although overshooting can occur below an external convective zone (see Alongi et al. 1991), this paper is exclusively concerned with core overshooting.

One of the first empirical determinations of convective core overshooting was obtained by Maeder & Mermilliod (1981) who used a set of 34 galactic open clusters and fitted the main sequence width with an additional mixing of about 20–40% in mass fraction. Mermilliod & Maeder (1986) derived an overshooting amount of about 0.3 H_p for solar-like chemical composition and for a 9–15 $M_\odot$ range. Stothers & Chin (1991) derived an overshooting amount <0.2 H_p for Pop. I stars using the metal-enriched opacity tables published in Rogers & Iglesias (1992).

During the last decade, many evolutionary model grids have been computed with an overshooting amount equal or close to 0.2 H_p: e.g. Charbonnel et al. (1996) or Bertelli et al. (1994). This second team (Padova group) uses a formalism (see Bressan et al. 1981) slightly different from the Geneva team one (e.g. see Schaller et al. 1992). Generally the same overshooting amount is used whatever the metallicity and mass are.

Kozhurina-Platais et al. (1997) obtained $l_{\rm over} = 0.2 \pm 0.05$ H_P for the galactic cluster NGC 3680 (solar metallicity) with the isochrone technique. This method consists of fitting the cluster CMD features (particularly the turn-off position) with model isochrones. Iwamoto & Saio (1999) compared evolutionary models with observations of three binary systems: V2291 Oph, α Aur and η And ("binary system" technique). The authors adjusted either the helium content or the overshooting parameter to get a better fit to observations. The best results were obtained with a moderate overshooting amount ($\lesssim$0.15 H_p). For super-solar metallicity ($Z_0 = 0.024$) Lebreton et al. (2001) derived $l_{\rm over} \lesssim 0.2$ H_P from the modeling of the Hyades cluster turn-off.

Maeder & Mermilliod (1981) have suggested an overshooting increasing with mass within the studied range of 2–6 $M_\odot$ which is also found by Schröder et al. (1997) with a study of binary systems. According to their results, the overshooting should increase from $\lesssim$0.24 H_p for 2.5 $M_\odot$ to $\lesssim$0.32 H_p for 6.5 $M_\odot$. With a similar study Ribas et al. (2000) also found a mass dependence.

Send offprint requests to: D. Cordier,
e-mail: daniel.cordier@ensc-rennes.fr

Article published by EDP Sciences and available at http://www.aanda.org or http://dx.doi.org/10.1051/0004-6361:20020934

Retour à la table des matières : p. v

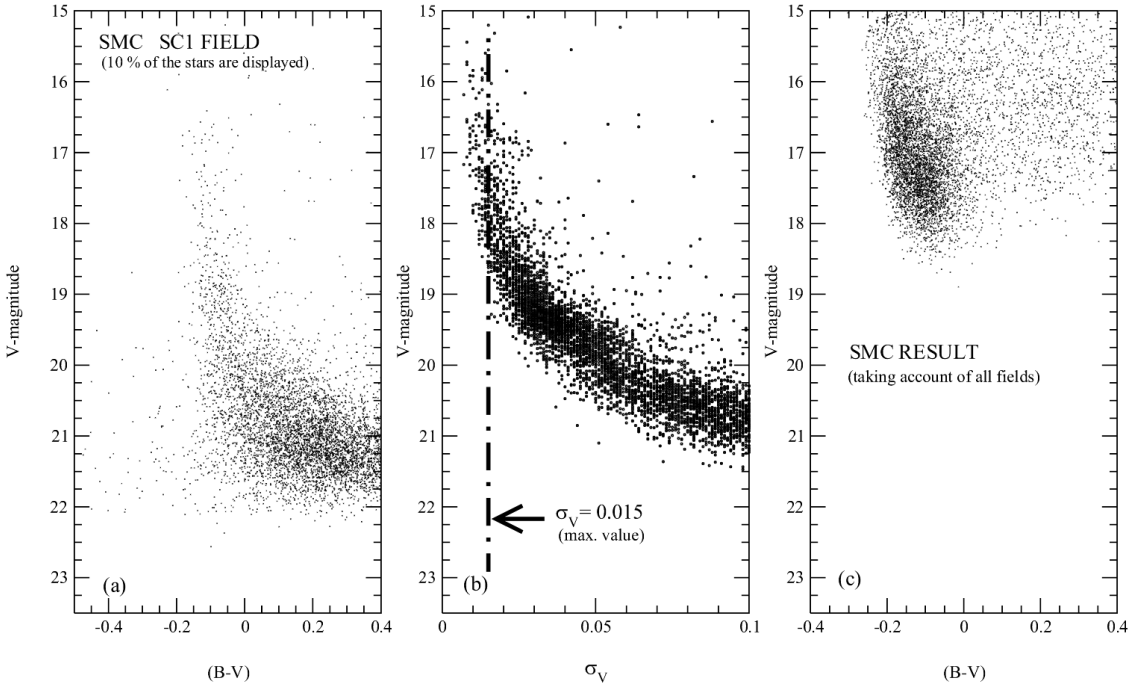

Fig. 1. a) CM-Diagram for the OGLE 2 SC 1 field, 10% of the data have been plotted for sake of clarity. **b)** Standard deviation of the measurements: σ_V versus magnitude V, the dot-dashed line indicates the limit-value considered (0.015). **c)** The resulting CM-diagram after selection (all the fields within SMC have been plotted).

The question of a metallicity dependence must also be addressed. Ribas et al. (2000)'s results suggest a slight metallicity dependence for a stellar mass around 2.40 $M_\odot$ (see their Table 1). The more metal poor star SZ Cen (in mass fraction: $Z_0 = 0.007$) is satisfactorily modelled with an overshooting distance 0.1 $H_p \lesssim l_{ov} \lesssim 0.2$ H_P and objects with Z_0 ranging between 0.015 and 0.020 seem to have an overshooting around 0.2 H_P. Keller et al. (2001) have recently explored the dependence of overshooting with metallicity by means of the isochrone technique using isochrone grids from the Padova group. Their study involves HST observations of four clusters: NGC 330 (SMC), 1818, 2004 and 2001 (LMC). Keller et al. (2001) find the best fit (with respect to age and overshooting) for an overshooting amount which is equivalent to $l_{\rm over} = 0.31 \pm 0.11$ H_p in the Geneva formalism ($l_{\rm over}^{\rm Padova} = 2 \times l_{\rm over}^{\rm Geneva}$).

In this paper, we carry out an independent study of a possible metallicity dependence of overshooting with a technique which differs from the "binary system" (Ribas et al. 2000; Andersen 1991) and "isochrone" techniques. Our method is based on star-count ratios, with comparisons between observational material and synthetic population results in color-magnitude (CMD) diagrams. We are then led to discuss several points: particularly distance modulus, reddening and binarity rate. If the dependence of overshooting on metallicity (or mass) was thereby to be firmly assessed, it would then be a challenge to understand its physical origin.

We are concerned with a metallicity range relevant to the Magellanic Clouds and take advantage of the homogeneous OGLE 2 data, which provide color magnitude diagrams for $\sim 2 \times 10^6$ stars in the Small Magellanic Cloud (hereafter SMC) and $\sim 7 \times 10^6$ in the Large Magellanic Cloud (hereafter LMC). On the theoretical side, we estimate the number of stars from evolutionary model sequences computed with different amounts of overshooting. From these data sets and using evolutionary models with intermediate and low metallicity, we estimate the overshooting value during the main sequence in the SMC and LMC for a stellar mass in the range 2.5 $M_\odot$–25 $M_\odot$.

In Sect. 2 we describe the observational data involved in this work. Section 3 is devoted to the method used: data selection and star counting. Section 4 gives the main features of our population synthesis procedure. Section 5 is devoted to astrophysical inputs, and Sect. 6 to results and effects of uncertainties. Section 7 discusses the results. It must be emphasized that we determine in fact the extent of the inner mixed core region which can be due either to true overshooting or to another process such as rotation; some observational evidence exists about correlation between metallicity and $v \sin i$ (see Venn et al. 1999). The problem of rotation is briefly discussed in Sect. 7. Finally, Sect. 8 gives some comments and concluding remarks. An appendix has been added to provide details about the population synthesis algorithm and error simulations.

2. Observational data

The observational data set considered here has been obtained by the Optical Gravitational Lensing Experiment (OGLE hereafter) consortium during its second operating phase

Retour à la table des matières : p. v

(for more details and references the reader can consult URL: `http://www.astrouw.edu.pl/ogle/`).

2.1. SMC and LMC data

We have downloaded the SMC data described in Udalski et al. (1998). The data used in this paper are from the post-Apr. 8, 2000 revision. The SMC is divided into 11 fields (labeled SC1 to SC11) covering $55' \times 14'$; each field contains between ~100 000 and ~350 000 objects. For each object several quantities are available: equatorial coordinates, BVI photometry and associated standard errors σ_B, σ_V and σ_I. This database has the great advantage of being extensive and very homogeneous.

The LMC data are described in Udalski et al. (2000). The BVI map of the LMC is composed of 26 fields (SC1 to SC26) in the central bar of the LMC. The dataset includes photometry and astrometry for about 7 million stars over a 5.7 square degree field.

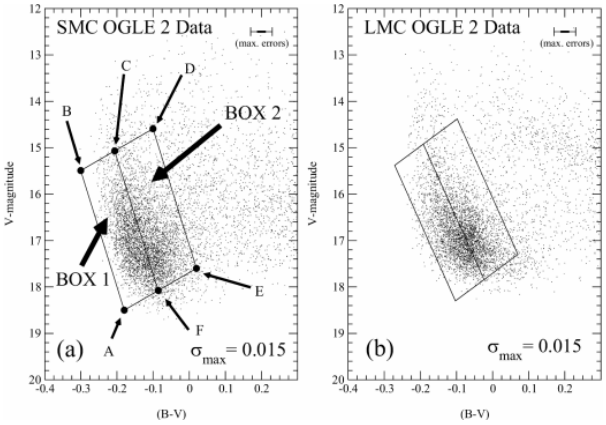

Fig. 2. a) Data from SMC with $\sigma_V \leq 0.015$ mag and box definitions ($N_1 + N_2 = 4653$ and $N_2/N_1 = 1.08$), **b)** the same for the LMC case ($N_1 + N_2 = 4113$ and $N_2/N_1 = 1.01$).

3. The star-count method

3.1. Data selection

As shown in Fig. 1b, the standard error on V-magnitude, σ_V, increases with the magnitude. This is also true for B or I-magnitudes. Hence the errors on $(B - V)$ or $(V - I)$ colors rapidly increase and reach values as large as 0.2 mag around a V-mag ~ 20: this is of the same order as the Main Sequence width.

As we are interested in the MS structure and as we must minimize error effects while keeping quite good statistics, we have chosen to take into account only data with σ_V and σ_B (or σ_I) lower or equal to 0.015 mag, leading to a maximum error on color of 0.02 mag. The value of 0.015 mag appears to be an optimal choice maintaining a good statistics with photometric errors remaining small compared with the MS width. Figure 1 sketches the proposed selection process and displays differences between the entire Color-Magnitude Diagram (Fig. 1a) and the final diagram (Fig. 1c): obviously, the remaining data are those corresponding to lower magnitudes.

This selection process leaves ~4700 objects on the SMC MS (over a total of more than 2.2 millions objects) in the BV system (~1100 objects in the VI system) and ~4000 objects on the LMC MS (over a total of more than 7.2 millions objects) in the BV system (~1600 objects in the VI system). As we can see, the BV system presents more favorable statistics, therefore in the following we will work only with this set of bands.

Tables 4 from Udalski et al. (1998, Udalski et al. 2000) indicate that completeness for $V \lesssim 18$ should be better than about 99% for the SMC; and should be around 96%−99% depending on the field crowding for the LMC.

3.2. Star count ratios: An observational constraint

As the absolute number of stars arriving on the ZAMS per unit of time for a given mass is unknown, we rather compute star count ratios. To count stars, we first define an area in the CM-diagram. As we are interested in the MS structure, we choose a region which contains the main sequence "bulge" revealed after the data selection process (see Fig. 2a) with the most convenient geometrical shape: a "parallelogram" (for automatic count purpose). A couple of opposite sides (AB and DE in Fig. 2a) are chosen to be more or less "parallel" to the main sequence axis.

In the CM-Diagram, main sequence stars evolve from the blue to the red side. The MS width is mainly an evolutionary effect connected to a characteristic time scale $\tau_{\rm MS}$ (time spent by a star on the Main Sequence). The distribution of the objects within the Main Sequence should be related to this time scale. Therefore we divide our parallelogram into two regions called "box 1" and "box 2" (see Fig. 2a) where the respective numbers of objects N_1 and N_2 are similar ($N_2/N_1 \sim 1$). This ratio is taken as an observational constraint and it will enable us to discriminate between theoretical grids of evolutionary tracks computed with various overshooting amounts.

We now turn to the method used to build a synthetic stellar sample comparable to the OGLE 2 ones (after selection) from evolution simulation outputs.

4. Population synthesis

4.1. Evolutionary models

Our evolutionary models are built with the 1D Henyey type code CESAM[1] (see Morel 1997) in which we brought several improvements. Applying modern techniques like the projection of the solutions on B-spline basis and automatic mesh refinements, CESAM allows robust, stable and highly accurate calculations. We use as physical inputs:

– the OPAL 96 opacities from Iglesias & Rogers (1996) at high temperatures ($T > 10\,000$ K) and the Alexander & Ferguson (1994) opacities for cooler domains. For metallicity higher than the solar one (that occurs during the He core

[1] CESAM: Code d'Évolution Stellaire Adaptatif et Modulaire.

Retour à la table des matières : p. v

burning phase) we use elemental opacities (Los Alamos) calculated by Magee et al. (1995);
- the EFF equation of state from Eggleton et al. (1973);
- elemental abundances are from Grevesse & Noels (1993) (the "GN93" mixture), the cosmological helium is from Izotov et al. (1997): $Y_P = 0.243$, and the helium content is scaled on the solar one following a standard helium-metallicity relation: $Y = Y_P + Z(\Delta Y/\Delta Z)$. The calibration of a solar model in luminosity yields $\Delta Y/\Delta Z = 2$ (Lebreton et al. 1999) from the calibration of the solar model radius. This value is compatible with the recent value $\Delta Y/\Delta Z = 2.17 \pm 0.40$ of Peimbert et al. (2000). We therefore adopt $\Delta Y/\Delta Z \approx 2$;
- for the chemical composition we adopt [Fe/H] derived from Cepheid measurements by Luck et al. (1998):
  - for the SMC they find a range from −0.84 to −0.65 with a mean value: [Fe/H] = −0.68 which leads to $X_0 = 0.745$, $Y_0 = 0.251$ and $Z_0 = 0.004$.
  - for the LMC they find a range from −0.55 to −0.19, combining all the values we obtain a mean value of [Fe/H] = −0.34 leading to: $X_0 = 0.733$, $Y_0 = 0.259$ and $Z_0 = 0.008$;
- The nuclear reaction rates are from Caughlan & Fowler (1988), except: $^{12}C(\alpha,\gamma)^{16}O$, $^{17}O(p,\gamma)^{18}F$ taken from Caughlan et al. (1985) and $^{17}O(p,\alpha)^{14}N$ taken from Landré et al. (1990). The adopted rate for $^{12}C(\alpha,\gamma)^{16}O$ is quite similar to the NACRE compilation (Angulo et al. 1999) one: a factor of about two higher than Caughlan & Fowler (1988) and about 80% of Caughlan et al.'s (1985) one.
- To take into account the metallicity effect on the mass loss rate (de Jager et al. 1988) we adopt the scaling factor $(Z_0/0.02)^{0.5}$ derived from the Kudritzki & Hummer (1986) models;
- The convective flux is computed according to the classical MLT. We use a mixing length value $l_{MLT} = 1.6\ H_P$. This value has been derived by Schaller et al. (1992) from the average location of the red giant branch of more than 75 clusters. A very similar value (1.64) has been found more recently by Lebreton et al. (1999). An extra-mixing zone is added above the Schwarzschild convective core: this "extra-mixing" zone is set to extend over the distance $l_{over} = \alpha_{over}\ H_P$, α_{over} being a free parameter, the value of which is discussed here;
- the external boundary conditions are determined in a layer within a simple grey model atmosphere built with an Eddington's $T(\tau)$ law.

4.2. Conversion of the theoretical quantities into observational ones

In order to compare theoretical results to observational data, conversions are needed. Transformations of the theoretical quantities, (M_{bol}, T_{eff}) into absolute magnitudes and colors are derived from the most recent version of the Basel Stellar Library (*BaSeL*, version 2.2), available electronically at `ftp://tangerine.astro.mat.uc.pt/pub/BaSeL/`. This library provides color-calibrated theoretical flux distributions for a large range of fundamental stellar parameters, T_{eff} (2000 to 50 000 K), $\log g$ (−1.0 to 5.5 dex), and [Fe/H] (−5.0 to +1.0 dex). The *BaSeL* flux distributions are calibrated on the stellar $UBVRIJHKL$ colors, using:

- *empirical* photometric calibrations for solar metallicity;
- *semi-empirical* relations constructed from the color differences predicted by stellar model atmospheres for non-solar metallicities.

Details about the calibration procedure are given in Lejeune et al. (1997) and Lejeune et al. (1998). Compared to the previous versions of the *BaSeL* library, all the model spectra of stars with $T_{eff} \geq 10\,000$ K are now calibrated on empirical colors from the T_{eff} versus $(B-V)$ relation of Flower (1996). In addition, the calibration procedure for the cool giant model spectra has been extended in the present models to the parameter ranges 2500 K $\leq T_{eff} <$ 6000 K and $-1.0 \leq \log g < 3.5$[2].

4.3. Population synthesis

In contrast with "classical" works on population synthesis where the CMD as a whole is simulated, we construct a small part of the CMD: the area containing the brighter MS stars. In this way the task is simplified. Artificial stellar samples have been generated from our evolutionary tracks with a specially designed population synthesis code `CReSyPS`[3].

In our framework the main hypothesis is that the Star Formation Rate (SFR) is constant during the time scales involved here: i.e. a few hundred megayears. So for a given mass the number of observed stars (i.e. those corresponding to a given evolutionary track) must be proportional to the time scale of the main sequence. We assume that the SFR is constant in time and mass (equal for all masses in the range explored in this work), if we note r the SFR: $\Delta t \approx 1/r$ represents the mean time elapsed between two consecutive star births. For the observational star samples, Δt is unknown but the objects numbers are available. We choose Δt to get similar total star numbers in boxes 1 and 2 (i.e. $N_1 + N_2$) both in the synthetic CMD and observational diagram. We point out that the ratios N_2/N_1 are not sensitive to the Δt value chosen.

The evolutionary track grids scan a mass range between 2.5 $M_\odot$ and 25 $M_\odot$ from the ZAMS to $\log T_{eff} \sim 3.8$ covering the entire box ranges in color and magnitude (defined in Sect. 3.2). The mass step is increasing from 0.5 $M_\odot$ around 3 $M_\odot$ stars to 5 $M_\odot$ above 15 $M_\odot$. Several overshooting amounts have been used from 0.0 to 0.8. `CReSyPS` treats the photometric errors by simulating OGLE 2 ones (see Appendix A) which is very important for our purposes. Our algorithm requires the knowledge of some input parameters: distance modulus, reddening and absorption, binarity rate, Initial Mass Function (hereafter IMF) slope and photometric errors.

[2] In the previous versions of the *BaSeL* models, we adopted T_{eff} = 5000 K and $\log g = 2.5$ as the upper limits for the calibration of giants (see Lejeune et al. 1998).

[3] Code Rennais de Synthèse de Populations Stellaires.

Retour à la table des matières : p. v

We summarize here the main steps of the algorithm:

- **STEP 1:** a mass distribution is generated between 2.5 $M_\odot$ and 25 $M_\odot$ following the Salpeter's law: $\mathrm{d}N/\mathrm{d}m \approx m^{-\alpha_{\rm Salp}}$ (see Sect. 5.4).
- **STEP 2:** for each mass, an evolutionary track is interpolated within the grid calculated by the evolutionary code. On each track, models are selected every time step Δt, which is adjusted in order to yield a total number of stars equivalent to the observed one.
- **STEP 3:** consistently with the value of the binary rate $<\beta>$ (see Sect. 5.3), objects are randomly selected to belong to a binary system and the magnitudes of these systems are calculated. Triple systems (and higher multiplicity systems) are neglected.
- **STEP 4:** distance modulus is added (and in the case of SMC a random "depth" inside the cloud) and synthetic photometric errors are attributed to magnitudes (see Appendix A).
- **STEP 5:** we use a "quality filter": objects with too large photometric errors are rejected from the synthetic sample.
- **STEP 6:** color is calculated, reddening and extinction coefficient are applied. Concerning reddening, a gaussian distribution is applied around the mean value in order to simulate object-to-object variations (see discussion in Sect. 5.2).

With the interpolation between evolutionary tracks, it is very important (particularly at low mass, i.e. 3.0 $M_\odot \lesssim M \lesssim 4.0\ M_\odot$) to reproduce the time scale $\tau_{\rm MS}$ with a good accuracy. A test at 3.25 $M_\odot$ has shown that the "interpolated time scale", $\tau_{\rm MS}^{\rm interpol}$, is very close to the calculated one (with the evolutionary code) $\tau_{\rm MS}^{\rm cal}$ with a difference not larger than about 1%. Also important are the magnitude interpolations on the Main Sequence: our tests also show a very good agreement between interpolated magnitudes and calculated ones, differences are unsignificant (about 10^{-3}–10^{-2} mag, whereas the photometric errors are much larger).

Our code intensively uses a random number generator. We have chosen an algorithm insuring a very large period about 2×10^{18} (program "**ran2**" from Press et al. 1992), which is much larger than the number of synthetized objects.

As a result, examples of synthetic samples generated by CReSyPS are displayed in Fig. 3 where the influence of overshooting is shown for both clouds.

5. Astrophysical inputs

5.1. Distance modulus

Large Magellanic Cloud. The LMC distance modulus has a key role in extragalactical distance determinations, but its value is still debated. The determinations range between "short" distance scales (i.e. Stanek et al. 1998) and "long" distance scales (i.e. Laney & Stobie 1994). Using the HIPPARCOS calibrated red clump stars, Stanek et al. (1998) found $\mu_{0,\ \rm LMC} = 18.065 \pm 0.031 \pm 0.09$ mag and Laney & Stobie (1994) from a study of Cepheids Period-Luminosity relation obtained $\mu_{0,\ \rm LMC} = 18.53$ mag with an internal error of 0.04 mag. Groenewegen & Salaris (2001) found $\mu_{0,\ \rm HV\ 2274} = 18.46 \pm 0.06$ mag from a study of the LMC-eclipsing binary system HV 2274. They indicate a LMC center distance at $\mu_{0,\ \rm LMC} = 18.42 \pm 0.07$ mag. Recently, from the DENIS survey data, Cioni et al. (2000) derived a distance modulus for the LMC of $\mu_{0,\ \rm LMC} = 18.55 \pm 0.04$ (formal) ± 0.08 (systematic) using a method based on the apparent magnitude of the tip of the red giant branch. The HST Key Project Team adopted $\mu_{0,\ \rm LMC} = 18.50 \pm 0.15$ mag (Mould et al. 2000). In order to bracket the most recent estimations, we have chosen the HST Key Project value:

$$\mu_{\rm LMC} = 18.50 \pm 0.15 \text{ mag.}$$

Van der Marel & Cioni (2001) give an order of magnitude of the depth of the LMC. They indicate small corrections to magnitude for well studied individual objects within the LMC, ranging between $\Delta\mu_{0,\ \rm LMC} = -0.013$ (SN 1987A) to $\Delta\mu_{0,\ \rm LMC} = +0.015$ (HV 2274). We neglect these corrections which have the same order of magnitude than the photometric errors.

Small Magellanic Cloud. Laney & Stobie (1994) suggest a distance modulus (based on Cepheids) of $\mu_{0,\ \rm LMC} = 18.94$ mag with an internal error of 0.04 mag; this modulus decreases by about 0.04 mag if calibrators are half-weighted. More recently Kovács (2000) (with a method based on double mode Cepheids), find $\mu_{0,\ \rm LMC} = 19.05 \pm 0.13$ mag and Cioni et al. (2000) have $\mu_{0,\ \rm LMC} = 18.99 \pm 0.03$ (formal) ± 0.08 (systematic) mag. We retain the following estimation:

$$\mu_{\rm SMC} = 18.99 \pm 0.10 \text{ mag.}$$

The SMC distance modulus only represents an average distance. Crowl et al. (2001) have evaluated the depth of the SMC along the line-of-sight by a study of populous clusters. They derived a depth between ~6 kpc and ~12 kpc; these values lead to magnitude differences of 0.2 and 0.4 mag respectively. Previous studies, see for instance Gardiner et al. (1991), show similar results with a line-of-sight SMC depth ranging between ~4–7 kpc and ~15 kpc strongly depending on the location in the SMC.

We have chosen to model the SMC depth with a gaussian distribution of distances around $\mu_{\rm SMC}$ with a standard deviation:

$$\sigma_{\rm SMC}^{\rm depth} = 0.05 \text{ mag}$$

which represents a total depth of ~8 kpc (about ~0.3 mag).

5.2. Reddening and absorption

We have to distinguish: foreground reddening $E(B-V)_{\rm MW}$ (due to material in Milky Way) and internal reddening $E(B-V)_{\rm i}$ with an origin into the Cloud itself. These quantities are expected to change along the line-of-sight. Here we model the total reddening as $E(B-V)_{\rm MW+i} = E(B-V)_{\rm MW} + E(B-V)_{\rm i}$ taking into account its non-uniformity. From the literature, we derive estimations for the mean value and the dispersion of $E(B-V)_{\rm MW+i}$, object-to-object variations can then be simulated.

We now discuss reddening determinations for the SMC and LMC. From a study of spectral properties of galactic nuclei behind the Magellanic Clouds, Dutra et al. (2001) have evaluated the foreground and background reddenings for both Clouds.

Retour à la table des matières : p. v

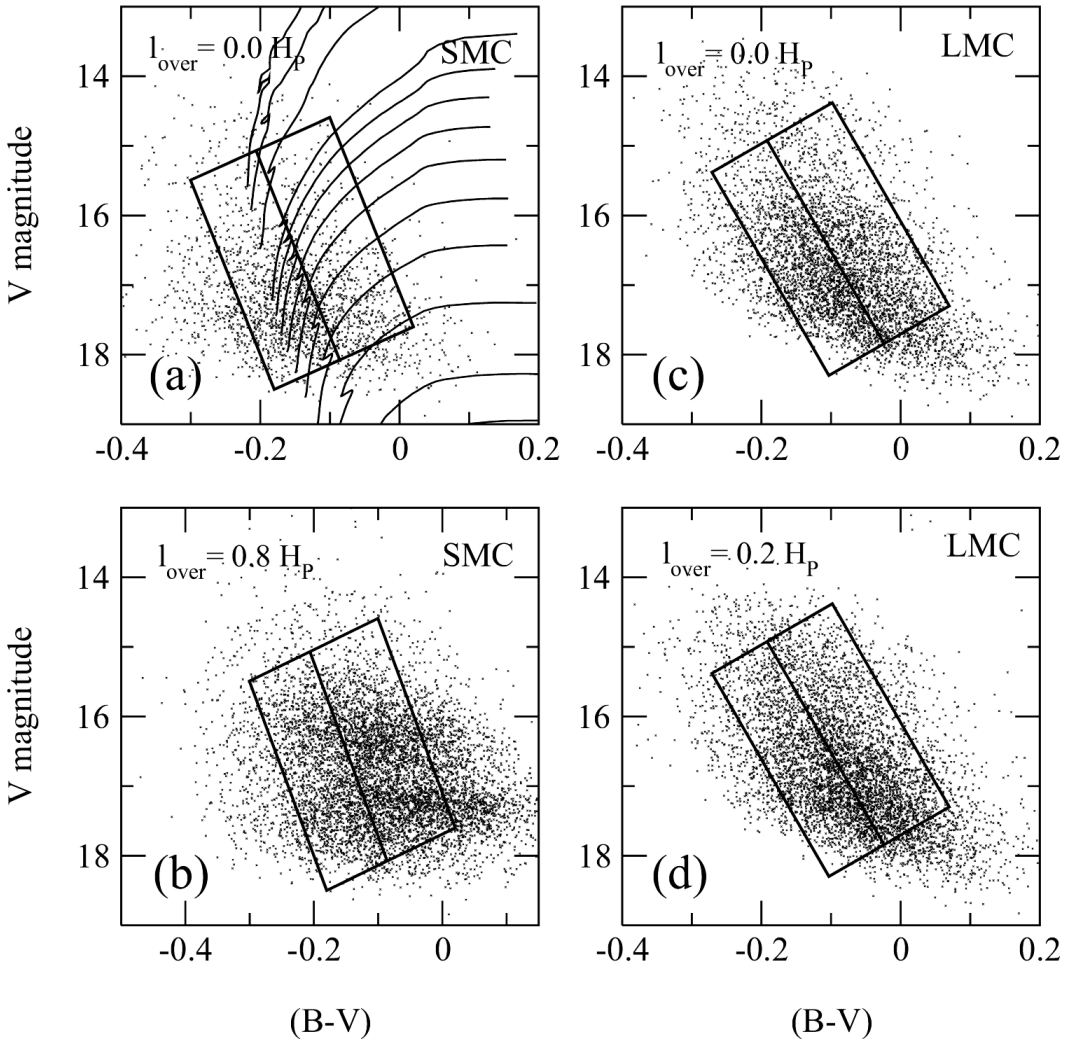

Fig. 3. Synthetic CM-Diagrams for SMC and LMC chemical compositions, panels **a)** and **b)** are for the SMC with two overshooting amounts: $\alpha_{\rm over} = 0.0$ and $\alpha_{\rm over} = 0.8$, panels **c)** and **d)** are for the LMC with: $\alpha_{\rm over} = 0.0$ and $\alpha_{\rm over} = 0.2$ respectively. For panel **a)** only 30% of the synthetic objects have been displayed for clarity purpose and corresponding evolutionary tracks have been plotted. For other panels: **b)–d)** the number of displayed objects has not be reduced. In all cases the total number of stars in the boxes -used for calculations- is close to the observational one: **a)** $N_1 + N_2 = 4403$ ($N_2/N_1 = 0.65$), **b)** $N_1 + N_2 = 5011$ ($N_2/N_1 = 1.59$), **c)** $N_1 + N_2 = 3582$ ($N_2/N_1 = 0.94$), **d)** $N_1 + N_2 = 4717$ ($N_2/N_1 = 1.13$). We recall that empirically we got for the SMC $N_1 + N_2 = 4653$ ($N_2/N_1 = 1.08$) and for the LMC $N_1 + N_2 = 4113$ ($N_2/N_1 = 1.01$). The ratios N_2/N_1 obtained theoretically are rather independant from the value of $N_1 + N_2$ in the synthetic CM-Diagram, for instance in the case of the panel **b)** we got $N_2/N_1 = 1.60$ with $N_1 + N_2 = 6399$. The cloud of dots in panel **b)** ($l_{\rm over} = 0.8$ H_P, SMC) calls a comment: it appears to be bimodal, i.e. showing over-populated regions around $V \sim 17.5$ mag and $V \sim 16.3$ mag. Indeed for high overshooting values the main sequence of masses as small as ~ 3 $M_\odot$ can reach $V \sim 17.5$ generating with their large evolutionary time scale an over-populated region. Moreover the binarity shifts a part of this population to a $\sim$0.8 mag brighter region, with a binarity rate $\beta = 0.0$, this "bimodal effect" disappears.

For the LMC, they found an average spectroscopic reddening of $E(B-V)_{\rm MW+i} = 0.12 \pm 0.10$ mag. The uncertainties essentially come from the determination of the stellar populations belonging to background galaxies: in the case of LMC, when Dutra et al. (2001) consider only red population galaxies, they find $E(B-V)_{\rm MW+i} = 0.15 \pm 0.11$ mag, which gives an idea of the global uncertainty on $E(B-V)$, which should be around $\sim$0.02–0.03 mag (about $\sim$13–20%). For the SMC Dutra et al. (2001) find $E(B-V)_{\rm MW+i} = 0.05 \pm 0.05$ mag. The OGLE 2 project provides reddening for each Cepheid star discovered in both Clouds. OGLE values are: $E(B-V)_{\rm MW+i} = 0.09 \pm 0.01$ (SMC) and $E(B-V)_{\rm MW+i} = 0.15 \pm 0.02$ (LMC). In Fig. 4 we have displayed the histogram of $E(B-V)_{\rm MW+i}$ values from Dutra et al. (2001) and OGLE group. OGLE data have a better statistics with respectively 1333 (SMC) and 2049 (LMC) objects, against 14 (SMC) and 22 (LMC) for Dutra et al. (2001). Dutra et al's data are systematically less red; this could be inherent to their method: they observed objects behind Clouds

Retour à la table des matières : p. v

and observations are easier through the more transparent regions of the clouds.

In addition, Oestreicher et al. (1995) have determined the reddening for 1503 LMC foreground stars with a UBV photometry based method: $E(B-V)_{\rm MW} = 0.06 \pm 0.02$ mag, a quite low value because it is related to foreground stars. It shows a spread (0.02) similar to the OGLE 2 one. Oestreicher et al.'s (1995) distribution is in very good agreement (see Fig. 4b) with Dutra et al.'s one, which tends to confirm that Dutra et al.'s result could be underestimated (Dutra et al.'s results are supposed to take account foreground and internal reddeing). Therefore in the case of LMC, we prefer to retain the OGLE average value for purpose of consistency:

$$\langle\, E(B-V)^{\rm LMC}_{\rm MW+i} \,\rangle = 0.15 \text{ mag.}$$

Figure 4b shows that the distribution shape is the same for Dutra et al. (2001) and Oestreicher et al. (1995), the OGLE one being quite narrow which appears slightly underestimated, thus we take a value similar to Dutra et al. one:

$$\sigma^{\rm LMC}_{E(B-V)_{\rm MW+i}} = 0.08 \text{ mag.}$$

We take into account an additional uncertainty on $\langle\, E(B-V)^{\rm LMC}_{\rm MW+i} \,\rangle$ of about:

$$\delta^{\rm LMC}_{E(B-V)} = 0.02 \text{ mag.}$$

The SMC case is more questionable (we only have two sets of data), we favor the OGLE values because they are likely more suitable for performing simulations which synthesize OGLE data. Moreover OGLE data have larger statistics. We adopt:

$$\langle\, E(B-V)^{\rm SMC}_{\rm MW+i} \,\rangle = 0.09 \text{ mag}$$

with a crudely estimated uncertainty of about:

$$\delta^{\rm SMC}_{E(B-V)} = 0.015 \text{ mag.}$$

In this case also, the OGLE standard deviation (see Fig. 4a) seems to be low, therefore we adopt the Dutra et al. (2001) one:

$$\sigma^{\rm SMC}_{E(B-V)_{\rm MW+i}} = 0.05 \text{ mag.}$$

The absorption coefficient is taken from Schlegel et al. (1998):

$$A_V = 3.24 \times E(B-V)_{\rm MW+i}$$

and is calculated for each object.

5.3. Binary rate

Evaluating the average binary rate $<\beta>$ in objects as extended as the Magellanic Clouds is not easy. Locally (i.e. within a particular area of the galaxy) this multiplicity rate depends – at least – on two factors: (1) the star density and the kinematics of the objects which influence the encounter probability; (2) the initial binary rate (relative number of binaries on the ZAMS). Within the Magellanic Clouds, the binary rate likely varies over a wide range and we only consider its spatial average value $<\beta>$.

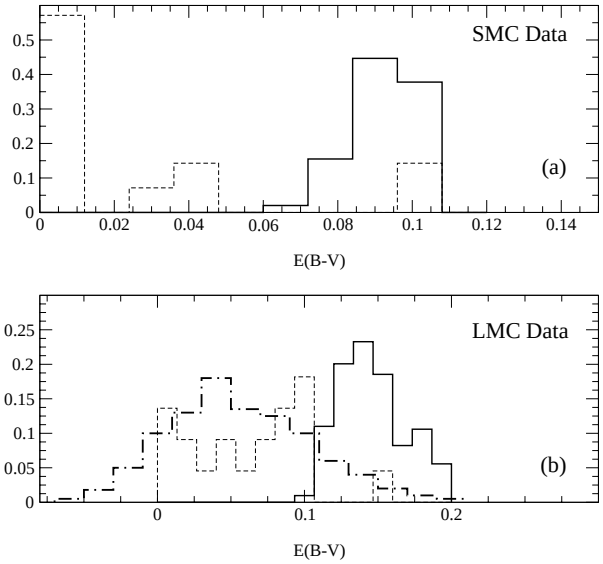

Fig. 4. Relative number of stars $N_{\rm stars}/N_{\rm tot}$ versus reddening from Dutra et al. (2001) (dashed curve), OGLE 2 experiment Cepheid catalogue: see Udalski et al. (1999) and Udalski et al. (1999), and data read in Fig. 24 of Oestreicher et al. (1995) (dot-dashed curve). **a)** Data for SMC, **b)** data for LMC.

Ghez (1995) finds in the solar neighbourhood that for main sequence stars and young stars the binary rate $<\beta>$ ranges between 0.10 and 0.50 (it peaks at $<\beta> = 0.50$). Therefore we tested the effects of binarity for these two extreme values.

In our population synthesis code, binaries are taken into account with a uniform probability for the mass ratio $q = M_2/M_1$ (in the considered mass range).

5.4. IMF slope

The IMF has been extensively discussed by many authors. Toward both Galactic poles and within a distance of 5.2 pc from the Sun, Kroupa et al. (1993) found a mass function: $\mathrm{d}N/\mathrm{d}m \approx m^{-\alpha_{\rm Salp}}$ with $\alpha_{\rm Salp} \approx 2.7$ for stars more massive than 1 $M_\odot$. In the LMC, Holtzman et al. (1997) inferred – from HST observations – a value consistent with the Salpeter (1955) one: $\alpha_{\rm Salp} \approx 2.35$. At very low metallicity, Grillmair et al. (1998) observed the Draco Dwarf spheroidal Galaxy ([Fe/H] ≈ -2) with the HST. They concluded that the Salpeter IMF slope remains valid in the Magellanic Clouds and we have chosen:

$$\alpha_{\rm Salp} = 2.30 \pm 0.30.$$

However we must keep in mind that some circularity in work exists when using an IMF. As described by Garcia & Mermilliod (2001) the IMF can be derived from the observed Present Day Mass Function (PDMF) using evolutionary tracks and their corresponding time scales which depend on the adopted value for the overshooting!

Retour à la table des matières : p. v

5.5. Star formation rate

For a given mass, the Star Formation Rate (SFR) represents the number of stars "created" per unit of time. Vallenari et al. (1996) have studied three stellar fields of the LMC and have found a time scale of about ∼2–∼4 Gyr for the "bulk of star formation". We therefore make the reasonable assumption that the SFR remained quite constant during the short galactic period relevant for this work, i.e. for the last ∼300 Myr. The SFR involved here is an average value over each cloud.

6. Resulting overshooting amounts

6.1. Large Magellanic Cloud

As a first step we choose the mean values for each astrophysical input (discussed in Sect. 5), this yields for the LMC the following overshooting:

$l_{\rm over} = 0.09\ {\rm H_p}$

which is a rather mild amount. We examine in Fig. 5 how the $l_{\rm over}$-value is affected by the uncertainties on the astrophysical inputs:

- Changing the IMF slope $\alpha_{\rm Salp}$ in the range 2.0−2.6 we obtain:

  $0.02 \lesssim\ l_{\rm over}^{\rm Salp}\ \lesssim 0.09\ {\rm H_p}$

  which tends to minimize the overshooting.
- Next, a test with the average binary rate $< \beta >$ in the range 0.10 − 0.50 leads to:

  $0.00 \lesssim\ l_{\rm over}^{<\beta>}\ \lesssim 0.14\ {\rm H_p}.$
- A distance modulus value in the range $18.35 \lesssim \mu_{\rm LMC} \lesssim 18.65$ enables us to derive: $l_{\rm over} = 0.0\ {\rm H_p}$ (in fact for $\mu_{\rm LMC} = 18.35$ all the values for simulated N_2/N_1 are larger than the observed one) and $l_{\rm over} = 0.21\ {\rm H_p}$ for $\mu_{\rm LMC} = 18.65$.
- An average reddening between 0.13 and 0.17 leads respectively to $l_{\rm over} = 0.0\ {\rm H_p}$ (in this case also all the values for simulated N_2/N_1 are larger than the observed one) and $l_{\rm over} = 0.27\ {\rm H_p}$.

We stress that uncertainties on distance modulus and reddening infer the largest uncertainties on the final overshooting values. We retain for the LMC average chemical composition:

$l_{\rm over}^{\rm LMC} = 0.10^{+0.17}_{-0.10}\ {\rm H_p}$

which indicates that a mild overshooting amount around ∼0.1−0.2 $\rm H_p$ is needed to model LMC stars as found in the majority of determinations involving solar chemical composition objects (see Sect. 1).

6.2. Small Magellanic Cloud

For the SMC, using the mean value of each astrophysical inputs we obtain (see also Fig. 5):

$l_{\rm over} = 0.41\ {\rm H_p}.$

- If the IMF slope varies between extreme values ($-2.0 \lesssim \alpha_{\rm Salp} \lesssim -2.6$), the overshooting varies within the following boundaries:

  $0.36 \lesssim\ l_{\rm over}^{\rm IMF}\ \lesssim 0.50\ {\rm H_p}$

  similarly, an average binary rate ranging between 0.10 and 0.50 leads to:

  $0.34 \lesssim\ l_{\rm over}^{<\beta>}\ \lesssim 0.45\ {\rm H_p}.$
- The uncertainty on SMC distance modulus ($18.89 \lesssim \mu_{\rm SMC} \lesssim 19.09$) leads to:

  $0.37 \lesssim\ l_{\rm over}^{\mu}\ \lesssim 0.46\ {\rm H_p}.$
- Similarly if one considers the uncertainty on the average reddening ($< E(B-V) >$ ranging between 0.075 and 0.105), the overshooting amount shows a high sensitivity to reddening:

  $0.36 \lesssim\ l_{\rm over}^{E(B-V)}\ \lesssim 0.52\ {\rm H_p}.$

Again, uncertainties on distance modulus and reddening are the largest. We retain for the SMC:

$l_{\rm over}^{\rm SMC} = 0.40^{+0.12}_{-0.04}\ {\rm H_p}.$

Whatever the simulation is, statistical errors are of the order of 0.01 $\rm H_p$ which can be safely neglected. In the SMC case, the required overshooting appears to be much larger than for LMC stars and for solar composition stars.

7. Discussion

7.1. An upper limit with Roxburgh's criterion

Roxburgh's criterion (Roxburgh 1989) is a very general constraint on the size of the convective core. It is written as an integral formulation over the stellar core radius:

$$\int_{r=0}^{r=R_{\rm core}} (L_{\rm rad} - L_{\rm nuc}) \frac{1}{T^2} \frac{{\rm d}T}{{\rm d}r} {\rm d}r = \int_{r=0}^{r=R_{\rm core}} \frac{\Phi}{T} 4\pi r^2 {\rm d}r \qquad (1)$$

where $L_{\rm rad}$ and $L_{\rm nuc}$ are respectively the radiative energy flux and the total energy flux (in $\rm J\,s^{-1}$) generated by nuclear processes, r is the radius, $R_{\rm core}$ is the core size including the "overshooting" region. Φ represents the viscous dissipation (in $\rm J\,s^{-1}\,m^{-3}$). In the whole stellar convective core the turbulence is supposed to be statistically stationary and the temperature gradient has to be almost adiabatic. In Eq. (1) the integrand is positive when r is lower than the Schwarzschild boundary where $L_{\rm rad} = L_{\rm nuc}$ and it becomes negative beyond.

The viscous dissipation Φ is unknown but the integral constraint is satisfied for larger $R_{\rm core}$ value when $\Phi = 0$. Hence, neglecting the dissipation by setting $\Phi = 0$ provides the maximum possible extent of the convective core which can be considered as the upper limit for overshooting. Evolutionary tracks have been calculated, using Roxburgh's criterion, for a representative mass of 6 $M_\odot$ and SMC and LMC metallicities. The equivalent overshooting amount (EOA), given in Table 1, is the time weighted average overshooting distance along the evolutionary tracks, expressed in pressure scale height.

Retour à la table des matières : p. v

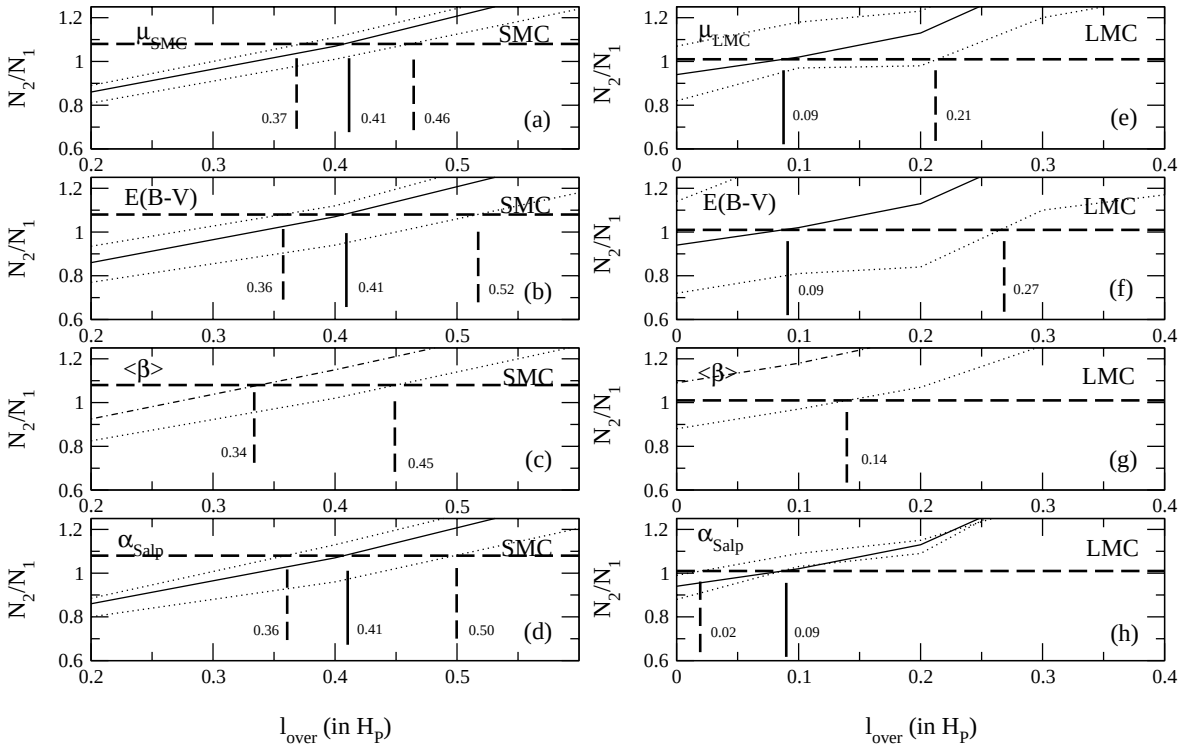

Fig. 5. Overshooting determinations for SMC (panels **a**–**d**)) and LMC (panels **e**–**h**)). The influence of distance modulus, reddening and IMF slope are considered for each cloud: continuous lines correspond to central values of these parameters discussed in Sect. 5 and dashed lines to the associated error bars. Inferred values of l_{over} (and uncertainties) are given on each figure. For **c)** and **g)** panels, dotted line is for $< \beta > = 0.0$ and dot-dashed for $< \beta > = 0.5$ (see text).

Table 1. Time weighted average overshooting distances for a 6 $M_\odot$ main sequence model, derived with the "Roxburgh's criterion" neglecting dissipative phenomenon ($\Phi = 0$).

Metallicity Z_0	0.004 (SMC)	0.008 (LMC)
Average EOA	0.6 H_p	0.6 H_p

In both cases (LMC and SMC), Roxburgh's criterion predicts a maximum value (i.e. neglecting viscous dissipation) around 0.6 H_p (see Table 1) independent from Z_0. Our determinations – i.e. $l_{over}^{SMC} = 0.40^{+0.12}_{-0.06}$ H_p and $l_{over}^{LMC} = 0.10^{+0.17}_{-0.10}$ H_p- therefore are compatible with the theoretical upper limit given by the Roxburgh's criterion.

7.2. Influence of rotation

In addition to convection, rotation is an other important phenomenon inducing mixing through shear effects and other instabilities. For instance Venn (1999) finds surface abundance variations in SMC A supergiants that could be explained by some kind of mixing related to rotation.

Taking account of the rotational effect brings new important unknown features: (1) the Ω-value distribution and (2) the $v \sin i$ distribution for the considered stellar population. Both features remain unconstrained by observational studies.

In addition, stellar rotation involves many effects and physical processes that are non-trivial to include in modern evolutionary codes. Talon et al. (1997) show that (see their Fig. 5) a rotating 1D-model with an initial surface velocity of 300 km s^{-1} leads to a main sequence track equivalent to an overshooting model using $l_{over} = 0.2$ H_p. Despite great theoretical efforts, a free parameter remains for horizontal diffusivity in Talon et al. (1997) treatment of rotational mixing (see Zahn 1992).

Rotation changes the global shape of an evolutionary track, through two distinct effects: (1) the material mixing inside the inner part of the star which brings more fuel into the nuclear burning zones like overshooting, (2) the effective surface gravity modification leading to color and magnitude changes (which depend on the angle between the line-of-sight and the rotational axis). In their Fig. 6, Maeder & Meynet (2001) show the influence of rotation on evolutionary tracks for low metallicity objects ($Z_0 = 0.004$). These tracks have been calculated taking into account: (1) an "average effect" on surface, (2) the internal mixing. These tracks are very similar to those calculated with different overshooting amounts values.

An additional effect which needs to be discussed here is the surface effect: modifications of colors and magnitudes of MS stars due to rotation (in absence of any mixing phenomenon) have been studied by Maeder & Peytremann (1970) with uniformly rotating models. Their Table 2 gives expected changes of M_V and $(B - V)$ as a function of Ω (angular velocity

Retour à la table des matières : p. v

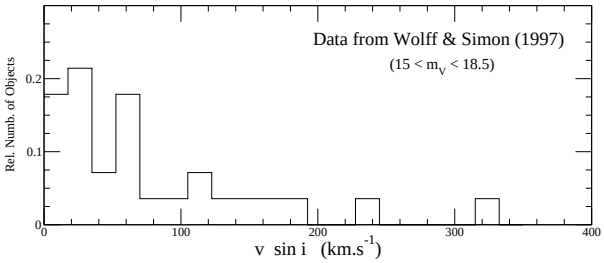

Fig. 6. Relative number of stars ($N_{\rm stars}/N_{\rm tot}$ versus $V \times \sin i$ for Wolff & Simon (1997) objects with magnitudes in our studied range.

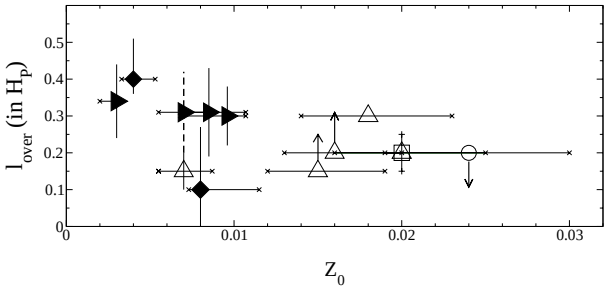

Fig. 7. Overshooting parameter $\alpha_{\rm over}$ versus metallicity Z_0 from various sources. Open triangles represent results from Ribas et al. (2000) for SZ Cen ($Z_0 \sim 0.007$) error bars have been indicated, arrows mean that the derived value is a minimum. The open square shows a result from Kozhurina-Platais et al. (1997) for the galactic cluster NGC 3680, error bars are indicated. Filled triangles are determinations from Keller et al. (2001): with continuous error bars amounts corresponding to the SMC cluster NGC 330, NGC 1818, NGC 2100 and with dashed error bars result for the LMC cluster NGC 2004. Open circle: determination in Hyades cluster from Lebreton et al. (2001) (upper limit for overshooting). Filled diamonds: SMC and LMC determinations performed in this work. Errors on Z have been evaluated assuming an internal error on [Fe/H] of 0.1 dex.

expressed in break-up velocity unit) and $v \sin i$ (this latter ranges from 0 to 457 km s^{-1}, for a 5 $M_\odot$ star). In this table standard deviation for M_V and $(B-V)$, are: $\sigma_{M_V} = 0.18$ mag and $\sigma_{(B-V)} = 0.01$ mag. Therefore the rotation effect has roughly the same order of magnitude than present uncertainties on magnitudes and colors. However, stars with $v \sin i$ greater than ~200 km s^{-1} are quite rare, as shown by the data of Wolff & Simon (1997) (see Fig. 6). Then keeping only data with $v \sin i \lesssim 200$ km s^{-1}, leads to: $\sigma_{M_V} = 0.20$ mag and $\sigma_{(B-V)} = 0.001$ mag. The effect on absolute magnitude remains of the same order, whereas the effect on color becomes largely negligible. We conclude that our results remain valid, even if the major mixing is due to rotation. In this case, the value of $l_{\rm over}$ would change its meaning. Major contribution to $l_{\rm over}$ value would represent a shear effect mixing.

7.3. Influence of chemical composition gradient

We have sofar assumed a uniform chemical composition. The chemical composition may vary inside each Magellanic Cloud. The existence of an abundance gradient in the Clouds is still debated and spectroscopic measurements with a statistics as large as the statistics of OGLE 2 data are not available. In their Table 4, Luck et al. (1998) give spectroscopic determinations of [Fe/H] for 7 SMC Cepheids and 10 LMC Cepheids. For SMC data, the standard deviation is $\sigma^{\rm SMC}_{\rm [Fe/H]} \sim 0.07$ dex leading to negligible variations for the heavy elements mass fraction Z_0. Therefore the SMC can be considered as chemically homogeneous for our purpose. For LMC, Luck et al. (1998) find a standard deviation $\sigma^{\rm LMC}_{\rm [Fe/H]} \sim 0.10$ dex giving $0.007 \lesssim Z_0 \lesssim 0.01$. From evolutionary tracks of typical mass (6 $M_\odot$) and an overshooting of 0.1 H_P, changing Z_0 from 0.007 to 0.01 has a negligible effect on magnitude and an effect of ~0.003 mag on color, which is largely lower than the photometric errors. We conclude that – in the light of the present knowledge – the chemical composition gradient does not change our results significantly.

7.4. Comparison with other works

From the investigation of young clusters in the Magellanic Clouds, Keller et al. (2001) did not find any noticeable overshooting dependence with metallicity. They obtained for NGC 330 ($Z_0 \sim 0.003$) $l^{\rm NGC\ 330}_{\rm over} = 0.34 \pm 0.10$ H_p, which is compatible with our determination for the SMC: $l^{\rm SMC}_{\rm over} = 0.40^{+0.12}_{-0.04}$ H_p. For NGC 2004 ($Z_0 \sim 0.007$) Keller et al. (2001) got $l^{\rm NGC\ 2004}_{\rm over} = 0.31 \pm 0.11$ H_p; while for similar metallicity we derived $l^{\rm LMC}_{\rm over} = 0.10^{+0.17}_{-0.10}$ H_p which is also compatible with Keller et al.'s result. One can note that masses involved in our simulations (average mass of ~7−8 $M_\odot$ with a standard deviation of 4 $M_\odot$) are higher than the Keller et al. (2001) one (terminus masses in the range 9−12 $M_\odot$ for the four clusters). Keller et al. (2001) do not discuss the influence of the uncertainty on distance modulus of the clusters and use $\mu_{\rm LMC} = 18.45$ mag and $\mu_{\rm SMC} = 18.85$ mag.

Ribas et al. (2000) derive overshooting amounts from evolutionary models of galactic binary systems. For SZ Cen ($Z_0 \sim 0.007$) they find $0.1 \lesssim l_{\rm over} \lesssim 0.2$ H_p which is close to our value for the LMC, but the mass of SZ Cen is 2.32 $M_\odot$ and some mass effect cannot be avoided, therefore any comparison with the present results must be considered with care. In Fig. 7 we summarize results from several authors. Despite the small number of points, a slight dependence of overshooting with metallicity cannot be excluded. However, at low and high metallicities, the considered mass ranges are different and the errors remain substantial, therefore a definite conclusion is not yet possible.

8. Conclusion

In this paper we have estimated the overshooting distance from a turbulent core for intermediate-mass main sequence stars. The result for SMC is $l^{\rm SMC}_{\rm over} = 0.40^{+0.12}_{-0.06}$ H_P, and for the LMC $l^{\rm LMC}_{\rm over} = 0.10^{+0.17}_{-0.10}$ H_P. The main contributions to errors are those brought by distance modulus and reddening uncertainties. We have shown that chemical gradients within the clouds and rotation surface effects of studied stars cannot significantly influence our results. Binary rate and IMF slope have no important effects as well. For SMC, despite different methods and data, we find a result very similar to Keller et al.'s (2001) one for

Retour à la table des matières : p. v

cluster NGC 330. The case of LMC is more questionable because of the rather large uncertainty on reddening.

Figure 7 tends to indicate a sensitivity of overshooting to metallicity. However a mass effect cannot be excluded; we can only stress that if such a dependence exists, it should be an increase of overshooting with decreasing metallicity. However, the overshooting is expected to increase with mass, unfortunately samples studied at solar metallicity have often lower masses than those at low metallicities. Therefore further investigations are needed to disentangle these effects. In any cases, if this dependence is confirmed the next challenge will be the physical explanation of this metallicity-overshooting effect.

Finally, the overshooting amounts derived in this work have a statistical meaning: they are average values over time (in real stars, "overshooting" likely changes during the main sequence) and over mass in the considered range. Moreover these amounts represent an extramixing above the classical core generated either by inertial penetration of convective bubbles or shear phenomena related to rotation. The real extent of the core likely results from a combination of both processes; indeed, rotating models Maeder & Meynet (2001)'s rotating models still need overshooting.

Acknowledgements. We thank Jean-Paul Zahn and Ian Roxburgh for helpful discussions; we are also grateful to the OGLE group for providing their data and to Pierre Morel for writing the CESAM code. We thank the referee Dr. S. C. Keller for valuable remarks and suggestions.

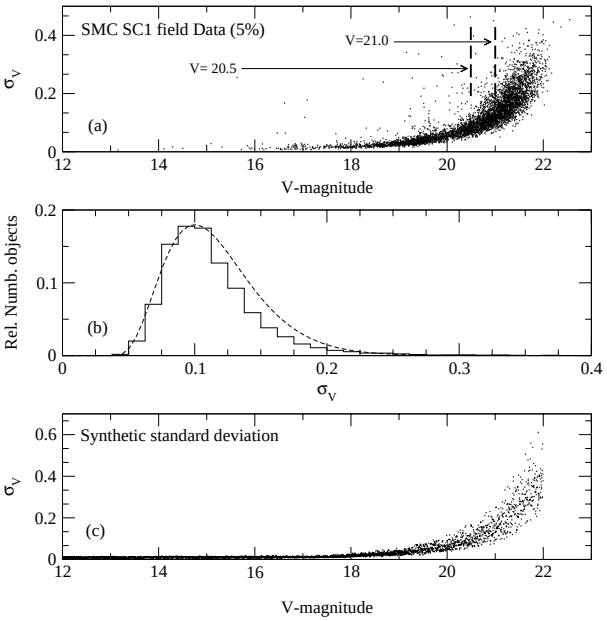

Fig. A.1. a) Standard deviation σ_V versus V-magnitude for objects belonging to the SC1 field of the SMC. **b)** Histogram of the σ_V values for magnitude V between 20.5 and 21.0, the fit (dashed curve) is performed with a function of a type given in the text. Differences between the fit and the histogram are clearly insignificant for our purpose. **c)** Synthetic σ_V distribution generated with our algorithm.

Appendix A: Photometric error simulations

As we selected the data using a criterion involving the photometric standard deviation of magnitude measurements, we have to generate an artificial standard deviation for the theoretical magnitude computed from evolutionary models. Moreover the general properties of the synthetic standard deviation distribution must be similar to the OGLE 2 one.

We describe here the scheme used to generate the pseudo-synthetic photometric standard error distributions. The prefix "pseudo" means that we have extracted information about the standard error distribution from the OGLE 2 data themselves (see Fig. A.1a). For that purpose, we divide the relevant range of magnitudes into bins; in each bin, we construct the histogram of standard deviation values (Fig. A.1b). This histogram then is fitted with a function of the form:

$$P(\sigma) = a \times (\sigma - \sigma_{\min})^4 \times \mathrm{e}^{-b(\sigma-\sigma_{\min})}$$

where the constants a, b, σ, $\sigma_{\min}$ are derived from the OGLE 2 data. $P(\sigma)$ represents the probability for having the standard deviation σ. The constants have been derived for each "magnitude bin", for each OGLE fields in SMC and LMC. Then average values have been calculated over SMC and LMC.

In our population synthesis code, for a given magnitude value m, a standard deviation value σ_m is randomly determined following the probability law derived from OGLE. After that, either the object is rejected (if the σ_m value is too large) or the magnitude m is changed into m^{noisy}, following a gaussian distribution having a standard deviation σ_m.

Let us comment about differences between Figs. A.1a and A.1c. Figure A.1a contains the "evolutionary information" – i.e. more objects at high magnitudes- whereas Fig. A.1c does not contain this information, objects have been uniformly distributed with respect to the magnitude. These facts explain the difference between both figures.

References

Alexander, D., & Ferguson, J. 1994, ApJ, 437, 879
Alongi, M., Bertelli, G., Bressan, A., & Chiosi, C. 1991, A&A, 244, 95
Andersen, J. 1991, A&AR, 3, 91
Angulo, C., Arnould, M., Rayet, M., et al. 1999, Nucl. Phys. A, 656, 3
Bertelli, G., Bressan, A., Chiosi, C., Fagatto, F., & Nasi, E. 1994, A&AS, 106, 275
Böhm-Vitense, E. 1958, Zs. f. Ap., 46, 135
Bressan, A. G., Chiosi, C., & Bertelli, G. 1981, A&A, 102, 25
Caughlan, G., & Fowler, W. 1988, Atomic Data Nuc. Data Tables, 40, 283
Caughlan, G., Fowler, W., Harris, M., & Zimmerman, B. 1985, Atomic Data Nuc. Data Tables, 32, 197
Charbonnel, C., Meynet, G., Maeder, A., & Schaerer, D. 1996, A&AS, 115, 339
Cioni, M.-R. L., Van der Marel, R. P., Loup, C., & Habing, H. J. 2000, A&A, 359, 601
Crowl, H. H., Sarajedini, A., Piatti, A., et al. 2001, AJ, 122, 220

Retour à la table des matières : p. v

de Jager, C., Nieuwenhuijzen, H., & van der Hucht, K. A. 1988, A&AS, 72, 259
Dutra, C. M., Bica, E., Clariá, J. J., Piatti, A. E., & Ahumada, A. V. 2001, A&A, 371, 895
Eggleton, P., Faulkner, J., & Flannery, B. 1973, A&A, 23, 325
Flower, P. J. 1996, ApJ, 469, 355
Garcia, B., & Mermilliod, J. C. 2001, A&A, 368, 122
Gardiner, L. T., Hatzidimitriou, D., & Hawkins, M. R. S. 1991, Proc. Astron. Soc. Austr., 9, 80
Ghez, A. 1996, in Evolutionary processes in Binary Stars, ed. R. A. M. J. Wijers, M. B. Davis, & C. A. Tout (Kluwer Academic Publishers), 1
Grevesse, N., & Noels, A. 1993, in Origin and Evolution of the Elements, ed. V.-F. E. Prantzos N., & C. M. (Cambridge University Press, Cambrigge), 14 (GN'93)
Grillmair Truc, T., & Truc, T. 1998, AJ, 115, 144
Groenewegen, M. A. T., & Salaris, M. 2001, A&A, 366, 752
Holtzman, Truc, T., & Truc, T. 1997, AJ, 113, 656
Iglesias, C. A., & Rogers, F. J. 1996, ApJ, 464, 943 (OPAL 96)
Iwamoto, N., & Saio, H. 1999, ApJ, 521, 297
Izotov, Y., Thuan, T., & Lipovetsky, V. 1997, ApJS, 108, 1
Keller, S. C., Da Costa, G. S., & Bessell, M. S. 2001, AJ, 121, 905
Kovács, G. 2000, A&A, 363, L1
Kozhurina-Platais, V., Demarque, P., Platais, I., Orosz, J. A., & Barnes, S. 1997, AJ, 113, 1045
Kroupa, P., Tout, C., & Gilmore, G. 1993, MNRAS, 262, 545
Kudritzki, R., & Hummer, D. 1986, in IAU Symp. 116, Luminous Stars and Associations in Galaxies, ed. P. L. C. de Loore, & A. J. Willis, 3
Landré, V., Prantzos, N., Aguer, P., et al. 1990, A&A, 240, 85
Laney, C. D., & Stobie, R. S. 1994, MNRAS, 266, 441
Lebreton, Y., Fernandes, J., & Lejeune, T. 2001, A&A, 374, 540
Lebreton, Y., Perrin, M.-N., Cayrel, R., Baglin, A., & Fernandes, J. 1999, A&A, 350, 587
Lejeune, T., Cuisinier, F., & Buser, R. 1997, A&AS, 125, 229
Lejeune, T., Cuisinier, F., & Buser, R. 1998, A&AS, 130, 65
Luck, R. E., Moffett, T. J., Barnes, T. G., & Gieren, W. P. 1998, AJ, 115, 605
Maeder, A., & Mermilliod, J. 1981, A&A, 93, 136
Maeder, A., & Meynet, G. 2001, A&A, 373, 555
Maeder, A., & Peytremann, E. 1970, A&A, 7, 120
Magee, N. H., Abdallah, J. Jr., Clark, R. E. H., et al. 1995, in Atomic Structure Calculations and New Los Alamos Astrophysical Opacities, ed. S. Adelman, & W. Wiese, vol. 78 (Astronomical Society of the Pacific Conf. Ser. (Astrophysical Applications of Powerful New Database)), 51
Massaguer, J. 1990, in Rotation and Mixing in Stellar Interiors, ed. M.-J. Goupil, & J.-P. Zahn (Springer, Berlin, Heidelberg, New York), 129
Mermilliod, J.-C., & Maeder, A. 1986, A&A, 158, 45
Morel, P. 1997, A&AS, 124, 597
Mould, J. R., Huchra, J. P., Freedman, W. L., et al. 2000, ApJ, 529, 786
Oestreicher, M. O., Gochermann, J., & Schmidt-Kaler, T. 1995, A&AS, 112, 495
Peimbert, M., Peimbert, A., & Ruiz, M. 2000, ApJ, 541, 688
Press, W., Teukolsky, S., Vetterling, W., & Flannery, B. 1992, Numerical Recipes in Fortran 77 (Cambridge University Press)
Ribas, I., Jordi, C., & Giménez, Á. 2000, MNRAS, 318, L55
Rogers, F. J., & Iglesias, C. A. 1992, ApJS, 79, 507
Roxburgh, I. 1989, A&A, 211, 361
Salpeter, E. 1955, ApJ, 121, 161S
Schaller, G., Schaerer, D., Meynet, G., & Maeder, A. 1992, A&AS, 96, 269
Schlegel, D. J., Finkbeiner, D. P., & Davis, M. 1998, ApJ, 500, 525
Schröder, K., Pols, O. R., & Eggleton, P. P. 1997, MNRAS, 285, 696
Stanek, K. Z., Zaritsky, D., & Harris, J. 1998, ApJ, 500, L141
Stothers, R. B., & Chin, C. 1991, ApJ, 381, L67
Talon, S., Zahn, J.-P., Maeder, A., & Meynet, G. 1997, A&A, 322, 209
Udalski, A., Soszynski, I., Szymanski, M., et al. 1999a, Acta Astron., 49, 223
Udalski, A., Soszynski, I., Szymanski, M., et al. 1999b, Acta Astron., 49, 437
Udalski, A., Szymański, M., Kubiak, M., et al. 1998, AcA, 48, 147
Udalski, A., Szymański, M., Kubiak, M., et al. 2000, AcA, 50, 307
Vallenari, A., Chiosi, C., Bertelli, G., Aparicio, A., & Ortolani, S. 1996, A&A, 309, 367
Van der Marel, R. P., & Cioni, M. L. 2001, AJ, 122, 1807
Venn, K. 1999, ApJ, 518, 405
Wolff, S., & Simon, T. 1997, PASP, 109, 759
Zahn, J. 1991, A&A, 252, 179
Zahn, J.-P. 1992, A&A, 265, 115

Retour à la table des matières : p. v

14.2 Article sur les céphéides du SMC

A&A 409, 491–501 (2003)
DOI: 10.1051/0004-6361:20031185
© ESO 2003

Astronomy & Astrophysics

The faint Cepheids of the Small Magellanic Cloud: An evolutionary selection effect?

D. Cordier[2,3], M. J. Goupil[1], and Y. Lebreton[2]

[1] LESIA, Observatoire de Paris-Meudon, 92195 Meudon Principal Cedex, France
[2] GEPI, Observatoire de Paris-Meudon, 92195 Meudon Principal Cedex, France
[3] École Nationale Supérieure de Chimie de Rennes, Campus de Beaulieu, 35700 Rennes, France

Received 21 November 2002 / Accepted 8 July 2003

Abstract. Two problems concerning the faintest Small Magellanic Cloud (SMC) Cepheids are addressed. On the one hand evolutionary tracks fail to cross the Cepheid Instability Strip for the highest magnitudes (i.e. I-mag ~ 17) where Cepheids are observed; mass–luminosity relations (ML) obtained from evolutionary tracks disagree with mass–luminosity relations derived from observations. We find that the above failures concern models built with standard input physics as well as with non-standard ones. The present work suggests that towards highest magnitudes, Cepheids stars undergo a selection effect caused by evolution: only the most metal poor stars cross the Instability Strip during the "blue loop" phase and are therefore the only ones that can be observed at low luminosity. This solution enables us to reproduce the shape of the lower part of the Instability Strip and improves the agreement between observed and theoretical ML-relations. Some issues are discussed, among them Beat Cepheid results that argue strongly in favor of our hypothesis.

Key words. galaxies: Magellanic Clouds – stars: evolution – stars: variables: general

1. Introduction

Cepheids are variable stars located in the color-magnitude diagram (CM-diagram) within the Instability Strip (IS) where pulsation phenomena take place via the κ-mechanism. Cepheid masses range between ~3 $M_\odot$ and ~15 $M_\odot$. During the past decade, microlensing experiments such as MACHO[1], EROS[2], MOA[3] or OGLE[4] have produced a huge flow of data. As by-products of these observational programs, a large number of new variable stars, and among them, Cepheids have been detected. OGLE 2 data provide a large and high quality sample of Cepheids belonging to the Small Magellanic Cloud (SMC) which we consider in this work. This extended and homogeneous data set has already brought several shortcomings of the SMC Cepheid modeling to light:

(1) The evolutionary tracks built with standard input physics and for a chemical composition $Z_0 = 0.004$ ($Y_0 = 0.251$) as usually assumed for the SMC fail to reproduce the observed Cepheid position within the CM-diagram for highest magnitudes (i.e. ~17 mag).

(2) The mass–luminosity relation (ML^{puls} hereafter) derived from pulsation properties (see Beaulieu et al. 2001) and the ML-relation from evolutionary tracks (ML^{evol} hereafter) do not agree.

The first problem arises because theoretical "blue loops" do not cross the observed IS over the whole Cepheid mass range. Indeed an evolutionary track for a mass of about 5 $M_\odot$ crosses the observed IS three times, the first time ("first crossing") is the fastest one – e.g. ~0.01 Myr for a 5 $M_\odot$ model –, the second time ("second crossing") is slower – e.g. ~0.20 Myr – and the third time ("third crossing") remains short, about ~0.01 Myr. These time scale considerations tell us that the majority of the observed objects should be in the second crossing stage. During this phase, the star burns He in its inner regions. The third and second crossings both belong to the so-called "blue loop" excursion towards the blue side of Hertzsprung Russell (HR) diagram. Consequently, theoretical blue loops should cross the observed IS for the *entire* Cepheid mass range. As we confirm in the first part of this work, theoretical tracks with standard physics and free parameters varying in a reasonable range are not able to provide blue loops that reach the observed SMC Cepheids at low magnitude, i.e. they are not able to model the low luminosity Cepheids in the SMC case.

The second problem has been underlined – among others – by Beaulieu et al. (2001) who found a strong disagreement between the mass–luminosity relation ML^{puls} and ML^{evol} in the SMC case. They determine a ML^{puls} for the LMC and SMC

Send offprint requests to: D. Cordier,
e-mail: daniel.cordier@ensc-rennes.fr

[1] http://wwwmacho.mcmaster.ca
[2] http://www.lal.in2p3.fr/recherche/eros
[3] http://www.phys.vuw.ac.nz
[4] http://www.astrouw.edu.pl/~ogle/

Article published by EDP Sciences and available at http://www.aanda.org or http://dx.doi.org/10.1051/0004-6361:20031185

Retour à la table des matières : p. v

using pulsation calculations, independent of evolutionary calculations: for a given Cepheid the mass $M_\star$ and the luminosity $L_\star$ are found iteratively solving an equation of the type $P_i^{\rm theo}(M_\star, L_\star) = P_i^{\rm obs}$, where $P_i^{\rm obs}$ is the observed period ($i = 0$ for fundamental pulsators and $i = 1$ first overtone ones) and $P_i^{\rm theo}$ the theoretical one calculated with a pulsation code. The results of Beaulieu et al. (2001) are based on calculations that assume a metallicity content $Z_0 = 0.004$ which is that assumed to represent the mean metallicity of the SMC.

We are therefore led, in the second part of this paper, to propose another possibility and show that it can reconcile both issues: the blue loops at low mass *and* the mass–luminosity relation problem. In our hypothesis no high magnitude (i.e. with a mass around $\sim 3\ M_\odot$) SMC Cepheids with a metallicity as high as the mean SMC value can exist because the evolution does not bring these stars far enough on the blue side to cross the instability strip. The observed high magnitude SMC Cepheids must therefore be undermetallic (i.e. $Z_0 \sim 0.001$) with respect to the mean SMC metallicity (i.e. $Z_0 \sim 0.004$).

During the recent past Baraffe et al. (1998), Alibert et al. (1999), Bono et al. (2000) and Bono et al. (2001) have done investigations involving evolutionary computations suited for Cepheids. These works focus on the period–luminosity relation and/or on the evolutionary ML-relation, but none of them shows a direct comparison between evolutionary tracks and Cepheid photometric data within the CM-diagram.

In Sect. 2 we recall the physical inputs used in our standard models, which are similar to what is found in the recent literature. We next compare our evolutionary tracks with OGLE 2 observed Cepheids within a CM-diagram. Following a method similar to that used by Beaulieu et al. (2001), we also compare $\mathrm{ML}^{\rm evol}$ and $\mathrm{ML}^{\rm puls}$. In both cases we confirm the discrepancy.

In Sect. 3 we discuss the above issues in view of the uncertainties of the standard models and discuss the effect of non-standard physics in cases when models including such physics are available. In Sect. 4 we compare models calculated with $Z_0 = 0.001$ with observations. Section 5 is devoted to discussion about the possibility of the existence of SMC low luminosity Cepheids with metallicity as low as $Z_0 = 0.001$.

2. Standard models versus observations

2.1. Inputs for standard evolutionary models

Our evolutionary models are built with the 1D Henyey type code CESAM[5] originally written by Morel (1997) to which we brought several improvements.

The equation of state is from Eggleton et al. (1973) and the external boundary condition is defined in a simplified model atmosphere involving the Eddington $T(\tau)$ law. The nuclear network involves 30 nuclear reactions; we have followed Schaller et al. (1992) who used the same networks as in Maeder (1983) for H-burning and Maeder & Meynet (1987) He-burning network supplemented with the $^{17}\mathrm{O}(\alpha, \mathrm{n})^{20}\mathrm{Ne}$ reaction. Nuclear reaction rates are from Caughlan & Fowler (1988) except $^{12}\mathrm{C}(\alpha,\gamma)^{16}\mathrm{O}$, $^{17}\mathrm{O}(\mathrm{p},\gamma)^{18}\mathrm{F}$ from Caughlan et al. (1985) and $^{17}\mathrm{O}(\mathrm{p},\alpha)^{14}\mathrm{N}$ from Landré et al. (1990). More recent nuclear rates do exist: NACRE by Angulo et al. (1999), however the adopted rate for $^{12}\mathrm{C}(\alpha,\gamma)^{16}\mathrm{O}$ is quite similar to the NACRE one (a factor of about two higher than Caughlan & Fowler (1988) and about 80% of the Caughlan & Fowler (1988) one.

The adopted mean chemical composition for the SMC is taken as $X_0 = 0.745$, $Y_0 = 0.251$ and $Z_0 = 0.004$, corresponding to a metal to helium enrichment of $\Delta Y_0/\Delta Z_0 = 2$ (see for instance Peimbert et al. 2000), to a primordial helium $Y_{\rm P} = 0.243$ (Izotov et al. 1997) and to $[\mathrm{Fe/H}] = -0.68$ (Luck et al. 1998). Elemental abundances correspond to the Grevesse & Noels (1993) (GN93) mixture consistent with OPAL96 calculations.

Opacities are from Iglesias & Rogers (1996) (OPAL96) for high temperatures ($T \geq 10\,000$ K) and Alexander & Ferguson (1994) for cooler domains. We stress that the central chemical composition during the He burning phase differs strongly from GN93 (e.g. 50% of $^{12}\mathrm{C}$ and 50% of $^{16}\mathrm{O}$). Thus we have used opacity tables allowing a variable composition in $^{12}\mathrm{C}$ and $^{16}\mathrm{O}$ with the aim of modeling the core as realistically as possible. These tables have been built with the Magee et al. (1995) elemental opacities (Los Alamos).

The convective flux is computed according to the prescription of the Mixing Length Theory (Böhm-Vitense 1958). The mixing length value $l_{\rm MLT}$ – derived from solar calibration – is equal to 1.6 $\mathrm{H_p}$. We used Schwarzschild's criterion to decide if the energy transport is radiative or convective, and an extra mixing zone is added above the convective core (i.e. overshooting). The extension of this zone is taken to be $l_{\rm over} = 0.2\ \mathrm{H_p}$ ($l_{\rm over} = \alpha_{\rm over}\ \mathrm{H_p}$).

For the transformation of theoretical quantities, ($M_{\rm bol}$, $T_{\rm eff}$) into absolute magnitudes and colors, we used the Basel Stellar Library (*BaSeL*, version 2.2) of Lejeune et al. (1998) which provides color-calibrated theoretical flux distributions for the largest possible range of fundamental stellar parameters, $T_{\rm eff}$ (2000 K to 50 000 K), $\log g$ (−1.0 to 5.5), and [Fe/H] (−5.0 to +1.0).

2.2. Comparison between models and observations: The "Blue Loop problem"

Cepheid data are from Udalski et al. (1999a). We have chosen to work with $(V - I)$ colors for which more data are available. Fundamental and first overtone Cepheids are plotted in Fig. 1b. A mean $(V - I)$ reddening is taken from Udalski (1998), $E(V - I) = 0.08$. The SMC distance modulus is fixed at 18.94 from Laney & Stobie (1994) with an internal error of 0.04 mag; this is a well accepted value, e.g. Groenewegen (2000) found 19.11 ± 0.11 or 19.04 ± 0.17 depending on the photometric band.

In both figures (Figs. 1a, b) evolutionary tracks involving standard input physics are displayed. Figure 1a is an HR-diagram showing $\log L/L_\odot$ versus $\log T_{\rm eff}$. The segment of the line shows the temperature that should be reached – according to OGLE observations – by the evolutionary tracks for a stellar mass of about 3 $M_\odot$; we will mention this mark in further discussions. An estimation of the uncertainties is also

[5] CESAM: Code d'Évolution Stellaire Adaptatif et Modulaire.

Retour à la table des matières : p. v

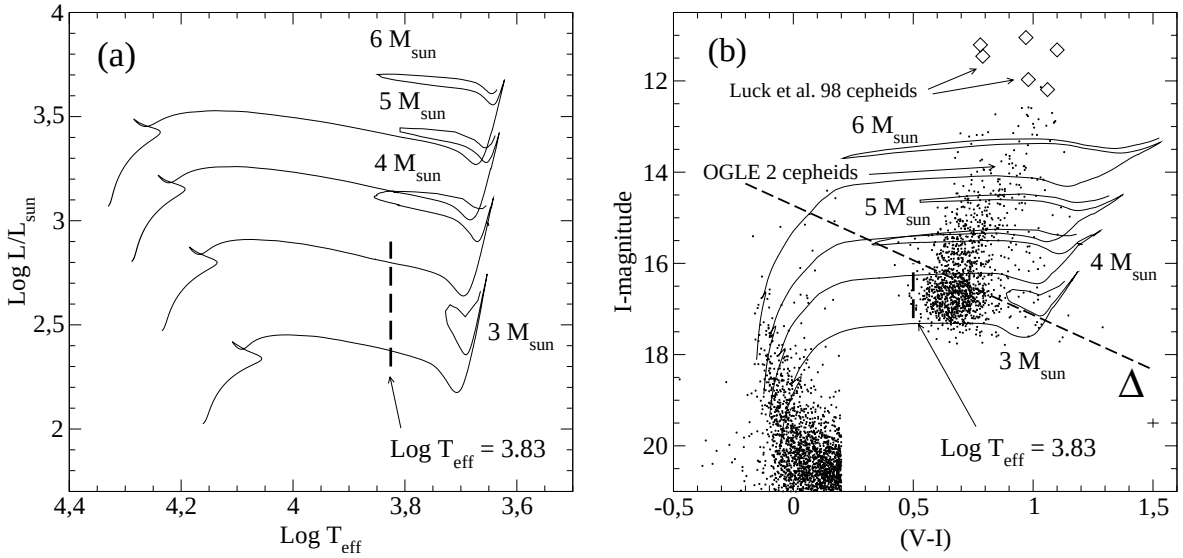

Fig. 1. a) Theoretical HR diagram showing our standard evolutionary tracks with masses 3.0, 4.0, 5.0 and 6.0 $M_\odot$. The adopted chemical composition is $X_0 = 0.745$ $Y_0 = 0.251$ $Z_0 = 0.004$. The heavy element mixture making up Z_0 is from GN'93. The core overshooting extension is 0.2 H_p along the entire tracks. **b)** CM-diagram showing OGLE2 data (black dots) including the sample of Cepheids (fundamental and first overtone pulsators). Only 10% of the stars belonging to the SC 1 OGLE 2 field main sequence are displayed for $(V - I) < 0.2$. The adopted reddening is $E(V - I) = 0.08$ from Udalski et al. (1999a). The cross on the right side indicates an estimation of errors: 30% of $E(V - I) = 0.08$ on color and 0.1 mag on I, for Cepheids. The effective temperature that should be reached by models with masses of about 3 $M_\odot$ is indicated by a vertical dashed straight line. The open diamonds are the sample of Cepheids used by Luck et al. (1998) in their study of chemical composition, values for I-magnitude and $(V - I)$ are those from Luck et al.'s (1998) Table 3. In panel **b)**, the evolutionary tracks of **a)** are also plotted (solid lines). The straight dashed line Δ represents the limit below which the evolutionary tracks fail to model the observed Cepheids.

plotted in Fig. 1b: we estimate the error on the colors to be roughly 30% of $E(V - I)$ (which is the typical variation of reddening within the sample) and determine an error of 0.1 dex on the I-magnitude which roughly represents the distance modulus uncertainty.

In Fig. 1b we have also plotted the stars from Luck et al. (1998) for information.

The general characteristics of these theoretical diagrams are similar to those shown by several groups like the Geneva one, see Charbonnel et al. (1993). This is not surprising because these authors have used similar physical inputs. For instance, the effective temperature at the tip of our 3 $M_\odot$ blue loop is $\log T_{\rm eff} = 3.728$ which compares well with the Charbonnel et al. (1993) $\log T_{\rm eff} = 3.734$. In all cases, the $\log T_{\rm eff}$ value is far from the required one of about 3.82, i.e. a temperature hotter by ∼1200 K.

The main features shown in Fig. 1 are that:

(1) the main sequence position seems to be reasonably well reproduced by the models;

(2) the position of the blue tip of the 3 $M_\odot$ blue loop is too red. For an I-magnitude corresponding to a mass of about 3 $M_\odot$, we can clearly see a bulge of the Cepheids. In fact, 93% of fundamental pulsators and 81% of first overtone pulsators are located between $I_{\rm min} \sim 16.5$ and $I_{\rm max} \sim 17.7$. Such a large number of objects – statistically significant – cannot be explained solely by ∼4.0 $M_\odot$ first crossing models. Indeed, for a 4.0 $M_\odot$ standard model, the time spent during the first crossing is $\tau_{\rm first} = 4.6 \times 10^{-2}$ Myr while the time it takes for the second and third crossing is $\tau_{\rm second\ crossing} + \tau_{\rm third\ crossing} = 3.433$ Myr. Hence, blue loops should cross the entire observational IS for the lowest masses. The adopted value of distance modulus μ does not affect this conclusion. Indeed, even if we take extreme evaluations: $\mu_1 = 18.66 \pm 0.16$ from Udalski (1998) and $\mu_2 = 19.05 \pm 0.13$ from Kovács (2000), the evolutionary track for ∼3 $M_\odot$ does not extend through the observational IS.

2.3. Comparison between observed and calculated mass–luminosity relations

2.3.1. Deriving mass–luminosity relations from observations

In order to derive a ML-relation from the observations, we use a method very similar to the one used by Beaulieu et al. (2001). For each object we solve iteratively the equation:

$$P_i^{\rm theo}(M_\star, L_\star, T_{\rm eff}, Y_0, Z_0) = P_i^{\rm obs} \quad (1)$$

where $P_i^{\rm obs}$ is the observed period value ($i = 0$ for fundamental pulsators and $i = 1$ for first overtones) and $P_i^{\rm theo}(M_\star, L_\star, T_{\rm eff}, Y_0, Z_0)$ the theoretical one, computed with the Florida LNA[6] pulsation code which is a Castor type code (see Castor 1971). During the iterative process, $M_\star$ is adjusted in order to match $P_i^{\rm obs}$ and $P_i^{\rm theo}$, for a given iteration $M_\star$ is fixed and we solve the following set of equations where the

[6] Linear Non-Adiabatic.

Retour à la table des matières : p. v

unknowns are ($\log T_{\rm eff}, \log R_\star, \log L_\star$):

$$\log T_{\rm eff} = 3.9224 + 0.0046 \log g + 0.0012\,[{\rm Fe/H}] - 0.2470\ (V-I-(R_V-R_I)E(B-V)) \quad (2)$$

$$2.5 \log L_\star = \mu_{\rm SMC} - V + R_V E(B-V) + BC + 4.75 \quad (3)$$

$$L_\star = 4\pi\sigma R_\star^2 T_{\rm eff}^4 \quad (4)$$

$$g = G\frac{M_\star}{R_\star^2}. \quad (5)$$

Equation (2) comes from Kovács (2000, Eq. (2)), in which we brought absorption corrections. Equation (3) is Beaulieu et al.'s Eq. (2). Kovács (2000), who made interpolations of the Castelli et al. (1997) stellar atmosphere models to convert magnitudes into bolometric and effective temperature into colors. The luminosity $L_\star$ is in solar units,

$$BC = 0.0411 + 2.0727\Delta T - 0.0274 \log g + 0.0482[{\rm Fe/H}] - 8.0634\Delta T^2$$

and $\Delta T = \log T_{\rm eff} - 3.772$. The magnitude and color V, $(V-I)$ are from OGLE observations, $\mu_{\rm SMC}$ has been taken equal to 18.9 consistent with Laney & Stobie (1994). Following Udalski et al. (1999b) we took $E(B-V) \sim 0.08$, $R_V = 3.24$ and $R_I = 1.96$.

In order to apply this method one has to select the data. Indeed on the CCD detector, a Cepheid may be "blended" with another star, the magnitude of the object being shifted towards lower magnitudes. These "over-luminous" objects lead to wrong couples ($\log M_\star$, $\log L_\star$), therefore it is crucial to reject from the sample the stars suspected to be blended with other object(s). From OGLE data we have extracted amplitudes of pulsation in B, V and I bands and then derived amplitude–$\log P$ relations. The criterion to suspect that an object is blended is the following: if a given object has a magnitude lower than the mean magnitude (at least 0.2 mag lower) given by the magnitude–$\log P$ law *and* an amplitude lower than the mean amplitude given by the amplitude–$\log P$ relation, this object is rejected. Moreover we have also rejected some objects that appear to be suspiciously too red. Finally we retain 1177 fundamental pulsators and 709 first overtone pulsators and obtain similar samples of objects to that of Beaulieu et al. (2001).

Figure 2 displays the resulting ML-relation derived with an assumed metallicity $Z_0 = 0.004$. We did not find significant differences to the results from Beaulieu et al. (2001).

2.3.2. Uncertainties in derived ML-relations

For years the question of Magellanic Cloud distances has been a subject of debate. There were supporters for "short" distance scales – e.g. Stanek et al. (1998) with $\mu_{\rm LMC} = 18.065 \pm 0.031 \pm 0.09$ mag – and for "long" distance scales – e.g. Laney & Stobie (1994) with $\mu_{\rm LMC} = 18.53 \pm 0.04$ mag – Cioni et al. (2000) derived a distance modulus for the LMC $\mu_{\rm LMC} = 18.53 \pm 0.04 \pm 0.08$ mag and Mould et al. (2000) (HST Key Project Team) have adopted $\mu_{\rm LMC} = 18.50 \pm 0.04 \pm 0.15$ mag. We made a test with "short" distance (i.e. $\mu_{\rm SMC} = 18.7$ mag);

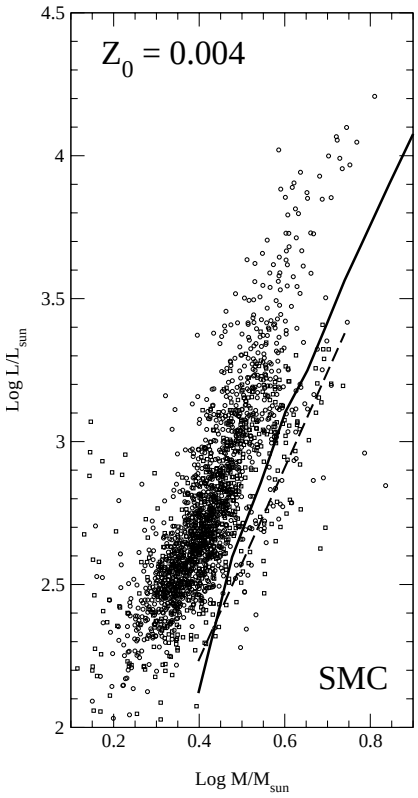

Fig. 2. Mass–luminosity relation derived from OGLE observations for $Z_0 = 0.004$ corresponding to [Fe/H] ~ -0.7. Circles: fundamental pulsators, squares: first overtone pulsators. Solid line: mass–luminosity relation from our evolutionary code with $Z_0 = 0.004$ and an overshooting amount $\alpha_{\rm over} = 0.2$ H_p; dashed line: mass–luminosity relation from Bono et al. (2000), which is almost identical with Alibert et al. (1999) one.

this leads to differences in mass of $\delta \log M/M_\odot \sim -0.1$ and in luminosity $\delta \log L/L_\odot \sim -0.08$ (consistent with Eq. (3)). We dismiss these "short" distance scales: (1) whatever the techniques used, recent works seem in agreement with "long" distance scales; (2) a difference in mass of $\delta \log M/M_\odot \sim -0.1$ would mean that evolutionary computations would be completely wrong. We stress that Beaulieu et al. (2001) have the same point of view. Therefore we adopted a "long" distance value for the SMC distance modulus: $\mu_{\rm SMC} = 18.9 \pm 0.15$ mag; this choice is supported by the recent result of Harries et al. (2003) who found $\mu_{\rm SMC} = 18.89 \pm 0.04$ (statistical) ± 0.15 (systematic) mag with a technique involving eclipsing binaries.

The depth of the LMC seems to be negligible (Van der Marel & Cioni 2001); the depth of the SMC has been evaluated to range between ~0.2 and ~0.4 mag (Crowl et al. 2001). Then – for extreme cases – a given object inside the SMC could have an actual distance modulus +0.2 mag larger or lower than $\mu_{\rm SMC} = 18.9$ mag, which has to be regarded as an average value. In order to estimate either the influence of an error on $\mu_{\rm SMC}$ or an effect of SMC depth, we have made a test with $\mu_{\rm SMC} = 19.1$ mag; we got $\delta \log M/M_\odot \sim +0.1$ and $\delta \log L/L_\odot \sim +0.08$.

Retour à la table des matières : p. v

Another source of uncertainty is the reddening; if we assume an error of ±0.03 mag on $E(B-V) = 0.08$ mag, we get a small uncertainty on masses and luminosity: $\delta \log M/M_\odot \sim \pm 0.01$ and $\delta \log L/L_\odot \sim \pm 0.05$.

Beside this, uncertainties connected to standardization of OGLE photometry are clearly negligible; with $\delta V = \pm 0.02$ mag we obtained $\delta \log M/M_\odot \sim \pm 0.01$ and $\delta \log L/L_\odot \sim \mp 0.01$.

Moreover Beaulieu et al. (2001) made some additional tests: introducing turbulent convection, computing non-linear models or changing the mesh size within models does not yield periods significantly different from those computed with LNA code. Therefore the uncertainty on distance (error on $\mu_{\rm SMC}$ or effect of SMC depth) remains the most important one.

2.3.3. Comparison with ML-relations from evolutionary tracks

From Fig. 2, we remark a large discrepancy between the ML-relations derived from OGLE observations and from evolutionary calculations. For each evolutionary track, luminosity has been read at the "tip" of the blue loop, where the model spent at lot of time. The discrepancy is also found using Bono et al. (2000) mass–luminosity relation. The disagreement increases when $\log M/M_\odot$ decreases. We must however emphasize that for $\log M/M_\odot \sim 0.4$ (i.e. $M/M_\odot \sim 2.5$), the evolutionary track does not cross the Cepheid Instability Strip and a comparison between $\mathrm{ML}^{\rm evol}$ and $\mathrm{ML}^{\rm puls}$ for $\log M/M_\odot \sim 0.4$ has no real meaning. Even an extreme value of $\mu_{\rm SMC}$ – i.e. 19.1 mag – cannot lead to a perfect agreement between all ML-relations.

3. Uncertainties in standard evolutionary models

In this section, we review the factors affecting the blue loop extension. Before presenting any models, we briefly recall a method allowing some predictions about the blue loop extension. We follow the work of Lauterborn et al. (1971) who have defined an "effective core potential":

$$\Phi_{\rm eff} = \frac{M_{\rm c}}{R_{\rm c}}\, {\rm e}^{(\alpha\, \Delta m\, \Delta X)} \qquad (6)$$

where $M_{\rm c}$ and $R_{\rm c}$ are respectively the mass and the radius of the $\mathrm{H_e}$ core and α is a constant. Δm is the width of the zone located between the $\mathrm{H_e}$ core and the beginning of the outer chemically homogeneous region. ΔX represents the total hydrogen mass fraction variation within Δm. Numerical experiments done by Lauterborn et al. (1971) have shown that a model undergoes a blue loop if this potential is lower than a critical value $\Phi_{\rm eff}^{\rm (crit)}$. We have to keep in mind this simple result: the lower $\Phi_{\rm eff}$, the bluer the blue loop tip.

In the next sections, we focus on a $3\,M_\odot$ track because the most severe discrepancy in the CM-diagram is observed around this mass.

3.1. Overshooting

If we reduce the overshooting amount from $\alpha_{\rm over} = 0.2$ $\mathrm{H_p}$ ("standard value") to $\alpha_{\rm over} = 0.0$ $\mathrm{H_p}$, the $\mathrm{H_e}$ core mass $M_{\rm c}$ decreases as a consequence of the less extended H-core on main sequence. As a consequence, loops more extended toward the blue are expected. This is confirmed in Fig. 3b where it clearly appears that even without any overshooting ($\alpha_0 = 0.0$ $\mathrm{H_p}$), a 3 solar mass loop still remains too short to account for the observational data.

3.2. Mixing length parameter

The mixing length parameter $\alpha_{\rm MLT} = l_{\rm MLT}/\mathrm{H_p}$ has been so far set equal to 1.6 in our standard models. This value is derived from solar calibration (Lebreton et al. 1999) and it is probably not universal: it may depend on metallicity, mass, etc. A priori, $\alpha_{\rm MLT}$ acts only on the convective flux ($\alpha_{\rm MLT}$ is involved in MLT temperature gradient calculation) and does not change the position of Schwarzschild limit, hence ΔX in Eq. (6) should remain unchanged and more blueward loops are not expected. The tracks computed with the extreme values $\alpha_{\rm MLT} = 1.0$ and $\alpha_{\rm MLT} = 2.0$ are plotted in Fig. 3a. Both tracks have been calculated with $\alpha_{\rm over} = 0.0$ which is the most favorable situation as explained in Sect. 3.1. As one can notice $\alpha_{\rm MLT}$ has a negligible influence on the blue tip position. The effective temperature of the bluest point of the loop remains approximatly equal to ~3.76 (in Log) which is not enough to reach the warmer edge of the observational IS; it still lacks ~850 K. We point out that a value of $\alpha_{\rm MLT} = 1.0$ is very unlikely because it leads to a giant branch around $(V-I) \sim 1.5$ where there are no stars within the CM-diagram.

3.3. Convective penetration

Similarly, although not identically to the overshooting process, turbulent eddies must penetrate to some extent downward in the convective envelope into stable radiative regions. However, we do not know how far they penetrate.

Here we have carried out a calculation setting the extension of convective penetration at $\alpha_{\rm cp} = 0.7$ $\mathrm{H_p}$ following the Alongi et al. (1991) prescription. They found that this value is needed to reproduce the properties of the red giant branch luminosity function. This amount (0.7 $\mathrm{H_p}$) must be understood as representing an order of magnitude as Alongi et al. (1991)'s calculations were performed before 1992 when the OPAL group published his new opacity tables.

During the giant branch (hereafter GB) episode, the convective penetration produces a deeper penetration of the external convective zone. In this way, ΔX in Eq. (6) decreases and yields a lower $\Phi_{\rm eff}$ and bluer loop tip. Evolutionary tracks are displayed in Fig. 3c for a 3 $M_\odot$ without overshooting (i.e. both with $\alpha_{\rm over} = 0.0$ $\mathrm{H_p}$) and show – as expected – that convective penetration slightly extends the loop but not enough to cross the entire IS. The extension difference reaches only a few ~130 K, remaining too cold by ~720 K.

3.4. Rotation

Maeder & Meynet (2001) present evolutionary tracks including the effect of stellar rotation at low metallicity $Z_0 = 0.004$

Retour à la table des matières : p. v

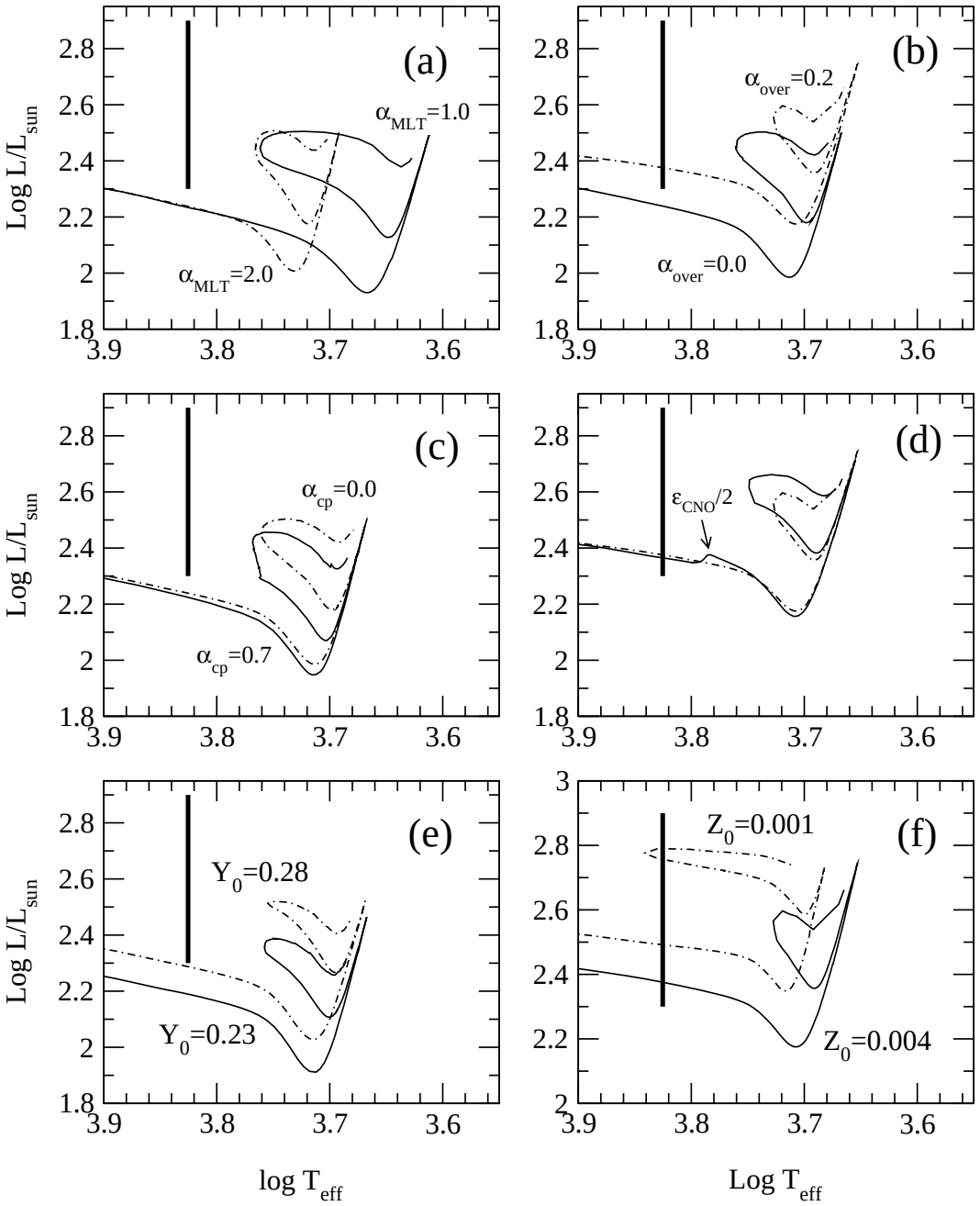

Fig. 3. Influence of free parameters on the blue loop extension for a 3 $M_\odot$ model. The parameters are: **a)** the mixing length, **b)** the overshooting, **c)** the convective penetration (overshooting below external convective zone), **d)** CNO nuclear cycle energy production rate, **e)** initial helium content and **f)** initial metallicity. For each plot, a vertical segment (defined in Fig. 1b) shows the temperature which the loop must reach to cross over the entire observational IS.

in the mass range 9.0 to 60.0 $M_\odot$. The smaller mass value remains in the Cepheid domain. In Fig. 6 of Maeder & Meynet (2001) the reader can see that the blue loop extension is substantially reduced from $\log T_{\rm eff} \sim 4.12$ to $\log T_{\rm eff} \sim 3.95$ ($\Delta \log T_{\rm eff} \sim -0.17$) whereas we need $\Delta \log T_{\rm eff} \sim +0.05$. This blue loop reduction is due to the core extra-mixing added by convection equivalent to an overshooting addition.

3.5. Influence of the CNO-cycle energy generation rate

Although the CNO nuclear reaction cycle is rather well known, we have performed evolutionary calculations with an energy generation rate $\epsilon_{\rm cno}$ artificially reduced by a factor of two, from an arbitrary chosen post-main sequence stage (indicated by an

Retour à la table des matières : p. v

arrow in Fig. 3d). This magnitude of uncertainty (a factor of two) is extremely large because the consequences during the Main Sequence phase would bring unavoidable disagreements between observations and models.

One can again predict what can be expected from such a numerical experiment. A lower $\epsilon_{\rm cno}$ leads to a lower $M_{\rm c}$ in Eq. (6), thus to a lower $\Phi_{\rm eff}$ and consequently to a bluer loop. Figure 3d confirms this argument. Again, the loop is not extended enough and even an unrealistic uncertainty of a factor of two on the global energy generation rate $\epsilon_{\rm cno}$ cannot explain the disagreement between observations and theory.

Enhancing by a factor of two the 3α reaction rate is also found to have a negligible influence on the blue loop extension.

3.6. Effects of helium

The initial helium content adopted, Y_0, is expected to have only a minor influence on the blue loop *extension*, indeed:

- The central helium content $Y_{\rm c}$ during the blue loop episode does not depend on the helium content of the initial homogeneous model Y_0. Hence Y_0 does not influence $\epsilon_{\rm He}$ the He-burning energy production rate because within the inner regions $Y_{\rm c} = 1 - Z_{\rm c}$ (with $Z_{\rm c}$ the central heavy elements mass fraction) whatever the Y_0 value is.
- During the blue loop the H-burning shell moves through the "X-profile" where Y varies between ∼1 (boundary of He core) and $Y = Y_0$ (chemically homogeneous region mixed during the dredge-up episode when the model is closed to the Red Giants Branch). These Intermediate Y values are independent of Y_0 (obviously excepted values being close to Y_0 itself).

Therefore the influence of Y_0 on the blue loop extension is expected to be very small. As a verification, models have been calculated with $Y_0 = 0.23$ and $Y_0 = 0.28$ which represent two extreme values: $Y_0 = 0.23$ is a rather low value for primordial helium and $Y_0 = 0.28$ which implies $\Delta Y_0/\Delta Z_0 \sim 9$ while "reasonable" values are around 2, for a review see Luridiana (2002). The tracks with $Y_0 = 0.23$ and $Y_0 = 0.28$ in (Fig. 3e) show that the initial helium content has no influence on the blue loop extension: the effective temperature of the tip remains equal to 3.76, i.e. ∼850 K colder than blue edge of IS, even in the favorable scheme of zero overshooting.

3.7. Effects of metallicity

The high sensivity of a blue loop extension to metallicity is well known. The physical origin of this phenomenon is in the H-burning shell where material is processed through CNO cycle. For a fixed heavy element mixture (here GN93) the lower Z_0, the lower $X_{\rm C}$, $X_{\rm N}$, $X_{\rm O}$ (respectively C, N and O mass fractions) are. These three elements play the same role of catalysts in chemical reactions, therefore a C, N, O deficiency leads to lower energy generated. Then, $M_{\rm c}$ in Eq. (6) remains lower for a longer time and one obtains more extended blue loops. On the one hand, the H-burning shell drives the star structure on the Giant Branch, on the other hand, during the blue loop episode, the He-burning core pulls the model towards the blue edge, where the He main sequence is located. The lower the $\epsilon_{\rm CNO}$, the stronger the He central burning effect.

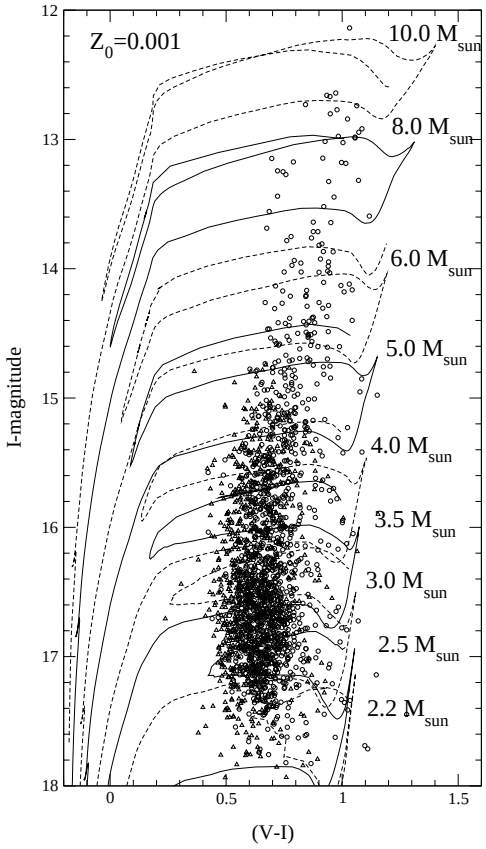

Fig. 4. Grid of evolutionary tracks for $Z_0 = 0.001$ with mass ranges between 2.5 $M_\odot$ and 10.0 $M_\odot$. All the tracks cross the observational Instability Strip even the low mass tracks. Fundamental pulsators are represented by open circles and first overtone ones by open triangles.

As a confirmation of this high metallicity sensivity, we have computed evolution at 3 $M_\odot$ taking a very low value: i.e. $Z_0 = 0.001$ which corresponds to [Fe/H] ∼ −1.3. We compare the resulting extensions in Fig. 3f. The blue loop crosses the entire IS, the tip reaching a position bluer than the blue edge of IS.

Therefore the only way we have found to extend blue loops towards the high temperature edge of the HR diagram is to decrease the metallicity. In the next section we compare observational constraints and models built with $Z_0 = 0.001$.

4. Models with $Z_0 = 0.001$

4.1. Blue loops at $Z_0 = 0.001$

We have calculated a grid of evolutionary tracks at very low metallicity, i.e. $Z_0 = 0.001$. The results are displayed in Fig. 4 where one can remark that the whole observed Instability Strip is crossed by the theoretical tracks, even the fainter part, i.e. the lower region of the color-magnitude diagram. These results

Retour à la table des matières : p. v

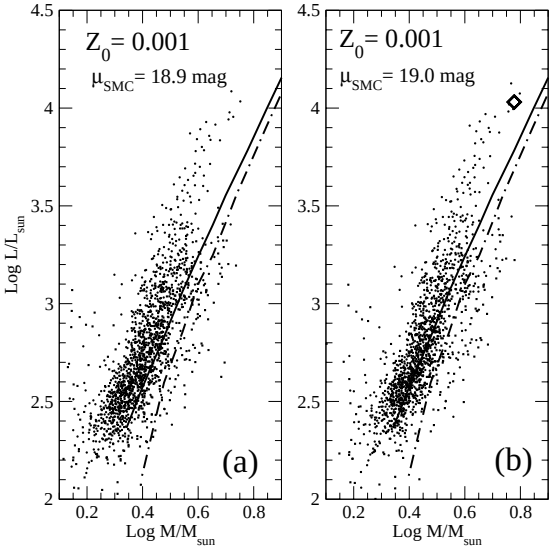

Fig. 5. Mass–luminosity relations derived from OGLE observations assuming $Z_0 = 0.001$ corresponding to [Fe/H] ~ -1.3. Solid line: mass–luminosity relation from our evolutionary code with $Z_0 = 0.001$ and an overshooting amount $\alpha_{over} = 0.2$ H_p; dot-dashed line: ML^{evol} for $Z_0 = 0.004$ and $\alpha_{over} = 0.2$ H_p (same as Fig. 2, for comparison). Panel **a)**: ML^{puls} has been computed assuming a distance modulus $\mu_{SMC} = 18.9$ mag; panel **b)**: same thing assuming $\mu_{SMC} = 19.0$. The diamond symbol shows the position of a 6 $M_\odot$, $Z_0 = 0.001$ model with $\alpha_{over} = 0.6$ H_p.

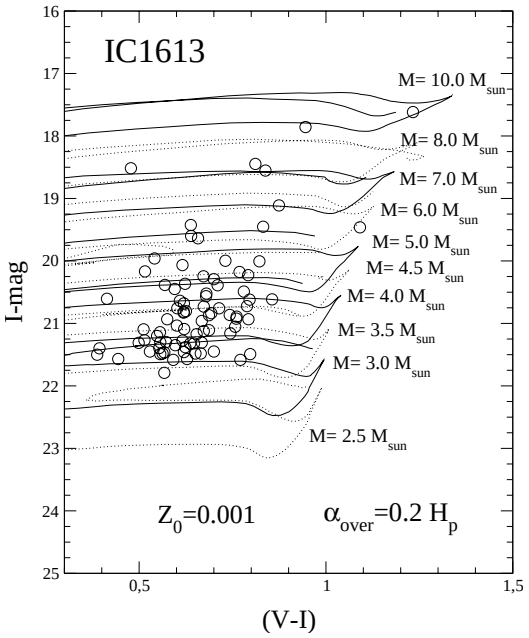

Fig. 6. Circles: Cepheids detected by the OGLE team towards IC1613, evolutionary tracks (solid and dotted lines) have been calculated with $Z_0 = 0.001$ and an overshooting $\alpha_{over} = 0.2$ H_p.

suggest that a large fraction of SMC Cepheids could be metal deficient compared to the mean metallicity of the Small Cloud.

One interesting point is that the shape of the Instability Strip at high magnitude is well reproduced by the decrease of the blue loop extension when going from higher to lower masses.

4.2. Mass–luminosity relation at $Z_0 = 0.001$

In Fig. 5 we have displayed the mass–luminosity relations derived from OGLE observations assuming a metallicity of $Z_0 = 0.001$. Figure 5b shows a better agreement between ML^{evol} and ML^{puls}, if we assume $\mu_{SMC} = 19.0$ mag – consistently with recent determinations – the agreement for low masses is excellent. Unfortunately it remains a discrepancy for higher masses – i.e. for $\log M/M_\odot \sim 0.7$, this point will be discussed in the next section.

5. Conclusion and discussion

Section 4 shows that looking for an agreement between models and SMC observations for both blue loop extensions and M–L relations for the SMC gives strong hints that high magnitude (i.e. low mass) SMC Cepheids could be metal deficient compared to the mean metallicity of the SMC; this fact could be explained by a "selection effect": only stars with low enough metallicity could have an evolutionary track crossing the Cepheid Instability Strip. Unfortunately direct spectroscopic determinations of [Fe/H] for the SMC Cepheids around I-mag ~ 17 are not yet available. We discuss now a few issues in favor of the above proposition. First we consider another metal-poor galaxy and then discuss the information that can be drawn from Cepheids in SMC clusters and beat Cepheids that supports the existence of SMC Cepheids as metal poor as [Fe/H] ~ -1.3 dex.

5.1. Comparison between our model and a very low metallicity Cepheid population

Udalski et al. (2001) provided a sample of Cepheids belonging to the galaxy IC1613 with a metallicity [Fe/H] $\sim -1.3 \pm 0.2$ (see Lee et al. 1993). This data set offers the opportunity to check whether our evolutionary models are valid for metallicity as low as the value suspected for SMC Cepheids located below the Δ line in a CM-diagram. Figure 6 displays OGLE objects and our evolutionary tracks for $Z_0 = 0.001$. The distance modulus for IC1613 is taken to be 24.2 ± 0.1 mag and absorption is $A_I = 0.05$ (see Udalski et al. 2001); reddening is given by Schlegel et al. (1998). Figure 6 shows that the evolutionary tracks cross the whole instability strip as defined by the observed Cepheids. For this galaxy, no problem of blue loops exists with our models indicating that the main features of our models likely capture the essential evolutionary properties at low metallicity. One can notice that even a cut-off of the OGLE detector around I-mag ~ 22 cannot really change our conclusion because the blue loop for 2.5 $M_\odot$ is extended enough to model Cepheids as faint as I-mag ~ 22.2.

Retour à la table des matières : p. v

5.2. Evidence for metal-poor stars within the SMC

Luck et al. (1998) have determined the chemical composition of Cepheids in SMC by means of high resolution spectroscopy. The [Fe/H] values found by the authors range between −0.84 and −0.65 corresponding to a mass fraction Z_0 ranging between ∼0.0030 and ∼0.0045; these values bracket the commonly assumed metallicity mean value for SMC, i.e. $Z_0 = 0.004$. However, two remarks are in order here: (1) the sample studied by Luck et al. (1998) has a quite poor statistical size (6 objects) while OGLE sample contains about 2000 objects; (2) more importantly, as shown by Fig. 1b the stars studied by Luck et al. (1998) are objects much brighter than those around I-magn ∼ 17 which are not reached by our blue loops. The reason for the choice of bright objects is that spectroscopic determinations are easier for brighter objects. Therefore biais concerning high magnitude SMC Cepheid metallicity cannot be excluded.

On the other hand, one may think that it is possible to infer some indirect information about the SMC Cepheid metallicity. The OGLE team has indeed discovered many stellar clusters in the SMC, (see Pietrzyński et al. 1998). Moreover Pietrzyński & Udalski (1999c) have detected 132 Cepheids belonging to these clusters. One of the main properties of stars belonging to a given cluster is that they present the same chemical composition. Therefore any indication about metallicity of these SMC clusters give information about the metallicity of Cepheids belonging to clusters. The literature is quite poor about metallicity determinations for SMC clusters. Table 1 mainly taken from Crowl et al. (2001) gives metallicity estimations for SMC clusters. Thanks to a cross identification we have found 2 clusters belonging to the catalogue of Pietrzyński & Udalski (1999c) and having a metallicity determination in the literature: NGC 330 (`SMC0107` in OGLE catalogue) and NGC 416 (`SMC0158`). However these clusters are known to be young or intermediate-age systems; one has to check whether the ages of Cepheids are compatible with age of the cluster hosting them.

In the case of NGC 330, Chiosi et al. (1995) have found a maximum age of 48 Myr; Pietrzyński & Udalski (1999b) have derived from their study $31.6^{+8.2}_{-6.5}$ Myr. From HST observations Mighell et al. (1998b) estimate an absolute age for NGC 416 of 6.6 ± 0.5 Gyr assuming that the Lindsay 1 cluster is 9 Gyr old; Pietrzyński & Udalski (1999b) confirm that NGC 416 is older than 1 Gyr. We underline that neither NGC 330 nor NGC 416 are mentioned in the erratum of Pietrzyński & Udalski (1999a).

For the Cepheid (`SMC_SC7 206038` in the OGLE catalogue) suspected to belong to NGC 330, if we assume a metallicity [Fe/H] = −0.7 ($Z_0 = 0.004$) and a mass about 3.5 $M_\odot$ consistent with its position within CMD, we find an age of ∼230 Myr; assuming [Fe/H] = −1.3 ($Z_0 = 0.001$) and 3.0 $M_\odot$ we obtain ∼300 Myr. Thus the Cepheid is likely to be a field star and does not belong to NGC 330.

Stars suspected to be NGC 416 objects have an I-magnitude between 15 and 16 mag; this corresponds to a mass around 4 $M_\odot$ for [Fe/H] = −1.3 (metallicity consistent with the cluster one). From our evolutionary calculations we get – for such mass and metallicity – an age of ∼150 Myr.

Unfortunately this value is not compatible with the estimated age for NGC 416; indeed the age spread (probably around ∼0.5 Gyr) does not allow such young objects to belong to the cluster. Nevertheless one can notice that the majority of SMC clusters in Table 1 are metal deficient, thus SMC stars with metallicity lower than $Z_0 \sim 0.004$ ([Fe/H] ∼ −0.7) do exist and the hypothesis of metal deficient SMC Cepheids appears to be reasonable.

5.3. Information brought by SMC Beat Cepheids

The OGLE Team has discovered a sample of 93 beat Cepheids in the SMC. Udalski et al. (1999a) found that 23 pulsate simultaneously on the fundamental mode (hereafter F) and the first overtone (hereafter 1OT); the remaining objects have been found to pulsate simultaneously on the first and second overtones (hereafter 2OT).

In order to derive their $\mathrm{ML}^{\mathrm{puls}}$, Beaulieu et al. (2001) chose three quantities among the four observational ones: T_{eff}, L and the periods P_k and P_{k+1} (P_0 for F/1OT and P_1 for 1OT/2OT); they calculate the theoretical value of P_{k+1} noted P_{k+1}(calc) (the observed one being P_{k+1}(obs)). They next define the parameter $\epsilon = P_{k+1}(\mathrm{calc})/P_{k+1}(\mathrm{obs})$) allowing a comparison between theory and observations. They explore the influence of different important parameters, particularly the distance modulus and reddening and finally conclude that a solution (i.e. $\epsilon \sim 1$) is found simultaneously for F/1OT pulsators *and* 1OT/2OT *only if* the metallicity is settled as $Z_0 = 0.001$ (i.e. [Fe/H] ∼ −1.3).

In Fig. 8 we have plotted the observed beat Cepheids together with evolutionary tracks and the straight line Δ defined in Sect. 2. This plot clearly shows that the beat Cepheids are located in the region where we suspect that objects are metal deficient (i.e. with a metallicity around $Z_0 \sim 0.001$). All 1OT/2OT pulsators are below Δ (excepted one object) while F/1OT pulsators are scattered slightly above and below.

Thus these pulsation/evolution models of SMC beat Cepheids argue in favor of a relation between a metal deficiency (with respect to the mean value of the SMC) and the existence of SMC Cepheids at low magnitude.

5.4. The case of high mass Cepheid

Although it is slightly out of the scope of this paper where we focus on faint SMC Cepheids, we will debate in this section the case of brighter objects: i.e. $\log M/M_\odot \sim 0.7$–∼0.8 corresponding to $3.6 \lesssim \log L/L_\odot \lesssim 4.1$. Whatever the assumed metallicity: $Z_0 = 0.004$ or $Z_0 = 0.001$, few objects with an evaluated mass around $\log M/M_\odot \sim 0.77$ ($M \sim 6\,M_\odot$) have a $\mathrm{ML}^{\mathrm{puls}}$ in discrepancy with the related $\mathrm{ML}^{\mathrm{evol}}$.

We can make some hypotheses: as shown in Sect. 2.3.2 with a larger distance modulus – i.e. $\mu_{\mathrm{SMC}} = 19.1$ mag – we get $\delta \log M/M_\odot \sim +0.1$ and $\delta \log M/M_\odot \sim +0.08$ (compared with the situation with 18.9 mag), but this extreme value is not able to bring a full agreement between $\mathrm{ML}^{\mathrm{puls}}$ and $\mathrm{ML}^{\mathrm{evol}}$ for brighter objects. On the other hand it is unlikely that all these stars would be located deeper in the SMC than others.

Retour à la table des matières : p. v

Table 1. Determinations of SMC clusters metallicity.

Cluster	[Fe/H]	Cepheid(s)?
NGC 330	-0.82 ± 0.11 (a)	**no**
NGC 411	-0.68 ± 0.07 (b)	no
NGC 152	-0.94 ± 0.15 (c)	no
Lindsay 113	-1.24 ± 0.11 (d)	no
Kron 3	-1.16 ± 0.09 (d)	no
NGC 339	-1.50 ± 0.14 (d)	no
NGC 416	-1.44 ± 0.12 (d)	**no**
NGC 361	-1.45 ± 0.11 (d)	no
Lindsay 1	-1.35 ± 0.08 (d)	no
NGC 121	-1.71 ± 0.10 (d)	no
Kron 28	-1.20 ± 0.13 (e)	no
Lindsay 38	-1.65 ± 0.12 (e)	no
Kron 44	-1.10 ± 0.11 (e)	no

(a) Hill (1999); (b) Alves & Sarajedini (1999); (c) Crowl et al. (2001); (d) Mighell et al. (1998a); (e) Piatti et al. (2001).

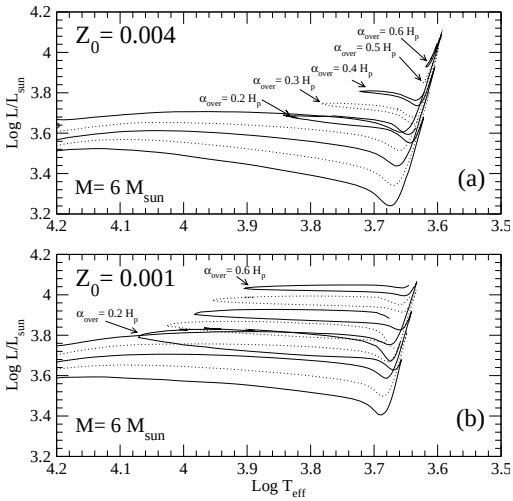

Fig. 7. Numerical experiments for a 6 $M_\odot$ model. For both metallicities $Z_0 = 0.004$ (panel **a)**) and $Z_0 = 0.001$ (panel **b)**), we have computed a grid of evolutionary tracks varying the overshooting amount from 0.2 H_p up to 0.6 H_p. For high metallicity, the blue loop disappears suddenly for overshooting larger than 0.4 H_p while the blue loop extension decreases monotonously in the low metallicity case.

For a given mass value, a way to enhance the luminosity is to consider a larger overshooting amount. As suggested by Cordier et al. (2002), it cannot be excluded that the average overshooting amount for intermediate mass stars increases when metallicity decreases; they have derived – assuming $Z_0 = 0.004$ for SMC main sequence stars – $\alpha_{\rm over} = 0.40^{+0.12}_{-0.06}$ H_p. With a LMC bump Cepheid study, Keller & Wood (2002) infer an overshooting amount $\Lambda_c = 0.63 \pm 0.03$ H_p (~0.3 H_p in our formalism).

We made a test involving all mass values with $\alpha_{\rm over} = 0.4$ H_p, as expected blue loop extensions are reduced (for low mass tracks the excursion of the blue loop within IS is less deep) and luminosity is not increased enough ($\delta \log L/L_\odot \sim +0.1$) to get an agreement between $ML^{\rm evol}$ and $ML^{\rm puls}$ for $\log M/M_\odot \sim 0.77$. Then, to increase the overshooting amount over the whole range of mass is not the solution.

Another possibility is that overshooting can depend on mass, increasing as mass increases as suggested for instance by Young et al. (2001). Thus we have concentrated on 6 $M_\odot$ models, varying the overshooting amount between 0.2 H_p (our "standard" value here) up to 0.6 H_p; this for both metallicities: $Z_0 = 0.001$ and $Z_0 = 0.004$. Results are shown in Fig. 7; it is clear that beyond 0.4 H_p one no longer get a blue loop for $Z_0 = 0.004$. In contrast with $Z_0 = 0.001$, the blue loop extension decreases, but where the Cepheid IS is crossed by tracks. $\log L/L_\odot$ increases reaching large enough values (for 0.6 H_p, see diamond symbol in Fig. 5b) to make $ML^{\rm evol}$ and $ML^{\rm puls}$ for $\log M/M_\odot \sim 0.77$. We stress that Keller & Wood (2002) found their quite "high" overshooting amount using a sample of bright LMC Cepheids; this support our proposal of a higher overshooting for brighter Cepheids. Our work favors a solution involving low metallicity. Towards high masses, another selection effect could occur if the overshooting increases with mass and reache ~0.6 H_p for masses larger than ~6 $M_\odot$ at low metallicity. A detailed study is needed on this topic and is beyond the main goal of this paper.

5.5. Summary

In this paper we have explored two main problems related to the SMC Cepheid population: (1) the blue loop extension for high magnitude stars, (2) the mass–luminosity relation. We have first shown that the blue loop extension is extended enough only if the metallicity is substantially lower than the commonly used value for SMC object models.

Evolutionary tracks computed with $Z_0 = 0.001$ correctly reproduce the Instability Strip shape for low masses and the mass–luminosity relation derived from these tracks is in rather good agreement with $ML^{\rm puls}$ deduced from observations using a technique similar to Beaulieu et al. (2001). The remaining discrepancy for the small population of brighter objects could be explained by a joint effect of low metallicity and a rather enhanced core mixing process. Further research is needed on this subject. We emphasize that Pietrukowicz (2002) – who estimates period change rates of SMC OGLE Cepheids – found also for brighter objects a rather bad agreement between models and observations. Our point is that all Cepheids below Δ are likely metal poor and stars above Δ belong probably to a "mixed" population. Finally, the present work strongly suggests the existence of an evolutionary selection effect for fainter Cepheids belonging to SMC. High resolution spectroscopic chemical composition determinations for SMC Cepheids through the entire IS and particularly around magnitude 17 are requested to bring definitive arguments in favor or against the present suggestion. This could be possible for a sample of a few stars with the UVES VLT spectrograph. Results would shed new light on the cosmologically important metallicity dependence of the Cepheid period–magnitude relation.

Retour à la table des matières : p. v

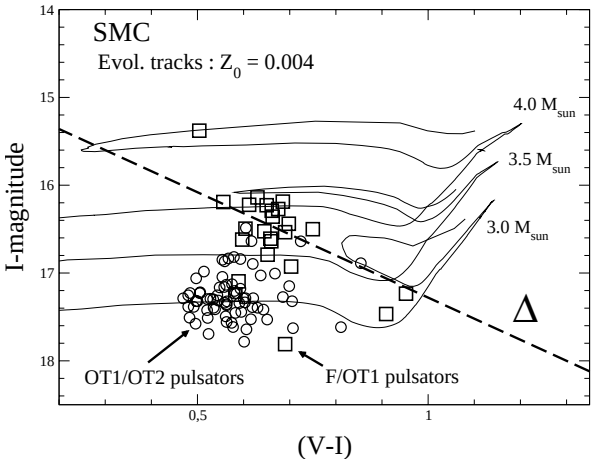

Fig. 8. Location of SMC beat Cepheids detected by the OGLE team in the CM diagram. Squares are F/1OT pulsators and circles are 1OT/2OT pulsators. The evolutionary tracks have been computed for the metallicity value $Z_0 = 0.004$ and the dashed line Δ limits the regions where the Cepheids are expected to be metal-deficient ($Z_0 = 0.001$).

Acknowledgements. We warmly thank the anonymous referee who contributed to the improvement of this paper with his/her remarks and suggestions. We also thank Jean-Philippe Beaulieu and J. Robert Buchler for valuable discussions; we are also grateful to the OGLE group for providing their data and to people involved in `GNU/Linux` projects. D. Cordier thanks ENSCR for working facilities and his "Aménagement de service" during 2002/2003 academic year.

References

Alexander, D., & Ferguson, J. 1994, ApJ, 437, 879
Alibert, Y., Baraffe, I., Hauschildt, P., & Allard, F. 1999, A&A, 344, 551
Alongi, M., Bertelli, G., Bressan, A., & Chiosi, C. 1991, A&A, 244, 95
Alves, D. R., & Sarajedini, A. 1999, ApJ, 511, 225
Angulo, C., Arnould, M., Rayet, M., et al. 1999, Nucl. Phys. A, 656, 3
Baraffe, I., Alibert, Y., M'era, D., Chabrier, G., & Beaulieu, J. 1998, ApJ, 499, L205
Beaulieu, J. P., Buchler, J. R., & Kolláth, Z. 2001, A&A, 373, 164
Böhm-Vitense, E. 1958, Zs. f. Ap., 46, 135
Bono, G., Caputo, F., Cassisi, S., et al. 2000, ApJ, 543, 955
Bono, G., Gieren, W. P., Marconi, M., Fouqué, P., & Caputo, F. 2001, ApJ, 563, 319
Castelli, F., Gratton, R. G., & Kurucz, R. L. 1997, A&A, 318, 841
Castor, J. I. 1971, ApJ, 166, 109
Caughlan, G., & Fowler, W. 1988, Atomic Data Nuc. Data Tables, 40, 283
Caughlan, G., Fowler, W., Harris, M., & Zimmerman, B. 1985, Atomic Data Nuc. Data Tables, 32, 197
Charbonnel, C., Meynet, G., Maeder, A., Schaller, G., & Schaerer, D. 1993, A&AS, 101, 415
Chiosi, C., Vallenari, A., Bressan, A., Deng, L., & Ortolani, S. 1995, A&A, 293, 710
Cioni, M.-R. L., Van der Marel, R. P., Loup, C., & Habing, H. J. 2000, A&A, 359, 601
Cordier, D., Lebreton, Y., Goupil, M.-J., et al. 2002, A&A, 392, 169
Crowl, H. H., Sarajedini, A., Piatti, A., et al. 2001, AJ, 122, 220
Eggleton, P., Faulkner, J., & Flannery, B. 1973, A&A, 23, 325
Grevesse, N., & Noels, A. 1993, in Origin and Evolution of the Elements, ed. N. Prantzos, E. Vangini-Flam & M. Cassé (Cambridge: Cambridge University Press), 14 (GN'93)
Groenewegen, M. A. T. 2000, A&A, 363, 901
Harries, T. J., Hilditch, R. W., & Howarth, I. D. 2003, MNRAS, 339, 157
Hill, V. 1999, A&A, 345, 430
Iglesias, C. A., & Rogers, F. J. 1996, ApJ, 464, 943 (OPAL 96)
Izotov, Y., Thuan, T., & Lipovetsky, V. 1997, ApJS, 108, 1
Keller, S. C., & Wood, P. R. 2002, ApJ, 578, 144
Kovács, G. 2000, A&A, 363, L1
Landré, V., Prantzos, N., Aguer, P., et al. 1990, A&A, 240, 85
Laney, C. D., & Stobie, R. S. 1994, MNRAS, 266, 441
Lauterborn, D., Refsdal, S., & Weigert, A. 1971, A&A, 10, 97
Lebreton, Y., Perrin, M.-N., Cayrel, R., Baglin, A., & Fernandes, J. 1999, A&A, 350, 587
Lee, M. G., Freedman, W. L., & Madore, B. F. 1993, ApJ, 417, 553
Lejeune, T., Cuisinier, F., & Buser, R. 1998, A&AS, 130, 65
Luck, R. E., Moffett, T. J., Barnes, T. G., & Gieren, W. P. 1998, AJ, 115, 605
Luridiana, V. 2002 [`astro-ph/0209177`]
Maeder, A. 1983, A&A, 120, 113
Maeder, A., & Meynet, G. 1987, A&A, 182, 243
Maeder, A., & Meynet, G. 2001, A&A, 373, 555
Magee, N. H., Abdallah, J. Jr., & Clark, R. E. H. 1995, in Atomic Structure Calculations and New Los Alamos Astrophysical Opacities, ed. S. Adelman, & W. Wiese, ASP Conf. Ser. (Astrophysical Applications of Powerful New Database), 78, 51
Mighell, K. J., Sarajedini, A., & French, R. S. 1998a, AJ, 116, 2395
Mighell, K. J., Sarajedini, A., & French, R. S. 1998b, ApJ, 494, L189
Morel, P. 1997, A&AS, 124, 597
Mould, J. R., Huchra, J. P., Freedman, W. L., et al. 2000, ApJ, 529, 786
Peimbert, M., Peimbert, A., & Ruiz, M. 2000, ApJ, 541, 688
Piatti, A., Santos, J. C., Clariá, J. J., et al. 2001, MNRAS, 325, 792
Pietrukowicz, P. 2002, Acta Astron., 52, 177
Pietrzyński, G., & Udalski, A. 1999a, Acta Astron., 49, 435
Pietrzyński, G., & Udalski, A. 1999b, Acta Astron., 49, 157
Pietrzyński, G., & Udalski, A. 1999c, Acta Astron., 49, 543
Pietrzyński, G., Udalski, A., Kubiak, M., et al. 1998, Acta Astron., 48, 175
Schaller, G., Schaerer, D., Meynet, G., & Maeder, A. 1992, A&AS, 96, 269
Schlegel, D. J., Finkbeiner, D. P., & Davis, M. 1998, ApJ, 500, 525
Stanek, K. Z., Zaritsky, D., & Harris, J. 1998, ApJ, 500, L141
Udalski, A. 1998, AcA, 48, 113
Udalski, A., Soszynski, I., Szymański, M., et al. 1999a, AcA, 49, 1
Udalski, A., Soszynski, I., Szymanski, M., et al. 1999b, Acta Astron., 49, 437
Udalski, A., Wyrzykowski, L., Pietrzynski, G., et al. 2001, Acta Astron., 51, 221
Van der Marel, R. P., & Cioni, M. L. 2001, AJ, 122, 1807
Young, P. A., Mamajek, E. E., Arnett, D., & Liebert, J. 2001, ApJ, 556, 230

Retour à la table des matières : p. v

14.3 Article sur la branche des géantes et BaSTI

The Astronomical Journal, 133:468–478, 2007 February
© 2007. The American Astronomical Society. All rights reserved. Printed in U.S.A.

A LARGE STELLAR EVOLUTION DATABASE FOR POPULATION SYNTHESIS STUDIES. III. INCLUSION OF THE FULL ASYMPTOTIC GIANT BRANCH PHASE AND WEB TOOLS FOR STELLAR POPULATION ANALYSES

Daniel Cordier
Ecole Nationale Superieure de Chimie de Rennes, Campus de Beaulieu, Rennes, France; daniel.cordier@ensc-rennes.fr

Adriano Pietrinferni[1] and Santi Cassisi[2]
INAF—Astronomical Observatory of Collurania, Teramo, Italy; pietrinferni@oa-teramo.inaf.it, cassisi@oa-teramo.inaf.it

and

Maurizio Salaris[3]
Astrophysics Research Institute, Liverpool John Moores University, Birkenhead, UK; ms@astro.livjm.ac.uk
Received 2006 March 10; accepted 2006 September 16

ABSTRACT

Stellar evolution tracks and isochrones are key inputs for a wide range of astrophysical studies; in particular, they are essential to the interpretation of photometric and spectroscopic observations of resolved and unresolved stellar populations. We have made available to the astrophysical community a large, homogenous database of up-to-date stellar tracks and isochrones and a set of programs useful in population synthesis studies. In this paper we first summarize the main properties of our stellar model database (BaSTI) already introduced by Pietrinferni and coworkers. We then discuss an important update of the database, i.e., the extension of all stellar models and isochrones until the end of the thermal pulses along the asymptotic giant branch. This extension of the library is particularly relevant for stellar population analyses in the near-infrared or longer wavelengths, where the contribution to the integrated photometric properties by cool and bright asymptotic giant branch stars is significant. A few comparisons with empirical data are also presented and briefly discussed. We then present three Web tools that allow an interactive access to the database and make it possible to compute user-specified evolutionary tracks, isochrones, stellar luminosity functions, and synthetic color-magnitude diagrams and integrated magnitudes for arbitrary star formation histories. All these Web tools are available at the BaSTI database official Web site.

Key words: astronomical data bases: miscellaneous — galaxies: stellar content — stars: AGB and post-AGB — stars: general

Online material: color figures

1. INTRODUCTION

The interpretation of photometric and spectroscopic observations of resolved and unresolved stellar populations is nowadays a fundamental tool to investigate the formation and evolution of galaxies. Large grids of stellar evolution models and isochrones are a necessary ingredient in this kind of analysis, together with appropriate tools to predict synthetic color-magnitude diagrams (CMDs)—and hence star counts along the various observed CMD branches—integrated magnitudes, and spectra of stellar populations with an arbitrary star formation history (SFH). To this purpose Pietrinferni et al. (2004, 2006) published a huge and homogeneous database of stellar evolution models that covers the relevant chemical composition range of stellar populations in galaxies of various morphological types, and allows one to choose among different treatments of core convection and stellar mass loss employed in the model calculations. These models are available on the World Wide Web as downloadable files from the BaSTI (Bag of Stellar Tracks and Isochrones) database,[4] together with three Web tools that allow user-friendly manipulation of the stellar evolution library. Thanks to these tools one can compute user-specified isochrones, interpolate among evolutionary tracks to obtain the evolution for a mass value not contained in the grid, determine the differential and cumulative luminosity functions from a set of isochrones, and finally, compute synthetic stellar populations with an arbitrary SFH and determine their integrated magnitudes and colors.

This paper describes comprehensively the BaSTI database, and in particular how to run the various Web tools, the necessary inputs, and their outputs. Section 2 describes the stellar evolution library, with particular emphasis on the most recent extensions not included in Pietrinferni et al. (2004, 2006); §§ 3–5 describe the individual Web tools that allow the computation of user-specified isochrones, models, luminosity functions, and synthetic CMDs. Section 6 contains our final conclusions, and the Appendix contains some more technical details about the implementation of the Web tools.

2. STELLAR EVOLUTION MODELS AND ISOCHRONES

We have computed stellar evolution models for 11 different metallicities, namely, $Z = 0.0001, 0.0003, 0.0006, 0.001, 0.002, 0.004, 0.008, 0.01, 0.0198, 0.03$, and 0.04, assuming two different heavy-element distributions: the scaled-solar one by Grevesse & Noels (1993) and the α-enhanced one with $\langle[\alpha/\mathrm{Fe}]\rangle = 0.40$ by Salaris & Weiss (1998). As for the initial He-mass fractions, we employed a value of $Y = 0.245$ for the cosmological He (see, e.g., Cassisi et al. 2003). To reproduce the solar initial He abundance obtained from the calibration of the solar model, we assume an

[1] Also at Universitá di Teramo, Teramo, Italy.
[2] Also at Instituto de Astrofisica de Canarias, La Laguna, Tenerife, Spain.
[3] Also at Max-Planck-Institut für Astrophysik, Garching, Germany.
[4] See http://terri1.oa-teramo.inaf.it/BASTI.

Retour à la table des matières : p. v

He-enrichment law equal to $\Delta Y/\Delta Z \sim 1.4$. For each initial chemical composition we have computed stellar evolutionary tracks with mass in the range $0.5\ M_{\odot} \leq M \leq 10\ M_{\odot}$ and a fine mass spacing. Mass loss from the stellar surface is accounted for using the Reimers (1975) law and two values of the free parameter η, namely, $\eta = 0.2$ and 0.4. For stars that develop convective cores during the central H-burning phase we have computed models with and without overshoot from the Schwarzschild boundary of the central convective regions.

All evolutions, with the exception of the least massive stars whose central H-burning timescale is longer than the Hubble time, have been computed from the pre-main-sequence phase until the C ignition or until the first thermal pulse along the asymptotic giant branch (AGB), depending on the initial stellar mass. Full details of these calculations can be found in Pietrinferni et al. (2004, 2006). Very recently we have extended the evolution of low- and intermediate-mass objects through the entire thermal pulse (TP) phase, until the end of the AGB stage. To this purpose we have used the synthetic-AGB technique (Iben & Truran 1978). Our simplified treatment of the TP-AGB phase satisfactorily reproduces several integrated properties (see below) of stellar populations in the near-IR bands, which are greatly affected by the presence of TP stars. Given that the purpose of this library of stellar models is to provide a reliable tool to be employed in stellar population synthesis studies, we feel confident that the following simplified treatment of the AGB evolution is adequate for our purposes. For each stellar model of a given initial chemical composition and mass, we started the synthetic AGB evolution at the beginning of the TP phase, where the stellar evolution calculations were terminated. The first model of the synthetic TP-AGB evolution is characterized by the total mass M, carbon-oxygen core mass $M_{\rm CO}$, luminosity L, effective temperature $T_{\rm eff}$, and surface chemical composition (X_f, Y_f, Z_f) of the last fully evolutionary model.

The TP-AGB phase is then followed by increasing (after a given time step dt) $M_{\rm CO}$ and L according to equations (5)–(7) in Wagenhuber & Groenewegen (1998), which contain a term mimicking the effect of the hot bottom burning, when appropriate. The hydrogen mass fraction in the envelope (an input of eq. [6] of Wagenhuber & Groenewegen 1998) is approximated as $1 - (Y_f + 0.01) - Z_f$ all along the TP evolution. During a time step the mass of the envelope $(M - M_{\rm CO})$ is reduced not only by the growth of $M_{\rm CO}$ but also by mass-loss processes, accounted for by using the mass-loss formulae of Vassiliadis & Wood (1993). For any given value of M and $M_{\rm CO}$, the effective temperatures are computed using the relationships in Wagenhuber (1996) that are plotted in Figure 8 of Wagenhuber & Groenewegen (1998). To ensure continuity, the zero points of the equations describing the evolution of L, $M_{\rm CO}$, and $T_{\rm eff}$ have been adjusted to reproduce the corresponding values of the last fully evolutionary model, at the beginning of the TP phase. The synthetic evolution is stopped when the models have started to evolve off the AGB, at constant luminosity, toward their white dwarf cooling sequence. The full models have been used to compute isochrones for ages ranging between 30 Myr and 19 Gyr. We provide separately models and isochrones with and without the inclusion of the TP-AGB phase, in case users wish to use their own description of the TP-AGB evolution, employing either fully evolutionary calculations or synthetic AGB models with different choices about, e.g., mass loss and/or the core mass-luminosity relationship. To this purpose we provide, as mentioned below, tables with He and CO core mass, as well as the luminosity and effective temperature at the beginning of the TP-AGB phase.

The reader is referred to Pietrinferni et al. (2004) for a detailed discussion about the normalization of the individual evolutionary tracks (the concept of the key point and normalized points between two successive key points) and isochrone computation. Here we simply mention two changes with respect to the discussion in Pietrinferni et al. (2004). The first change is the inclusion of two additional key points along the red giant branch (RGB), one to mark the maximum luminosity during the RGB bump and another to mark the minimum RGB bump luminosity (key points 6 and 7). A total of 370 normalized points are distributed between key point 6 and its predecessor, 30 points are distributed between key points 6 and 7, and 400 points are distributed between key point 7 and the following one, the tip of the RGB. Due to the TP-AGB extension, we have added an additional key point (number 17) after the beginning of the TP phase to mark the termination of the AGB phase, when the model evolution turns to the blue. A total of 250 normalized points cover the TP-AGB phase, between key points 16 and 17. The resulting isochrones have a total of 2250 points.

TABLE 1

Initial Chemical Composition of the Model Grid

Z	Y	[Fe/H] (Scaled-Solar Mixture)	[Fe/H] (α-Enhanced Mixture)
0.0001	0.245	−2.27	−2.62
0.0003	0.245	−1.79	−2.14
0.0006	0.246	−1.49	−1.84
0.0010	0.246	−1.27	−1.62
0.0020	0.248	−0.96	−1.31
0.0040	0.251	−0.66	−1.01
0.0080	0.256	−0.35	−0.70
0.0100	0.259	−0.25	−0.60
0.0198	0.273	+0.06	−0.29
0.0300	0.288	+0.26	−0.09
0.0400	0.303	+0.40	+0.05

The main characteristics of the stellar model database are summarized in Tables 1 and 2. Table 1 lists the grid of initial chemical compositions; Table 2 summarizes the available sets of models and isochrones. For a given heavy-element mixture (either scaled-solar or α-enhanced) we have computed models for 11 Z-values (Table 1) using both $\eta = 0.2$ and 0.4 for the evolution until the TP-AGB phase. For each value of η we have computed models with and without overshoot from the central convective core (in the appropriate mass range). The extension of the overshooting region $\lambda_{\rm OV}$ is $0.2H_p$ (H_p is the local pressure scale height at the Schwarzschild convective boundary), decreasing to zero when the convective cores vanish, as described in Pietrinferni et al. (2004). For each choice of the metal mixture, Z, η, and convective core extension we specify the number of tracks available, their mass range, the number of isochrones available, and their age range. Note that for masses above $\sim 2.4\ M_{\odot}$ the evolution with $\eta = 0.4$ is identical to the case of $\eta = 0.2$ (because of the negligible amount of mass lost during their evolution, according to the Reimers' law).

Broadband magnitudes and colors of the stellar evolution tracks and isochrones are predicted using color-$T_{\rm eff}$ transformations and bolometric corrections based on an updated set of model atmospheres described in Pietrinferni et al. (2004) and Cassisi et al. (2004). The evolutionary results are available in the photometric filters listed in Table 2. Additional filters will be added with time. It is worth pointing out that, for the first time, we have homogeneous transformations for both scaled-solar and α-enhanced mixtures even for supersolar metallicities. At present, the transformations for the *Hubble Space Telescope* (*HST*) ACS filters are available only for a scaled-solar chemical composition.

Retour à la table des matières : p. v

TABLE 2
SUMMARY OF THE BaSTI MODEL AND ISOCHRONE DATABASE

η	λ_{OV}	No. Tracks	M_{min} ($M_\odot$)	M_{max} ($M_\odot$)	No. Isochrones	Age_{min} (Myr)	Age_{max} (Gyr)
			Scaled-Solar Mixture				
0.2.....	0	20	0.5	2.4	63	30	19
	0.2	20	1.1	2.4	44	30	9.5
0.4.....	0	40	0.5	10	54	30	14.5
	0.2	20	1.1	10	44	30	9.5
			α-Enhanced Mixture				
0.2.....	0	20	0.5	2.4	63	30	19
	0.2	20	1.1	2.4	44	30	9.5
0.4.....	0	40	0.5	10	54	30	14.5
	0.2	20	1.1	10	44	30	9.5

NOTE.— Color-T_{eff}: *HST* ACS *UBVRIJHKL*.

For the TP-AGB section of the models and isochrones, broadband colors and magnitudes have been computed by supplementing the transformations used up to the beginning of the TP phase with the Westera et al. (2002) ones for RGB and AGB stars with $T_{eff} < 3750$ K. To ensure continuity, the bolometric corrections and colors of Westera et al. (2002) have been shifted to match the other sets of transformations when $T_{eff} = 3750$ K. Along the TP-AGB phase, when the $(J - K)$ colors reach $(J - K) = 1.2$ mag, we use the $(J - K)$–T_{eff} and $(H - K)$–T_{eff} relationships by Bergeat et al. (2001) that are appropriate in the carbon star regime. Models and isochrones extended along the TP-AGB phase are at the moment transformed only to the *UBVRIJHKL* system.

All models described above have been computed under the assumption that a star of a given mass and initial chemical composition loses during its evolution a fixed amount of mass, determined by the adopted mass-loss law. An isochrone for an old population will therefore display on the CMD a clumpy horizontal branch (HB) phase, comprising stars all with essentially the same total mass, because of both the constant mass of their progenitor and the constant value of the mass lost along the previous RGB phase. If one wants to simulate the extended HBs observed in Galactic globular clusters, a spread in the amount of mass lost by the RGB progenitor has to be accounted for. To this purpose, for each chemical composition we have also computed additional large sets of core-He-burning models, with the He core mass and envelope chemical profile fixed by a RGB progenitor having an age of ~13 Gyr at the RGB tip, and a range of values of the total stellar mass, to simulate the effect of a spread in the mass lost along the RGB. These HB models (~30 for each chemical composition) constitute a valuable tool to perform synthetic HB modeling and to investigate pulsational and evolutionary properties of different kinds of variable stars.

Users can directly download from the BaSTI database evolutionary tracks and HB models as single files or as tar gzipped archive files, selecting among the following options (11 initial chemical compositions for each choice): scaled-solar, α-enhanced, canonical (no overshoot), noncanonical (overshoot included), $\eta = 0.2$, $\eta = 0.4$, TP-AGB excluded, and TP-AGB included. We have included on the Web site appropriate "README" files and also provide tables (both in ASCII and HTML format) summarizing the main properties of the theoretical models (not including the TP-AGB phase) and also providing the CMD location of the zero-age HB and the central He exhaustion stages. These two latter sets of tables can be found at the pages containing the $\eta = 0.4$ models. A large number of precomputed isochrones for each of the individual options described before, spanning the full age range allowed by the computed models, can be downloaded as tar gzipped archive files.

The models and isochrones contained in BaSTI have been extensively tested in Pietrinferni et al. (2004, 2006) and already employed in a number of investigations (e.g., Gallart et al. 2005). We conclude this section by showing a few tests for the TP-AGB extension that we introduce in this paper. We first tested our isochrones against near-IR surface brightness fluctuation (SBF) magnitudes, which are very sensitive to the brightness and evolutionary timescales of AGB stars (see, e.g., Liu et al. 2000; Cantiello et al. 2003; Mouhcine et al. 2005; Raimondo et al. 2005).

We considered the *J*- and *K*-band SBF magnitudes determined by González et al. (2004) for a sample of Magellanic Cloud superclusters. A supercluster is obtained by co-adding individual clusters belonging to the same SWB class (see Searle et al. [1980] for the definition of the SWB classes, which are essentially age ranges). González et al. (2004) also provide the mean metallicity and age of the objects grouped in each supercluster. The original SBF magnitudes were on the Two Micron All Sky Survey system and have been transformed to the Johnson system following Bessell & Brett (1988) and Carpenter (2001).

Figures 1 and 2 display the observed SBF absolute magnitudes in *K* and *J* [González et al. (2004) assume $(m - M)_0 = 18.50 \pm 0.13$ for the Large Magellanic Cloud (LMC) and $(m - M)_0 = 18.99 \pm 0.05$ for the Small Magellanic Cloud (SMC)] of six superclusters, whose age range is covered by our models, as a function of age. Different symbols correspond to different mean metallicities; the three youngest superclusters all share the same metallicity. Horizontal error bars correspond to the age spread around the mean supercluster ages, as given by González et al. (2004).

We have compared these data with the SBF magnitudes obtained from our isochrones for the appropriate mean metallicities of the individual superclusters. Note that for each individual value of *Z* considered, we have plotted the theoretical SBF magnitudes only in the age range spanned by the one (or more) supercluster with that mean value of *Z*. We employed the BaSTI models with $\eta = 0.2$, including overshooting in the appropriate age range. For the lowest metallicity (oldest) supercluster we also display the results obtained with $\eta = 0.4$. Theory is able to

Retour à la table des matières : p. v

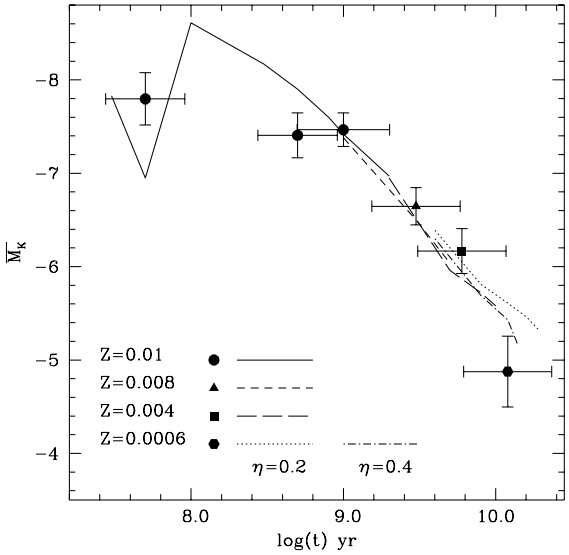

FIG. 1.—Run of the *K*-band SBF magnitudes of Magellanic Cloud superclusters as a function of their age. Theoretical SBF magnitudes for the appropriate metallicity and age range (denoted with different line styles) of the individual superclusters (superclusters of different metallicities are denoted with different symbols) are also displayed. These theoretical values are obtained from the scaled-solar isochrones including overshooting and with $\eta = 0.2$, extended along the TP-AGB phase. At $Z = 0.0006$ we also display values obtained with $\eta = 0.4$ (*dash-dotted line*; see text for details).

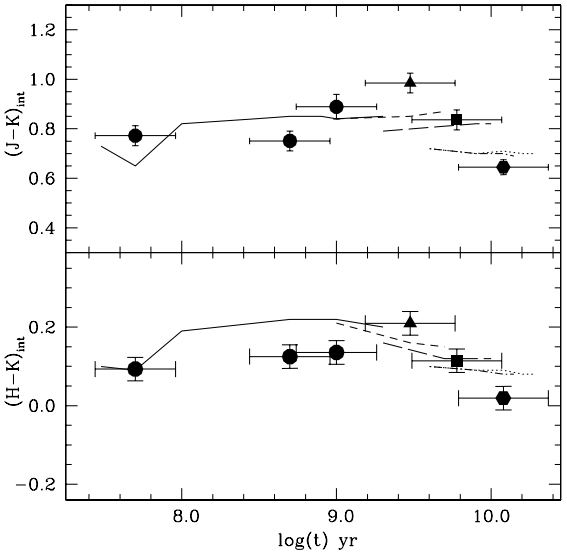

FIG. 3.—Same as Fig. 1, but for the integrated $(H - K)$ and $(J - K)$ colors of Magellanic Cloud superclusters (see text for details).

fit the data points within the observational errors, the only exception being the *J*-band SBF of the oldest supercluster.

Figure 3 compares the dereddened integrated $(J - K)$ and $(H - K)$ colors provided by González et al. (2004) for the six superclusters—transformed to the Johnson system as done for the SBF—with theoretical predictions from the same models employed for the SBF analysis. Theoretical colors appear consistent with their observational counterparts; the mean difference between theory and observations is equal to ∼0.03 mag in both $(J - K)$ and $(H - K)$. This value can be considered a reasonable estimate of the accuracy of our predicted integrated near-IR colors. Finally, Figure 4 compares the combined [K, $(J - K)$] CMDs of AGB stars in a sample of LMC clusters with theoretical isochrones. The individual stars have been co-added according to the SWB class of the parent clusters. Reddenings are from Frogel & Cohen (1982), and we use an LMC distance modulus $(m - M)_0 = 18.50$. The metallicities and ages of the theoretical isochrones are selected on the basis of the SWB class, following

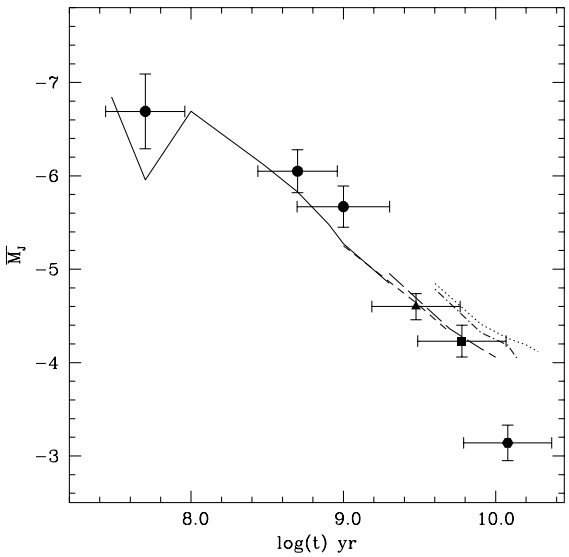

FIG. 2.—Same as Fig. 1, but for the *J*-band SBF magnitudes (see text for details).

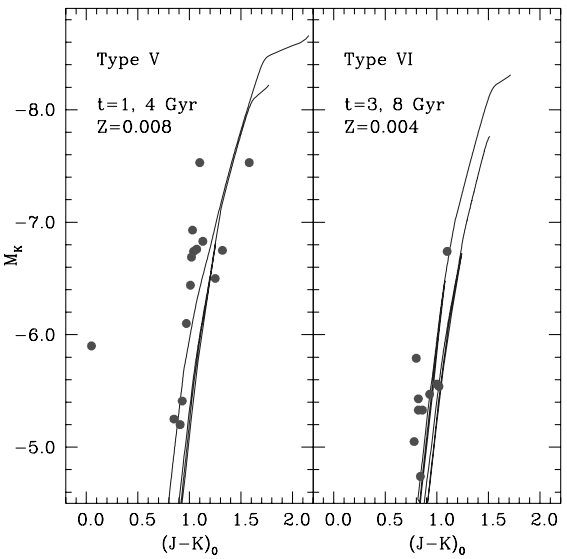

FIG. 4.—Cumulative [K, $(J - K)$] CMDs of AGB stars in a sample of LMC clusters. Theoretical isochrones for the appropriate age and metallicity range are also displayed (see text for details). [*See the electronic edition of the Journal for a color version of this figure.*]

Retour à la table des matières : p. v

FIG. 5.— Web interface for the tool dedicated to isochrones and evolutionary tracks. [*See the electronic edition of the Journal for a color version of this figure.*]

again González et al. (2004). One can see a good overlap between the theoretical AGB sequences and the observed near-IR CMDs.

3. ISOCHRONE MAKER AND TRACK INTERPOLATION PROGRAM

We have created a dedicated World Wide Web interface that allows the direct computation of isochrones for any given choice of age, for the chemical compositions and age ranges listed in Tables 1 and 2. It also enables the user to compute interpolated evolutionary tracks in the mass range 0.5–10 $M_{\odot}$ for any chemical composition in the grid. A linear interpolation on a point-by-point basis between two neighboring evolutionary tracks stored in the database is performed to determine the track for the specified mass. The mass spacing of the tracks included in BaSTI is small enough that a linear interpolation is sufficient to guarantee a high accuracy. Once the track is computed, it is immediately transposed in the chosen photometric system.

The use of this interface is particularly simple: first of all one has to go to the BaSTI Web site[5] and click on the link "Isochrones—Tracks" in the "Web Tool" section; a page like the one displayed in Figure 5 will appear. The user has now to choose among a number of options:

1. The output type, i.e., isochrone or interpolated evolutionary track.
2. The heavy-elements mixture, i.e., scaled-solar or α-enhanced.

[5] See http://terri1.oa-teramo.inaf.it/BASTI. In case of network and/or technical problems with this official Web site, the user can connect to D. C.'s personal Web site, http://astro.ensc-rennes.fr, where the BaSTI Web tools have been mirrored in the "BaSTI Web Tools" section.

Retour à la table des matières : p. v

3. The photometric system of interest; at the moment we allow a choice between the standard *UBVRIJHKL* filters and the *HST* ACS ones.
4. Core convection treatment, i.e., with or without convective core overshoot.
5. The initial chemical composition (Y, Z).

Once these input parameters are fixed, the next screen allows the choice of the isochrone age (in megayears) or the track initial total mass in solar units. Outputs (in the same format as the tracks and isochrones stored in the database) are directly sent to the user's browser.

4. LUMINOSITY FUNCTION PROGRAM

The isochrones stored in the BaSTI database, or obtained with the Web tool described in § 3, can be used as input for the tool described here, which computes the luminosity functions (e.g., differential and cumulative star counts as a function of the magnitude in a given wavelength band) of single-age, single-metallicity stellar populations.

To run this Web tool the user has to provide four parameters: the number of isochrones whose luminosity functions are needed (maximum 20), the photometric filter (in the *UBVRIJKLH* system), the initial mass function (IMF) exponent, and the size of the magnitude bins within which the star counts are performed (e.g., 0.15 mag; these bins have to be larger than 0.05 mag). We adopt for the IMF a form of the type $dN_*/dM = CM^{-\alpha}$, where dN_* is the number of stars formed with mass between M and $M + dM$ and C is a normalization constant whose value is fixed by imposing the total number of stars populating the isochrones to be equal to 10^6. A value of α equal to 2.35 corresponds to the Salpeter (1955) IMF.

One has then to choose between the options of computing the luminosity functions only until the RGB tip, along the whole isochrone until the early AGB, or including also the TP-AGB phase. Star counts are then computed analytically by convolving the IMF with the distribution of the initial stellar mass values along the isochrones. For example, the number of stars N between two consecutive points $i - 1$ and i along a chosen isochrone is given by $N = C/1 - \alpha(M_i^{1-\alpha} - M_{i-1}^{1-\alpha})$.

As a final step one has to upload the isochrone files and submit the job. Results are directly sent to the user's Internet browser as ASCII data divided into several sections, each of them corresponding to one individual isochrone. The input parameters are recalled: metallicity, IMF exponent, age, etc. The data themselves are displayed in three columns: the mean magnitude of the bin and the differential (where N denotes the star counts per magnitude bin as a function of the magnitude) and cumulative (where $N+$ denotes the sum of the star counts from the faintest bin to the actual one as a function of the magnitude) luminosity functions.

5. SYNTHETIC CMD CODE

The computation of synthetic CMDs is often required to interpret observations of resolved or unresolved stellar populations. The simplest form of a synthetic CMD is an isochrone that represents the sequence occupied by stars all formed at the same time and with the same initial chemical composition. Clearly, an isochrone does not directly contain information about the number of stars populating the various CMD branches, nor the effect of photometric errors and reddening, and cannot represent composite stellar populations comprising multiple generations of stars. To include these effects one needs a synthetic CMD generator. On the BaSTI Web site the user can access the SYNTHETIC MAN code, which is an evolution of the version briefly described in Pietrinferni et al. (2004). This code computes the magnitudes and colors of objects belonging to a synthetic stellar population with an arbitrary SFH. The program employs a grid of isochrones with ages between 30 Myr and 14 Gyr (we employ 49 isochrones extended until the end of the TP-AGB phase for each of the 11 metallicities included in our model grid).

The SYNTHETIC MAN code is based on a Monte Carlo algorithm that allows one to include in a simple way observation-related effects such as the reddening/distance/metallicity dispersion and photometric errors and to identify on a star-by-star basis the various types of pulsating stars that may be present in the synthetic population. Synthetic CMDs and observation-related effects can also be efficiently determined by means of analytical integrations, as done in Dolphin (2002). It is worth noting that Skillman et al. (2003) applied three different methods to determine the SFH of the galaxy IC 1613. One of them is the analytical technique by Dolphin (2002), and another is a Monte Carlo method similar to the one we implemented. A comparison of the results with the different techniques shows striking agreement.

The general structure of the SYNTHETIC MAN code is as follows. A SFH file has to be specified first. The SFH contains a grid of N ages t_i (the upper limit for N is set to 200), increasing with increasing running index i (the present time is assigned $t = 0$), and for each age one has to specify a scale factor SF_i proportional to the relative number of stars formed at that time. Also, the metallicity (parameterized by [Fe/H]) of the stars formed at that age has to be given ($[\mathrm{Fe/H}]_i$), together with a 1 σ Gaussian spread around this value. The scale factor and [Fe/H] for ages in the range $t_i \leq t < t_{(i+1)}$ are then assumed to be equal to SF_i and $[\mathrm{Fe/H}]_i$, respectively. In other words, the SFH is considered to be a sequence of step functions. The scale factor and [Fe/H] at $i = N$ are not considered and can be set to any arbitrary value; the last point in the SFH file is important only because it provides the upper age limit for the simulated stellar population. If one or more single burst stellar populations are needed, one or more pairs of identical ages (i.e., $t_i = t_{(i+1)}$) need to be included in the SFH file.

After the SFH is read by the code, the following cycle starts, running along the SFH index from $i = 0$ to $i = N$. The age difference between two generic t_i and $t_{(i+1)}$ values is computed, and for each star formed in this time interval (the number of stars formed in a generic time interval is determined from the input SFH) a random value of the stellar age $t_i \leq t < t_{(i+1)}$ is drawn with a flat probability distribution, together with a mass M selected randomly according to a user-specified IMF (the default mass range goes from 0.1 to 120 $M_\odot$, although a different lower mass limit can be specified by the user) and a random value of [Fe/H] assigned according to the value of $[\mathrm{Fe/H}]_i$ plus the 1 σ spread given in the SFH. With the three specified values of t, M, and [Fe/H] the program interpolates quadratically in age, metallicity, and then mass among the isochrones in the grid to determine the star luminosity, effective temperature, actual value of the mass (in principle different from the initial value because of mass loss), and photometric properties in the *UBVRIJHKL* system.

For each generated mass an additional random number determines whether the star is a member of an unresolved binary system (the percentage of unresolved binaries has to be specified as an input); if this is true, the mass of the second component is selected randomly following Woo et al. (2003), and the fluxes of the two unresolved components are properly added.

Once the photometric properties of an object (single or belonging to an unresolved binary system) are determined, the depth effects

Retour à la table des matières : p. v

TABLE 3
VARIABLE TYPE INDEX AND SOURCES USED IN THE POPULATION SYNTHESIS PROGRAM

Variable Type Index	Variable Type	Source for Instability Strip Boundaries
0	No variable	
1	Fundamental RR Lyrae	Marconi et al. (2003), Di Criscienzo et al. (2004)
2	First-overtone RR Lyrae	Marconi et al. (2003), Di Criscienzo et al. (2004)
3	Fundamental anomalous Cepheid	Marconi et al. (2004)
4	First-overtone anomalous Cepheid	Marconi et al. (2004)
5	Fundamental classical Cepheid	Bono et al. (2000)

of the synthetic stellar population are simulated probabilistically according to a uniform stellar distribution with a user-specified total depth (in magnitudes). After depth effects are included, the individual magnitudes are modified by adding the effect of extinction (another input parameter; we have employed the extinction ratios from the Asiago Database on Photometric Systems [see Moro & Munari 2000] and $R_V = 3.1$) and then further perturbed according to a Gaussian distribution to simulate the photometric errors, with a user-specified 1 σ width. The star [Fe/H] value is also perturbed according to a Gaussian error with user-specified 1 σ width to mimic the effect of spectroscopic observational errors. As an additional option, the code can search for variable stars, according to their location with respect to the boundary of RR Lyrae and Cepheid instability strips; pulsation periods are then determined. Table 3 shows literature references for the relevant types of variables.

Once all stars formed between ages t_i and $t_{(i+1)}$ are generated, the next interval ($t_{(i+1)} \leq t < t_{(i+2)}$) is considered, and the cycle continues, ending when all stars in the final age bin $t_{(N-1)} \leq t < t_{(N)}$ are generated.

As a technical comment, if the value of M for a star generated by the Monte Carlo procedure is too large to be still evolving at its age t or is lower than 0.5 $M_\odot$, the contribution to the total mass of stars formed in the population is taken into account, but the star photometric properties are not determined. The total mass of the objects formed, the total number of the stars whose photometric properties have been determined (in principle different from the total number generated for the reasons mentioned above), and the integrated magnitudes (in the *UBVRIJHKL* system) of the synthetic population are also computed.

Like all Monte Carlo–based simulations, our program makes extensive use of random numbers. Our random number generator (initially written by James 1990) needs "seeds" to be initialized; these seeds can be either provided by the user or obtained from the True Random Number Service Web site,[6] which derives "true" random numbers from atmospheric electromagnetic noise.

The World Wide Web interface to SYNTHETIC MAN can been found in the BaSTI section "Synthetic Color-Magnitude Diagrams." This software is as simple to use as the others, but a registration is required before its first use. The user receives a notification by e-mail when the computations are completed. In order to get a user identification, one needs to contact S. Cassisi or D. Cordier. In the following we summarize the input parameters for a run of SYNTHETIC MAN.

1. A scale factor for the SFH. As explained before, the SFH contains the relative weight of the star formation episodes in the various age bins. In order to fix the absolute number of objects in each stellar generation, a scale factor has to be chosen. The product of this scale factor times the relative weight in the input SFH gives the total number of stars created in a generic age bin, with mass between 0.1 (or a user specified lower mass limit) and 120 $M_\odot$. If more than 2×10^6 objects are expected to be formed at a given time step, the program will stop to highlight the excessive amount of computational time needed for the whole simulation.

2. A choice for the mean photometric error. The user can adopt a 1 σ constant error that it is applied to all stars in the simulation, in all nine photometric bands. The size of this constant error (between 0.0 and 1.0 mag) has to be specified. Alternatively, the user can choose to adopt an error varying with the actual star magnitude and/or photometric band. The exact values have to be specified by the user in an appropriate input file. This photometric error input file contains 18 columns and an arbitrary number N of rows (upper limit $N = 200$). The first nine columns display N magnitudes M_J^i (i running from 1 to N), in order of increasing value, for the *UBVRIJHKL* photometric bands, respectively. The remaining nine columns are the corresponding 1 σ photometric errors in the *UBVRIJHKL* filters, respectively (e.g., σ_U, σ_B, and σ_V). The choice of the error for any individual synthetic star proceeds as follows. If M_V^* is the star magnitude in the V band, the program searches for a pair of neighboring tabulated M_V^i magnitudes such that $M_V^i < M_V^* \leq M_V^{i+1}$ and assigns to the star σ_V the value tabulated for M_V^{i+1}. If M_V^* is smaller than M_V^1 or larger than M_V^N, the error corresponding to M_V^1 or M_V^N is used, respectively. The same procedure is repeated for all other photometric bands considered.

3. The 1 σ mean spectroscopic error (between 0.01 and 1.0 dex).

4. A choice for the range considered in the stellar mass random extraction. An upper limit of 120 $M_\odot$ is always considered. The user can decide to use a different lower mass limit (larger than 0.1 $M_\odot$) that must then be specified by the user.

5. The total spatial depth of the population (between 0.0 and 10.0 mag).

6. The color excess $E(B - V)$ (between 0.0 and 10.0 mag).

7. The fraction of unresolved binaries.

8. The minimum mass ratio for the unresolved binary systems (between 0.0 and 1.0)

TABLE 4
INDEX FOR THE ISOCHRONE SETS EMPLOYED BY THE SYNTHETIC MAN CODE

Index	Isochrone Set
1	Scaled-solar, no overshooting, $\eta = 0.2$
2	Scaled-solar, overshooting, $\eta = 0.2$
3	Scaled-solar, no overshooting, $\eta = 0.4$
4	Scaled-solar, overshooting, $\eta = 0.4$
5	α-enhanced, no overshooting, $\eta = 0.2$
6	α-enhanced, overshooting, $\eta = 0.2$
7	α-enhanced, no overshooting, $\eta = 0.4$
8	α-enhanced, overshooting, $\eta = 0.4$

[6] See http://www.random.org.

Retour à la table des matières : p. v

TABLE 5
AVAILABLE STAR FORMATION HISTORIES

Stellar Population	Source
NGC 6822 (global SFH)	Gallart et al. (1996)
SMC (global SFH)	Harris & Zaritsky (2004)
LMC (bar field)	Holtzman et al. (1999)
Local disk	Rocha-Pinto et al. (2000)
Milky Way bulge	Mollá et al. (2000)
Sextans A	Dolphin et al. (2003)
LGS3	Miller et al. (2001)

9. The IMF. The user can adopt a power law of the form M^{-x}. The exponent x must then be specified. Alternatively, the user is allowed to choose the Kroupa et al. (1993) IMF.

10. A choice of the isochrone set to use according to the value of an integer index between 1 and 8. The correspondence between integer value and isochrone set is reported in Table 4.

11. The possibility to search for pulsating variable stars harbored by the synthetic population and compute their periods. An integer value equal to 1 enables the search, and a value equal to 0 prevents the search.

12. The desired SFH. A number of prespecified SFHs for selected galaxies are also provided (see Table 5).

13. As in all simulations based on a Monte Carlo method, our program needs seeds for random number generator initialization. The user can choose the values of the seeds or let the program automatically get seeds from the True Random Number Service Web site.[7] We underline that all computations initialized with the same seeds will lead to identical outputs.

After specifying the input parameters, users can start their computations by clicking the "Submit" button. The calculation may take some time (from a few minutes to hours, mainly depending on the requested number of stars). After the calculation is

[7] See http://www.random.org.

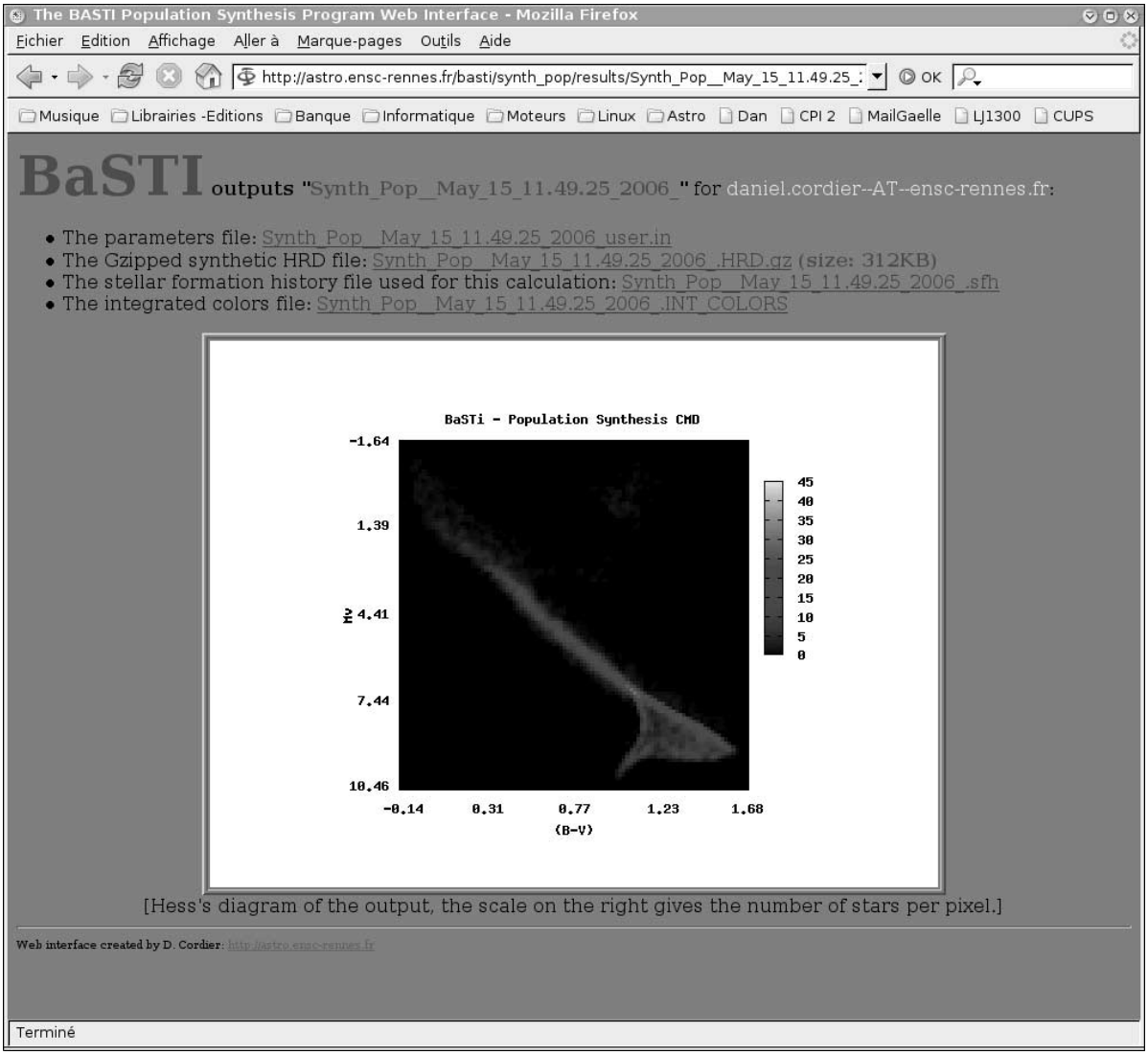

FIG. 6.— Example of the output Web page for the SYNTHETIC MAN Web tool. [*See the electronic edition of the Journal for a color version of this figure.*]

Retour à la table des matières : p. v

completed the user receives an e-mail as notification. As the size of the output files can amount to several megabytes, they cannot be sent by e-mail, and a solution involving a dynamically generated Web page has been found to be preferable. In the output Web page four data files are available:

1. `Synth_Pop_*_user.in`. This ASCII file recalls the parameters used for the calculation.
2. `Synth_Pop_*_.HRD.gz`. This gzipped file contains data for the individual stars, in which one can find the following quantities: identification number, $\log t$ (yr), [Fe/H], the value of the actual mass, $\log L$ ($L_\odot$), $\log T_{\rm eff}$ (K), M_V, $(B-V)$, $(U-B)$, $(V-I)$, $(V-R)$, $(V-J)$, $(V-K)$, $(V-L)$, $(H-K)$, the value of the initial mass, the initial mass of the unresolved binary companion (if present; for stars without a companion this quantity is set to 0.0), logarithm of the pulsation period (in days; if the search for variable is off or if the star is not pulsating, this quantity is set to 99.99), and an index denoting the type of variable (see Table 3 for explanations). This file can be uncompressed with the standard GNU software GUNZIP. As this file can be relatively large, downloading is automatically forced when users click on the link.
3. `Synth_Pop_*_.sfh`. This file contains the SFH data used for the calculations.
4. `Synth_Pop_*_.INT_PROPERTIES`. This file contains the integrated *UBVRIJHKL* absolute magnitudes produced by the stars evolving in the synthetic population, several selected integrated colors, the total number of stars with computed photometric properties, the total mass of stars formed (within the mass range specified in the input file) according to the specified SFH, and a summary of the various types of variable stars found (if the search for variables is off, the values are all equal to zero).

The asterisk denotes a string chosen by the Web tool to avoid the possibility of output files corresponding to a specific simulation being overwritten by those related to a different run. The string is selected according to the time when the numerical run is launched. For example, if the run is launched at 16.51.34 of 2006 May 3, the string will be "`May_3_16.51.34_2006.`"An example of the output Web page is displayed in Figure 6. The [V, $(B-V)$] Hess's diagram taking into account all the synthetic objects drawn for the simulation is also automatically displayed, with stars' numbers being encoded with colors. The user should be aware that, for obvious reasons, Web pages displaying program outputs are deleted by the software manager 1 month after the end of the computation.

6. CONCLUSION

In this paper we have presented the content of the BaSTI database for stellar population synthesis studies. In particular, we have discussed the recent extension of the models to the end of the TP-AGB phase and described three Web tools used to compute synthetic CMDs, luminosity functions, and user-specified isochrones and stellar evolution tracks.

In the near future the BaSTI database will be developed following two directions: the extension of the database itself and the development of an online version of our stellar evolution code.

We plan to extend the mass range spanned by our database by adding tracks for very low mass objects (below 0.5 $M_\odot$) and very massive stars (above 10 $M_\odot$), the latter until C-burning ignition.

With a Web-based version of our evolution code, people who are not expert in stellar evolution calculations will be able to compute models with their customized set of parameters (mixing-length value, extension of the overshooting region, metallicity, etc.), avoiding inaccurate interpolation and/or extrapolation between and/or from existing models. This could also allow for more complex tuning such as opacity tables or nuclear rate table switching, and changes to the equation of state. We think that this Web-based evolutionary code, as well as the BaSTI database, could be relevant tools for the whole scientific community within the ongoing Virtual Observatory project (Pasian 2004).

We wish to thank the anonymous referee for suggestions that helped us to improve the content and readability of the manuscript. D. C. thanks the Ecole Nationale Supérieure de Chimie de Rennes for working facilities and M. J. Goupil and Y. Lebreton for so many things. We wish also to acknowledge all the people who have already used and/or will be using the BaSTI Web tools for their own research and who will send us their comments/suggestions. We warmly thank E. Sandquist for all the useful comments and for pointing out the existence of some problems in a preliminary version of our Web tools. S. C. warmly thanks financial support from Ministero dell'Università e della Ricerca and INAF.

APPENDIX

BaSTI WEB TOOLS: SOME TECHNICAL ASPECTS

The World Wide Web, originally conceived for document delivery, has evolved into a medium supporting interactive computations. One way for a Web server (in our case APACHE)[8] to interact with data-generating programs is the well-known Common Gateway Interface (hereafter CGI). Input parameters and data provided by the user are passed to our three FORTRAN programs through PERL programs. PERL is probably the most common CGI scripting language, for which a huge collection of modules is available in the Comprehensive PERL Archive Network.[9]

The track/isochrone interpolation program and the luminosity function program are simply driven with a specific PERL interface, and their outputs are directly displayed as an ASCII file that can be saved in the user's hard disk and used by other programs without any difficulty.

The CMD generator is probably, at the moment, our most sophisticated Web-based software. When it is invoked, a computation identification string of characters (CISC) is assigned. The files are handled and stored with this CISC as part of the file name, so even if multiple users from different parts of the world submit simulations at the same time, they can all be processed separately. When the computation is completed, an HTML page is created on the fly, displaying data output files and a previsualization made with GNUPLOT. The PERL module NET allows automatic e-mail sending for user notification.

Figure 7 summarizes the BaSTI Web tools' general scheme. Some details have been omitted, such as interaction with the plotting software GNUPLOT and random seeds downloaded from the True Random Number Service Web site.[10] At the moment all calculations are treated after each user's clicking, and consequently, several computations can be running at the same time on our machine, an occurrence that could seriously affect the computation time. Depending on the success of our online programs, we could implement as a new feature a more elaborate computation-managing system that could "queue" the users requests, decreasing individual computation times.

[8] See http://www.apache.org.
[9] See http://www.cpan.org.
[10] See http://www.random.org.

Retour à la table des matières : p. v

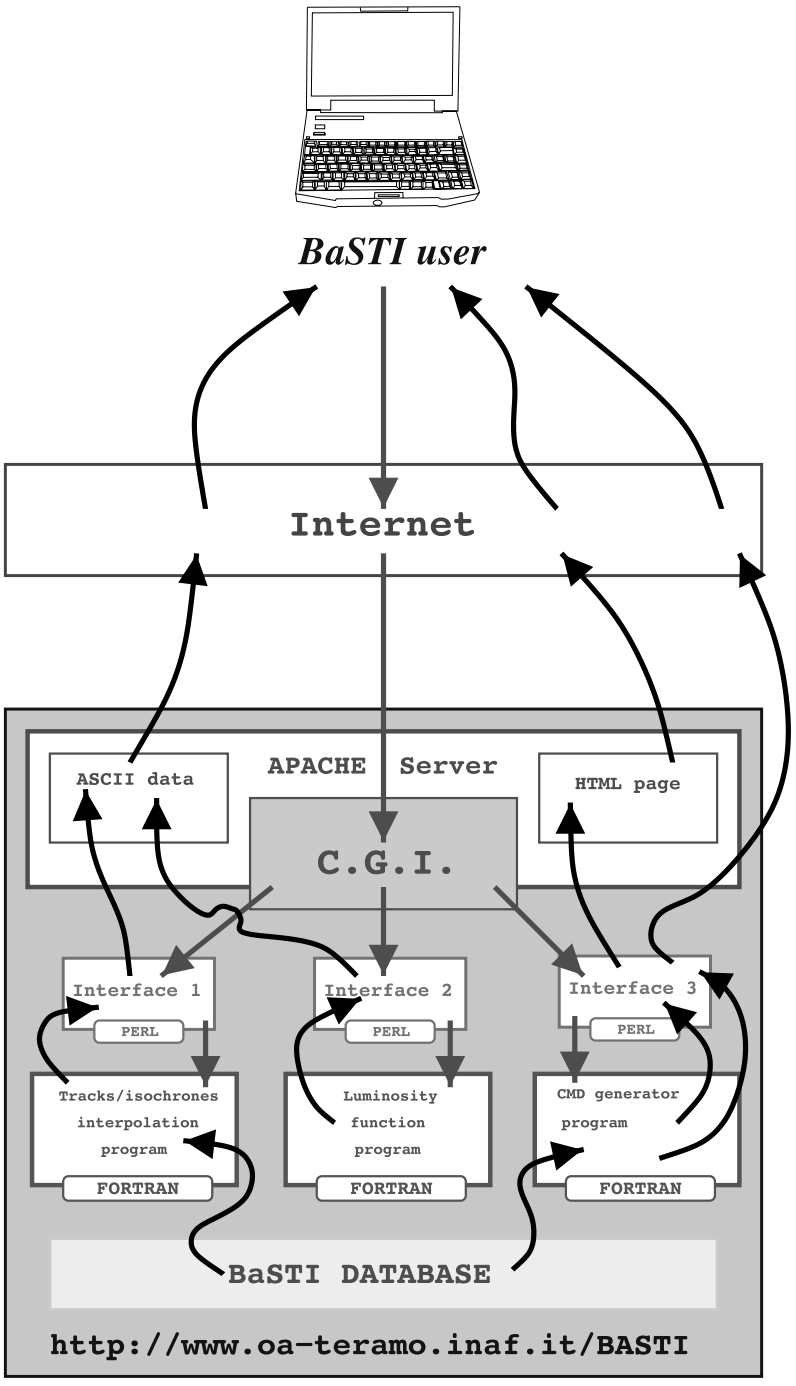

FIG. 7.—Data fluxes in the BaSTI Web tools. Random number generator seeds provided by the True Random Number Service Web site have been omitted. [*See the electronic edition of the Journal for a color version of this figure.*]

Retour à la table des matières : p. v

REFERENCES

Bergeat, J., Knapik, A., & Rutily, B. 2001, A&A, 369, 178
Bessell, M. S., & Brett, J. M. 1988, PASP, 100, 1134
Bono, G., Castellani, V., & Marconi, M. 2000, ApJ, 529, 293
Cantiello, M., Raimondo, G., Brocato, E., & Capaccioli, M. 2003, AJ, 125, 2783
Carpenter, J. M. 2001, AJ, 121, 2851
Cassisi, S., Salaris, M., Castelli, F., & Pietrinferni, A. 2004, ApJ, 616, 498
Cassisi, S., Salaris, M., & Irwin, A. W. 2003, ApJ, 588, 862
Di Criscienzo, M., Marconi, M., & Caputo, F. 2004, ApJ, 612, 1092
Dolphin, A. E. 2002, MNRAS, 332, 91
Dolphin, A. E., et al. 2003, AJ, 126, 187
Frogel, J. A., & Cohen, J. G. 1982, ApJ, 253, 580
Gallart, C., Aparicio, A., Bertelli, G., & Chiosi, C. 1996, AJ, 112, 2596
Gallart, C., Zoccali, M., & Aparicio, A. 2005, ARA&A, 43, 387
González, R. A., Liu, M. C., & Bruzual A., G. 2004, ApJ, 611, 270
Grevesse, N., & Noels, A. 1993, in Origin and Evolution of the Elements, ed. N. Prantzos, E. Vangioni-Flam, & M. Casse (Cambridge: Cambridge Univ. Press), 14
Harris, J., & Zaritsky, D. 2004, AJ, 127, 1531
Holtzman, J. A., et al. 1999, AJ, 118, 2262
Iben, I., & Truran, J. W. 1978, ApJ, 220, 980
James, F. 1990, Comput. Phys. Commun., 60, 329
Kroupa, P., Tout, C. A., & Gilmore, G. 1993, MNRAS, 262, 545
Liu, M. C., Charlot, S., & Graham, J. R. 2000, ApJ, 543, 644
Marconi, M., Caputo, F., Di Criscienzo, M., & Castellani, M. 2003, ApJ, 596, 299
Marconi, M., Fiorentino, G., & Caputo, F. 2004, A&A, 417, 1101
Miller, B. W., Dolphin, A. E., Lee, M. G., Kim, S. C., & Hodge, P. 2001, ApJ, 562, 713
Mollá, M., Ferrini, F., & Gozzi, G. 2000, MNRAS, 316, 345
Moro, D., & Munari, U. 2000, A&AS, 147, 361
Mouhcine, M., González, R. A., & Liu, M. C. 2005, MNRAS, 362, 1208
Pasian, F. 2004, Mem. Soc. Astron. Italiana, 4, 86
Pietrinferni, A., Cassisi, S., Salaris, M., & Castelli, F. 2004, ApJ, 612, 168
———. 2006, ApJ, 642, 797
Raimondo, G., Brocato, E., Cantiello, M., & Capaccioli, M. 2005, AJ, 130, 2625
Reimers, D. 1975, Mem. Soc. R. Sci. Liege, 8, 369
Rocha-Pinto, H. J., Scalo, J., Maciel, W. J., & Flynn, C. 2000, A&A, 358, 869
Salaris, M., & Weiss, A. 1998, A&A, 335, 943
Salpeter, E. 1955, ApJ, 121, 161
Searle, L., Wilkinson, A., & Bagnuolo, W. G. 1980, ApJ, 239, 803
Skillman, E. D., Tolstoy, E., Cole, A. A., Dolphin, A. E., Saha, A., Gallagher, J. S., Dohm-Palmer, R. C., & Mateo, M. 2003, ApJ, 596, 253
Vassiliadis, E., & Wood, P. R. 1993, ApJ, 413, 641
Wagenhuber, J. 1996, Ph.D. thesis, Tech. Univ. München
Wagenhuber, J., & Groenewegen, M. A. T. 1998, A&A, 340, 183
Westera, P., Lejeune, T., Buser, R., Cuisinier, F., & Bruzual, G. 2002, A&A, 381, 524
Woo, J.-H., Gallart, C., Demarque, P., Yi, S., & Zoccali, M. 2003, AJ, 125, 754

Retour à la table des matières : p. v

———————————————————————————————————————-

Retour à la table des matières : p. v

14.4 Article sur BaSTI comme part du Virtual Observatory italien

CHICAGO JOURNALS

BaSTI, a Bridge between Grid and Virtual Observatory Part 1: BaSTI inside the VO
Author(s): P. Manzato, A. Pietrinferni, F. Gasparo, G. Taffoni and D. Cordier
Source: *Publications of the Astronomical Society of the Pacific*, Vol. 120, No. 870 (August 2008), pp. 922-932
Published by: The University of Chicago Press on behalf of the Astronomical Society of the Pacific
Stable URL: http://www.jstor.org/stable/10.1086/591294
Accessed: 08/12/2014 10:42

Your use of the JSTOR archive indicates your acceptance of the Terms & Conditions of Use, available at
http://www.jstor.org/page/info/about/policies/terms.jsp

JSTOR is a not-for-profit service that helps scholars, researchers, and students discover, use, and build upon a wide range of content in a trusted digital archive. We use information technology and tools to increase productivity and facilitate new forms of scholarship. For more information about JSTOR, please contact support@jstor.org.

The University of Chicago Press and *Astronomical Society of the Pacific* are collaborating with JSTOR to digitize, preserve and extend access to *Publications of the Astronomical Society of the Pacific.*

http://www.jstor.org

This content downloaded from 194.199.64.71 on Mon, 8 Dec 2014 10:42:13 AM
All use subject to JSTOR Terms and Conditions

PUBLICATIONS OF THE ASTRONOMICAL SOCIETY OF THE PACIFIC, **120**:922–932, 2008 July
© 2008. The Astronomical Society of the Pacific. All rights reserved. Printed in U.S.A.

BaSTI, a Bridge between Grid and Virtual Observatory Part 1: BaSTI inside the VO

P. MANZATO

INAF-SI / Trieste Astronomical Observatory, via G.B. Tiepolo 11, 34143 Trieste, Italy; manzato@oats.inaf.it

A. PIETRINFERNI

INAF / Collurania Astronomical Observatory, via M. Maggini 64100 Teramo, Italy; pietrinferni@oa-teramo.inaf.it

F. GASPARO, G. TAFFONI

INAF-SI / Trieste Astronomical Observatory, via G.B. Tiepolo 11, 34143 Trieste, Italy

D. CORDIER

Institut de Physique de Rennes Université de Rennes 1, Campus de Beaulieu, 35 700 Rennes, France and Ecole Nationale Suprieure de Chimie de Rennes, Campus de Beaulieu, 35 700 Rennes, France

Received 2008 April 24; accepted 2008 June 20; published 2008 July 29

ABSTRACT. In the first part of this work we describe a new relational database (DB) created for storing metadata of stellar evolution models for a large range of masses and initial chemical compositions, which allows searching for data by scientific quantities and useful parameters. These data users can access the DB and might select a good catalog of evolutionary tracks and/or isochrones for making scientific studies and comparison with observational data. We also present a new Web portal where users can download scientific data of interest. This work has been conduced within the Italian Theoretical Virtual Observatory (ITVO) project , which aims to register these theoretical data under the Virtual Observatory standard and provide a set of standard tools able to visualize and analyze observational and also theoretical data. In the second part of the work we describe the link between the Grid infrastructure and the Virtual Observatory services as delineated by G. Taffoni and colleagues in 2006 and by F. Pasian and colleagues in 2008.

Online material: color figures

1. INTRODUCTION

This work is the second step inside the Italian Theoretical Virtual Observatory (ITVO) project (Pasian et al. 2006), whose first step consisted of archiving and publishing the data of many cosmological simulations (see Manzato et al. 2007), to offer the scientific community the possibility of reusing these data. As very long central processing unit (CPU) time was required to obtain these simulations, it was decided to insert other simulation data, like theoretical stellar data, in the virtual observatory (VO; see Hanisch & Quinn 2003) standards as part of VO–Data Centre Alliance (VO-DCA) WP4 and WP5 European asset and the ITVO Italian project.

In consideration of the covered wide range of stellar masses and chemical compositions, as well as of choices about important parameters such as mass loss and core convective overshooting efficiency, the Bag of Stellar Tracks and Isochrones (BaSTI) database (DB) (see Pietrinferni et al. 2004, 2006; Cassisi et al. 2006; Cordier et al. 2007) represents a fundamental tool to investigate the properties of stellar populations in both galactic and extragalactic systems.

The DB is structured to archive all the parameters regarding a stellar model simulation, starting from the initial chemical composition to their proprieties such as type of model, photometric system, heavy element distribution, mass loss, and even type of scenario,[1] and all parameters regarding the numerical evolutionary code linked to the metadata of the simulation output files. This relational DB offers the possibility of storing and easily searching the obtained data by many set of stellar simulations, and it also gives user-friendly access to a huge amount of homogeneous data such as these tracks and isochrones computed by using the Fraseati Raphson Newton Evolutionary Code (FRANEC) evolutionary code (see Pietrinferni et al. 2004

[1] In this context, with 'scenario' we refer to the fact that the stellar models are computed under various assumptions about the efficiency of noncanonical physical processes such as core convective overshooting, atomic diffusion, and rotation.

This content downloaded from 194.199.64.71 on Mon, 8 Dec 2014 10:42:13 AM
All use subject to JSTOR Terms and Conditions

Retour à la table des matières : p. v

TABLE 1
THE MAIN CHARACTERISTICS OF THE BASTI EVOLUTIONARY MODELS DATABASE

Mixture	Scaled-solar				α-enhanced			
η	0.2		0.4		0.2		0.4	
λ_{OV}	0	0.2	0	0.2	0	0.2	0	0.2
N^O tracks	20	20	40	20	20	20	40	20
$M_{min}(M_\odot)$	0.5	1.1	0.5	1.1	0.5	1.1	0.5	1.1
$M_{max}(M_\odot)$	2.4	2.4	10	10	2.4	2.4	10	10
N^O isoc.	63	44	54	44	63	44	54	44
Age_{min}(Myr)	30	30	30	30	30	30	30	30
Age_{max}(Gyr)	19	9.5	14.5	9.5	19	9.5	14.5	9.5
Photometric system	*UBVRIJKLH*—ACS *HST*—Ströemgren—Sloan—Walraven							

and references therein). So, the new Web portal provides users with the opportunity of downloading a single tar file within stellar tracks and/or isochrones of interest. We assigned a plus value to these data, thus developing a structure: archive +DB+ Web portal. In the past, one could only access the data archive through the links on a Web portal. Now we are creating a much more flexible structure that will allow many additional services in the future.

2. THE STORED STELLAR SIMULATIONS

Our model DB has been computed by using a recent version of the FRANEC evolutionary code, updated in many aspects concerning both the numerical scheme for treating the nuclear burnings and the accuracy of the numerics. Almost all the adopted physical inputs have been updated as well. In particular, the radiative opacity tables (Iglesias & Rogers 1996; Alexander & Ferguson 1994), thermal conduction (Potekhin 1999), plasma-neutrino processes (Haft et al. 1994) were updated. The nuclear reaction rates have been updated by using the NACRE compilation (Angulo et al. 1999), with the exception of the $^{12}C(\alpha,\gamma)^{16}O$ reaction (Kunz et al. 2002). As for the equation of state (EOS), we have employed the new EOS by A. Irwin[2] (see also Cassisi et al. 2003), which covers all relevant evolutionary stages from the Main Sequence to the initial phases of White Dwarf cooling sequence or advanced burning stages, for a large mass range. All models have been computed by fixing the extension of the convective core during the core H-burning phase classically (i.e., according to the canonical Schwarzschild's criterion) and also considering a nonnegligible efficiency of the overshoot process ($\lambda_{OV} = 0.2Hp$). We have also accounted for mass loss by using the Reimers (1975) formula with the free parameter η set to 0.2 and 0.4. A more detailed discussion about the physical inputs can be found in Pietrinferni et al. 2004.

With the aim of covering a wide range of chemical compositions, we provide models for 11 different metallicities, namely $Z = 0.0001$, 0.0003, 0.0006, 0.001, 0.002, 0.004, 0.008, 0.01, 0.0198 (i.e. $Z_\odot$), 0.03 and 0.04, assuming two different heavy element distributions: scaled-solar (Grevesse & Noel 1993) and α-enhanced (Salaris & Weiss 1998). As for the primordial He abundance, we have adopted the value ($Y = 0.245$) provided by Cassisi et al. (2003). Through the calibration of the standard solar model we have set the following: the solar initial metal abundance $Z_\odot = 0.0198$, the mixing-length parameter[3] $m_l = 1.913$, and the initial Helium abundance for the Sun $Y_\odot = 0.2734$. As a consequence, we assume an Helium enrichment law equal to $\Delta Y/\Delta Z \approx 1.4$, in good agreement with the recent estimation $\Delta Y/\Delta Z = 2.1 \pm 0.9$ provided by Casagrande et al. (2007).

For each fixed chemical composition we have computed models in the mass range $0.5 \leq M/M_\odot \leq 10$ with a very fine mass spacing (see details in Pietrinferni et al. 2004). All models, with the exception of the least massive ones whose central H-burning time scale is longer than the Hubble time, have been evolved from the Pre-Main Sequence phase up to the C-ignition, or until the first thermal pulses along the asymptotic giant branch. The main characteristics of our archive are listed in Table 1. These models have been used to compute isochrones for a wide range of ages, from 30 Myr to the upper limit listed in Table 1. An extensive comparison between our isochrones and ones computed by other groups can be found in Pietrinferni et al. (2004, 2006) and Dotter et al. (2007).

For each chemical composition we have also computed additional He-burning low-mass stellar models with He core mass and envelope chemical profile fixed by a red giant branch (RGB) progenitor having an age of ~13 Gyr at the RGB tip, and a range of values of the total stellar mass. These horizontal

[2] More informations about this new EOS can be found at the following uniform resource locator (URL) site http://freeeos.sourceforge.net.

[3] The mixing-length theory (Böhm-Vitense 1958) is a phenomenological, local, and time-independent approach to the stellar convective transport. This treatment introduces, for the computation of the temperature gradient, an adimensional parameter $m_l = l/H_P$ (where H_P is the local pressure height and l is the mean free path of the convective element), which has to be calibrated.

This content downloaded from 194.199.64.71 on Mon, 8 Dec 2014 10:42:13 AM
All use subject to JSTOR Terms and Conditions

Retour à la table des matières : p. v

branch (HB) models (~30 for each chemical composition) constitute a valuable tool to perform synthetic HB modeling, and to investigate pulsational and evolutionary properties of different kinds of pulsating variable stars.

From the theoretical plane all evolutionary results have been transferred to magnitudes and colors in various photometric filters, by using color-$T_{\rm eff}$ transformations and bolometric corrections based on an updated set of model atmospheres (see Castelli & Kurucz 2003 for more details). The evolutionary results are available in the *UBVRIJKLH*, Advanced Camera for Surveys (ACS) on the *Hubble Space Telescope* (*HST*), Strömegren, Sloan, and Walraven photometric filters; in the near future we will also provide models in the *HST* WFC3 photometric filters. It should be noted that, for the first time, these transformations are available for both scaled-solar and α-enhanced mixtures. The importance of adopting appropriate color-$T_{\rm eff}$ transformations and bolometric corrections has been pointed out by Cassisi et al. (2004); moreover, several comparisons have been made to verify that theoretical models coupled with consistent color-$T_{\rm eff}$ transformations and bolometric corrections properly reproduce observational data (see Bergbusch & Vandenberg 2001; Pietrinferni et al. 2004, 2006; Dotter et al. 2007 and references therein).

We have also provided tables for each chemical composition with relevant data about the theoretical models and the loci in the H-R diagram corresponding to the Zero Age Horizontal Branch (ZAHB) and to the central He exhaustion.

3. BaSTI DATABASE, ARCHIVE, AND WEB PORTAL

The metadata of the simulated stellar files are stored in an Oracle 10g DB.[4] All data are stored in tables that are linked each other by foreign keys on primary keys to avoid any duplication of the information. There is also one auxiliary table to take into account the units used for the different quantities.

The metadata of the stored stellar simulation are as follows: all program parameters such as name code, version, initial conditions, boundary conditions, EOS, radiative and conductive opacities, nuclear reaction rates, neutrino losses. In addition, there are also stored the quantities of chemical compositions, for example, global metallicity Z, initial helium abundance Y, iron content [Fe/H], and the corresponding [M/H] value obtained from the adopted heavy elements mixture. More stored parameters include mass loss, type of model, photometrical system, heavy element distribution, and the scenario (canonical, overshooting, diffusion, rotation). All these tables have a link with the table where they are stored: the name of the output file, the directory where it is archived, the type of the files—i.e., if

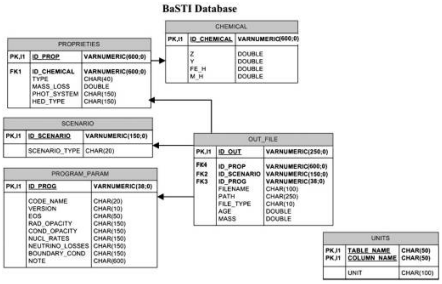

FIG. 1.—BaSTI relational DB schema: PK indicates a primary key of a table and FK indicates a foreign key to link two tables. See the electronic edition of the PASP for a color version of this figure.

the file refers to an isochrone, a track, an HB track, a ZAHB table or summary table, though at the moment all are American Standard Code for Information Interchange (ASCII) files. See the DB structure in the Figure 1.

The BaSTI Web portal is realized in hyper text mark-up language (HTML) for the static part, while the dynamic portion is written in Hypertext Preprocessor (PHP),[5] a server-side scripting language especially suited for Web development that can be embedded into HTML. The Web server used for our purposes is Apache 2.0 [6], the most famous open-source HTTP server for modern operating systems. At present the DB access is allowed from two different sites:

1. Italian Astronomical Archives Center (IA2) Web site[7]
2. OA-Teramo Web site[8]

This functionality permits a search over a large amount of scientific parameters allowing a simple and direct query to find the data that better satisfy the characteristics of a research typology. From the Web portal it is also possible to personalize the Simple Query Language (SQL) query, by making a more complex one and/or filtering on fields like a ratio of two quantities; see Figure 2. One example of a scientific query for the DB is discovering a set of simulated tracks for a given mass range and a ratio between mass and metallicity. The resulting catalog is shown in the Figure 3, where users can select and download a group of files and create a single tar file.

There is also a Help Web page[9] where the user can read a definition of the used quantities and get an idea of the value by which he/she can search into the archive.

[4] The Oracle Web site is found at http://www.oracle.com.

[5] For more information on PHP, or to download the code, see http://www.php.net/.

[6] Apache Software Foundation is found online at http://www.apache.org/.

[7] The Italian Astronomical Archives Center is found at the URL http://wwwas.oats.inaf.it/IA2/BaSTI/.

[8] The OA-Teramo Web site is at URL http://albione.oa-teramo.inaf.it/.

[9] For BaSTI help, see http://albione.oa-teramo.inaf.it/index.html.

This content downloaded from 194.199.64.71 on Mon, 8 Dec 2014 10:42:13 AM
All use subject to JSTOR Terms and Conditions

Retour à la table des matières : p. v

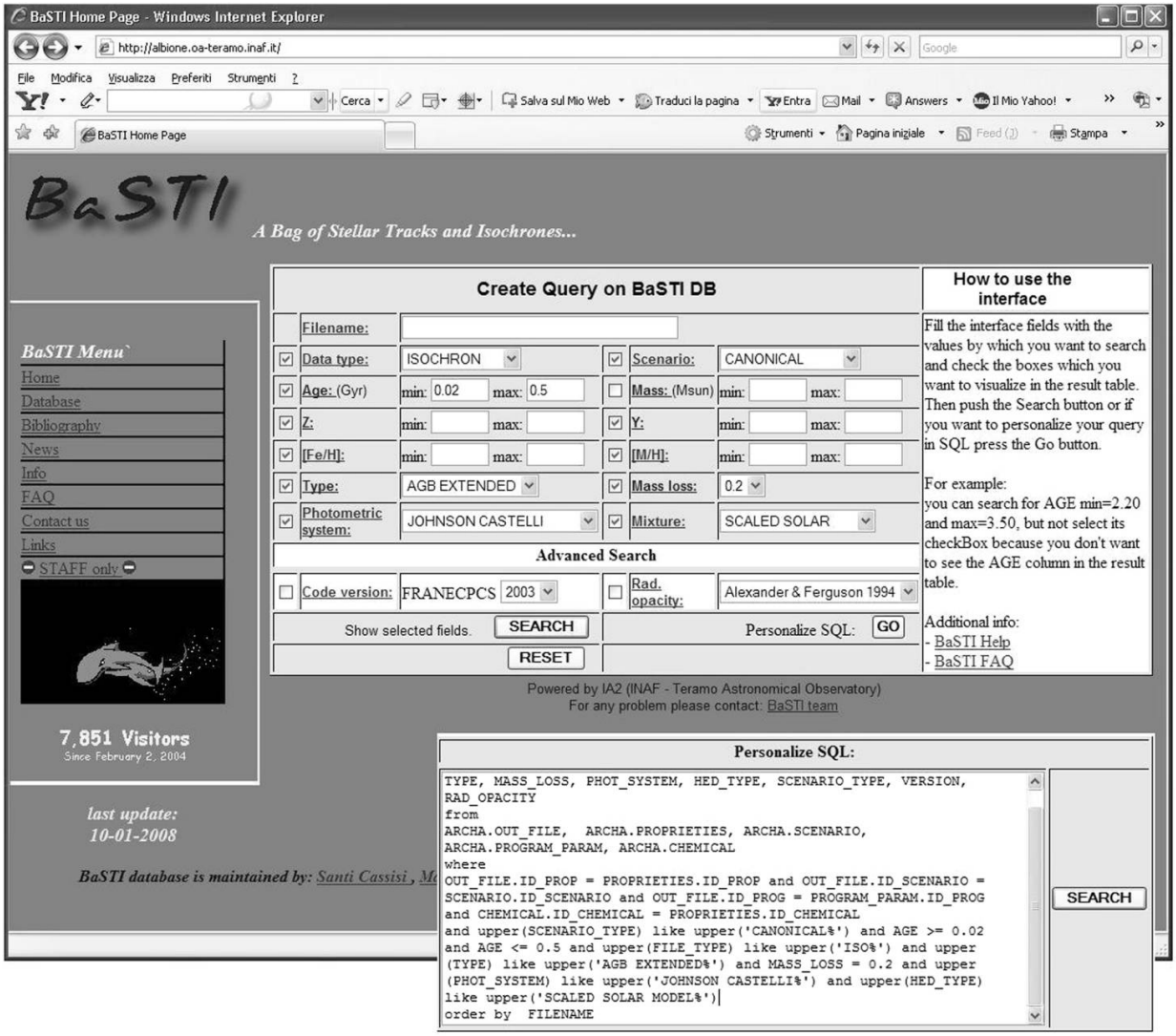

FIG. 2.—BaSTI Web portal: query form, personalized SQL form. See the electronic edition of the PASP for a color version of this figure.

The diagram flux of the data between the BaSTI Web portal and the Archive is shown in Figure 4.

3.1. BaSTI Web tools

In addition to tracks, isochrones, and tables, the BaSTI archive also includes three WEB TOOLS, which allow user-friendly manipulations on the stellar evolution library. Thanks to these tools one can compute user-specified isochrones, interpolate among evolutionary tracks to obtain the evolution for a mass value not contained in the grid, determine the differential and cumulative luminosity functions from a set of isochrones previously downloaded and, finally, compute synthetic stellar populations with an arbitrary star formation history (SFH) and determine their integrated magnitudes and colors. One way for a Web server to interact with data generating program is by using the Common Getaway Interface (CGI). Input data provided by the user are transferred to our three Formula Translation (FORTRAN) programs through Practical Extraction and Report Language (Perl) programs.

This content downloaded from 194.199.64.71 on Mon, 8 Dec 2014 10:42:13 AM
All use subject to JSTOR Terms and Conditions

Retour à la table des matières : p. v

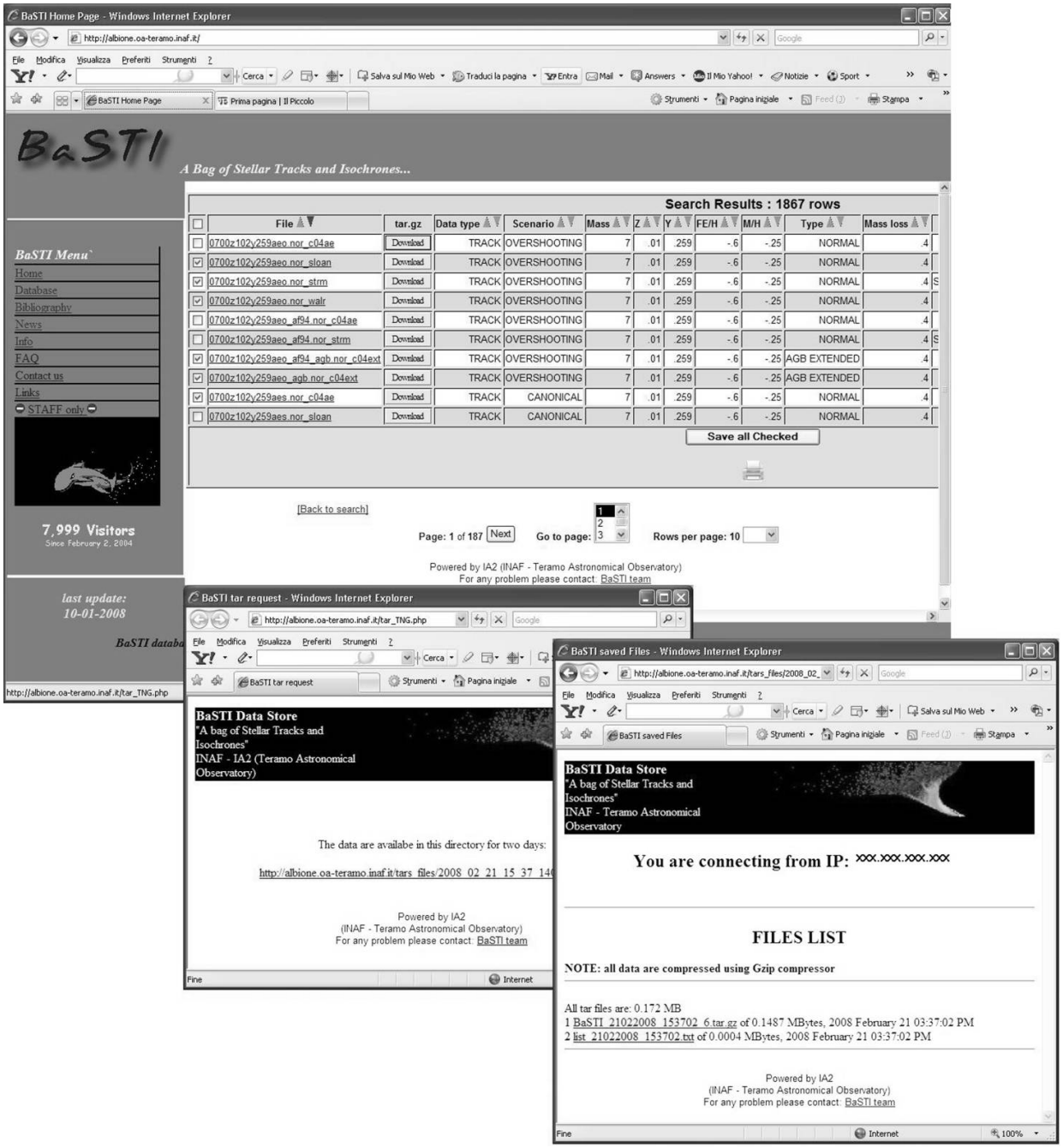

FIG. 3.—BaSTI Web portal result table: downloadable ASCII files. See the electronic edition of the PASP for a color version of this figure.

This content downloaded from 194.199.64.71 on Mon, 8 Dec 2014 10:42:13 AM
All use subject to JSTOR Terms and Conditions

Retour à la table des matières : p. v

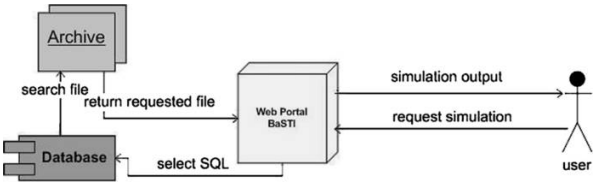

FIG. 4.—Diagram of the data flux from the Web portal to DB and Archive. See the electronic edition of the PASP for a color version of this figure.

3.1.1. Isochrone Maker and Track Interpolation Program

A dedicated Web interface has been empowered to allow a direct computation of isochrone for any given age, for chemical compositions and within the age range listed in Table 1. Using the same interface, it is also possible to compute interpolated evolutionary tracks in the mass range 0.5–10 $M_{\odot}$ for any chemical composition in the grid. To determine the track for the specified mass a linear interpolation on a point-by-point basis between two neighboring evolutionary tracks stored in the archive is performed. Due to the fine mass spacing of the tracks included in the BaSTI archive, a linear interpolation proves highly accurate. Once the track/isochrone has been computed, it is immediately transposed in the chosen photometric system.

This interface is particularly easy to use; the user has now to choose among a number of options:

1. The output type, i.e., isochrone or interpolated evolutionary track
2. The heavy elements mixture, i.e., scaled-solar or α-enhanced
3. The photometric system of interest; at the moment we allow a choice between the standard *UBVRIJKLH* filters and the ACS-*HST* ones
4. Core convection treatment, i.e., with or without convective core overshoot
5. The initial chemical composition (Y, Z).

Once these input parameters are fixed, the next screen allows the choice of the isochrone age (in Myr) or of the track initial total mass in solar units, as well as the job submission. The output tables (in the same format as the tracks and isochrones stored in the DB) are directly sent to the user's browser.

3.1.2. Luminosity Function Program

This tool provides differential and cumulative star counts as a function of the magnitude in a given wavelength band of single-age and single-metallicity stellar populations (e.g., the luminosity function). The isochrones stored in the BaSTI DB, or those obtained with the Web tool described in the previous section, represent the input files for the tool described here. To run this Web tool the user has to provide five parameters: the number of isochrones whose luminosity functions are needed (maximum 20); the final stage of the isochrone, i.e., computing the luminosity functions only until the RGB tip, along the whole isochrone until the early asymptotic giant branch (early-AGB), or also including the thermal pulses–AGB (TP-AGB) phase; the photometric filter (in the *UBVRIJKLH* system); the initial mass function (IMF) exponent; the size of the magnitude bins within which the star counts are performed (e.g., 0.15 mag; these bins have to be larger than 0.05 mag). We adopt for the IMF a form of this type: $\frac{dN_{\star}}{dM} = CM^{-\alpha}$ where $dN_{\star}$ is the number of stars formed with mass between M and $M + dM$, and C is a normalization constant. A value of α of 2.35 corresponds to the Salpeter (1955) IMF.

As a final step one has to upload the isochrone files and submit the job. The output is directly sent to the user Internet browser as an ASCII file, which is divided into several sections, each of them corresponding to one individual isochrone. A summary of the selected input parameters is forwarded (age, metallicity, IMF exponent, etc.) into the output file, while the data themselves are displayed in three columns: the mean magnitude of the bin, the differential ($\log N$—where N denotes the star counts per magnitude bin as a function of the magnitude) and cumulative ($\log N+$—where $N+$ denotes the sum of the star counts from the faintest bin to the actual one, as a function of their magnitude) luminosity functions.

3.1.3. Synthetic CMD Code

The synthetic color-magnitude diagram (CMD) is often a fundamental tool to interpret observations of resolved or unresolved stellar populations. The simplest example of a synthetic CMD is an isochrone, because it represents the sequence occupied by stars formed at the same time and with the same initial chemical composition. Clearly, an isochrone cannot represent a multiple ages stellar population; moreover, it does not directly contain information about the distribution of stars along the various CMD branches. To include these effects one needs a synthetic CMD generator. In the BaSTI Web site the user can access the SYNTHETIC MAN(ager). This code computes magnitudes and colors of objects belonging to a synthetic stellar population with an arbitrary SFH. The program employs the grid of isochrones with TP-AGB included in the BaSTI archive.

The most important input is the SFH file through which one sets the grid of ages and for each age: the scale factor (which is proportional to the relative number of stars formed at that time), the metallicity [Fe/H] of the stars formed at that age, and the eventual 1 σ spread around this value.

The general structure of the code is as follows. At each age step t, the program sets the number of stars formed and their [Fe/H], as specified by the SFH. Then, according to the

This content downloaded from 194.199.64.71 on Mon, 8 Dec 2014 10:42:13 AM
All use subject to JSTOR Terms and Conditions

Retour à la table des matières : p. v

TABLE 2
VARIABLE TYPE INDEX AND SOURCES USED IN THE POPULATION SYNTHESIS PROGRAM

Variables Type Index	Variable Type	Source for Instability Strip Boundaries
0	no variable	...
1	fundamental RR Lyrae	Marconi et al. (2003); Di Criscienzo et al. (2004)
2	first overtone RR Lyrae	Marconi et al. (2003); Di Criscienzo et al. (2004)
3	fundamental anomalous cepheid	Marconi et al. (2004)
4	first overtone anomalous cepheid	Marconi et al. (2004)
5	fundamental classical cepheid	Bono et al. (2000)

prescribed IMF, the values of the initial masses of the individual stars are randomly determined. For each value of the mass, the program interpolates among all the isochrones of age t in the grid (linear interpolation in mass, quadratic interpolation in metallicity), to determine its luminosity, effective temperature, actual value of the mass (in principle different from the initial value because of mass loss) and photometric properties. If the mass is too large to be still evolving at the age t, the next value of the mass is considered. For each mass an additional random number determines whether the generated star is a member of an unresolved binary system (the percentage of unresolved binaries has to be specified as input); if this is true, the mass of the second component is selected randomly, following Woo et al. (2003), and the fluxes of the unresolved components are properly added.

Once the photometric properties of an object (single or belonging to an unresolved binary system) are determined, additional effects are simulated, such as

1. Depth effects—according to a uniform stellar distribution with a user-specified total depth (in mag)
2. The effect of extinction—we have employed the extinction ratios by Bessel et al. (1998)
3. The photometric error—the individual magnitudes are perturbed according to a Gaussian distribution, with a user-specified 1 σ width (the same for all stars and for all photometric bands)
4. The effect of spectroscopic observational errors—the individual [Fe/H] values (that is, the [Fe/H] values at that age obtained from the SFH) are also perturbed according to a Gaussian error with user-specified 1 σ width.

The code can also search for variable stars, according to their location with respect to the boundary of RR Lyrae and Cepheid instability strips; pulsation periods are then determined. Table 2 shows literature references for the relevant type of variables.

Like all Monte-Carlo-method–based simulations, our program makes an extensive use of random numbers. Our random number generator (initially written by James 1990) needs seeds to be initialized; these seeds can be either provided by the user or got from Random.org,[10] which derived true random numbers from atmospheric electromagnetic noise.

The Web interface to SYNTHETIC MAN can been found in the BaSTI section called Synthetic Color—Magnitude Diagrams. This software is as simple to use as the others, but a registration is required before its first use. In order to get an user identification, one needs to contact S. Cassisi,[11] A. Pietrinferni,[12] or D. Cordier.[13]

In the following we summarize the input parameters for a run of SYNTHETIC MAN.

1. **Photometric error.** Photometric measurements are affected by observational errors that here are modeled following a Gaussian distribution. The user can fix a 1 σ constant error that is applied to all stars in the simulation for all 9 photometric bands. Another option is to employ an error that varies with the actual star magnitude and/or photometric band. The exact values have to be specified in an appropriate table. This table contains 18 columns. The first 9 columns display magnitudes in the 9 photometric bands, in order of increasing values. The remaining 9 columns are the corresponding photometric errors.[14]
2. **Mean spectroscopic error.** Spectroscopical abundances determinations are affected by observational errors that have been modeled following a Gaussian distribution. The allowed range of the 1 σ dispersion is between 0.0 and 1.0 dex.
3. **Color excess** $E(B-V)$. The color excess $E(B-V)$ toward the synthetic stellar population, are caused by the interstellar medium. The extinctions in the individual photometric bands are computed from the value of $E(B-V)$ employing the reddening low by Bessel et al. (1998).
4. **Total spatial depth of the population.** If stars belonging to the simulated stellar population cannot be assumed to be all at

[10] x
Random.org is a random number service, accessed online at http://www.random.org.
[11] S. Cassisi can be reached at cassisi@oa-teramo.inaf.it.
[12] A. Pietrinferni can be reached at pietrinferni@oa-teramo.inaf.it.
[13] D. Cordier can be reached at daniel.cordier@ensc-rennes.fr.
[14] See the online help for more details http://albione.ao-teramo.inaf.it/BASTI/WEB_TOOLS/syn-th_pop/mean_phot_error_help.html.

This content downloaded from 194.199.64.71 on Mon, 8 Dec 2014 10:42:13 AM
All use subject to JSTOR Terms and Conditions

Retour à la table des matières : p. v

the same distance, the population shows a spatial depth. At the moment the spatial depth is modeled with a uniform distribution in distance modulus.

5. **Fraction of unresolved binaries.** A fraction of the objects detected in a generic stellar population are unresolved multiple stellar systems. Only unresolved binaries are accounted for in our code. Their fraction is a free parameter.

6. **Minimum mass ratio for the unresolved binary systems.** The minimum mass ratio in the Woo et al. (2003) relationship (between 0.0 and 1.0, the suggested value is 0.7).

7. **Lower mass limit.** The lower limit of the mass of the stars in the simulation (the minimum allowed value at the moment is 0.50 $M_{\odot}$).

8. **Scale factor for the SFR.** The star formation rate (SFR) contains the relative weight of the star formation episodes at the various ages. In order to fix the absolute number of objects in each stellar generation, a scale factor has to be chosen. The product of this scale factor times the relative weight in the input SFR gives the total number of stars created at a given time, with mass between 0.5 and 120 $M_{\odot}$. If more than 2×10^6 objects are expected to be formed at a given time step, the program will stop to highlight the excessive amount of computational time needed for the whole simulation.

9. **Exponent α of the IMF.** Assumed to be of the form $M^{-\alpha}$.

10. **Choice of the isochrone set to use.** That is, scaled-solar or α-enhanced, η00.2 or $\eta = 0.4$ and standard (without overshooting) or overshooting ($\lambda_{\rm OV} = 0.2$).

11. **Possibility of searching for pulsating stars.** Search for pulsating stars harbored by the synthetic population and compute their periods.

12. **Desired SFH.** A number of prespecified SFHs for selected galaxies are also provided (see Table 3).

13. **Random number generation.** As with all simulations based on a Monte-Carlo method, our program needs seeds for random numbers generator initialization. The user can choose the values of the seeds, or let the program automatically get seeds from the server of entropy. We underline that all computations initialized with the same seeds will lead to identical outputs.

TABLE 3

AVAILABLE STAR FORMATION HISTORIES

Stellar Population	Source
NGC6822 (global SFH)	Gallart et al. (1996)
SMC (global SFH)	Harris & Zaritsky (2004)
LMC (bar field)	Holtzman et al. (1999)
Local disk	Rocha-Pinto et al. (2000a, 2000b)
Milky Way bulge	Molla et al. (2000)
Sextans A	Dolphin et al. (2003)
LGS3	Miller et al. (2001)

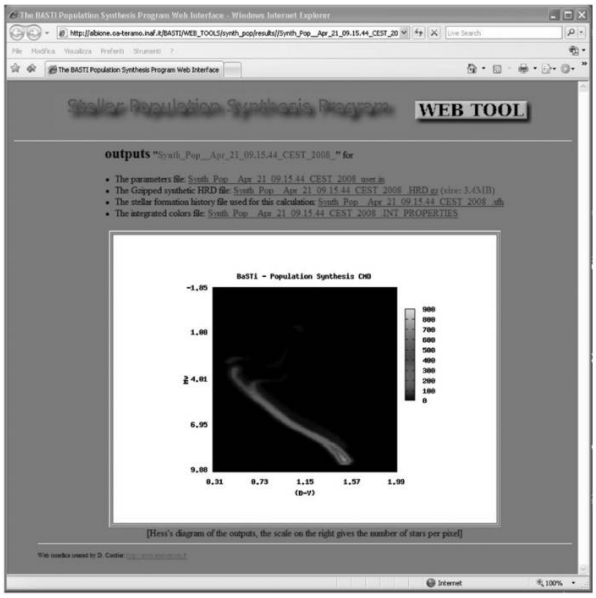

FIG. 5.—Example of the output Web page for the SYNTHETIC MAN Web tool. See the electronic edition of the PASP for a color version of this figure.

After specifying the input parameters, users can start their computations by clicking the "Submit" button. The calculation may take from a few minutes to hours, mainly depending on the requested number of stars. Because the size of the output files can amount to several MBytes, they cannot be sent directly to the user Internet browser, nor by email. So, once the computation is completed, an HTML page is created on the fly, and the user receives an email as notification, which includes the page URL. In the output Web page four data files are available:

1. `Synth_Pop_*_user.in`:[15] this ASCII file recalls the parameters used for the calculation.

2. `Synth_Pop_*_.HRD.gz`: this gzipped file contains data for the individual stars, in which one can find the following quantities: identification number, $\log(t)$ (yr), [Fe/H], the value of the actual mass, $\log(L/L_{\odot})$, $\log(T_{\rm eff})$, M_V, $(B-V)$, $(U-B)$, $(V-I)$, $(V-R)$, $(V-J)$, $(V-K)$, $(V-L)$, $(H-K)$, the value of the initial mass, the initial mass of the unresolved binary companion (if present—for stars without companion this quantity is set to 0.0), logarithm of the pulsation period (in days—if the search for variable is off or if the star is not pulsating this quantity is set to 99.99), an index denoting the

[15] The symbol * indicates the date at which the calculation is obtained.

This content downloaded from 194.199.64.71 on Mon, 8 Dec 2014 10:42:13 AM
All use subject to JSTOR Terms and Conditions

Retour à la table des matières : p. v

type of variable (see Table 2 for an explanation). This file can be uncompressed with the standard GNU software `gunzip`. As this file can be relatively large, the downloading is automatically forced when users click on the link.

3. `Synth_Pop_*_.sfh`: contains the Star Formation History data used for the calculations.

4. `Synth_Pop_*_.INT_COLORS`: file with the integrated *UBVRIJHKL* absolute magnitudes produced by the stars evolving in the synthetic population, several selected integrated colors, the total number of stars in the simulation, and their total mass.

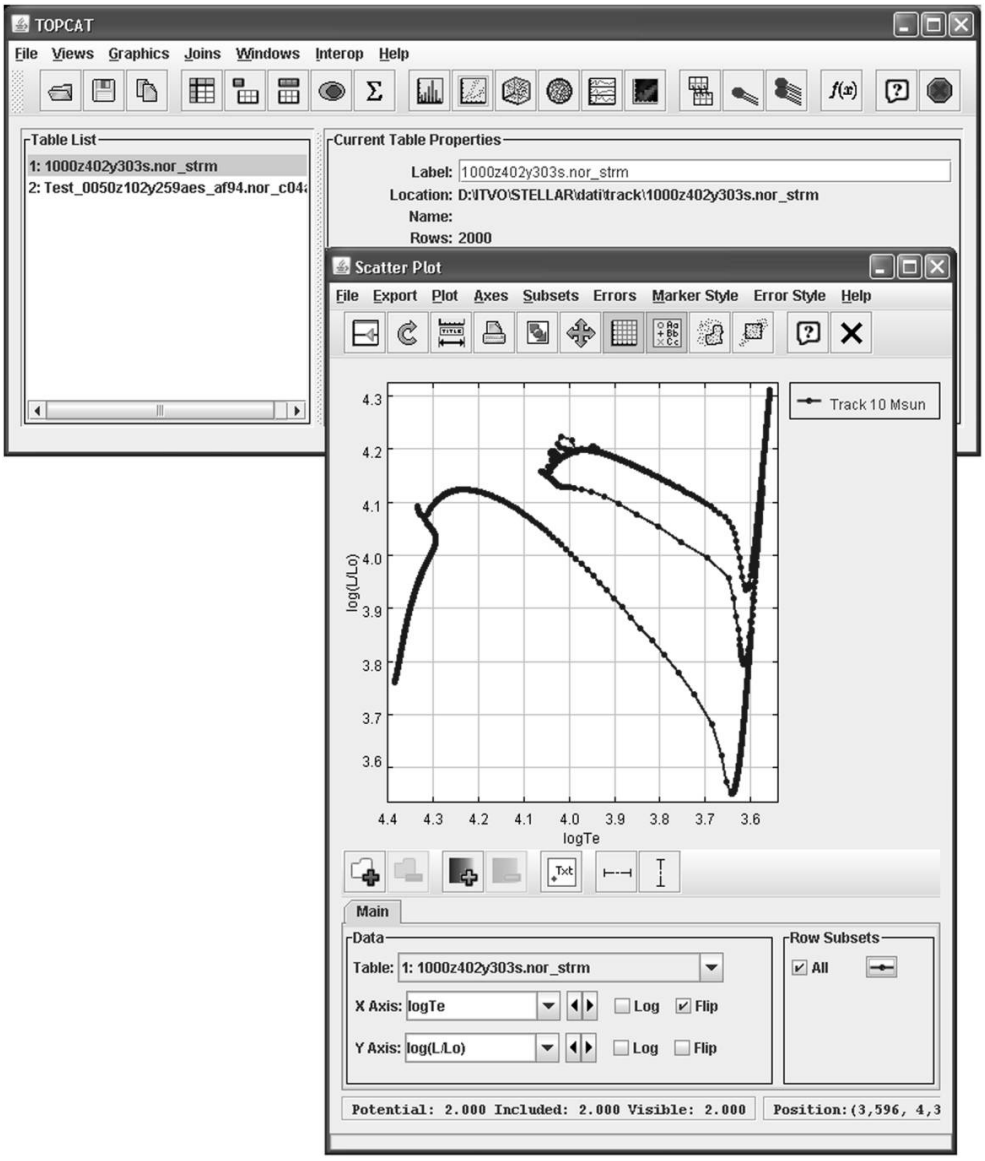

FIG. 6.—Plot of one track of a 10 $M_{\odot}$ star with $[M/H] = 0.395$, $Z = 0.04$ and $Y = 0.303$ created loading into TOPCAT tool a ASCII table downloaded from the BaSTI Web portal. See the electronic edition of the PASP for a color version of this figure.

This content downloaded from 194.199.64.71 on Mon, 8 Dec 2014 10:42:13 AM
All use subject to JSTOR Terms and Conditions

Retour à la table des matières : p. v

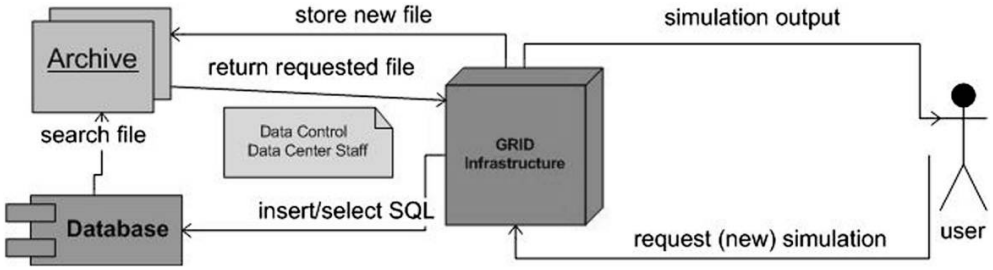

FIG. 7.—Future data flux diagram for the new request of simulated stellar data via grid infrastructure. See the electronic edition of the PASP for a color version of this figure.

An example of the output Web page is displayed in Figure 5. The $V-(B-V)$ Hess's diagram taking into account all the synthetic objects drawn for the simulation is also automatically displayed, stars number being encoded with colors. The user should be aware that—for obvious reasons—Web pages displaying program outputs are deleted by the software manager one month after the end of the computation.

4. VO TOOLS AND FUTURE DEVELOPMENT

The output format for all files at the moment are ASCII tables, so a user can open them with the TOPCAT VO tool to easily create a plots of the contained quantities, as shown for example in the Figure 6.

The problem is that the ASCII file is not a standard, so to see the column names in TOPCAT you have to remove the comment line between the column name and the column values, because for TOPCAT the last line starting with "#" must contain the column name. The idea for the future is obtain as output a FITS BINTABLE that is codified in a standard also well accepted by VO. The next step will be create a VOTable format for save or transform the data in this new extensible mark-up language (XML) VO standard.

In the future, we wish to create a data model inside the IVOA theoretical interest group as we are making for cosmological simulations (Lemson et al. 2007). That data model will be the future standard schema to use for accessing and creating services for these data. The theory data model consists in a unified modeling language (UML) diagram of classes including all the variables and quantities used and calculated in the simulations. The data model has to be validated from more than one real DB schema that contains the metadata of these simulations in order to enable future queries on distributed DBs and archives. We also have to write a standard access protocol for these data, to enable a simply and uniform query to retrieve the stellar simulations.

Another progress will be to install a Web service using the Symbolic Optimal Assembly Program (SOAP) engine Axis,[16] SOAP[17] is an XML-based communication protocol, an encoding format for interapplication communication, that will allow development of tools and process via a Web service, in order to include these in the VO registry. For example, as a first step one can query the DB via the Web service or transform all the tools available from the BaSTI Web portal in Web services. Another future development could be seeing the header of these ASCII table or in future FITS Tables and also creating on-the-fly profiles of some quantities to get a better view of the data before downloading them. See the first work on this (Costa et al. 2008).

Another future development will be link to VO-Data Center Alliance project Work Package 5, which can produce new simulations using the Grid infrastructure (see Taffoni et al. 2006; Pasian et al. 2008), so that users may request new full-fledged simulations for personal use and their inclusion in the archive and database for wider use is filtered by the Data Centre staff (see the future data flux diagram in the Fig. 7).

5. CONCLUSION

This work includes the first relational database created to store and access the stellar simulation data in order to publish and to reuse very expensive—in term of computing time and man power—results like theoretical outputs, which took a long time to write and run the code. This work allows scientists to access and compare theoretical and observational data in an easy and homogeneous way using IVOA standards. Furthermore, this database is continuously updated by including additional stellar evolution data.

The authors wish to thank Santi Cassisi for his precious suggestions and Fabio Pasian for his support to this project.

[16] Axis Web Services can be found online at http://ws.apache.org/axis/.

[17] Simple Object Access Protocol information is available online at http://www.w3.org/TR/2000/NOTE-SOAP-20000508/.

This content downloaded from 194.199.64.71 on Mon, 8 Dec 2014 10:42:13 AM
All use subject to JSTOR Terms and Conditions

REFERENCES

Alexander, D. R., & Ferguson, J. W. 1994, ApJ, 437, 879
Angulo, C., et al. (NACRE Coll.) 1999, Nucl. Phys. A, 656, 3
Bergbusch, P. A., & Vandenberg, D. A. 2001, ApJ, 556, 322
Bessell, M. S., Castelli, F., & Plez, B. 1998, A&A, 333, 231
Böhm-Vitense, E. 1958, Z. Astrophys., 46, 108
Bono, G., Castellani, V., & Marconi, M. 2000, ApJ, 529, 293
Casagrande, L., Flynn, C., portinari, L., Girardi, L., & Jimenez, R. 2007, MNRAS, 382, 1516
Cassisi, S., Salaris, M., & Irwin, A. W. 2003, ApJ, 588, 862
Cassisi, S., Salaris, M., Castelli, F., & Pietrinferni, A. 2004, ApJ, 616, 498
Cassisi, S., et al. 2006 Mem. Soc. Astron. Italiana, 77, 71
Castelli, F., & Kurucz, R.L. 2003, in Poster Papers, IAU Symp. 210, Modeling of Stellar Atmospheres, ed. N. E. Piskunov, W. W. Weiss, & D. F. Gray (San Francisco: ASP) (astro-ph/0405087)
Cordier, D., Pietrinferni, A., Cassisi, S., & Salaris, M. 2007, AJ, 133, 468
Costa, A., et al. 2008, PASP, in press
Di Criscienzo, M., Marconi, M., & Caputo, F. 2004, ApJ, 612, 1092
Dolphin, A. E., Saha, A., Skillman, E. D., Dohm-Palmer, R. C., Tolstoy, E., Cole, A. A., Gallagher, J. S., Hoessel, J. G., & Mateo, M. 2003, AJ, 126, 187
Doetter, A., Chaboyer, B., Jevremovic, D., Baron, E., Ferguson, J. W., Sarajedini, A., & Anderson, J. 2007, AJ, 134, 376
Gallart, C., Aparicio, A., Bertelli, G., & Chiosi, C. 1996, AJ, 112, 2596
Grevesse, N., & Noels, A. 1993, in: Origin and Evolution of the Elements, ed. N. Prantzos, E. Vangioni-Flam, & M. Casse (New York: Cambridge Univ. Press), 15
Haft, M., Raffelt, G., & Weiss, A. 1994, ApJ, 425, 222
Hanisch, R. J., & Quinn, P. J. 2003, International Virtual Observatory Alliance, (http://www.ivoa.net/pub/info/)
Harris, J., & Zaritsky, D. 2004, AJ, 127, 1531
Holtzman, J. A., et al. 1999, AJ, 118, 2262
Kunz, R., et al. 2002, ApJ, 567, 643
Iglesias, C. A., & Rogers, F. J. 1996, ApJ, 464, 943
James, F. 1990, Comput. Phys. Commun., 60, 329
Lemson, G., et al. 2007, Data Model for Theoretical (Meta-)data, (http://www.ivoa.net/)
Manzato, P., et al. 2007, Proc. EFMCSC, An Archive of Cosmological Simulations and the ITVO Multi-Level Database (River Edge, NJ: World Scientific)
Marconi, M., Caputo, F., Di Criscienzo, M., & Castellani, M. 2003, ApJ, 596, 299
Marconi, M., Fiorentino, G., & Caputo, F. 2004, A&A, 417, 1101
Miller, B. W., Dolphin, A. E., Lee, M.-G., Kim, Sang C., & Hodge, P. 2001, ApJ, 562, 713
Mollá, M., Ferrini, F., & Gozzi, G. 2000, MNRAS, 316, 345
Pasian, F., et al. 2006, in Proc. IAU 2, Highlights of Astronomy 14, ed. K. A. van der Hucht (Cambridge: Cambridge Univ. Press)
Pasian, F., et al. 2008, in ADASS XVII, ed. J. Lewis, R. Argyle, P. Bunclark, D. Evans, & E. Gonzales-Solares (ASP Conf. Ser. 394; San Francisco: ASP)
Pietrinferni, A., Cassisi, S., Salaris, M., & Castelli, F. 2004, ApJ, 612, 168
Pietrinferni, A., Cassisi, S., Salaris, M., & Castelli, F. 2006, ApJ, 642, 797
Potekhin, A. Y. 1999, A&A, 351, 787
Reimers, D. 1975, Mem. Soc. R. Sci. Liège, 8, 369
Rocha-Pinto, H. J., Maciel, W. J., Scalo, J., & Flynn, J. 2000a, A&A, 358, 850
Rocha-Pinto, H. J., Scalo, J., Maciel, W. J., & Flynn, J. 2000b, A&A, 358, 869
Salaris, M., & Weiss, A. 1998, A&A, 335, 943
Salpeter, E. E. 1955, ApJ, 121, 161
Taffoni, G., et al. 2006, preprint (astro-ph/0605165)
Woo, J.-H., Gallart, C., Demarque, P., Yi, S., & Zoccali, M. 2003, AJ, 125, 754

This content downloaded from 194.199.64.71 on Mon, 8 Dec 2014 10:42:13 AM
All use subject to JSTOR Terms and Conditions

Retour à la table des matières : p. v

14.5 Article sur Omega Centauri

The Astronomical Journal, 144:5 (11pp), 2012 July doi:10.1088/0004-6256/144/1/5
© 2012. The American Astronomical Society. All rights reserved. Printed in the U.S.A.

HUBBLE SPACE TELESCOPE OBSERVATIONS OF AN OUTER FIELD IN OMEGA CENTAURI: A DEFINITIVE HELIUM ABUNDANCE*

I. R. King[1], L. R. Bedin[2,3], S. Cassisi[4], A. P. Milone[5,6], A. Bellini[2], G. Piotto[7], J. Anderson[2], A. Pietrinferni[4], and D. Cordier[8]

[1] Department of Astronomy, University of Washington, Box 351580, Seattle, WA 98195-1580, USA; king@astro.washington.edu
[2] Space Telescope Science Institute, 3700 San Martin Drive, Baltimore, MD 21218, USA; bellini@stsci.edu, jayander@stsci.edu
[3] INAF-Osservatorio Astronomico di Padova, Vicolo dell'Osservatorio 5, I-35122 Padova, Italy; luigi.bedin@oapd.inaf.it
[4] Osservatorio Astronomico di Teramo, Via Mentore Maggini s.n.c., I-64100 Teramo, Italy; cassisi@oa-teramo.inaf.it, adriano@oa-teramo.inaf.it
[5] Instituto de Astrofisica de Canarias, E-38200 La Laguna, Tenerife, Canary Islands, Spain; milone@iac.es
[6] Department of Astrophysics, University of La Laguna, E-38200 La Laguna, Tenerife, Canary Islands, Spain
[7] Dipartimento di Astronomia, Università di Padova, Vicolo dell'Osservatorio 2, I-35122 Padova, Italy; giampaolo.piotto@unipd.it
[8] Institut UTINAM, Observatoire de Besançon-UMR CNRS 6213, 41 bis avenue de lObservatoire, F-25000 Besançon, France; daniel.cordier@obs-besancon.fr
Received 2011 July 13; accepted 2012 March 21; published 2012 June 6

ABSTRACT

We revisit the problem of the split main sequence (MS) of the globular cluster ω Centauri, and report the results of two-epoch *Hubble Space Telescope* observations of an outer field, for which proper motions give us a pure sample of cluster members, and an improved separation of the two branches of the MS. Using a new set of stellar models covering a grid of values of helium and metallicity, we find that the best possible estimate of the helium abundance of the bluer branch of the MS is $Y = 0.39 \pm 0.02$. For the cluster center, we apply new techniques to old observations: we use indices of photometric quality to select a high-quality sample of stars, which we also correct for differential reddening. We then superpose the color–magnitude diagram of the outer field on that of the cluster center, and suggest a connection of the bluer branch of the MS with one of the more prominent among the many sequences in the subgiant region. We also report a group of undoubted cluster members that are well to the red of the lower MS.

Key words: globular clusters: individual (NGC 5139) – Hertzsprung-Russell and C-M diagram – proper motions – stars: abundances – stars: Population II

Online-only material: color figures

1. INTRODUCTION

The stellar system ω Centauri (NGC 5139) is one of the most puzzling objects in our Galaxy. In an intriguing way, the large amount of attention devoted to this globular cluster has served to increase rather than decrease the number of mysteries that surround it. For several decades, it had been recognized that the red giant branch (RGB) of ω Cen shows a spread in metallicity (Dickens & Woolley 1967; Cannon & Stobie 1973). The breadth in color of the RGB was interpreted as an indication of an intrinsic spread in chemical abundance, as subsequently confirmed by spectroscopic data (Freeman & Rodgers 1975); and Norris et al. (1996) suggested that two epochs of star formation have occurred. Today we know that there are many more populations than that (Lee et al. 1999; Pancino et al. 2000; Sollima et al. 2005; Villanova et al. 2007; Bellini et al. 2010, and references therein). It has been suggested further that at each metallicity there is a range in age (Sollima et al. 2005; Villanova et al. 2007).

More than a decade ago, our group found that the main sequence (MS) of the cluster is double (Anderson 1997, 2002; Bedin et al. 2004). Because of the lack of information on the heavy elements in the MS components, the original version of Bedin et al. (2004) had proposed several explanations for the split, none of them conclusive. The referee, John Norris, strongly suggested, however, "TRY HELIUM," in spite of the improbably high He abundance that would be required, and published his suggestion (Norris 2004).

The turning point was the work by Piotto et al. (2005), who actually measured the heavy elements along the two branches of the MS. They found that contrary to expectation, the bluer branch (bMS) has a higher rather than a lower metallicity than the redder branch (rMS), and that the only way to explain the photometric and spectroscopic results was that the helium abundance of the bMS is $Y \sim 0.4$—far beyond what its metallicity would imply. Very recently Dupree et al. (2011) have found direct evidence for an enhancement in He, from the analysis of the λ10830 transition of He I in the RGB stars of ω Cen. The correlation of He-line detection with [Fe/H], Al, and Na supports the assumption that He is enhanced in stars of the bMS. (It is still totally unclear, however, where a large enrichment of He could have come from, and how it could fit with current stellar-evolution models.)

In other clusters too, studies of the RGB (Bragaglia et al. 2010a) and of the horizontal branch (Gratton et al. 2010) have suggested a spread in He abundances. In both of these studies, NGC 2808 has stood out especially as showing a clear spread in helium—not surprisingly, since that cluster has an MS that is split into three branches (Piotto et al. 2007). And in that cluster, Pasquini et al. (2011) have used the He λ10830 line to estimate a helium value $Y \geqslant 0.39$, confirming suggestions by D'Antona & Caloi (2008) and by Bragaglia et al. (2010a); furthermore, Bragaglia et al. (2010b) have obtained spectra of MS stars on the reddest and on the bluest MS branches of NGC 2808, and find that abundances of individual heavy elements are very much

* Based on observations with the NASA/ESA *Hubble Space Telescope*, obtained at the Space Telescope Science Institute, which is operated by AURA, Inc., under NASA contract NAS 5-26555.

in agreement with the scenario of normal He for the rMS and enhanced He for the bMS.

In the present paper, we describe an outer field of ω Cen that has relatively few stars, but minimal crowding. This field has already been used in our paper on the splitting of the MS (Bedin et al. 2004), and also in a study of the radial behavior of the numbers of stars in the bMS and the rMS, by Bellini et al. (2009); the present paper is the fuller discussion that the latter authors promised for this field. In addition to our presentation of the MS split in this outer field, we sharpen our view of the central field, we fit theoretical isochrones to the two branches of the MS, and, importantly, we estimate the difference in their helium abundances, along with the quantitative uncertainty of that difference.

2. THE OUTER FIELD

2.1. Observations, Measurements, and Reductions

In the outer field ($13^h25^m35\overset{s}{.}5$, $-47°40'6\overset{''}{.}7$, same as the $17'$ field in Bedin et al. 2004), we combined a new data set with an earlier one. We had already imaged this field, $17'$ from the center of ω Cen (core radius $2\overset{'}{.}37$, half-mass radius $5\overset{'}{.}0$, tidal limit $53\overset{'}{.}4$), using the Wide Field Channel (WFC) of the *Hubble Space Telescope*'s (*HST*'s) Advanced Camera for Surveys (ACS). Those images (GO-9444, PI: King), taken 2002 July 3, consisted of 2 × 1300 s + 2 × 1375 s with F606W and 2 × 1340 s + 2 × 1375 s with F814W. Our follow-up program (GO-10101, PI: King) was to have had second epoch images in F814W only, but in view of the extreme interest ignited by the results presented in Bedin et al. (2004) and Piotto et al. (2005), we were able to get Director's Discretion time that allowed us to repeat the F606W images as well. After a delay caused by a failed guide star, the second epoch images were taken 2005 December 24, with exposures 2 × 1285 s + 2 × 1331 s in F606W and 4 × 1331 s in F814W. Because of the delay, however, the orientation differed by 180°. As we shall see, this change improved the photometry, but at the cost of somewhat complicating the astrometry.

The photometry was carried out using the procedures and software tools developed for the Globular Cluster Treasury program (Sarajedini et al. 2007), as described in detail by Anderson et al. (2008). We summarize here briefly: to each star image in each exposure, we fit a point-spread function (PSF) interpolated expressly for that star, using a 9 × 5 array of PSFs in each of the two chips of the ACS/WFC. These arrays model the spatial variation of the PSF, but for each individual exposure we add a "perturbation PSF" that fine tunes the fitting to allow for small differences in focus, temperature, etc.

The fitting of each star uses its central 5 × 5 pixels, and yields a flux and a position. In addition, we created a model of the extended outer parts of the PSF that allowed us to eliminate the artifacts that arise from outer features in the PSFs of bright stars, while excluding very few legitimate stars. (The PSFs are described in great detail in Anderson et al. 2008.)

We transformed our zero points to those of the WFC/ACS Vega-mag system following the procedure given in Bedin et al. (2005), and using the encircled energy and zero points given by Sirianni et al. (2005). Because of the high background ($\gtrsim$100 e^- pixel^{-1}), combined with the fact that our exposures were taken at a time when inefficiencies in charge transfer were less serious than they are now, this field did not need any corrections for inadequate charge transfer efficiency.

2.2. The Saturated Stars

Since the primary aim of the programs for which the images were taken had been the faint stars, neither of our epochs included short exposures. For the bright stars, we had to derive the best photometry that we could, from their saturated images. We used the method developed by Gilliland (2004), which works by recovering electrons that have bled into neighboring pixels. Our application of this method is described in Section 8.1 of Anderson et al. (2008). The method depends, however, on having a detector GAIN greater than 1. Unfortunately, our first epoch images were taken with GAIN = 1, but in the second epoch we had GAIN = 2 and were able to do effective photometry on the saturated images. Thus, for saturated stars we had only the second epoch available.

Because Gilliland's method uses so different a procedure, we had to adjust the zero points of the magnitudes that it produced. The necessary shifts (<0.02 mag in each band) were easily determined from the stars in the 0.5 mag interval just below the saturation limit, where both methods are valid. Figure 1 shows the impressive improvement that the use of Gilliland's method gave us for a stretch of about 3 mag at the bright end. It also shows, however, that for stars brighter than $m_{\rm F606W} \sim 17.1$ even that method is unable to cope with saturation. (From the onset of saturation at magnitude 20.4 up to a magnitude about 17.1, however, there is a considerable improvement.)

2.3. Proper Motions

For the astrometry, we did not need the elaborate procedures that we had used for the photometry; for our data set it was more appropriate simply to use the program described by Anderson & King (2006), to get position coordinates for each star in each `_flt` image. (These are the images that have been bias-subtracted and flat-fielded via the standard ACS pipeline, but have not been resampled; as such they are suitable for derivation of positions and fluxes by high-precision PSF-type analysis.)

Our next step was to apply the distortion corrections of Anderson (2002, 2006). We then needed to transform these positions into a common reference frame at each epoch, for which we arbitrarily chose one image at that epoch. For the transformations, we selected among the brighter stars a set of stars that were in the MS region of the color–magnitude diagram (CMD), so as to minimize any disturbing influence that inadvertent inclusion of field stars might have on our transformations.

Once we had all the positions in a single reference frame at each epoch, we measured the displacement of each star from the first epoch to the second, relative to a set of at least 10 of its immediate neighbors (dropping the few stars that did not have 10 near neighbors), so that each cluster star would have a near-zero displacement between the two epochs, while field stars would show noticeable motions.

Since the astrometry depends very little on the filter band, we were able to treat each filter the same, and combine the results. With a precision of better than 0.05 pixel for the coordinates of individual star images, the precision of a displacement from the mean of eight exposures at each epoch should be 1/2 of that, so that over the 3.5 year baseline the proper motions should be good to 0.007 pixel yr^{-1}, which for a 50 mas pixel is 0.35 mas yr^{-1}. Since the distance to ω Cen is about 5 kpc, this is equivalent to an uncertainty of ∼4 km s^{-1} in the transverse motion of each star (appreciably less than the 10 km s^{-1} internal velocity dispersion of the cluster at this distance from the center; Merritt

Retour à la table des matières : p. v

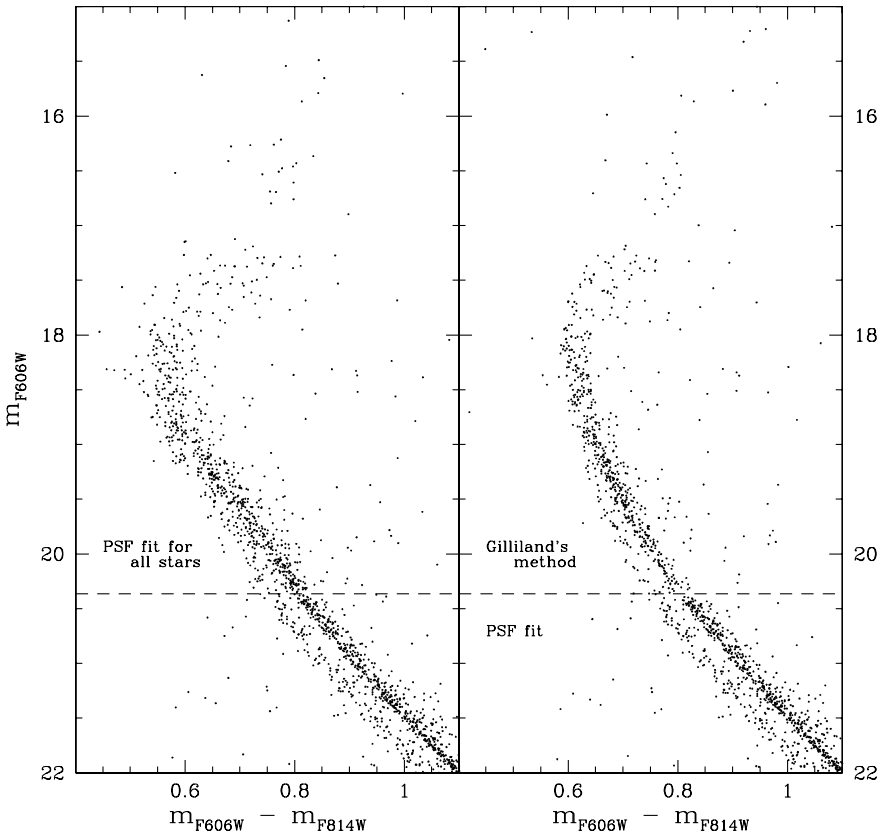

Figure 1. Left: the color–magnitude diagram (CMD) as obtained from PSF fitting of unsaturated pixels. The horizontal dashed line marks the beginning of saturation in filter F606W. Right: the same CMD, with photometry for saturated stars obtained as described in Section 2.2.

et al. 1997). In practice, moreover, the field-star motions turn out to differ from the cluster motions by much more than the internal dispersion of the latter.

2.4. The Cleaned Color–Magnitude Diagram of the Outer Field

Because this field is so far from the center of ω Cen, it suffers relatively greater contamination by field stars than inner fields do; we therefore made careful use of proper motions to remove field stars from our CMD. Our first step was to plot the *x*- and *y*-components of proper motion for each unit interval of magnitude. From these plots, it was clear that most of the motions—those of cluster members—were concentrated around a common centroid, while the motions of field stars scattered much more widely about another center. For bright stars there was little or no overlap between the two distributions, but with increasing measurement error at faint magnitudes the separation became less clear.

In the left-hand panel of Figure 2, we show the sizes of the motions as a function of magnitude. We drew an arbitrary line (magenta in the online journal) to separate members from non-members. Rather than just throwing away the stars that we call non-members, however, we have colored each star from black to gray according to the palette shown at the top of the figure. Stars whose motions are very close to that of the cluster centroid are black; with increasing difference from the mean cluster motion the symbols become a paler and paler gray.

With the likelihood that each star is a cluster member coded in this intuitive way, in the right-hand panel of the figure we plot the stars in the CMD. The symbol that represents each star now has the same degree of grayness that the star was assigned in the left-hand panel, so that we can see where in the CMD the cluster members and the non-members lie, and conversely, from the gray level of the symbol, which stars should be rejected as non-members. Finally, in Figure 3 we show the CMD of the stars whose proper motions lie to the left of the broken line in the preceding figure, which we therefore consider to be cluster members. The dashed line, 0.75 mag above the rMS, marks the upper limit of its binaries (those with equal mass).

As we have already noted, the flaring out of the MS at magnitudes brighter than 17 is due to the inability of our methods to cope with the most extreme levels of saturation. This anomaly aside, our CMD shows a number of interesting features: (1) the MS shows the best separation of its two branches that has yet been seen. (It should be noted that Figure 3 is similar to Figure 1(d) of Bedin et al. 2004, but now the interfering field stars have been removed. For the relative number of rMS and bMS stars, one should see Bellini et al. 2009, whose study of the radial variation of the rMS/bMS ratio includes the results whose details we present here.) Also, in the following section, we will use the distance between the bMS and the rMS to derive a definitive value for the helium abundance of the bMS. (2) The bMS appears to cross over the rMS and emerge on the other side of it, in the subgiant region; we will discuss this further in

Retour à la table des matières : p. v

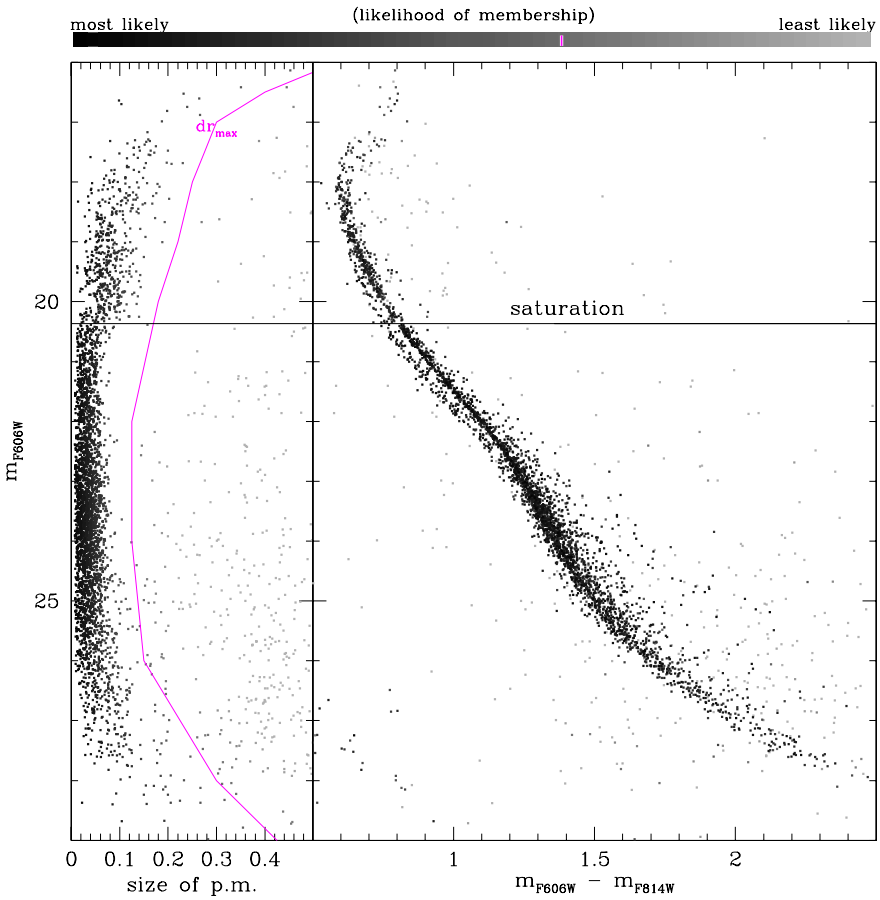

Figure 2. At left, the sizes of the proper motions (in pixel units), with the symbol for each star grayscale-coded so as to show in an intuitive way the likelihood that it is a cluster member (as indicated in the palette at the top). The magenta lines in this panel and in the palette show our proper-motion cutoff for membership. In the right-hand panel is the CMD of the same stars, with the same gray-scale coding, so that one can see the membership likelihood of each star in the CMD.

(A color version of this figure is available in the online journal.)

Section 5. (3) A part of the white dwarf sequence can be seen at the lower left (but we will not discuss it in this paper). (4) A considerable number of undoubted cluster members lie too far above and to the redward of the MS to be interpreted as binaries. Although they suggest some sort of sequence, their region is too ill defined to be called a sequence. We will discuss this group too in Section 5, in conjunction with the CMD of the much richer central region of the cluster.

3. THE HELIUM ABUNDANCE OF THE bMS

Ever since the surprising discovery that the bMS has higher metallicity than the rMS (Piotto et al. 2005, hereafter P05), it has become increasingly evident that this reversal of the usual color progression with MS metallicity must indicate that the stars of the bMS contain a higher proportion of helium. Here, we apply theoretical models of stellar structure to the question of what helium abundance the location of the observed blue sequence actually implies.

3.1. Fitting the Color Separation of the bMS and the rMS

For the comparison of observation with theory, we select a single salient characteristic of the bifurcation of the MS: the color separation between the two branches. We measure this at a magnitude where the separation is large and the photometry is also quite reliable. Examining Figure 3, we see that within the magnitude range in which our photometry is free from saturation, the separation of the two sequences appears to remain nearly constant over a stretch of about 2 mag, giving us a large enough number of stars to get a good value of the color separation of the two sequences. We will refer to this separation as ΔC. Specifically, we chose the magnitude interval $20.6 \leqslant m_{\rm F606W} \leqslant 21.8$ so that we can consider our observed ΔC to apply to the entire middle part of this range, i.e., for several tenths of a magnitude on either side of the midpoint, $m_{\rm F606W} = 21.2$.

For the actual determination of the color separation, we made use of a procedure that is described in great detail by Bellini et al. (2009). Briefly, we drew a fiducial color sequence along the gap between the two branches, and made the sequences approximately vertical by subtracting from the color of each star the fiducial color at its magnitude. We then plotted a histogram of the resulting colors, and fitted it with a pair of Gaussians. The separation that we find is 0.057 ± 0.0017 mag, where the uncertainty is due only to the Poisson statistics of the star numbers in the two sequences. As a more conservative figure,

Retour à la table des matières : p. v

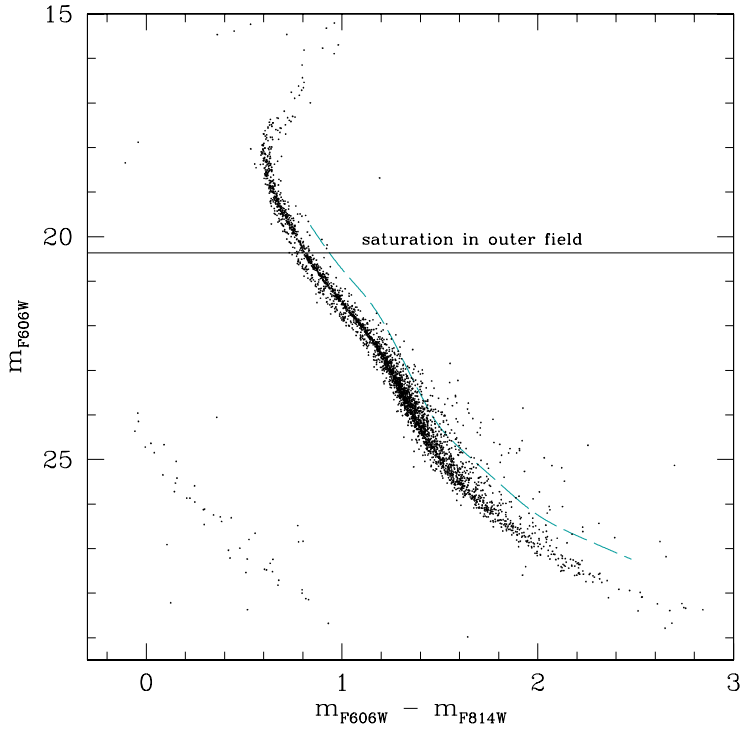

Figure 3. Color–magnitude diagram of cluster members in the outer field (stars whose proper motions lie to the left of the magenta line in the preceding figure). The dashed blue line marks the locus of equal-mass rMS binaries, 0.75 mag above the rMS.

(A color version of this figure is available in the online journal.)

however, we prefer to assign a 3σ uncertainty, and to quote a color separation of 0.057 ± 0.005.

For calculation of theoretical values of ΔC, we chose an absolute magnitude of 7.0. For our distance modulus, we took $(m-M)_0 = 13.70$ (Del Principe et al. 2006), $E(B-V) = 0.12$ (Harris 2010, revision of Harris 1996), and $A_V = 3.1\,E(B-V)$ (Cardelli et al. 1989); these give $(m-M)_V = 14.072$, which we rounded to 14.1, so that $M_{F606W} = 7.0$ corresponds to $m_{F606W} = 21.1$, close to the middle of the magnitude range that we used for our observational ΔC. (We note that the results that we derive below are insensitive to our exact choice of distance modulus, since the bMS and rMS run so closely parallel at these magnitudes.)

We wished to compare theoretical isochrones with the whole stretch of MS that is shown in Figure 3, and we therefore extended our models to lower masses ($M < 0.5\,M_\odot$). We again took $[\alpha/\mathrm{Fe}] = +0.4$ and used the physical scenario described by Pietrinferni et al. (2004, 2006). For these low masses, we rely on the equation of state by Saumon et al. (1995) for dense, cool matter, and on low-temperature opacities by Ferguson et al. (2005) and high-temperature opacities by Rogers & Iglesias (1992). The outer boundary conditions were fixed by adopting the Next Generation model atmospheres provided by Allard et al. (1997) and Hauschildt et al. (1999a, 1999b). We fixed the base of the atmosphere at Rosseland optical depth $\tau = 100$, i.e., deep enough for the diffusion approximation to be valid. We note also that although detailed atmospheres are available only for canonical He abundances, helium does not appreciably affect the atmosphere, because its only effect would be on pressure-induced H_2–He absorption, which matters only in stars of lower mass than we discuss here (F. Allard 2008, private communication). At any given metallicity, the match between the more massive models and the low-mass ones was made at a mass level where the transition in luminosity and effective temperature between the two regimes is smooth (usually $\sim 0.5\,M_\odot$).

We computed stellar models for $[\mathrm{Fe/H}] = -1.62$ and -1.32 to represent the rMS and bMS, respectively; to allow for the uncertainty of 0.2 dex in the relative metallicities of the bMS and the rMS, we also computed models with $[\mathrm{Fe/H}] = -1.52$ and -1.12, to represent alternative [Fe/H] values for the bMS. For each value of [Fe/H] for the bMS, we calculated models for a set of helium abundances that reached beyond $Y = 0.4$. Within the heavy elements, we used the α-enhanced mixture of Pietrinferni et al. (2006).

For the transformation of the theoretical stellar models into the observational plane, we used the semi-empirical colors and bolometric corrections of Pietrinferni et al. (2004), transformed according to Appendix D of Sirianni et al. (2005). We also verified, however, that using the color–T_{eff} relations and bolometric corrections of Hauschildt et al. (1999a, 1999b) would produce practically the same result. (In any case, whatever inaccuracies there may be in our transformation are greatly reduced by the fact that the quantity that we use is the *difference* between two colors.)

We used our theoretical models for a comparison with the observed ΔC between the two branches of the MS. To do this, we derived the equivalent theoretical quantity from our set of isochrones, and transformed it into the observational plane, as just indicated.

Retour à la table des matières : p. v

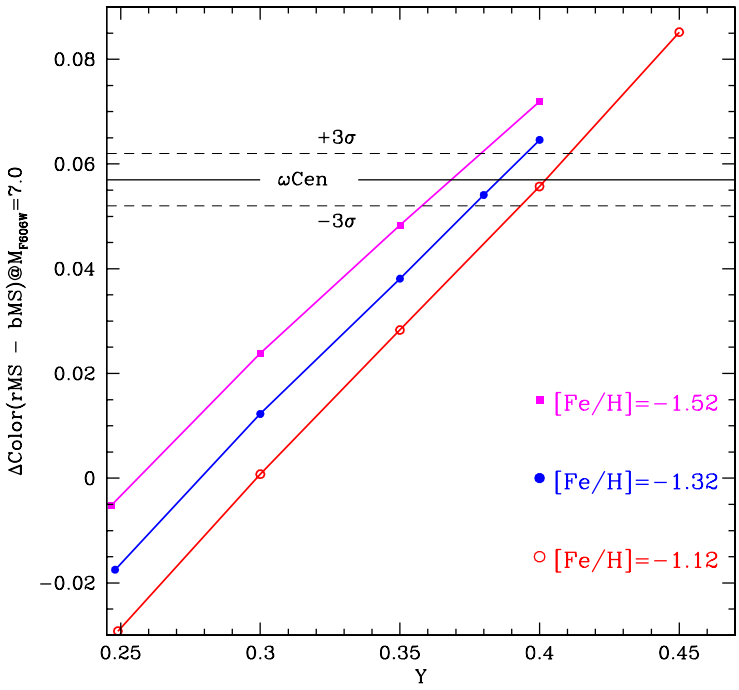

Figure 4. Theoretical estimate of the parameter ΔC as a function of the initial He content of the bMS and for various assumptions about its iron content [Fe/H]. The horizontal solid line marks our measured value of ΔC. The horizontal dashed lines represent the 3σ uncertainty of that measurement.

The next step was to choose metallicity values for the rMS and for the bMS, within the broad range of metal abundances that has been found in spectroscopic studies—a choice that is hampered, however, by the lack of knowledge of how the two MS branches connect to the upper parts of the H-R diagram, from which all of our good abundance information comes. Thus, all that we really have to go on is the uncertain result of P05 that the metallicities of the rMS and the bMS are about -1.6 and -1.3, respectively, with a somewhat less uncertain result that the difference of the two metallicities is 0.3 ± 0.2. (They italicize the difference, marking it as their prime result concerning metallicity.)

We accordingly chose for the rMS our [Fe/H] $= -1.62$ isochrone, with primeval He (i.e., $Y = 0.246$), and for the bMS the isochrones with [Fe/H] $= -1.32$ and various He abundances. In doing so, we note that it is the *difference* of the metallicities that matters, rather than the absolute value of either of them. We could shift these [Fe/H] values by 0.1–0.2 dex or so, without any appreciable effect on the helium abundance that we will derive for the bMS or its uncertainty. (We have, in fact, verified that our results remain the same if we choose [Fe/H] $= -1.75$ for the rMS and also shift all the bMS [Fe/H] values by the same 0.13.)

For comparison with observation, then, we calculated the color difference at $M_{\rm F606W} = 7.0$ between the rMS isochrone and the bMS isochrones, with various assumed values of the helium abundance Y. Bearing in mind, however, that P05 considered the metallicity difference between the bMS and rMS to be uncertain by 0.2, we also carried out the same procedure for assumed bMS metallicities of -1.12 or -1.52 (i.e., higher or lower by 0.2).

Figure 4 shows these theoretical ΔC estimates. In order to make our procedures clear, we explain at length the meanings of the various lines in the figure: each of the three sloping lines corresponds to the bMS metallicity that is indicated for that line in the color key. Each point on the line shows the value of ΔC that comes from assuming that value of metallicity for the bMS, along with a particular value of Y, while always using for the rMS [Fe/H] $= -1.62$ and $Y = 0.246$. The lines themselves were created by connecting with straight lines the points belonging to the same bMS metallicity.

We used the figure to determine the value of the helium abundance Y, and also its uncertainty. The latter arises from two sources: the uncertainty in the metallicity difference between the bMS and the rMS, and our observational error in measuring ΔC.

The solid horizontal line in the figure corresponds to our measured value of ΔC. It serves two purposes: first, its intersection with the sloping line for [Fe/H] $= -1.32$ (our preferred value for the bMS) is at $Y = 0.0386$; this is our result for the helium abundance. Second, this line also tells us the uncertainty in Y that results from the uncertainty of 0.2 in the metallicity of the bMS relative to the rMS. To evaluate that uncertainty, we simply measure the distance from the intersection of the solid horizontal line with the [Fe/H] $= -1.32$ line to its intersection point with either the [Fe/H] $= -1.12$ or the -1.52 line. These distances are each 0.016, which is thus the uncertainty in Y due to this cause.

The second source of uncertainty in Y comes from the measuring error in ΔC. To represent this, we drew the two horizontal dashed lines, which are above and below the solid line by the $3\sigma = \pm0.005$ that we chose as a conservative error estimate. They intersect the sloping [Fe/H] $= -1.32$ line at $Y =$ 0.375 and 0.397, respectively, 0.011 greater or less than our Y value of 0.386.

When we combine this ±0.011 with the ±0.016 that came from the uncertainty in the metallicity difference, our result for the helium abundance of the bMS is $Y = 0.39 \pm 0.02$. Not only is this a more reliable estimate than has been available before;

Retour à la table des matières : p. v

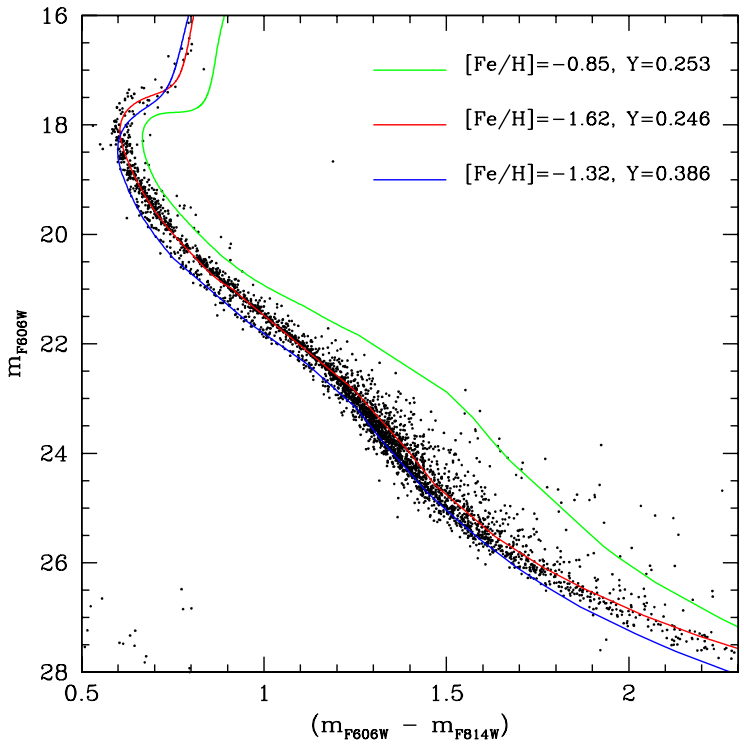

Figure 5. Comparison of selected theoretical isochrones with the CMD of the outer field. The isochrones drawn in red and in blue were chosen by merely matching the colors of the bMS and the rMS at $m_{F606W} = 21.17$. The isochrone in green will be discussed in Section 5.

it is the first estimate that has had a quantitative uncertainty attached.

Recently, Pasquini et al. (2011) have used the He λ10830 line in the spectra of two red giant stars in NGC 2808 to estimate that the He abundance of those stars is $Y \geqslant 0.39$. It is interesting to see the similarity with what we find in ω Cen. Additionally, in ω Cen itself, Dupree et al. (2011) have detected the λ10830 line in some RGB stars but not in others, in agreement with our suggestion that some of the cluster stars have enhanced helium.

3.2. The Isochrones

Figure 5 shows the isochrones that correspond to the abundances with which we have fitted the color separation between the bMS and the rMS (along with a third isochrone that will be discussed in Section 5). An isochrone with primeval helium and a metallicity appropriate for ω Cen fits the rMS, while, as just explained, we fit the bMS with an [Fe/H] that is higher by ∼0.3, and helium content $Y = 0.386$. We find it gratifying that the theoretical isochrones fit the bMS and the rMS as well as they do, especially since the fitting is a direct overplot, with no adjustments other than our having chosen the abundances so as to match the observed colors at $m_{F606W} = 21.1$.

4. A NEW COLOR–MAGNITUDE DIAGRAM FOR THE CENTRAL FIELD

Our CMD of the outer field is photometrically accurate, and free of field stars, but it has too few stars for us to draw clear conclusions from it alone. To illuminate what the outer field is telling us, we will compare its CMD with that of the much richer central field, as measured through the same pair of filters. For this purpose, we improve on the results of the *HST* Treasury Survey of globular clusters (Sarajedini et al. 2007; Anderson et al. 2008), in two ways: first, we follow the suggestions of Anderson et al. (2008, Section 7.1) regarding the use of quality indices to select a sample of the best-measured stars, and then we correct the Treasury photometry of the selected stars for differential reddening. We do not make a proper-motion selection, however, because the central field is so rich that only a tiny fraction of the total number of stars are field stars, and restricting our attention to a proper-motion sample would have caused us to lose all the faint stars.

4.1. Photometric Quality Selection

Our photometric quality criteria were four in number: the first two were the rms residuals of the magnitude measures in each band (columns headed "err" in the Globular Cluster Treasury files at http://www.astro.ufl.edu/∼ata/public_hstgc/), while the other two were `xsig` and `ysig`, which are not internal errors but rather the differences between the mean positions measured in F606W and in F814W, for the x- and y-coordinates, respectively. (Experience in working with the Treasury results had shown that stars with low-quality photometry tended also to have larger values of `xsig` and `ysig`.) We plotted each criterion against magnitude, and then tried rejecting stars at various percentile levels of the criteria. We found that a good compromise between improving the CMD, on the one hand, and rejecting too many stars, on the other hand, was to reject stars that were above the 75th percentile of any of the four criteria. This process, illustrated in Figure 6, selected 109,782 of the 317,680 stars that had at least two deep exposures in each filter. The cut is

Retour à la table des matières : p. v

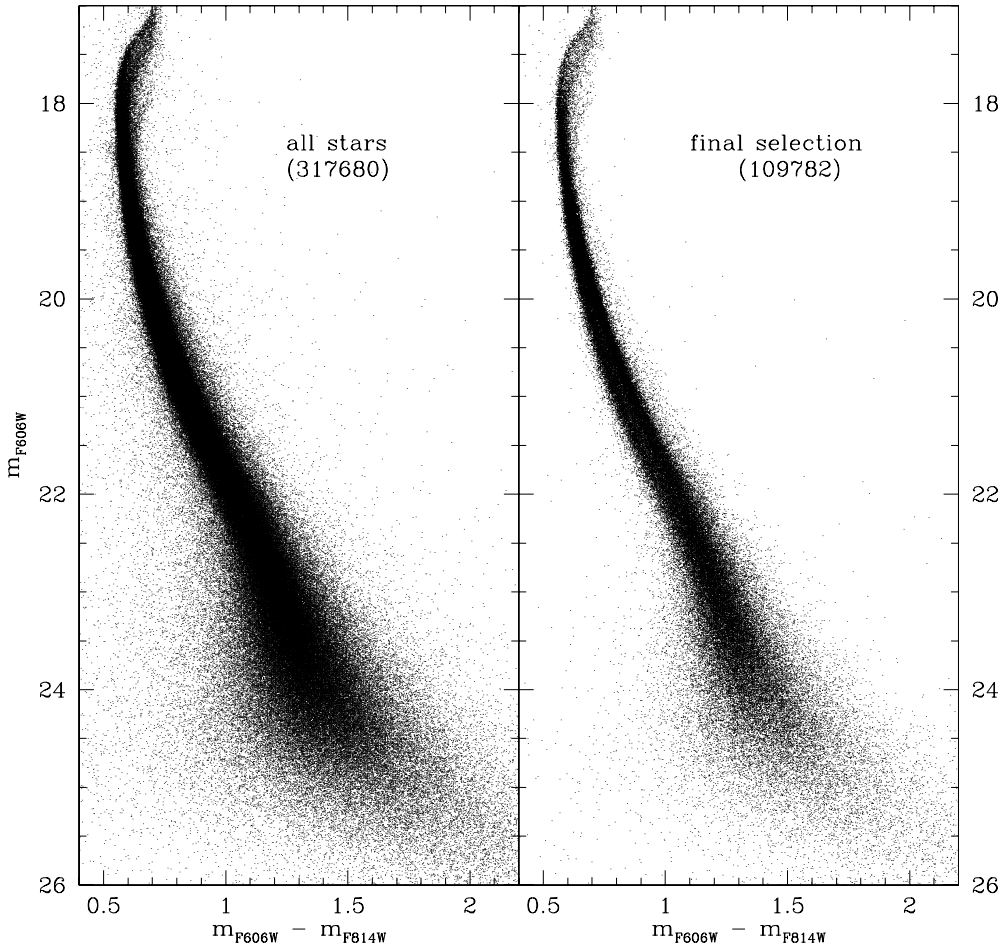

Figure 6. Comparison of a portion of the CMD of the central field, before and after selection of the stars that are the most likely to be photometrically reliable.

severe, but that is understandable in a field as crowded as the center of ω Centauri, and we believe that the resulting CMD is as good as we can produce for this field by quality selection alone.

(As a test of the efficacy of the individual criteria, we verified that each of them rejected numerous stars that had passed all the other criteria at the 75th percentile level. We note that we also tried four additional criteria, which measure the quality of the PSF fit and the amount of encroaching light from neighboring stars, for each filter—called `qv`, `qi`, `ov`, and `oi` by Anderson et al. 2008. We found that these criteria rejected few stars that were not already flagged by the four that we did use; we concluded that such low levels of rejection could be attributed to random scatter of the values of those criteria, and we therefore did not use them at all.)

4.2. Corrections for Differential Reddening

The sequences in the CMD of ω Cen are somewhat broadened by differential reddening. The Harris catalog (Harris 2010, revision of Harris 1996) gives for this cluster $E(B-V) = 0.12$, and reddening as large as this is rarely uniform. The basic method that we used to construct a reddening map of our field depends on drawing a fiducial sequence to follow the course of the MS, subgiant branch (SGB), and RGB, and then deriving an approximate reddening from the observed color of each star, by seeing how far it needs to be slid up or down a reddening line in order to meet the fiducial sequence. Our usual procedure would then be to designate the well-observed stars in a bright interval of magnitude as reference stars, and to take for the reddening correction of each individual star the mean reddening of the 75 nearest reference stars. For ω Cen, however, there are special problems, because the multiplicity of sequences confuses the procedure. In this case we proceeded as follows.

We began, as we have for other clusters, by rotating the CMD through an angle,

$$\theta = \tan^{-1} \frac{A_{F606W}}{A_{F606W} - A_{F814W}},$$

around an arbitrarily chosen point. This rotation makes the reddening line into the new x-axis, greatly simplifying the dereddening operation, which is now just a shift along the x-axis.

For the special problem of ω Cen, we iterated the first part of our usual procedure. As a first approximation to a fiducial sequence, we arbitrarily drew a line along the rMS, simply because it is the more populous of the MS components. We then applied our usual procedure, even though it is imperfect because

Retour à la table des matières : p. v

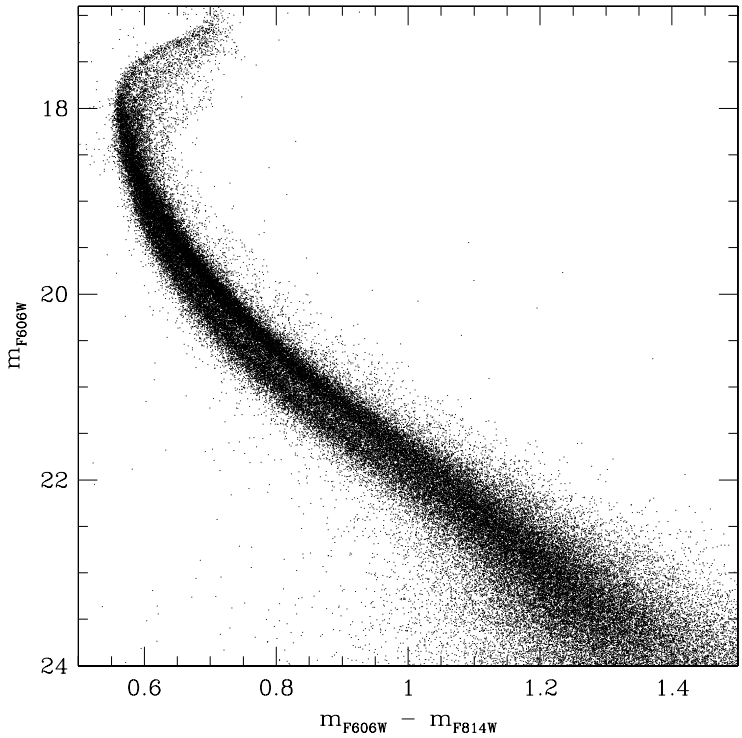

Figure 7. CMD of the central field, after quality selection and reddening correction.

of the multiple sequences; it did produce enough differential-reddening correction to effect some narrowing of the MS. (Because the rMS is so dominant numerically, any attempt to move bMS stars onto the rMS merely introduces noise that slows the convergence.) Four iterations of the correction procedure sufficed to give as good a correction as we could get.

In the corrected CMD (Figure 7), the subgiant region is split into multiple branches (a foretaste of what we may hope to find with a richer set of filters). The MS split has become less prominent here, but only as a result of printing the CMD heavily enough to show the details of the subgiant region. Figure 8 is a Hess diagram made from the same colors and magnitudes. The split in the MS can be seen more clearly now—strikingly well, in fact, for the crowded center of the cluster.

5. SUPERPOSITION OF THE TWO COLOR–MAGNITUDE DIAGRAMS

We now have a CMD of the outer field, quite sharp and almost completely free of field stars, but with few stars overall; and we have a CMD of the central field in the same two filters, with a much larger number of stars but with photometry of lower quality, in that crowded region. A fruitful step now is to compare the two CMDs by laying one on top of the other. In order to make this superposition, however, we need to adjust the zero points of the reddening-corrected magnitudes, because the corrections did not preserve zero points. We did this adjustment by eye, simply by getting the best match that we could.

The superposition, which now allows us to combine the clarity and purity of the outer field with the richness and continuity of the sequences that we see in the central field, is shown in Figures 9 and 10. The first of them shows the bright part of the magnitude range, and the second shows the faint part (with considerable magnitude overlap between the two).

In Figure 9, the rMS appears to continue upward into the bright edge of the SGB stars, while the bMS seems to emerge from the crossing of the bMS and rMS at a magnitude level that takes it into the next-most-prominent of the SGB sequences. Although a result that depends on photometry of saturated star images must always be taken with some reserve, it is hard to see how any other connection of branches of the MS with branches in the SGB region could be possible, given the numbers of stars along each of the two sequences, on the MS and then in the SGB region. (It is interesting to note that the detailed study of Villanova et al. 2007, which was limited to ground-based resolution beyond the central $10' \times 10'$ of the cluster, made SGB connections for the rMS and for the reddest branch of the MS (which they called MS-a), but they were unable to make a connection for the bMS. It is our superposition of the CMD of the outer field on that of the central field that has allowed us to suggest an SGB connection for the bMS.)

In Figure 10, we show the fainter part of the superposed CMDs. Here, the bMS seems to intersect the rMS at magnitude ~22.8, but it is not at all clear whether this is a crossing or a merger. There is a faint hint that the bMS might emerge on the red side of the rMS at fainter magnitudes, but it is impossible to be sure of this, because the photometry in the central field rapidly loses accuracy, and below $m_{\rm F606W} \sim 23$ photometric error begins to spread the MS hopelessly.

We have already called attention to the group of faint red stars well to the red of the MS, in the outer field; we see now that they are prominent in the central field too. Although we have given up hope of tracing sequences at such faint magnitudes, what we can say nevertheless is that the magnitude spread is

Retour à la table des matières : p. v

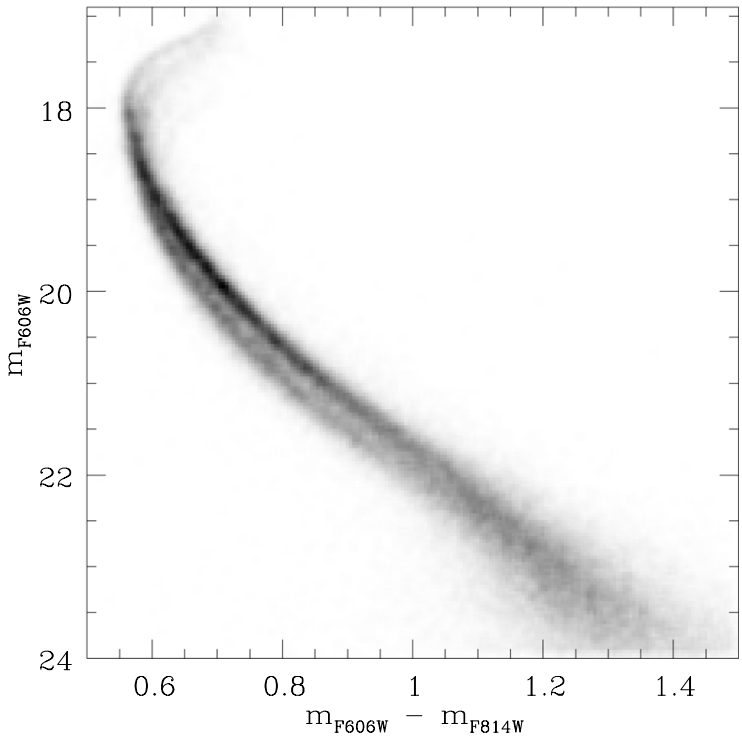

Figure 8. CMD of the central field, after quality selection and reddening correction, shown as a Hess diagram. This gray-scale representation was made from the same colors and magnitudes that were shown in Figure 7.

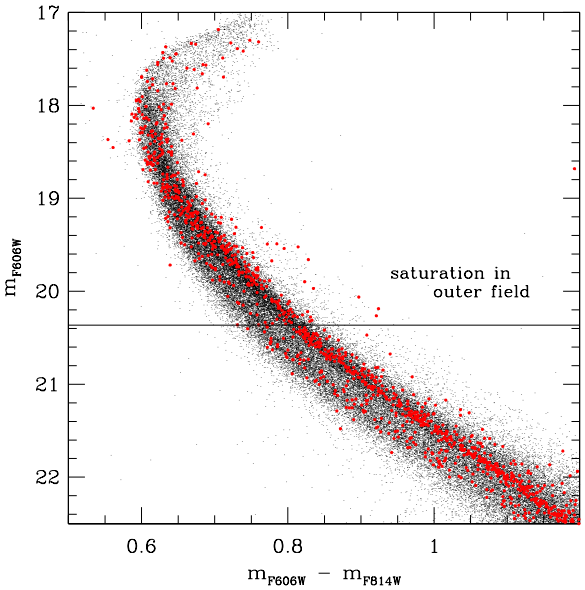

Figure 9. Points from the outer field, in red, superposed on points from the central field, in black. This figure shows the bright part of the magnitude range covered by our observations, while Figure 10 shows the faint part of the range (with considerable magnitude overlap between the two).

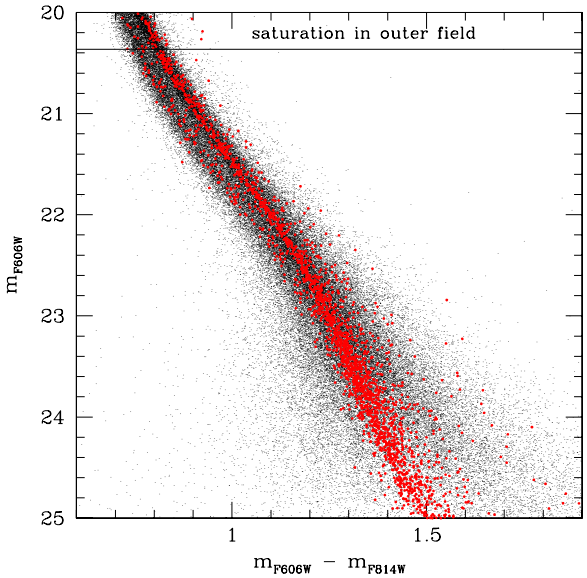

Figure 10. Faint end of the superposition of the CMD of the outer field (red) on that of the central field (black).

clearly greater on the red side of the MS than on the blue side, so that this redward extension must be something real.

We have noted that the faint red stars cannot be explained away as binaries, since they were shown in Figure 3 to be well above the upper limit of the region in the CMD where binaries lie. Since a redder MS color is usually associated with a higher metallicity (with the notable exception of the bMS!), these stars might be suspected to be the lower end of the faintest SGB sequence (the region that Villanova et al. 2007 called MS-a). This component of ω Cen is known to be much less metal-poor,

Retour à la table des matières : p. v

with [Fe/H] −0.8 to −0.7 (Johnson & Pilachowski 2010). In Figure 5, we have chosen from our library of isochrones the one with [Fe/H] = −0.85, $Y = 0.253$, and age 13 Gyr. (Noting that the highly enhanced helium in the bMS and in a few stars in NGC 2808 is an unusual anomaly, we chose to revert to a more normal Y, raising its value just a little as a consequence of the increased metallicity, and using a conventional value of dY/dZ.)

On the other hand, the spread of the red stars in color is far greater than can be expected in any single sequence; neither can we confidently trace in the observed CMD a sequence that connects SGB-a with these stars—and in fact in Villanova et al. (2007) we suggested tentatively that MS-a continues down into the rMS at a brighter magnitude than this. It is unfortunate that the outer field does not have enough stars to allow the tracing of any but the two richest sequences, while at faint magnitudes the photometry of the central field is too damaged by crowding to yield further enlightenment.

With observations that are confined to these two filters, we can go no farther in tracing sequences. It has recently been shown by Bellini et al. (2010), however, that when observations with the ultraviolet filters of WFC3 are brought into the picture, all sorts of details emerge. We will therefore leave further pursuit of the continuity of sequences to future papers that include results from more filters.

6. SUMMARY

We have used *HST* ACS/WFC imaging of an outer field of ω Centauri at two epochs to derive a CMD, cleaned of field stars, that shows the clearest separation of the blue and red branches of the MS that has yet been achieved. We have calculated new stellar structure models for a mesh of abundances of helium and metals, and have fitted isochrones to our observed sequences, deducing for the blue branch of the MS $Y = 0.39 \pm 0.02$—the first time that this anomalous abundance of helium has been given a solid base in theory, and assigned a quantitative uncertainty. We show a plausible fit of the ω Cen sequences with three different isochrones that have different abundances of helium and metals.

We have re-examined the CMD of the central part of ω Cen, selected a subset of stars that are likely to have the most reliable photometry, and corrected its photometry for differential reddening. When we superpose the CMDs of the two regions, we tentatively identify the SGB continuation of the bMS with one of the many branches that the rich central field shows in the SGB region. We also find a striking new group of stars to the red of the MS. We look forward to new insights from combining these results with the leverage that UV photometry with WFC3 now applies to this extraordinarily complex CMD.

S.C. warmly thanks F. Allard for interesting discussions and for kindly sharing her own results. S.C., A.P., and G.P. acknowledge partial support by MIUR under grants PRIN2007 (prot. 20075TP5K9) and PRIN-INAF 2009, and G.P. acknowledges support by ASI under grants ASI-INAF I/016/07/0 and I/009/10/0. J.A. and I.R.K. acknowledge support from STScI grants GO-9444, GO-10101, and GO-11233.

REFERENCES

Allard, F., Hauschildt, P. H., Alexander, D. R., & Starrfield, S. M. 1997, ARA&A, 35, 137
Anderson, J. 1997, PhD thesis, Univ. California, Berkeley
Anderson, J. 2002, in Proceedings of the 2002 HST Calibration Workshop, ed. S. Arribas, A. Koekemoer, & B. Whitmore (Baltimore, MD: STScI), 13
Anderson, J. 2006, in Proceedings of the 2005 Calibration Workshop, ed. A. Koekemoer, P. Goudfrooij, & L. Dressel (Baltimore, MD: STScI), 11
Anderson, J., & King, I. R. 2006, ACS Instrument Science Report 2006-01
Anderson, J., Sarajedini, A., Bedin, L. R., et al. 2008, AJ, 135, 2055
Bedin, L. R., Cassisi, S., Castelli, F., et al. 2005, MNRAS, 357, 1038
Bedin, L. R., Piotto, G., Anderson, J., et al. 2004, ApJ, 605, L125
Bellini, A., Bedin, L. R., Piotto, G., et al. 2010, AJ, 140, 631
Bellini, A., Piotto, G., Bedin, L. R., et al. 2009, A&A, 507, 1393
Bragaglia, A., Carretta, E., Gratton, R., et al. 2010a, A&A, 519, A60
Bragaglia, A., Carretta, E., Gratton, R. G., et al. 2010b, ApJ, 720, L41
Cannon, R. D., & Stobie, R. S. 1973, MNRAS, 162, 207
Cardelli, J. A., Clayton, G. C., & Mathis, J. S. 1989, ApJ, 345, 245
D'Antona, F., & Caloi, V. 2008, MNRAS, 390, 693
Del Principe, M., Piersimoni, A. M., Storm, J., et al. 2006, ApJ, 652, 362
Dickens, R. J., & Woolley, R. v. d. R. 1967, R. Obs. Bull., 128, 255
Dupree, A. K., Strader, J., & Smith, G. H. 2011, ApJ, 728, 155
Ferguson, J. W., Alexander, D. R., Allard, F., et al. 2005, ApJ, 623, 585
Freeman, K. C., & Rodgers, A. W. 1975, ApJ, 201, L71
Gilliland, R. 2004, ACS Instrument Science Report 2004-01
Gratton, R. G., Carretta, E., Bragaglia, A., Lucatello, S., & D'Orazi, V. 2010, A&A, 517, A81
Harris, W. E. 1996, AJ, 112, 1487
Harris, W. E. 2010, arXiv:1012.3224
Hauschildt, P. H., Allard, F., & Baron, E. 1999a, ApJ, 512, 377
Hauschildt, P. H., Allard, F., Ferguson, J., Baron, E., & Alexander, D. 1999b, ApJ, 525, 871
Johnson, C. I., & Pilachowski, C. A. 2010, ApJ, 722, 1373
Lee, Y.-W., Joo, J.-M., Sohn, Y.-J., et al. 1999, Nature, 402, 55
Merritt, D., Meylan, G., & Mayor, M. 1997, AJ, 114, 1074
Norris, J. 2004, ApJ, 612, L25
Norris, J. E., Freeman, K. C., & Mighell, K. J. 1996, ApJ, 462, 241
Pancino, E., Ferraro, F., Bellazzini, M., Piotto, G., & Zoccali, M. 2000, ApJ, 534, 83
Pasquini, L., Mauas, P., Käufl, H. U., & Cacciari, C. 2011, A&A, 531, A35
Pietrinferni, A., Cassisi, S., Salaris, M., & Castelli, F. 2004, ApJ, 612, 168
Pietrinferni, A., Cassisi, S., Salaris, M., & Castelli, F. 2006, ApJ, 642, 797
Piotto, G., Bedin, L. R., Anderson, J., et al. 2007, ApJ, 661, L53
Piotto, G., Villanova, S., Bedin, L. R., et al. 2005, ApJ, 621, 777
Rogers, F. J., & Iglesias, C. A. 1992, ApJS, 79, 507
Sarajedini, A., Bedin, L. R., Chaboyer, B., et al. 2007, AJ, 133, 1658
Saumon, D., Chabrier, G., & van Horn, H. M. 1995, ApJS, 99, 713
Sirianni, M., Jee, M. J., Benítez, N., et al. 2005, PASP, 117, 1049
Sollima, A., Pancino, E., Ferraro, F. R., et al. 2005, ApJ, 634, 332
Villanova, S., Piotto, G., King, I. R., et al. 2007, ApJ, 663, 296

Retour à la table des matières : p. v

Retour à la table des matières : p. v

Conclusion

« *A conclusion is simply the place where you got tired of thinking.* »

Dan Chaon,
Stay Awake, Ballantine Books (2012),
repris sur https://www.goodreads.com

à moins que le lecteur préfère :

« *A conclusion is the place where you got tired thinking.* »

Martin H. Fischer,
In Charlie Walker, *My Few Wise Words of Wisdom* (2000),
repris sur https://todayinsci.com

J'ai toujours apprécié les méthodes de Monte-Carlo, elles doivent être présentes dans presque tous les domaines de la physique. Le transfert des photons dans une atmosphère planétaire peut se traiter avec une méthode de Monte-Carlo, mais cette approche peut bien sûr s'appliquer au nuage formé lors d'un débouchage d'une bouteille de champagne, tout autant qu'au cas de l'irradiation d'une nébuleuse protoplanétaire. Dans les années à venir, un joli aboutissement serait de réaliser une confluence surface planétaire-champagne-nébuleuse protosolaire, ceci via une telle méthode.

En décembre 2017, la NASA a retenu, pour son programme *New Frontiers*, deux concepts de missions spatiales : *Dragonfly*[1] qui est un mission d'exploration de la surface de Titan (voir Fig. 14.1), en concurrence avec une mission de retour d'échantillons de la comète 67P/Churyumov–Gerasimenko : *CAESAR*[2] (Comet Astrobiology Exploration Sample Return). Le choix de la sonde qui sera construite va se faire mi-2019, je souhaite bien sûr que *Dragonfly* soit choisie, les analyses de la surface de Titan qui pourront être faites sont irremplaçables, même par les plus sophistiqués des modèles numériques. Un tel engin, profitant des conditions titanienne particulièrement favorables au vol, serait un des premiers drones extraterrestres, et pourrait révéler d'innombrables surprises.

Laissons la parole à l'avenir.

1. voir http://dragonfly.jhuapl.edu
2. voir http://caesar.cornell.edu/

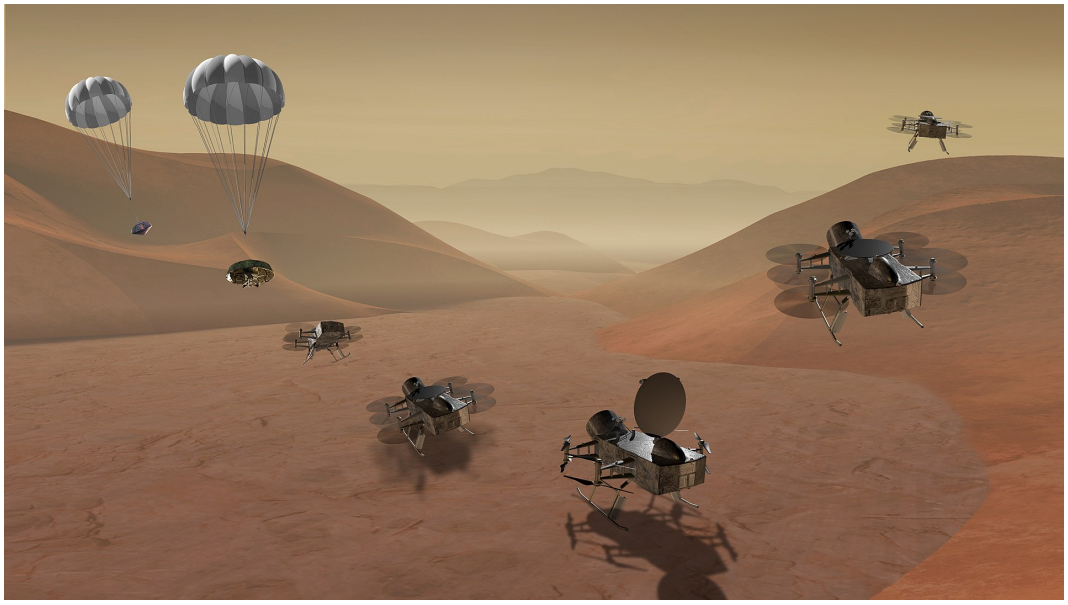

FIGURE 14.1 – La sonde *Dragonfly* telle qu'elle opérera peut être dans les zones équatoriales de Titan vers le milieu des années 2030, après un lancement vers 2025 (Image : Johns Hopkins APL/Steve Gribben).

Retour à la table des matières : p. v

Annexe A

Curriculum vitæ

Daniel Cordier
Né le 5 juillet 1966 à Nancy

Adresses : 7, rue Gerbert
51 100 Reims

E-mail : daniel.cordier@univ-reims.fr

Marié, père de quatre enfants :

Hippolyte, né le 28 mai 1998
Léopold, né le 2 février 2001
Sibylle et Marianne, nées le 11 octobre 2005

Déroulement de carrière

- **1993-1994 :** obtention de l'agrégation de physique, professeur stagiaire au lycée Condorcet de Méru (Oise).
- **1994-2009 :** professeur de physique au Cycle Préparatoire Intégré de la Fédération Gay-Lussac, hébergé l'Ecole Nationale Supérieure de Chimie de Rennes (ENSCR).
- **2009-2011 :** détachement dans le corps de Chargés de Recherche de 1ère Classe, affectation l'Institut de Physique de Rennes (UMR 6251).
- **2011-2015 :** intégration au CNRS et affectation à l'Institut UTINAM de Besançon (6213).
- **2015- :** affection au *Groupe de Spectrométrie Moléculaire et Atmosphérique* (UMR CNRS 7331), Reims.

Encadrement d'étudiant(e)s en Master

- encadrement de Melle Laëtitia Néraudeau en M1 et M2 du Master MEFF de l'ESPE de Franche-Comté (années 2012-2013 et 2013-2014), sujet : «Les conceptions initiales dans l'enseignement de l'astronomie au cycle 3».

- ☐ encadrement d'un stage de M1 de Jonathan Barreaux (mai-juin 2009, Institut de Physique de Rennes), sujet : «Equation d'état adaptée au cas des étoiles céphéides».

- ☐ encadrement d'un stage de M1 «astrophysique» de Jimmy Leray (30/03/2011–25/06/2011, Institut de Physique de Rennes), sujet : «Construction d'un modèle simple d'atmosphère à une dimension et en équilibre avec une phase liquide».

Co-encadrement d'étudiant(e)s en thèse

- ☐ co-encadrement (avec Robert Georges, Institut de Physique de Rennes) d'Audrey Moudens, sujet : «Formation de complexes moléculaires hydratés appliquée aux sciences planétaires» (soutenance : octobre 2010).

- ☐ co-encadrement (avec Vincent Chevrier, Université d'Arkansas) d'Adrienn Luspay-Kuti, sujet : «Experimental constraints on the composition and dynamics of Titan's polar lakes» (soutenance : mars 2014).

- ☐ co-encadrement (avec Vincent Chevrier, Université d'Arkansas) de Sandeep Singh, sujet : «Experimental determination of acetylene and ethylene solubility in liquid methane and ethane : Implications to Titan's surface» (soutenance : juillet 2015).

- ☐ co-encadrement (avec Pascal Rannou, Université de Reims) de Maélie Coutelier, sujet : «Analyse des images hyperspectrales de VIMS : Etude du système atmosphère-surface-lacs de Titan – Application aux cas d'ExoTitans.» (date de soutenance prévue : septembre 2020).

Retour à la table des matières : p. v

Annexe B

Production bibliographique complète

B.1 Travaux Publiés

B.1.1 Livres

— **Cordier**, D.,
«Cours de physique - Licence : Tome 1 : Electrostatique et magnétostatique», Editions Dunod, **2004**, 288 pages (ISBN : 9782100068531).

— **Cordier**, D.,
«Cours de physique - Licence : Tome 2 : Phénomènes d'induction et ondes électromagnétiques», Editions Dunod, **2007**, 328 pages (ISBN : 9782100068548).

B.1.2 Articles de vulgarisation

2018 – 1. Liger-Belair, G., **Cordier**, D., Cilindre, C., Honvault, J.,
«Champagne ! Un nuage bleu lorsque le bouchon saute»,
Revue des Œnologues, N^{o} 167, avril 2018.

2. Liger-Belair, G., **Cordier**, D., Honvault, J.,
«Le fugace nuage bleu du champagne»,
Pour la Science, N^{o} 488, Juin 2018.

3. Liger-Belair, G., **Cordier**, D., Cilindre, C., Honvault, J.,
«Champagne ! Un nuage bleu lorsque le bouchon saute»,
Revue des œnologues et des techniques vitivinicoles et œnologiques, N^{o} 168, Juillet 2018.

B.1.3 Publications à comité de lecture

Articles dans des revues internationales à comité de lecture

2002 – 1. **Cordier**, D., Lebreton, Y., Goupil, M.-J., Lejeune, T., Beaulieu, J.-P and Arenou, F.,
«Convective core mixing : a metallicity dependence ?»,
2002, *Astronomy & Astrophysics*, 392, 169.
doi: 10.1051/0004-6361:20020934.

2003 – 2. **Cordier**, D., Goupil, M.-J. and Lebreton, Y.,
«Cepheids of the Small Magellanic Cloud : a selection effect ?»,
2003, *Astronomy & Astrophysics*, 409, 491.
doi: 10.1051/0004-6361:20031185.

2007 – 3. **Cordier**, D., Pietrinferni, A., Cassisi, S. et Salaris, M.,
«A Large Stellar Evolution Database for Population Synthesis Studies. III. Inclusion of the Full Asymptotic Giant Branch Phase and Web Tools for Stellar Population Analyses»,
2007, *Astronomical Journal*, 133, 468.
doi: 10.1086/509870.

2008 – 4. Manzato, P., Pietrinferni, A., Gasparo, F., Taffoni, G. & **Cordier**, D.,
«BaSTI, a Bridge between Grid and Virtual Observatory Part 1 : BaSTI inside the VO»,
2008, *Publication of the Astronomical Society of the Pacific* (PASP), 120, 922.
doi: 10.1086/591294.

5. **Cordier**, D., Mousis, O., Lunine, J.-I., Moudens, A. & Vuitton, V.,
«Photochemical enrichment of deuterium in Titan's atmosphere»,
2008, *The Astrophysical Journal Letter*, 689, 61C.
doi: 10.1086/595677.

2009 – 6. Mousis, O., Lunine, J.-I. ; Thomas, C., Pasek, M, Marboeuf, U., Alibert, Y., Ballenegger, V., **Cordier**, D., Ellinger, Y., Pauzat, F. & Picaud, S.
«Clathration of Volatiles in the Solar Nebula and Implications for the Origin of Titan's atmosphere»,
2009, *The Astrophysical Journal*, 691, 1780.
doi: 10.1088/0004-637X/691/2/1780.

7. Mousis, O., Lunine, J.-I., Waite, J. H., Magee, B.,
Lewis, W. S., Mandt, K. E., Marquer, D., **Cordier**, D.,
«Formation Conditions of Enceladus and Origin of Its Methane Reservoir»,
2009, *The Astrophysical Journal Letter*, 701, 39.
doi: 10.1088/0004-637X/701/1/L39.

8. **Cordier**, D., Mousis, O., Lunine, J.-I., Lavvas, P., Vuitton, V.,
«An Estimate of the Chemical Composition of Titan's Lakes»,
2009, *The Astrophysical Journal Letter*, 707, 128.
doi: 10.1088/0004-637X/707/2/L128.

9. Mousis, O., Lunine, J.I., Pasek, M., **Cordier**, D., Waite, J.H., Mandt, K., Lewis, W.S. & Nguyen M.J.,
«A primordial origin for the atmospheric methane of Saturn's Moon Titan»,
2009, *Icarus*, 204, 749.
doi: 10.1016/j.icarus.2009.07.040.

10. Mandt, K.E., Waite, J.H., Lewis, W., Magee, B., Bell, J., Lunine, J.I., Mousis, O., & **Cordier**, D.,
«Isotopic evolution of the major constituents of Titan's atmosphere based on Cassini data»,
2009, *Planetary and Space Science* (PSS), 57, 1917.
doi: 10.1016/j.pss.2009.06.005.

2010 – 11. Mousis, O., Jonathan I. Lunine, J.I., Picaud, S., **Cordier, D.**,
«Volatile inventories in clathrate hydrates formed in the primordial nebula»,
2010, *Faraday Discussion*, 147, 509–525 (http ://arxiv.org/abs/1011.4171).
doi: 10.1039/c003658g.

12. **Cordier**, D., Mousis, O., Lunine, J. I., Lebonnois, S., Lavvas, P., Lobo, L. Q., Ferreira, A. G. M.,
«About the Possible Role of Hydrocarbon Lakes in the Origin of Titan's Noble Gas Atmospheric Depletion»,
2010, *The Astrophysical Journal Letter*, 721, 117.
doi: 10.1088/2041-8205/721/2/L117.

2011 – 13. Mousis, O., Lunine, J.I., Petit, J.-M., Zahnle, K., Biennier, L., Picaud, S.,
Johnson, T. V., Mitchell, J.B.A, Boudon, V., **Cordier**, D., Devel, M., Georges, R., Griffith, C., Iro, N., Marley, M.S., Marboeuf, U.,
«On the volatile enrichments and heavy element content in HD 189733b»,

Retour à la table des matières : p. v

2011, *The Astrophysical Journal*, 727, 77.
doi: 10.1088/0004-637X/727/2/77.

14. Moudens, A., Mousis, O., Petit, J.M., Wurm, G., **Cordier**, D., Charnoz, N.,
«Photophoretic transport of hot minerals in the solar nebula»,
2011, *Astronomy & Astrophysics*, 531, 106.
doi: 10.1051/0004-6361/201116476.

15. Mousis, O., Lunine, J. I., Picaud, S., **Cordier**, D., Waite, Jr., J. H., Mandt, K. E.,
«Removal of Titan's Atmospheric Noble Gases by Their Sequestration in Surface Clathrates»,
2011, *The Astrophysical Journal Letter*, 740, L9.
doi: 10.1088/2041-8205/740/1/L9.

2012 – 16. **Cordier**, D., Mousis, O., Lunine, J.I., Lebonnois, S., Rannou, P.,
Lavvas, P., Lobo, L.Q., Ferreira, A.G.M., «Titan's lakes chemical composition : sources of uncertainties and variability»,
2012, *Planetary and Space Science*, 61, 99.
doi: 10.1016/j.pss.2011.05.009.

17. Mousis, O., Lunine, J. I., Chassefière, E., Montmessin, F., Lakhlifi, A., Picaud, S., Petit, J.-M. & **Cordier**, D.,
«Mars cryosphere : A potential reservoir for heavy noble gases ?»,
2012, *Icarus*, 218, 80-87.
doi: 10.1016/j.icarus.2011.12.007.

18. King, I. R., Bedin, L. R., Cassisi, S., Milone, A. P., Bellini, A., Piotto, G., Anderson, J., Pietrinferni, A., **Cordier**, D.,
«Hubble Space Telescope Observations of an Outer Field in Omega Centauri : A Definitive Helium Abundance»,
2012, *Astronomical Journal*, 144, 5.
doi: 10.1088/0004-6256/144/1/5.

2013 – 19. **Cordier**, D., Barnes, J. W. & Ferreira, A.,
«On the chemical composition of Titan's dry lakebed evaporites»,
2013, *Icarus*, 226, 1431-1437.
doi: 10.1016/j.icarus.2013.07.026.
Paper highlighted by the journal *Nature Geoscience*

— **Cordier**, D., Mousis, O., Lunine, J.I., lavvas, P. & Vuitton, V.,
«Erratum : "An Estimate of the Chemical Composition of Titan's Lakes" (2009, ApJL, 707, L128)»,
2013, *The Astrophysical Journal Letter*, 768, L23.
doi: 10.1088/2041-8205/768/1/L23

2014 – 20. Biennier, L., Carles, S., **Cordier**, D., Guillemin, J.-C., Le Picard, S. & Faure, A.,
«Low temperature reaction kinetics of $CN^- + HC_3N$ and implications for the growth of anions in Titan's atmosphere»,
2014, *Icarus*, 227, 123-131.
doi: 10.1016/j.icarus.2013.09.004.

21. Rousselot, P., Pirali, O., Jehin, E., Vervloet, M., Hutsemékers, D., Manfroid, J., **Cordier**, D., Martin-Drumel, M.-A., Gruet, S., Arpigny, C., Decock, A., Mousis, O.,
«Toward a unique nitrogen isotopic ratio in cometary ices»,
2014, *The Astrophysical Journal*, 780L, 17R.
doi: 10.1088/2041-8205/780/2/L17.

22. Tobie, G., Teanby, N.A., Coustenis, A., Jaumann, R., Raulin, F., Schmidt, J., Carrasco, N., Coates, A.J., **Cordier**, D., DeKok, R., Geppert, W.D., Lebreton, J.-P., Lefevre, A., Livengood, T.A., Mandt, K.E., Mitri, G., Nimmo, F., Nixon, C.A., Norman, L., Pappalardo, R.T., Postberg, F., Rodriguez,

S., Schulze-Makuch, D., Soderblom, J.M., Solomonidou, A., Stephan, K., Stofan, E.R., Turtle, E.P., Wagner, R.J., West, R.A., Westlake, J.H., «Science goals and mission concept for the future exploration of Titan and Enceladus»,
2014, *Planetary and Space Science*, 104, 59-77.
doi: 10.1016/j.pss.2014.10.002.

2015 – 23. Luspay-Kuti, A., Chevrier, V. F., **Cordier**, D., Rivera-Valentin, E.G., Singh, S., Wagner, A., Wasiak, F.C.,
«Experimental Constraints on the Composition and Dynamics of Titan's Polar Lakes»,
2015, *Earth and Planetary Science Letters*, 410C, 75-83.
doi: 10.1016/j.epsl.2014.11.023.

24. Cornet, T., **Cordier**, D., Le Bahers, T., Bourgeois, O., Fleurant, C., Le Mouélic, S., Altobelli, N., «Dissolution on Titan and on Earth : Toward the age of Titan's karstic landscapes»,
2015, *Journal of Geophysical Research*, 120, 1044-1074.
doi: 10.1002/2014JE004738.
Paper highlighted by the journal *Nature Geoscience*

25. Tinetti, G, Drossart, P., Eccleston, P., Hartogh, P., Isaak, K., Linder, M., Lovis, C., Micela, G., Ollivier, M., Puig, L., Ribas, I., Snellen, I., Swinyard, B., Allard, F., Barstow, J., Cho, J., Coustenis, A., Cockell, C., Correia, A., Decin, L., Kok, R., Deroo, P., Encrenaz, T., Forget, F., Glasse, A., Griffith, C., Guillot, T., Koskinen, T., Lammer, H., Leconte, J., Maxted, P., Mueller-Wodarg, I., Nelson, R., North, C., Pallé, E., Pagano, I., Piccioni, G.,Pinfield, D.,Selsis, F., Sozzetti, A., Stixrude, L.,Tennyson, J., Turrini, D., Zapatero-Osorio, M., Beaulieu, J.-P., Grodent, D., Guedel, M., Luz, D., Nørgaard-Nielsen, H. U., Ray, T., Rickman, H., Selig, A., Swain, M., Banaszkiewicz, M., Barlow, M., Bowles, N., Branduardi-Raymont, G., Foresto, V. C., Gerard, J.-C., Gizon, L., Hornstrup, A., Jarchow, C., Kerschbaum, F., Kovacs, G., Lagage, P.-O., Lim, T., Lopez-Morales, M., Malaguti, G., Pace, E., Pascale, E., Vandenbussche, B., Wright, G., Zapata, G. R., Adriani, A., Azzollini, R., Balado, A., Bryson, I., Burston, R., Colomé, J., Crook, M., Giorgio, A., Griffin, M., Hoogeveen, R., Ottensamer, R., Irshad, R., Middleton, K., Morgante, G., Pinsard, F., Rataj, M., Reess, J.-M., Savini, G., Schrader, J.-R., Stamper, R., Winter, B., Abe, L., Abreu, M., Achilleos, N., Ade, P., Adybekian, V., Affer, L., Agnor, C., Agundez, M., Alard, C., Alcala, J., Allende Prieto, C., Alonso Floriano, F. J., Altieri, F., Alvarez Iglesias, C. A., Amado, P., Andersen, A., Aylward, A., Baffa, C., Bakos, G., Ballerini, P., Banaszkiewicz, M., Barber, R. J., Barrado, D., Barton, E. J., Batista, V., Bellucci, G., Belmonte Avilés, J. A., Berry, D., Bézard, B., Biondi, D., Błęcka, M., Boisse, I., Bonfond, B., Bordé, P., Börner, P., Bouy, H., Brown, L., Buchhave, L., Budaj, J., Bulgarelli, A., Burleigh, M., Cabral, A., Capria, M. T., Cassan, A., Cavarroc, C., Cecchi-Pestellini, C., Cerulli, R., Chadney, J., Chamberlain, S., Charnoz, S., Christian Jessen, N., Ciaravella, A., Claret, A., Claudi, R., Coates, A., Cole, R., Collura, A., **Cordier**, D., Covino, E., Danielski, C., Damasso, M., Deeg, H. J., Delgado-Mena, E., Vecchio, C., Demangeon, O., Sio, A., Wit, J., Dobrijévic, M., Doel, P., Dominic, C., Dorfi, E., Eales, S., Eiroa, C., Espinoza Contreras, M., Esposito, M., Eymet, V., Fabrizio, N., Fernández, M., Femenía Castella, B., Figueira, P., Filacchione, G., Fletcher, L., Focardi, M., Fossey, S., Fouqué, P., Frith, J., Galand, M., Gambicorti, L., Gaulme, P., García López, R. J., Garcia-Piquer, A., Gear, W., Gerard, J.-C., Gesa, L., Giani, E., Gianotti, F., Gillon, M., Giro, E., Giuranna, M., Gomez, H., Gomez-Leal, I., Gonzalez Hernandez, J., González Merino, B., Graczyk, R., Grassi, D., Guardia, J., Guio, P., Gustin, J., Hargrave, P., Haigh, J., Hébrard, E., Heiter, U., Heredero, R. L., Herrero, E., Hersant, F., Heyrovsky, D., Hollis, M., Hubert, B., Hueso, R., Israelian, G., Iro, N., Irwin, P., Jacquemoud, S., Jones, G., Jones, H., Justtanont, K., Kehoe, T., Kerschbaum, F., Kerins, E., Kervella, P., Kipping, D., Koskinen, T., Krupp, N., Lahav, O., Laken, B., Lanza, N., Lellouch, E., Leto, G., Licandro Goldaracena, J., Lithgow-Bertelloni, C., Liu, S. J., Lo Cicero, U., Lodieu, N., Lognonné, P., Lopez-Puertas, M., Lopez-Valverde, M. A., Lundgaard Rasmussen, I., Luntzer, A., Machado, P., MacTavish, C., Maggio, A., Maillard, J.-P., Magnes, W., Maldonado, J., Mall, U., Marquette, J.-B., Mauskopf, P., Massi, F., Maurin, A.-S., Medvedev, A., Michaut, C., Miles-Paez, P., Montalto, M., Montañés Rodríguez, P., Monteiro, M., Montes, D., Morais, H.,

Retour à la table des matières : p. v

Morales, J. C., Morales-Calderón, M., Morello, G., Moro Martín, A., Moses, J., Moya Bedon, A., Murgas Alcaino, F., Oliva, E., Orton, G., Palla, F., Pancrazzi, M., Pantin, E., Parmentier, V., Parviainen, H., Peña Ramírez, K. Y., Peralta, J., Perez-Hoyos, S., Petrov, R., Pezzuto, S., Pietrzak, R., Pilat-Lohinger, E., Piskunov, N., Prinja, R., Prisinzano, L., Polichtchouk, I., Poretti, E., Radioti, A., Ramos, A. A., Rank-Lüftinger, T., Read, P., Readorn, K., Rebolo López, R., Rebordão, J., Rengel, M., Rezac, L., Rocchetto, M., Rodler, F., Sánchez Béjar, V. J., Sanchez Lavega, A., Sanromá, E., Santos, N., Sanz Forcada, J., Scandariato, G., Schmider, F.-X., Scholz, A., Scuderi, S., Sethenadh, J., Shore, S., Showman, A., Sicardy, B., Sitek, P., Smith, A., Soret, L., Sousa, S., Stiepen, A., Stolarski, M., Strazzulla, G., Tabernero, H. M., Tanga, P., Tecsa, M., Temple, J., Terenzi, L., Tessenyi, M., Testi, L., Thompson, S., Thrastarson, H., Tingley, B. W., Trifoglio, M., Martín Torres, J., Tozzi, A., Turrini, D., Varley, R., Vakili, F., Val-Borro, M., Valdivieso, M. L., Venot, O., Villaver, E., Vinatier, S., Viti, S., Waldmann, I., Waltham, D., Ward-Thompson, D., Waters, R., Watkins, C., Watson, D., Wawer, P., Wawrzaszk, A., White, G., Widemann, T., Winek, W., Wiśniowski, T., Yelle, R., Yung, Y., Yurchenko, S. N.,
«The EChO science case»,
2015, *Experimental Astronomy*, 40, 329-391.
doi: 10.1007/s10686-015-9484-8.

2016 – 26. **Cordier**, D., Prada Moroni, P. G., Tognelli, E.,
«Dust Photophoretic transport around a T Tauri star : implications for comets composition»,
2016, *Icarus*, 268, 281-294.
doi: 10.1016/j.icarus.2015.11.037.

27. **Cordier**, D., Cornet, T., Barnes, J. W., MacKenzie, S. M, Le Bahers, T., Nna Mvondo, D., Rannou, P., Ferreira, A. G.,
«Structure of Titan's evaporites»,
2016, *Icarus*, 270, 41-56.
doi: 10.1016/j.icarus.2015.12.034

28. **Cordier**, D.,
«How speed of sound measurements could bring constraints on the composition of Titan's seas»,
2016, *Monthly Notices of the Royal Astronomical Society*, 459, 2008-2013.
doi: 10.1093/mnras/stw732

2017 – 29. **Cordier**, D., García-Sánchez, F., Justo-García, D. N., Liger-Belair, G.,
«Bubble streams in Titan's seas as product of liquid N_2-CH_4-C_2H_6 cryogenic mixture»,
2017, *Nature Astronomy*, 1, 102.
doi: 10.1038/s41550-017-0102

30. Singh, S., Combe, J.-P., **Cordier**, D., Chevrier, V.F., Wagner, A., McMahon, Z.,
«Experimental Determination of Acetylene and Ethylene Solubility in liquid Methane and Ethane : Implications to Titan's Surface»,
2017, *Geochimica et Cosmochimica Acta*, 208, 86-101.
doi: 10.1016/j.gca.2017.03.007

31. Nyaupana, P. R., Diez-y-Riega, H., Camejo, E., Manzanares, C. E., **Cordier**, D.
«C-H infrared absorption and solubility ef ethylene, methyl-caetylene, 2-methyl-2-butene, and 2-methyl-1,3butadiene (iroprene) in liquid argon solutions»,
2017, *Applied Spectroscopy*, 71(9) 2146–2153.
doi: 10.1177/0003702817702387

32. Liger-Belair, G., **Cordier**, D., Honvault, J., Cilindre, C.,
«Unveiling CO_2 heterogeneous freezing plumes during champagne cork popping»,
2017, *Scientific Reports*, 7, Article number : 10938.
doi: 10.1038/s41598-017-10702-6
Article classé, en 2017, dans le «Top 100» des articles de chimie, parus dans *Scientific Reports*, les plus lus.

Retour à la table des matières : p. v

2018 – 33. **Cordier**, D., Liger-Belair, G.,
«Bubbles in Titan's seas: nucleation, growth and RADAR signature»,
2018, *The Astrophysical Journal*, 859, 26.
doi: 10.3847/1538-4357/aabc10
Paper highlighted by the *American Astronomical Society* (AAS) :
https://aasnova.org/2018/05/21/bubbles-in-titans-seas/

34. **Cordier**, D., Carrasco, N.,
«The floatability of aerosols on Titan's seas and Marangoni waves damping»,
2018, *Nature Geoscience*, soumis, **en cours de révision**.

Récapitulatif

— Nombre total d'articles : 34.

— Nombre de publications en premier auteur : 13.

— Nombre annuel moyen de publications, par année passée en qualité de chercheur à temps plein : 3.78.

Articles dans des revues nationales à comité de lecture

— **Cordier** D.,
«Expériences simples de densitométrie»,
Bulletin de l'Union des Physiciens N° 777, Octobre **1995**, Vol. 89, p. 1567.

— **Cordier** D. et Roussel J.,
«Analyse harmonique du bruit d'un moteur de voiture»,
Bulletin de l'Union des Physiciens N° 882, Mars **2006**, p. 311-322.

— **Cordier** D.
«A propos de la chute d'une barre conductrice dans un champ magnétique – Influence d'un effet non-linéaire»,
Bulletin de l'Union des Physiciens N° 911, Février **2009**.

— **Cordier** D., Mousis O.
«Arpenter l'Univers grâce à des systèmes oscillants : les étoiles céphéides»,
Bulletin de l'Union des Physiciens N° 918, Novembre **2009**.

— Roussel, J., **Cordier** D.
«Courants de Foucault induits dans un cylindre conducteur – Approche numérique»,
Bulletin de l'Union des Physiciens N° 938, Novembre **2011**.

B.2 Actes de colloques

2000 – **Cordier**, D., Lejeune, T., Lebreton, Y. and Goupil, M.-J,
«Mixing in the SMC Stars : Implication for Cepheids», 2000, ASP Conf. Ser. 203 : IAU Colloq. 176 : The Impact of Large-Scale Surveys on Pulsating Star Research, Ed. L. Szabados and D. Kurtz., p. 381.

2001 – **Cordier**, D., Lebreton, Y. and Goupil, M.-J,
«Cepheids in the SMC : Blue Loops and Mass-Luminosity Relation», 2001, ASP Conf. Ser., in press, IAU Colloq. : Observed HR diagrams and stellar evolution : the interplay between observational constraints and theory, Ed. T. Lejeune and J. Fernandes.

Retour à la table des matières : p. v

2006 – Cassisi, S., Pietrinferni, A., Salaris, M., Castelli, F., **Cordier**, D., Castellani, M.,
«BASTI : an interactive database of updated stellar evolution models», 2006, Memorie della Societa Astronomica Italiana, v.77, p.71.

2007 – Pietrinferni, A., Cassisi, S., Salaris, M., **Cordier**, D., Castelli, F.,
«BaSTI - a library of stellar evolution models : updates and applications», 2007, IAU Symposium, v. 241, p. 39-40.

2008 – **Cordier**, D.,
«WEBCESAM : a web interface for stellar evolution calculations», 2008, *Memorie della Societa Astronomica Italiana*, 79, 689.

— **Cordier**, D., Mousis, O. Lunine, J.I., Moudens, A.,
«A Dual Origin for the Deuterium Enrichment in the Atmosphere of Titan», 2008, *Lunar and Planetary Science XXXIX*, 39.1691C.

— Moudens, A., **Cordier**, D., Mousis, O., Lunine, J. I., Vuitton, V.
«Photochemical Enrichment of Deuterium in Titan's Atmosphere : new lights from Cassini-Huygens», 2008, *SF2A-2008*, Nov., p. 427.

— Mousis, O., Lunine, J. I., Thomas, C., Pasek, M., Marboeuf, U., Alibert, Y., Ballenegger, V., **Cordier**, D., Ellinger, Y., Pauzat, F., Picaud, S.
«Origin of Titan and its Atmosphere : New Lights from Cassini-Huygens», 2008, *EPSC Meeting 2008*, Sep., p. 688.

— **Cordier**, D., Mousis, O. Lunine, J.I., Moudens, A., Vuitton, V.,
«New Constraints on Photochemical Enrichment of Deuterium in Titan's Atmosphere from Cassini-huygens Data», 2008, *Division for Planetary Science*, 40.3107C.

2009 – Mousis, O., **Cordier**, D., Lunine, J. I., Lavvas, P., Vuitton, V.,
«Composition of the lakes of Titan», 2009, *Conférence SF2A*, 245M.

— Mousis, O., Lunine, J. I., Pasek, M., **Cordier**, D., Waite, J. H., Mandt, K. E., Lewis, W. S., Nguyen, M.-J.
«Is Serpentinization the Source of Titan's Atmospheric Methane ?», 2009, *Lunar and Planetary Science*, 40.1182M.

2010 – Lunine, J. I., **Cordier**, D., Mousis, O., Lavvas, P.,
«Solubilities of Hydrocarbons in the Seas of Titan and Tests for Exotic Life», **2010**, *LPICo*, 1538.5365L.

— **Cordier**, D., Mousis, O., Luni

— Liger-Belair, G., **Cordier**, D., Cilindre, C., Honvault, J.,
«Champagne ! Un nuage bleu lorsque le bouchon saute»,
Revue des œnologues et des techniques vitivinicoles et œnologiques, N° 168, Juillet 2018. ne, J.-I., Lavvas, P., Lobo, L., Ferreira, A.,
«Chemical composition of Titan's lakes and noble gases sequestration», 2010, *Titan Through Time Workshop – GSFC*.

Retour à la table des matières : p. v

— Mousis, O., Lunine, J. I., Pasek, M., **Cordier**, D., Waite, Jr., J. H., Mandt, K. E., Lewis, W. S., «Evidence for a primordial origin of Titan's atmospheric methane», **2010**, *EGU General Assembly Conference Abstracts*, vol. 12, p. 9410.

— Mousis, O., Moudens, A., Petit, J.-M., **Cordier**, D., Wurm, S. C. G., Alibert, Y. «Radial transport of hot minerals in the primordial nebula», 2010, *European Planetary Science Congress 2010*, Sep., p. 504.

— **Cordier**, D., Mousis, O., Lunine, J., Lebonnois, S., Rannou, P., Lavvas, P., Lobo, L., Ferreira, A., «Titan's Lakes Chemical Composition : Sources of Uncertainties And Variability, Implications For Noble Gases Sequestration»,

— Liger-Belair, G., **Cordier**, D., Cilindre, C., Honvault, J., «Champagne ! Un nuage bleu lorsque le bouchon saute», *Revue des œnologues et des techniques vitivinicoles et œnologiques*, N^{o} 168, Juillet 2018. **2010**, *Division for Planetary Science*, 42.3606C.

— Mousis, O., Lunine, J. I., Zahnle, K., Biennier, L., Picaud, S., Johnson, T. V., Petit, J., Mitchell, J. B. A., Beaulieu, J., Boudon, V., **Cordier**, D., Devel, M., Georges, R., Griffith, C., Iro, N., Marley, M. S., Marboeuf, U., Tinetti, G. «Constraints On The Volatile Enrichments In Hd189733b From Internal Structure Models», 2010, *Division for Planetary Science*, 42.5603M.

2011 – Mousis, O., Lunine, J. I., Picaud, S., **Cordier**, D., Waite, J. H. and Mandt, K. E. «The role of clathrate hydrates in cleaning the noble gases of Titan's atmosphere», 2011, *EPSC-DPS Joint Meeting 2011*, Oct., p. 63.

— Liger-Belair, G., **Cordier**, D., Cilindre, C., Honvault, J., «Champagne ! Un nuage bleu lorsque le bouchon saute», *Revue des œnologues et des techniques vitivinicoles et œnologiques*, N^{o} 168, Juillet 2018.

— **Cordier**, D., Mousis, O., Lunine, J.I., Lebonnois, S., Rannou, P., Lavvas, P., Lobo, L. Q., Ferreira, A. G. M. «The hydrocarbon lakes of Titan : uncertainties on their chemical composition», 2011, *EPSC-DPS Joint Meeting 2011*, Oct., p. 595.

2012 – **Cordier**, D., Mousis, O., Lunine, J. I., Lebonnois, S., Rannou, P., Lavvas, P., Lobo, L., Ferreira, A. «Chemical Composition of Titan's lakes : estimates and uncertainties», 2012, *European Planetary Science Congress 2012*, Sep., p. 940.

2013 – **Cordier**, D., Barnes, J. W., Ferreira, A. «Composition of Titan's Dry Lakebeds : What can be Inferred from the Solubility Theory», 2013, *Lunar and Planetary Institute Science Conference Abstracts*, vol. 44, p. 1468.

— Biennier, L., Carles, S., **Cordier**, D., Guillemin, J.-C., Bourgalais, J., Le Picard, S., Faure, A. «How do anions grow in the cold upper atmosphere of Titan ? Insights from the laboratory», 2013, *European Planetary Science Congress 2013*, Sep., p. XXX.

Retour à la table des matières : p. v

— **Cordier**, D., Barnes, J. W., Ferreira, A., Cornet, T.,
«Solids dissolution theory : implications for dry lakebeds composition and lake formation time-scale», 2013, *European Planetary Science Congress 2013*, Sep., p. XXX.

2014 – Rousselot, P., Pirali, O., Jehin, E., Vervloet, M., HutsemÃ©kers, D., Manfroid, J., **Cordier**, D., Martin-Drumel, M.-A., Gruet, S., Arpigny, C., Decock, A., Mousis, O.,
«The Nitrogen Isotopic Ratio in Comet's Ammonia»,
2014, *Comets as Tracers of Solar System Formation and Evolution*, April 1-3, 2014, Toulouse, France.

— Decock, A., Jehin, E., Rousselot, P., Hutsemékers, D., Manfroid, J., **Cordier**, D.,
«Isotopic ratios of the light elements in comet C/2012 F6 (LEMMON)»,
2014, *Comets as Tracers of Solar System Formation and Evolution*, April 1-3, 2014, Toulouse, France.

— Cornet, T., **Cordier**, D., Le Bahers, T., Bourgeois, O., Fleurant, C., Le Mouélic, S.,
«Kinetics of surface dissolution : A coupled thermodynamics-climatic approach for Titan and the Earth»,
2014, *European Geoscience Union (EGU) Congress 2014*, avril 2014, Vienne.

— Cornet, T., **Cordier**, D., Le Bahers, D., Bourgeois, O., Fleurant, C., and Le Mouélic, S.,
«Karstification processes on Titan and on Earth : Denudation rates and timescales»,
2014, *European Planetary Science Congress 2014*, 7-12 septembre, Cascais, Portugal.

— **Cordier**, D., Barnes, J.W., Le Bahers, T., Cornet, T. and Ferreira, A.,
«Titan's evaporites structure and their formation time-scale»,
2014, *European Planetary Science Congress 2014*, 7-12 septembre, Cascais, Portugal.

— **Cordier**, D., Prada Moroni, P.G. and Tognelli, E.,
«Dust photophoretic transport in a disk irradiated by an evolving PMS star»,
2014, *European Planetary Science Congress 2014*, 7-12 septembre, Cascais, Portugal.

— **Cordier**, D., Barnes, J. W., Le Bahers, T., Cornet, T., Ferreira, A.,
«Structure des évaporites de Titan et composition des séquences évaporitiques»,
2014, *Colloque quadriannuel du Programme Nationale de Planétologie 2014*, 1-2-3 octobre 2014, Paris.

2015 – **Cordier**, D., Roussel, J., Rannou, P.,
«About the vertical gradient of composition in Titan's lakes», 2015, *European Planetary Science Congress 2015, held 27 September - 2 October, 2015 in Nantes, France.*

— Cornet, T., **Cordier**, D., Le Bahers, T., Bourgeois, O., Fleurant, C., Le Mouélic, S., Altobelli, N.,
«Dissolution on Titan and on Earth : Towards the age of Titan's karstic landscapes», 2015, *European Planetary Science Congress 2015, held 27 September - 2 October, 2015 in Nantes, France*

— Cornet, T., **Cordier**, D., Le Bahers, T., Bourgeois, O., Fleurant, C., Le Mouélic, S., Altobelli, N., «Dissolution on Titan and on Earth : Towards the Age of Titan's Karstic-like Landscapes», 2015, *American Geophysical Union, Fall Meeting 2015, abstract #P13B-2139*

Retour à la table des matières : p. v

2016 – Cornet, T. ; **Cordier**, D. ; Marounina, N. ; Le Bahers, T. ; Altobelli, N.,
«Constraining the Sources of Uncertainty of the RST Thermodynamic Model Applied to Titan», 2016, *Lunar and Planetary Institute Science Conference Abstracts*, vol. 47, p. 1932.

— **Cordier**, D., Cours, T., Rey, M. ; Maltagliati, L., Seignovert, B., Biennier, L.,
«Could PAH or HAC explain the Titan's stratosphere absorption around 3.4 µm revealed by solar occultations ?», 2016, *Titan Aeronomy and Climate. Proceedings of the Workshop held 27-29 June, 2016 in Reims, Champagne-Ardenne, France.*

— **Cordier**, D., Cours, T., Rey, M., Maltagliati, L., Seignovert, B., Biennier, L.,
«Presence of PAH or HAC below 900 km in the Titan's stratosphere ?», 2016, *American Astronomical Society, DPS meeting #48, id.515.03, Pasadena, CA, USA.*

— **Cordier**, D., «Thermodynamics at the surface of Titan», 2016, *Titan Surface Workshop – Paris, 2-4 th November 2016.*

2017 – Cornet, T., Fleurant, C., Seignovert, B., **Cordier**, D., Bourgeois, O., Le Mouélic, S.,
«Landscape Formation Through Dissolution Processes on Titan : a 3D Landscape Evolution Modeling Approach», 2017, *Lunar and Planetary Institute Science Conference Abstracts*, vol. XX, p. YYYY.

— Cornet, T., Seignovert, B., Fleurant, C., **Cordier**, D., Bourgeois, O., Le Mouélic, S., Rodriguez, S., Lucas, A.,
«Landscape Formation on Titan : a 3D Karst Landscape Evolution Model», 2017, *EPSC 2017, 16– 21 October, Riga, Latvia*

— **Cordier**, D., Carrasco, N.,
«The Interaction of Titan's Aerosols with Hydrocarbon Seas», 2017, *EPSC 2017, 16– 21 October, Riga, Latvia*

— **Cordier**, D., Liger-Belair, G.,
«How bubbles can form and grow in a Titan's sea ?», 2017, *Titan Surface Workshop – Boston, 3-5 October*

2018 – Cornet, T., Seignovert, B., Fleurant, C., **Cordier**, D., Bourgeois, O., Le Mouelic, S., Rodriguez, S., Lucas, A.,
«Development of labyrinths on Titan : A numerical model based on surface dissolution», 2018, *European Geosciences Union General Assembly 2018, Vienna, Austria, –13 April 2018*

B.2.1 Autres types de publications

— **Cordier** D.,
«Les étoiles de type céphéide : tests de la théorie de la structure interne stellaire»,
2000, Thèse de l'Université de Rennes 1, France.

Retour à la table des matières : p. v

Annexe C

Articles divers

C.1 Article sur HD 189733b

The Astrophysical Journal, 727:77 (7pp), 2011 February 1 doi:10.1088/0004-637X/727/2/77
© 2011. The American Astronomical Society. All rights reserved. Printed in the U.S.A.

ON THE VOLATILE ENRICHMENTS AND HEAVY ELEMENT CONTENT IN HD189733b

O. Mousis[1], J. I. Lunine[2], J.-M. Petit[1], K. Zahnle[3], L. Biennier[4,5], S. Picaud[1], T. V. Johnson[6], J. B. A. Mitchell[4,5], V. Boudon[7], D. Cordier[4,5,8], M. Devel[9], R. Georges[4,5], C. Griffith[10], N. Iro[11], M. S. Marley[3], and U. Marboeuf[12]
[1] Institut UTINAM, CNRS-UMR 6213, Observatoire de Besançon, Université de Franche-Comté, BP 1615, 25010 Besançon Cedex, France; olivier.mousis@obs-besancon.fr
[2] Dipartimento di Fisica, Università degli Studi di Roma "Tor Vergata," Roma, Italy
[3] NASA Ames Research Center, Moffett Field, CA 94035, USA
[4] Université européenne de Bretagne, Rennes, France
[5] Institut de Physique de Rennes, CNRS, UMR 6251, Université de Rennes 1, Campus de Beaulieu, 35042 Rennes, France
[6] Jet Propulsion Laboratory, California Institute of Technology, Pasadena, CA 91109, USA
[7] Laboratoire Interdisciplinaire Carnot de Bourgogne, UMR 5209 CNRS-Université de Bourgogne, 9 Avenue Alain Savary, BP 47870, F-21078 Dijon Cedex France
[8] Ecole Nationale Supérieure de Chimie de Rennes, CNRS, UMR 6226, Avenue du Général Leclerc, CS 50837, 35708 Rennes Cedex 7, France
[9] FEMTO-ST, CNRS, UFC, UTBM, ENSMM, Besançon, France
[10] Lunar and Planetary Laboratory, University of Arizona, Tucson, AZ, USA
[11] NASA/Goddard Space Flight Center, Greenbelt, MD, USA
[12] Laboratoire de Planétologie de Grenoble, Université Joseph Fourier, CNRS INSU, France
Received 2010 November 16; accepted 2010 November 16; published 2011 January 5

ABSTRACT

Favored theories of giant planet formation center around two main paradigms, namely the core accretion model and the gravitational instability model. These two formation scenarios support the hypothesis that the giant planet metallicities should be higher or equal to that of the parent star. Meanwhile, spectra of the transiting hot Jupiter HD189733b suggest that carbon and oxygen abundances range from depleted to enriched with respect to the star. Here, using a model describing the formation sequence and composition of planetesimals in the protoplanetary disk, we determine the range of volatile abundances in the envelope of HD189733b that is consistent with the 20–80 $M_{\oplus}$ of heavy elements estimated to be present in the planet's envelope. We then compare the inferred carbon and oxygen abundances to those retrieved from spectroscopy, and we find a range of supersolar values that directly fit both spectra and internal structure models. In some cases, we find that the apparent contradiction between the subsolar elemental abundances and the mass of heavy elements predicted in HD189733b by internal structure models can be explained by the presence of large amounts of carbon molecules in the form of polycyclic aromatic hydrocarbons and soots in the upper layers of the envelope, as suggested by recent photochemical models. A diagnostic test that would confirm the presence of these compounds in the envelope is the detection of acetylene. Several alternative hypotheses that could also explain the subsolar metallicity of HD189733b are formulated: the possibility of differential settling in its envelope, the presence of a larger core that did not erode with time, a mass of heavy elements lower than the one predicted by interior models, a heavy element budget resulting from the accretion of volatile-poor planetesimals in specific circumstances, or the combination of all these mechanisms.

Key words: planets and satellites: composition – planets and satellites: formation – planets and satellites: general – planets and satellites: individual (HD189733b) – protoplanetary disks – stars: abundances

1. INTRODUCTION

Favored theories of giant planet formation center around two main paradigms, namely the core accretion model (Safronov 1969; Goldreich & Ward 1973; Pollack et al. 1996) and the gravitational instability model (Cameron 1978; Boss 1997). In the frame of the core accretion model, a solid core forms from the accretion of planetesimals and becomes massive enough (∼5–10 $M_{\oplus}$) to initiate runaway gravitational infall of a large gaseous envelope in which gas-coupled solids continue their accretion (Alibert et al. 2005b; Hubickyj et al. 2005; Mordasini et al. 2009). This model provides the large amount of heavy elements necessary to explain the supersolar metallicities observed in Jupiter and Saturn via the accretion of planetesimals in their envelopes (Gautier et al. 2001; Saumon & Guillot 2004; Alibert et al. 2005b; Mousis et al. 2006, 2009b). In the frame of the gravitational instability model, gas giant protoplanets form rapidly through a gravitational instability of the gaseous portion of the disk and then more slowly contract to planetary densities (Boss 1997, 2005). In this scenario, due to the limited efficiency of planetesimals accretion during the planet formation, its metallicity should be slightly higher or equal to that of the parent star (Helled & Bodenheimer 2010).

A puzzling feature of the transiting hot Jupiter HD189733b ($M = 1.15 \pm 0.04\ M_J$) orbiting a K2V stellar primary at the distance of 0.03 AU (Bouchy et al. 2005) is its metallicity, whose estimates have been found to range between subsolar to supersolar (see Figure 1) from determinations of carbon and oxygen atmospheric abundances. Because the metallicity of the parent star is solar ([Fe/H] $= -0.03 \pm 0.04$; Bouchy et al. 2005), we still compare the metallicity of HD189733b to this value in the following. Several sources of data were used by two different groups in order to retrieve these volatile abundances. A first set of data was collected by Swain et al. 2009 (hereafter S09) from the dayside spectrum of HD189733b with *HST* NICMOS spectrophotometry in the 1.5–2.5 μm range, leading them to find subsolar carbon and oxygen abundances. In contrast, from the same set of data and with their own model, Madhusudhan & Seager 2009 (hereafter MS09) found these spectra consistent with supersolar C and O abundances. However, MS09 also found that these species could be in subsolar abundances from spectra of the planet's atmosphere during secondary eclipses with *Spitzer* broadband photometry. This huge variation of

Retour à la table des matières : p. v

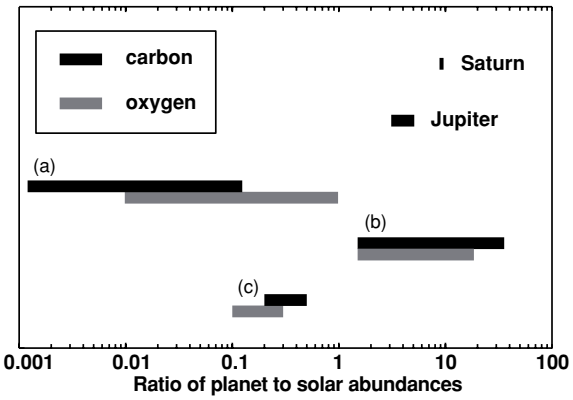

Figure 1. Carbon and oxygen abundances (relative to hydrogen) in HD189733b compared with solar values. Elemental abundances derived from the analysis by MS09 (bars a) of the planet spectra acquired with *Spitzer* broadband photometry during secondary eclipses and from the interpretation by MS09 (bars b) and S09 (bars c) of the same spectra obtained during dayside observations by *HST* NICMOS spectrophotometry in the 1.5–2.5 μm range. Carbon abundances measured in Jupiter and Saturn are shown for comparison (values taken from Mousis et al. 2009a). The oxygen abundance is still unconstrained in these two planets.

elemental abundances derived by the two groups is due to a wide variety of atmospheric pressure–temperature profiles that are found consistent with the planet's spectra (S09; MS09).

Although consensus has not yet been reached on the metallicity of HD189733b, the possibility that this—or potentially other—hot Jupiters[13] have subsolar metallicity raises the challenging theoretical question of whether and how a giant planet may achieve subsolar metallicity during its formation. In order to account for this discrepancy, Mousis et al. (2009a) have proposed that gravitational settling, due to strong irradiation, could lower the carbon and oxygen abundances in the upper layers of HD189733b's atmosphere. However, this possibility has not been yet tested by models detailing the envelope's evolution under the influence of irradiation and might be contradicted by the possible increase of the atmospheric opacities that is required to explain the large radii of irradiated planets (Burrows et al. 2007).

In this work, we determine the range of volatile abundances in the envelope of HD189733b that matches the 20–80 $M_{\oplus}$ mass range of heavy elements predicted by the interior models of Guillot (2008). The latter rejected the models predicting masses of heavy elements lower than 20 $M_{\oplus}$ in HD189733b on the basis that they are not able to explain in a consistent manner the observed radius measurements of all known transiting giant exoplanets. We also use a model describing the formation sequence of planetesimals in the protoplanetary disk and the composition of the incorporated ices, assuming that the distribution of heavy elements is homogeneous within the planet's envelope. We then compare the inferred carbon and oxygen abundances to those retrieved from spectroscopy and we infer the range of supersolar values that can directly fit both spectra and internal structure models. We also investigate the role that can be played by carbon molecules in the form of polycyclic aromatic hydrocarbons (PAHs) and soots possibly present in the upper layers of the envelope (Marley et al. 2009; Zahnle et al. 2010) in the apparent contradiction between the subsolar elemental abundances and the important mass of heavy elements predicted in HD189733b. We finally discuss the alternative mechanisms that could explain this possible discrepancy.

[13] O and C minimum elemental abundances in the transiting hot Jupiter HD209458b have also been found ~0.3 and 0.7 times solar, respectively (MS09).

2. DELIVERY OF HEAVY ELEMENTS TO PROTO-HD189733b

2.1. Formation Conditions of HD189733b

Irrespective of the details of their formation, close-in giant planets are thought to have originated in the cold outer region of protoplanetary disks and migrated inward until they stopped at closer orbital radii to the star (Goldreich & Tremaine 1980; Lin et al. 1996; Fogg & Nelson 2005, 2007; Mandell et al. 2007). In this context, it has been proposed that core accretion is a method by which planets may form at small distances to the star (~10 AU) while gravitational instability may be the mechanism by which planets may form at much larger distances ($\geqslant$100 AU; Boley 2009; Meru & Bate 2010). Because a bimodal distribution of gas giant planet semi-major axes should remain present after scattering and planet–disk interaction (Boley 2009), implying that giant planets formed by core accretion should migrate closer to the star than those formed by gravitational instability, we follow here the core accretion model to describe the formation of HD189733b. In this scenario, building blocks accreted by proto-HD189733b may have formed all along its radial migration pathway in the protoplanetary disk. However, in this work, we assume that only the planetesimals produced beyond the snow line, i.e., those possessing a significant fraction of volatiles, materially affected the observed O and C abundances due to their vaporization when they entered the envelope of the planet. This hypothesis is supported by the work of Guillot & Gladman (2000) who showed that planetesimals delivered to a planet owning a mass similar or greater than that of Jupiter are rather ejected than accreted. This mechanism should then prevent further noticeable accretion of solids by the planet during its migration below the snow line.

2.2. Composition of Icy Planetesimals

In order to compare the amount of heavy elements inferred from measurements of elemental abundances in HD189733b with theoretical determinations of the planet metal content, we have used a model describing the formation sequence and the composition of the different ices formed beyond the snow line of the protoplanetary disk from which HD189733b was formed (Mousis et al. 2009a). This model has already been used to interpret the observed volatile enrichments in the atmospheres

Retour à la table des matières : p. v

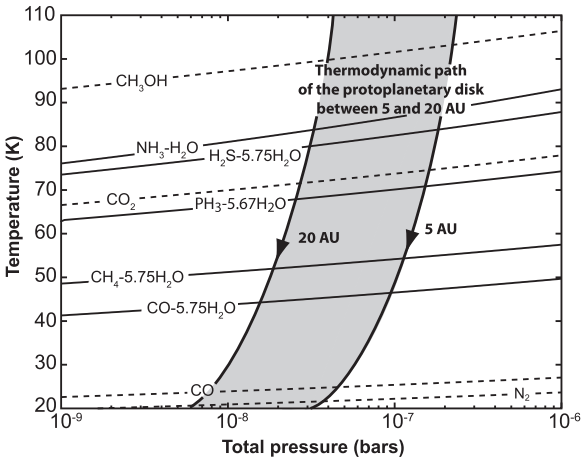

Figure 2. Equilibrium curves of hydrate (NH_3–H_2O), clathrates (X-5.75H_2O or X-5.67H_2O) (solid lines), pure condensates (dotted lines), and the ensemble of thermodynamic paths (gray area) ranging between 5 and 20 AU in the pressure–temperature space of the disk, assuming full efficiency of clathration. Species remain in the gas phase above the equilibrium curves. Below, they are trapped as clathrates or simply condense.

Table 1
Gas Phase Abundances in the Solar Nebula

Species X	(X/H_2)	Species X	(X/H_2)
O	1.16×10^{-3}	N_2	5.33×10^{-5}
C	5.82×10^{-4}	NH_3	5.33×10^{-5}
N	1.60×10^{-4}	CO	4.91×10^{-4}
S	3.66×10^{-5}	CO_2	7.01×10^{-5}
P	6.88×10^{-7}	CH_3OH	1.40×10^{-5}
Ar	8.43×10^{-6}	CH_4	7.01×10^{-6}
Kr	4.54×10^{-9}	H_2S	1.83×10^{-5}
Xe	4.44×10^{-10}	PH_3	6.88×10^{-7}
H_2O	5.15×10^{-4}		

Notes. Elemental abundances derived from Lodders (2003). Molecular abundances resulted from the distribution of elements described in the text.

of Jupiter and Saturn in a way consistent with the heavy element content predicted by interior models (Mousis et al. 2009b). It is based on a predefined initial gas phase composition in which all elements are in solar abundance (Lodders 2003; see Table 1) and describes the process by which volatiles are trapped in icy planetesimals formed in the protoplanetary disk. Oxygen, carbon, nitrogen, and sulfur are postulated to exist only in the form of H_2O, CO, CO_2, CH_3OH, CH_4, N_2, NH_3, and H_2S with $CO/CO_2/CH_3OH/CH_4 = 70/10/2/1$, $N_2/NH_3 = 1/1$ and $H_2S/H_2 = 0.5 \times (S/H_2)_\odot$ in the gas phase of the disk (values taken from Mousis et al. 2009b who investigated the composition of ices formed in the protosolar nebula and accreted by Jupiter and Saturn). Once the abundances of these molecules have been fixed, the remaining O gives the abundance of H_2O.

The process of volatile trapping in planetesimals, illustrated in Figure 2, is calculated using the stability curves of hydrates, clathrates and pure condensates, and the ensemble of thermodynamic paths detailing the evolution of temperature and pressure in the 5–20 AU range of the protoplanetary disk. We refer the reader to the works of Papaloizou & Terquem (1999) and Alibert et al. (2005a) for a full description of the turbulent model of accretion disk used here. This model postulates that viscous heating is the predominant heating source, assuming that the outer parts of the disk are protected from solar irradiation by a shadowing effect of the inner disk parts. In these conditions, temperature in the planet-forming region can decrease down to very low values (∼20 K; Mousis et al. 2009b). However, irradiation onto the central parts of the disk could modify the disk structure so much that shadowing is limited or absent in the outer parts. In this case, the temperature in the planet-forming region would be higher. On the other hand, the same model as the one used in this work has been used to explain the noble gas enrichments observed by the Galileo probe in the atmosphere of Jupiter (Owen et al. 1999; Mousis et al. 2009b). In order to account for the measured supersolar abundance of argon, the accretion of planetesimals formed at temperatures as low as ∼20 K has been invoked in the feeding zone of Jupiter. Here, because the K2V parent star of HD189733b is cooler than the Sun, we assume that the temperature and pressure conditions in the formation zone of HD189733b were as low as for Jupiter.

For each ice considered in Figure 2, the domain of stability is the region located below its corresponding stability curve. The clathration process stops when no more crystalline water ice is available to trap the volatile species. Note that, in the pressure conditions of the disk, CO_2 crystallizes at a higher temperature than its associated clathrate. We then assume that solid CO_2 is the only existing condensed form of CO_2 in this environment. In addition, we have considered only the formation of pure ice of CH_3OH in our calculations because no experimental data concerning the equilibrium curve of its associated clathrate have been reported in the literature. The intersection of a thermodynamic path at a given distance from the star with the stability curves of the different ices allows determination of the amount of volatiles that are condensed or trapped in clathrates at this location in the disk. Assuming that, once condensed, the ices add to the composition of planetesimals accreted by the growing planet along its migration pathway, this allows us to reproduce the volatile abundances by adjusting the mass of planetesimals that vaporized when entering the envelope. Our approach is supported by the simulations of Baraffe et al. (2006) that show that planetesimals are ablated in the envelope once the core mass reaches ∼6 $M_\oplus$. Note that, because the migration path followed by the forming HD189733b is unknown, the 5–20 AU distance range of the ensemble of thermodynamic paths has been arbitrarily chosen to determine the composition of the accreted ices. The adoption of any other distance range for the planet's path beyond the snow line would not affect the composition of the ices (and thus HD189733b's global volatile enrichments) because it remains almost identical irrespective of (1) their formation distance and (2) the input parameters of the disk, provided that the initial gas phase composition is homogeneous (Marboeuf et al. 2008). Table 2 gives the mean composition of ices incorporated in planetesimals formed in the cold part of the protoplanetary disk and ultimately accreted by proto-HD189733b.

3. VOLATILE ENRICHMENTS INFERRED FROM THE HEAVY ELEMENT CONTENT

Figure 1 shows the carbon and oxygen abundances (relative to solar) determined in HD189733b by S09 and MS09. Both studies suggest that carbon and oxygen abundances could be subsolar but MS09 also find that strongly supersolar elemental abundances are consistent with the spectra. If carbon only exists in the form of spectroscopically identified species, then the simultaneous fit of carbon and oxygen abundances retrieved by S09 in HD189733b requires the accretion of ∼1.2 $M_\oplus$ of

Retour à la table des matières : p. v

Table 2
Ratio of the Mass of Ice to the Global Mass of Ices in Planetesimals Formed in the Protoplanetary Disk

Ice	Mass Fraction
H_2O	5.03×10^{-1}
CO	2.79×10^{-1}
CO_2	1.13×10^{-1}
NH_3	3.61×10^{-2}
H_2S	2.37×10^{-2}
N_2	2.17×10^{-2}
CH_3OH	1.94×10^{-2}
CH_4	3.44×10^{-3}
PH_3	8.24×10^{-4}

ices in the envelope (see Mousis et al. 2009a for details). This translates into the accretion of 2.3–4.6 $M_\oplus$ of planetesimals in HD189733b's envelope if one assumes that the fraction of rocks and metals f_{r-m} varies between 0.47 and 0.74 in these solids, as for those formed in the outer solar nebula (Johnson & Lunine 2005; Wong et al. 2008; Johnson & Estrada 2009). This mass range is well below the one predicted by interior models (20–80 $M_\oplus$; Guillot 2008). Similarly, if each extreme abundance value found by MS09 is presumed representative of the composition of HD189733b's envelope, this also poses a problem of consistency with interior models. Indeed, considering the minimum carbon abundance of $\sim 1.2 \times 10^{-3}$ times the solar value inferred by MS09 in HD189733b, this corresponds to a maximum of $\sim 3 \times 10^{-2}$ $M_\oplus$ of heavy elements dissolved in the envelope, assuming a fraction of rocks and metals f_{r-m} of 0.74 in planetesimals. Alternatively, if one considers a carbon abundance of ~35.6 times the solar value in HD189733b, i.e., the upper value retrieved by MS09, this directly translates into a minimum of ~250 $M_\oplus$ of heavy elements dissolved in the envelope, with $f_{r-m} = 0$ in planetesimals. We conclude that both extreme determinations found by MS09 require a mass of heavy elements that is well outside the 20–80 $M_\oplus$ range predicted in HD189733b. These considerations imply that the determinations of S09 and MS09 are unable to constrain the mass range of heavy elements predicted by internal structure models.

Figure 3 represents the volatile enrichments (relative to solar) in the envelope of HD189733b as a function of the fraction of rocks and metals in accreted planetesimals. Note that the enrichment values of S, N, and P are shown together with those of O and C because they may be tested by future observations of HD189733b's atmosphere. In particular, S is expected to be contained mainly in H_2S at altitudes of 0.002–1 bar in HD189733b (Zahnle et al. 2009). Its abundance at these levels may be sampled provided observations at sufficiently high spectral resolution of its strong 2 μm feature become available. The elemental abundances of N and P are likely more difficult to measure in HD189733b. The main nitrogen-bearing and phosphorus-bearing gases are predicted to be N_2 and P_2 (Visscher et al. 2006). Both species lack a dipole moment, and are therefore challenging to measure at IR wavelengths. In exoplanets cooler than HD189733b, elemental N and P are mainly in NH_3 and PH_3 forms below altitudes where photolysis occurs (Saumon et al. 2000; Visscher et al. 2006), and these molecular species are spectroscopically much easier to detect. The volatile enrichments have been calculated for the two extreme values covering the 20–80 $M_\oplus$ range of heavy elements estimated to be present in HD189733b (Guillot 2008). If 20 $M_\oplus$

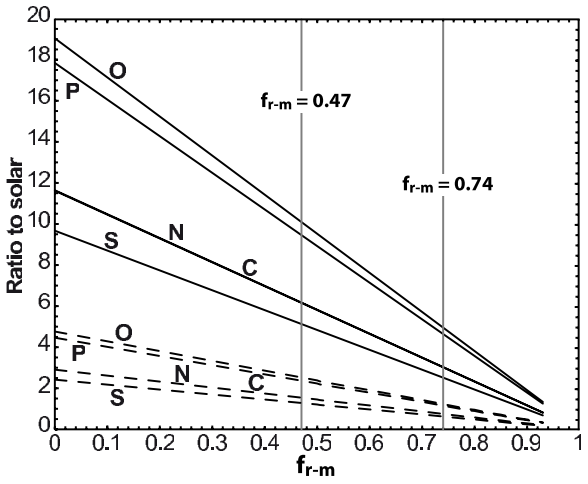

Figure 3. Volatile enrichments in the envelope of HD189733b as a function of the fraction of rocks and metals f_{r-m} in accreted planetesimals. Volatile enrichments have been calculated in the case of the presence of 20 $M_\oplus$ (dashed lines) and 80 $M_\oplus$ (solid lines) of heavy elements in the envelope, respectively. The two vertical lines enclose the range of plausible f_{r-m} values in planetesimals for which volatile enrichments are predicted in HD189733b (see the text). N and C lines appear superimposed. If 80 $M_\oplus$ of heavy elements is present in the envelope, our enrichment predictions are within the range of determinations of MS09 from *HST* NICMOS spectrophotometry, irrespective of the f_{r-m} value in the 0.47–0.74 range. If 20 $M_\oplus$ of heavy elements is present in the envelope, the simultaneous fit of the O and C determinations by MS09 from *HST* NICMOS spectrophotometry leads to a unique common solution for $f_{r-m} = 0.48$.

of heavy elements are dissolved in the envelope, O, C, N, S, and P are found to be 1.2–2.5, 0.8–1.5, 0.8–1.5, 0.6–1.3, and 1.2–2.3 times supersolar for f_{r-m} ranging between 0.47 and 0.74 in planetesimals, respectively. In contrast, if 80 $M_\oplus$ of heavy elements are present in the envelope, then O, C, N, S, and P become 5.0–10.1, 3.0–6.2, 3.0–6.2, 2.5–5.1, and 4.6–9.5 times supersolar for the same f_{r-m} range in planetesimals, respectively. The comparison of our calculations with the full range of subsolar C and O abundances retrieved by MS09 from *Spitzer* broadband photometry data suggest that their values do not correspond to the global heavy element enhancement presumed to exist in HD189733b. In contrast, when comparing our enrichment predictions with the supersolar values retrieved by MS09 from *HST* NICMOS spectrophotometry, we find that our values calculated for a mass of 80 $M_\oplus$ of heavy elements present in the envelope are within their range of determinations, irrespective of the f_{r-m} value. In the case of 20 $M_\oplus$ of heavy elements present in the envelope, the simultaneous fit of the O and C determinations by MS09 from *HST* NICMOS spectrophotometry leads to a unique common solution, which corresponds to O, C, N, S, and P found to be 2.5, 1.5, 1.5, 1.3, and 2.3 times supersolar for $f_{r-m} = 0.48$, respectively.

4. INFLUENCE OF HIDDEN CARBON

Recent photochemical models of HD189733b's atmosphere suggest that a substantial part of carbon could be present in the form of ethylene, acetylene, PAHs, and probably soots at the sampled pressure levels, implying that the retrieved carbon abundances could be underestimated (Marley et al. 2009; Zahnle et al. 2010). Depending on the efficiency of the vertical mixing and for an optimum temperature of ~1000 K in the envelope, up to ~90% of carbon could exist in the form of soots and

Retour à la table des matières : p. v

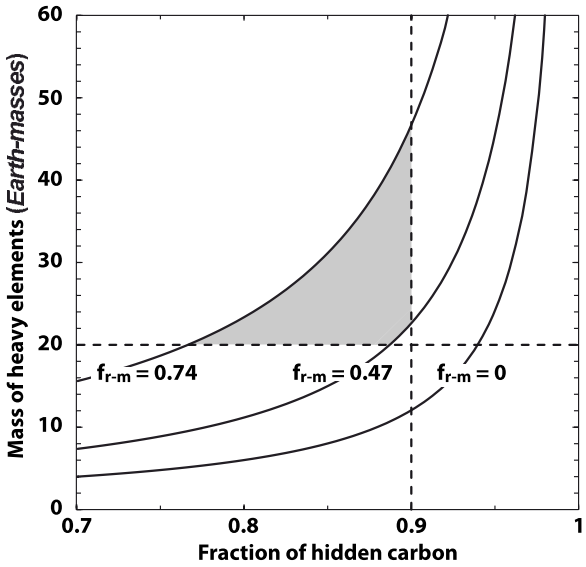

Figure 4. Mass of heavy elements in HD189733b as a function of the fraction of carbon hidden in the atmosphere (see the text). The horizontal dashed line corresponds to the minimum mass of heavy elements predicted in HD189733b (Guillot 2008). The vertical dashed line corresponds to the upper value of the carbon fraction that can exist in the form of soots and organic molecules at sampled pressure levels. The three solid curves correspond to different fractions of rocks and metals f_{r-m} in planetesimals accreted by HD189733b during its formation (see the text). The gray area represents the range of fractions of hidden carbon matching the global heavy element content predicted in HD189733b's interior, which is enclosed by the two most plausible values of f_{r-m}, assuming a composition of planetesimals similar to those formed in the solar nebula (see the text).

organic molecules (Zahnle et al. 2010). In these conditions, a range of the subsolar abundances inferred in the planet could be consistent with its metal content if a fraction of carbon is postulated to exist in the form of the not yet detected molecules. Figure 4 represents the mass of heavy elements in HD189733b as a function of the fraction of "hidden" carbon at the sampled pressure levels, assuming that the abundances of spectroscopically visible oxygen and carbon are within the range of values found by S09. In this case, the observable oxygen and carbon abundances have been set to ∼0.3 and 0.15 times solar, i.e., values corresponding to the fit of our model to the highest oxygen abundance found by S09. The figure shows that if 77%–90% of carbon is contained in these compounds, then the mass of heavy elements needed to fit the observed volatile abundances is now between ∼20 and 46.5 $M_\oplus$ and matches the mass range predicted by interior models for the 0.47–0.74 range of f_{r-m} values in planetesimals. In this case, our model also predicts an oxygen abundance ranging between 1.3 and 2.9 times the solar value in HD189733b's envelope.

5. ALTERNATIVE SCENARIOS

Several alternative hypotheses to the presence of soots in HD189733b can be formulated in order to account for the possible discrepancy between the elemental atmospheric abundances and the global budget of heavy elements in the planet. This discrepancy could have been engendered by processes that, similarly to the hypothesis of the presence of soots previously detailed, take place in the atmosphere of HD189733b during its postaccretion evolution. For example, a plausible alternative could be the presence of differential settling in HD189733b, which would result from the combination of gravity and irradiation effects that took place inside the atmosphere of HD189733b, thus lowering the C and O (and any other volatile) abundances in the upper layers (Mousis et al. 2009a). In this case, the measured C and O atmospheric abundances would not be representative of the envelope composition because the atmosphere is isolated from the interior by a radiative zone. This idea has not yet been investigated by numerical modeling.

On the other hand, the assumptions of our model depicting the volatile enrichments in HD189733b are based on a given mass range of accreted solids defined by interior models (Guillot 2008), on the temperature at which the solids/ices condensed in the solar nebula, and on the presence of a core with a defined size. The basis of our comparison here is Jupiter, but HD189733b may not have followed the same accretional and dynamical history as Jupiter did because it migrated so far inward. For example, our volatile abundance calculations have been performed assuming that the core of HD189733b has eroded with time, implying that all the heavy elements are included in the envelope. This assumption derives from Jupiter's interior models that also predict that the mass of its core may actually be as low as zero (Saumon & Guillot 2004). Neglecting the possibility of erosion and adopting a core mass corresponding to the maximum one predicted for Jupiter (∼13 $M_\oplus$; Saumon & Guillot 2004) would decrease our volatile enrichment predictions by a factor between ∼0.35 and 0.84, depending on the considered total mass of heavy elements (20 to 80 $M_\oplus$) in HD189733b. In the case of a 0.35 factor, the O and C predicted abundances already become 0.4 and 0.3 times solar, respectively. If the core mass of HD189733b is equal to 15 $M_\oplus$, and assuming a total mass of heavy elements of 20 $M_\oplus$ in the planet, then the O and C predicted abundances become, respectively, 0.3 and 0.2 times solar and are within the range of subsolar abundances retrieved by MS09. The assumption of any larger core in HD189733b would imply lower abundances of heavy elements in the envelope.

An alternative explanation is that the mass of heavy elements present in HD189733b is lower than the 20–80 $M_\oplus$ mass range in the models preferred by Guillot (2008) on the basis that the same hypothesis (modified equation of state or increased opacity scenario) allows us to account for the properties of all known transiting giant extrasolar planets. Indeed, while the 20–80 $M_\oplus$ mass range of heavy elements is based on an explanation consistent for the masses-radii of all planets, the mass and radius of HD189733b itself is consistent with a larger mass range (including zero). A low mass of heavy elements in HD189733b could be due to the formation of large planetesimals by the time the giant planet accreted its gas envelope. Planetesimals would then dynamically decouple from and not necessarily be accreted with the gas, and thus the giant planet's gas envelope would actually be metal-poor. This would leave the planet with a heavy-element poor envelope if core erosion did not take place and little planetesimal accretion occurred after the giant planet grew to Jupiter size. The key point is whether planetesimal mass is dynamically coupled to the gas or not. If most of the mass of solids is in lunar-size objects, then this mass will certainly not be coupled to the gas. Another question is related to what extent C and O condense out of the gas because if these volatiles were not incorporated in planetesimals, then they should remain in solar abundances in the planet's envelope.

Another possibility is that the subsolar abundances in HD189733b would result from the accretion of volatile-poor planetesimals, if one postulates that the heavy element budget

Retour à la table des matières : p. v

of the planet was mainly acquired inward of the nebula snow line. This might run into difficulty because of the eventual poor efficiency of the planetesimals accretion during the formation of HD189733b: dynamical models of Guillot & Gladman (2000) suggest that the ratio of accreted to ejected planetesimals converges toward zero in the case of giant planets with masses reaching or exceeding that of Jupiter. However, the simulations of Guillot & Gladman (2000) were performed without addressing the inward migration of giant planets. In this case, as planets move inward, the Safronov number decreases and more accretion could occur. This scenario can lead to two extreme possibilities. The first possibility consists in the accretion of gas and planetesimals at the same location and at temperatures greater than ∼160 K in the disk (i.e., the condensation temperature of water) by the growing HD189733b. In this case, the envelope of the planet should contain solar abundances of volatiles because the accreted gas would have never been fractionated by their condensation. In the second possibility, if the planet accreted most of its gas at very low temperature (∼20 K) beyond the snowline, migrated inward and accreted its heavy elements in the warm part of the disk, then it should display oxygen and carbon subsolar abundances. Indeed, the gas accreted by the planet should be oxygen- and carbon-poor because these species would have mostly formed pure ices or been incorporated into clathrates that decoupled from gas. An intermediate case could be that the temperature of the gas accreted by the planet beyond the snow line is low enough to allow the condensation of water ($\leqslant$160 K) but remains too high to allow the condensation or trapping of carbon ($>$ 100 K). In these conditions, the oxygen abundance should be subsolar in the envelope while that of carbon remains solar.

Finally, other alternative possibilities can be envisaged but none of them is found satisfying. Indeed, the subsolar C and O abundances in HD189733b could result from the fact that the planetesimals accreted by the growing planet did not ablate in the atmosphere but carried their volatiles intact to the deep interior, where they remain. However, simulations by Baraffe et al. (2006) show that 100 km planetesimals are destroyed in the envelope once the core mass reaches around 6 $M_{\oplus}$, making this hypothesis unlikely. Alternatively, it is possible for oxygen to be depleted relative to carbon inward of the snow line thanks to the cold-trapping or cold-finger effect of water forming ice at the snowline and drying the nebula inward, but this event involves principally oxygen (Stevenson & Lunine 1988; Cyr et al. 1999) and does not account for the subsolar abundance of carbon.

6. CONCLUSIONS

Using a model describing the formation sequence and composition of planetesimals in the protoplanetary disk, we determined the range of volatile abundances in the envelope of HD189733b that is consistent with the 20–80 $M_{\oplus}$ of heavy elements estimated to be present in the planet's envelope. This model has been used in the framework of the core accretion model but the results obtained here may be valid in the case of the gravitational instability model if planetesimals accretion was possible during or after the collapse of gas to form HD189733b. Assuming that carbon exists only in the form of spectroscopically detected species, we find that none of the volatile abundances determined from our model is consistent with the volatile subsolar abundances retrieved by S09 and MS09. The same statement applies to the largest supersolar volatile abundances inferred by MS09 from which the corresponding mass of heavy elements largely exceeds the mass range derived from interior models. In contrast, the volatile abundances inferred from the mass range of heavy elements estimated to be present in the planet are found within the range of supersolar abundances determined by MS09 from *HST* NICMOS photometry.

On the other hand, the presence of soots, PAHs, and organic molecules as suggested by the photochemical model of Zahnle et al. (2010) in HD189733b's envelope could compensate for the subsolar carbon abundances inferred from spectroscopically active species. The presence of the additional carbon-bearing species leads to supersolar abundances that match the predicted heavy element content for this planet, as was the case in an earlier study of Jupiter (Mousis et al. 2009b). The calculated oxygen abundance in HD189733b is larger than that inferred from observations but the discrepancy could have resulted from an oxygen depletion in the envelope during its thermal history, due to the immiscibility of oxygen and hydrogen under high temperature conditions (Fortney & Hubbard 2003), again similar to a possible evolutionary scenario for Jupiter and Saturn that also accounts for their apparent oxygen deficiencies (Owen et al. 1999; Gautier et al. 2001; Mousis et al. 2009b). A preliminary diagnostic test that would strongly support the presence of soots in the atmosphere of HD189733b is the detection of molecular precursors such as acetylene (C_2H_2) via the measurement of its C-H stretch at 3.03 μm in the brightest part of the infrared spectrum. This band has been fully characterized in the laboratory up to 1500 K (Amyay et al. 2009). At the temperature of ∼1000 K, C_2H_2 initiates a carbon-rich chemistry that ultimately leads to the formation of soots (Zahnle et al. 2010) via a large number of different potential physical and chemical pathways. The measurement of the aromatic/aliphatic content of the carbonaceous material embedded in the envelope of HD189733b, which allows one to trace its stage of evolution, could be constrained via the measurement of the C-H stretch absorption features at 3.3 μm (aromatic compounds) and 3.4 μm (aliphatic compounds) (Dartois et al. 2004). Similarly, the position of the C-C aromatic stretch region can also be used as a tracer of the aromaticity of the material at 6.2 μm (aromatic compounds) and 6.3 μm (aliphatic compounds). Because it is difficult to investigate directly the spectral features of soots (Jäger et al. 2009; Pino et al. 2008; Biennier et al. 2009), spectroscopic identification of chemical precursors is the best way to test the model described in this paper.

Several alternative hypotheses to the presence of soots in HD189733b have also been formulated in order to reconcile the apparent discrepancy between the observed elemental atmospheric abundances and the global budget of heavy elements in the planet inferred by interior models. Among these hypotheses, the possibility of differential settling in the envelope of HD189733b, the presence of a larger core that did not erode with time, a mass of heavy elements lower than the one predicted by interior models, a heavy element budget resulting from the accretion of volatile-poor planetesimals in specific circumstances or the combination of all the mechanisms invoked in this work could also explain the observed subsolar elemental abundances.

We thank J.-P. Beaulieu and G. Tinetti for their valuable comments on the manuscript. O.M. acknowledges support from CNES. J.I.L.'s work was supported within the scope of the program "Incentivazione alla mobilita" di studiosi straineri e italiani residenti all'estero. We acknowledge T. Guillot for enlightening discussions and information on his work. We thank

Retour à la table des matières : p. v

an anonymous reviewer for his constructive comments which helped us improve our manuscript.

REFERENCES

Alibert, Y., Mordasini, C., Benz, W., & Winisdoerffer, C. 2005a, A&A, 434, 343
Alibert, Y., Mousis, O., Mordasini, C., & Benz, W. 2005b, ApJ, 626, L57
Amyay, B., et al. 2009, J. Chem. Phys., 131, 114301
Baraffe, I., Alibert, Y., Chabrier, G., & Benz, W. 2006, A&A, 450, 1221
Biennier, L., Georges, R., Chandrasekaran, V., Rowe, B. R., Bataille, T., Jayaram, V., Reddy, K. P. J., & Arunan, E. 2009, Carbon, 47, 3295
Boley, A. C. 2009, ApJ, 695, L53
Boss, A. P. 1997, Science, 276, 1836
Boss, A. P. 2005, ApJ, 629, 535
Bouchy, F., et al. 2005, A&A, 444, L15
Burrows, A., Hubeny, I., Budaj, J., & Hubbard, W. B. 2007, ApJ, 661, 502
Cameron, A. G. W. 1978, Moon Planets, 18, 5
Cyr, K. E., Sharp, C. M., & Lunine, J. I. 1999, J. Geophys. Res., 104, 19003
Dartois, E., Muñoz Caro, G. M., Deboffle, D., & d'Hendecourt, L. 2004, A&A, 423, L33
Fogg, M. J., & Nelson, R. P. 2005, A&A, 441, 79
Fogg, M. J., & Nelson, R. P. 2007, A&A, 472, 1003
Fortney, J. J., & Hubbard, W. B. 2003, Icarus, 164, 228
Gautier, D., Hersant, F., Mousis, O., & Lunine, J. I. 2001, ApJ, 550, L227
Goldreich, P., & Tremaine, S. 1980, ApJ, 241, 425
Goldreich, P., & Ward, W. R. 1973, ApJ, 183, 1051
Guillot, T. 2008, Phys. Scr., 130, 014023
Guillot, T., & Gladman, B. 2000, in ASP Conf. Ser. 219, Disks, Planetesimals, and Planets, ed. F. Garzón, C. Eiroa, D. de Winter, & T. J. Mahoney (San Francisco, CA: ASP), 475
Helled, R., & Bodenheimer, P. 2010, Icarus, 207, 503
Hubickyj, O., Bodenheimer, P., & Lissauer, J. J. 2005, Icarus, 179, 415
Jäger, C., Huisken, F., Mutschke, H., Jansa, I. L., & Henning, T. 2009, ApJ, 696, 706
Johnson, T. V., & Estrada, P. R. 2009, in Saturn from Cassini-Huygens, ed. M. K. Dougherty, L. W. Esposito, & S. M. Krimigis (Berlin: Springer), 55
Johnson, T. V., & Lunine, J. I. 2005, Nature, 435, 69
Lin, D. N. C., Bodenheimer, P., & Richardson, D. C. 1996, Nature, 380, 606
Lodders, K. 2003, ApJ, 591, 1220
Madhusudhan, N., & Seager, S. 2009, ApJ, 707, 24 (MS09)
Mandell, A. M., Raymond, S. N., & Sigurdsson, S. 2007, ApJ, 660, 823
Marboeuf, U., Mousis, O., Ehrenreich, D., Alibert, Y., Cassan, A., Wakelam, V., & Beaulieu, J.-P. 2008, ApJ, 681, 1624
Marley, M. S., Zahnle, K., Freedman, R., Lodders, K., & Fortney, J. 2009, AAS/Division for Planetary Sciences Meeting Abstracts, 41, 42.02
Meru, F., & Bate, M. R. 2010, MNRAS, 406, 2279
Mordasini, C., Alibert, Y., Benz, W., & Naef, D. 2009, A&A, 501, 1161
Mousis, O., Alibert, Y., & Benz, W. 2006, A&A, 449, 411
Mousis, O., Lunine, J. I., Tinetti, G., Griffith, C. A., Showman, A. P., Alibert, Y., Beaulieu, J.-P., & the Holmes Collaboration 2009a, A&A, 507, 1671
Mousis, O., Marboeuf, U., Lunine, J. I., Alibert, Y., Fletcher, L. N., Orton, G. S., Pauzat, F., & Ellinger, Y. 2009b, ApJ, 696, 1348
Owen, T., Mahaffy, P., Niemann, H. B., Atreya, S., Donahue, T., Bar-Nun, A., & de Pater, I. 1999, Nature, 402, 269
Papaloizou, J. C. B., & Terquem, C. 1999, ApJ, 521, 823
Pino, T., et al. 2008, A&A, 490, 665
Pollack, J. B., Hubickyj, O., Bodenheimer, P., Lissauer, J. J., Podolak, M., & Greenzweig, Y. 1996, Icarus, 124, 62
Safronov, V. S. 1969, Evoliutsiia Doplanetnogo Oblaka (Moscow: Nauka)
Saumon, D., Geballe, T. R., Leggett, S. K., Marley, M. S., Freedman, R. S., Lodders, K., Fegley, B., Jr., & Sengupta, S. K. 2000, ApJ, 541, 374
Saumon, D., & Guillot, T. 2004, ApJ, 609, 1170
Stevenson, D. J., & Lunine, J. I. 1988, Icarus, 75, 146
Swain, M. R., Vasisht, G., Tinetti, G., Bouwman, J., Chen, P., Yung, Y., Deming, D., & Deroo, P. 2009, ApJ, 690, L114 (S09)
Visscher, C., Lodders, K., & Fegley, B., Jr. 2006, ApJ, 648, 1181
Wong, M. H., Lunine, J. I., Atreya, S. K., Johnson, T., Mahaffy, P. R., Owen, T. C., & Encrenaz, T. 2008, Rev. Mineral. Geochem., 68, 219
Zahnle, K., Marley, M. S., & Fortney, J. J. 2010, ApJ, submitted (http://arxiv.org/abs/0911.0728)
Zahnle, K., Marley, M. S., Freedman, R. S., Lodders, K., & Fortney, J. J. 2009, ApJ, 701, L20

Retour à la table des matières : p. v

C.2 Article sur la séquestration des gaz rares dans la cryosphère de Mars

Icarus 218 (2012) 80–87

Contents lists available at SciVerse ScienceDirect

Icarus

journal homepage: www.elsevier.com/locate/icarus

Mars cryosphere: A potential reservoir for heavy noble gases?

Olivier Mousis [a,*], Jonathan I. Lunine [b], Eric Chassefière [c], Franck Montmessin [d], Azzedine Lakhlifi [a], Sylvain Picaud [a], Jean-Marc Petit [a], Daniel Cordier [a]

[a] Université de Franche-Comté, Institut UTINAM, CNRS/INSU, UMR 6213, 25030 Besançon Cedex, France
[b] CRSR, Cornell University, Ithaca, NY 14853, USA
[c] Université Paris-Sud, Laboratoire IDES, CNRS/INSU, UMR8148, Orsay 91405, France
[d] Laboratoire Atmosphères, Milieux, Observations Spatiales (LATMOS), 78280 Guyancourt, France

ARTICLE INFO

Article history:
Received 11 July 2011
Revised 9 November 2011
Accepted 4 December 2011
Available online 23 December 2011

Keywords:
Mars, Atmosphere
Abundances, Atmospheres
Ices
Origin, Solar System

ABSTRACT

The two orders of magnitude drop between the measured atmospheric abundances of non-radiogenic argon, krypton and xenon in Earth *versus* Mars is striking. Here, in order to account for this difference, we explore the hypothesis that clathrate deposits incorporated into the current martian cryosphere have sequestered significant amounts of these noble gases assuming they were initially present in the paleoatmosphere in quantities similar to those measured on Earth (in mass of noble gas per unit mass of the planet). To do so, we use a statistical-thermodynamic model that predicts the clathrate composition formed from a carbon dioxide-dominated paleoatmosphere whose surface pressure ranges up to 3 bars. The influence of the presence of atmospheric sulfur dioxide on clathrate composition is investigated and we find that it does not alter the trapping efficiencies of other minor species. Assuming nominal structural parameters for the clathrate cages, we find that a carbon dioxide equivalent pressure of 0.03 and 0.9 bar is sufficient to trap masses of xenon and krypton, respectively, equivalent to those found on Earth in the clathrate deposits of the cryosphere. In this case, the amount of trapped argon is not sufficient to explain the measured Earth/Mars argon abundance ratio in the considered pressure range. In contrast, with a 2% contraction of the clathrate cages, masses of xenon, krypton and argon at least equivalent to those found on Earth can be incorporated into clathrates if one assumes the trapping of carbon dioxide at equivalent atmospheric pressures of ~2.3 bar. The proposed clathrate trapping mechanism could have then played an important role in the shaping of the current martian atmosphere.

© 2012 Published by Elsevier Inc.

1. Introduction

The differences among the terrestrial planets in their measured atmospheric abundances of non-radiogenic noble gases is striking. It is well known that these abundances dramatically decline when one moves outward from the Sun within the inner Solar System (Pepin, 1991 and references therein). This variation is particularly important when comparing the atmospheres of Earth and Mars, where argon, krypton and xenon abundances simultaneously differ by about two orders of magnitude (see Table 1). Indeed, the measured noble gas abundance discrepancy (also close to two orders of magnitude for argon but nonexistent for krypton and xenon) remains hypothetical between Earth and Venus because large uncertainties are associated with *in situ* determinations made in the latter planet (see Mousis et al., 2010a and references therein). Another interesting feature of the atmospheric noble gas abundances in terrestrial planets is that they all exhibit significant depletion relative to solar composition (see Pepin, 1991, 2006). This depletion depends, at a first approximation, on the mass of the element in question, with the light gases being more depleted and isotopically fractionated than the heavy ones. Moreover, the nature of the main source of noble gases remains controversial because only a relatively small fraction was supplied to the atmospheres of terrestrial planets via the outgassing of their mantles (Marty and Meibom, 2007). In this context, constraining the physical processes that engendered the variation of noble gas abundances between Earth and Mars is key to understanding how the primordial atmospheres of the terrestrial planets evolved to their current composition. This requires us to study the delivery mechanisms of the volatiles initially accreted by these planets and also the nature of the different sink mechanisms that might have shaped their current atmospheric abundances (Pepin, 1991, 2006; Owen et al., 1992; Owen and Bar-Nun, 1995; Dauphas, 2003; Marty and Meibom, 2007; Mousis et al., 2010a).

It has been proposed that noble gases could have been acquired by the terrestrial planets through the gravitational capture of their primary atmospheres (Pepin, 1991, 2006). These gases would have initially been captured in approximately solar-like abundances,

* Corresponding author.
E-mail address: olivier.mousis@obs-besancon.fr (O. Mousis).

0019-1035/$ - see front matter © 2012 Published by Elsevier Inc.
doi:10.1016/j.icarus.2011.12.007

Table 1
The ratio of observed heavy noble gas abundances normalized in g/g-planet between Earth and Mars (values derived from Pepin (1991) and references therein).

Noble gas	X_{Earth}/X_{Mars}
^{36}Ar	126.9–214.9
^{84}Kr	80.4–113.5
^{130}Xe	55.4–85.0

then experienced subsequent fractionation as a result of gravitational escape, driven on Earth by a giant Moon-forming impact, on Mars by sputtering at high altitudes (and may be by the putative giant impact which formed the observed martian crustal dichotomy (Andrews-Hanna et al., 2008; Golabek et al., 2011)). The fractionation process could also have been driven by the absorption of intense ultraviolet radiation from the young Sun on each of the terrestrial planets (Pepin, 2006). Others scenarios suggest that bombardment by icy planetesimals or comets could be the main delivery mechanism of argon, krypton and xenon to the terrestrial planets (Owen et al., 1992; Owen and Bar-Nun, 1995). In order to account for the differences between the noble gas abundances observed today among these planets, Owen et al. (1992) argued that giant impacts would have eroded their atmospheres without inducing any fractionation. In their model, gravitational escape would have played a role restricted to the fractionation of atmospheric neon. Two separate sources, i.e. fractionated nebular gases and accreted cometary volatiles, have also been invoked to contribute to the current noble gas budget on Earth (Dauphas, 2003). In this case, hydrothermal escape would have fractionated the heavy noble gases acquired from the solar nebula and the resulting transient atmosphere would have mixed with cometary material in order to reproduce the Earth's noble gas abundances.

Alternatively, in order to account for the krypton and xenon abundance differences between Earth and Mars, Mousis et al. (2010a) proposed that the presence of large amounts of carbon dioxide-dominated clathrate deposits in the martian soil would have efficiently sequestered these noble gases. Because they found that the trapping of argon into these clathrates was poor, Mousis et al. (2010a) argued that, irrespective of its possible source (comets or gravitational capture), this volatile was probably fractionated, similarly to neon,[1] via the gravitational escape that affected the primary atmospheres. However, these authors based their conclusions on calculations of clathrate composition performed at current martian temperature and pressure conditions at the surface (Musselwhite and Lunine, 1995; Swindle et al., 2009) while they were investigating their formation in ancient Mars, in which the paleoatmosphere might have been orders of magnitude denser than the current atmosphere. Since the relative abundances of guest species incorporated in clathrate strongly depend on the temperature and pressure conditions at which it forms, the calculations used by Mousis et al. (2010a) may not be relevant to the study of clathrate composition in the context of the ancient martian climate.

In this paper, we reinvestigate the hypothesis that clathrate deposits present in the martian cryosphere have sequestered significant amounts of heavy noble gases initially present in the paleoatmosphere. To do so, we use a statistical-thermodynamic model derived from the approach of van der Waals and Platteeuw (1959) that gives the clathrate composition in a carbon dioxide-dominated atmosphere for a surface pressure range up to 3 bars, encompassing essentially all the values mentioned in the literature (Pollack et al., 1987; Fanale et al., 1992; Bridges and Wright, 2006; Tian et al., 2010). We also assess the stability of clathrate on ancient Mars, a nontrivial question since the global mean surface temperature may have been higher than today's due to a greenhouse effect induced by a denser carbon dioxide-dominated atmosphere. Because SO_2 could have been present in the ancient martian atmosphere as a result of volcanic activity (Tian et al., 2010), its influence on clathrate composition is also quantified.

[1] Neon is found to be an extremely poor clathrate former (Lunine and Stevenson, 1985). This results from the small size of this atom inducing exceedingly weak interactions with the cages.

2. Stability of CO_2-dominated clathrates on ancient Mars

In order to efficiently trap the atmospheric noble gases, our model requires that CO_2-dominated clathrate formed at the interface at which crystalline water ice is in contact with the atmosphere of ancient Mars. This interface should be located at the martian surface or in the close subsurface if this latter is assumed to be porous (Longhi, 2006). The thermodynamic conditions needed for the formation of CO_2-dominated clathrate could be encountered nowadays at the surface of martian polar caps (Miller and Smythe, 1970; Longhi, 2006) but many studies show that deposits of these crystalline structures are thermodynamically stable only at several meters depth in the subsurface at lower latitudes (Longhi, 2006; Prieto-Ballesteros et al., 2006; Chastain and Chevrier, 2007). On the other hand, various models of the martian paleoatmosphere support the notion that the mass of atmospheric CO_2 could have been up to several hundreds times *larger* than the current one, leading to surface pressures reaching values as high as 1 to a few bars (Pollack et al., 1987; Fanale et al., 1992; Bridges and Wright, 2006; Tian et al., 2010). One could then argue that this increase of CO_2 pressure at the surface in ancient times should favor clathrate formation. However, more infrared absorption associated with the increase of CO_2 atmospheric pressure may have implied a higher global mean surface temperature (Forget and Pierrehumbert, 1997) and its value could have exceeded that needed for clathrate stability at the given pressure. In order to investigate this effect on the putative stability of CO_2-dominated clathrates at the martian surface, we have used some recent calculations performed by Tian et al. (2010) who determined the climate consequences of SO_2 outgassing in a dense CO_2-dominated atmosphere.

Fig. 1 presents the stability domain of CO_2-dominated clathrate (assumed here to correspond to the equilibrium curve of CO_2 clathrate) against several global mean surface temperature profiles of ancient Mars expressed as a function of CO_2 atmospheric pressure. These temperature profiles have been computed with a photochemical model for different SO_2 atmospheric mole fractions

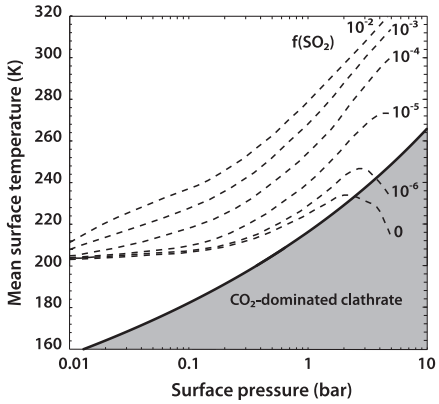

Fig. 1. Mean surface temperature of the early Mars (dashed lines) represented as a function of the surface pressure of CO_2 for different mole fractions of SO_2 f (SO_2) in the atmosphere (adapted from Fig. 2 of Tian et al., 2010). The bold solid line and gray area correspond to the equilibrium curve and domain of stability of CO_2-dominated clathrate, respectively.

Retour à la table des matières : p. v

f (SO_2) ranging between 0 and 10^{-2}, assuming no presence of aerosols in the atmosphere and a solar luminosity 0.75 times the current value (see Tian et al. (2010) for details). The figure shows that the clathrate is stable at the surface only at CO_2 atmospheric pressures exceeding ~2.5 bar for f (SO_2) = 0 and ~3.7 bar for f (SO_2) = 10^{-6}, respectively. Note that the considered range of f (SO_2) is too small to induce visible changes of the clathrate's global equilibrium curve used in the plot. On the other hand, even if the global mean surface temperature of Mars were higher than the clathrate equilibrium temperature at lower atmospheric pressure, this would not preclude clathrate formation in some areas of the planet benefiting from cooler climates. For example, assuming a 13 K decrease of the surface temperature, the clathrate is stable at CO_2 atmospheric pressures reaching or exceeding 0.5 bar for f (SO_2) $\leqslant 10^{-6}$ in the atmosphere. At the same surface pressure, which seems to be a reasonable value according to the literature (Johnson et al., 2008, 2009), a 23 K decrease of the soil temperature would also be needed to allow clathrate formation for f (SO_2) = 10^{-5}.

As shown by the figure, we note that high f (SO_2) values ($\geqslant 10^{-5}$) do not help clathrate formation on the planet due to the significant increase of the global mean surface temperature, but recent photochemical models suggest that the lifetime of SO_2 was very short in the ancient martian atmosphere and that only mixing ratios in the 10^{-8}–10^{-6} range could have persisted for hundreds of years (Johnson et al., 2009). Moreover, Tian et al. (2010) showed that the greenhouse effect induced by SO_2 injection into the atmosphere would have been ineffective in warming early Mars for timescales longer than a few months because it would have been outweighed by surface cooling from the inevitable formation of sulfate aerosols. We therefore assume in the present study, that either significant temperature variations have existed on the martian surface as a result of climate change at different latitudes or that the paleoatmosphere was dense enough to allow formation of significant amounts of permanent clathrate deposits.

3. The statistical-thermodynamic model

To investigate the possibility that clathrate deposits potentially present in the current martian cryosphere have incorporated a significant mass of heavy noble gases, we postulate that the mole fractions of volatile species measured in the present atmosphere (Moroz, 1998) were similar in the paleoatmosphere. In addition, we have assumed the presence of atmospheric SO_2 (f (SO_2) = 10^{-6}) due to volcanic activity in order to test the influence of this species on clathrate composition. Following the considerations of Section 2, we are aware that hypothesizing the presence of a *larger* mole fraction of atmospheric SO_2 makes more uncertain the thermodynamic stability of clathrate at given surface pressure and temperature. Table 2 summarizes the atmosphere composition considered in this work.

Table 2
Relative abundances of CO_2, N_2, O_2, SO_2, CO, Ar, Kr and Xe in the initial gas phase x_G (values derived from Moroz (1998)).

Species	x_G
CO_2	0.954
N_2	2.71×10^{-2}
O_2	1.31×10^{-3}
SO_2	1×10^{-6}
CO	7.03×10^{-4}
Ar	1.61×10^{-2}
Kr	2.01×10^{-7}
Xe	8.03×10^{-8}

To calculate the relative abundances of guest species incorporated in a clathrate from a coexisting gas of specified composition at given temperature and pressure, we follow the method described by Lunine and Stevenson (1985), Thomas et al. (2007, 2008, 2009) and Mousis et al. (2010b) which uses classical statistical mechanics to relate the macroscopic thermodynamic properties of clathrates to the molecular structure and interaction energies. It is based on the original ideas of van der Waals and Platteeuw (1959) for clathrate formation, which assume that trapping of guest molecules into cages corresponds to the three-dimensional generalization of ideal localized adsorption. This approach is based on four key assumptions:

1. The host molecules contribution to the free energy is independent of the clathrate occupancy. This assumption implies in particular that the guest species do not distort the cages.
2. (a) The cages are singly occupied. (b) Guest molecules rotate freely within the cage.
3. Guest molecules do not interact with each other.
4. Classical statistics is valid, i.e., quantum effects are negligible.

In this formalism, the fractional occupancy of a guest molecule K for a given type t (t = small or large) of cage can be written as

$$y_{K,t} = \frac{C_{K,t}P_K}{1 + \sum_J C_{J,t}P_J}, \quad (1)$$

where the sum in the denominator includes all the species which are present in the initial gas phase. $C_{K,t}$ is the Langmuir constant of species K in the cage of type t, and P_K is the partial pressure of species K. This partial pressure is given by $P_K = x_K \times P$ (we assume that the sample behaves as an ideal gas), with x_K the mole fraction of species K in the initial gas phase, and P the total gas pressure, which is dominated by CO_2.

The Langmuir constant depends on the strength of the interaction between each guest species and each type of cage, and can be determined by integrating the molecular potential energy within the cavity as

$$C_{K,t} = \frac{4\pi}{k_B T}\int_0^{R_c} \exp\left(-\frac{w_{K,t}(r)}{k_B T}\right) r^2\, dr, \quad (2)$$

where R_c represents the radius of the cavity assumed to be spherical, k_B the Boltzmann constant, T the temperature and $w_{K,t}(r)$ is the spherically averaged potential (here Kihara or Lennard-Jones potential) representing the interactions between the guest molecules K and the H_2O molecules forming the surrounding cage t. This potential $w(r)$ can be written for a spherical guest molecule, as (McKoy and Sinanoğlu, 1963)

$$w(r) = 2z\epsilon\left[\frac{\sigma^{12}}{R_c^{11} r}\left(\delta^{10}(r) + \frac{a}{R_c}\delta^{11}(r)\right) - \frac{\sigma^6}{R_c^5 r}\left(\delta^4(r) + \frac{a}{R_c}\delta^5(r)\right)\right], \quad (3)$$

with the mathematical function $\delta^N(r)$ in the form

Table 3
Parameters for the cavities.

Clathrate structure	I		II	
Cavity type	Small	Large	Small	Large
R_c (Å)	3.975	4.300	3.910	4.730
b	2	6	16	8
z	20	24	20	28

R_c is the radius of the cavity (values taken from Parrish and Prausnitz (1972)). b represents the number of small (b_s) or large (b_ℓ) cages per unit cell for a given structure of clathrate (I or II), z is the coordination number in a cavity.

Retour à la table des matières : p. v

$$\delta^N(r) = \frac{1}{N}\left[\left(1 - \frac{r}{R_c} - \frac{a}{R_c}\right)^{-N} - \left(1 + \frac{r}{R_c} - \frac{a}{R_c}\right)^{-N}\right]. \quad (4)$$

In Eq. (3), z is the coordination number of the cell. Parameters z and R_c, which depend on the structure of the clathrate (I or II) and on the type of the cage (small or large), are given in Table 3. The intermolecular parameters a, σ and ϵ describing the guest molecule–water interactions in the form of a Kihara or Lennard-Jones potential are listed in Table 4. Note that, due to the lack of experimental or theoretical data, the mixed Lennard-Jones parameters for SO_2–H_2O interactions were obtained using the standard Lorentz–Berthelot combination rules $\epsilon_{K-W} = \sqrt{\epsilon_K \times \epsilon_W}$ and $\sigma_{K-W} = (\sigma_K + \sigma_W)/2$ in which the guest molecule parameters ϵ_K and σ_K were derived from quantum mechanical calculations (Churakov and Gottschalk, 2003) and the water molecule parameters ϵ_W and σ_W from Alavi et al. (2009).

Finally, the mole fraction f_K of a guest molecule K in a clathrate can be calculated with respect to the whole set of species considered in the system as

$$f_K = \frac{b_s y_{K,s} + b_\ell y_{K,\ell}}{b_s \sum_J y_{J,s} + b_\ell \sum_J y_{J,\ell}}, \quad (5)$$

where b_s and b_l are the number of small and large cages per unit cell respectively, for the clathrate structure under consideration, and with the sum of the mole fractions of enclathrated species normalized to 1.

4. Results

As shown by Eqs. (1) and (2) in Section 3, the clathrate composition strongly depends on the temperature and pressure conditions at which it forms. We have then computed the clathrate composition for atmospheric pressures up to 3 bars allowing us to encompass all the plausible values discussed in the literature. At each pressure considered, the temperature used in our computations is the equilibrium temperature of CO_2-dominated clathrate represented in Fig. 1. We have also taken into account the influence of variation of the cage sizes on the mole fractions of guests encaged in clathrates by modifying their nominal radius (see Table 3) by ±2%. Indeed, it has been shown that the size of the cages can vary as a function of temperature (thermal expansion or contraction) and also of the size of the guest species (Shpakov et al., 1998; Belosludov et al., 2003; Takeya et al., 2006; Hester et al., 2007). As a result, the induced thermal expansion or contraction can significantly affect the composition of clathrates (Thomas et al., 2008; Mousis et al., 2010b).

Fig. 2 presents the clathrate composition calculated as a function of the surface pressure of CO_2 in the cases of our nominal structural parameters and of a ±2% variation of the cage sizes. Note that all our calculations have been performed in the case of structure I clathrate because the martian atmosphere is by far dominated by CO_2 and that CO_2 clathrate is of structure I (Lunine and Stevenson, 1985; Sloan and Koh, 2008). Except for values lower than ∼0.1 bar, the mole fractions of encaged volatiles are found to vary only weakly with pressure for the given structural parameters. However, the trapping efficiency of the volatiles strongly differs in clathrate when considering different values of the cage sizes. For example, at the atmospheric pressure of 0.5 bar at the surface and assuming a 2% expansion of the cage sizes compared to the nominal structural parameters listed in Table 3, the mole fractions of Ar, Kr and Xe are found to be 3.5×10^{-4}, 4.2×10^{-8}, and 5.7×10^{-7}, respectively. On the other hand, if one assumes a 2% contraction of the cage sizes compared to the nominal structural values, the mole fractions of Ar, Kr and Xe substantially increase and become 5.0×10^{-3}, 8.8×10^{-7} and 9.0×10^{-7}, respectively. These calculations suggest that Xe is very well trapped in clathrate irrespective of the considered cage sizes since its mole fraction still remains larger than the atmospheric value. Kr is also well trapped, in particular when adopting cage sizes equal to or larger than the nominal structural parameters, thus favoring *larger* mole fractions in clathrate than in the atmosphere. With a mole fraction in clathrate always lower than in the atmosphere, Ar remains the less efficiently sequestered noble gas. However, we note that the amount of trapped Ar is not negligible in the case of a 2% contraction of the cage sizes since its mole fraction in clathrate is then ∼1/3 the atmospheric value. Interestingly, with a mole

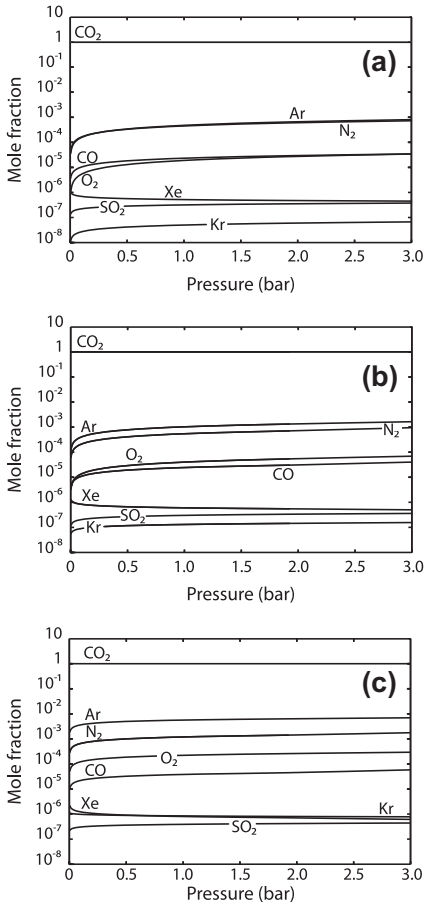

Fig. 2. Mole fractions of volatiles encaged in clathrates calculated as a function of the surface pressure of CO_2 in the cases of (a) a 2% increase of the cage sizes, (b) no cage variation and (c) a 2% contraction of the cage sizes.

Table 4
Parameters for Kihara and Lennard-Jones potentials.

Molecule	σ_{K-W} (Å)	ϵ_{K-W}/k_B (K)	a_{K-W} (Å)	Reference
CO_2	2.97638	175.405	0.6805	Sloan and Koh (2008)
N_2	3.13512	127.426	0.3526	Sloan and Koh (2008)
O_2	2.7673	166.37	0.3600	Parrish and Prausnitz (1972)
SO_2	3.5343	153.85	0	This work
CO	3.1515	133.61	0.3976	Mohammadi et al. (2005)
Ar	2.9434	170.50	0.184	Parrish and Prausnitz (1972)
Kr	2.9739	198.34	0.230	Parrish and Prausnitz (1972)
Xe	3.32968	193.708	0.2357	Sloan and Koh (2008)

σ_{K-W} is the Lennard-Jones diameter, ϵ_{K-W} is the depth of the potential well, and a_{K-W} is the radius of the impenetrable core, for the guest–water pairs.

Retour à la table des matières : p. v

fraction of order $\sim 2\text{–}4 \times 10^{-7}$ in clathrate, corresponding to a value ~2.5–5 times smaller than the postulated mole fraction in the atmosphere, SO_2 is found to be a very poor clathrate former in the presence of a CO_2-dominated gas.

Our calculations show that the amount of atmospheric noble gases trapped into the martian cryosphere is proportional to the quantity of enclathrated CO_2. Fig. 3 displays the ratios of heavy noble gas abundances initially present in the martian atmosphere and subsequently sequestered into the cryosphere to the ones measured nowadays expressed as a function of the equivalent CO_2 pressure trapped into clathrates for the three cases of varying cage sizes. For each noble gas, the corresponding ratio R_{NG} is given by

$$R_{NG} = \frac{P_{ancient}}{P_{present}} \times \frac{f_{NG}}{x_{NG}}, \quad (6)$$

where $P_{ancient}$ is the assumed CO_2 surface pressure at the time of clathrate formation and $P_{present}$ the CO_2 surface pressure at present times (i.e. 7 mbar), f_K and x_K the mole fractions calculated in clathrate and measured in the present atmosphere, respectively. These computations are based on the assumption that the initial concentrations of noble gases (mass of noble gas per unit mass of planet) on Earth and Mars are the same, implying that the proportions of volatiles delivered to these planets were similar at their accretion epoch. This allows us to investigate whether or not the sole presence of clathrates on Mars can explain its lower noble gas atmospheric abundance compared to the Earth instead of assuming a variation of the volatile delivery between these planets at their formation epoch. Panel (a) of Fig. 3 shows that amounts of xenon and krypton (normalized in mass of noble gas per unit mass of planet or g/g-planet) equivalent to those found on Earth can be incorporated into the martian cryosphere provided that the CO_2 equivalent pressure exceeds ~0.04 and 1.9 bar at their respective clathration epoch when postulating a 2% expansion of the cages. In this case and at the pressure range considered, the amount of trapped Ar is not sufficient to explain the measured Earth/Mars argon abundance ratio. Conclusions are similar for calculations performed in the case of the nominal structural parameters and displayed in Panel (b) of Fig. 3 but the amount of CO_2 needed to be clathrated in order to trap masses of Kr and Xe equivalent to those found on Earth is lower. In this case, a CO_2 equivalent pressure of 0.03 and 0.9 bar is sufficient to trap masses of Xe and Kr in the cryosphere equivalent to those found on Earth, respectively. In contrast, Panel (c) of Fig. 3 shows that, assuming a 2% contraction of the cages, it is possible to incorporate masses of all three noble gases equivalent to those found on Earth over the atmospheric pressure range considered. Indeed, enough mass of Xe, Kr and Ar can be incorporated if one assumes the trapping of CO_2 at equivalent atmospheric pressures of ~0.02, 0.12, and 2.3 bar, respectively.

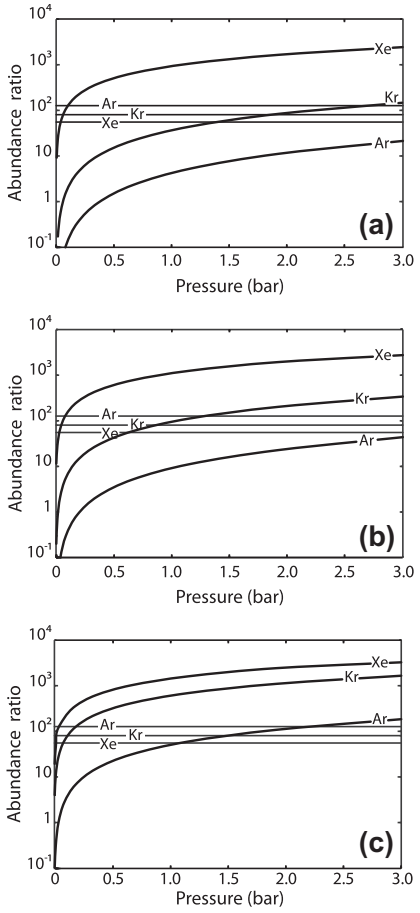

Fig. 3. Ratios of heavy noble gas abundances initially present in the martian atmosphere and subsequently incorporated into the cryosphere to the measured ones represented as a function of the amount of enclathrated CO_2 (expressed in equivalent surface pressure) in the cases of (a) a 2% increase of the cage sizes, (b) no cage variation and (c) a 2% contraction of the cage sizes. The three horizontal lines represent the ratios of measured heavy noble gas abundances between the Earth and Mars. These computations are based on the assumption that the initial concentration of noble gases (mass of noble gas per unit mass of planet) on Earth and Mars are the same.

5. Discussion

The calculations presented in this work have been conducted assuming that the atmospheric mole fraction of SO_2 is 10^{-6}. Additional tests show that the trapping efficiencies of other minor species present in the atmosphere, including heavy noble gases, are insensitive to the f(SO_2) variation in the $0\text{–}10^{-2}$ range. This conclusion can apply to any other minor species whose variation of the mole fraction in the gas phase will hardly alter the trapped mole fractions of other volatiles. In addition, the trapping efficiency of SO_2 in clathrate remains poor in this mole fraction range. Interestingly, because the mole fraction of enclathrated SO_2 is at most ~40% of the atmospheric value, this confirms that another sink mechanism, most likely photochemistry (Johnson et al., 2009), must be invoked in order to explain the complete extinction of this molecule in the martian atmosphere.

Our model indicates that the minimum CO_2 surface pressure allowing the clathration of amounts of Ar, Kr and Xe initially present in the martian paleoatmosphere and equivalent to those estimated on Earth (in mass of noble gas per unit mass of planet) is ~2.3 bar. This atmospheric pressure corresponds to a layer of pure CO_2 clathrate globally averaged on Mars of ~183 m, a value lower than the global equivalent layer (GEL) of water estimated to be in the 0.5–1 km range (Clifford et al., 2010). The hypothesis examined here, that large quantities of heavy noble gases can be trapped in martian clathrates, is consistent with the inventory of water available on the planet. The formation kinetics of a CO_2 clathrate formed from crystalline water ice and gas has been estimated to be in the $0.3\text{–}1 \times 10^{-12}$ mol m^{-2} Pa^{-1} s^{-1} range from laboratory experiments (Schmitt, 1986). Based on these numbers, and assuming the initial presence of a layer of crystalline ice with a high porosity on Mars, we find that ~1–4 Myr would be needed at 2.3 bar of surface pressure for the formation of the 183 m clathrate layer. Note that clathrates formed at a higher CO_2 surface pressure should have destabilized with time if they remained in contact with the

Retour à la table des matières : p. v

atmosphere, due to the progressive decrease of its pressure down to the present value. Our scenario is then based on the assumption that large amounts of clathrates are buried today in the martian soil and are preserved from the atmosphere. Only a few meters of depth are needed to preserve the stability of this clathrate layer (Longhi, 2006). Our scenario also implies that a substantial fraction of the missing CO_2 inferred in the present Mars is hidden in its cryosphere. This potential reservoir should be taken into account along with the carbonate budget when estimating the amount of CO_2 burried into the martian soil.

In drawing Fig. 3, we have implicitely assumed that the initial concentration of noble gases (mass of noble gas per unit mass of planet) on Earth and Mars are the same. Hence, considering Panel (b) of Fig. 3, we see that for a CO_2 pressure of 1 bar, there would be 100 times more Kr trapped in clathrates than remaining in the atmosphere, which is exactly the atmospheric depletion we are looking for to explain the numbers given in Table 1. However, Mousis et al. (2010a), using the impact rates of comets on Earth and Mars derived by Horner et al. (2009), showed that combining the reduced impact rate on Mars (a factor of 3 less) and the reduced mass of the planet (a factor of 10), one expects an initial concentration of noble gases of cometary origin 3 times larger on Mars than on Earth. Hence one should move the horizontal lines in Fig. 3 up by a factor of 3. The trapping of these noble gases into clathrates would then imply a higher CO_2 surface pressure.

Alternatively, it has been also shown that comets might not be the only carriers of heavy noble gases. According to the Nice model, the mass of cometary and asteroidal origin impacting the Moon are essentially the same (Gomes et al., 2005). The impact per unit surface area on the Moon and on Earth are also the same. So, the ratio of impacts from comets and asteroids on Mars compared to Earth are the same as compared to the Moon. Using the ratios given in Table 4 of Horner et al. (2009), we conclude that in the context of the Nice model, the impact mass on Mars of asteroidal origin is 4–8 times larger than that of cometary origin. They may have a profound effect on the initial noble gas content of Earth and Mars. In particular, Mars would have initially been comparatively richer in ^{132}Xe than the Earth if asteroids have a composition close to that of CI meteorites. This fits well with the fact that ^{132}Xe can be trapped in larger quantities than ^{84}Kr or ^{36}Ar (our calculations of clathrate composition are not sensitive to the different existing isotopes). On the other hand, as mentioned in Horner et al. (2009), the Nice group (A. Morbidelli, private communication) has carried out simulations of the Late Heavy Bombardment which show the opposite result – that with certain initial conditions, Mars actually receives more cometary material, and less asteroidal impacts per unit area than the Moon. In their simulation, Mars receives twice as many cometary impacts per unit area as the Moon, a surprising result given the high impact velocity of the comets in the inner Solar System. Horner et al. (2009) on the contrary found that the cometary impact flux per unit area is essentially the same for all terrestrial planets. In the same time, the Nice group found an asteroidal impact flux per unit area that is the same for Mars and the Moon, while Horner et al. found an increased impact flux on Mars due to lower impact velocities and proximity of the asteroids to Mars. Therefore, given the strong uncertainties concerning the relative levels of hydration of the Earth and Mars, we assert that the assumption that these two planets initially experienced the delivery of the same amount of volatiles (in mass of noble gas per unit mass of planet) is a reasonable one.

Atmospheric escape is generally assumed to have removed large amounts of volatiles from Mars' atmosphere. Noble gases in the martian atmosphere are globally depleted by a factor of 100 with respect to Earth. Several escape mechanisms may have played an important role in removing the noble gases. Impact erosion, which does not result in elemental or isotopic fractionation, has been proposed to remove large amounts of volatiles. A lunar-size object may drive off the entire atmosphere of the Earth (Ahrens, 1993). Nevertheless, recent simulations suggest that impact erosion is less efficient than previously assumed, except if planetary embryos possess an ocean of liquid water (Genda and Abe, 2005). Other mechanisms, like hydrodynamic escape or sputtering could have been active at early times (Pepin, 1991). The high value of the $^{40}Ar/^{36}Ar$ on Mars, of the order of 3000 ± 500, that is 10 times larger than Earth's ratio (Biemann et al., 1976), acts in favor of a large primitive escape. ^{40}Ar is formed from the radioactive decay of ^{40}K with a half life of 1.2 Gyr (Xie and Tackley, 2004). ^{40}Ar is therefore degassed in Mars' atmosphere much later than ^{36}Ar. The high $^{40}Ar/^{36}Ar$ on Mars suggests that ^{36}Ar massively escaped before the bulk of ^{40}Ar was degassed to the atmosphere, and it could have been the fate of other non-radiogenic noble gases. Nevertheless, because impact erosion could not be as efficient as previously thought (Genda and Abe, 2005), and considering difficulties to reconcile elemental and isotopic fractionation pattern of noble gases in terrestrial planets by considering escape as their only sink (Pepin, 1991), trapping of noble gases in clathrate clearly deserves to be considered and further studied. Because trapping in clathrate is more efficient for heavy noble gases, and escape more efficient for light ones, a combination of these two sinks could result in a relatively uniform depletion rate of noble gases in Mars + atmosphere. The proposed clathrate trapping mechanism could have played an important role in the shaping of the current martian atmosphere.

Recent works suggest that the early martian atmosphere was not CO_2-rich, based on equilibrium models of phases at the Noachian (Chevrier et al., 2007), the stability of liquid solutions below freezing point of pure water (Fairén et al., 2009), and the extrapolation of the presently observed carbon escape rates back to the past suggesting that CO_2 loss by escape has been small along most of Mars' history (Barabash et al., 2007). It is nevertheless unlikely that the CO_2 pressure has been low, similar to its present pressure, during the entire history of Mars. Although thermal escape of carbon is expected to have removed most of the primordial CO_2, with a characteristic time to lose 1 bar of CO_2 in the range from 1 to 10 Myr (Tian et al., 2009), a secondary atmosphere is expected to have progressively formed through volcanic outgassing of CO_2. According to the morphological analysis, 0.3 bar of CO_2 would have been released during the last 4 Gyr (Graddock and Greeley, 2009). Crust formation modeling suggests that a total 0.5–1 bar of CO_2 have been outgassed, mostly during the Pre-Noachian and the Noachian (Grott et al., 2011). At least ~1 bar of CO_2 has been released to the atmosphere along martian history. Non-thermal escape is likely a minor sink of carbon during the last 4 Gyr, but carbonate deposition in crustal hydrothermal system could have resulted in a significant decrease of atmospheric CO_2 during the late Noachian and the Hesperian (Chassefière and Leblanc, 2011). The expected strong primitive thermal escape of C could have prevented CO_2 from accumulating in the atmosphere until 4 Gyr b.p. (Tian et al., 2009), with possibly low or moderate CO_2 pressure at the Pre-Noachian, in the range from a few hundred millibars to a few bars. After the end of intense C thermal escape, during the Noachian, mantle outgassing should have led to a significant CO_2 pressure of typically 0.5 bar or more, followed by a subsequent decrease through sequestration of atmospheric carbon in the crust.

Finally, it is clear that the model used to determine the composition of martian clathrates has some limitations. In particular, the transferability of the intermolecular potential parameters to temperatures and pressures beyond the range for which they have been fitted is uncertain (Ballard and Sloan, 2000; Clarke and Bishnoi, 2003). Inconsistencies have also been seen between intermolecular potential parameters derived from different sets of experimental data (Tee et al., 1966). In these conditions, supple-

Retour à la table des matières : p. v

mentary measurements of the equilibrium pressure of clathrates formed from species listed in Table 2 in the temperature range appropriate for martian conditions would be needed in order to derive a consistent set of intermolecular potential parameters. Because the size of the clathrate cages is very critical to the inference of the correct trapping propensities of the different species, laboratory experiments (in the form of Raman spectroscopy measurements) are also needed to determine their variation laws as a function of temperature in martian conditions. Moreover, it has been claimed in the literature that Kihara or Lennard-Jones intermolecular potentials may not accurately describe the interaction between guest and water molecules (Sun and Duan, 2005). Futhermore, future theoretical developments aimed at predicting the relative trapping efficiencies of various species in multiple guest clathrates should be based on atom–atom descriptions of the intermolecular guest–clathrate interactions, in which effective parameters for these interactions are fitted from results of *ab initio* quantum mechanical methods (Sun and Duan, 2005; Klauda and Sandler, 2002, 2003; Thomas et al., 2010).

Acknowledgments

This work was supported in part by the French Centre National d'Etudes Spatiales and the Italian program "Incentivazione alla mobilità di studiosi stranieri e italiani residenti all'estero". We thank Vincent F. Chevrier and an anonymous Referee for their useful comments and corrections. E.Chassefière. and A. Lakhlifi acknowledge support from CNRS EPOV interdisciplinary program. A. Morbidelli is acknowledged for enlightening discussions and information on his work.

References

Ahrens, T.J., 1993. Impact erosion of terrestrial planetary atmospheres. Annu. Rev. Earth Planet. Sci. 21, 525–555.
Alavi, S., Susilo, R., Ripmeester, J.A., 2009. Linking microscopic guest properties to macroscopic observables in clathrate hydrates: Guest–host hydrogen bonding. J. Chem. Phys. 130, 174501-1–174501-9.
Andrews-Hanna, J.C., Zuber, M.T., Banerdt, W.B., 2008. The Borealis basin and the origin of the martian crustal dichotomy. Nature 453, 1212–1215.
Ballard, A.L., Sloan, E.D., 2000. Structural transitions in methane plus ethane gas hydrates–Part II: modeling beyond incipient conditions. Chem. Eng. Sci. 55 (23), 5773–5782.
Barabash, S., Fedorov, A., Lundin, R., Sauvaud, J.-A., 2007. Martian atmospheric erosion rates. Science 315, 501–503.
Belosludov, V.R., Inerbaev, T.M., Subbotin, O.S., Belosludov, R.V., Kudoh, J., Kawazoe, Y., 2003. Thermal expansion and lattice distortion of clathrate hydrates of cubic structures I and II. J. Supramol. Chem. 2 (4–5), 453–458.
Biemann, K. et al., 1976. The atmosphere of Mars near surface: Isotope ratios and upper limits on Noble gases. Science 194, 76–78.
Bridges, J.C., Wright, I.P., 2006. Atmospheric thickness on ancient Mars: Constraints from SNC meteorites. Ann. Lunar Planet. Sci. Conf., 37, 1990.
Chassefière, E., Leblanc, F., 2011. Methane release and the carbon cycle on Mars. Planet. Space Sci. 59, 207–217.
Chastain, B.K., Chevrier, V., 2007. Methane clathrate hydrates as a potential source for martian atmospheric methane. Planet. Space Sci. 55, 1246–1256.
Chevrier, V., Poulet, F., Bibring, J.-P., 2007. Early geochemical environment of Mars as determined from thermodynamics of phyllosilicates. Nature 448, 60–63.
Churakov, S.V., Gottschalk, M., 2003. Perturbation theory based equation of state for polar molecular fluids: I. Pure fluids. Geochem. Cosmochim. Acta 67 (13), 2397–2414.
Clarke, M.A., Bishnoi, P.R., 2003. Development of an implicit least squares optimisation scheme for the determination of Kihara potential parameters using gas hydrate equilibrium data. Fluid Phase Equilibria 211, 51–60.
Clifford, S.M., Lasue, J., Heggy, E., Boisson, J., McGovern, P., Max, M.D., 2010. Depth of the martian cryosphere: Revised estimates and implications for the existence and detection of subpermafrost groundwater. J. Geophys. Res. (Planets) 115, 7001.
Dauphas, N., 2003. The dual origin of the terrestrial atmosphere. Icarus 165, 326–339.
Fairén, A.G., Davila, A.F., Gago-Duport, L., Amils, R., McKay, C.P., 2009. Stability against freezing of aqueous solutions on early Mars. Nature 459, 401–404.
Fanale, F.P., Postawko, S.E., Pollack, J.B., Carr, M.H., Pepin, R.O., 1992. Mars – Epochal climate change and volatile history. Mars, 1135–1179.
Forget, F., Pierrehumbert, R.T., 1997. Warming early Mars with carbon dioxide clouds that scatter infrared radiation. Science 278, 1273–1276.
Genda, H., Abe, Y., 2005. Enhanced atmospheric loss on protoplanets at the giant impact phase in the presence of oceans. Nature 433, 842–844.
Golabek, G.J., Keller, T., Gerya, T.V., Zhu, G., Tackley, P.J., Connolly, J.A.D., 2011. Origin of the martian dichotomy and Tharsis from a giant impact causing massive magmatism. Icarus 215, 346–357.
Gomes, R., Levison, H.F., Tsiganis, K., Morbidelli, A., 2005. Origin of the cataclysmic Late Heavy Bombardment period of the terrestrial planets. Nature 435, 466–469.
Graddock, R.A., Greeley, R., 2009. Minimum estimates of the amount and timing of gases released into the martian atmosphere from volcanic eruptions. Icarus 204, 512–526.
Grott, M., Morschhauser, A., Breuer, D., Hauber, E., 2011. Volcanic outgassing of CO_2 and H_2O on Mars. Earth Planet. Sci. Lett. 308, 291–400.
Hester, K.C., Huo, Z., Ballard, A.L., Koh, C.A., Miller, K.T., Sloan, E.D., 2007. Thermal expansivity for sI and sII clathrate hydrates. J. Phys. Chem. B 111, 8830–8835.
Horner, J., Mousis, O., Petit, J.-M., Jones, B.W., 2009. Differences between the impact regimes of the terrestrial planets: Implications for primordial D:H ratios. Planet. Space Sci. 57, 1338–1345.
Johnson, S.S., Mischna, M.A., Grove, T.L., Zuber, M.T., 2008. Sulfur-induced greenhouse warming on early Mars. J. Geophys. Res. (Planets) 113, 8005.
Johnson, S.S., Pavlov, A.A., Mischna, M.A., 2009. Fate of SO_2 in the ancient martian atmosphere: Implications for transient greenhouse warming. J. Geophys. Res. (Planets) 114, 11011.
Klauda, J.B., Sandler, S.I., 2002. Ab initio intermolecular potentials for gas hydrates and their predictions. J. Phys. Chem. B 106, 5722–5732.
Klauda, J.B., Sandler, S.I., 2003. Predictions of gas hydrate phase equilibria and amounts in natural sediment porous media. Marine Petroleum Geol. 20, 459–470.
Longhi, J., 2006. Phase equilibrium in the system CO_2–H_2O: Application to Mars. J. Geophys. Res. (Planets) 111, 6011.
Lunine, J.I., Stevenson, D.J., 1985. Thermodynamics of clathrate hydrate at low and high pressures with application to the outer Solar System. Astrophys. J. Suppl. Series 58, 493–531.
Marty, B., Meibom, A., 2007. Noble gas signature of the late heavy bombardment in the Earth's atmosphere. eEarth Discuss. 2, 99–113.
McKoy, V., Sinanoğlu, O., 1963. Theory of dissociation pressures of some gas hydrates. J. Chem. Phys. 38 (12), 2946–2956.
Miller, S.L., Smythe, W.D., 1970. Carbon dioxide clathrate in the martian ice cap. Science 170, 531–533.
Mohammadi, A.H., Anderson, R., Tohidi, B., 2005. Carbon monoxide clathrate hydrates: Equilibrium data and thermodynamic modeling. AIChE J. 51, 2825–2833.
Moroz, V.I., 1998. Chemical composition of the atmosphere of Mars. Adv. Space Res. 22, 449–457.
Mousis, O. et al., 2010a. Impact regimes and post-formation sequestration processes: Implications for the origin of heavy noble gases in terrestrial planets. Astrophys. J. 714, 1418–1423.
Mousis, O., Lunine, J.I., Picaud, S., Cordier, D., 2010b. Volatile inventories in clathrate hydrates formed in the primordial nebula. Faraday Discuss. 147, 509–525.
Musselwhite, D., Lunine, J.I., 1995. Alteration of volatile inventories by polar clathrate formation on Mars. J. Geophys. Res. 100, 23301–23306.
Owen, T., Bar-Nun, A., 1995. Comets, impacts and atmospheres. Icarus 116, 215–226.
Owen, T., Bar-Nun, A., Kleinfeld, I., 1992. Possible cometary origin of heavy noble gases in the atmospheres of Venus, Earth, and Mars. Nature 358, 43–46.
Parrish, W.R., Prausnitz, J.M., 1972. Dissociation pressures of gas hydrates formed by gas mixtures. Ind. Eng. Chem.: Process Des. Develop. 11 (1), 26–35 (Erratum: Parrish, W.R., Prausnitz, J.M., 1972. Ind. Eng. Chem.: Process Des. Develop. 11 (3), 462).
Pepin, R.O., 1991. On the origin and early evolution of terrestrial planet atmospheres and meteoritic volatiles. Icarus 92, 2–79.
Pepin, R.O., 2006. Atmospheres on the terrestrial planets: Clues to origin and evolution. Earth Planet. Sci. Lett. 252, 1–14.
Pollack, J.B., Kasting, J.F., Richardson, S.M., Poliakoff, K., 1987. The case for a wet, warm climate on early Mars. Icarus 71, 203–224.
Prieto-Ballesteros, O. et al., 2006. Interglacial clathrate destabilization on Mars: Possible contributing source of its atmospheric methane. Geology 34, 149.
Schmitt, B., 1986. La surface de la glace. Structure, dynamique et interactions. Implications astrophysiques. Ph.D. Thesis.
Shpakov, V.P., Tse, J.S., Tulk, C.A., Kvamme, B., Belosludov, V.R., 1998. Elastic moduli calculation and instability in structure I methane clathrate hydrate. Chem. Phys. Lett. 282 (2), 107–114.
Sloan, E.D., Koh, C.A., 2008. Clathrate Hydrates of Natural Gases, third ed. CRC Press, Taylor & Francis Group, Boca Raton.
Sun, R., Duan, Z.H., 2005. Prediction of CH_4 and CO_2 hydrate phase equilibrium and cage occupancy from ab initio intermolecular potentials. Geochim. Cosmochim. Acta 69, 4411–4424.
Swindle, T.D., Thomas, C., Mousis, O., Lunine, J.I., Picaud, S., 2009. Incorporation of argon, krypton and xenon into clathrates on Mars. Icarus 203, 66–70.
Takeya, S. et al., 2006. Structure and thermal expansion of natural gas clathrate hydrates. Chem. Eng. Sci. 61 (8), 2670–2674.
Tee, L.S., Gotoh, S., Stewart, W.E., 1966. Molecular parameters for normal fluids: The Kihara potential with spherical core. Ind. Eng. Chem. Fund. 5, 363–367.

Retour à la table des matières : p. v

Thomas, C., Mousis, O., Ballenegger, V., Picaud, S., 2007. Clathrate hydrates as a sink of noble gases in Titan's atmosphere. Astron. Astrophys. 474, L17–L20.
Thomas, C., Picaud, S., Mousis, O., Ballenegger, V., 2008. A theoretical investigation into the trapping of noble gases by clathrates on Titan. Planet. Space Sci. 56, 1607–1617.
Thomas, C., Mousis, O., Picaud, S., Ballenegger, V., 2009. Variability of the methane trapping in martian subsurface clathrate hydrates. Planet. Space Sci. 57, 42–47.
Thomas, C., Picaud, S., Ballenegger, V., Mousis, O., 2010. Sensitivity of predicted gas hydrate occupancies on treatment of intermolecular interactions. J. Chem. Phys. 132, 104510.
Tian, F. et al., 2010. Photochemical and climate consequences of sulfur outgassing on early Mars. Earth Planet. Sci. Lett. 295, 412–418.
Tian, F., Kasting, J.F., Solomon, S.C., 2009. Thermal escape of carbon from the early martian atmosphere. Geophys. Res. Lett. 308, 391–400.
van der Waals, J.H., Platteeuw, J.C., 1959. Clathrate solutions. Advances in Chemical Physics, vol. 2. Interscience, New York.
Xie, S., Tackley, P.J., 2004. Evolution of helium and argon isotopes in a convecting mantle. Phys. Earth Planet. Int. 146, 417–439.

Retour à la table des matières : p. v

C.3 Article sur la détermination du rapport $^{14}N/^{15}N$ dans les comètes

The Astrophysical Journal Letters, 780:L17 (5pp), 2014 January 10 doi:10.1088/2041-8205/780/2/L17
© 2014. The American Astronomical Society. All rights reserved. Printed in the U.S.A.

TOWARD A UNIQUE NITROGEN ISOTOPIC RATIO IN COMETARY ICES

Philippe Rousselot[1], Olivier Pirali[2], Emmanuël Jehin[3], Michel Vervloet[2], Damien Hutsemékers[3], Jean Manfroid[3], Daniel Cordier[1], Marie-Aline Martin-Drumel[2], Sébastien Gruet[2], Claude Arpigny[3], Alice Decock[3], and Olivier Mousis[1]
[1] Institut UTINAM-UMR CNRS 6213, Observatoire des Sciences de l'Univers THETA, University of Franche-Comté, BP 1615, F-25010 Besançon Cedex, France; rousselot@obs-besancon.fr
[2] Synchrotron SOLEIL, ligne AILES, UMR 8214 CNRS, L'orme des Merisiers, Saint-Aubin, F-91192 Gif-Sur-Yvette, France
[3] Département d'Astrophysique, de Géophysique et d'Océanographie, Université de Liège, Allée du Six Août, B-4000 Liège, Belgium
Received 2013 October 28; accepted 2013 November 19; published 2013 December 16

ABSTRACT

Determination of the nitrogen isotopic ratios in different bodies of the solar system provides important information regarding the solar system's origin. We unambiguously identified emission lines in comets due to the $^{15}NH_2$ radical produced by the photodissociation of $^{15}NH_3$. Analysis of our data has permitted us to measure the $^{14}N/^{15}N$ isotopic ratio in comets for a molecule carrying the amine (–NH) functional group. This ratio, within the error, appears similar to that measured in comets in the HCN molecule and the CN radical, and lower than the protosolar value, suggesting that N_2 and NH_3 result from the separation of nitrogen into two distinct reservoirs in the solar nebula. This ratio also appears similar to that measured in Titan's atmospheric N_2, supporting the hypothesis that, if the latter is representative of its primordial value in NH_3, these bodies were assembled from building blocks sharing a common formation location.

Key words: comets: general – line: identification – molecular data – techniques: spectroscopic

Online-only material: color figure

1. INTRODUCTION

The determination of nitrogen isotopic ratios in solar system objects is of primary importance to achieve a better understanding of the origins of these objects. Measurements of the $^{14}N/^{15}N$ isotopic ratio in different solar system objects and molecules have revealed great diversity. This ratio ranges from 441 ± 5 for the present-day Sun (Marty et al. 2011), considered to be representative of the protosolar nebula, to 50 in some organic materials of chondrite and interplanetary dust particles (Messenger 2000; Bonal et al. 2010). Any object of the solar system (except Jupiter) is actually enriched in ^{15}N compared to the protosolar nebula.

Different hypotheses have been proposed to explain this enrichment. Chemical models (Rodgers & Charnley 2008) have shown that interstellar chemistry can produce ^{15}N enrichment for both molecules carrying the nitrile (–CN) functional group and those carrying the amine (–NH) functional group. A recent work suggests that these differences would simply reflect the different interstellar N reservoirs from which N-bearing molecules originate (Hily-Blant et al. 2013). Based on observations of $H^{13}CN$ and $HC^{15}N$ in two prestellar cores, the authors suggested that the molecules carrying the nitrile functional group would be more enriched in ^{15}N than the molecules carrying the amine functional group. Nevertheless, such a theory still requires further observations and modeling before it can be confirmed.

Comets are interesting targets with which to test this theory because they contain both HCN and NH_3 molecules (leading to CN and NH_2 radicals after photodissociation by solar radiation). So far, the $^{14}N/^{15}N$ ratio has only been measured in comets from HCN and CN (Jehin et al. 2009). It has been measured in about 20 bright comets through optical observations of the CN radical (Arpigny et al. 2003; Manfroid et al. 2009) and for a few comets from millimeter observations of HCN (Bockelée-Morvan et al. 2005, 2008). For both species, the measurements give the same non-terrestrial isotopic composition ($^{14}N/^{15}N \simeq 150$ in comets versus 272 in Earth's atmosphere) and do not depend on the origin of the comets (Jehin et al. 2009).

In this work our objective is to measure the $^{14}N/^{15}N$ isotopic ratio in comets for a radical bearing the amine functional group, NH_2. This radical is assumed to be produced by photodissociation of the NH_3 molecule since: (1) 95% of photodissociated NH_3 molecules in comets produce NH_2 radicals, (2) NH_3 is, by far, the most abundant molecule observed in comets able to produce NH_2, and (3) simultaneous measurements of NH_3 and NH_2 abundances in comets have provided similar values (Kawakita & Mumma 2011). We first conducted laboratory experiments to measure the wavelengths of the most intense $^{15}NH_2$ lines, which were poorly known, with sufficient accuracy. In addition, we processed a large sample of high-resolution cometary spectra obtained during the last decade and coadded them in the corresponding wavelength range. We then obtained an average spectrum with a very high signal-to-noise ratio to search for the faint $^{15}NH_2$ emission lines. We succeeded in detecting seven of them. From this positive detection of $^{15}NH_2$ emission lines, for the first time, it was possible to derive an estimate of the $^{14}N/^{15}N$ isotopic ratio in comets for a species bearing the amine functional group.

2. DETERMINATION OF $^{15}NH_2$ LINE WAVELENGTHS

Cometary spectra show emission of $^{14}NH_2$ bands around 5700 Å and 6000 Å ((0, 10, 0)–(0, 0, 0) and (0, 9, 0)–(0, 0, 0) bands in linear notation, respectively). Due to the lack of precise line lists with which to identify the cometary $^{15}NH_2$ lines, in the laboratory, we investigated the emission spectrum of $^{15}NH_2$ in the 5550–6250 Å (16,000–18,000 cm^{-1}) spectral range where the most intense lines are expected.

The emission spectrum has been recorded using the Fourier transform (FT) interferometer of the AILES beamline of the synchrotron SOLEIL equipped with a quartz-visible beamsplitter

Retour à la table des matières : p. v

and an avalanche photodiode detector. The experiment was implanted on the AILES beamline as described in Yu et al. (2010) except that in the present case one plane mirror and a single 30 cm focal length lense collected the plasma emission and focused it on the entrance aperture of the FT interferometer. The $^{15}NH_2$ radical was produced in a 13.5 MHz radiofrequency (RF) discharge of about 1 mbar of pure $^{15}NH_3$ continuously flowing through a 100 cm length and 2 cm diameter pyrex cell placed collinear to the RF coil axis. The spectral resolution was set to 0.05 cm^{-1} (0.017 Å) and the final spectrum is a coaddition of 288 interferograms corresponding to a total of about 2 hr of acquisition time. Together with the weak emission lines of $^{15}NH_2$, we detected numerous intense transitions of $^{15}N_2$ and H_2 in the spectrum. The presence of these spurious lines complicated the spectroscopic analysis of the $^{15}NH_2$ optical transitions but allowed accurate calibration of their frequencies (Bailly & Vervloet 2007; Salumbides et al. 2008; Bailly et al. 2010).

The emission lines measured in this work (both from laboratory and observational spectra) correspond to rovibronic transitions between the two Renner–Teller components of NH_2 which correlate to the $^2\Pi_u$ electronic ground state in the linear configuration. As for $^{14}NH_2$, the $\tilde{X}^2B_1$ electronic ground state of $^{15}NH_2$ is bent, whereas the $\tilde{A}^2A_1$ excited state is quasilinear (Herzberg 1966). Numerous studies have been devoted to experimental and theoretical understanding of the complex Renner–Teller effect for $^{14}NH_2$, and we refer to Dressler & Ramsay (1959) for the detailed description of the spectroscopic notations. In the following, we adopt the usual description of rotational quantum numbers $N_{K_aK_c}$ for asymmetric top molecules. Due to its unpaired electron each $N_{K_aK_c}$ level is split in two sublevels through spin-rotation interaction identified as F_1 ($N = J - 1/2$) and F_2 ($N = J + 1/2$). The vibrational quantum numbers are described as: (ν_1, ν_2, ν_3).

3. OBSERVATIONAL DATA

The cometary data are high-resolution spectra obtained at the European Southern Observatory (ESO) using the 8.2 m Kueyen telescope (UT2) of the Very Large Telescope with the Ultraviolet and Visual Echelle Spectrograph (UVES) instrument (Dekker et al. 2000). This instrument is a cross-dispersed echelle spectrograph designed to operate with high efficiency from the atmospheric cut-off at 300 nm to the long-wavelength limit of the CCD detectors (about 1100 nm).

We searched for the $^{15}NH_2$ emission lines in a series of high-resolution spectra collected with UVES on 12 different comets between 2002 and 2011 (resolving power $\lambda/\Delta\lambda \simeq 80{,}000$). The reduction procedure is detailed in Manfroid et al. (2009) and Decock et al. (2013). The UVES arc lamp wavelength calibration was corrected using the [O I] night sky emission lines. The BASS2000 solar spectrum was used to remove the absorption features of the cometary dust scattered light. Table 1 presents the detail of the 39 spectra used for our study. Because of the expected faintness of $^{15}NH_2$ emission lines we combined the normalized spectra using weights proportional to the square of the signal-to-noise ratio (column "Ratio" in Table 1). We obtained a single combined spectrum with the best signal-to-noise ratio that could be obtained from all our observational data.

4. SEARCH FOR $^{15}NH_2$ EMISSION LINES

We used the combined spectrum to search for $^{15}NH_2$ emission lines. To perform this search we established a list of all the $^{14}NH_2$ emission lines having a significant intensity and searched for their equivalent $^{15}NH_2$ lines for both the (0, 10, 0)–(0, 0, 0) and (0, 9, 0)–(0, 0, 0) bands. Unfortunately the spectral region corresponding to the (0, 9, 0)–(0, 0, 0) band contains numerous bright $^{14}NH_2$ and C_2 emission lines, preventing the detection of faint $^{15}NH_2$ emission lines. In the spectral region corresponding to the (0, 10, 0)–(0, 0, 0) band it was possible to detect seven different faint emission lines corresponding exactly to the $^{15}NH_2$ wavelengths resulting from the rotational analysis of the laboratory spectrum.

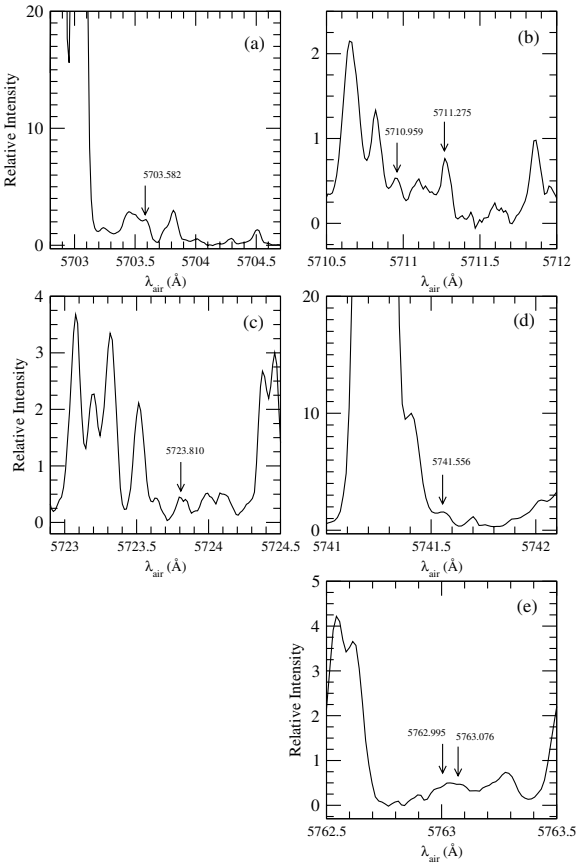

Figure 1. Emission lines of the average cometary spectrum attributed to $^{15}NH_2$ in the (0, 10, 0)–(0, 0, 0) band.

Table 2 presents the assignments and the wavelengths of the identified $^{15}NH_2$ lines with their $^{14}NH_2$ counterparts. Figure 1 shows the details of each emission line attributed to $^{15}NH_2$ (two of them, at 5762.995 and 5763.076 Å being unresolved). To identify the lines due to other species we used the cometary line atlas based on spectra obtained on comet 122P/de Vico (Cochran & Cochran 2002).

5. DISCUSSION

From the detected $^{15}NH_2$ emission lines it is possible to derive a $^{14}N/^{15}N$ ratio for NH_3, the parent molecule of NH_2. In fact, a rigorous calculation of this ratio requires an important work of calculations and significant complementary laboratory experiments. Nevertheless it is possible to get a good estimate

Retour à la table des matières : p. v

Table 1
Spectra of Comets Used for This Study

Comet	UT Date	MJD	Exp. Time (s)	r (au)	$\dot{r}$ (km s^{-1})	Δ (au)	$\dot{\Delta}$ (km s^{-1})	Ratio
C/2000 WM1 (LINEAR)	2002 Mar 7	52340.3623	1550	1.084	28.258	1.237	0.258	359
C/2000 WM1 (LINEAR)	2002 Mar 7	52340.3808	1550	1.084	28.258	1.237	0.278	386
C/2000 WM1 (LINEAR)	2002 Mar 8	52341.3682	1550	1.100	28.266	1.237	0.132	493
C/2000 WM1 (LINEAR)	2002 Mar 8	52341.3867	1550	1.100	28.266	1.237	0.155	301
C/2002 V1 (NEAT)	2003 Jan 8	52647.0373	2100	1.222	−36.514	0.833	7.871	700
C/2002 V1 (NEAT)	2003 Jan 8	52647.0622	2100	1.221	−36.521	0.833	7.916	723
C/2002 V1 (NEAT)	2003 Jan 10	52649.0312	2100	1.180	−37.105	0.842	8.272	741
C/2002 V1 (NEAT)	2003 Jan 10	52649.0562	1987	1.179	−37.113	0.842	8.313	555
C/2002 X5 (Kudo-Fujikawa)	2003 Feb 19	52689.0132	2000	0.697	43.032	0.865	−5.052	885
C/2002 V1 (NEAT)	2003 Mar 21	52719.9854	600	1.012	39.761	1.626	42.003	467
C/2002 Y1 (Juels-Holvorcem)	2003 May 29	52788.3943	1800	1.142	24.091	1.556	−7.220	682
C/2002 Y1 (Juels-Holvorcem)	2003 May 29	52788.4157	1800	1.142	24.093	1.556	−7.195	600
C/2002 Y1 (Juels-Holvorcem)	2003 May 30	52789.3935	1800	1.156	24.184	1.552	−7.198	508
C/2002 Y1 (Juels-Holvorcem)	2003 May 30	52789.4149	1800	1.156	24.186	1.552	−7.172	517
C/2001 Q4 (NEAT)	2003 Sep 1	52883.2929	4500	3.730	−18.803	3.448	−25.411	724
88P/Howell	2004 May 2	53127.3723	3600	1.385	2.988	1.648	−3.250	382
88P/Howell	2004 May 3	53128.3630	3600	1.387	3.131	1.646	−3.198	350
88P/Howell	2004 May 4	53129.3715	3600	1.388	3.276	1.644	−3.126	163
C/2001 Q4 (NEAT)	2004 May 5	53130.9577	119	0.978	−5.426	0.322	−4.120	269
C/2001 Q4 (NEAT)	2004 May 6	53131.0658	2189	0.977	−5.363	0.322	−3.287	928
C/2002 T7 (LINEAR)	2004 May 6	53131.4214	1080	0.680	15.835	0.607	−65.603	1115
C/2001 Q4 (NEAT)	2004 May 7	53132.0650	2148	0.974	−4.841	0.321	2.228	863
C/2002 T7 (LINEAR)	2004 May 26	53151.9760	2678	0.940	25.576	0.414	54.973	1922
C/2002 T7 (LINEAR)	2004 May 27	53152.0357	1800	0.941	25.585	0.416	55.188	1467
C/2003 K4 (LINEAR)	2004 Nov 20	53329.3438	1499	1.202	14.810	1.510	−28.215	632
73P-C/SW 3	2006 May 27	53882.3666	4799	0.952	−4.168	0.151	12.320	128
8P/Tuttle	2008 Jan 16	54481.0208	3599	1.041	−4.292	0.358	21.631	185
8P/Tuttle	2008 Jan 28	54493.0178	3899	1.027	0.404	0.522	24.711	959
8P/Tuttle	2008 Feb 4	54500.0169	3899	1.034	3.159	0.621	24.155	1033
103P/Hartley 2	2010 Nov 5	55505.3044	2899	1.065	2.533	0.159	7.081	701
103P/Hartley 2	2010 Nov 5	55505.3470	3199	1.065	2.546	0.159	7.194	500
103P/Hartley 2	2010 Nov 10	55510.3036	2899	1.074	4.054	0.181	7.961	716
103P/Hartley 2	2010 Nov 10	55510.3466	3199	1.074	4.067	0.182	8.072	807
103P/Hartley 2	2010 Nov 11	55511.2453	4499	1.076	4.333	0.186	7.954	522
103P/Hartley 2	2010 Nov 11	55511.3048	3599	1.077	4.351	0.186	8.088	506
103P/Hartley 2	2010 Nov 11	55511.3447	2399	1.077	4.363	0.186	8.191	579
C/2009 P1 (Garradd)	2011 Sep 10	55814.0190	4799	2.092	−14.825	1.474	14.622	272
C/2009 P1 (Garradd)	2011 Sep 11	55815.0020	4799	2.084	−14.769	1.482	15.126	330
C/2009 P1 (Garradd)	2011 Sep 12	55816.0102	4799	2.075	−14.710	1.491	15.675	430

Notes. UT Date is for mid-exposure, r is the heliocentric distance, $\dot{r}$ the heliocentric velocity, Δ the geocentric distance, $\dot{\Delta}$ the geocentric velocity, and the ratio is the ratio between the brightest emission line in the range 3899–5695 Å range and the noise.

of the $^{14}N/^{15}N$ ratio in NH_3 by adopting reasonable assumptions. These assumptions, discussed below, are: (1) a similar photodissociation efficiency for $^{14}NH_3$ and $^{15}NH_3$ to produce, respectively, $^{14}NH_2$ and $^{15}NH_2$ radicals and (2) similar transition probabilities for both $^{14}NH_2$ and $^{15}NH_2$.

For the photodissociation efficiency with respect to the solar radiation it would be necessary to conduct complementary laboratory experiments for measuring the absorption cross section for both $^{14}NH_3$ and $^{15}NH_3$. Some results of laboratory experiments relative to this problem have, nevertheless, already been published (Suto & Lee 1983; Liang et al. 2007). These papers show that the oscillator strength f, defined by $1.13 \times 10^{-6} \int \sigma d\nu$ (where σ is the absorption cross section in megabarns ($= 10^{-18}$ cm^2) and ν the wavenumber (cm^{-1})) is only 7.3% greater for $^{15}NH_3$ compared to $^{14}NH_3$ (Liang et al. 2007) in the 165–220 nm range (corresponding to the main region of photodissociation for these molecules). For shorter wavelengths, especially the Lyα region, only $^{14}NH_3$ absorption cross sections are available (Suto & Lee 1983). At the Lyα wavelength the $^{14}NH_3$ cross section is smaller than in the 165–220 nm range (about 10×10^{-18} cm^2 versus about 20×10^{-18} cm^2). Even if the Lyα emission line would correspond to very different absorption cross sections for $^{15}NH_3$ and $^{14}NH_3$ it could not lead to a large overall difference in the photodissociation rate for these two molecules because the solar Lyα flux represents only a few percent of the total solar flux in the 165–220 nm range.[4] Complementary laboratory data would be welcome to evaluate accurately the difference of photodissociation efficiency for $^{14}NH_3$ and $^{15}NH_3$. It is nevertheless highly probable that no significant difference exists.

Equal transition probabilities are generally adopted for the two isotopic species when measuring isotopic ratios from line intensity ratios. In the case of the $^{14}NH_2$ and $^{15}NH_2$ radicals,

[4] See data from the LASP Interactive Solar Irradiance Data Center available at http://lasp.colorado.edu/lisird/whi_ref_spectra/.

Retour à la table des matières : p. v

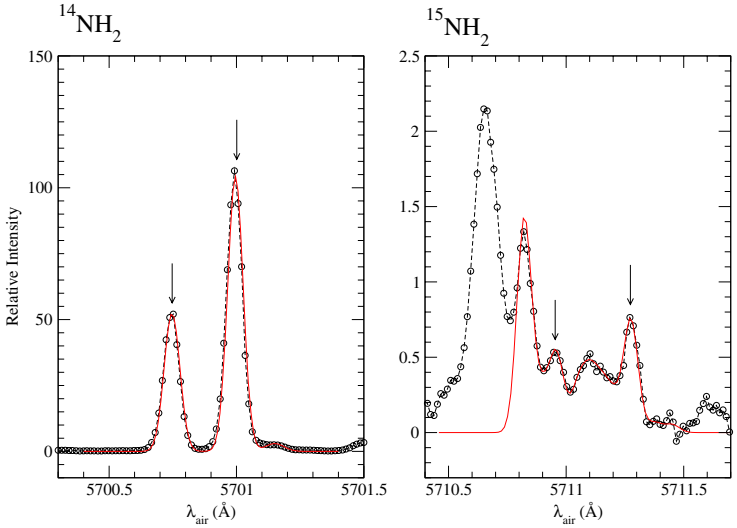

Figure 2. Modeling used to derive the $^{14}NH_2/^{15}NH_2$ emission line ratio on the average cometary spectrum for the $^{15}NH_2$ lines located at 5710.959 and 5711.275 Å. (A color version of this figure is available in the online journal.)

Table 2
$^{15}NH_2$ Emission Lines Identified in the Average Cometary Spectrum

Line Identification	Air Wavelength (Å)	$^{14}NH_2$ Counterpart Air Wavelength (Å)	Ratio
$1_{10} - 0_{00}$ $(F_1 - F_1)$	5703.582	5693.594	91^{+50}_{-30}
$1_{11} - 1_{01}$ $(F_2 - F_2)$	5710.959	5700.747	101^{+60}_{-40}
$1_{11} - 1_{01}$ $(F_1 - F_1)$	5711.275	5700.996	137^{+50}_{-30}
$1_{10} - 2_{02}$ $(F_1 - F_1)$	5723.810	5713.790	118^{+60}_{-40}
$1_{10} - 2_{20}$ $(F_1 - F_1)$	5741.556	5731.683	180 ± 80
$3_{12} - 4_{22}$ $(F_1 - F_1)$	5762.995	5752.752	135^{+60}_{-40}
$3_{12} - 4_{22}$ $(F_2 - F_2)$	5763.076	5752.800	135^{+60}_{-40}

Notes. The $^{14}NH_2$ wavelengths are computed from the wavenumbers given in Ross et al. (1988). The ratio is the intensity ratio of $^{14}NH_2$ emission lines with the associated $^{15}NH_2$ lines (note identical ratios for the last two lines which appear blended).

this assumption could be invalidated by the Renner–Teller effect. This effect concerns the low-lying rovibronic levels (with $K_a \neq 0$) of the electronic excited state with higher rovibronic levels of the electronic ground state. In point of fact, the almost constant isotopic shift between the wavelengths of the selected transitions of Table 2 indicates that no severe perturbations resulting from a strong resonance between two interacting levels occur for the excited rovibronic levels of the subband $K_a = 1$ (0, 10, 0)–(0, 0, 0) of Table 2.

The intensity ratio between $^{14}NH_2$ and $^{15}NH_2$ emission lines was measured for each detected $^{15}NH_2$ line using the $^{14}NH_2$ corresponding line. In some cases, because of a blend of the $^{15}NH_2$ line with another emission line (due to either $^{14}NH_2$ or C_2) we used an ad hoc fitting of these perturbing lines before measuring the $^{15}NH_2$ line intensity by fitting it with a synthetic line convolved with the instrument response function.

Adopting a Gaussian analytical expression for the line profiles, we have simultaneously adjusted the intensities of the N lines considered in a wavelength range bracketing the line(s) of interest (i.e., for $^{14}NH_2$ or $^{15}NH_2$). This task was performed thanks to a classical Levenberg–Marquardt algorithm (Press et al. 1992). The FWHM, thought to be uniform, has been determined previously in applying the same technique.

In order to maximize the signal-to-noise ratio this analysis has been applied to the combined cometary spectrum. Table 2 presents the ratios measured for each couple of $^{14}NH_2$ and associated $^{15}NH_2$ lines. The uncertainties cited give the deviations of the values for which acceptable fits are obtained using various procedures. From this table it can be seen that, within the error, all the intensity ratios are compatible with each other. In some cases a blend with other very weak and unidentified emission lines cannot be excluded. Such a blend could lead to an underestimation of the $^{14}N/^{15}N$ ratio in one or two lines. From Table 2 we can compute an average $^{14}NH_2/^{15}NH_2$ ratio of 127. A simple computation of the standard deviation gives $\sigma = 32$ but the average of the uncertainties provides a range of values from ~80 to ~190. The latter range of values is probably more appropriate because of the difficulty in accurately subtracting the solar continuum for each region of interest. Figure 2 presents the modeling done for the $^{15}NH_2$ lines located at 5710.959 and 5711.275 Å and their $^{14}NH_2$ counterparts.

This ratio of 127 obtained with the average spectrum is probably very close to the $^{14}N/^{15}N$ ratio in the NH_3 molecules, with the two reasonable assumptions mentioned above. It is close to the $^{14}N/^{15}N$ ratio measured both in HCN and in CN.

So far, the $^{14}N/^{15}N$ ratio measured in solar system objects presents variations that remain difficult to interpret. The analysis of Genesis solar wind samples (Marty et al. 2011) suggests a $^{14}N/^{15}N$ ratio of 441 ± 5, in agreement with the in situ measurements made in the ammonia of Jupiter's atmosphere (Fouchet et al. 2004) which probably comes from primordial N_2 (Owen et al. 2001). In contrast, with a value of 272 in the atmospheric N_2, Earth's ratio is enriched in ^{15}N compared to Jupiter and is similar to the bulk of ratios derived from the analysis of comet 81P/wild 2 grains (Mckeegan et al. 2006). Nitrogen isotopic ratios have also been measured in Titan's

Retour à la table des matières : p. v

atmosphere, which is dominated by N_2 molecules. The two existing measurements, found to be 167.7 ± 0.6 and 143 from the *Cassini* GCMS and INMS data (Niemann et al. 2010; Mandt et al. 2009), respectively, are found to be lower than the Earth's value. Because of the low abundance of primordial Ar observed by *Cassini-Huygens*, it is generally assumed that N_2 is of secondary origin in this atmosphere and was delivered in a less volatile form, probably NH_3. Different mechanisms have been proposed for the conversion of NH_3 to N_2: photolysis (Atreya et al. 1978), atmospheric shock heating (McKay et al. 1988), endogenic production (Glein et al. 2009), and impacts during the late heavy bombardment (Sekine et al. 2011). Isotopic fractionation may have occurred for nitrogen in Titan's atmosphere, nevertheless the atmospheric model published by Mandt et al. (2009) suggests that the current $^{14}N/^{15}N$ ratio observed in N_2 is close to the value acquired by the primordial ammonia of Titan. Sekine et al. (2011) also predict that $^{14}N/^{15}N$ values in NH_3 in comets and Enceladus' plume would be as high as that of Titan's N_2. A $^{14}N/^{15}N$ ratio in the ammonia of comets significantly lower than the "primordial" solar wind/Jupiter value, and similar to the one measured on Titan, assumed to be representative of its primordial value, favors the hypothesis that comets and Titan were assembled from building blocks sharing a common formation location in the nebula. This idea is supported by the measurement of the D/H ratio in the plumes emitted from Saturn's other moon, Enceladus, by the INMS instrument aboard the *Cassini* spacecraft, which is found to be similar to the values derived from Oort Cloud comets (Waite et al. 2009; Kavelaars et al. 2011).

The aforementioned measurements suggest that N_2 and NH_3 result from the separation of nitrogen into at least two distinct reservoirs, with distinct ^{15}N enrichment, which never equilibrated. Ion–molecule chemistry in dense interstellar and/or protostellar material could create ^{15}N enrichment in the ammonia ice that is produced in these environments (Charnley & Rodgers 2002). Alternatively, the ^{15}N enrichment observed in cometary ices could result from isotopic fractionation processes that occurred in the late protosolar nebula (Aléon 2010). More observational constraints are needed to test these scenarios such as more accurate and independent measurements of the nitrogen ratio in NH_2 for comets of different origins. Our work demonstrates that such measurements are now possible in the near future.

REFERENCES

Aléon, J. 2010, ApJ, 722, 1342
Arpigny, C., Jehin, E., Manfroid, J., et al. 2003, Sci, 301, 1522
Atreya, S. K., Donahue, T. M., & Kuhn, W. R. 1978, Sci, 201, 611
Bailly, D., Salumbides, E. J., Vervloet, M., & Ubachs, W. 2010, MolPh, 108, 827
Bailly, D., & Vervloet, M. 2007, MolPh, 105, 1559
Bockelée-Morvan, D., Biver, N., Jehin, E., et al. 2008, ApJL, 679, L49
Bockelée-Morvan, D., Crovisier, J., Mumma, M., & Weaver, H. 2005, in Comets II, ed. M. Festou, H. U. Keller, & H. A. Weaver (Tucson, AZ: Univ. Arizona Press), 391
Bonal, L., Huss, G. R., Krot, A. N., et al. 2010, GeCoA, 74, 6590
Charnley, S. B., & Rodgers, S. D. 2002, ApJL, 569, L133
Cochran, A. L., & Cochran, W. D. 2002, Icar, 157, 297
Decock, A., Jehin, E., Hutsemékers, D., & Manfroid, J. 2013, A&A, 555, A34
Dekker, H., D'Odorico, S., Kaufer, A., Delabre, B., & Kotzlowski, H. 2000, Proc. SPIE, 4008, 534
Dressler, K., & Ramsay, D. A. 1959, RSPTA, 251, 553
Fouchet, T., Irwin, P. G. J., Parrish, P., et al. 2004, Icar, 172, 50
Glein, C. R., Desch, S. J., & Shock, E. L. 2009, Icar, 204, 637
Herzberg, G. 1966, Molecular Spectra and Molecular Structure: III. Electronic Spectra and Electronic Structure of Polyatomic Molecules (New York: Van Nostrand-Reinhold)
Hily-Blant, P., Bonal, L., Faure, A., & Quirico, E. 2013, Icar, 223, 582
Jehin, E., Manfroid, J., Hutsemékers, D., Arpigny, C., & Zucconi, J.-M. 2009, EM&P, 105, 167
Kavelaars, J. J., Mousis, O., Petit, J.-M., & Weaver, H. A. 2011, ApJL, 734, L30
Kawakita, H., & Mumma, M. J. 2011, ApJ, 727, 91
Liang, M.-C., Cheng, B.-M., Lu, H.-C., et al. 2007, ApJL, 657, L117
Mandt, K. E., Waite, J. H., Lewis, W., et al. 2009, PASS, 57, 1917
Manfroid, J., Jehin, E., Hutsemékers, D., et al. 2009, A&A, 503, 613
Marty, B., Chaussidon, M., Wiens, R. C., Jurewicz, A. J. G., & Burnett, D. S. 2011, Sci, 332, 1533
McKay, C. P., Scattergood, T. W., Pollack, J. B., Borucki, W. J., & van Ghyseghem, H. T. 1988, Natur, 332, 520
McKeegan, K. D., Aléon, J., Bradley, J., et al. 2006, Sci, 314, 1724
Messenger, S. 2000, Natur, 404, 968
Niemann, H. B., Atreya, S. K., Demick, J. E., et al. 2010, JGRE, 115, 12006
Owen, T., Mahaffy, P. R., Niemann, H. B., Atreya, S., & Wong, M. 2001, ApJL, 553, L77
Press, W., Teukolsky, S., Vetterling, W., & Flannery, B. 1992, Numerical Recipes in Fortran 77 (Cambridge: Cambridge Univ. Press)
Rodgers, S. D., & Charnley, S. B. 2008, ApJ, 689, 1448
Ross, S. C., Birss, F. W., Vervloet, M., & Ramsay, D. A. 1988, JMoSp, 129, 436
Salumbides, E. J., Bailly, D., Khramov, A., et al. 2008, PhRvL, 101, 223001
Sekine, Y., Genda, H., Sugita, S., Kadono, T., & Matsui, T. 2011, NatGe, 4, 359
Suto, M., & Lee, L. C. 1983, JCP, 78, 4515
Waite, J. H., Jr., Lewis, W. S., Magee, B. A., et al. 2009, Natur, 460, 487
Yu, S., Pearson, J. C., Drouin, B. J., et al. 2010, JChPh, 133, 174317

Retour à la table des matières : p. v

C.4 Article sur le concept de mission EChO

Exp Astron (2015) 40:329–391
DOI 10.1007/s10686-015-9484-8

ORIGINAL ARTICLE

The EChO science case

Giovanna Tinetti[1] · Pierre Drossart[2] · Paul Eccleston[3] · Paul Hartogh[4] · Kate Isaak[5] · Martin Linder[5] · Christophe Lovis[6] · Giusi Micela[7] · Marc Ollivier[8,2] · Ludovic Puig[5] · Ignasi Ribas[9] · Ignas Snellen[10] · Bruce Swinyard[3,1] · France Allard[11] · Joanna Barstow[12] · James Cho[13] · Athena Coustenis[2] · Charles Cockell[14] · Alexandre Correia[15] · Leen Decin[16] · Remco de Kok[17] · Pieter Deroo[18] · Therese Encrenaz[2] · Francois Forget[19] · Alistair Glasse[20] · Caitlin Griffith[21] · Tristan Guillot[22] · Tommi Koskinen[21] · Helmut Lammer[23] · Jeremy Leconte[24,19] · Pierre Maxted[25] · Ingo Mueller-Wodarg[26] · Richard Nelson[13] · Chris North[27] · Enric Pallé[28] · Isabella Pagano[29] · Guseppe Piccioni[30] · David Pinfield[31] · Franck Selsis[32] · Alessandro Sozzetti[33] · Lars Stixrude[1] · Jonathan Tennyson[1] · Diego Turrini[30] · Mariarosa Zapatero-Osorio[34] · Jean-Philippe Beaulieu[35] · Denis Grodent[36] · Manuel Guedel[37] · David Luz[38] · Hans Ulrik Nørgaard-Nielsen[39] · Tom Ray[40] · Hans Rickman[41,42] · Avri Selig[17] · Mark Swain[18] · Marek Banaszkiewicz[41] · Mike Barlow[1] · Neil Bowles[12] · Graziella Branduardi-Raymont[43] · Vincent Coudé du Foresto[2] · Jean-Claude Gerard[36] · Laurent Gizon[4] · Allan Hornstrup[45] · Christopher Jarchow[4] · Franz Kerschbaum[37] · Géza Kovacs[45] · Pierre-Olivier Lagage[46] · Tanya Lim[3] · Mercedes Lopez-Morales[9] · Giuseppe Malaguti[47] · Emanuele Pace[48] · Enzo Pascale[27] · Bart Vandenbussche[16] · Gillian Wright[20] ·

✉ Giovanna Tinetti
g.tinetti@ucl.ac.uk

[1] Department of Physics & Astronomy, University College London, WC1E6BT London, UK

[2] LESIA, Observatoire de Paris, Meudon, France

[3] STFC Rutherford Appleton Laboratory, Harwell Campus, Didcot OX11 0QX, UK

[4] Max-Planck-Institut für Sonnensystemforschung, Katlenburg-Lindau, Germany

[5] European Space Agency-ESTEC, Noordwijk, The Netherlands

[6] Geneva Observatory, Geneva, Switzerland

[7] INAF: Osservatorio Astronomico di Palermo G.S. Vaiana, Palermo, Italy

[8] Institut d'Astrophysique Spatiale, Orsay, France

[9] Institut d'Estudis Espacials de Catalunya (ICE-CSIC), Barcelona, Spain

[10] Leiden University, Leiden, The Netherlands

[11] Ecole Normale Superieure, Lyon, France

[12] Oxford University, Oxford, UK

[13] Queen Mary University London, London, UK

Retour à la table des matières : p. v

Gonzalo Ramos Zapata[49] · Alberto Adriani[30] · Ruymán Azzollini[40] · Ana Balado[49] · Ian Bryson[20] · Raymond Burston[4] · Josep Colomé[9] · Martin Crook[3] · Anna Di Giorgio[30] · Matt Griffin[27] · Ruud Hoogeveen[17] · Roland Ottensamer[37] · Ranah Irshad[3] · Kevin Middleton[3] · Gianluca Morgante[47] · Frederic Pinsard[46] · Mirek Rataj[41] · Jean-Michel Reess[2] · Giorgio Savini[1] · Jan-Rutger Schrader[17] · Richard Stamper[3] · Berend Winter[43] · L. Abe[22] · M. Abreu[63] · N. Achilleos[1] · P. Ade[27] · V. Adybekian[62] · L. Affer[7] · C. Agnor[13] · M. Agundez[32] · C. Alard[35] · J. Alcala[58] · C. Allende Prieto[28] · F. J. Alonso Floriano[68] · F. Altieri[30] · C. A. Alvarez Iglesias[28] · P. Amado[66] · A. Andersen[51] · A. Aylward[1] · C. Baffa[56] · G. Bakos[79] · P. Ballerini[29] · M. Banaszkiewicz[41] · R. J. Barber[1] · D. Barrado[34,49] · E. J. Barton[1] · V. Batista[35] · G. Bellucci[30] · J. A. Belmonte Avilés[28] · D. Berry[63] · B. Bézard[2] · D. Biondi[30] · M. Błęcka[41] · I. Boisse[62] · B. Bonfond[36] · P. Bordé[8] · P. Börner[4] · H. Bouy[34,49] · L. Brown[18] · L. Buchhave[51] · J. Budaj[65] · A. Bulgarelli[47] · M. Burleigh[74] · A. Cabral[63] · M. T. Capria[30] · A. Cassan[35] · C. Cavarroc[46] · C. Cecchi-Pestellini[7] · R. Cerulli[30] · J. Chadney[26] · S. Chamberlain[63] · S. Charnoz[46] · N. Christian Jessen[44] · A. Ciaravella[7] · A. Claret[66] · R. Claudi[59] · A. Coates[43] · R. Cole[43] · A. Collura[7] · D. Cordier[52] · E. Covino[58] · C. Danielski[8] · M. Damasso[33] · H. J. Deeg[28] · E. Delgado-Mena[62] · C. Del Vecchio[56] · O. Demangeon[8] · A. De Sio[48] · J. De Wit[78] · M. Dobrijévic[32] · P. Doel[1] · C. Dominic[61] · E. Dorfi[37] · S. Eales[27] · C. Eiroa[67] · M. Espinoza Contreras[28] · M. Esposito[28] · V. Eymet[32] · N. Fabrizio[30] · M. Fernández[66] ·

[14] Royal Observatory Edinburgh, Edinburgh, UK

[15] Aveiro University, Aveiro, Portugal

[16] University of Leuven, Leuven, Belgium

[17] SRON, Institute for Space Research, Utrecht, The Netherlands

[18] NASA Jet Propulsion Laboratory, Pasadena, CA, USA

[19] LMD, Jussieu, Paris, France

[20] STFC UK-ATC, Edinburgh, UK

[21] University of Arizona, Tucson, AZ, USA

[22] Observatoire de Nice, Nice, France

[23] IWF, Graz, Austria

[24] Canadian Institute of Theoretical Astrophysics, University of Toronto, Toronto, ON, Canada

[25] Keele University, Keele, UK

[26] Imperial College, London, UK

[27] Cardiff University, Cardiff, UK

[28] Instituto de Astrofisica de Canarias, La Laguna, Tenerife, Spain

[29] INAF- OAT, Catania, Italy

[30] INAF-IAPS, Rome, Italy

[31] University of Hertfordshire, Hatfield, UK

Retour à la table des matières : p. v

B. Femenía Castella[28] · P. Figueira[62] · G. Filacchione[30] · L. Fletcher[12] · M. Focardi[48] · S. Fossey[1] · P. Fouqué[54] · J. Frith[31] · M. Galand[26] · L. Gambicorti[56] · P. Gaulme[8] · R. J. García López[28] · A. Garcia-Piquer[9] · W. Gear[27] · J.-C. Gerard[36] · L. Gesa[9] · E. Giani[56] · F. Gianotti[47] · M. Gillon[36] · E. Giro[59] · M. Giuranna[30] · H. Gomez[27] · I. Gomez-Leal[32] · J. Gonzalez Hernandez[28] · B. González Merino[28] · R. Graczyk[41] · D. Grassi[30] · J. Guardia[9] · P. Guio[1] · J. Gustin[36] · P. Hargrave[27] · J. Haigh[26] · E. Hébrard[32] · U. Heiter[42] · R. L. Heredero[63] · E. Herrero[9] · F. Hersant[32] · D. Heyrovsky[50] · M. Hollis[1] · B. Hubert[36] · R. Hueso[69] · G. Israelian[28] · N. Iro[55] · P. Irwin[12] · S. Jacquemoud[53] · G. Jones[43] · H. Jones[31] · K. Justtanont[70] · T. Kehoe[15] · F. Kerschbaum[37] · E. Kerins[75] · P. Kervella[2] · D. Kipping[78] · T. Koskinen[21] · N. Krupp[4] · O. Lahav[1] · B. Laken[28] · N. Lanza[29] · E. Lellouch[2] · G. Leto[29] · J. Licandro Goldaracena[28] · C. Lithgow-Bertelloni[1] · S. J. Liu[30] · U. Lo Cicero[7] · N. Lodieu[28] · P. Lognonné[53] · M. Lopez-Puertas[66] · M. A. Lopez-Valverde[66] · I. Lundgaard Rasmussen[44] · A. Luntzer[37] · P. Machado[63] · C. MacTavish[71] · A. Maggio[7] · J.-P. Maillard[35] · W. Magnes[23] · J. Maldonado[67] · U. Mall[4] · J.-B. Marquette[35] · P. Mauskopf[21] · F. Massi[56] · A.-S. Maurin[32] · A. Medvedev[4] · C. Michaut[53] · P. Miles-Paez[28] · M. Montalto[62] · P. Montañés Rodríguez[28] · M. Monteiro[62] · D. Montes[68] · H. Morais[15] · J. C. Morales[2] · M. Morales-Calderón[34,49] · G. Morello[1] · A. Moro Martín[34,49] · J. Moses[80] · A. Moya Bedon[34,49] · F. Murgas Alcaino[28] · E. Oliva[56] · G. Orton[18] · F. Palla[56] · M. Pancrazzi[48] · E. Pantin[46] · V. Parmentier[22] ·

[32] Université de Bordeaux, Bordeaux, France

[33] INAF, Torino, Italy

[34] CAB, Madrid, Spain

[35] Institut d'Astrophysique de Paris, Paris, France

[36] Université de Liège, Liège, Belgium

[37] University of Vienna, Vienna, Austria

[38] Universidade de Lisboa, Lisbon, Portugal

[39] DSRI, Lyngby, Denmark

[40] Dublin Institute for Advanced Studies, Dublin, Ireland

[41] Space Research Centre, Polish Academy of Science, Warsaw, Poland

[42] Department of Physics and Astronomy, Uppsala University, Uppsala, Sweden

[43] Mullard Space Science Laboratory, University College London, Surrey RH5 6NT, UK

[44] DTU Space, Kongens Lyngby, Denmark

[45] Konkoly Observatory, Budapest, Hungary

[46] Centre Energie Atomique – Saclay, Gif-sur-Yvette, France

[47] INAF – IASF – Bologna, Bologna, Italy

[48] Università di Firenze, Florence, Italy

[49] INTA, Águilas, Spain

Retour à la table des matières : p. v

H. Parviainen[28] · K. Y. Peña Ramírez[28] · J. Peralta[63] · S. Perez-Hoyos[69] · R. Petrov[22] · S. Pezzuto[30] · R. Pietrzak[41] · E. Pilat-Lohinger[37] · N. Piskunov[42] · R. Prinja[1] · L. Prisinzano[7] · I. Polichtchouk[13] · E. Poretti[57] · A. Radioti[36] · A. A. Ramos[28] · T. Rank-Lüftinger[37] · P. Read[12] · K. Readorn[56] · R. Rebolo López[28] · J. Rebordão[63] · M. Rengel[4] · L. Rezac[4] · M. Rocchetto[1] · F. Rodler[9] · V. J. Sánchez Béjar[28] · A. Sanchez Lavega · E. Sanromá[28] · N. Santos[62] · J. Sanz Forcada[34,49] · G. Scandariato[7] · F.-X. Schmider[22] · A. Scholz[40] · S. Scuderi[29] · J. Sethenadh[4] · S. Shore[60] · A. Showman[21] · B. Sicardy[2] · P. Sitek[41] · A. Smith[43] · L. Soret[36] · S. Sousa[62] · A. Stiepen[36] · M. Stolarski[41] · G. Strazzulla[29] · H. M. Tabernero[68] · P. Tanga[22] · M. Tecsa[12] · J. Temple[12] · L. Terenzi[47] · M. Tessenyi[1] · L. Testi[64] · S. Thompson[71] · H. Thrastarson[77] · B. W. Tingley[28] · M. Trifoglio[47] · J. Martín Torres[81,82] · A. Tozzi[56] · D. Turrini[30] · R. Varley[1] · F. Vakili[22] · M. de Val-Borro[4] · M. L. Valdivieso[28] · O. Venot[16] · E. Villaver[67] · S. Vinatier[2] · S. Viti[1] · I. Waldmann[1] · D. Waltham[73] · D. Ward-Thompson[76] · R. Waters[17] · C. Watkins[13] · D. Watson[51] · P. Wawer[41] · A. Wawrzaszk[41] · G. White[72] · T. Widemann[2] · W. Winek[41] · T. Wiśniowski[41] · R. Yelle[21] · Y. Yung[77] · S. N. Yurchenko[1]

Received: 10 December 2014 / Accepted: 26 October 2015 / Published online: 29 November 2015
© The Author(s) 2015. This article is published with open access at Springerlink.com

[50] Charles University, Prague, Czech Republic

[51] DARK Cosmology Center, Copenhagen, Denmark

[52] Observatoire de Besancon, Besancon, France

[53] IPGP, Paris, France

[54] LATT, Toulouse, France

[55] University of Hamburg, Hamburg, Germany

[56] INAF – Arcetri, Florence, Italy

[57] INAF – Brera, Milan, Italy

[58] INAF – Capodimonte, Naples, Italy

[59] INAF – Padova, Padova, Italy

[60] Università di Pisa, Pisa, Italy

[61] University of Amsterdam, Amsterdam, The Netherlands

[62] CAUP, Porto, Portugal

[63] CAAUL, Lisbon, Portugal

[64] ESO, Garching, Germany

[65] Slovak Academy of Sciences, Bratislava, Slovakia

Retour à la table des matières : p. v

Abstract The discovery of almost two thousand exoplanets has revealed an unexpectedly diverse planet population. We see gas giants in few-day orbits, whole multi-planet systems within the orbit of Mercury, and new populations of planets with masses between that of the Earth and Neptune—all unknown in the Solar System. Observations to date have shown that our Solar System is certainly not representative of the general population of planets in our Milky Way. The key science questions that urgently need addressing are therefore: *What are exoplanets made of? Why are planets as they are? How do planetary systems work and what causes the exceptional diversity observed as compared to the Solar System*? The EChO (Exoplanet Characterisation Observatory) space mission was conceived to take up the challenge to explain this diversity in terms of formation, evolution, internal structure and planet and atmospheric composition. This requires in-depth spectroscopic knowledge of the atmospheres of a large and well-defined planet sample for which precise physical, chemical and dynamical information can be obtained. In order to fulfil this ambitious scientific program, EChO was designed as a dedicated survey mission for transit and eclipse spectroscopy capable of observing a large, diverse and well-defined planet sample within its 4-year mission lifetime. The transit and eclipse spectroscopy method, whereby the signal from the star and planet are differentiated using knowledge of the planetary ephemerides, allows us to measure atmospheric signals from the planet at levels of at least 10^{-4} relative to the star. This can only be achieved in conjunction with a carefully designed stable payload and satellite platform. It is also necessary to provide broad instantaneous wavelength coverage to detect as many molecular species as possible, to probe the thermal structure of the planetary atmospheres and to correct for the contaminating effects of the stellar photosphere. This requires wavelength coverage of at least 0.55 to 11 μm with a goal of covering from 0.4 to 16 μm. Only modest spectral resolving power is needed, with R~300 for wavelengths less than 5 μm and R~30 for wavelengths greater than this. The transit

[66] IAA, Madrid, Spain

[67] UAM, Madrid, Spain

[68] UCM, Madrid, Spain

[69] UPV, Valencia, Spain

[70] Onsala Space Observatory, Onsala, Sweden

[71] Cambridge University, Cambridge, UK

[72] Open University, Milton Keynes, UK

[73] Royal Holloway University of London, Surrey, UK

[74] University of Leicester, Leicester, UK

[75] University of Manchester, Manchester, UK

[76] University of Lancaster, Lancaster, UK

[77] California Institute of Technology, Pasadena, CA, USA

[78] Harvard Smithsonian Center for Astrophysics, Cambridge, MA, USA

[79] Princeton University, Princeton, NJ, USA

[80] Space Science Institute, Seabrook, TX, USA

[81] Instituto Andaluz de Ciencias de la Tierra (CSIC-UGR), Granada, Spain

[82] Luleå Technical University, Kiruna, Sweden

Retour à la table des matières : p. v

spectroscopy technique means that no spatial resolution is required. A telescope collecting area of about 1 m^2 is sufficiently large to achieve the necessary spectro-photometric precision: for the Phase A study a 1.13 m^2 telescope, diffraction limited at 3 μm has been adopted. Placing the satellite at L2 provides a cold and stable thermal environment as well as a large field of regard to allow efficient time-critical observation of targets randomly distributed over the sky. EChO has been conceived to achieve a single goal: exoplanet spectroscopy. The spectral coverage and signal-to-noise to be achieved by EChO, thanks to its high stability and dedicated design, would be a game changer by allowing atmospheric composition to be measured with unparalleled exactness: at least a factor 10 more precise and a factor 10 to 1000 more accurate than current observations. This would enable the detection of molecular abundances three orders of magnitude lower than currently possible and a fourfold increase from the handful of molecules detected to date. Combining these data with estimates of planetary bulk compositions from accurate measurements of their radii and masses would allow degeneracies associated with planetary interior modelling to be broken, giving unique insight into the interior structure and elemental abundances of these alien worlds. EChO would allow scientists to study exoplanets both as a population and as individuals. The mission can target super-Earths, Neptune-like, and Jupiter-like planets, in the very hot to temperate zones (planet temperatures of 300–3000 K) of F to M-type host stars. The EChO core science would be delivered by a three-tier survey. The EChO *Chemical Census*: This is a broad survey of a few-hundred exoplanets, which allows us to explore the spectroscopic and chemical diversity of the exoplanet population as a whole. The EChO *Origin*: This is a deep survey of a subsample of tens of exoplanets for which significantly higher signal to noise and spectral resolution spectra can be obtained to explain the origin of the exoplanet diversity (such as formation mechanisms, chemical processes, atmospheric escape). The EChO *Rosetta Stones*: This is an ultra-high accuracy survey targeting a subsample of select exoplanets. These will be the bright "benchmark" cases for which a large number of measurements would be taken to explore temporal variations, and to obtain two and three dimensional spatial information on the atmospheric conditions through eclipse-mapping techniques. If EChO were launched today, the exoplanets currently observed are sufficient to provide a large and diverse sample. The Chemical Census survey would consist of>160 exoplanets with a range of planetary sizes, temperatures, orbital parameters and stellar host properties. Additionally, over the next 10 years, several new ground- and space-based transit photometric surveys and missions will come on-line (e.g. NGTS, CHEOPS, TESS, PLATO), which will specifically focus on finding bright, nearby systems. The current rapid rate of discovery would allow the target list to be further optimised in the years prior to EChO's launch and enable the atmospheric characterisation of hundreds of planets.

Keywords Exoplanets · Spectroscopy · Atmospheric science · IR astronomy · Space missions

1 Introduction

1.1 Exoplanets today

Roughly 400 years ago, Galileo's observations of the Jovian moons sealed the Copernican Revolution, and the Earth was no longer considered the centre of the Universe (*Sidereus*

Retour à la table des matières : p. v

Nuncius, 1610). We are now poised to extend this revolution to the Solar System. The detection and characterisation of exoplanets force the Sun and its cohorts to abdicate from their privileged position as the archetype of a planetary system.

Recent exoplanet discoveries have profoundly changed our understanding of the formation, structure, and composition of planets. Current statistics show that planets are common; data from the Kepler Mission and microlensing surveys indicate that the majority of stars have planets [35, 68]. Detected planets range in size from sub-Earths to larger than Jupiter (Fig. 1). Unlike the Solar System, the distribution of planetary radii appears continuous [18], with no gap between 2 and 4 Earth radii. That is, there appears to be no distinct transition from telluric planets, with a thin, if any, secondary atmosphere, to the gaseous and icy giants, which retain a substantial amount of hydrogen and helium accreted from the protoplanetary disk.

The orbital characteristics among the almost 2000 exoplanets detected also do not follow the Solar System trend, with small rocky bodies orbiting close to a G star and giant gas planets orbiting further out, in roughly circular orbits. Instead giant planets can be found within 1/10 the semi-major axis of Mercury. Planets can orbit host stars with an eccentricity well above 0.9 (e.g. HD 80606b), comparable to Halley's comet. Planets can orbit two mother stars (e.g. Kepler-34b, Kepler-35b, and Kepler-38b): this is not an oddity any more. Planetary systems appear much more diverse than expected. The Solar System template does not seem to be generally applicable.

The range of orbital parameters and stellar hosts translates into planetary temperatures that span two orders of magnitude. This range of temperatures arises from the range of planet-star proximities, where a year can be less than 6 Earth-hours (e.g. KOI-55b), or over 450 Earth-years (e.g. HR 8799b), and host star temperatures, which can range from 2200 to 14,000 K. Conditions not witnessed in the Solar System lead to exotic planets whose compositions we can only speculate about. Currently, we can only guess that the extraordinarily hot and rocky planets CoRoT-7b, Kepler-10b, Kepler-78b and 55 Cnc-e sport silicate compounds in the gaseous and liquid phases [96, 137]. "Ocean planets" that have densities in between those of giant and rocky planets [73, 97,

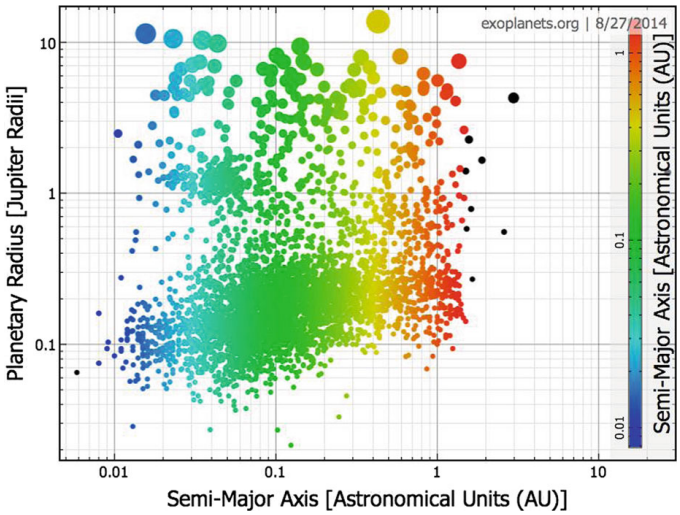

Fig. 1 Currently known exoplanets, plotted as a function of distance to the star and planetary radii (courtesy of exoplanets.org). The graph suggests a continuous distribution of planetary sizes – from sub-Earths to super-Jupiters– and planetary temperatures than span two orders of magnitude

Retour à la table des matières : p. v

153] and effective temperatures between the triple and critical temperatures of water, i.e. between 273 and 647 K (e.g. GJ 1214b) may have large water-rich atmospheres. The "Mega-Earth", Kepler-10c [59], is twice the Earth's size but is 17 times heavier than our planet, making it among the densest planets currently known.

The diversity of currently detected exoplanets not only extends the regime of known conditions, it indicates environments completely alien to the Solar System. *Observations demonstrate that the Solar System is not the paradigm in our Galaxy: one of the outstanding questions of modern astrophysics is to understand why.*

Over the past two decades, primary transit and radial velocity measurements have determined the sizes and masses of exoplanets, thereby yielding constraints on the bulk composition of exoplanets. The missions NASA-K2 and TESS and ESA-Cheops and PLATO, together with ground-based surveys, will increase by a factor of five the number of planets for which we have an accurate measurement of mass and radius. While measurements of the masses and radii of planetary systems have revealed the great diversity of planets and of the systems in which planets originate and evolve, these investigations generate a host of important questions:

(i) *What is the relationship between a planet's bulk and atmospheric composition?* The planetary density alone does not provide unique solutions. The degeneracy is higher for super-earths and small Neptunes [176]. As an example, it must be noted that a silicate-rich planet surrounded by a very thick atmosphere could have the same mass and radius as an ice-rich planet without an atmosphere [1].

(ii) *Why are many of the known transiting gaseous planets larger than expected?* These planets are larger than expected even when the possibility that they could be coreless hydrogen-helium planets is allowed for [27, 76]. There is missing physics that needs to be identified.

(iii) *For the gaseous planets, are elements heavier than hydrogen and helium kept inside a central core or distributed inside the planet?* The distribution of heavy elements influences how they cool [9, 75] and is crucial in the context of formation scenarios [103].

(iv) *How do the diverse conditions witnessed in planetary systems dictate the atmospheric composition?* An understanding of the processes that steer planetary composition bears on our ability to extrapolate to the whole galaxy, and perhaps universe, what we will learn in the solar neighbourhood.

(v) *How does the large range of insolation, planetary spin, orbital elements and compositions in these diverse planetary systems affect the atmospheric dynamics?* This has direct consequences for our ability to predict the evolution of these planets [41, 42, 130, 134, 147].

(vi) *Are planets around low mass, active stars able to keep their atmospheres*? This question is relevant e.g. to the study habitability, as given the meagre energy output of M dwarfs, their habitable zones are located much closer to the primary than those of more massive stars (e.g.~0.03 AU for stars weighting one tenth of the Sun) [93].

We cannot fully understand the atmospheres and interiors of these varied planetary systems by simple analogy with the Solar System, nor from mass and

Retour à la table des matières : p. v

radii measurements alone. As shown by the historical investigations of planets in our own Solar System, these questions are best addressed through spectroscopic measurements. However, as shown by the historical path taken in astronomy, a large sample and range of planetary atmospheres are needed to place the Solar System in an astronomical context. Spectroscopic measurements of a large sample of planetary atmospheres may divulge their atmospheric chemistry, dynamics, and interior structure, which can be used to trace back to planetary formation and evolution(Fig. 2).

In the past decade, pioneering results have been obtained using transit spectroscopy with Hubble, Spitzer and ground-based facilities, enabling the detection of a few of the most abundant ionic, atomic and molecular species and to constrain the planet's thermal structure (e.g. [36, 86, 101, 107, 108, 150, 151 160, 182]). The infrared range, in particular, offers the possibility of probing the neutral atmospheres of exoplanets. In the IR the molecular features are more intense and broader than in the visible [169] and less perturbed by clouds, hence easier to detect. On a large scale, the IR transit and eclipse spectra of hot-Jupiters seem to be dominated by the signature of water vapour (e.g. [10, 21, 26, 34, 38, 47, 48, 50, 54, 74, 91, 111, 159–161, 168–171]), similarly, the atmosphere of hot-Neptune HAT-P-11b appears to be water-rich [67]. The data available for other warm Neptunes, such as GJ 436b, GJ 3470b are suggestive of cloudy atmospheres and do not always allow a conclusive identification of their composition [22, 65, 70, 88, 117, 156]. The analysis of the transmission and day-side spectra for the transiting 6.5 M_{Earth} super-Earth GJ 1214b suggests either a metal-rich or a cloudy atmosphere [19, 25, 90, 91, 157].

Despite these early successes, the data available are still too sparse to provide a consistent interpretation, or any meaningful classification of the planets analysed. The degeneracy of solutions embedded in the current transit observations [95, 100, 105, 159, 161, 187] inhibits any serious attempt to estimate the elemental abundances. New and better quality data are needed for this purpose.

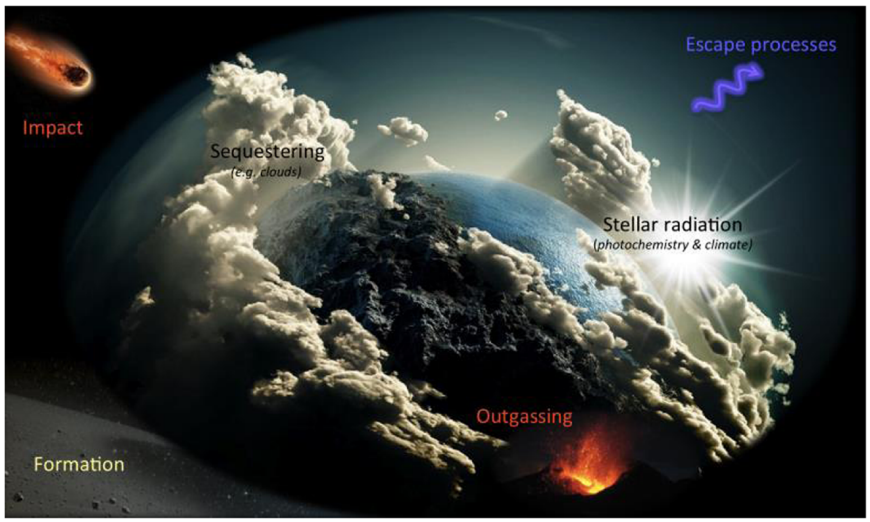

Fig. 2 Key physical processes influencing the composition and structure of a planetary atmosphere. While the analysis of a single planet cannot establish the relative impact of all these processes on the atmosphere, by expanding observations to a large number of very diverse exoplanets, we can use the information obtained to disentangle the various effects

Retour à la table des matières : p. v

Although these and other data pertaining to extrasolar planet atmospheres are tantalising, uncertainties originating in the narrow-band spectra and sparsity/non simultaneity of the data and, in some cases, low signal to noise ratio, mean that definitive conclusions concerning atmospheric abundances cannot be made today. Current data do not allow one to discriminate between different formation and evolution scenarios for the observed planets.

The Exoplanet Characterisation Observatory (EChO) [166] is a dedicated spaceborne telescope concept whose characteristics are summarised in Table 1. The spectral coverage and stability to be achieved by an EChO-like mission would be a game changer, allowing atmospheric compositions to be measured with unparalleled exactness: statistically speaking, at least a factor 10 more precisely and a factor 10 to 1000 more accurately than current observations. This would enable the detection of molecular abundances three orders of magnitude smaller than currently possible. We would anticipate at least a fourfold increase from the handful of molecules currently detected today. Each of these molecules tells us a story, and having access to a larger number means understanding aspects of these exotic planets that are today completely ignored. Combining these data with estimates of planetary bulk compositions from accurate measurements of their radii and masses will allow degeneracies associated with planetary interior modelling to be broken [2, 176], giving unique insight into the interior structure and elemental abundances of these alien worlds.

1.1.1 Major classes of planetary atmospheres: what should we expect?

EChO would address the fundamental questions "*what are exoplanets made of?*" and "*how do planets form and evolve*?" through direct measurement of bulk and atmospheric chemical composition. EChO can observe super-Earths, Neptune-like and Jupiter-like exoplanets around stars of various masses. These broad classes of planets are all expected to have very different formation, migration and evolution histories that will be imprinted on their atmospheric and bulk chemical signatures. Many theoretical studies have tried to understand and model the various processes controlling the formation and evolution of planetary atmospheres, with some success for the Solar System. However, such atmospheric evolution models need confirmation and tight calibrations from observations. In Fig. 3 we show the predicted bulk atmospheric compositions as a function of planetary temperature and mass [66, 94] and we briefly describe in the following paragraphs the possible origins of the various scenarios.

H/He dominated–Hydrogen and helium being the lightest elements and the first to be accreted, they can most easily escape. The occurrence of H/He dominated atmospheres should thus be limited to objects more massive than the Earth. Because giant planets play a pivotal role in shaping planetary systems (e.g. [172, 173]), determining precisely their internal structure and composition is essential to understand how planets form. In particular, the abundances of high-Z elements compared to the stellar values and the relative ratios of the different elements (e.g. C, N, S) represent a window on the past histories of the extrasolar systems hosting the observed planets.

In the Solar System, none of the terrestrial planetary bodies managed to accrete or keep their primordial H/He envelope, not even the coldest ones which are less

Retour à la table des matières : p. v

Table 1 EChO – Exoplanet characterisation observatory—mission summary

Key science questions to be addressed	• Why are exoplanets as they are? • What are the causes for the observed diversity? • Can their formation history be traced back from their current composition and evolution? • How does the Solar System work compared to other planetary systems?
Science objectives	• Detection of planetary atmospheres, their composition and structure • Determine vertical and horizontal temperature structure and their diurnal and seasonal variations • Identify chemical processes at work (thermochemistry, photochemistry, transport quenching) • Constrain planetary interiors (breaking the radius-mass degeneracy) • Quantify the energy budget (albedo, effective temperature) • Constrain formation and evolution models (evidence for migration) • Detect secondary atmospheres around terrestrial planets (evolution) • Investigate the impact of stellar and planetary environment on exoplanet properties
EChO core survey	• Three-tier survey of 150–300 transiting exoplanets from gas giants to super-Earths, in the very hot to temperate zones of F to M type host stars • Target selection before launch based on ESA science team and community inputs • Chemical Census: statistically complete sample detecting strongest atmospheric molecular features • Origin: retrieval of vertical thermal profiles and abundances of trace gases • Rosetta Stone: high signal-to-noise observations yielding refined molecular abundances, chemical gradients and atmospheric structure; diurnal and seasonal variations; presence of clouds and measurement of albedo • Delivery of a homogeneous catalogue of planetary spectra
EChO observational strategy	• Transit and eclipse spectroscopy with broad, instantaneous, and uninterrupted spectra covering all key molecules • High photometric stability on transit timescales • Required SNR obtained by summing a sufficient number of transits or eclipses • Large instantaneous sky coverage
Payload telescope	• Afocal 3-mirror, off-axis Korsch-like system, 1.5 m×1 m elliptical M1, unobstructed (effective area 1.13 m^2), diffraction-limited at 3 μm; <3 μm, 80 % encircled energy within diameter of 1.6 arcsec.
Payload instrument	• Highly-integrated broadband spectrometer instrument with modular architecture • Common optical train for all spectrometers and the fine guidance system optical module • Continuous wavelength coverage from 0.4 to 11 μm in baseline design • Goal wavelength coverage from 0.4 to 16 μm. • Resolving powers of $\lambda/\Delta\lambda$ >300 below 5 μm, and >30 above 5 μm • Passively cooled MCT detectors at ~40 K for FGS and science channels<5 μm • Active Ne JT Cooler provides cooling to ~28 K for science channels>5 μm
Spacecraft 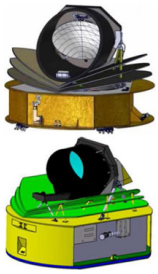	• Launch mass~1.5 tonnes • Dimensions: Ø 3.6 m×2.6 m. Designs from the two industrial studies shown to the left. • Pointing requirements: coarse APE of 10 arcsec (3σ); fine APE of 1 arcsec (3σ); PDE of 20 milli-arcseconds (1σ) over 90s to 10 h; RPE of 50 milli-arcsecond over 90s (1σ) • Attitude control system: reaction wheels and cold gas system complemented by a Fine-Guidance System operating in the visible within the AOCS control loop. • Thermal Control System: Passive cooling via 3 V-grooves to≤47 K • Telecommand, Telemetry and Communication: X-band, 35 Gbit of science data per week transmitted with a High Gain Antenna to a 35 m ESTRACK station
Launcher, orbit, mission phases and operations	• Launch from Kourou on a Soyuz-Fregat MT into L2 orbit in 2024 (possible option of launch in 2022) • Nominal mission duration 4 years (goal 6 years) • MOC at ESOC, SOC at ESAC, Instrument Operations and Science Data Centre distributed across consortium members states • 14 h ground contact/week: 2×2 h for telecommand uplink and science downlink, remainder for determination of orbital parameters
Data policy	• Short proprietary period after nominal SNR is reached, shrinking to 1 month after 3 years

Retour à la table des matières : p. v

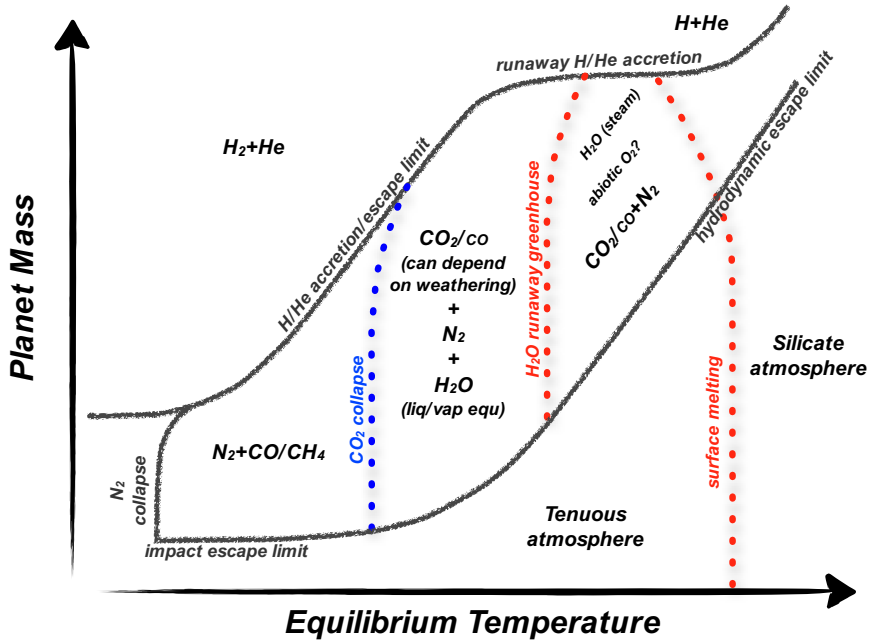

Fig. 3 Schematic summary of the various classes of atmospheres as predicted by Leconte et al. [94]. Only the expected dominant species are indicated, other (trace) gases will be present. Each line represents a transition from one regime to another, but these "transitions" need tight calibrations from observations. Interestingly, many atmospheric-regime transitions occur in the high-mass/high-temperature, domain, which is exactly where EChO is most sensitive

prone to escape. The presence of a large fraction of primordial nebular gas in the atmosphere of warm to cold planets above a few Earth masses should be fairly common. However, being more massive than that is by no means a sufficient condition: some objects have a bulk density similar to the Earth up to 8–10 M_{Earth}. Possibly planets forming on closer orbits can accrete less nebular gas [84], or hotter planets exhibit higher escape rates.

Thin silicate atmospheres–For very hot or low mass objects (lower part of Fig. 3), the escape of the lightest elements at the top of the atmosphere is a very efficient process. Bodies in this part of the diagram are thus expected to have tenuous atmospheres, if any. Among the most extreme examples, some rocky exoplanets, such as CoRoT- 7 b or 55 Cnc e, are so close to their host star that the temperatures reached on the dayside are sufficient to melt the surface itself. As a result some elements, usually referred to as "refractory", become more volatile and can form a thin "silicate" atmosphere [96]. Depending on the composition of the crust, the most abundant species should be, by decreasing abundance, Na, K, O_2, O and SiO. In addition, silicate clouds could form.

$H_2O/CO_2/N_2$ atmospheres–In current formation models, if the planet is formed much closer to –or even beyond– the snow line,[1] the water content of the planetesimals could be significantly large and tens to thousands of Earth oceans of water could be accreted [61]. This suggests the existence of a vast population of planets with deep oceans (aqua-planets) or whose bulk composition is dominated

[1] *Snow line*: distance from a central protostar at which ice grains can form. This occurs at temperatures of~ 150–170 K

Retour à la table des matières : p. v

by water (Ocean planets [97]). Another source of volatiles are the planetesimals that accrete to form the bulk of the planet itself. These will be the major sources of carbon compounds (mainly CO_2 and possibly CH_4), water (especially if they formed beyond the snow line), and, to a lesser extent, N_2/NH_3 and other trace gases. In the case of rocky planets, their low gravity field leads to H_2 escape. On a much longer, geological timescale, the volatiles that remained trapped in the mantle during the solidification can be released through volcanic outgassing. Along with H_2O and CO_2, this process can bring trace gases to the surface, such as H_2S, SO_2, CH_4, NH_3, HF, H_2, CO and noble gases. On Earth and Mars, there is strong evidence that this secondary outgassing has played a major role in shaping the present atmosphere [66].

Water vapour has a tendency to escape, as illustrated by the atmospheric evolutions of Mars and Venus. This certainly happened to the terrestrial planets in our Solar System. In Venus' and Mars' atmospheres the D/H ratio is between 5 and 200 times the Solar ratio, suggesting water on the surface was lost through time. Also their global atmospheric composition, with mostly CO_2 and a few percent of N_2, are similar. The surface pressures and temperatures are very different, though, as a result of their different initial masses and evolutions. The Earth is an exception in the Solar System, with the large abundance of O_2 and its photodissociation product O_3 as a consequence of the appearance of life [104, 139] and the conversion of CO_2 in the water oceans to $CaCO_3$.

Within each of the above planet taxonomic classes, the stochastic nature of planetary formation and evolution will be reflected in significant variations in the measured abundances, providing important information about the diverse pathways experienced by planets that reside within the same broad class. Our Solar System only provides one or two particular examples, if any, for each of the aforementioned planetary classes. It is therefore impossible to understand the "big picture" on this basis. This is where extrasolar planets are an invaluable asset. This means that, even before being able to characterise an Earth-like planet in the habitable zone, we need to be able to characterise giant planets' atmospheres and exotic terrestrial planet atmospheres in key regimes that are mostly unheard of in the Solar System. Thus, the first observations of exoplanet atmospheres, whatever they show, will allow us to make a leap forward in our understanding of planetary formation, chemistry, evolution, climates and, therefore, in our estimation of the likelihood of life elsewhere in the universe. Only a dedicated transit spectroscopy mission can tackle such an issue.

1.2 The case for a dedicated space mission

EChO has been designed as a dedicated survey mission for transit and eclipse spectroscopy capable of observing a large, diverse and well-defined planet sample within its 4 years mission lifetime. The transit and eclipse spectroscopy method, whereby the signal from the star and planet are differentiated using knowledge of the planetary ephemerides, allows us to measure atmospheric signals from the planet at levels of at least 10^{-4} relative to the star. This can only be achieved in conjunction with a carefully designed stable payload and satellite platform.

Retour à la table des matières : p. v

It is also necessary to have a broad instantaneous wavelength coverage to detect as many molecular species as possible, to probe the thermal structure of the planetary atmospheres and to correct for the contaminating effects of the stellar photosphere. Since the EChO investigation include planets with temperatures spanning from~300 K up to ~3000 K, this requires a wavelength coverage~0.55 to 11 μm with a goal of covering from 0.4 to 16 μm. Only modest spectral resolving power is needed, with R~100 for wavelengths less than 5 μm and R~30 for wavelengths greater than this.

The transit spectroscopy technique means that no angular resolution is required. A telescope collecting area of about 1 m^2 is sufficiently large to achieve the necessary spectro-photometric precision: for this study the telescope has been assumed 1.13 m^2, diffraction limited at 3 μm. Placing the satellite at L2 provides a cold and stable thermal environment as well as a large field of regard to allow efficient time-critical observation of targets randomly distributed over the sky. EChO was designed to achieve a single goal: exoplanet spectroscopy.

It is important to realise that a statistically significant number of observations must be made in order to fully test models and understand which are the relevant physical parameters. Even individual classes of planets, like hot Jupiters, exhibit great diversity, so it insufficient to study a few planets in great detail. This requires observations of a large sample of objects, generally on long timescales, which can only be done with a dedicated instrument like EChO, rather than with multi-purpose telescopes such as the James Web Space Telescope (JWST) or the European Extremely Large Telescope (E-ELT). Another significant aspect of the search relates to the possibility to discover unexpected "Rosetta Stone" objects, i.e. objects that definitively confirm or inform theories. This requires wide searches that are again possible only through dedicated instruments. EChO would allow planetary science to expand beyond the narrow boundaries of our Solar System to encompass our Galaxy. EChO would enable a paradigm shift by identifying and quantifying the chemical constituents of hundred(s) of exoplanets in various mass/temperature regimes, we would be looking no longer at individual cases but at populations. Such a universal view is critical if we truly want to understand the processes of planet formation and evolution and how they behave in various environments.

2 EChO science objectives

In this section we explain the key science objectives addressed by EChO, and how we would tackle these questions through the observations provided by EChO, combined with modeling tools and laboratory data

2.1 Key science questions addressed by EChO

EChO has been conceived to address the following fundamental questions:

- Why are exoplanets as they are?
- What are the causes for the observed diversity?
- Can their formation and evolution history be traced back from their current composition?

Retour à la table des matières : p. v

EChO would provide spectroscopic information on the atmospheres of a large, select sample of exoplanets allowing the composition, temperature (including profile), size and variability to be determined at a level never previously attempted. This information can be used to address a wide range of key scientific questions relative to exoplanets:

- *What are they made of?*
- *Do they have an atmosphere?*
- *What is the energy budget?*
- *How were they formed?*
- *Did they migrate and, if so, how?*
- *How do they evolve?*
- *How are they affected by starlight, stellar winds and other time-dependent processes?*
- *How do weather conditions vary with time?*

And of course:

- *Do any of the planets observed have habitable conditions?*

These objectives, tailored for gaseous and terrestrial planets, are detailed in the next sections and summarised in Fig. 4 and Table 2.

In the next sections we also explain how these questions can be tackled through the observations provided by EChO, combined with modelling tools and auxiliary information from laboratory data and preparatory observations with other facilities prior to the EChO launch.

2.2 Terrestrial-type planets (predominantly solid)

Several scenarios may occur for the formation and evolution of terrestrial-type planets (see 1.1.1 and Fig. 3). To start with, these objects could have formed *in situ*, or have moved from their original location because of dynamical interaction with other bodies, or they could be remnant cores of more gaseous objects which have migrated in. Due to the low planetary mass, terrestrial planets' atmospheres could have evolved quite dramatically from the initial composition, with lighter molecules, such as hydrogen, escaping more easily. Impacts with other bodies, such

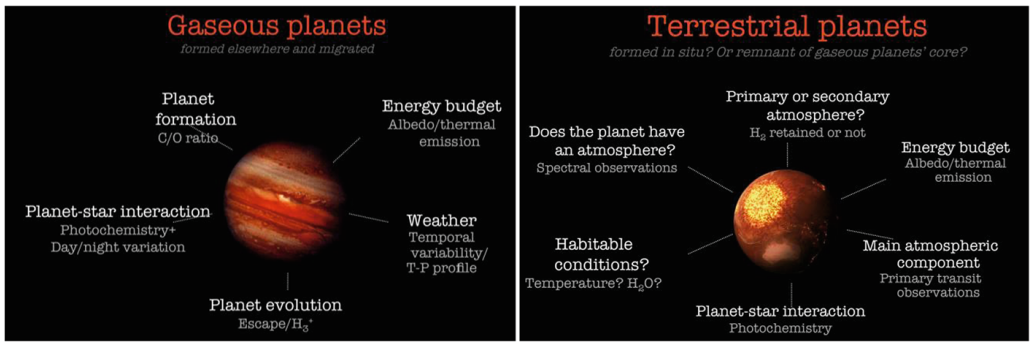

Fig. 4 Key questions for gaseous & rocky planets that will be addressed by EChO [167]

Retour à la table des matières : p. v

Table 2 Traceability matrix

Planet type	Scientific question	Observable	Observational strategy	Survey type
Gaseous planets	Energy budget	Incoming and outgoing radiation	Stellar flux+planetary albedo and thermal emission with VIS and IR photometry during eclipses	Chemical Census
	Planetary interior	a. Density b. Hints from atmospheric composition?	a. Transit spectra b. Transit and eclipse spectra	Chemical Census
	Chemical processes: Thermochemistry? Transport+quenching? Photochemistry?	a. Chemistry of planets around different stars & different temperatures b. Day/night chemical variations c. Vertical mixing ratios	a. Transit and eclipse spectra of planets around different stars & different temps. b. Relative abundances of minor molecular species (HCN, NH_3, C_2H_2, etc.) c. Phase observations	Origin
	Dynamics: Time scale of horizontal and vertical mixing	a. Vertical thermal profile b. Horizontal gradients c. Diurnal variations d. Temporal variability, seasonal/inter-seasonal variations for tilted/eccentric planets.	a. IR eclipse spectra b. IR Eclipse mapping c. IR orbital phase lightcurves d. Repeated observations & use of chemical species as tracers (e.g. CH_4, NH_3, CO_2, and HCN etc.)	Origin & Rosetta Stone
	Formation: Core accretion or gravitation instability? Where did the planet form in the planetary disk?	a. Planetary density b. C/O ratio and metallicity	a. Transit+mass from Radial Velocity b. Relative abundances of carbon versus oxygen-bearing molecules	Origin
	Migration: Any evidence of the initial conditions?	a. Comparison star/planet metallicity (C/O, O/H, C/H..) b. Chemistry of planets around different stars.	a. Relative abundances of carbon-, oxygen-, bearing molecules, etc. b. Transit and eclipse spectra of planets around different stars & different T	Origin
	2D and 3D maps	Exoplanet image at multiple wavelengths	Ingress and egress eclipse spectra Orbital phase-curves Full orbit spectra	Rosetta Stone
	Evolution: Escape processes	H_3^+ detection and ionospheric temperature measurement	Transit and eclipse spectra	Origin

Retour à la table des matières : p. v

Table 2 (continued)

Planet type	Scientific question	Observable	Observational strategy	Survey type
Terrestrial planets	Energy budget Albedo & Temperature	Incoming and outgoing radiation	Stellar flux+planetary albedo and thermal emission with VIS and IR photometry during eclipses	Chemical Census
	Is there an atmosphere?	Featureless spectrum over a broad wavelength range or not	Transit spectra at multiple λ (IR in particular) to constrain the scale height. Thermal phase variations.	Chemical Census
	Primary or secondary atmosphere?	Hydrogen rich atmosphere?	Transit spectra at multiple λ (IR in particular) to constrain the scale height	Chemical Census
	Main atmospheric component	Scale height	Transit spectra at multiple λ (IR in particular) to constrain the scale height	Chemical Census
	Planetary interior	a. Density b. Hints from atmospheric composition?	a. Transit+mass from Radial Velocity b. Transit and eclipse spectra	Chemical Census
	Formation: Formed in situ? Migrated? Core of a giant planet? Frequency of Venus-like, Mercury-like, Ocean planets..	a. Density b. Is there an atmosphere? c. Primary (H_2-rich) or secondary atmosphere? d. Atmospheric composition?	a. Transit + mass from Radial Velocity b. c. d. Transit and eclipse spectra	Chemical Census
Temperate terrestrial planets	Habitability	a. Temperature b. Chemical composition (H_2O? CO_2? O_3?)	a. Eclipse measurements b. Transit or eclipse measurements at low resolution.	Challenging, need a late M star, bright in the IR

Retour à la table des matières : p. v

as asteroids or comets, or volcanic activity might also alter significantly the composition of the primordial atmosphere. EChO can confirm the presence or absence of an atmosphere enveloping terrestrial planets. On top of this, EChO can detect the composition of their atmospheres (CO_2, SiO, H_2O etc.), so we can test the validity of current theoretical predictions (Section 1.1.1 and Fig. 3). In particular:

(i) A very thick atmosphere (several Earth masses) of heavy gas, such as carbon dioxide, ammonia, water vapour or nitrogen, is not realistic because it requires amounts of nitrogen, carbon, and oxygen with respect to silicon much higher than all the stellar ratios detected so far [66]. If EChO detects an atmosphere which is not made of hydrogen and helium, the planet is almost certainly from the terrestrial family, which means that the thickness of the atmosphere is negligible with respect to the planetary radius. In that case, theoretical works provided by many authors in the last decade [1, 73, 97, 174, 175] can be fully exploited in order to characterise the inner structure of the planet (Fig. 5).

(ii) If an object exhibits a radius that is bigger than that of a pure water world (water being the least dense, most abundant material except for H/He) of the same mass, this tells us that at least a few % of the total mass of the planet is made of low density species, most likely H_2 and He. The fact that many objects less massive than Neptune are in this regime shows that it is possible to accrete a large fraction of gas down to 2–3 M_{Earth}, the mass of Kepler-11 f (Fig. 5). EChO can test this hypothesis by probing the presence of H_2, He and H_2O through transit spectroscopy (Fig. 5). While the presence of clouds can sometimes mimic the effect of an atmosphere denser than H/He, the broad wavelength range of EChO will maximize the chance of finding a transparent spot where the deeper atmospheric regions can be probed.

(iii) A major motivation for exoplanet characterisation is to understand the probability of occurrence of habitable worlds, i.e. suitable for surface liquid water. While EChO may reveal the habitability of one or more planets – temperate super-Earths around nearby M-dwarfs are within reach of EChO's capabilities [164] – its major contribution to this topic results from its capability to detect the presence of atmospheres on many terrestrial planets even outside the habitable zone and, in many cases, characterise them.

2.3 The intermediate family (Neptunes and Sub-Neptunes)

Planets with masses between the small solid terrestrial and the gas giants planets are key to understanding the formation of planetary systems [77]. The existence of these intermediate planets close to their star, as found by radial velocity and transit surveys (see Fig. 1), already highlights the shortcomings of current theoretical models.

(i) Standard planet formation scenarios predict that embryos of sufficient mass (typically above 5 M_{Earth}) should retain some of the primordial hydrogen and helium from the protoplanetary disc. With EChO's primary transit spectroscopic measurements, we may probe which planets possess a hydrogen helium atmosphere and directly test the conditions of planet formation (Fig. 5).

Retour à la table des matières : p. v

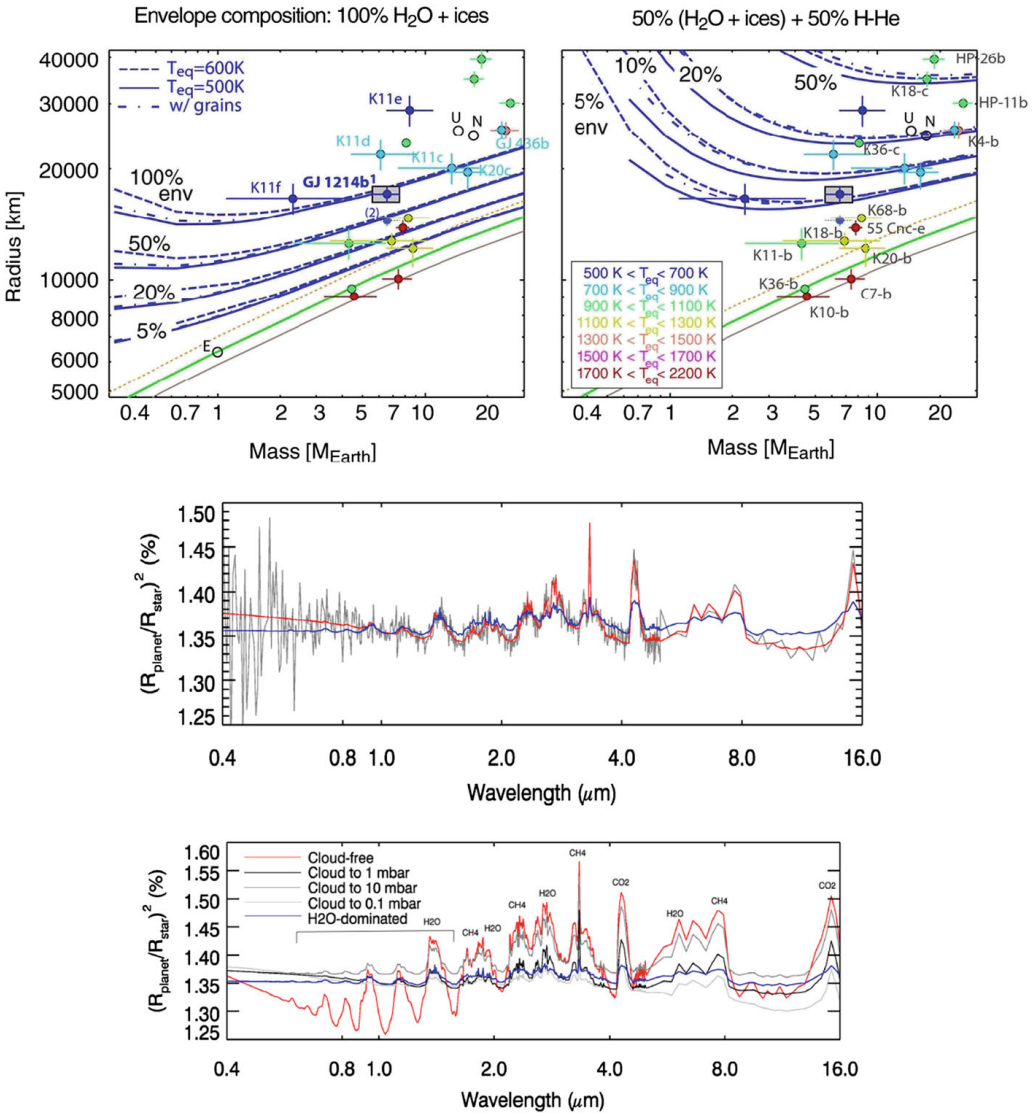

Fig. 5 *Top*: Mass–radius relationships for Ocean planets and sub-Neptunes and degeneracy of interpretation [176]. Two envelope compositions are shown: 100 % H_2O/ices (*left*) and with 50 % (H_2O/ices)+50 % H/He (*right*): they both explain the densities of the planets identified with *blue dots*. *Bottom*: Synthetic spectra between 0.4 and 16 μm of the super-Earth GJ1214b for a range of atmospheric scenarios [11]. Centre: Two retrieval fits to a noisy EChO-like simulated spectrum, with a H_2-He rich atmosphere (*red*) and a 50 % H_2O model (*blue*). EChO is able to distinguish between the two competing scenarios. *Bottom*: simulations of cloudy and cloud-free atmospheres. EChO's broad wavelength range and sensitivity would enable the identification of different molecular species and type of clouds

(ii) The only two intermediate solar system planets that we can characterise –Uranus and Neptune– are significantly enriched in heavy elements, in the form of methane. The reason for this enrichment is unclear: is it due to upward mixing, early or late delivery of planetesimals, or because they formed at the CO ice line [6]? EChO would guarantee these measurements in many planets, thereby providing observations that are crucial to constrain models.

(iii) We do not know where to put the limits between solid, liquid and gaseous planets. While EChO cannot measure directly the phase of a planet as a

Retour à la table des matières : p. v

whole, the determination of its size and of the composition of its atmosphere will be key to determining whether its interior is solid, partially liquid, or gaseous.

2.4 Gaseous exoplanets

Giant planets are mostly made of hydrogen and helium and are expected to be always in gaseous form. Unlike solid planets, they are relatively compressible and the progressive loss of heat acquired during their formation is accompanied by a global contraction. Inferring their internal composition thus amounts to understanding how they cool [75]. The dominance of hydrogen and helium implies that the degeneracy in composition (i.e. uncertainty on the mixture of ices/rocks/iron) is much less pronounced than for solid planets, so that the relevant question concerns the amounts of all elements other than hydrogen and helium, i.e. heavy elements, that are present. A fundamental question is by how much are these atmospheres enriched in heavy elements compared to their parent star. Such information will be critical to:

- understand the early stage of planetary and atmospheric formation during the nebular phase and the immediately following few millions years [173]
- test the effectiveness of the physical processes directly responsible for their evolution.

We detail below the outstanding questions to be addressed by an EChO-like mission and how these can be achieved.

2.4.1 The chemistry of gaseous planets' atmospheres

(i) *The relative importance of thermochemical equilibrium, photochemistry, and transport-induced quenching* in controlling the atmospheric composition of gaseous exoplanets largely depends on the thermal structure of the planets. Transport-induced quenching of disequilibrium species allows species present in the deep atmosphere of a planet to be transported upward in regions where they should be unstable, on a time scale shorter than the chemical destruction time. The disequilibrium species are then "quenched" at observationally accessible atmospheric levels. In the solar system, this is the case, in particular, for CO in the giant planets, as well as PH_3 and GeH_4 in Jupiter and Saturn [63]. Another key process, which also leads to the production of disequilibrium species, is photochemistry [194]. The energy delivered by the absorption of stellar UV radiation can break chemical bonds and lead to the formation of new species. In the solar system, the photochemistry of methane is responsible for the presence of numerous hydrocarbons in the giant planets. In the case of highly irradiated hot Jupiters, these disequilibrium species are expected to be important. In some of the known hot-Jupiters, CH_4 and NH_3 are expected to be enhanced with respect to their equilibrium abundances due to vertical transport-induced quenching. These species should be dissociated by

Retour à la table des matières : p. v

photochemistry at higher altitude, leading, in particular, to the formation of C_2H_2 and HCN on the day side [118, 178]. EChO can address these open questions, by deriving the abundances of both key and minor molecular species, with mixing ratios down to 10^{-5} to 10^{-7} (Fig. 6), temporally and spatially resolved in the case of very bright sources (see 2.3.2.3).

(ii) *Chemistry and dynamics* are often entangled. Agúndez et al. [4, 5] showed that for hot-Jupiters, for instance, the molecules CO, H_2O, and N_2 and H_2 show a uniform abundance with height and longitude, even including the contributions of horizontal or vertical mixing. For these molecules it is therefore of no relevance whether horizontal or vertical quenching dominates. The vertical abundance profile of the other major molecules CH_4, NH_3, CO_2, and HCN shows, conversely, important differences when calculated with the horizontal and vertical mixing. EChO spectroscopic measurements of the dayside and terminator regions would provide a key observational test to constrain the range of models of the thermochemical, photochemical and transport processes shaping the composition and vertical structure of these atmospheres.

2.4.2 Energy budget: heating and cooling processes

(i) *Albedo and thermal emission*. The spectrum of a planet is composed mainly of reflected stellar light and thermal emission from the planet; the measurement of the energy balance is an essential parameter in quantifying the energy source of dynamical activity of the planet (stellar versus internal sources). The Voyager observations of the Giant Planets in the Solar System have allowed an accurate determination of the energy budget by measuring the Bond albedo of the planets (Jupiter: [78]; Saturn: [79]; Uranus: [123]; Neptune: [124]). EChO extends these methods to exoplanets: the reliable determination of the spectrum in reflected versus thermal range will provide a powerful tool for classifying the dynamical activity of exoplanets.

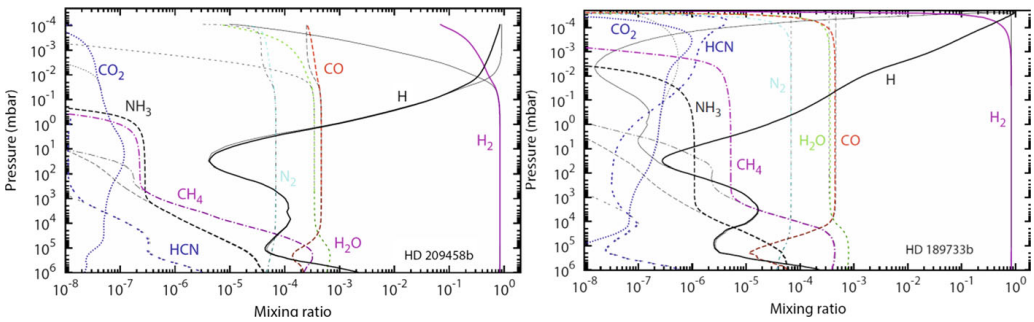

Fig. 6 Steady-state composition of HD 209458b (*left*) and HD 189733b (*right*) calculated with a non-equilibrium model (*colour lines*), compared to the thermodynamic equilibrium (*thin black lines*) [178]. For HD 189733b, one can clearly notice the higher sensitivity to photolyses and vertical mixing, with all species affected, except the main reservoirs, H_2, H_2O, CO, and N_2. Since the atmosphere of HD209458b is hotter, it is mostly regulated by thermochemistry. The EChO Origin survey would measure these differences by deriving the abundances of both key and minor molecular species, with mole fractions down to 10^{-5} to 10^{-7} (see Section 3.2.2 and 3.2.3)

Retour à la table des matières : p. v

(ii) *Non-LTE emissions.* Observation of the CH_4 non-LTE emission on the day side of Jupiter and Saturn [49, 64, 58] is an important new tool to sound the upper atmosphere levels around the homopause (typically at the microbar level for giant planets), the layer separating the turbulent mixing from the diffusive layers where molecules are separated by their molecular weight. This region is an important transition between the internal dynamical activity and the radiatively controlled upper atmosphere, with gravity waves being identified as an important mechanism responsible of high thermospheric temperatures in giant planets. Swain et al. [158] and Waldmann et al. [184] identified an unexpected spectral feature near 3.25 μm in the atmosphere of the hot-Jupiter HD 189733b which was found to be inconsistent with LTE conditions holding at pressures typically sampled by infrared measurements. They proposed that this feature results from non-LTE emission by CH_4, indicating that non-LTE effects may need to be considered, as is also the case in our Solar System for Jupiter and Saturn as well as for Titan. While these types of measurements are challenging from the ground [109], EChO can conclusively unveil the nature of this feature and address the same question for many hot gaseous planets, making use of the improved observing conditions from space.

(iii) H_3^+ emission (3.5–4.1 μm). Of particular interest in the study of gas giants within our own solar system are emissions of H_3^+ which dominate their emissions between 3 and 4 μm. H_3^+ is a powerful indicator of energy inputs into the upper atmosphere of Jupiter [106], suggesting a possible significance in exoplanet atmospheres as well. As the unique atmospheric constituent radiatively active, H_3^+ plays a major role in regulating the ionospheric temperature. Simulations by Yelle [193] and Koskinen et al. [92] have investigated the importance of H_3^+ as a constituent and IR emitter in exoplanet atmospheres. A finding of these calculations is that close-orbiting extrasolar planets (0.2 AU) may host only relatively small abundances of H_3^+ due to the efficient dissociation of H_2, a parent molecule in the creation path of H_3^+. As a result, the detectability of H_3^+ may depend on the distance of the planet from the star. EChO can test this hypothesis by detecting or setting an upper limit on the H_3^+ abundance in many giant planets.

(iv) Clouds may modify the albedo and contribute to the green-house effect, therefore their presence can have a non-negligible impact on the atmospheric energy budget. If present, clouds will be revealed by EChO through transit and eclipse spectroscopy in the VIS-NIR**.** Clouds show, in fact, distinctive spectroscopic signatures depending on their particle size, shape and distribution (see Figs. 14 and 19). Current observations in the VIS and NIR with Hubble and MOST have suggested their presence in some of the atmospheres analysed (e.g. [55, 89–91, 138, 142, 147]). We do not know, though, their chemical composition, how they are spatially distributed and whether they are a transient phenomenon or not. Further observations over a broad spectral window and through time are needed to start answering these questions (see most recent work done for brown dwarfs [7, 33] or eclipse/phase mapping observations).

2.4.3 Spatial and temporal variability: weather, climate and exo-cartography

(i) *Temporal variability*: Tidally synchronised and unsynchronised gaseous planets are expected to possess different flow and temperature structures. Unencumbered by

Retour à la table des matières : p. v

complicating factors, such as physical topography and thermal orography, the primary difference will be in the amplitude and variability of the structures. An example is shown in Fig. 7 for the case of HD 209458b, a synchronised hot-Jupiter. The state-of-the-art, high-resolution simulation shows giant, tropical storms (cyclones) generated by large-amplitude planetary waves near the substellar point. Once formed, the storms move off poleward toward the nightside, carrying with them heat and chemical species, which are observable. The storms then dissipate to repeat the cycle after a few planet rotations [41, 42]. Storms of such size and dynamism are characteristic of synchronized planets, much more so than unsynchronized ones. There are other even more prominent periodicities (e.g., approximately 1.1, 2.1, 4.3, 8.3, 15 and 55 planet rotations), all linked to specific dynamical features. Through its excellent temporal coverage of individual objects (i.e. tens of repeated observations as part of the Rosetta Stone survey, see Section 3.2.2), EChO can well distinguish the two different models and type of rotation.

(ii) *Horizontal thermal structure*: phase curves, spherical harmonics & eclipse mapping. Longitudinal variations in the thermal properties of the planet cause a variation in the brightness of the planet with orbital phase (Fig. 7). This orbital modulation has been observed in the IR in transiting [86, 87] and non-transiting systems [45, 46]. In Stevenson et al. [157] full orbit spectra have been obtained. One of the great difficulties in studying extrasolar planets is that we cannot directly resolve the surfaces of these bodies, as we do for planets in our solar system. The use of occultations or eclipses to spatially resolve astronomical bodies, has been used successfully for stars in the past. Most recently Majeu et al. [108] and De Wit et al. [52, 53] derived the two-dimensional map of the hot-Jupiter HD189733b in the IR. Majeu et al. [107] combined 7 observations at 8 μm with Spitzer-IRAC and used two techniques: slice mapping & spherical harmonic mapping (see Fig. 12). Both techniques give similar maps for the IR dayside flux of the planet. EChO can provide phase curves and 2D-IR maps recorded simultaneously at multiple wavelengths, for several gaseous planets, an unprecedented achievement outside the solar system. These curves and maps will allow one to determine horizontal and vertical, thermal and chemical gradients and exo-cartography (Fig. 8).

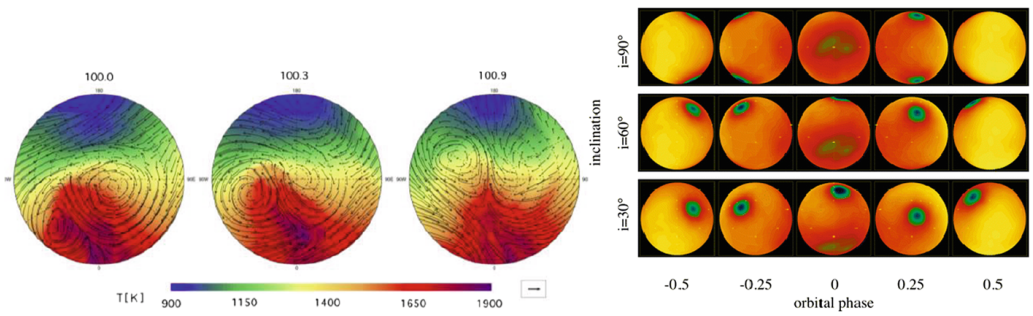

Fig. 7 *Left*: Giant storms on a synchronized, gaseous planet. Wind vectors superimposed on temperature map over approximately one planet rotation period, viewed from the north pole. Synchronized planets experience intense irradiation from the host star (at lon=0 point), exciting large-amplitude planetary waves and active storms that move off to the night side (top half in each frame). The storms dissipate and regenerate with a distinct period of a few planet rotations [41, 42]. Other dynamically-induced periodicities are present on synchronized planets. The periodicities can be used to distinguish synchronized and unsynchronized planets, among other things. *Right*: Simulated phase variations for a hot-Jupiter with different inclinations [129]

Retour à la table des matières : p. v

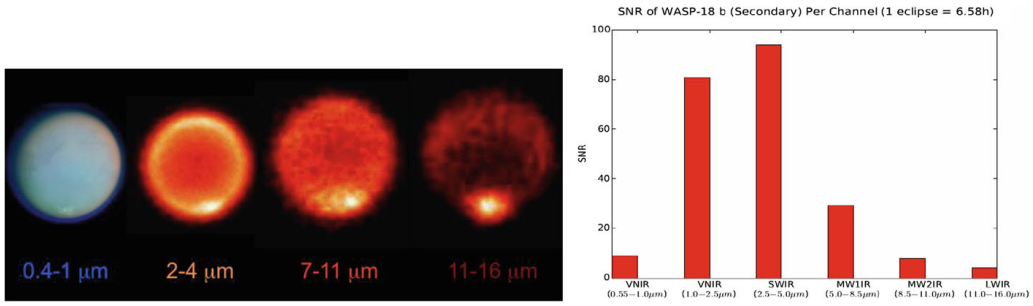

Fig. 8 *Left*: Demonstration of possible results from exo-cartography of a planet at multiple photometric bands. *Right*: simulations of EChO performances for the planet WASP-18b: the SNR in one eclipse is high enough at certain wavelength to allow one to resolve spatially the planet through eclipse mapping

2.4.4 Planetary interior

Although EChO has been conceived to measure the characteristics of planetary atmospheres it can also be crucial in improving our knowledge of planetary interiors [77]. EChO can measure with exquisite accuracy the depth of the primary transit and therefore the planetary size (see e.g. Figs. 19 and 23). But the major improvements for interior models will come from the ability to characterise the atmosphere in its composition, dynamics and structure. As described in the previous sections, this can be achieved by a combination of observations of transits and of observations of the planetary lightcurve during a full orbital cycle.

EChO directly contributes to the understanding of the interiors of giant exoplanets through the following measurements:

(i) *Measurements on short time scales.* A few hours of continuous observations of the transit or eclipse reveal the abundances of important chemical species globally on the terminator or on the dayside. The comparison of these measurements with the characteristics of the star and of the planet, in particular the stellar metallicity and the mass of heavy elements required to fit the planetary size is key in the determination of whether the heavy elements are mixed all the way to the atmosphere or mostly present in the form of a central core.

(ii) *Measurements on long time scales.* A half or a full planetary orbit, i.e. hours/days of continuous observations, enable the observation of the atmospheric dynamics (wind speed, vertical mixing from disequilibrium species), atmospheric structure (vertical and longitudinal temperature field, presence of clouds) and variability. This is essential to estimate the depth at which the atmosphere becomes well mixed and therefore the heat that is allowed to escape.

2.4.5 Chemical composition of gaseous planets: a pointer to planet formation and migration history

Formation and migration processes play fundamental roles in determining planetary bulk and atmospheric compositions that ultimately reflect the chemical structure and fractionation within nascent protoplanetary discs. For the purpose of illustration, Turrini et al. [173] have considered a number of simplified planetary accretion and migration

Retour à la table des matières : p. v

scenarios within discs with Solar chemical abundance. They show that models of accretion onto planetary cores can lead to final envelope C/O values that range from less than 0.54 up to 1, and correlate with where and how the planet forms and migrates in a predictable manner. EChO can provide much needed observational constraints on the C/O values for many gaseous planets. In the following paragraphs we outline how key formation and migration processes may lead to diverse chemical signatures.

(i) Giant planet formation via *gravitational instability* that occurs during the earliest phases of protoplanetary disc evolution will result initially in planets with bulk and atmospheric abundances reflecting that of the protoplanetary disc. Recent studies show that formation is followed by rapid inward migration on time scales~ 10^3 years [14, 196], too short for significant dust growth or planetesimal formation to arise between formation and significant migration occurring. Migration and accompanying gas/dust accretion should therefore maintain initial planetary abundances if protoplanetary discs possess uniform elemental abundances. Post-formation enrichment may occur through bombardment from neighbouring planetesimals or star-grazing comets, but this enrichment will occur in an atmosphere with abundances that are essentially equal to the stellar values, assuming these reflect the abundances present in the protoplanetary disc.

In its simplest form, the *core accretion model* of planet formation begins with the growth and settling of dust grains, followed by the formation of planetesimals that accrete to form a planetary core. Growth of the core to a mass in excess of a few Earth masses allows for the settling of a significant gaseous envelope from the surrounding nebula. Halting growth at this point results in a super-Earth or Neptune-like planet. Continued growth through gas and planetesimal accretion leads to a gas giant planet. A key issue for determining the atmospheric abundances in a forming planet is the presence of ice-lines at various distances from the central star, beyond which volatiles such as water, carbon dioxide and carbon monoxide freeze-out onto grains and are incorporated into planetesimals. Figure 9 shows the effect of ice-lines associated with these species on the local gas- and solid-phase C/O ratios in a protoplanetary disc with solar C/O ratio~0.54. A H_2O ice-line is located at 1–3 AU, a CO_2 ice-line at ~10 AU, and a CO ice-line at~40 AU [120]). Interior to the H_2O ice-line, carbon- and silicate-rich grains condense, leading to a gas-phase C/O~0.6 (due to the slight overabundance of oxygen relative to carbon in these refractory species). The atmospheric abundances of a planet clearly depend on where it forms, the ratio of gas to planetesimals accreted at late times, and the amount of accretion that occurs as the planet migrates. As a way of illustrating basic principles, we note that a planet whose core forms beyond the H_2O ice-line, and which then accretes gas but no planetesimals interior to 2 AU as it migrates inward will have an atmospheric C/O~0.54. Additional accretion of planetesimals interior to 2 AU would drive C/O below 0.54. Similarly, a planet that forms a core and accretes all of its gas beyond the CO_2 ice-line at 10 AU before migrating inward without further accretion will have an envelope C/O~1. More realistic N-body simulations of planet formation that include migration, gas accretion and disc models with the chemical structure shown in Fig. 10 have been performed recently by Coleman & Nelson [44]). These show a range of final C/O values for short-period planets, as illustrated by the example run shown in Fig. 10.

Retour à la table des matières : p. v

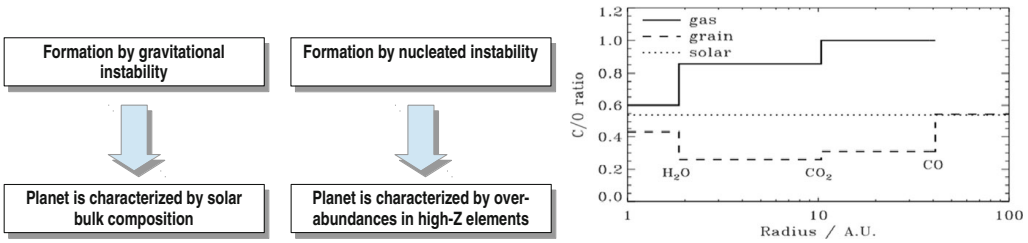

Fig. 9 *Left*: expected differences in the atmospheric composition due to different formation scenarios. *Right*: Locations of the ice-lines and their influence on the C/O ratios for the gas and solids (adapted from [120])

(ii) Gas disc-driven migration is only one plausible mechanism by which planets can migrate. The large eccentricities (and obliquities) of the extrasolar planet population suggest that planet-planet gravitational scattering ("Jumping Jupiters") may be important [39, 192], and this is likely to occur toward the end of the gas disc lifetime, when its ability to damp orbital eccentricities is diminished. When combined with tidal interactions with the central star, planet-planet scattering onto highly eccentric orbits can form short-period planets that have not migrated toward the central star while accreting from the protoplanetary disc. These planets are likely to show chemical signatures that reflect this alternative formation history, being composed of higher volatile fractions if they form exterior to the H_2O ice line. Measurements of bulk and atmospheric chemical compositions by EChO will provide important clues regarding the full diversity of the formation and migration pathways that were followed by the observed planetary sample.

3 EChO observational techniques

In this section we detail the observational techniques and strategies that EChO may adopt to maximise the scientific return.

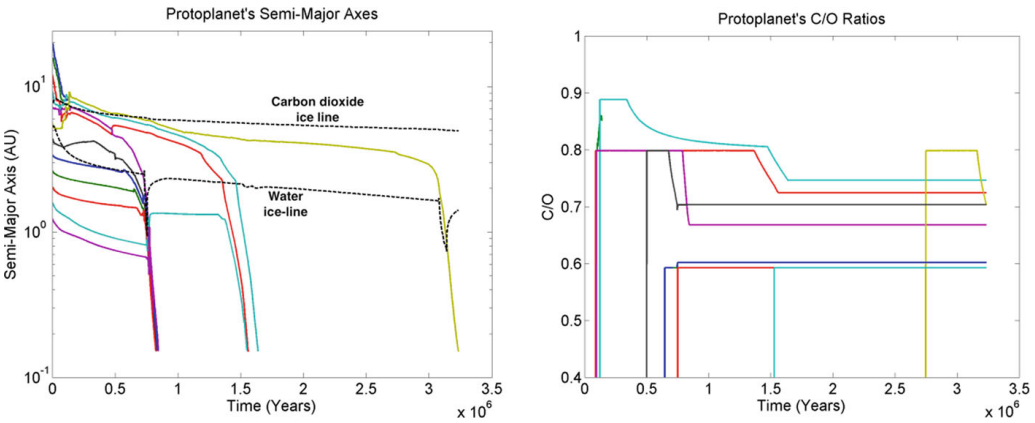

Fig. 10 *Left panel*: migration trajectories of forming planets. *Right panel*: Corresponding C/O ratios of planetary envelopes as they accrete and migrate. Note the initially high C/O ratios of planets forming beyond CO_2 ice-line and reductions in C/O as planets migrate inward where the local disc gas C/O ratio is close to the solar value of~0.54. Images taken from Coleman & Nelson [44]

Retour à la table des matières : p. v

The transit and eclipse spectroscopy allow us to measure atmospheric signals from the planet at levels of at least 10^{-4} relative to the star. Analysis techniques to decorrelate the planetary signal from the astrophysical and instrumental noise are presented.

A broad instantaneous wavelength coverage is essential to detect as many chemical species as possible, to probe the thermal structure of the planetary atmospheres and to correct for the contaminating effects of the stellar photosphere.

The EChO core science may be optimised by a three-tier survey, distinguished by the SNR and the resolving power of the observations. Those are tailored to achieve well defined scientific objectives and might need to be revised at a later stage, closer to launch, to account for the new developments and achievements of the field.

3.1 Transits, eclipses and phase-curves

EChO will probe the atmospheres of extrasolar planets using temporal variations to separate out planet light from the star—a technique that has grown to be incredibly powerful over the last decade. It makes use of (a) planet transits, (b) secondary eclipses, and (c) planet phase variations (Fig. 11).

(i) *Transit spectroscopy*: When a planet moves in front of its host star, starlight filters through the planet's atmosphere. The spectral imprint of the atmospheric constituents can be distilled from the spectrum of the host star by comparing in-transit with out-of-transit spectra [32, 143, 168]. Transit spectroscopy probes the high-altitude atmosphere at the day/night terminator region of the planet. The absorption signals mainly depend on the temperature and the mean molecular weight of the atmosphere, and on the volume mixing ratio of the absorbing gas. If present, clouds can be detected mainly in the VIS/NIR.

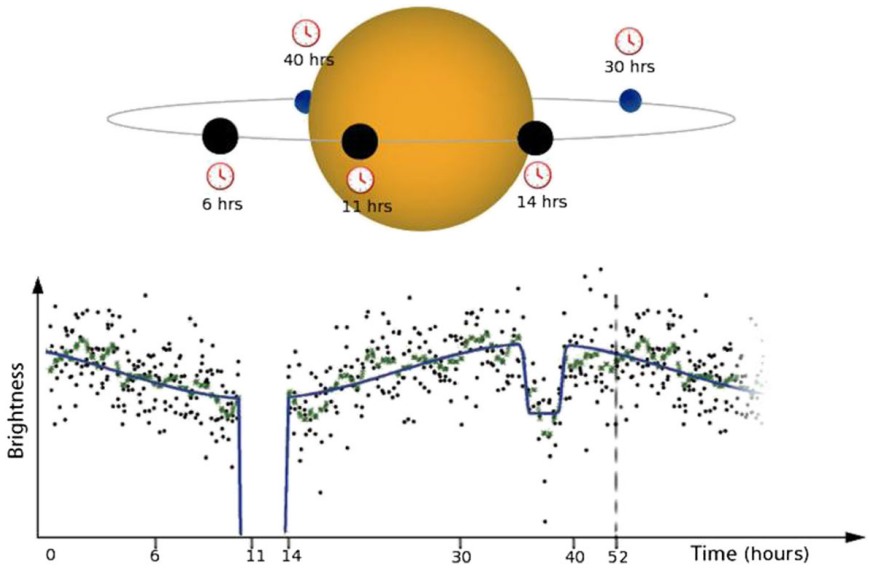

Fig. 11 Optical phase curve of planet HAT-P-7b observed by Kepler [29] showing the transit, eclipse, and variations in brightness of system due to the varying contribution from the planet's day and night-side as function of orbital phase

Retour à la table des matières : p. v

(ii) *Eclipse spectroscopy*: On the opposite side of the orbit, the planet is occulted by the star (the eclipse), and therefore temporarily blocked from our view. The difference between in-eclipse and out-of-eclipse observations provides the planet day-side spectrum. In the near- and mid-infrared, the radiation is dominated by thermal emission, modulated by molecular features [37, 53]. This is highly dependent on the vertical temperature structure of the atmosphere, and probes the atmosphere at higher pressure-levels than transmission spectroscopy. At visible wavelengths, the planet's spectrum is dominated by Rayleigh and/or Mie scattering of light from the host star (e.g. [51]). For the latter, clouds can play an important role.

(iii) *Planet phase variations*: During a planet's orbit, varying parts of the planet's day- and night-side are seen. By measuring the minute changes in brightness as a function of orbital phase, the longitudinal brightness distribution of a planet can be determined [29, 86, 149]. On the one hand, such observations are more challenging since the time-scales over which the planet contributions vary are significantly longer than for transit and eclipse spectroscopy. On the other hand, this method can also be applied to non-transiting planet systems [46] and to measure the significant variations in atmospheric temperature throughout the orbit of eccentric planets [99]. Phase variations in the IR are important in understanding a planet's atmospheric dynamics and redistribution of absorbed stellar energy from their irradiated day-side to the night-side. Phase variations in the VIS are very useful to infer the cloud distribution [55].

(iv) *Exoplanet mapping and meteorological monitoring*: The combination of the three prime observational techniques utilized by EChO provides us with information from different parts of the planet atmosphere; from the terminator region via transit spectroscopy, from the day-side hemisphere via eclipse spectroscopy, and from the unilluminated night-side hemisphere using phase variations. In addition, eclipses can be used to spatially resolve the day-side hemisphere. During ingress and egress, the partial occultation effectively maps the photospheric emission region of the planet [128]. Figure 12 illustrates the results from eclipse mapping observations [107]. In addition, an important aspect of EChO is the repeated observations of a number of key planet targets in both transmission and secondary eclipse mode. This will allow the monitoring of global meteorological variations in the planetary atmospheres (see Section 2.4.3).

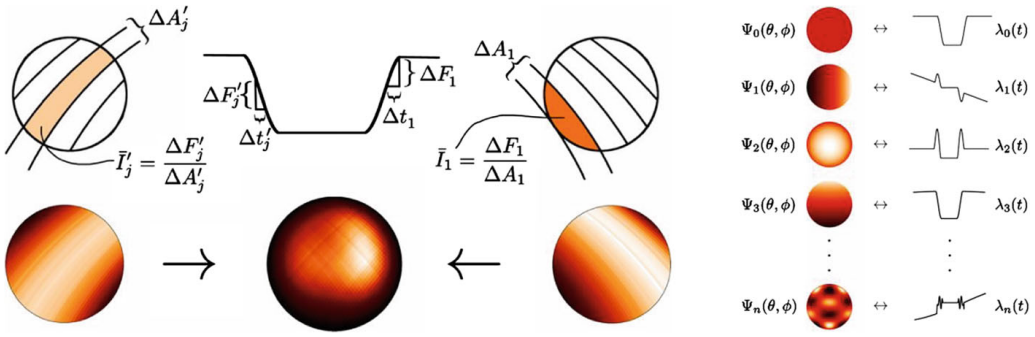

Fig. 12 Two techniques to resolve spatially the planet. Right: spherical harmonics. *Left*: slice mapping with ingress and egress maps as well as a combined map of HD189733b at 8 μm. These were achieved with Spitzer [107]. See also [52, 56, 121]

Retour à la table des matières : p. v

All three techniques have already been used very successfully from the optical to the near- and mid-infrared, showing molecular, atomic absorption and Rayleigh scattering features in transmission [21, 25, 36, 47, 48, 55, 86, 89, 101, 132, 147, 148, 160, 168–170, 182] and/or emission spectra [38, 74, 91, 156, 159, 161, 171] of a few of the brightest and hottest transiting gas giants, using the Hubble and Spitzer space telescopes. In addition, infrared phase variations have been measured at several wavelengths using Spitzer, showing only a relatively small temperature difference (300 K) between the planet's day and night-side - implying an efficient redistribution of the absorbed stellar energy [86]. These same observations show that the hottest (brightest) part of this planet is significantly offset with respect to the sub-stellar point, indicative of a longitudinal jet-stream transporting the absorbed heat to the night-side.

3.2 EChO observational strategy

To maximise the science return, EChO would study exoplanets both as a population & as individual objects. We describe in the following sections how EChO would achieve its objectives.

3.2.1 EChO spectral coverage & resolving power

To maximise the scientific impact achievable by EChO, we need to access all the molecular species expected to play a key role in the physics and chemistry of planetary atmospheres. It is also essential that we can observe planets at different temperatures (nominally from 300 to 3000 K, Fig. 13) to probe the differences in composition potentially linked to formation and evolution scenarios. A broad wavelength coverage is therefore required to:

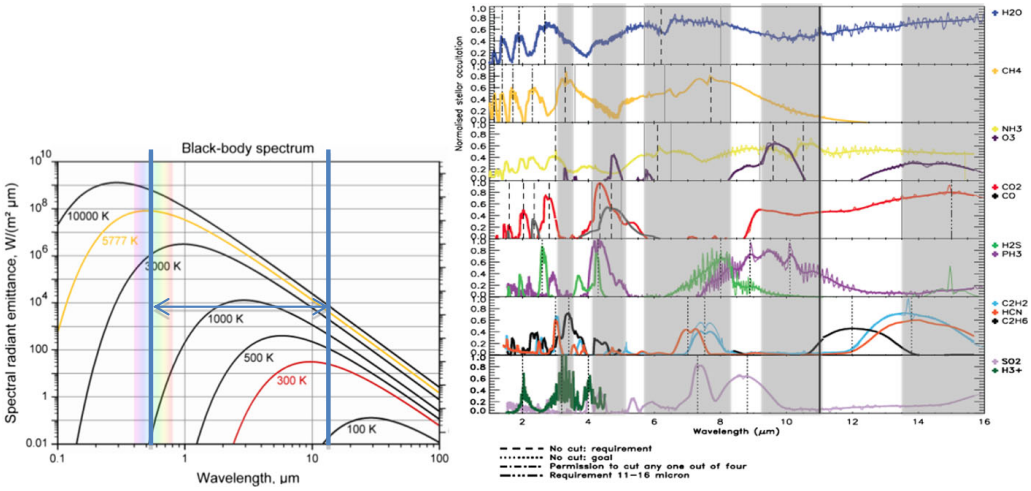

Fig. 13 *Left*: *Blackbody curves* corresponding to different temperatures: the colder the temperature, the longer the wavelengths where the Planckian curves peak. The two *blue lines* show optimal wavelength range to characterise planets from 300 to 3000 K. *Right*: molecular signatures in the 1–16 μm range at the required and goal spectral resolving power proposed for EChO. *Dashed lines* indicate the key spectral features. *Grey* bands indicate the protected spectral windows, i.e. where no split between spectrometer channels should occur

Retour à la table des matières : p. v

- Measure both albedo and thermal emission to determine the planetary energy budget.
- Capture the variety of planets at different temperatures [164].
- Detect the variety of chemical components present in exoplanet atmospheres [165] .
- Guarantee redundancy (i.e. molecules detected in multiple bands of the spectrum) to secure the reliability of the detection—especially when multiple chemical species overlap in a particular spectral range ([165]; see Tables 4, 5 and 6).
- Enable an optimal retrieval of the chemical abundances and thermal profile, Fig. 17 [11, 12].

This means covering the largest wavelength range feasible given the temperature limits (i.e. from the visible to the Mid-IR, ~0.4 to 16 μm). Some spectral regions are more critical than others, as it is explained in the following paragraphs [62, 167].

(i) The wavelength coverage 0.55–11 μm is critical for EChO, as it guarantees that ALL the key chemical species (H_2O, CH_4, CO, CO_2, NH_3) and all other species (Na, K, H_2S, SO_2, SiO, H_3^+, C_2H_2, C_2H_4, C_2H_6, PH_3, HCN etc.) can be detected, if present, in all the exoplanet types observed by EChO, with the exception of CO_2 and C_2H_6 in temperate planetary atmospheres (see Fig. 13).

Molecular species such as H_2O, CH_4, CO_2, CO, NH_3 are key to understand the chemistry of those planets: the broad wavelength coverage guarantees that these species can be detected in multiple spectral bands, even at low SNR, optimising their detectability in atmospheres at different temperatures. Redundancy (i.e. molecules detected in multiple bands of the spectrum) significantly improves the reliability of the detection, especially when multiple chemical species overlap in a particular spectral range. Redundancy in molecular detection is also necessary to allow the retrieval of the vertical thermal structure and molecular abundances. The wavelength range 0.55-11 μm guarantees the retrieval of molecular abundances and thermal profiles, especially for gaseous planets, with an increasing difficulty in retrieving said information for colder atmospheres [13].

In hot planets, opacities in the visible range are dominated by metallic resonance lines (Na at 0.59 μm, K at 0.77 μm, and possibly weaker Cs transitions at 0.85 and 0.89 μm). TiO, VO and metal hydrides are also expected by analogy to brown dwarfs [144].

(ii) The target wavelength coverage of 0.55–16 μm guarantees that CO_2 and C_2H_6 can be detected in temperate planetary atmospheres. It also offers the possibility of detecting additional absorption features for HCN, C_2H_2, CO_2 and C_2H_6 for all other planets and improves the retrieval of thermal profiles [13].

(iii) The target wavelength coverage of 0.4–11 μm might improve the detection of Rayleigh scattering in hot and warm gaseous planets if clouds are not present. In a cloud-free atmosphere, the continuum in the UV–VIS is given by Rayleigh scattering on the blue side, i.e. for wavelengths shorter than 1 μm (Rayleigh scattering varies as $1/\lambda^4$). If there are clouds or hazes with small-size particles, those should be detectable in the visible even beyond 0.55 μm (see Fig. 19).

(iv) A spectral resolving power of R=300 for λ<5 μm will permit the detection of most molecules at any temperature. At λ>5 μm, R=30 is enough to detect the key molecules at hot temperatures, due to broadening of their spectral signatures.

Retour à la table des matières : p. v

For temperate planets, R=30 at longer wavelengths is also an acceptable solution, given there are fewer photons [167].

In Fig. 14 left, two values (300 and 30) are used for the spectral resolving power of the simulated transmission spectra. In addition to the main candidate absorbers (H_2O, CH_4, NH_3, CO, CO_2), Fig. 13 shows the contributions from HCN, O_3, H_2S, PH_3, SO_2, C_2H_2, C_2H_6 and H_3^+. Among those, H_3^+ around 2 μm and 3–4 μm is detectable with a resolving power of>100.

While R=30 enables the detection of most of the molecules absorbing at λ>5 μm, especially at higher temperatures, we would lose the possibility of resolving the CO_2, HCN and other hydrocarbon Q-branches, for which R> 100 is needed. The current instrument design allows a spectral resolving power between the two.

In the visible, for cloud-free atmospheres, a resolving power of~100 is still sufficient for identifying the resonance lines of Na and K, but not to resolve the centre of the lines. For the star, Hα can be easily identified at 0.656 μm.

3.2.2 EChO's three surveys

An optimised way to capture the EChO science case is through three survey tiers. These are briefly described below and summarised in Table 3 and in Figs. 15 and 16.

Chemical Census

- This tier will measure the planetary albedos and effective temperatures for the complete EChO sample (hundreds of planets).
- This tier enables the detection of the strongest features in the measured spectra of the EChO sample. These include the presence of clouds or hazes, and the major atomic and molecular species (e.g. Na, K, CH_4, CO, CO_2, NH_3, H_2O,

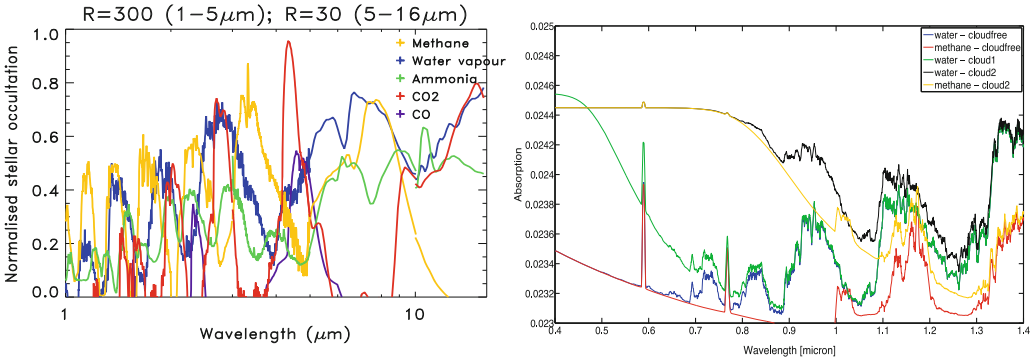

Fig. 14 Simulated transmission spectra of a gaseous exoplanet at 800 K [81]. The atmospheric absorption is normalised to 1; typically the fraction of stellar flux absorbed by the atmosphere of a hot planet is 10^{-4}-10^{-3}. The spectra were generated at a resolving power R=300 for λ<5 μm and R =30 for λ>5 μm (*left*). *Right*: transmission spectra of cloud-free and cloudy atmosphere of a gaseous planet [81]. Particle size, shape, distribution and the pressure of the atmospheric layer where clouds/hazes form cause changes in the spectra in the VIS-NIR [102]

Retour à la table des matières : p. v

Table 3 Summary of EChO's three tiers: objectives addressed and observational strategies adopted

Tier	Key science objectives	Observables & derived products	Observational strategy
Chemical Census (Survey)	• Exploring the diversity of exoplanet atmospheres • What are exoplanets made of?	- Presence of most abundant atmospheric components, e.g. H_2O, CH_4, CO, CO_2, NH_3 etc.	A sample of planets (hundreds) which is representative of the local volume (super-earths, Neptunes & Jupiters, with a range of temperatures, orbital and stellar parameters).
		- Albedo and thermal emission	R~50 for λ<5μm R~30 for λ>5μm SNR~5
		- Presence of clouds/hazes	Transits or eclipses until the required R & SNR is reached to detect most abundant atmospheric molecules.
Origin (Deep survey)	a. Understanding the origin of exoplanet diversity & the physical mechanisms in place b. How do planet form and evolve?	- Molecular abundances of both key components and trace gases in the atmosphere, - vertical thermal profiles, - constraints on clouds/albedo.	A subset (tens) of the planets analysed through the Chemical Census tier, with a prevalence of Neptunes and Jupiters.
			R~100 for λ<5μm R~30 for λ>5μm SNR~10
			Transits+eclipses until the required SNR & R are reached to retrieve molecular abundances for most trace gases and vertical thermal profiles.
Weather, Exo-maps & Rosetta Stones (Ultra deep survey)	A very detailed and exhaustive study of a select sample of benchmark cases.	- Very precise molecular abundances of key components and trace gases, - vertical and horizontal thermal profiles and chemical gradients, - spatial and temporal variability, - orbital modulations, - constraints on clouds/albedo.	A select sample chosen among the most favourable exoplanets in their own category (typically 10 or 20). For the Exo-Meteo and Exo-Maps, exoplanets whose stars are very bright should be selected (e.g. HD 189733b).
			R~300 for λ<5μm R~30 for λ>5μm SNR~20
			Many repeated obs. of transits and/or eclipses + orbital lightcurves + eclipse mapping.

Retour à la table des matières : p. v

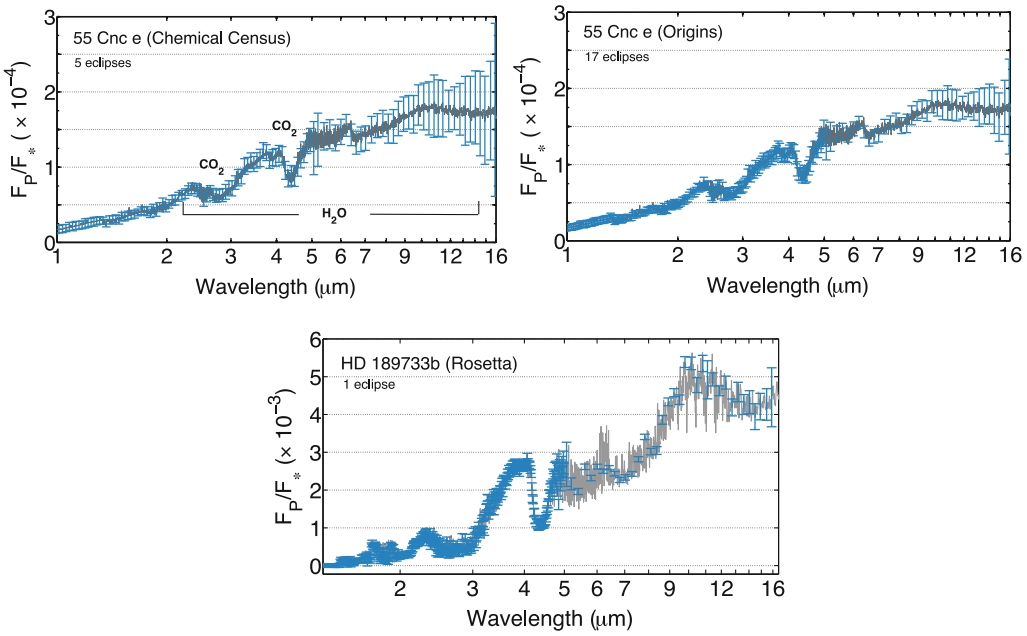

Fig. 15 EChOSim simulations (see Section 3.4) of transmission and emission spectra as observed by EChO with different survey programs. The transits or eclipses needed are reported in the figure. *Top*: emission spectra of super-Earth 55 Cnc e with Chemical Census and Origin surveys. The spectral features of CO_2 and water vapour are detectable in Chemical Census, their abundances and thermal profile retrievable in Origin. *Bottom*: emission spectrum of hot Jupiter HD 189733b (Rosetta Stones program). The key gases are retrievable very precisely, see Figs. 17 and 18

C_2H_2, C_2H_6, HCN, H_2S and PH_3), provided the atomic/molecular abundances are large enough (e.g. mixing ratios~$10^{-6}/10^{-7}$ for CO_2, $10^{-4}/10^{-5}$ for H_2O), see Tables 3, 4 and 5.

- For the temperate super-Earths, we also show that with R=30 and SNR=5, O_3 can be detected with an abundance of 10^{-7} at 9.6 μm, see Table 6.

Origin survey

A subsample of the Chemical Census (tens of planets). The Origin tier allows:

- Higher degree of confidence in the detection of key molecular features in multiple bands (see Tables 3, 4, 5 and 6, Fig. 18) enabling the retrieval of the vertical thermal profile (Figs. 17 and 18)
- Measurement of the abundances of trace gases (see Tables 3, 4 and 5) constraining the current proposed scenarios for the chemical and physical processes for exoplanet atmospheres (see Section 2.4).
- Allow determination of the C/O ratio and constrain planetary formation/migration scenarios (see Section 2.4.5)
- Constrain the type of clouds and cloud parameters when condensates are present (thickness, distribution, particle size, cloud-deck pressure)

Rosetta Stones

Benchmark cases, which we plan to observe in great detail to understand an entire class of objects. For these planets we can observe:

Retour à la table des matières : p. v

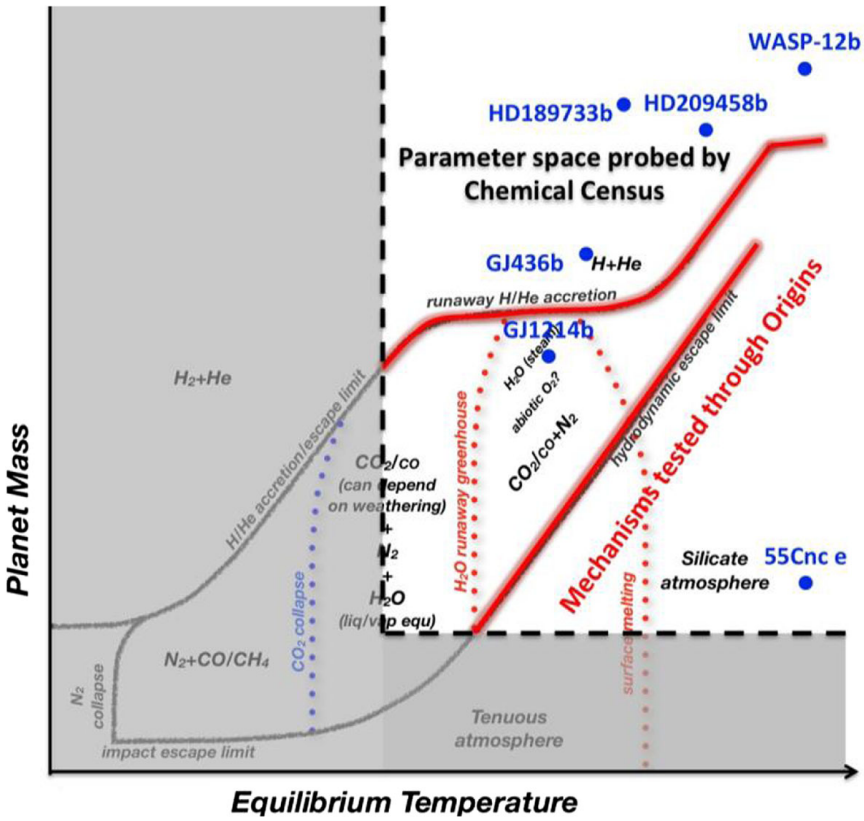

Fig. 16 Parameter space probed by the Chemical Census, i.e. a large number of planets with masses ranging from~5 Earth Masses to very massive Jupiters, and temperatures spanning two orders of magnitude, i.e. from temperate, where water can exist in a liquid phase, to extremely hot, where iron melts. A few known planets, benchmark cases representative of classes of objects, are shown in the diagram to orientate the reader. These are excellent objects to study as Rosetta Stones. Key physical processes responsible of transitions among classes of exoplanets are identified: these mechanisms can be tested through the Origin survey

- Weak spectral features for which the highest resolving power and SNR are needed.

Among Rosetta Stones, a good candidate for the Exo-Meteo & Exo-Maps survey, is a planet whose requirements for the Chemical Census can be achieved in one transit or

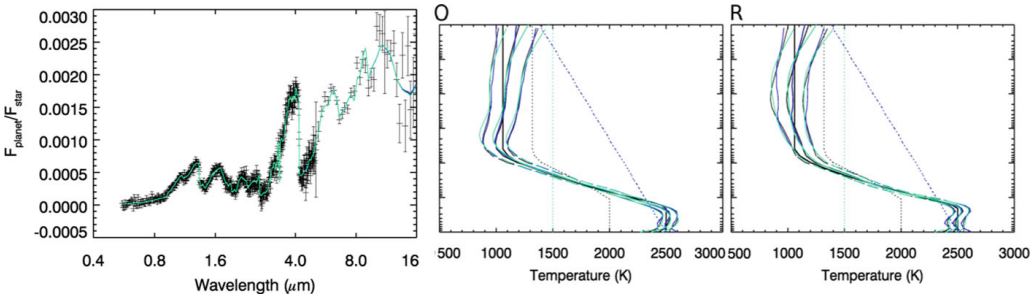

Fig. 17 *Left* Eclipse spectra for a hot-Jupiter observed in Rosetta Stone program. The *fitted spectra colours* correspond to different temperature priors, as on the *right*. The temperature prior used does not affect the resultant spectral fit. *Right*: Temperature retrievals of a hot-Jupiter from eclipse observations (L-R: Origin, Rosetta Stone). The three different temperature priors used are shown by *dotted lines*; the *thick black line* is the input profile, and the three retrieved profiles are shown by the *thin solid lines*. The retrieval error is shown by the *dashed lines*

Retour à la table des matières : p. v

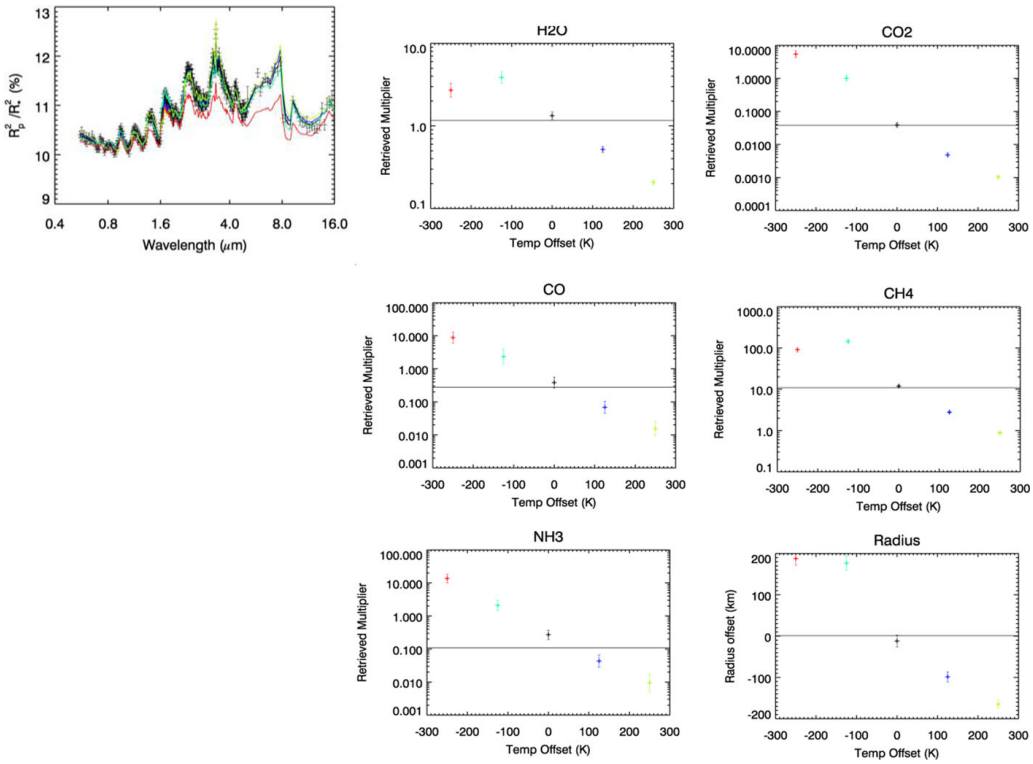

Fig. 18 Retrieved results for a hot Neptune transit spectrum observed in the Rosetta Stone tier. *Colours* correspond to different reduced χ^2: *red*=17.1, *green*=2.0, *black*=1.2 (best fit), *blue*=1.6, *yellow*=2.8. For a good retrieval the reduced χ^2 should be close to 1. The best fit is the *black* one, for which the temperature and gases are correctly retrieved

eclipse. Gaseous planets such as HD 189733b, HD 209458b, or GJ 436b are the most obvious candidates for this type of observations today, meaning we can observe:

- Temporal variability, i.e. Exo-Meteo (weather, Section 2.4)
- Spatial resolution, i.e. Exo-Maps (2D and 3D maps, Section 2.4)

3.2.3 Optimal SNR & information retrieved

Most of the science objectives detailed in Section 3.2, are based on the assumption that EChO can retrieve the molecular composition and the thermal structure of a large number of exoplanet atmospheres at various levels of accuracy and confidence, depending on the scientific question and target selected.

We consider here the goal wavelength coverage assumed for EChO, i.e. 0.4 to 16 μm, and investigate the key molecular features present in a range of planetary atmospheres with a temperature between ~300 and 3000 K. In a planetary spectrum, as measured through a transit or an eclipse, the molecular features appear as departures from the continuum. At a fixed temperature-pressure profile, the absorption depth or emission features will depend only on the abundance of the molecular species. Tables 4 to 6 show the minimum abundance detectable for a selected molecule absorbing in a planetary atmosphere, as a function of wavelength and observing tier, i.e. Chemical

Retour à la table des matières : p. v

Table 4 Examples of average detectable abundances for a warm-Neptune (e.g. GJ 436b) for the three tiers [165]. The molecular abundance is expressed as mixing ratio

	CH_4		CO		CO_2			NH_3			H_2O		
Obs. mode	3.3 μm	8 μm	2.3 μm	4.6 μm	2.8 μm	4.3 μm	15 μm	3 μm	6.1 μm	10.5 μm	2.8 μm	5–8 μm	11–16 μm
Rosetta St.	10^{-7}	10^{-6}	10^{-4}	10^{-6}	10^{-7}	10^{-7}	10^{-7}	10^{-7}	10^{-6}	10^{-7}	10^{-6}	10^{-6}	10^{-5}
Origins	10^{-7}	10^{-6}	10^{-3}	10^{-5}	10^{-6}	10^{-7}	10^{-6}	10^{-6}	10^{-6}	10^{-6}	10^{-6}	10^{-5}	10^{-4}
Ch. Census	10^{-7}	10^{-5}	10^{-3}	10^{-4}	10^{-6}	10^{-7}	10^{-5}	10^{-5}	10^{-5}	10^{-5}	10^{-5}	10^{-5}	10^{-4}
	HCN			PH_3		C_2H_6		H_2S			C_2H_2		
Obs. mode	3 μm	7 μm	14 μm	4.3 μm	10 μm	3.3 μm	12.2 μm	2.6-μm	4.25-μm	8 μm	3 μm	7.5 μm	13.7-μm
Rosetta St.	10^{-7}	10^{-5}	10^{-7}	10^{-7}	10^{-6}	10^{-6}	10^{-6}	10^{-5}	10^{-4}	10^{-4}	10^{-7}	10^{-5}	10^{-7}
Origins	10^{-6}	10^{-5}	10^{-6}	10^{-7}	10^{-6}	10^{-5}	10^{-5}	10^{-5}	10^{-4}	10^{-3}	10^{-7}	10^{-4}	10^{-6}
Ch. Census	10^{-6}	10^{-4}	10^{-5}	10^{-7}	10^{-5}	10^{-5}	10^{-5}	10^{-4}	10^{-3}	–	10^{-7}	10^{-3}	10^{-5}

Retour à la table des matières : p. v

Table 5 Examples of average detectable abundances for a hot super-Earth around a G-type star (e.g. 55 Cnc e) for the three tiers. The molecular abundance is expressed as mixing ratio

	H_2O			CO_2		
Obs. Mode	2.8 μm	5–8 μm	11–16 μm	2.8 μm	4.3 μm	15 μm
Rosetta St.	10^{-4}	10^{-4}	10^{-4}	10^{-5}	10^{-7}	10^{-5}
Origins	10^{-4}	10^{-3}	10^{-3}	10^{-5}	10^{-6}	10^{-4}
Ch. Census	10^{-3}	–	–	10^{-4}	10^{-5}	–

Census, Origin, Rosetta Stones (see Table 3). We show here the results for three planetary cases: warm Neptune, hot and temperate super-Earth. The spectral resolving power is lowered to R=20 in the 5 to 16 μm spectral interval for the temperate super-Earth, being the most challenging planet type that EChO might observe. For simulations on hot and temperate Jupiters see [165].

As shown by Tables 4, 5 and 6, for most planetary cases, the Chemical Census tier is enough to detect the very strongest spectral features for the most abundant molecules, whereas the Origin tier can reveal most molecules with mixing ratios of 10^{-6} or lower, often at multiple wavelengths, which is excellent for constraining the type of chemistry or the C/O ratio. The robustness of these results was tested by exploring the sensitivity to parameters such as the vertical thermal profile, the mean molecular weight of the atmosphere and the relative water abundances: the main conclusions remain valid except for the most extreme cases [165]. Should clouds/hazes be present, having multiple absorption bands available greatly help the molecular detection. In general, small cloud particles affect mainly the short wavelengths (i.e. VIS and NIR), while the atmosphere becomes more transparent at longer wavelengths Fig. 19 [102]. Further simulations will be done in the future using the TauRex retrieval models [189, 190]

Similar conclusions were reached through simulations with the NEMESIS (Non-linear optimal Estimator for Multivariate spectral analysis) radiative transfer and retrieval tool [11, 12]. NEMESIS was used to explore the potentials of the proposed EChO payload to solve the retrieval problem for a range of H_2-He planets orbiting different stars and Ocean planets such as GJ 1214b.

NEMESIS results show that EChO should be capable of recovering all gases in the atmosphere of a hot-Jupiter to within 2-sigma for all tiers. However, we see differences

Table 6 Examples of average molecular detectability for a temperate super-Earth (~320 K) around a late M for fixed SNR and R=20. The molecular abundance is expressed as mixing ratio

	H_2O		CO_2	NH_3		O_3	
SNR	5–8 μm	11–16 μm	15 μm	6 μm	11 μm	9.6 μm	14.3 μm
10	10^{-6}	10^{-4}	10^{-6}	10^{-5}	10^{-6}	10^{-7}	10^{-5}
5	10^{-6}	10^{-4}	10^{-6}	10^{-6}	10^{-6}	10^{-7}	10^{-5}

Retour à la table des matières : p. v

in the retrieved T-p profile between the Chemical Census, Origin and Rosetta Stone tiers. As expected, for the Chemical Census the spectral resolution is too low to fully break the degeneracy between temperature and gas mixing ratios, so the retrieved profile is less accurate. This is not the case for Origin and Rosetta Stone (Fig. 17). Examples of spectral fits for the Rosetta case are also shown in Fig. 17. The temperature prior chosen does not affect the retrieval or the spectral fit.

Similar results were obtained for the hot-Jupiter's transit spectra and for the hot-Neptune's transit and eclipse spectra (Fig. 18; [13]). In primary transit, it is not possible to retrieve independently the T-p profile due to the limited sensitivity to temperature, but by performing multiple retrievals with different assumed T-p profiles and comparing the goodness-of-fit of the resulting spectra, we can obtain the constraints needed. In Fig. 18, the different colours correspond to retrievals using different model T-p profiles, with the best fit being provided by the input temperature profile, as expected. From this, we can correctly infer the temperature and gaseous abundances from primary transit.

As well as constraining the temperature of hot Jupiters and Neptunes, with a few tens of eclipses we can obtain sufficient signal-to-noise to allow a retrieval of the stratospheric temperature of super-Earths atmospheres, such as GJ 1214b, which has not been achieved to date [11]. An independent constraint on the temperature will be valuable for interpreting the better-studied transit spectrum of GJ 1214b, which will also be significantly improved in quality by EChO observations (see Fig. 5).

3.3 Laboratory data for EChO

3.3.1 Linelists

Interpreting exoplanetary spectra requires access to appropriate laboratory spectroscopic data, as does the construction of associated radiative transport and atmospheric models. These objects may reach temperatures up to about 3000 K meaning that billions of transitions are required for an accurate model [163, 195]. A dedicated project is in progress to provide comprehensive sets of line lists for all the key molecules expected to important in exoplanet atmospheres (both hydrogen-

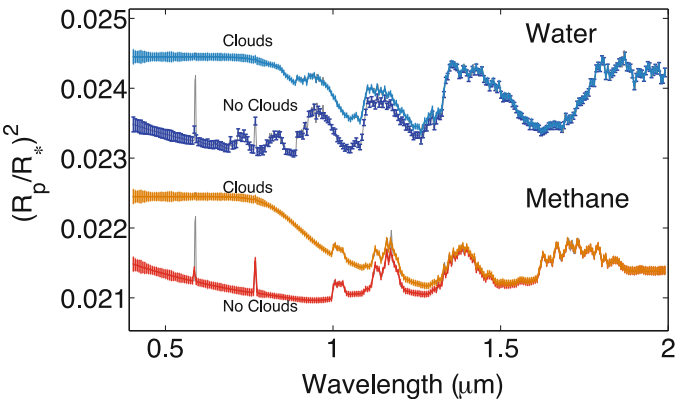

Fig. 19 Examples of cloudy and clear-sky gaseous planet spectra with different molecular compositions as observed by EChO. The performances obtainable with EChO allow the detection of clouds/hazes and their characteristics, as well as the extraction of the molecular abundances. For clarity, we have included an offset between the methane-rich and the water-rich spectra

Retour à la table des matières : p. v

rich gas giants and oxygen-rich terrestrial-like atmospheres). The ExoMol project (www.exomol.com) aims at providing complete lists for the 30 most important species (including methane, water, ammonia, phosphine, hydrogen sulphide, a variety of hydrocarbons and a long list of stable and open shell diatomics) by 2016 [162]. These data will therefore be available for pre-launch testing and design studies [163].

3.3.2 Reaction / photodissociation rates

The diversity of exoplanetary atmospheres observable with EChO spans a broad range of physical conditions. Individual reaction rates must therefore be known at temperature ranging from below room temperature to above 2500 K and – because the deep atmospheric layers are chemically mixed with the layers probed by spectroscopic observations – at pressures up to about 100 bars. Today these rates are well-known at room temperature, but only rarely determined at high temperature. The teams from University of Bordeaux and LISA Créteil, France, are measuring new photoabsorption cross-section at high temperatures, at wavelengths shorter than 200 nm [180]. The first measurements for CO_2 have been performed at the synchrotron radiation facility BESSY, in Berlin, and at LISA, Créteil.

3.3.3 Optical properties of gases at high Pressure-Temperature

Despite various measurements and theoretical models dedicated to the optical properties of gases, accurate data at different temperatures and pressures are still lacking in numerous spectral regions. Little or no data in some case are available for continuum absorption, line mixing, far wings and collision induced absorption, even for the well-studied carbon dioxide molecule. The scenario is further complicated by the need to reproduce in the laboratory very long path lengths to be able to measure weak but important absorption and/or to boost the sensitivity and accuracy of the setup. New data will become available due to experiments performed in support to operational or planned solar system missions. In particular, measurements are available from the laboratory at INAF-IAPS Rome (http://exact.iaps.inaf.it) performed for Venus Express orbiting around Venus [155], and more measurements are planned for JUNO presently in cruise to Jupiter. Finally, the increasing availability of new tunable lasers in the EChO spectral range makes possible the use of the cavity ring down technique, which has been proven to be very effective e.g. in the continuum measurements of the Venus' atmospheric windows [152].

3.4 Dealing with systematic & astrophysical noise

3.4.1 EChO performance requirements

EChO's top-level requirement is that the photometric stability over the frequency band of interest shall not add significantly to the photometric noise from the astrophysical scene (star, planet and zodiacal light). The frequency band over which the requirement applies is between 2.8×10^{-5} Hz and 3.7 mHz, or ~5 min to 10 h [60, 122, 127, 187]. This implies having the capability to remove any residual

Retour à la table des matières : p. v

systematics and to co-add the elementary observations from many repeat visits to a given target.

The photometric stability budget is described by Puig et al. [127], Pascale et al. [122], and Waldmann and Pascale [187]. To achieve the required performance, particular attention is required to:

- the design of the instrument
- the calibration strategy to characterise all possible systematic variations in performance
- the data processing pipeline(s).

We briefly discuss these topics in the following sections.

3.4.2 Design of the instrument and knowledge of its characteristics

The most important factor determining the final performance of the mission is the way the instrument is designed. Even though the whole wavelength range is divided into bands observed using different physical spectrometer modules, the instrument is designed to operate as a single entity within the same thermal, optical, electrical and mechanical environment.

Particular care has been given to the way the modules are designed in order to share similar technological solutions for each module. For example, the detector technology is similar among all the modules and the readout units and the common electronics are designed as a single unit to simplify the electro-magnetic compatibility. All the modules as well as the Fine Guiding Sensor (FGS) share a common field of view and telescope optical train with specific dichroics mounted on the same optical bench. They are thus at the same temperature and see the same mechanical environment. In this way optical path errors between modules and the common optics are reduced to a minimum and thermo-mechanical drift within the instrument is eliminated by having an isothermal design of the optical modules. Any pointing jitter is seen directly by both the FGS and the spectrometer instrument and this information can be accounted for in the data processing. Likewise, through calibration, performance monitoring and use of the FGS data, changes in optical path between the telescope and the instrument (such as “breathing” of the point spread function or changes in telescope focus) can be identified and calibrated out of the data.

During the development phase all the critical components, particularly the detectors, will be intensively tested to determine their intrinsic characteristics. This will include determining their sensitivity to environmental variations such as temperature variations, pointing jitter, high-energy particles, electro-magnetic contamination etc. The aim is to understand and predict the evolution of the instrument response when the environmental conditions vary, and therefore to optimise the correction pipeline and the housekeeping monitoring needed as input to the pipeline. The overall instrument will thus be fully calibrated and its performance verified at subsystem and system level before launch in order to check its global behaviour and evaluate its performance using laboratory calibration sources.

Retour à la table des matières : p. v

3.4.3 The calibration strategy

As described in Eccleston et al., [60], photovoltaic detectors based on MCT (mercury cadmium telluride) will be used for EChO. They are known to have various non-linear behaviours both in regard to responsivity and dark current. Whilst we have designed an instrument that allows to monitor continuously this behaviour during observation phases, it will also be necessary to verify the behaviour of the detectors and instrument in flight over a number of timescales (in-flight calibration). These will range from determining the short-term response of the detectors through to slow changes in the instrument performance due to the effects of the space environment and component ageing. It is therefore necessary to consider regular calibration phases between the observations and, possibly, during them. Depending on the final temporal stability of the instrument, several parameters will be checked at different timescales from several hours to days. The calibration strategy includes the use of both an internal calibration unit within the instrument and a list of stable stars (known to be stable to 10^{-5} over the necessary timescales) spread all over the sky.

3.4.4 The data processing

It is crucial to correct the raw observed signal time series to account for variations in the signal which are not directly linked to the planetary transit or occultation. The methods for doing this will be encapsulated in the data processing algorithms to be employed in the data pipeline; the final data quality and performance of EChO are highly dependent on the performance of these algorithms. There may be many systematic variations to account for, most of which will be negligible, but we highlight two areas requiring particular attention:

- *The astrophysical scene contributions*: the stellar variability, the local zodiacal cloud contribution, the exozodiacal cloud contribution and any contaminating stars. These are independent of the instrument performance but may add systematic signals resembling the transiting planet.
- *The instrument drifts, pointing jitter, detector non-linearity and any dependence on environmental variations and ageing*. These effects will be highly correlated between the spectral bands and many of the effects will be monitored by, for example, off axis detectors, thermistors, the Fine Guidance Sensor and will ultimately be assessed through dedicated calibration observations.

These issues will be addressed by data reduction techniques validated on current instruments as described in Sections 3.4.5 and 3.4.6. These techniques use the inherent redundancy in the data, knowledge of the target planetary orbital phase and secondary information from the instrument and satellite to remove unwanted systematic effects.

3.4.5 Decorrelating instrument systematics

Detecting the atmospheric signal of an exoplanet requires high precision measurements (Fig. 20). Limitations to said precision come from the systematic noise associated with the instrument with which the data are observed. This is particularly true for general,

Retour à la table des matières : p. v

non-dedicated observatories. In the past, parametric models have been used extensively by most teams in the field of exoplanet spectroscopy/differential band photometry to remove instrument systematics [3, 20–22, 37, 38, 47, 48, 54, 74, 86, 89–91, 156, 159–161, 169–171]. Parametric models approximate systematic noise via the use of auxiliary information about the instrument, the so called Optical State Vectors (OSVs). Such OSVs often include the X and Y-positional drifts of the star or the spectrum on the detector, the focus and the detector temperature changes, as well as positional angles of the telescope on the sky. By fitting a linear combination of OSVs to the data, the parametric approach derives its systematic noise model. We refer to this as the "linear, parametric" method. In many cases precisions of a few parts in 10,000 with respect to the stellar flux were reached.

In the case of dedicated missions, such as Kepler [28, 85], the instrument response functions are well characterised in advance and conceived to reach the required 10^{-4} to10^{-5} photometric precision. EChO aims at reaching the same level of photometric precision. For general purpose instruments, not calibrated to reach this required precision, poorly sampled OSVs or a missing parameterisation of the instrument often become critical issues. Even if the parameterisation is sufficient, it is often difficult to determine which combination of these OSVs may best capture the systematic effects of the instrument. This approach has caused some debates for current instruments regarding the use of different parametric choices for the removal of systematic errors.

Given the potential intricacies of a parametric approach, in the past years alternative methods have been developed to de-correlate the data from instrumental and stellar noise. The issue of poorly constrained parameter spaces is not new in astrophysics and has given rise to an increased interest in unsupervised (and supervised) machine learning algorithms (e.g. [191]). Unsupervised machine learning algorithms do not need to be trained prior to use and do not require auxiliary or prior information on the star, instrument or planet but only the observed data themselves. The machine learning approach will then (from observations) 'learn' the characteristics of an instrument and allows us to de-trend systematics from the astrophysical signal. This guarantees the highest degree of objectivity when analysing

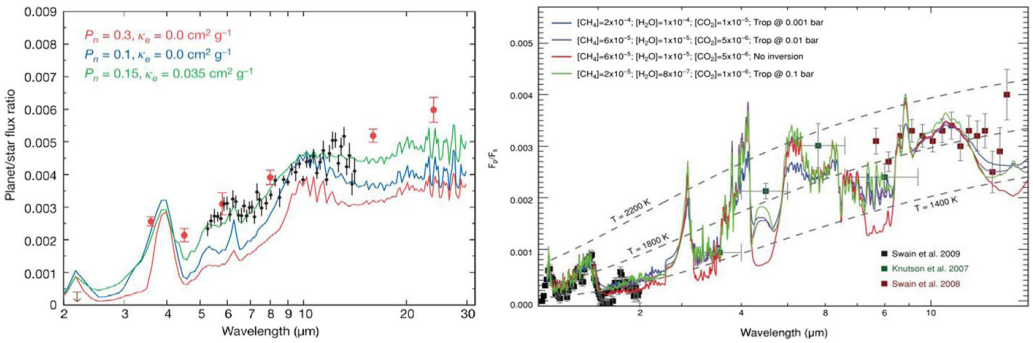

Fig. 20 Eclipse spectra and photometric data for hot-Jupiters observed with Hubble (NICMOS) and Spitzer (IRS & IRAC). *Left*: MIR observations of HD 189733b. Simulated spectra of water vapour are overlapped [74]. *Right*: NIR and MIR observations compared to synthetic spectra for three models that illustrate the range of temperature/composition possibilities consistent with the data [159, 161]. For each model case, the molecular abundance of CH_4, H_2O, and CO_2 and the location of the tropopause is given. Note that the mid-infrared data are not contemporaneous with the near-infrared data, and attempting to "connect" these data sets with a model spectrum is potentially problematic if significant variability is present

Retour à la table des matières : p. v

observed data. In Waldmann [183, 186], Waldmann et al. [185] and Morello et al. [116], Independent Component Analysis – ICA [83] has been adopted as an effective way to decorrelate the exoplanetary signal from the instrument in the case of Hubble-NICMOS and Spitzer/IRS data or to decorrelate the stellar activity from the exoplanet transit lightcurve, in Kepler data. The error-bars for non-parametric approaches can be sometimes larger than those reported by parametric approaches. This difference is due to the higher amount of auxiliary information injected in the parametric approach. Ultimately, it is a trade-off between a higher degree of objectivity for the non-parametric methods and smaller errors for the parametric detrending.

For the EChO data, both methods will be used to correct instrumental systematics and astrophysical noise. Very thorough tests and calibration of the instrument before launch (especially detector performances), will substantially help to constrain the auxiliary information of the instrument hence the decorrelation process.

3.4.6 Correcting for stellar activity

The impact of stellar activity on the EChO data has been carefully evaluated by many teams working on EChO. Results from the Kepler mission [15] indicate that most G dwarfs have photometric dispersions less than 50 ppm over a period of 6 h (typical dispersions for the Sun over the same period range between 10 and 30 ppm), while most late-K and M dwarfs vary at a level of some 500 ppm. Note that Kepler operates in the visible where stellar photometric variability is over a factor of 2 higher than in the "sweet spot" of EChO—the NIR and MIR—because of the contrast between spots and the stellar photosphere. The effects of stellar activity on EChO's observations will vary for transit and eclipse observations. Alterations in the spot distribution across the stellar surface can modify the transit depth (because of the changing ratio of photosphere and spotted areas on the face of the star) when multiple transit observations are combined, potentially giving rise to spurious planetary radius variations. The situation is simpler for occultations, where the planetary emission follows directly from the depth measurement. In this case, only activity-induced variations on the timescale of the duration of the occultation need to be corrected for to ensure that the proper stellar flux baseline is used. The EChO mission has been designed to be self-sufficient in its ability to correct for the effects of stellar activity. This is possible thanks to the instantaneous, broad-wavelength coverage and the strong chromatic dependence of light modulations caused by stellar photospheric inhomogeneities (star-spots and faculae). We have explored several possible approaches to evaluate the effect of stellar activity and developed methodologies to prove the performance of EChO data in reaching the required precision ([80, 113, 140]; Danielski et al., 2015, in preparation).

Method 1 Herrero et al. [80] investigated a direct method of correlating activity-induced variations in the visible with those in the IR. The underlying hypothesis is that variations of the transit depth in the visible are solely caused by stellar activity effects and not influenced by the atmosphere of the transiting planet. To test this approach, a realistic stellar simulator has been developed that produces time series data with the same properties as the measurements from EChO. The simulator considers surface inhomogeneities in the form of (dark) starspots and (bright) faculae, takes into account limb darkening (or brightening in the case of faculae), and includes time-variable effects such as differential rotation and active region evolution. A series of transits at wavelengths 0.8,

Retour à la table des matières : p. v

2.5, and 5.0 μm have been generated. Then, they have measured the transit depths and calculated the variations of those depths with time. They have found that there is a well-defined correlation between activity-induced transit depth variations in the visible (0.8 μm) and the IR (2.5 and 5.0 μm). An illustration of the transit light curves generated by the simulator and the correlation between visible and IR transit depth variations (TDV) can be seen in Fig. 21 (top panels). In practice, the correction of EChO data for stellar activity using, for example, a series of measurements in the visible and an IR band can be done using the following expression: $d_{IR}^{corr}=d_{IR}+a_0+a_1\cdot(d_{VIS}-\langle d_{VIS}\rangle)$, where d stands for the transit depth, and a_0 and a_1 are the coefficients of a linear fit that can be determined from simulations.

A number of combinations of stellar photospheres and active region parameters (size and location of spots, temperature contrast) were considered to obtain a statistical view of the method. The results can be seen in Herrero et al. [80]. The cases analysed represent standard stars of GKM spectral types with filling factors of 1–7 %, i.e., corresponding to stars that are ~4–30 times more spotted than the active Sun. The procedure explained in Herrero et al. [80] provides a correction of the transit data to a few times 10^{-5}, and thus is fully compliant with EChO noise requirements.

Method 2 A complementary method has been developed by Micela [113] to reconstruct the spectral energy distribution of the target stars in the IR using the visible spectrum (0.55–1 μm) as an instantaneous calibrator. Having a sufficient number of spectra of a given stars observed at different levels of activity, it is possible to calibrate the method for each star. The approach has been developed on a grid (in spot temperature and filling factor) of models of active stars and has been tested through simulations taking into account for photon noise. The method is based on principal component analysis. Since the new variables are chosen to maximize the variance, it is possible to reduce the dimensionality of the space, eliminating the dependences among the original variables and noise. In all the explored cases the first two components are retained: the first component is related to the slope of the spectrum while higher order components are related to features of the spectrum.

The procedure involves the following steps: 1) generation of 1000 simulations of the input model assuming an average SNR per resolution element; 2) projection of the simulated spectra into the space of the first two components; 3) identification of the best fit spectrum in the principal component space and selection of the corresponding NIR spectrum as the "best estimate" of the NIR stellar spectrum; and 4) comparison between the spectral distortion with no correction (assuming an unspotted star) and the residual after adopting the best estimate. Figure 21 shows as an example the median correction of the 1000 simulations and the 25 and 75 % quartiles for T_{eff}=5200 K and stellar SNR=500. We compare the distortion before applying the correction, measured as the average value in the 1–2 μm band where the

Fig. 21 *Top left*: Transit light curves at 2.5 μm (*red*) and 5.0 μm (*green*) for one of the cases generated in the sample, compared with the transit light curve of an immaculate star. Note the small systematic deviations and the more apparent spot crossing events. *Top right*: Correlation of activity-induced transit depth variations (TDV) in the visible (0.8 μm) and the IR (2.5 and 5.0 μm). The *top panels* are from Herrero et al. [80]. *Bottom*: distortion of the near IR stellar spectrum for three cases (stars with temperatures of 6000, 5200 and 4200, spot ΔT=700 K and filling factor=0.01). *Black lines*: spectral distortions without corrections, *red lines*: residual distortion after the correction with method 2, the three lines correspond to the 25th, 50th, and 75th percentiles of 1000 simulations [113]

Retour à la table des matières : p. v

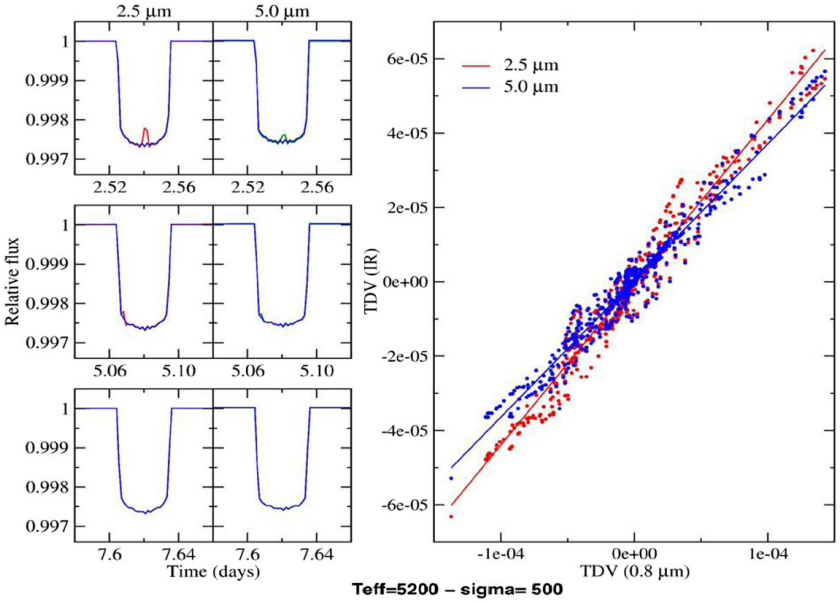

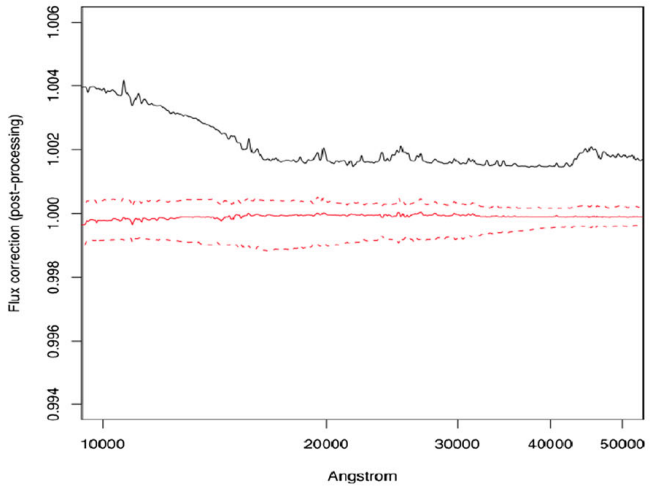

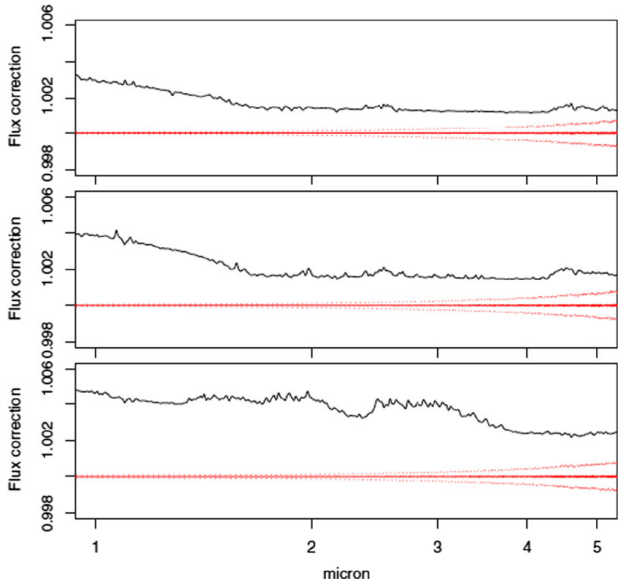

Retour à la table des matières : p. v

effect is larger, and the equivalent average of the median and 25–75 % quartiles of the residuals after the correction. This method allows for a significant reduction of the spectral distortion, see Fig. 21 and Micela [113].

Method 3 A further approach has focused on statistical methods to de-correlate astrophysical noise from the desired science signal. Whilst the statistical fundamental of these methods are very different and often complementary, they all try to disentangle the astrophysical signal from various noise sources using the coherence of the exoplanetary transit/eclipse signature over time and/or frequencies of light. Figure 22 shows two examples of such a decorrelation. Given single time series on an active star with various modes of pulsation obtained by the Kepler space telescope, Waldmann [183] showed that a randomly chosen pulsation mode of the star could be isolated and the remaining autocorrelative noise of the star suppressed, resulting in a strong reduction of the stellar noise component (Fig. 22 left). Similar concepts apply to periodic exoplanetary lightcurves observed over multiple transits and/or wavelengths.

The results were repeated successfully for a sample of Kepler stellar light curves, spanning from M to G types. In all cases a correction of the order of 10^{-5} to 5 10^{-4}

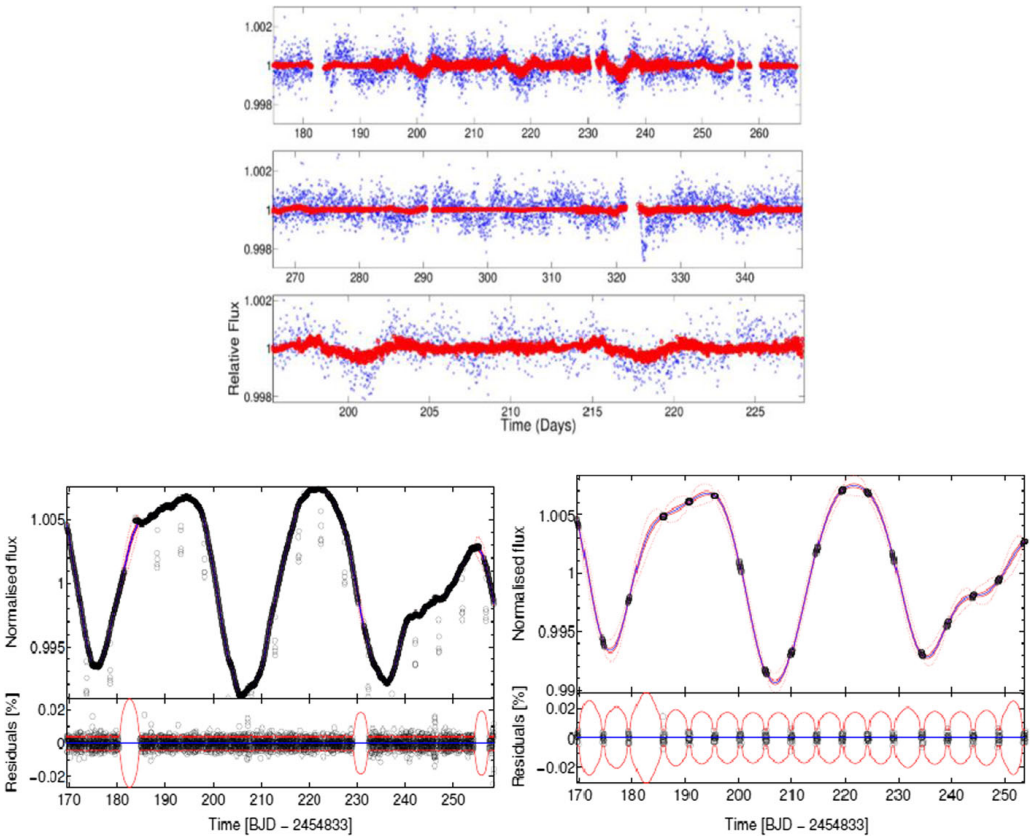

Fig. 22 *Left*: Kepler time series of an active M0 star (*blue dots*). Using Independent Component Analysis, the periodic pulsation filter at t=202, 218 and 235 was filtered from other correlated noise in the time series. The filtered signal is shown in red [183]. *Centre and Right*: Kepler time series of another active K4 star. Using a Gaussian Process based method the stellar activity was successfully filtered out, with residuals as small as 10^{-5} when considering daily observations of 10 h (*Centre*) and 10^{-4} when data are acquired for 10 h every 5 days (Right) (Danielski et al., 2015, in preparation)

Retour à la table des matières : p. v

depending on the frequency of the sampling (i.e. 10 h continuous observations every day or 10 h once a week), was obtained (Danielski et al. 2015, in preparation).

3.5 Evaluation of EChO performance

In this section, we briefly describe the strategy developed for the evaluation of EChO's performance, and the evaluation done during the Phase A study.

3.5.1 Performance evaluation tools

The performance of EChO has been assessed using computational models based on two approaches. The first approach taken is based on a static radiometric model that takes the required performance figures for the payload to 'size' the mission. This model has been used to calculate the number of transit/occultation revisits necessary to achieve a specified SNR in the transit spectral features and the possible revisits during a given mission lifetime [127]. The second approach is to construct a model that simulates the actual performance of the mission as realistically as possible (EChOSim). This end-to-end simulation is fully dynamic and accounts for the major systematic influences on the performance such as pointing jitter, internal thermal radiation sources, detector dark current and noise [122, 187]. Both models have been used to calculate the observation duration needed for the targets in the EChO sample. We find that a nominal mission lifetime of 4 years is sufficient to fulfill the science requirements and a mission of 6 years would fulfill the most ambitious EChO goals. The use of separate performance models with similar results gives confidence that the mission can be undertaken as planned and can deliver the science described in this paper.

3.5.2 Overall noise allocation

Using the EChOSim tool, we can evaluate the performance by calculating the overall noise allocation and comparing this to the scientific requirements. The procedure is extensively described in [122] and here we only summarise the main results.

- Noise associated to the astrophysical scene:
  The number of detected photons from the planet and star, N_0, and the zodiacal background photons in a sampling interval Δt, *Zodi*, are used to estimate the level of photon noise from the astrophysical scene:

$$\sigma_N^S = \sqrt{N_0 + Zodi} \quad \frac{e^-}{pixel} - rms \tag{1}$$

  It is convenient to refer the noise in one sampling interval to the noise per unit time:

$$\sigma_N = \sigma_N^S / \sqrt{\Delta t} \qquad \left[e^- pixel^{-1} s^{-1/2} - rms \right] \tag{2}$$

Retour à la table des matières : p. v

- Noise associated with the instrument:

  All sources of instrumental noise contribute to the total system noise level, σ_{SN}. The system noise level is then given by the sum in quadrature of all individual noise components:

$$\sigma_{SN} = \sqrt{\sigma^2_{RO} + \sigma^2_{DC} + \sigma^2_{Tel} + \sigma^2_{Opt} + \sigma^2_{RPE+PDE}} \qquad \left[e^- pixel^{-1} s^{-1/2} - rms\right] \quad (3)$$

  σ_{RO} is the detector readout noise, σ_{DC} is the dark current noise, σ_{Tel} is the combined photon noise associated to the thermal emission of all optical surfaces in the line of sight, σ_{Opt} is the photon noise associated to the thermal emission of the module enclosure, and $\sigma_{RPE+PDE}$ expresses the photometric noise associated to the pointing jitter.

3.5.3 Simulations of EChO planetary spectra

Using the EChOSim tool, we can simulate the observation of key targets and see how the overall requirements translate into reconstructed spectra. We show here two cases: the transit of a warm Neptune around a faint object (GJ 3470b) in the Rosetta Stone tier, and the eclipse of this same object in the Origin tier.

GJ 3470b is a 0.0437 M_J planet with a radius of 0.374 R_J (where M_J and R_J are respectively the mass and the radius of Jupiter), orbiting at 0.036 AU with a period of 3.3367 days around its parent star (M1.5 V star, mV=12.27, T_{eff}=3600 K at 30.7 pc). The transit and eclipse duration is about 1 h and 45 min. The atmospheric composition and thermal properties used for our simulation are taken from Venot et al. [179, 181].

The transit observation of GJ3470b in the Rosetta Stone tier requires the co-addition of 21 transits, assuming the current design of the mission and the known parameters of the planetary system. We estimated the observable $(R_p/R_s)^2$ (the transit depth, where R_p and R_s are the planetary and the stellar radius respectively) as a function of the wavelength (Fig. 23). The associated error bars are computed using a dynamical fitting method implemented in the observation pipeline [122]. This figure clearly shows that the transit depth chromatic variations associated with atmospheric

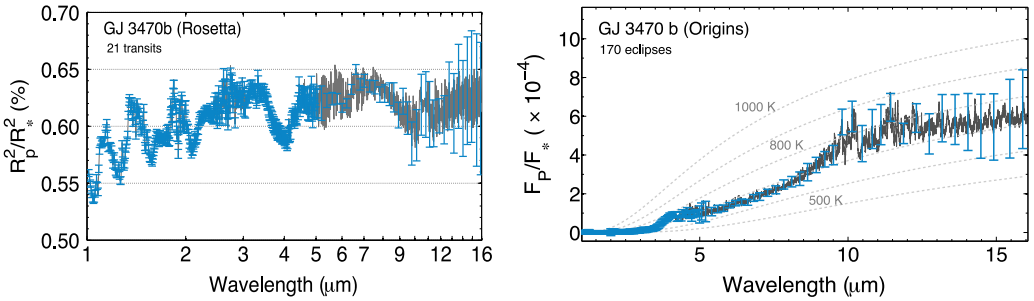

Fig. 23 *Left*: Transit depth as a function of wavelength for GJ3470b as observed with EChO. We assumed the co-addition of 21 transits and the current design of the instrument and data processing pipeline. *Right*: Planet to star contrast as a function of wavelength assuming the co-addition of 170 eclipses

Retour à la table des matières : p. v

absorptions can be detected in the IR spectral range even with a limited number of transit observations. The SNR decreases over 12 μm due to the increase noise in the detection chain and the contribution from thermal noise. The transit spectrum exhibits various spectral features associated not only with water vapour but numerous other molecules.

Similar simulations have been done for the eclipse spectra, which provide the planet to star contrast as a function of wavelength (Fig. 23)

Using both transit and eclipse spectra together, one can determine the mean molecular weight of the atmosphere, the atmospheric components, the temperature as a function of pressure, the presence and type of clouds. These calculations have been repeated for all the targets observable by EChO (see next section).

4 Mission strategy

In this section we describe the list of currently available targets for EChO (>150), and we discuss the foreseen developments for the future, given the large number of ground and space dedicated facilities to discover new exoplanets in the next decade. The final list is expected to include hundreds of exoplanets, with a variety of sizes, temperatures, stellar hosts and orbital parameters.

4.1 EChO's current Core Sample

To produce a sample of potential targets for EChO using known systems we first drew up a "long list" of known targets with well characterised stellar and planetary parameters. This list has been generated using the EChO Target List Observation Simulator (ETLOS) [177] and will be continuously updated. ETLOS extracts the star/planet information from the Open Exoplanet Catalogue [132]; further verification is done using SIMBAD, the 2MASS catalogue and exoplanet.eu [141] where appropriate. The Core Survey targets were then selected to ensure as diverse range stellar types, metallicities and temperatures as possible to fulfil the requirements of the Chemical Census. Suitable targets for the Origin and Rosetta Stone tiers were further selected to fulfil the requirements expressed in Table 3.

To assess the total time needed to observe the required number of targets in the three survey tiers we have undertaken simulations of the mission and instrument performance. As explained in Section 3.5, two rather different approaches were taken for this. The first is a static model built using more generic assumptions about the instrument and mission performance (ESA Radiometric Model, [127]). The second approach models the instrument as designed and uses a dynamic approach to the performance simulation using realistic stellar and planetary parameters to model to actual time domain signal from the observation (*EChOSim,* [122]). The list of known targets was run through the ESA–RM and *EChOSim* performance models. Although some differences are expected due to the different parameterisation of the instrument and other model assumptions, the results spread over the Core Survey are consistent, and the discrepancies for specific targets are understood and traceable. We are therefore confident of the robustness of the estimates obtained.

Retour à la table des matières : p. v

The integration times needed for each observing mode and the detectability for key molecular species are reported in [177]: http://www.ucl.ac.uk/exoplanets/echotargetlist. The diversity of the selection is shown in Figs. 24 and 25 where we show how current select targets are distributed between stellar type, metallicity, orbit type, density and temperature.

4.2 The future EChO Core Sample

A comprehensive exercise has been run to establish a target statistical sample of transiting targets for EChO that would cover the widest possible range of exoplanet/host star parameter space [133]. As a first step, star counts were estimated using (a) new catalogues [69, 98] making cuts based on spectral type and magnitude directly, and (b) using the combination of the stellar mass function derived from the 10-pc RECONS sample and the mass-luminosity-K-band relationship from [8]. Estimates were then made of the maximum number of exoplanets of a given exoplanet class (mean radius/mass: Jupiter-like 10 R_{Earth}/300 M_{Earth}; Neptune-like 4 R_{Earth}/15 M_{Earth}; Small Neptune 2.6 R_{Earth}/6 M_{Earth}; Super-Earth-like 1.8 R_{Earth}/7 M_{Earth}) and fiducial equilibrium temperature (T_{hot}=1500 K; T_{warm}=600 K; $T_{temperate}$=320 K) that transit a selection of stellar spectral types from K to M. This was done using statistics from the Kepler mission and adopting a methodology similar to that described in a recent paper by Fressin et al. [68].

Planet occurrence rates based on Kepler results were calculated for all spectral types. These rates are weighted towards solar-like stars because of the predominance of FGK hosts in the Kepler survey itself. An analysis of the planet occurrence rates for M hosts observed by Kepler indicates that the rates are consistent with those found for earlier spectral types, albeit at low statistical significance (e.g. [57]). Star counts, planet temperatures and types, and the transiting planet occurrence rate were then used to determine the numbers and types of transiting exoplanets around host stars down to a K-band magnitude of 9, with the overall total number in good agreement with estimates from HARPS [110] as well as other estimates based on Kepler data [82]. Figure 26 illustrates a possible parameter space that EChO may observe in the Chemical Census and Origin surveys according to current SNR requirements and conservative assumptions on instrument performance. These predictions are in line with the expected science yield from the future surveys (see Table 7 and Fig. 29).

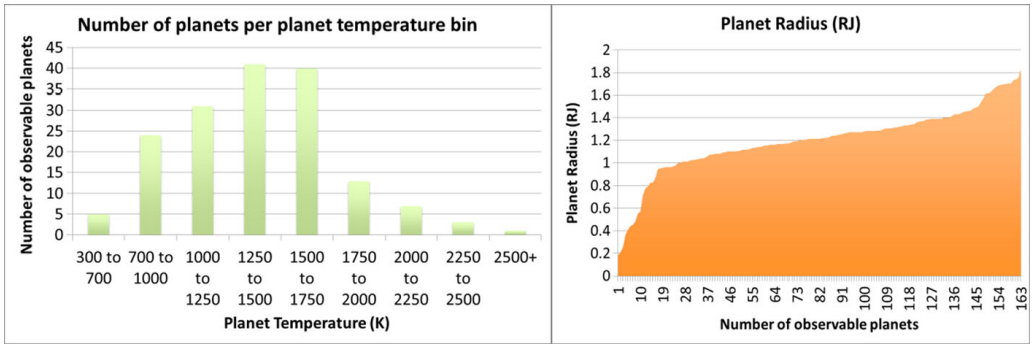

Fig. 24 *Left*: known planets observable by EChO (i.e. satisfying the requirements in Table 3) classified as function of the planetary temperature in K. *Right*: cumulative distribution function showing known planets observable by EChO classified as function of the planetary radius

Retour à la table des matières : p. v

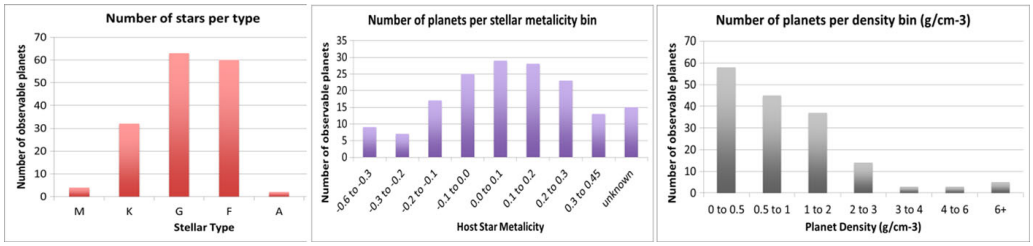

Fig. 25 Known planets observable by EChO (i.e. satisfying the requirements in Table 3) classified as function of the: *Left*: Stellar Type, *Middle*: Stellar Metallicity, *Right*: Planetary density in g/cm^3

4.3 Sky visibility/source accessibility

EChO will visit a large and well-defined set of targets (see Section 4.1 & 4.2). Repeated visits may be required to build up the SNR of individual target spectra. The maximum duration of a visit to a target system will be ~10 h—the time of the transit itself, plus about that time before and then after the transit. The time between successive transit observations will depend on orbital period and scheduling, and could be as little as a day, to as long as a few tens of days. In principle, the targets may be in any part of the sky, and as such the satellite needs a large field of regard, with minimal constraints (due to Earth/Sun) on the direction in which it can be pointed. The most challenging targets for EChO will be temperate super-Earths around M-type stars. Given the orbital radius and so period of a typical temperate planet (T_p~300 K), a maximum number of a couple of hundred transits (depending on the effective temperature/spectral type of the host star) would occur during a mission lifetime of 4 years. The complete sky shall be accessible within a year, with a source at the ecliptic observable for 40 % of the mission lifetime. Shown in Fig. 27 is a plot of the sky visibility for EChO, superposed on which are targets from the different tires of the EChO core survey.

4.4 New targets for EChO

Target selection is a key aspect of EChO. The choice of the targets will determine the planetary parameter space we will explore. The scientific outcome of the mission clearly depends on the observed sample.

There is no need to select the sample more than 10 years before launch but we need a good plan to select the best sample immediately prior to launch. In the present phase we are defining the primary physical planetary parameters that define the "diversity" of planet population. These include:

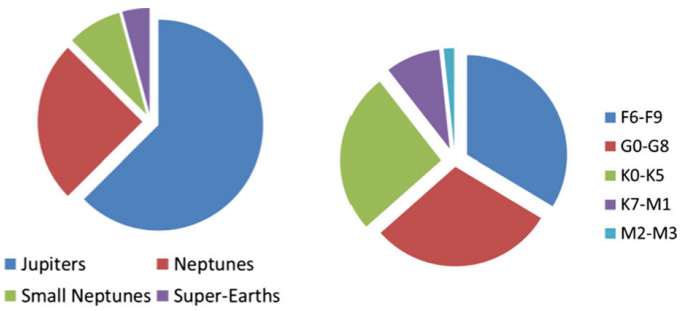

Fig. 26 Pie charts illustrating the different planetary classes considered for the future core sample

Retour à la table des matières : p. v

Table 7 Summary of the main surveys/projects that will provide targets for EChO in the next 10 years

Name of Survey/Mission	Key characteristics	Target stars relevant for EChO	Expected planets relevant for EChO	Notes
WASP/SuperWASP [126]	• Ground photometric survey—broad band • All sky • Ongoing	G-early K	100*J* Few *N*	P_{orb}<10 days; >70 J already discovered
K2 [23]	• Space survey • Survey in the ecliptic plane • Ongoing	All	~500*J* ~500 *SE, N*	P_{orb}<5 days
HATNet/HATSouth [16, 17]	• Ground photometric survey—broad band • All sky • Ongoing	G/K	100*J* Few *N*	P_{orb}<10 days; >50 J already discovered
HARPS, HARPS-N, Keck, ESPRESSO, CARMENES, SPiROU	• Ground Doppler surveys - VIS/IR • Transit search through photometric follow-up • All sky, bright stars • Ongoing/being built	G/K/M	See below	Discovered the brightest targets in each category
CHEOPS [30]	• Space photom. follow-up • 2017–2021 (3.5 years) • Monitoring of bright stars with Doppler-detected planets	G/K/M	10*N* 5 *SE*	Also used to refine parameters of planets detected by ground-based transit surveys
NGTS [40]	• Ground photometric survey – broad band • Coverage 1920° • −50<dec<−30 • 2014–2019	G/K/M	100*J* 20*N* 20 *SE*	P_{orb}<16 days
APACHE et al. [154]	• Ground photom. survey • Monitoring of 3000 M • 2012–2017	M	5 *SN/SE*	P_{orb}<10 days
GAIA [125]	• Space astrometric survey • All sky	All	10–15*J*	Around M stars 0.5–3 AU

Retour à la table des matières : p. v

Table 7 (continued)

Name of Survey/Mission	Key characteristics	Target stars relevant for EChO	Expected planets relevant for EChO	Notes
	• 2014–2019			
MEarth [119]	• Ground photom. survey • Ongoing	Late-M	5 *SN/SE*	P_{orb}<10 days; GJ 1214b
TESS [135]	• Space photometric survey • 45,000 sq degree • 2017-	G/K/M	650*J* 1000*N* 700 *SN* 300 *E & SE*	P_{orb}<50 days
PLATO [128]	• Space photometric survey • sq degree • 2024	All	~1000 J 1200 N 700 SN 600 SE	

The columns on target stars and expected planets refer specifically to the observations relevant for EChO. Legend: (*J* Jupiters, *N* Neptunes, *SN* sub-Neptunes, *SE* Super-Earths, *E* Earths)

Retour à la table des matières : p. v

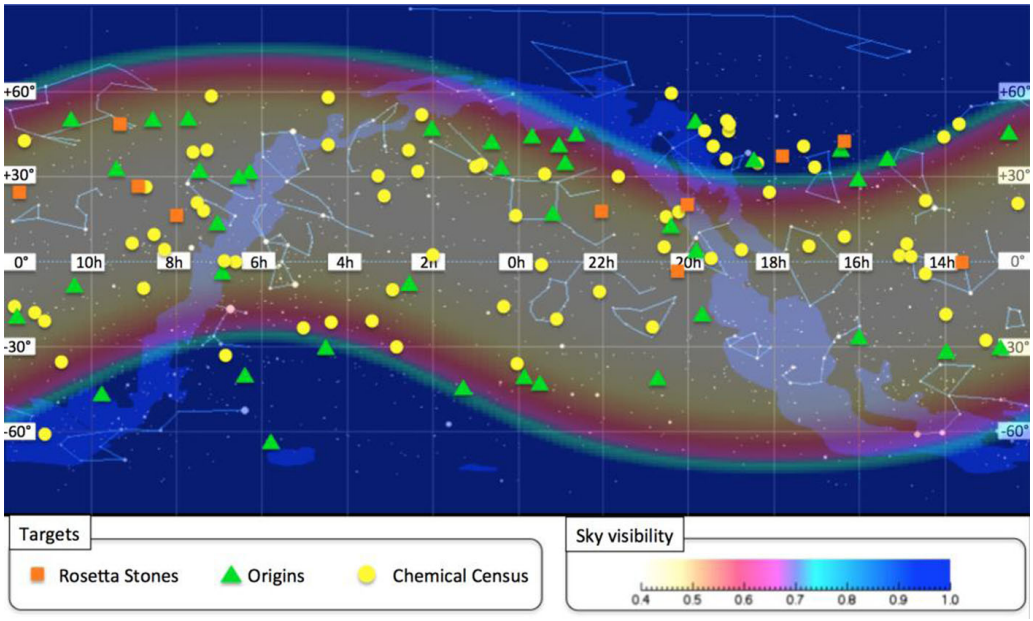

Fig. 27 A plot illustrating the fraction of the year for which a given location in the sky (in equatorial coordinates) is visible to EChO (courtesy of M. Ollivier), as seen from a representative operational orbit of EChO at L2. Superposed are known exoplanets that would be targets in the EChO Core Survey, as described in Section 4.1). Each target is accessible for at least 5 months (40 % of time)

- Stellar metallicity, age, temperature,
- Planetary temperature, mass and density.

A sub-set of this parameter space can be explored by EChO. Several surveys both from ground and from space will provide targets with the necessary characteristics to meet the objectives of the mission [112] (Figs. 28 and 29). Table 7 summarises the most important surveys from which we expect a significant contribution to the final core sample. The list is not exhaustive.

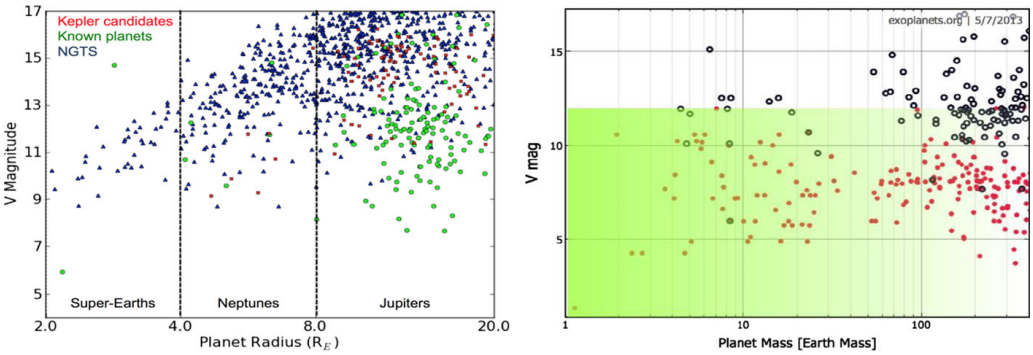

Fig. 28 *Left*: Simulated planet population from NGTS. This assumes a survey of 1920 square degrees over 5 years. Each of the plotted simulated planets can be confirmed with HARPS or ESPRESSO in less than 10 h exposure time. This instance of the simulation shows 39 confirmable super-Earths and 231 Neptunes. Of these, 23 super-Earths and 25 Neptunes orbit stars brighter than I=11. These planets will be the optimal targets for EChO. *Right*: Existing planets with measured mass from RV survey (*red dots*). Existing planets with measured radius from transit survey (*black circles*). The *green shaded area* is where CHEOPS will provide accurate radius measurements

Retour à la table des matières : p. v

4.5 The optimization of the observation program

The ability to fulfil the scientific program strongly depends on the optimization of the observation program. Because the planetary transits and occultations happen at specific epochs (given by ephemerides), the observation program, the data transfer sequences and the on-board calibration phases have to be well-defined and are time critical. The final performance evaluation of EChO also needs to take into account the way the observation and calibration/data transfer phases are optimized.

We have simulated an observing programme with an assumed target reference sample using scheduling simulation tools [71, 115]. These tools aim to check the

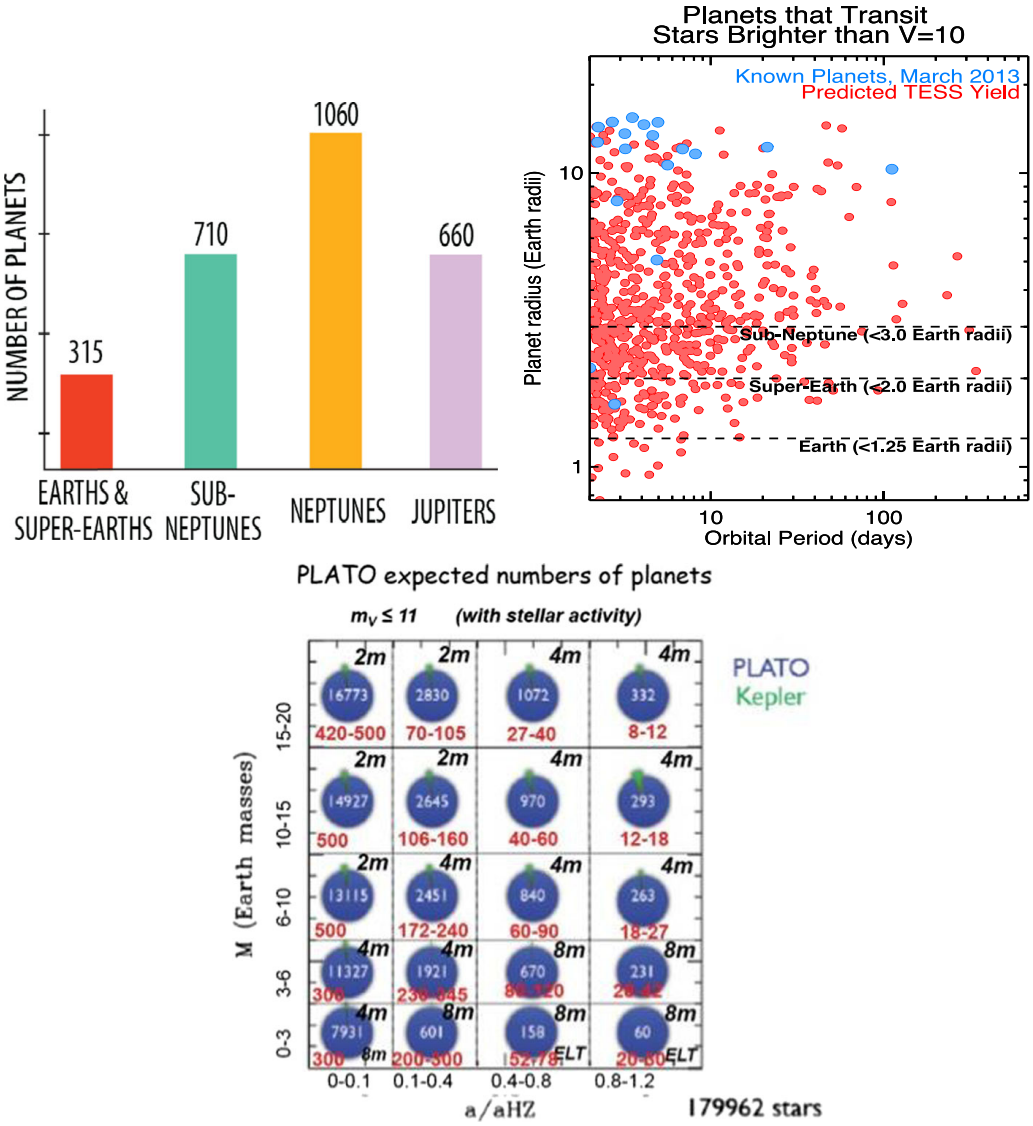

Fig. 29 *Top left*: Expected science yield from the TESS mission. *Top right*: Radius-Orbital period distribution of transiting exoplanets found around nearby stars brighter than $V=10$ as of March 2013 (*blue dots*), versus the number of such planets expected to be discovered by TESS (*red dots*). These planets will be the optimal targets for EChO. *Bottom*: Expected science yield from the PLATO mission

Retour à la table des matières : p. v

feasibility and efficiency of the observation program. They include optimisation routines that allow the scheduling assuming knowledge of the visibility of the objects, the transit/occultation ephemerides, the expected spacecraft performance and some assumed calibration and data transfer phases. The net result of the overall process is that, using the target lists described in Section 4.1 & 4.2, the EChO mission would meet its scientific objectives.

5 Synergy with other facilities

EChO, JWST and E-ELT observations are highly complementary and mutually beneficial. While JWST will provide state-of-the-art measurements for a few tens of planets, the E-ELT will provide targeted observations for a few tens of planets at ultra-high spectral resolving power at specific wavelengths. *The role of EChO is to provide the broad picture by performing a systematic and uniform survey of hundreds of exoplanets*. EChO instantaneous broad wavelength coverage is also essential to correct for the stellar activity (see Section 3.4.6). The three observatories together would deliver transformational science.

5.1 EChO & the JWST

JWST is the largest space telescope ever conceived, with an equivalent telescope diameter of 5.8 m and 22 m^2 collecting area. It is designed to operate over the visible (~0.6 μm) to mid-IR waveband (28 μm) providing very high sensitivity imaging and spectroscopy of faint astronomical targets. It is a true observatory with multiple capabilities, instruments and operating modes, optimised for background limited observations. JWST is scheduled for launch in late 2018. Although

Table 8 JWST instruments and observing modes useful for transit spectroscopy

Instrument	Mode	Resolving power	Wavelength range (μm)	Comments
NIRISS	Grism, cross-dispersed, slit-less	700	0.6–2.5	Saturates at $K<9$ at some part of band
NIRCam	Grism, slit-less	2000	2.4–5.0	Not proposed for transit spectroscopy in SODRM
NIRSpec	Prism, wide slit (1.6”)	100	0.6–5.0	Saturates at $J<11$ (see Fig. 30) Wavelength range covered using 3 separate orders
NIRSpec	Grating, wide slit (1.6”)	1000 or 2700	(0.7) 1.0–1.8 1.7–3.0 2.9–5.0	Uses three grating settings to cover wavelength range. Effective SW cut on is 0.9 μm
MIRI	Prism, 0.6” slit or slit-less	100	5.0–11.0	
MIRI	IFU (0.2”–0.27”/pixel)	2400–3600	5.0–7.7 7.7–11.9 11.9–18.3 18.3–28.3	Each band uses 3 sub-bands with separate gratings [72].

Retour à la table des matières : p. v

primarily designed for observations of very faint targets (in the μJy range), JWST will do a great deal of ground breaking exoplanetary science. Table 8 summarises the JWST instruments and operating modes that will be useful for exoplanet transit spectroscopy. Studies of the performance of the instruments for transit spectroscopy have been carried out notably for NIRISS and NIRSpec (Dorner Phd Thesis Universite de Lyon 2012, [43], http://www.cosmos.esa.int/web/jwst/exoplanets). Both transit & eclipse measurements over the full waveband from 0.6 to 28 μm are possible with the combination of the instruments and modes on JWST [24]. However, both its extremely high sensitivity and observatory nature mean there are significant restrictions on the type and number of targets that will be observable (see Table 8 and Fig. 30).

In addition to transits, there are a number of direct imaging possibilities using JWST—for a full summary see the exo-planet "white papers" (see http://www.stsci.edu/jwst/doc-archive/white-papers). A first cut, notional observing program for the JWST is encompassed in the Science Observations Design Reference Mission (SODRM - http://www.stsci.edu/jwst/science/sodrm/jwst/science/sodrm/): this consists of a number of observing programs built around seven science themes designed to allow the mission team test the observation planning tools.

5.2 EChO & the E-ELT

E-ELT and EChO observations will be highly complementary and mutually beneficial (Table 9). Ground-based observations of exoplanet atmospheres have many challenges and limitations. Large parts of the electromagnetic spectrum are blocked from view due to absorption and scattering in the Earth's atmosphere. In addition, the thermal background from the sky and telescope are strongly variable, making high-precision ground-based transit or eclipse spectroscopy practically impossible

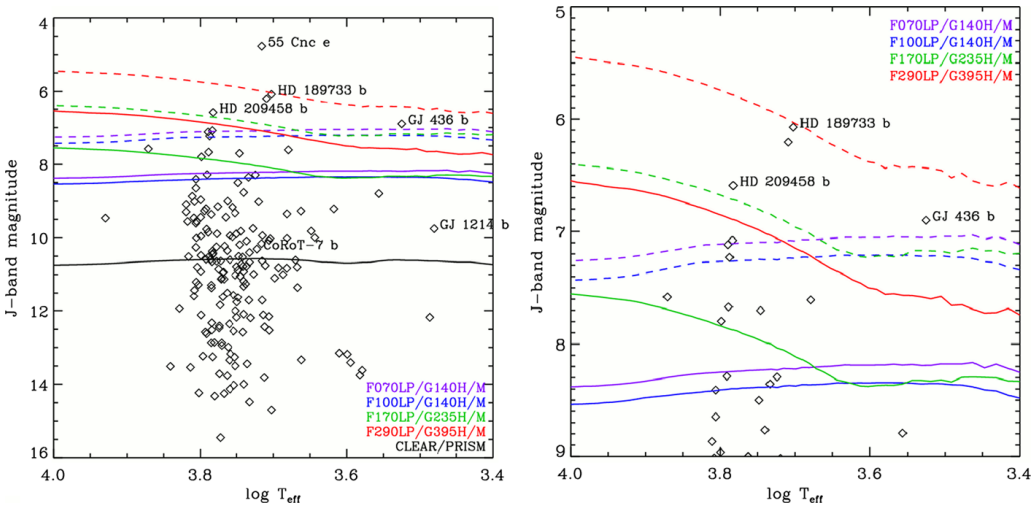

Fig. 30 J-band limiting magnitudes for the different NIRSpec modes as a function of host star temperature (http://www.cosmos.esa.int/web/jwst/exoplanets). The *colored dashed lines* are for the high resolution gratings, the *coloured solid lines* for the medium resolution gratings, and the *solid black line* for the prism. Sources below the lines can be observed in the full wavelength range of the given mode as specified in the table above. The *black symbols* denote the host stars of known transiting exoplanet

Retour à la table des matières : p. v

Table 9 Planned next-generation telescopes and their instrumentation relevant to transiting exoplanet characterization science. Currently, three next generation telescopes are on the drawing board, the European Extra Large Telescope (E-ELT - http://www.eso.org/public/teles-instr/e-elt.html), the Giant Magellan Telescope (GMT - http://www.gmto.org), and the Thirty-Meter Telescope (TMT - http://www.tmt.org/). Note that at the time of writing, funding has not been completely secured for any of the three telescope projects. The earliest deployment for any of these will be the early 2020s. Also, the instrumentation for the telescopes has by no means been finalised, and a significant fraction of these instruments may never be developed, or change

Telescope	Diameter	Instrument	Spectral range	Instant coverage	spectral dispersion
E-ELT	39 m	METIS	2.9–5.3 μm	0.1 μm	R=100,000
		HIRES	0.4–2.3 μm	0.4–2.3 μm	R=100,000
		MOS	0.4–1.7 μm	0.4–1.7 μm	R<30,000
GMT	24.5 m	MOS	0.4–1.0 μm	0.4–1.0 μm	R<5000
		NIR-HRS	1.0–5.0 μm	TBD	R~50–100,000
		G-CLEF	0.4–1.0 μm	0.4–1.0 μm	TBD
TMT	30 m	WFOS	0.3–1.0 μm	0.3–1.0 μm	R<7500
		HROS	0.3–1.0 μm	0.3–1.0 μm	R~50–90,000
		IRMOS	0.8–2.5 μm	0.3 μm	R=2000–10,000
		MIRES	9–18 μm	8–14 μm	R=100,000
		NIRES	1–5 μm	~2 μm	R=100,000

from the ground at >5 micron. However, the E-ELT will be very valuable in specific ways. One particularly successful observing strategy makes use of spectroscopy at a very high dispersion of R=100,000. At this resolution, molecular bands in exoplanet spectra are resolved into hundred(s) to thousands of individual lines, whose signals can be combined to secure a more robust molecular detection. Only astrophysical information over small wavelength scales is preserved, hence the line-contrast is being measured with respect to a local pseudo-continuum. This technique has been used very successfully using the VLT, for both exoplanet transmission spectroscopy [150] and emission spectroscopy [31], and will be more powerful on the next-generation of extra-large telescopes.

E-ELT observations will be highly complementary to EChO. The EChO spectra, which will be obtained over a large instantaneous wavelength range, are crucial for measuring the most important planetary atmosphere parameters−the temperature-pressure profile and the main molecular abundances. With these parameters determined by EChO, high-resolution E-ELT observations, providing planet differential transmission and day-side spectra at specific wavelengths, can be calibrated and used to target other, specific aspects of the planetary atmospheres. For the best observable targets, e.g. those targeted by EChO in the Origin and Rosetta tiers, the E-ELT can provide information on the rotation of the planet and high-altitude wind speeds using the absorption line profiles – important ingredients for global circulation models (e.g. see [146] for theoretical simulations). Using the high-dispersion technique, the line-contrasts can be measured for a large part of the planet orbit, meaning that variations in molecular abundance ratios (when linked to EChO observations) and/or the atmospheric temperature-pressure profile could be traced

Retour à la table des matières : p. v

from the night, morning, to evening-side of the planet, revealing the influences of possible photo-chemical processes.

6 EChO science beyond exoplanets

In addition to the science of exoplanets, EChO has the capability to make important observations in the field of planetology, stellar physics, disks and brown dwarf studies, exploring a continuum of objects between planets and stars, in particular:

(i) **Stellar physics**—A relevant part of stellar science will come from the activity analysis that is needed to extract the planetary signal. So most of the material is described in the main activity plan.
(ii) **Physics of circumstellar disks around young stars**—a list of accessible objects shows that tens of T Tauri stars are potentially accessible for EChO. Physics of circumstellar disks with spectral variability in the 0.4/11 micron range is of interest for disk astrophysics and planetary systems' formation.
(iii) **Solar System objects**—Planetary objects can be observed with EChO (even with the slit aperture of 2×10 arcsec in the visible channel limiting the FOV) mainly for calibration purpose. Planetary satellites are also good reference objects to observe. This can be done with limited pointing accuracy (~1 arcsec). Comets (if a bright comet is available) can also be observed with EChO.
(iv) **Stellar occultations on Solar System Kuiper Belt Objects**—Planetary occultations can search for atmospheric perturbations during occultation. An occurrence of ~1 event/year for large KBO objects (Pluto, Quaoar, Eris…) is expected. Nevertheless, these occultations are rare.
(v) **Planetary seismology**—Due to the EChO aperture, only Uranus and Neptune are observable. Search for planetary oscillations through long duration continuous spectral observations in the infrared.
(vi) **Brown dwarf observations**—Homogenous sample of brown dwarfs (K=10–15), spanning the range of known spectral types, each observed during one rotational period (typically 10 h) [114].

7 Conclusions

Our knowledge of planets other than the eight "classical" Solar System bodies is in its infancy. We have discovered over a thousand planets orbiting stars other than our own, and yet we know little or nothing about their chemistry, formation and evolution. Planetary science therefore stands at the threshold of a revolution in our knowledge and understanding of our place in the Universe: just how special are the Earth and our Solar System? It is only by undertaking a comprehensive chemical survey of the exo-planet zoo that we will answer this critical question.

Acknowledgments We would like to thank all the National Space Agencies who supported the EChO phase-A study. We also thank Nick Cowan for useful comments.

Retour à la table des matières : p. v

Open Access This article is distributed under the terms of the Creative Commons Attribution 4.0 International License (http://creativecommons.org/licenses/by/4.0/), which permits unrestricted use, distribution, and reproduction in any medium, provided you give appropriate credit to the original author(s) and the source, provide a link to the Creative Commons license, and indicate if changes were made.

References

1. Adams, E.R., Seager, S.: ApJ **673**, 1160 (2008)
2. Adams, E.R., et al.: Astron. J **673,** 1160–1164 (2008)
3. Agol, E., et al.: ApJ **721**, 1861 (2010)
4. Agúndez, M., Venot, O., Iro, N., et al.: A&A **548**, A73 (2012)
5. Agúndez, M., et al.: A&A **564**, A73 (2014). 21
6. Ali-Dib, M., Mousis, O., Petit, J.-M., Lunine, J.I.: ApJ **793**, 9 (2014)
7. Apai, D., et al.: ApJ **768**, 121 (2013)
8. Baraffe, I., Chabrier, G., Barman, T.S., Allard, F., Hauschildt, P.H.: A&A **337**, 403 (1998)
9. Baraffe, I., Chabrier, G., Barman, T.: A&A **482**, 315 (2008)
10. Barman, T.S.: ApJ **661**, L191 (2007)
11. Barstow, J.K., et al.: MNRAS **430**, 1188 (2013)
12. Barstow, J.K., et al.: MNRAS **434**, 2616 (2013)
13. Barstow, J.K., et al.: Exoplanet atmospheres with EChO: spectral retrievals using EChOSim. Exp. Astron. (2014). doi:10.1007/s10686-014-9397-y
14. Baruteau, C., Meru, F., Paardekooper, S.-J.: MNRAS **416**, 1971 (2011)
15. Basri, G., Walkowicz, L.M., Batalha, N., et al.: AJ **141**, 20 (2011)
16. Bakos et al.: PASP **114**, 974 (2002)
17. Bakos et al.: PASP **125**, 154 (2013)
18. Batalha, N., et al.: ApJS **204**, 24 (2013)
19. Bean, J.L., Miller-Ricci Kempton, E., Homeier, D.: Nature **468**, 669 (2010)
20. Beaulieu, J.-P., Carey, S., Ribas, I., et al.: ApJ **677**, 1343 (2008)
21. Beaulieu, J.-P., Kipping, D.M., Batista, V., et al.: MNRAS **409**, 963 (2010)
22. Beaulieu, J.-P., Tinetti, G., Kipping, D.M., et al.: ApJ **731**, 16 (2011)
23. Beichman, C., et al.: New uses for the Kepler telescope: a survey of the Ecliptic plane for transiting planets and star formation. White Paper, http://keplerscience.arc.nasa.gov/K2/docs/WhitePapers/Beichman_Kepler.pdf (2013)
24. Beichman, C., et al.: Publ. Astron. Soc. Pac. **126**, 1134 (2014)
25. Berta, Z., et al.: ApJ **747**, 35 (2012)
26. Birkby, J.L., et al.: MNRAS **436**, L35 (2013)
27. Bodenheimer, P., et al.: ApJ **548**, 466 (2001)
28. Borucki, W.J., et al.: Astrophys. Space Sci. **241**(1), 111 (1996)
29. Borucki, W.J., et al.: Science **325**, 709 (2009)
30. Broeg et al.: EPJWC **47**, 3005 (2013)
31. Brogi, M., et al.: Nature **486**, 502 (2012)
32. Brown, T.M.: ApJ **553**, 1006 (2001)
33. Buenzli, E., et al.: ApJ **782**, 77 (2014)
34. Burrows, A., Hubeny, I., Budaj, J., Hubbard, W.B.: ApJ **661**, 502 (2007)
35. Cassan, A., et al.: Nature **481**, 167 (2012)
36. Charbonneau, D., Brown, T.M., Noyes, R.W., Gilliland, R.L.: ApJ **568**, 377 (2002)
37. Charbonneau, D., Allen, L.E., Megeath, S.T., et al.: ApJ **626**, 529 (2005)
38. Charbonneau, D., et al.: ApJ **686**, 1341 (2008)
39. Chatterjee, S., Ford, E., Matsumura, S., Rasio, F.A.: ApJ **686**, 580 (2008)
40. Chazelas et al.: SPIE 8444 (2012)
41. Cho, J.Y.-K., Menou, K., Hansen, B.M.S., Seager, S.: ApJ **587**, L117 (2003)
42. Cho, J.Y.-K., Menou, K., Hansen, B.M.S., Seager, S.: ApJ **675**, 817 (2008)
43. Clampin M: In: Pathways toward habitable planets: ASP **430**, 167 (2010)
44. Coleman, G., Nelson, R.P.: MNRAS **445**, 479 (2014)
45. Cowan, N.B., et al.: MNRAS **379**, 641 (2007)
46. Crossfield, I.J.M., Hansen, B.M.S., Harrington, J., et al.: ApJ **723**, 1436 (2010)
47. Crouzet, N., McCullough, P.R., Burke, C., Long, D.: ApJ **761**, 7 (2012)

Retour à la table des matières : p. v

48. Crouzet, N., et al.: Water vapor in the spectrum of the extrasolar planet HD 189733b: 2. The eclipse. ApJ **795**, 166 (2014)
49. de Graauw, T., et al.: A&A **321**, L13 (2007)
50. Danielski, C., et al.: ApJ **785**, 35 (2014)
51. De Kok, R.J., Stam, D.M.: Icarus **221**, 517 (2012)
52. De Wit, J., Gillon, M., Demory, B.O., Seager, S., A&A **548**, id.A128, 19 pp. (2012)
53. De Wit, J., Gillion, M., Demory, B.O., Seager, S.: A&A **548**, 128 (2012)
54. Deming, D., Seager, D., Richardson, L.J., et al.: Nature **434**, 740 (2005)
55. Deming, D., et al.: ApJ **774**, 95 (2013)
56. Demory, B.O., et al.: ApJ **776**, L25 (2013)
57. Dressing, C.D., Charbonneau, D.: ApJ **767**, 20 (2013)
58. Drossart, P., et al.: Nature **340**, 539 (1989)
59. Dumusque, X., et al.: ApJ **789**, 154 (2014)
60. Eccleston, P., et al. Exp. Astron., 11 (2014), doi:10.1007/s10686-014-9428-8
61. Elkins-Tanton: Astrophys. Space Sci. **332**, 359 (2011)
62. Encrenaz, T., et al.: Transit spectroscopy of exoplanets from space: how to optimize the wavelength coverage and spectral resolving power, Exp. Astron., doi:10.1007/s10686-014-9415-0 (2014)
63. Encrenaz, T.: Space Sci. Rev. **116**, 99 (2004)
64. Encrenaz, et al.: A&A **315**, L397 (1996)
65. Ehrenreich, D., et al., A&A in press, arXiv:1405.1056 (2014)
66. Forget, F., Leconte, J., Phil. Trans. R. So. **372**, #20130084 (2014) http://dx.doi.org/10.1098/rsta
67. Fraine, J., et al.: Nature **513**, 526 (2014)
68. Fressin, F., et al.: ApJ **766**, 81 (2013)
69. Frith, J.: MNRAS **435**, 2161 (2013)
70. Fukui, A., et al.: ApJ **770**, 95 (2013)
71. Garcia-Piquer, A., et al.: Artificial intelligence for the EChO mission planning tool. Exp. Astron. (2014). doi:10.1007/s10686-014-9411-4
72. Glasse, A., et al.: Mid-infrared instrument for James Webb space telescope IX: Predicted sensitivity (2014)
73. Grasset, O., Schneider, J., Sotin, C.: ApJ **693**, 722 (2009)
74. Grillmair, C.J., Burrows, A., Charbonneau, D., et al.: Nature **456**, 767 (2008)
75. Guillot, T.: Annu. Rev. Earth Planet. Sci. **33**, 493 (2005)
76. Guillot, T., Santos, N.C., Pont, F., et al.: A&A **453**, L21 (2006)
77. Guillot T., Stixrude L.: Characterizing planetary interiors with EChO, ECHO-TN-0001-OCA (2014)
78. Hanel, R., et al.: J. Geophys. Res. **86**, 8705 (1981)
79. Hanel, R.A., et al.: Icarus **53**, 262 (1983)
80. Herrero, E., et al.: Correcting EChO data for stellar activity, by direct scaling of activity signals. Exp. Astron. (2014). doi:10.1007/s10686-014-9387-0
81. Hollis, M.D.J., et al.: Comput. Phys. Commun. **184**, 2351 (2014)
82. Howard, A., et al.: ApJS **201**, 15 (2012)
83. Hyvarinen, A.: IEEE Signal Processing Lett. **6**, 145 (1999)
84. Ikoma, M., Hori, Y.: ApJ **753**, 6 (2012)
85. Jenkins, J.M., et al.: ApJ **713**, L87–L91 (2010)
86. Knutson, H.A., Charbonneau, D., Allen, L.E.: Nature **447**, 183 (2007)
87. Knutson, H.A., et al.: ApJ **690**, 822 (2009)
88. Knutson, H.A., et al.: ApJ **735**, 23 (2011)
89. Knutson, H.A., et al.: Nature **505**, 66 (2014)
90. Kreidberg, L., et al.: Nature **505**, 69 (2014)
91. Kreidberg, L., et al.: ApJL **793**, L27 (2014)
92. Koskinen, T.T., Aylward, A.D., Miller, S.: Nature **450**, 845 (2007)
93. Lammer H.: Origin and evolution of planetary atmospheres, springer briefs in astronomy. ISBN 978-3-642-32086-6. Springer (2013)
94. Leconte, J., Forget, F., Lammer, H.: On the (anticipated) diversity of terrestrial planet atmospheres. Exp. Astron. (2014). doi:10.1007/s10686-014-9403-4
95. Lee, J.-M., Fletcher, L.N., Irwin, P.: MNRAS **420**, 170 (2012)
96. Léger, A., et al.: Icarus **213**, 1 (2011)
97. Léger, A., Selsis, F., Sotin, C., et al.: Icarus **169**, 499 (2004)
98. Lepine, S., et al.: AJ **145**, 102 (2013)
99. Lewis, N.K., et al.: ApJ **766**, 95 (2013)

Retour à la table des matières : p. v

100. Line, M.R., Yung, Y.: ApJ **779**, 6 (2013)
101. Linsky, J.L., et al.: ApJ **717**, 1291 (2010)
102. Liou, K.N.: International geophysics series, vol 84, p. 583. Academic, San Diego (2002). 583 pp
103. Lissauer, J.J., Stevenson, D.J.: In Protostars and planets V, 591 (2007)
104. Lovelock, J.E.: Nature **207**, 568 (1965)
105. Madhusudhan, N., Seager, S.: ApJ **707**, 24 (2009)
106. Maillard, J-P., Miller, S.: In: Molecules in the atmospheres of extrasolar planets. ASP Conference Series, Vol. 450. Edited by J.P. Beaulieu, S. Dieteres, and G. Tinetti. San Francisco: Astronomical Society of the Pacific, p.19 (2011)
107. Majeau, C., Agol, E., Cowan, N.B.: ApJ **747**, L20 (2012)
108. Majeau, C., Agol, E., Cowan, N.B.: A two-demensional map of the extrasolar planet HD 189733b, ApJ **757**, L32 (2012)
109. Mandell, A.M., et al.: ApJ **728**, 18 (2011)
110. Mayor, M., Marmier, M., Lovis, C., et al., arXiv: 1109.2497 (2011)
111. McCullough, P., et al.: ApJ **791**, 55 (2014)
112. Micela, G., et al.: The contribution of the major planet search surveys to EChO target selection. Exp. Astron. (2014). doi:10.1007/s10686-014-9412-3
113. Micela, G.: Correcting for stellar activity, I. Exp. Astron. (2014). doi:10.1007/s10686-014-9430-1
114. Morales, J.C., et al.: Brown dwarf characterization with EChO. Exp. Astron. (2015). doi:10.1007/s10686-014-9434-x
115. Morales, J.C., et al.: Scheduling the EChO survey with known exoplanets. Exp. Astron. (2014). doi:10.1007/s10686-014-9409-y
116. Morello, G., et al.: ApJ **786**, 22 (2014)
117. Morello, G., et al.: Revisiting Spitzer transit observations with Independent Component Analysis: new results for the GJ436 system, ApJ, in press arXiv:1501.05866 (2015)
118. Moses, J., Visscher, C., Fortney, J., et al.: ApJ **737**, 15 (2011)
119. Nutzman et al.: PASP **120**, 317 (2008)
120. Oberg, K.I., Murray-Clay, R., Bergin, E.A.: ApJ **743**, 16 (2011)
121. Parmentier, V., Showman, A., de Wit, J.: Unveiling the atmospheres of giant exoplanets. Exp. Astron. (2014). doi:10.1007/s10686-014-9395-0
122. Pascale, E., et al.: EChOSim: The exoplanet characterisation observatory software simulator. Exp. Astron., arXiv:1406.3984 (2014)
123. Pearl, J.C., et al.: Icarus **84**, 12 (1990)
124. Pearl, J. C., Conrath, B. J., JGR **96**, (S01) 18921–18930 (1991)
125. Perryman, M., et al.: ApJ **797**, 14 (2014)
126. Pollacco, D. et al.: PASP **118**, 1407 (2006)
127. Puig, L., et al.: The phase 0/A study of the ESA M3 mission candidate EChO. Exp. Astron. (2014). doi:10.1007/s10686-014-9419-9
128. Rauer, H., et al.: Experimental Astronomy **38**, 249 (2014)
129. Rauscher, E., Menou, K., Cho, J.Y.-K., Seager, S., Hansen, B.M.S.: ApJ **662**, L115 (2007)
130. Rauscher, E., Menou, K., Cho, J.Y.-K., Seager, S., Hansen, B.M.S.: ApJ **681**, 1646 (2008)
131. Read, P.L.: Planet. Space Sci. **59**, 900 (2011)
132. Redfield, et al.: ApJ **673**, L87 (2008)
133. Rein H., http://www.openexoplanetcatalogue.com (2015)
134. Ribas, I., Lovis, C.: The EChO science study team EChO-SRE-SA-PhaseA-001. (2013). http://sci.esa.int/echo/53396-echo-phase-a-assessment-study-documentation/
135. Ricker et al.: J. Ast. Inst. Sys. 1(1) 014003. doi:10.1117/1.JATIS.1.1.014003 (2014)
136. Rogers, T.M., Komacek, T.D.: ApJ **794**, 132 (2014)
137. Rouan, D., et al.: ApJ **741**, L30 (2011)
138. Rowe, J., et al.: ApJ **689**, 1345 (2008)
139. Rye, R., Holland, H.D.: Am. J. Sci. **298**, 621 (1998)
140. Scandariato, G., et al.: EChO spectra and stellar activity II. The case of dM stars. Exp. Astron. (2014). doi:10.1007/s10686-014-9390-5
141. Schneider, J., http://exoplanet.eu (2015)
142. Schwartz, J.C., Cowan, N.B.: MNRAS **449**, 4192 (2015)
143. Seager, S., Sasselov, D.D.: ApJ **537**, 916 (2000)
144. Sharp, C.M., Burrows, A.: ApJS **168**, 140 (2007)
145. Showman, A., et al.: ApJ **762**, 24 (2013)
146. Showman, Polvani: ApJ **738**, 24 (2011)

Retour à la table des matières : p. v

147. Sing, D.K., et al.: MNRAS **416**, 1443 (2011)
148. Snellen, I., et al.: A&A **487**, 357 (2008)
149. Snellen, I., et al.: Nature **459**, 543 (2009)
150. Snellen, I., et al.: Nature **465**, 1049 (2010)
151. Snellen, I., et al.: Nature **509**, 63–65 (2014)
152. Snels, M., et al.: J. Quant. Spectrosc. Radiat. Transf. **133**, 464 (2014)
153. Sotin, C., Grasset, O., Mocquet, A.: Icarus **191**, 337 (2007)
154. Sozzetti, A., Bernagozzi, A., Bertolini, E., et al.: EPJWC 47, 3006 (2013)
155. Stefani, S., et al.: J. Quant. Spectrosc. Radiat. Transf. **117**, 21 (2013)
156. Stevenson, K.B., et al.: Nature **464**, 1161 (2010)
157. Stevenson, K.B., et al.: Science **14**, 838 (2014)
158. Swain, M.R., et al.: Nature **463**, 637 (2010)
159. Swain, M.R., et al.: ApJ **704**, 1616 (2009)
160. Swain, M.R., Vasisht, G., Tinetti, G.: Nature **452**, 329 (2008)
161. Swain, M.R., et al.: ApJ **690**, L114 (2009)
162. Tennyson, J., Yurchenko, S.N.: MNRAS **425**, 21 (2012)
163. Tennyson, J., Yurchenko, S.N.: The status of spectroscopic data for the EChO mission. Exp. Astron. (2014). doi:10.1007/s10686-014-9385-2
164. Tessenyi, M., Ollivier, M., Tinetti, G., et al.: ApJ **746**, 45 (2012)
165. Tessenyi, M., et al.: Icarus **226**, 1654 (2013)
166. Tinetti, G., et al.: Exp. Astron. **34**, 311 (2012)
167. Tinetti, G., Encrenaz, E., Coustenis, A.: Astron. Astrophys. Rev. **21**, 63 (2013)
168. Tinetti, G., Liang, M.C., et al.: ApJ **654**, L99 (2007)
169. Tinetti, G., et al.: Nature **448**, 169 (2007)
170. Tinetti, G., Deroo, P., Swain, M., et al.: ApJ **712**, L139 (2010)
171. Todorov, K.O., et al.: ApJ **796**, 100 (2014)
172. Tsiganis, K., Gomes, R., Morbidelli, A., Levison, H.F.: Nature **435**, 459 (2005)
173. Turrini, D., Nelson, R., Barbieri, M.: The role of planetary formation and evolution in shaping the composition of exoplanetary atmospheres, Exp. Astron., doi:10.1007/s10686-014-9401-6 arXiv:1401.5119 (2014)
174. Valencia, D., O'Connel, R.J., Sasselov, D.: Icarus **181**, 545 (2006)
175. Valencia, D., Sasselov, D.D., O'Connell, R.J.: ApJ **665**, 1413 (2007)
176. Valencia, D., Guillot, T., Parmentier, V., Freeman, R.: ApJ **775**, 10 (2013)
177. Varley, R., et al.: Generation of a target list of observable exoplanets for EChO. Exp. Astron. (2015). doi:10.1007/s10686-014-9436-8
178. Venot, O., Hébrard, E., Agundez, M., et al.: A&A **546**, A43 (2012)
179. Venot, O., et al.: A&A **562**, A51 (2014). 11
180. Venot, O., Fray, N., Bénilan, Y., et al.: A&A **551**, A131 (2013)
181. Venot, O., et al.: Chemical modelling of exoplanet atmospheres. Exp. Astron. (2014). doi:10.1007/s10686-014-9406-1
182. Vidal-Madjiar, A., et al.: Nature **422**, 143 (2003)
183. Waldmann, I.P.: ApJ **747**, 12 (2012)
184. Waldmann, I.P., Tinetti, G., Drossart, P., Swain, M.R., et al.: ApJ **744**, 35 (2012)
185. Waldmann, I.P., et al.: ApJ **766**, 9 (2013)
186. Waldmann, I.P.: ApJ **780**, 10 (2014)
187. Waldmann, I.P., Pascale, E.: Data analysis pipeline for EChO end-to-end simulations, Exp. Astron., doi:10.1007/s10686-014-9408-z, arXiv:1402.4408 (2014)
188. Waldmann, I.P., et al.: Tau-REx I: A next generation retrieval code for exoplanetary atmospheres, ApJ in press, arXiv:1409.2312 (2014)
189. Waldmann, I. P., et al.: ApJ **813**, 13 (2015a)
190. Waldmann, I. P., et al.: ApJ **802**, 107 (2015b)
191. Wang, F., Yan, P., Suzuki, K., Shen, D. (eds.): Machine learning in medical imaging. Springer Lecture 1750 Notes in Computer Science (2010)
192. Weidenschilling, S.J., Marzari, F.: Nature **384**, 619 (1996)
193. Yelle, R.V.: Icarus **170**, 167 (2004)
194. Yung, Y.L., DeMore, W.B.: Photochemistry of planetary atmospheres. Oxford University Press, New York (1999)
195. Yurchenko, S.N., Tennyson, J., Bailey, J., Hollis, M.D.J., Tinetti, G.: Proc. Natl. Acad. Sci. **111**, 9379 (2014)
196. Zhu, Z., et al.: ApJL **758**, L42 (2012)

Retour à la table des matières : p. v

Retour à la table des matières : p. v